

Modern Acoustics and Signal Processing

Douglas A. Abraham

Underwater Acoustic Signal Processing

Modeling, Detection, and Estimation

Foreword by
Martin Siderius



Modern Acoustics and Signal Processing

Springer

Modern Acoustics and Signal Processing

Editor-in-chief

William M. Hartmann, East Lansing, USA

Editorial Board

Yoichi Ando, Kobe, Japan

Whitlow W.L. Au, Kane'ohe, USA

Arthur B. Baggeroer, Cambridge, USA

Christopher R. Fuller, Blacksburg, USA

William A. Kuperman, La Jolla, USA

Joanne L. Miller, Boston, USA

Alexandra I. Tolstoy, McLean, USA

More information about this series at <http://www.springer.com/series/3754>

The ASA Press

The ASA Press imprint represents a collaboration between the Acoustical Society of America and Springer dedicated to encouraging the publication of important new books in acoustics. Published titles are intended to reflect the full range of research in acoustics. ASA Press books can include all types of books published by Springer and may appear in any appropriate Springer book series.

Editorial Board

Mark F. Hamilton (Chair), University of Texas at Austin

James Cottingham, Coe College

Diana Deutsch, University of California, San Diego

Timothy F. Duda, Woods Hole Oceanographic Institution

Robin Glosemeyer Petrone, Threshold Acoustics

William M. Hartmann (Ex Officio), Michigan State University

Darlene R. Ketten, Boston University

James F. Lynch (Ex Officio), Woods Hole Oceanographic Institution

Philip L. Marston, Washington State University

Arthur N. Popper (Ex Officio), University of Maryland

Martin Siderius, Portland State University

G. Christopher Stecker, Vanderbilt University School of Medicine

Ning Xiang, Rensselaer Polytechnic Institute



Douglas A. Abraham

Underwater Acoustic Signal Processing

Modeling, Detection, and Estimation

Foreword by Martin Siderius



Modern Acoustics and Signal Processing



Springer

Douglas A. Abraham
Ellicott City, MD, USA

ISSN 2364-4915 ISSN 2364-4923 (electronic)
Modern Acoustics and Signal Processing
ISBN 978-3-319-92981-1 ISBN 978-3-319-92983-5 (eBook)
<https://doi.org/10.1007/978-3-319-92983-5>

Library of Congress Control Number: 2018950408

© Springer Nature Switzerland AG 2019

This work is subject to copyright. All rights are reserved by the Publisher, whether the whole or part of the material is concerned, specifically the rights of translation, reprinting, reuse of illustrations, recitation, broadcasting, reproduction on microfilms or in any other physical way, and transmission or information storage and retrieval, electronic adaptation, computer software, or by similar or dissimilar methodology now known or hereafter developed.

The use of general descriptive names, registered names, trademarks, service marks, etc. in this publication does not imply, even in the absence of a specific statement, that such names are exempt from the relevant protective laws and regulations and therefore free for general use.

The publisher, the authors and the editors are safe to assume that the advice and information in this book are believed to be true and accurate at the date of publication. Neither the publisher nor the authors or the editors give a warranty, express or implied, with respect to the material contained herein or for any errors or omissions that may have been made. The publisher remains neutral with regard to jurisdictional claims in published maps and institutional affiliations.

This Springer imprint is published by the registered company Springer Nature Switzerland AG
The registered company address is: Gewerbestrasse 11, 6330 Cham, Switzerland

The Acoustical Society of America

On 27 December 1928 a group of scientists and engineers met at Bell Telephone Laboratories in New York City to discuss organizing a society dedicated to the field of acoustics. Plans developed rapidly and the Acoustical Society of America (ASA) held its first meeting on 10–11 May 1929 with a charter membership of about 450. Today ASA has a worldwide membership of 7000.

The scope of this new society incorporated a broad range of technical areas that continues to be reflected in ASA's present-day endeavors. Today, ASA serves the interests of its members and the acoustics community in all branches of acoustics, both theoretical and applied. To achieve this goal, ASA has established technical committees charged with keeping abreast of the developments and needs of membership in specialized fields as well as identifying new ones as they develop.

The Technical Committees include acoustical oceanography, animal bioacoustics, architectural acoustics, biomedical acoustics, engineering acoustics, musical acoustics, noise, physical acoustics, psychological and physiological acoustics, signal processing in acoustics, speech communication, structural acoustics and vibration, and underwater acoustics. This diversity is one of the Society's unique and strongest assets since it so strongly fosters and encourages cross-disciplinary learning, collaboration, and interactions.

ASA publications and meetings incorporate the diversity of these Technical Committees. In particular, publications play a major role in the Society. *The Journal of the Acoustical Society of America* (JASA) includes contributed papers and patent reviews. *JASA Express Letters* (JASA-EL) and *Proceedings of Meetings on Acoustics* (POMA) are online, open-access publications, offering rapid publication. *Acoustics Today*, published quarterly, is a popular open-access magazine. Other key features of ASA's publishing program include books, reprints of classic acoustics texts, and videos.

ASA's biannual meetings offer opportunities for attendees to share information, with strong support throughout the career continuum, from students to retirees. Meetings incorporate many opportunities for professional and social interactions and attendees find the personal contacts a rewarding experience. These experiences result in building a robust network of fellow scientists and engineers, many of whom became lifelong friends and colleagues.

From the Society's inception, members recognized the importance of developing acoustical standards with a focus on terminology, measurement procedures, and criteria for determining the effects of noise and vibration. The ASA Standards Program serves as the Secretariat for four American National Standards Institute Committees and provides administrative support for several international standards committees.

Throughout its history to present day, ASA's strength resides in attracting the interest and commitment of scholars devoted to promoting the knowledge and practical applications of acoustics. The unselfish activity of these individuals in the development of the Society is largely responsible for ASA's growth and present stature.

Series Preface for Modern Acoustics and Signal Processing

In the popular mind, the term “acoustics” refers to the properties of a room or other environment—the acoustics of a room are good or the acoustics are bad. But as understood in the professional acoustical societies of the world, such as the highly influential Acoustical Society of America, the concept of acoustics is much broader. Of course, it is concerned with the acoustical properties of concert halls, classrooms, offices, and factories—a topic generally known as architectural acoustics, but it also is concerned with vibrations and waves too high or too low to be audible. Acousticians employ ultrasound in probing the properties of materials, or in medicine for imaging, diagnosis, therapy, and surgery. Acoustics includes infrasound—the wind driven motions of skyscrapers, the vibrations of the earth, and the macroscopic dynamics of the sun.

Acoustics studies the interaction of waves with structures, from the detection of submarines in the sea to the buffeting of spacecraft. The scope of acoustics ranges from the electronic recording of rock and roll and the control of noise in our environments to the inhomogeneous distribution of matter in the cosmos.

Acoustics extends to the production and reception of speech and to the songs of humans and animals. It is in music, from the generation of sounds by musical instruments to the emotional response of listeners. Along this path, acoustics encounters the complex processing in the auditory nervous system, its anatomy, genetics, and physiology—perception and behavior of living things.

Acoustics is a practical science, and modern acoustics is so tightly coupled to digital signal processing that the two fields have become inseparable. Signal processing is not only an indispensable tool for synthesis and analysis, it informs many of our most fundamental models for how acoustical communication systems work.

Given the importance of acoustics to modern science, industry, and human welfare Springer presents this series of scientific literature, entitled *Modern Acoustics and Signal Processing*. This series of monographs and reference books is intended to cover all areas of today’s acoustics as an interdisciplinary field. We expect that scientists, engineers, and graduate students will find the books in this series useful in their research, teaching and studies.

William M. Hartmann
Series Editor-in-Chief

*I dedicate this book to my parents, Pat and
Don, for shaping who and what I am, and to
my wife Mary who loves me just the same.*

Foreword

I was first introduced to statistical signal processing when I met the author of this book, Dr. Douglas Abraham. We met in 1996 while working for the NATO SACLANT Undersea Research Centre in La Spezia, Italy (now called the Centre for Maritime Research and Experimentation). When I arrived, I was told (by several people) that Doug was the go-to person for signal processing questions. I soon found out why-Doug is a great teacher, and tricky concepts could often be cleared up with a short visit to his office. Sometimes we even took these discussions to the road. While at the Centre, a group of us often jogged up to the nearby hill town of Pitelli. Doug and I had about the same pace so typically suffered this together. Before starting, we would usually chat about an idea and, often just as we would begin our ascent, Doug (huffing and puffing) would start in on an explanation. I am fairly sure these sessions, out of necessity, contributed to his ability to efficiently lay out an argument.

Over the years, Doug has remained the go-to person, but with this book, he brings his knack for removing some of the mystery of statistical signal processing to the entire underwater acoustics community. Doug is one of the foremost experts in statistical signal processing for sonar systems; this is made clear throughout this book. He has been working in this area for over 30 years. He spent the early part of his career at the Naval Undersea Warfare Center (NUWC), and in addition to his time with NATO, he has also been a Senior Research Associate at the Applied Research Laboratory at The Pennsylvania State University and a Program Officer at the Office of Naval Research (ONR) and taught at the University of Connecticut. His many years spent "in the trenches" developing and analyzing algorithms is combined with a variety of senior level positions. This allows him to present, in this book, the most relevant material for the modern sonar system scientist and engineer.

I have been doing research in underwater acoustics for many years, and starting with those early encounters with Doug and continuing until now, it has become clearer to me that most problems in this field are random in nature, so solutions often require knowledge of statistical signal processing. The early chapters of this book provide the necessary introductory material that lays the foundation for the in-depth descriptions that are in the later chapters. Ample material is provided

on underwater acoustics, linear systems, signal processing, and statistics. One feature is that details are not glossed over; specifics are included throughout the book. Important treatments include proper use of the sonar equation for detection applications and the thorough derivation and analysis of matched filters and energy detectors.

This book contains a wealth of information and is very well organized in its presentation. I believe the contents are essential reading for the present-day scientist or researcher working in underwater acoustics.

Portland State University
Portland, OR, USA

Martin Siderius

Preface

Underwater acoustic signal processing is an application of signal processing in a multidisciplinary field where engineers, acousticians, physicists, oceanographers, and marine biologists employ signal processing as part of an underwater remote sensing system to achieve a diverse set of inferential objectives. The purpose of this book is to support both the users of and those performing research and development in underwater acoustic signal processing across the many common objectives encountered in real-life applications, which are often typified by *detection*, *classification*, *localization*, and *tracking* (DCLT). To encourage the use of this book in the classroom or for self-study, derivations are presented for many of the principal results and a number of exercises are included to explore important concepts more fully. When possible, key information has been summarized in tables and a detailed index has been crafted to support use as a reference.

This book is structured in three parts: (1) an introduction to sonar and underwater acoustics; (2) background material on systems, signal processing, and mathematical statistics; and (3) a treatise on detection in underwater acoustics accompanied by several estimation applications. The first and second parts are predominantly accessible to those with an undergraduate STEM background, although some sections require a level of comfort or familiarity with partial differential equations or mathematical statistics. The complexity of the third part arises less from the technical depth of the material than from amalgamating and applying concepts across acoustics, signal processing, and statistics to derive and analyze detection and estimation algorithms.

As with many other books in underwater acoustics, the sonar equation and its terms dominate the theme of the first part (i.e., sound source levels, propagation, target scattering, ambient noise, and reverberation). However, the material presented on underwater acoustics expands beyond the signal-to-noise-ratio basis of the sonar equation to characterize signals and noise so as to support the development of detection and estimation algorithms. The localization aspect of remote sensing is also described in terms of its dependence on both the sonar system and the acoustic propagation conditions.

The second part of the book first conveys the fundamentals of signal processing: linear systems, Fourier analysis, sampling, filtering, and windowing. The basics of mathematical statistics (probability, random variables, and random processes) follow along with a brief introduction to the statistical signal processing topics of detection and estimation. This background material is intended as both a refresher and a light introduction to the most important concepts. Complete books have been written on the section-level topics, so the depth or breadth of such material clearly cannot be conveyed in so short a format. The focus, therefore, is on the material most commonly used in practice and that necessary for the development and analysis of detection and estimation algorithms found in the final part of this book.

Many signal processing books focus on and emphasize the tools of the trade, often at the expense of describing how and where they are applied. In the third part of this book, the process is reversed to start with the problem and then develop the solution. The benefit of this approach is that it clearly identifies the assumptions required to derive detection and estimation algorithms for use in underwater acoustics applications and emphasizes the conditions under which they are optimal or why they are not. The third part of this book begins with a characterization of the signals and noise encountered in various applications of underwater acoustics, importantly including the effect of propagation through an underwater channel. Most signals of interest in underwater acoustics fall into one of three broad categories: signals with known form, signals with unknown form, or signals with unknown starting time and/or duration. In the remaining chapters, detection algorithms are developed for each signal type: matched filters for signals with known form, energy detectors for signals with unknown form, and sequential detectors for signals with unknown starting time and/or duration. Several practical aspects are also covered, including normalization, estimation of unknown parameters, and techniques for analyzing algorithm performance.

My foremost goal in writing this book was to provide a modern treatment of underwater acoustic signal processing that was comprehensive with respect to signal detection while retaining the rigor found in earlier literature. In the end, I hope the underwater acoustics community finds this book a useful resource in studying, developing, analyzing, and applying signal processing algorithms.

Ellicott City, MD, USA
April 2018

Douglas A. Abraham

Acknowledgements

I was exposed to the content found in this book throughout my career in underwater acoustic signal processing, the majority of which has been funded by the Undersea Signal Processing Team at the U.S. Office of Naval Research (ONR 321US). I am grateful to the current and past ONR 321US program officers for their encouragement and support of my ideas and the ensuing research. I also need to recognize and thank the teachers, mentors, and colleagues I have had throughout my career. A number of excellent teachers and mentors guided me early on, conveying their knowledge and skills, much of which can be found in this book. They were also exemplary examples of how research in a team environment and teaching should be done. The interdisciplinary nature of underwater acoustic signal processing, however, requires that we learn a good part of it on the job. I was fortunate enough to work with and learn from experts across a number of fields, many of whom very patiently answered the numerous questions I posed to them over the years.

At times it can be difficult to write a four-page conference paper that is free of errors. Writing a book of this size guarantees (with probability one!) that there are errors. I am indebted to the very generous people who reviewed full chapters or numerous sections (M. A. Ainslie, J. Gebbie, T. E. Luginbuhl, N. Parrish, D. P. Williams) and sections (J. Bates, T. D. Cuprak, J. K. Nelson). Their feedback helped me avoid several mistakes and significantly improved the content and presentation. The errors that remain are my own—please let me know, dear reader, when you find them so they can be fixed in the future (email to uaspbook@gmail.com).

Signal processing can be a very dry topic. This is in part because it is the “dry end” of a sonar system and not the more exciting “wet end” where the sensor meets the water, but also owing to its foundations in equation-laden mathematics and statistics. The number of real-life examples found in this book helped make writing it more interesting, and I hope it does the same when you read it. Some of the data presented in this book came from experiments in which I participated over the years and some were proffered by colleagues specifically for this book. Acknowledgements are provided when the processed data examples are presented,

and I am deeply grateful to my colleagues for their efforts in obtaining and providing the data to me. It is equally important to thank and acknowledge all the other participants in these experiments (engineers, technicians, scientists, ships crews, and ships officers) for their vital efforts in obtaining this important link between theory and reality.

Contents

Part I Sonar and Underwater Acoustics

1	Introduction to Underwater Acoustic Signal Processing	3
1.1	Overview of Underwater Acoustic Signal Processing	3
1.1.1	Sonar Systems	4
1.1.2	Common Applications	6
1.1.3	Signal Processing in Underwater Acoustics	7
1.1.4	Development Process for Novel Applications	9
1.1.5	Example Signals of Interest	10
1.1.6	Examples of Signal and Information Processing	15
1.1.6.1	Detection	16
1.1.6.2	Localization	18
1.1.6.3	Tracking	21
1.1.6.4	Classification	24
1.2	Intended Use and Organization of This Book	27
References		31
2	Sonar Systems and the Sonar Equation	33
2.1	Introduction	33
2.2	Remote Sensing with Sonar Systems	33
2.2.1	Components of a Sonar System	34
2.2.2	Monostatic, Bistatic, and Distributed Sonar Systems	36
2.2.3	Localization: Estimating the Position of a Sound or Scattering Source	37
2.2.3.1	Active vs. Passive Localization	38
2.2.3.2	Array Design and Angle Estimation	39
2.2.3.3	Localization with Distributed and Moving Sonar Systems	40
2.2.3.4	Localization and the Effects of Propagation ...	43
2.2.4	Bistatic Active Sonar	45
2.2.4.1	Active Sonar Resolution Cell	47

2.2.5	Doppler Scale and Shift	48
2.2.5.1	Doppler Effect via Waveform and Platform Trajectories	51
2.2.6	Doppler Sensitive and Insensitive Waveforms	54
2.3	The Sonar Equation	56
2.3.1	Decibel Notation	58
2.3.2	The Basic Passive Sonar Equation	60
2.3.2.1	Example: Passive Submarine Radiated Noise Detection	66
2.3.3	The Basic Active Sonar Equation	67
2.3.3.1	Example: Reverberation- and Noise-Limited Active Sonar Detection	71
2.3.4	Summary of Sonar Equation Terms	73
2.3.5	Relating SNR to Detection Performance: Detection Threshold	75
2.3.5.1	Gaussian-Fluctuating Signal	76
2.3.5.2	Non-fluctuating or Deterministic Signal	78
2.3.5.3	Extensions to Other Signal and Noise Models	79
2.3.5.4	Example Signal-Model Performance Comparison	80
2.3.5.5	Detection Threshold (DT)	81
2.3.6	Relating SNR to Estimation Performance	85
2.3.7	Other Applications of the Sonar Equation	87
2.3.7.1	Signal Excess (SE)	88
2.3.7.2	Figure of Merit (FOM)	90
	References	91
3	Underwater Acoustics	95
3.1	Introduction	95
3.2	Acoustic Wave Propagation in the Ocean	95
3.2.1	Acoustical Field and Power Quantities	97
3.2.1.1	Acoustic Pressure and Pressure Levels	98
3.2.1.2	Particle Velocity	99
3.2.1.3	Acoustic Intensity	100
3.2.1.4	Acoustic Power	100
3.2.1.5	Acoustic Energy Flux Density	101
3.2.2	Propagation and Spreading	101
3.2.2.1	The Wave Equation, Spherical Waves, and Spherical Spreading	102
3.2.2.2	Periodic Signals, Wavelength, and Wavenumber	104
3.2.2.3	Cylindrical Spreading	106
3.2.2.4	Plane Waves	107
3.2.2.5	Near-Field and Far-Field Propagation	109

3.2.3	Sound Projection and Propagation	111
3.2.3.1	Inhomogeneous Wave Equation and the Channel Impulse Response	111
3.2.3.2	Helmholtz Equation and Channel Frequency Response	114
3.2.3.3	Doppler Effect via the Inhomogeneous Wave Equation	115
3.2.3.4	Source Factor and Source Level (SL)	118
3.2.4	Propagation Loss (PL)	120
3.2.4.1	Propagation Loss for Different Spreading Models	121
3.2.4.2	Propagation Loss and the Channel Frequency Response	122
3.2.4.3	Coherent and Incoherent Propagation Loss	123
3.2.5	Absorption and Dispersion	124
3.2.5.1	Absorption	124
3.2.5.2	Dispersion	124
3.2.6	Sound-Speed, Snell's Law, and Refraction	125
3.2.6.1	Sound Speed Profiles and Ray Tracing	128
3.2.7	Boundaries and Reflection Loss	131
3.2.7.1	Boundary Conditions Between Layers	132
3.2.7.2	Constant-Density Layers	133
3.2.7.3	Reflection at the Ocean Surface	134
3.2.7.4	Reflection at the Ocean Bottom	136
3.2.7.5	Total Internal Reflection and Phase Change	138
3.2.7.6	Rough Surface Reflection	142
3.2.8	Rays and Modes in Shallow Water	148
3.2.8.1	Ray-Based Solution and Multipath	149
3.2.8.2	Mode-Based Solution	150
3.2.8.3	Dispersion in a Waveguide	154
3.2.9	Reciprocity	156
3.3	Ambient Noise	158
3.3.1	Overview and Ambient Noise Spectrum Curves	158
3.3.1.1	Converting Spectrum Rates of Change from per Octave to per Decade	160
3.3.2	Very Low Frequency	160
3.3.3	Low Frequency: Distant Shipping Noise	161
3.3.4	Low to High Frequency: Wind-Related Surface Noise	162
3.3.5	Very High Frequency: Thermal Noise	163
3.3.6	Spatio-Temporal and Statistical Properties of Ambient Noise	164
3.4	Scattering from Objects: Target Echoes and Target Strength	164
3.4.1	Target Strength (TS)	165
3.4.1.1	Relationship to Radar Cross Section	168

3.4.2	Target Impulse Response	169
3.4.2.1	Impulse Response of a Rigid Sphere	170
3.4.3	Scattering from Objects: The ka Dependence	172
3.4.3.1	Rayleigh Scattering Regime ($ka \ll 1$)	173
3.4.3.2	Geometric Scattering Regime ($ka \gg 1$)	174
3.4.3.3	Exact Modal Solutions	177
3.5	Reverberation	180
3.5.1	Sources of Reverberation	182
3.5.2	Volume Reverberation	182
3.5.3	Boundary Reverberation	186
3.5.4	Signal to Reverberation Ratio	189
3.5.5	Statistical Characterization of Reverberation	190
3.5.6	Spectral Properties of Reverberation	191
3.5.7	Reverberation from a Moving Source	193
	References	196

Part II Systems, Signal Processing and Mathematical Statistics Background

4	Linear Systems and Signal Processing	203
4.1	Introduction	203
4.2	Linear-Time-Invariant (LTI) Systems and Convolution	203
4.2.1	Impulse Response of an LTI System	204
4.2.2	Frequency Response of an LTI System	207
4.3	Fourier Transforms	208
4.3.1	Inverse Fourier Transform	209
4.3.2	Properties of the Fourier Transform	211
4.4	Hilbert Transform	215
4.5	Signal Time-Bandwidth Product	216
4.6	Converting Analog Signals to Digital Signals	219
4.6.1	Sampling and Aliasing	219
4.6.2	Quantization	223
4.7	Discrete-Time Signals and Systems	225
4.7.1	Fourier Transform of a Discrete-Time Signal	226
4.7.2	Properties of the Fourier Transform of Discrete-Time Signals	227
4.8	Discrete and Fast Fourier Transforms (DFT and FFT)	228
4.9	Discrete-Time Filtering (LPF, HPF, and BPF)	231
4.9.1	FIR and IIR Filters	232
4.9.2	FIR Filter Design	234
4.9.3	Bandpass and High-Pass Filters	236
4.9.4	FIR Filter Implementation	237
4.10	Windowing and Window Functions	239
4.10.1	Rectangular, Uniform, or Boxcar Window	242
4.10.2	Tukey Window	243

4.10.3	Hamming Window	243
4.10.4	Taylor Window	244
4.10.5	Kaiser Window	245
4.10.6	Hann Window	245
4.10.7	Blackman Window	246
4.11	Decimation and Interpolation	246
	References	249
5	Mathematical Statistics	251
5.1	Introduction	251
5.2	Probability	251
5.3	Random Variables	253
5.3.1	Random Variables, Distributions, and Densities	253
5.3.2	Moments and Expectations	257
5.3.3	Functions of Random Variables	259
5.3.4	Simulating Random Variables	262
5.3.5	Histogram Estimates of the PDF and CDF	263
5.3.6	Multiple Random Variables, Joint Densities, and Independence	265
5.3.7	Central Limit Theorem (CLT)	268
5.3.8	Conditional Distributions and Bayes' Theorem	269
5.3.9	Transform-Domain Functions	271
5.3.9.1	Moment Generating Function	271
5.3.9.2	Characteristic Function	272
5.3.9.3	Cumulant Generating Function	272
5.4	Random Processes	273
5.4.1	Stationarity and Ergodicity	275
5.4.2	Power Spectral Density	278
5.5	Complex Random Variables and Random Processes	281
5.6	Common Statistical Distributions	284
5.6.1	Bernoulli Distribution	285
5.6.2	Binomial Distribution	286
5.6.3	Poisson Distribution	286
5.6.4	Uniform Distribution	287
5.6.5	Beta Distribution	288
5.6.6	Gaussian or Normal Distribution	289
5.6.7	Complex Gaussian Distribution	290
5.6.8	Multivariate Gaussian Distribution	291
5.6.9	Complex Multivariate Gaussian Distribution	291
5.6.10	Exponential Distribution	292
5.6.11	Gamma Distribution	293
5.6.12	Rayleigh Distribution	294
5.6.13	Rician Distribution	295
5.6.14	Chi-Squared Distribution	296
5.6.15	Non-central Chi-Squared Distribution	297

5.6.16	<i>F</i> Distribution	298
5.6.17	Non-central <i>F</i> Distribution.....	299
5.6.18	Weibull Distribution	300
5.6.19	<i>K</i> Distribution	301
5.6.20	Generalized Pareto Distribution.....	302
5.6.21	Log Normal Distribution	303
	References.....	303
6	Statistical Signal Processing	307
6.1	Introduction.....	307
6.2	Signal Detection Theory	307
6.2.1	Hypothesis Testing in Underwater Acoustics	308
6.2.2	Performance Measures, Implementation, and Analysis of Detectors.....	309
6.2.2.1	Receiver Operating Characteristic (ROC) Curves	312
6.2.2.2	Estimating P_d and P_f	314
6.2.2.3	Importance Sampling	315
6.2.2.4	Equal-Error Point and Area Under the Curve	315
6.2.3	Design of Detectors: Neyman–Pearson Optimal	316
6.2.4	Composite Hypothesis Testing: Detecting When There Are Unknown Parameters	318
6.2.5	Design of Detectors: Uniformly Most Powerful Tests and Invariance	319
6.2.6	Design of Detectors: Small-Signal Situations	320
6.2.7	Design of Detectors: Generalized Likelihood Ratio (GLR)	321
6.2.7.1	Asymptotic Distribution of the GLR Detector Decision Statistic	324
6.2.8	Design of Detectors: Bayesian Approaches	325
6.3	Estimation Theory	325
6.3.1	Point Estimation in Underwater Acoustics	326
6.3.2	Performance Measures and Analysis of Estimators.....	327
6.3.3	Cramér–Rao Lower Bound (CRLB)	329
6.3.3.1	CRLB for Multiple Parameters.....	331
6.3.3.2	CRLB for Transformations	332
6.3.3.3	CRLB for a Multivariate Gaussian Model.....	334
6.3.3.4	CRLB for a Complex Multivariate Gaussian Model	334
6.3.4	Estimation Techniques: Maximum Likelihood.....	335
6.3.4.1	Properties of the MLE	336
6.3.5	Estimation Techniques: Method of Moments	337
6.3.6	Estimation Techniques: Bayesian Inference.....	340

6.3.7	Estimation Techniques: Expectation-Maximization (EM) Algorithm	341
6.3.7.1	Example: Exponential Mixture	342
6.3.8	Confidence Intervals and Bayesian Credible Sets	344
References		345

Part III Detection in Underwater Acoustics

7	Underwater Acoustic Signal and Noise Modeling	349
7.1	Introduction	349
7.2	Characterizing Underwater Acoustic Signals	351
7.2.1	Signal Consistency and Knowledge	353
7.2.2	Time-Frequency Characterization of the Signal	356
7.2.2.1	Finite-Duration Signal Measurement as a Stationary Random Processes	358
7.2.2.2	Narrowband, Broadband, and Bandpass Signals	359
7.2.3	Effect of Propagation on Source-Signal Characterization	362
7.2.3.1	Unknown and Random Phases	363
7.2.3.2	Unknown and Random Amplitudes	364
7.3	Bandpass and Baseband Representations of Signal and Noise	367
7.3.1	Analytic Signals	368
7.3.2	Basebanding and the Complex Envelope	371
7.3.2.1	Signal Envelope and Instantaneous Intensity ..	373
7.3.2.2	Different Ways to Baseband a Signal	374
7.3.2.3	Basebanding a Signal Subject to Delay and Doppler	375
7.3.3	Bandpass Signals and Linear Time-Invariant Systems ...	377
7.3.4	Complex Envelope of Bandpass Noise	378
7.3.5	Modeling the Complex Envelope After Sampling in Time	382
7.3.5.1	Deterministic Signal Energy	382
7.3.5.2	Noise Covariance Matrix	383
7.3.6	Statistics of the Complex Envelope, Envelope, and Instantaneous Intensity	385
7.3.6.1	Uniformly Random Phase	386
7.4	Noise and Interference Models	388
7.4.1	Ambient Noise	389
7.4.2	Reverberation	392
7.4.2.1	Reverberation as a Random Process	392
7.4.2.2	Reverberation Autocorrelation Function	393
7.4.2.3	Reverberation Power Spectral Density	394
7.4.2.4	Doppler Spreading of Reverberation	396
7.4.3	Heavy-Tailed Noise and Reverberation	403
7.4.3.1	Effect of Beamforming and Matched Filtering on Reverberation Statistics	404

7.4.3.2	Statistical Models for Heavy-Tailed Data	406
7.4.3.3	K Distribution	408
7.4.3.4	Poisson-Rayleigh Distribution	413
7.4.3.5	Other Common Models	415
7.4.3.6	Performance Bounds on Parameter Estimation	420
7.4.3.7	Mixture Distributions	423
7.5	Signal and Signal-Plus-Noise Statistical Models	429
7.5.1	Deterministic Signal	430
7.5.1.1	Probability of Detection	434
7.5.1.2	Sum of Instantaneous-Intensity Samples	434
7.5.2	Gaussian-Fluctuating Signal	435
7.5.2.1	Probability of Detection	436
7.5.2.2	Sum of Instantaneous-Intensity Samples	436
7.5.3	Rician Signal	437
7.5.3.1	Probability of Detection	438
7.5.3.2	Sum of Instantaneous-Intensity Samples	439
7.5.4	Gamma-Fluctuating-Intensity (GFI) Signal	440
7.5.4.1	Probability of Detection	441
7.5.4.2	Sum of Instantaneous-Intensity Samples	442
7.5.5	Hankel Transform for Signal-Plus-Noise PDFs and CDFs	442
7.5.6	Approximations to the CDF of Signals in Heavy-Tailed Noise	445
7.5.6.1	Signal in Gaussian Noise	446
7.5.6.2	Three-Moment Shifted-Gamma (TMSG) Approximation	446
7.5.6.3	Three-Moment Non-central-gamma (TMNCG) Approximation	448
7.5.6.4	Sums of Instantaneous-Intensity Samples	451
7.5.6.5	Signal and Noise Model Instantaneous-Intensity Moments	452
	References	452
8	Detecting Signals with Known Form: Matched Filters	457
8.1	Introduction	457
8.1.1	Introductory Examples	459
8.2	Matched-Filter Detectors	464
8.2.1	SNR Gain of the Matched Filter	469
8.2.2	Detector for Signals with Known Form, Known Amplitude, and Known Phase	471
8.2.3	Detector for Signals with Known Form and Unknown Phase	475
8.2.4	Detector for Signals with Known Form and Uniformly Random Phase	477
8.2.5	Detector for Signals with Known Form and Gaussian Amplitude Fluctuations	479

8.2.6	Detector for Signals with Known Form and an Arbitrary Amplitude Distribution	481
8.2.7	Detector for Signals with Known Form and a Rician Distributed Amplitude	482
8.2.8	Detectors When Parameters Other Than Phase and Amplitude Are Unknown	485
8.2.8.1	Detectors for Unknown Noise Parameters	485
8.2.8.2	Detectors for Unknown Signal Parameters	488
8.2.9	Noise-Normalized and Adaptive Matched Filters	489
8.2.10	Effect of Oversampling on a Matched-Filter Detector	491
8.2.11	False-Alarm Rate (FAR)	494
8.2.11.1	FAR Under Oversampling	497
8.3	Waveform Autocorrelation and Ambiguity Functions	498
8.3.1	SNR Loss from Waveform Mismatch	500
8.3.1.1	Coherent Matched Filter	500
8.3.1.2	Quadrature Matched Filter	501
8.3.1.3	The Complex Ambiguity Function and SNR Loss	502
8.3.2	Ambiguity Functions	507
8.3.2.1	Narrowband Signals	508
8.3.2.2	Cross-Ambiguity	509
8.3.3	Autocorrelation Functions	510
8.3.4	CW Pulses	511
8.3.4.1	Autocorrelation Function for a CW Pulse	511
8.3.4.2	Ambiguity Function for a CW Pulse	513
8.3.5	LFM Pulses	515
8.3.5.1	Autocorrelation Function for an LFM Pulse	516
8.3.5.2	Narrowband Ambiguity Function for an LFM Pulse	517
8.3.5.3	Wideband Ambiguity Function for an LFM Pulse	519
8.3.6	HFM Pulses	520
8.3.6.1	Autocorrelation Function for an HFM Pulse	522
8.3.6.2	Ambiguity Function for an HFM Pulse	524
8.4	Beamforming as a Detection Process	527
8.4.1	Plane Waves and Line Arrays	527
8.4.2	Narrowband Beamformer	528
8.4.2.1	Array Signal and Noise Models	529
8.4.3	Array Beam Response and Beampattern	531
8.4.4	Array Gain and Directivity	533
8.5	Signal-Parameter Estimation Performance	535
8.5.1	Waveform Resolution vs. Estimation Accuracy	537
8.5.1.1	Resolution of the Standard Sonar Pulses	537
8.5.1.2	Accuracy vs. Resolution	540

8.5.2	Performance Bounds for Estimating Signal Strength and Phase	541
8.5.3	Performance Bounds for Estimating Arrival Time	545
8.5.3.1	Frequency-Modulated Pulses.....	550
8.5.3.2	Continuous-Wave Pulses	552
8.5.4	Performance Bounds for Estimating Doppler Scale	553
8.5.4.1	Shaded CW-Pulse Example	556
8.5.5	Performance Bounds for Joint Estimation of Arrival Time and Doppler Scale	558
8.5.5.1	LFM-Pulse Example	560
8.6	Normalization: Background Power Estimation	562
8.6.1	Cell-Averaging CFAR Normalizer.....	566
8.6.1.1	Decision-Threshold Analysis.....	567
8.6.1.2	Equivalent Number of Independent Samples	569
8.6.1.3	Performance Analysis and CFAR Loss	572
8.6.2	Target Masking and False-Alarm-Rate Inflation	574
8.6.3	Order-Statistic CFAR Normalizer	575
8.6.3.1	Decision-Threshold Analysis.....	577
8.6.3.2	Performance Analysis	578
8.6.3.3	Which Order Statistic to Use?.....	582
8.7	Doppler Processing.....	584
8.7.1	Doppler Filter Bank	586
8.7.1.1	Probability of False Alarm in a Filter Bank ...	587
8.7.1.2	Probability of Detection in a Filter Bank	588
8.7.1.3	Doppler Filter Bank Example	590
8.7.1.4	FFT Implementation of a CW-Pulse Doppler Filter Bank.....	592
8.7.2	Reverberation in a Doppler Filter Bank	594
8.7.2.1	Detection in Reverberation and Noise	596
8.7.2.2	Reverberation Temporal-Support Function for CW and FM Pulses	597
8.7.3	Normalization for CW Pulses	599
8.8	Temporal Spreading and Incoherent Integration	603
8.8.1	Energy Spreading Loss (ESL)	604
8.8.2	Incoherent Integration	610
8.8.2.1	Decision-Threshold Analysis.....	612
8.8.2.2	Performance Analysis	614
	Appendix 8.A: Example MATLAB® Code for a Doppler Filter Bank.....	616
	References	617
9	Detecting Signals with Unknown Form: Energy Detectors	621
9.1	Introduction.....	621
9.2	Energy Detectors	625
9.2.1	Statistical Characterization of the Signal and Noise	628
9.2.2	SNR After the Coherent Portion of Detection Processing	630

9.2.3	Detector for Random Signals and Noise Having Constant Spectra in a Known Frequency Band	632
9.2.3.1	The Basic Energy Detector and Its Performance Analysis	634
9.2.4	Frequency-Domain Processing for Shaped Signal and Noise Spectra.....	638
9.2.4.1	Decorrelation of DFT Bin Data	640
9.2.5	Detectors for Random Signals with Known Spectra in a Known Frequency Band	642
9.2.5.1	Optimal Detector for a Signal with a Known Spectrum	642
9.2.5.2	Locally Optimal Detector for a Signal with a Known Spectral Shape	643
9.2.5.3	Eckart Filter for Maximum Detection Index ..	644
9.2.6	Detectors for Random Signals with Unknown Spectra in a Known Frequency Band	646
9.2.6.1	Large and Small Signal-to-Noise Spectral-Density Ratios.....	646
9.2.6.2	Generalized Likelihood Ratio Energy Detector for an Unknown Signal Spectrum ...	647
9.2.7	Performance of a Weighted-Sum Energy Detector for Gaussian Random Signals and Noise	648
9.2.7.1	Exact Solution via the Characteristic Function	651
9.2.7.2	Numerical Evaluation of the CDF from the Characteristic Function	652
9.2.7.3	Gaussian Approximation	655
9.2.7.4	Gamma Approximation.....	656
9.2.7.5	Shifted Gamma Approximation	656
9.2.8	Detectors for Random Signals with Unknown Spectra in an Unknown Frequency Band	657
9.2.8.1	Modified Generalized Likelihood Ratio Energy Detector	658
9.2.8.2	Power-Law Energy Detector	659
9.2.9	Detectors for Deterministic Signals with Unknown or Partially Known Form	663
9.2.9.1	Deterministic Signals with Unknown Structure in a Known Frequency Band	664
9.2.9.2	Deterministic Signals with Partially Known Form	666
9.2.9.3	Completely Unknown Deterministic Signals ..	668

9.2.10	Time-Domain Energy Detector: Coherent and Incoherent Averaging	669
9.2.10.1	Choosing the Coherent-Processing-Window Size and Spacing	674
9.2.10.2	Choosing the Analysis Window Extent	675
9.2.11	Detection Threshold for the Noise-Normalized Energy Detector	676
9.2.11.1	Deterministic Signals	677
9.2.11.2	Gaussian-Based Approximation for Gaussian Random Signals	679
9.2.11.3	Gamma-Based Approximation for Gaussian Random Signals	681
9.3	Normalization: Background Power Estimation	682
9.3.1	Auxiliary Data for Narrowband and Broadband Processing	683
9.3.2	Cell-Averaging Normalizer	685
9.3.3	Exponential-Average Normalizers	688
9.3.4	Weighted-Average Normalizers	692
9.3.4.1	Characteristic Function of a Weighted-Average Background Estimate	693
9.3.4.2	Single-Sample Normalizer Distribution, Characteristic Function and Moments	693
9.4	Time-Delay Estimation	698
9.4.1	Cross-Correlation Processing	701
9.4.1.1	Inter-Sensor-Delay Estimation	706
9.4.1.2	Cramér-Rao Lower Bound for Inter-Sensor Delay	710
9.4.2	Autocorrelation Processing	713
9.4.2.1	Estimating Parameters of a PSD	714
9.4.2.2	Multipath-Delay Estimation	715
9.4.2.3	Cramér-Rao Lower Bound for Multipath Delay	720
9.5	Narrowband-Signal Parameter Estimation	721
9.5.1	Sinusoidal Signals	722
9.5.1.1	Estimation of the Frequency, Phase, and Amplitude of a Sinusoid	723
9.5.1.2	Phase Estimator Distribution	725
9.5.1.3	Cramér-Rao Lower Bounds	727
9.5.2	Narrowband Gaussian Random Signals	728
9.5.2.1	Cramér-Rao Lower Bounds	729
9.5.2.2	Estimation of the Center Frequency and Bandwidth	732

Appendix 9.A: Numerical Evaluation of the CDF of a Sum of Exponential Random Variables	733
Appendix 9.B: Moments of the Modified GLR Energy Detector Decision Statistic	735
Appendix 9.C: Algorithm for Estimating the Bandwidth and Center-Frequency of a Narrowband Random Signal in Noise	736
References	739
10 Detecting Signals with Unknown Duration and/or Starting Time: Sequential Detectors	743
10.1 Introduction	743
10.2 Performance Measures for Sequential Signal Detectors	747
10.3 Detectors for Signals with Known Duration and Known Starting Time	752
10.3.1 M -of- N Detector: Binary Integration	753
10.3.1.1 M -of- N Detector Design: Choosing Thresholds	755
10.4 Detectors for Signals with Known Duration and Unknown Starting Time	758
10.4.1 Sliding Incoherent Sum Detector	760
10.4.2 Sliding M -of- N Detector	763
10.5 Detectors for Long-Duration Signals	766
10.5.1 Known Starting Time: Sequential Probability Ratio Test (SPRT)	767
10.5.1.1 Decision Thresholds and Error Probabilities ..	769
10.5.1.2 Average Sample Numbers for the SPRT	770
10.5.1.3 Overshoot Corrections to the SPRT Average Sample Numbers	774
10.5.2 Unknown Starting Time: Page's Test	776
10.5.2.1 Average Sample Numbers for Page's Test	780
10.5.2.2 Unity Roots of the Moment Generating Function	784
10.5.2.3 ROC Curves and Asymptotic Performance of Page's Test	786
10.5.2.4 Biasing a General Input to Page's Test	789
10.5.2.5 Page's Test with Nuisance Parameter Estimation	791
10.5.2.6 Overshoot Corrections to Page's Test Average Sample Numbers	792
10.6 Detectors for Signals with Unknown, Intermediate Duration	793
10.6.1 Known Starting Time: Sequential Probability Ratio Test (SPRT)	795
10.6.1.1 SPRT Analysis by Quantization	797
10.6.1.2 Truncated SPRT	802

10.6.2	Unknown Starting Time: Page's Test	804
10.6.2.1	Alternating Hypothesis Page's Test	804
10.6.2.2	Page's Test Analysis by Quantization.....	807
10.6.2.3	Design Example.....	810
	References.....	817
Index	819

Acronyms and Abbreviations

ACF	Autocorrelation function
ADT	Average detection threshold
AF	Ambiguity function
AG	Array gain
AHPT	Alternating hypothesis Page's test
ASN	Average sample number
AUC	Area under the curve
BB	Broadband
BPF	Bandpass filter
BRL	Bottom reflection loss
BTR	Bearing time record
CA	Cell averaging
CDF	Cumulative distribution function
CF	Characteristic function
CFAR	Constant false alarm rate
CGF	Cumulant generating function
CLT	Central limit theorem
CMF	Coherent matched filter
CPI	Coherent processing interval
CRLB	Cramér-Rao lower bound
CTBTO	Comprehensive Nuclear-Test-Ban Treaty Organization
CUSUM	Cumulative summation
CW	Continuous wave
CZ	Convergence zone
dB	Decibel
DCLT	Detection, classification, localization, and tracking
DFT	Discrete Fourier transform
DI	Detection index or directivity index (context)
DT	Detection threshold
ED	Energy detector
EDF	Exceedance distribution function

EM	Expectation maximization (algorithm)
ESL	Energy spreading loss
FA	False alarm
FAR	False alarm rate
FFT	Fast Fourier transform
FIFO	First-in first-out
FIM	Fisher information matrix
FIR	Finite impulse response
FM	Frequency modulation
FOM	Figure of merit
GFI	Gamma fluctuating intensity
GLR	Generalized likelihood ratio
GO	Greater of
GPD	Generalized Pareto distribution
HFM	Hyperbolic frequency modulated
HPD	Highest posterior density
HPF	High-pass filter
Hz	Hertz
iid	Independent and identically distributed
IIR	Infinite impulse response
IMS	(CTBTO) International Monitoring System
INB	Instantaneously narrowband
ISO	International Organization for Standardization
J	Joule
kn	Knot
LFM	Linear frequency modulated
LHS	Left-hand side
LLF	Log likelihood function
LLR	Log likelihood ratio
LO	Locally optimal or (rarely) lesser of
LPF	Low-pass filter
LPM	Linear period modulation
LR	Likelihood ratio
LTI	Linear time invariant
MAP	Maximum a posteriori
MDL	Minimum detectable level
MF	Matched filter
MGF	Moment generating function
MGLR	Modified GLR
ML	Maximum likelihood
MLE	Maximum-likelihood estimate (or estimator)
MM	Method of moments
MSE	Mean squared error
MSP	Mean squared pressure
MVUE	Minimum-variance unbiased estimator

NAF	Narrowband ambiguity function
NB	Narrowband
NN	Noise normalized
NP	Neyman Pearson
NPO	Neyman–Pearson optimal
NURC	NATO Undersea Research Centre
ODN	Ownship Doppler nullification
OS	Order statistic
Pa	Pascal
PDE	Partial differential equation
PDF	Probability density function
PL	Propagation loss
PMF	Probability mass function
PMFI	Post-matched-filter integration
PSD	Power spectral density
QMF	Quadrature matched filter
RAP	Reliable acoustic path
RCS	Radar cross section
RD	Recognition differential
RHS	Right-hand side
RL	Reverberation level
RMS	Root-mean-square
RMSE	Root-mean-squared error
ROC	Receiver operating characteristic
RV	Random variable
SE	Signal excess
SF	Single filter
SI	Scintillation index or international system of units (context)
SINR	Signal to interference-and-noise ratio
SIPC	Signal and information processing chain
SIRV	Spherically invariant random vector
SL	Source level
SNR	Signal-to-noise ratio
SoI	Signal of interest
SoN	State of nature
SPL	Sound pressure level
SPRT	Sequential probability ratio test
SQNR	Signal to quantization noise ratio
SRL	Surface reflection loss
SRR	Signal to reverberation ratio
SSP	Sound-speed profile
SSS	Strict-sense stationary
STD or Std	Standard deviation
STEM	Science, technology, engineering, or math
TL	Transmission loss

TMNCG	Three-moment non-central gamma
TMSG	Three-moment shifted gamma
TS	Target strength
UASP	Underwater acoustic signal processing
UMP	Uniformly most powerful
VAR or Var	Variance
VLA	Vertical line array
W	Watt
WAF	Wideband ambiguity function
WSS	Wide-sense stationary

Notation Conventions, Function, and Transform Definitions

The notation and definitions for terms in the sonar equation can be found in the list in Sect. 2.3.4 on p. 73. The notation for probability distributions can be found in Table 5.3 on p. 285.

Mathematical Notation Convention

Analytic signal of $x(t)$	$\dot{x}(t) = x(t) + jx_h(t)$ where $x_h(t)$ is the Hilbert transform of $x(t)$ (see following page)
Complex envelope of $x(t)$	$\tilde{x}(t) = e^{-j2\pi f_c t} \dot{x}(t)$
Conjugation	x^*
Convolution of $h(t)$ and $x(t)$ (continuous time)	$h(t) * x(t) = \int_{-\infty}^{\infty} h(\tau)x(t - \tau) d\tau \\ = \int_{-\infty}^{\infty} x(\tau)h(t - \tau) d\tau = x(t) * h(t)$
Convolution of $h[n]$ and $x[n]$ (discrete time)	$h[n] * x[n] = \sum_{m=-\infty}^{\infty} h[m]x[n - m] \\ = \sum_{m=-\infty}^{\infty} x[m]h[n - m] = x[n] * h[n]$
Imaginary unit	$j = \sqrt{-1}$
Integers	generally i, j, \dots, n
Logarithm, base 10	$\log_{10} x$
Logarithm, natural	$\log x = \log_e x$
Matrix	uppercase bold, \mathbf{X}
Vector	lowercase bold, \mathbf{x}
Vector, direction or position	\vec{x}
Vector transpose	\mathbf{x}^T
Vector, transpose and conjugate (Hermitian)	$\mathbf{x}^H = (\mathbf{x}^T)^*$

Function Notations and Definitions

Beta function

$$B(\alpha, \beta) = \int_0^1 x^{\alpha-1} (1-x)^{\beta-1} dx = \frac{\Gamma(\alpha)\Gamma(\beta)}{\Gamma(\alpha+\beta)}$$

Gamma function

$$\begin{aligned}\Gamma(\alpha) &= \int_0^\infty t^{\alpha-1} e^{-t} dt = (\alpha-1)\Gamma(\alpha-1) \\ &= (\alpha-1)! \text{ if } \alpha > 0 \text{ is an integer}\end{aligned}$$

Gamma function,
normalized incomplete

$$\tilde{\gamma}(x; \alpha) = \int_0^x \frac{t^{\alpha-1} e^{-t}}{\Gamma(\alpha)} dt = \frac{\gamma(\alpha, x)}{\Gamma(\alpha)}$$

Impulse function

$$\delta(t) \text{ or } \delta[n]$$

Indicator function

$\mathbb{I}(\text{boolean})$ = one when the argument is true and zero when it is false

Marcum Q function,
generalized

$$Q_M(a, b) = \frac{1}{a^{M-1}} \int_b^\infty x^M e^{-(x^2+a^2)/2} I_{M-1}(ax) dx$$

Rectangular window

$\text{rect}(t)$ is one when $|t| < 1/2$ and is otherwise zero

Sinc function

$$\text{sinc}(x) = \sin(\pi x)/(\pi x)$$

Standard normal cumulative
distribution function

$$\Phi(x) = \frac{1}{\sqrt{2\pi}} \int_{-\infty}^x e^{-z^2/2} dz$$

Transform Notations and Definitions

Characteristic function of
 $X \sim f_X(x)$

$$\Phi_X(\omega) = E[e^{j\omega X}] = \int_{-\infty}^\infty e^{j\omega x} f_X(x) dx$$

Fourier transform

$$X(f) = \mathcal{F}\{x(t)\} = \int_{-\infty}^\infty x(t) e^{-j2\pi ft} dt$$

Fourier transform, inverse

$$x(t) = \mathcal{F}^{-1}\{X(f)\} = \int_{-\infty}^\infty X(f) e^{j2\pi ft} df$$

Fourier transform, discrete

$$X_p(k) = \sum_{n=0}^{N-1} x_d[n] e^{-j2\pi kn/N}$$

Fourier transform,
discrete inverse

$$x_d[n] = \frac{1}{N} \sum_{k=0}^{N-1} X_p(k) e^{j2\pi kn/N}$$

Fourier transform,
discrete frequencies

$$f_k = \begin{cases} \left(\frac{k}{N}\right) f_s & \text{for } 0 \leq k < \frac{N}{2} \\ \left(\frac{k-N}{N}\right) f_s & \text{for } \frac{N}{2} \leq k \leq N-1 \end{cases}$$

Hankel transform of $g(x)$
(order ν)

$$\mathcal{H}_\nu\{a, g(x)\} = \int_0^\infty x g(x) J_\nu(ax) dx \text{ where } J_\nu(x) \text{ is a Bessel function of the first kind}$$

Hilbert transform

$$x_h(t) = \mathcal{H}\{x(t)\} = \frac{1}{\pi} \int_{-\infty}^{\infty} \frac{x(\tau)}{\tau-t} d\tau$$

Moment generating function
of $X \sim f_X(x)$

$$M_X(t) = E[e^{tX}] = \int_{-\infty}^{\infty} e^{tX} f_X(x) dx$$

Part I

Sonar and Underwater Acoustics

Chapter 1

Introduction to Underwater Acoustic Signal Processing



The topic of this book is the theory and application of *signal processing* in *underwater acoustics*. The majority of applications in underwater acoustics can be described as remote sensing where an electro-mechanical system exploits acoustic signals underwater to achieve a desired purpose. The most recognized application is sonar (*sound navigation and ranging*) for which the stated purpose is navigation and ranging (i.e., determining the distance or range from the sonar platform to an object of interest). The techniques by which underwater measurements of acoustic pressure are converted into navigation and ranging information are what comprise the signal-processing component of a sonar system. In this chapter, underwater acoustic signal processing is introduced according to the more general *detection, classification, localization, and tracking* (DCLT) paradigm. Common applications of underwater acoustic signal processing are described along with specific examples of signals of interest and each of the topics in the DCLT paradigm. The chapter is concluded with an explanation of how this book is organized, who the intended audience is, and how it might be used.

1.1 Overview of Underwater Acoustic Signal Processing

Most applications in underwater acoustics can be described as a *remote sensing* problem [1]. In remote sensing there is an object, condition, or phenomena (call this the *object of interest*) about which information is desired without an ability to directly observe it. Acoustic signals are used to indirectly obtain information about the object of interest and allow inference about the *state of nature* being investigated. The state of nature in an inference problem is the underlying truth about or condition of the object of interest.

One of the early applications of acoustical¹ remote sensing underwater was depth sounding, where the depth of the ocean bottom under a ship is estimated by projecting a pulse and measuring the two-way travel time. The *object of interest* is the bottom and the *state of nature* is the bottom depth, which has obvious relevance to navigation. The propagation delay between the time the pulse is projected and the time its echo is measured after reflecting off the bottom encodes the desired information about the state of nature.

An example of a more distant remote-sensing application can be found in the acoustical monitoring system used by the Comprehensive Nuclear-Test-Ban Treaty Organization (CTBTO) to verify compliance with the treaty. Descriptions of the hydroacoustic portion of the International Monitoring System (IMS) can be found in [3–5]. The *state of nature* being investigated is whether or not a nuclear test has occurred. If a nuclear test occurred in or near an ocean, the ensuing explosion acts as a low-frequency sound source that can be heard underwater at great distances. The underwater acoustic signals remotely measured by the CTBTO monitoring system are used to infer if a nuclear test occurred or not. The acoustic waves measured by the sensing system can be called *signals of interest* if they are necessary and sufficient to describe the state of nature under investigation.

An indication of how distant the source of a low-frequency underwater sound can be from the sensing platform is found in the spectrogram (i.e., time-frequency analysis) of a measurement² from a CTBTO IMS hydrophone station shown in Fig. 1.1. The two wavering signals above the arrow in the 2–30 Hz band are possibly the sounds produced by the grounding of an iceberg. The measurement was obtained at the CTBTO IMS hydrophone station off Cape Leeuwin, Australia, which is over 3000 km from Antarctica, the most likely source of the iceberg. As noted in [4], it is common for the CTBTO IMS hydrophone stations to observe sounds having propagated over 10,000 km, which is one quarter of the earth’s circumference. In a different application (measuring ocean temperature), the Heard Island Feasibility Test [7] demonstrated a sensing capability with ranges over 18,000 km. Such long-distance sensing exploits the minimal attenuation of low-frequency sound propagating in the SOFAR (sound fixing and ranging) channel, which is also known as the deep sound channel.

1.1.1 Sonar Systems

In many applications of underwater acoustics, the remote sensing system is simply referred to as the *sonar system*. In its most basic form, the sensing components of a sonar system can consist of a single sensor converting acoustic pressure underwater

¹The choice of the adjective *acoustic* or *acoustical* is made following the paradigm of [2].

²Acknowledgement: CTBTO [6] with gratitude to Drs. G. Haralabus, M. Zampolli, P. Nielsen, and A. Brouwer for their assistance in identifying, accessing, and interpreting the data.

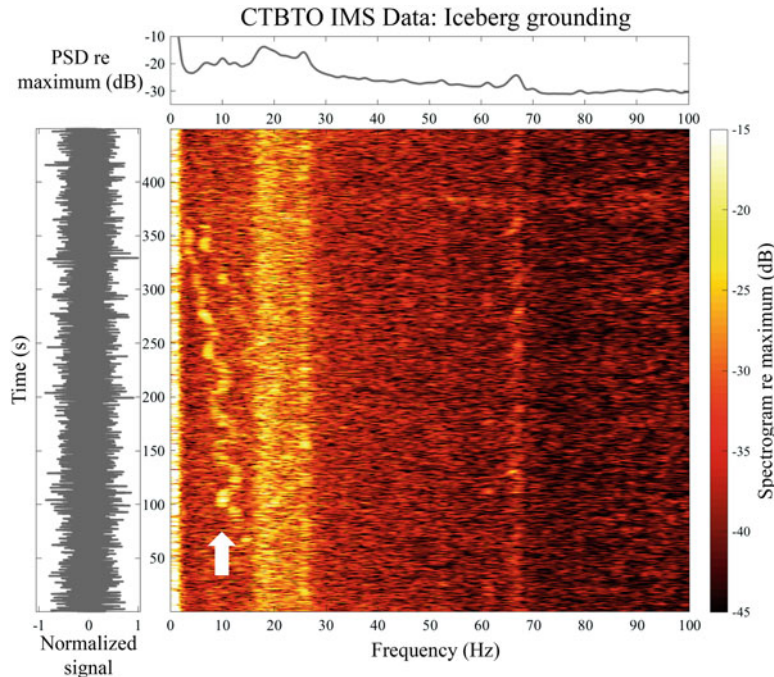


Fig. 1.1 Possible iceberg grounding (waving signals above the white arrow) measured on April 15, 2017 at the CTBTO IMS hydrophone station off Cape Leeuwin, Australia. Acknowledgement: CTBTO [6]

to an electrical voltage. Such sensors are called hydrophones and are similar to a microphone used to sense acoustic waves in air. In many sonar systems there are multiple hydrophones that are configured in geometric patterns and called an *array* of sensors. Having multiple sensors in a sonar system not only improves its performance, but often allows inference that is otherwise very difficult or impossible with a single sensor.

The CTBTO application is an example of *passive* remote sensing where acoustic signals indigenous to the object of interest are measured and used in the inference. Passive sonar systems require the object of interest to emit an acoustic signal that can be measured by the sensor array despite having to propagate through the underwater environment. A basic assumption in passive sonar applications is that all of the necessary and sufficient information regarding the state of nature resides in these acoustic emissions.

Remote sensing can also be *active* where an acoustic pulse is projected into the underwater environment and the ensuing reflections measured on a sensor and used to achieve the inferential objective (e.g., the aforementioned depth sounder). Active sonar systems therefore minimally require a sound projector and a hydrophone. In active sensing the object of interest is a source of sound reflection or scattering

and the state of nature must therefore be encoded in the reflected signals. Although this poses some limitations relative to passive sensing, active sensing enjoys other advantages with respect to localization and tracking (see Sects. 1.1.6.2 and 1.1.6.3). The most prominent advantage lies in the ability to estimate the distance to an object through echo ranging. It is also possible to estimate the radial velocity between the sensing platform and the object of interest with a single transmission (e.g., how fast a moving object is approaching is important in an object-avoidance sonar system). The advantages of passive sensing over active sensing include the obvious non-invasiveness of the process and the lower cost from not requiring a sound projector. From a DCLT-performance perspective, passive systems benefit from sensing signals emitted by the object of interest across wide frequency bands, whereas active sensing is essentially restricted to the bandwidth of the projected waveform.

Observation time is important in both active and passive sensing. Qualitatively, the information available in signals of interest increases with observation time and an increase in information can enable an improvement in system performance. Long observation times are more natural to passive systems where the signals of interest are often persistent. However, some signals of interest in passive systems are inherently short in duration (e.g., as in the CTBTO application or when sensing marine mammals by their sound emissions). In active systems a long observation time is obtained by projecting multiple consecutive *pings*, with each comprising a pulse transmission followed by a period of listening up to the two-way travel time for the farthest range of interest.

1.1.2 Common Applications

There are many standard applications of remote sensing in underwater acoustics. These include, but are not limited to, the following:

- Navigation (e.g., depth sounder, autonomous-vehicle navigation)
- Fish and marine mammal finding/censusing/monitoring
- Finding and following moving and stationary objects underwater (there are a plethora of military and civilian applications)
- Asset protection or intruder prosecution (e.g., harbor or ship defense)
- Communications (data and voice)
- Passive monitoring of activity (e.g., noise, nuclear testing)
- Research in the underwater environment (biologic, geologic, oceanographic, acoustical, etc.)

Each application has its own particular object of interest, state of nature under investigation, and the associated signals of interest. As depicted in Fig. 1.2, the signals of interest are affected by propagation through the underwater environment and measured by a remote sensing system. Although this can be beneficial when it encodes the state of nature in the signals of interest, the underwater acoustical

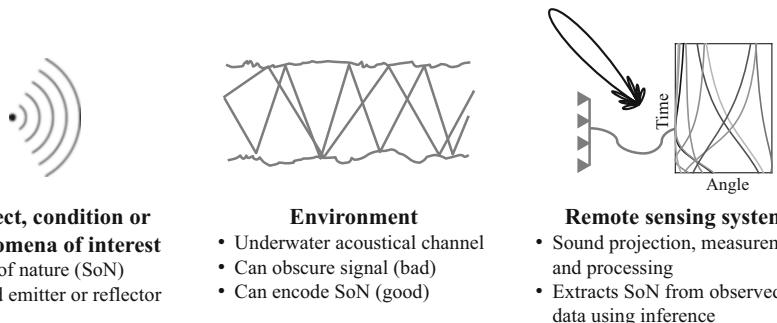


Fig. 1.2 Applications in underwater acoustics: sonar as a remote sensing system used to make inferences about the state of nature (SoN) of an object of interest as viewed through the lens of the underwater acoustical environment

channel is generally considered detrimental to inference because of how it distorts signals of interest.

The signal processing applied to the acoustic measurements in order to extract the state of nature in each of the aforementioned applications has many common elements. For example, when measurements are made on multiple closely spaced sensors (i.e., an array of sensors), they are usually combined in the same manner. Such *array signal processing* implements a spatial filtering process called *beamforming* (see Sects. 1.1.6.1 and 8.4) whereby signals from a specific direction are emphasized and signals or interferences from other directions are attenuated. Similarly, signals of interest can often be characterized by one of several standard statistical models for which detection algorithms are well established. These detection algorithms can generally be described as filtering measurements to the frequency band of the signal followed by coherent and incoherent integration.

Although examples from the above list are used throughout this book, the theme is on the elements that are common across most applications in underwater acoustic signal processing. As might be expected, the majority of applications are enacted in ocean environments, which is therefore the basis for the material presented in this book. However, the design of signal processing algorithms for fresh-water applications is generally the same.

1.1.3 Signal Processing in Underwater Acoustics

Signal processing is a fundamental part of any remote sensing system. It arises as part of the inference process by which the state of nature is extracted from measurements of signals of interest. The principal disciplines of statistical inference are *hypothesis testing* and *estimation theory*. Nearly all applications of underwater acoustics entail one or both of these. The “no explosion”-vs.-“explosion” decision

Table 1.1 Signal-processing oriented inferential objectives and the relevant branch of statistical inference

Inferential objective	State of nature described as a question	Type of statistical inference
Detection	Is a signal of interest present or not?	Hypothesis testing
Classification	What class of object generated the signal of interest?	Multiple hypothesis testing
Localization	Where is the object of interest now?	Estimation (descriptive)
Tracking	Where will the object of interest be in the future?	Estimation (predictive)

of the CTBTO application is a binary hypothesis test that can be described as a *detection* problem. Given an explosion was detected, examples of estimation problems might include *when did it occur?* and *where did it occur?* These examples illustrate how the state of nature being investigated can be phrased as a question. If the answer to the question is a decision (e.g., “the measurement contains a signal of interest” or “there is no signal of interest in the measurement”), then the application is most likely a hypothesis test and if the answer is a physical quantity associated with the object of interest (e.g., its range, bearing, depth, scattering strength or source power level), then it is an estimation problem. Most underwater acoustic signal processing algorithms can be described as either a detection or an estimation algorithm or as a component of one.

The advantages obtained by characterizing an application of underwater acoustics as an inference problem lie in the wealth of solutions from the fields of mathematical statistics and statistical signal processing and the associated standard performance measures. Structured design approaches yielding optimal or nearly-optimal solutions exist for both detection and estimation problems over a wide range of assumptions. Once the inferential objective of an underwater acoustics application is determined, the process for designing the signal processing algorithms required to achieve it is straightforward, although not necessarily easy or even able to be implemented.

From a signal-processing perspective, inference in underwater acoustics can often be categorized as detection, classification, localization, or tracking. The combined objectives are referred to by the acronym “DCLT.” **Detection** is a binary hypothesis test determining if a signal is present in a measurement or if it is simply background noise. **Classification** is a multiple hypothesis test deciding to which class a detected signal belongs among a finite set of classes. **Localization** entails forming an estimate of the location of the object of interest. **Tracking** is localization coupled with estimation of where the object of interest will be at some time in the future (e.g., from estimates of the course and speed of the object of interest). These inferential objectives, the question-form of the state of nature being investigated and the relevant branch of statistical inference are summarized in Table 1.1.

In some contexts there is a distinction between *signal* processing and *information* processing. When a signal is defined as a continuous or regularly sampled function

of time and/or space, *signal* processing refers to operations performed regularly as a function of the relevant independent variable. In this context, detection and some forms of localization (e.g., beamforming) are considered signal processing functions. The output of a detection process in most underwater acoustics applications is a sequence of irregularly spaced points in time and/or space. Because detector output data do not satisfy the above *signal* definition, operations utilizing such data are at times called *information* processing. Classification, tracking, and some forms of localization can fall into this category.

1.1.4 Development Process for Novel Applications

Although most applications of underwater acoustic signal processing will be similar to at least one of those listed in Sect. 1.1.2, it is useful to describe the process by which signal processing algorithms should be developed for novel applications. This process involves more than algorithm development. It is preceded by a statement of the problem and design of a sensing system. Nor is it complete until the performance of the algorithm is examined to understand when it should and should not be used. The primary steps in the process include:

1. Identify the state of nature under investigation.
 - What information related to the object of interest is important?
 - What is the inferential objective: detection or estimation?
2. Define or design the sensing system (e.g., the sonar system) used to obtain underwater acoustic measurements that encode the state of nature.
3. Characterize the available measurements with a statistical model using parameters related to the state of nature.
4. Develop a detection or estimation algorithm based on the assumed statistical model and the inferential objective.
5. Evaluate the performance of the algorithm both in general (e.g., at what point does it fail) and for specific situations of interest.
6. Iterate beginning with Step 2, as necessary, to achieve the desired remote-sensing performance.

This process is described as an iterative one with the goal of achieving a desired performance. When Steps 3–5 yield essentially the same signal processing algorithms across a set of sensing-system permutations (e.g., varying processing bandwidth or array size), the design process can be simplified through the *sonar equation* (see Sect. 2.3 or [8]), which uses the signal-to-noise power ratio (SNR) as a performance metric. This restricts the iteration to Step 2 where the sensing system is designed to achieve an SNR known to provide the desired performance in the ensuing detection or estimation algorithms. Although the emphasis of this book is on Steps 3–5 for the detection inferential objective, the means to obtain the SNR

required to achieve a desired detection or estimation performance is included for several standard signal models.

1.1.5 Example Signals of Interest

The first step in the development process considered in detail in this text is Step 3, to characterize the available measurements. In this section example signals of interest are presented from various applications of underwater acoustical remote sensing. As can be seen in the first example (Fig. 1.3), the signals are represented as a time series in a narrow panel on the left side of the figure and by their spectrum in a narrow panel at the top. The joint time-frequency content is displayed in the large panel using a spectrogram. The scaling for each panel is that for the content after normalization by the peak value (i.e., a value of “1” in the time-series plot is the peak whereas it is zero decibels in the others).

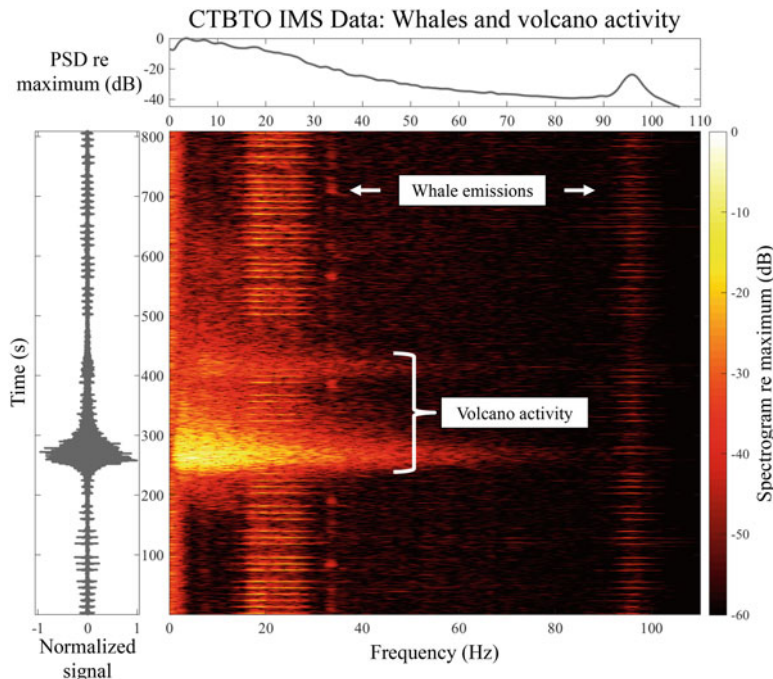


Fig. 1.3 Possible volcano activity and whale emissions measured on May 10, 2017 at the CTBTO IMS hydrophone station off the Crozet Islands, France. Acknowledgement: CTBTO [6]

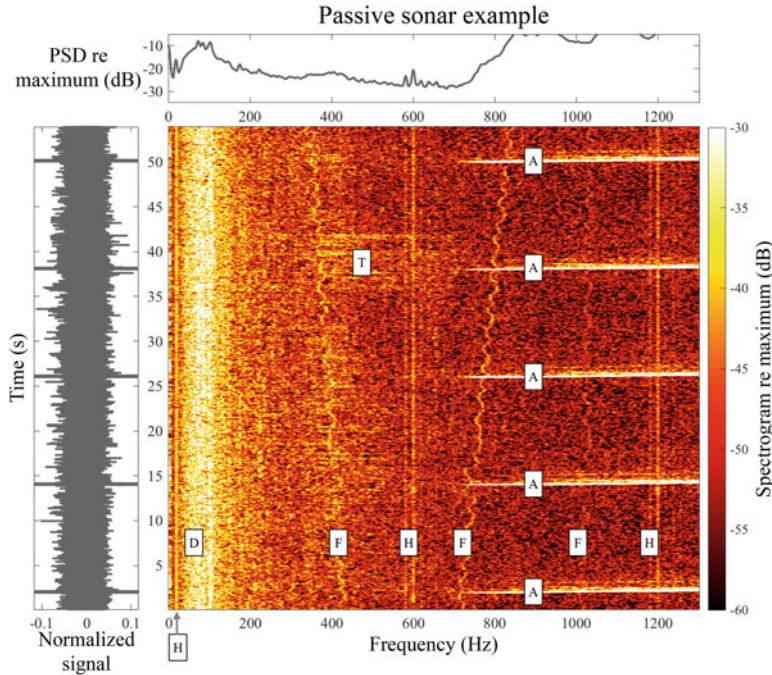


Fig. 1.4 Example of passive sonar signals and noise from the horizontal beam of a vertical line array. Acknowledgement: NURC Clutter JRP [12]

The spectrogram in Fig. 1.3 is from measurements³ made at the CTBTO IMS hydrophone station off the Crozet Islands, France. The acoustic emissions of a fin whale are seen as a long sequence of pulses in the 18–35 Hz band as well as a narrow band just below 100 Hz. Although not visible on this temporal scale, the lower frequency whale emissions are down-swept frequency-modulated pulses [9, Sect. 10.2.1]. Occluding these for a period of time are sounds arising from volcano activity (possibly volcano jet noise; see [10, 11]). These two examples illustrate the diversity that can be observed in the time and frequency characteristics of underwater sound as well as the potential for overlap that can hinder inference.

The signals seen in Fig. 1.3 are indigenous to the underwater environment. Examples of anthropogenic (man-made) sounds are shown in Fig. 1.4. The data were obtained on a vertical line array (VLA) during the NATO Undersea Research Centre (NURC) Clutter 2007 Experiment.⁴ The signals and noise seen in this figure include narrowband radiated noise from a nearby fishing vessel (marked F), harmonically

³Acknowledgement: CTBTO [6] with gratitude to Drs. G. Haralabus, M. Zampolli, P. Nielsen, and A. Brouwer for their assistance in identifying, accessing, and interpreting the data.

⁴Acknowledgement: NURC Clutter JRP [12] with gratitude to Dr. P. Nielsen (scientist in charge, Clutter 2007 Experiment) and Dr. C. Holland (ARL/PSU) who led this particular investigation.

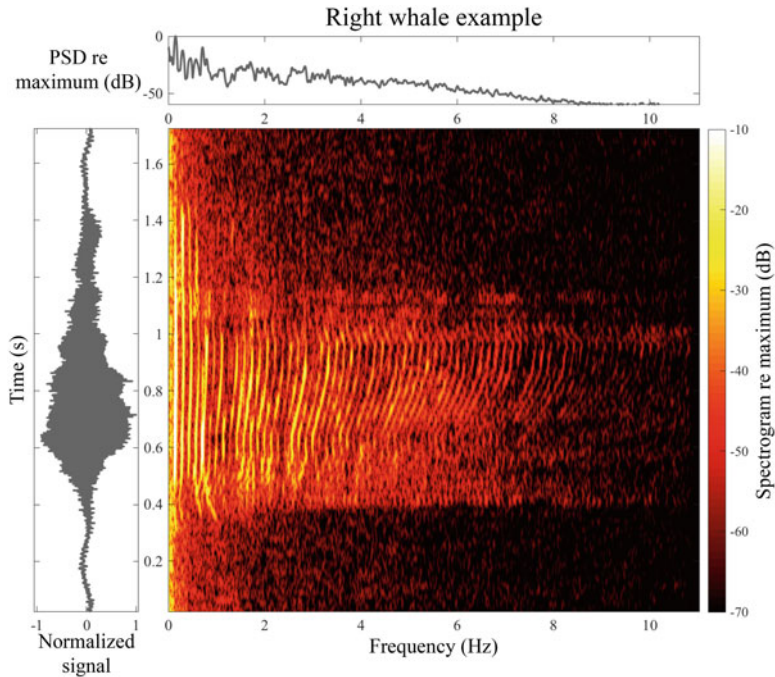


Fig. 1.5 Example spectrogram of right-whale call. Acknowledgement: data provided by Prof. S. Parks, Syracuse University

related signals from power generation (H), broader-band distant-shipping noise (D), a burst of broadband transient signals from the fishing vessel (T), and a sequence of active sonar pulses (A) and their ensuing reverberation. The wavering narrowband signals marked as F illustrate how radiated ship noise can have unstable frequency characteristics, be narrowband at any instant in time, and yet traverse a large frequency band over a short period.

A sound emission from a right whale is shown in Fig. 1.5. The data were obtained by Prof. S. Parks (Syracuse University) in the Bay of Fundy using a single hydrophone that was deployed from the surface.⁵ As described in [13], this is an example of a “low-frequency tonal” right-whale call. Although the peak occurs near 150 Hz, there is significant energy at much higher frequencies. This one example cannot represent the immense diversity of sound emissions produced by marine mammals, which is articulated in [9, Ch. 10]. However, it does convey the complexity inherent in the sounds produced by marine mammals.

⁵Acknowledgment with gratitude to Prof. S. Parks, Biology Dept., Syracuse University, who acquired the data under funding from the National Oceanic and Atmospheric Administration (NOAA) and a Department of Fisheries and Oceans (DFO) Canada permit.

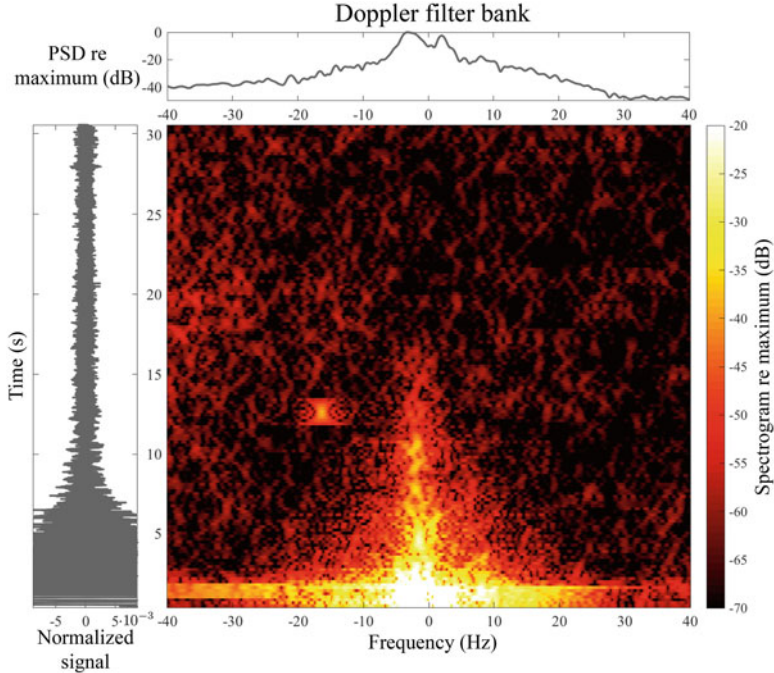


Fig. 1.6 Example Doppler filter bank showing the reverberation ridge and an echo near -18 Hz and 12-s delay. Acknowledgement: NURC Clutter JRP [12]

An example response of a Doppler filter bank (see Sect. 8.7.1) is shown in Fig. 1.6 using the same analysis tool as the previous figures. The data arise from projection of a continuous-wave (CW) pulse. They were measured on a towed line array during the NURC Clutter 2007 Experiment⁶ and beamformed to point in the direction of a passing ship. The echo from the ship is visible near a Doppler shift of -18 Hz and a 12-s time delay. One of the hindrances in active sensing is the reflection or backscattering of the projected pulse from a myriad of sources other than the object of interest, collectively termed *reverberation* in underwater acoustics (see Sect. 3.5). In Fig. 1.6, reverberation dominates the first few seconds of data over a wide frequency range, but eventually decays into the ambient noise, persisting the longest in the zero-Hz Doppler-shift channel. Note that the echo is not visible in the time series, which is before the matched filtering accomplished by the spectrogram.

An echo from the Campo Vega oil rig produced by transmitting a linear-frequency-modulated (LFM) active-sonar pulse is shown in Fig. 1.7. The data were obtained on a towed line array during the NURC Clutter 2009 Experiment

⁶Acknowledgement: NURC Clutter JRP [12] with gratitude to Dr. P. Nielsen (scientist in charge, Clutter 2007 Experiment).

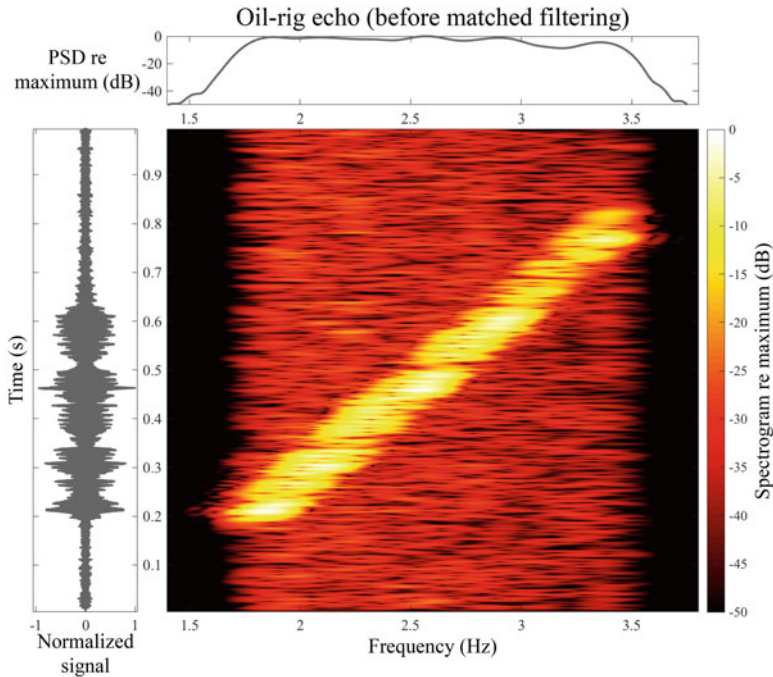


Fig. 1.7 Example spectrogram of an echo from the Campo Vega oil rig before matched filtering.
Acknowledgement: NURC Clutter JRP [12]

and beamformed to point in the direction of the oil rig.⁷ The echo shown has a bandwidth of 1700 Hz and a duration of approximately 0.62 s, which is evident from the spectrogram. Although the echo is clearly visible above the noise, very little structure is discernible because no matched filtering has been applied to the measurement. Application of a matched filter (see Sect. 8.2), as seen in Fig. 1.8, has the effect of removing the frequency modulation to align the echo temporally across frequency. This in turn makes the temporal structure induced by reflection from the oil-rig pylons visible.

These examples illustrate the variety of signals of interest that can be encountered in applications of underwater acoustic signal processing. In order to develop signal processing algorithms for these signals, they must be characterized not only in terms of their time and frequency content, but also in terms of their consistency over repeated observations and how much information is known about the signal structure. Obtaining the proper characterization, which is one focus area of this book (Chap. 7), allows using standard signal processing algorithms to accomplish the inferential objective.

⁷Acknowledgement: NURC Clutter JRP [12] with gratitude to Dr. P. Nielsen (scientist in charge, Clutter 2009 Experiment) and Dr. P. Hines, Mr. J. Scrutton, and Mr. S. Murphy (DRDC) who designed and led this particular investigation, collated and labeled the echoes.

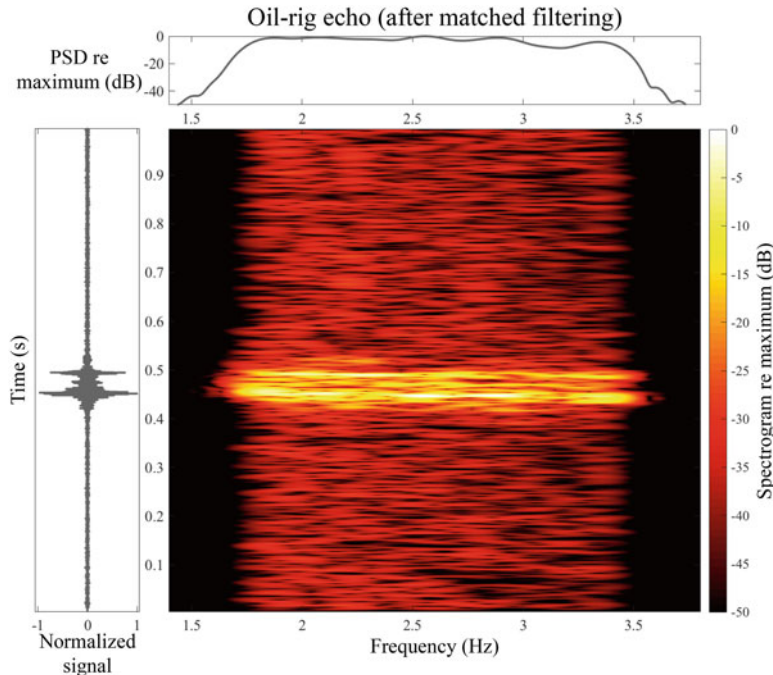


Fig. 1.8 Example spectrogram of an echo from the Campo Vega oil rig after matched filtering.
Acknowledgement: NURC Clutter JRP [12]

1.1.6 Examples of Signal and Information Processing

The signal and information processing chain (SIPC) in many applications of underwater acoustics will comprise the modules shown in Fig. 1.9. These modules are not in one-to-one correspondence to the DCLT inferential objectives. For example, the beamforming (array signal processing) module contributes to both detection and localization. How these modules relate to the DCLT objectives is described in the following subsections along with examples of each module. With respect to underwater acoustics, detailed examples and derivation of detection and localization algorithms can be found in the classic texts by Burdic [14] and Nielsen [15] as well as [16, 17] and for tracking in [18]. More general resources for the development and analysis of tracking algorithms include [19–22]. Useful resources for classification techniques, which is also called pattern recognition, machine or statistical learning, include [23–25].

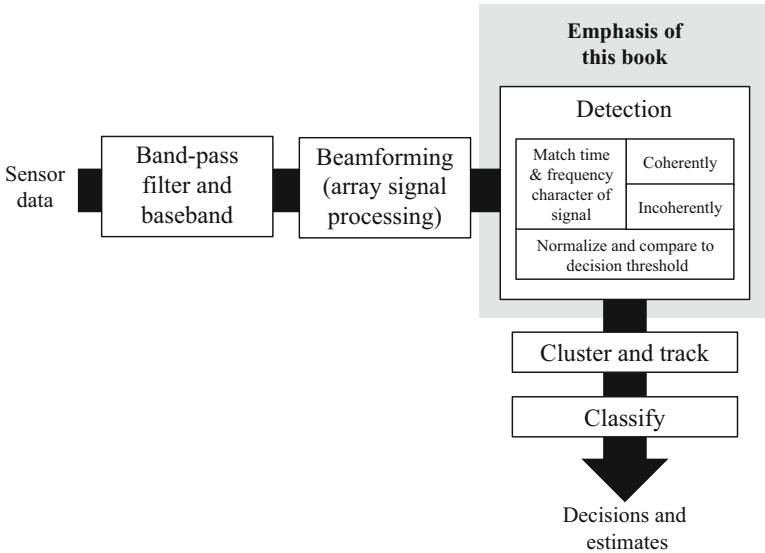


Fig. 1.9 Generic signal and information processing chain (SIPC) in an underwater acoustical remote sensing system

1.1.6.1 Detection

Detection is the most fundamental of the inferential objectives in remote sensing. No other objectives can be accomplished without first performing detection. The signal processing operations that go into a detection algorithm can be described as exploiting all the known characteristics of the signal of interest to isolate it in the dimensions of time, frequency, and space. As seen in Fig. 1.9, this starts by restricting consideration to the frequency band of the signal of interest through bandpass filtering. This is often done in conjunction with basebanding, which simply shifts and isolates the signal's frequency band to be centered at zero frequency (see Sect. 7.3.2). Basebanding can reduce the computational requirements of digital signal processing and is a step in forming many detectors.

Systems containing multiple sensors (e.g., an array of hydrophones) utilize beamforming to focus on signals coming from particular directions. The focusing is accomplished by placing the sensors (either physically like pointing a satellite dish or electronically through time delays) so they all sense the same wavefront of an acoustic wave arriving from the desired direction. Rejecting noise and interference from directions other than from where the signal of interest is emanating improves SNR, which has a direct effect on detection performance. As will be seen, beamforming can be derived as part of a detection algorithm despite its obvious relevance to localization. The wavefront of an acoustic wave is the region in space at a given time carrying the same source-signal information from the object of interest. The shape of the wavefront, which must be known to implement a beamformer,

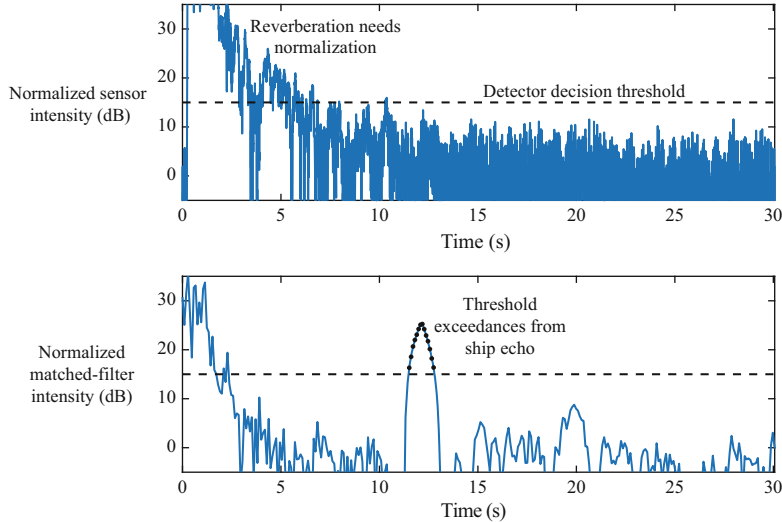


Fig. 1.10 Instantaneous intensity of measurements from a CW pulse before matched filtering (upper panel) and after (lower panel). The data have been normalized according to the ambient noise power. Acknowledgement: NURC Clutter JRP [12]

depends on how the acoustic wave propagates. This illustrates the dependence of signal processing algorithms on the physical processes conveying the information from the object of interest to the remote sensing system.

The next signal-processing step in a detector is to match the time and frequency content of the signal. This is generally followed by a coherent integration stage and a stage of incoherent integration. Coherent integration essentially assumes a constant signal phase so the signal accrues constructively as it is combined. At the point where the phase changes too much to combine constructively, an incoherent integration is employed by removing the phase.

The final stage of detection involves identifying when a signal of interest has occurred. In order for a detection to occur, the signal of interest must be visible against the background noise and interference observed in the system. For example, in the Doppler filter bank of Fig. 1.6 the ship echo is not visible in the time series, but it is visible in the spectrogram. This is illustrated for the Doppler channel containing the echo in Fig. 1.10 where the upper pane displays the sensor data (in a 200-Hz band) before matching to the time and frequency characteristics of the pulse in the lower panel. While the signal may and may not be visible in the upper pane, it is clearly visible in the lower pane.

The actual detection decision process is accomplished by forming a *detector decision statistic* that is compared to a *decision threshold*. A “decision statistic” is a distillation of the data measured during a processing period into a scalar function. For the purpose of detection, it should contain all the information required to decide if a signal is present or not. If the data measurements are represented by the vector

$\mathbf{x} = [x_1 \ \cdots \ x_n]^T$, then the detector decision statistic can be described by the scalar function $T(\mathbf{x})$. A signal of interest is then declared detected when $T(\mathbf{x})$ exceeds the aforementioned decision threshold. In the example of Fig. 1.10, it can be seen that if the output of a bandpass filter tuned to a 200-Hz-wide frequency band is used as a decision statistic, there is no detection at the time of the ship echo. However, by matching the time and frequency characteristics of the CW pulse through the use of a matched filter, the ship echo is easily detected from the exceedances of the detector decision threshold.

At early times, the data shown in both panes of Fig. 1.10 are dominated by reverberation that eventually recedes to the point where the data become dominated by ambient noise. If a constant detector decision threshold is used as shown in Fig. 1.10, there will be many threshold exceedances leading to incorrect detections. Such incorrect detections are called *false alarms* and their occurrence should be kept to a minimum. If the signal of interest were observed in the reverberation-dominated region and the same level of “visibility” were desired as was obtained in the noise-dominated region, the decision threshold could be increased so as to be the same level above the reverberation power as it was above the noise power. An equivalent way of implementing this time-varying decision threshold is to divide the matched-filter intensity by the estimated reverberation and noise power so a constant decision threshold can be used. This process is called *normalization* and is an important part of any detector because the noise and interference (e.g., reverberation) background can change over time, frequency, and space.

As noted in Fig. 1.9, the emphasis of this book is on signal detection. This includes characterizing signals of interest, derivation of an appropriate detection algorithm, accounting for an unknown noise and interference power through normalization, and evaluating the performance of the detector. The primary performance metrics for detection algorithms are the probability of detection (P_d) and the probability of false alarm (P_f). The design process ideally results in an optimal detector that maximizes P_d while constraining P_f to be below some acceptable level.

1.1.6.2 Localization

In the localization inferential objective, the position of the object of interest is estimated from the measurement of the signal of interest. Several factors affect the localization capability of a remote sensing system with the foremost being whether the system has an active or passive modality. An active sensing system exploits estimates of the time it takes for an acoustic pulse to propagate from a projector to the object of interest and then on to the sensor having reflected off the object of interest. This is known as *echo ranging* and has been employed by bats and marine mammals longer than humans.

An example of the echoes produced by a linear frequency modulated (LFM) pulse and measured on a line array of sensors is shown in Fig. 1.11. The sensor

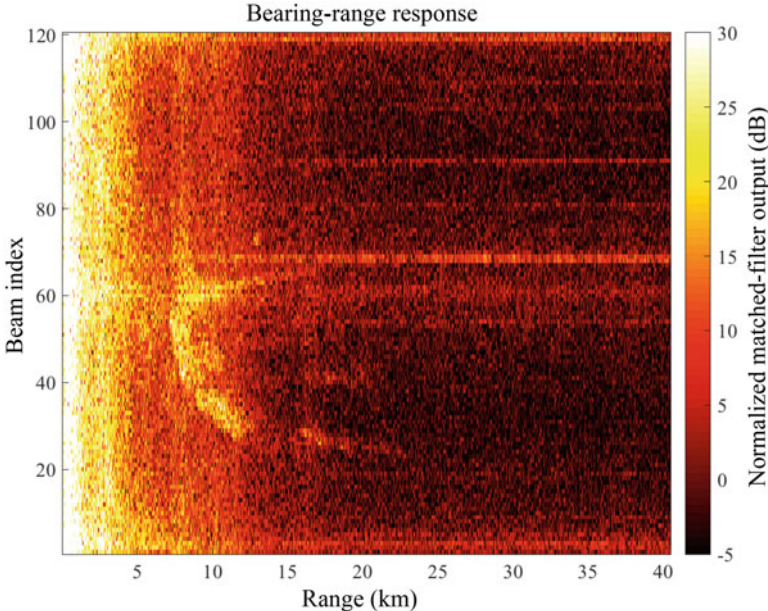


Fig. 1.11 Beamformed and matched-filtered response of an active sonar system using a line array of sensors. Detection of a signal of interest in a beam localizes the object of interest in range and bearing. The data have been normalized by an estimate of the ambient noise power. Acknowledgement: NURC Clutter JRP [12]

array measurements were obtained during the NURC Clutter 2007 Experiment⁸ and combined to produce *beams* pointing to specific directions (i.e., the data were beamformed). The image in Fig. 1.11 is displayed using the beam index number and on the abscissa the time delay has been converted to a range estimate. When a signal of interest is detected on a particular beam, the object of interest can be localized in terms of its range and bearing. This is illustrated in Fig. 1.12 where the range and bearing of each threshold exceedance is shown in a geographic display. These data represent ten consecutive pings of the active sonar, occurring 1 min apart, and a detector decision threshold of 15 dB. Echoes from an object of interest moving at 15 kn were injected into the data to illustrate realistic motion. A disadvantage of active sensing can be seen in the plethora of reflections producing false alarms. Examples seen in Fig. 1.12 include echoes from geologic features (an exposed rocky ridge) and a potential set of false alarms that appear related to the motion of the sonar platform, but may be a moving object of interest.

⁸Acknowledgement: NURC Clutter JRP [12] with gratitude to Dr. P. Nielsen (scientist in charge, Clutter 2007 Experiment).

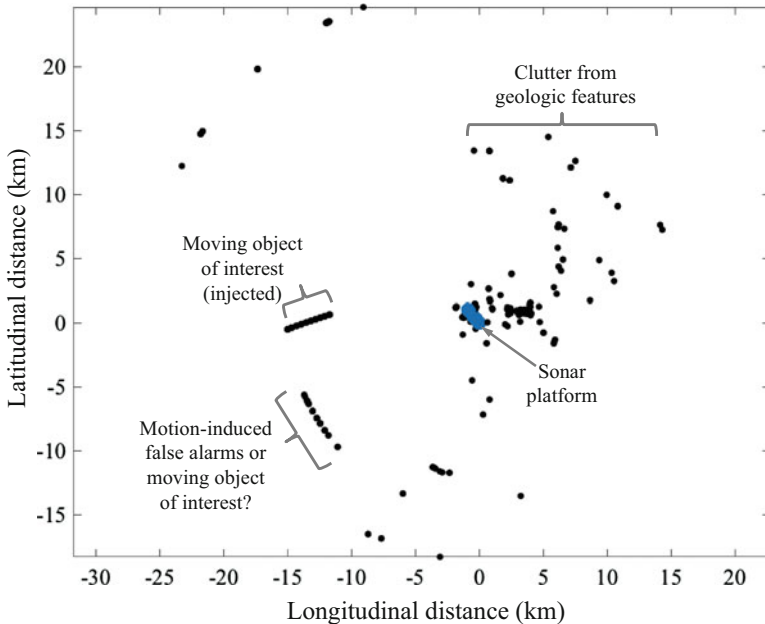


Fig. 1.12 Geographic display of detection data from ten consecutive pings of an active sonar system illustrating localization in the horizontal plane. Acknowledgement: NURC Clutter JRP [12]

The horizontal lines seen in Fig. 1.11 are from the radiated noise of nearby surface ships. To an active sonar system, these represent interferences. However, to a passive sonar system these are potentially signals of interest as was shown in Fig. 1.4. This also hints at the difficulty in estimating range in the passive sensing modality. The propagation model used in the beamforming for Fig. 1.11 assumed the acoustic wave was planar as it passed the sensor array. This allows estimation of the bearing⁹ of the object of interest with a linear sensor array in a passive sensing system, but not the range. Suppose, however, that the array was large enough that the acoustic wavefront was distinctly spherical (i.e., the object of interest is in the *near-field* of the array). The sensor measurements could then be used to estimate the curvature of the wavefront and through that estimate the range and bearing to the object of interest. If the sensors of the array are arranged so the array is two-dimensional (i.e., it is planar) or three-dimensional (i.e., it is volumetric), an object of interest can be localized in bearing and the depression/elevation angle under a plane-wave model and in three dimensions for objects in the near-field of the array.

⁹More properly, a conical angle is estimated. The bearing is obtained, subject to a left/right ambiguity, by assuming the line array is horizontal and restricting the solution to the horizontal plane.

The size of sensor arrays is limited by physical and engineering constraints as well as cost. From a sensing perspective, there is a limit where the signal of interest decorrelates over the physical extent or span of the array. This is similar to how detectors only integrate coherently up to the point permitted by the phase of the signal of interest. In localization, where the shape of the wavefront over the array is important, there is little benefit in building arrays larger than what can be combined coherently. A more effective approach is to build multiple sensor arrays that can be physically separated (e.g., like the CTBTO monitoring system). If the sensor array in each *node* of such a distributed sensing system detects the same signal of interest and estimates a bearing, then the object of interest can be localized through triangulation. When only a single hydrophone (with no ability to estimate a bearing) is available at each node, an object of interest can still be localized using multilateration (see Sect. 2.2.3.3) if the time-of-arrival differences can be measured between multiple pairs of nodes.

These examples illustrate how localization depends on sensing modality, array geometry, acoustic propagation, and whether there is more than one sensing node or not (i.e., the number of sensing platforms). A more detailed description of the localization inferential objective can be found in Sect. 2.2.3

1.1.6.3 Tracking

The tracking inferential objective is closely related to localization. The two are distinguished by noting that localization answers the question “where is the object of interest now?”, whereas tracking couples in estimating where the object of interest will be in the future (i.e., “where is it going?”). The motion of the object of interest is typically parameterized by its position, velocity, and (sometimes) acceleration in Cartesian coordinates as a function of time. These variables defining the motion are called *state variables*, similar to how the voltage across capacitors and current through inductors are all that is needed to determine the response of an RLC circuit (i.e., a circuit comprising resistors, capacitors, and/or inductors). The objective in a tracker is to estimate and predict the states as they change over time using the data measured by the sonar system. Like many signal processing algorithms, trackers accomplish this by using a model to describe how the states evolve. This can be interpreted as a *motion filter*: the tracker filters out data with motion unlike that represented by the model and promotes data exhibiting the expected motion. A synthetic example of the tracking process is shown in Fig. 1.13 where measurements in range and cross-range obtained over a number of temporal epochs, which are called *frames* in tracking, are used to estimate the motion of the object of interest. The underlying motion has a constant velocity on the first leg followed by a turn and acceleration. Using a “nearly constant-velocity” model (often just called a constant-velocity model) in the first leg provides a better estimate than assuming a “nearly constant-acceleration” model. This is because the latter model, while still accurate, is more general and therefore incurs a larger *estimation error* than the constant-velocity model which more succinctly describes the motion (i.e., two parameters

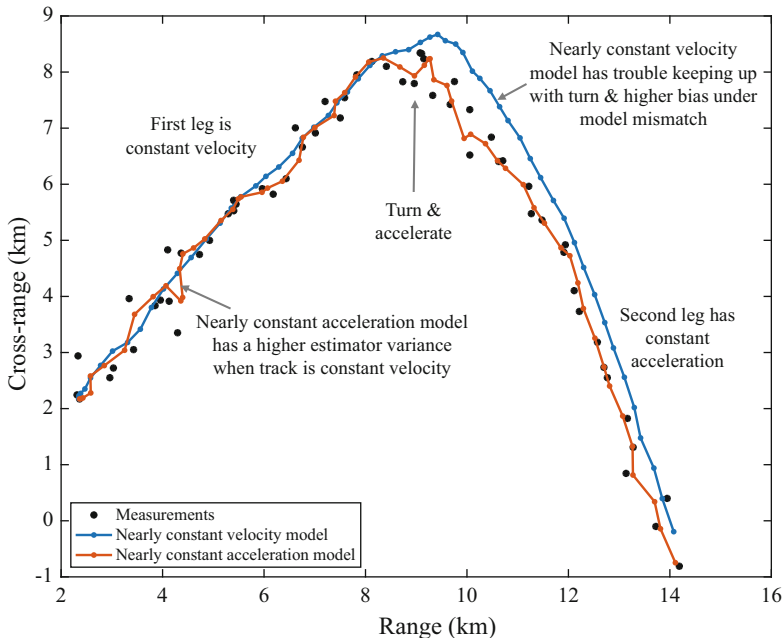


Fig. 1.13 Tracking of an object of interest using different motion models (synthetic example)

instead of three, per dimension). However, when the object of interest enters the turn and then maintains an acceleration the nearly constant-velocity model is no longer accurate because it assumes there is always zero acceleration. This is manifested in the tracker as a larger bias in the state estimates obtained using the nearly constant-velocity model during and after the turn and represents a *mismatch error*. This example identifies one of the tenets of using models in signal processing: *model only as much of the physics and statistics as necessary to solve the problem*. Models that are too general lead to estimation errors and models that are not general enough lead to mismatch errors.

The nearly-constant-velocity and nearly-constant-acceleration motion models are examples of using a linear dynamical system to describe the motion of an object of interest. The states in the next frame are a linear combination of the states in the current frame, a known input (which can be zero) and a process noise. An impact of the process noise, which is random, is that the state variables describing motion are themselves random and this must be taken into account during their estimation. The process noise essentially allows the model to deviate in a random manner from the otherwise deterministic linear progression. Choosing a low process noise means the estimation exploits the deterministic component of the model to combine data over many frames, which can result in a low estimation error when the model is accurate but a high mismatch error when it is not. Using a high process noise results in less data being combined across frames, which increases the estimation error but limits

the potential for a large mismatch error. Choosing the process noise is part of the art in designing and implementing a tracking algorithm.

The input data to a tracking algorithm are the output of the detection process; however, the raw detector data require some manipulation before they are appropriate for use in a tracker. In the first step, the threshold exceedances in a given frame are grouped or clustered into those believed to arise from unique signals of interest. A frame represents one ping of data in an active system and one coherent processing interval in a passive system. This *clustering* stage accounts for oversampling in the detector decision statistic, an example of which can be seen in the lower panel of Fig. 1.10 where there are a large number of threshold exceedances for what should be the detection of a single signal of interest. Clustering is also required when a signal of interest is spread so as to span multiple resolution cells (e.g., as occurs by propagating through the underwater environment along multiple paths.)

The data from each unique “cluster” are then used to form parameter estimates for intermediate quantities linked to the motion of the object of interest. In the tracking literature, these parameter estimates are called “measurements” although they are typically quantities derived from the measurements of acoustic pressure made at each sensor. In this section they will be referred to as *tracker measurements*. Examples of such parameters include the range and bearing estimated during localization in an active sensing system and an estimate of the radial velocity if the projected waveform is Doppler sensitive. In passive sensing where range and radial velocity cannot easily be estimated from the data in a single temporal epoch, the tracker measurements can include bearing, center frequency (for narrowband signals of interest), and time delay estimates. A *measurement model* that is specific to the sensing application relates the tracker measurements to the motion state variables. Defining this model is a straightforward application of kinematics when starting with the state variables (i.e., what the sensor observes given a particular motion for the object of interest). A key assumption in tracking is that this relationship is invertible so the motion states can be estimated from the observations of the remote sensing system. A classic example of how conditional this assumption can be found when estimating range with a passive sonar system where only the bearing estimates are available over time. This “bearings-only-tracking” problem does not result in an invertible measurement model unless there is an acceleration component in the relative motion between the object of interest and the sensing platform [26, 27].

In any frame there are likely to be a number of clusters (e.g., imagine one tenth of the points seen in Fig. 1.12, which spans ten pings). Clearly many of these will belong to unique objects of interest, which introduces the problem of how to associate clusters across frames. The solutions to this problem and how to deal with the concurrent tracking of multiple objects of interest (called multi-target tracking) are beyond the scope of this introduction. Consideration is therefore restricted to tracking a single object of interest given tracker measurements over a sequence of frames. How the state parameter estimates are obtained from the tracker measurements depends on whether the measurement and motion models are linear or non-linear and whether the tracker measurement noise (i.e., the errors in

estimating the intermediate quantities from the sensor measurements) is Gaussian distributed or not. If both models are linear and the noise is Gaussian, the Kalman filter [28, 29] is optimal in terms of minimizing the mean squared error of the state parameter estimates. Several other common trackers are formed as specific cases of the Kalman filter. For example, the Kalman filter simplifies to a recursive least-squared-error estimator when there is no process noise. Kalman filters are generally implemented recursively owing to a simple update procedure and the on-line nature of the data. However, batch trackers are not uncommon. When the Kalman filter reaches a steady state (i.e., the effect of its initialization has subsided), the nearly-constant-velocity model produces what is known as an α - β filter and the nearly-constant-acceleration model produces what is known as an α - β - γ filter (the variables represent filter gains). When the change in the states is small from one temporal epoch to the next, linear motion and measurement models may be good approximations. When they are not or if the noises are not Gaussian distributed, there exist extensions of the Kalman filter (e.g., the extended Kalman filter and the unscented Kalman filter) as well as particle-filter trackers that can be brought to bear.

It is important to note that the description of tracking in this section has focused on estimating and predicting the physical motion of the object of interest. There are, however, many other applications of tracking in underwater acoustics because the techniques can be used to estimate other temporally or spatially varying quantities (e.g., the center frequency of a narrowband signal, the shape of a towed array, and even physical properties of the ocean).

1.1.6.4 Classification

The final stage of signal and information processing in many applications of underwater acoustics is classification, where the category or class to which a signal of interest belongs is determined from the sensor measurements. Examples of classification include the following: identifying which type of marine mammal produced an observed acoustic emission; determining if a very low frequency measurement was an earthquake or a nuclear test in the CTBTO application; deciding if an object moving toward a ship is a fish school or a diver in asset protection; deciding if the object in a sonar image is a cylindrical mine, a sand ripple, or sea grasses; or assessing if an active sonar echo is from a rock outcrop or a submarine.

From the perspective of statistical inference, a classifier is a multiple-hypothesis test. Noting that detection is simply a multiple-hypothesis test with two classes, it is useful to compare and contrast the two inferential objectives. Detectors exploit as much of the time-frequency properties of signals of interest as are reasonably known and generally assume a benign background when no signal is present. Thus the two hypotheses being tested by a detector are (1) is there a signal with these

time-frequency properties, or (2) is there a benign noise background. The majority of data processed by most systems can be considered benign, as can be seen in Figs. 1.1, 1.3, 1.4, 1.6, and 1.11 where the background predominantly appears with a consistent speckle. As such, this set of detection hypotheses is appropriate most of the time. However, most systems also sense signals other than the desired one that have enough similarities in their time-frequency structure to those used to build the detector that these confusables are detected. This is clearly true in active sensing where most detections are echoes of the projected pulse. However, it can also be true in passive sensing when little is known a priori about the signals of interest, which requires detectors with low specificity in the time-frequency structure they exploit.

In many applications, there is enough information in the time-frequency structure of the signal of interest and the confusable signals that the signal measurement can be labeled (i.e., classified) with a useful accuracy. From communications theory, the Shannon-Hartley theorem dictates that channel capacity (e.g., see [30, Sect. 15.3]) in bits per second is

$$C = W \log_2(1 + \text{SNR}) \quad (1.1)$$

where W is the channel bandwidth. Thus by limiting a signal to bandwidth W and a duration or processing time T_p , the total information potentially available is proportional to the processing time-bandwidth product $T_p W$ and SNR in decibels. The amount of information in the signal can be taken as a bound on classification performance, but not necessarily the performance achieved by any particular algorithm. This implies that an increase in the processing time, bandwidth, or SNR has the potential to improve classification performance. For example, the broadband nature of marine-mammal acoustic emissions and their diversity in time-frequency structure often makes classification easy (e.g., distinguishing the low frequency calls of a right whale from the high frequency clicks of a common dolphin).

Where classification algorithms work hardest is when there is significant overlap in the time-frequency structure of the signal of interest and confusable signals. As an example, consider the active sonar echoes shown in Fig. 1.14 which are from an echo repeater (essentially a point source), an oil rig, a single-point mooring, an air hose, and two unknown sources (see [31] for detailed descriptions). The data were obtained during the NURC Clutter 2009 Experiment,¹⁰ beamformed and matched-filtered. Because these all represent reflections (or a re-transmission) of a common waveform, their spectral content is limited to the same frequency band. Examination of the echoes leads to little insight as to how they might be classified without resorting to specialized algorithms, which illustrates the difficulty of classification in active remote sensing.

¹⁰Acknowledgement: NURC Clutter JRP [12] with gratitude to Dr. P. Nielsen (scientist in charge, Clutter 2009 Experiment) and Dr. P. Hines, Mr. J. Scrutton, and Mr. S. Murphy (DRDC) who designed and led this particular investigation, collated and labeled the echoes.

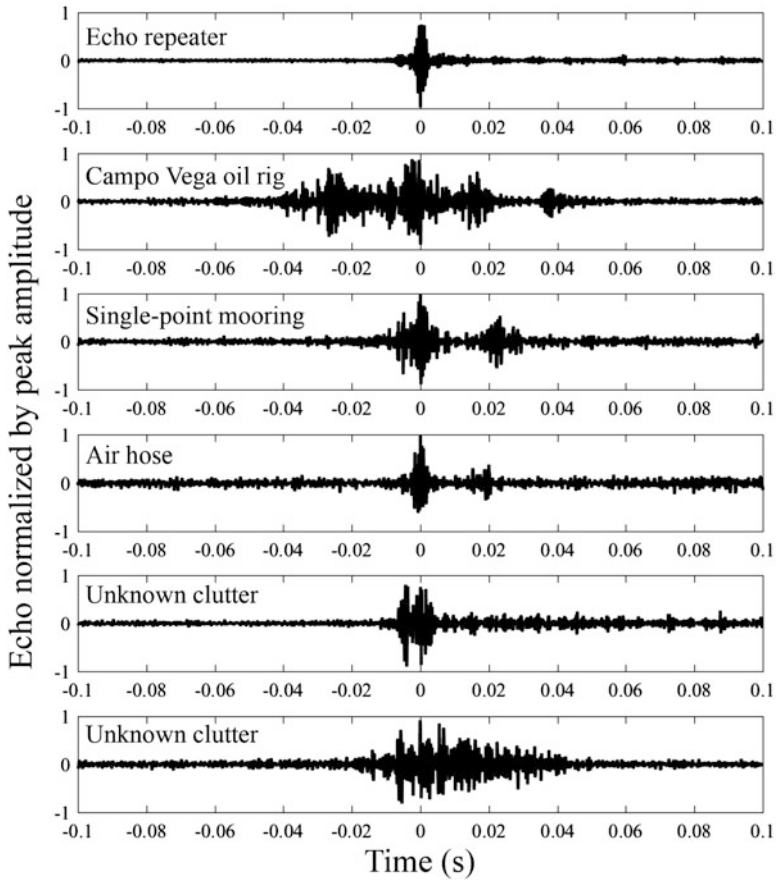


Fig. 1.14 Various echoes from Clutter 2009. Acknowledgement: NURC Clutter JRP [12]

Most classification algorithms have two basic steps: (1) extract some pertinent characteristics from the data into a set of features and (2) use the observed features to choose one of the classes. The classification *features* essentially distill from the signal measurement the information necessary and sufficient to separate the hypotheses under consideration. There are three basic means for obtaining features: as sufficient statistics of a statistical model of the data, identifying physics-based features that naturally separate the different hypotheses, and extracting descriptive features that characterize the signal measurement but may not reliably separate the hypotheses. Sufficient statistics are ideal, but difficult to obtain owing to what are generally complicated models. Physics-based features are useful because their relationship to the hypotheses is often obvious, but are rare. Descriptive features are readily available, but deciding which ones to use is laborious. Examples of physics-based features include radial velocity to identify moving objects, or texture to identify anthropogenic objects that are less complex than natural ones. Neither

feature is perfect because there will be objects of interest and confusables that violate the assumptions. However, separation between the classes can be improved by using multiple features.

Given a set of features, there are many different ways in which classifiers can decide which hypothesis best represents the data. These are beyond the scope of this introduction, however it is important to highlight the difference between *statistical classifiers* that require a set of labeled observations and those that do not. Many of the ‘off-the-shelf’ classification algorithms work by using labeled historical data to estimate parameters that define when a particular class is chosen. For example, if the parameters defining the joint probability density function of the features are estimated for each class, they can be used on new data to pick the class resulting in the highest likelihood. In most applications, the amount of labeled historical data available for *training* the classifier (i.e., estimating its parameters) is limited. This implies that the number of features (or parameters in the modeling) must be small enough that the estimation error is acceptably small. It is also imperative that the labeled historical data have the same characteristics as the data to which the classifier is applied in the field. Important characteristics include, but are not limited to, the following: SNR, propagation conditions, sensor characteristics, types of confusable signals. When implemented properly, statistical classifiers can provide very good performance in what are otherwise difficult classification scenarios.

1.2 Intended Use and Organization of This Book

This book has been written primarily to guide and inform those performing analysis, development, or research in underwater acoustic signal processing. Underwater acoustical remote sensing is inherently a multi-disciplinary subject. The various pedagogical areas involved include engineering (electrical, mechanical and ocean), physics with a focus on acoustics, marine biology, and physical oceanography. The intended audience therefore extends across several scientific and technical fields. Although the focus of this book is on signal processing in underwater acoustics applications, background material from other fields is necessary for a proper treatment. Complementarily, this book has also been constructed for use as a textbook in graduate-level courses on sonar signal processing. In deference to this usage, many results include derivations and examples are used liberally throughout the book. Although there are no formal problem sets at the end of each chapter, there are exercises at the end of many sections to encourage the reader to examine important topics in more detail.

Because the target audience spans several diverse disciplines, this book includes background material in underwater acoustics, linear systems, signal processing, and mathematical statistics. The intent is to provide enough information in each of these supporting disciplines for a reader to follow the development and analysis of underwater acoustic signal processing algorithms as presented without access to an eclectic set of reference texts. A working knowledge of undergraduate

mathematics is assumed throughout. Inclusion of background material should make this book a useful reference and has the advantage of clarifying (through concrete definitions) many of the differences encountered between physics, mathematics, and engineering, which go far beyond the $\sqrt{-1} = i$ or j dilemma.

This book is organized into the following three parts.

Part I: Sonar and underwater acoustics

Part II: Systems, signal processing, and mathematical statistics background

Part III: Detection in underwater acoustics

Part I begins with an introduction to underwater acoustic signal processing as a component of a remote sensing system (this chapter). The sonar application is then introduced in Chap. 2 by describing the components, types, and properties of sonar systems followed by an explanation of the sonar equation and its many uses. Part I concludes by introducing the topics of underwater acoustic propagation, ambient noise, scattering from objects, and reverberation in Chap. 3. Owing to the importance of understanding how the underwater acoustical environment affects the derivation and performance of signal processing algorithms, the material in Chap. 3 is more extensive than what is usually found in a book with a signal-processing focus. Part I of the book should be accessible to those with an undergraduate science, technology, engineering, or math (STEM) background.

Part II of this book is primarily background material in the areas of linear systems theory, signal processing, and mathematical statistics. It begins in Chap. 4 with basic concepts in linear systems and signal processing including impulse and frequency responses, convolution, Fourier transforms, sampling, filtering, and windowing. The mathematical statistics concepts of probability, random variables, and random processes are presented in Chap. 5. Part II ends with a brief presentation in Chap. 6 of the statistical signal processing topics of detection and estimation. Although the topics presented in Part II are not unique to the underwater acoustic signal processing theme of this book, the information is condensed from multiple diverse textbooks to form a light introduction and reference for each topic area and includes a number of apropos examples. More importantly, this part of the book contains the tools necessary for deriving and understanding the techniques and concepts presented in Part III.

The final part of this book (Part III) is the focal point of the theme of detection in underwater acoustics. Before deriving detection algorithms, the signals produced by objects of interest must be characterized. In Chap. 7 this begins by using the standard time and frequency characterizations, but also includes how to represent signals according to their consistency over repeated observations and by how much knowledge is available about the structure of the signal. Also considered is how the characterization of the source signal produced by the object of interest changes as it propagates through the underwater environment to the sensor array. Because most signals in underwater acoustics are bandpass in nature (i.e., their spectral content is limited to a finite frequency band and the signals have no zero-frequency component), both signal processing and detector derivation are often performed after *basebanding* the signals to be centered around zero frequency. The

process of basebanding a signal is described along with how the result is related to the analytic signal and complex envelope. In order to facilitate derivation of detection algorithms, a statistical model is presented for the complex envelope of a signal measured in the presence of Gaussian noise and sampled in time. When properly formed, the sampled complex envelope of a measurement contains all the information necessary for both signal detection and parameter estimation. Given a statistical model for a complex envelope sample, the ensuing statistical models for the envelope and instantaneous intensity, which are used to evaluate detection performance, are then derived under an assumption of uniformly random phase. Delving back into the underwater acoustics application, characterizations of ambient noise and reverberation are presented along with a number of heavy-tailed distribution models capable of representing real data with more fluctuations than expected from the Gaussian models. The chapter then ends with a presentation of four standard signal models along with the means to evaluate their distribution functions.

Armed now with statistical models for both signals and noise, the focus shifts to deriving detectors for various signal types. Owing to the general applicability of many signal processing techniques, it is common to describe algorithms generically and then how they apply to different problems. Because of the focus in this text on the underwater acoustics application, a different approach is taken where the various types of signals expected to be encountered are categorized and then detectors are derived for each category. Three broad categories have been identified as covering the majority of signals encountered in underwater acoustics: (1) signals with known form, (2) signals with unknown form, and (3) signals with unknown duration and starting time. Detectors for these signal types under various assumptions in the time, frequency, consistency, and knowledge dimensions are derived in Chaps. 8–10 using the standard design approaches described in Chap. 6. In addition to deriving detection algorithms, techniques for evaluating their performance are presented along with several other practical topics such as normalization and the estimation of signal parameters. In an important connection to the sonar equation that is presented in Chap. 2, the detection threshold (DT) term describing the SNR required to achieve a specific performance is related to the probability of detection and probability of false alarm for common signal types and their detectors.

Signals of known form, which are most common in active remote sensing and communications applications, are shown to require *matched filters* for detection in Chap. 8. When there is mismatch between the assumed form of the signal that is used in the detector and the form measured at a sensor, there is a loss in performance. The waveform autocorrelation and ambiguity functions characterize this as a function of a mismatch in time and Doppler scale. These are presented for the most common active sonar waveforms: continuous wave (CW) pulses and linear- and hyperbolic-frequency-modulated (LFM and HFM) pulses. The ambiguity function also provides information on the resolution capability of the waveforms and can be used to describe the accuracy of unbiased estimators through the Cramér-Rao Lower Bound (CRLB) on the variance. CRLBs are derived for the time and Doppler parameters using the standard active-sonar waveforms as

examples. The bounds for estimating Doppler, both when the delay is known and when it is not, are presented using Doppler scale rather than Doppler shift. This supports application to broadband-Doppler-sensitive waveforms and simplifies to the standard Doppler-shift results for narrowband waveforms. The chapter closes covering practical aspects of detection for signals with known form: normalization to account for an unknown background power, accounting for an unknown Doppler through Doppler filter banks, and characterizing and accounting for the temporal spreading of a signal induced by propagation.

In passive remote sensing the signals of interest usually have either an unknown or only partially known form. In Chap. 9 it is shown how such signals require *energy detectors* that are commonly implemented in the frequency domain. How the frequency-domain data are combined depends on how much is known about the signal and can result in an Eckart filter, a noise-normalized energy detector, or even a power-law energy detector. Before the frequency-domain data are combined they need to be normalized by the average noise power. Different techniques are presented for estimating the noise power and evaluating the effect on detection performance. Two of the localization approaches described in Sect. 2 require estimation of the time delay between broadband signals measured on different nodes in a distributed system or between different propagation paths between the source and sensor. The estimation algorithms, respectively a cross- and auto-correlation, are derived along with the CRLB to describe their performance limits. Parameter estimation for narrowband signals is also presented, including sinusoidal and narrowband Gaussian random signals.

The detectors derived for signals of known and unknown form in Chaps. 8 and 9 assume the signal exists in a fixed processing interval (e.g., the length of the signal with known form or the coherence time of a random signal). In most cases the starting time of the signal is unknown and in many cases its duration is also unknown. As shown in Chap. 10, such signals require *sequential detectors* where data are observed until enough evidence is accumulated to warrant declaring a signal is present. The various combinations of signal characterizations (e.g., known and unknown starting time and duration; short, intermediate and long duration) lead to algorithms such as M -of- N detectors, sliding M -of- N detectors, the sequential probability ratio test (SPRT), and Page's test. A key difference about these detectors from those already considered is that the amount of data required for detection changes from one realization to the next. By representing the number of samples used in the detection as a random variable, the appropriate performance measures can be evaluated. This includes the standard probability of detection for signals with a finite duration, but also requires evaluation of the average number of samples to characterize detection of long-duration signals and false-alarm performance.

To summarize, this text includes: an introduction to signal processing in underwater acoustics; a review of sonar systems, localization, and the sonar equation; the rudiments of underwater acoustics as they apply to signal processing; background material on linear systems, signal processing, and mathematical statistics; a process to describe and model underwater acoustic signals and noise in terms of their temporal and spectral characteristics, consistency over multiple observations, and

how much is known about them; and the derivation, analysis, and practicalities of matched filters for signals with known form, energy detectors for signals with unknown form, and sequential detectors for signals with unknown starting time or duration.

References

1. M. Denny, *Blip, Ping & Buzz: Making Sense of Radar and Sonar* (The Johns Hopkins University Press, Baltimore, 2007)
2. F.V. Hunt, Acoustic vs acoustical. J. Acoust. Soc. Am. **27**(5), 975–976 (1955)
3. M.W. Lawrence, P. Grenard, Hydroacoustic monitoring system for the Comprehensive Nuclear-Test-Ban Treaty, in *OCEANS '98 Conference Proceedings*, vol. 2 (1998), pp. 694–697
4. M.W. Lawrence, Acoustic monitoring of the global ocean for the CTBT, in *Proceedings of the Annual Conference of the Australian Acoustical Society* (2004), pp. 455–459
5. M.K. Prior, D.J. Brown, G. Haralabus, J. Stanley, Long-term monitoring of ambient noise at CTBTO hydrophone stations, in *Proceedings of 11th European Conference on Underwater Acoustics* (2012), pp. 1018–1025
6. Acknowledgement: The author thanks and acknowledges the Preparatory Commission for the Comprehensive Nuclear-Test-Ban Treaty Organization (CTBTO; <https://www.ctbto.org/specials/vdec/>) for providing access to the data used to produce these figures. The CTBTO is not responsible for the views of the author
7. W.H. Munk, R.C. Spindel, A. Baggeroer, T.G. Birdsall, The Heard Island feasibility test. J. Acoust. Soc. Am. **96**(4), 2330–2342 (1994)
8. R.J. Urick, *Principles of Underwater Sound*, 3rd edn. (McGraw-Hill, Inc., New York, 1983)
9. W.W.L. Au, M.C. Hastings, *Principles of Marine Bioacoustics* (Springer, Berlin, 2008)
10. R.S. Matoza, D. Fee, M.A. Garcés, J.M. Seiner, P.A. Ramón, M.A.H. Hedlin, Infrasonic jet noise from volcanic eruptions. Geophys. Res. Lett. **36**(L08303), 1–5 (2009)
11. R.S. Matoza, D. Fee, The inaudible rumble of volcanic eruptions. Acoust. Today **14**(1), 17–25 (2018)
12. Acknowledgement: These data were made possible by funding from the Office of Naval Research (Codes 321US and 322OA) and the CLUTTER Joint Research Project (JRP), including as Participants the NATO Undersea Research Centre (NURC), Pennsylvania State University—ARL-PSU (USA), Defence Research and Development Canada—DRDC-A (CAN), and the Naval Research Laboratory—NRL (USA). Scientist in charge: Dr. P. Nielsen
13. S.E. Parks, A. Searby, A. Célérier, M.P. Johnson, D.P. Nowacek, P.L. Tyack, Sound production behavior of individual North Atlantic right whales: implications for passive acoustic monitoring. Endanger. Species Res. **15**, 63–76 (2011)
14. W.S. Burdic, *Underwater Acoustic System Analysis*, 2nd edn. (Peninsula Publishing, Los Altos, 1991)
15. R.O. Nielsen, *Sonar Signal Processing* (Artech House, Inc., Norwood, 1991)
16. A.A. Winder, Underwater sound, a review: Part II-Sonar system technology. IEEE Trans. Sonics Ultrason. **22**(5), 291–332 (1975)
17. W.C. Knight, R.G. Pridham, S.M. Kay, Digital signal processing for sonar. Proc. IEEE **69**(11), 1451–1506 (1981)
18. J.C. Hassab, *Underwater Signal and Data Processing* (CRC Press, Boca Raton, 1989)
19. Y. Bar-Shalom, X.R. Li, T. Kirubarajan, *Estimation with Applications to Tracking and Navigation* (Wiley-Interscience, New York, 2001)
20. J.V. Candy, *Model-Based Signal Processing* (Wiley, New York, 2006)

21. Y. Bar-Shalom, P.K. Willett, X. Tian, *Tracking and Data Fusion: A Handbook of Algorithms* (YBS Publishing, Storrs, 2011)
22. L.D. Stone, R.L. Streit, T.L. Corwin, K.L. Bell, *Bayesian Multiple Target Tracking*, 2nd edn. (Artech House, Norwood, 2014)
23. C.M. Bishop, *Pattern Recognition and Machine Learning* (Springer Science, New York, 2006)
24. T. Hastie, R. Tibshirani, J. Friedman, *The Elements of Statistical Learning* (Springer, Berlin, 2009)
25. K. Fukunaga, *Statistical Pattern Recognition*, 2nd edn. (Academic, Boston, 1990)
26. S.C. Nardone, V.J. Aidala, Observability criteria for bearings-only target motion analysis. *IEEE Trans. Aerosp. Electron. Syst.* **AES-17**(2), 162–166 (1981)
27. V.J. Aidala, S.E. Hammel, Utilization of modified polar coordinates for bearings-only tracking. *IEEE Trans. Autom. Control* **28**(3), 283–294 (1983)
28. R.E. Kalman, A new approach to linear filtering and prediction problems. *Trans. ASME—J. Basic Eng.* **82**(Series D), 35–45 (1960)
29. R.E. Kalman, R.S. Bucy, New results in linear filtering and prediction theory. *Trans. ASME—J. Basic Eng.* **96**, 95–108 (1961)
30. A.B. Carlson, *Communication Systems* (McGraw-Hill, New York, 1986)
31. S.M. Murphy, P.C. Hines, Examining the robustness of automated aural classification of active sonar echoes. *J. Acoust. Soc. Am.* **135**(2), 626–636 (2014)

Chapter 2

Sonar Systems and the Sonar Equation



2.1 Introduction

The purpose of this chapter is to introduce several basic concepts related to sonar systems and their analysis through the sonar equation. The components of a sonar system are described in Sect. 2.2 along with examples of how they can be used to perform the localization inferential objective. The focus of Sect. 2.3 is the sonar equation, which is a performance evaluation of a sonar system in terms of the signal-to-noise power ratio (SNR). A key part of Sect. 2.3 lies in how to relate specific detection and localization performance measures to the SNR required to achieve them.

The material found in this chapter is presented as a brief overview of sonar systems in a remote sensing context and a review of sonar equation analysis. More detailed descriptions of sonar and sonar systems can be found in any of the several books written on the topic [1–4]. With the intent of motivating the need for the more detailed derivations and analysis of detection algorithms found in Part III, a very basic representation of the effects on acoustic waves as they propagate through the ocean environment has been assumed. This chapter should therefore be accessible to a wider audience, but also provide the means for a more detailed analysis when coupled with the more representative effects of the underwater acoustical environment presented in Chap. 3 and the derivation and analysis of detection algorithms found in Part III.

2.2 Remote Sensing with Sonar Systems

A *sonar system* is the set of hardware and software accomplishing the navigation and ranging remote-sensing objectives. In a more general context the set of hardware and software required to accomplish one of the objectives listed in Sect. 1.1.3 might be

called an underwater acoustical remote sensing system. However, the sonar acronym has come to represent the more general application, which in most cases will be similar to one of the many standard types of sonar systems.

In this section the basic components of a sonar system are described in Sect. 2.2.1. The differences between monostatic, bistatic, and distributed system geometries are articulated in Sect. 2.2.2 with more detail on bistatic sonar systems found in Sect. 2.2.4. A variety of localization techniques are described in Sect. 2.2.3, illustrating their dependence on the sensing modality, sonar system geometry, sensor-array design, and assumed propagation conditions. The section concludes with Sects. 2.2.5 and 2.2.6 where the Doppler effect, arising from motion of the sonar platform or object of interest, is explained.

2.2.1 Components of a Sonar System

The basic components of a sonar system, as depicted in Fig. 2.1, include a

- sound source,
- sensor array,
- telemetry,
- signal and information processing,
- display and analysis.

For active sonar systems, the sound source is a projector like an underwater loudspeaker, emitting a prescribed acoustic pulse called the *transmit waveform*. The sound projector is a *transducer* converting an electrical input voltage to an acoustic pressure. In passive sonar systems, the sound source is part of the state of nature being explored. It arises naturally and although it is an inherent part of the remote sensing application it is not a physical component of the sonar system.

For both active and passive sonar systems, sounds are measured underwater by sensors that are transducers converting acoustic pressure at a specific point in space to a voltage signal. Such transducers are essentially underwater microphones and known as *hydrophones*. The spatial period of a spatially periodic underwater

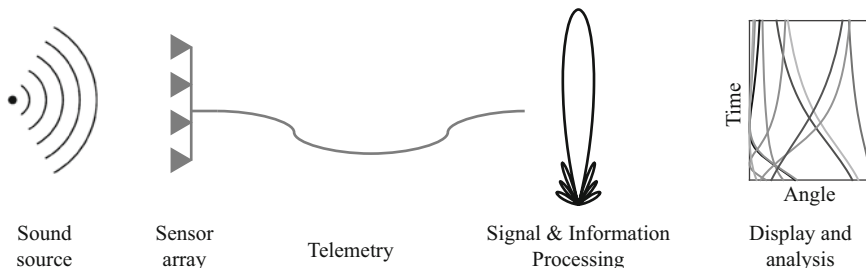


Fig. 2.1 Components of a sonar system

acoustic wave is called the wavelength (see Sect. 3.2.2.1). Assuming the speed of sound underwater is $c_w = 1500 \text{ m/s}$, a wavelength ($\lambda = c_w/f$) is

- 150 m at 10 Hz,
- 15 m at 100 Hz,
- 1.5 m at 1 kHz,
- 15 cm at 10 kHz, and
- 1.5 cm at 100 kHz.

When a hydrophone is small relative to a wavelength (e.g., a hydrophone with a diameter of 2-cm is small even at 10 kHz), its response is nearly constant in frequency and with respect to the angle at which it is ensonified (i.e., it has omnidirectional response). Owing to the mechanics of converting acoustic pressure to an electrical voltage (e.g., see [2, Sect. 3.2.1] or [5, Sect. 4.1.3] for the equivalent electrical circuit of a hydrophone) there is a low-frequency cut-off, though it is often no more than a few hertz which is more than adequate for most underwater acoustic applications. The high-frequency cut-off, which can be in the 10 s to 100 s of kilohertz, is dictated by the size of the hydrophone, which at some point becomes appreciable relative to the wavelength. The importance of a flat frequency response lies in capturing the acoustic pressure accurately as a voltage to which signal processing may be applied in order to extract the state of nature from the measurements.

Hydrophones are typically arranged in groups and called a sensor *array*. Sampling the acoustic field spatially by separating the hydrophones can improve sonar performance when the signals from the object of interest are stable over a larger physical scale than the ambient noise or when there is an interference impinging on the sensor array from a different direction than the signal from the object of interest. However, a sensor array cannot be made arbitrarily large owing to not only the engineering constraints but also the diminishing return encountered when the scale of the array exceeds the spatial stability of the signal from the object of interest. The physical configuration of the sensors in an array depends on both the remote-sensing application and the physical constraints of the sonar platform [5, Sect. 1.5]. For example, arrays towed behind ships are usually configured with sensors equally spaced in a line [6, Sect. 1.4], [7]. Towing the array behind the ship keeps it away from ship-generated noise which improves remote sensing performance, but creates an additional problem in that the sensor signals need to be conveyed to a processing unit on the ship. The combined process of automatically measuring acoustic pressure and communicating the signals to a physically displaced processor is called *telemetry* and is a common part of remote sensing systems.

The image in Fig. 2.1 chosen to represent signal and information processing is that of a beampattern arising from processing the signals measured on an array of sensors. There are many other topics within the signal and information processing component as described in Sect. 1.1.6. The final image in Fig. 2.1 under *display*

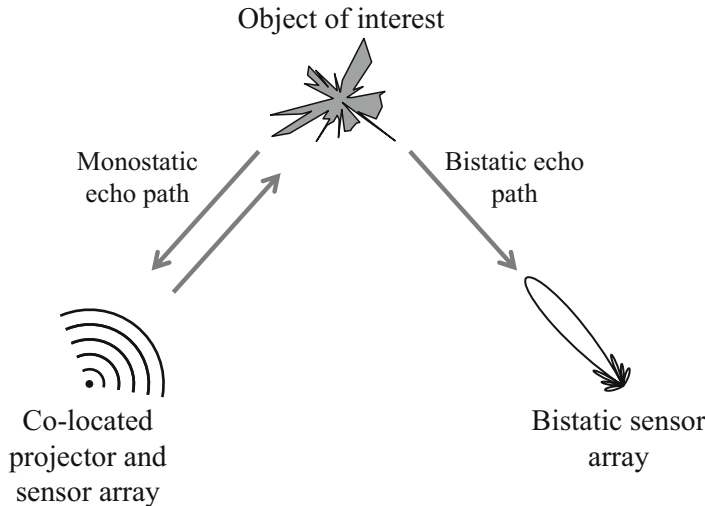


Fig. 2.2 Monostatic and bistatic sonar configurations (top-down view)

and analysis is that of a bearing-time record (BTR) representing the intensity of acoustic pressure measured by a passive sonar array as a function of time and angle. Although display techniques are not a focus point here, conveying information obtained through remote sensing is an important part of any sonar system.

2.2.2 **Monostatic, Bistatic, and Distributed Sonar Systems**

Sonar systems are used in what is inherently a time-varying 3-dimensional (3-D) environment. Let the horizontal axes (x, y) represent, respectively, the local longitudinal and latitudinal directions. Define the vertical axis z as depth with positive values pointing down from the sea surface, which is defined as being at $z = 0$. Depending on the application, different subsets of the dimensions will take priority. For example, the primary focus of a depth-sounder is the z dimension whereas a search or surveillance sonar would focus on the horizontal plane, (x, y). The majority of examples considered in this text focus on the horizontal plane and view depth as secondary information. In a 2-D horizontal plane the sensor is usually considered at the origin and polar coordinates (r, θ) are as common as their Cartesian counterparts. The distance r from the sensor to the object of interest is called the *range* whereas θ is the relative angle from some predefined angular origin (e.g., north or the platform heading if the sensor is attached to a moving body).

Most sonar systems, as described in Sect. 2.2.1, are single units operating from one place or platform (e.g., a single fixed installation, ship, autonomous vehicle, or buoy) although the processing or display and analysis can be performed remotely.

When the sound projector and sensor in an active sonar system are close enough together to assume they are co-located (as occurs when the same transducers are used both to project sound and measure it), the configuration is called a *monostatic* geometry. In the monostatic sonar geometry shown in Fig. 2.2, both the sound ensonifying the object of interest and the ensuing echo propagate along the same part of the ocean. By appealing to reciprocity of acoustic propagation (see Sect. 3.2.9), which dictates that the effects of propagation from point A to point B are the same as propagating from point B to point A, the processing and analysis of monostatic sonar geometries is simplified compared to bistatic geometries.

When the projector and sensor in an active sonar system are placed far enough apart to violate reciprocity of the acoustical paths, the sonar geometry is considered *bistatic* as opposed to the monostatic geometry of the co-located scenario. Although localization in bistatic active sonar systems [8] is more complicated than in monostatic systems (see Sect. 2.2.4), they can be designed to provide more robust detection performance [9].

When a sonar system comprises multiple sensor arrays spaced some distance apart, it is called a *distributed* sonar system. For example, the CTBTO underwater acoustical monitoring system includes a number of three-hydrophone stations [10] placed around the world. Distributed systems bring an additional complexity to telemetry, requiring either raw data, partially processed data, or sensor-level decisions to be communicated to a central processing station for fusion into a final analysis product. While distributed systems can be both passive and active, they solve a difficult problem for passive sonar with respect to localization as discussed in the following section.

2.2.3 *Localization: Estimating the Position of a Sound or Scattering Source*

After signal detection, the most basic and ubiquitous inferential objective in underwater acoustic signal processing is localization. Localization techniques are driven by the following conditions:

- remote-sensing modality (active or passive),
- sonar system configuration (single stationary platform, platform in motion, or distributed system),
- sensor-array design (number and arrangement of sensors), and
- the assumed propagation conditions (near-field, far-field, or multiple paths/modes).

The impact of these conditions on localization is so important that the design of a sonar system can be driven by what is required to achieve a localization performance specification.

Ideally the location of the object of interest is determined in all three spatial dimensions. Achieving this, however, is the exception rather than the rule as most systems are not capable of estimating all three dimensions. Because of this, the coordinate system is usually adapted to the capabilities of a specific system. Common situations will be described as the impact of each of the above conditions on localization is discussed. With the large number of possible localization scenarios, only the most basic scenarios are introduced. Unless noted otherwise, sensors are assumed to be omni-directional hydrophones, sonar systems and objects of interest are assumed to be stationary, and acoustic propagation is assumed to occur in the *basic ocean model* described in Sect. 3.2 consisting of a homogenous, lossless, and dispersionless transmission medium with no boundaries.

2.2.3.1 Active vs. Passive Localization

The primary advantage of an active sensing system over a passive one lies in the ability to infer range, even with a single stationary sensor. When the object of interest is far from the sensor array, a passive sonar system can only estimate the direction from which the sound arrives at the array. Active sonar systems allow estimation of the time an acoustic pulse takes to travel from a sound projector to an object of interest and then on to a sensor. For a monostatic sonar system, this is two times the one-way travel time and allows estimation of the range from the sonar system to the object of interest as

$$r = \frac{c_w \tau}{2} \quad (2.1)$$

where τ is the two-way travel time and c_w is the speed of sound in water, which is assumed to be constant.

When both the sound projector and sensor are omni-directional, knowing the range r localizes the object of interest to a sphere of radius r about the sonar. In the search or surveillance situation where the (x, y) plane is of primary interest the sphere becomes a circle of radius r in the horizontal plane assuming the sonar and object of interest are at the same depth and the propagation paths are horizontal. Without additional information, it is not known where on the circle the object of interest might lie. Any point on the circle produces the same two-way travel time.

In a bistatic active sonar system, propagation from the object of interest to the sensor is different from that between the sound projector and the object of interest. Because of this difference, localization results in an ellipsoid (specifically, an ellipse rotated about its major axis) rather than a sphere in 3-D or an ellipse in the 2-D scenario. The bistatic equal-travel-time ellipse and other information related to bistatic active sonar systems are described in Sect. 2.2.4.

More realistically, the acoustic waves do not propagate in straight lines or at constant speeds, so (2.1) is an approximation.

2.2.3.2 Array Design and Angle Estimation

Recall from Sect. 2.2.1 that a hydrophone has an omnidirectional response when it is small relative to a wavelength. If the length of a cylindrical hydrophone is made large relative to a wavelength, the response is no longer omnidirectional but has greater sensitivity to sound arriving from the direction perpendicular to the axis of the cylinder, which is called the broadside direction. Signals arriving from angles more closely aligned to the hydrophone axis are attenuated relative to the broadside direction. Of course making a hydrophone exceed even one wavelength at low frequencies is not feasible. Fortunately, an array of omni-directional hydrophones arranged in a line (i.e., co-linearly) approximates this response which has width inversely related to the extent of the array. Because of this directional sensitivity, the direction of arrival of an acoustic signal impinging on a sensor array can be estimated through the array signal processing technique called beamforming.

With the line-array design, the angle being estimated represents a cone. That is, signals impinging on a line array from anywhere on a cone at angle θ to the array axis appear the same. The rotational angle cannot be estimated and is therefore ambiguous. For a passive sonar system with a line array, both range and rotational angle are ambiguous (i.e., the cone in Fig. 2.3). For an active sonar system, only the rotational angle is ambiguous as range can be obtained from time delay as previously described. Recall that in a search/surveillance scenario, the emphasis is on locating the object of interest in the (x, y) plane. When the line array is horizontal and it can be assumed that most of the acoustic energy arrives at the line array near the horizontal plane (e.g., when the distance between the sonar and object of interest is large), the cone of ambiguity simplifies to lines for passive sonar or points for active sonar at angle θ to the left and right sides of the array (i.e., the so-called left/right ambiguity).

The line array only has sensors in one dimension (1-D). As might be expected, placing sensors in 2-D (i.e., a planar array) and 3-D (a volumetric array) reduces

Fig. 2.3 Line array and cone of ambiguity

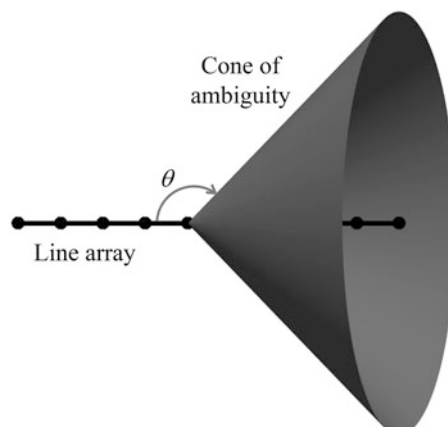
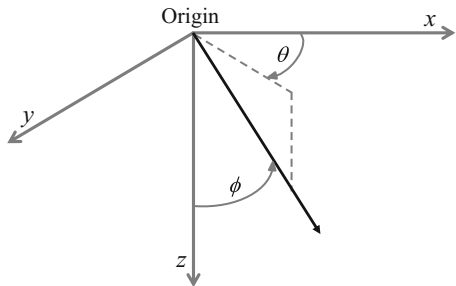


Fig. 2.4 Coordinate system definition. The vertical (z) axis is positive when pointing down with the ocean surface at $z = 0$. θ is the angle from the positive x axis in the (x, y) plane and ϕ is the angle from the positive z axis



localization ambiguity. The coordinate system used in this book is shown in Fig. 2.4. The (x, y) plane is generally taken as horizontal so θ is an azimuthal angle. Note that the positive vertical axis (z) points down under the assumption that the surface is at $z = 0$. The vertical angle ϕ is defined as originating from the positive z axis. However, it is common to describe vertical angles as relative to horizontal (e.g., $\tilde{\phi} = \pi/2 - \phi$). In such cases, angles pointing down from horizontal are called depression angles and those pointing up are elevation angles.

Conversion from spherical coordinates to and from Cartesian is accomplished by

$$\begin{aligned} x &= r \sin \phi \cos \theta, \\ y &= r \sin \phi \sin \theta, \text{ and} \\ z &= r \cos \phi \end{aligned} \tag{2.2}$$

and

$$\begin{aligned} r &= \sqrt{x^2 + y^2 + z^2}, \\ \theta &= \arctan(y/x), \text{ and} \\ \phi &= \arctan\left(z^{-1}\sqrt{x^2 + y^2}\right). \end{aligned} \tag{2.3}$$

2.2.3.3 Localization with Distributed and Moving Sonar Systems

The passive ranging problem can be resolved by using multiple sensor arrays (called nodes) placed so as to allow triangulation of the two angle measurements as depicted in Fig. 2.5a. When individual nodes have localization ambiguities (e.g., the left/right ambiguity of a line array), the distributed-system localization can also

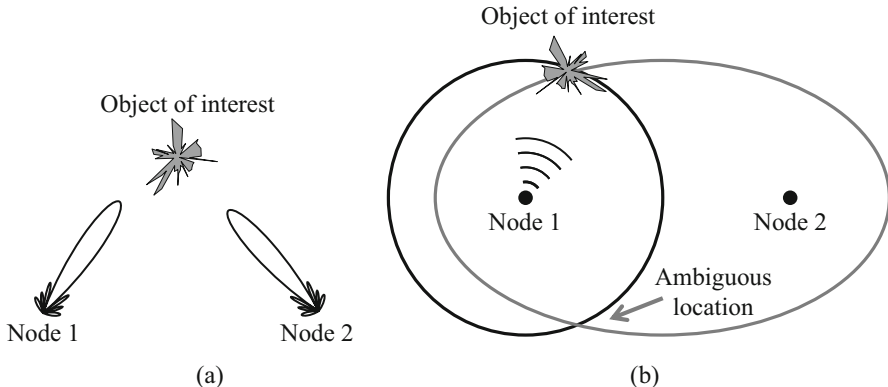


Fig. 2.5 Localization in distributed systems. (a) Triangulation in a passive distributed system. (b) Time-delay localization in an active distributed system

have ambiguities (e.g., two line arrays would produce up to four potential locations for an object of interest).

When there is only a single hydrophone at each node in a passive sensing system there is no means to measure the direction of arrival; triangulation is not possible. However, measurement of the difference in the time of arrival of a signal at two different nodes results in a hyperbolic line of location [11]. That is, the sound source must lie on a hyperbola defined by the two node locations and the time-of-arrival difference. Combination of multiple such time-of-arrival difference measurements and their associated lines of location allows localization through a process called *multilateration*,¹ as depicted for a horizontal application in Fig. 2.6. Accurate measurement of the time differences requires broadband signals and a cross-correlation processor as described in Sect. 9.4.1.

For a distributed active system, equal-travel-time circles and ellipses can be used with omni-directional sensors to localize an object as shown in Fig. 2.5b. In the depiction, Node 1 is a monostatic active system producing an equal-travel-time circle and Node 2 is the sensor array of a bistatic sonar configuration (using the sound projected by Node 1) producing an equal-travel-time ellipse. The circle and ellipse intersect at two points, one of which would be the location of the object of interest.

Theoretically, using additional nodes in a distributed system can resolve localization ambiguities as the ambiguous locations for different node pairs will generally not be coincident. However, localization errors complicate the problem even for two nodes. Common sources of error include those from estimating the angle of arrival or travel time of the acoustic signal, errors in the knowledge of node locations and

¹Multilateration is the same localization technique as that used in the long-range navigation (LORAN) system.

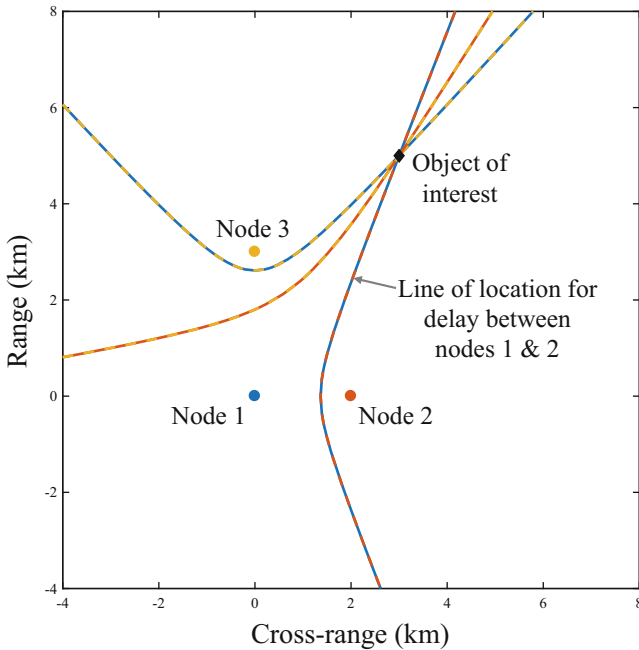
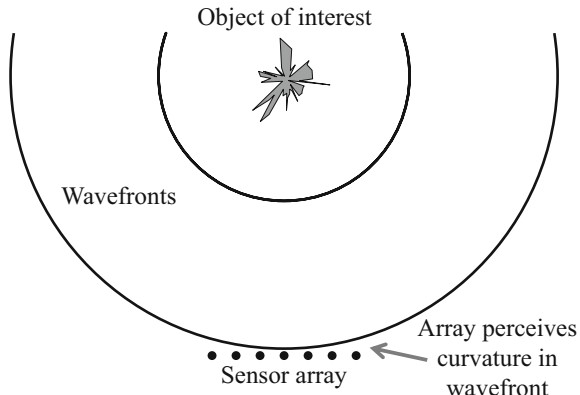


Fig. 2.6 Localization by multilateration using time-of-arrival difference measurements between pairs of nodes

orientations, and errors in the assumptions about sound speed and the conversion from travel-time to range. The errors can be large enough that point estimates from three nodes will often not produce a common intersection without accounting for the aforementioned errors.

In the examples depicted in Fig. 2.5, measurements from the different nodes are taken at the same time. However, the same principles apply if the object of interest is stationary and multiple measurements are taken from a single moving sonar platform. When the object of interest is moving, localization can still be performed by using a parametric model of the motion (e.g., constant velocity). Use of a motion model is equivalent to estimating not only the location but also the velocity (speed and course) of the object of interest, which allows predicting where it will be in the future. The process of associating and combining localization estimates over multiple consecutive temporal epochs to estimate the position, course, and speed of objects of interest describes the field of *target tracking* [12].

Fig. 2.7 Wavefront curvature and passive ranging



2.2.3.4 Localization and the Effects of Propagation

The localization techniques previously described assumed very simple conditions with respect to the environment and that the object of interest was far from the sensor array. Suppose, however, the object of interest is close enough to the sensor array for the curvature of a spherical acoustic wavefront to be measurable as depicted in Fig. 2.7. In this situation, the object of interest is said to be in the *near-field* of the sensor array (described more precisely in Sect. 3.2.2.5) and means range can be estimated with a passive sonar. The signal processing algorithm exploiting this condition, known as wavefront-curvature beamforming [13, 14] forms beams as a function of both angle of arrival and range where the curvature differences at different ranges provide enough discrimination to estimate range. As would be expected, performance degrades as range increases and the object of interest moves from the near-field to the far-field of the sensor array.

In shallow water, spherical propagation can only extend to the point where the wavefront encounters a boundary. Beyond this point propagation can be much more complicated, which is both good and bad. When the propagation channel is complicated enough, it can encode the location of the object of interest in the imprint it leaves on the acoustic signal. For example, consider the multiple-path propagation scenario of [2, Ch. 15] as shown in Fig. 2.8 where sound from an object of interest near the surface at range r propagates to the sensor array along two different paths. If z_a is the depth of the sensor array and z_b the bottom depth, the two paths effectively produce *image* sensors at depths $2z_b - z_a$ and $2z_b + z_a$ (see Sect. 3.2.8.1 for more information on image sources). The path-length difference can then be obtained as a function of the range r of the object of interest,

$$\delta_r = \sqrt{r^2 + (2z_b + z_a)^2} - \sqrt{r^2 + (2z_b - z_a)^2}. \quad (2.4)$$

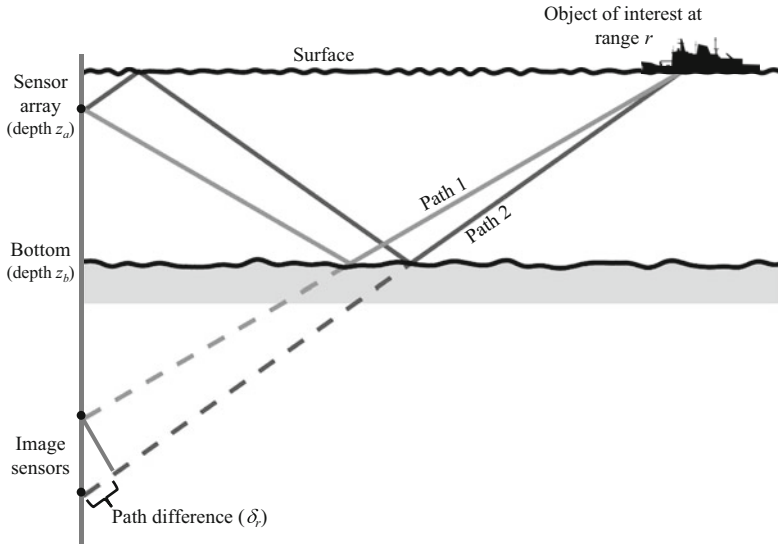


Fig. 2.8 Multipath passive ranging example (adapted from Burdic [2, Fig. 15-6], 1991, Peninsula Publishing, with permission)

When the range r is much larger than the bottom depth, (2.4) can be inverted using a first-order Maclaurin series approximation to obtain range as a function of the sensor-array and bottom depths and the path-length difference,

$$r \approx \frac{4z_a z_b}{\delta_r}. \quad (2.5)$$

The path-length difference can be obtained from the path time-delay difference as $\delta_r = \delta_\tau c_w$ and δ_τ can be estimated from an autocorrelation analysis of the acoustic signal measured by the sensor array. As described in Sect. 9.4.2, this requires a broadband signal from the object of interest. Measurement of two path-length differences allows localization in both range and depth [15, 16].

In shallow water and at lower frequencies, propagation may be more appropriately represented using a normal-mode solution to the wave equation in a waveguide than the ray-based solution exploited in the previous example (e.g., see Sect. 3.2.8). In these conditions the waveguide invariant [17, Sect. 2.4.6], which characterizes a coupling in range and frequency, can be used to estimate range (e.g., see [18, 19]).

The examples of this section illustrate how the effects of propagation can be exploited to enable passive localization of the object of interest with a sensor array. Research in the area of matched-field processing (e.g., see [20, 21]) extends these techniques to more complicated propagation conditions and includes estimating the depth of the object of interest as well as any unknown environmental parameters. Exploiting the effects of propagation to perform localization is a difficult task requir-

ing balance between adequately representing propagation and using a propagation model simple enough that all the model parameters can be obtained accurately.

2.2.4 Bistatic Active Sonar

In a bistatic active sonar system [8] the sound projector and sensor array are physically separated. Sound travels from the projector to the object of interest, reflects off the object of interest, and travels to the sensor array. Suppose only the time delay τ between sound projection and measurement of the reflection at the sensor array is estimated. If the distance from the sound projector to the object of interest is r_S and from the object of interest to the sensor array is r_R (the subscript R denotes receiver) and the speed of sound is a constant c_w , then the travel time is

$$\tau = \frac{r_S + r_R}{c_w} \quad (2.6)$$

and the distance traveled by the sonar pulse is $r = r_S + r_R = c_w \tau$. For a monostatic system, the range $r_M = r_S = r_R$ and (2.6) clearly simplifies to produce (2.1), $r_M = c_w \tau / 2$.

For a given total distance travelled (r) the locus of points in the (x, y) plane at which the object of interest might be located is described by an ellipse formed with the sound projector and sensor array at the foci as shown in Fig. 2.9. If the distance between the sound projector and sensor array (i.e., the baseline) is r_B , the major and minor axes are, respectively

$$2a = r \quad (2.7)$$

and

$$2b = \sqrt{r^2 - r_B^2}. \quad (2.8)$$

The equi-travel-time ellipse is then defined by (x, y) satisfying

$$\frac{x^2}{a^2} + \frac{y^2}{b^2} = 1. \quad (2.9)$$

As signal processing is performed on data from the sensor array, it is convenient to put the equi-travel-time ellipse equation into a receiver-centric coordinate system. That is, in terms of range r_R of the object of interest from the sensor array and the relative angle θ pointing at the object of interest from the direction of the sound projector. The sensor array measures both the *direct blast*, which is the projected sound impinging on the sensor array through the most direct (i.e., shortest) propagation path, and the echo from the object of interest. If τ_B is the travel time of

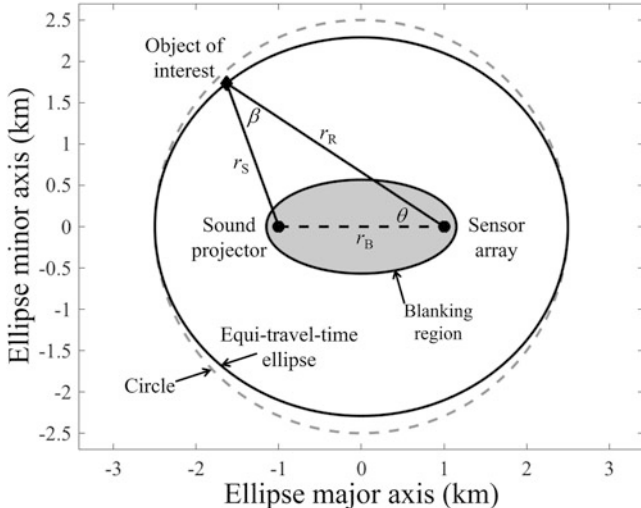


Fig. 2.9 Bistatic active sonar geometry

the direct blast from the sound projector to the sensor array, the time difference between these two arrivals, $\tau_M = \tau - \tau_B > 0$, produces what is called an equivalent monostatic range [8],

$$r_M = \frac{c_w(\tau - \tau_B)}{2} = \frac{r_s + r_R - r_B}{2}. \quad (2.10)$$

Using (2.10) along with the law of cosines (relating θ to r_s , r_R , and r_B), the receiver-centric coordinate system produces the range equation

$$r_R = r_M \left[\frac{1 + r_B/r_M}{1 + 0.5(1 - \cos \theta) r_B/r_M} \right]. \quad (2.11)$$

Given the measured time delay difference τ_M and therefore r_M , varying $\theta \in [0, 2\pi]$ produces the same locus of points as those satisfying (2.9). Examining (2.11), it can be seen that $r_R \rightarrow r_M$ as $r_B \rightarrow 0$ or as $r_M \rightarrow \infty$. That is, the equation simplifies appropriately in the monostatic case ($r_B = 0$) and the monostatic case is a good approximation when r_M is large relative to the baseline, r_B .

In both monostatic and bistatic active sonar systems, the direct blast can exceed the linear regions of amplifiers in the sonar telemetry or the dynamic range of the analog-to-digital converters. When this occurs, the sensor array is considered blanked (ineffective) until $\tau_B + T_p$ where T_p is the duration of the transmit waveform. As such, listening for echoes can only begin after $\tau_B + T_p$ so $\tau > \tau_B + T_p$ and the minimum equivalent monostatic range is

$$r_M \geq \frac{c_w T_p}{2}, \quad (2.12)$$

which also represents the minimum un-blanked range for a monostatic sonar system. Using the minimum value of r_M from (2.12) in (2.11) produces the blanking region as shown in Fig. 2.9.

Exercise 2.1 For the bistatic sonar configuration shown in Fig. 2.9, show that if $x = a \cos \phi$ and $y = b \sin \phi$ with a and b as defined in (2.7) and (2.8) the distance from the sound projector to the object of interest and then to sensor array is r .

2.2.4.1 Active Sonar Resolution Cell

Similar to a monostatic sonar system, when the sensor array is such that the direction of arrival θ of the echo can be estimated through beamforming, then the object of interest can be localized to a specific point in (x, y) rather than an equal-travel-time ellipse. Although a point estimate is obtained for the range and bearing of the object of interest relative to the sensor array, uncertainty in the estimate is in part related to the size of the sonar resolution cell, which is the region in range-and-bearing space isolated by spatial and temporal signal processing. Beamforming isolates the object of interest to within the beamwidth ψ of the beamformer and temporal processing (matched filtering) to within $\delta_r = c_w T_r / 2$ in range where T_r is the temporal resolution of the transmit waveform after matched filtering. As discussed in Sect. 8.5.1, T_r is generally one over the bandwidth of the waveform.

If the object of interest is at range r , then the area of the sonar resolution cell for a monostatic sonar is approximately the product of the down-range extent δ_r and the length of the arc subtended by the beamformer,

$$A_M = \delta_r r \psi \left(1 + \frac{\delta_r}{2r} \right) \approx \delta_r r \psi. \quad (2.13)$$

The approximation represents the sonar resolution cell as a rectangle and is adequate when the down-range extent is small relative to the range.

For a bistatic sonar, the shape of the equi-time-delay ellipses can make the resolution cell more like a parallelogram than a rectangle [22, Sect. 5.6.1], as can be seen in Fig. 2.10. The sides of the parallelogram are $\delta_r / \cos(\beta/2)$ and $r\psi / \cos(\beta/2)$ where β is the bistatic angle, which from the perspective of the object of interest is the angle between the sensor array and the sound projector (see Fig. 2.9). Based on the parallelogram approximation, the area of the bistatic sonar resolution cell is

$$A_B = \frac{\delta_r r \psi}{\cos^2(\beta/2)}, \quad (2.14)$$

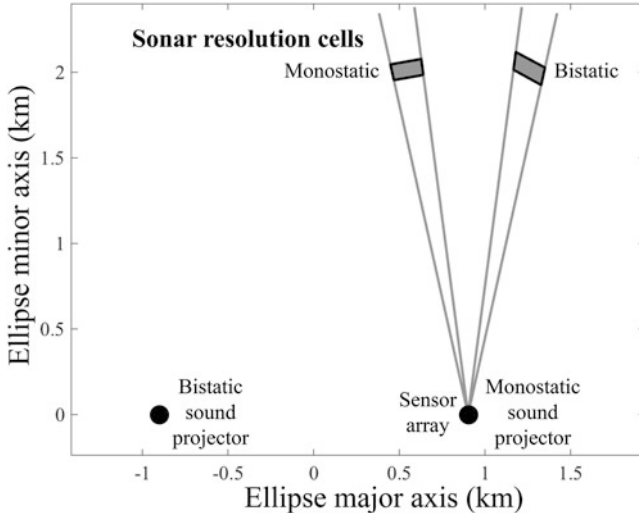


Fig. 2.10 Sonar resolution cell shapes for monostatic and bistatic geometries

which is greater than A_M except when $\beta = 0$, which results in a monostatic sonar geometry. Similar to the rectangle approximation of the monostatic geometry, the parallelogram approximation requires the range-to-baseline ratio to be large.

2.2.5 Doppler Scale and Shift

When an object of interest and/or a sonar platform is in motion the acoustic signals incident on an object of interest or measured by a sensor are altered by the Doppler effect. The effect of the motion on the measured signals can be determined by evaluating the intersection between the space-time trajectories of the acoustic wavefront and observation point or measurement platform (e.g., see Sect. 2.2.5.1 or [23, Ch. 2]) or by solution of the inhomogeneous wave equation for a moving source (e.g., see Sect. 3.2.3.3 or [24, Sect. 11.2]). Suppose the object of interest emits a signal $s(t)$ either as indigenous sound or by scattering an incident active sonar pulse. The signal measured by a sensor, assuming the previously described basic ocean environment, is a delayed and scaled version of the emitted signal,

$$x(t) = a(t)s(t - \tau(t)), \quad (2.15)$$

where the amplitude $a(t)$ and delay $\tau(t)$ are in general time-varying. The delay describes which part of the wavefront the sensor intersects at time t whereas the amplitude represents the change in the pressure envelope from spreading (e.g., $1/r$ for spherical or $1/\sqrt{r}$ for cylindrical). Generally, $a(t)$ will vary slowly and can

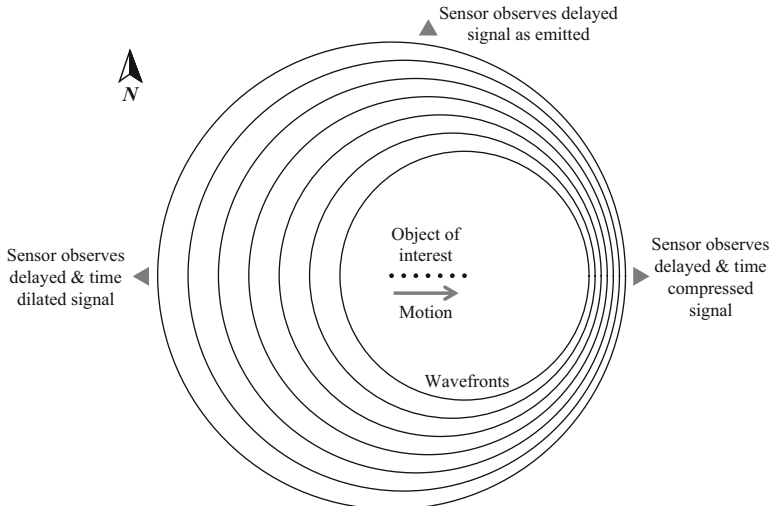


Fig. 2.11 Doppler: the effect of motion on acoustic wavefronts

be assumed a constant \bar{a} over the duration of an active sonar pulse or a coherent processing interval in passive sonar. In the simple example shown in Fig. 2.11, the object of interest is moving east with constant speed. Consider the observation point to the north where the range r between the object of interest and the sensor is essentially constant with time. For this case the time delay $\tau(t)$ is approximately constant at r/c_w and the sensor observes a delayed version of the signal as it was emitted.

At the observation point to the east, the wavefronts appear more rapidly than to the north as the object of interest is moving closer over time. The measured signal is subjected to a time compression and has the form

$$x(t) = \bar{a}s(\eta t - \eta\tau_0) = \bar{a}s(\eta(t - \tau_0)) \quad (2.16)$$

where $\tau_0 = r/c_w$ is the time delay associated with the initial range and η is a time scale parameter,

$$\eta = \frac{c_w}{c_w - v_0}, \quad (2.17)$$

related to the speed of sound in water and the speed of the object of interest (v_0) toward the observation point. When $\eta > 1$ the measured signal is a time-compressed version of the emitted signal. Conversely, when $\eta < 1$ the signal undergoes a time dilation.

If the emitted signal is a sinusoid with frequency f_0 , the measured signal is also a sinusoid,

$$\begin{aligned} x(t) &= \bar{a} \cos(2\pi f_0(\eta t - \eta \tau_0)) \\ &= \bar{a} \cos(2\pi(f_0 \eta)(t - \tau_0)), \end{aligned} \quad (2.18)$$

but with a frequency $f_1 = f_0 \eta$. When v_0 is positive (i.e., the range between the object of interest and the sensor is decreasing), $\eta > 1$ and $f_1 > f_0$. When v_0 is negative (i.e., the range between the object of interest and the sensor is increasing), the measured signal is a time-dilated version of the emitted signal, $\eta < 1$, and the perceived frequency f_1 is less than the emitted frequency f_0 .

In underwater acoustics, most sonar platforms and objects of interest move much more slowly than the speed of sound. For example, a container ship might travel at 25 kn (12.8 m/s) which is less than 1% of the nominal speed of sound (1500 m/s) in the ocean. When v_0/c_w is small, the approximation

$$\eta \approx 1 + \frac{v_0}{c_w} \quad (2.19)$$

is accurate and leads to the *Doppler shift* (for one-way propagation)

$$\Delta_f = f_1 - f_0 \approx \frac{v_0 f_0}{c_w}. \quad (2.20)$$

This describes the difference between the perceived frequency of an emitted sinusoid and the original frequency. For a monostatic active sonar system where an echo propagates back to the sonar on reciprocal paths, a case considered in more detail below, the Doppler shift is twice that shown in (2.20),

$$\delta_f = 2\Delta_f \approx \frac{2v_0 f_0}{c_w}. \quad (2.21)$$

When both the object of interest and sonar platform are in motion, the velocity v_0 is replaced by the relative radial velocity Δ_v such that $\Delta_v > 0$ represents closing range and $\Delta_v < 0$ opening range.

Although a frequency shift is an accurate representation for how Doppler affects a sinusoidal signal, it is not necessarily so for a broadband signal. From the time-scaling property of the Fourier transform (see Sect. 4.3), the effect of a time scale in the frequency domain is an inverse scale on both frequency and amplitude. If $S(f)$ is the Fourier transform of $s(t)$, then the Fourier transform of the observed signal subject to a Doppler scale η is

$$X(f) = \frac{\bar{a}}{|\eta|} S\left(\frac{f}{\eta}\right) e^{-j2\pi f \tau_0}. \quad (2.22)$$

The linear phase term in (2.22) (i.e., the $e^{-j2\pi f \tau_0}$) arises from the delay. If the emitted signal had duration T_p and bandwidth W centered at f_c , then a Doppler scale η produces a signal with duration T_p/η and a spectrum centered at ηf_c but

with bandwidth ηW . If the Doppler-shift approximation had been applied to the broadband waveform, it would result in a waveform with bandwidth W . Although the total change in bandwidth might be small, it can have a large impact on broadband Doppler sensitive waveforms.

2.2.5.1 Doppler Effect via Waveform and Platform Trajectories

The precise temporal effect of motion on the measured signal can be assessed by determining when the wavefronts of the sound emitted by the sound projector intersect the trajectory of the sensor (e.g., see [23, Ch. 2]). Suppose both the sound emitter (platform A in Fig. 2.12) and sensor (platform B) are in motion in such a way that they have constant range rate (i.e., the distance separating them changes linearly with time), their distance from an arbitrary reference point along the line connecting them can be described as

$$r_i(t) = \bar{r}_i + v_i t \quad (2.23)$$

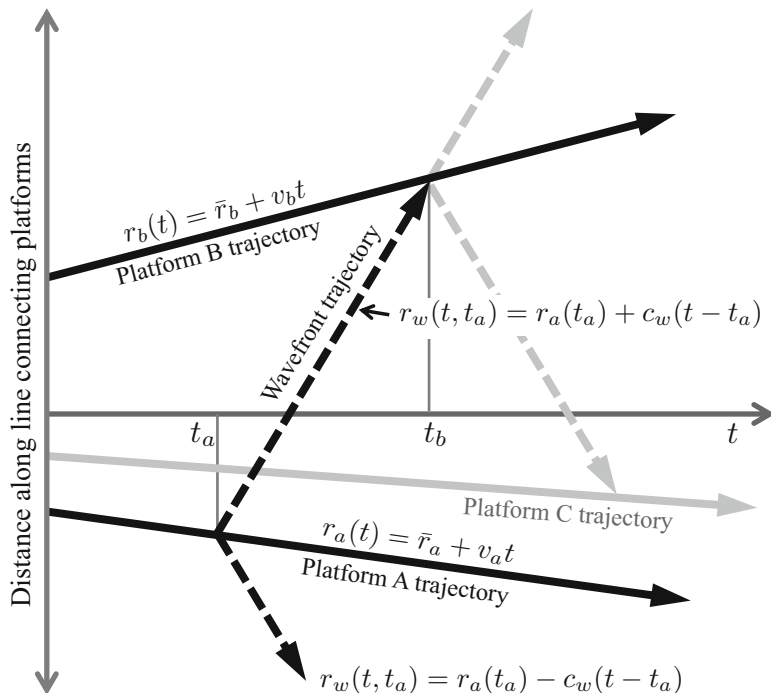


Fig. 2.12 Platform and wavefront trajectories for the constant-radial-velocity model

for $i = a$ and b , as depicted in Fig. 2.12. If platform A emits a signal at time t_a , the acoustic wavefront propagates in both directions along the connecting line with speed c_w as represented by the dashed lines in Fig. 2.12, so its location at time $t \geq t_a$ is

$$r_w(t, t_a) = r_a(t_a) \pm c_w(t - t_a). \quad (2.24)$$

At time t_b , platform B observes the signal emitted from platform A at time t_a if the trajectories of platform B and the wavefront coincide. Using (2.23) and (2.24) to solve for t_a results in

$$t_a = \left(\frac{c_w - v_b}{c_w - v_a} \right) t_b - \left(\frac{\bar{r}_b - \bar{r}_a}{c_w - v_a} \right) \quad (2.25)$$

where it has been assumed $r_b(t_a) > r_a(t_a)$ so the + of the \pm in (2.24) is used. In terms of the delay-and-time-scale form of (2.16), $x(t_b) = s(t_a) = s(\eta(t_b - \tau_0))$, the Doppler scale is

$$\eta = \frac{c_w - v_b}{c_w - v_a} \quad (2.26)$$

and the delay is

$$\tau_0 = \frac{\bar{r}_b - \bar{r}_a}{c_w - v_b}. \quad (2.27)$$

The above analysis can be extended to a bistatic active sonar geometry when the object of interest and both the sound-projector and sensor-array platforms have co-linear motion with linear radial velocity. In Fig. 2.12 the sensor-array platform is shown as platform C with constant radial velocity v_c , initial range \bar{r}_c , and motion following (2.23). The Doppler scale from (2.16) can be shown to be

$$\eta = \frac{(c_w - v_b)(c_w + v_c)}{(c_w + v_b)(c_w - v_a)} \quad (2.28)$$

where it has been assumed that $r_c(t_b) < r_b(t_b)$ so the acoustic wavefront emanating from platform B at time t_b and intersecting platform C is at range

$$r_w(t, t_b) = r_b(t_b) - c_w(t - t_b) \quad (2.29)$$

at time t . The corresponding time delay in (2.16) is

$$\tau_0 = \frac{(\bar{r}_b - \bar{r}_c)(c_w - v_b) + (\bar{r}_b - \bar{r}_a)(c_w + v_b)}{(c_w - v_b)(c_w + v_c)} \quad (2.30)$$

For a monostatic system with a co-located sound projector and sensor, $v_a = v_c$ and $\bar{r}_a = \bar{r}_c$ which leads to

$$\eta = \frac{(c_w - v_b)(c_w + v_a)}{(c_w + v_b)(c_w - v_a)} \quad (2.31)$$

and

$$\tau_0 = \frac{2c_w(\bar{r}_b - \bar{r}_a)}{(c_w + v_a)(c_w - v_b)}. \quad (2.32)$$

The conditions producing bistatic linear radial velocity are unlikely; most realistic scenarios will include radial acceleration. As seen in [25] the time delay $\tau(t)$ in the presence of an acceleration component can be approximated as a quadratic function in t that simplifies to a linear function when radial acceleration is zero. Except for very extreme accelerations (relative to the sonar application), the quadratic function is very well approximated by the linear functions presented here.

Exercise 2.2 (Monostatic Doppler Shift Approximation for Two-Way Propagation) Show (2.31) results in δ_f as in (2.21) when the speed of sound c_w is large relative to the platform velocities. Note that based on the definition of v_0 (positive values represent a reduction in the distance between the platforms), $v_0 = v_a - v_b$.

Exercise 2.3 (Non-radial Velocity) Suppose platform A produces an acoustic wavefront at time t_a from a position $\vec{x}_a(t_a)$. The wavefront will reach a stationary sonar (platform B) at position \vec{x}_b at time t if the travel time $t - t_a$ is equal to the distance between platforms A and B at time t_a divided by c_w ; that is, if $t - t_a = r_{ab}(t_a)/c_w$. Suppose platform A has constant-velocity motion with speed v_a in the direction \vec{u}_0 described by the position vector

$$\vec{x}_a(t) = \vec{x}_0 + v_a(t - t_0)\vec{u}_0 \quad (2.33)$$

for some time t_0 close to t_a (i.e., $\delta_{t_a} = t_a - t_0$ is small). Using the law of cosines, show that the range at time t_a is

$$\begin{aligned} r_{ab}(t_a) &= \|\vec{x}_b - \vec{x}_a(t_a)\|_2 \\ &= |r_0 - \delta_{t_a} v_a \cos \theta_a| \sqrt{1 + \frac{\delta_{t_a}^2 v_a^2 \sin^2 \theta_a}{(r_0 - \delta_{t_a} v_a \cos \theta_a)^2}} \end{aligned} \quad (2.34)$$

where $\|\vec{x}\|_2 = \sqrt{\vec{x} \cdot \vec{x}}$ is the 2-norm of the vector \vec{x} , r_0 is the distance between the platforms at time t_0 , and θ_a is the angle between the direction of travel (\vec{u}_0) and the vector pointing at platform B from platform A at time t_0 , $\vec{x}_b - \vec{x}_a(t_0)$. Now by assuming $r_0 \gg |\delta_{t_a} v_a|$, show that

$$t_a \approx \left(\frac{c_w}{c_w - v_a \cos \theta_a} \right) \left[t - \frac{r_0 + t_0 v_a \cos \theta_a}{c_w} \right] \quad (2.35)$$

and relate the term in parentheses to η in (2.17). For what value of θ_a is η the same as in (2.17)? This exercise illustrates how, at long ranges, the radial component of platform velocity ($v_a \cos \theta_a$) dominates the Doppler effect even when motion is not strictly radial.

2.2.6 Doppler Sensitive and Insensitive Waveforms

The waveforms used in active remote sensing can be categorized as either being sensitive or insensitive to the effects of Doppler. The three most common active sensing waveforms are (1) continuous wave (CW) pulses, (2) linear frequency modulated (LFM) pulses, and (3) hyperbolic frequency modulated (HFM) pulses. The HFM pulse is also known as having a linear period modulation. CW pulses are considered Doppler sensitive whereas LFM and HFM pulses are viewed as being insensitive to Doppler. The HFM pulse is considered “optimally Doppler tolerant” [26, 27] in that the shape of the matched-filter response does not depend on Doppler (although its position in delay does). More details on active sensing waveforms can be found in Sect. 3.5.6 for waveform and reverberation spectra, in Sect. 8.3 for waveform autocorrelation and ambiguity functions, and in [23, Ch. 5] or [28, Ch. 4].

As described in Sect. 2.2.5, the effect of Doppler on a sinusoidal signal is approximated well by a shift in frequency proportional to the relative radial velocity between the sound projector and object of interest (see (2.21)). This is illustrated on the left side of Fig. 2.13 for the CW pulse where the echo spectrum is clearly seen to shift away from the spectrum of an echo not exhibiting Doppler. Noting that the latter is also the spectrum of reverberation, the CW pulse echo will often be masked by reverberation when the relative radial speed is small. However, when the relative radial speed is large, the CW-pulse echo spectrum only overlaps the reverberation spectrum in the sidelobes and performance is therefore likely to be limited by ambient noise rather than reverberation. If the DCLT objective is to estimate the relative radial velocity of the object of interest, performance is in part related to the mismatch between the zero-Doppler replica and the filter matched to the correct radial velocity (i.e., how much the reverberation is suppressed). The example shown in Fig. 2.13 (a 0.5-s duration CW pulse at 2 kHz) exhibits a mismatch of 7 dB when the object of interest has a 1-knot [kn] relative radial velocity, 19 dB at 4 kn, and 25 dB at 8 kn. This implies estimating the relative radial velocity with a CW pulse will be very effective: mistaking an object of interest closing at 8 kn from a stationary one will be very unlikely. Thus, a Doppler-sensitive waveform is useful in a detection context when the object of interest exhibits high relative radial velocity or when relative radial velocity estimation is the primary concern. A disadvantage in the detection context is that Doppler sensitive waveforms require detection processing in the form of multiple matched filters across the extent of relative radial velocities expected to be observed (e.g., the Doppler filter bank described in Sect. 8.7).

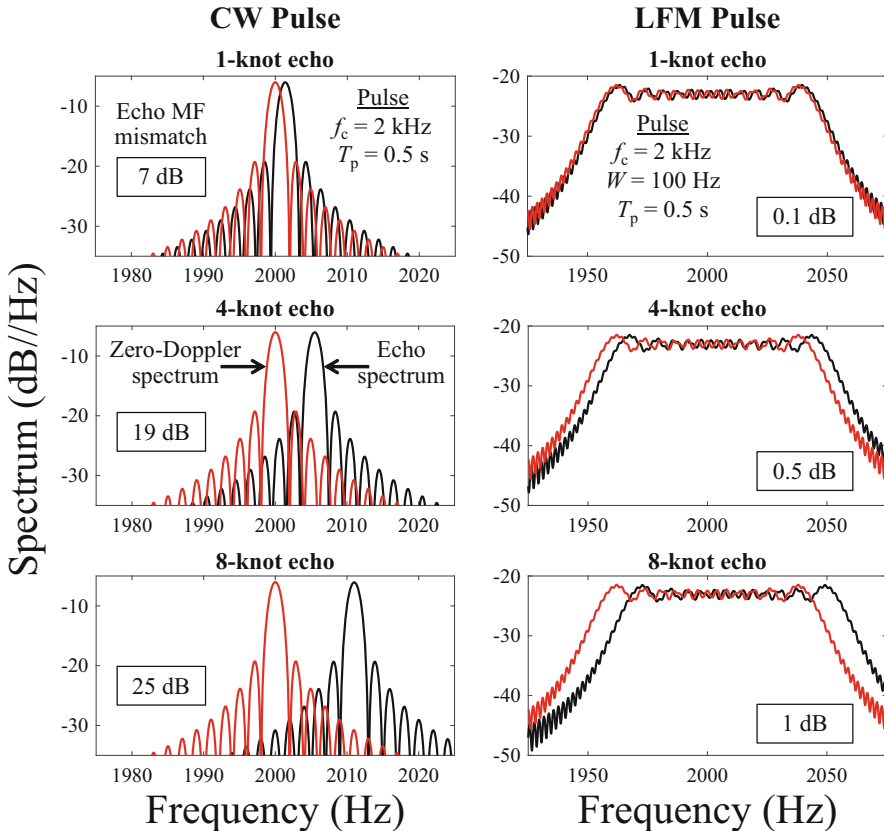


Fig. 2.13 Frequency spectrum for CW and LFM pulses for an echo arising from a stationary object of interest (red lines) and the echo from an object of interest at different relative velocities (black lines). The number in the box is the mismatch loss in a matched filter designed assuming no Doppler when applied to an echo with the given target radial velocity

For broadband waveforms, the effect of Doppler on an echo must be described as a temporal dilation or contraction, which results in both an amplitude and frequency scale in the spectrum (see (2.22)). The effect on the spectrum of an LFM pulse is shown on the right side of Fig. 2.13. The echo spectrum almost completely overlaps the spectrum of the echo with no Doppler effect, even at high relative radial velocities. An overlap of the echo spectrum is a necessary but not sufficient condition for a sonar pulse to be considered Doppler insensitive. For the LFM pulse shown in the figure, the small values of echo matched-filter mismatch (respectively 0.1, 0.5, and 1 dB for relative radial velocities of 1, 4, and 8 kn) imply that, for this example, only 1 dB of SNR is lost when using a zero-Doppler replica in a matched filter for an echo having an 8-kn relative radial velocity. Thus the

bank of filters matched to different relative radial velocities required by the CW pulse are not required for the LFM (or HFM) pulse. As shown in Sect. 8.3, the ambiguity function describes how detection processing responds to echoes having a different relative radial velocity than the one assumed in the matched filter. Based on their ambiguity functions, both the LFM and HFM pulses are considered Doppler insensitive. However, from the perspective of estimating the relative radial velocity of an echo neither the LFM or HFM pulse can provide the performance of a CW pulse, which improves with duration. Conversely, when estimating the range to the object of interest through time-delay estimation is important, the CW pulse has resolution proportional to its duration (implying it cannot have simultaneously good delay and Doppler resolution). Broadband pulses generally have delay resolution inversely proportional to their bandwidth and are therefore useful for time-delay estimation.

In reverberation limited conditions, broadband waveforms that allow separate control over the bandwidth and pulse duration are seen in Sect. 2.3.3 to have an advantage over CW pulses (whose bandwidth is inversely proportional to duration). Increasing bandwidth increases the signal to reverberation power ratio and therefore sonar performance in reverberation-limited conditions. As described in [23, Ch. 5] broadband waveforms that are also sensitive to Doppler exist. Although the waveforms are designed to combine some of the desirable delay and Doppler resolution properties of CW and FM pulses, they often do not perform well in reverberation-limited scenarios.

2.3 The Sonar Equation

Understanding the performance of a sonar system in a given remote-sensing application can be useful both in the design process and in terms of deciding where and when to employ the system. Assessing the performance of a sonar system requires accounting for the effect of each part of the remote sensing application. This includes each component in the sonar system, the effects of the underwater acoustical environment, and the characteristics of the sound or scattering from the object of interest. Ideally, the performance measure is chosen according to the inferential objective (e.g., one of the DCLT objectives listed in Sect. 1.1.6). When the inferential objective is described as either a detection or an estimation problem, the appropriate performance measure (e.g., detection and false-alarm probabilities or mean-squared estimation error) can be identified from statistical theory as described in Sects. 6.2.2 and 6.3.2. One of the difficulties in using performance measures from detection and estimation theory lies in the statistical or probabilistic nature of their formation. For example, evaluation of the probability of detection requires many repeated experimental observations under identical conditions, which can be very difficult to obtain in practice.

A simpler and more common approach is to focus on how each component in the remote-sensing system affects the signal-to-noise power ratio (SNR) under

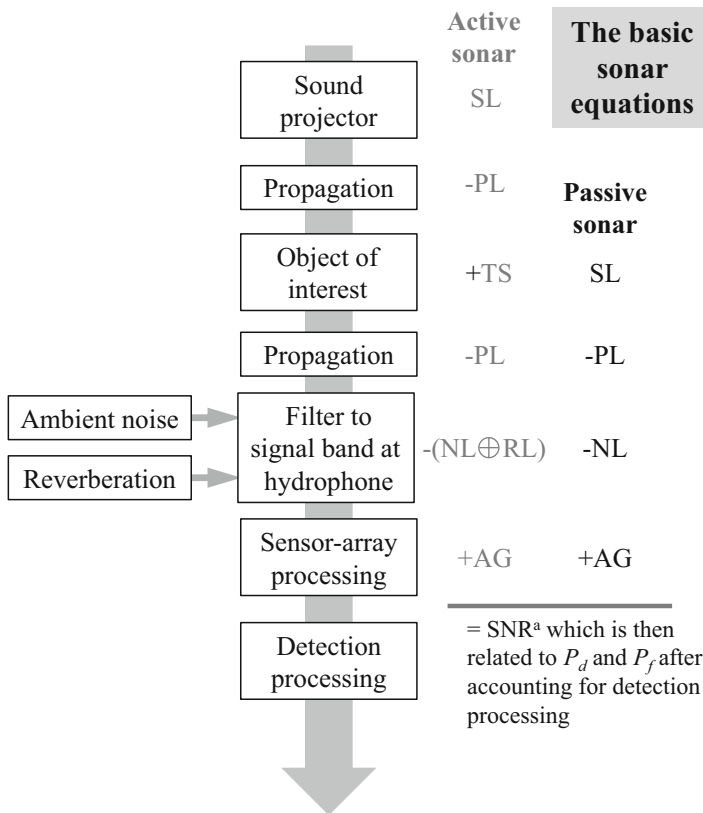


Fig. 2.14 Basic sonar equations for passive and active sonar

an inherent assumption that the performance in each of the DCLT objectives improves as SNR increases, which is generally true. As a simple power ratio, SNR is easier to predict and estimate from experimental observations than most probabilistic measures. The SNR analysis can easily be carried forward through each component of the remote-sensing system as illustrated in Fig. 2.14 and the signal and information processing chain (as described in Fig. 1.9) to include the linear portion of detection processing. At this point theoretical models describing signal and noise statistics can be used to evaluate detection and localization performance given a sonar system achieves a particular SNR. Alternatively, if a specific performance is desired, the SNR required to achieve it at various points in the signal processing chain can be determined and then used to make design decisions. Although the theoretical models providing the link between SNR and DCLT performance are not always accurate, they are often close enough to be useful. When they are not, more realistic statistical models for both signal and noise are available to improve the accuracy of performance prediction (e.g., see Sects. 7.4 and 7.5).

The tool by which an SNR analysis is made is called the *sonar equation*. Within the sonar equation, the effect of each part of the remote sensing application on the “power” in the signal of interest and noise is accounted for and accrued to produce an overall SNR. In the context of the sonar equation, “power” implies the square of any appropriate *field* quantity (e.g., voltage, current, or pressure are field quantities). Identical concepts to the sonar equation exist for other applications in the form of the radar equation (e.g., see [29, Ch. 4]) and the link budget in telecommunications. The sonar equation has roots in early analysis [30] where it was used to determine the maximum range for operating a sonar as defined by the range at which an echo was recognizable “half the time.” It is also a very useful tool for organizing the various components of the remote sensing application as is done in many texts on sonar and underwater acoustics (e.g., [3, 6, 31]).

Because of the large dynamic range inherent in underwater acoustic signals, the sonar equation is formulated using the decibel logarithmic scale, which is introduced in Sect. 2.3.1. The basic sonar equations for passive and active sonar are then presented in Sects. 2.3.2 and 2.3.3, carrying the SNR analysis through sensor array processing and the linear portion of detection processing. Techniques for easily relating detection performance to the SNR required to achieve it are described in Sect. 2.3.5 and to estimation performance in Sect. 2.3.6. The various ways in which the sonar equation can be used (e.g., to find the maximum operating range of a system or to assess how far a system’s performance is from a desired operating point) are presented in Sect. 2.3.7.

2.3.1 Decibel Notation

Power levels in sonar systems span a great extent—from very loud sound projectors to hydrophones sensitive to very low levels of acoustic pressure. The ratio of the largest to smallest acoustic powers of interest exceeds 10^{20} , which is even more than the world population ($7.349 \cdot 10^9$ in 2015 [32]) squared! To facilitate handle this wide range of values it is common to work in a logarithmic rather than linear scale. The most common logarithmic scale in use is the *decibel* scale, which converts an intensity or power ratio (P_1/P_0) to a base-10 logarithmic scale according to

$$L = 10 \log_{10} \left(\frac{P_1}{P_0} \right). \quad (2.36)$$

For example, if the power ratio $P_1/P_0 = 100$, then $L = 10 \log_{10} 100$ is said to equal 20 dB where “dB” stands for decibels. The “B” in dB is capitalized because a decibel is one tenth of a *bel*, which was named for Alexander Graham Bell. As seen in Table 2.1, zero decibels represents equal powers in the ratio and an increase (or decrease) of 10 decibels represents a multiplicative factor of 10 (or 0.1) in the power ratio. The ratio of largest to smallest of acoustic powers of interest spans at least 200 decibels.

Table 2.1 Commonly used decibel values and their equivalent linear-scale power and amplitude ratios

Decibel value (dB): R	Linear power ratio: $10^{R/10}$	Linear amplitude ratio: $10^{R/20}$
30	1000	31.6
20	100	10
10	10	$\sqrt{10} \approx 3.16$
6	≈ 4	≈ 2
3	≈ 2	$\approx \sqrt{2}$
0	1	1
-3	≈ 0.5	$\approx \sqrt{0.5}$
-6	≈ 0.25	≈ 0.5
-10	0.1	$\sqrt{0.1} \approx 0.316$
-20	0.01	0.0316
-30	0.001	0.00316

Suppose the powers P_1 and P_0 arise from, respectively, voltages V_1 and V_0 across a resistor of R ohms. The power ratio in decibels is

$$\begin{aligned} L &= 10 \log_{10} \left(\frac{V_1^2/R}{V_0^2/R} \right) \\ &= 10 \log_{10} \left(\frac{V_1^2}{V_0^2} \right) \end{aligned} \quad (2.37)$$

$$= 20 \log_{10} \left(\frac{|V_1|}{|V_0|} \right) \quad (2.38)$$

which is seen to be mathematically equivalent to starting with a ratio of squared voltages or their absolute value with the latter requiring using a multiplicative factor of 20 rather than 10 after taking the logarithm of the ratio. Since the decibel level L is the same for all three, these equations can be used to convert a decibel value to any of the ratios. However, there is an implicit assumption that the resistances across which the voltages are measured are identical. In the sonar equation where the amplitude function could be acoustic pressure measured at two different locations, this might not necessarily be the case [33, App. B].

A decibel value always represents a power or intensity *ratio*. However, it can be used to describe absolute levels by replacing the denominator (P_0) within the logarithm by a reference quantity. For example, if $P_1 = 100$ mW and a reference unit of 1 mW is used, then $L = 10 \log_{10}(100 \text{ mW}/1 \text{ mW}) = 20 \text{ dB}$. In this context, “20 dB” by itself represents the decibel value of the ratio between 100 mW and the 1 mW reference unit. In order to know the absolute level, the reference unit must be provided along with the decibel value of the ratio, as in “20 dB relative to 1 mW.” Conventions for describing the reference value include assuming a unit quantity in the given

measure and replacing “relative” with “re” or a double backslash (//), respectively,

“20 dB re mW” or “20 dB//mW.”

In underwater acoustics, the standard unit for pressure is the micropascal (μPa) and 1 μPa is the standard reference pressure [34, Sect. 3.2]. It is common to use the pressure equivalent to (2.37) (i.e., ratios of squared pressures rather than ratios of acoustic powers or intensities). For example, if a hydrophone measurement had a peak value of 10,000 μPa , it could be described in decibels as

“80 dB re μPa^2 ” or “80 dB re μPa .”

The “re μPa^2 ” reference implies use of (2.37) whereas “re μPa ” implies use of (2.38). As previously noted, the “80 dB” is the same in both cases and so the choice of reference unit comes down to personal preference. Following the reasoning in [33, App. B], the reference representing (2.37) is used in this text to avoid the confusion accompanying (2.38) when applied to spectral densities.²

The use of one micropascal as the reference unit is not ubiquitous in acoustical applications. For example, the standard in air is 20 μPa (e.g., see [35, Sect. 10.1.3]) and older literature uses one dyne per square centimeter, which equates to 0.1 Pa [6, Sect. 1.6]. Inclusion of the reference level and measurement unit is clearly paramount to relating decibel levels to physical field or power quantities. The confusion often encountered in comparing sound in air and water is described aptly in [36].

2.3.2 The Basic Passive Sonar Equation

In this section the basic sonar equations for passive sonar systems are derived according to the SNR after each component of the remote sensing system and signal processing through the linear portion of detection processing, as represented in Fig. 2.14. Only a brief description of each term in the passive sonar equation is presented in this section and summarized in Sect. 2.3.4. More detailed information can be found for most of the terms elsewhere in this text as noted in Sect. 2.3.4.

Sonar equation analysis starts with an *input* to the remote-sensing system. In passive sonar, the input is the source signal (or waveform) $u_o(t)$ generated by the object of interest. This produces an acoustic pressure signal

$$p_o(t) = \frac{u_o(t - r/c_w)}{r} \quad (2.39)$$

²The spectral density of a pressure signal measured in μPa has units $\mu\text{Pa}^2/\text{Hz}$ so applying (2.38) results in the reference $1 \mu\text{Pa}/\sqrt{\text{Hz}}$, which can lead to confusion because it characterizes the square root of a spectral density, which is not a commonly used quantity.

at a short distance r from the source where c_w is the speed of sound in water. The ‘power’ of the acoustic signal at range r is its average intensity,

$$\mathcal{I}_o(r) = \frac{\frac{1}{T} \int_t^{t+T} p_o^2(\tau + r/c_w) d\tau}{\rho_w c_w} \quad (2.40)$$

where ρ_w is water density. In passive sonar, signals of interest are usually modeled as band-limited Gaussian random processes with bandwidth W . Based on this, the time extent over which this average is formed for the passive sonar application is assumed to be at least the temporal extent to which the signal of interest is highly correlated $T_{coh} = 1/W$.

The product $\rho_w c_w$ is called the characteristic impedance of the transmission medium. When $\rho_w c_w$ is the same at both the sound generation and measurement points, the sonar equation can equivalently be constructed using the mean squared pressure (MSP),

$$P_o(r) = \frac{1}{T} \int_t^{t+T} p_o^2(\tau + r/c_w) d\tau. \quad (2.41)$$

The choice between MSP and average intensity is similar to the choice between the squared voltage or electrical power described in Sect. 2.3.1 where the ratio is identical when the resistances are the same. Owing to the simplicity of the examples used in this text, the MSP will be used. However, in scenarios where there is a significant change in density or sound speed between the sound source and sensor, the intensity in (2.40) should be used (e.g., when the sound source or sensor are buried).

With pressure in units of micropascals (μPa), $P_o(r)$ will have units μPa^2 . In representing the remote sensing system as a linear system, $u_o(t)$ is the input. The ‘power’ equivalent to the MSP for this source waveform, which is called the *source factor*, is

$$U_o = \frac{1}{T} \int_t^{t+T} u_o^2(\tau) d\tau. \quad (2.42)$$

As will be shown in Sect. 3.2.3.1, $u_o(t)$ has units of pressure times distance (i.e., $\mu\text{Pa m}$), which implies U_o has units $\mu\text{Pa}^2 \text{ m}^2$. Converting U_o to decibels then results in the source level (SL) term

$$\text{SL} = 10 \log_{10}(U_o) \text{ dB re } \mu\text{Pa}^2 \text{ m}^2, \quad (2.43)$$

which begins the sonar equation.

The next component of the remote sensing system is propagation of the acoustic signal from the object of interest to the sensor array. The intensity of an acoustic wave emanating from the object of interest generally decays as it propagates away from the object of interest. Define the reduction factor as the quantity L_p (which is generally greater than one) so that the MSP of the signal of interest when measured

at the sensor array is U_o/L_p . Note that if U_o has units $\mu\text{Pa}^2\text{m}^2$ and MSP has units μPa^2 , then L_p has units m^2 . The propagation loss (PL) term in the sonar equation is the decibel equivalent to L_p ,

$$\text{PL} = 10 \log_{10}(L_p) \text{ dB re m}^2. \quad (2.44)$$

If the ambient noise power at the sensor array is P_n , the SNR at the hydrophone level is

$$S^h = \frac{U_o}{P_n L_p} \quad (2.45)$$

where the superscript in S^h denotes at which point in the system the SNR is being evaluated. Because U_o/L_p is the MSP of the signal of interest as measured by a hydrophone, the quantity P_n must be taken as the MSP of the noise measured by the hydrophone and, similar to the power of the signal of interest, will have units μPa^2 . However, ambient noise generally has a much broader bandwidth than the signal of interest. To account for this, the hydrophone measurements (which contain both signal and noise) are assumed to be filtered to the frequency band of the signal (called the processing band) with unit-gain in the filter's pass band. For such filtering, the MSP of the signal of interest is the same before and after the filtering. The MSP of the noise after filtering (P_n) represents all of the noise found in the processing band. That is, P_n is the total noise power in the processing band; it is not the total noise power over all frequencies nor is it the noise power spectral density (e.g., the noise in a 1-Hz band). Owing to the linearity of array processing, this is similar to performing the linear portion of passive detection processing before array processing rather than after.

As described in Sect. 3.3, ambient ocean noise generally has a frequency dependence with a decreasing power spectral density as frequency increases until thermal noise begins to dominate at very high frequencies. If the processing band width (W) is small compared to the variation, the noise power spectral density can be assumed a constant $S_n(f) = P_n/W$ where $S_n(f)$ is in units of $\mu\text{Pa}^2/\text{Hz}$. Similarly, an average or representative value of L_p should be used to represent the effects of propagation, which can also have frequency dependence (e.g., see Sect. 3.2.4.2). Two important points follow from the derivation of (2.45). First, any processing applied to the measurements must be applied identically to both the signal and noise terms. Second, because (2.45) is a ratio of MSPs, it and any other terms representable as a proper SNR must be unitless, which provides a good check for evaluating various forms of the sonar equation.

The effect of signal processing operations in the sonar equation is quantified by the gain in SNR. For example, *array gain* is defined as the ratio of the SNR after array processing (S^a) to the SNR on a single hydrophone,

$$G_a = \frac{S^a}{S^h} = \frac{G_{a,s}}{G_{a,n}}. \quad (2.46)$$

It can also be described as the ratio of the array signal gain $G_{a,s}$ to the array noise gain $G_{a,n}$, which can be confusing when signal processing functions are designed with unit signal or noise gain (e.g., $G_{a,n} = 1$) so all the gain resides in the other component (e.g., $G_a = G_{a,s}$). Combining (2.46) with (2.45) provides the SNR after array processing as

$$S^a = G_a S^h = \frac{U_o G_a}{P_n L_p}. \quad (2.47)$$

As with the effect of propagation, a representative or average array gain is typically used to describe array processing performance over the frequency band of the detection processing.

By converting the ratio in (2.47) to decibels, the multiplications and divisions are converted to additions and subtractions, resulting in the basic passive sonar equation

$$\text{SNR}^a = 10 \log_{10} S^a = \text{SL} - \text{PL} - \text{NL} + \text{AG} \quad (2.48)$$

where the components are the decibel equivalents of each term in (2.47):

$\text{SL} = 10 \log_{10}(U_o)$ dB re $\mu\text{Pa}^2 \text{ m}^2$ is the source level,

$\text{PL} = 10 \log_{10}(L_p)$ dB re m^2 is the propagation loss,

$\text{NL} = 10 \log_{10}(P_n)$ dB re μPa^2 is the total noise power level in the processing band,
and

$\text{AG} = 10 \log_{10}(G_a)$ dB is the array gain in decibels.

There are two ways in which some descriptions of the sonar equation will differ from the above definitions. First, most older texts use definitions of SL and PL that do not include the m^2 units. Note that these units cancel when the difference SL-PL is formed in (2.48), which represents the ratio of the linear-form terms in (2.47) (i.e., U_o/L_p). The above approach, which follows [33, Sect. 3.2.2.3], properly accounts for the units of the functions producing these terms in explicit examples and so is preferred. Using either the newer or older nomenclature in the sonar equation produces the same end result in SNR. The second difference is in the definition of NL as representing the noise spectrum level rather than the level of all of the noise in the processing band (e.g., see [3, Sect. 7.3] and [6, Ch. 7]). The noise spectrum level is the decibel form of the noise power spectral density,

$$\text{NL}_f = 10 \log_{10}\{S_n(f)\} = 10 \log_{10}\left(\frac{P_n}{W}\right) \text{ dB re } \mu\text{Pa}^2/\text{Hz}, \quad (2.49)$$

and is often referred to as the noise level in a 1-Hz band. As will be described in Sect. 2.3.5, both approaches ultimately produce the same results as long as the definitions are applied consistently. These and other terms in the sonar equation are compiled in Sect. 2.3.4 along with their definitions. With respect to notation, quantities in decibels are either denoted in plain text with capital letters (e.g., SNR, SL or NL) or by a variable with a subscript (e.g., S_{dB}^a).

Array gain can be obtained for very complicated scenarios involving interferences and advanced sensor array processing. For sonar equation analysis, however, the simple condition of array gain in isotropic noise and plane-wave propagation across the array is usually sufficient. This simplification is called the *directivity index* (DI) of an array. Directivity index and array gain are covered in more detail in Sect. 8.4; a useful approximation to DI for an equally spaced line array in the broadside direction with conventional beamforming is presented here. If the line array comprises n sensors with equal spacing d , DI is approximately

$$\text{DI} \approx 10 \log_{10} \left(\frac{nf}{\gamma_w f_d} \right) \text{ dB} \quad (2.50)$$

where f is the operating frequency, $f_d = c_w/(2d)$ is the design frequency of the array and γ_w is the relative noise gain of the window function used to shade the array from Table 4.2 (e.g., $\gamma_w = 1$ for uniform shading and $\gamma_w = 1.51$ for Hann shading). The approximation is reasonably accurate when $nf/f_d > 2$ and $f < 2f_d$.

The most common use of the sonar equation is to assess detection performance. Detection algorithms applied to time-series data typically have both linear and non-linear components. The linear portion is often considered a ‘coherent’ combination of the data in that the phase is important and therefore retained. The non-linear component then continues to combine the data over longer periods of time in an incoherent manner (i.e., discarding phase) to form a detector decision statistic for comparison against a decision threshold. For example, the bandpass filtering to the signal band shown in Fig. 2.15 is the linear/coherent component of the processing whereas integrating the squared-envelope is the non-linear/incoherent component. This processing structure, which is known as an energy detector, applies to both narrowband and broadband passive sonar signals with the only difference lying in the width of the processing band. More details on passive sonar detection can be found in Sect. 9.2 or [2, Sect. 15.2]. Because there is no signal structure to exploit in a random signal and because filtering to the processing band was assumed to have been applied at the hydrophone level in the definition of (2.45), the SNR after the linear component of passive-sonar detection processing is (in this analysis) the same as it is after array processing,

$$\text{SNR}^d = \text{SNR}^a = \text{SL} - \text{PL} - \text{NL} + \text{AG}. \quad (2.51)$$

The separation of detection processing into linear and non-linear components has two different motivations. The first comes from the difficulty in properly forming an SNR after non-linear processing, for which the superposition principle does not apply. For example, the cross-terms (signal-noise products) inherent in the squared-envelope operation shown in Fig. 2.15 preclude definition of which components are signal and which are noise, so no sensible SNR can be formed. The second motivation for defining an SNR after linear detection processing arises when the data measured at a hydrophone can be assumed to be a Gaussian random process. In this situation, the data are also a Gaussian random process after the linear portion of

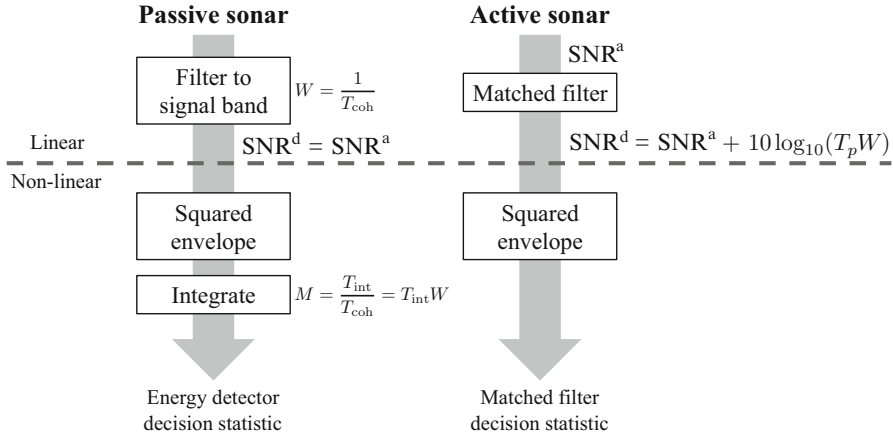


Fig. 2.15 Basic detection processing for passive and active sonar

detection processing and, under some basic assumptions about the signal and noise, can be completely characterized by the SNR.

The process of forming a squared envelope alters the statistical distribution of the data. In particular, the previously mentioned Gaussian-distributed data will no longer be Gaussian distributed after the squared-envelope is formed. For the basic signal models considered later in this section, the impact of the non-linear component of the energy detector shown in Fig. 2.15 (i.e., integrating the squared envelope) can be summarized by the processing time-bandwidth product,

$$M = T_{\text{int}} W = \frac{T_{\text{int}}}{T_{\text{coh}}}, \quad (2.52)$$

where T_{int} is the total integration time and $T_{\text{coh}} = 1/W$ is (approximately) the correlation time of a random signal with bandwidth W . The minimum value for T_{int} is T_{coh} , so $M \geq 1$ and equals one only when there is no integration. Clearly M increases as the incoherent integration time increases. As would be expected, detection performance also improves as M increases. However, it is important to note that M is not a gain in SNR achieved by incoherent integration. Rather it aids in describing how the statistical distribution of the detector decision statistic changes as a function of incoherent integration time. M is essentially the number of statistically independent observations of the signal characterized by SNR^d that are combined incoherently to form the detector decision statistic.

The final part of sonar-equation analysis, which relates SNR^d and M to detection and estimation performance metrics, will be covered in Sects. 2.3.5 and 2.3.6. Because there are common results for both active and passive sonar analysis, the basic active sonar equation is introduced first.

2.3.2.1 Example: Passive Submarine Radiated Noise Detection

Determine the SNR after linear detection processing for the following scenario.

- Distance between the submarine and sensor array is 1 km
- Propagation is represented by spherical spreading so $PL = 20 \log_{10} r$ dB re m² for range r
- Ambient noise for a light shipping density and a 6 m/s wind speed (sea state 2 to 3)
- An array with $n = 15$ sensors equally spaced every 0.75 m and beamforming with Hann shading
- Processing band is 100 Hz wide and centered at 1 kHz
- Total processing time is 0.5 s

Suppose the radiated noise from a submarine has a source spectrum level of 110 dB re $\mu\text{Pa}^2/\text{m}^2/\text{Hz}$ for a 100 Hz band centered at 1 kHz (from [3, Fig. 8.2], but using the modern reference units for a source spectrum level). The source level of the signal of interest in the processing band in decibels is

$$SL = 110 + 10 \log_{10} 100 = 130 \text{ dB re } \mu\text{Pa}^2 \text{ m}^2 \quad (2.53)$$

From Fig. 3.19 in Sect. 3.3.4 wind-generated surface noise for the given wind speed dominates that of light shipping activity at 1 kHz. The spectrum level of wind-generated surface noise for a wind speed of 6 m/s is approximately 60 dB re $\mu\text{Pa}^2/\text{Hz}$ at 1 kHz, so the total-noise level in the processing band is $NL = 80 \text{ dB re } \mu\text{Pa}^2$.

A sensor spacing of 0.75 m implies an array design frequency of $f_d = c_w/(2d) = 1 \text{ kHz}$. Using (2.50) with $n = 15$, $\gamma_w = 1.51$ for the Hann window, and at the center frequency provides an approximate array gain of $AG = 10 \text{ dB}$.

By combining the above information into (2.51), the SNR after linear detection processing is seen to be

$$\begin{aligned} \text{SNR}^d &= SL - PL - NL + AG \\ &= 130 - 20 \log_{10} 1000 - 80 + 10 \\ &= 0 \text{ dB}. \end{aligned} \quad (2.54)$$

An SNR of 0 dB, where the signal and noise have the same MSP after beamforming and the coherent portion of detection processing, might not be expected to provide very good performance. However, this value does not include the effect of incoherent detection processing over time. The SNR in (2.54) represents the data for one correlation length of the signal or $1/W = 0.01 \text{ s}$. Radiated noise is considered a broadband random signal for which detection processing entails filtering to the desired band followed by integrating the squared envelope of the filter output. Integrating for 0.5 s provides $M = T_{\text{int}} W = 50$ independent observations, all with

an SNR of 0 dB, which will be seen to provide quite good detection performance in Sect. 2.3.5.

2.3.3 *The Basic Active Sonar Equation*

In active sonar, the sound ‘emitted’ by the object of interest is the reflection or scattering of the acoustic waves originally produced by the sound projector and having propagated to the object of interest. For the purposes of sonar equation analysis, the projected sound, as defined by the transmit waveform, can be characterized by its amplitude, duration, and bandwidth. When forming the MSP of acoustic signals or noise, the time duration over which the average is formed should be taken to include the complete echo—the duration of the signal and any spreading arising from propagation and scattering. An alternative approach not considered here is to use the energy form of the active sonar equation [33, Ch. 3], which integrates the squared pressure but does not form the average. When done properly, the final results for each approach are the same. As previously mentioned, only brief descriptions of each term in the active sonar equation are presented in this section. A summary of the terms and an indication of where more details may be found is provided in Sect. 2.3.4.

Compared with the passive sonar equation, the active sonar equation must account for the effect of an additional propagation leg from the sound projector to the object of interest and the interaction of the projected sound with the object of interest. Building on (2.48), the active sonar equation after array processing can be described as

$$\text{SNR}^a = \text{SL} - \text{PL}_a + \text{TS} - \text{PL}_b - \text{NL} + \text{AG} \quad (2.55)$$

where SL is now the source level of the sound projector, TS (target strength) represents the interaction of the projected sound with the object of interest, and PL_a and PL_b represent the propagation loss, respectively, from the sound projector to the object of interest and from the object of interest to the sensor array. For a monostatic active sonar system, the propagation loss on each propagation leg is assumed to be the same so the total propagation loss is twice the one-way propagation loss,

$$\text{PL}_{\text{2-way}} = \text{PL}_a + \text{PL}_b = 2 \cdot \text{PL}_{\text{1-way}} = 10 \log_{10}(L_p^2) \text{ dB re m}^4. \quad (2.56)$$

The target strength term of the sonar equation,

$$\text{TS} = 10 \log_{10}(G_t) \text{ dB re m}^2, \quad (2.57)$$

uses a characterization of the reflection or scattering of the acoustic waves incident on the object of interest to convert the incident sound pressure level to a source-

level type term (which explains the units of dB re m²). The linear form of TS is called target gain, G_t , and has units of m² representing a differential scattering cross section. As described in Sect. 3.4 or [6, Ch. 9], TS is highly dependent on the size, shape, orientation, and composition of the object of interest. Note that the m² units accompanying the TS term are cancelled by the second propagation loss term (PL_b) similar to how PL_a cancels the units from the SL term.

One of the fundamental hindrances in active remote sensing comes from the backscattering of the projected sound from boundaries and inhomogeneities in the environment, collectively termed reverberation in the sonar application. In the presence of reverberation, SNR is more properly the ratio of the signal power to the power of the total interfering background, comprising both noise and reverberation. If P_r is the power of the reverberation in the processing band as measured by a hydrophone at the sensor array, the reverberation level is $RL = 10 \log_{10}(P_r) \text{ re } \mu\text{Pa}^2$ and the basic monostatic active sonar equation becomes

$$\text{SNR}^a = \text{SL} - 2\text{PL} + \text{TS} - (\text{NL} \oplus \text{RL}) + \text{AG} \quad (2.58)$$

where \oplus indicates a power sum. That is, the sum of the linear power terms converted to decibels,

$$\text{NL} \oplus \text{RL} = 10 \log_{10}(P_n + P_r) \text{ dB re } \mu\text{Pa}^2. \quad (2.59)$$

When ambient noise is much louder than the reverberation (i.e., $P_n \gg P_r$), the sonar is said to be *ambient-noise limited*. Under this condition, $\text{NL} \oplus \text{RL} \approx \text{NL}$ and the SNR after sensor-array processing simplifies to

$$\text{SNR}^a = \text{SL} - 2\text{PL} + \text{TS} - \text{NL} + \text{AG}. \quad (2.60)$$

Conversely, when reverberation dominates ambient noise ($P_r \gg P_n$) the sonar is said to be *reverberation limited* and the SNR after sensor-array processing is approximately

$$\text{SNR}^a = \text{SL} - 2\text{PL} + \text{TS} - \text{RL} + \text{AG}. \quad (2.61)$$

Three important characteristics about RL are (1) it varies as a function of the range from the sound projector, (2) RL can be sensitive or insensitive to the Doppler assumed for the matched-filter replica depending on whether the transmit waveform is Doppler sensitive or insensitive, and (3) RL is directly related to the source level. In shallow water environments, RL is often a decreasing function with range, so if a sonar is reverberation limited at close ranges, it will transition to being ambient-noise limited at some point as RL decays. In deep-water scenarios where a convergence zone (CZ) exists, RL can increase above the ambient-noise level through the extent of the CZ only to decay again beyond the CZ. Narrowband Doppler-sensitive transmit waveforms can produce echoes occupying a completely

different frequency band than the transmit waveform when the object of interest has enough motion relative to the source platform. For such scenarios, RL is very small relative to NL so the sonar is always noise limited. However, when a transmit waveform is insensitive to Doppler, RL may still be large even when the object of interest has significant relative motion.

To examine the relationship between SL and RL, consider Waite's ([3, Ch. 6] or here in Sect. 3.5.4) simplified characterization of RL for a monostatic sonar system in a shallow-water environment. The reverberation power level as measured by a hydrophone is approximated through the use of a *reverberation target strength* (TS_r) in the same manner as the echo reflected off the object of interest,

$$\text{RL} = \text{SL} - 2\text{PL} + \text{TS}_r. \quad (2.62)$$

The reverberation target strength describes the scattering contributions from the ocean at an annulus with range r and down-range extent $c_w T_p / 2$ for a transmit pulse with duration T_p . When boundary reverberation dominates (e.g., the surface or bottom),

$$\text{TS}_r = S_b + 10 \log_{10} \left[\left(\frac{c_w T_p}{2} \right) (2\pi r) \right] \text{ dB re m}^2 \quad (2.63)$$

where S_b is the boundary scattering strength in decibels. Converting (2.62) to linear units results in

$$P_r = \frac{U_o S_b \left(\frac{c_w T_p}{2} \right) (2\pi r)}{L_p^2} \quad (2.64)$$

where $U_o = 10^{\text{SL}/10}$ and $S_b = 10^{S_b/10}$. Note that this analysis is not expected to represent even rather benign scenarios with high accuracy because reverberation is a complicated combination of propagation and scattering. However, it is useful in making the following two points. The first is that P_r and therefore RL increase with both source level and pulse duration. The second is that P_r and RL decrease with range for both spherical spreading ($L_p = r^2$) and cylindrical ($L_p = r$), notwithstanding the expected changes in S_b with range.

Detection processing for active sonar signals involves matched filtering (also called pulse compression) as will be discussed in Chap. 8. Because matched filtering is a linear operation, the SNR at the matched filter output can be evaluated and incorporated into the sonar equation. When the transmit waveform has duration T_p and bandwidth W , matched filtering gain (i.e., the ratio of the output SNR to the input SNR) is the *processing* time-bandwidth product, $T_p W$. The active sonar equation after matched filtering then simplifies to

$$\begin{aligned} \text{SNR}^d &= \text{SNR}^a + 10 \log_{10}(T_p W) \\ &= \text{SL} - 2\text{PL} + \text{TS} - (\text{NL} \oplus \text{RL}) + \text{AG} + 10 \log_{10}(T_p W) \end{aligned} \quad (2.65)$$

where the superscript d represents the coherent portion of detection processing. In a noise-limited scenario with $NL = NL_f + 10 \log_{10} W$, where as before NL_f is the noise spectral level, the sonar equation becomes

$$\begin{aligned} SNR^d &= SL - 2PL + TS - NL + AG + 10 \log_{10}(T_p W) \\ &= SL - 2PL + TS - NL_f + AG + 10 \log_{10}(T_p). \end{aligned} \quad (2.66)$$

Here it can be seen that under noise-limited conditions increasing source level (SL) or signal duration (T_p) directly improves SNR irrespective of bandwidth.

When reverberation dominates ambient noise, $NL \oplus RL \approx RL$ and the SNR after matched filtering is

$$\begin{aligned} SNR^d &= SL - 2PL + TS - (SL - 2PL + TS_R) + AG + 10 \log_{10}(T_p W) \\ &= TS - TS_R + AG + 10 \log_{10}(T_p W) \\ &= TS - S_b - 10 \log_{10}(c_w \pi r) + AG + 10 \log_{10} W \end{aligned} \quad (2.67)$$

where (2.62) and (2.63) have been used to define RL. This illustrates that under reverberation-limited conditions, increasing SL or transmit waveform duration do not improve SNR; however, increasing transmit-waveform bandwidth does. Pulsed sinusoidal or continuous-wave (CW) transmit waveforms have bandwidth inversely proportional to pulse duration, $W = 1/T_p$. Thus, increasing bandwidth can only be done by shortening the CW pulse duration, which will also impact the extent to which the sonar is reverberation limited. As such, frequency-modulated waveforms are generally used in reverberation-limited conditions as they can provide separate control over the bandwidth and pulse duration.

In Fig. 2.15, the active sonar detection processing includes formation of the squared envelope, but does not include incoherent integration. Formation of the squared envelope represents what is known as a *quadrature matched filter* (QMF) accounting for an unknown or uniformly random phase in a deterministic signal (see Sect. 8.2 in Part III or [37, Sect. 7.6.2] for more details on the QMF). An unknown or uniformly random phase can arise from the interaction of sound with a boundary as described in Sect. 3.2.7 as well as from propagation through a multipath channel. Propagation over multiple paths also spreads an active sonar signal in time, potentially resulting in a loss in performance. Incoherent integration can be used to recoup some of these detection losses (e.g., see Sect. 8.8.2). The performance improvement from incoherent integration is, similar to the passive case, related to $M = T_{int} W$ when the SNR for each squared-envelope sample is constant throughout the spreading. As this is not typically the case, the formulas of this section can be used under the assumption that SNR^d is an average SNR over the spreading.

By allowing incoherent integration in the active sonar detector, the detection algorithms shown in Fig. 2.15 are essentially identical when relating SNR^d and M to the primary detection performance measures, the probability of detection (P_d) and

probability of false alarm (P_f). For both cases the total integration time (T_{int}) has a minimum value of $1/W$, which arises from the duration of the impulse response of the filtering to the band of the signal of interest. As such, $M \geq 1$ with the lower bound arising when no incoherent integration occurs. A useful interpretation of M is that it represents the number of independent squared-envelope samples contained in the integrated signal [38, App. A].

2.3.3.1 Example: Reverberation- and Noise-Limited Active Sonar Detection

In the scenario described below consider the following:

1. At what range does the sonar begin to become ambient-noise limited (i.e., the range where $\text{NL} = \text{RL}$)? How does this change if bandwidth is reduced or increased?
 2. Plot the SNR and signal-to-reverberation ratio (SRR) after array processing using (2.60) and (2.61) as a function of range. Compare them with the SNR in (2.58). What SNR does the system achieve at the range found in step 1? Would you expect the signal to be noticeable without detection processing?
 3. Plot the SNR after linear detection processing using (2.65). If SNR at this point must be at least 10 dB for performance to be considered adequate, what is the maximum range of the system? How does this change with pulse duration?
 - Omnidirectional source with SL of 200 dB re $\mu\text{Pa}^2 \text{ m}^2$
 - Transmit waveform with pulse length $T_p = 1 \text{ s}$ and bandwidth $W = 100 \text{ Hz}$ centered at $f_c = 2 \text{ kHz}$
 - Propagation for deep water with spherical spreading so $\text{PL} = 20 \log_{10} r \text{ dB re m}^2$
 - Reverberation dominated by the sea surface; assume a constant grazing angle of $\theta_g = 10^\circ$ for the ranges of interest
 - Wind speed of 10 kn, which is approximately sea-state 3
 - Array gain is 20 dB
 - Target strength for a rigid sphere with a 2-m radius.
 1. At what range does the sonar begin to become ambient-noise limited (i.e., the range where $\text{NL} = \text{RL}$)? How does this change if bandwidth is reduced or increased?
- In this frequency regime, wind-generated noise dominates the ambient noise. Using the formula from Sect. 3.3.4, the noise spectrum level at 2 kHz for a 10 kn (=5.1 m/s) wind speed is approximately 56 dB re $\mu\text{Pa}^2/\text{Hz}$. If the ambient noise spectrum level NL_f is assumed to be flat over the transmit band, the total noise power level, as obtained from (2.49), is $\text{NL} = \text{NL}_f + 10 \log_{10} W = 76 \text{ dB re } \mu\text{Pa}^2$.

From Sect. 3.5.3, RL for boundary reverberation is

$$\text{RL} = \text{SL} - 2\text{PL} + \mathcal{S}_a + 10 \log_{10} \left(\frac{\pi r c_w T_p}{\cos \theta_g} \right) \quad (2.68)$$

where \mathcal{S}_a is the surface scattering strength. As described in Sect. 3.5.3, this can be obtained using the Chapman-Harris formula [39],

$$\mathcal{S}_a = 3.3\beta \log_{10} \left(\frac{\theta_{\text{deg}}}{30} \right) - 42.4 \log_{10}(\beta) + 2.6, \quad (2.69)$$

where θ_{deg} is the grazing angle in degrees and

$$\beta = 158 \left(v_{\text{kn}} f^{1/3} \right)^{-0.58} \quad (2.70)$$

with v_{kn} as the wind speed in knots. For the case at hand, $\mathcal{S}_a = -54$ dB.

Range enters through both PL and the last term in (2.68), so by equating NL to RL it can be isolated producing

$$30 \log_{10} r = \text{SL} + \mathcal{S}_a + 10 \log_{10} \left(\frac{\pi c_w T_p}{\cos \theta_g} \right) - \text{NL}. \quad (2.71)$$

Assuming $c_w = 1500$ m/s results in $r \approx 3.7$ km as the transition point from reverberation to ambient limited. Noting that $\text{NL} = \text{NL}_f + 10 \log_{10} W$, it can be seen that if r_0 is the cross-over range for bandwidth W_0 , using a bandwidth W changes the cross-over range to

$$r = \left(\frac{W_0}{W} \right)^{1/3} r_0. \quad (2.72)$$

Thus, doubling the bandwidth reduces the cross-over range to 3 km whereas halving the bandwidth means the system is reverberation-limited out to a range of 4.7 km. Note that this result is for spherical spreading with the given (simplistic) reverberation model and assumes the noise spectrum level is constant over the signal band.

2. Plot the SNR and signal-to-reverberation ratio (SRR) after array processing using (2.60) and (2.61) as a function of range. Compare them with the SNR in (2.58). What SNR does the system achieve at the range found in step 1? Would you expect the signal to be noticeable without detection processing?

To compute SNR, target strength for the object of interest must be determined. From (3.197) in Sect. 3.4.1, the TS of a rigid sphere with radius $a = 2$ m is 0 dB re m^2 in the geometric scattering regime. The geometric scattering regime is valid for $ka = (2\pi f/c_w)a \gg 1$, which requires a sensing frequency $f \gg 120$ Hz when $a = 1$ m. Although the transmit waveform band (2 kHz \pm 50 Hz)

clearly satisfies this, the geometric scattering regime result may be a reasonable approximation for values of ka only moderately greater than unity (e.g., see Fig. 3.22).

Application of (2.60) and (2.61) to obtain SNR is then straightforward and illustrates how the two functions cross at the range computed in Step 1 above. The SNR at this point using (2.58) is approximately -1.5 dB whereas the others are 3-dB higher because they only consider half the noise or interference observed by the system. An SNR of -1.5 dB implies the signal power is smaller than the noise power. At this SNR, it is not likely to be observable before performing matched filtering.

3. Plot the SNR after linear detection processing using (2.65). If SNR at this point must be at least 10 dB for performance to be considered adequate, what is the maximum range of the system? How does this change with pulse duration?

The SNR after detection processing simply requires adding $10 \log_{10} T_p W = 20$ dB to the SNR after array processing as shown in (2.65). This yields an SNR of 18.5 dB at the transition range from step 1, which satisfies the 10 -dB minimum SNR for adequate performance. Beyond this point the sonar is ambient-noise limited so (2.66) can be used to isolate r , which is now only found in PL,

$$40 \log_{10} r = \text{SL} + \text{TS} - \text{NL}_f + \text{AG} + 10 \log_{10}(T_p) - 10. \quad (2.73)$$

This results in a maximum range of 7 km satisfying the performance requirement.

From (2.73), it can be seen that if the maximum detection range of the system is r_0 for a pulse duration T_0 , then it becomes

$$r = \left(\frac{T_p}{T_0} \right)^{1/4} r_0 \quad (2.74)$$

if a pulse duration of T_p is used (assuming spherical propagation and continuing to be noise-limited). Thus doubling the pulse duration extends the maximum range to $1.2 \cdot 7 = 8.4$ km while halving the pulse duration reduces it to $0.84 \cdot 7 = 5.9$ km.

2.3.4 Summary of Sonar Equation Terms

Source Level: $\text{SL} = 10 \log_{10}(U_o) \text{ dB re } \mu\text{Pa}^2 \text{ m}^2$

The source level (SL) represents the power introduced into the remote sensing system and is therefore the first term in the sonar equation. It is the decibel equivalent of the source factor (U_o ; units $\mu\text{Pa}^2 \text{ m}^2$), which is the mean-squared source waveform produced by the object of interest in the processing band in passive sonar or the sound projector in active sonar. See Sect. 3.2.3.4 for more detail.

Propagation Loss: $PL = 10 \log_{10}(L_p) \text{ dB re m}^2$

PL represents the reduction of the source level in decibels re m^2 arising from propagation between the object of interest and the sensor array or a sound projector and the object of interest. Because L_p is a loss appearing in the denominator of (2.47), PL is generally, but not always, a positive quantity. See Sect. 3.2.4 for more detail.

Noise Level: $NL = 10 \log_{10}(P_n) \text{ dB re } \mu\text{Pa}^2$

NL is the mean squared pressure (MSP) of all of the ambient noise in the processing band in decibels relative to a squared reference pressure of $1 \mu\text{Pa}^2$, as measured at the sensor array. See Sect. 3.3 for more detail.

Array Gain: $AG = 10 \log_{10}(G_a) \text{ dB}$

AG is the SNR improvement in decibels achieved by array processing. It is common to use the directivity index (DI) of an array in lieu of AG where DI is AG when calculated for isotropic noise and plane-wave propagation conditions. See Sect. 8.4 for more detail.

Target Strength: $TS = 10 \log_{10}(G_t) \text{ dB re m}^2$

TS represents the impact of reflection or scattering from the object of interest as the decibel equivalent of G_t , the differential scattering cross section, which has units of m^2 . It converts an incident pressure into a source-level type term. See Sect. 3.4 for more detail.

Reverberation Level: $RL = 10 \log_{10}(P_r) \text{ dB re } \mu\text{Pa}^2$

RL is the MSP of reverberation in the processing band in decibels relative to a squared reference pressure of $1 \mu\text{Pa}^2$, as measured at the sensor array. See Sect. 3.5 for more detail.

SNR: Signal-to-noise power ratio in decibels. The noise power is the total power in the processing band so SNR represents a unitless ratio.

- $\text{SNR}^h = 10 \log_{10} S^h$ is the hydrophone-level SNR after filtering to the frequency band of the signal of interest (i.e., the processing band).
- $\text{SNR}^a = 10 \log_{10} S^a$ is the SNR after sensor array processing.
- $\text{SNR}^d = 10 \log_{10} S^d$ is the SNR after the linear portion of detection processing. This SNR is related to detection performance in Sect. 2.3.5.

When SNR contains an over-line (e.g., $\overline{\text{SNR}}^d$) it represents the SNR required to achieve a specific detection operating point (i.e., it is a function of P_d and P_f) or to achieve a desired estimation performance. See Sects. 2.3.2–2.3.6 for more detail.

Detection Threshold: DT describes the SNR in decibels required to achieve a specific operating point (e.g., $DT^d = \overline{\text{SNR}}^d$). It can be applied at different points in the processing chain (e.g., DT^d and DT^a). In this text DT represents SNR as described above and so is the decibel representation of a unitless power ratio. When used with the subscript “Hz,” as in DT_{Hz} , it represents SNR formed using noise power spectral density (i.e., noise in a 1-Hz band) and therefore has units dB re Hz. When used with the subscript “50,” as in DT_{50} , it represents the case of $P_d = 0.5$ and is called minimum detectable level (MDL). See Sect. 2.3.5 for more detail.

Recognition Differential: RD is the same as DT. See Sect. 2.3.5 for more detail.

Signal Excess: SE is the difference in decibels between the achieved SNR and DT. It describes how far, in terms of SNR, a sonar system is from a desired operating point. It is the same regardless of where in the signal processing chain SNR and DT are defined or if they are defined using the total noise power in the processing band or the noise power in a 1-Hz band. See Sect. 2.3.7 for more detail.

Figure of Merit: FOM is a re-organization of the sonar equation to define the PL such that the achieved SNR equals DT_{50} . See Sect. 2.3.7 for more detail.

2.3.5 Relating SNR to Detection Performance: Detection Threshold

A common application of the sonar equation is to assess the detection performance of a sonar system. Detection performance is quantified by the probabilities of detection (P_d) and false alarm (P_f), which define what is called the operating point of a detector (detection performance measures are described in detail in Sect. 6.2.2). Given the SNR after coherent detection processing (SNR^d) as obtained through the sonar equation and the benefit associated with incoherent processing (the processing time-bandwidth product, M), the “forward” problem of evaluating P_f and P_d is a straightforward evaluation of the cumulative distribution function (CDF) of standard random variables. It is described in detail for several standard signal models in the sonar application in Part III, including more complicated scenarios than those typically considered in sonar-equation analysis (e.g., signal spreading, normalization, and non-Gaussian data). In many applications of the sonar equation, however, it is desired to determine what condition (e.g., range to an object of interest, size of an array, or sea-state) will achieve a pre-determined or desired level of sonar detection performance. The sonar equation can easily be manipulated to describe the unknown parameter, but it is then a function of the SNR required to achieve the desired detection performance. Historically, the SNR required to achieve a specific detection operating point has been called *detection threshold* (DT).

Obtaining the SNR as a function of a detection operating point (i.e., a (P_d, P_f) pair) and a prescribed amount of processing time-bandwidth product (M) defines the “inverse” of the aforementioned forward problem. Clearly this can be accomplished through iterative solution of the forward problem. However, accurate approximations or simple numerical solutions exist for deterministic and Gaussian-fluctuating signals, which are the two most common signal models. Techniques for obtaining the required SNR for various combinations of signal type and detector structure are provided in the following sub-sections and summarized at the end of the section. In this text, when the SNR required to achieve an operating point is obtained as a solution to the inverse problem it will be denoted by a line over SNR; for example, \overline{SNR}^d or \overline{SNR}^a .

2.3.5.1 Gaussian-Fluctuating Signal

The Gaussian-fluctuating signal is typically used to represent passive sonar signals arising from radiated noise or when propagating over large distances, but can also be useful in active sonar when channel fluctuations significantly degrade the coherent echo. When $M = 1$, the required SNR can be explicitly related to the desired operating point according to

$$\overline{\text{SNR}}^d = 10 \log_{10} \left[\frac{\log P_f}{\log P_d} - 1 \right]. \quad (2.75)$$

This equation illustrates how improving the operating point by decreasing P_f or increasing P_d leads to a requirement for a higher SNR. Such a relationship is expected for all signal types and all (good) detection algorithms.

At the other extreme, where M is large, the decision statistic can be described as the sum of many independent observations. Therefore, by appealing to the central limit theorem (CLT, see Sect. 5.3.7), it can be approximated by a Gaussian random variable. This leads to the required SNR of

$$\overline{\text{SNR}}^d = -5 \log_{10} M + 10 \log_{10}(\phi_f - \phi_d) - 10 \log_{10} \left(1 + \frac{\phi_d}{\sqrt{M}} \right) \quad (2.76)$$

$$\approx -5 \log_{10} M + 10 \log_{10}(\phi_f - \phi_d) \quad (2.77)$$

where the approximation in the second line assumes \sqrt{M} is large relative to ϕ_d . The variables

$$\phi_f = \Phi^{-1}(1 - P_f) \quad (2.78)$$

and

$$\phi_d = \Phi^{-1}(1 - P_d) \quad (2.79)$$

are obtained from the cumulative distribution function (CDF) of the standard normal random variable, $\Phi(z)$, according to $P_f = 1 - \Phi(\phi_f)$ and $P_d = 1 - \Phi(\phi_d)$; that is, $z = \Phi^{-1}(p)$ is the functional inverse of $p = \Phi(z)$. From (2.77) it can be seen that as M increases, the SNR required to achieve the operating point decreases according to $5 \log_{10} M$, illustrating the performance improvement attained by incoherent processing. Unfortunately, unless $P_d \approx 0.5$, M needs to be quite large for (2.77) to be highly accurate: the error is generally more than 1 dB for $M = 10$ and on the order of 0.5 dB for $M = 100$.

The exact solution to the inverse problem for the Gaussian-fluctuating signal can be described by using the inverse of the normalized incomplete gamma function. If $\tilde{\gamma}(h; M)$ is the incomplete gamma function including normalization by $\Gamma(M)$,

$$\tilde{\gamma}(h; M) = \int_0^h \frac{x^{M-1} e^{-x}}{\Gamma(M)} dx = p \quad (2.80)$$

then its functional inverse is $h = \tilde{\gamma}^{-1}(p; M)$. The SNR required to achieve the desired operating point is then

$$\overline{\text{SNR}}^d = 10 \log_{10} \left[\frac{\tilde{\gamma}^{-1}(1 - P_f; M)}{\tilde{\gamma}^{-1}(1 - P_d; M)} - 1 \right]. \quad (2.81)$$

Computational routines for evaluating $\Phi(z)$, $\tilde{\gamma}(z; M)$ and their functional inverses are readily available. Note the error function (erf) can be used to obtain $\Phi(z)$ (see Sect. 5.6.6). When these standard routines are not available, approximations for $M \leq 20$ can be found in [40], although they require different coefficients (provided as a table in [40]) for each value of M .

Example: Array Gain Required to Achieve a Performance Specification

Recall the passive-sonar example from Sect. 2.3.2 where a submarine at 1-km range with 0.5 s of incoherent integration in a $W = 100$ Hz band resulted in $\overline{\text{SNR}}^d = 0$ dB with $M = 50$ independent samples in the incoherent integration. If the probability of false alarm is set to $P_f = 10^{-6}$, the scenario results in $P_d = 0.73$ which is quite good considering the signal is no larger than the noise after filtering.

Now suppose the sensor array was being redesigned to meet a performance specification of near perfect detection, $P_d = 0.99$ and $P_f = 10^{-6}$, with all other conditions remaining the same. To determine the AG necessary to meet the performance specification, the sonar equation from (2.54) becomes

$$\begin{aligned} \overline{\text{SNR}}^d &= \text{SL} - \text{PL} - \text{NL} + \text{AG} \\ &= 130 - 20 \log_{10}(1000) - 80 + \text{AG} = -10 + \text{AG}. \end{aligned} \quad (2.82)$$

Then, $\overline{\text{SNR}}^d = 2$ dB is obtained from (2.81) with $M = 50$ for $P_d = 0.99$. Using this in (2.82) results in a requirement for $\text{AG} = 12$ dB where the initial array gain was only 10 dB. Thus, to improve detection performance to $P_d = 0.99$ requires a 2 dB increase in array gain. Although this might not appear significant, it would require almost a 60% increase in the size of a linear array (a factor $10^{2/10} \approx 1.6$).

2.3.5.2 Non-fluctuating or Deterministic Signal

The non-fluctuating or deterministic signal is commonly used in evaluating active sonar performance, especially when environmental conditions do not change significantly from ping to ping. It can also be useful in passive remote sensing for signals with some measure of repeatability over multiple observations such as marine mammal vocalizations. As will be described in Sect. 8.2, the most common scenario for a deterministic signal is one in which the phase of the signal is unknown and where detection is performed using a quadrature matched filter (QMF).

As with the Gaussian-fluctuating signal, when M is large, the CLT can be used to approximate the detector decision statistic by a Gaussian random variable. This leads to the SNR required to achieve the operating point,

$$\overline{\text{SNR}}^d = -5 \log_{10} M + 10 \log_{10} \left[\phi_f - \phi_d \sqrt{1 + \frac{\phi_f}{\sqrt{M}} + \frac{\phi_d^2}{M}} + \frac{\phi_d^2}{\sqrt{M}} \right] \quad (2.83)$$

$$\approx -5 \log_{10} M + 10 \log_{10} [\phi_f - \phi_d] \quad (2.84)$$

which has the same asymptotic ($M \rightarrow \infty$) form as for the Gaussian-fluctuating signal in (2.77).

The forward solution to obtain P_d for the deterministic signal requires evaluation of the CDF of a non-central chi-squared random variable. The inverse solution obtaining the SNR required to achieve an operating point requires inversion of the CDF in terms of the non-centrality parameter. Owing to the difficulty in this calculation, several empirically derived formulas have been developed to approximate the solution. The most well known in the sonar community is Albersheim's equation [41],

$$\overline{\text{SNR}}^d = -5 \log_{10} M + \left(6.2 + \frac{4.54}{\sqrt{M + 0.44}} \right) \log_{10}(A + 0.12AB + 1.7B) \quad (2.85)$$

where

$$A = \log_e \left(\frac{0.62}{P_f} \right) \text{ and } B = \log_e \left(\frac{P_d}{1 - P_d} \right). \quad (2.86)$$

Albersheim's equation was derived to represent Robertson's curves [42] for incoherent detection performed by integrating the *envelope* of the filter output rather than the *squared envelope* as shown in Fig. 2.15. Integrating the envelope as opposed to the squared envelope is simpler when signal processing is implemented in analog hardware. With most modern signal processing implementations occurring digitally, the exigency for the integrated-envelope detector is now rare. As noted in [43], the required SNR when integrating the envelope is very similar (less than 0.2 dB of difference) to integrating the squared envelope, so Albersheim's equation is still

quite useful. From [43], Albersheim's equation is accurate to within 0.2 dB (for the integrated-envelope detector) for at least $P_d \in [0.3, 0.95]$, $P_f \in [10^{-8}, 10^{-4}]$, and $M \in [1, 16]$.

In [40], Hmam presents similar empirically derived equations specific to the integrated-squared-envelope detector,

$$\overline{\text{SNR}}^d = -10 \log_{10} M + 10 \log_{10} \left[\left(\sqrt{h - M/2 + 0.25} - A \right)^2 - \frac{M}{2} + 0.25 \right] \quad (2.87)$$

where

$$A = \text{sign}(0.5 - P_d) \sqrt{0.85616 \log_e B}, \quad (2.88)$$

$$B = \frac{0.19}{\sqrt{0.819025 + 1.5206P_d(0.9998 - P_d)} - 0.905}, \quad (2.89)$$

and

$$h = \tilde{\gamma}^{-1}(1 - P_f; M). \quad (2.90)$$

Hmam also provides an approximation to the decision threshold h , though coefficients are required as a function of M . As previously noted, the inverse normalized incomplete gamma function can be obtained through standard computational packages. When $M = 1$, the decision threshold can be described explicitly in terms of P_f ,

$$h = -\log(P_f). \quad (2.91)$$

Hmam's equation is accurate [40] to within 0.085 dB (for the integrated-squared-envelope detector) for at least $P_d \in [0.05, 0.999]$, $P_f \in [10^{-12}, 10^{-3}]$, and $M \in [1, 20]$. This presentation of Hmam's equation has been adapted from [40] to provide the per sample SNR (i.e., Hmam's result in [40] is for $\overline{\text{SNR}}^d + 10 \log_{10} M$).

2.3.5.3 Extensions to Other Signal and Noise Models

A Rician signal model arises when the signal of interest contains both deterministic and Gaussian-fluctuating components. Hmam's equation can be used to relate P_d , P_f , and M to the power of the coherent component relative to the power in the fluctuating component if the latter is fixed relative to the noise background. Historically the Rician signal has been approximated by a model termed *one-dominant plus Rayleigh* or “1-D+R,” where the squared envelope of the signal is assumed to be chi-squared distributed with four degrees of freedom. Approximations to the required SNR for the 1-D+R and the more general Weinstock [44] model (described in Sect. 7.5.4 as a gamma-fluctuating-intensity) as developed by Shnidman [45] can also be found in [28, Ch. 6].

All of the aforementioned approximations to the SNR required to achieve a specified detector operating point assume the additive noise is Gaussian. Extensions for the $M = 1$ case to account for non-Gaussian background noise by appropriately calculating the detector decision threshold can be found in [46]. Although detectors with incoherent integration ($M > 1$) were not evaluated in [46], the approach is likely to work there as well.

2.3.5.4 Example Signal-Model Performance Comparison

A comparison of the SNR required to detect either a deterministic or a Gaussian-fluctuating signal is shown in Fig. 2.16. Hmam's equation from (2.87)–(2.90) is used for the deterministic signal and the exact results of (2.81) are used for the Gaussian-fluctuating signal. The SNR obtained by a Gaussian approximation to the detector decision statistic from (2.77) or (2.84) is shown to illustrate how inaccurate the approach is for small to moderate values of M . Because the Gaussian approximation inherently assumes M is large, this comparison is not particularly fair. However, it is not uncommon for it to be used inappropriately when M is too small for it to be accurate. The disparity seen in Fig. 2.16 (ranging from 3–14 dB for $M = 1$) should discourage such misuse.

Two different operating points are shown: minimum detectable level (MDL for which $P_d = 0.5$) for $P_f = 10^{-4}$ and a high quality operating point with $P_d = 0.9$ and $P_f = 10^{-8}$. The additional SNR required to achieve the high quality operating point relative to MDL is less than 3 dB when M is large, but can be significantly higher when M is small (nearly 5 dB for the deterministic signal and over 10 dB for the Gaussian-fluctuating signal). This may be explained by noting that $\overline{\text{SNR}}^d$ is the SNR in each independent sample in the incoherent integration, so a small increase can produce a significant effect when M is large.

In both operating points, the deterministic signal model requires a lower SNR than the Gaussian-fluctuating signal. Although this appears obvious, the result depends on the interaction between the signal fluctuations, the number of independent observations (M), and the detection algorithm. For a detector performing incoherent integration, the deterministic signal is easier to detect than the Gaussian-fluctuating signal at high quality operating points. The case of lower quality operating points is examined in one of the following exercises.

The $M = 1$ case represents no integration, which is common for the matched-filter detector. The disparity between the two signal models is greatest when $M = 1$ and is exacerbated by the higher quality operating point. A higher value of P_d emphasizes the tails of the probability density function (PDF) of the signal model, where the two models will differ more. The disparity decreases as M increases because of the homogenizing effect of incoherent summation of identically distributed data; the PDF of the detector decision statistic becomes closer to Gaussian for both signal models.

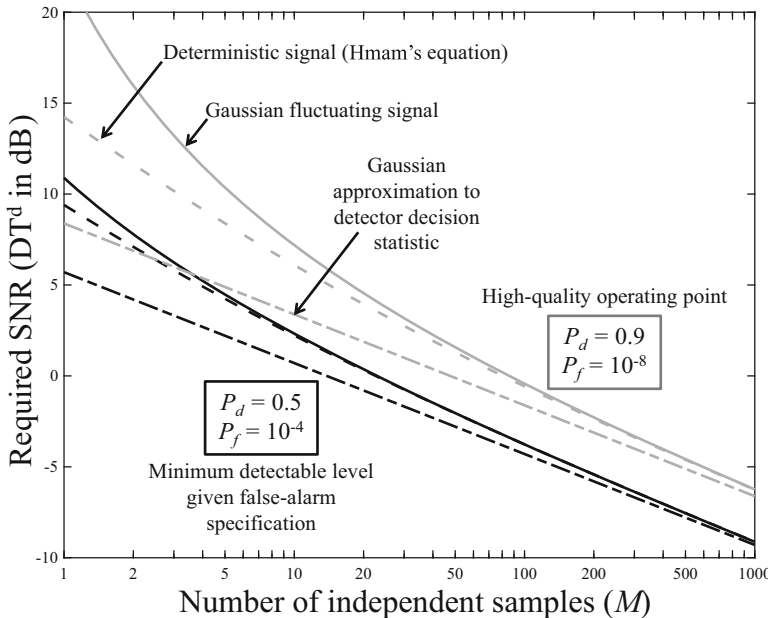


Fig. 2.16 Required SNR after coherent detection processing ($\overline{\text{SNR}}^d$) as a function of M for Gaussian-fluctuating and deterministic signals at MDL and a high-quality operating point. The inaccuracy of the Gaussian approximation to the detector decision statistic is evident for all but the largest values of M

Exercise 2.4 Compare the Gaussian approximations to the SNR required to achieve the operating point in (2.76) and (2.83). Show that when $P_d = 0.5$ (and $\phi_d = 0$) they are equal, when $P_d > 0.5$ the fluctuating signal requires a higher SNR than the deterministic signal to achieve the operating point but when $P_d < 0.5$ the converse results. Note that P_f should always be less than P_d . What conclusions can be drawn from these results?

Exercise 2.5 Evaluate the derivative of $\overline{\text{SNR}}^d$ in (2.85) with respect to $\log_{10} M$ and plot it as a function of M for various values of P_f and P_d . Observe that as $M \rightarrow \infty$ it tends to -5 , but that it can be several decibels lower for small values of M . Does this imply the incoherent processing improvement for small values of M is better or worse than the asymptotic value of $5 \log_{10} M$?

2.3.5.5 Detection Threshold (DT)

One of the most complicated terms in the sonar equation is the Detection Threshold (DT) term. DT is defined as the SNR in decibels required to achieve a specific (P_d, P_f) operating point for a given statistical signal model, noise model, and detector structure. Although its definition is straightforward, there are a myriad of

ways in which it can be applied and some common misuses. The difficulties and hazards in using and deriving DT are summarized as follows.

- DT can be defined as an SNR using either the total noise power in the processing band or the noise spectrum level (i.e., noise in a 1-Hz band).
- The concept can be applied at different parts of the signal processing chain (e.g., at a hydrophone, after sensor array processing or after coherent detection processing).
- The $-5 \log_{10} M$ term found in some approximations to DT (e.g., from $\overline{\text{SNR}}^d$ in (2.77) or (2.85)) can be misinterpreted as how SNR changes with incoherent integration.
- DT can be misinterpreted as a detector decision threshold and incorrectly used in the implementation of detection algorithms on real data rather than its correct use in system design or analysis as the SNR required to achieve a detector operating point.

When done properly and consistently, any combination of definition and application point (the first two bullets above) will lead to the same end result. Early use of the concept labeled the required SNR the *recognition differential* (RD) [1, 6]. Some applications restrict its use to the MDL case where the probability of detection is 0.5 for a given P_f . Following the convention of [6, 33] et al., the subscript 50 will be used to identify MDL, as in DT_{50} .

Several texts define DT (e.g., see [2, 3, 6]) after sensor array processing as

$$\text{DT}_{\text{Hz}}^a = 10 \log_{10} \frac{P_o^a}{S_n^a(f)} \quad \text{dB re Hz} \quad (2.92)$$

where P_o^a is the MSP of the signal of interest (units of μPa^2) and $S_n^a(f)$ is the noise spectral density (units of $\mu\text{Pa}^2/\text{Hz}$). The subscript notation DT_{Hz} from [2, Ch. 15] has been adopted to highlight the use of the noise in a 1-Hz band (spectral density) rather than the noise in the processing band. Because the ratio within the logarithm in (2.92) is not a unitless ratio, DT_{Hz} has units of dB re Hz. As shown by Urick in [6, Ch. 12], this form most likely arose from early research in the detection of signals in Gaussian noise [47]. When the signal is known exactly, a coherent matched filter (CMF) is the optimal processor (see Sect. 8.2.2) and results in Gaussian-distributed detector decision statistics. Peterson et al. [47] related detection performance to $d = 2\mathcal{E}/N_0$, where \mathcal{E} is the total signal energy, $N_0 = P_n/W$ is the noise power spectral density, and d is called the *detection index*. For this signal, noise, and detector combination, detection index can be related to P_f and P_d according to

$$d = (\phi_f - \phi_d)^2 \quad (2.93)$$

where ϕ_f and ϕ_d are as in (2.78) and (2.79). If T is the time over which the MSP is formed, then $\mathcal{E} = T P_o^a$ and detection index can be described in terms of the linear

forms of the SNR after array processing (S^a) or coherent detection (S^d). Using the results of Sect. 2.3.3, this results in

$$d = \frac{2\mathcal{E}}{N_0} = 2\left(\frac{\mathcal{E}/T}{N_0 W}\right) WT = 2S^a WT = 2S^d. \quad (2.94)$$

The WT term applied to S^a to arrive at S^d is precisely the processing time-bandwidth product representing the gain in SNR from coherent detection processing. Combining (2.93) and (2.94) results in the required SNR

$$\overline{\text{SNR}}^d = 10 \log_{10} \left[\frac{(\phi_f - \phi_d)^2}{2} \right]. \quad (2.95)$$

It is important to note that the required SNR in (2.95) differs from the results presented for the deterministic signal, which most closely resembles the above assumptions, when applied to the active-sonar detector shown in Fig. 2.15. As previously mentioned, the detector structure shown in Fig. 2.15 represents a *quadrature matched filter* for signals with an unknown or uniformly random phase. When the signal is assumed to be known exactly (including its phase, as described in Sect. 8.2.2), there is no formation of the envelope and the SNR required to achieve an operating point as shown in (2.95) will generally be lower than that obtained from Albersheim's or Hmam's equations with $M = 1$.

From (2.94), it can be seen that \mathcal{E}/N_0 is a unitless ratio. So, by using the total noise power in the processing band, as is done in [33, Ch. 3], a unitless (i.e., proper) SNR is obtained. Although this is the approach taken in this text, the means to relate the various definitions and application points is provided as follows. The required-SNR definitions developed earlier in this section are for the SNR after coherent detection processing. As such, DT after coherent detection processing is simply the required SNR,

$$\text{DT}^d = \overline{\text{SNR}}^d. \quad (2.96)$$

Recall formation of $\overline{\text{SNR}}^d$ requires choosing a signal type, defining the amount of incoherent integration (M), and specifying the detector operating point (P_f, P_d).

DT after array processing,

$$\text{DT}^a = \overline{\text{SNR}}^a = \text{DT}^d - 10 \log_{10} WT_{\text{coh}}, \quad (2.97)$$

is related to DT after coherent detection processing according to the gain in SNR achieved by the filtering portion of the detector. As described in Sect. 2.3.2, this is the processing time-bandwidth product WT_{coh} where T_{coh} is the temporal extent of coherent processing (e.g., T_p , the duration of an active sonar waveform). When the signal is assumed to be a band-limited random process (e.g., many narrow- and broad-band passive sonar signals), $T_{\text{coh}} = 1/W$ so the processing time-bandwidth product is one and $\text{DT}^a = \text{DT}^d$.

The historical definition of $DT_{\text{Hz}}^{\text{a}}$, which some may argue provides intuition on performance, is obtained from DT formed using a proper SNR by adding $10 \log_{10} W$,

$$DT_{\text{Hz}}^{\text{a}} = DT^{\text{a}} + 10 \log_{10} W \quad \text{dB re Hz.} \quad (2.98)$$

For example, consider a Gaussian-fluctuating signal with bandwidth $W = 1/T_{\text{coh}}$ and an energy detector with integration time T_{int} . From (2.77) and (2.93), the Gaussian approximation to the energy-detector decision statistic leads to

$$DT^{\text{d}} = \overline{\text{SNR}}^{\text{d}} = -5 \log_{10}(WT_{\text{int}}) + 5 \log_{10} d. \quad (2.99)$$

Now applying (2.97) and (2.98) leads to the result found in [6, Sect. 12.3],

$$DT_{\text{Hz}}^{\text{a}} = 5 \log_{10} \left(\frac{dW}{T_{\text{int}}} \right) \quad \text{dB re Hz.} \quad (2.100)$$

When $M = WT_{\text{int}}$ is small, more accurate results can be obtained by using (2.81) for $\overline{\text{SNR}}^{\text{d}}$ compared with the Gaussian approximation.

With respect to interpreting performance of sonar systems (e.g., comparing noise- to reverberation-limited performance in active sonar), rather than using DT_{Hz} , it is often better to use SNR as developed in Sects. 2.3.2 or 2.3.3 and rely on the monotonically increasing relationship between SNR and P_d given a fixed P_f .

Summary of Required-SNR/DT for Various Signal Model and Detector Combinations

The following table provides the equation numbers for the SNR required to achieve a desired detection operating point (after the linear portion of detection processing; $\overline{\text{SNR}}^{\text{d}} = 10 \log_{10} S^{\text{d}}$) for various combinations of signal type and detector configuration. Recall that $M = WT_{\text{int}}$ is the processing time-bandwidth product when there is incoherent integration over time T_{int} in the quadrature matched filter (QMF) or energy detector (ED). The statistical distributions of the detector decision statistic under the noise and signal-plus-noise hypotheses are in the notation described in Table 5.3 in Sect. 5.6. In some cases the decision statistics have been converted to simpler forms in such a way that the relationship between P_d and P_f does not change (e.g., subtracting M in the CLT approximations).

(continued)

Signal-detector Combination	Required SNR/DT $\overline{\text{SNR}}^d$ or DT^d	Statistical model Noise	Signal+Noise
Signal known exactly (deterministic) with coherent matched filter (CMF)			
Exact result	(2.95)	$\mathcal{N}(0, 1)$	$\mathcal{N}\left(\sqrt{2S^d}, 1\right)$
Deterministic signal with integrated QMF or ED (unknown/uniformly random phase)			
Exact for $M \geq 1$	Sects. 7.5.1 or 8.8.2	χ_{2M}^2	$\chi_{2M, 2MS^d}$
Approx. for $M \geq 1$	Albersheim's (2.85) or Hmam's (2.87) equations		
CLT approx. ($M \gg 1$)	(2.84)	$\mathcal{N}(0, M)$	$\mathcal{N}(MS^d, M[1 + 2S^d])$
Gaussian-fluctuating signal with integrated QMF or ED			
Exact for $M = 1$	(2.75)	Expon(1)	Expon($1 + S^d$)
Exact for $M \geq 1$	(2.81) and Sect. 9.2.7	Gamma($M, 1$)	Gamma($M, 1 + S^d$)
CLT approx. ($M \gg 1$)	(2.77)	$\mathcal{N}(0, M)$	$\mathcal{N}(MS^d, M[1 + S^d]^2)$

Note that SNR^d is defined as the SNR per CPI (coherent processing interval), which is assumed to be constant. The total or integrated SNR used in detection is therefore MS^d .

2.3.6 Relating SNR to Estimation Performance

Similar to how detection threshold is used to describe the SNR required to achieve a specified detection performance, the SNR required to achieve a specified estimation performance can be used in the sonar design process. Ideally, SNR is related to the appropriate estimator performance measure such as variance or mean-squared error (see Sect. 6.3.2) for the specific estimation algorithm to be used. As this is often difficult, use of the Cramér-Rao lower bound (CRLB, see Sect. 6.3.3) on the variance of all unbiased estimators is a common alternative.

As an example, consider the CRLB for estimation of the relative bearing of an object of interest using an equally spaced line array when the signal is deterministic but with unknown phase. The results of [48] provide the CRLB for the relative bearing

$$\text{Var}(\hat{\theta}) \geq \frac{6 \cdot 180^2}{S^h T W n \gamma (n^2 \gamma^2 - 1) \pi^4 \sin^2(\theta)} \quad (2.101)$$

where the estimator $\hat{\theta}$ is in degrees, θ is the angle (relative to the forward array direction) of the object-of-interest, S^h is SNR observed at a hydrophone, TW is the processing time-bandwidth product, and n is the number of hydrophones in the array with spacing d . The parameter $\gamma = f/f_d$ describes the operating frequency of the array (f) relative to the design frequency, $f_d = c_w/(2d)$, and has the effect of reducing the array length when $f < f_d$. The result in (2.101), which is slightly different from the result of [48],³ assumes narrowband beamforming of a deterministic signal in spatially isotropic and temporally white Gaussian noise followed by coherent temporal processing over time T .

Rearranging (2.101) to define the *minimum possible* SNR required to achieve a specific standard deviation in angle estimation ($\sigma_{\hat{\theta}}$) and converting to decibels results in

$$\begin{aligned} \overline{\text{SNR}}^h &= 10 \log_{10} \left(\frac{6 \cdot 180^2}{\pi^4} \right) - 10 \log_{10}(TW) - 10 \log_{10} \left[n\gamma(n^2\gamma^2 - 1) \right] \\ &\quad - 20 \log_{10}(\sigma_{\hat{\theta}}) - 20 \log_{10}|\sin \theta| \\ &\approx 33 - 10 \log_{10}(TW) - 30 \log_{10}(n\gamma) - 20 \log_{10}(\sigma_{\hat{\theta}}) - 20 \log_{10}|\sin \theta| \end{aligned} \quad (2.102)$$

Because these results use the CRLB, there is no guarantee any particular estimator will achieve the desired performance. However, estimating the relative bearing by finding the maximum output of a conventional beamformer with rectangular shading achieves the CRLB when SNR is above a threshold value [48, 49]. Below the threshold, the probability of the maximum beamformer output being far from the true value is large, in which case detection probability will be low (see [49] for the related case of estimating the frequency of a sinusoid in noise). Thus, the above equations are predominantly useful when SNR at the beamformer output is large enough to support a high quality detection operating point.

Although (2.102) is presented in terms of the SNR required at the hydrophone, it can be mapped to the SNR after sensor array processing (by adding $10 \log_{10}(n\gamma)$, which assumes conventional beamforming with a rectangular window) or after coherent detection processing (by additionally adding $10 \log_{10}(TW)$). The SNR after sensor array processing required to achieve various relative-bearing estimation accuracies is shown in Fig. 2.17 as a function of effective array size (i.e., $n\gamma$). The example illustrates how improving estimation performance by a factor of two reduction in the lower bound on the error standard deviation requires an increase in

³The CRLB derived in [48], which begins with sampled data, assumes the in-phase and quadrature components of the noise each have variance σ^2 . The result presented here uses $\sigma^2/2$ so the SNR is S^h formed as a ratio of MSPs. This follows from the discussion of basebanding and sampling signals and noise in Sects. 7.3.1–7.3.5. The result in (2.101) also converts the result to a physical angle from an electronic one and includes the effect of using an array at frequencies below the design.

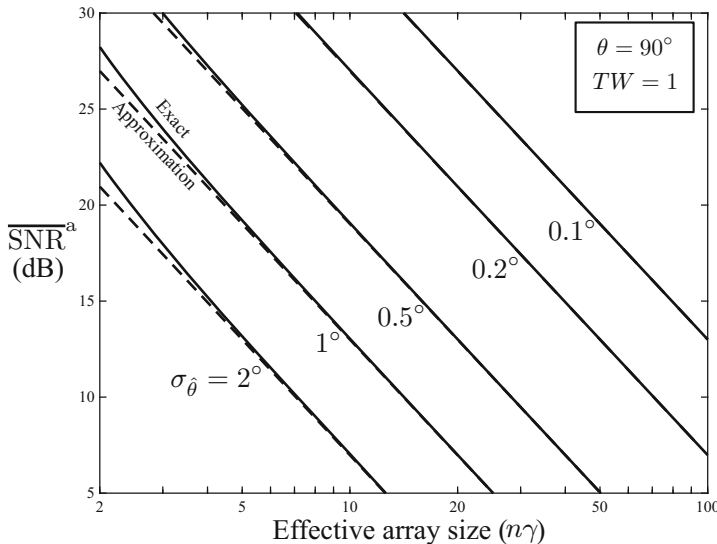


Fig. 2.17 Minimum SNR required to achieve a desired estimation performance as defined by the CRLB for a deterministic signal in isotropic noise

SNR of approximately 6 dB. As previously mentioned, low values of SNR may be in a region where large errors dominate performance. For example, the CRLB for a Gaussian-fluctuating signal is very similar to the result in (2.101)—only marginally larger. However, the fluctuations when no incoherent averaging is applied cause a much higher probability of large error than for the deterministic signal, so the CRLB is too loose of a bound even for higher SNR.

2.3.7 Other Applications of the Sonar Equation

There are many ways in which the sonar equation can be applied. Examples in Sect. 2.3.5 derived the SNR achieved in a particular scenario, which can then be related to detection or estimation performance. Alternatively, the achieved SNR can be related to that required to achieve a specific operating point (i.e., DT) to evaluate what is called signal excess (SE) as described below.

Another use of the sonar equations is to isolate one term to aid in system design or application. This was done in a Sect. 2.3.5 example where the array gain necessary to achieve a performance specification was used for array design. Applying this approach to propagation loss produces what is called the *figure of merit* (FOM).

Both SE and FOM are discussed in the following sections.

2.3.7.1 Signal Excess (SE)

The desired performance of a sonar system produces DT, the SNR required to achieve it, as described in Sect. 2.3.5. Noting that SNR varies with the range to the object of interest it can be useful to assess where the sonar meets, exceeds, or fails to achieve the performance specification. This is accomplished by forming the difference between the achieved SNR and DT, a quantity called the signal excess (SE)

$$\text{SE} = \text{SNR}^d - \text{DT}^d, \quad (2.103)$$

where here it has been defined using SNR and DT after coherent detection processing. Similar to SNR and DT and subject to a consistent development, the SE concept can be applied after sensor array processing and defined using noise spectrum level or total noise power in the processing band. However, conversion from one definition or application point to another, as described in Sect. 2.3.5, must be applied equally to both the SNR and DT terms implying SE is the same for all approaches.

SE describes how close to achieving a specific operating point a sonar is in a given scenario. When $\text{SE} = 0 \text{ dB}$, the sonar achieves the desired performance, when $\text{SE} > 0 \text{ dB}$ it exceeds it and when $\text{SE} < 0 \text{ dB}$ it does not. Our intuition tells us that if SNR increases or decreases by 10 dB detection performance should get, respectively, significantly better or worse. Although this is true, the degree of change depends on the probability distribution function of the detector decision statistic. Consider the plot of P_d against SE shown in Fig. 2.18 where DT is defined for an operating point of $P_d = 0.5$ (MDL) and $P_f = 10^{-4}$. Such a plot is called a *transition curve* [6, Sect. 12.4] as it can be used to determine P_d when SNR differs from DT_{50} by a given amount (i.e., SE). For example, a 5-dB signal excess provides $P_d \approx 1$ for a deterministic signal but is just under 0.8 for a Gaussian-fluctuating signal and even lower for the gamma-fluctuating intensity signal with a scintillation index (SI) of 2.5.

Mathematically, the transition-curve P_d is obtained as

$$P_d(\text{SE}) = \Pr\left\{T \geq h; \text{SNR}^d = \text{DT}_{50}^d + \text{SE}\right\} \quad (2.104)$$

where T is the detector decision statistic and h is the decision threshold yielding the desired P_f . When there is significant incoherent integration (i.e., large M) and the detector decision statistic can be assumed to be Gaussian distributed, the transition-curve P_d is

$$P_d(\text{SE}) = \Phi\left(\phi_f\left[10^{\text{SE}/10} - 1\right]\right) \quad (2.105)$$

where $\Phi(z)$ is the standard normal distribution CDF and $\phi_f = \Phi^{-1}(1 - P_f)$ from (2.78). As seen in Fig. 2.18 the Gaussian assumption produces a steep transition

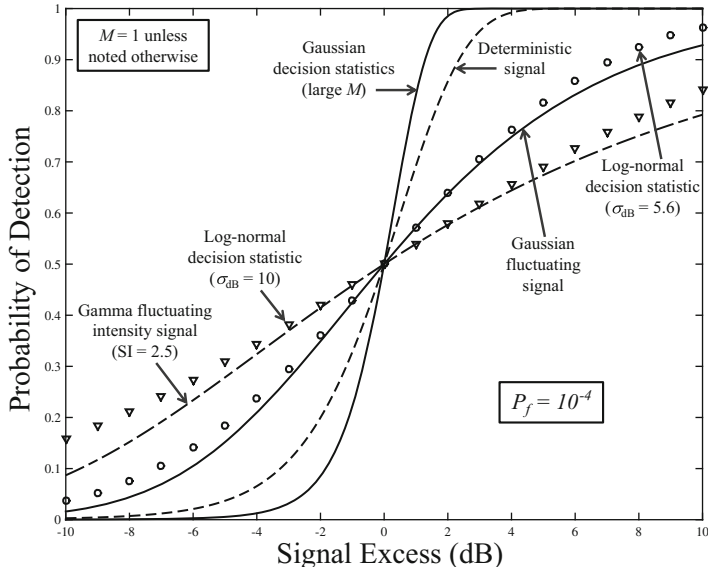


Fig. 2.18 Probability of detection as a function of signal excess with an operating point of $P_d = 0.5$ and $P_f = 10^{-4}$ for various signal or decision-statistic models

from very low P_d to very high P_d as SE varies from negative to positive. The steepness of the transition has been exploited to approximate detection performance over a set of conditions with varying SE, but otherwise equal probability of occurrence. For example, suppose the location (θ) of an object of interest is unknown. By evaluating SE over a set of n equally likely locations $\{\theta_1, \dots, \theta_n\}$, P_d can be approximated by the fraction of locations with a positive SE,

$$P_d \approx \frac{1}{m} \sum_{i=1}^n \mathbb{I}\{\text{SE}(\theta_i) \geq 0\}, \quad (2.106)$$

where $\mathbb{I}\{\cdot\}$ is the indicator function returning unity when the argument is true and zero otherwise. This technique, which assumes the object of interest at location θ_i is either detected perfectly ($P_d(\theta_i) = 1$) or not at all ($P_d(\theta_i) = 0$), is a simple means for obtaining average performance and works when the transition curve is sufficiently steep (the steepness increases as P_f decreases). However, as seen in Fig. 2.18 for the other signal types, the transition curve is not always steep. An alternative approach improving accuracy would be to form a histogram of SE values (e.g., in 1-dB increments) and applying the fraction of counts in each SE bin to the P_d in the bin from the transition curve.

The transition-curve results shown as lines in Fig. 2.18 were generated using (2.104) for each signal model, first adjusting the achieved SNR according to the assumed SE and then using the forward calculation of P_d given the achieved SNR

and the detector decision threshold as dictated by P_f . An approximate technique, as shown in [6, Fig. 12.10], entails assuming the detector decision statistic follows a log-normal distribution under the signal-plus-noise condition so that converting it to decibels (T_{dB}) produces a Gaussian random variable with a mean value of the achieved SNR ($= \text{DT} + \text{SE}$) and a standard deviation (σ_{dB}) related to the extent of signal fluctuations. The transition-curve P_d can then be easily calculated as

$$P_d(\text{SE}) = \Pr\{T \geq h\} = \Pr\{T_{\text{dB}} \geq \text{DT}\} \quad (2.107)$$

$$= \Phi\left(\frac{\text{SE}}{\sigma_{\text{dB}}}\right) \quad (2.108)$$

where $\Phi(\cdot)$ is the standard normal cumulative distribution function. Such a model is convenient to work with because signal fluctuations can be easily quantified from the variance of measurements on a decibel scale. For example, Dyer's [50] saturated multipath phase results yielding $\sigma_{\text{dB}} = 5.6$ can be seen in Fig. 2.18 to approximate the Gaussian-fluctuating signal, from which the 5.6 dB result is derived. The fit is quite good when SE is close to zero; however, the log-normal approximation appears optimistic when SE is further from zero.

Although the log-normal assumption is very simple to apply it can lead to an incorrect use of DT as a threshold in a detector (the form of (2.107) contributes greatly to the confusion) and, as noted in [50] and [6, Sect. 12.4], Gaussian approximations to decibel quantities are not always accurate. An additional disadvantage in assuming the detector decision statistic is log-normal distributed lies in the transition-curve P_d produced as $\sigma_{\text{dB}} \rightarrow 0$, which is a step function at $\text{SE} = 0$. In particular it does not produce the " $\sigma = 0$ " curve in [6, Fig. 12.10] nor does it converge to the deterministic signal as would be desired. A more appealing approach is to employ a more general signal model such as the gamma fluctuating intensity (GFI) model described in Sect. 7.5.4 and use (2.104). The GFI model, which can be defined by an SNR and the scintillation index (SI) of the signal, contains both the deterministic signal ($\text{SI} = 0$) and Gaussian-fluctuating signal ($\text{SI} = 1$) as sub-members. Increasing SI increases signal fluctuations. For example, as seen in Fig. 2.18, the $\text{SI} = 2.5$ case produces results similar to the $\sigma_{\text{dB}} = 10$ case found in [6, Fig. 12.10].

2.3.7.2 Figure of Merit (FOM)

The sonar equation can be re-arranged from defining SNR to describe PL such that SNR equals DT (i.e., the sonar is at the desired operating point). When the performance specification is MDL ($P_d = 0.5$), this value of PL is termed the figure of merit (FOM) of the sonar and describes the maximum PL the system can withstand while still meeting the MDL performance specification. From the basic passive sonar equation in (2.48),

$$\text{FOM} = \text{SL} - \text{NL} + \text{AG} - \text{DT}_{50}^a \quad (2.109)$$

where DT_{50}^a is detection threshold after sensor array processing for $P_d = 0.5$.

For an active sonar system, the link between RL and PL (e.g., see (2.62)) makes evaluating FOM primarily of interest in a noise-limited scenario. By re-arranging (2.60), FOM is seen to be

$$\text{FOM} = \frac{1}{2}[\text{SL} + \text{TS} - \text{NL} + \text{AG} - \text{DT}_{50}^a] \quad (2.110)$$

which is the maximum one-way PL allowable for the system to achieve the desired operating point.

In an environment where PL increases with range, FOM can be used to determine the maximum range at which the sonar system achieves the desired operating point, which is useful in an operational context. However, as noted in [2, Sect. 15.1], FOM requires specification of several situation-specific quantities such as NL, TS for active systems, and SL for passive systems. As such, it may not be useful as a general measure of the performance of a sonar system.

References

1. J.W. Horton, *Fundamentals of SONAR* (United States Naval Institute, Annapolis, 1959)
2. W.S. Burdic, *Underwater Acoustic System Analysis*, 2nd edn. (Peninsula Publishing, Los Altos, 1991)
3. A.D. Waite, *SONAR for Practising Engineers*, 3rd edn. (Wiley, New York, 2002)
4. M. Denny, *Blip, Ping & Buzz: Making Sense of Radar and Sonar* (The Johns Hopkins University Press, Baltimore, 2007)
5. C.H. Sherman, J.L. Butler, *Transducers and Arrays for Underwater Sound* (Springer, Berlin, 2007)
6. R.J. Urick, *Principles of Underwater Sound*, 3rd edn. (McGraw-Hill, Inc., New York, 1983)
7. S.G. Lemon, Towed-array history, 1917-2003. *IEEE J. Ocean. Eng.* **29**(2), 365–373 (2004)
8. H. Cox, Fundamentals of bistatic active sonar, in *Underwater Acoustic Data Processing*, ed. by Y.T. Chan. NATO Science Series E (Kluwer Academic Publishers, Dordrecht, 1989), pp. 3–24
9. D. Grimmett, Multi-sensor placement to exploit complementary properties of diverse sonar waveforms, in *9th International Conference on Information Fusion* (2006), pp. 1–8
10. M.W. Lawrence, Acoustic monitoring of the global ocean for the CTBT, in *Proceedings of the Annual Conference of the Australian Acoustical Society* (2004), pp. 455–459
11. H.E. Daniels, The theory of position finding. *J. R. Stat. Soc. Ser. B Methodol.* **13**(2), 186–207 (1951)
12. Y. Bar-Shalom, P.K. Willett, X. Tian, *Tracking and Data Fusion: A Handbook of Algorithms* (YBS Publishing, Storrs, 2011)
13. W.J. Bangs II, Array processing with generalized beamformers. PhD thesis, Yale University, 1971
14. W.R. Hahn, Optimum signal processing for passive sonar range and bearing estimation. *J. Acoust. Soc. Am.* **58**(1), 201–207 (1975)
15. J.C. Hassab, Passive tracking of a moving source by a single observer in shallow water. *J. Sound Vib.* **44**(1), 127–145 (1976)

16. J.C. Hassab, Contact localization and motion analysis in the ocean environment: a perspective. *IEEE J. Ocean. Eng.* **8**(3), 136–147 (1983)
17. F.B. Jensen, W.A. Kuperman, M.B. Porter, H. Schmidt, *Computational Ocean Acoustics*, 2nd edn. (Springer, New York, 2011)
18. H. Tao, G. Hickman, J.L. Krolik, M. Kemp, Single hydrophone passive localization of transiting acoustic sources, in *OCEANS 2007 - Europe* (2007), pp. 1–3
19. K.L. Cockrell, H. Schmidt, Robust passive range estimation using the waveguide invariant. *J. Acoust. Soc. Am.* **127**(5), 2780–2789 (2010)
20. A.B. Baggeroer, W.A. Kuperman, P.N. Mikhalevsky, An overview of matched field methods in ocean acoustics. *IEEE J. Ocean. Eng.* **18**(4), 401–424 (1993)
21. A. Tolstoy, *Matched Field Processing for Underwater Acoustics* (World Scientific Pub. Co., River Edge 1993)
22. N.J. Willis, *Bistatic Radar* (Artech House, Inc., Norwood, 1991)
23. D.W. Ricker, *Echo Signal Processing* (Kluwer Academic Publishers, Boston, 2003)
24. P.M. Morse, K.U. Ingard, *Theoretical Acoustics* (Princeton University Press, Princeton, 1968)
25. E.J. Kelly, R.P. Wishner, Matched-filter theory for high-velocity accelerating targets. *IEEE Trans. Mil. Electron.* **Mil-9**, 56–69 (1965)
26. J.J. Kroszczynski, Pulse compression by means of linear-period modulation. *Proc. IEEE* **57**(7), 1260–1266 (1969)
27. R.A. Altes, E.L. Titlebaum, Bat signals as optimally Doppler tolerant waveforms. *J. Acoust. Soc. Am.* **48**(4), 1014–1020 (1970)
28. M.A. Richards, *Fundamentals of Radar Signal Processing* (McGraw-Hill, New York, 2005)
29. P.Z. Peebles Jr., *Radar Principles* (Wiley, New York, 1998)
30. Principles and applications of underwater sound. Sum. Tech. Rep. Volume 7, Office of Scientific Research and Development, Nat. Def. Res. Comm. Div. 6, 1946. DTIC accession number AD200786
31. R.P. Hodges, *Underwater Acoustics: Analysis, Design and Performance of Sonar* (Wiley, New York, 2010)
32. World population prospects: The 2015 revision, key findings and advance tables. Technical Report ESA/P/WP.241, United Nations, Department of Economic and Social Affairs, Population Division, New York, 2015
33. M.A. Ainslie, *Principles of Sonar Performance Modeling* (Springer, New York, 2010)
34. ISO 18405.2 International Standard for Terminology in Underwater Acoustics. <https://www.iso.org/obp/ui/#iso:std:iso:18405>
35. W. Benenson, J.W. Harris, H. Stocker, H. Lutz, *Handbook of Physics* (Springer, Berlin, 2000)
36. D.M.F. Chapman, D.D. Ellis, The elusive decibel: thoughts on sonars and marine mammals. *Can. Acoust.* **26**(2), 29–31 (1998)
37. S.M. Kay, *Fundamentals of Statistical Signal Processing: Detection Theory* (Prentice Hall PTR, Upper Saddle River, 1998)
38. A.H. Nuttall, A.F. Magaraci, Signal-to-noise ratios required for short-term narrowband detection of Gaussian processes. Tech. Rpt. 4417, Naval Underwater Systems Center, Newport, October 1972
39. R.P. Chapman, J.H. Harris, Surface backscattering strengths measured with explosive sound sources. *J. Acoust. Soc. Am.* **34**(10), 1592–1597 (1962)
40. H. Hmam, SNR calculation procedure for target types 0, 1, 2, 3. *IEEE Trans. Aerosp. Electron. Syst.* **41**(3), 1091–1096 (2005)
41. W.J. Albersheim, A closed-form approximation to Robertson's detection characteristics. *Proc. IEEE* **69**(7), 839 (1981)
42. G.H. Robertson, Operating characteristics for a linear detector of CW signals in narrow-band Gaussian noise. *Bell Syst. Tech. J.* **46**, 755–774 (1967)
43. D.W. Tufts, A.J. Cann, On Albersheim's detection equation. *IEEE Trans. Aerosp. Electron. Syst.* **AES-19**(4), 643–646 (1983)
44. W.W. Weinstock, *Target Cross Section Models for Radar Systems Analysis*. Ph.D. dissertation, University of Pennsylvania, Philadelphia, 1964

45. D.A. Shnidman, Determination of required SNR values. *IEEE Trans. Aerosp. Electron. Syst.* **38**(3), 1059–1064 (2002)
46. D.A. Abraham, Detection-threshold approximation for non-Gaussian backgrounds. *IEEE J. Ocean. Eng.* **35**(2), 355–365 (2010)
47. W.W. Peterson, T.G. Birdsall, W.C. Fox, The theory of signal detectability. *Trans. IRE Prof. Group Inform. Theory* **4**(4), 171–212 (1954)
48. L. Brennan, Angular accuracy of a phased array radar. *IRE Trans. Antennas Propag.* **9**(3), 268–275 (1961)
49. D. Rife, R. Boorstyn, Single tone parameter estimation from discrete-time observations. *IEEE Trans. Inform. Theory* **20**(5), 591–598 (1974)
50. I. Dyer, Statistics of sound propagation in the ocean. *J. Acoust. Soc. Am.* **48**(1B), 337–345 (1970)

Chapter 3

Underwater Acoustics



3.1 Introduction

The topic of this chapter is underwater acoustics, with an emphasis on the aspects important to signal processing. Within the context of the development process for novel applications presented in Sect. 1.1.4, the material in this chapter is presented to aid in describing the measurements obtained by an underwater acoustic remote sensing system. The inherent assumption of distance in remote sensing applications implies the most important aspect of underwater acoustics is how propagation affects the signal of interest. Several topics related to acoustic propagation in the ocean are covered in Sect. 3.2, including time- and frequency-domain characterizations of the wave equation, the propagation loss term in the sonar equation, and the effects of source motion, refraction and boundary reflection on an acoustic wave. The properties of ambient noise relevant to sonar-equation analysis are covered in Sect. 3.3, including which sources dominate different frequency regimes. The target strength term in the sonar equation and scattering off of objects is covered in Sect. 3.4. Finally, the reverberation level term in the sonar equation and a statistical and spectral characterization of reverberation is presented in Sect. 3.5.

3.2 Acoustic Wave Propagation in the Ocean

Acoustic waves in the ocean arise from a disturbance to the quiescent or equilibrium state at a particular point in space and time. The disturbance causes an oscillation of the adjacent particles and produces a mechanical wave emanating from that point. The mechanical wave transports energy as the disturbance moves away from its

source without bulk transport of the ocean water particles. The resulting acoustic pressure wave is generally assumed to be a small part of the total pressure.¹

In the remote-sensing application of underwater acoustics, the disturbance arises from the object of interest and is represented by the signal $u_o(t)$ which is termed the *source waveform*. The acoustic wave emanating from the source conveys this information through space over time. The subject of underwater acoustic propagation can be defined as determining the acoustic pressure $p(t, \vec{x})$ measured through time and space ($\vec{x} = (x, y, z)$) in terms of the source waveform $u_o(t)$ as the wave propagates through the ocean. In this section, only propagation from the sound projector to the remote sensor measuring it will be considered. To simplify the discussion, propagation will be described as occurring between a sound *source* and a *receiver*. In active sensing systems where there is a second propagation leg, the effects can be accrued.

For several simple scenarios, the spatio-temporal pressure signal $p(t, \vec{x})$ arising from the source can be described precisely as a function of the source waveform $u_o(t)$. The simplest characterization of the ocean as a transmission medium, called the *basic ocean model* in this text, is to assume it is homogenous with respect to propagation characteristics, lossless, dispersionless, and boundaryless. If the source is a pulsating sphere, then the acoustic wave it generates in such an environment is a spherical one, propagating away from the source at the same speed in all directions. The *wavefronts*, which are the points in space concurrently undergoing the same disturbance [1, Sect. 17-2], comprise spheres centered on the source. When the radius of the sphere is large, the wavefront in a small region can be approximated by a plane, which greatly simplifies modeling and analysis in some applications.

However, the ocean can be a very complex environment with respect to its characterization. Physical characterization of the ocean environment is the fundamental objective of the field of physical oceanography [2]. There are many ways in which the realism of the modeling can be improved over the basic ocean model, including:

- boundaries, losses, and/or dispersion;
- depth-dependent propagation characteristics (constant in (x, y));
- bottom layers and propagation through the bottom;
- range, (x, y) , or (x, y, z) dependence to propagation characteristics;
- range or (x, y) dependence to bottom depth;
- rough surfaces, temporal dependence, random components, etc.

Although some of these complexities will be addressed in this section, the intent is primarily to introduce the basic concepts governing how sound propagates in the ocean and provide the models necessary for developing and analyzing underwater

¹In this text the only portion of the pressure measurement considered is that arising from acoustic signals; static pressure is assumed to be constant over time and removed during sensing.

acoustic signal processing algorithms. From a signal-processing perspective it is important to balance the need for realism in the modeling with the tractability of the analysis. This often leads to simple acoustic propagation models, which are acceptable if they retain the pertinent effects. For example, in sonar-equation analysis only the change between the source level and the mean squared pressure as a function of range is required (i.e., propagation loss). In beamforming, however, the phase structure of the wavefront as it passes over the receiving array is of paramount importance.

This section begins by describing the relationship between acoustic pressure, particle velocity and intensity in Sect. 3.2.1. The wave equation and spherical propagation are introduced in Sect. 3.2.2.1. The relationship between periodic signals, wavelength, and wavenumber is described in Sect. 3.2.2.2. Cylindrical spreading and plane waves are described in Sects. 3.2.2.3 and 3.2.2.4 followed by near-field and far-field propagation in Sect. 3.2.2.5. The inhomogeneous wave equation is introduced in Sect. 3.2.3.1 and used to describe the channel impulse response. Their frequency-domain counterparts, the Helmholtz equation and channel frequency response are then described in Sect. 3.2.3.2. How constant-velocity source motion produces a time-scale Doppler effect is derived in Sect. 3.2.3.3 using the inhomogeneous wave equation. The source level and propagation loss terms from the sonar equation are described in Sects. 3.2.3.4 and 3.2.4. The effects of absorption and dispersion are presented in Sect. 3.2.5. How acoustic waves reflect and refract at boundaries and propagate in ocean environments with a depth-dependent sound speed are described in Sects. 3.2.6 and 3.2.7. Ray and normal-mode solutions to the wave equation for a shallow water channel are presented in Sect. 3.2.8. Finally, the concept of reciprocity in acoustic propagation is presented in Sect. 3.2.9.

Basic information on mechanical waves in general and acoustic waves in particular can be found in physics textbooks such as [1] and general acoustics books such as [3, 4]. More detailed examinations of underwater acoustic propagation can be found in texts such as [5–9]. Basic information on physical oceanography can be found in introductory texts such as [2, 10].

3.2.1 Acoustical Field and Power Quantities

The primary objective in Sect. 3.2 is to characterize an acoustic signal as it propagates through the ocean from a sound source to a receiver. From a signal-processing perspective, a description of the acoustic pressure is paramount. However, other quantities such as the mean-squared-pressure, acoustic intensity, power or energy are needed for performance prediction and to characterize sound projectors. Here they are related to the pressure and particle velocity.

Table 3.1 International system units for various acoustic wave quantities and pertinent properties of water in the ocean

Description	Variable	Units	Note
Acoustic pressure	$p(t, \vec{x})$	μPa	Scalar quantity of time and space
Mean squared pressure	$P(\vec{x})$	μPa^2	A function of time for pulses
Particle velocity	$\vec{v}(t, \vec{x})$	m/s	Vector quantity of time and space
Acoustic intensity	$\vec{J}(\vec{x})$ or $J(\vec{x})$	pW/m^2	Power or energy flux density
Acoustic power	\mathcal{P}	pW	Energy flux
Acoustic energy flux density	$\mathcal{E}(\vec{x})$	pJ/m^2	
Speed of sound in water	c_w	m/s	Nominal value is 1500 m/s
Water density	ρ_w	kg/m^3	Nominal value is 1027 kg/m^3

Notes: μ = micro = 10^{-6} ; $\text{pico} = 10^{-12}$

3.2.1.1 Acoustic Pressure and Pressure Levels

The acoustic pressure signal $p(t, \vec{x})$ describes the change in pressure from the static condition at time t and position \vec{x} . By definition as a change from the static condition it is assumed to be on average zero,

$$\frac{1}{T} \int_t^{t+T} p(\tau, \vec{x}) d\tau = 0, \quad (3.1)$$

when T spans many cycles of the lowest frequency under consideration.² The International System of Units convention for pressure is pascals (Pa). Owing to the generally small values of acoustic pressure measured in underwater acoustics, micropascals ($1 \mu\text{Pa} = 10^{-6} \text{ Pa}$) are the accepted standard. A list of units and variables for common quantities in underwater acoustics is found in Table 3.1.

Because most acoustic signals have a temporal variability, pertinent distillations are often extracted to represent the character of the signal. For example, the peak pressure might be of importance to underwater acoustic noise pollution measurements. In the sonar equation analysis of Sect. 2.3, the mean-squared pressure (MSP) is used to determine the performance of a sonar system. MSP is defined as the average of the squared pressure over a time span T ,

$$P(\vec{x}) = \frac{1}{T} \int_t^{t+T} p^2(\tau, \vec{x}) d\tau \quad (3.2)$$

²The acoustic pressure is assumed to be on-average zero in order to simplify various results in later sections; it may not be strictly accurate in all cases, especially if T is not overly large.

where t and T are taken to encompass the pertinent characteristics of the signal (e.g., the extent of an active sonar echo or many cycles of a narrowband noise process). When referring to pressure signals, it is common (but not ubiquitous) for the pressure *level* to represent MSP in decibels. For example, if $P(\vec{x})$ is the MSP at \vec{x} in μPa^2 , the *acoustic pressure level* or *sound pressure level* is $10 \log_{10} P(\vec{x}) \text{ dB}$ re μPa^2 .

3.2.1.2 Particle Velocity

When an acoustic wave travels through water, the water particles oscillate in the same direction as the wave travels.³ Particle velocity is therefore a directional quantity, $\vec{v}(t, \vec{x})$, whereas pressure is a scalar quantity. The relationship between particle velocity and pressure depends on the type of propagating wave (e.g., spherical, planar, or cylindrical) and can be derived from the principles of fluid mechanics yielding the wave equation. Under several simplifying assumptions, which are satisfied by the basic ocean model, the portion of particle velocity attributable to acoustic pressure is related to the spatio-temporal pressure signal through [11, Sect. 1.4]

$$\vec{v}(t, \vec{x}) = \frac{-1}{\rho_w} \int \nabla p(t, \vec{x}) \, dt, \quad (3.3)$$

where ∇ is a spatial gradient and ρ_w is the density of water.

The particle velocity for a plane wave is

$$\vec{v}(t, \vec{x}) = \left[\frac{p(t, \vec{x})}{\rho_w c_w} \right] \vec{u} \quad (3.4)$$

where \vec{u} is the direction of travel (i.e., perpendicular to the planar wavefront) and c_w is the speed of sound. Because a plane wave is a good approximation to a spherical or cylindrical wavefront at long ranges (see Sect. 3.2.2.4), (3.4) approximates the particle velocity when taking \vec{u} as perpendicular to the spherical or cylindrical wavefront, which results in a unit vector in the range dimension. Because the particles only move in one effective dimension for the plane wave, it is common to describe (3.4) in terms of the particle velocity in the direction of travel,

$$v_{\vec{u}}(t, \vec{x}) = \vec{v}(t, \vec{x}) \cdot \vec{u} = \frac{p(t, \vec{x})}{\rho_w c_w}. \quad (3.5)$$

However, it is important to remember that particle velocity is a directional quantity.

³Particle oscillation in the same direction as a wave is traveling defines a longitudinal wave. When an acoustic wave travels through the ocean bottom, it may also include a transverse wave with particles oscillating in the perpendicular direction.

3.2.1.3 Acoustic Intensity

The intensity of an acoustic wave is a measure of power density. It is the time-averaged product of the pressure and particle velocity,

$$\vec{J}(\vec{x}) = \frac{1}{T} \int_t^{t+T} p(\tau, \vec{x}) \vec{v}(\tau, \vec{x}) d\tau, \quad (3.6)$$

and therefore inherently a vector quantity. Similar to forming MSP, the integral should encompass enough time to capture the pertinent signal characteristics. By exploiting the relationship between pressure and particle velocity from (3.4) and only considering the component in the direction of the propagating wave as in (3.5), the intensity for a plane wave is seen to be the mean squared pressure divided by the characteristic impedance of water ($\rho_w c_w$),

$$J(\vec{x}) = \frac{\frac{1}{T} \int_t^{t+T} p^2(\tau, \vec{x}) d\tau}{\rho_w c_w} = \frac{P(\vec{x})}{\rho_w c_w}. \quad (3.7)$$

It is common to use (3.7) to describe an *equivalent plane wave intensity* when the wavefront is not planar [9, Sect. 3.2.2.1]. When pressure is in units of μPa , intensity has units of picowatts per square meter (pW/m^2), which illustrates it is a power density.

In the processing of acoustic signals it is common to describe the integrand in (3.6) as the instantaneous intensity,

$$\vec{I}(t, \vec{x}) = p(t, \vec{x}) \vec{v}(t, \vec{x}) \quad (3.8)$$

or from (3.7) for the plane wave

$$I(t, \vec{x}) = p(t, \vec{x}) v_{\vec{u}}(t, \vec{x}) = \frac{p^2(t, \vec{x})}{\rho_w c_w}. \quad (3.9)$$

Exercise 3.1 Show that the units of intensity formed via (3.7) with $p(t, \vec{x})$ in μPa are pW/m^2 .

3.2.1.4 Acoustic Power

Acoustic power, which is the energy transferred through a surface per unit time (i.e., energy flux), is used to characterize a sound projector. It can be obtained from the intensity as the integral over a surface S enclosing the source [4, Sect. 1-11]

$$\mathcal{P} = \iint_S \vec{J}(\vec{x}) \cdot \vec{n} dS \quad (3.10)$$

where \vec{n} is a unit vector normal to the surface.

Suppose a sound projector produces a spherical wave with MSP $P_o(r)$ at range r . The average intensity on the sphere at range r is then $\mathcal{I}_o(r) = P_o(r)/(\rho_w c_w)$ and the surface integral in (3.10) simplifies to

$$\mathcal{P} = 4\pi r^2 \mathcal{I}_o(r) = 4\pi \frac{r^2 P_o(r)}{\rho_w c_w} = 4\pi \frac{U_o}{\rho_w c_w}, \quad (3.11)$$

where the term $U_o = r^2 P_o(r)$ is called the source factor, which is described in detail in Sect. 3.2.3.4. When pressure is in units of μPa , the acoustic power has units of picowatts (pW).

3.2.1.5 Acoustic Energy Flux Density

Many acoustic signals are short duration and have varying amplitudes (e.g., a marine mammal acoustic emissions, an active sonar echo, or a communications packet). In practice such signals are called transient signals; however, in a mathematical sense they are energy signals because their total energy is finite,

$$\int_{-\infty}^{\infty} p^2(t, \vec{x}) dt < \infty. \quad (3.12)$$

Depending on the application, the energy flux density of a transient signal may be more appropriate to use than the intensity, which is a power density. For example, this is used in an energy form of the sonar equation [9, Sect. 3.3]. The energy flux density for a plane-wave signal is

$$\mathcal{E}(\vec{x}) = \frac{1}{\rho_w c_w} \int_{-\infty}^{\infty} p^2(t, \vec{x}) dt. \quad (3.13)$$

If pressure is in units of μPa , energy flux density will be in units of picojoules per square meter (pJ/m^2).

3.2.2 Propagation and Spreading

With a remote-sensing application in mind, the acoustic waves of interest are those that propagate or travel through the water and so carry information about the object of interest to a sensor. In this section the wave equation, which governs how acoustic waves propagate, is introduced under different coordinate systems (Cartesian, spherical, and cylindrical). The spherical-wave solution to the wave

equation in the basic ocean model is used to identify exploitable structure in the space-time acoustic pressure field when sensing at long ranges, including the plane-wave approximation and how temporal periodicity induces spatial periodicity.

3.2.2.1 The Wave Equation, Spherical Waves, and Spherical Spreading

The basic ocean model (homogeneous sound speed and density with no losses, dispersion, or boundaries) is useful not only in understanding how acoustic waves travel in the ocean, but also because it is an accurate representation over small distances. The latter is important when an acoustic propagation model is necessary in a signal processing algorithm. For example, wavefront shape and propagation delays over an array are used in beamforming as described in Sect. 8.4.

If the source produces a signal $u_o(t)$ at the origin of the coordinate system (i.e., $\vec{x}_o = (0, 0, 0)$), then the resulting acoustic pressure field as a function of time and space, $p(t, \vec{x})$, must satisfy the *wave equation*

$$\nabla^2 p = \frac{1}{c_w^2} \frac{\partial^2 p}{\partial t^2} \quad (3.14)$$

where c_w is the speed of sound and $\nabla^2 = \nabla \cdot \nabla$ is the Laplacian operator, here representing a second-order spatial derivative. In Cartesian coordinates, the Laplacian operator is

$$\nabla^2 p = \frac{\partial^2 p}{\partial x^2} + \frac{\partial^2 p}{\partial y^2} + \frac{\partial^2 p}{\partial z^2}. \quad (3.15)$$

The wave equation can be derived from the principles of fluid mechanics as shown in [4, 9, 12]. It is important to note (3.14) is a linear approximation derived assuming pressure amplitudes are small [4, Sect. 1-5]. The non-linear effects of propagation are usually only encountered at short ranges to very loud disturbances, as is the case when they are induced by parametric sound projectors (e.g., see [6, Sect. 5.3]).

By assuming the source is a point source in the basic ocean model, the acoustic disturbance $u_o(t)$ propagates equally in all directions (i.e., omni-directionally) in expanding concentric spheres. Because there is no dispersion, all frequencies propagate at a constant speed (c_w). Suppose the signal emitted by the source has peak MSP at time \hat{t} . In the following discussion, the wavefront created by the source at time \hat{t} is used to identify one particular wavefront; however, the concepts apply to any wavefront. Spherical propagation and lack of dispersion imply the time at which the peak MSP is observed at range r is $\hat{t} + r/c_w$. Because the pressure of the propagating acoustic wave is identical anywhere on a sphere with radius r , the pressure signal $p(t, \vec{x})$ can be written as a spatial function of range, $p(t, r)$.

Even though the basic ocean model is assumed to be loss-less (i.e., no acoustic energy is lost in a conversion to heat), the peak MSP at range r is not the same as

it was for the original disturbance near the origin. The MSP can be determined as a function of range by appealing to the law of conservation of energy in a closed system. Conservation of energy in a loss-less environment implies here that the acoustic power \mathcal{P} passing through a sphere of radius r does not change with r . Noting acoustic intensity is acoustic power per unit area (see Sect. 3.2.1.3), the intensity of the peak-MSP wavefront on the sphere at range r_1 (and surface area $4\pi r_1^2$) can be related to the intensity at range r_0 according to

$$\mathcal{I}(r_1) = \frac{\mathcal{P}}{4\pi r_1^2} = \frac{r_0^2}{r_1^2} \mathcal{I}(r_0). \quad (3.16)$$

Thus, the intensity and therefore MSP changes with a $1/r^2$ relationship with range. Because intensity and MSP are proportional to the square of pressure (e.g., see (3.2) or (3.7)), the pressure envelope will have a $1/r$ relationship with range. As described in Sect. 3.2.4.1, this result also leads to the propagation-loss formula for spherical spreading, $PL = 10 \log_{10}(r^2) = 20 \log_{10} r \text{ dB re m}^2$.

By combining the time delay and decaying pressure with range, the propagating wave can be surmised to have form

$$p(t, r) = \frac{u_o(t - r/c_w)}{r}, \quad (3.17)$$

which describes a spherical wave propagating away from the source at speed c_w . This development of the spherical wave is intuitive rather than a direct solution to the wave equation and clearly produces an issue as $r \rightarrow 0$, which will be resolved in Sect. 3.2.3.1 when sources are considered. The primary question is, however, does (3.17) satisfy the wave equation in (3.14)? To answer this, the Laplacian operator in (3.15) must be converted to spherical coordinates, for which it is [13]

$$\nabla^2 p = \frac{\partial^2 p}{\partial r^2} + \frac{2}{r} \frac{\partial p}{\partial r} + \frac{1}{r^2} \frac{\partial^2 p}{\partial \phi^2} + \frac{\cos \phi}{r \sin \phi} \frac{\partial p}{\partial \phi} + \frac{1}{r^2 \sin \phi} \frac{\partial^2 p}{\partial \theta^2} \quad (3.18)$$

with the angles θ and ϕ as defined in Fig. 2.4.

As there is no dependence of the spherically propagating wave on either θ or ϕ , the last three terms of the Laplacian operator in (3.18) are zero and (3.14) simplifies to what is known as the spherical wave equation,

$$\frac{\partial^2 p}{\partial r^2} + \frac{2}{r} \frac{\partial p}{\partial r} = \frac{1}{c_w^2} \frac{\partial^2 p}{\partial t^2}. \quad (3.19)$$

The first and second partial derivatives of $p(t, r)$ in (3.17) with respect to r are, for $r > 0$,

$$\frac{\partial p}{\partial r} = -\frac{u_o(t - r/c_w)}{r^2} - \frac{u'_o(t - r/c_w)}{c_w r} \quad (3.20)$$

and

$$\frac{\partial^2 p}{\partial r^2} = \frac{2u_o(t - r/c_w)}{r^3} + \frac{2u'_o(t - r/c_w)}{c_w r^2} + \frac{u''_o(t - r/c_w)}{c_w^2 r}. \quad (3.21)$$

Combining these according to the left side of (3.19) yields

$$\nabla^2 p = \frac{u''_o(t - r/c_w)}{c_w^2 r} = \frac{1}{c_w^2 r} \frac{\partial^2 p}{\partial t^2} \quad (3.22)$$

which is clearly equal to the right side of (3.19) so $p(t, r)$ from (3.17) satisfies the wave equation subject to the differentiability of $u_o(t)$.

The particle velocity of a spherical wave can be determined from (3.3) using the gradient in spherical coordinates,

$$\nabla p(t, r, \theta, \phi) = \frac{\partial p}{\partial r} \vec{e}_r + \frac{1}{r} \frac{\partial p}{\partial \theta} \vec{e}_\theta + \frac{1}{r \sin \theta} \frac{\partial p}{\partial \phi} \vec{e}_\phi, \quad (3.23)$$

where \vec{e}_d is a unit vector in the dimension of d (e.g., $\vec{e}_r = (1, 0, 0)$ in spherical coordinates or $\vec{e}_y = (0, 1, 0)$ in Cartesian coordinates). Because the pressure signal of the spherical wave in (3.17) does not depend on θ or ϕ , water particles will only oscillate in the range dimension,

$$\begin{aligned} \vec{v}(t, r) &= \left[\frac{u_o(t - r/c_w)}{\rho_w c_w r} + \frac{1}{\rho_w r^2} \int u_o(t - r/c_w) dt \right] \vec{e}_r \\ &\approx \frac{p(t, r)}{\rho_w c_w} \vec{e}_r. \end{aligned} \quad (3.24)$$

The approximation arises by noting that acoustic pressure was presumed to be small relative to static pressure and zero mean (see (3.1)), so its integral over time will be small and the second term inconsequential as range increases.

3.2.2.2 Periodic Signals, Wavelength, and Wavenumber

A periodic signal is one having a repetitive structure over time. Although some natural signals are periodic (e.g., short segments of marine mammal whistles), many anthropogenic signals are intentionally so (e.g., those often used in sound projectors or those generated from rotating machinery). The most common periodic signal is the sinusoid,

$$u_o(t) = A_o \cos(2\pi f_o t + \phi_o) \quad (3.25)$$

where A_o is the amplitude, f_o the frequency, and ϕ_o the phase. More generally, however, a periodic signal can be described as satisfying

$$u_o(t) = u_o(t + mT_o) \quad (3.26)$$

for all t and all integer values of m where T_o is called the period. When a periodic signal is emitted by a source at the origin in the basic ocean model, the acoustic pressure satisfies the relationship

$$\begin{aligned} p(t, r) &= \frac{u_o(t - r/c_w)}{r} \\ &= \frac{u_o(t - r/c_w + mT_o)}{r} \\ &= \frac{u_o\left(t - \frac{r - mc_w T_o}{c_w}\right)}{r - mc_w T_o} \left(1 - \frac{mc_w T_o}{r}\right) \\ &\approx p(t, r - mc_w T_o) \end{aligned} \quad (3.27)$$

where the approximation is valid when $r \gg mc_w T_o$. Thus, periodicity in time induces periodicity in space when the acoustic wave propagates. If $u_o(t)$ is periodic with period T_o , then under spherical propagation $p(t, r)$ will be approximately periodic in range with range period

$$\lambda_o = c_w T_o = \frac{c_w}{f_o} \quad (3.28)$$

where $f_o = 1/T_o$ is the fundamental frequency of the periodic signal. The spatial period λ_o is called the *wavelength* of the acoustic wave—the distance between identical wavefronts. The spatial equivalent to radian frequency ($\omega_o = 2\pi f_o = 2\pi/T_o$) is the wavenumber,

$$k_o = 2\pi \left(\frac{1}{\lambda_o}\right) = \frac{2\pi f_o}{c_w}, \quad (3.29)$$

which has units of radians per meter.

The development presented earlier in this section to describe what waveforms satisfy the spherical wave equation allowed the initial acoustic source to be a general signal $u_o(t)$ and only required differentiability. As seen here, if that waveform is periodic in time it will be (approximately) periodic in space. For some applications, periodicity or sinusoidal waveforms in space can be exploited. However, for many applications this is not required. Because of this, the general form of $u_o(t)$ will be used as often as possible in the discussion of propagation.

Exercise 3.2 (Sums of Sinusoids) Show that a weighted sum of sinusoids with different amplitudes, frequencies, and phases is periodic if all the frequencies are rational numbers (i.e., can be represented as a ratio of integers). What is the fundamental frequency of the sum? When there are only two sinusoids and the frequency of one is an irrational number, under what condition is the sum periodic?

3.2.2.3 Cylindrical Spreading

Suppose the basic ocean model is restricted by the surface and bottom boundaries. A spherical wave propagating from a sound source in the water continues until the wavefront encounters a boundary where it can then be reflected back into the ocean. Suppose the reflected waves incur no losses from interaction with the boundaries and when the range is large enough conspire to produce concentric cylindrical wavefronts centered in (x, y) at the location of the source. Applying the same conservation-of-energy logic to cylindrical surface area (area = $2\pi r z_b$ where z_b is bottom depth) as was done for spherical spreading implies the intensity has a $1/r$ relationship with range so pressure will follow a $1/\sqrt{r}$ relationship. This leads to the presumed functional form

$$p(t, r) \approx \frac{u_o(t - r/c_w)}{\sqrt{r_{cs}r}}, \quad (3.30)$$

where the r_{cs} term in the denominator accounts for the losses in the initial spherical spreading and out to the point where the cylindrical wavefronts present themselves. This carries an implicit assumption that $r > r_{cs}$ for the cylindrical wavefronts to occur. Expanding the Laplacian operator in cylindrical coordinates [13] produces the wave equation in cylindrical coordinates,

$$\nabla^2 p = \frac{\partial^2 p}{\partial r^2} + \frac{1}{r} \frac{\partial p}{\partial r} + \frac{1}{r^2} \frac{\partial^2 p}{\partial \theta^2} + \frac{\partial^2 p}{\partial z^2} = \frac{1}{c_w^2} \frac{\partial^2 p}{\partial t^2}. \quad (3.31)$$

For cylindrical wavefronts there is no dependence on z or θ so only the first two terms of the Laplacian operator in (3.31) need to be evaluated, which results in

$$\begin{aligned} \nabla^2 p &= \frac{u''_o(t - r/c_w)}{c_w^2 \sqrt{r_{cs}r}} + \frac{u_o(t - r/c_w)}{4r_{cs}r^{5/2}} \\ &= \left[\frac{u''_o(t - r/c_w)}{c_w^2 \sqrt{r_{cs}r}} \right] \left[1 + \frac{c_w^2}{4r^2} \frac{u_o(t - r/c_w)}{u''_o(t - r/c_w)} \right] \end{aligned} \quad (3.32)$$

when applied to the assumed form of $p(t, r)$ in (3.30). Noting that the first term in brackets is the right-hand side of the wave equation in (3.31) when applied to (3.30), it can be seen that a pure cylindrical wavefront with pressure proportional to $1/\sqrt{r_{cs}r}$ does not strictly satisfy the wave equation because of the latter term in brackets. However, it could be an approximate solution at long ranges because this latter term will tend to one as long as $u_o(t)/u''_o(t)$ is finite. The proper solution to the wave equation in this situation, as shown in Sect. 3.2.8, is a sum over the ray paths connecting the source and receiver or the sum over the modes of a waveguide. Although the cylindrical wave approximation in (3.30) ignores many of the interesting effects of propagation in a waveguide, it does accurately represent

the $1/\sqrt{r_{\text{cs}}r}$ amplitude decay at long ranges. As described in Sect. 3.2.4.1, this formulation leads to the cylindrical-spreading propagation-loss formula,

$$\text{PL} = 10 \log_{10}(r_{\text{cs}}) + 10 \log_{10}(r) \text{ dB re m}^2. \quad (3.33)$$

3.2.2.4 Plane Waves

At long ranges, a spherical or cylindrical wavefront can be approximated locally (i.e., in a small region) by a planar wavefront. For the spherical wavefront, consider a point $\vec{x}_0 = (x_0, y_0, z_0)$ at range $r_0 = \sqrt{x_0^2 + y_0^2 + z_0^2}$. If the source is at the origin, the wavefront at \vec{x}_0 propagates in the direction $\vec{u}_0 = \vec{x}_0/r_0 = (u_{x,0}, u_{y,0}, u_{z,0})$. Using a first-order Taylor series about \vec{x}_0 , the range from the origin to a point \vec{x} near \vec{x}_0 can be approximated by

$$\begin{aligned} r &= \sqrt{x^2 + y^2 + z^2} \\ &\approx r_0 + (\vec{x} - \vec{x}_0) \cdot [\nabla r|_{\vec{x}=\vec{x}_0}] \\ &= r_0 + (\vec{x} - \vec{x}_0) \cdot \vec{x}_0/r_0 \\ &= \vec{x} \cdot \vec{u}_0 \\ &= x u_{x,0} + y u_{y,0} + z u_{z,0}. \end{aligned} \quad (3.34)$$

Inserting this into the solution to the spherical wave equation (3.17) yields

$$p(t, \vec{x}) \approx \frac{u_o \left(t - \frac{1}{c_w} \vec{u}_0 \cdot \vec{x} \right)}{r_0 + (r - r_0)} \quad (3.35)$$

$$\approx \frac{u_o \left(t - \frac{1}{c_w} \vec{u}_0 \cdot \vec{x} \right)}{r_0} \equiv p_o \left(t - \frac{1}{c_w} \vec{u}_0 \cdot \vec{x} \right) \quad (3.36)$$

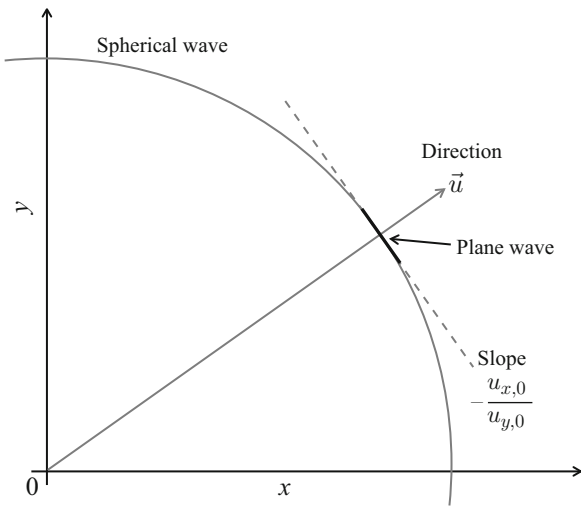
where because $|r_0 - r|$ is assumed to be small relative to r_0 the r in the denominator can be replaced with r_0 . The function $\vec{u}_0 \cdot \vec{x}/c_w = t_p$ describes a plane perpendicular to \vec{u}_0 . For example, in two dimensions it is the line

$$y = -\frac{u_{x,0}}{u_{y,0}} x + \frac{t_p c_w}{u_{y,0}} \quad (3.37)$$

which is depicted in Fig. 3.1.

As might be expected, propagating waves of the form described in (3.36) are called *plane waves*. Their importance lies in the much simpler analysis arising from the linear form of $\vec{u}_0 \cdot \vec{x}$ in (3.36) compared with the non-linear $r = \sqrt{x^2 + y^2 + z^2}$ in (3.17). However, by using the Laplacian operator in cartesian coordinates from

Fig. 3.1 Local approximation of a spherical wave by a plane wave at long range



(3.15) it is easily shown (see exercise) that (3.36) also satisfies the wave equation. This implies that once a plane wave is formed in the basic ocean model, it will continue to propagate as one.

Exercise 3.3 Suppose a plane wave has form

$$p(t, \vec{x}) = p_o(\omega_o t - \vec{k} \cdot \vec{x}) \quad (3.38)$$

where $\vec{k} = [k_x \ k_y \ k_z]^T$ is a vector of wavenumbers. Derive the second-order time and space partial derivatives and use them to show the function satisfies the wave equation in (3.14) only if

$$k_x^2 + k_y^2 + k_z^2 = \frac{\omega_o^2}{c_w^2}. \quad (3.39)$$

Exercise 3.4 Using (3.3) show that the particle velocity of the plane wave in (3.38) is

$$\vec{v}(t, \vec{x}) = \frac{[k_x \ k_y \ k_z]^T}{\|\vec{k}\|} \left[\frac{1}{\rho_w c_w} p_o(\omega_o t - \vec{k} \cdot \vec{x}) \right] \quad (3.40)$$

where $\|\vec{x}\|$ is the length of the vector \vec{x} .

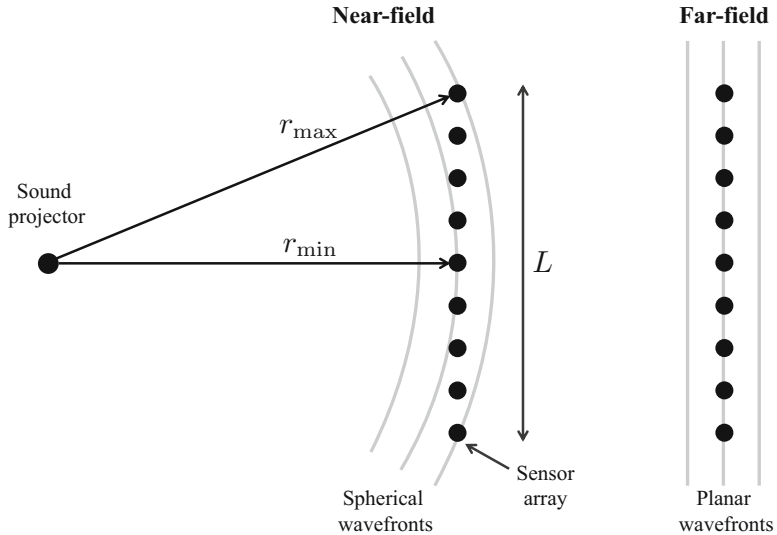


Fig. 3.2 Spherical and planar wavefronts relative to a tangentially aligned line array

3.2.2.5 Near-Field and Far-Field Propagation

When the range from a sensor array to an acoustical source is small enough for spherical wavefronts to have distinct curvature over the array, it is said to be in the *near-field* of the source. In this region, the plane-wave approximation is not valid and the more complicated spherical wavefront must be used. Conversely, when the sensor array is in the *far-field* of the source the plane-wave approximation is accurate.

Suppose a planar wavefront passes over an array of sensors perfectly aligned to the wavefront, as depicted in the far-field scenario shown in Fig. 3.2. When all of the sensors are on the same wavefront, the acoustic pressure can be estimated by averaging the measurements with a gain in performance when the noise is independent from sensor to sensor. If the wavefront is appreciably curved, as shown in the near-field scenario in Fig. 3.2, the sensors will not all measure the same part of the acoustic wave so averaging them may not produce a good estimate of the acoustic pressure.

For a periodic acoustic wave with wavelength λ , a common approximation used to define the far-field condition is to require the difference between the maximum and minimum sensor range (in the plane tangent to the wavefront) to be less than one half wavelength. If the array has length L (more generally L can be taken as cross-range extent), the maximum range difference is less than $\lambda/2$ when

$$r > \frac{L^2}{4\lambda}. \quad (3.41)$$

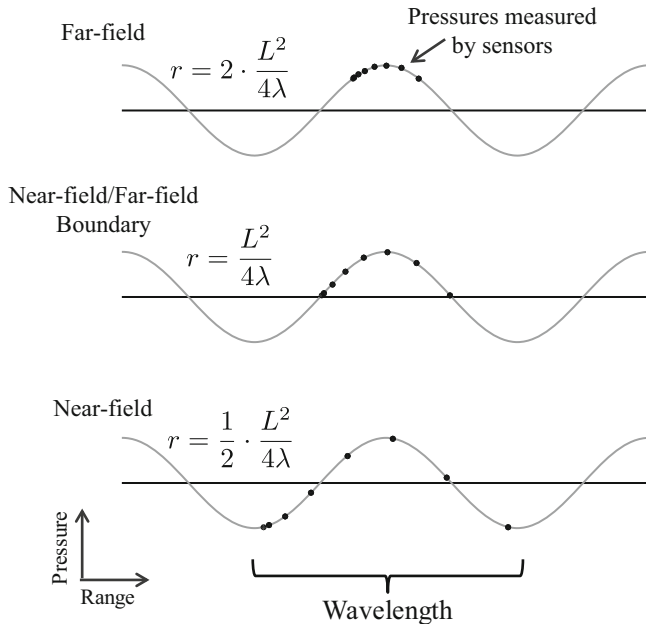


Fig. 3.3 How a spherical wavefront is sampled by a tangentially aligned line array in near-field and far-field conditions. Under a plane-wave assumption, sensor measurements are averaged to estimate the wavefront

The impact of this choice on estimation can be seen in Fig. 3.3 where for the far-field condition (top panel), the pressures measured by the sensors are tightly grouped. For this example, the intent is to measure the crest of the acoustic wave, although the concept applies to any part. At the boundary between near-field and far-field (middle panel), the sensor measurements spread over half the spatial period. Although this results in some loss in performance, it is not as detrimental as when the sensor array is in the near-field (bottom panel). In the near-field the sensor measurements are spread over more than half of a spatial period and necessarily include regions of compression and rarefaction. Because of this, the average of the sensor array measurements may have little in common with the acoustic wave crest intended to be measured. However, if the shape of the wavefront is known, delays can be applied to each sensor to align the measurements before averaging and reduce the mismatch loss. This is known as wavefront curvature processing and is described in [14, 15].

Exercise 3.5 Suppose an array has a fixed number of sensors (n) spaced every half wavelength. Show that the far-field condition described by (3.41) is

$$r > \frac{(n-1)^2 \lambda}{16}. \quad (3.42)$$

Thus when the length of the array is proportional to wavelength, then the far-field condition occurs farther away from the sound source at lower frequencies than higher ones. If $n = 32$, show that the far-field condition begins at 900, 90, and 9 m, respectively, when $f = 100$ Hz, 1 kHz, and 10 kHz for $c_w = 1500$ m/s.

3.2.3 Sound Projection and Propagation

When describing an application of underwater acoustics as a remote-sensing problem, the object of interest either projects or reflects acoustic waves into the water, where they then propagate to a distant sensor. Several topics related to this projection and propagation of sound are covered in this section. A key enabler is found by describing the input/output relationship of the source signal and the ensuing remote pressure measurement through the inhomogeneous wave equation and the channel impulse response in Sect. 3.2.3.1. The corresponding frequency-domain representations, the Helmholtz equation and the channel frequency response, are described in Sect. 3.2.3.2. The time-scale Doppler effect is shown to arise from constant-velocity motion of the sound source in Sect. 3.2.3.3. Finally, the source level term in the sonar equation and its linear form (the source factor) are explained in Sect. 3.2.3.4.

3.2.3.1 Inhomogeneous Wave Equation and the Channel Impulse Response

The linear wave equation is a partial differential equation (PDE) in space and time. The form in (3.14) represents the homogenous PDE for which initial and boundary conditions must be used to elicit a usable solution. Complete solutions first require defining the inhomogeneous wave equation [16, Sect. 5.15], [7, Sect. 4.2]

$$\nabla^2 p(t, \vec{x}) - \frac{1}{c_w^2} \frac{\partial^2 p(t, \vec{x})}{\partial t^2} = u(t, \vec{x}) \quad (3.43)$$

where $u(t, \vec{x})$ is the forcing function and the temporal and spatial dependencies are made explicit. The homogenous PDE shown in (3.14) clearly arises when $u(t, \vec{x}) = 0$. The form of the forcing function depends on how sound is introduced to the propagation medium (e.g., from mass injection or from body forces [16, Sect. 5.15]).

Consider as an example the spherical wave $p(t, r) = u_o(t - r/c_w)/r$ from (3.17), which was produced by a source at the coordinate origin of the basic ocean model. The spherical wave was shown to satisfy the homogenous wave equation (3.14) when $r > 0$, but not at the location of the source ($r \rightarrow 0$). For a point source at the origin the forcing function becomes [16, Sect. 5.16]

$$u(t, \vec{x}) = -4\pi u_o(t)\delta(\vec{x}) \quad (3.44)$$

where $\delta(\vec{x}) = \delta(x)\delta(y)\delta(z)$ is the Dirac delta function in Cartesian coordinates. The Dirac delta function in a single dimension, $\delta(x)$, is only non-zero near $x = 0$ where it has infinite height and infinitesimal width so that the area under the function is one (see Sect. 4.2). With this forcing function zero everywhere in space except the origin, it is not surprising that the spherical wave is a solution to the inhomogeneous wave equation when $r > 0$. More importantly, it is also a solution as $r \rightarrow 0$ (see the second exercise below) so the complete solution to the PDE in the basic ocean model is the spherical wave. An implication of this is that the units of the source waveform $u_o(t)$ will be distance times pressure so that $u_o(t - r/c_w)/r$ will have units of pressure.⁴

The analysis of linear, time-invariant systems is significantly simplified through the use of the system *impulse response* and *convolution*. Any input signal to a system can be described as a weighted combination of delayed impulse functions. Linearity and time-invariance then allow the system output to be described as a similarly weighted combination of delayed versions of the system impulse response (i.e., a convolution of the input signal and the system impulse response). Background information on the impulse response of a linear time-invariant system and convolution can be found in Sect. 4.2. In the present application, the effects of propagation from a sound source at \vec{x}_o through an underwater channel to a receiver at \vec{x} can be described by the *channel impulse response*, which is the solution to (3.43) when the source waveform is an impulse in time at the location of the source,

$$u(t, \vec{x}) = -4\pi\delta(t)\delta(\vec{x} - \vec{x}_o), \quad (3.45)$$

and the initial conditions are zero. By letting $u_o(t) = \delta(t)$ in the aforementioned spherical wave solution and translating the source position to \vec{x}_o , the channel impulse response for the basic ocean model is

$$h(t, \vec{x}) = \frac{\delta(t - \|\vec{x} - \vec{x}_o\|/c_w)}{\|\vec{x} - \vec{x}_o\|} \quad (3.46)$$

where $\|\vec{x}\|$ is the length of the vector \vec{x} . The effect of propagation on the sound projected by the source and measured at \vec{x} is then evaluated through the convolution (denoted by the operator $*$) between $u_o(t)$ and $h(t, \vec{x})$,

$$p(t, \vec{x}) = u_o(t) * h(t, \vec{x}) = \int_{-\infty}^{\infty} u_o(\tau)h(t - \tau, \vec{x}) d\tau. \quad (3.47)$$

Noting that $u_o(t)$ has units of pressure times distance, $h(t)$ must have units of one over the product of distance and time (e.g., $1/(ms)$) in order for $p(t, \vec{x})$ to be pressure. It is important to note that some characterizations of propagation from a

⁴These units are codified by international standard in [17, Sect. 3.3.1.4].

point source to a receiver as a linear system utilize $4\pi u_o(t)$ or $-4\pi u_o(t)$ (e.g., [5, 8]) as an input rather than $u_o(t)$ (e.g., [7]). Although the resulting impulse response will differ by a scale of $(4\pi)^{-1}$ or $-(4\pi)^{-1}$, the output $y(t, \vec{x})$ in (3.47) will be identical as long as all approaches are applied consistently (i.e., any scale β applied to the input signal $u_o(t)$ appears as $1/\beta$ in $h(t)$ so they cancel in (3.47)).

The complete solution to the linear wave equation requires the particular solution from (3.43) linearly combined with solutions to the homogenous wave equation in (3.14) while accounting for initial and/or boundary conditions. For most problems of interest, the initial conditions will be zero so the input sources and boundary conditions are paramount to the solution. Analytical solutions exist for a variety of simple ocean environments [7, 8]. Of particular interest in this text are those resulting in multiple propagation paths or multiple modes. For example, when multiple propagation paths connect the source and receiver, the channel impulse response is a sum of delayed and scaled impulse functions,

$$h(t, \vec{x}) = \sum_{i=1}^N a_i \delta(t - \tau_i), \quad (3.48)$$

where a_i and τ_i are the amplitude and propagation delay of the i th path (e.g., $a_1 = 1/\|\vec{x} - \vec{x}_o\|$ and $\tau_1 = \|\vec{x} - \vec{x}_o\|/c_w$ for the spherical wave). Such a propagation scenario is called a *multipath channel*. When the ocean can be described as a horizontally stratified waveguide, the complete solution to (3.43) results in a sum over mode functions, which will be covered in Sect. 3.2.8.2.

Exercise 3.6 Confirm that using the channel impulse response from (3.46) in the convolution from (3.47) produces the general form of the spherical wave solution in (3.17) when the source is at the origin.

Exercise 3.7 Show $p(t, \vec{x}) = u_o(t - r/c_w)/r$ satisfies (3.43) as $r \rightarrow 0$ when $u(t, \vec{x}) = \delta(\vec{x})u_o(t)$. Start by describing $p(t, \vec{x})$ as the limit of a function $p_\varepsilon(t, \vec{x})$ without a singularity at the origin,

$$p_\varepsilon(t, \vec{x}) = \frac{u_o(t - r/c)}{r + \varepsilon}. \quad (3.49)$$

Then, using $p_\varepsilon(t, \vec{x})$, simplify the left side of (3.43) using the Laplacian in spherical coordinates from (3.18). Next, integrate both sides over a spherical volume \mathcal{V} centered at the origin and with radius δ . Use the sifting property of the multi-dimensional impulse function,

$$\int_{\mathcal{V}} \delta(\vec{x}) dV = 1, \quad (3.50)$$

to simplify the right-hand side. Note that in spherical coordinates the differential volume element is $dV = r^2 \sin \phi dr d\phi d\theta$. Finally, take the limit as $\varepsilon \rightarrow 0$.

3.2.3.2 Helmholtz Equation and Channel Frequency Response

Because the coefficients in the wave equation ((3.14) or (3.43)) do not depend on time, the temporal dimension can be removed by a transformation to the frequency domain, resulting in a PDE only in the spatial dimensions. Applying the Fourier transform (see Sect. 4.3) to the temporal dimension of $p(t, \vec{x})$ results in

$$\mathcal{F}\{p(t, \vec{x})\} = \int_{-\infty}^{\infty} p(t, \vec{x}) e^{-j2\pi ft} dt = P(f, \vec{x}), \quad (3.51)$$

which is a function of frequency and space. The Helmholtz equation, which is simply the wave equation in the frequency domain [8, Sect. 2.2], can be obtained by taking the Fourier transform of each side of (3.43). Interchanging the order of the Fourier integral and Laplacian operator and using the derivative property of the Fourier transform (see (4.37) in Sect. 4.3) yields the Helmholtz equation,

$$\nabla^2 P(f, \vec{x}) + k^2 P(f, \vec{x}) = U(f, \vec{x}) \quad (3.52)$$

where $k = 2\pi f/c_w$ is the wavenumber and $U(f, \vec{x})$ is the Fourier transform of $u(t, \vec{x})$.

The *channel frequency response* $H(f, \vec{x})$ to a point source at \vec{x}_o is the complete solution to (3.52) for the impulsive source signal in (3.45) which yields $U(f, \vec{x}) = -4\pi\delta(\vec{x} - \vec{x}_o)$. $H(f, \vec{x})$ is also the Fourier transform of the channel impulse response $h(t, \vec{x})$ and is known in the ocean acoustics literature as the Green's function where it is generally used as a function of \vec{x} and \vec{x}_o . The convenience of the frequency domain representation of the system lies in the simplification of a convolution to a product. If $U_o(f)$ is the Fourier transform of the point source input signal $u_o(t)$, the Fourier transform of the pressure signal measured at \vec{x} is

$$P(f, \vec{x}) = H(f, \vec{x})U_o(f). \quad (3.53)$$

As an example, consider the multipath channel described by (3.48). The channel frequency response is the weighted sum over the paths of a complex phase term depending on each path's delay,

$$H(f, \vec{x}) = \mathcal{F}\{h(t, \vec{x})\} = \sum_{i=1}^N a_i e^{-j2\pi f \tau_i}. \quad (3.54)$$

As noted in Sect. 3.2.3.1, there can be a scale difference of $\pm 4\pi$ in the definition of the system input (here $U_o(f)$), depending on the derivation. Similar to the impulse response, this results in a scale difference in the frequency response of $\pm(4\pi)^{-1}$, but no difference in $P(f, \vec{x})$ in (3.53).

A variety of analytical and numerical techniques exist to solve the Helmholtz equation [8]. Because the solution is in the frequency domain, any time-domain representation of the pressure requires solving (3.52) or (3.53) at the frequencies comprising the signal followed by an inverse Fourier transform,

$$p(t, \vec{x}) = \int_{-\infty}^{\infty} P(f, \vec{x}) e^{j2\pi ft} df. \quad (3.55)$$

In utilizing solutions to (3.52), it is important to note that there are multiple conventions for defining the Fourier transform, with variations potentially altering the sign in the exponent, amplitude scaling, and use of frequency (f) or angular frequency ($\omega = 2\pi f$). The convention followed in this text is denoted by the transform pair in (3.51) and (3.55) and detailed in Sect. 4.3. The choice can affect $P(f, \vec{x})$ by scale or complex conjugation, but not $p(t, \vec{x})$ when the transform, solution, and inverse transform are performed consistently with respect to the definition.

3.2.3.3 Doppler Effect via the Inhomogeneous Wave Equation

The time-scale Doppler effect was derived in Sect. 2.2.5.1 by matching the trajectories of the platform and acoustic wavefront over time. In this section it is derived by allowing the source in the inhomogeneous wave equation to have motion. Suppose the sound projector moves away from the origin at a constant velocity v in the x dimension while projecting a source signal $u_o(t)$. The inhomogeneous wave equation from (3.43) and (3.44) then becomes

$$\nabla^2 p(t, \vec{x}) - \frac{1}{c_w^2} \frac{\partial^2 p(t, \vec{x})}{\partial t^2} = -4\pi u_o(t) \delta(x - vt) \delta(y) \delta(z). \quad (3.56)$$

As described in [18, Sect. 11.2] or [19], this can be converted to a wave equation with a stationary source, such as that in (3.44), through a sequence of two linear coordinate transformations. The first transformation is to the variables

$$\tilde{t} = \gamma \left(t - \frac{v}{c_w^2} x \right), \quad \tilde{x} = \gamma(x - vt), \quad \tilde{y} = y, \quad \text{and} \quad \tilde{z} = z \quad (3.57)$$

where

$$\gamma = \frac{1}{\sqrt{1 - \frac{v^2}{c_w^2}}} \quad (3.58)$$

keeps the Jacobian of the transformation equal to one. Evaluating the effect on (3.56) first requires inverting the transformation for the two coupled variables, which results in

$$x = \gamma(\tilde{x} + v\tilde{t}) \quad \text{and} \quad t = \gamma\left(\tilde{t} + \frac{v}{c_w^2}\tilde{x}\right). \quad (3.59)$$

Noting that $\delta(x/a) = a\delta(x)$ when preserving the sifting property of the impulse function, the right-hand side (RHS) of (3.56) under the first transformation becomes

$$\text{RHS}(3.56) = -4\pi\gamma u_o\left(\gamma\tilde{t} + \frac{v}{c_w^2}\gamma\tilde{x}\right)\delta(\tilde{x})\delta(\tilde{y})\delta(\tilde{z}) \quad (3.60)$$

$$= -4\pi\gamma u_o(\gamma\tilde{t})\delta(\tilde{x})\delta(\tilde{y})\delta(\tilde{z}) \quad (3.61)$$

where the argument of u_o in (3.60) can be simplified to that in (3.61) because $\delta(\tilde{x})$ is only non-zero when $\tilde{x} = 0$.

As described in [18, Sect. 11.2] for the acoustic velocity potential (an integrated pressure) the form of the left-hand side of (3.56) does not change under this linear transformation. Define $\tilde{p}(\tilde{t}, \tilde{x})$ as simply $p(t, \tilde{x})$ taken as a function of the transformed variables in (3.57). The inhomogeneous wave equation from (3.56) then becomes

$$\nabla^2 \tilde{p}(\tilde{t}, \tilde{x}) - \frac{1}{c_w^2} \frac{\partial^2 \tilde{p}(\tilde{t}, \tilde{x})}{\partial \tilde{t}^2} = -4\pi\gamma u_o(\gamma\tilde{t})\delta(\tilde{x})\delta(\tilde{y})\delta(\tilde{z}) \quad (3.62)$$

in the coordinates of the first transformation, $(\tilde{t}, \tilde{x}, \tilde{y}, \tilde{z})$.

The second transformation simply scales all the variables by γ ; that is, $\check{t} = \gamma\tilde{t}$, $\check{x} = \gamma\tilde{x}$, $\check{y} = \gamma\tilde{y}$, and $\check{z} = \gamma\tilde{z}$. Using the chain rule on the left-hand side (LHS) of (3.62) shows that the transformation produces a multiplicative scale factor of γ^2 in each term,

$$\text{LHS}(3.62) = \gamma^2 \nabla^2 \check{p}(\check{t}, \check{x}) + \gamma^2 \frac{\partial^2 \check{p}(\check{t}, \check{x})}{\partial \check{t}^2}, \quad (3.63)$$

where

$$\check{p}(\check{t}, \check{x}) = \tilde{p}(\check{t}/\gamma, \check{x}/\gamma) \quad (3.64)$$

is the space-time pressure field in the coordinate system of the second transformation. Applying the second transformation to the RHS of (3.62) and combining with (3.63) then produces an inhomogeneous wave equation,

$$\nabla^2 \check{p}(\check{t}, \check{x}) + \frac{1}{c_w^2} \frac{\partial^2 \check{p}(\check{t}, \check{x})}{\partial \check{t}^2} = -4\pi\gamma^2 u_o(\check{t})\delta(\check{x})\delta(\check{y})\delta(\check{z}), \quad (3.65)$$

in the coordinates $(\check{t}, \check{x}, \check{y}, \check{z})$ with the desired stationary source. Note, however, that the source signal in this coordinate system is a multiplicative factor γ^2 larger than

the original one in (3.56). The time-varying pressure observed at $\vec{x} = (x, y, z)$ is then obtained by solving this wave equation to obtain $\check{p}(\check{t}, \check{\vec{x}})$ and mapping the solution back to the original coordinate system through the relationships

$$\check{t} = \gamma^2 \left(t - \frac{v}{c_w^2} x \right), \quad \check{x} = \gamma^2 (x - vt), \quad \check{y} = \gamma y, \quad \text{and} \quad \check{z} = \gamma z. \quad (3.66)$$

For example, using the spherical-wave solution from (3.17) for the basic ocean model produces

$$\check{p}(\check{t}, \check{\vec{x}}) = \gamma^2 \frac{u_o(\check{t} - \check{r}/c_w)}{\check{r}} = p(t, \vec{x}) \quad (3.67)$$

where $\check{r} = \sqrt{\check{x}^2 + \check{y}^2 + \check{z}^2}$ and the dependence on t and \vec{x} is obtained through (3.66). Thus, the pressure observed at \vec{x} from a source projecting $u_o(t)$ while moving with constant course and speed in the basic ocean model is the source signal with a time-varying argument ($\tau(t) = \check{t} - \check{r}/c_w$) and a time-varying amplitude (γ^2/\check{r}). Given a sensor position \vec{x} , the time-varying argument of the source signal is

$$\tau(t) = \check{t} - \frac{\check{r}}{c_w} = \gamma^2 \left(t - \frac{v}{c_w^2} x \right) - \frac{\gamma}{c_w} \sqrt{\gamma^2(x - vt)^2 + y^2 + z^2}. \quad (3.68)$$

If \vec{x} lies on the x axis, this form simplifies considerably to an affine function of t (e.g., see [19]). However, when $|v| \ll c_w$ it is very close to an affine function in the more general scenario and so may be approximated by a Maclaurin series. This requires

$$\tau(0) = -\frac{\gamma r_\gamma}{c_w} \left(1 + \frac{v \cos \theta}{c_w} \right) \quad (3.69)$$

where

$$r_\gamma = \sqrt{\gamma^2 x^2 + y^2 + z^2} \quad (3.70)$$

and $\cos \theta = \gamma x / r_\gamma$ so θ is approximately the angle between the axis of the sound projector's motion and the direction of the sensor at \vec{x} (because $\gamma \approx 1$ when $|v| \ll c_w$). It can then be shown that

$$\tau'(0) = \gamma^2 \left(1 + \frac{v \cos \theta}{c_w} \right) \quad (3.71)$$

and

$$\tau''(0) = -\frac{\gamma^3 v^2 \sin^2 \theta}{c_w r_\gamma}. \quad (3.72)$$

Because $\tau''(0)$ is proportional to v/c_w and inversely proportional to the range r_γ , a first-order Maclaurin series is sufficient to describe $\tau(t)$ even when θ is not near zero, which occurs when the projector is approximately moving toward or away from the sensor. This approximation to the argument of the source function is then

$$\tau(t) \approx \left[\frac{1 + \frac{v \cos \theta}{c_w}}{1 - \frac{v^2}{c_w^2}} \right] \left(t - \frac{r_\gamma}{\gamma c_w} \right) \quad (3.73)$$

$$\approx \left[\frac{1}{1 - \frac{v \cos \theta}{c_w}} \right] \left(t - \frac{r}{c_w} \right), \quad (3.74)$$

where (3.74) is formed from (3.73) as a first-order Maclaurin series in v/c_w applied to the inverse of the term in brackets. Using this in (3.67) then produces the form found in (2.16),

$$p(t, \vec{x}) \approx \frac{u_o(\eta[t - r/c_w])}{r} \quad (3.75)$$

with the Doppler scale

$$\eta = \frac{1}{1 - \frac{v \cos \theta}{c_w}} \quad (3.76)$$

where the approximation $\check{r}/\gamma^2 \approx |\vec{x}| = r$ arises from assuming the projector does not move very far over the temporal extent of the signal compared to the range of the sensor.

3.2.3.4 Source Factor and Source Level (SL)

The source level (SL) term is the starting point for the sonar equation and describes how much sound is introduced into the ocean either by the object of interest (passive sonar) or a sound projector (active sonar). In an analytical context, it is convenient to represent the sound projector as a point source located at the acoustical center of the physical source (\vec{x}_o). Suppose a point source produces a source waveform $u_o(t)$ that enters the forcing function of the inhomogeneous wave equation (via (3.43) and (3.44)) in the basic ocean model. The average “power” in the input to this system is then the averaged squared mean of the initial disturbance created by the object of interest,

$$U_o = \frac{1}{T} \int_t^{t+T} u_o^2(\tau) d\tau, \quad (3.77)$$

which is called the source factor [9, Sect. 3.2.2] and [17, Sect. 3.3.1.6]. Recall from the discussion in Sect. 3.2.3.1 that the source waveform $u_o(t)$ had units of pressure times distance (e.g., $\mu\text{Pa} \cdot \text{m}$), which implies that U_o has units of $\mu\text{Pa}^2\text{m}^2$. The SL term in the sonar equation is then the decibel equivalent of the source factor,

$$\text{SL} = 10 \log_{10}(U_o) \text{ dB re } \mu\text{Pa}^2\text{m}^2. \quad (3.78)$$

To provide some physical context for the source factor U_o and the SL term in the sonar equation, consider the MSP at range r from the point source at \vec{x}_o under spherical spreading. From (3.17) the pressure at range r is $p(t, r) = u_o(t - r/c_w)/r$, which results in MSP

$$P(r) = \frac{1}{r^2} \left[\frac{1}{T} \int_t^{t+T} u_o^2(\tau - r/c_w) d\tau \right]. \quad (3.79)$$

Clearly U_o is not related to the MSP at the location of the point source because letting $r \rightarrow 0$ results in an infinitely large MSP. While this was treated in Sect. 3.2.3.1 using an impulse function at \vec{x}_o , it does not lend itself to a satisfying physical interpretation. By adjusting t in (3.79) to account for propagation delay it can be seen that

$$P(r) = \frac{U_o}{r^2} = \frac{U_o}{L_p(r)} \quad (3.80)$$

where $L_p(r) = r^2$ is the propagation loss factor for spherical spreading. It can now be seen from (3.80) that the source factor is the propagation loss factor times the MSP measured at a range r ,

$$U_o = L_p(r) P(r) = r^2 P(r). \quad (3.81)$$

This implies that U_o is the same irrespective of the range at which the MSP is measured (while spherical spreading holds)—it represents the “power” of the input to the system. From (3.81) it appears that by hypothetically considering range $r = 1 \text{ m}$, that the source factor is the MSP a distance 1 m from the source (i.e., $U_o = P(1)$). Although these two quantities have the same numerical value, the MSP interpretation lacks the m^2 in the units of the source factor, which have been codified in an international standard [17].

In practice, projector source levels must be obtained from in-water measurements that are usually made far enough away from the source for the wavefront to be in the far-field [20, Sect. 12.7] and in conditions subject to spherical spreading. The

far-field measurements are then used to obtain the source factor through (3.81) and yield the source level

$$SL = 10 \log_{10} \left\{ r^2 P(r) \right\} \text{ dB re } \mu\text{Pa}^2\text{m}^2. \quad (3.82)$$

Note that the reference units required to make the ratio inside the logarithm unitless are $\mu\text{Pa}^2\text{m}^2$. With this notation there is no need for the “at 1 m” qualification that often accompanies SL; the reference units properly account for it. For example, suppose an MSP of 160 dB re μPa^2 was measured a distance of 100 m from the source. The source level is then $SL = 160 + 10 \log_{10} \{100^2\} = 200$ dB re $\mu\text{Pa}^2\text{m}^2$. Although one could say the source has sound pressure level 160 dB re μPa^2 at 100 m, this is not the SL term in the sonar equation. One could also say that the MSP hypothetically measured at 1 m distance from the source is 200 dB re μPa^2 . Although this is numerically equivalent to the SL term in the sonar equation, the reference units are different and do not work correctly with the other terms in the sonar equation, in particular the propagation loss term.

3.2.4 Propagation Loss (PL)

Recall that the sonar equation is used to describe pressure levels throughout the remote sensing system in a simple fashion using decibel notation. The propagation-loss (PL) term maps the source level, which represents the initial disturbance caused by the object of interest and the input to the inhomogeneous wave equation, to the sound pressure level measured at the receiver. By converting (3.80) to decibels, the MSP level at a receiver at range r ,

$$\begin{aligned} 10 \log_{10} \left\{ \frac{P(r)}{(1 \mu\text{Pa})^2} \right\} &= 10 \log_{10} \left\{ \frac{U_o}{(1 \mu\text{Pa})^2 (1 \text{ m})^2} \right\} - 10 \log_{10} \left\{ \frac{L_p(r)}{(1 \text{ m})^2} \right\} \text{ dB} \\ &= SL - PL, \end{aligned} \quad (3.83)$$

is seen to be the source level minus the propagation loss (PL), where

$$PL = 10 \log_{10} \left\{ L_p(r) \right\} \text{ dB re } \text{m}^2. \quad (3.84)$$

It is important to note that the propagation loss factor $L_p(r)$ has units of m^2 and PL is in dB re m^2 . To reiterate, this arises because $L_p(r) = U_o/P(r)$ is the ratio of the source factor (units: $\mu\text{Pa}^2\text{m}^2$) to the MSP at a particular location (units: μPa^2). The International Organization for Standardization (ISO) standard for terminology in underwater acoustics [17] calls out a separate definition for *transmission loss* (TL), which is the decibel equivalent of the ratio of a particular quantity (e.g., MSP or average intensity) as measured at two different points. Because the ratio is unitless, TL has units of decibels.

3.2.4.1 Propagation Loss for Different Spreading Models

As previously mentioned, propagation loss for spherical spreading is

$$PL = 20 \log_{10}(r) \text{ dB re m}^2. \quad (3.85)$$

As described in [9, Sect. 9.1.1.2], an approximation to PL for cylindrical spreading can be obtained when the source and receiver are not too close to the boundaries and by making the following assumptions: (i) multipath propagation, (ii) rough enough boundaries for the paths connecting the source and receiver to not combine coherently, and (iii) that the reflection coefficient of the bottom is one for grazing angles below the critical angle (θ_c^g , measured from the horizontal). These concepts are covered later in this text and so are not discussed here. The resulting propagation loss factor⁵ for cylindrical spreading can then be described as

$$L_p(r) = r_{\text{cs}} r \quad (3.86)$$

where

$$r_{\text{cs}} = \frac{z_b}{2\theta_c^g} \quad (3.87)$$

and z_b is the bottom depth. This leads to the cylindrical-spreading propagation loss formula,

$$PL = 10 \log_{10}(r_{\text{cs}}) + 10 \log_{10}(r) \text{ dB re m}^2 \quad (3.88)$$

Interpreting the θ_c^g in the denominator of (3.87) as an approximation to $\tan(\theta_c^g)$ implies r_{cs} can be viewed as a range term that characterizes when spherical spreading is no longer applicable.

At longer ranges a better approximation to the bottom reflection loss is required to account for the accumulated losses of multiple bottom reflections. As shown in [9, Sect. 9.1.1.2], by approximating the bottom reflection loss as exponentially decaying in grazing angle, but still set to zero for angles beyond the critical angle, the propagation loss factor can be described approximately by

$$L_p(r) \approx r_{\text{ms}}^{1/2} r^{3/2} \quad (3.89)$$

where

$$r_{\text{ms}} = \frac{\eta z_b}{\pi} \quad (3.90)$$

⁵Note that the propagation loss factor is one over the propagation factor (i.e., $L_p = 1/F_{\text{MP}}$) in the notation of [9, Sect. 3.2.2.1].

has distance units and η is a type of reflection loss gradient. From [9, Table 9.1], $\eta = 0.28$ nepers/radian for medium sand. This *mode-stripping* regime should be used for ranges

$$r \geq \frac{r_{\text{cs}}^2}{r_{\text{ms}}} \quad (3.91)$$

which is simply where (3.86) is less than (3.89).

Converting (3.89) to decibels then results in the propagation-loss formula for the mode-stripping regime,

$$\text{PL} = 5 \log_{10}(r_{\text{ms}}) + 15 \log_{10}(r) \text{ dB re m}^2. \quad (3.92)$$

A key point to be seen in (3.85), (3.88), and (3.92) is that the units are properly represented both in the reference and in the originating propagation loss factor.

3.2.4.2 Propagation Loss and the Channel Frequency Response

From (3.80), the propagation loss factor is the ratio

$$L_p = \frac{U_o}{P(\vec{x})} = \frac{\frac{1}{T} \int_0^T u_o^2(t) dt}{\frac{1}{T} \int_{t_b}^{t_b+T} p^2(t, \vec{x}) dt} \quad (3.93)$$

where the receiver is assumed to be at position \vec{x} and dependence of L_p on \vec{x} is implicit. Through the use of Parseval's theorem (see Sect. 4.3.2) L_p can be described in the frequency domain as

$$L_p = \frac{\frac{\int_{f_0}^{f_1} |U_o(f)|^2 df}{\int_{f_0}^{f_1} |H(f, \vec{x}) U_o(f)|^2 df}}{\frac{\int_{f_0}^{f_1} |H(f, \vec{x}) U_o(f)|^2 df}{\int_{f_0}^{f_1} |H(f, \vec{x})|^2 df}}. \quad (3.94)$$

where $H(f, \vec{x})$ is the frequency response of the channel and $U_o(f)$ is the Fourier transform of the disturbance produced by the source, which is assumed to have content only for $f \in (f_0, f_1)$.

For narrowband signals where $U_o(f)$ predominantly has energy at frequency f_c , L_p simplifies to

$$L_p = \frac{1}{|H(f_c, \vec{x})|^2}. \quad (3.95)$$

Frequency-domain solutions to the wave equation (i.e., the Helmholtz equation) are therefore very efficient for narrowband signals. For broadband signals, L_p can be bounded above by the inverse of the average spectral channel response (i.e., $|H(f, \vec{x})|^2$) using Chebyshev's integral inequality [21, 11.314]

$$L_p \leq \left[\frac{1}{(f_1 - f_0)} \int_{f_0}^{f_1} |H(f, \vec{x})|^2 \, df \right]^{-1}. \quad (3.96)$$

The equality in (3.96) holds when $U_o(f)$ is constant for $f \in (f_0, f_1)$, which is approximately true for linear frequency modulated (LFM) pulses with constant envelopes and, when the bandwidth-to-center-frequency ratio is not too large, for hyperbolic frequency-modulated (HFM) pulses.

Exercise 3.8 Starting with $h(t)$ in units of the inverse of the product of distance times time (e.g., $1/(ms)$), show that the upper bound on L_p in (3.96) has units of m^2 .

3.2.4.3 Coherent and Incoherent Propagation Loss

As previously mentioned, propagation between a source and receiver can occur through multiple distinct paths. The definitions of L_p in (3.93) and (3.94) combine the waves traveling each path coherently, which can lead to constructive and destructive interference patterns. Because it is often difficult to know the phase of each path precisely, particularly for bottom interacting paths, it is common to consider an incoherent combination [8, Sect. 3.3.5.3]. For the multipath channel, with frequency response as in (3.54), this results in summing the magnitude-squared of each path amplitude,

$$|H(f, \vec{x})|^2 = \sum_{i=1}^N |a_i(f, \vec{x})|^2, \quad (3.97)$$

where the path amplitudes are given an explicit dependence on frequency and location. Propagation loss calculated using (3.97) is known as incoherent PL. It can be interpreted as the PL assuming each path incurs a uniformly random phase that is independent of the phase on all other paths. As shown in [8, Sect. 5.2.1], the concept can be applied to a summation over propagation modes as well as paths.

3.2.5 Absorption and Dispersion

3.2.5.1 Absorption

Absorption occurs when some acoustic energy is lost from conversion to heat in forcing water particles to oscillate. The impact on MSP is an exponential decay with range in addition to, for example, spherical spreading,

$$P(r_1) = e^{-2\beta(r_1-r_0)} \left[\frac{r_0^2}{r_1^2} P(r_0) \right] \quad (3.98)$$

where β is an attenuation coefficient in units of nepers per meter [Np/m].⁶ Converting (3.98) to propagation loss results in the form

$$\begin{aligned} PL &= 20 \log_{10} \left(\frac{r_1}{r_0} \right) + 10 \log_{10} e^{2\beta(r_1-r_0)} \\ &= 20 \log_{10} \left(\frac{r_1}{r_0} \right) + \alpha \frac{(r_1 - r_0)}{10^3} \quad \text{dB re m}^2 \end{aligned} \quad (3.99)$$

where $\alpha = 10^3 \beta [20 \log_{10}(e)]$ is the attenuation in dB/km and the ranges r_1 and r_0 are in meters. Although β and α are shown as being constant in (3.98) and (3.99), they increase with frequency as shown in Fig. 3.4 for α . The equations producing the curve shown in Fig. 3.4 can be found in [9, Sect. 4.1.5].

At very low frequencies (e.g., below 200 Hz), there are other mechanisms that lead to higher values than the values shown in Fig. 3.4 (e.g., see [22] or [9, Sect. 4.1.5]). However, absorption is primarily an issue for high-frequency acoustical systems. For example, the approximate range at which absorption results in three decibels of attenuation (i.e., the MSP is halved) is 3000 km at 100 Hz, 50 km at 1 kHz, 3 km at 10 kHz, and less than 90 m at 100 kHz.

3.2.5.2 Dispersion

A propagation medium is called *dispersive* when the speed of sound changes with frequency [1]. From [3, Sect. 8.2], the speed of sound accounting for dispersion is

$$c = c_w \sqrt{\frac{2[1 + (2\pi f \tau_s)^2]}{1 + \sqrt{1 + (2\pi f \tau_s)^2}}} \quad (3.100)$$

⁶Nepers are the units of the natural logarithm of a ratio of a measured (i.e., field) quantity such as pressure, so $1 \text{ Np} = 20 \log_{10}(e) \text{ dB}$.

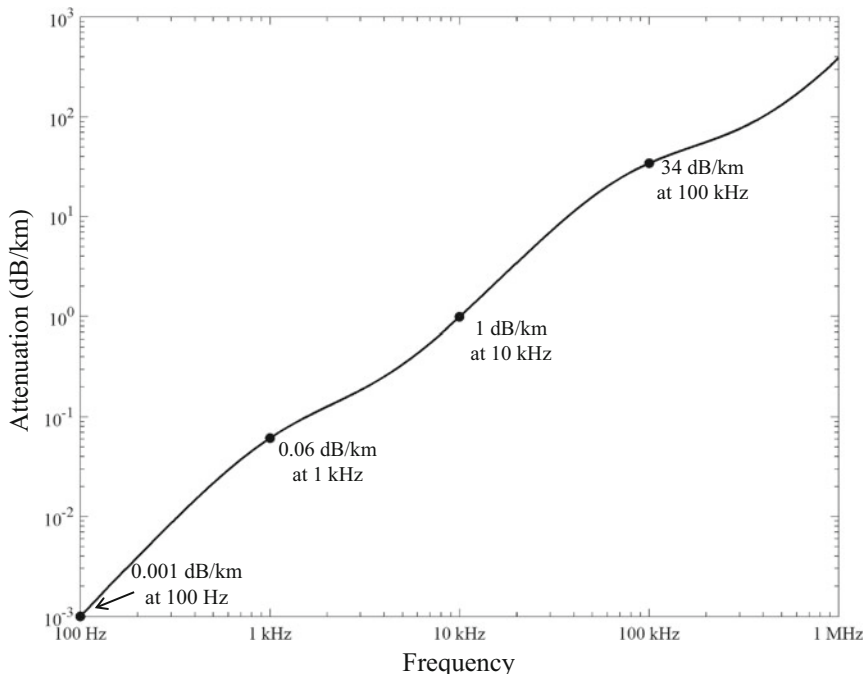


Fig. 3.4 Frequency dependence of attenuation for representative conditions

where τ_s is a relaxation time, which is about 10^{-12} s for most liquids. Thus, for most applications of underwater acoustics, dispersion intrinsic to propagation of sound through water is generally not a concern. However, there are circumstances in underwater acoustics where propagation can be frequency dependent. When the water contains a large enough fraction of impurities (e.g., bubbles) [6, Sect. 8.3.3], [9, Sect. 5.5.3.1], the compressibility (bulk modulus) changes and results in a frequency dependence to sound speed. Another example of dispersive propagation characteristics arises in a waveguide where the preference of different frequencies to take different paths results in frequency-dependent propagation delays [8, Sect. 8.5.2]. Such *geometric* dispersion is described further here in Sect. 3.2.8.3.

3.2.6 Sound-Speed, Snell's Law, and Refraction

To this point in the text, the speed of sound in the ocean has been assumed constant in space and time. Although variations in each of the dimensions are not uncommon, as illustrated by the values seen in Table 3.2, a common scenario entails variation only in the depth dimension. One of the simplifying properties of the ocean is that it is typically stratified into horizontal layers with constant physical characteristics.

Table 3.2 Nominal values and ranges for characteristic properties of the ocean

Description	Sound speed (m/s)	Density (kg/m ³)
Air	332–350	1.3
Water	1450–1550	1010–1050 [nominally 1027]
Bottom (clay to silt to sand)	$0.98c_w$ – $1.34c_w$	$1.3\rho_w$ – $2.5\rho_w$
Bottom (rock)	2050–5350	1500–2700

Bottom parameters are condensed from [9, Sec. 4.4] for mid-frequency (1–10 kHz). For the clay-silt-sand range they are provided as a factor of the water sound speed (c_w) or density (ρ_w)

This arises from stratified flow where mixing is more prevalent in the horizontal than the vertical [2, Ch. 2]. Several empirical models for the variation of sound speed with depth, temperature, and salinity have been developed, including [6, eq. 1.3.1]

$$\begin{aligned} c_w(z, T, S) = & 1449.2 + 4.6T - 0.055T^2 + 0.00029T^3 \\ & + (1.34 - 0.01T)(S - 35) + 0.016z \end{aligned} \quad (3.101)$$

where z is depth [m], T is temperature [$^{\circ}$ C], and S is salinity in parts per thousand. The difficulty in applying (3.101) lies in knowing how temperature varies with depth near the surface. However, it is clear that sound speed increases with both water temperature and depth. Salinity plays a minor role relative to temperature and depth and in most environments does not vary significantly.

The homogenous wave equation for an ocean environment with spatially varying density and sound speed has the form [7, eq. 1.1],

$$\rho(\vec{x}) \nabla \cdot \left[\frac{1}{\rho(\vec{x})} \nabla p(t, \vec{x}) \right] = \frac{1}{c_w^2(\vec{x})} \frac{\partial^2 p(t, \vec{x})}{\partial t^2}. \quad (3.102)$$

Under the stratified-ocean model, $\rho(\vec{x})$ and $c_w(\vec{x})$ only depend on depth z and not (x, y) ; however, density is generally assumed constant within the water column which simplifies (3.102) to

$$\nabla^2 p(t, \vec{x}) = \frac{1}{c_w^2(\vec{x})} \frac{\partial^2 p(t, \vec{x})}{\partial t^2}. \quad (3.103)$$

Analytical and numerical solutions for the stratified-ocean case include normal modes (Sect. 3.2.8.2) and ray tracing where acoustic wave propagation is determined by following a plane wave as it moves through the layers. The direction of propagation of a plane wave within a homogenous layer is constant until it reaches the layer boundary. The plane wave's direction of travel within the layer is represented by a *ray* starting at the source and departing at a given angle. The trajectory of the plane wave as it propagates through the various layers of the ocean is called a *ray path*. For example, consider two adjacent fluid layers as shown in

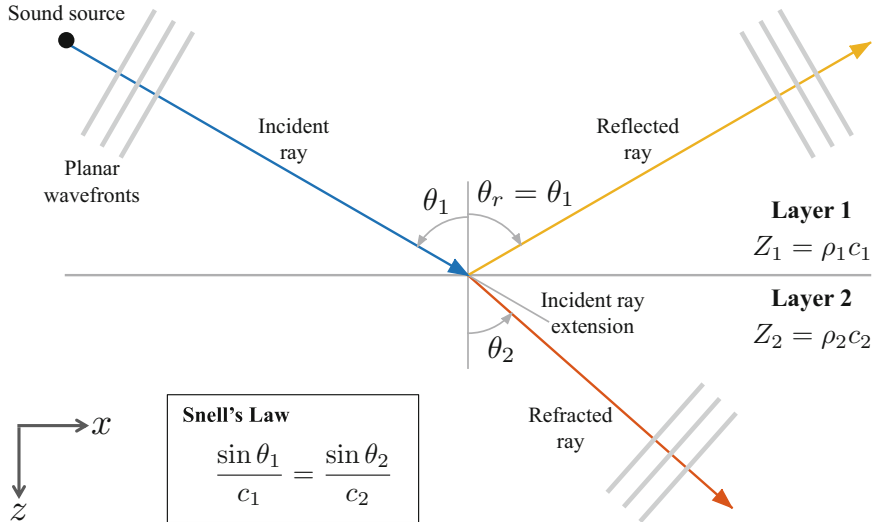


Fig. 3.5 Incident, reflected, and transmitted wavefronts at a layer boundary. Snell's law dictates the angle at which the transmitted ray is refracted into the second layer

Fig. 3.5 where a sound source in Layer 1 produces a ray that eventually meets the boundary between Layer 1 and Layer 2 at incidence angle θ_1 . In this discussion, the angles describing the rays at the boundary are incidence angles which are measured from the line perpendicular to the boundary between the two layers. At the boundary, some portion of the wave represented by this incident ray is reflected back into Layer 1 and some portion is transmitted or refracted into Layer 2. The angle at which the reflected wave propagates back into Layer 1 is the same as for the incident wave ($\theta_r = \theta_1$). However, the angle θ_2 at which the refracted wave propagates into Layer 2 can be altered from θ_1 by a difference in the speed of sound in the two layers. If c_1 and c_2 are the sound speeds in the two layers, Snell's law [1] defines the relationship between the two angles as

$$\frac{\sin \theta_1}{c_1} = \frac{\sin \theta_2}{c_2}. \quad (3.104)$$

By solving (3.104) for θ_2 ,

$$\theta_2 = \arcsin\left(\frac{c_2}{c_1} \sin \theta_1\right), \quad (3.105)$$

it can be seen that when $c_2 > c_1$ refraction places the wave at an angle closer to the boundary between the layers ($\theta_2 < \theta_1$) and when $c_2 < c_1$ farther from the boundary ($\theta_2 > \theta_1$). However, if the incident wave impacts the boundary head-on (i.e., $\theta_1 = 0$), the wave is transmitted into Layer 2 with no change in direction

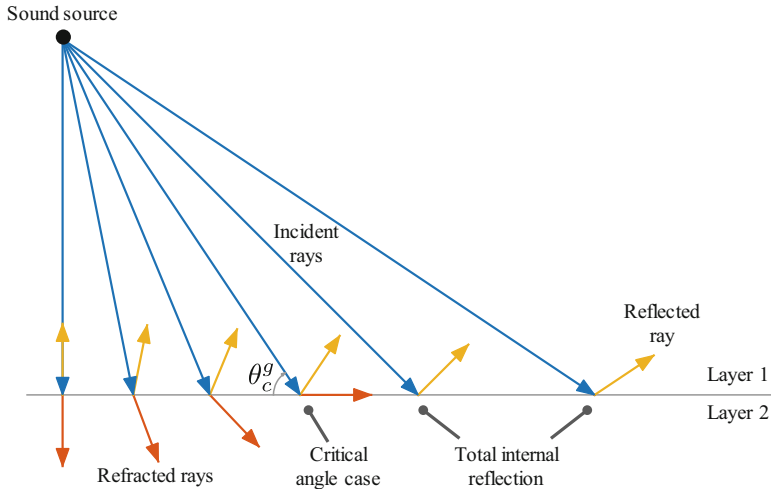


Fig. 3.6 Reflected and refracted rays for various grazing angles. When the grazing angle is below the critical angle, there is no transmitted ray

($\theta_2 = \theta_1 = 0$) irrespective of c_1 and c_2 . The example shown in Fig. 3.5 demonstrates the $c_2 < c_1$ case where the refracted wave forms in a direction farther from the layer boundary than the direction of the incident wave.

Because the argument of the arcsin function in (3.105) must be less than or equal to one, there is a limit at which there is no transmitted or refracted wave. When the incidence angle is

$$\theta_c = \arcsin\left(\frac{c_1}{c_2}\right) \quad (3.106)$$

the refracted angle is $\pi/2$ or at the horizontal. Beyond this *critical angle* ($\theta_1 > \theta_c$), no refraction or transmission into the second layer occurs. Some texts define the critical angle as a grazing angle rather than an incidence angle. The grazing angle is the angle between the ray and the boundary between the layers, $\theta_c^g = \arccos(c_1/c_2) = \pi/2 - \theta_c$. No transmission or refraction occurs in Layer 2 when the *grazing angle* of the incident wave is *below* the critical grazing angle. When there is no refraction, the wave is completely reflected into Layer 1 in a condition known as *total internal reflection*. The rays for various incident angles below, at, and above the critical angle of incidence are illustrated in Fig. 3.6.

3.2.6.1 Sound Speed Profiles and Ray Tracing

Armed with Snell's law, a horizontally stratified ocean, and sound speed as a function of depth, the propagation of a ray emanating from a sound source can be determined analytically for certain sound-speed profiles (SSPs) or numerically

through ray-trace codes. The examples in this book take the latter approach and use the Bellhop model by M. Porter based on [23]. Code for Bellhop is available at the Ocean Acoustics Library [24]. The dependence of sound speed on depth, temperature, and salinity described in (3.101) often produces an SSP that initially decreases as depth increases owing to the temperature dependence. Eventually, the depth dependence begins to dominate causing the SSP to reach a minimum and then begin to increase. Representative of these characteristics is the SSP for an idealized sound channel as defined by Munk [25],

$$c(z) = c_{\min} \left[1 + \frac{\gamma_A z_{\min}}{2} \left(\eta(z) + e^{-\eta(z)} - 1 \right) \right] \quad (3.107)$$

where $\eta(z) = 2(z - z_{\min})/z_{\min}$ for z ranging from the surface ($z = 0$) to the bottom ($z = z_b$). The parameter $\gamma_A = 1.14 \cdot 10^{-5} \text{ m}^{-1}$ describes the rate of change of the SSP at large depths relative to c_{\min} (i.e., the slope of the SSP at large depths is approximately $c_{\min}\gamma_A$). Using the values from Munk's example in [25], the SSP is seen in the left pane of Fig. 3.7 to have a minimum of $c_{\min} = 1492 \text{ m/s}$ at depth $z_{\min} = 1300 \text{ m}$, which is the axis of the deep sound channel.

Given a source at 100-m depth and a ray departing horizontally, the ray begins to curve downward as seen in the inset in the right pane of Fig. 3.7. Three rays are shown in the figure with departure angles of -1° , 0° , and 1° relative to horizontal (positive angles relative to horizontal point down). The path of the ray pointing slightly up is at first toward the surface, but then it turns down before reaching the surface. At this point, all three of the rays propagate deeper until they

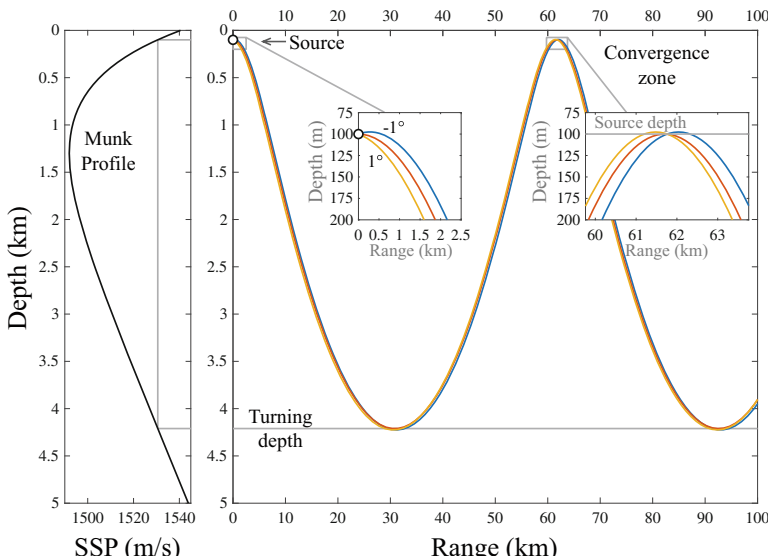


Fig. 3.7 Ray trace for convergence zone example with Munk SSP [computed using Bellhop]

turn upward. The turning depth is the depth at which the sound speed equals that of the largest potentially encountered by the ray. For the ray departing at 0° , it is the sound speed at the depth of the source. For the other rays it is the sound speed at a shallower depth, implying their turning point is deeper than the 0° -departure-angle ray. After the rays turn toward the surface, they are seen to come together again at the depth of the source in a region called a *convergence zone*. Ray traces provide a visual representation of where acoustic energy propagates in a given environment. A confluence of rays, as shown in the convergence zone, is generally indicative of higher acoustic pressure and therefore more effective remote sensing.

If the ocean is deep enough that the sound speed at the bottom exceeds that at the surface, as shown in the example of Fig. 3.7, there will be a range of departure angles from which rays will form a convergence zone with neither surface nor bottom interaction. The depth at which the sound speed equals that at the surface is called the *critical depth* and when the bottom is deeper than the critical depth there is said to be *depth excess* [8, Sect. 1.4.1]. When the ocean is not deep enough to support depth excess, the rays interact with the bottom, which inherently involves a loss in power in the reflected wave relative to the incident wave.

The ray trace shown in Fig. 3.7 also illustrates what is known as the *reliable acoustic path* (RAP) [26, Sect. 5.8], which consists of the paths connecting the shallow and deep portions of the trace. When a receiver is placed deep in the ocean, but not so deep that the sound speed is greater than it is at the surface, rays departing at different angles will span a large region in range near the surface without interacting with the bottom. Such coverage is said to afford a “reliable” propagation path between the sound source and receiver.

Another underwater sound propagation phenomenon is the *deep sound channel*, as shown in Fig. 3.8 for the Munk SSP. When the source is near the nadir of the SSP, ray paths going up or down eventually refract back toward the source depth. Similar to CZ propagation, the ray paths coalesce at the depth of the source at certain range intervals, resulting in regions of low propagation loss.

Exercise 3.9 (Snell’s Law and Huygen’s Principle) Snell’s law can be explained in a physical sense by applying Huygen’s principle [1], which dictates that propagation of a wavefront can be represented by populating it with point sources emanating spherical waves. The new wavefront is defined by the surface tangent to the spherical waves. To derive Snell’s law, suppose a plane wave is incident at a horizontal boundary layer as in Fig. 3.5. Place a point source at the boundary where the incident ray intersects it. It produces a spherical wave which propagates into the second layer with speed c_2 . Now place a second point source a distance d farther along the boundary. Determine the time Δ_t it takes for the incident wavefront to propagate from the first point source to the second within the first layer (i.e., with sound speed c_1). The wavefront of the refracted wave is then represented by the line containing the second point source and tangent to the spherical wave produced by the first point source after propagating for a time Δ_t into the second layer. Derive Snell’s law from the above geometric description of the refracted wavefront. Draw

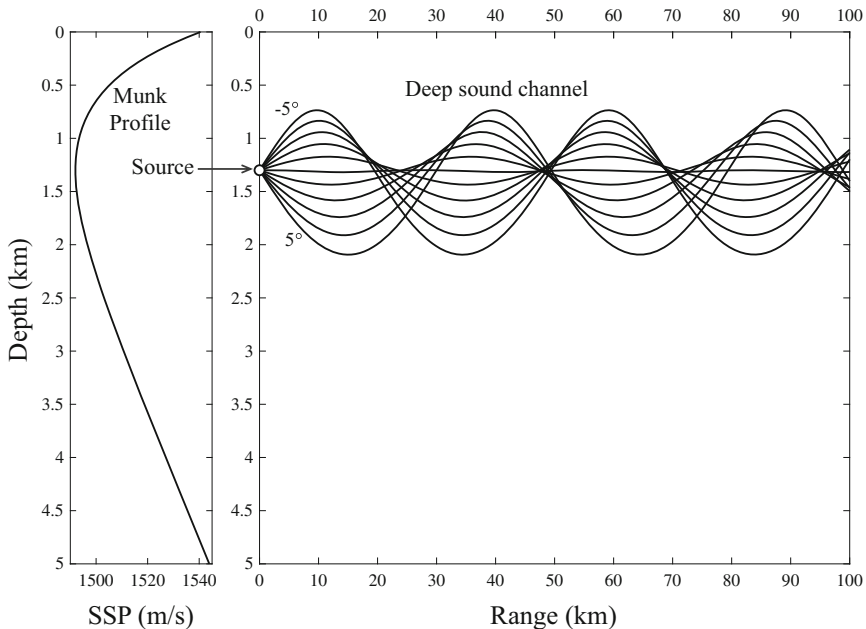


Fig. 3.8 Ray trace for deep sound channel with Munk SSP showing rays with departure angles every degree from -5° to 5° [computed using Bellhop]

diagrams for cases where $c_2 \gg c_1$ and $c_2 \ll c_1$ to illustrate when the refracted wave forms as propagating closer to a horizontal or vertical direction than for the incident wave.

3.2.7 Boundaries and Reflection Loss

As described in the previous section, when an acoustic wave in a layered ocean meets a boundary, some portion of the incident energy is reflected back into the current layer and some is transmitted into the next layer. Absent from the discussion was how much of the incident wave is reflected or transmitted. In this section, the amplitudes of the reflected or transmitted waves are determined by applying boundary conditions where the layers meet. The surface and bottom are then considered to determine how sound waves react at the ocean boundaries. Generally, the wave reflected at the boundary is of most importance to remote sensing. *Reflection loss* describes the decibel reduction in intensity of the reflected wave relative to the incident wave. Reflection loss arises both when a portion of the incident wave is transmitted in the bottom and when the boundary is considered acoustically rough (i.e., it is not flat relative to the sensing wavelength).

3.2.7.1 Boundary Conditions Between Layers

Although Snell's law describes how the refracted wave propagates into a subsequent layer, boundary conditions are required to fully define the transmitted and reflected waves in terms of the incident wave. In order for two fluid layers to remain in contact with each other, the pressure and normal component of particle velocity must be continuous at the boundary. To define the pressure, (3.36) is used to represent the incident plane wave within Layer 1,

$$p_1(t, \vec{x}) = A_1 p_o(t - \vec{u}_1 \cdot (\vec{x} - \vec{x}_b)/c_1) \quad (3.108)$$

where \vec{x}_b is the point in Fig. 3.5 where the incident ray intersects the layer boundary and \vec{u}_1 is a unit vector in the direction of the incident ray. The 2-D scenario of Fig. 3.5 is taken as x in the horizontal and z in the vertical with down as the positive direction so $\vec{u}_1 = (\sin \theta_1, \cos \theta_1)$ (recall θ_1 is the incident angle referencing the vertical axis and not the horizontal). The pressure arising from the incident wave in (3.108) can then be described as

$$p_1(t, x, z) = A_1 p_o(t - [(x - x_b) \sin \theta_1 + (z - z_b) \cos \theta_1]/c_1) \quad (3.109)$$

where $\vec{x}_b = (x_b, z_b)$. The direction vector for the reflected wave is $\vec{u}_{1,r} = (\sin \theta_1, -\cos \theta_1)$ and the direction vector for the refracted wave is similar to the incident wave, with θ_2 replacing θ_1 . With these, the reflected and refracted waves can be defined by, respectively,

$$p_{1,r}(t, x, z) = A_{1,r} p_o(t - [(x - x_b) \sin \theta_1 - (z - z_b) \cos \theta_1]/c_1). \quad (3.110)$$

and

$$p_2(t, x, z) = A_2 p_o(t - [(x - x_b) \sin \theta_2 + (z - z_b) \cos \theta_2]/c_2). \quad (3.111)$$

The ratio of the amplitudes of the reflected or refracted wave to the incident wave (respectively, $A_{1,r}/A_1$ and A_2/A_1) can be obtained by applying the boundary conditions. Continuity of the pressure at the boundary requires

$$p_1(t, x, z_b) + p_{1,r}(t, x, z_b) = p_2(t, x, z_b), \quad (3.112)$$

which results in requiring

$$\begin{aligned} & A_1 p_o \left(t - (x - x_b) \frac{\sin \theta_1}{c_1} \right) + A_{1,r} p_o \left(t - (x - x_b) \frac{\sin \theta_1}{c_1} \right) \\ &= A_2 p_o \left(t - (x - x_b) \frac{\sin \theta_2}{c_2} \right). \end{aligned} \quad (3.113)$$

By applying Snell's law to replace $\sin(\theta_2)/c_2$ with $\sin(\theta_1)/c_1$ on the right side of (3.113), the pressure-continuity boundary condition is seen to simplify to

$$A_1 + A_{1,r} = A_2. \quad (3.114)$$

When the layers are horizontal, the component of particle velocity normal to the boundary is obtained by a dot product between particle velocity from (3.4) and a unit vector in the vertical dimension, $\vec{u}_z = (0, 1)$. For the incident wave this results in

$$v_{1,z}(t, \mathbf{x}) = \frac{p_1(t, \mathbf{x})}{\rho_1 c_1} \cos \theta_1 \quad (3.115)$$

with similar results for the reflected and refracted waves. Similar to the pressure-continuity boundary condition, the vertical component of particle velocity will be continuous at the layer boundary if

$$\frac{A_1 \cos \theta_1}{Z_1} - \frac{A_{1,r} \cos \theta_1}{Z_1} = \frac{A_2 \cos \theta_2}{Z_2} \quad (3.116)$$

where $Z_i = \rho_i c_i$ is the characteristic impedance of layer i for $i = 1, 2$.

Using (3.114) and (3.116), the ratio of the amplitudes of the reflected wave to the incident wave is seen to be

$$\frac{A_{1,r}}{A_1} = \frac{Z_2 \cos \theta_1 - Z_1 \cos \theta_2}{Z_2 \cos \theta_1 + Z_1 \cos \theta_2} \quad (3.117)$$

and the ratio of the amplitudes of the refracted wave to the incident wave

$$\frac{A_2}{A_1} = \frac{2Z_2 \cos \theta_1}{Z_2 \cos \theta_1 + Z_1 \cos \theta_2}. \quad (3.118)$$

Thus, A_1 and θ_1 in conjunction with the layer characteristics and Snell's law are all that are required to describe the reflected and refracted waves at the boundary between the two layers. These ratios are commonly called, respectively, the reflection and transmission coefficients.

3.2.7.2 Constant-Density Layers

Within the water column, the density can be assumed constant with only the sound speed varying as a function of depth. For two water-column layers with $\rho_1 = \rho_2$, (3.117) and (3.118) simplify to a function of the ratio between the sound speeds in the layers, c_2/c_1 . When the sound speed varies slowly enough with depth or the layers are very thin, a Taylor-series expansion of the reflected and refracted wave amplitudes about $c_2/c_1 = 1$ yields

$$\frac{A_{1,r}}{A_1} \approx \frac{c_2 - c_1}{2c_1 \cos^2 \theta_1} \quad (3.119)$$

and

$$\frac{A_2}{A_1} \approx 1 + \frac{c_2 - c_1}{2c_1 \cos^2 \theta_1}, \quad (3.120)$$

assuming $\cos \theta_1$ is not too close to zero. This illustrates how the reflected wave has a small amplitude and the refracted wave is nearly the same amplitude as the incident wave when there is very little impedance mismatch between constant-density layers (i.e., $c_2 \approx c_1$).

3.2.7.3 Reflection at the Ocean Surface

When a plane wave is incident on the ocean surface, the second layer is air. The speed of sound in air and its density are nominally $c_a = 338$ m/s and $\rho_a = 1.3$ kg/m³, yielding a very low characteristic impedance relative to that normally seen in water ($\rho_a c_a = 440$ vs. $\rho_w c_w = 1.54 \cdot 10^6$ kg/m²s). In this situation ($Z_1 \gg Z_2$), the reflected wave amplitude is

$$A_{1,r} \approx -A_1, \quad (3.121)$$

and the refracted wave amplitude is much smaller than the incident wave amplitude ($A_2 \ll A_1$). Thus, nearly all of the incident wave energy is reflected back into the ocean but with an inversion in sign. When the propagating wave function is described as a bandpass signal (e.g., see Sect. 7.3.1), the sign inversion represents a phase shift of 180°.

Suppose propagation is dominated by just two paths, as shown in Fig. 3.9, with one reflecting from the surface and one traveling directly from the source to the receiver. If the source signal is narrowband, the time difference between the two paths can lead to constructive and destructive interference when they are combined at a receiver. This phenomena is known as a Lloyd mirror [27], [28, Sect. 5.7], [8, Sect. 1.4.2.1] and produces a propagation loss function as shown in Fig. 3.9. If the source emits the acoustic signal $p_o(t)$ and only the direct and surface-reflected paths reach a receiver, the measured signal is

$$y(t) = a_1 p_o(t - \tau_1) + a_2 p_o(t - \tau_2) \quad (3.122)$$

where a_i and τ_i are, respectively, the i th path's amplitude and delay for $i = 1$ and 2. If the paths have approximately the same length (e.g., when range is much larger than the depth of the source or receiver), their amplitudes will have nearly the same magnitude. However, the surface-reflected path undergoes a sign inversion, so $a_2 \approx -a_1$ and

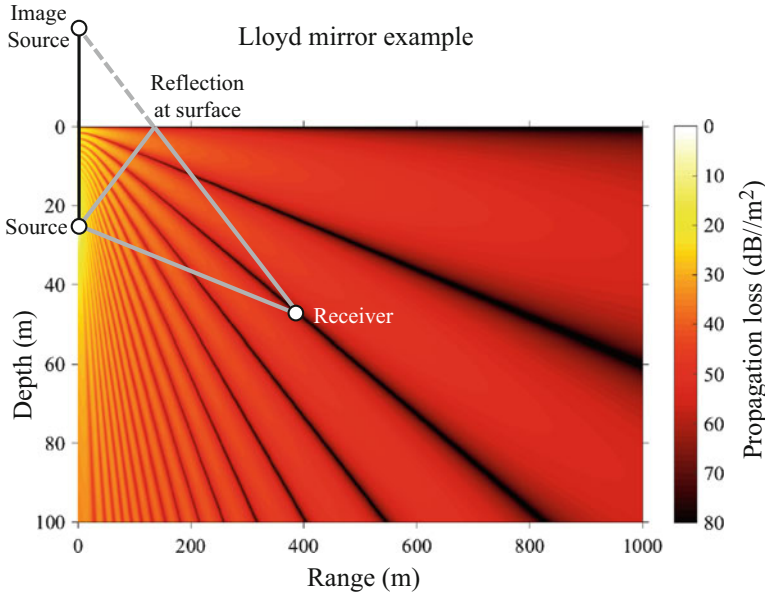


Fig. 3.9 Propagation loss for a direct and surface-reflected path producing the Lloyd mirror for a source projecting a 500 Hz tone at 25 m depth in water with 100 m depth, and a constant sound speed profile ($c_w = 1500 \text{ m/s}$)

$$y(t) \approx a_1[p_o(t - \tau_1) - p_o(t - \tau_1 - \delta_\tau)] \quad (3.123)$$

where $\delta_\tau = \tau_2 - \tau_1$ is the path delay difference.

If $p_o(t)$ is periodic with period T , then $p_o(t) = p_o(t - mT)$ for any integer m . Clearly, if the path delay difference is an integer multiple of the signal's period ($\delta_\tau = mT$), the signals arriving on the two paths are “in phase” and the sign inversion from the surface-interacting path causes destructive combination. If the signal is sinusoidal (e.g., $p_o(t) = \cos(2\pi f_o t)$), then the paths clearly add constructively when the delay difference is an integer-and-a-half-period off,

$$p_o(t - \delta_\tau) = \cos(2\pi f_o(t - (m + 0.5)/f_o)) = -\cos(2\pi f_o t) = -p_o(t). \quad (3.124)$$

More general signals may be considered by representing the propagation as a linear time-invariant system. The transfer function for the Lloyd mirror scenario is obtained from the Fourier transform of (3.122) as

$$\begin{aligned} H(f) &= \frac{Y(f)}{P_o(f)} = a_1 e^{j2\pi f \tau_1} - a_2 e^{j2\pi f \tau_2} \\ &\approx a_1 e^{j2\pi f \tau_1} \left[1 - e^{j2\pi f \delta_\tau} \right] \end{aligned} \quad (3.125)$$

where the path delays and amplitudes depend on the range and depth of the receiver.

The propagation loss shown in Fig. 3.9 is $-20 \log_{10} |H(f)|$ where the source is at 25 m depth and emits a tone at frequency $f = 500$ Hz. The propagation delays are formed assuming a constant sound speed ($c_w = 1500$ m/s) and spherical spreading (i.e., $\tau_i = r_i/c_w$ and $a_i = 1/r_i$ where r_i is the path length). If the receiver is at range x and depth z , the length of the direct path is easily obtained using the Pythagorean theorem. The length of the surface-reflected path can be similarly obtained by noting it is the same as if the sound originated from the *image source* shown a distance above the ocean surface equal to the source depth.

Exercise 3.10 (Image Source) Use the image-source technique to determine the effect of the path connecting the source and receiver through one bottom reflection. The image-source technique entails creating image oceans above and below the existing one and connecting the receiver to the image sources. The image source shown in Fig. 3.9 is at a height z_s above the ocean surface where z_s is the source depth. For the first image ocean below the real one, the source is at an apparent depth of $2z_b - z_s$ where z_b is the bottom depth. If the receiver is at depth z_a and horizontal distance x , show that the length of the bottom-reflected path is $\sqrt{x^2 + (2z_b - z_s - z_a)^2}$. Use this path length to add a path to the transfer function in (3.125) and determine the effect on propagation loss as a function of receiver position. Assume the bottom is very hard so all of the incident energy is reflected back into the water. Continue the process by adding the two paths with one surface and one bottom reflection.

3.2.7.4 Reflection at the Ocean Bottom

Although conditions at the ocean bottom vary slowly enough in time relative to the sound speed near the surface to be considered constant in most applications, they vary significantly with location. As seen in Table 3.2, sound speed in the bottom can range from approximately that of water (e.g., for clay) to being several times faster (e.g., rock). As must be expected, the bottom is denser than water with a range from about 1.3 times that of water to over 2.5 times. When focus is on the reflected ray, the loss incurred by a single reflection off the bottom is quantified by the ratio in (3.117) converted to decibels,

$$\text{BL} = -20 \log_{10} \left| \frac{A_{1,r}}{A_1} \right|. \quad (3.126)$$

When the acoustic impedance mismatch between water and the bottom is small, most of the energy is transmitted into the bottom. For example, a medium clay bottom has a small impedance mismatch, $(Z_2/Z_1) = 1.3$,⁷ and therefore results

⁷Sound speed and density values for the various examples in this section are from [9, Sect. 4.4]; for example, medium clay has $c_b = 0.9846c_w$ and $\rho_b = 1.331\rho_w$. The acoustic impedances are computed assuming $c_w = 1500$ m/s and $\rho_w = 1027$ kg/m³.

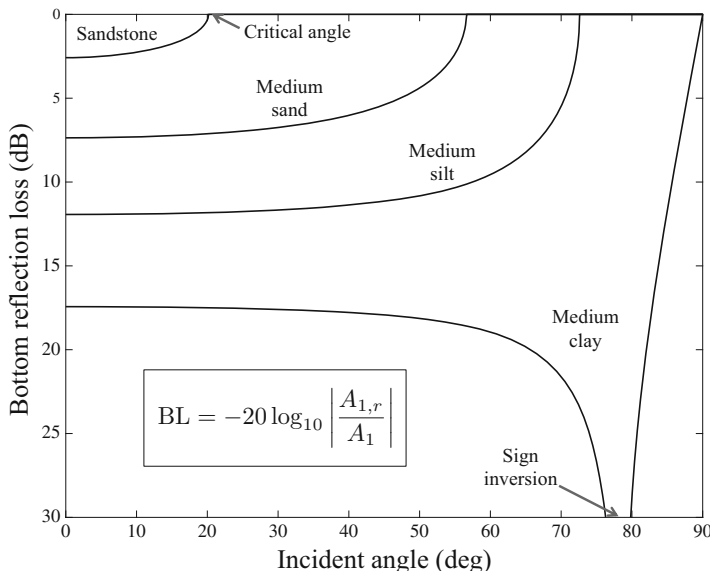


Fig. 3.10 Bottom reflection loss (dB) for various bottom types as a function of incident angle when $c_w = 1500 \text{ m/s}$ and $\rho_w = 1027 \text{ kg/m}^3$

in a significantly smaller reflected wave as can be seen in Fig. 3.10 which shows a bottom reflection loss $\approx 17 \text{ dB}$ over a wide range of incidence angles. As the impedance mismatch increases to 1.7 for medium silt, 2.5 for medium sand, and 6.8 for sandstone, the bottom loss decreases. Because the sound speed is also increasing through this range of examples, the critical angle where total internal reflection begins becomes smaller, thereby increasing the range over which there is no reflection loss.

Qualitatively, a hard dense bottom is acoustically reflective, leading to very little bottom reflection loss, whereas a soft bottom is more transparent and therefore incurs a higher reflection loss. When each reflection off the bottom incurs a large loss, it is clear that very few such interactions can occur in a successful remote sensing system. For example, consider the plot of propagation loss shown in Fig. 3.11 as a function of the receiver's range and depth for a medium clay bottom. In this example the source is projecting a 1-kHz tone at a depth of 25 m in water with a bottom depth of 100 m and a constant sound speed ($c_w = 1500 \text{ m/s}$). The trend of increasing PL with range is evident as is the nearly complete disappearance of energy into the bottom at short ranges where the grazing angle is large (i.e., very little energy is reflected back into the water). As range increases to the point where the grazing angle is less than 10° (i.e., about 425 m), the effect of bottom reflected waves can be seen in the interference pattern formed in the surface-reflected waves.

In contrast to the sound absorbing clay bottom, the medium sand bottom shown in Fig. 3.12 reflects the incident wave quite well. The PL is seen to decay more

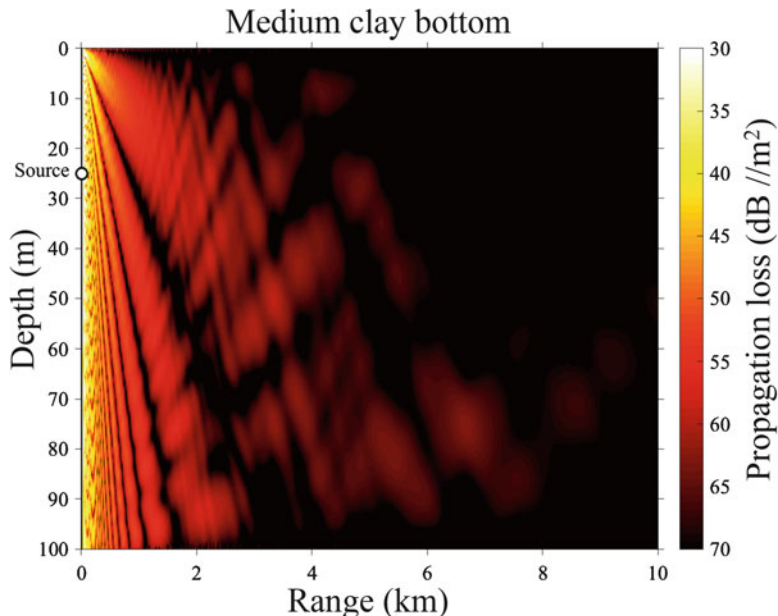


Fig. 3.11 Propagation loss for a source projecting a 1 kHz tone at 25 m depth in water with 100 m depth, a constant sound speed profile ($c_w = 1500$ m/s) and a medium clay bottom [computed using Bellhop]

slowly with range, which also implies reverberation will be a larger issue for active sonar systems compared with the clay bottom. The interaction of a large number of rays is also seen to produce a very intricate interference pattern. The interference pattern is created by constructive and destructive combination of the different paths the projected signal takes from the source to receiver.

3.2.7.5 Total Internal Reflection and Phase Change

When a plane wave undergoes total internal reflection, the reflection coefficient magnitude is one. However, the interaction imparts a phase change on the reflected wave, which results in a complex reflection coefficient in (3.117). Recall that total internal reflection occurs when $\theta_1 > \theta_c$ or

$$\sin \theta_2 = \frac{c_2}{c_1} \sin \theta_1 > 1. \quad (3.127)$$

This requires a purely imaginary value for $\cos \theta_2$ (via $\cos^2 \theta_2 = 1 - \sin^2 \theta_2$),

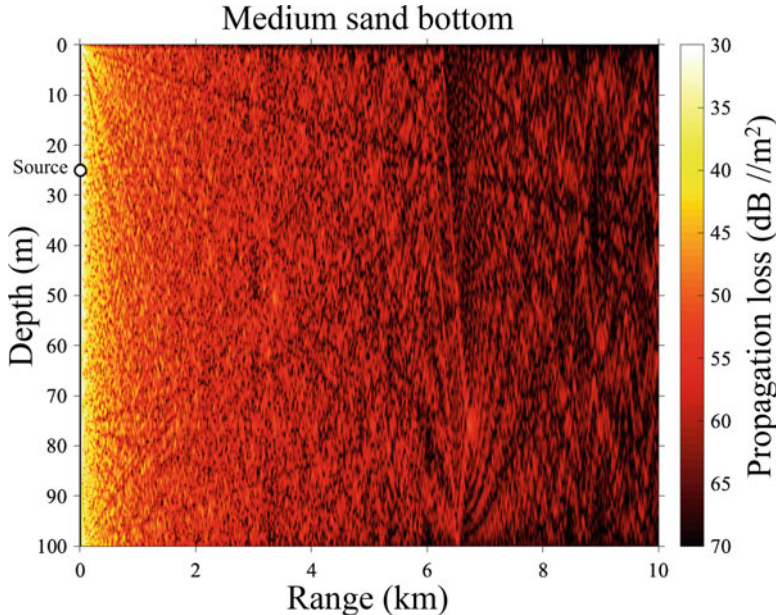


Fig. 3.12 Propagation loss for a source projecting a 1 kHz tone at 25 m depth in water with 100 m depth, a constant sound speed profile ($c_w = 1500$ m/s) and a medium sand bottom [computed using Bellhop]

$$\cos \theta_2 = \pm j \sqrt{\left(\frac{c_2}{c_1} \sin \theta_1\right)^2 - 1} = \pm j \gamma_2, \quad (3.128)$$

where $\gamma_2 = \sqrt{(\sin(\theta_1)c_2/c_1)^2 - 1}$. The phase changes for the typical bottom conditions (with reflection loss found in Fig. 3.10) are shown in Fig. 3.13 as a function of the incident angle. When the incident angle exceeds the critical angle and enters the total internal reflection regime, the phase begins to change toward a complete sign inversion (i.e., phase is -180°) in the horizontal limit.

A change in the phase of a signal is easily understood for either a pure sinusoid or, more generally, a narrowband signal. A narrowband signal can be represented by

$$s(t) = a(t) \cos(2\pi f_c t + \theta(t)) \quad (3.129)$$

where the amplitude $a(t)$ and phase $\theta(t)$ vary slowly with respect to the carrier $\cos(2\pi f_c t)$. Introducing a phase change of $-\phi$ simply results in a change in the carrier phase, $a(t) \cos(2\pi f_c t + \theta(t) - \phi)$. For an infinite-duration sinusoid ($a(t)$ and $\theta(t)$ are constant) it is equivalent to a time delay in the pressure wave, $\cos(2\pi f_c(t - \phi/(2\pi f_c)))$, which allows representing the effect by replacing the actual boundary with a slightly deeper “virtual” pressure-release boundary as

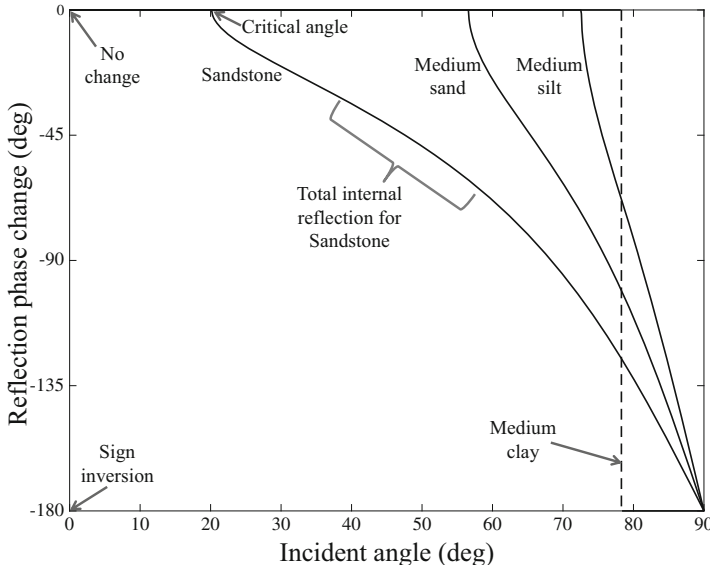


Fig. 3.13 Phase change with bottom reflection for various bottom types as a function of incident angle when $c_w = 1500 \text{ m/s}$ and $\rho_w = 1027 \text{ kg/m}^3$

described in [6, Sect. 2.6.4]. However, for all other signals (e.g., pulses or broadband signals) the composition of the reflected signal is more complicated than a delay because the phase change is not linear with frequency. This can be seen by considering the Fourier transform of the transmitted wave from (3.111)

$$P_2(f, x, z) = A_2 e^{-j2\pi f[(x-x_b)\sin\theta_2 + (z-z_b)\cos\theta_2]/c_2} P_o(f), \quad (3.130)$$

which is valid only for $z \geq z_b$. Substituting (3.128) into (3.130) results in

$$P_2(f, x, z) = A_2 e^{\pm 2\pi f(z-z_b)\gamma_2/c_2} e^{-j2\pi f[(x-x_b)\sin\theta_2]/c_2} P_o(f) \quad (3.131)$$

which describes a horizontally propagating wave at the boundary and an exponentially decaying amplitude as z increases beyond z_b (i.e., deeper into the bottom). In order for the amplitude to decay rather than grow as depth increases, $\pm f\gamma_2$ must be negative, which requires choosing the negative root in (3.128) for $f > 0$ and the positive root when $f < 0$. The reflection coefficient in (3.117) is then not only complex with unit magnitude, but also frequency dependent in a non-linear manner,

$$\begin{aligned} R(f) &= \frac{A_{1,r}(f)}{A_1} = \frac{Z_2 \cos \theta_1 + j Z_1 \gamma_2 \operatorname{sign}(f)}{Z_2 \cos \theta_1 - j Z_1 \gamma_2 \operatorname{sign}(f)} \\ &= e^{j \operatorname{sign}(f) \phi}, \end{aligned} \quad (3.132)$$

where

$$\phi = 2 \arctan \left(\frac{Z_1 \gamma_2}{Z_2 \cos \theta_1} \right). \quad (3.133)$$

To determine the effect of a non-zero phase change in the time domain, first define the Fourier transform of the reflected wave from (3.110) as $P_{1,r}(f, x, z) = R(f)S(f)$ where

$$S(f) = A_1 e^{-j2\pi f[(x-x_b) \sin \theta_1 + (z-z_b) \cos \theta_1] / c_1} P_o(f) \quad (3.134)$$

and

$$s(t) = A_1 p_o(t - [(x - x_b) \sin \theta_1 + (z - z_b) \cos \theta_1] / c_1) \quad (3.135)$$

represent the reflected wave at the critical angle (i.e., when $R(f) = 1$). By expanding (3.132) into separate sine and cosine terms,

$$P_{1,r}(f, x, z) = [\cos \phi + j \operatorname{sign}(f) \sin \phi] S(f) \quad (3.136)$$

the reflected wave is seen to be a weighted sum of the pulse and its Hilbert transform [29, Sect. 5.2],

$$p_{1,r}(t) = \cos(\phi)s(t) + \sin(\phi)s_h(t) \quad (3.137)$$

where $s_h(t) = \mathcal{H}\{s(t)\}$ represents the Hilbert transform of $s(t)$ (e.g., see Sect. 4.4 or [30, pg. 267]).

Exercise 3.11 Show that (3.137) results in a change in the carrier phase for the narrowband signal in (3.129). Note that if a signal $g(t)$ is band-limited to have frequency content below f_c , the Hilbert transforms of the modulated signals [31, Sect. 3.3] are

$$\mathcal{H}\{g(t) \cos(2\pi f_c t)\} = -g(t) \sin(2\pi f_c t) \quad (3.138)$$

and

$$\mathcal{H}\{g(t) \sin(2\pi f_c t)\} = g(t) \cos(2\pi f_c t). \quad (3.139)$$

3.2.7.6 Rough Surface Reflection

The previous discussions of reflection off of boundaries have assumed the boundary layers to be perfectly flat. However, in many situations the ocean surface and bottom are more appropriately represented as being rough surfaces. How rough or smooth the surface is depends on the wavelength of the acoustic wave and the apparent size of the surface variations when taking into account the incidence angle. As described in [6, Sect. 13.2.1], the *acoustical roughness* of a surface is defined by the Rayleigh parameter⁸

$$g_r = 4k^2\sigma_z^2 \cos^2\theta \quad (3.140)$$

where σ_z is the standard deviation or RMS height of the roughness (e.g., surface waveheight), θ is the incidence angle (relative to vertical), and $k = 2\pi/\lambda = 2\pi f/c_w$ is the wavenumber. When $g_r \ll 1$, the surface is smooth and when $g_r \gg 1$ it is rough, so higher frequency signals are impacted more when they reflect off a surface with a fixed RMS roughness. However, at low grazing angles (i.e., incidence angles θ near $\pi/2$) even high frequency signals can be minimally disturbed by surface roughness. The example found in Fig. 3.14 illustrates how the reflected wavefront for an incident plane wave is distorted. The example exploits the geometric optics or Kirchhoff approximation to describe the reflected wave, which requires the local radius of curvature of the surface a to satisfy $ka \gg 1$. For example, if $f = 1$ kHz, the surface waves must have curvature much greater than a 24-cm radius. At 100 Hz it would be 2.4 m so this example is more relevant for high frequencies. The connecting lines and dots in Fig. 3.14 represent reflections off horizontal facets in the surface (i.e., specular reflections). Notice that they are distorted from the planar wavefront expected for a smooth surface (the reflected wave for a flat surface is shown with a 5-ms propagation offset relative to the rough-surface reflection).

To determine the effect of the distortion on sonar performance, consider the surface reflection shown in Fig. 3.15. This scenario assumes the reflecting surface is fixed throughout the time the pulse interacts with it, that the source and receiver are in fixed positions, that the surface has a horizontal facet at the point where an incident plane wave would intersect the nominal (flat) surface, and that the time delay after pulse transmission that is evaluated is that for the scenario of a flat surface reflection. Suppose a wave at incident angle θ reflects off the nominal surface to produce a pressure signal $\hat{p}_r(t)$ at the receiver. Note that the analytic form of the signals, which are described in Sect. 7.3.1 and denoted by circles over the variable, are used here to facilitate evaluating their response in linear-time-invariant (LTI) systems. If the surface is displaced vertically by an amount z_s , the wave must travel an additional distance of $2z_s \cos \theta$, represented in the figure by the thick portion of the ray for the displaced surface. This distance is the displacement of each

⁸Note that the square root of (3.140) is also commonly defined as the Rayleigh parameter.

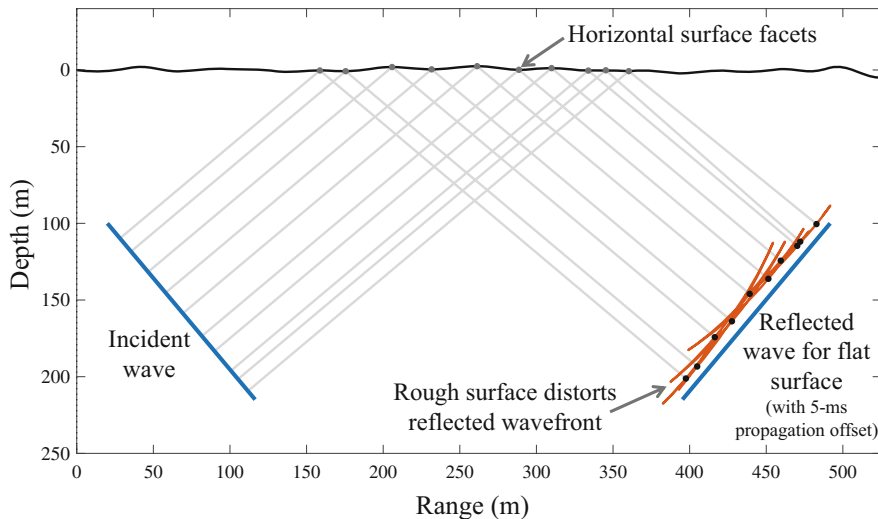


Fig. 3.14 Example of how reflection off a rough surface distorts the reflected wavefront

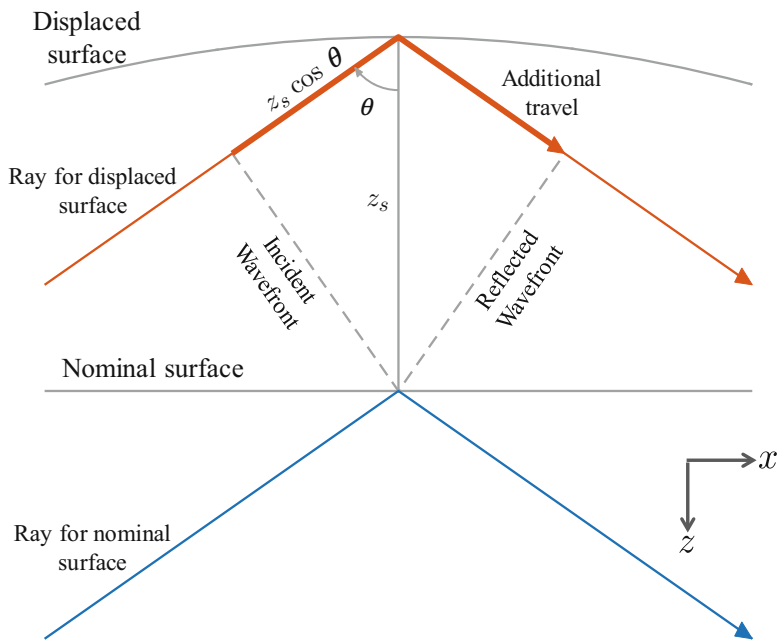


Fig. 3.15 Additional distance traveled for reflection off displaced surface relative to nominal

dot in Fig. 3.14 from a planar wavefront. The additional propagation distance is represented in the reflected signal as a time delay,

$$\dot{\bar{p}}_r \left(t - \frac{2z_s \cos \theta}{c_w} \right). \quad (3.141)$$

If the effective ensonified area on the surface is large relative to the correlation length of the surface, many such horizontal facets will contribute to the reflection. If the number of contributing points is large enough, the total reflected signal can be approximated by an expectation over a random surface height (z_s),

$$\dot{\bar{p}}_r^c(t) \approx E_{z_s} \left[\dot{\bar{p}}_r \left(t - \frac{2z_s \cos \theta}{c_w} \right) \right]. \quad (3.142)$$

Note that the expectation in (3.142) is a mathematical convenience in representing a sum over a large number of surface heights selected from a single instantiation of a random rough surface with a large effective ensonified area. Because the result does not otherwise depend on the specific instantiation, the result is the same for each instantiation and is therefore known as the coherent component (which explains the superscript c). It is also called the specular reflection because it arises from the horizontal facets of the surface. It is important to note that the reflection can also include an incoherent component arising from the multitude of other-sloped facets that will be discussed shortly.

The expectation in (3.142) can be described as the signal produced by the nominal surface reflection after applying a low-pass filter,

$$\begin{aligned} \dot{\bar{p}}_r^c(t) &= \int_{-\infty}^{\infty} \dot{\bar{p}}_r \left(t - \frac{2z \cos \theta}{c_w} \right) f_Z(z) dz \\ &= \dot{\bar{p}}_r(t) * h(t) \end{aligned} \quad (3.143)$$

where $f_Z(z)$ is the probability density function (PDF) of the random vertical displacement of the surface, $*$ is the convolution operator, and $h(t)$ is the impulse response of the filter,

$$h(t) = \left(\frac{c_w}{2 \cos \theta} \right) f_Z \left(\frac{c_w t}{2 \cos \theta} \right). \quad (3.144)$$

The impulse response in (3.144) is itself a proper PDF of the same form or family as $f_Z(z)$, but with standard deviation $\sigma_c = 2 \cos(\theta) \sigma_z / c_w$ when σ_z is the standard deviation of the surface's random vertical displacement. When $\sigma_c \rightarrow 0$, as would occur for a flat surface or very low grazing angle, $h(t) \rightarrow \delta(t)$ so $\dot{\bar{p}}_r^c(t) \rightarrow \dot{\bar{p}}_r(t)$. Conversely, if $\dot{\bar{p}}_r(t)$ is narrowband and σ_c becomes large relative to the period of the center (carrier) frequency, the average reflected signal will be small owing to the smoothing over many periods of the carrier.

In the frequency domain, the Fourier transform of the coherent reflection is the product of the Fourier transforms of $\dot{p}_r(t)$ and $h(t)$,

$$\dot{P}_r^c(f) = H(f)\dot{P}_r(f) \quad (3.145)$$

where $\dot{P}_r(f) = \mathcal{F}\{\dot{p}_r(t)\}$ and $H(f) = \mathcal{F}\{h(t)\}$. Because $h(t)$ is a proper PDF, its Fourier transform can be obtained from the characteristic function of the PDF (see Sect. 5.3.9.2). For example, if the displacement is assumed to be Gaussian with zero mean and standard deviation σ_z ,

$$\begin{aligned} H(f) &= e^{-(2\pi f)^2 \sigma_c^2 / 2} \\ &= e^{-2k^2 \sigma_z^2 \cos^2 \theta} \end{aligned} \quad (3.146)$$

where $k = 2\pi f/c_w$ is the wavenumber.

For narrowband signals, $H(f)$ may not vary significantly over the frequency content of the signal so the effect of the coherent rough surface reflection is a product rather than a convolution. The reflected wave is then approximately a scaled version of the flat surface reflection,

$$\dot{p}_r^c(t) \approx H(f_c) \dot{p}_r(t) \quad (3.147)$$

$$= e^{-2k_c^2 \sigma_z^2 \cos^2 \theta} \dot{p}_r(t), \quad (3.148)$$

where f_c is the center frequency of the signal, k_c the corresponding wavenumber, and the second equation is for Gaussian-distributed displacements. When incorporating the effect of the coherent surface reflection loss from (3.148) in propagation loss, the per bounce loss in decibels is

$$\alpha_s = -20 \log_{10} \left[e^{-2k_c^2 \sigma_z^2 \cos^2 \theta} \right] = 4.3 g_r \quad (3.149)$$

where the $20 \log_{10}$ form is used because $\dot{p}_r^c(t)$ is a pressure quantity rather than a mean-squared pressure or intensity.

The loss in the coherent component arising from rough surface scattering is only part of the effect of rough surface scattering. As described in [6, Sect. 13.2.4], [5, Ch. 6], there is also an incoherent component reflected from the surface. The incoherent component can be interpreted as arising from facets with path delays that span enough temporal carrier-frequency cycles of a zero-mean narrowband signal that the average pressure signal of their sum is essentially zero. For this incoherent component, the surface reflection loss must be evaluated through its average intensity or mean squared pressure. The underlying process is essentially the same as that for the coherent component in that reflections from the horizontal facets can also produce delays spanning multiple cycles of a narrowband signal. For example, suppose the surface roughness is large enough that the span of the delay in (3.141) is much larger than one cycle of a narrowband signal ($= 1/f_c$). If the span

of surface heights is assumed to be restricted to within three standard deviations of the flat surface (i.e., $\pm 3\sigma_z$), this then results in

$$\frac{2(6\sigma_z) \cos \theta}{c_w} \gg \frac{1}{f_c} \quad (3.150)$$

which can be converted to the inequality

$$\sqrt{g_r} \gg \frac{\pi}{3} \approx 1. \quad (3.151)$$

This implies that the horizontal-facet reflections will span more than one cycle of a narrowband signal when the Rayleigh parameter is greater than about one. This leads to enough cancellation of the horizontal-facet reflections that the reflections from the non-horizontal surface slopes play a significant role in defining the surface reflection. Similarly, when the Rayleigh parameter is much less than one the coherent component dominates the incoherent. As would be expected, the average reflected intensity or mean squared pressure of the combined coherent and incoherent contributions decreases as roughness (g_r) increases (e.g., see Fig. 13.2.5 of [6]), but not as fast as that solely predicted by the coherent component in (3.149) when $g_r > 1$.

From a remote-sensing perspective, the dependence of surface roughness losses on incidence/grazing angle reinforces the importance of low-grazing-angle paths (which have little loss due to roughness) in achieving good performance at long ranges. From a signal-processing perspective, however, the temporal composition of the reflected wave at a single receiver can be just as important as the average pressure or intensity. By examining Fig. 3.14 it can be seen that the pressure signal measured at a receiver is formed from multiple reflections from the particular portions of the rough surface where the slope directs the incident wave at the receiver upon reflection. Importantly, each reflection will have a different time delay (and possibly amplitude, which is ignored in the following analysis). Mathematically, let the surface height in this one-dimensional scenario be the random process $Z(x)$ and its slope be $M(x) = Z'(x)$ where x is the horizontal distance from the mid-point between a source and receiver. The measured signal can be represented as an integral over x picking off the points where the random slope $M(x)$ equals the desired slope $\mathcal{M}(x)$, which directs the reflected wave to the receiver and therefore depends on the geometry. When the roughness is small relative to the distance to the receiver, the minor change in $\mathcal{M}(x)$ with the surface displacement $Z(x)$ can be ignored (so $\mathcal{M}(x)$ only depends on x and not $Z(x)$) and the time delay for the path connecting the source, surface, and receiver can be approximated as $\tau_{x,z} = \tau_x + \tau_z$ where τ_x is the delay for the nominal surface at x and $\tau_z = 2z \cos(\theta)/c_w$ is the additional delay for the height variation as was used in (3.141). These simplifications result in the distorted *total* surface reflection having the form

$$\dot{p}_r^t(t) \approx \int_{-\infty}^{\infty} \dot{p}_r(t - \tau_x - \tau_z) \delta(M(x) - \mathcal{M}(x)) \, dx \quad (3.152)$$

where $\delta(\cdot)$ is the Dirac delta function.

If the surface height is a stationary random process, the height and the slope are uncorrelated when evaluated at the same position (i.e., $E[Z(x)Z'(x)] = 0$). If the height distribution is Gaussian with zero mean, then the slope distribution is also Gaussian with zero-mean. As such, the random variables $Z(x)$ and $Z'(x)$ are independent and their PDFs factor. Under these conditions, the total reflected signal is

$$\dot{p}_r^t(t) \approx \int_{-\infty}^{\infty} \left[\int_{-\infty}^{\infty} \dot{p}_r(t - \tau_x - \tau_z) f_Z(z) \, dz \right] f_M(\mathcal{M}(x)) \, dx \quad (3.153)$$

$$= \int_{-\infty}^{\infty} \dot{p}_r^c(t - \tau_x) f_M(\mathcal{M}(x)) \, dx \quad (3.154)$$

where $f_M(m)$ is the PDF of the slope and as before $f_Z(z)$ is the PDF of the surface height. Noting that the function within the brackets in (3.153) is the coherently reflected signal from (3.143) evaluated at $t - \tau_x$, incorporating reflections from non-horizontal slopes can be seen to have the effect of further smoothing the initial signal $\dot{p}_r(t)$. The degree to which it is smoothed depends on the geometry and the distribution of the slopes, which is related to the surface height distribution and spatial correlation function. The form of (3.154) illustrates how the coherent component arises when there is significant weight on or near zero slope (i.e., $f_M(m)$ is peaked around $m = 0$), noting that $\mathcal{M}(0) = 0$ and $\tau_0 = 0$. When the distribution of slopes spreads out, the incoherent component begins to play a role. Following [5, Sect. 6.5], [6, Sect. 13.2.4], if the spatial correlation function is Gaussian-shaped with correlation length L ,

$$R_{ZZ}(\chi) = E[Z(x)Z(x + \chi)] = \sigma_z^2 e^{-\chi^2/L^2}, \quad (3.155)$$

the variance of the slope is $\sigma_m^2 = 2\sigma_z^2/L^2$. This supports our intuition that surfaces with longer correlation lengths should have larger coherent components than those with shorter correlation lengths.

Suppose that for a given instantiation of the surface only N points contribute to the reflection,

$$\dot{p}_r^t(t) \approx \frac{1}{N} \sum_{i=1}^N \dot{p}_r^c(t - \tau_{x_i}) f_M(\mathcal{M}(x_i)). \quad (3.156)$$

If the signal is narrowband with respect to this linear system, the response is then approximately $\hat{p}_r^t(t) \approx H^t(f_c)\hat{p}_r(t)$ where the transfer function

$$H^t(f) = \sum_{i=1}^N f_M(\mathcal{M}(x_i)) e^{-j2\pi f \tau_{x_i}} \quad (3.157)$$

is a random quantity depending on the surface instantiation. At low roughnesses the squared modulus of the average is much larger than the variance, $E[|H^t(f_c)|^2] \gg \text{Var}\{H^t(f_c)\}$, because the delays and slopes are all clustered near zero. At large roughnesses, where the delays spread across multiple periods of the narrowband signal, $H^t(f_c)$ tends toward having a mean of zero and so the variance dominates. This is an example of how propagation can affect the statistical characterization of a source signal, which is discussed in more detail in Sect. 7.2.3.

Additional details on rough surface scattering can be found in [6, Ch. 13], [5, Ch. 6], and [32, Sect. 3.5 & App. A.3.3]. Models appropriate for use in the sonar equation to more accurately approximate surface reflection loss due to roughness can be found in [9, Ch. 8], including appropriate models for sea-surface height distributions and extensions to account for the effect of bubbles which can lead to additional losses. Recent work extending the modeling of the coherent component of surface reflection loss to broadband pulses and incorporating the pulse duration can be found in [33, 34]. The key intuitive points arising from this work are (i) increasing bandwidth reduces the reflection loss after matched filtering because the smaller sonar resolution cell reduces the effective number of independent surface heights that are ensonified and (ii) reflection loss increases with pulse duration because more independent surface heights are encountered, until the duration equals the dominant surface wave period where the loss saturates. Thus, a short broadband pulse incurs very low coherent surface reflection loss compared with a long narrowband one.

3.2.8 Rays and Modes in Shallow Water

As previously mentioned, numerical codes can be used to determine how acoustic wavefronts propagate in complex ocean environments with a ray-based solution. In shallow water the number of paths can be quite large when the bottom is highly reflective (e.g., as in Fig. 3.12). Additionally, the ray model is a solution to the Eikonal equations [8, Ch. 3] which are an approximation to the wave equation valid at high frequency and therefore potentially inaccurate at low frequency. An appealing alternative in shallow water and for low frequencies is to describe the propagation in terms of modes rather than rays. Consider a *basic ocean waveguide* identical to the basic ocean model described at the beginning of Sect. 3.2 but having constant depth z_b . The basic ocean waveguide is useful to compare the ray and mode approaches because exact solutions to the wave equation can be found for both. For a *range-independent* waveguide (i.e., the properties do not change with range) it

is convenient to work in cylindrical coordinates using range r and depth z , while restricting azimuth to that containing the source and receiver.

3.2.8.1 Ray-Based Solution and Multipath

The method of image sources [1, Ch. 39], [16, Sect. 6.8] can be used to describe the impulse response of an iso-speed waveguide. The technique requires placing sources in *image* oceans reflected above and below the real ocean. As seen in Fig. 3.16, the sources are at depths $2nz_b \pm z_o$ for all integers n where z_b is the bottom depth and z_o is the source depth. The straight lines in Fig. 3.16 represent (unfolded) reflected paths connecting the source and receiver. The impulse response for this *multipath channel* is then the sum of the single-path response in the basic ocean model from (3.46) over all of the sources, each of which represents a different propagation path connecting the source and receiver.

In the simplest case, as considered in [5, Sect. 3.6], both boundaries of the waveguide are assumed to be free surfaces. That is, an incident wave at either boundary undergoes total internal reflection for all incident angles and the reflected wave is subject to a sign change at both boundaries. The impulse response of this iso-speed waveguide is⁹

$$h(t, z, r) = \sum_{n=-\infty}^{\infty} \left[\frac{1}{r_n^e} \delta(t - r_n^e/c_w) - \frac{1}{r_n^o} \delta(t - r_n^o/c_w) \right] \quad (3.158)$$

where

$$r_n^e = \sqrt{r^2 + (z - z_o + 2nz_b)^2} \quad (3.159)$$

and

$$r_n^o = \sqrt{r^2 + (z + z_o + 2nz_b)^2} \quad (3.160)$$

are the distances travelled to the receiver at range r and depth z from image sources at zero range and, respectively, depths of $2nz_b - z_o$ and $2nz_b + z_o$. As can be seen in Fig. 3.16, the r_n^o image sources (dashed gray lines) have an odd number of boundary reflections and therefore incur a net sign inversion whereas the r_n^e sources (solid gray lines) have an even number of reflections. The frequency response of the channel is the Fourier transform of (3.158),

⁹Note that (3.158) differs from that presented in [5, eq. 3.83] by the -4π scale noted in Sect. 3.2.3.1.

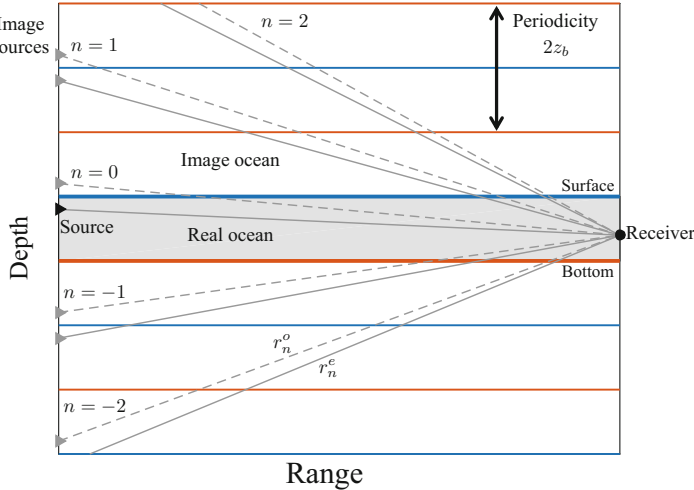


Fig. 3.16 Method of images applied to a shallow-water iso-speed environment

$$H(f, z, r) = \sum_{n=-\infty}^{\infty} \left[\frac{1}{r_n^e} e^{-j2\pi f r_n^e / c_w} - \frac{1}{r_n^o} e^{-j2\pi f r_n^o / c_w} \right]. \quad (3.161)$$

It is straightforward to extend (3.158) or (3.161) to account for reflection loss due to transmission into the bottom or roughness in either boundary by including an incident-angle-dependent per-bounce loss and summing over the four combinations of paths with even and odd numbered surface and bottom reflections (e.g., see [32, Sect. 2.4.3]). Closed-form solutions also exist when the sound-speed variation is linear in depth or range [8, Sect. 3.7.3], for which the ray paths are described by arcs of circles.

3.2.8.2 Mode-Based Solution

The normal-mode solution to the wave equation is derived from the Helmholtz equation (3.52) by assuming that for a given frequency the solution is separable in depth and range (i.e., $P(f, r, z) = G(f, r)\Phi(f, z)$). The solution, for which derivations may be found in [5, Sects. 3.6 & 4.2], [7, Sect. 5.2], and [8, Sect. 5.2.1], results in separate differential equations in depth and range. For the general case of depth-dependent sound speed and density, the depth differential equation solution is an eigen-function of a Sturm-Liouville problem with boundary conditions [7, 8]. The solution to the range differential equation is a Hankel function of the first or second kind (which one depends on how the Fourier transform is defined).

The general solution is then found by summing over all the Sturm-Liouville eigenfunctions $\Phi_m(z)$,

$$H(f, z, r) = \frac{-j\pi}{\rho(z_o)} \sum_{m=1}^{\infty} \Phi_m(z_o) \Phi_m(z) H_0^{(2)}(k_{hm}r), \quad (3.162)$$

where k_{hm}^2 are the eigenvalues, and $H_0^{(2)}(x)$ is a Hankel function of the second kind. Note that (3.162) is the complex conjugate¹⁰ of the result found in [7, eq. 5.20] owing to different definitions of the Fourier transform. The eigenfunctions, which are also called mode functions, are scaled so as to be orthonormal with respect to $\rho(z)$,

$$\int_0^{z_b} \frac{1}{\rho(z)} \Phi_m(z) \Phi_n(z) dz = \delta[m - n], \quad (3.163)$$

where $\delta[i]$ is the Kronecker delta function which is one when $i = 0$ and zero otherwise.

By applying the Hankel function's large-argument approximation, $H_0^{(2)}(x) \approx \sqrt{2/(\pi x)} e^{-j(x-\pi/4)}$ [35, 10.2.6], the frequency response becomes

$$H(f, z, r) \approx \frac{e^{-j\pi/4}}{\rho(z_o)} \sqrt{\frac{2\pi}{r}} \sum_{m=1}^{\infty} \Phi_m(z_o) \Phi_m(z) \frac{e^{-jk_{hm}r}}{\sqrt{k_{hm}}} \quad (3.164)$$

The \sqrt{r} in the denominator illustrates the $10 \log_{10} r$ cylindrical spreading loss described in Sects. 3.2.2.3 and 3.2.4. When k_{hm} is real, the complex exponential $e^{-jk_{hm}r}$ in (3.164) indicates k_{hm} can be interpreted as the horizontal wavenumber of the m th mode. The error in the Hankel-function approximation is larger for the magnitude than for the phase when the argument is small. However, it is accurate to within 5% for arguments $x \geq 1$, so it can be used for $r > 1/k_{hm}$. This will apply in most cases, although care must be taken for the smallest values of k_{hm} .

In forming the mode function and eigenvalues ($\Phi_m(z)$ and k_{hm}^2), boundary conditions such as requiring the pressure at the ocean surface to be zero must be applied. For the basic ocean waveguide (constant sound speed and density) with two free boundaries previously described, the mode functions are sinusoids in depth,

$$\Phi_m(z) = \sqrt{\frac{2\rho}{z_b}} \sin(\gamma_m z) \quad (3.165)$$

¹⁰Because $H_0^{(2)}(x) = J_0(x) - jY_0(x) = [J_0(x) + jY_0(x)]^* = [H_0^{(1)}(x)]^*$ for real $x > 0$, where $J_v(x)$ and $Y_v(x)$ are Bessel functions of the first and second kind, respectively.

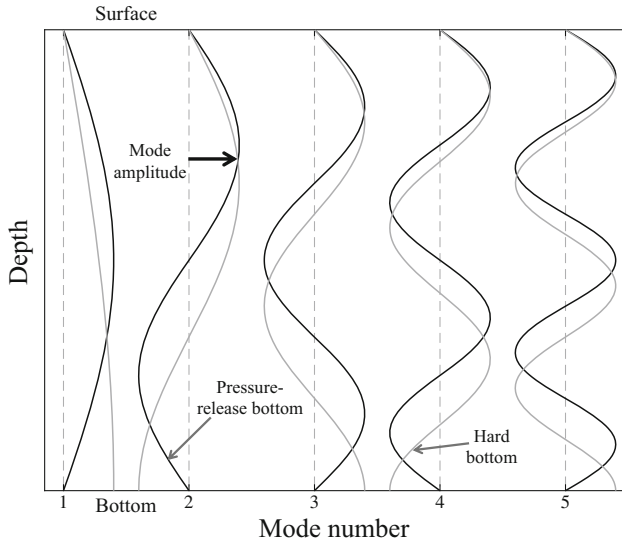


Fig. 3.17 Mode shapes for a shallow-water waveguide

with frequency $\gamma_m = \pi m / z_b$ and the eigenvalues are

$$k_{hm}^2 = k^2 - \gamma_m^2. \quad (3.166)$$

As seen in Fig. 3.17, the mode functions for the dual pressure-release-boundary waveguide (dark lines) have zero amplitude at both the surface and the bottom. Had the bottom been assumed rigid, the particle velocity at depth z_b would need to be zero resulting in $\gamma_m = \pi(m - 0.5)/z_b$. The mode functions for the rigid bottom (gray lines in Fig. 3.17), which are still sine waves with zero phase at the surface, have zero slope at the bottom.

A number of other waveguide scenarios are treated theoretically in [7, 8]. More complicated scenarios such as depth-varying sound speed, a layered bottom, and even range dependence can be solved through numerical approaches such as those described in [8, Sect. 5.7]. The KRAKEN code by M. Porter, which is based on [36, 37] and available at the Ocean Acoustics Library [24], is an example.

Using the mode and eigenvalue functions from (3.165) and (3.166) in (3.162) results in the frequency response for the basic ocean waveguide,

$$H(f, z, r) = \frac{-j2\pi}{z_b} \sum_{m=1}^{\infty} \sin(\gamma_m z_o) \sin(\gamma_m z) H_0^{(2)}\left(r\sqrt{k^2 - \gamma_m^2}\right). \quad (3.167)$$

Note that frequency only enters (3.167) in the argument of the Hankel function via $k = 2\pi f/c_w$; the mode functions do not depend on frequency unless the boundary

conditions constraining them do. For a given frequency, modes producing purely imaginary horizontal wavenumber (i.e., $\gamma_m > k$) result in evanescent waves with an exponential decay of the frequency response amplitude with range (this can be seen from the aforementioned approximation to the Hankel function). For a given mode, this implies it is not evaluated for frequencies below $mc_w/(2z_b)$, which is known as the low-frequency mode cut-off [8, Sect. 2.4.5.2]. If f_{\max} is the largest frequency of interest, the sum over modes can be truncated to retain only modes with real horizontal wavenumbers. This requires

$$m < \frac{2z_b f_{\max}}{c_w} = \frac{z_b}{\lambda/2} \quad (3.168)$$

which indicates the number of modes required to represent a waveguide is the number of half-wavelengths required to span the water column. This will be much less computationally intensive than evaluating (3.158) or (3.161) until the ray amplitudes are negligible. The advantage accorded the normal-mode solution for low frequencies in shallow water is compelling: at 100 Hz in 100 m of water only 13 modes are required to completely describe the channel response.

The mode-form of the impulse response for the basic ocean waveguide with two pressure-relief boundaries is obtained by taking the inverse Fourier transform of (3.167),

$$h(t, z, r) = \frac{4c_w}{z_b} \sum_{m=1}^{\infty} \sin(\gamma_m z_o) \sin(\gamma_m z) \frac{\cos(\gamma_m \sqrt{c_w^2 t^2 - r^2})}{\sqrt{c_w^2 t^2 - r^2}} \quad (3.169)$$

for $t \geq r/c_w$. Although this may not appear to be the same as the ray-based solution in (3.158), it is an equivalent representation. Guidance for proof of the equivalence between the two can be found in [5, App. B].

Exercise 3.12 Show that particle velocity perpendicular to the bottom is zero for the m th mode in a waveguide when $\Phi'_m(z_b) = 0$. Hint: use (3.3) with (3.162), which requires the gradient in cylindrical coordinates,

$$\nabla p(t, r, \theta, z) = \frac{\partial p}{\partial r} \vec{e}_r + \frac{1}{r} \frac{\partial p}{\partial \theta} \vec{e}_{\theta} + \frac{\partial p}{\partial z} \vec{e}_z. \quad (3.170)$$

Exercise 3.13 Using the Helmholtz equation in (3.52) and the Laplacian operator in cylindrical coordinates from (3.31), assume a separable solution $P(f, \vec{x}) = G(r)\Phi(z)$ (suppressing any potential dependence on f) and simplify the homogeneous partial differential equation (i.e., $U(f, \vec{x}) = 0$) to the form

$$\left[\frac{G''(r) + r^{-1}G'(r) + k^2G(r)}{G(r)} \right] + \left[\frac{\Phi''(z)}{\Phi(z)} \right] = 0. \quad (3.171)$$

In order for this equation to hold for all r and z , the terms in brackets must both be constant and opposite. The term in the first set of brackets results in Bessel's equation, for which the Hankel function is a solution. If the latter term equals $-\gamma^2$ for some real $\gamma > 0$, show that it forms the differential equation

$$\Phi''(z) + \gamma^2 \Phi(z) = 0. \quad (3.172)$$

Solve (3.172) with boundary conditions requiring the pressure at the surface and bottom to be zero (i.e., $\Phi(0) = 0$ and $\Phi(z_b) = 0$). How does the solution change if the particle velocity normal to the boundary at the bottom is zero (i.e., $\Phi'(z_b) = 0$) as it must be for a rigid bottom?

3.2.8.3 Dispersion in a Waveguide

With respect to wave propagation, *dispersion* is defined as a frequency dependence to the wave speed for a given medium. As will be seen, propagation in a waveguide does have a frequency dependence to the time it takes a pulse to propagate to a given range. However, the dependency arises from the naturally preferred propagation paths each frequency component takes as opposed to dispersion intrinsic to the sea water medium (which is small enough to be negligible as discussed in Sect. 3.2.5). The frequency dependence of propagation in a waveguide is therefore called *geometric dispersion*.

Mode propagation in the iso-speed waveguide can be visualized by considering each mode as comprising a pair of planar wavefronts propagating down the waveguide in tandem, but with opposite vertical directions. Mathematically, this can be seen by inserting (3.165) into (3.164) and expanding $\sin(\gamma_m z)$ into complex exponentials yielding

$$H(f, z, r) \approx \frac{\sqrt{2\pi}}{z_b} e^{-j3\pi/4} \sum_{m=1}^{\infty} \frac{\sin(\gamma_m z_o)}{\sqrt{r k_{hm}}} \left[e^{-j(k_{hm}r - \gamma_m z)} - e^{-j(k_{hm}r + \gamma_m z)} \right] \quad (3.173)$$

At long ranges, the exponential terms within the brackets are approximately planar wavefronts (i.e., they represent the planar approximation to a spherical wave in Sect. 3.2.2.4) with the same horizontal wavenumber (k_{hm}) but opposing vertical wavenumbers ($\pm\gamma_m$). For the basic ocean waveguide, the grazing angles of the rays representing the wavefront pair are

$$\theta_m = \pm \arcsin\left(\frac{\gamma_m}{k}\right) = \pm \arcsin\left(\frac{mc_w}{2z_b f}\right). \quad (3.174)$$

Thus the lowest mode ($m = 1$ for which $\gamma_1 = \pi/z_b$) travels at a nearly horizontal grazing angle as long as the waveguide depth is many half-wavelengths (i.e., $z_b \gg c_w/(2f) = \lambda/2$) and higher order modes are represented by steeper rays.

The horizontal progression of rays with steep grazing angles is obviously slower than for shallow-grazing-angle rays, so higher order modes take longer to propagate to a given range than lower order modes. Similarly, lower frequencies for a given mode have a larger grazing angle and therefore a slower horizontal progression. The frequency dependence of the horizontal progression is quantified by the *group delay* of the channel (Sect. 4.9). Recalling the time-delay property of the Fourier transform ($\mathcal{F}\{x(t - \tau_d)\} = e^{-j2\pi f \tau_d} X(f)$), the group delay of a filter with transfer function $H(f)$,

$$\tau_d(f) = \frac{-1}{2\pi} \frac{\partial}{\partial f} \angle H(f), \quad (3.175)$$

describes the time delay between the input and the output. When the transfer function phase $\angle H(f)$ is not linear with frequency, $\tau_d(f)$ is frequency dependent. For the present application, the group delay is frequency dependent and represents the time a particular frequency component of a pulse needs to propagate to range r . Applying (3.175) directly to (3.162) or (3.164) requires summing over all the modes active for a particular frequency to reduce a complicated inter-mode phase interaction to a single group delay as a function of frequency. A simpler alternative is to evaluate the group delay for individual modes assuming the overall group delay may be inferred from the per-mode delays. As frequency f only enters the phase of a single mode in the large- r result of (3.164) through $k_{hm} = \sqrt{k^2 - \gamma_m^2}$ with $k = 2\pi f/c_w$, the group delay for the m th mode only depends on frequency and range,

$$\tau_d(f, r) = \frac{r}{2\pi} \frac{\partial k_{hm}}{\partial f} \quad (3.176)$$

$$= \frac{r/c_w}{\sqrt{1 - (\gamma_m/k)^2}} = \frac{r/c_w}{\cos \theta_m}, \quad (3.177)$$

where (3.176) applies to the general waveguide and (3.177) to the basic ocean waveguide.

The grazing-angle dependence in (3.176) illustrates how each mode takes a factor $1/\cos \theta_m$ longer than the nominal time of r/c_w to reach range r . An example of the group delay for a 100-m deep iso-speed waveguide at a 15-km range is shown for the first five modes in Fig. 3.18 (black lines). The first mode is seen to arrive before all others, very close to the nominal 10-s group delay for this range except at the lowest frequencies. At higher frequencies, the fifth mode arrives very close to the first, but can be much later at lower frequencies. For example, at 50 Hz it arrives almost 5 s later than the first mode. Because of the dependence of group delay on range, the separation between modes may be difficult to measure at short range but can be dramatic at long range. Also shown in Fig. 3.18 is the full-channel group delay (gray dots) when the source and receiver are both at depth $z_o = z = 10$ m. At the lowest frequencies shown only the first mode is active and so the full-

channel result is identical to the single-mode result. As frequency increases, the full-channel delay appears to mostly track the single-mode results as they enter into $H(f, r, z)$ with small values of k_{hm} , which dominate the other modes because of the Hankel function's inverse dependence on its argument. Eventually, however, no single mode dominates and the interaction between modes becomes too complicated for the single-mode results to simply represent, resulting in a rapidly varying group delay with frequency.

In the waveguide application, the speed at which the various frequency components of the pulse travel horizontally through the water is called the *group velocity*. As an incremental change in range arising from an incremental change in time, it can be obtained as the inverse of the derivative of the group delay in (3.176) with respect to range,

$$\frac{\partial r}{\partial \tau_d(f, r)} = \left\{ \frac{\partial \tau_d(f, r)}{\partial r} \right\}^{-1} = -2\pi \left\{ \frac{\partial^2 \angle H(f)}{\partial r \partial f} \right\}^{-1} \quad (3.178)$$

$$= c_w \sqrt{1 - (\gamma_m/k)^2}. \quad (3.179)$$

Noting that $\gamma_m < \gamma_{m+1}$ for all modes,¹¹ clearly the first mode has the highest group velocity (also explaining why it arrives first in Fig. 3.18) and it is less than c_w .

Although the modal characterization of group delay and group velocity is a convenient representation, geometric dispersion should not be construed as only applying to modes: it is a characteristic of the waveguide itself. Owing to the equivalence of (3.161) and (3.162) (with (3.165)), either the ray or mode characterization of $H(f, r, z)$ can be used in (3.175) or (3.178) to obtain the full channel group delay or group velocity.

3.2.9 Reciprocity

The reciprocity principle [3, Sect. 7.2] describes a symmetry to propagation between a source and receiver when their positions are exchanged. This can greatly simplify analysis of monostatic active sonar systems because the effects of propagation only need to be evaluated once.

While a proof of the reciprocity principle is beyond the scope of this text (the interested reader is referred to [3, Sect. 7.2] or [8, Ch. 2, App. 1]), several examples of reciprocity have already been encountered in this chapter. The simplest case is for the basic ocean model where the channel impulse response in (3.46) only depends on the range $r = \|\vec{x} - \vec{x}_o\|$ between the source and receiver, which does not change when their positions are exchanged. For a monostatic active sonar, the two-way

¹¹A property of the Sturm-Liouville system eigenvalues.

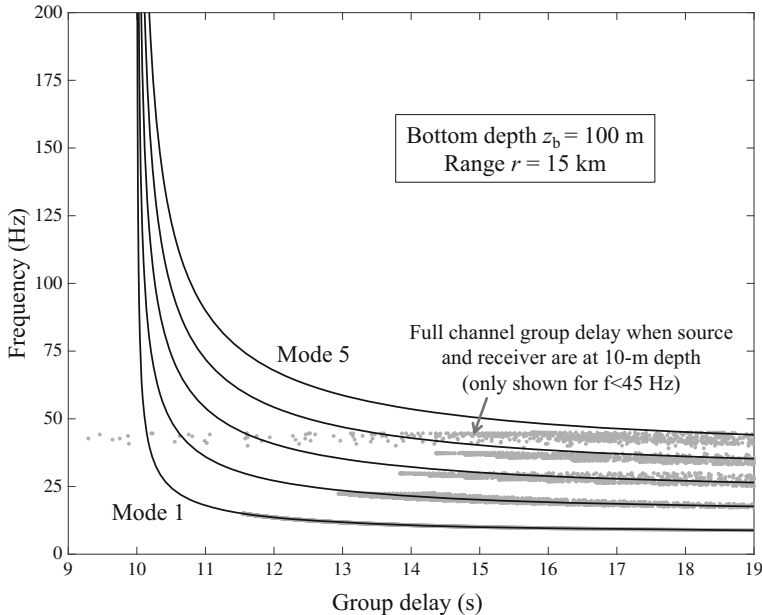


Fig. 3.18 Geometric dispersion of modes in a shallow-water waveguide

channel impulse response is the convolution of the one-way response ($h_1(t)$) with itself,

$$h_2(t) = h_1(t) * h_1(t) = \frac{\delta(t - 2r/c_w)}{r^2}. \quad (3.180)$$

This illustrates the $r/(c_w/2)$ time delay arising from propagation out to and back from range r .

Reciprocity is also seen in the basic ocean waveguide example of Sect. 3.2.8. The ray-based solution in (3.158) is a function of the distances between the receiver and the image sources, which depend on the range and depths of the source (z_o) and receiver (z). Exchanging the source and receiver positions only requires exchanging z_o and z . Although this clearly does not affect r_n^o in (3.160), r_n^e simply becomes r_{-n}^e and the channel impulse response in (3.158) remains the same.

The mode-based solution to the Helmholtz equation in (3.162), which allows a depth-dependence to sound speed and density, illuminates how reciprocity depends on density at the source and receiver. Let the frequency response of the channel be written as $H(f, \vec{x}; \vec{x}_o)$ where \vec{x} is the position of the receiver and \vec{x}_o the position of the source. The mode-based solution from (3.162),

$$H(f, \vec{x}; \vec{x}_o) = \frac{-j\pi}{\rho(z_o)} \sum_{m=1}^{\infty} \Phi_m(z_o) \Phi_m(z) H_0^{(2)}(k_{hmr}), \quad (3.181)$$

can then be seen to satisfy

$$\rho(\vec{x}_o)H(f, \vec{x}; \vec{x}_o) = \rho(\vec{x})H(f, \vec{x}_o; \vec{x}), \quad (3.182)$$

when the source and receiver are exchanged. Equation (3.182) is the more general reciprocity relation [8, eq. 2.274] accounting for changes in density.

3.3 Ambient Noise

Ambient noise is defined as the ever present interfering sounds measured by hydrophones used in the ocean. Of particular interest are the noises producing the constant background hum of a noisy environment—akin to the drone of a distant highway. This definition in particular excludes temporary, loud, and distinct sounds such as the fleeting passage of a nearby train. Such noises are treated as interferences that are ephemeral in time and localized in space. The intent of this section is to review the primary ambient noise sources in each of several frequency bands and describe approximate equations for noise spectrum levels as a function of frequency.

3.3.1 Overview and Ambient Noise Spectrum Curves

As can be seen in several overviews [38–41], ambient noise has many sources, each with their own dependencies and ensuing variations. An appropriate description of ambient noise worth quoting comes from [42, pg. 249]:

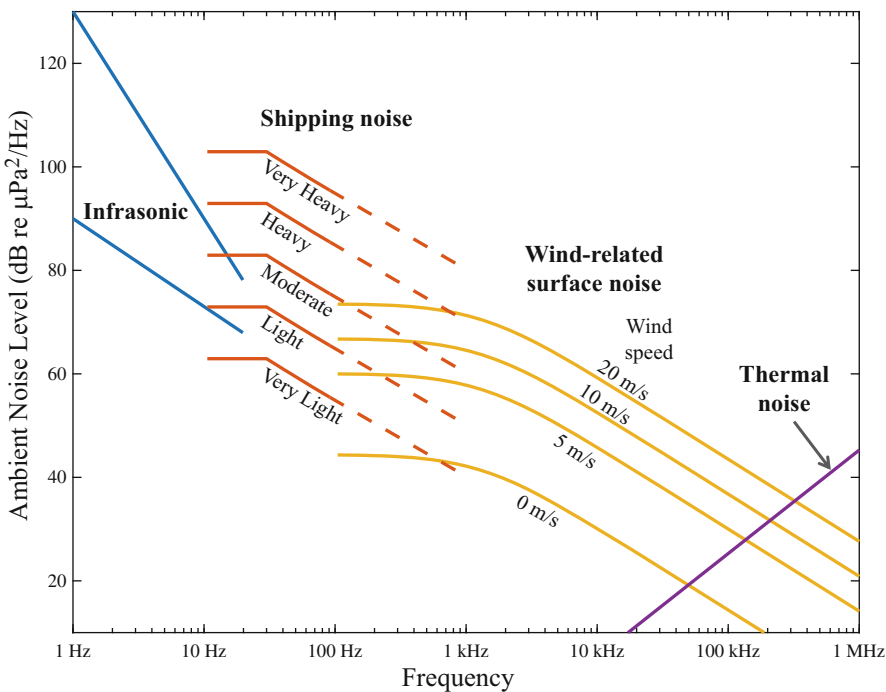
“The outstanding characteristic of ambient noise is its great variability.”

Despite the numerous origins and their inherent variability, four frequency regimes can be defined where one or two ambient noise sources tend to dominate the others [43, Sect. 7.1]. The four (overlapping) regimes, along with their dominant sources and references where more detail may be found, are shown in Table 3.3. Ambient noise levels have famously been summarized by a graph produced by Wenz [38] (see [9, Fig. 8.13] or [41, Fig. 4.2] for expanded versions). The graph succinctly illustrates the variety of sources, their frequency dependence, and the variability over which noise spectrum levels can range: the minimum spread for a given frequency is approximately 50 dB!

Example noise level curves are shown in Fig. 3.19 illustrating how the different noise sources dominate in each band, but also overlap each other. The formulae required to generate them follow for each frequency band in Sects. 3.3.2–3.3.5. The primary application of these ambient noise curves is for sonar-equation analysis. Although they are useful for performance prediction, actual noise levels can be dramatically different in practice. This is both because one set of curves does not have universal applicability to all locations or receiver depths and because local

Table 3.3 Dominant noise by frequency band

Frequency band	Dominant noise source	References
Very low (<20 Hz)	Wave interaction and turbulence	Carey [41] or Urick [43]
Low (10 Hz to 1 kHz)	Distant shipping noise	[9, 32, 38, 44]
Low to high (100 Hz to 100 kHz)	Surface-related noise	Ainslie [9] or Knudsen [45]
Very high (>50 kHz)	Thermal noise	Mellen [46]

**Fig. 3.19** Ambient noise spectrum level vs. frequency. The four regions are dominated by, respectively, ocean turbulence, shipping noise, wind-related surface noise, and thermal noise. Shipping noise treats each ship as a dipole source

conditions can include situations not covered by these models. For example, ambient noise arising from precipitation (e.g., rain) can exceed wind-induced surface noise or persistent noise from anthropogenic structures such as oil rigs may overwhelm distant shipping noise.

3.3.1.1 Converting Spectrum Rates of Change from per Octave to per Decade

Ambient noise spectrum levels are often linear when plotted logarithmically in frequency. The decay rate, which is the negative slope of the line, is at times described by referencing the reduction over an octave (i.e., a doubling) in frequency, a decade (i.e., a factor of ten), or other frequency ratios such as a third-octave or the nearly equivalent and preferred decidecade (tenth of a decade, also called a frequency logit). For example, a decay rate of 5 dB per octave above 100 Hz has been quoted for surface-related noise [42] and noise from distant shipping is described as falling off at 2 dB per frequency logit (decidecade) [47, Sect. 2B-1], which is about 6 dB per octave.

In order to relate the decay rate from one frequency ratio to another, suppose the noise power spectral density has a power-law form over the frequency range of interest,

$$P_N(f) \propto \frac{1}{f^p}. \quad (3.183)$$

The decay rate of the noise spectrum level relative to a factor R change in frequency can then be found by converting (3.183) to decibels and differentiating with respect to $-\log_R(f)$, yielding

$$C_R = 10p \log_{10}(R). \quad (3.184)$$

Thus the slope per octave is $C_2 = 10p \log_2(10) \approx 3p$ and the slope per decade is $C_{10} = 10p$. The two can be related as

$$C_{10} = \frac{C_2}{\log_{10} 2} \approx \frac{10}{3} C_2. \quad (3.185)$$

The two previously mentioned decay rates of $C_2 = 5$ and 6 dB per octave produce $C_{10} = 16.6$ and 19.9 dB per decade, respectively, or 17 and 20 with rounding to an integer.

A frequency logit uses the ratio $R = 10^{0.1} \approx 1.2589$, which yields $C_{10^{0.1}} = p$, precisely the exponent in the denominator of (3.183). The frequency logit is very similar to a third-octave where $R = 2^{1/3} \approx 1.2599$ which yields $C_{2^{1/3}} = (10/3)p \log_{10} 2 \approx p$.

3.3.2 Very Low Frequency

Several sources contribute to noise in the very low frequency band ($f < 20$ Hz) including wave–wave interaction and turbulence [41, 48]. Both oceanic and atmo-

spheric turbulence have been identified as a noise source in this frequency regime [48]. According to Carey [41], ambient noise spectrum measurements in the 0.2–5 Hz regime exhibit decays in the range 17–40 dB per decade (5–12 dB per octave). These extremes are shown in Fig. 3.19 with intercepts to illustrate the variation potentially observed. For example, the upper plot is

$$NL_f^{\text{vlf}} = 130 - 40 \log_{10} f. \quad (3.186)$$

Although not shown in Fig. 3.19, wave–wave interaction can exhibit a peak in the spectrum (e.g., in the 0.2–0.5 Hz regime) related to wave frequency.

3.3.3 Low Frequency: Distant Shipping Noise

As noted in Sect. 3.2, low-frequency sound is subject to less attenuation as it propagates and therefore can be heard farther away than higher frequency sound having the same source level. With most of the radiated noise produced by commercial shipping lying below 1 kHz (e.g., see [9, Sect. 8.3.1]) it is not surprising that it can dominate in the low-frequency regime of about 10 Hz to 300 Hz. Spectrally, distant shipping noise has been characterized as having maximum value below 100 Hz, being relative flat from 10–100 Hz, and having a 20 dB per decade (6 dB per octave) fall-off above 100 Hz [12, 32, 38, 44]. As such, a reasonable model promulgated by Lurton [32, Sect. 4.2.2] uses a constant level from 10 to 100 Hz followed by a constant decay at 20 dB per decade. Shipping density variations cause the constant level to vary from 60 to 90 dB re $\mu\text{Pa}^2/\text{Hz}$.

An alternative approach proposed by Ainslie [9, Sect. 8.3.1] incorporating measurements of noise radiated from many merchant ships is presented in Fig. 3.19. Ainslie treats distant shipping noise as arising from a sheet of monopole or dipole sources near the surface, each having the same average source spectrum. The average source spectrum level for a single ship is taken from [49] as

$$SL_f^{\text{mp}} = 230 - 35.94 \log_{10} f + 9.17 \log_{10} \left[1 + (f/340)^2 \right] \text{ dB re } \mu\text{Pa}^2 \text{m}^2/\text{Hz} \quad (3.187)$$

for $f \in [30, 1200]$ Hz. As seen in Fig. 3.19, the level of the overall noise spectrum at 30 Hz is held constant down to 10 Hz based on the aforementioned reports of a near constant level in this region. If each ship is treated as a monopole source, the ambient noise level from distant shipping is simply

$$NL_f^{\text{sh,mp}} = \begin{cases} NL_{30}^{\text{sh,mp}} & 10 \leq f < 30 \\ 10 \log_{10} \left(\frac{D^{\text{sh}}}{10^{12}} \right) + SL_f^{\text{mp}} & 30 \leq f \leq 1200 \end{cases} \quad (3.188)$$

in units of dB re $\mu\text{Pa}^2/\text{Hz}$ where D^{sh} is the shipping density in terms of the average number of ships per square mega-meter (Mm^2). Shipping density is suggested in [9, Table 9.3] to vary from 5 per Mm^2 for very light shipping to 50,000 per Mm^2 for very heavy shipping. Each incremental level shown in Fig. 3.19 represents an order of magnitude change in shipping density (i.e., 50 per Mm^2 for light shipping, 500 for moderate, and 5000 for heavy).

By treating each ship as a dipole source at depth d (m), the ambient noise level is

$$\text{NL}_f^{\text{sh,dp}} = \begin{cases} \text{NL}_{30}^{\text{sh,dp}} & 10 \leq f < 30 \\ 10 \log_{10}[4\pi(kd)^2] + 10 \log_{10}\left(\frac{D^{\text{sh}}}{10^{12}}\right) + \text{SL}_f^{\text{mp}} & 30 \leq f \leq f_e \\ \text{NL}_{f_e}^{\text{sh,dp}} - C_{10}(f_e) \log_{10}\left(\frac{f}{f_e}\right) & f_e < f \leq 1200 \end{cases} \quad (3.189)$$

in units of dB re $\mu\text{Pa}^2/\text{Hz}$ where $k = 2\pi f/c_w$ is the wavenumber. The result in the middle line of (3.189), which is from [9, eqs. 8.198 & 8.217], requires $kd < \pi/4$. For frequencies above this limit ($f_e = c_w/(8d)$) a linear (in dB) extension has been applied as seen in Fig. 3.19. The decay rate of the middle line in (3.189) is

$$C_{10}(f) = 15.94 - 18.34 \left[\frac{(f/340)^2}{1 + (f/340)^2} \right] \quad \text{dB per decade.} \quad (3.190)$$

The decay rate of the linear extension in (3.189) was calculated using (3.190) at $f = f_e$, where $kd = \pi/4$. The example in Fig. 3.19 used $d = 2$ m and the decay rate of the extension was 14.6 dB per decade (4.4 dB per octave). Although this may not decay as rapidly as other models, it originates with measurements from [49] yielding (3.187) for which the decay rate is that shown in (3.190) plus 20 from the $10 \log_{10}(k^2)$ in (3.189).

The models presented in this section are generally applied for deep-water conditions. In deep water, low-frequency sound from very distant ships will be observed. However, in shallow water where significant interaction with the bottom attenuates the very distant shipping noise, ambient noise is expected to be more diverse than (3.188) or (3.189) can represent.

3.3.4 Low to High Frequency: Wind-Related Surface Noise

Above 100 Hz ambient noise from distant shipping decays to the point where wind-generated surface noise can dominate. The physical mechanism [9, Sect. 8.3.2.1] is attributed to the pulsation of bubbles generated by breaking waves. Early reports show a spectrum decay rate of 5 dB per octave (16.6 dB per decade) [42, Sect. 13.5.2]. The curves produced by Knudsen [45] as found in [38] were long considered the standard. Ainslie [9, Sect. 8.3.2.1] proposes combining the high-

frequency model from [50, Sect. II-D] with the low-frequency measurements of [51]. The combined model,

$$\begin{aligned} \text{NL}_f^{\text{wind}} &= 41.2 + 10 \log_{10} \pi + 22.4 \log_{10} [\max(1, v)] \\ &\quad - 10 \log_{10} \left[1.5 + \left(\frac{f}{1000} \right)^{1.59} \right] - \Delta_T^{\text{dB}} \text{dB re } \mu\text{Pa}^2/\text{Hz}, \end{aligned} \quad (3.191)$$

depends on wind speed (v , m/s) as measured at a height of 10 m and the difference in temperature between the air (T_a , °C) and water (T_w , °C) through

$$\Delta_T^{\text{dB}} = \begin{cases} 0 & T_a - T_w < 1 \\ 0.26(T_a - T_w - 1)^2 & T_a - T_w \geq 1 \end{cases}. \quad (3.192)$$

The high-frequency model of [50, Sect. II-D] was derived for an omni-directional hydrophone in a deep water scenario (i.e., it only accounted for direct-path propagation). Although the low-frequency measurements of [51] were in a shallow-water environment, the effects of propagation were removed to obtain the wind-noise source levels represented in (3.191) and the results were shown to be similar to a deep water scenario.

Precipitation can create noise in a similar manner to wind [9], exhibiting higher noise levels (up to 10s of decibels higher) in this frequency band and with a peak in the 16–24 kHz band [50]. Approximate spectrum levels can be obtained from [50, Sect. II-D.5] or [9, Sect. 8.3.2.2].

3.3.5 Very High Frequency: Thermal Noise

A fundamental limitation in sensing acoustic pressure under water arises in the noise generated by a hydrophone from the thermal agitation of water molecules. Such thermal noise is always present and can be a system limitation for high-frequency sonars (e.g., $f > 50$ kHz).

Mellen [46] (also see [9, Sect. 10.2.1.1]) describes the power spectral density of an acoustic noise representative of the hydrophone response to thermal noise as

$$P_n^{\text{th}}(f) = 4\pi K T \left(\frac{\rho_w}{c_w} \right) f^2 \text{ Pa}^2/\text{Hz} \quad (3.193)$$

where $K = 1.381 \times 10^{-23}$ J/K is Boltzmann's constant, T is temperature (kelvin), ρ_w is water density, and c_w is the speed of sound in water. It should be noted that the units of f are Hz and of $P_n^{\text{th}}(f)$ in (3.193) are Pa^2/Hz . Converting to decibels for nominal values ($\rho_w = 1027 \text{ kg/m}^3$, $c_w = 1500 \text{ m/s}$, and $T = 283^\circ \text{ K}$ which is 10° C) and using the standard $\mu\text{Pa}^2/\text{Hz}$ reference units produces the noise spectral level

$$\text{NL}_f^{\text{th}} = -74.7 + 20 \log_{10} f \text{ dB re } \mu\text{Pa}^2/\text{Hz}. \quad (3.194)$$

As seen in Fig. 3.19, thermal noise only plays a role at very high frequencies. As such, some texts describe (3.194) using frequency defined in kHz rather than Hz, which changes the -74.7 to -14.7 .

3.3.6 Spatio-Temporal and Statistical Properties of Ambient Noise

The previous sections provide a spectral characterization of the various dominating ambient noise sources. This spectral characterization comes under the assumption that the noise is a wide-sense-stationary random process (see Sect. 5.4). Under this assumption, the power spectral density (i.e., $P_n(f) = 10^{\text{NL}_f/10}$) also defines the pertinent temporal correlation properties through an inverse Fourier transform to obtain the autocorrelation function. When ambient noise arises from many contributions of statistically independent sources, the measured signals will have a Gaussian probability density function owing to the central limit theorem (see Sect. 5.3.7). Although there are ambient noise situations where the CLT will not hold (e.g., low shipping density), that ambient noise is generally Gaussian distributed greatly simplifies the derivation and analysis of signal processing algorithms. Non-Gaussian probability distributions that can be used to represent ambient noise when the CLT is violated are described in Sects. 7.4.1 and 7.4.3.

In terms of a spatial characterization, ambient noise can generally be assumed to be isotropic azimuthally. Clearly there will be conditions violating this; for example, relative proximity to a shipping lane can make one direction preferentially louder than another. With respect to elevation angle, ambient noise arising from distant shipping generally arrives through very low grazing-angle paths (i.e., near horizontal). Any sounds traveling higher-angle paths are stripped off before they reach the sensor. Wind-generated surface noise, however, is a more local phenomena and therefore is stronger in some upward-looking angles than horizontal or downward-looking.

3.4 Scattering from Objects: Target Echoes and Target Strength

Reflection and scattering both describe an interaction of an incident acoustic wave with an object in its path. In Sect. 3.2.6 the reflection of an incident wave at a horizontal boundary was described as occurring in the specular direction; that is, the angle of reflection is the same as the angle of incidence but on the opposite side of the line perpendicular to the boundary. Scattering occurs when a wave

ensonifies an object with the resulting energy radiated either in many directions or a random direction. For example, in Sect. 3.2.7, the random rough surface distributed or diffused the reflected sound in many directions. This may be termed *diffuse reflection* but is essentially the same as scattering. As described in [52, Sect. 2.3], reflection is often treated as a deterministic effect arising from an incident wave producing a specular reflection from a non-random surface whereas scattering is considered a random redistribution of the incident wave to other angles.

The subject of wave interaction with objects and surfaces is extensive. Topics found in the literature include evaluating the dependence of the scattered wave on object or surface shape, size, orientation, and composition as well as the sensing geometry. The focus of this section is necessarily narrow and restricted to topics necessary for the design and analysis of signal processing algorithms in active remote sensing. The focus is on reflection and scattering from generic shapes representing objects of interest. The section begins by describing the target strength (TS) term in the sonar equation as the simplest representation of reflection and scattering from an object of interest. To support the design of active sonar detection algorithms, the reflection or scattering from an object of interest is characterized as a convolution of an incident pulse with a target impulse response in Sect. 3.4.2. Finally, the dependence of the reflected and scattered acoustic signal on sensing frequency is categorized through a dependence on the product of the sensing wavenumber and characteristic size of the object (i.e., ka) in Sect. 3.4.3.

3.4.1 Target Strength (TS)

Active remote sensing systems rely on the reflection or scattering of a projected wave off the object of interest to produce an echo carrying the information needed to achieve the DCLT objective. The sonar equation exploits the simplest possible representation of the interaction between the incident sound wave and the object of interest through the *target strength* term, which was defined in Sect. 2.3.3 as the means to convert the sound pressure level of the incident wave to the source level of the resulting echo. The predominance of military applications of early radar and sonar research and development led to describing the object of interest as a “target” and terms such as *target strength* and *target impulse response*. As seen in Sect. 3.4.2, the target impulse response is a more general characterization than target strength of the relationship between a sound wave incident on an object of interest and the resulting echo. Both the frequency dependence of target strength and the target impulse response can be useful in the design and analysis of signal processing algorithms.

The target strength term in the sonar equation is defined as follows. Suppose the target is far enough from the sound projector that the acoustic wave incident on it is planar. Let the MSP of the incident wave ensonifying the target be P_o^{ens} at the position of the target, but in its absence. Now measure the MSP of the signal reflected and scattered from the target at a distance r from its acoustical center and

let that be $P_o^{\text{ref}}(r)$. Let the range r be large enough to be in the far-field of the re-radiation but close enough for spherical spreading in the basic ocean model. The target strength is then

$$\text{TS} = 10 \log_{10} \left[\frac{r^2 P_o^{\text{ref}}(r)}{P_o^{\text{ens}}} \right] = 10 \log_{10} \left[\frac{U_o^{\text{ref}}}{P_o^{\text{ens}}} \right] \text{ dB re m}^2 \quad (3.195)$$

where $U_o^{\text{ref}} = r^2 P_o^{\text{ref}}(r)$ is the source factor for the target re-radiation of the incident acoustic wave (i.e., the target source factor).

Although the sonar equation requires target strength as represented in decibels (TS), the focus in this section is on the linear equivalent called the *target gain*,

$$G_t = \frac{r^2 P_o^{\text{ref}}(r)}{P_o^{\text{ens}}} = \frac{U_o^{\text{ref}}}{P_o^{\text{ens}}} = 10^{\text{TS}/10}. \quad (3.196)$$

Target gain, which has units of squared distance (e.g., m²), is the fractional amount of the MSP from the incident wave (P_o^{ens}) contributed to the target source factor (U_o^{ref}).

As an example, consider a rigid and fixed sphere with radius a [units: m], for which the target gain at high frequencies is $G_t = a^2/4$ (see Sect. 3.4.3). Converting this to target strength results in

$$\text{TS} = 10 \log_{10} \left(\frac{a^2}{4} \right) \text{ dB re m}^2. \quad (3.197)$$

This appears to indicate TS > 0 dB re m² when $a > 2$ m, which might be misinterpreted as producing a reflected wave louder than the incident one. The correct interpretation of this can be obtained from TS in (3.195), which properly defines the target source factor and encourages retaining the dependence on the range at which the MSP of the echo is measured,

$$P_o^{\text{ref}}(r) = \frac{U_o^{\text{ref}}}{r^2} = \frac{G_t}{r^2} P_o^{\text{ens}}. \quad (3.198)$$

Using the target gain of a sphere in (3.198) results in

$$P_o^{\text{ref}}(r) = \frac{a^2}{4r^2} P_o^{\text{ens}} \quad (3.199)$$

which can only be evaluated for $r \geq a$ and so is always less than the MSP of the incident wave.

In general G_t depends on both the angles of ensonification and angles of reflection. For many remote sensing applications, the primary acoustical paths have small grazing angles and so it is common to assume the vertical angles are zero

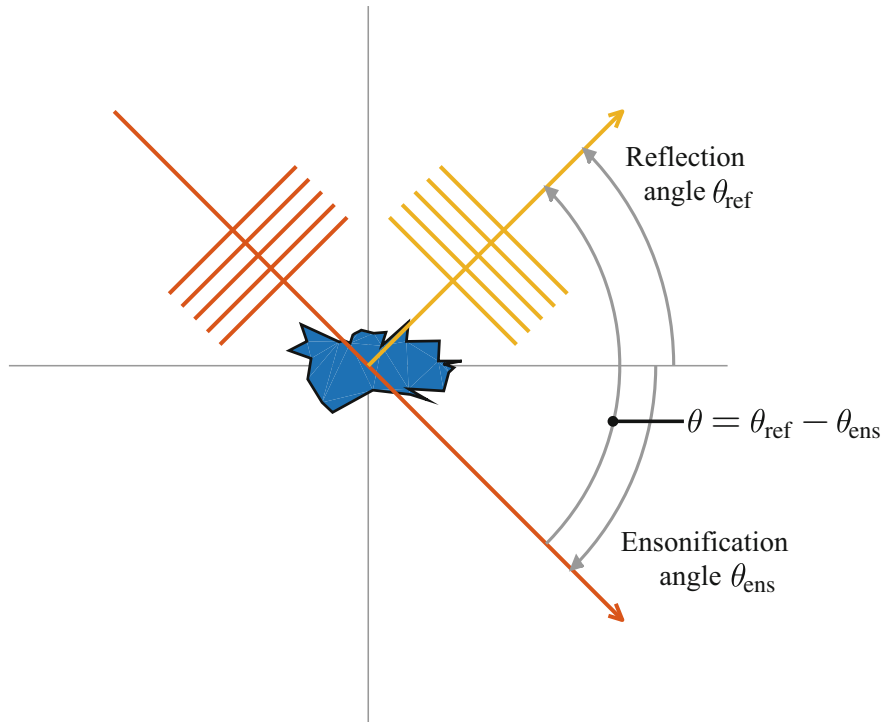


Fig. 3.20 Angles of ensonification and reflection for use in describing target strength

and focus on the azimuthal angles. In this section only the azimuthal angles are considered and when necessary TS, G_t , or other descriptors are described as a function of the azimuthal angle of ensonification θ_{ens} and the angle of the reflected or scattered wave θ_{ref} ; e.g., $G_t(\theta_{\text{ens}}, \theta_{\text{ref}})$. As seen in Fig. 3.20, the ensonification angle is the direction in which the ensonifying waves are propagating and the angle θ is defined as the difference between the reflection and ensonification angles,

$$\theta = \theta_{\text{ref}} - \theta_{\text{ens}}. \quad (3.200)$$

In a monostatic sensing system the reflection points back to the co-located source and receiver, so $\theta = \pi$ and the *backscattering* target strength or gain is obtained. In a bistatic system (described in Sect. 2.2.4 or Fig. 2.9), $\theta = \beta + \pi$ where β is the bistatic angle, which was defined as the difference between the angle pointing to the receiver (θ_{ref}) and the angle of incidence ($= \theta_{\text{ens}} + \pi$).

As a cautionary note, the aforementioned assumptions that the wavefront of the wave ensonifying the object of interest is planar or traveling horizontally will generally not be true, especially when the object of interest is near a boundary (e.g., shallow water or shallow targets in deep water) and ensonified from more than

one vertical direction. This is an inherent and difficult-to-avoid limitation of sonar-equation analysis where the effects of propagation and target scattering are treated independently. The more general formulation is described in [9, Sect. 11.4.2].

3.4.1.1 Relationship to Radar Cross Section

Target gain has an equivalent term in the radar equation called the *radar cross section* (RCS) [53, Ch. 5]. The description of RCS differs from target gain in a subtle manner. To illuminate the difference, consider Fuhs' [54] description of RCS (σ) by the equation

$$\frac{\sigma \mathcal{I}_o^{\text{ens}}}{4\pi} = r^2 \mathcal{I}_o^{\text{ref}}(r) \quad (3.201)$$

where $\mathcal{I}_o^{\text{ens}}$ is the intensity of the incident wave and $\mathcal{I}_o^{\text{ref}}(r)$ is the intensity of the reflected wave at range r (i.e., $\mathcal{I}_o^{\text{ens}} = P_o^{\text{ens}}/(\rho_w c_w)$ and similarly for $\mathcal{I}_o^{\text{ref}}(r)$). The quantity in the numerator on the left side of (3.201) is the power intercepted by the object of interest in units of W when the cross-section σ has units m². The left side of (3.201) is then the power in any direction as if the total intercepted power were scattered isotropically (i.e., equally over 4π steradians) with no loss. Combining the definition of σ from (3.201) with (3.196) shows that

$$G_t = \frac{\sigma}{4\pi}. \quad (3.202)$$

This relationship leads to describing $G_t = d\sigma/d\Omega$ as the *differential scattering cross section* [4, Sect. 9-1], [9, Sect. 2.2.3.1] where Ω is solid angle.

Similar to sonar, RCS depends on the frequency and size of the scattering object. For radar there is also a dependence on the polarization of the waves.¹² The utility of RCS to the sonar application primarily lies in the high-frequency, geometric scattering regime where polarization is not an issue and tables of RCS for various shapes apply to sonar through (3.202). Resources for radar or acoustical cross section include [4, 6, 9, 43, 53–58]. Not all definitions of cross section or differential cross section are consistent, so results should always be used with knowledge of the definition.

¹²Note that some radar texts (e.g., [53, Sect. 5.2]) differentiate RCS from *scattering cross section* by restricting RCS to the polarization the antenna can sense.

3.4.2 Target Impulse Response

The target impulse response characterizes the interaction of a pulse with an object of interest from the perspective of a linear time-invariant system (e.g., see Sect. 4.2). The input to the system is the plane-wave signal $p_i(t)$ incident at the acoustical center of the object and the output is $u_o(t)$, the disturbance of an equivalent point source representing re-radiation of the incident sound waves by the target. This can then be used in the forcing function of the inhomogeneous wave equation to determine the echo as measured at the receiver.

The target impulse response $h_o(t)$ relates the input and output through a convolution,

$$u_o(t) = h_o(t) * p_i(t) = \int_{-\infty}^{\infty} h_o(\tau) p_i(t - \tau) d\tau. \quad (3.203)$$

Recalling that $u_o(t)$ has units of pressure times distance, it can be seen that the units of $h_o(t)$ are distance per unit time (e.g., m/s). If the incident wave is a temporal impulse function, $p_i(t) = \delta(t)$, the output $u_o(t)$ is then precisely $h_o(t)$. In the frequency domain, the convolution in (3.203) becomes the product

$$U_o(f) = H_o(f) P_i(f) \quad (3.204)$$

where $H_o(f)$ is the Fourier transform of $h_o(t)$ and represents the frequency response of the target reflection or scattering.

As described in (3.196) and Sect. 2.3.3, target gain is the ratio of the target source factor to the MSP of the incident wave,

$$G_t = \frac{\frac{1}{T} \int_t^{t+T} u_o^2(t) dt}{\frac{1}{T} \int_t^{t+T} p_i^2(t) dt} \quad (3.205)$$

where t and T are chosen to include the full extent of the incident wave and echo in the integrals. Similar to the development of propagation loss in Sect. 3.2.4.2, target gain can be related to the target frequency response through Parseval's theorem (Sect. 4.3.2)

$$G_t = \frac{\int_{f_0}^{f_1} |H_o(f) P_i(f)|^2 df}{\int_{f_0}^{f_1} |P_i(f)|^2 df} \quad (3.206)$$

where the frequency content of the signal is restricted to the interval (f_0, f_1) . For narrowband signals with frequency content centered at f_c , target gain simplifies to

$$G_t = |H_o(f_c)|^2 = S_t(f_c) \quad (3.207)$$

where $S_t(f) = |H_o(f)|^2$ is the target spectral response. This scenario, for which target strength is

$$\text{TS} = 10 \log_{10} G_t = 10 \log_{10}\{S_t(f_c)\} \quad (3.208)$$

is the most common one encountered in sonar system analysis. For broadband signals the target gain in (3.206) can be shown to be at least the average spectral response

$$G_t \geq \frac{1}{(f_1 - f_0)} \int_{f_0}^{f_1} S_t(f) df \quad (3.209)$$

by using Chebyshev's integral inequality [21, 11.314]. The equality in (3.209) holds only if $|P_i(f)|$ in (3.206) is constant for $f \in (f_0, f_1)$, which will be approximately true for constant-envelope LFM pulses or HFM pulses with small bandwidth-to-center-frequency ratios.

The formation of target strength with G_t defined in (3.205) as a ratio of MSPs is called an *integrated target strength* [59, Sect. 42.7], [60, Sect. 4.2]. An alternative form represents the target gain by the change in peak squared disturbance to the peak squared pressure,

$$G_t^{\text{peak}} = \frac{\max_t u_o^2(t)}{\max_t p_i^2(t)^2}. \quad (3.210)$$

If the source waveform is an infinite duration sinusoid with frequency f_c , then $G_t^{\text{peak}} = G_t^{\text{int}} = S_t(f_c)$ where G_t^{int} refers to (3.205). The equality will also hold for pulsed sinusoids as long as $H_o(f)$ varies slowly near f_c over the bandwidth of the Fourier transform of the pulse amplitude weighting (nominally inversely proportional to pulse duration).

Exercise 3.14 Starting with $h_o(t)$ in units of m/s, show that G_t in (3.206) has units of m^2 .

3.4.2.1 Impulse Response of a Rigid Sphere

The impulse response for a rigid and fixed sphere can be found in [61] for a monostatic sensing scenario with the sphere a distance r from a co-located source and receiver in the basic ocean model. The scenario is depicted in Fig. 3.21. If the source emits a unit-area temporal impulse, the echo measured at the receiver using the physical optics method is

$$x_r(t) = \frac{a}{2r(r-a)} \delta(t - \tau_o) - \frac{1}{2rt} \text{rect}\left(\frac{t - \tau_o - \tau_a/2}{\tau_a}\right) \quad (3.211)$$

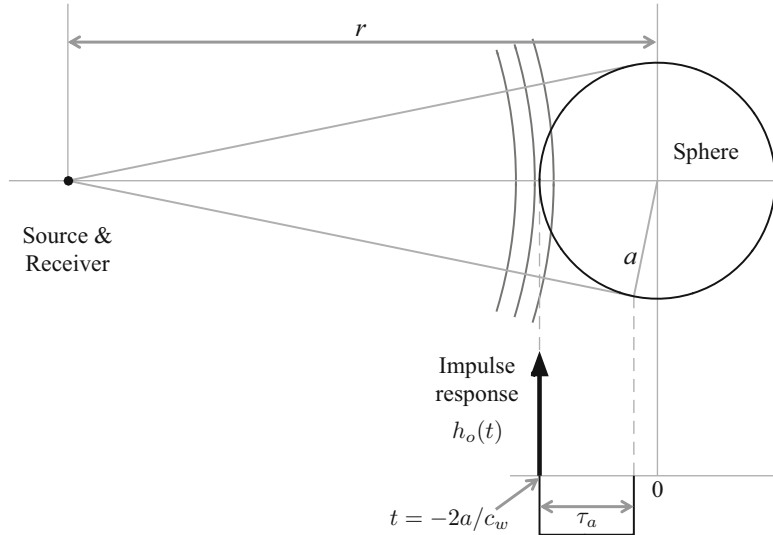


Fig. 3.21 Geometry for scattering from a sphere in [61] and the corresponding target impulse response from (3.213) for the geometric scattering (high ka) regime

where $\text{rect}(t)$ is the rectangular pulse function¹³ $\tau_o = 2(r - a)/c$ is the propagation delay to and from the closest point on the sphere (see Fig. 3.21), and

$$\tau_a = \frac{2}{c_w} \left[a - r \left(1 - \sqrt{1 - a^2/r^2} \right) \right] \quad (3.212)$$

is the temporal extent of the scattering, which is related to how much of the sphere is ensonified. The target impulse response can be obtained from (3.211) by multiplying by r^2 to account for two-way spherical spreading and shifting the time origin to the acoustical center of the sphere,

$$\begin{aligned} h_o(t) &= r^2 x_r(t + 2r/c_w) \\ &\approx \frac{a}{2(1 - a/r)} \delta(t + 2a/c_w) - \frac{c_w}{4(1 + tc_w/(2r))} \text{rect}\left(\frac{t + 2a/c_w - \tau_a/2}{\tau_a}\right) \\ &\approx \frac{a}{2} \delta(t + \Delta) - \frac{c_w}{4} \text{rect}\left(\frac{t + \Delta/2}{\Delta}\right). \end{aligned} \quad (3.213)$$

¹³The rectangular pulse function is one when the magnitude of the argument is less than 0.5 and zero otherwise; see Sect. 4.2.1.

The approximation in (3.213) arises when the range to the sphere is much larger than its radius, $r \gg a$, in which case $\tau_a \rightarrow \Delta = \frac{2a}{c_w}$ and the whole front half of the sphere is ensonified. The latter term in (3.213) clearly has units of distance per unit time. Although less obvious, the first term does too because the Dirac delta function can be approximated by a rectangular function with a small temporal width ε and height $1/\varepsilon$.

The physical optics method used in [61] to derive (3.211) is accurate at high frequencies (essentially high enough so the temporal extent of the response, τ_a , encompasses many cycles). It is a frequency-dependent extension of the geometric scattering to be described in Sect. 3.4.3. This example illustrates the characteristics of geometric scattering where the echo consists of an impulse arising at the front edge of the sphere followed by a spread response covering the extent of the sphere that is ensonified (i.e., the front half of the sphere as the back half is in the acoustical shadow and therefore not ensonified). In general, discontinuities in the surface of the object produce impulsive responses that will dominate the scattering. Resonances, which are not treated by the physical optics method, can extend the temporal extent of the impulse response beyond that accounted for by the size of the object.

Clearly one can take the Fourier transform of (3.213) to obtain the frequency response $H_o(f)$ as a function of frequency. However, as pointed out in [61] and [56, Ch. 2], the results will only be accurate for high frequencies (i.e., those corresponding to wavelengths that are small relative to the diameter of the sphere) because of the assumptions in the physical optics approach. The following section describes the dependence of scattering on frequency through wavenumber (k) and object size (a).

3.4.3 Scattering from Objects: The ka Dependence

An important concept in wave scattering from objects is how the dominant scattering physics change with the size of an object relative to the wavelength of the signal impinging on it. Suppose the nominal dimension of an object is a (e.g., the radius of a sphere) and the sensing wavelength is characterized by the wavenumber $k = 2\pi/\lambda$. The product $ka = 2\pi a/\lambda$ describes the object's size relative to the sensing wavelength and is commonly used to delineate the different regimes of scattering physics. When ka is small ($ka \ll 1$), the size of the object is small relative to the sensing wavelength and the scattering depends primarily on the object's volume irrespective of its shape. However, when the object is large relative to a wavelength ($ka \gg 1$), the reflected or scattered wave depends on the object's shape through the scattering cross-section. These two extremes are known as the Rayleigh scattering regime (small ka) and the geometric scattering regime (large ka). In between is a regime where at least one dimension of the object is on the order of a wavelength, potentially producing scattering components from resonance and diffraction.

As will be seen through the examples of this section, target gain has different characteristics for large and small ka . For rigid objects, target gain G_t is proportional

to f^4 when $ka \ll 1$. However, for $ka \gg 1$, G_t can (coarsely¹⁴) range from being constant with frequency to having an f^2 dependence. This implies a significant advantage to increasing the sensing frequency when in the Rayleigh scattering regime and less or no advantage to increasing frequency when $ka \gg 1$. Although many other factors must be considered when designing a sonar system, generally the frequency band will be chosen to be in the high ka regime for the size of the objects of interest. To provide some perspective, $ka = 1$ when $a = 24$ cm at 1 kHz with $c_w = 1500$ m/s. Thus scattering from objects larger than about a quarter meter will be outside of the Rayleigh regime when the sensing frequency is above 1 kHz.

The frequency dependence of target scattering enters the ka product through the wavenumber ($k = 2\pi f/c_w$). Exact derivations of the wave scattered from an object generally assume an infinite duration complex sinusoidal incident wave with a specific frequency f_c (i.e., $p_{\text{in}}(t) = e^{j2\pi f_c t}$), and derive the target frequency response $H_o(f_c)$ or spectral response $S_t(f_c)$. Because some derivations use $e^{-j2\pi f_c t}$ to define a sinusoidal signal rather than $e^{j2\pi f_c t}$, which results in a conjugation of the frequency response from that defined here, the focus of this section is on the spectral response, $S_t(f) = |H_o(f)|^2$. The low- and high- ka extremes are described, followed by the complete solutions for simple objects such as a sphere and cylinder. Consideration is mostly restricted to the rigid and fixed sphere or cylinder with references provided for other scenarios.

3.4.3.1 Rayleigh Scattering Regime ($ka \ll 1$)

As can be found in [62, Sect. 334] or [63, 64], a rigid object with volume V that is fixed in the water (i.e., does not move when subjected to acoustic pressure) with dimension much less than a wavelength ($ka \ll 1$) results in

$$S_t^R(f, \theta_{\text{ens}}, \theta_{\text{ref}}) = \left(\frac{V}{4\pi} \right)^2 k^4 \left[1 - \frac{3}{2} \cos \theta \right]^2 \quad (3.214)$$

where θ is the scattering angle relative to the ensonifying angle ($\theta = \theta_{\text{ref}} - \theta_{\text{ens}} = \pi$ represents back-scatter) and the superscript R is used to emphasize the result is only for the Rayleigh scattering regime. Noting that wavenumber is proportional to frequency, $S_t^R(f)$ has an f^4 dependence which clearly shows why high frequencies are more suitable for sensing small objects than low frequencies.

Consider as an example a rigid and fixed sphere in the backscattering direction ($\theta = \pi$), for which the target spectral response in the Rayleigh scattering regime is

$$S_t^R(f, \theta_{\text{ens}}, \theta_{\text{ens}} + \pi) = \frac{25}{36} a^2 (ka)^4. \quad (3.215)$$

¹⁴This description describes the general trend of G_t ; most objects will exhibit nulls and peaks with frequency.

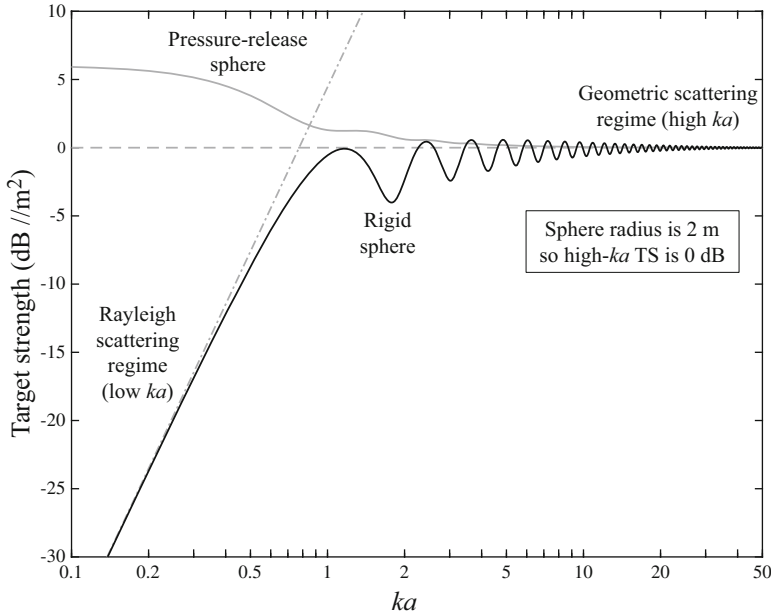


Fig. 3.22 Monostatic target strength of a rigid or pressure-release sphere via the modal solution in (3.224) and (3.225) as a function of ka where $k = 2\pi f/c_w$ and a is the radius of the sphere. The Rayleigh- and geometric-scattering results are also shown

The target strength arising from (3.215) via (3.208) (i.e., for a long sinusoidal pulse) is shown in Fig. 3.22 (dash-dot line) for a sphere with 2-m radius as a function of ka . The solid line is the modal solution (to be described later in this section) illustrating where the small- ka approximation in (3.214) begins to fail for the sphere (e.g., $ka > 0.5$). Because the scattered wave only depends on the object's volume, there is no aspect dependence (i.e., dependence on θ_{ens}). However, the shape will dictate how small ka must be for the approximation to be accurate.

As can be seen from the term in brackets in (3.214), the scattered wave has both a monopole and a dipole component [6, Sect. 7.5.2]. The net effect on the bistatic response is shown in Fig. 3.23 (dashed line) for $ka = 0.5$ and seen to have maximum response in the backscattering direction. Note that the plot in Fig. 3.23 is a normalization of (3.214) by $a^2/4$ so the high- ka backscattered target spectral response is one (0 dB).

3.4.3.2 Geometric Scattering Regime ($ka \gg 1$)

When the dimension of an object encompasses many wavelengths, scattering can be approximately described using a geometric approach where the interaction is characterized with rays. A ray incident on the object is treated as if it were reflecting

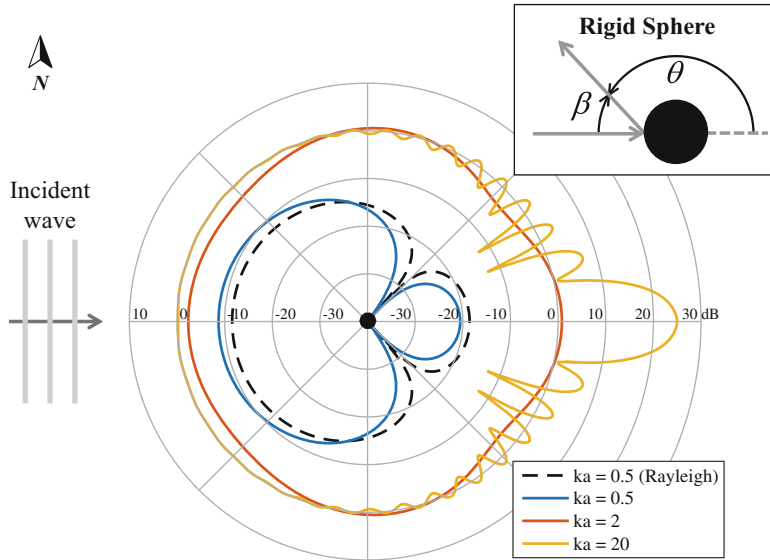


Fig. 3.23 Form function for a rigid sphere as a function of bistatic angle with $ka = 0.5, 2$, and 20 . The curves are shown in decibels (i.e., $20 \log_{10}|f(ka, \theta)|$) with each ring representing 10 dB and the center point absorbing all values below -40 dB. The incident wave arrives from the west, so backscattering is to the west and forward scattering to the east

off a plane tangent to the object's surface, leading to a specular reflection (i.e., angle of reflection equals angle of incidence). A particularly useful interpretation of the scattered wave in this regime can be obtained by describing it as the high-frequency limit of a physical-optics approach, which is wave based. Suppose an incident plane wave ensonifies an object (e.g., as depicted in Fig. 3.21 with a spherical wave) where x describes the range in the direction of propagation and the ensonified portion of the object occupies ranges x_0 to x_1 . If $A(x)$ is the cross-sectional area of the ensonified object as a function of range, then the portion of the object contributing to the scattering from range x can be described by the differential cross-section dA/dx . The target spectral response can then be described by (adapted from [43, Sect. 9.1] and [55, eq. 57])

$$S_t(f) = \frac{1}{\lambda^2} \left| \int_{x_0}^{x_1} \frac{dA}{dx} e^{j2k(x-x_0)} dx \right|^2 \quad (3.216)$$

The integral describes the scattered wave as a weighted combination of the reflection from the object over range. All the contributions at a particular range x combine coherently as they have the same relative phase, $2k(x - x_0) = 2\pi f[2(x - x_0)/c_w]$, which arises from the travel time $2(x - x_0)/c_w$ from range x_0 to x and then back to x_0 .

When ka is very large and the object is smooth, dA/dx changes slowly with respect to the complex exponential e^{j2kx} . For this scenario, consecutive half cycles of the sinusoid approximately cancel each other out leaving primarily the first and last half cycles. These represent the discontinuities at the front and back edges of the object of interest, illustrating how sharp changes (discontinuities in the cross-sectional area) dominate the scattering in the geometric regime. As described in [55, Sect. 6-3], the contribution from the last half-cycle is negligible either when the object has an irregular shape or is a closed surface. This leaves the contribution from the first half-cycle, where the incident wave first hits the object, as the dominant source of scattering in the geometric regime. Evaluating (3.216) is complicated for all but the simplest of objects. Fortunately, tables of target strength or radar cross section in this regime exist for many shapes (e.g., see [43, Table 9.1] or [57, Table 3.1]).

For a smooth, convex object with principal radii a_1 and a_2 at the closest point of the object to the sonar, the target spectral response is [55, Sect. 6.3], [58, Sect. 43-2.2]

$$S_t^g(f, \theta_{ens}, \theta_{ref}) = \frac{a_1 a_2}{4} \quad (3.217)$$

where the superscript g is used to emphasize the result is only for the high- ka , geometric scattering regime. For a rigid sphere with radius a , this becomes

$$S_t^g(f, \theta_{ens}, \theta_{ref}) = \frac{a^2}{4}, \quad (3.218)$$

which is shown in Fig. 3.22 as a dashed horizontal line. For the rigid sphere, the geometric-scattering approximation is reasonably accurate when $ka > 10$. It is interesting to note that there is no dependence in (3.218) on either wavelength λ or the scattering angle θ ; the latter of course assumes the receiver is not in the shadow created by the object. Because the geometric optics approach does not include diffraction, it is not necessarily accurate at useful values of ka for scattering angles $|\theta| < \pi/2$. This can be seen in Fig. 3.23 where the exact target spectral response of a rigid sphere is plotted for $ka = 20$ as a function of θ . The plot shows $S_t(f)$ with normalization by $a^2/4$ so the back-scattered target spectral response is one (0 dB) at high frequency. The geometric scattering regime result (0 dB for $|\theta| > \pi/2$) is quite accurate at $ka = 20$, even into the region of $|\theta| < \pi/2$, but fails at angles near forward scattering (i.e., θ near 0).

In the forward scattering direction ($\theta = 0$) of a smooth object, the physical optics approach [43, Sect. 9.6] leads to a target spectral response of

$$S_t^{po}(f) = \frac{A_p^2}{\lambda^2} \quad (3.219)$$

at high ka where A_p is the projected area of the object. For the sphere, this results in

$$S_t^{po}(f) = \left[\frac{a^2}{4} \right] (ka)^2 \quad (3.220)$$

which produces a normalized level of 26 dB for $ka = 20$, very close to the 25 dB seen in Fig. 3.23 for the exact solution.

The backscattering target spectral response of a rigid horizontal cylinder with radius a and length L in the geometric scattering regime has the form [43, Table 9.1]

$$S_t^g(f; \theta_{ens}, \theta_{ens} + \pi) = \frac{aL^2}{2\lambda} \left[\frac{\sin \beta_{cyl}}{\beta_{cyl}} \right]^2 \cos^2 \theta_{ens} \quad (3.221)$$

where the azimuthal angle of ensonification θ_{ens} is the angle from perpendicular to the cylinder axis and $\beta_{cyl} = kL \sin \theta_{ens}$. When the incident wave is perpendicular to the axis of the cylinder (i.e., broadside where $\theta_{ens} = 0$), $\beta_{cyl} = 0$ and the back-scattered target spectral response

$$S_t^g(f; 0, \pi) = \frac{aL^2}{2\lambda} \quad (3.222)$$

is at a maximum, as can be seen in Fig. 3.24. From (3.221) it can be seen the cylinder exhibits both a frequency dependence (through λ) and an aspect dependence. The aspect dependence is driven by β_{cyl} , which depends on the length of the cylinder in terms of wavelengths (i.e., through $kL = 2\pi L/\lambda$). When the cylinder is many wavelengths long, the angular response will be narrower than if it is only a few wavelengths long. This can be seen by noting the null-to-null width of the response about broadside is $\arcsin(\lambda/(2L)) \approx \lambda/(2L)$, which is inversely proportional to L/λ .

It is important to note that the function in (3.221) is only valid for some range of ensonification angles near broadside, which is obvious when noting (3.221) is zero when $\theta_{ens} = \pi/2$ even though the cylinder end-caps would produce a response. This is illustrated in Fig. 3.24 where the target strength for different end-cap shapes is shown in comparison to the target strength of the cylinder. An approximation to the target strength of a cylinder with a spherical end-cap (formed by adding their target gains) is shown in Fig. 3.25.

3.4.3.3 Exact Modal Solutions

As previously mentioned, scattering for objects between the Rayleigh and geometric regimes can be complicated by object resonances (e.g., producing Lamb waves) and diffraction (e.g., producing creeping waves). For simple shapes, scattering solutions

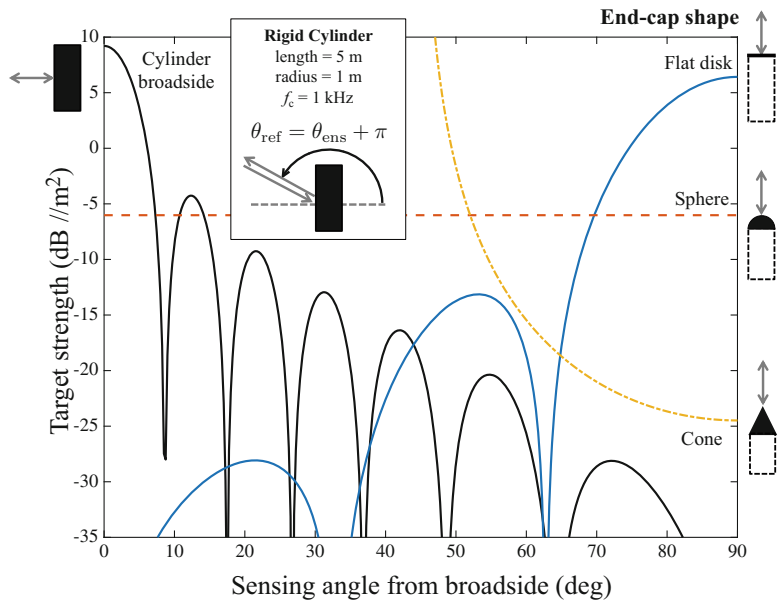


Fig. 3.24 Monostatic, geometric-regime target strength of a rigid cylinder with 1-m radius and 5-m length at $f_c = 1 \text{ kHz}$ as a function of sensing angle from broadside. Because (3.221) is only valid near broadside, TS for various end-cap shapes is also shown

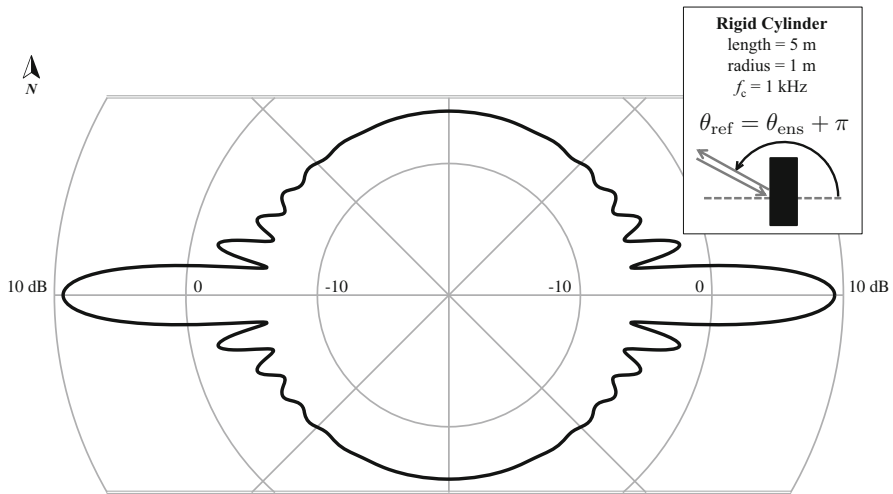


Fig. 3.25 Polar plot of the combined geometric-regime target strength of a cylinder with a spherical end-cap as approximated by adding the target gains

are formulated by decomposing the incident plane wave, and therefore the scattered wave, into a sum over modes [63, 65]. The ka -dependence of the scattering for a specific shape is isolated into a unitless ratio, $f(ka)$, called the *form function*. The form function describes the far-field response to a sinusoidal input normalized in such a manner that the high ka response for a rigid object is one; that is,

$$S_t(f) = S_t^g(f)|f(ka)|^2, \quad (3.223)$$

where it is assumed the geometric-regime response is formulated for a rigid object. For a long-duration sinusoidal signal, the target strength is then the TS from the geometric scattering regime plus the decibel equivalent of the form function

$$\text{TS} = 10 \log_{10} \{S_t^g(f)\} + 20 \log_{10}|f(ka)|. \quad (3.224)$$

From [59, 63, 65, 66] the form function for a sphere is

$$f(ka) = \frac{2}{ka} \sum_{n=0}^{\infty} (2n+1) P_n(\cos \theta) \sin(\eta_n) e^{j\eta_n} \quad (3.225)$$

where $P_n(x)$ is the n th-degree Legendre polynomial [67, Ch. 21] and η_n is the phase shift of the n th mode. For backscattering where $\theta = \pi$, the Legendre polynomial simplifies to $P_n(-1) = (-1)^n$. From [59, eq. 3], the combined $\sin(\eta_n)e^{j\eta_n}$ term for the sphere has the form

$$\sin(\eta_n)e^{j\eta_n} = \frac{j_n(ka)L_n - (ka)j'_n(ka)}{h_n^{(2)}(ka)L_n - (ka)h_n^{(2)'}(ka)} \quad (3.226)$$

where L_n depends on the sphere's characteristics, $j_n(x)$ is an n th-order spherical Bessel function of the first kind and $j'_n(x)$ its derivative, $h_n^{(2)}(x)$ is an n th-order spherical Hankel function of the second kind and $h_n^{(2)'}(x)$ its derivative. When the sphere is rigid $L_n = 0$ and when it has a pressure-release surface $L_n \rightarrow \infty$. As shown in Fig. 3.22, TS using the modal solution (solid lines) via (3.224)–(3.226) appropriately tends to the geometric-scattering solution at high ka and, for the rigid sphere, the Rayleigh-scattering solution at low ka . The region between exhibits an oscillatory behavior where different scattering components partially interfere with or complement each other [6, Ch. 7]. TS for a pressure-release sphere is also shown in Fig. 3.22. Although it has the same high- ka TS it differs significantly at low ka , exhibiting an increase in TS as opposed to the k^4 dependence of Rayleigh scattering.

The form function for an infinite length cylinder with radius a as found in [59, 63, 68] is

$$f(ka) = \frac{2}{\sqrt{\pi ka}} \sum_{n=0}^{\infty} \varepsilon_n \cos(n\theta) \sin(\eta_n) e^{j\eta_n} \quad (3.227)$$

where ε_n is the Neumann factor with $\varepsilon_0 = 1$ and $\varepsilon_n = 2$ for $n \geq 1$. The weighting of the n th mode for the cylinder is

$$\sin(\eta_n) e^{j\eta_n} = \frac{J_n(ka)L_n - (ka)J'_n(ka)}{H_n^{(2)}(ka)L_n - (ka)H_n^{(2)\prime}(ka)} \quad (3.228)$$

where $J_n(x)$ and $H_n^{(2)}(x)$ are, respectively, the Bessel function of the first kind and the Hankel function of the second kind, both of order n . Similar to the sphere, the extreme case of a rigid cylinder results in $L_n = 0$ and $L_n \rightarrow \infty$ for a pressure-release cylinder.

As noted in [59, Sect. 42.7], TS for a finite-length cylinder can be approximated via (3.224) by using the finite-length cylinder's geometric-regime response (e.g., from (3.221)) with the form function of the infinite-length cylinder from (3.227) and (3.228). The resulting TS for normal incidence ($\theta_{\text{ens}} = 0$) is shown in Fig. 3.26 for back and forward scattering as a function of frequency when $a = 1$ m and $L = 5$ m. The oscillations from interfering scattering components is coupled with the frequency dependence of the geometric scattering result for the backscattering. Forward scattering at high ka exhibits the f^2 dependence predicted by the physical optics result of (3.219).

Form functions for solid spheres and infinite-length cylinders composed of various materials are depicted in [59, 68]. They exhibit more complicated resonances than the rigid-shape form function. The modal solution can be decomposed into terms related to the rigid object shape plus resonance terms [66], which can be important for object classification [59] in remote sensing. The focus of this section has been on solid spheres and cylinders [63]; however, results for elastic spherical shells [64] and elastic cylindrical shells [69] are readily accessible.

3.5 Reverberation

One of the fundamental hindrances in active remote sensing lies in discerning the echo generated by the object of interest from echoes generated by other sources. These latter echoes represent signal-dependent interferences to the DCLT objectives and, in the sonar context, are collectively termed *reverberation*. Several sources of reverberation are described in Sect. 3.5.1 and the reverberation level (RL) term in the sonar equation is characterized for volume and boundary reverberation in

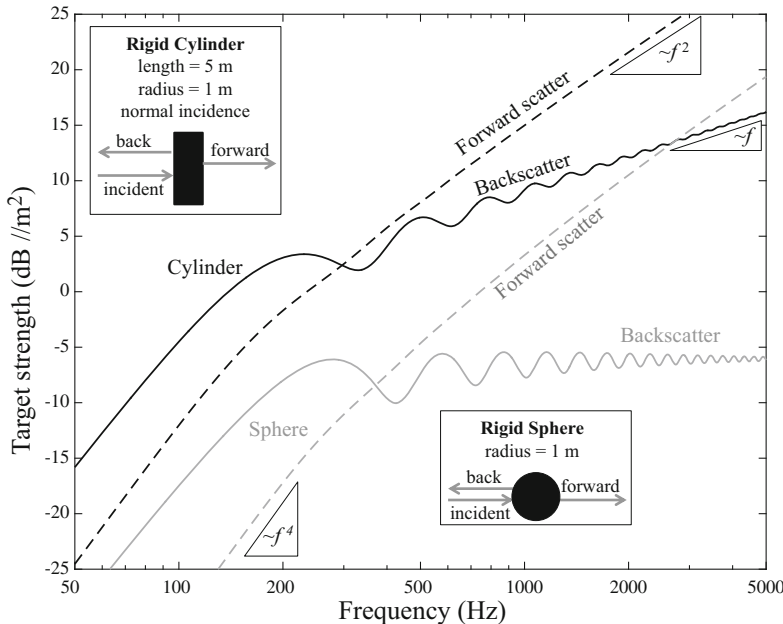


Fig. 3.26 Target strength of a rigid sphere and cylinder (normal incidence) as a function of frequency for back and forward scattering

Sects. 3.5.2 and 3.5.3. RL is then used to describe the signal to reverberation power ratio in Sect. 3.5.4, which drives sonar performance when reverberation dominates ambient noise. A basic characterization of the statistical and spectral properties of reverberation is presented in Sects. 3.5.5 and 3.5.6. Finally, the effect of a moving sonar platform on the spectrum of reverberation coming from different directions is described in Sect. 3.5.7 along with the ownship-Doppler-nullification (ODN) processing technique used to map the different reverberation spectra back to that for a stationary scenario. Several reverberation-focused topics are covered later in Part III. More general statistical models, in terms of probability density functions, random processes, reverberation frequency spectra and their spreading, are presented in Sect. 7.4.2. The impact of reverberation on the performance of a Doppler filter bank is discussed in Sect. 8.7.2 and how a normalizer provides constant-false-alarm-rate detection when there is a time-varying reverberation level is presented in Sect. 8.6.

Except where noted otherwise, the development of this section assumes both an omni-directional projector and an omni-directional sensor. The effect of array processing through the array gain (AG) term in the sonar equation is assumed to capture the improvement in SNR obtained by spatial filtering for reverberation as well as ambient noise.

3.5.1 Sources of Reverberation

As described by Ol'shevskii [70, Sect. 1.2], reverberation arises when the transmitted waveform is “*partially scattered by various inhomogeneities of the medium and irregularities of the boundary.*” Inhomogeneities in the ocean environment include obvious ones such as fish and air bubbles, but also changes in sound speed or density or changes in the ocean bottom such as rock outcrops and patches of shells or sea grasses. Boundary irregularities in the form of varying ocean surface or bottom heights are typically described as rough surfaces that produce reverberation as well as affect the forward reflection of an acoustic wave (e.g., see rough-surface reflection in Sect. 3.2.7).

These sources of reverberation can be described generically as arising either from the ocean volume or the ocean boundaries. In both cases, the reverberation level (RL) measured at a sensor represents an accumulation of scattering from a multitude of elemental scattering sources (e.g., individual fish, air bubbles, or portions of a randomly rough surface oriented to scatter sound to the sensor). Scattering from an elemental source is characterized by a target impulse or frequency response as described in Sect. 3.4. Under some basic assumptions, the elemental scattering sources combine independently so RL can be characterized solely by the volumetric or areal density of scatterers and the total contributing volume or boundary area. The portion of the environment contributing to reverberation changes over time as the transmitted pulse propagates farther from the source. The larger volume/area encountered as the pulse propagates implies an increasing number of scatterers contributing to reverberation. However, the losses from propagation generally lead to RL decreasing with time. An obvious exception arises for surface reverberation in a convergence zone (CZ) where propagation limits ensonification of the elemental scatterers until the CZ is encountered.

3.5.2 Volume Reverberation

To determine RL for volume reverberation, suppose a source waveform $u_o(t)$ with duration T_p is projected by a monostatic sonar system with an omni-directional source in the basic ocean model. Let an elemental reverberation scattering source be in the ocean volume at range r_i and be small enough relative to the sensing wavelength to have a backscattering target impulse response $h_t(t) \approx A_i \delta(t)$ with respect to the source waveform.¹⁵ The pressure measured at the receiver (co-located with the source) is found by convolving the transmitted pulse with both the target impulse response and the two-way channel impulse response from (3.180) to produce

¹⁵This essentially requires a flat target spectral response over the frequency band of the source waveform.

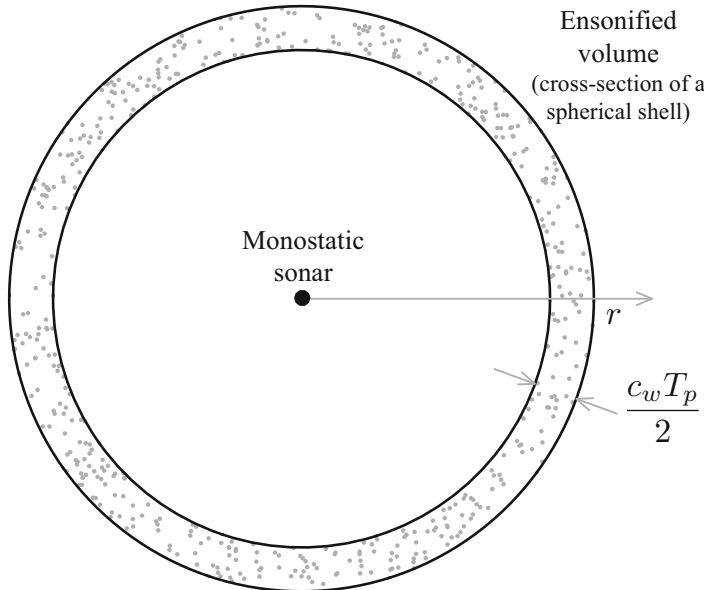


Fig. 3.27 Reverberation ensonified volume (cross-section of a spherical shell) in the basic ocean model

$$p_i(t) = \frac{A_i}{r_i^2} u_o \left(t - \frac{2r_i}{c_w} \right) \quad (3.229)$$

By noting $u_o(t)$ is only non-zero for $t \in [0, T_p]$, it can be seen that only scatterers from range $r - c_w T_p / 2$ to range $r = c_w t / 2$ will contribute to the signal measured at time t . The *ensonified volume* is therefore described by a spherical shell with outside radius r and thickness $c_w T_p / 2$ as depicted (via a cross-section) in Fig. 3.27.

If there are n elemental scatterers within the ensonified volume, the total reverberation measurement is

$$r(t) = \sum_{i=1}^n \frac{A_i}{r_i^2} u_o \left(t - \frac{2r_i}{c_w} \right). \quad (3.230)$$

To obtain the MSP of the reverberation measured at the sensor, a few assumptions about the geometry and the statistical nature of the elemental scatterers are necessary. First, the elemental scatterers are assumed to be randomly placed in the ensonified volume and independent of each other. This implies r_i is a uniform random variable on the interval $[r - c_w T_p / 2, r]$ which means $\tau_i = 2(r - r_i)/c_w$ is also a uniform random variable but on the interval $[0, T_p]$. The random time delays in (3.230) are most easily handled in the frequency domain. When the range is large

relative to the extent of the ensonified area, $r \approx r_i$ and the Fourier transform of $r(t)$ is approximately

$$R(f) \approx \frac{1}{r^2} U_o(f) e^{-j4\pi f r/c_w} \sum_{i=1}^n A_i e^{j2\pi f \tau_i} \quad (3.231)$$

where $U_o(f)$ is the Fourier transform of $u_o(t)$. Now by Parseval's theorem (see (4.50) in Sect. 4.3.2), the reverberation MSP (P_r) can be defined by using the Fourier transform of the reverberation measurement

$$P_r = \frac{1}{T} \int_{t-T/2}^{t+T/2} r^2(t) dt = \frac{1}{T} \int_{-\infty}^{\infty} |R(f)|^2 df \quad (3.232)$$

where T is taken large enough to encompass the echoes from all scattering elements contributing at time t (i.e., $r(t)$ is assumed to be zero outside of the integral). Because $R(f)$ contains random time delays (τ_i), it is also random and an expectation must be applied to (3.232) to obtain an average MSP. By restricting consideration to frequencies such that $f T_p \gg 1$ (which is not a significant restriction for most sonar systems), it can be shown that

$$E \left[\left| \sum_{i=1}^n A_i e^{j2\pi f \tau_i} \right|^2 \right] \approx \sum_{i=1}^n E[A_i^2] \quad (3.233)$$

where the amplitude gain of the scattered signal (A_i) has also been assumed random. If the scatterer amplitude gains (A_i) are identically distributed in a statistical sense (i.e., they have a common probability density function), then (3.233) is nG_r , where $G_r = E[A_i^2]$ is the change in power induced by an elemental scatterer. Combining (3.231)–(3.233) produces the average reverberation MSP at the sensor,

$$P_r = \frac{U_o G_r \beta_v V}{r^4} \quad (3.234)$$

where U_o is the source factor and β_v is the density of elemental scatterers in the volume V (i.e., $n = \beta_v V$). Converting (3.234) to decibels results in the volume-reverberation level,

$$\text{RL} = \text{SL} - 2\text{PL} + \mathcal{S}_v + 10 \log_{10} V, \quad (3.235)$$

where $\text{PL} = 20 \log_{10}(r)$ dB for spherical spreading and $\mathcal{S}_v = 10 \log_{10}(G_r \beta_v)$ dB is the volume scattering strength. Because the scattering strength represents a power

ratio, the units are decibels.¹⁶ When the range extent of the ensonified volume ($\delta_r = c_w T_p / 2$) is small relative to range, the ensonified volume V in the basic ocean model is approximately

$$V \approx 4\pi \delta_r r^2. \quad (3.236)$$

Using (3.236) in (3.235), it can be seen that RL for volume reverberation decays with range by $20 \log_{10} r$ (i.e., a 6-dB reduction per doubling of range).

This analysis assumes the scattering sources are uniformly distributed in the ocean volume. However, the predominant source of volume reverberation is from fish and other biota, particularly in what is termed the deep scattering layer [43, Sect. 8.10]. Thus, S_v will vary with range (i.e., time delay) as the projected pulse propagates down to the layer and back. It also varies as a function of the time of day as the fish move shallower at night. At shallower depths the size of fish swim bladders increases, which has the effect of reducing the resonant frequency [43, Sect. 8.10] as can be seen in Fig. 3.28. The figure contains the target strength of a single 30-cm-long fish with a swim bladder as a function of frequency at

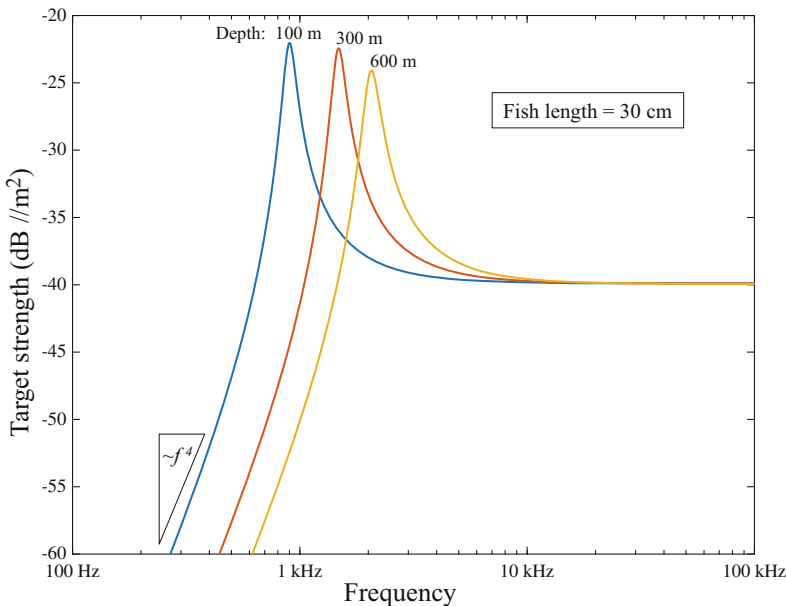


Fig. 3.28 Example target strength of a single fish (length 30 cm) with a swim bladder at different depths as a function of frequency. The contribution from the fish flesh at high frequencies is not included

¹⁶As described in [52, Sec. 2.3.2], scattering strength does not have units of dB relative to a unit volume or area.

three different depths (100, 300, and 600 m). The curves are generated using the approximations described in [9, Sect. 5.4.3.6] and do not include the effect of scattering from the flesh of the fish that might be apparent as a minor increase at high frequencies. Swim-bladder size (specifically, the radius of a sphere with an equivalent surface area to the bladder) is assumed proportional to fish length. In addition to the depth-dependence of the resonant frequency, the curves also illustrate the relatively flat response above the resonant frequency and an f^4 dependence of fish TS for frequencies below resonance. These correspond, respectively, to the geometric and Rayleigh scattering regimes described in Sect. 3.4.3.

The TS of a fish, which corresponds to $10 \log_{10} G_r$ dB, is only part of the volume scattering strength S_v . The density of scatterers dictates how much the fish population impacts the sensing through the volume scattering strength. From [32, Sect. 3.4.2.3], fish density can be approximated (roughly) by one over the length (L) cubed, $\beta_v \approx 1/L^3$, which would result in $S_v \approx -24$ dB for the 30-cm fish for frequencies well above resonance. S_v will be larger near resonance, but different sizes of fish within the ensonified volume will spread the resonance peak in frequency. As noted in [43, Sect. 8.10] and [32, Sect. 3.4.2.4], above about 20 kHz, volume reverberation in the deep scattering layer arises from very small biota (e.g., zooplankton) and produces volume scattering strengths in the range of -70 to -80 dB.

This simplified description of volume scattering from ocean biota excludes many effects, including dependence on type, orientation, shape, shoaling, and multiple scattering. The interested reader is referred to [6, 9, 32] for detailed treatments.

3.5.3 Boundary Reverberation

In many situations reverberation from the ocean surface or bottom will dominate that from the volume. This is particularly true for downward-refracting sound-speed profiles or in shallow water where remote sensing at large ranges almost guarantees the sound waves interact with the boundaries. How boundary reverberation differs from volume reverberation can be understood by envisioning the spherical-shell shaped ensonified volume (e.g., from Fig. 3.27) intersecting a planar boundary to form an ensonified annulus on the boundary. A cross-section of such an interaction is shown in Fig. 3.29 for a rough boundary.

A simple approximation to RL for boundary reverberation can be obtained in a similar manner to that developed for volume reverberation in Sect. 3.5.2. Assuming that the acoustic waves incident on the boundary arrive at a single angle, the “volume” and “volume scattering strength” in (3.235) can be replaced with an area (A) and an areal scattering strength (S_a),

$$\text{RL} = \text{SL} - 2\text{PL} + S_a + 10 \log_{10} A. \quad (3.237)$$

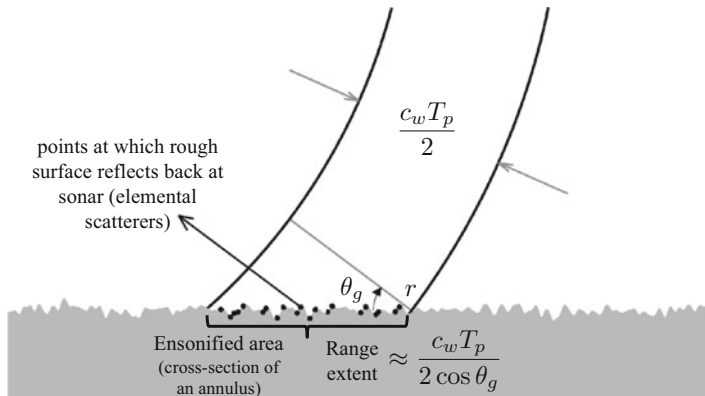


Fig. 3.29 Reverberation ensonified area (cross-section in range of an annulus) in the basic ocean model

For a monostatic sonar system, S_a is called the “back” scattering strength (i.e., representing the scattering back toward the co-located source and receiver). For a bi-static sonar system, it necessarily represents the scattering toward the sensor.¹⁷ The backscattering strength for the ocean surface is commonly referred to as S_s whereas that from the bottom is termed S_b .

If the grazing angle of the incident wave is θ_g , the ensonified area is approximately

$$A \approx 2\pi r \delta_r \quad (3.238)$$

where the down-range extent of the annulus,

$$\delta_r \approx \frac{c_w T_p}{2 \cos \theta_g}, \quad (3.239)$$

is assumed to be small relative to the range (i.e., $r \gg \delta_r$). The approximation to δ_r , which assumes the spherical wave is planar (locally) where it intersects the boundary, will be accurate when range is large. The down-range extent of the annulus decreases with the grazing angle to a minimum of $c_w T_p / 2$ when $\theta_g \rightarrow 0^\circ$. Using (3.238) in (3.237) with PL from spherical spreading (indicative of a single interaction with the boundary) implies RL for boundary reverberation decays with range according to $30 \log_{10} r$ (i.e., a 9-dB reduction per doubling of range). In a shallow-water mode-stripping region where $PL = 15 \log_{10} r$ dB, the reverberation decay would follow $20 \log_{10} r$, although this assumes S_a is constant with range (i.e., grazing angle) when it is not.

¹⁷This distinction was not made for volume reverberation, although it is relevant.

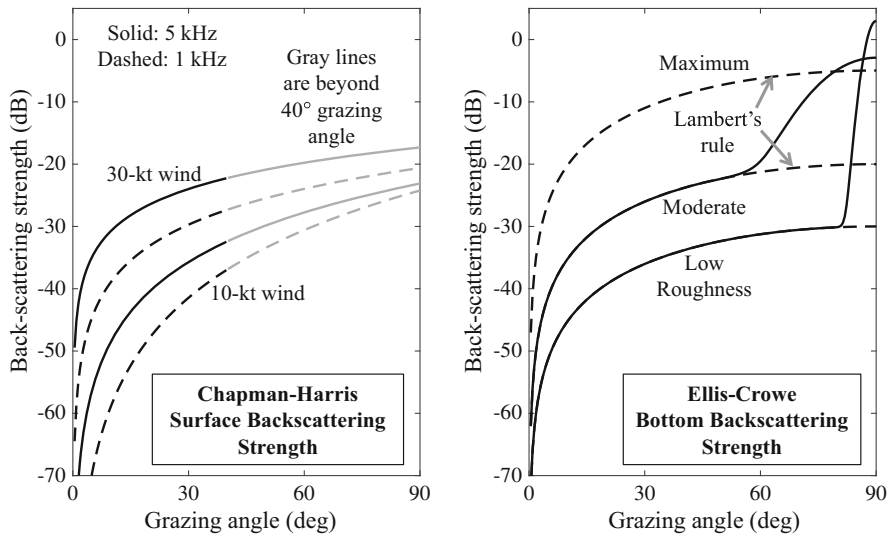


Fig. 3.30 Backscattering strength examples for the ocean surface (Chapman-Harris) and bottom (Ellis-Crowe). The former are based on data below a 40° grazing angle

In Fig. 3.29, the portions of the rough boundary within the ensonified area that reflect sound back toward a co-located source and receiver are designated by the black dots and may be thought of as elemental scatterers. The areal backscattering strength can be described as a density times a per scatterer contribution, as was done for volume reverberation, although the actual derivations are more complicated. The areal backscattering strength clearly depends on grazing angle and the acoustical properties of the material on the other side of the boundary (i.e., air or the ocean bottom). It also depends on the spatial characteristics of the ocean surface or bottom and frequency. For example, at some frequencies the dominant source of surface reverberation could be bubbles generated by surface waves whereas at other frequencies the dominant mechanism might be the rough ocean surface itself. Empirical formulae for surface backscattering strength (S_s) illuminate the dependencies on wind-speed, grazing angle, and frequency. Examples using the results of Chapman and Harris [71] are shown in Fig. 3.30 (left side) for 10- and 30-kn wind speeds and 1- and 5-kHz frequencies. S_s increases with both frequency and wind speed. The Chapman-Harris formula was described in the example of Sect. 2.3.3, specifically in (2.69). Note that the Chapman-Harris model was derived from measurements with less than a 40° grazing angle so the region in the figure beyond 40° are gray lines. Empirical models for higher and lower frequencies can be found in [9, Sect. 8.1.2].

The most common model for bottom backscattering strength (S_b) at low grazing angles is Lambert's rule,

$$\mathcal{S}_b = 10 \log_{10} \mu + 10 \log_{10} \left\{ \sin^2 \theta_g \right\} \quad (3.240)$$

where μ (called the Lambert parameter [72]) encapsulates the bulk loss of the scattering from the surface and the latter term in (3.240) accounts for the change with grazing angle. For surfaces with low roughness μ will be small; however, from [43, Sect. 8.13] it has a maximum value of $1/\pi$ for diffuse scattering. The maximum arises from a conservation of energy argument requiring the total reflected and scattered power to be no more than the incident power [52, Sect. 2.3.2]. The maximum along with examples of a low and moderately rough bottom are shown in Fig. 3.30 (right side, dashed lines). At high grazing angles, facet scattering dominates [72], [32, Sect. 3.5.3.3], [9, Sect. 8.1] and can be included in \mathcal{S}_b as seen in the Ellis-Crowe [72] model examples in Fig. 3.30 (right side, solid lines).

From the backscattering strength examples shown in Fig. 3.30, there is a wide range of values and scenarios where surface reverberation will dominate bottom reverberation or vice versa. The simple description of boundary reverberation presented in this section excludes the majority of the theoretical and empirical models for \mathcal{S}_a to present an introduction to the concept along with a few simple formulae to use in examples. Detailed descriptions of the theory and measurements related to boundary reverberation can be found in [9, 32, 43, 52].

3.5.4 Signal to Reverberation Ratio

The form of the RL equations in (3.235) and (3.237) is very similar to that describing the MSP level of the echo from the object of interest at a receiver in a monostatic sonar ($= \text{SL} - 2\text{PL} + \text{TS}$). The collective effect of the elemental volume or boundary scatterers on the MSP level can in fact be described as a *reverberation target strength* (TS_r) [60, Sect. 6.6]. For example, in (3.237) the boundary reverberation target strength is simply

$$\text{TS}_r = \mathcal{S}_a + 10 \log_{10} A \quad \text{dB re m}^2. \quad (3.241)$$

Note that this approximation carries with it the assumptions and simplifications made for (3.237), which include requiring the acoustic waves incident on the boundary to arrive at a single angle. In reverberation-limited conditions, the SNR at a hydrophone is the signal-to-reverberation ratio (SRR), which simplifies to

$$\text{SRR}^h = \text{TS} - \text{TS}_r, \quad (3.242)$$

when it is assumed that PL is the same for propagation to the object of interest and the reverberation sources at that range. This result implies that as long as the sonar system is reverberation limited, SRR will decay with range according to $20 \log_{10} r$ (i.e., a 6-dB reduction for every doubling of range) in volume

reverberation and $10 \log_{10} r$ (i.e., a 3-dB reduction for every doubling of range) for boundary reverberation. The boundary-reverberation result assumes S_a is constant even though it will decrease with range as grazing angles become shallower and generally ignores the effects of propagation in a waveguide. Zhou [73] and Harrison [74] show much more precisely that for boundary scattering following Lambert's rule, both the echo level and RL decay at a $30 \log_{10} r$ rate at large ranges relative to water depth so SRR becomes constant.

3.5.5 Statistical Characterization of Reverberation

Recall the characterization of reverberation as a sum of elemental scatterers randomly placed in the ensonified volume from (3.230),

$$r(t) = \sum_{i=1}^n \frac{A_i}{r_i^2} u_o\left(t - \frac{2r_i}{c_w}\right). \quad (3.243)$$

Taken as a time series, $r(t)$ is in the parlance of mathematical statistics a random process (Sect. 5.4), which is essentially a time-varying random variable. While this characterization of reverberation will be elaborated upon in Sect. 7.4.2.1, in this section the focus is on the reverberation at a particular time t for which $r(t)$ is a random variable (Sect. 5.3). A random variable is defined by its probability density function (PDF), which is important because the design of detection algorithms and their false-alarm performance depend on it.

Suppose that the range r corresponding to the time of interest t ($r = c_w t / 2$) is large relative to the down-range extent of the ensonified volume (i.e., $r \gg c_w T_p / 2$). For this scenario, the value of r_i in the denominator of (3.243) is approximately r and

$$R = r(t) \approx \frac{1}{r^2} \sum_{i=1}^n A_i u_o(\tau_i) \quad (3.244)$$

where the random variable representing reverberation at time t is R and $\tau_i = t - 2r_i/c_w$ is a uniform random variable on $(0, T_p)$.

When reverberation in (3.244) is the sum over many independent and identically distributed elemental scatterers, the central limit theorem (CLT; see Sect. 5.3.7) implies R is approximately Gaussian distributed. The Gaussian distribution (Sect. 5.6.6) is characterized by its mean and variance. Because the elemental scatterers are assumed to be independent and identically distributed, the mean and variance of the sum in (3.244) are simply n times the mean and variance (respectively) of one scatterer. The average value of $u_o(\tau_i)$ is the average of the source waveform,

$$E[u_o(\tau_i)] = \frac{1}{T_p} \int_0^{T_p} u_o(t) dt = 0, \quad (3.245)$$

which will generally be zero so R is also zero mean (i.e., $E[R] = 0$). Because R is zero mean, its variance is the same as its statistical power ($\text{Var}\{R\} = E[R^2]$) and has the form

$$\begin{aligned} \text{Var}\{R\} &= \frac{n}{r^4} E[A_i^2] \frac{1}{T_p} \int_0^{T_p} u_o^2(t) dt \\ &= \frac{U_o G_r n}{r^4} \end{aligned} \quad (3.246)$$

where $G_r = E[A_i^2]$ and U_o is the source factor. Noting that $n = \beta_v V$, it can be seen that the average reverberation MSP from (3.234) is also the variance of the reverberation at a given time. This result is not surprising as the MSP is in reality a surrogate for the reverberation power ($E[R^2]$) and the development in Sect. 3.5.2 only included the elemental scatterers contributing to reverberation at time t as opposed to those contributing at any time throughout the course of the integral in (3.232).

3.5.6 Spectral Properties of Reverberation

Spectral analysis of a temporal signal provides insight into its frequency-domain characteristics. Because reverberation arises from the scattering of sound projected into a linear system, its spectral content is expected to be driven by that of the transmitted signal. The characterization in the previous section of the reverberation time series as a random process implies that the power spectral density (PSD) should be used to represent its frequency content. However, as described in Sect. 5.4.2, this requires the random process to be wide-sense stationary (WSS) and because of the time-varying RL, $r(t)$ is not WSS. As shown in Sect. 7.4.2.1, scaling $r(t)$ can produce a WSS random process for which an autocorrelation function and PSD can be constructed.

In this section, a simplified characterization of the spectral content of reverberation is evaluated from the Fourier transform of the reverberation arising from scatterers contributing at time t (i.e., $R(f)$ in (3.231)). Using the results of Sect. 3.5.2, the average squared modulus of the Fourier transform of $r(t)$ is seen to be

$$E[|R(f)|^2] = \frac{nG_r}{r^4} |U_o(f)|^2 = \frac{nG_r}{r^4} S_o(f) \quad (3.247)$$

which is simply a scale of the spectrum of the source waveform, $S_o(f) = |U_o(f)|^2$, confirming the aforementioned intuitive relationship.

When evaluating the spectrum of band-limited source waveforms, it is often more convenient to work with the *analytic* form of the signal rather than the real-valued source waveform. The analytic signal (see Sect. 7.3.1) is formed by discarding the (redundant) negative frequency components of a real-valued signal, resulting in a complex signal with only positive frequency components. A real-valued band-limited signal can be represented by

$$u(t) = a(t) \cos(2\pi f_c t + \theta(t)) = \frac{1}{2} [\dot{u}(t) + \dot{u}^*(t)] \quad (3.248)$$

where $a(t)$ is the amplitude modulation, $\theta(t)$ is the phase, and

$$\dot{u}(t) = a(t)e^{j2\pi f_c t + j\theta(t)} \quad (3.249)$$

is the analytic signal of $u(t)$. The Fourier transform of $u(t)$ can then be found in terms of the Fourier transform of the analytic signal, $U(f) = [\dot{U}(f) + \dot{U}^*(-f)]/2$. The spectrum is formed similarly,

$$S_u(f) = |U(f)|^2 = \frac{1}{4} [S_{\dot{u}}(f) + S_{\dot{u}}(-f)] \quad (3.250)$$

where $S_{\dot{u}}(f) = |\dot{U}(f)|^2$. For example, consider a CW pulse with frequency f_c , duration T_p , and amplitude A : $u_o(t) = A \cos(2\pi f_c t)$ for $t \in (0, T_p)$ and is zero elsewhere. The analytic signal of the transmit pulse is the complex sinusoid $\dot{u}(t) = Ae^{j2\pi f_c t}$ for $t \in (0, T_p)$ and its spectrum is a sinc function ($\text{sinc}(x) = \sin(\pi x)/(\pi x)$) centered about the transmit frequency,

$$S_{\dot{u}}(f) = A^2 T_p^2 \text{sinc}^2(T_p(f - f_c)). \quad (3.251)$$

The analytic signal of an LFM pulse with duration T_p , amplitude A , and spanning the frequency interval (f_0, f_1) is $u_o(t) = e^{j2\pi[f_0 t + t^2 W/(2T_p)]}$ for $t \in (0, T_p)$ and zero elsewhere, where $f_c = (f_0 + f_1)/2$ is the center frequency and $W = f_1 - f_0$ is the bandwidth. The spectrum of the analytic signal of the LFM pulse can be shown to have form

$$S_{\dot{u}}(f) = \frac{A^2 T_p}{2W} \left| [C(\beta_1) - C(\beta_0)] + j [S(\beta_1) - S(\beta_0)] \right|^2 \quad (3.252)$$

where $\beta_0 = (f_0 - f)\sqrt{\pi T_p/W}$, $\beta_1 = (f_1 - f)\sqrt{\pi T_p/W}$, and $C(x) = \sqrt{2/\pi} \int_0^x \cos(t^2) dt$ and $S(x) = \sqrt{2/\pi} \int_0^x \sin(t^2) dt$ are, respectively, the cosine and sine Fresnel integrals as defined in [67, Ch. 39]. As shown in [75, Sect. 4.6.2], a stationary-phase approximation to the spectrum results in a constant level $A^2 T_p / W$ in the transmit band (f_0, f_1) and zero elsewhere. The accuracy of

the stationary-phase approximation increases with the duration-bandwidth product $T_p W$. Applying the stationary-phase approximation to an HFM pulse results in

$$\dot{S}_u(f) \approx \frac{A^2 T_p f_0 f_1}{W f^2} \quad (3.253)$$

for $f \in (f_0, f_1)$ and zero elsewhere. When the bandwidth is not very large relative to the center frequency, the LFM spectrum of (3.252) is a reasonable approximation. The exact HFM-pulse spectrum can be found in [76].

Exercise 3.15 Integrate (3.253) to show the total energy in the HFM transmit pulse is $A^2 T_p$. How large does W/f_c need to be before the HFM spectrum is 3 dB above the LFM spectrum level at $f_0 = f_c - W/2$?

3.5.7 Reverberation from a Moving Source

An important characteristic of the spectral properties of reverberation lies in how it changes when the sound projector is in motion. Suppose the sound projector with a co-located sensor is on a sonar platform traveling in a straight line at speed v . From Sect. 2.2.5 or 3.2.3.3, the reverberation measured from stationary elemental scatterers ahead of the platform will be subject to a Doppler scale (see (2.31))

$$\eta = \frac{c_w + v}{c_w - v}. \quad (3.254)$$

The effect of the motion on the i th elemental scatterer is a time scale applied to (3.229), resulting in

$$p_i(t) = \frac{A_i}{r_i^2} u_o \left(\eta t - \frac{2r_i}{c_w} \right). \quad (3.255)$$

The impact on the average squared modulus of the Fourier transform is both an amplitude and a frequency scale (see Sect. 4.3.2),

$$E\left[|P_i(f)|^2\right] \approx \frac{G_r}{r^2 \eta^2} \left| U_o\left(\frac{f}{\eta}\right) \right|^2. \quad (3.256)$$

For stationary elemental scatterers at a relative angle θ to the platform heading, the Doppler scale becomes

$$\eta_0(\theta) = \frac{c_w + v \cos \theta}{c_w - v \cos \theta} \quad (3.257)$$

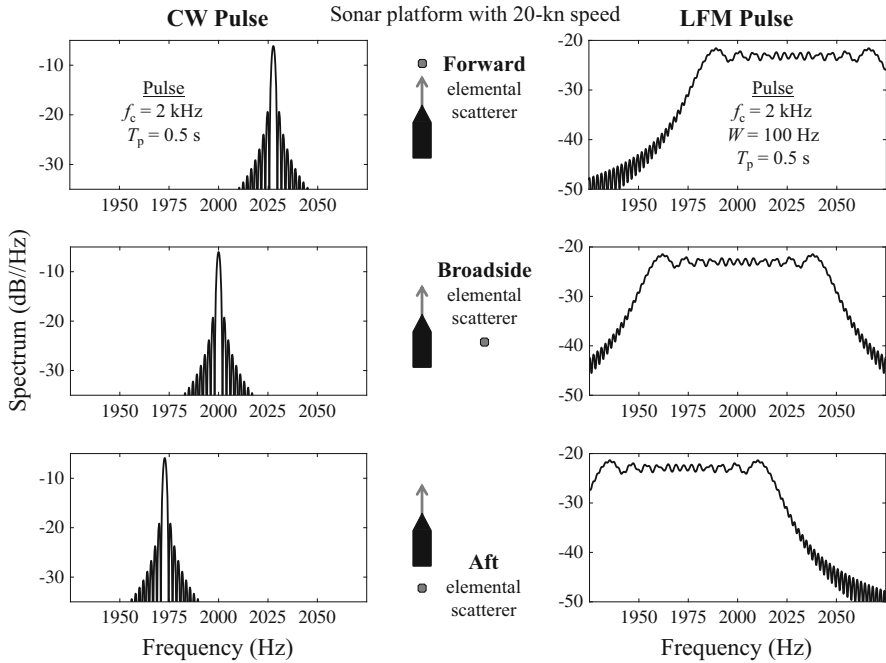


Fig. 3.31 Spectrum of the reverberation for forward, broadside, and aft directions when the sonar platform speed is 20 kn

which produces the result in (3.254) for the forward direction ($\theta = 0$) and the inverse of (3.254) in the aft direction ($\theta = \pi$). At broadside ($\theta = \pi/2$), $\eta_0(\theta) = 1$ which implies there is no Doppler effect on the reverberation. These three cases are illustrated in Fig. 3.31 for a sonar platform with a 20-kn speed. The plots on the left side are for a CW pulse with 0.5-s duration and a 2-kHz frequency. The plots on the right side are for an LFM pulse with the same duration and center frequency as the CW pulse but a 100-Hz bandwidth. For both pulse types, the reverberation spectrum shifts (scales) to higher frequencies in the forward direction and to lower frequencies in the aft direction relative to the spectrum of the source waveform.

An omni-directional sensor on a moving sonar platform measures reverberation from all directions, which results in a spectrum spread to both higher and lower frequencies. A sensor array is generally used to increase the signal-to-noise-or-reverberation power ratio through spatial filtering (i.e., beamforming). When the sonar platform is moving it also has the effect of reducing the spreading of the reverberation spectrum to that observed within the angular sector of each beam (e.g., see Sect. 7.4.2.4 or [26, Sect. 12.3]). To simplify detection processing on each beam, it is common to construct a fixed set of Doppler filters (e.g., see Sect. 8.7) matched to the relative radial velocities of interest under the assumption the sonar platform is stationary. Applying the fixed set of Doppler filters to beams pointing in different

directions then results in different spans of hypothesized relative radial velocities for the object of interest. A process called *ownship Doppler nullification* (ODN) [77, Sect. 5.2] accounts for the angular dependence of the Doppler induced by motion of the sonar platform. Recall from (2.28) in Sect. 2.2.5 that the Doppler scale of an echo when the source (with radial velocity v_a), object of interest (v_b), and receiver (v_c) are all in motion is

$$\eta = \left[\frac{c_w - v_b}{c_w + v_b} \right] \left[\frac{c_w + v_c}{c_w - v_a} \right]. \quad (3.258)$$

The bank of Doppler filters spans a range of values for v_b , but must account for the velocity of the source and receiver platforms in the direction of the beam. The total Doppler scale in (3.258) can be factored into an echo component and a sonar-platform component,

$$\eta = \eta_e \eta_0(\theta) \quad (3.259)$$

where η_e is the first term in brackets in (3.258) and $\eta_0(\theta)$ is as in (3.257) for a monostatic sonar or is the second term in brackets in (3.258) for a bistatic system. Note that when platform motion is not constant, the motion of the source platform is required at the time of pulse transmission and the motion of the receiver platform at the time the echo is measured.

After factoring η into its two components, ODN can be described as the process of removing the effect of $\eta_0(\theta)$ from the signal $x_\theta(t)$ measured on the beam pointing in the direction θ . Suppose the beam signal

$$x_\theta(t) = A_o u_o(\eta t - \tau) + r_\theta(t) \quad (3.260)$$

contains an echo with amplitude A_o , delay τ , and Doppler scale η , as well as a reverberation component $r_\theta(t)$. ODN is accomplished by applying a time scale countering the effect of the sonar-platform component of the Doppler scale,

$$\begin{aligned} y_\theta(t) &= x_\theta\left(\frac{t}{\eta_0(\theta)}\right) \\ &= A_o u_o(\eta_e t - \tau) + r_\theta\left(\frac{t}{\eta_0(\theta)}\right). \end{aligned} \quad (3.261)$$

Clearly the effect of platform motion has been removed from the echo, leaving only a dependence on η_e . Thus a fixed Doppler filter bank can be applied to $y_\theta(t)$ to obtain the full range of radial velocities of interest irrespective of the direction θ or speed of the sonar platform. The effect of ODN on the reverberation component is most easily explained in the frequency domain. Assuming the beamwidth is narrow enough for the reverberation spectrum to not have much spreading, the Fourier transform of the reverberation signal is proportional to that of the source waveform

after accounting for the sonar-platform component of the Doppler scale,

$$R_\theta(f) = \mathcal{F}\{r(t)\} = \frac{A_r}{|\eta_0(\theta)|} U_o\left(\frac{f}{\eta_0(\theta)}\right). \quad (3.262)$$

By taking the Fourier transform of $y_\theta(t)$ it can be seen that the reverberation component has been mapped to that for the stationary platform scenario,

$$Y_\theta(f) = \frac{1}{|\eta_0(\theta)|} X_\theta(\eta_0(\theta)f) \quad (3.263)$$

$$= \frac{A_o}{|\eta_e|} U_o\left(\frac{f}{\eta_e}\right) e^{-j2\pi f\tau} + A_r U_o(f). \quad (3.264)$$

When the sonar-platform speed is slow relative to the speed of sound, $\eta_0(\theta) \approx 1 + 2v \cos(\theta)/c_w$ for the monostatic sonar scenario. Using this in (3.263),

$$Y_\theta(f) = \frac{1}{|\eta_0(\theta)|} X_\theta(f[1 + 2v \cos(\theta)/c_w]), \quad (3.265)$$

illustrates how the ODN process for a CW pulse (e.g., at frequency f_c) involves recentering the spectrum of the beam with an angle dependent shift of $\Delta_f = -2f_c v \cos(\theta)/c_w$. Referring to the example shown in Fig. 3.31, this would require shifting the spectrum in the forward direction down by 27 Hz and the spectrum in the aft direction up by 27 Hz, thereby centering the reverberation spectrum at 2 kHz irrespective of θ .

References

1. D. Halliday, R. Resnick, *Fundamentals of Physics* (Wiley, New York, 1981)
2. J.A. Knauss, *Introduction to Physical Oceanography*, second, reissued in 2005 edition (Waveland Press, Inc., Long Grove, 1997)
3. L.E. Kinsler, A.R. Frey, A.B. Coppens, J.V. Sanders, *Fundamentals of Acoustics*, 3rd edn. (Wiley, New York, 1982)
4. A.D. Pierce, *Acoustics: An Introduction to Its Physical Principles and Applications* (Acoustical Society of America, Woodbury, 1989)
5. I. Tolstoy, C.S. Clay, *Ocean Acoustics: Theory and Experiment in Underwater Sound* (American Institute of Physics, Inc., New York, 1987)
6. H. Medwin, C.S. Clay, *Fundamentals of Acoustical Oceanography* (Academic Press, Inc., Boston, 1998)
7. G.V. Frisk, *Ocean and Seabed Acoustics* (Prentice Hall, Inc., Englewood Cliffs, 1994)
8. F.B. Jensen, W.A. Kuperman, M.B. Porter, H. Schmidt, *Computational Ocean Acoustics*, 2nd edn. (Springer, New York, 2011)
9. M.A. Ainslie, *Principles of Sonar Performance Modeling* (Springer, New York, 2010)
10. R.H. Stewart, *Introduction to Physical Oceanography* (Orange Grove Texts Plus, Tallahassee, 2008)

11. L.J. Ziomek, *Acoustic Field Theory and Space-Time Signal Processing* (CRC Press, Boca Raton, 1995)
12. W.S. Burdic, *Underwater Acoustic System Analysis*, 2nd edn. (Peninsula Publishing, Los Altos, 1991)
13. J.F. Hurley, *Intermediate Calculus: Multivariable Functions and Differential Equations with Applications* (Saunders College, Philadelphia, 1980)
14. W.J. Bangs II, *Array Processing with Generalized Beamformers*. PhD thesis, Yale University, 1971
15. W.R. Hahn, Optimum signal processing for passive sonar range and bearing estimation. *J. Acoust. Soc. Am.* **58**(1), 201–207 (1975)
16. L.E. Kinsler, A.R. Frey, A.B. Coppens, J.V. Sanders, *Fundamentals of Acoustics*, 4th edn. (Wiley, New York, 2000)
17. ISO 18405.2 International Standard for Terminology in Underwater Acoustics. <https://www.iso.org/obp/ui/#iso:std:iso:18405>
18. P.M. Morse, K.U. Ingard, *Theoretical Acoustics* (Princeton University Press, Princeton, 1968)
19. L.H. Sibul, L.G. Weiss, T.L. Dixon, Characterization of stochastic propagation and scattering via Gabor and wavelet transforms. *J. Comput. Acoust.* **2**(3), 345–369 (1994)
20. C.H. Sherman, J.L. Butler, *Transducers and Arrays for Underwater Sound* (Springer, New York, 2007)
21. I.S. Gradshteyn, I.M. Ryzhik, *Table of Integrals, Series, and Products*, 8th edn., ed. by D. Zwillinger. (Elsevier Academic Press, Waltham, 2015)
22. A.C. Kibblewhite, L.D. Hampton, A review of deep ocean sound attenuation data at very low frequencies. *J. Acoust. Soc. Am.* **67**(1), 147–157 (1980)
23. M.B. Porter, Y.C. Liu, Finite-element ray tracing, in *Proceedings of the International Conference on Theoretical and Computational Acoustics*, ed. by D. Lee, M.H. Schultz (1994), pp. 947–956
24. Ocean Acoustics Library. <http://oalib.hlsresearch.com>
25. W.H. Munk, Sound channel in an exponentially stratified ocean, with application to SOFAR. *J. Acoust. Soc. Am.* **55**(2), 220–226 (1974)
26. W.S. Burdic, *Underwater Acoustic System Analysis* (Prentice Hall, Englewood Cliffs, 1984)
27. W.M. Carey, Lloyd's mirror—image interference effects. *Acoust. Today* **5**(2), 14–20 (2009)
28. R.J. Urick, Models for the amplitude fluctuations of narrow-band signals and noise in the sea. *J. Acoust. Soc. Am.* **62**(4), 878–887 (1977)
29. L.M. Brekhovskikh, O.A. Godin, *Acoustics of Layered Media I: Plane and Quasi-Plane Waves* (Springer, Berlin, 1998)
30. R.N. Bracewell, *The Fourier Transform and Its Applications*, 2nd edn. (McGraw-Hill, Inc., New York, 1986)
31. R.N. McDonough, A.D. Whalen, *Detection of Signals in Noise*, 2nd edn. (Academic Press, Inc., San Diego, 1995)
32. X. Lurton, *An Introduction to Underwater Acoustics* (Springer-Praxis, Berlin, 2002)
33. D.A. Abraham, S.M. Murphy, P.C. Hines, A.P. Lyons, Matched-filter loss from time-varying rough-surface reflection with a small effective ensonified area. *IEEE J. Ocean. Eng.* <https://doi.org/10.1109/JOE.2017.2704198>
34. D.A. Abraham, Coherent matched-filter surface reflection loss as a function of pulse duration and ensonified extent, in *Proceedings of the Underwater Acoustics Conference and Exhibition*, Skiathos, September 2017, pp. 177–183
35. F.W.J. Olver, D.W. Lozier, R.F. Boisvert, C.W. Clark (eds.), *NIST Handbook of Mathematical Functions* (Cambridge University Press, Cambridge, 2010)
36. M.B. Porter, E.L. Reiss, A numerical method for ocean-acoustic normal modes. *J. Acoust. Soc. Am.* **76**(1), 244–252 (1984)
37. M.B. Porter, E.L. Reiss, A numerical method for bottom interacting ocean acoustic normal modes. *J. Acoust. Soc. Am.* **77**(5), 1760–1767 (1985)
38. G.M. Wenz, Acoustic ambient noise in the ocean: spectra and sources. *J. Acoust. Soc. Am.* **34**(12), 1936–1956 (1962)

39. G.M. Wenz, Review of underwater acoustics research: noise. *J. Acoust. Soc. Am.* **51**(3), 1010–1024 (1972)
40. R.J. Urick, *Ambient Noise in the Sea*. Undersea Warfare Technology Office, Naval Sea Systems Command, Department of the Navy, Washington, D.C., 1984
41. W.M. Carey, R.B. Evans, *Ocean Ambient Noise: Measurement and Theory* (Springer, New York, 2011)
42. Principles and applications of underwater sound. Sum. Tech. Rep. Volume 7, Office of Scientific Research and Development, Nat. Def. Res. Comm. Div. 6, 1946. DTIC accession number AD200786
43. R.J. Urick, *Principles of Underwater Sound*, 3rd edn. (McGraw-Hill, Inc., New York, 1983)
44. J.W. Horton, *Fundamentals of SONAR* (United States Naval Institute, Annapolis, 1959)
45. V.O. Knudsen, R.S. Alford, J.W. Emling, Underwater ambient noise. *J. Mar. Res.* **7**, 410–429 (1948)
46. R.H. Mellen, The thermal-noise limit in the detection of underwater acoustic signals. *J. Acoust. Soc. Am.* **24**(5), 478–480 (1952)
47. J.W. Horton, *Signal Processing of Underwater Acoustic Waves* (Government Printing Office, Washington, 1969)
48. J.H. Wilson, Very low frequency (vlf) wind-generated noise produced by turbulent pressure fluctuations in the atmosphere near the ocean surface. *J. Acoust. Soc. Am.* **66**(5), 1499–1507 (1979)
49. S.C. Wales, R.M. Heitmeyer, An ensemble source spectra model for merchant ship-radiated noise. *J. Acoust. Soc. Am.* **111**(3), 1211–1231 (2002)
50. APL-UW, APL-UW high-frequency ocean environmental acoustic models handbook. Technical Report TR9407, Applied Physics Laboratory, University of Washington, 1994
51. W.A. Kuperman, M.C. Ferla, A shallow water experiment to determine the source spectrum level of wind-generated noise. *J. Acoust. Soc. Am.* **77**(6), 2067–2073 (1985)
52. D.R. Jackson, M.D. Richardson, *High-Frequency Seafloor Acoustics* (Springer, New York, 2007)
53. P.Z. Peebles Jr., *Radar Principles* (Wiley, New York, 1998)
54. A.E. Fuhs, Radar cross section lectures. Technical Report DTIC A125576, Naval Post Graduate School, Monterey, California, 1982
55. D.E. Kerr, H. Goldstein, Radar targets and echoes, in *Propagation of Short Radio Waves*, chapter 6, ed. by D.E. Kerr (McGraw-Hill Book Company, Inc., New York, 1951). reprinted by Peninsula Publishing in 1988
56. J.W. Crispin Jr., K.M. Siegel (eds.), *Methods of Radar Cross-Section Analysis* (Academic Press, New York, 1968)
57. D.K. Barton, *Modern Radar System Analysis* (Artech House, Inc., Norwood, 1988)
58. P.L. Marston, Quantitative ray methods for scattering, in *Encyclopedia of Acoustics*, vol. 1, chapter 43, ed. by M.J. Crocker (Wiley, New York, 1997), pp. 483–500
59. L.R. Dragonette, C.F. Gaumond, Transient and steady-state scattering and diffraction from underwater targets, in *Encyclopedia of Acoustics*, vol. 1, chapter 42, ed. by M.J. Crocker (Wiley, New York, 1997), pp. 469–482
60. A.D. Waite, *SONAR for Practising Engineers*, 3rd edn. (Wiley, New York, 2002)
61. Z. Sun, G. Gimenez, D. Vray, F. Denis, Calculation of the impulse response of a rigid sphere using the physical optic method and modal method jointly. *J. Acoust. Soc. Am.* **89**, 10–18 (1991)
62. Lord Rayleigh, *The Theory of Sound*, vol. II (Dover Publications, New York, 1896). Second revised and enlarged edition
63. J.J. Faran, Sound scattering by solid cylinders and spheres. *J. Acoust. Soc. Am.* **23**(4), 405–418 (1951)
64. R.R. Goodman, R. Stern, Reflection and transmission of sound by elastic spherical shells. *J. Acoust. Soc. Am.* **34**(3), 338–344 (1962)
65. H. Überall, Interference and steady-state scattering of sound waves, in *Encyclopedia of Acoustics*, vol. 1, chapter 5, ed. by M.J. Crocker (Wiley, New York, 1997), pp. 55–67

66. L. Flax, L.R. Dragonette, H. Überall, Theory of elastic resonance excitation by sound scattering. *J. Acoust. Soc. Am.* **63**(3), 723–731 (1978)
67. K. Oldham, J. Myland, J. Spanier, *An Atlas of Functions*, 2nd edn. (Springer, New York, 2009)
68. R. Hickling, Analysis of echoes from a solid elastic sphere in water. *J. Acoust. Soc. Am.* **34**(10), 1582–1592 (1962)
69. R.D. Doolittle, H. Überall, Sound scattering by elastic cylindrical shells. *J. Acoust. Soc. Am.* **39**(2), 272–275 (1966)
70. V.V. Ol'shevskii, *Characteristics of Sea Reverberation* (Consultants Bureau, New York, 1967)
71. R.P. Chapman, J.H. Harris, Surface backscattering strengths measured with explosive sound sources. *J. Acoust. Soc. Am.* **34**(10), 1592–1597 (1962)
72. D.D. Ellis, D.V. Crowe, Bistatic reverberation calculations using a three-dimensional scattering function. *J. Acoust. Soc. Am.* **89**(5), 2207–2214 (1991)
73. J.X. Zhou, The analytical method of angular power spectrum, range and depth structure of the echo-to-reverberation ratio in shallow water sound field. *Acta Acust.* **5**(2), 86–99 (1980)
74. C.H. Harrison, Closed-form expressions for ocean reverberation and signal excess with mode stripping and Lambert's law. *J. Acoust. Soc. Am.* **114**(5), 2744–2756 (2003)
75. M.A. Richards, *Fundamentals of Radar Signal Processing* (McGraw-Hill, New York, 2005)
76. J.J. Kroszczynski, Pulse compression by means of linear-period modulation. *Proc. IEEE* **57**(7), 1260–1266 (1969)
77. R.O. Nielsen, *Sonar Signal Processing* (Artech House, Inc., Norwood, 1991)

Part II

Systems, Signal Processing and

Mathematical Statistics Background

Chapter 4

Linear Systems and Signal Processing



4.1 Introduction

Many of the most important topics in applied signal processing are introduced in this chapter. The material begins with continuous-time signals, systems, and their Fourier analysis. Sampling and quantization of continuous-time signals follows along with discrete-time signals, systems, and Fourier analysis, including the discrete Fourier transform (DFT), its interpretations, and implementation via the fast Fourier transform (FFT). The chapter is concluded with practical signal processing topics including filtering, filter design, windowing, decimation, and interpolation.

4.2 Linear-Time-Invariant (LTI) Systems and Convolution

Systems analysis is a basic part of signal processing and encompasses not only many signal processing functions (e.g., filtering, estimation and prediction, spectral analysis) but is also used in characterizing physical processes in order to develop signal processing for specific applications. For example, the remote-sensing interpretation of underwater acoustic applications can be described as a system with an input signal ($x(t)$) and an output signal ($y(t)$) as shown in Fig. 4.1. For a specific case, consider an active sonar system for which $x(t)$ would be the transmit waveform and $y(t)$ the measured echoes. However, in other underwater acoustic applications the input signal might be the noise generated by breaking waves or the height of the seafloor as a function of latitude and longitude. Systems can have multiple inputs (e.g., an echo and noise) and multiple outputs (e.g., acoustic pressure measured at multiple points).

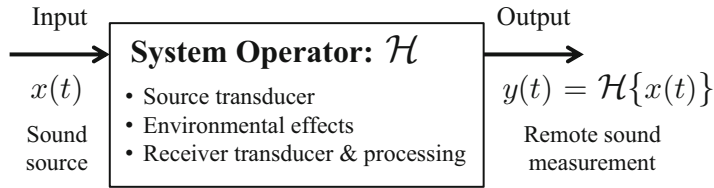


Fig. 4.1 System interpretation of remote sensing

The physics relating the input signals to the output signals can be represented mathematically by an operator \mathcal{H} such that

$$y(t) = \mathcal{H}\{x(t)\}. \quad (4.1)$$

In this section the system is considered to be at rest; that is, the initial conditions of the state variables are zero. As such, the output $y(t)$ is the zero-state response of the system to input $x(t)$. This mathematical representation $y(t) = \mathcal{H}\{x(t)\}$ allows many properties of the system to be described. Two of the most important properties are linearity and time invariance. A system is linear if it satisfies super-position; i.e., if the input signal is a linear combination of a distinct set of individual signals, then the output will be a corresponding linear combination of the system output to each of the individual signals. If $x(t) = a_1x_1(t) + a_2x_2(t)$, this requires

$$\begin{aligned} y(t) &= \mathcal{H}\{a_1x_1(t) + a_2x_2(t)\} \\ &= a_1\mathcal{H}\{x_1(t)\} + a_2\mathcal{H}\{x_2(t)\} \\ &= a_1y_1(t) + a_2y_2(t) \end{aligned} \quad (4.2)$$

where $y_i(t) = \mathcal{H}\{x_i(t)\}$ for $i = 1$ and 2 .

A system is time-invariant if its characterization does not change over time. From an input–output perspective, time invariance requires that delaying an input signal by an arbitrary amount results in an identical delay in the output

$$\mathcal{H}\{x(t - \tau)\} = y(t - \tau) \text{ for all } \tau \quad (4.3)$$

where $y(t) = \mathcal{H}\{x(t)\}$.

4.2.1 Impulse Response of an LTI System

When a system is linear and time invariant (LTI), the operator \mathcal{H} has the form

$$y(t) = \mathcal{H}\{x(t)\} = \int_{-\infty}^{\infty} h(\tau)x(t - \tau) d\tau \quad (4.4)$$

where $h(t)$ is the impulse response of the system. The name *impulse response* comes from assuming the input signal to an LTI system is an impulse. To define an impulse, first define a rectangular pulse centered at zero with unit height and unit width (and therefore unit area) by the function

$$\text{rect}(t) = \begin{cases} 1 & \text{for } -\frac{1}{2} < t \leq \frac{1}{2} \\ 0 & \text{otherwise} \end{cases}. \quad (4.5)$$

The width of the pulse can be changed to ε by multiplying the argument by $1/\varepsilon$,

$$\text{rect}(t/\varepsilon) = \begin{cases} 1 & \text{for } -\frac{\varepsilon}{2} < t \leq \frac{\varepsilon}{2} \\ 0 & \text{otherwise} \end{cases}. \quad (4.6)$$

An impulse function can then be constructed by starting with a rectangular pulse with width ε , scaling it to have unit area (e.g., see Fig. 4.2), and then taking the limit as $\varepsilon \rightarrow 0$,

$$\delta(t) = \lim_{\varepsilon \rightarrow 0} \frac{1}{\varepsilon} \text{rect}(t/\varepsilon). \quad (4.7)$$

The function $\delta(t)$ is known as a Dirac delta function ([1, Sect. 15] or [2, Ch. 5]) and is represented graphically as a vertical arrow on the abscissa at the point where the argument is zero as shown in Fig. 4.2. This derivation of $\delta(t)$ is not unique; it can generally be described as the limit of a function growing in amplitude at the origin, decreasing in width, and integrating to one. The resulting function is zero for all arguments except the origin where it is undefined, but may be considered infinitely large. A key property of the delta function is known as *sifting*, where $\delta(t - t_0)$ sifts out of an integral the value of a function for the time at which the delta function is non-zero,

$$\int_{-\infty}^{\infty} f(t) \delta(t - t_0) dt = f(t_0). \quad (4.8)$$

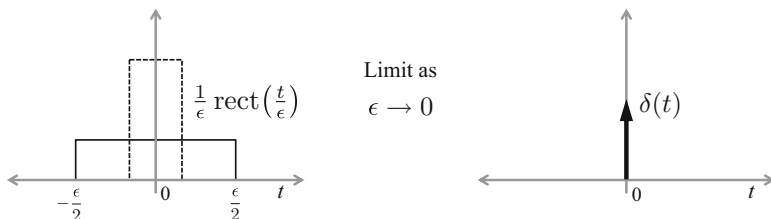


Fig. 4.2 Dirac delta function as the limit of a unit-area rectangular pulse

Applying the sifting property of the delta function to (4.4) when the input is an impulse function produces the impulse response; that is, if $x(t) = \delta(t)$, then $y(t) = h(t)$.

The operator in (4.4) for an LTI system is called a *convolution* operator and represented by an asterisk (*),

$$h(t) * x(t) = \int_{-\infty}^{\infty} h(\tau)x(t - \tau) d\tau = \int_{-\infty}^{\infty} x(\tau)h(t - \tau) d\tau = x(t) * h(t). \quad (4.9)$$

From the right side of (4.9), convolution is seen to be a commutative operation (i.e., $x(t) * h(t) = h(t) * x(t)$).

Example: Multipath Signal

Suppose an acoustic signal $x(t)$ propagates through an underwater channel and is measured some distance away as $y(t)$. If the underwater channel can be characterized by having n distinct paths where the i th path imparts an attenuation (a_i) and a delay (τ_i), the received signal is

$$y(t) = \sum_{i=1}^n a_i x(t - \tau_i). \quad (4.10)$$

The system is easily seen to be both linear and time invariant. Additionally, the impulse response of the channel has the form

$$h(t) = \sum_{i=1}^n a_i \delta(t - \tau_i). \quad (4.11)$$

Suppose, however, there is just one path and it is subject to Doppler from motion of the source, receiver, or a boundary (see Sect. 2.2.5). The measured signal will then have the form

$$y(t) = a_1 x(\eta_1 t - \tau_1) \quad (4.12)$$

where η_1 is the Doppler scale. The Doppler scale will be greater than one when the motion reduces the distance between the source and receiver and less than one when the distance increases. It only equals one when there is no Doppler effect. Although the system is linear, it is not time-invariant if $\eta_1 \neq 1$. To see this let $x_0(t) = x(t - \tau_0)$ and evaluate the system output to $x_0(t)$,

(continued)

$$\begin{aligned}
 \mathcal{H}\{x_0(t)\} &= a_1 x_0(\eta_1 t - \tau_1) \\
 &= a_1 x(\eta_1 t - \tau_1 - \tau_0) \\
 &= y(t - \tau_0/\eta_1) \\
 &\neq y(t - \tau_0).
 \end{aligned} \tag{4.13}$$

4.2.2 Frequency Response of an LTI System

Sinusoidal signals are both naturally occurring and a signal of choice in underwater acoustics as well as many other applications. They are also helpful in characterizing the input–output relationships of LTI systems. Suppose the input signal is a complex sinusoid with frequency f_0 . Using the first form of the convolution integral in (4.9), the output will be

$$\begin{aligned}
 y(t) &= \mathcal{H}\left\{e^{j2\pi f_0 t}\right\} \\
 &= \int_{-\infty}^{\infty} h(\tau) e^{j2\pi f_0(t-\tau)} d\tau \\
 &= \left[\int_{-\infty}^{\infty} h(\tau) e^{-j2\pi f_0 \tau} d\tau \right] e^{j2\pi f_0 t} \\
 &= H(f_0) e^{j2\pi f_0 t}
 \end{aligned} \tag{4.14}$$

where

$$H(f) = \int_{-\infty}^{\infty} h(t) e^{-j2\pi f t} dt \tag{4.15}$$

is the Fourier transform (see Sect. 4.3) of the impulse response. Noting that $H(f)$ is in general complex, the output signal can be described as

$$y(t) = |H(f_0)| e^{j\angle H(f_0)} e^{j2\pi f_0 t} \tag{4.16}$$

where $\angle H(f_0)$ is the angle or phase of $H(f_0)$ in radians. Thus the zero-state response of an LTI system to a complex sinusoid is another complex sinusoid with the same frequency, scaled by the magnitude of $H(f_0)$, and with an additional phase term equal to that of $H(f_0)$. For this reason the Fourier transform of the impulse

response ($H(f)$) is called the *frequency response* of the system. It completely characterizes the response of an LTI system to a sinusoidal input.

Recall the multipath example where Doppler caused time invariance. Were the input signal a sinusoid, the output in the presence of Doppler is still a sinusoid but one with a different frequency ($\eta_0 f_0$). As this cannot be possible within the confines of (4.16), which requires the output sinusoid to be the same frequency as the input, the system cannot be LTI.

4.3 Fourier Transforms

Fourier transforms are an integral part of many signal processing functions. This is particularly true in underwater acoustic signal processing where frequency-domain signal characteristics are diverse and often very informative. The Fourier transform of the signal $x(t)$ is

$$X(f) = \mathcal{F}\{x(t)\} = \int_{-\infty}^{\infty} x(t) e^{-j2\pi f t} dt \quad (4.17)$$

where f is the frequency in hertz (Hz) when t is time in seconds (s).

The Fourier transform most commonly describes the frequency content of a time-domain signal. However, it can be applied to other signal dimensions such as space as is done in array signal processing. It can also be applied to deterministic (i.e., repeatable or non-random) and random signals. In this section treatment is restricted to deterministic signals. Fourier analysis of random signals, commonly known as the power spectrum or power spectral density is covered in Sect. 5.4.2.

Example: Rectangular Window

A rectangular window function on the interval $t \in (-T/2, T/2)$ can be defined using the rectangular pulse from Sect. 4.2,

$$\text{rect}(t/T) = \begin{cases} 1 & \text{for } -\frac{T}{2} < t \leq \frac{T}{2} \\ 0 & \text{otherwise} \end{cases} \quad (4.18)$$

Its Fourier transform is

$$\begin{aligned} X(f) &= \int_{-T/2}^{T/2} e^{-j2\pi f t} dt \\ &= T \text{sinc}(fT) \end{aligned} \quad (4.19)$$

(continued)

where the *sinc* function is

$$\text{sinc}(x) = \frac{\sin(\pi x)}{\pi x}. \quad (4.20)$$

The Fourier transform exists for any signal that is absolutely integrable, which requires

$$\int_{-\infty}^{\infty} |x(t)| dt < \infty. \quad (4.21)$$

Many signals of interest (e.g., constant signals or sinusoidal signals) do not satisfy the absolutely integrable requirement of (4.21) because they are power signals rather than energy signals. In such cases a generalized Fourier transform can be used where the signals are defined as the limit of a function satisfying (4.21). For example, let $x_T(t)$ be the uniform window with width T as in (4.18). By letting $T \rightarrow \infty$, the uniform window becomes a constant for all time

$$x(t) = \lim_{T \rightarrow \infty} x_T(t) = 1 \quad (4.22)$$

which is not absolutely integrable. However, by starting with (4.19) it can be seen that the generalized Fourier transform

$$\begin{aligned} X(f) &= \lim_{T \rightarrow \infty} \mathcal{F}\{x_T(t)\} \\ &= \lim_{T \rightarrow \infty} T \text{sinc}(fT) = \delta(f) \end{aligned} \quad (4.23)$$

where the function $T \text{sinc}(fT)$ within the limit is seen to satisfy the requirements for forming an impulse function as $T \rightarrow \infty$. Of course, one would expect the Fourier transform of a constant signal to place all frequency content at $f = 0$. In practice, most signals are of finite duration and finite amplitude and therefore will satisfy (4.21).

4.3.1 Inverse Fourier Transform

The Fourier transform is an invertible transform. The time-domain signal can be obtained from the frequency-domain signal through the inverse Fourier transform

$$x(t) = \mathcal{F}^{-1}\{X(f)\} = \int_{-\infty}^{\infty} X(f) e^{j2\pi ft} df. \quad (4.24)$$

It is common to see the Fourier transform described as a function of angular frequency (i.e., ω in radians per second [rad/s]) rather than temporal frequency (i.e., f in cycles per sec [Hz]). In the transform itself, this simply requires taking (4.17) as a function of $\omega = 2\pi f$ rather than f . However in (4.24), the change of variables in the integral results in

$$x(t) = \mathcal{F}^{-1}\{X(\omega)\} = \frac{1}{2\pi} \int_{-\infty}^{\infty} X(\omega) e^{j\omega t} d\omega. \quad (4.25)$$

The time- and frequency-domain functions form what is called a Fourier transform pair, denoted by

$$x(t) \xleftrightarrow{\mathcal{F}} X(f). \quad (4.26)$$

Fourier transform pairs can be derived from the definitions in (4.17) and (4.24). However it is more common to use tables (e.g., see [3, Table 7.1] or most *Signals and Systems* textbooks) and to exploit the many properties of the Fourier transform.

As an example of deriving a time-domain signal from a frequency-domain characterization, suppose a signal contained just one frequency (f_0), such that its Fourier transform was

$$X(f) = \delta(f - f_0) \quad (4.27)$$

where $\delta(f - f_0)$ is a Dirac delta function with argument $f - f_0$, which places infinite weight at $f = f_0$ and is zero everywhere else. Using the inverse Fourier transform definition from (4.24) and the sifting property of the Dirac delta function, the corresponding time-domain signal,

$$\begin{aligned} x(t) &= \int_{-\infty}^{\infty} \delta(f - f_0) e^{j2\pi f t} df \\ &= e^{j2\pi f_0 t}, \end{aligned} \quad (4.28)$$

is seen to be a complex sinusoid with frequency f_0 . By using this Fourier transform pair for the complex sinusoidal signal,

$$e^{j2\pi f_0 t} \xleftrightarrow{\mathcal{F}} \delta(f - f_0), \quad (4.29)$$

the Fourier transform of a real sinusoidal signal can be obtained by decomposing it into two complex sinusoids,

$$\begin{aligned}\mathcal{F}\{\cos(2\pi f_0 t)\} &= \mathcal{F}\left\{\frac{1}{2}\left[e^{j2\pi f_0 t} + e^{-j2\pi f_0 t}\right]\right\} \\ &= \frac{\delta(f - f_0)}{2} + \frac{\delta(f + f_0)}{2}.\end{aligned}\quad (4.30)$$

These examples illustrate how complex sinusoids are the basis functions for the Fourier transform, which can also be seen by examining the definition in (4.17).

4.3.2 Properties of the Fourier Transform

Articulating several properties of the Fourier transform significantly simplifies its use in signal processing. Some of the most useful properties follow. For many signals the Fourier transform is a complex function,

$$X(f) = |X(f)| e^{j\angle X(f)} \quad (4.31)$$

where $|X(f)|$ is the magnitude and $\angle X(f)$ the phase. The magnitude of the Fourier transform is often the most important characteristic; however, as seen below, the phase is important for signals subject to time delays.

Linearity If a signal is a linear combination of two individual signals, $x(t) = a_1x_1(t) + a_2x_2(t)$, then its Fourier transform is an identical linear combination of the Fourier transforms of the individual signals,

$$\begin{aligned}X(f) &= \int_{-\infty}^{\infty} [a_1x_1(t) + a_2x_2(t)] e^{-j2\pi ft} dt \\ &= a_1 \int_{-\infty}^{\infty} x_1(t) e^{-j2\pi ft} dt + a_2 \int_{-\infty}^{\infty} x_2(t) e^{-j2\pi ft} dt \\ &= a_1X_1(f) + a_2X_2(f)\end{aligned}\quad (4.32)$$

where $x_i(t) \xrightarrow{\mathcal{F}} X_i(f)$ for $i = 1$ and 2 .

Time Delay If a signal $x(t)$ is delayed by τ , its Fourier transform changes only in the phase,

$$\mathcal{F}\{x(t - \tau)\} = \int_{-\infty}^{\infty} x(t - \tau) e^{-j2\pi ft} dt$$

$$\begin{aligned}
&= e^{-j2\pi f\tau} \int_{-\infty}^{\infty} x(s)e^{-j2\pi fs} ds \\
&= e^{-j2\pi f\tau} X(f).
\end{aligned} \tag{4.33}$$

Time Scale The Fourier transform of $x(\gamma t)$ for $\gamma \neq 0$ results in an inverse frequency scale and a scale of the transform,

$$\begin{aligned}
\mathcal{F}\{x(\gamma t)\} &= \int_{-\infty}^{\infty} x(\gamma t)e^{-j2\pi ft} dt \\
&= \frac{1}{|\gamma|} \int_{-\infty}^{\infty} x(s)e^{-j2\pi(f/\gamma)s} ds \\
&= \frac{1}{|\gamma|} X\left(\frac{f}{\gamma}\right).
\end{aligned} \tag{4.34}$$

Modulation Suppose a signal $x(t)$ is modulated (i.e., multiplied) by a complex sinusoid with frequency f_0 . The Fourier transform of the modulated signal,

$$\begin{aligned}
\mathcal{F}\{x(t)e^{j2\pi f_0 t}\} &= \int_{-\infty}^{\infty} [x(t)e^{j2\pi f_0 t}] e^{-j2\pi ft} dt \\
&= \int_{-\infty}^{\infty} x(t)e^{-j2\pi(f-f_0)t} dt \\
&= X(f - f_0),
\end{aligned} \tag{4.35}$$

is a frequency-shifted version of the Fourier transform of the original signal, illustrating how modulation moves the frequency content of a signal from being centered at $f = 0$ to being centered at $f = f_0$. Modulating a signal by a cosine results in the Fourier transform pair

$$\cos(2\pi f_0 t)x(t) \xleftrightarrow{\mathcal{F}} \frac{X(f - f_0)}{2} + \frac{X(f + f_0)}{2} \tag{4.36}$$

which can be seen by expanding the cosine into the sum of complex sinusoids with frequencies $\pm f_0$.

Differentiation The Fourier transform of the derivative of a signal, $x'(t)$, is $j2\pi f$ times the Fourier transform of the signal,

$$\mathcal{F}\{x'(t)\} = j2\pi f X(f). \quad (4.37)$$

This can be shown by differentiating the signal as defined by the inverse Fourier transform,

$$\begin{aligned} x'(t) &= \frac{d}{dt} \int_{-\infty}^{\infty} X(f) e^{j2\pi f t} df \\ &= \int_{-\infty}^{\infty} [j2\pi f X(f)] e^{j2\pi f t} df. \end{aligned} \quad (4.38)$$

Duality Noting the similarity between the Fourier transform and its inverse, there is a duality between transform pairs. Suppose $x(t) \xleftrightarrow{\mathcal{F}} X(f)$, then by treating $X(f)$ as a function of time and taking its Fourier transform,

$$\begin{aligned} \mathcal{F}\{X(t)\} &= \int_{-\infty}^{\infty} X(t) e^{-j2\pi f t} dt \\ &= \int_{-\infty}^{\infty} X(t) e^{j2\pi(-f)t} dt \\ &= x(-f). \end{aligned} \quad (4.39)$$

The duality property can be compactly described as follows. If $x(t)$ and $X(f)$ are a known Fourier transform pair,

$$x(t) \xleftrightarrow{\mathcal{F}} X(f) \quad (4.40)$$

then $X(t)$ and $x(-f)$ are also a Fourier transform pair

$$X(t) \xleftrightarrow{\mathcal{F}} x(-f). \quad (4.41)$$

Recall the example of a uniform window function for $t \in (-T/2, T/2)$ which yielded the Fourier transform pair

$$\text{rect}(t/T) \xleftrightarrow{\mathcal{F}} T \text{sinc}(fT). \quad (4.42)$$

The duality property indicates a signal with Fourier transform

$$Y(f) = \text{rect}(f/W) \quad (4.43)$$

has inverse Fourier transform

$$y(t) = W \text{sinc}(t/W) \quad (4.44)$$

noting that the sinc function is even; i.e., $\text{sinc}(x) = \sin(\pi x)/(\pi x) = \text{sinc}(-x)$.

Convolution One of the most useful properties of the Fourier transform is the convolution property. Recall the output ($y(t)$) of a linear-time-invariant (LTI) system is the convolution between the input ($x(t)$) and the impulse response ($h(t)$) of the system,

$$y(t) = x(t) * h(t) = \int_{-\infty}^{\infty} h(\tau)x(t - \tau) d\tau. \quad (4.45)$$

In the frequency domain, the Fourier transform of the output is the product of the Fourier transforms of the input and the impulse response,

$$\begin{aligned} Y(f) &= \int_{-\infty}^{\infty} \left\{ \int_{-\infty}^{\infty} h(\tau)x(t - \tau) d\tau \right\} e^{-j2\pi f t} dt \\ &= \int_{-\infty}^{\infty} h(\tau) \int_{-\infty}^{\infty} x(t - \tau) e^{-j2\pi f t} dt d\tau \\ &= \int_{-\infty}^{\infty} h(\tau) e^{-j2\pi f \tau} d\tau \int_{-\infty}^{\infty} x(t) e^{-j2\pi f t} dt \\ &= H(f)X(f), \end{aligned} \quad (4.46)$$

where $h(t) \xleftrightarrow{\mathcal{F}} H(f)$. Thus a convolution in the time domain equates to a (much simpler) product in the frequency domain,

$$x(t) * y(t) \xleftrightarrow{\mathcal{F}} X(f)Y(f). \quad (4.47)$$

It can also be shown that the converse is true: a product in the time domain results in a convolution in the frequency domain,

$$x(t)y(t) \xleftrightarrow{\mathcal{F}} X(f)*Y(f). \quad (4.48)$$

Parseval's Theorem An energy signal (in the mathematical sense) is defined as one having finite energy; that is,

$$\mathcal{E} = \int_{-\infty}^{\infty} |x(t)|^2 dt < \infty. \quad (4.49)$$

Parseval's theorem for energy signals allows evaluation of \mathcal{E} from the frequency-domain characterization as follows:

$$\begin{aligned} \mathcal{E} &= \int_{-\infty}^{\infty} |x(t)|^2 dt = \int_{-\infty}^{\infty} x(t)x^*(t) dt \\ &= \int_{-\infty}^{\infty} x(t) \left[\int_{-\infty}^{\infty} X(f)e^{j2\pi ft} df \right]^* dt \\ &= \int_{-\infty}^{\infty} X^*(f) \left[\int_{-\infty}^{\infty} x(t)e^{-j2\pi ft} dt \right] df \\ &= \int_{-\infty}^{\infty} |X(f)|^2 df. \end{aligned} \quad (4.50)$$

For example, consider the Fourier transform pair from (4.43) and (4.44),

$$W \text{sinc}(tW) \xleftrightarrow{\mathcal{F}} \text{rect}(f/W). \quad (4.51)$$

Using (4.50), the energy is easily seen to be

$$\mathcal{E} = \int_{-W/2}^{W/2} 1^2 df = W \quad (4.52)$$

whereas direct evaluation of (4.49) would require evaluating

$$\int_{-\infty}^{\infty} W^2 \text{sinc}^2(tW) dt = W. \quad (4.53)$$

4.4 Hilbert Transform

The Hilbert transform is useful in describing the analytic representation of a real signal. It is defined as [2, p. 267]

$$s_h(t) = \mathcal{H}\{s(t)\} = \frac{1}{\pi} \int_{-\infty}^{\infty} \frac{s(\tau)}{\tau - t} d\tau. \quad (4.54)$$

The Hilbert transform of cosine, sine, and impulse functions,

$$\mathcal{H}\{\cos t\} = -\sin t$$

$$\mathcal{H}\{\sin t\} = \cos t$$

$$\mathcal{H}\{\delta(t)\} = -\frac{1}{\pi t}$$

can be found in [2, Table 12.11].

Noting that the Hilbert transform of an impulse function is $-1/(\pi t)$, it can be seen that $s_h(t)$ might also be obtained through the convolution

$$s_h(t) = \left(-\frac{1}{\pi t}\right) * s(t). \quad (4.55)$$

Converting (4.55) to the frequency domain yields

$$S_h(f) = \mathcal{F}\{s_h(t)\} = j \operatorname{sign}(f) S(f) \quad (4.56)$$

where $S(f)$ is the Fourier transform of $s(t)$ and $\operatorname{sign}(f)$ is the signum function which equals one when $f > 0$, minus one when $f < 0$ and zero when $f = 0$.

It is important to note that some definitions of the Hilbert transform (e.g., [4, Sect. 3.3] or [5, Sect. 3.4]) use $t - \tau$ in the denominator of (4.54) rather than the $\tau - t$ used here and found in [2, p. 267] or [6, Sect. 13.7]. That is, the definition and transformed function differ by a factor of -1 .

4.5 Signal Time-Bandwidth Product

The bandwidth of a signal is a measure of the extent of its frequency content. In most applications the frequency range available for use is limited making bandwidth a precious commodity. The Fourier transform can aid in understanding the time and frequency extents of signals. Consider a rectangular pulse with temporal extent T , $\operatorname{rect}(t/T)$. Its Fourier transform is the sinc function

$$\operatorname{rect}(t/T) \xleftrightarrow{\mathcal{F}} T \operatorname{sinc}(fT) \quad (4.57)$$

which is centered at $f = 0$ and decays with oscillations as $|f|$ increases. Suppose the bandwidth is taken as the distance between the zeros on either side of the peak value of the Fourier transform. For the rectangular pulse, the bandwidth is then

$2/T$ because $\text{sinc}(fT)$ first equals zero when $fT = \pm 1$. Thus, as this signal becomes longer it consumes less bandwidth and if it is made shorter it will consume more. This intuitive inverse relationship between temporal extent and bandwidth can be more formally codified by the *time-bandwidth product*. First, however, it is necessary to precisely define the duration and bandwidth of a signal.

The bandwidth of a signal can have several definitions. The definition used in the previous example is the *null-to-null* bandwidth, taken as the extent in frequency between the nulls on either side of the peak of the Fourier transform magnitude. A more common definition of bandwidth is the *3-dB-down* bandwidth. It is the extent of the frequency band required to retain any portion of the Fourier transform with magnitude within 3 dB of the peak value. This definition essentially retains any portion of the band at least half as strong as the peak value when evaluating the squared magnitude of the Fourier transform, so it is sometimes called the *half-power bandwidth*. A third definition of bandwidth is called the *root-mean-square* (RMS) bandwidth,

$$W_{\text{RMS}} = \left[\frac{\int_{-\infty}^{\infty} (f - f_c)^2 |X(f)|^2 df}{\int_{-\infty}^{\infty} |X(f)|^2 df} \right]^{\frac{1}{2}} \quad (4.58)$$

where f_c is a measure of the center of the magnitude-squared Fourier transform,

$$f_c = \frac{\int_{-\infty}^{\infty} f |X(f)|^2 df}{\int_{-\infty}^{\infty} |X(f)|^2 df}. \quad (4.59)$$

Similar definitions can be constructed to describe the temporal extent or duration of a signal. Of particular interest is the RMS duration, defined as

$$T_{\text{RMS}} = \left[\frac{\int_{-\infty}^{\infty} (t - t_c)^2 |x(t)|^2 dt}{\int_{-\infty}^{\infty} |x(t)|^2 dt} \right]^{\frac{1}{2}} \quad (4.60)$$

where t_c is a measure of the temporal center of the signal,

$$t_c = \frac{\int_{-\infty}^{\infty} t |x(t)|^2 dt}{\int_{-\infty}^{\infty} |x(t)|^2 dt}. \quad (4.61)$$

The time-bandwidth product of a signal is simply the product of its duration and bandwidth. It typically identifies the inverse relationship between the duration of a signal and its bandwidth. For example, for real signals the time-bandwidth product, when formed using the RMS definitions, can be shown to satisfy the inequality

$$T_{\text{RMS}} W_{\text{RMS}} \geq \frac{1}{4\pi}. \quad (4.62)$$

Design constraints restricting either T_{RMS} or W_{RMS} clearly have inverse impact in the other domain. For example, designing a low-pass filter with a very low cut-off frequency (see Sect. 4.9) will require a filter with a long-duration impulse response.

The *signal* time-bandwidth product described by (4.62) relates the time- and frequency-domain extents of a signal. There is a second type of time-bandwidth product commonly used in signal processing to describe detection or estimation performance (e.g., see Sect. 2.3.5). To differentiate between the two, the one described in this section will be referred to as a *signal* time-bandwidth product whereas the other will be called a *processing* time-bandwidth product.

Example: Gaussian Shaped Signal

Consider a signal with a Gaussian shape

$$x(t) = e^{-t^2/(4\lambda^2)} \quad (4.63)$$

where λ is related to the standard deviation of the Gaussian probability distribution (see Sect. 5.6.6). The Fourier transform of (4.63) also has a Gaussian shape,

$$X(f) = 2\lambda\sqrt{\pi}e^{-4\lambda^2\pi^2f^2}. \quad (4.64)$$

The RMS bandwidth and duration of the signal are, respectively,

$$W_{\text{RMS}} = \frac{1}{4\pi\lambda} \quad (4.65)$$

and

$$T_{\text{RMS}} = \lambda. \quad (4.66)$$

Recalling that the standard deviation (and therefore λ in this example) is a measure of spread in a probability density function, it is not surprising for the RMS duration of $x(t)$ to be related to λ . The inverse relationship between

(continued)

bandwidth and signal duration is clearly seen in (4.65), indicating a shorter duration signal requires a commensurately higher bandwidth.

The *signal* time-bandwidth product for a Gaussian shaped function is a constant with respect to λ ,

$$T_{\text{RMS}} W_{\text{RMS}} = \frac{1}{4\pi}, \quad (4.67)$$

which achieves the lower bound in (4.62). Thus, the Gaussian shaped signal may be considered efficient with respect to the RMS bandwidth required to achieve a specific RMS duration. Unfortunately, in practice it is usually more important to ensure signals do not extend significantly beyond a design frequency band and this is not captured in the RMS measure of bandwidth.

4.6 Converting Analog Signals to Digital Signals

As described in Sect. 2.2.1, acoustical remote sensing systems convert acoustic pressure measurements into voltages. The voltage signals are analog; that is, they are continuous in time and continuous in value (although usually bounded). Most signal processing is implemented after the continuous signals have been digitized, which means they are *sampled* in time and *quantized* in value. The sampling process converts a continuous-time signal to a discrete-time signal, retaining the continuity of value. The quantization step is a sampling in value to convert the discrete-time, continuous-valued signal to a finite set of levels. When a continuous signal has been digitized properly, it can be reconstructed with negligible error.

Signal processing algorithms can be designed and analyzed using either or both continuous-time and discrete-time signal and system representations. Both approaches will be used throughout this book, depending on the situation. For discrete-time analysis, it is usually assumed the signals are continuous-valued (i.e., the effects of quantization are negligible).

4.6.1 Sampling and Aliasing

Sampling a continuous signal in time entails extracting the signal value at periodic intervals. If the period of the sampling is T and the sampling begins at $t = 0$, the continuous-time signal $x(t)$ becomes the sequence

$$x(0), x(T), x(2T), x(3T), \dots \quad (4.68)$$

These samples form a discrete-time signal. To distinguish discrete-time signals from continuous-time signals, a bracket is used as opposed to parentheses and an integer time-sample index is used in lieu of a continuous independent variable; e.g.,

$$x[n] = x(nT) \quad (4.69)$$

for $n = 0, \pm 1, \pm 2, \dots$. The general rule for choosing a sampling time is that the signal should change very little between samples. Consider a sinusoidal signal with frequency f_0 as shown in Fig. 4.3. Three sampling scenarios are shown in the figure. Undersampling occurs when there is too much change in the signal between consecutive samples (i.e., the samples are too far apart). The consequence of undersampling is a failure to capture all of the information in a continuous-time signal, resulting in an inability to accurately represent or recreate the signal. In the example shown in Fig. 4.3, undersampling would lead to assuming the sinusoid had a much lower frequency, a phenomena called aliasing. Oversampling occurs when not enough happens between samples. The primary consequences of oversampling are the additional storage and computational requirements of processing digital signals at a higher rate than necessary. Good sampling obtains enough samples to accurately represent and reconstruct the continuous-time signal without wasting computational resources.

In order to satisfy the requirement for *no significant changes between samples*, the frequency content of a signal must be limited prior to sampling. If the highest

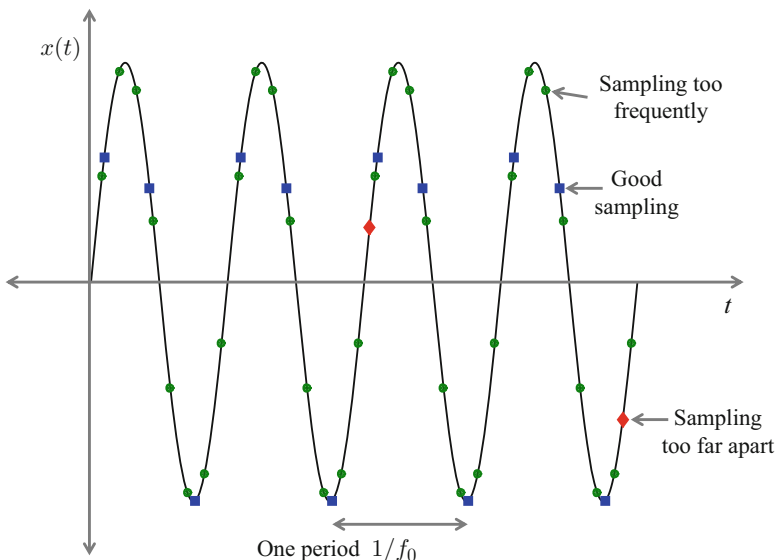


Fig. 4.3 Sampling a sinusoidal signal

frequency in the signal to be sampled is f_{\max} , then the signal must be sampled at sampling rate

$$f_s \geq 2f_{\max}. \quad (4.70)$$

The sampling rate $f_s = 2f_{\max}$ is known as the *Nyquist rate*; it is the lowest sampling rate for which a signal with maximum frequency f_{\max} can be reconstructed [7, Sect. 3.3]. The *Nyquist frequency* is half the Nyquist rate and represents the highest frequency in a signal that can be reconstructed when sampling occurs at the Nyquist rate.

To evaluate the impact of sampling on the frequency content of a signal, the sampled signal is represented as a continuous signal comprising a sequence of impulse functions spaced every T with weight $x[n] = x(nT)$,

$$x_s(t) = x(t) \sum_{i=-\infty}^{\infty} \delta(t - iT) \quad (4.71)$$

so $x_s(t)$ is zero when t is not an integer multiple of T and the information in the sampled signal (i.e., $x(nT)$) is retained by the impulse at $t = nT$. The impulse train in (4.71) is a periodic signal and can be described by a Fourier series (e.g., see [3, Ch. 6] or [2, Ch. 10]) expansion,

$$\begin{aligned} p(t) &= \sum_{i=-\infty}^{\infty} \delta(t - iT) \\ &= \frac{1}{T} \sum_{k=-\infty}^{\infty} e^{j2\pi kf_st} \end{aligned} \quad (4.72)$$

where $f_s = 1/T$. Using the modulation property from (4.35), the Fourier transform of $x_s(t)$ is seen to be the Fourier transform of the original continuous signal repeated at integer multiples of the sampling frequency,

$$X_s(f) = \frac{1}{T} \sum_{k=-\infty}^{\infty} X(f - kf_s). \quad (4.73)$$

A graphical representation of the repeated Fourier transforms is shown in Fig. 4.4 where the maximum frequency is less than half the sampling rate (i.e., satisfying (4.70)). The Nyquist sampling requirement can be described as being satisfied when the repetitions of the Fourier transform of the original signal (centered at $0, \pm f_s, \pm 2f_s, \dots$) do not overlap. An exact copy of the Fourier transform of the original signal is found centered at every integer multiple of the sampling rate.

When the sampling frequency is less than twice the highest frequency component of a signal, the repetitions of $X(f)$ overlap, as seen in Fig. 4.5. The folding of higher frequency signal components to lower frequencies is called *aliasing*. When aliasing occurs, there is no exact copy of the Fourier transform of the original signal, but

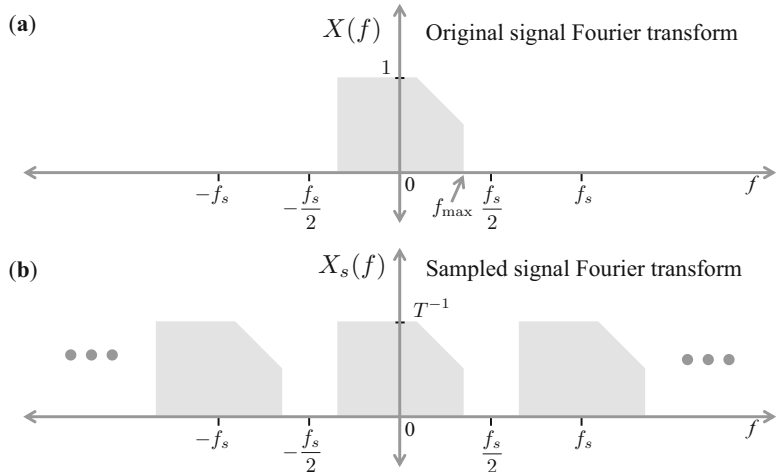


Fig. 4.4 Fourier transform of (a) original signal and (b) sampled signal with proper sampling

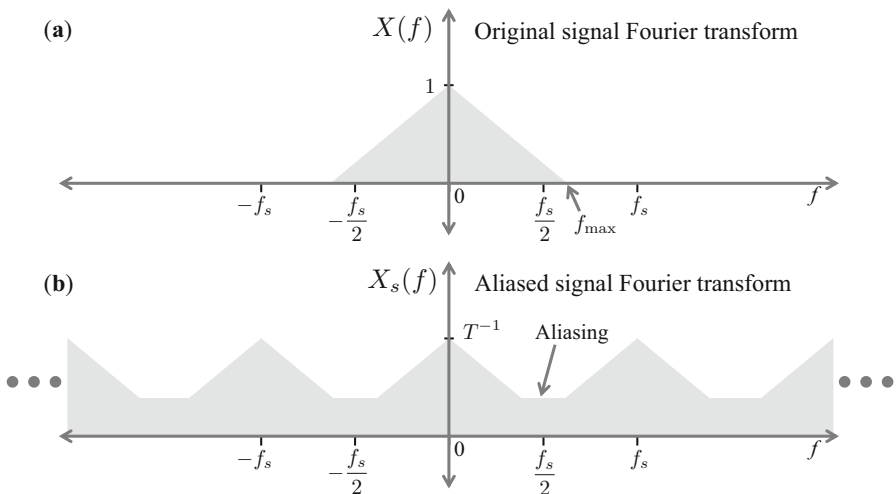


Fig. 4.5 Fourier transform of (a) original signal and (b) sampled signal with aliasing

rather an indistinguishable combination of the signal components at frequencies above and below the Nyquist frequency. Because of this corruption, the sampled signal cannot be reconstructed to the original one.

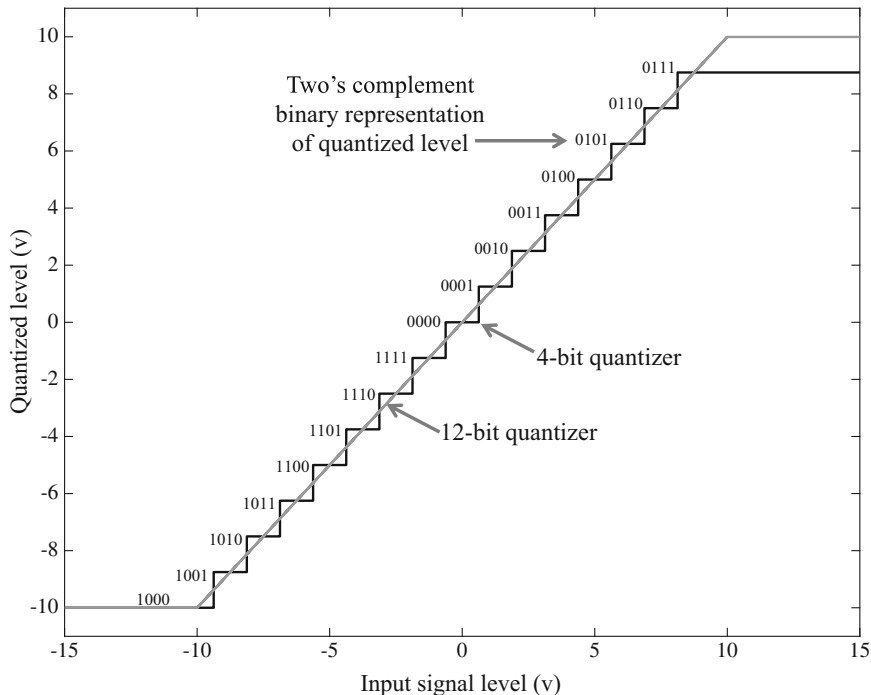


Fig. 4.6 Quantization example showing 4- and 12-bit quantization functions for a maximum amplitude of 10 v

4.6.2 Quantization

The discussion of sampling and aliasing earlier in this section assumed the sampled signal was still continuously valued (recall $x[n] = x(nT)$ and $x(t)$ was continuously valued). In practice sampled signals are represented by finite-length binary numbers in a process called *quantization* to enable digital signal processing. Quantization is performed by mapping continuous values to a finite set of quantization levels as illustrated by the example quantization functions shown in Fig. 4.6. The $B = 4$ bit quantizer uses one bit to represent sign and three bits to represent magnitude, leading to $2^B = 16$ levels. The two's complement [8, Sect. 6.7.1] binary representation, where the most-significant-bit is used to represent sign, is shown for the 4-bit quantizer. Clearly a 4-bit quantizer leads to a coarse sampling of the continuous-valued input. The 12-bit quantizer is seen to provide a much lower quantization error and will be adequate for most applications.

Quantization error is usually assumed to be uniformly distributed (see Example 5.3.2 or Sect. 5.6.4) about each quantization level, extending halfway to the adjacent levels. Thus, the variance of the quantization error is

$$\sigma_Q^2 = \frac{\Delta^2}{12} \quad (4.74)$$

where $\Delta = A/2^{B-1}$ is the distance between levels when the maximum amplitude to be quantized is A and B bits are used in the quantizer. As seen in Fig. 4.6, the range of values quantized is $[-A, A - \Delta]$ and one of the levels is zero. An alternative quantization technique shifts the step function in Fig. 4.6 up by $\Delta/2$ so there are levels at $\pm\Delta/2$ but not zero.

When implementing a quantizer, it is important to ensure not only to choose A to capture the largest magnitude signal of interest, but also to choose B large enough to capture the smallest magnitude signal of interest. For example, if the smallest signal of interest was always in the range ± 1 v, the 4-bit quantizer in Fig. 4.6 (for which $\Delta = 1.25$) would only return the three levels 1111, 0000, and 0001. Depending on the application, this might be too coarse of a quantization. The dynamic range of a quantizer measures its ability to represent small signals relative to the saturation limit (A). The dynamic range of the quantizer is the ratio in decibels of the largest to smallest magnitude signals representable,

$$DR_Q = 20 \log_{10}(2^{B-1}) \approx 6.021(B - 1). \quad (4.75)$$

In the above example, the smallest signal of interest is $20 \log_{10}(10/1) = 20$ dB below the largest. The 4-bit quantizer yields a dynamic range of 18 dB, which is insufficient to represent the 1-v signal. The 12-bit quantizer with a 66 dB dynamic range is clearly sufficient.

The dynamic range criterion does not provide a clear indication of how accurately a small signal is represented. If the amplitude of the smallest signal of interest has peak amplitude A_0 , then the peak signal-of-interest to quantization noise power ratio (SQNR) is

$$\begin{aligned} SQNR &= 10 \log_{10} \left(\frac{A_0^2}{\sigma_Q^2} \right) \\ &= DR_Q + 10 \log_{10}(12) - DR_s \\ &\approx 6.021(B - 1) + 10.8 - DR_s \end{aligned} \quad (4.76)$$

where

$$DR_s = 20 \log_{10} \left(\frac{A}{A_0} \right) \quad (4.77)$$

is the dynamic range between the largest and smallest signal of interest. Ideally, quantization noise is small relative to the dominating physical noise inherent in the sensing application (e.g., reverberation or ambient ocean noise). In the example where $DR_s = 20$ dB, the 4-bit quantizer yields $SQNR = 9$ dB, indicating

quantization noise will dominate in many applications; the 12-bit quantizer with SQNR = 57 dB will almost always be adequate.

4.7 Discrete-Time Signals and Systems

The continuous-time signal and system theory and analysis presented in Sects. 4.2 and 4.3 can be extended to discrete-time signals and systems. The basic representations and formulas are presented here for LTI systems without derivation. References for discrete-time signals and systems include [3, 8].

Let the operator \mathcal{H} represent the input–output relationship of a discrete-time system with input $x[n]$ and output $y[n]$,

$$y[n] = \mathcal{H}\{x[n]\}. \quad (4.78)$$

An impulse function in discrete time is the Kronecker delta function,

$$\delta[n] = \begin{cases} 1 & \text{if } n = 0 \\ 0 & \text{otherwise.} \end{cases} \quad (4.79)$$

When the input to a discrete-time system is $\delta[n]$, the output is the impulse response,

$$h[n] = \mathcal{H}\{\delta[n]\}. \quad (4.80)$$

If the system is linear and time invariant, then the operator \mathcal{H} can be represented as a convolution sum,

$$\begin{aligned} y[n] &= \sum_{m=-\infty}^{\infty} h[m]x[n-m] = \sum_{m=-\infty}^{\infty} x[m]h[n-m] \\ &= h[n] * x[n] = x[n] * h[n]. \end{aligned} \quad (4.81)$$

If the input to an LTI system with impulse response $h[n]$ is a complex sinusoid with frequency ψ ,

$$x[n] = e^{j2\pi\psi n} \quad (4.82)$$

the output is

$$\begin{aligned} y[n] &= \mathcal{H}\left\{e^{j2\pi\psi n}\right\} \\ &= \sum_{m=-\infty}^{\infty} \left[h[m]e^{-j2\pi\psi m} \right] e^{j2\pi\psi n} \end{aligned}$$

$$= H(\psi) e^{j2\pi\psi n}. \quad (4.83)$$

The function

$$H(\psi) = \sum_{n=-\infty}^{\infty} h[n] e^{-j2\pi\psi n} \quad (4.84)$$

is the frequency response of the system and the Fourier transform of $h[n]$. As with continuous-time LTI systems, the zero-state response to a complex sinusoid is a sinusoid of the same frequency with amplitude and phase altered by the frequency response of the system, $H(\psi)$.

4.7.1 Fourier Transform of a Discrete-Time Signal

In Sect. 4.6, the Fourier transform of a sampled continuous-time signal was shown to be the transform of the continuous signal repeated about integer multiples of the sampling frequency. More formally, the Fourier transform of a discrete-time signal $x_d[n]$ is

$$X_d(\psi) = \sum_{n=-\infty}^{\infty} x_d[n] e^{-j2\pi\psi n} \quad (4.85)$$

where ψ is frequency in cycles per sample. The subscript d is used to emphasize the discrete-time nature of the signal and its Fourier transform. Because of the periodicity of the complex sinusoid for any integer k ,

$$e^{-j2\pi\psi n} = e^{-j2\pi(\psi+k)n}, \quad (4.86)$$

the Fourier transform is also periodic

$$X_d(\psi) = X_d(\psi + k). \quad (4.87)$$

As such, $X_d(\psi)$ only needs to be evaluated for $\psi \in [-0.5, 0.5]$ or any other suitable interval covering one full period. The form of (4.85) can be recognized as the Z transform of $x_d[n]$ evaluated on the unit circle with $2\pi\psi$ representing the angle in radians, which also explains why only one period needs to be evaluated. The Fourier transform in (4.85) can also be related to that in (4.73) for a sampled continuous-time signal according to

$$X_d(\psi) = X_s(\psi f_s), \quad (4.88)$$

which converts ψ in cycles per sample to $f = \psi f_s$ in cycles per second. This can also be seen by noting ψn in the exponent of (4.85) is identical to the corresponding term in the definition of the Fourier transform (i.e., ft) used to form (4.73),

$$\psi n = (\psi f_s)(nT) = ft. \quad (4.89)$$

To recover the discrete-time signal from its Fourier transform, the inverse transform of the original continuous-time signal (assuming no aliasing) can be used when it is evaluated at $t = nT$,

$$\begin{aligned} x_d[n] = x(nT) &= \int_{-f_s/2}^{f_s/2} X(f) e^{j2\pi fnT} df \\ &= \int_{-\frac{1}{2}}^{\frac{1}{2}} f_s X(\psi f_s) e^{j2\pi \psi f_s nT} d\psi = \int_{-\frac{1}{2}}^{\frac{1}{2}} X_d(\psi) e^{j2\pi \psi n} d\psi. \end{aligned} \quad (4.90)$$

4.7.2 Properties of the Fourier Transform of Discrete-Time Signals

Fourier transforms of discrete-time signals have very similar properties to those discussed in Sect. 4.3. Properties not having an essentially identical form to those for continuous-time signals are shown here.

Time Delay If a signal $x[n]$ is delayed by m time samples, its Fourier transform changes only in the phase,

$$x[n - m] \xleftrightarrow{\mathcal{F}} e^{-j2\pi \psi m} X(\psi). \quad (4.91)$$

Modulation Suppose a signal $x[n]$ is modulated by a complex sinusoid with frequency ψ_0 . The Fourier transform of the modulated signal,

$$x[n] e^{j2\pi \psi_0 n} \xleftrightarrow{\mathcal{F}} X(\psi - \psi_0), \quad (4.92)$$

is a frequency-shifted version of the Fourier transform of the original signal. Modulating a signal by a cosine results in the Fourier transform pair

$$\cos(2\pi \psi_0 n) x[n] \xleftrightarrow{\mathcal{F}} \frac{X(\psi - \psi_0)}{2} + \frac{X(\psi + \psi_0)}{2}. \quad (4.93)$$

Convolution The Fourier transform of the discrete-time convolution between two signals is the product of the Fourier transforms of the individual signals,

$$x[n] * y[n] \xleftrightarrow{\mathcal{F}} X(\psi)Y(\psi), \quad (4.94)$$

where $y[n] \xleftrightarrow{\mathcal{F}} Y(\psi)$. Similarly, a convolution in the frequency domain results in a product in the time domain,

$$x[n]y[n] \xleftrightarrow{\mathcal{F}} X(\psi) * Y(\psi) = \int_{-\frac{1}{2}}^{\frac{1}{2}} X(\psi - s)Y(s) ds. \quad (4.95)$$

Parseval's Theorem The energy in a discrete time signal can be obtained from its Fourier transform according to

$$\begin{aligned} \mathcal{E} &= \sum_{n=-\infty}^{\infty} |x[n]|^2 \\ &= \int_{-\frac{1}{2}}^{\frac{1}{2}} |X(\psi)|^2 d\psi. \end{aligned} \quad (4.96)$$

4.8 Discrete and Fast Fourier Transforms (DFT and FFT)

In practical applications signals are generally measured and analyzed over short time periods. This is often required when signals are time-varying but can be assumed stationary over short durations. It also ameliorates the computational difficulties in analyzing very long signals. Suppose a continuous-time signal $x_c(t)$ is sampled every $T = 1/f_s$ to produce the discrete time signal $x_d[n]$ for $n = 0, \pm 1, \pm 2, \dots$. If only the samples $x_d[0], \dots, x_d[N-1]$ are available for analysis and the signal is assumed to be zero outside of these samples, the Fourier transform is

$$X_d(\psi) = \sum_{n=0}^{N-1} x_d[n]e^{-j2\pi\psi n}. \quad (4.97)$$

Although $X_d(\psi)$ only needs to be evaluated for $\psi \in [-0.5, 0.5]$, the range $[0, 1]$ may be used equivalently noting the periodicity in ψ (i.e., $X_d(\psi) = X_d(\psi \pm 1)$). Evaluating $X_d(\psi)$ at frequencies $\psi_k = k/N$ for $k = 0, \dots, N-1$ produces what is called the *discrete Fourier transform* (DFT),

$$X_p(k) = X_d\left(\frac{k}{N}\right) = \sum_{n=0}^{N-1} x_d[n]e^{-j2\pi kn/N} \quad (4.98)$$

where the meaning of the subscript p will be explained shortly. The frequency ψ_k in terms of cycles per second is

$$f_k = \begin{cases} \left(\frac{k}{N}\right) f_s & \text{for } 0 \leq k < \frac{N}{2} \\ \left(\frac{k-N}{N}\right) f_s & \text{for } \frac{N}{2} \leq k \leq N-1 \end{cases} \quad (4.99)$$

where the periodicity of $X_d(\psi)$ is exploited to map the range $\psi \in [0.5, 1)$ to $f \in [-f_s/2, 0)$. These are the frequencies evaluated when the DFT is used to determine the spectral content of the continuous signal $x_c(t)$ from which the samples $x_d[n] = x_c(nT)$ are obtained.

The DFT is an important tool in signal processing owing to an algorithm [9] providing an efficient computational evaluation of $X_p(k)$ when N is a power of 2. The algorithm is known as the *fast Fourier transform* (FFT) and provides $X_p(k)$ with $O(N \log_2 N)$ operations as opposed to the $O(N^2)$ operations of a direct implementation. The FFT exploits symmetry and periodicity in the complex exponential terms $e^{-j2\pi kn/N}$ of (4.98). Although the most common algorithms require N to be a power of two, fast algorithms can be developed for other factorizations [10, Sect. 8.10].

The DFT forms a set of N linear equations mapping the temporal values $x_d[0], \dots, x_d[N - 1]$ to the frequency values $X_p(0), \dots, X_p(N - 1)$. Given the frequency values, the temporal values can be reconstructed precisely using the inverse mapping (i.e., the inverse DFT),

$$x_d[n] = \frac{1}{N} \sum_{k=0}^{N-1} X_p(k) e^{j2\pi kn/N}, \quad (4.100)$$

for $n = 0, \dots, N - 1$. If the definition in (4.100) is used to define a time domain signal for all integer values of n , say $x_p[n]$, the reconstructed signal is seen to be periodic with period N ,

$$\begin{aligned} x_p[n] &= \frac{1}{N} \sum_{k=0}^{N-1} X_p(k) e^{j2\pi kn/N} \text{ for } n = 0, \pm 1, \pm 2, \dots \\ &= \frac{1}{N} \sum_{k=0}^{N-1} X_p(k) e^{j2\pi k(n+N)/N} \\ &= x_p[n + N], \end{aligned} \quad (4.101)$$

which explains the subscript p in (4.98). The signal $x_p[n]$ is called the periodic extension of $x_d[n]$. Recalling how sampling in time resulted in a repeated (or periodic) spectrum in the frequency domain, it is not surprising (based on the duality of the Fourier transform) that the sampling in frequency enacted by the DFT has resulted in periodicity in time. If $x_p[n]$ is periodic with period N , it can also be represented through the discrete Fourier series, which is a weighted sum of the fundamental frequency and harmonics of a complex sinusoid. The discrete Fourier series coefficients of $x_p[n]$ are $X_p(k)$ from (4.98) and the synthesis equation is precisely the inverse DFT in (4.100).

The DFT is often used to approximate the Fourier transform of a continuous-time signal. Suppose the signal $x_c(t)$ is non-zero only for $t \in [-T/2, NT - T/2]$ and

Table 4.1 Sampled signal and Fourier transform relationships

Description	Continuous	Discrete	Discrete/periodic extension
Signal	$x_c(t)$	$x_d[n] = x_c(nT)$	$x_p[n] = x_d[n]$ for $n \in [0, N - 1]$ $x_p[n] = x_p[n + N]$ for all n
Signal support	$t \in (-\infty, \infty)$	$n = 0, \pm 1, \pm 2, \dots$	Unique for $n \in [0, N - 1]$
Fourier transform	$X_c(f)$	$X_d(\psi) = f_s X_c(\psi f_s)$	$X_p(k) = X_d\left(\frac{k}{N}\right)$
Frequency support	$f \in (-\infty, \infty)$	$\psi \in \left(-\frac{1}{2}, \frac{1}{2}\right)$	$k = 0, \dots, N - 1$
Frequency units	Cycles/s	Cycles/sample	DFT index
Section	4.3	4.7	4.8

$x_p[n] = x_c(nT)$ for $n = 0, \dots, N - 1$. Then the Fourier transform $X_c(f)$, evaluated at the frequencies defined by (4.99), is approximated by

$$\begin{aligned}
 X_c(f_k) &= \int_{-\infty}^{\infty} x_c(t) e^{-j2\pi f_k t} dt \\
 &\approx T \sum_{n=0}^{N-1} x_c(nT) e^{-j2\pi f_k nT} \\
 &= T \sum_{n=0}^{N-1} x_p[n] e^{-j2\pi kn/N} \\
 &= T X_p(k).
 \end{aligned} \tag{4.102}$$

Three interpretations of the DFT have been discussed in this section. To summarize, the DFT can be considered as

- the Fourier transform of a discrete-time signal $x_d[n]$ assumed to be zero outside of $n \in [0, N - 1]$,
- an approximation to the Fourier transform of a continuous-time signal $x_c(t)$ assumed to be zero outside of $t \in [-T/2, N - T/2)$ when $x_d[n] = x_c(nT)$, or
- the coefficients of the discrete Fourier series of $x_p[n]$, the periodic extension of $x_d[n]$.

The relationships between the continuous-time, discrete-time, and discrete-time-periodic-extensions signals and their Fourier transforms are summarized in Table 4.1.

4.9 Discrete-Time Filtering (LPF, HPF, and BPF)

One of the most common operations in the processing of underwater acoustic signals is filtering. Sensors in measurement systems are often sensitive over a wide range of frequencies, extending well beyond those necessary for any given application. The frequency content of interest can be isolated with a bandpass filter, which ideally allows any signal within the desired band (called the pass-band) through with unit gain and no change in phase while rejecting any signal content at other frequencies (the stop-band). In practice a filter's frequency response, as seen in Fig. 4.7, only approximates the ideal. It typically exhibits ripple in the pass-band, does not fully reject signals in the stop-band, and requires a non-zero gap in the transition between the pass-band and stop-band (i.e., the transition band).

There are several other common types of filters similar to bandpass filters for isolating different portions of the frequency domain [7, Sect. 8.2], [11, Ch. 8]. Low-pass filters (LPFs) retain signals below a cut-off frequency f_c whereas high-pass filters (HPFs) retain signals above f_c . A notch filter, which is the inverse of a bandpass filter, rejects signals within a given band. An all-pass filter ideally allows all signals through while imparting a specific delay. Most of these filter types can be designed by starting with an LPF and transforming it to the appropriate shape [11, Sect. 8.3]. As such, design often focuses on LPFs.

Although filters are generally designed to attenuate specific frequencies, practical filters also impart a non-zero delay between the input and output. The delay the signal envelope incurs when passing through the filter is known as the *group delay*. In general group delay is frequency dependent and proportional to the negative slope of the phase response ($\angle H(\psi)$) of the filter,

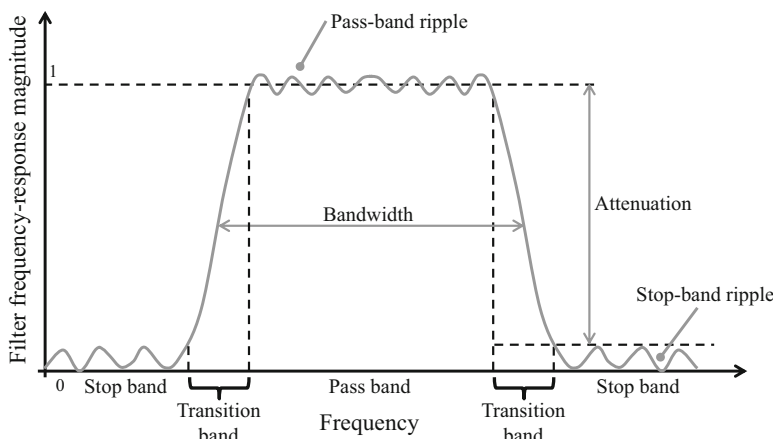


Fig. 4.7 Bandpass filter example frequency-response magnitude and design parameters

$$\tau_d(\psi) = -\frac{1}{2\pi} \frac{\partial}{\partial \psi} \angle H(\psi). \quad (4.103)$$

Because ψ has units of cycles per sample and $\angle H(\psi)$ radians, $\tau_d(\psi)$ has units of samples. When the phase response of a filter is linear in the pass-band, the group delay is constant and equates to a frequency-independent time delay of the input signal. In underwater acoustic signal processing applications for which time-delay estimation is the objective, properly accounting for the time delays introduced by filtering is imperative.

4.9.1 FIR and IIR Filters

As with LTI continuous-time systems, discrete-time LTI filters are completely described by their impulse response, which can be described as having either finite or infinite temporal extent. A finite-impulse-response (FIR) filter has non-zero impulse response only over a finite number of time samples. In contrast, an infinite-impulse-response (IIR) filter has an impulse response that continues infinitely, although it necessarily decays to zero. Examples of impulse responses for bandpass FIR and IIR filters are shown in Fig. 4.8 illustrating the difference.

In the example, both the FIR and IIR filters have 16 coefficients implying the computational costs of a direct implementation are equivalent. However, the impulse

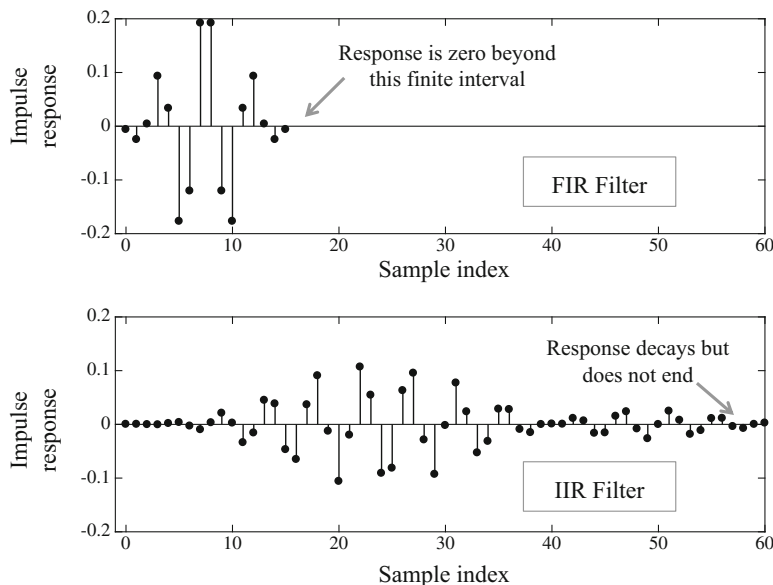


Fig. 4.8 Bandpass-filter impulse response examples for FIR and IIR filters

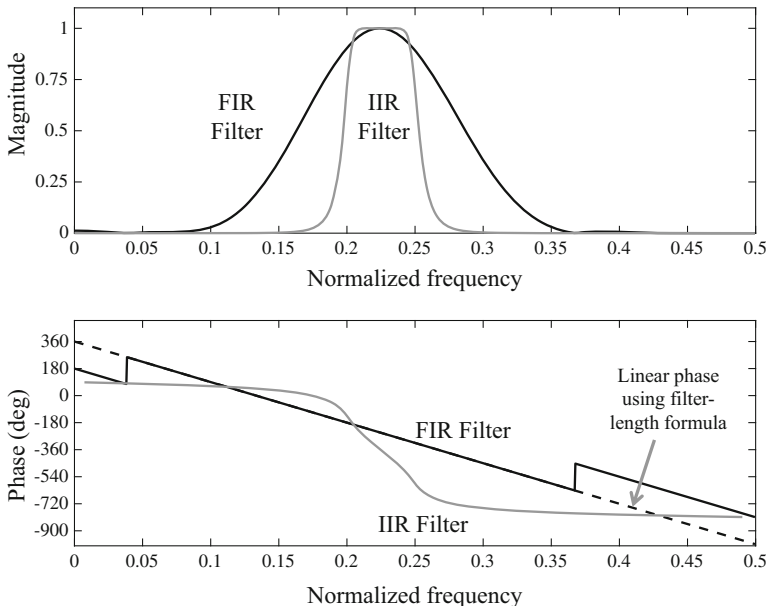


Fig. 4.9 Bandpass-filter frequency response examples for FIR and IIR filters

response of the IIR filter appears delayed relative to the FIR filter and it has a larger RMS duration. The difference in the frequency response of the filters is even more dramatic as seen in Fig. 4.9. The filters were designed to pass the frequency band [0.2, 0.25], which the IIR filter does quite well. The sharp transition from the pass-band to the stop-band is typical of IIR filters; FIR filters with the same number of coefficients cannot match this. The cost, however, is evident in the phase response seen in the bottom pane of Fig. 4.9 where the IIR filter exhibits a non-linear phase with a steeper slope in the pass-band. The steeper slope of the phase implies a longer group delay, which is related to the delayed impulse response seen in Fig. 4.8. The non-linear phase implies signals at different frequencies are subject to different delays, which can distort acoustic signals. This is the primary reason to use FIR filters over IIR filters when processing underwater acoustic signals and why the focus of this section is on FIR filters rather than IIR filters.

Any FIR filter with symmetric or anti-symmetric coefficients will have a linear phase in the pass-band. The group delay is therefore constant over frequency and equal to

$$\tau_d(\psi) = \frac{M - 1}{2} \quad (4.104)$$

where M is the size of the filter. The size of an FIR filter is the number of coefficients required to implement the filter (assuming no delays are skipped). An FIR filter

of size M is said to have order $M - 1$ because it is the order of the Z -transform polynomial describing the filter transfer function. This is also representative of the number of input delays required to implement the filter.

4.9.2 FIR Filter Design

There are many techniques available for designing filters [7, Ch. 8], even when restricting consideration to discrete-time FIR filters. Common approaches include (i) converting analog filters to digital, (ii) specifying the frequency response and computationally obtaining the best filter of a given size, and (iii) approximating the optimal filter. Even a partial treatment of filter design is beyond the scope of this review section, so only one procedure is provided (the last in the above list) with enough details to enable design of an LPF or BPF meeting a design specification.

An approximation technique that is straightforward to apply entails using a window function (see Sect. 4.10) to smoothly shorten the impulse response of an ideal filter. The ideal filter, as previously described, has unit gain in the pass-band, immediately transitions from the pass-band to the stop-band, and fully rejects all signals in the stop-band. For example, the frequency response of an ideal LPF with cut-off frequency $\psi_c = f_c/f_s$ is $H(\psi) = \text{rect}(\psi/(2\psi_c))$. The impulse response of this ideal LPF is

$$h_{\text{ILP}}[n] = 2\psi_c \text{sinc}(2\psi_c n), \quad (4.105)$$

which peaks at and is centered about $n = 0$. As the ideal filter is non-causal (i.e., the impulse response has non-zero values for some $n < 0$), a practical filter must apply a delay of $(M - 1)/2$ where M is the desired filter size and remove all non-zero values from the impulse response for $n < 0$. The windowing approach to filter design accomplishes this by applying a window $w[n]$ active only on $[0, M - 1]$ to the ideal filter impulse response ($h_{\text{Ideal}}[n]$) after it is delayed by $(M - 1)/2$ samples to produce the FIR filter coefficients

$$h[n] = w[n]h_{\text{Ideal}}\left[n - \frac{M - 1}{2}\right] \quad (4.106)$$

for $n = 0, \dots, M - 1$. As window functions are generally symmetric about their center and because $h_{\text{ILP}}[n]$ is symmetric about the origin, the practical LPF designed by this technique will be linear phase. When the maximum of the window function $w[n]$ is set to one, the average pass-band gain remains at unity as in the ideal LPF. Scaling the filter coefficients $h[n]$ so they sum to one produces unit gain for a constant input, which is very similar to unit average pass-band gain for an LPF, but not precisely the same.

LPF design starts by specifying the pertinent filter characteristics:

Cut-off frequency: $\psi_c = f_c/f_s$ where $\psi_c = 0.5$ represents half the sampling rate,

Transition-band width: $\psi_{tb} = f_{tb}/f_s$; the transition band spans $\psi_c \pm \psi_{tb}/2$,

Pass-band ripple: Δ_{dB} , the maximum deviation from zero decibels (unit gain) in the pass band, and

Stop-band attenuation: A_{dB} , a positive number of decibels.

One of the difficulties in filter design lies in choosing the filter size M . From [12, Sect. 5.10.5], M can be approximately related to attenuation and transition-band width according to

$$M \approx \frac{A_{dB}}{22\psi_{tb}} \quad (4.107)$$

where the pass-band ripple is assumed to be approximately 0.1 dB. As might be expected, a narrow transition band or high attenuation in the stop band requires a large filter order. As this is an approximation, it should be used as a starting point for design with the final filter evaluated to determine if it meets the specification.

Consider as an example using a Kaiser window (Sect. 4.10.5), which can be designed to trade off main-lobe width and sidelobe energy by appropriately choosing the window parameter β . Porat [7, Sect. 9.3] provides empirical relationships (shown below) between the filter specification and the Kaiser window design parameters, significantly simplifying filter design.

Recalling the convolution property of the Fourier transform, windowing the ideal-filter impulse response is equivalent to convolving the ideal-filter frequency response and the Fourier transform of the window function. Thus, the sidelobes of the Fourier transform of the window function affect both the filter attenuation and the pass-band ripple. To account for this in a manner similar to (4.107), an equivalent *attenuation* requirement related to pass-band ripple is defined as

$$P_{dB} = -20 \log_{10} \left(10^{\Delta_{dB}/20} - 1 \right) \quad (4.108)$$

and the overall attenuation is chosen to satisfy the stricter requirement,

$$\tilde{A}_{dB} = \max\{A_{dB}, P_{dB}\}. \quad (4.109)$$

When the stop-band attenuation dominates the pass-band attenuation requirement, the pass-band ripple will be dominated by the filter response at the lower end of the transition band. The Kaiser window parameter β and the filter size M are then chosen according to [7, Sect. 9.3],

$$\beta = \begin{cases} 0.1102(\tilde{A}_{dB} - 8.7) & \text{for } \tilde{A}_{dB} > 50 \\ 0.5842(\tilde{A}_{dB} - 21)^{0.4} + 0.07886(\tilde{A}_{dB} - 21) & \text{for } 21 < \tilde{A}_{dB} \leq 50 \\ 0 & \text{for } \tilde{A}_{dB} \leq 21 \end{cases} \quad (4.110)$$

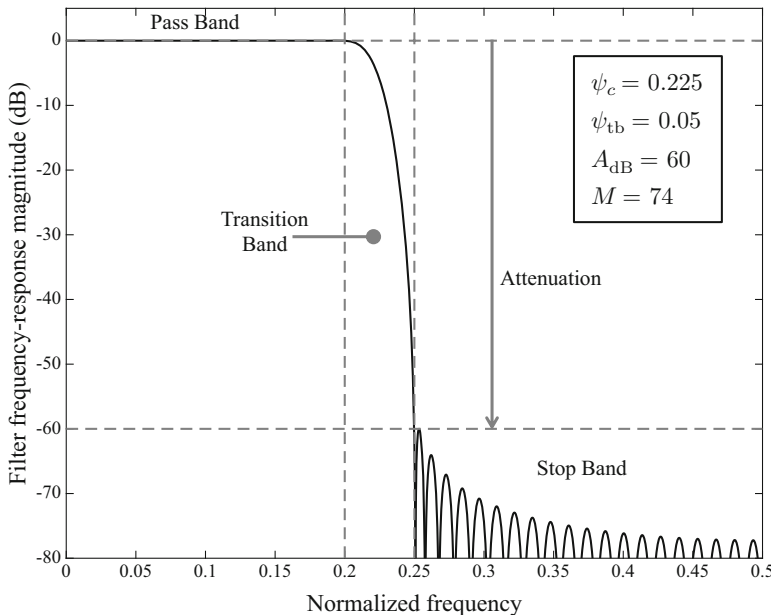


Fig. 4.10 Low-pass-filter design example

and

$$M = \frac{\tilde{A}_{\text{dB}} - 7.95}{2.285(2\pi\psi_{\text{tb}})} + 1 \approx \frac{\tilde{A}_{\text{dB}} - 7.95}{14.36\psi_{\text{tb}}} + 1. \quad (4.111)$$

When M is not an integer, it needs to be increased to the nearest odd or even one depending on the situation. For example, if the Kaiser window is to be used to form an HPF, then M should be odd (which is an even filter order) so as to not reject signals exactly at the Nyquist frequency.

An example LPF frequency-response magnitude arising from the specification $\psi_c = 0.225$, $\psi_{\text{tb}} = 0.05$, $A_{\text{dB}} = 60$, and $M = 74$ is shown in Fig. 4.10. Using (4.111), a filter size of $M = 74$ is observed to meet the specification.

4.9.3 Bandpass and High-Pass Filters

Recalling the modulation property of the Fourier transform, a BPF can be constructed from an LPF by modulating the impulse response with a cosine at the center frequency of the desired pass-band ($\psi_{\text{BP}} = f_{\text{BP}}/f_s$). Taking the impulse response of an ideal LPF with cutoff frequency $\psi_c = f_c/f_s$ from (4.105), which is centered at the origin, the transformation

$$\begin{aligned} h_{\text{IBP}}[n] &= 2h_{\text{ILP}}[n] \cos(2\pi n \psi_{\text{BP}}) \\ &= 2\psi_w \text{sinc}(\psi_w n) \cos(2\pi n \psi_{\text{BP}}) \end{aligned} \quad (4.112)$$

creates an ideal BPF with pass-band width $\psi_w = 2\psi_c$ (i.e., $f_w = 2f_c$) because the LPF is designed to pass both positive and negative frequencies, $\psi \in (-\psi_c, \psi_c)$, and the modulation shifts the whole pass-band to be centered at ψ_{BP} rather than being centered at $\psi = 0$.

The ideal impulse response of an HPF with cut-off frequency ψ_c is

$$h_{\text{IHP}}[n] = \text{sinc}(n) - 2\psi_c \text{sinc}(2\psi_c n), \quad (4.113)$$

which is essentially an ideal all-pass filter minus an ideal low-pass filter. When (4.113) is delayed by $(M - 1)/2$ for M odd, the $\text{sinc}(n)$ simplifies to an impulse function $\delta[n]$. When M is even, the $\text{sinc}(n)$ must be used to obtain the proper response. However, when M is even the HPF will have zero gain at the Nyquist frequency $\psi = 1/2$. As such, only odd size FIR filters should be used for HPFs.

4.9.4 FIR Filter Implementation

The convolution sum in (4.81) for an FIR filter of size M simplifies to

$$y[n] = \sum_{m=0}^{M-1} x[n-m]h[m]. \quad (4.114)$$

Implementing the filter requires M multiplications and $M - 1$ additions for every output sample; that is, on the order of M computational operations, $O(M)$.

Recalling that convolution in the time domain is a product in the frequency domain, the output $y[n]$ could be obtained by forming the DFT of the input and impulse response (respectively, $X(\psi)$ and $H(\psi)$) and then taking the inverse DFT of their product. If the size of the DFT is a power of 2, an FFT can be used as an efficient means to compute the DFT and its inverse. This is important when the data record and filter sizes are large as the $O(M)$ operations required per sample in the direct method can be significantly reduced.

The two primary approaches for implementing an FIR filter using DFTs are called *overlap-and-add* and *overlap-and-save* [11, Sect. 9.2.2]. As both approaches achieve similar computational savings, only the former is discussed here. The overlap-and-add method first breaks the input signal into non-overlapping blocks of length L ,

$$x[n] = \sum_{l=-\infty}^{\infty} x_l[n - lL] \quad (4.115)$$

where

$$x_l[n] = \begin{cases} x[n + lL] & 0 \leq n < L - 1 \\ 0 & \text{otherwise} \end{cases}. \quad (4.116)$$

The L active input values in each block are then convolved with the filter impulse response of length M to produce $y_l[n] = \mathcal{H}\{x_l[n]\}$ which has $M + L - 1$ active time samples. Linearity of the convolution operator then allows the FIR filter output to be reconstructed as the sum of the outputs of each of the individual blocks,

$$y[n] = \sum_{l=-\infty}^{\infty} y_l[n + lL]. \quad (4.117)$$

The overlap-and-add process entails obtaining $y_l[n]$ by implementing the convolution in the frequency domain using a DFT only for the length L block of input data. The resulting output has length $L + M - 1$ for an FIR filter of size M . The delay in (4.117) causes the $M - 1$ samples trailing the end of the l th block to overlap with the first $M - 1$ samples in the $(l + 1)$ st block to which they are added, thereby giving the technique its name.

When convolution is accomplished using a DFT, it is known as a *circular convolution*, which arises from the periodic extension produced by the inverse DFT. The convolution in (4.114) is known as a *linear convolution*. To produce the linear convolution between two sequences of length M and L a length $N = M + L - 1$ or larger circular convolution (i.e., DFT) must be used with each sequence *zero-padded* to length N . Generally, N is chosen as a power of two to enable use of the FFT, which only requires $O(N \log_2 N)$ operations compared with the $O(N^2)$ operations of direct computation of the DFT. The overall computational load per sample using the overlap-and-add method is

$$O\left(\frac{N \log_2 N}{N - M + 1}\right). \quad (4.118)$$

As shown in [7, Sect. 5.6] the optimal (in terms of minimum computational requirements) FFT size $N = 2^v$ varies with M . For example, if $M = 100$, the overlap-and-add method with $N = 1024$ requires $O(11.1)$ computations per sample compared with the $O(100)$ for the direct method. Using a larger or smaller FFT requires more computations. If $M = 75$, the optimal FFT size is $N = 512$. When M is small enough (less than 19 according to [7, Table 5.2] when only counting multiplication operations), direct computation is more efficient.

4.10 Windowing and Window Functions

Window functions are used in signal processing to limit the harsh effects of analyzing a short segment of a longer signal. As seen in Fig. 4.11, window functions smoothly de-emphasize data near the edges of the window compared with the rectangular window, which extracts the data with no tapering. An excellent resource for the characteristics of common window functions can be found in the classic 1978 article by Harris [13], although most practical signal processing or spectral estimation texts (e.g., [7, Sect. 6.3], [14, Table 4.1], [12, Sect. 3.9]) include a section on windows. Throughout this section, the window function $w[n]$ is assumed to be size N with the function active only for $n = 0, \dots, N - 1$ and zero elsewhere. Additionally, all window functions considered are non-negative, $w[n] \geq 0$ for all n .

There are several negative effects to windowing data. First, there is a loss in signal compared with using all of the data in the window with equal weighting. The signal loss is defined as the reduction in amplitude of a signal coherently combined with a given window relative to the gain for a rectangular window,

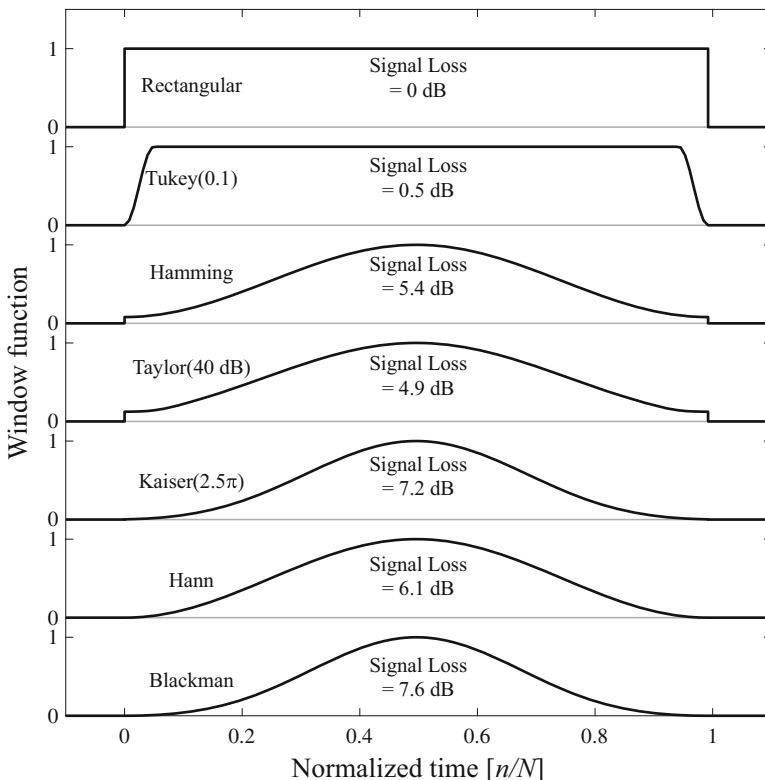


Fig. 4.11 Window functions and the associated signal loss

Table 4.2 Characteristics of various window functions as calculated for $N = 128$

Window name	Main-lobe width ^a [DFT index]	Maximum sidelobe level [dB]	Sidelobe decay rate [dB/octave]	Relative noise gain [γ_w]	Signal loss [dB]	Independent sample rate (η_w)
Rectangular	0.89	-13.3	6	1.00	0	1.5
Tukey						
$\alpha = 0.1$	0.94	-13.3	6	1.05	0.5	1.55
Hamming	1.31	-45.4	6	1.37	5.4	1.91
Taylor						
$R_{\text{dB}} = 40$	1.24	-40.1	6	1.29	4.9	1.80
Kaiser						
$\beta = 2.5\pi$	1.59	-57.3	6	1.66	7.2	2.33
Hann	1.45	-31.5	18	1.51	6.1	2.10
Blackman	1.66	-58.1	18	1.74	7.6	2.43

^aThe main-lobe width is as measured between the 3-dB-down points

$$\text{Signal Loss} = 20 \log_{10} \left(\frac{\sum_{n=0}^{N-1} w[n]}{\max_n w[n]} \right) \quad (4.119)$$

which is in decibels. As seen in Table 4.2, this is usually near or above 6 dB, which equates to a 50% reduction in signal amplitude.

The second negative effect of using windows is best described using the Fourier transform of the window function. Recall the convolution property of the Fourier transform where a product in the time domain is a convolution in the frequency domain. Thus applying a window ($w[n]$) to a signal ($x[n]$) is the same as convolving the Fourier transform of the window ($W(\psi)$) with the signal's Fourier transform ($X(\psi)$). When the intent is to isolate specific frequencies (as is done in spectral estimation) or specific directions (as is done in beamforming) the ideal shape for $W(\psi)$ is an impulse function. However, de-emphasizing the data near the window edges has the effect of shortening the RMS duration and therefore broadening the RMS bandwidth (see Sect. 4.5), making $W(\psi)$ less like an impulse function. The broadening of the main-lobe of $W(\psi)$ is seen visually in Fig. 4.12 for several window types. In Fig. 4.12 and Table 4.2, frequency and bandwidth are defined in units of DFT frequency index (sometimes called DFT bins), $k = \psi N = Nf/f_s$ for a window with size N . The values in the table are representative of large windows (large N) and not necessarily precise for smaller window sizes ($N = 128$ was used to form the entries in Table 4.2 with the exception of the sidelobe decay rate). The increase in the frequency extent of $W(\psi)$ is quantified by the 3-dB-down bandwidth listed in Table 4.2 and also in the relative noise gain.

To define relative noise gain, first assume the window is scaled so it sums to one,

$$\sum_{n=0}^{N-1} w[n] = 1. \quad (4.120)$$

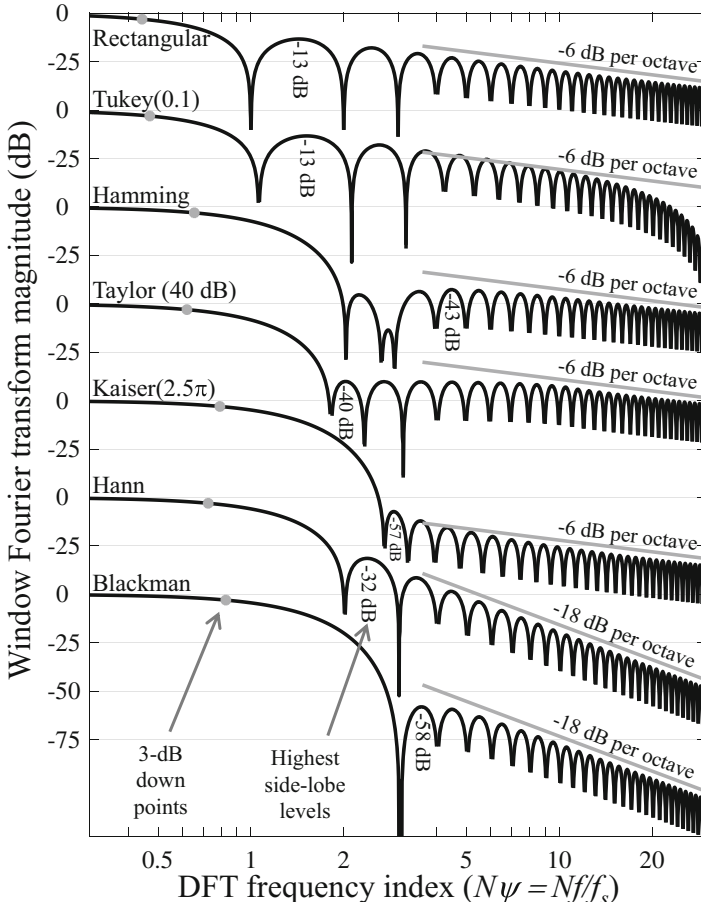


Fig. 4.12 Window function Fourier-transform magnitudes normalized to unit gain at $\psi = 0$. Note the frequency axis is logarithmically spaced

Under this *distortionless response* constraint, the output signal amplitude is the same as the input signal and noise gain is the ratio of the output noise power to the input noise power,

$$G_w = \frac{\sum_{n=0}^{N-1} w^2[n]}{\left(\sum_{n=0}^{N-1} w[n]\right)^2} \quad (4.121)$$

where the scaling in (4.120) has been incorporated. For a rectangular window the noise gain is $1/N$, which is its minimum for all window functions. The distortionless-response noise gain is the same as the equivalent noise bandwidth in [13]. The relative noise gain, found in Table 4.2 and [13], describes noise gain for the window $w[n]$ relative to that for a rectangular window, $\gamma_w = G_w/G_{\text{rect}} = NG_w$.

There are also advantages to using window functions in data analysis. One of the most significant lies in an increased ability to reject signals outside of the main-lobe of $W(\psi)$. As seen in Fig. 4.12 and Table 4.2, the highest sidelobe for the rectangular window is approximately 13 dB below the peak, which does not provide much suppression for strong interfering signals. At the expense of an increase in the main-lobe width, the maximum sidelobe can be made very small. Thus windows provide a means for trading accuracy in terms of main-lobe width for purity in terms of rejecting signals outside the main-lobe.

A final window metric is the *independent sample rate* produced by a particular window. In spectral estimation (Sect. 5.4.2), a window of size N is used to filter a signal so the power level in a particular band can be estimated. When only M samples of the signal are available for analysis, the choice of N elicits a trade-off between bias (large N reduces bias) and variance (small N reduces variance). As might be expected, the shape of the window also plays a role in the trade-off. Windows with strong tapers (e.g., the Hann and Blackman windows) shorten the effective window length, thereby increasing the bias and reducing the variance compared with a rectangular window. The variance of power-level estimates is inversely proportional to the number of independent samples in the analysis window, which is $M\eta_w/N$ where η_w is the *independent sample rate*. Assuming spectrally white noise in the band, a large analysis time, and following [15, App. A], the rate at which independent (squared-envelope) samples arise is

$$\begin{aligned}\eta_w &= N \frac{\left[\int_{-\frac{1}{2}}^{\frac{1}{2}} |W(\psi)|^2 d\psi \right]^2}{\int_{-\frac{1}{2}}^{\frac{1}{2}} |W(\psi)|^4 d\psi} \\ &= N \frac{\left[\sum_{n=0}^{N-1} w^2[n] \right]^2}{\sum_{n=-(N-1)}^{N-1} R_w^2[n]} \quad (4.122)\end{aligned}$$

where $R_w[n] = w[n] * w[-n]$ is the autocorrelation function of the window. The results for small analysis times can be found in [15, App. A].

4.10.1 Rectangular, Uniform, or Boxcar Window

The most basic window is the rectangular window; it is commonly called a uniform or boxcar window. The window equally weights each sample being extracted,

$$w[n] = 1 \text{ for } n = 0, \dots, N - 1. \quad (4.123)$$

As previously mentioned, window functions are assumed here to be size N and are therefore zero outside of $n \in [0, N - 1]$.

The Fourier transform of the rectangular window is

$$\begin{aligned} W_R(\psi) &= \frac{\sin(\pi N \psi)}{\sin(\pi \psi)} e^{-j\pi \psi(N-1)} \\ &= N \frac{\text{sinc}(N \psi)}{\text{sinc}(\psi)} e^{-j\pi \psi(N-1)}. \end{aligned} \quad (4.124)$$

The phase term represents the temporal centering of the window at sample $(N-1)/2$ and the ratio of *sin* or *sinc* functions produces the shape known as a Dirichlet kernel. The decay rate of the sidelobes is dominated by the numerator *sinc* function, which has envelope ψ^{-1} yielding 20 dB per decade or 6 dB per octave,

$$\frac{1}{\psi} \Rightarrow -20 \log_{10} \psi = \frac{-20}{\log_2 10} \log_2 \psi \approx -6 \log_2 \psi. \quad (4.125)$$

4.10.2 Tukey Window

The Tukey window replaces the beginning and ending fraction $\alpha/2$ of the rectangular window with a raised cosine (i.e., Hann), while leaving the center portion of the window at full amplitude, to reduce the effects of the sharp transition. The window function is

$$w[n] = \begin{cases} 0.5 \left[1 + \cos\left(\pi \left[\frac{2n}{\alpha(N-1)} - 1 \right] \right) \right] & 0 \leq \frac{n}{N-1} \leq \frac{\alpha}{2} \\ 1 & \frac{\alpha}{2} \leq \frac{n}{N-1} \leq 1 - \frac{\alpha}{2} \\ 0.5 \left[1 + \cos\left(\pi \left[\frac{2n}{\alpha(N-1)} + 1 - \frac{2}{\alpha} \right] \right) \right] & 1 - \frac{\alpha}{2} \leq \frac{n}{N-1} \leq 1 \end{cases} \quad (4.126)$$

for $n = 0, \dots, N-1$.

It is common to shade transmit signals with a 5% or 10% (i.e., $\alpha = 0.05$ or 0.1) Tukey window to reduce the effects of sharp transitions in amplifiers. When $\alpha = 0$, a rectangular window is obtained and when $\alpha = 1$ a Hann window is obtained. As such, the Tukey window can have the characteristics of either the rectangular or Hann windows, depending on α .

4.10.3 Hamming Window

The Hamming window,

$$w[n] = 0.54 - 0.46 \cos\left(\frac{2\pi n}{N-1}\right) \text{ for } n = 0, \dots, N-1, \quad (4.127)$$

is a common choice owing to the low sidelobe level (43 dB below the peak) and low signal loss relative to many other windows.

The Fourier transform of the Hamming window function can be described in terms of that of the rectangular window in (4.124),

$$W(\psi) = 0.54 W_R(\psi) - 0.23 W_R\left(\psi - \frac{1}{N-1}\right) - 0.23 W_R\left(\psi + \frac{1}{N-1}\right). \quad (4.128)$$

An interesting point about the Hamming window Fourier transform, which can be seen in Fig. 4.12, is that the highest sidelobe is not the first.

4.10.4 Taylor Window

The Taylor window function [16], [17, Sect. 3.4] is defined by its Fourier transform and is a compromise between a rectangular window and the Dolph-Chebyshev window function. The Dolph-Chebyshev window function places all sidelobes at a constant, definable level [7, Sect. 6.3.7] by trading main-lobe width for sidelobe suppression. The sidelobe suppression is defined by the peak-to-sidelobe ratio R_{dB} , which is a positive quantity (e.g., $R_{dB} = 40$). The Taylor window retains approximately \bar{n} of the sidelobes at R_{dB} below the peak with the remaining sidelobes roughly decaying at the 6-dB-per-octave rate of the rectangular window. As discussed in [17, Sect. 3.4], [18, Sect. 3.4.3], this is accomplished by moving the first $\bar{n} - 1$ zeros of the Fourier transform of the rectangular window.

To obtain the Taylor window given a desired peak-to-sidelobe ratio (R_{dB}) and \bar{n} , first define the locations of the $\bar{n} - 1$ zeros as

$$z_l = \bar{n} \sqrt{\frac{A^2 + (l - 0.5)^2}{A^2 + (\bar{n} - 0.5)^2}} \quad (4.129)$$

for $l = 1, \dots, \bar{n} - 1$ where A depends on the peak-to-sidelobe ratio in linear terms, $R = 10^{R_{dB}/20}$, according to

$$A = \frac{1}{\pi} \log(R + \sqrt{R^2 - 1}) \quad (4.130)$$

or, equivalently, $R = \cosh A$.

The window function is then

$$w[n] = 1 + 2 \sum_{m=1}^{\bar{n}-1} C_m \cos\left(\frac{2\pi m}{N} \left[n - \frac{(N-1)}{2}\right]\right) \quad (4.131)$$

for $n = 0, \dots, N - 1$ where C_m are Fourier series coefficients,

$$C_m = C_{-m} = \frac{\Gamma^2(\bar{n})}{\Gamma(\bar{n}+m)\Gamma(\bar{n}-m)} \prod_{l=1}^{\bar{n}-1} \left(1 - \frac{m^2}{z_l^2}\right) \quad (4.132)$$

for $m = 0, \dots, \bar{n} - 1$. When \bar{n} is too large, the window function becomes non-monotonically decreasing from its middle to its edges; in particular, it can have larger values at the edges than just in from the edges. As such, a common way [18, Sect. 3.4.3] to choose \bar{n} is as the largest value providing a monotonically decreasing window function.

Similar to the Hamming window, the Fourier transform of the Taylor window can be described as a weighted sum of the Fourier transform of the rectangular window,

$$W(\psi) = \sum_{m=-(\bar{n}-1)}^{\bar{n}-1} C_m W_R\left(\psi + \frac{m}{N}\right). \quad (4.133)$$

This can also be seen directly from (4.131) through the modulation property of the Fourier transform.

4.10.5 Kaiser Window

The Kaiser window function is

$$w[n] = [I_0(\beta)]^{-1} I_0\left(\beta \sqrt{1 - \left(\frac{|2n - N + 1|}{N - 1}\right)^2}\right) \text{ for } n = 0, \dots, N - 1 \quad (4.134)$$

where $\beta \geq 0$ and $I_0(x)$ is a zeroth order modified Bessel function.

The parameter β of the Kaiser window allows the shape to vary from a rectangular window ($\beta = 0$) to a very narrow window function (large β) with a large main-lobe and low sidelobes in the Fourier transform. From [13], the largest sidelobe is 46 dB below the peak when $\beta = 2\pi$ and 82 dB below the peak when $\beta = 3.5\pi$.

4.10.6 Hann Window

The Hann window is often called a raised-cosine, von Hann, or Hanning window. The window function is

$$w[n] = 0.5 - 0.5 \cos\left(\frac{2\pi n}{N - 1}\right) \text{ for } n = 0, \dots, N - 1. \quad (4.135)$$

The Fourier transform of the Hann window function is

$$W(\psi) = 0.5 W_R(\psi) - 0.25 W_R\left(\psi - \frac{1}{N-1}\right) - 0.25 W_R\left(\psi + \frac{1}{N-1}\right). \quad (4.136)$$

The placement and weight of the latter two terms reduce the largest sidelobe to 32 dB below the peak. They also produce cancellation in the extended sidelobes so that the decay rate is 18 dB per octave compared with the 6 dB per octave of the rectangular, Hamming, and Kaiser windows. This additional suppression can be advantageous when strong interferences exist far from the band of interest.

It is important to note the end points of this window ($w[0]$ and $w[N-1]$) are both zero. In applications such as beamforming, where a limited number of sensors are available, it is common to construct the window using $N+2$ samples rather than N and discarding the end points. This yields the window definition

$$w[n] = 0.5 - 0.5 \cos\left(\frac{2\pi(n+1)}{N+1}\right) \text{ for } n = 0, \dots, N-1. \quad (4.137)$$

4.10.7 Blackman Window

The Blackman window function is

$$w[n] = 0.42 - 0.5 \cos\left(\frac{2\pi n}{N-1}\right) + 0.08 \cos\left(\frac{4\pi n}{N-1}\right) \text{ for } n = 0, \dots, N-1. \quad (4.138)$$

The Fourier transform of the Blackman window function is

$$\begin{aligned} W(\psi) &= 0.42 W_R(\psi) - 0.25 W_R\left(\psi - \frac{1}{N-1}\right) - 0.25 W_R\left(\psi + \frac{1}{N-1}\right) \\ &\quad + 0.04 W_R\left(\psi - \frac{2}{N-1}\right) + 0.04 W_R\left(\psi + \frac{2}{N-1}\right). \end{aligned} \quad (4.139)$$

Similar to the Hann window, the Blackman window has a sidelobe slope of -18 dB per octave. However, it provides more suppression in the maximum sidelobe (58 dB compared to 32 dB) at the expense of a 17% larger main-lobe width and 1.5 dB more signal loss.

4.11 Decimation and Interpolation

For various reasons it can be necessary to change the sampling rate of a discrete-time signal. Reducing the sampling rate is called *decimation* or *down-sampling* whereas increasing the sampling rate is *interpolation* or *up-sampling*.

A signal is decimated by a factor D simply by extracting every D samples,

$$y[n] = x[Dn]. \quad (4.140)$$

If the sampling period of $x[n]$ is $T_x = 1/f_s$, the time between samples of $y[n]$ is $T_y = DT_x = D/f_s$, yielding a sampling rate a factor D smaller, f_s/D . The effect of decimation on the frequency content of a signal can be determined by relating the Fourier transform of $y[n]$ to that of $x[n]$. To accomplish this, consider the signal $p[n]x[n]$ where $p[n]$ is a periodic signal isolating every D samples and setting others to zero,

$$\begin{aligned} p[n] &= \begin{cases} 1 & n = 0, \pm D, \pm 2D, \dots \\ 0 & \text{otherwise} \end{cases} \\ &= \frac{1}{D} \sum_{k=0}^{D-1} e^{j2\pi kn/D}. \end{aligned} \quad (4.141)$$

The summation representation of $p[m]$ in (4.141) is its discrete Fourier series (e.g., see [8, Sect. 8.1]). Now, the Fourier transform of $y[n]$ is seen to be that of the product $p[n]x[n]$ evaluated at ψ/D ,

$$\begin{aligned} Y(\psi) &= \sum_{n=-\infty}^{\infty} y[n]e^{-j2\pi\psi n} \\ &= \sum_{n=-\infty}^{\infty} p[n]x[n]e^{-j2\pi(\psi/D)n}. \end{aligned} \quad (4.142)$$

Replacing $p[n]$ by its discrete Fourier series representation leads to

$$Y(\psi) = \frac{1}{D} \sum_{k=0}^{D-1} X\left(\frac{\psi - k}{D}\right). \quad (4.143)$$

Thus, decimation produces repeated spectra in a similar manner to sampling but with an accompanying dilation in frequency.

As decimation by a factor D is identical to an original sampling at a sampling rate of f_s/D , clearly any frequency content above the corresponding Nyquist frequency of $f_s/(2D)$ will result in aliasing. Suppose the highest frequency in $x[n]$ is band-limited to $|\psi| < 1/(2D)$ as depicted in the upper panel of Fig. 4.13. Then the Fourier transform of the decimated signal, which is seen in the lower panel of Fig. 4.13 to dilate to the Nyquist frequency, does not exhibit any aliasing.

The sampling rate of a discrete-time signal can be increased through up-sampling which, because it is an interpolation process, does not introduce any new information. If the original signal is $x[n]$ and an up-sampling rate of I is desired,

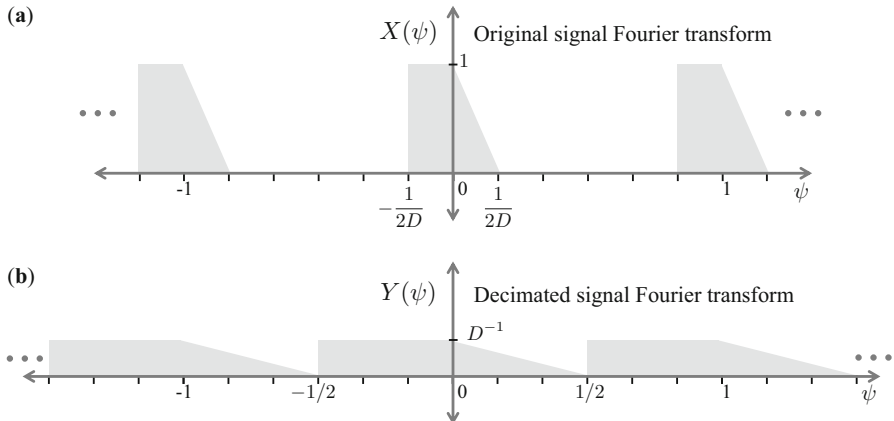


Fig. 4.13 Example Fourier transform of a signal (a) before and (b) after decimation

an intermediate signal $v[n]$ is formed at the higher sampling rate by placing $I - 1$ zeros in between samples of $x[n]$,

$$\begin{aligned} v[n] &= \dots, 0, x[0], 0, 0, 0, 0, x[1], 0, 0, 0, 0, x[2], 0, \dots \\ &= \begin{cases} x[n/I] & n = 0, \pm I, \pm 2I, \dots \\ 0 & \text{otherwise} \end{cases} \end{aligned} \quad (4.144)$$

The Fourier transform of $v[n]$ is simply a frequency-compressed version of the Fourier transform of $x[n]$, $V(\psi) = X(\psi I)$. As such, the unique frequency content in $X(\psi)$ for $|\psi| < 1/2$ is completely replicated in $V(\psi)$ on $|\psi| < 1/(2I)$ and repeated at every integer multiple of $1/I$. As only the first copy is desired, a LPF with cut-off frequency $\psi_c = 1/(2I)$ must be applied to $v[n]$ to obtain the up-sampled signal. An ideal LPF results in the Fourier transform of $y[n]$ having no frequency content above $\psi_c = 1/(2I)$.

Suppose the signal $x[n]$ came from a continuous-time signal sampled at rate f_s and had a maximum frequency f_0 , which was below the Nyquist frequency, $f_0 < f_s/2$. In terms of cycles per sample, the frequency in $x[n]$ is $\psi_0 = f_0/f_s$. After interpolation, the frequency of the signal in $y[n]$ is $\psi'_0 = \psi_0/I = f_0/(If_s)$, which is smaller in terms of cycles per sample than ψ_0 . However, the equivalent new sampling rate for the interpolated signal $y[n]$ is $f'_s = If_s$. So the frequency of the interpolated signal in cycles per second is still $f_0 = \psi f_s = \psi' f'_s$. In other words, interpolation does not provide additional higher frequency content of a continuous-time signal after it has been sampled.

A linear-phase FIR filter is generally used for interpolation, which incurs a delay as described in Sect. 4.9. If the size of the FIR filter is M , then the delay is $(M - 1)/2$ samples. When M is even, the delay is in between samples which might not be desirable. In particular, if the specific values of $x[n]$ are to be reproduced every I

samples in the up-sampled signal $y[n]$, then an odd-size linear-phase FIR filter must be used. For a linear-phase FIR filter with group delay $(M - 1)/2$, the interpolated signal is therefore

$$y[n] = \text{LPF}\{v[n + (M - 1)/2]\}. \quad (4.145)$$

Interpolation increases the sampling rate by an integer multiple (I) whereas decimation reduces the sampling rate by an integer factor (D). A non-integer multiple of the original sampling rate can be obtained by combining the processes if the ratio between the new and old sampling rates is rational,

$$\frac{f_{s,\text{new}}}{f_{s,\text{old}}} = \frac{I}{D}. \quad (4.146)$$

References

1. P.A.M. Dirac, *The Principles of Quantum Mechanics* (Oxford University Press, Oxford, 1930)
2. R.N. Bracewell, *The Fourier Transform and Its Applications*, 2nd edn. (McGraw-Hill, Inc., New York, 1986)
3. B.P. Lathi, *Linear Systems and Signals* (Berkeley-Cambridge Press, Carmichael, 1992)
4. R.N. McDonough, A.D. Whalen, *Detection of Signals in Noise*, 2nd edn. (Academic, San Diego, 1995)
5. A.B. Carlson, *Communication Systems* (McGraw-Hill, New York, 1986)
6. L. Råde, B. Westergren, *Mathematics Handbook*, 5th edn. (Springer, Berlin, 2004)
7. B. Porat, *A Course in Digital Signal Processing* (Wiley, New York, 1997)
8. A.V. Oppenheim, R.W. Schafer, *Discrete-Time Signal Processing*, 5th edn. (Pearson Higher Education, Inc., Upper Saddle River, 2010)
9. J.W. Cooley, J.W. Tukey, An algorithm for the machine calculation of complex Fourier series. *Math. Comput.* **19**(90), 297–301 (1965)
10. E.O. Brigham, *The Fast Fourier Transform and Its Applications* (Prentice Hall, Englewood Cliffs, 1988)
11. J.G. Proakis, D.G. Manolakis, *Digital Signal Processing*, 2nd edn. (Macmillan Pub. Co., New York, 1992)
12. R.G. Lyons, *Understanding Digital Signal Processing* (Prentice Hall, Englewood Cliffs, 2011)
13. F.J. Harris, On the use of windows for harmonic analysis with the discrete Fourier transform. *Proc. IEEE* **66**(1), 51–83 (1978)
14. S.M. Kay, *Modern Spectral Estimation Theory and Application* (Prentice Hall, Englewood Cliffs, 1988)
15. A.H. Nuttall, A.F. Magaraci, Signal-to-noise ratios required for short-term narrowband detection of Gaussian processes. Technical Report 4417, Naval Underwater Systems Center, Newport, October 1972
16. T.T. Taylor, Design of line-source antennas for narrow beamwidth and low sidelobes. *IRE Trans. Antennas Propag.* **AP-3**, 16–28 (1955)
17. R.C. Hansen, *Phased Array Antennas* (Wiley, New York, 1998)
18. H.L. Van Trees, *Optimum Array Processing* (Wiley, New York, 2002)

Chapter 5

Mathematical Statistics



5.1 Introduction

Many of the underwater acoustic signal processing applications discussed in this text have their roots in detection and estimation, both of which require a statistical characterization of the data prior to development. This section covers some basic statistical concepts enabling the derivation of algorithms in statistical signal processing. Some excellent reference texts for “mathematical statistics” include the engineering-oriented [1, 2] and those from the statistics community [3–5].

The three concepts covered in this section are (1) probability, (2) random variables, and (3) random processes. Probability provides the foundation for describing outcomes of experiments. Random variables quantify the experiment outcome numerically in a statistical sense. Random processes are an extension of random variables to functions of time. In underwater acoustic signal processing applications, the functions of time are generally acoustic pressures measured by hydrophones.

5.2 Probability

Probability is a “measure” (not too dissimilar to a physical measurement [2, Sect. 1.2]) related to a particular event. The relative-frequency interpretation assumes an experiment is repeated n times. If event \mathcal{A} occurs $n_{\mathcal{A}}$ times, then the probability associated with event \mathcal{A} is

$$\Pr\{\mathcal{A}\} = \lim_{n \rightarrow \infty} \frac{n_{\mathcal{A}}}{n} \quad (5.1)$$

so the “measurement” related to probability is the number of occurrences of the event under consideration.

Table 5.1 Subjective interpretation of probability: the measure of belief on the occurrence of event \mathcal{A}

$\Pr\{\mathcal{A}\}$	Occurrence (“measure”)
0	Never
0.001	Very rarely
0.01	Rarely
0.5	Half the time
0.8	Often
0.95	Most of the time
0.999	Almost always
1	Always

The event \mathcal{A} is one of many comprising a probability space. Based on the above relative-frequency interpretation, $\Pr\{\mathcal{A}\}$ will lie between zero and one and represents a measure of the frequency in the occurrence of event \mathcal{A} . It can also be described as the belief¹ in the potential for the event \mathcal{A} to occur. In the design and analysis of signal processing algorithms (particularly detection algorithms), it is necessary to choose a particular probability as an operating point. To assist this, it is useful to define in words how certain probability levels are generally interpreted. The list shown in Table 5.1 describes several levels of probability and how they are often interpreted in underwater acoustic signal processing. Although some of the interpretations are universal ($\Pr\{\mathcal{A}\} = 0, 0.5$, or 1), the others are subjective and could change for a different field.

Several concepts from set theory are used in mathematical statistics to describe and deal with events related to random variables. These concepts are covered briefly in this section without delving into the specific mathematical concepts required to derive random variables from probability spaces. Consider two events \mathcal{A} and \mathcal{B} . The union of the two events $\mathcal{A} \cup \mathcal{B}$ is the event such that either \mathcal{A} or \mathcal{B} has occurred. The intersection of the two events $\mathcal{A} \cap \mathcal{B}$ is the event requiring both \mathcal{A} and \mathcal{B} to occur. These can be related according to

$$\Pr\{\mathcal{A} \cup \mathcal{B}\} = \Pr\{\mathcal{A}\} + \Pr\{\mathcal{B}\} - \Pr\{\mathcal{A} \cap \mathcal{B}\} \quad (5.2)$$

which is easily shown through the use of a Venn diagram.

Conditional probability arises from considering the probability of an event given the occurrence of some other event. The relative-frequency interpretation starts with running an experiment n times and counting the occurrences of the events \mathcal{A} , \mathcal{B} , and $\mathcal{A} \cap \mathcal{B}$, respectively, $n_{\mathcal{A}}$, $n_{\mathcal{B}}$, and $n_{\mathcal{AB}}$. The conditional probability of observing event \mathcal{A} given event \mathcal{B} has occurred is then

¹Describing probability as belief in the potential occurrence of an event comes from the classical interpretation rather than the relative-frequency interpretation. The classical interpretation enumerates all the elements of the probability space before the experiment occurs and counts those in \mathcal{A} to assign a belief (the proportion of elements in \mathcal{A} to the total number) that \mathcal{A} will occur.

$$\Pr\{\mathcal{A}|\mathcal{B}\} = \lim_{n \rightarrow \infty} \frac{n_{\mathcal{AB}}}{n_{\mathcal{B}}} = \frac{\Pr\{\mathcal{A} \cap \mathcal{B}\}}{\Pr\{\mathcal{B}\}}. \quad (5.3)$$

Conditional probability can be used to derive Bayes' theorem,

$$\Pr\{\mathcal{A}|\mathcal{B}\} = \frac{\Pr\{\mathcal{B}|\mathcal{A}\} \Pr\{\mathcal{A}\}}{\Pr\{\mathcal{B}\}}, \quad (5.4)$$

which has had extensive application in combining prior information about an event with the occurrence of new, partially related events to form an improved understanding. Suppose, however, that the new event (\mathcal{B} on the right side of (5.4)) was independent of event \mathcal{A} . The conditional probability $\Pr\{\mathcal{B}|\mathcal{A}\}$ would not depend on the occurrence of \mathcal{A} and would simply be $\Pr\{\mathcal{B}\}$. That is,

$$\Pr\{\mathcal{B}|\mathcal{A}\} = \Pr\{\mathcal{B}\} \text{ and } \Pr\{\mathcal{A}|\mathcal{B}\} = \Pr\{\mathcal{A}\} \quad (5.5)$$

if \mathcal{A} and \mathcal{B} are independent, which leads to

$$\Pr\{\mathcal{A} \cap \mathcal{B}\} = \Pr\{\mathcal{A}\} \Pr\{\mathcal{B}\}. \quad (5.6)$$

5.3 Random Variables

5.3.1 *Random Variables, Distributions, and Densities*

A random variable is a mapping from the sample space of a probability experiment to the real line. It can be interpreted as an ordering or organizing of the sample space of possible events. In practical terms, random variables allow us to develop algorithms and evaluate their performance when the situations in which they are used contain some definable levels of uncertainty. As with physical models, it is important that statistical models incorporating random variables accurately represent the physical conditions in which the algorithms are used.

Standard statistical notation denotes random variables by a capital letter, e.g., X , whereas a specific value observed for the random variable (i.e., after the probability experiment has occurred) uses the lower case, x . A random variable is most easily understood by its probability density function (PDF). Nearly everyone is familiar with the Gaussian or normal PDF and its bell-shaped curve illustrating that observing a value near the mean is more likely than one farther away in the tails of the PDF. Mathematically, however, it is easier to first define the random variable's cumulative distribution function (CDF), which is the probability that the random variable X is below some specific value x ,

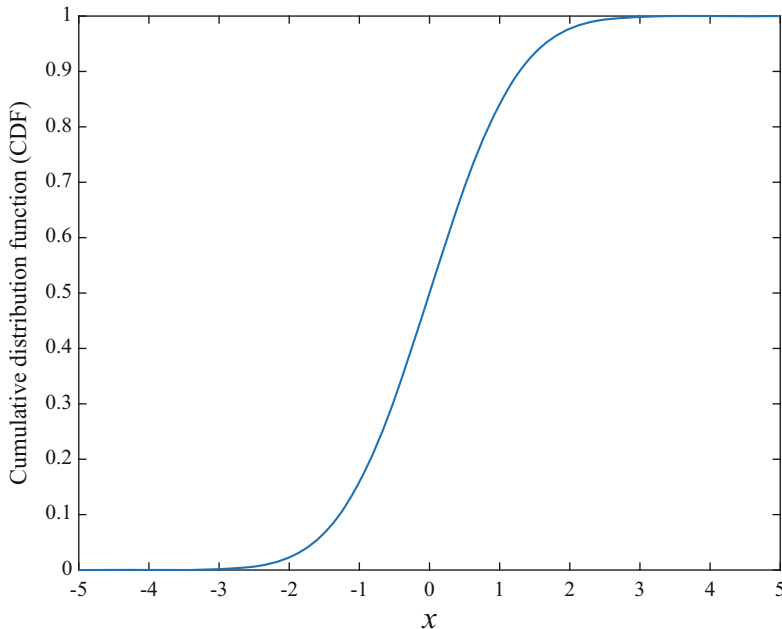


Fig. 5.1 Cumulative distribution function (CDF) of the standard normal distribution (zero mean and unit variance)

$$F_X(x) = \Pr\{X \leq x\}. \quad (5.7)$$

The variable F is usually taken to describe the CDF of a random variable with the subscript X , which is often suppressed for convenience, denoting the random variable to which the CDF belongs. Some pertinent characteristics of $F_X(x)$ are seen in Fig. 5.1: it starts at zero when $x = -\infty$ and rises monotonically to 1 as $x \rightarrow \infty$; because it is the probability of observing the event $\{X \leq x\}$, $F_X(x)$ must lie on $[0, 1]$.

The PDF of a random variable, typically using the variable f (with or without a subscript), is defined as the derivative of the CDF,

$$f_X(x) = \frac{d}{dx} F_X(x). \quad (5.8)$$

Noting the properties of the CDF, the PDF (e.g., see the Gaussian PDF in Fig. 5.2) is seen to be non-negative ($f_X(x) \geq 0$ for all x) and to integrate to one (i.e., $\int_{-\infty}^{\infty} f_X(x) dx = 1$). The CDF can be obtained from the PDF by integrating from $-\infty$ to x ,

$$F_X(x) = \int_{y=-\infty}^x f_X(y) dy. \quad (5.9)$$

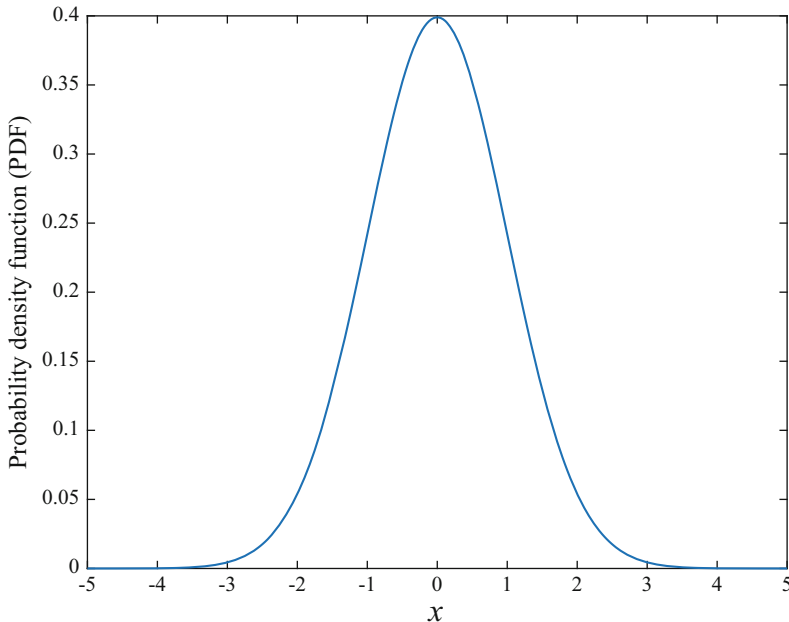


Fig. 5.2 Probability density function (PDF) of the standard normal distribution

A function related to the CDF often used in detection theory is the exceedance distribution function (EDF). The EDF is simply one minus the CDF ($1 - F_X(x)$) and represents the probability a random variable is larger than the argument. In statistics, the EDF is commonly called the survival function [6, Sect. 2.3 & Table 2.1].

Many common statistical distributions and their pertinent characteristics are presented in Sect. 5.6. Generally, the shape of the PDF is what distinguishes one statistical distribution from another. For example, the uniform distribution has a constant or uniform PDF over its region of support. Given a particular shape, some small number of parameters provide the specifics of each distribution. When the PDF or CDF of a random variable X depends on a parameter θ , it will be denoted as $f_X(x; \theta)$ or $F_X(x; \theta)$, respectively. The parameters of a distribution are not necessarily unique, but are often taken from the moments of a distribution (see Sect. 5.3.2). For example, the mean and variance characterize the Gaussian distribution. Parameters can often be described as controlling different facets of the PDF shape. These include [6, Sect. 3.5]

- **bound parameter:** describes the support of the distribution (e.g., a uniform distribution on $[a, b]$)
- **location parameter:** shifts the whole PDF along the abscissa (e.g., shifting the mean of a Gaussian distribution)

- **scale parameter:** dilates or contracts the PDF from some reference point (e.g., the exponential distribution parameter controls scale)
- **shape parameter:** otherwise alters the shape, often with respect to the tails (small values) of the PDF (e.g., varying the gamma-distribution shape parameter can produce an exponential distribution or one that is nearly Gaussian)
- **non-centrality parameter:** a type of shape parameter often used to describe a departure from a nominal distribution (e.g., a non-central chi-squared distribution with non-centrality parameter equal to zero is a (central) chi-squared distribution)

The most common and historic distributions have what are known as standard parameter values. For example, the *standard* normal distribution has zero mean and unit variance. Others include a standard uniform distribution (ranging from zero to one) and a standard exponential distribution (unit mean). Shorthand notation also exists for many distributions to describe how certain random variables are distributed. For example,

$$X \sim \mathcal{N}(\mu, \sigma^2) \quad (5.10)$$

implies the random variable X is Gaussian distributed with mean μ and variance σ^2 . A list of common distributions and the notation used in this book can be found in Table 5.3.

Random variables can be classified as continuous, discrete, or mixed. Continuous random variables have a continuous CDF. Discrete random variables can take on a countable number of discrete values. As might be expected, mixed random variables are part continuous and part discrete. An abstruse property of continuous random variables is that the probability of observing a continuous random variable X equal to a specific value x is zero,

$$\begin{aligned} \Pr\{X = x\} &= \lim_{\delta \rightarrow 0} \Pr\{x < X \leq x + \delta\} \\ &= \lim_{\delta \rightarrow 0} F_X(x + \delta) - F_X(x) \\ &= F_X(x^+) - F_X(x) = 0 \end{aligned} \quad (5.11)$$

where $F_X(x^+)$ is $F_X(x)$ evaluated from the right. Essentially, the range of X is so large (uncountably so) that the probability of observing any one event is zero. When it is necessary to describe this probability (e.g., to derive conditional PDFs), limits over events with non-zero probability are used as above.

Exercise 5.1 Plot the PDF and CDF of a Gaussian random variable with mean 1 and variance 4. If you do not have access to an advanced statistics package, use the error function to obtain the CDF. See Sect. 5.6 for the equations.

Exercise 5.2 Derive the CDF of a uniform distribution on (a, b) .

5.3.2 Moments and Expectations

It is often cumbersome to describe random variables by their CDF or PDF (e.g., consider alpha-stable distributions [7] that do not have a closed-form equation for either). At times, it is simpler to only consider standard characteristics of the distribution such as the average value (μ) and the spread about it. These are known as moments of the distribution and are formed through a mathematical device called an *expectation* operator.

The average value or mean is the expectation of the random variable,

$$\mu = E_X[X] = \int_{-\infty}^{\infty} x f_X(x) dx. \quad (5.12)$$

In general, the expectation operator $E_X[\cdot]$ takes an argument that is a function of the random variable X and provides its average value,

$$E_X[g(X)] = \int_{-\infty}^{\infty} g(x) f_X(x) dx. \quad (5.13)$$

The subscript on the expectation operator can be used to indicate over which random variable the expectation is to be formed, but is often not used when it is unambiguous. As might be expected, the expectation of a constant (a) is the constant itself,

$$E_X[a] = \int_{-\infty}^{\infty} a f_X(x) dx = a. \quad (5.14)$$

Additionally, the expectation is a linear operator,

$$E_{X,Y}[aX + bY] = aE_X[X] + bE_Y[Y] \quad (5.15)$$

where a and b are constants and X and Y are random variables.

The variance is defined as the expected squared difference between the random variable and its mean,

$$\text{Var}[X] = \sigma^2 = E_X[(X - \mu)^2] = \int_{-\infty}^{\infty} (x - \mu)^2 f_X(x) dx. \quad (5.16)$$

The square root of the variance is called the standard deviation (i.e., σ). It is often used in lieu of the variance to facilitate an understanding of how likely it is to observe a random variable one, two, or three standard deviations above or below the mean. For a Gaussian random variable, the probabilities are, respectively, approximately 32%, 4.6%, and 0.27%. Because the Gaussian PDF is symmetric about its mean, the probability of the random variable being distant on just one side of the mean is half of these percentages. Thus, although it is common to observe a

Gaussian random variable more than one σ away from the mean, it is rare to see it more than 3σ away.

Example: Uniform Random Variable on (a, b)

The PDF of a uniform random variable U on $[a, b]$ is simply $1/(b - a)$ for values of $u \in [a, b]$ and zero elsewhere. Therefore, its mean is

$$\mu_U = E_U[U] = \int_a^b \frac{u}{b-a} du = \frac{a+b}{2} \quad (5.17)$$

and variance

$$\sigma_U^2 = E_U[(U - \mu_U)^2] = \int_a^b \frac{[u - (a+b)/2]^2}{b-a} du = \frac{(b-a)^2}{12} \quad (5.18)$$

While the mean describes the average value of a random variable, other measures of the “center” of the distribution include the median and mode. The median of a random variable (η) is the value for which half the mass of the PDF lies above and below; that is, where the CDF equals 0.5,

$$F_X(\eta) = 0.5. \quad (5.19)$$

The mode is the value at which the PDF has maximum value. For some distributions (e.g., symmetric, unimodal PDFs), the mean, median, and mode are identical.

In addition to the first and second moments, higher-order moments further characterize the PDF of a random variable. Higher-order moments about the origin (μ'_k) are obtained by raising X to a power,

$$\mu'_k = E_X[X^k] = \int_{-\infty}^{\infty} x^k f_X(x) dx. \quad (5.20)$$

With respect to moments of random variables, the superscript ' is used to differentiate moments about the origin from central moments, which are taken about the mean. A k th-order central moment has form

$$\mu_k = E_X[(X - \mu)^k]. \quad (5.21)$$

Central moments can be related to moments taken about the origin by expanding the binomial argument of the expectation. For example, the variance (which is a second-order central moment)

$$\begin{aligned}\sigma^2 &= E_X[(X - \mu)^2] = E_X[X^2 - 2\mu X + \mu^2] \\ &= \mu'_2 - \mu^2.\end{aligned}\quad (5.22)$$

is related to the mean and power, $\mu_2 = E_X[X^2]$, of the random variable. The k th central moment, in terms of moments about the origin, is

$$\begin{aligned}\mu_k &= E_X[(X - \mu)^k] = \sum_{i=0}^k (-1)^i \binom{k}{i} E_X[X^{k-i}] \mu^i \\ &= \sum_{i=0}^k (-1)^i \binom{k}{i} \mu'_{k-i} \mu^i.\end{aligned}\quad (5.23)$$

The third-order central moment, scaled by the standard deviation raised to the third power, is known as the skewness of a distribution,

$$\eta_3 = E_X\left[\left(\frac{X - \mu}{\sigma}\right)^3\right] = \frac{\mu_3}{\sigma^3}. \quad (5.24)$$

The skewness can provide information regarding which side of the mean the bulk of the distribution lies. Similarly, normalizing the fourth central moment yields the kurtosis,

$$\eta_4 = E_X\left[\left(\frac{X - \mu}{\sigma}\right)^4\right] = \frac{\mu_4}{\sigma^4} \quad (5.25)$$

Extracting meaning from kurtosis is tenuous at best. By raising the distance from the mean to the fourth power, it emphasizes regions of the PDF farther away than the variance does and therefore is sometimes interpreted as characterizing the heaviness of the tails of the PDF.

5.3.3 Functions of Random Variables

When deriving or analyzing signal and information processing algorithms, a common requirement is to obtain the distributions of functions of random variables. For example, a detection algorithm (see Sect. 6.2 and Part III) maps a set of measured data samples (represented by a set of random variables) to a “signal present” or “signal absent” decision. The process involves evaluating what is called a detection statistic (a scalar function of the multiple random variables) and choosing “signal present” if it exceeds a predefined threshold and “signal absent” otherwise.

To evaluate detection performance, the distribution of the detection statistic must be derived from the distribution of the data from which it is formed.

A detailed discussion of how to derive the distribution of functions of random variables is beyond the scope of this text; the reader is referred to [5, Sect. 4.4], [1, Chs. 5 & 6], or [6, Ch. 3]. The simplest case involves a scalar function of one random variable, $Y = g(X)$. Suppose the function g is a one-to-one mapping (so the functional inverse $x = g^{-1}(y)$ exists and is unique) and that g is increasing and differentiable on the range of X (i.e., the region of the real line where $f_X(x) > 0$). Then, the CDF of Y is

$$\begin{aligned} F_Y(y) &= \Pr\{Y \leq y\} \\ &= \Pr\{g(X) \leq y\} = \Pr\left\{X \leq g^{-1}(y)\right\} \\ &= F_X\left(g^{-1}(y)\right) \end{aligned} \tag{5.26}$$

Differentiating with respect to y yields the PDF

$$f_Y(y) = f_X(x) \left| \frac{dx}{dy} \right| \tag{5.27}$$

where $x = g(y)$, dx/dy is the Jacobian of the transformation, and the absolute value signs extend the result to cases where $g(x)$ is monotonically decreasing. Simple extensions to this result exist when g has regions of zero slope or is a many-to-one mapping.

Example:

Suppose U is a uniform random variable on $(0, 1)$ and $V = -\log U$. Noting that $U = e^{-V}$, the Jacobian of the transformation is

$$\frac{du}{dv} = -e^{-v} \tag{5.28}$$

and the PDF of V

$$f_V(v) = e^{-v} \tag{5.29}$$

for $v \in (0, \infty)$, which equates to $v \in (0, \infty)$. Thus, $V = -\log U$ is an exponential random variable with unit mean.

Example: Rayleigh Distributed Envelope Yields Exponentially Distributed Intensity

As will be discussed in Sect. 7.3.6, the envelope of a bandpass Gaussian random process has a Rayleigh distribution. Suppose X is a Rayleigh-distributed random variable with scale σ and PDF

$$f_X(x) = \frac{x}{\sigma^2} e^{-x^2/2\sigma^2} \quad (5.30)$$

for $x \geq 0$. The instantaneous intensity, found by squaring the envelope, is typically used in detection and is often easier to work with than the envelope. To find the distribution of the instantaneous intensity, let $Y = X^2$ and note that $X = \sqrt{Y}$ and $dx/dy = 0.5/\sqrt{y}$. The PDF of Y is then

$$\begin{aligned} f_Y(y) &= f_X(\sqrt{y}) \frac{0.5}{\sqrt{y}} \\ &= \frac{1}{2\sigma^2} e^{-y/2\sigma^2} \end{aligned} \quad (5.31)$$

for $y \geq 0$, which can be recognized as an exponential distribution with mean $\lambda = 2\sigma^2$.

Beyond the simple case of a one-to-one mapping, the approaches for obtaining the PDF of a function of one or more random variables vary. For the specific case of an invertible mapping of n random variables jointly to n new random variables (i.e., n functions of n random variables), an extension to (5.27) exists where the PDFs are joint PDFs and the absolute value of the Jacobian becomes the absolute value of the determinant of the Jacobian matrix of the transformation. For a mapping of m random variables to $n < m$ new random variables, the process involves forming $m-n$ auxiliary random variables, determining the joint PDF of the resulting m random variables, and finally marginalizing (integrating) out the auxiliary random variables.

Exercise 5.3 Show that the square of a Rician random variable with scale $\sigma = 1$ is a non-central chi-squared random variable.

Exercise 5.4 Show that the sum of two exponentially distributed random variables with mean λ is a gamma-distributed random variable.

Exercise 5.5 Show that the PDF of the sum of two independent random variables is the convolution of their PDFs.

5.3.4 Simulating Random Variables

Simulation of random variables provides a powerful means for evaluating the performance of underwater acoustic signal processing algorithms. Most computational platforms provide random-variable generators for uniform and normal random variables and specialty packages are often available for other random variables. In the absence of the latter, several techniques exist for converting uniform or normal random variables to other distributions [8, 9].

The most straightforward technique is known as CDF inversion. Suppose samples of random variable X with PDF $f_X(x)$ are required when only a standard uniform (i.e., uniform on $(0, 1)$) random variable U is available. The approach exploits the PDF of a one-to-one mapping from (5.27) in order to discern what transformation is necessary to convert a standard uniform random variable to have PDF $f_X(x)$. Noting that $f_U(u) = 1$ for $u \in [0, 1]$, the PDF from (5.27) simplifies to

$$f_X(x) = f_U(u) \left| \frac{du}{dx} \right| = \left| \frac{du}{dx} \right| \quad (5.32)$$

If du/dx is positive, then $du = f_X(x) dx$, $u = F_X(x)$, and $x = F_X^{-1}(u)$ where $F_X^{-1}(u)$ is the functional inverse of $u = F_X(x)$. Thus, the random variable formed by evaluating the (functionally) inverted CDF at a standard uniform random variable,

$$X = F_X^{-1}(U), \quad (5.33)$$

has PDF $f_X(x)$.

Example: Exponential Random Variables

To generate an exponential random variable with mean λ , first invert the CDF

$$u = F_X(x) = 1 - e^{-x/\lambda} \quad (5.34)$$

to obtain $X = -\lambda \log(1 - U)$, which produces the desired exponential random variable. Noting that $1 - U$ is also a standard uniform random variable, the transformation $X = -\lambda \log(U)$ will also produce an exponential random variable with mean λ .

When the CDF of the random variable to be simulated is not amenable to simple inversion, it may be possible to form the random variable as a function of multiple random variables that are easier to simulate. For example, F-distributed random variables can be simulated as scaled ratios of chi-squared random variables. Similarly, K-distributed random variables are easily simulated as the product of gamma and exponential random variables. Unfortunately, this approach requires

some art in relating the desired random variable to others that are easier to simulate, a task made somewhat easier by extensive lists of relationships between random variables (e.g., see [10, Ch. 4] or [11]). A somewhat more general approach lies in the so-called rejection method [9, Sects. 4.4 & 5.2] where a functional relationship is not required, but multiple iterations may need to be performed before a suitable random variable is generated.

5.3.5 Histogram Estimates of the PDF and CDF

As previously mentioned, it is important that statistical models used in developing statistical signal processing algorithms accurately represent the real data on which the algorithms are to be used. Although there exist statistical tests (e.g., chi-squared goodness-of-fit tests or Kolmogorov–Smirnov tests [4, Sect. 11.2]) to evaluate the degree to which a hypothesized model fits observed data, a common first step is to visualize the fit of the model to a non-parametric estimator such as the histogram. Given an observed set of data, a histogram consists of the counts of the number of occurrences within each of a set of bins spanning the range of a random variable.

The following MATLAB® code was used to simulate a Gaussian random variable, estimate the PDF and CDF through a histogram, and compare it with the exact distribution. Note that the error function (erf) is used to evaluate the CDF. The histogram PDF estimate seen in Fig. 5.3 shows a good fit to the exact PDF, but appears noisy near the mode. The CDF estimate is formed by a cumulative sum of the counts in consecutive bins as shown in Fig. 5.4. The primary design choice when using a histogram is how large to make the bins. If they are too small, the estimate is very noisy. When too large, the histogram will not capture the shape of the underlying distribution.

Code to compare distribution model with histogram:

```
x=randn(5000,1)*2+1;
[f,h]=hist(x,100);
F=cumsum(f)/sum(f);
f=f/(sum(f)*(h(2)-h(1)));
u=1; v=4;
fg=exp(-(h-u).^2/(2*v))/sqrt(2*pi*v);
Fg=(1+erf((h-u)/sqrt(2*v)))/2;
figure; plot(h,f,h,fg,'--');
figure; plot(h,F,h,Fg,'--');
```

Histogram-based CDF estimates are often used to evaluate the performance of detection algorithms. In order to understand how accurate the performance estimate is, a confidence interval is calculated (e.g., see Sect. 6.3.8 for a brief description or [5, Ch. 9] for more detail). A confidence interval provides an estimate of the range over which the true value might lie as opposed to choosing a single point estimate of the unknown parameter. Suppose the data X_1, \dots, X_n are identically distributed and statistically independent of each other. The histogram CDF estimate for a given

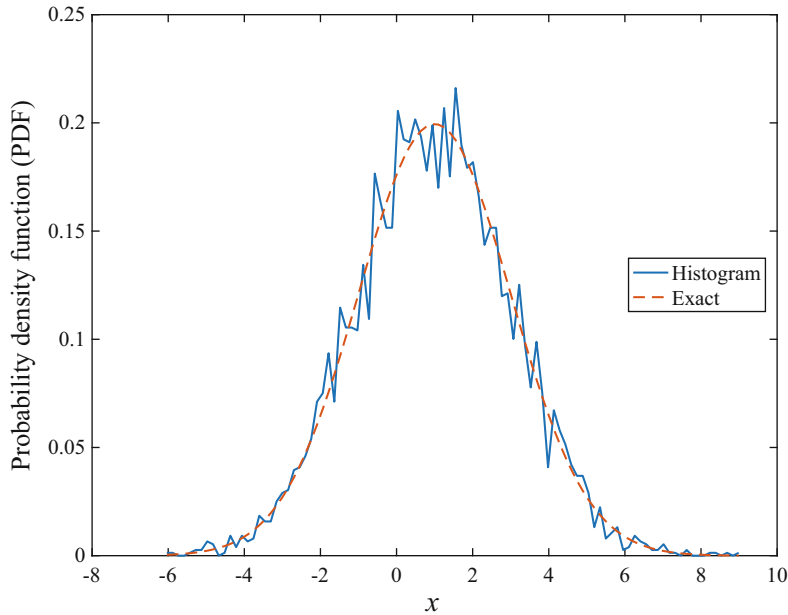


Fig. 5.3 Histogram PDF estimate compared with exact PDF. Note the noisiness of the estimate compared with the CDF estimate in the next figure

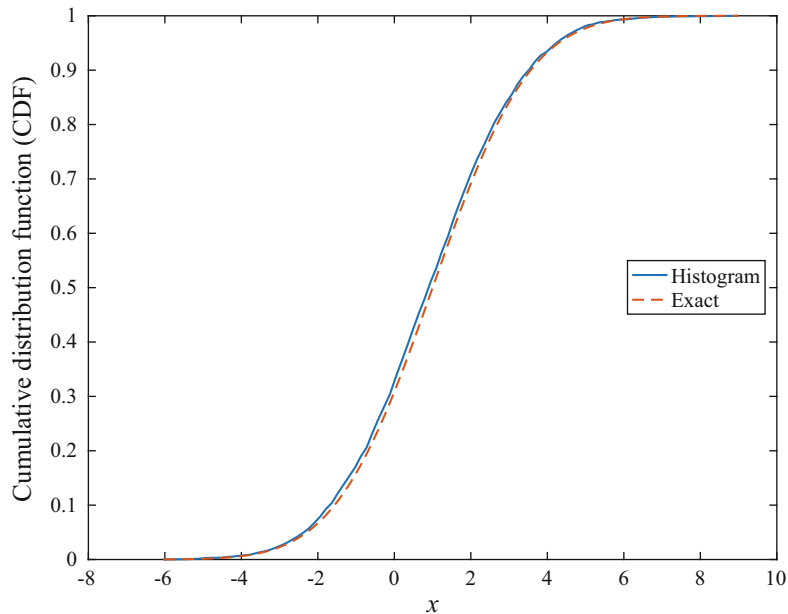


Fig. 5.4 Histogram CDF estimate compared with exact CDF

value h is the number of occurrences of X_i less than or equal to h divided by n . Mathematically, this can be described as

$$\hat{p} = \frac{1}{n} \sum_{i=1}^n \mathbb{I}\{X_i \leq h\} \quad (5.35)$$

where $\mathbb{I}\{\cdot\}$ is the indicator function returning one when the argument is true and zero otherwise. Each term within the sum is a Bernoulli random variable with parameter $p = F_x(h)$ (Sect. 5.6.1) and the sum itself is a binomial random variable with parameters n and p . The confidence interval for the estimate \hat{p} is formed by assuming it is approximately Gaussian, which is accurate if n is large enough,

$$\hat{p} \sim \mathcal{N}\left(p, \sigma_p^2\right) \quad (5.36)$$

where the mean is the true value p and the variance is $\sigma_p^2 = p(1 - p)/n$. Since p is not known, the estimate itself is used to form the confidence interval,

$$\hat{p} \mp z_{\alpha/2} \sqrt{\frac{\hat{p}(1 - \hat{p})}{n}} \quad (5.37)$$

where $z_{\alpha/2}$ is the $\alpha/2$ quantile² of the standard normal distribution, which is the negative of the $1 - \alpha/2$ quantile owing to symmetry in the Gaussian PDF. The interval is said to have confidence coefficient or coverage probability $1 - \alpha$ with the following interpretation. Were the estimation performed many times, the probability the interval includes the true value is $1 - \alpha$ (see Sect. 6.3.8 or [5, Sect. 9.2.3]).

Exercise 5.6 Simulate 5000 exponential random variables with mean 2, estimate the PDF and CDF with a histogram, and compare to the exact functions.

5.3.6 Multiple Random Variables, Joint Densities, and Independence

In most applications, more than one random variable will be observed and they may and may not be related. To describe this situation, consider two random variables X and Y . The joint CDF of X and Y represents the joint occurrence of the events $\{X \leq x\}$ and $\{Y \leq y\}$,

$$F_{X,Y}(x, y) = \Pr\{X \leq x \cap Y \leq y\} \quad (5.38)$$

²The β quantile of the random variable Z is the value z_β such that the CDF $F_Z(z_\beta) = \beta$.

where \cap represents the “and” operation providing the intersection of the two events. Similar to the development of the PDF in Sect. 5.3, the joint PDF is defined as the derivative

$$f_{X,Y}(x, y) = \frac{\partial^2}{\partial x \partial y} F_{X,Y}(x, y) \quad (5.39)$$

leading to the relationship

$$F_{X,Y}(x, y) = \int_{-\infty}^x \int_{-\infty}^y f_{X,Y}(s, t) dt ds. \quad (5.40)$$

Extension to n random variables results in the joint PDF $f(x_1, \dots, x_n)$ and joint CDF $F(x_1, \dots, x_n)$.

The distribution of one of the random variables taken without regard to the other random variables is called the marginal distribution. It can be obtained from the joint PDF by integrating out all other random variables (shown here for two random variables),

$$f_X(x) = \int_{-\infty}^{\infty} f_{X,Y}(x, y) dy. \quad (5.41)$$

The marginal CDF of X is obtained by integrating the marginal PDF,

$$\begin{aligned} F_X(x) &= \int_{-\infty}^x f_X(s) ds \\ &= \int_{-\infty}^x \int_{-\infty}^{\infty} f_{X,Y}(u, v) dv du \\ &= F_{X,Y}(x, \infty) \end{aligned} \quad (5.42)$$

and seen to be the joint CDF after evaluating all other random variables at ∞ .

Random variables are *independent* of each other if there is no information in one about any of the others. Mathematically, the events defined by the CDF (i.e., $\{X_i \leq x_i\}$ for $i = 1, \dots, n$) must be independent for all n -tuples (x_1, \dots, x_n) so the probability of their intersection is the product of the individual probabilities,

$$\begin{aligned} F(x_1, \dots, x_n) &= \Pr\{X_1 \leq x_1 \cap X_2 \leq x_2 \cap \dots \cap X_n \leq x_n\} \\ &= \prod_{i=1}^n \Pr\{X_i \leq x_i\} = \prod_{i=1}^n F_{X_i}(x_i). \end{aligned} \quad (5.43)$$

Differentiating the joint CDF of independent random variables shows the joint PDF is similarly separable into a product of the marginal PDFs,

$$\begin{aligned} f(x_1, \dots, x_n) &= \frac{\partial^n}{\partial x_1 \cdots \partial x_n} F(x_1, \dots, x_n) \\ &= \prod_{i=1}^n \frac{\partial}{\partial x_i} F_{X_i}(x_i) = \prod_{i=1}^n f_{X_i}(x_i). \end{aligned} \quad (5.44)$$

In many situations, a set of random variables is assumed to be independent and identically distributed, for which the acronym *iid* and notation $\stackrel{iid}{\sim}$ will be used. For example, $X_i \stackrel{iid}{\sim} \mathcal{N}(\mu, \sigma^2)$ for $i = 1, \dots, n$ implies the data are independent and identically Gaussian distributed with mean μ and variance σ^2 .

The correlation coefficient between two random variables X and Y is defined as

$$\rho = \frac{E[(X - \mu_X)(Y - \mu_Y)]}{\sigma_X \sigma_Y}, \quad (5.45)$$

which is the covariance divided by the square root of the product of the variances. When $\rho = 0$, X and Y are said to be uncorrelated. If two random variables are independent, their correlation coefficient is zero and so they are also uncorrelated. However, in general if two random variables are uncorrelated ($\rho = 0$), they are not necessarily independent. An example often causing confusion arises from jointly Gaussian-distributed random variables. Suppose X and Y are Gaussian distributed with joint PDF

$$f_{X,Y}(x, y) = \frac{\exp\left\{-\frac{1}{2(1-\rho^2)}\left[\frac{(x-\mu_X)^2}{\sigma_X^2} - 2\rho \frac{(x-\mu_X)(y-\mu_Y)}{\sigma_X \sigma_Y} + \frac{(y-\mu_Y)^2}{\sigma_Y^2}\right]\right\}}{2\pi\sigma_X\sigma_Y\sqrt{1-\rho^2}}. \quad (5.46)$$

The parameter ρ is the correlation coefficient and when $\rho = 0$, the joint PDF is seen to factor into the product of the marginal PDFs. Thus, uncorrelated ($\rho = 0$) Gaussian random variables are actually independent. Although other distributions may produce this case-specific result, it is important to remember that

independence implies two random variables are uncorrelated, whereas

uncorrelated does not necessarily imply independence.

As an example illustrating how two dependent variables can have zero correlation, suppose $Y = X^2$ where the PDF of X is symmetric about zero, which means all odd moments are zero. Clearly, the variables are not statistically independent and yet it is straightforward to show that ρ in (5.45) is zero.

To simplify notation, multiple random variables are often described as a random vector, $\mathbf{x} = [X_1 \dots X_n]^T$. However, this presents a conflict in notation between standard matrix-vector notation (where lower-case bold letters are vectors and upper-case bold letters are matrices) and mathematical statistics notation (where the upper-case letter denotes a random variable and the lower-case letters are their observed values). Because of the visual importance of matrix-vector notation, it will

take precedence over the mathematical statistics notation in this text. Thus, whether $\mathbf{x} = [X_1 \cdots X_n]^T$ is a vector of random variables or $\mathbf{x} = [x_1 \cdots x_n]^T$ represents its observed values must be discerned from the context in which it is used.

The first- and second-order moments are then described in matrix-vector form. The first-order moments are described by the mean vector,

$$\boldsymbol{\mu} = E[\mathbf{x}] = \begin{bmatrix} E[X_1] \\ E[X_2] \\ \vdots \\ E[X_n] \end{bmatrix}. \quad (5.47)$$

The second-order moments can be characterized by a correlation matrix or a covariance matrix. The correlation matrix is

$$\mathbf{R} = E[\mathbf{x}\mathbf{x}^T] \quad (5.48)$$

with element (i, j) containing the correlation between the i th and j th random variables, $E[X_i X_j]$. The covariance matrix is a generalization to the variance that forms a squared vector moment about the mean,

$$\boldsymbol{\Sigma} = E[(\mathbf{x} - \boldsymbol{\mu})(\mathbf{x} - \boldsymbol{\mu})^T] \quad (5.49)$$

with element (i, j) equal to

$$\{\boldsymbol{\Sigma}\}_{i,j} = E[(X_i - \mu_i)(X_j - \mu_j)]. \quad (5.50)$$

Thus, the diagonal terms of $\boldsymbol{\Sigma}$ are the variances of the random variables.

In general, the term *correlation* implies an expectation of a product of two random quantities as in (5.48) and the term *covariance* implies a correlation formed after subtracting mean values as in (5.49). The exception to this is the *correlation coefficient* in (5.45) which is defined as a normalized covariance. Clearly, when the mean of the random quantities is zero, the two results are identical.

5.3.7 Central Limit Theorem (CLT)

The central limit theorem (CLT) is an extremely useful tool for approximately characterizing the statistical distribution of the sum of independent and identically distributed random variables. Suppose X_1, \dots, X_n are *iid* random variables with mean μ and finite variance σ^2 . When their sum is normalized by its mean ($n\mu$) and standard deviation $\sqrt{n}\sigma$,

$$Z_n = \frac{\left[\sum_{i=1}^n X_i \right] - n\mu}{\sqrt{n}\sigma}, \quad (5.51)$$

the CLT [5, Sect. 5.3.2], [3, Sect. 5.4] dictates that it (Z_n) converges in distribution to a standard normal random variable as $n \rightarrow \infty$. This implies that when n is large enough Z_n is approximately $\sim \mathcal{N}(0, 1)$. The importance of this result is that it assumes very little about the actual distribution $f_X(x)$ of X_i (finite variance) and the data set (*iid*). In practice, the quality of the approximation depends on both the number of terms in the sum and how similar $f_X(x)$ is to the Gaussian distribution. Clearly, when X_i is Gaussian, the approximation is exact for all n . The following exercise illustrates how slowly the distribution of the sum converges when the data PDF is not close to Gaussian.

Exercise 5.7 If X_i is a standard exponential random variable, which has unit mean and unit standard deviation, then the sum over n such *iid* random variables is gamma distributed with shape parameter equal to n and unit scale. Show that Z_n from (5.51) is a shifted gamma random variable with distribution

$$f_Z(z) = \frac{n^{n/2}}{\Gamma(n)} (z + \sqrt{n})^{n-1} e^{-\sqrt{n}(z+\sqrt{n})} \quad (5.52)$$

for $z > -\sqrt{n}$. Plot (5.52) for $n = 1, 2, 10$, and 100 and compare with the PDF of the standard normal distribution. The asymmetry of the exponential distribution (and its one-sidedness) produces a very slow convergence of the PDF of the sum to the normal distribution. How noticeable is the difference between the PDF of the sum for $n = 100$ and the normal distribution? Plot the exceedance probability distribution (one minus the CDF) on a logarithmic scale and compare the approximations for large values of z . This illustrates how large n must be for an accurate approximation in the tails of a distribution as is the case when evaluating the performance of a detection algorithm.

5.3.8 Conditional Distributions and Bayes' Theorem

Because CDFs describe the probability of observing an event, conditional probability from Sect. 5.2 can be exploited to determine the CDF of one random variable conditioned on the probability of another random variable being less than a certain value,

$$\Pr\{X < x | Y < y\} = \frac{\Pr\{X \leq x \cap Y \leq y\}}{\Pr\{Y \leq y\}} \quad (5.53)$$

$$= \frac{F_{X,Y}(x, y)}{F_Y(y)}. \quad (5.54)$$

In practice, conditional distributions are useful (e.g., for the purposes of detection or estimation) in describing an unobserved random variable X when a related random variable Y has been measured at the specific value y . Ideally, the conditioning would be on occurrence of the event $\{Y = y\}$. However, a limiting argument must be used for continuous random variables because $\Pr\{Y = y\} = 0$, as was noted in Sect. 5.3.1. This would result in the undefined 0/0 if it were used directly in (5.53) in lieu of the event $\{Y \leq y\}$. Consider, therefore, the CDF of X conditioned on the event $\{y < Y \leq y + \delta\}$ with δ tending to zero,

$$\begin{aligned} F_{X|Y}(x|y) &= \lim_{\delta \rightarrow 0} \Pr\{X \leq x | y < Y \leq y + \delta\} \\ &= \lim_{\delta \rightarrow 0} \frac{F_{X,Y}(x, y + \delta) - F_{X,Y}(x, y)}{F_Y(y + \delta) - F_Y(y)} \\ &= \lim_{\delta \rightarrow 0} \frac{\int_{-\infty}^x \int_y^{y+\delta} f_{X,Y}(s, t) dt ds}{\int_y^{y+\delta} f_Y(t) dt} \end{aligned} \quad (5.55)$$

$$\begin{aligned} &= \lim_{\delta \rightarrow 0} \frac{\int_{-\infty}^x f_{X,Y}(s, y) \delta ds}{f_Y(y) \delta} \\ &= \frac{\int_{-\infty}^x f_{X,Y}(s, y) ds}{f_Y(y)}. \end{aligned} \quad (5.56)$$

It can be seen that conditioning on the probabilistic event $\{y < Y \leq y + \delta\}$ only requires letting δ be small enough that the joint PDF $f_{X,Y}(x, y)$ and the marginal PDF $f_Y(y)$ are approximately constant on $(y, y + \delta]$. This illustrates how the conditional CDF in (5.56) allows extracting as much information about X as possible from the joint distribution over X and Y given that $Y = y$ is observed (e.g., if δ is left too large, the integration over $(y, y + \delta]$ in (5.55) results in a smoother conditional distribution).

Differentiating $F_{X|Y}(x|y)$ with respect to x produces the conditional PDF,

$$\begin{aligned} f_{X|Y}(x|y) &= \frac{\partial}{\partial x} F_{X|Y}(x|y) \\ &= \frac{f_{X,Y}(x, y)}{f_Y(y)}. \end{aligned} \quad (5.57)$$

From the conditional PDF, two important theorems are derived. The first is the total probability theorem,

$$\begin{aligned} f_X(x) &= \int_{-\infty}^{\infty} f_{X,Y}(x, y) dy = \int_{-\infty}^{\infty} f_{X|Y}(x|y) f_Y(y) dy \\ &= E_Y[f_{X|Y}(x|Y)]. \end{aligned} \quad (5.58)$$

The second is Bayes' theorem for PDFs,

$$f_{X|Y}(x|y) = \frac{f_{Y|X}(y|x)f_X(x)}{f_Y(y)} = \frac{f_{Y|X}(y|x)f_X(x)}{\int_{-\infty}^{\infty} f_{Y|X}(y|x)f_X(x) dx}. \quad (5.59)$$

Noting the denominator does not depend on x , it can be seen that the shape of $f_{X|Y}(x|y)$ is driven by the numerator with the denominator simply a scale to ensure the PDF integrates to one. Bayes' theorem is particularly useful when making inferences about an unknown quantity X given some measured data $Y = y$.

5.3.9 Transform-Domain Functions

Similar to temporal signals, there exist frequency-domain-type transformations for PDFs. Although there is no equivalent physical interpretation, the mechanics of the transforms make them useful in statistical analysis.

5.3.9.1 Moment Generating Function

The moment generating function (MGF) is defined as

$$M_X(t) = E[e^{tX}] = \int_{-\infty}^{\infty} e^{tX} f_X(x) dx \quad (5.60)$$

which is the Laplace transform [12, Sect. 4.1] of the PDF $f_X(x)$ evaluated at $-t$ (note in engineering texts, t is usually the argument of the time-domain signal whereas in the statistics literature t is often the argument of the MGF).

The MGF takes its name from its utility in obtaining the moments of a distribution. For example, consider the k th derivative of $M_X(t)$ with respect to t ,

$$M_X^{(k)}(t) = \int_{-\infty}^{\infty} x^k e^{tX} f_X(x) dx. \quad (5.61)$$

Evaluating this function at $t = 0$ yields the k th moment of X about the origin

$$M_X^{(k)}(0) = \int_{-\infty}^{\infty} x^k f_X(x) dx = \mu'_k. \quad (5.62)$$

A very useful application of the MGF is for obtaining the distribution of the sum of independent random variables. Suppose $Y = X_1 + X_2 + \dots + X_L$ where X_l for $l = 1, \dots, L$ are independent and identically distributed with PDF $f_X(x)$. The MGF of Y is seen to be the MGF of X raised to the L th power,

$$\begin{aligned} M_Y(t) &= E[e^{tY}] = E[e^{t(X_1+X_2+\dots+X_L)}] \\ &= \prod_{l=1}^L E[e^{tX_l}] = [M_X(t)]^L. \end{aligned} \quad (5.63)$$

This result is related to the convolution property of the Laplace transform where a convolution in the temporal (PDF) domain equates to a product in the frequency (MGF) domain. In order to determine the PDF of Y , the inverse MGF must be formed. As with the Laplace transform, this can be tedious [12, Sect. 4.1-1] and is normally performed by recognizing the form of the MGF as one of a known distribution.

5.3.9.2 Characteristic Function

Evaluating the MGF at $t = j\omega$ produces the characteristic function (CF) of a distribution,

$$\Phi_X(\omega) = E[e^{j\omega X}] = \int_{-\infty}^{\infty} e^{j\omega x} f_X(x) dx. \quad (5.64)$$

This is easily recognized as the Fourier transform of $f_X(x)$ evaluated at $-\omega$ (see Sect. 4.3). An advantage of using the CF lies in the application of the fast Fourier transform (FFT) (Sect. 4.8) to numerically obtain the PDF or CDF of a random variable from the CF (e.g., via [13] which is described in detail in Sect. 9.2.7.2).

All the properties of the Laplace and Fourier transforms can be applied, respectively, to the MGF and CF, taking care to account for the sign on the argument. However, there are many resources to obtain the functions for common statistical distributions (e.g., Sect. 5.6 or [6]).

The variable Φ is also commonly used to represent the CDF of a standard normal random variable (see Sect. 5.6.6). Although it is generally easy to distinguish them by context (e.g., by the difference in their arguments), in this text the CF is represented by $\Phi(\omega)$ and the standard normal CDF by the variant $\Phi(z)$.

5.3.9.3 Cumulant Generating Function

Related to the MGF is the *cumulant generating function*,

$$K_X(t) = \log M_X(t) = \sum_{j=1}^{\infty} \kappa_j \frac{t^j}{j!}. \quad (5.65)$$

The cumulants are the coefficients of a Taylor series expansion of $K_X(t)$ about the origin,

$$\kappa_j = K_X^{(j)}(0) = \frac{d^j K_X(t)}{dt^j}. \quad (5.66)$$

They can be related to the moments of a random variable about zero (μ'_j) or the central moments (μ_j) about the mean. The first four cumulants and their moment relationships [14, pg. 229] are

$$\begin{aligned} \kappa_1 &= \mu'_1 = \mu, \\ \kappa_2 &= \mu'_2 - \mu'^2_1 = \mu_2 = \sigma^2, \\ \kappa_3 &= \mu'_3 - 3\mu'_1\mu'_2 + 2\mu'^3_1 = \mu_3, \\ \kappa_4 &= \mu'_4 - 3\mu'^2_2 - 4\mu'_1\mu'_3 + 12\mu'^2_1\mu'_2 - 6\mu'^4_1 \\ &= \mu_4 - 3\mu^2_2. \end{aligned} \quad (5.67)$$

In addition to providing easy access to the central moments, it is often easier to take derivatives of $K_X(t)$ than $M_X(t)$.

Exercise 5.8 Use the MGF to find the mean and variance of a non-central chi-squared random variable.

Exercise 5.9 Show that the sum of n independent non-central chi-squared random variables with non-centrality parameters δ_i for $i = 1, \dots, n$ is still non-centrally chi-squared distributed.

Exercise 5.10 Obtain the PDF of a sum of n independent exponentially distributed random variables where the mean of each is unique ($\lambda_i \neq \lambda_j$ if $i \neq j$). Hint: apply partial fraction expansion to the MGF.

Exercise 5.11 Show the cumulants κ_3 and higher for a normal distribution are zero.

5.4 Random Processes

Recall from Sect. 5.3 that a random variable mapped an experiment outcome to the real line. Similarly, a stochastic or random process maps a time-dependent experiment outcome to the real line to form a function of time with random characteristics, $X(t)$. By considering one particular time (say t_*), the random process at that time, $X(t_*)$, is a random variable with all the properties and characteristics previously described. Most physically measured signals (e.g., acoustic pressure, temperature, salinity, etc.) can be represented as a random process. In many cases, there will be more than one independent variable; for example, measuring pressure in space and

time leads to a four-dimensional random process. This section covers the very basics of random processes, limiting consideration to the few properties and characteristics necessary for use in subsequent chapters. References containing general information on random processes include [1, 2]; however, the subject is extensive enough for books to be written solely on specific types of random processes (e.g., [15]).

A complete statistical characterization of a random process requires an n th-order joint distribution function

$$F(x_1, \dots, x_n; t_1, \dots, t_n) = \Pr\{X(t_1) \leq x_1, \dots, X(t_n) \leq x_n\} \quad (5.68)$$

for all t_1, \dots, t_n as $n \rightarrow \infty$ where x_i is the observation of the random process at time t_i . In general, this information is difficult or impossible to obtain, so it is common to work with the first- and second-order properties of the random process. In certain situations (e.g., Gaussian random processes), these moments can completely characterize the process.

With respect to random processes, first-order properties are obtained by considering only one time. Since the random process at any given time is a random variable, the CDF and PDF are, respectively,

$$F(x; t) = \Pr\{X(t) \leq x\} \quad \text{and} \quad f(x; t) = \frac{\partial}{\partial x} F(x; t). \quad (5.69)$$

The PDF is used to determine the mean

$$\mu(t) = E[X(t)] = \int_{-\infty}^{\infty} x f(x; t) dx \quad (5.70)$$

and variance

$$\sigma^2(t) = E[(X(t) - \mu(t))^2] = E[X^2(t)] - \mu^2(t). \quad (5.71)$$

Second-order properties are obtained by considering the random process at two times, t_1 and t_2 , to obtain the random variables $X(t_1)$ and $X(t_2)$. From Sect. 5.3.6, the joint CDF is

$$F(x_1, x_2; t_1, t_2) = \Pr\{X(t_1) \leq x_1 \cap X(t_2) \leq x_2\} \quad (5.72)$$

and the joint PDF is

$$f(x_1, x_2; t_1, t_2) = \frac{\partial^2}{\partial x_1 \partial x_2} F(x_1, x_2; t_1, t_2). \quad (5.73)$$

An important second-order property of random processes is the autocorrelation function (ACF),

$$R_{XX}(t_1, t_2) = E[X(t_1)X(t_2)] = \int_{-\infty}^{\infty} \int_{-\infty}^{\infty} x_1 x_2 f(x_1, x_2; t_1, t_2) dx_1 dx_2 \quad (5.74)$$

which describes the second-order moment of the random process over two potentially different times. When it is evaluated at the same times ($t_1 = t_2 = t$), it produces the power

$$R_{XX}(t, t) = E[X^2(t)] = \sigma^2(t) + \mu^2(t). \quad (5.75)$$

Gaussian random processes are completely described by the mean and ACF.

Related to the ACF is the autocovariance function, which first removes the means

$$C_{XX}(t_1, t_2) = E[(X(t_1) - \mu(t_1))(X(t_2) - \mu(t_2))] = R(t_1, t_2) - \mu(t_1)\mu(t_2). \quad (5.76)$$

Often, these functions are described in terms of a time (t) and a time difference (τ) rather than two times. For example, the ACF can be parameterized as

$$R_{XX}(t, \tau) = E[X(t)X(t + \tau)] \quad (5.77)$$

where $t_1 = t$ and $t_2 = t + \tau$ (so $\tau = t_2 - t_1$).

5.4.1 Stationarity and Ergodicity

In order to make analysis of random processes tractable, it is necessary to restrict consideration to specific types of processes. In particular, the concepts of stationarity and ergodicity enable many types of analysis (the most common of which is evaluation of the frequency spectrum). A random process is *strict-sense-stationary* (SSS) if its properties do not change with time. Mathematically, this requires

$$F(x_1, \dots, x_n; t_1, \dots, t_n) = F(x_1, \dots, x_n; t_1 + t_0, \dots, t_n + t_0) \quad (5.78)$$

for all n and all t_0 . If the joint CDF does not change with time, then the joint PDF, mean, and variance are similarly constant. The ACF satisfies the relationship

$$\begin{aligned} R_{XX}(t_1, t_2) &= \int_{-\infty}^{\infty} \int_{-\infty}^{\infty} x_1 x_2 f(x_1, x_2; t_1, t_2) dx_1 dx_2 \\ &= \int_{-\infty}^{\infty} \int_{-\infty}^{\infty} x_1 x_2 f(x_1, x_2; t_1 + t_0, t_2 + t_0) dx_1 dx_2 \\ &= R_{XX}(t_1 + t_0, t_2 + t_0) \end{aligned} \quad (5.79)$$

for all t_0 , implying it is only a function of the difference $t_2 - t_1 = (t_2 + t_0) - (t_1 + t_0) = \tau$, which explains why some ACF definitions use a delay.

In most situations, it will not be possible to prove a random process is SSS, so the conditions are relaxed to satisfy only the first- and second-order conditions for what are termed wide-sense stationary (WSS) random processes. That is, a random process is WSS if the mean

$$E[X(t)] = \mu \quad (5.80)$$

is a constant and the ACF

$$R_{XX}(t, t + \tau) = R_{XX}(\tau) \quad (5.81)$$

is only a function of delay τ . Any SSS random process will be WSS; however, the converse is not true in general. A specific case where WSS does imply SSS is the Gaussian random process. In practice, most measurements will be neither SSS nor WSS, but are often assumed to be WSS over short periods of time. A function related to the ACF by a Fourier transform is the power spectral density of a WSS random process, which is discussed in Sect. 5.4.2.

After stationarity, a second desirable property of a random process is that of ergodicity, which relates the *ensemble* characteristics of a random process to its temporal characteristics. The ensemble is the space of all possible outcomes of the experiment; $X(t)$ is one random draw or realization from the ensemble. Quantities of interest are often described in terms of moments over the ensemble. For example, consider the mean from (5.70). If many observations of the random process were available (identified by ζ_i in the following equation), it could be approximated by a sample mean

$$\hat{\mu}(t) = \frac{1}{n} \sum_{i=1}^n X(t, \zeta_i) \quad (5.82)$$

where ζ_i represents the i th observation from the ensemble for $i = 1, \dots, n$. The estimate is unbiased (i.e., its expected value is the true value, $E[\hat{\mu}(t)] = \mu(t)$) and the variance inversely proportional to n , implying increasing accuracy as n increases.

Suppose, however, that only one observation of the random process is available. If the random process is WSS, the mean is constant $\mu(t) = \mu$ and therefore may be estimated from a temporal average,

$$\hat{\mu}_T = \frac{1}{T} \int_{-T/2}^{T/2} X(t) dt. \quad (5.83)$$

The estimate is unbiased and has variance

$$\begin{aligned}
 \text{Var}[\hat{\mu}_T] &= E[(\hat{\mu}_T - \mu)^2] \\
 &= \frac{1}{T^2} E\left[\left(\int_{-T/2}^{T/2} (X(t) - \mu) dt\right)^2\right] \\
 &= \frac{1}{T^2} \int_{-T/2}^{T/2} \int_{-T/2}^{T/2} E[(X(t) - \mu)(X(s) - \mu)] dt ds \\
 &= \frac{1}{T} \int_{-T}^T \left(1 - \frac{|\tau|}{T}\right) C_{XX}(\tau) d\tau. \tag{5.84}
 \end{aligned}$$

If the random process decorrelates quickly enough in time (i.e., the autocovariance $C_{XX}(\tau)$ goes to zero quickly enough as $|\tau|$ increases), then $\text{Var}[\hat{\mu}_T]$ will be inversely proportional to T as $T \rightarrow \infty$, implying increasing accuracy as T increases. Under these conditions, the time average can be used in lieu of the ensemble average. Such a random process is called *mean ergodic* and requires

$$\int_0^\infty C_{XX}(\tau) d\tau < \infty. \tag{5.85}$$

A random process is considered *power ergodic* when the autocovariance of $X^2(t)$ satisfies (5.85) and *distribution ergodic* when $X(t)$ and $X(t + \tau)$ become independent as $\tau \rightarrow \infty$. These cases extend to estimates of the power or CDF, the important concept of replacing ensemble averaging with time averaging for WSS random processes.

Many signal processing functions entail filtering a signal. Generally, the filters are linear and time invariant (LTI) (see Sect. 4.9 for details on LTI filters). When the input to an LTI filter is a WSS random process, the output is also a WSS random process. If the input mean and ACF are μ_X and $R_{XX}(\tau)$ and the impulse response of the filter is $h(t)$, the mean of the output is

$$\mu_Y = \mu_X \int_{-\infty}^{\infty} h(t) dt \tag{5.86}$$

and the ACF of the output is

$$R_{YY}(\tau) = \int_{-\infty}^{\infty} \int_{-\infty}^{\infty} R_{XX}(\tau - \alpha + \beta) h(\alpha) h(\beta) d\alpha d\beta. \tag{5.87}$$

By describing the output of the filter as the convolution between the input and the impulse response,

$$\begin{aligned}
Y(t) &= \int_{-\infty}^{\infty} X(t - \tau) h(\tau) d\tau \\
&\approx \sum_{i=-\infty}^{\infty} X(t - iT) h(iT) T
\end{aligned} \tag{5.88}$$

it is clearly a linear combination of the input random process. This implies that if the input random process is WSS and Gaussian, then the output will also be WSS and Gaussian. The importance of this result lies in the ability to perform any LTI filtering on a measured signal (described as a WSS Gaussian random process) and obtain a statistical characterization of the filter output from (5.86) and (5.87).

Exercise 5.12 Show that if a random process $X(t)$ is stationary, it is point-wise uncorrelated with the random process defined by its derivative $X'(t)$. That is, show $E[X(t)X'(t)] = 0$. Hint: note that

$$X(t)X'(t) = \frac{d}{dt} \frac{1}{2} X^2(t) \tag{5.89}$$

and that the order of differentiation and integration (expectation) can be exchanged. Does the same hold if $X(t)$ and $X'(t)$ are taken at different times?

5.4.2 Power Spectral Density

As described in Sect. 4.3, the Fourier transform of a signal $x(t)$ describes its frequency content. Only deterministic signals were considered in Sect. 4.3; here, Fourier analysis of random signals is introduced. To ensure the Fourier transform exists (i.e., to satisfy the absolutely integrable requirement), consider the truncation of a random process $X(t)$ with a window function,

$$X_T(t) = w(t)X(t) \tag{5.90}$$

where it is assumed that $w(t) = 0$ for $|t| > T/2$. The Fourier transform of $X_T(t)$ is

$$\mathcal{X}_T(f) = \int_{-\infty}^{\infty} X_T(t) e^{-j2\pi f t} dt \tag{5.91}$$

where here $\mathcal{X}_T(f)$ is used to represent the Fourier transform of a random process to avoid confusion with the random process being defined with a capital letter. The Fourier transform $\mathcal{X}_T(f)$ is itself a random function and will have zero mean if $X(t)$ does. Of primary interest is the expected value of the squared modulus of the Fourier transform,

$$\begin{aligned}
S_T(f) &= E[|\mathcal{X}_T(f)|^2] \\
&= E\left[\int_{-\infty}^{\infty} \int_{-\infty}^{\infty} X_T(t) X_T(s) e^{-j2\pi f(t-s)} dt ds\right] \\
&= \int_{-\infty}^{\infty} \int_{-\infty}^{\infty} w(t) w(s) R_{XX}(t-s) e^{-j2\pi f(t-s)} dt ds \\
&= \int_{-\infty}^{\infty} \left[\int_{-\infty}^{\infty} w(s) w(s+\tau) ds \right] R_{XX}(\tau) e^{-j2\pi f\tau} d\tau \\
&= \int_{-\infty}^{\infty} R_{ww}(\tau) R_{XX}(\tau) e^{-j2\pi f\tau} d\tau.
\end{aligned} \tag{5.92}$$

In deriving (5.92), $X(t)$ is assumed to be WSS, $R_{XX}(\tau)$ is assumed to decay to zero rapidly enough with $|\tau|$, and the effect of the window is represented by the correlation function

$$R_{ww}(\tau) = \int_{-\infty}^{\infty} w(s) w(s+\tau) ds = \mathcal{F}^{-1}\{|W(f)|^2\} \tag{5.93}$$

which is the inverse Fourier transform of the squared modulus of the Fourier transform of the window function,

$$S_w(f) = |W(f)|^2. \tag{5.94}$$

Further, suppose the window function $w(t)$ is scaled to have unit energy,

$$\int_{-\infty}^{\infty} w^2(t) dt = 1 = \int_{-\infty}^{\infty} S_w(f) df \tag{5.95}$$

which, by Parseval's theorem, implies the squared modulus of the Fourier transform also integrates to one.

Because $S_T(f)$ is the Fourier transform of a product in the time (delay) domain, it can be described as a convolution in the frequency domain,

$$S_T(f) = \int_{-\infty}^{\infty} S_w(\gamma) S_{XX}(f - \gamma) d\gamma \tag{5.96}$$

where the Fourier transform of $R_{XX}(\tau)$,

$$S_{XX}(f) = \int_{-\infty}^{\infty} R_{XX}(\tau) e^{-j2\pi f\tau} d\tau \tag{5.97}$$

is defined as the *power spectral density* (PSD) of the WSS random process $X(t)$.

If the temporal extent of $w(t)$ is large, then $S_w(f)$ will be narrow. For example, consider a rectangular window $w(t) = \text{rect}(t/T)/\sqrt{T}$, resulting in

$$S_w(f) = T \text{sinc}^2(ft) \quad (5.98)$$

which has null-to-null width $2/T$. By letting $T \rightarrow \infty$, $S_w(f) \rightarrow \delta(f)$ and the PSD of $X(t)$ is extracted from the convolution,

$$\lim_{T \rightarrow \infty} S_T(f) = S_{XX}(f). \quad (5.99)$$

Suppose, however, that T is finite but large enough so $S_{XX}(f)$ varies slowly with respect to the width of $S_w(f)$. Then, $S_T(f)$ approximates the PSD of $X(t)$,

$$S_T(f) \approx S_{XX}(f) \int_{-\infty}^{\infty} S_w(\gamma) d\gamma = S_{XX}(f) \quad (5.100)$$

and the need for $w(t)$ to satisfy (5.95) is evident.

When a linear-time-invariant (LTI) filter is applied to a wide-sense-stationary random process, the PSD of the filter output can be related to the PSD of the input and the transfer function $H(f)$ of the LTI system. By taking the Fourier transform of (5.87), it can be shown that

$$S_{YY}(f) = |H(f)|^2 S_{XX}(f) \quad (5.101)$$

where $X(t)$ and $Y(t)$ are, respectively, the input and output of the LTI system.

Why is $S_{XX}(f)$ called the *power spectral density*? The power of a random process $X(t)$ is its average intensity,

$$\mathcal{P}_X = \frac{1}{T} \int_0^T X^2(t) dt. \quad (5.102)$$

If a random process is ergodic, then the temporal and ensemble moments are equal so the power is also the ACF evaluated at zero delay,

$$\mathcal{P}_X = E[X^2(t)] = R_{XX}(0). \quad (5.103)$$

Finally, by using the definition of the inverse Fourier transform evaluated at $\tau = 0$, the power in $X(t)$ is seen to be the integral of the PSD over all frequency,

$$\mathcal{P}_X = R_{XX}(0) = \int_{-\infty}^{\infty} S_{XX}(f) df. \quad (5.104)$$

Therefore, $S_{XX}(f)$ describes the density of power as a function of frequency. Suppose $X(t)$ represents an acoustic pressure measurement with units in the μPa scale. Then, \mathcal{P}_X has units $(\mu\text{Pa})^2$ and $S_{XX}(f)$ will have units $(\mu\text{Pa})^2/\text{Hz}$.

Spectral estimation is the process of estimating $S_{XX}(f)$ from finite data records. The reader is referred to [16, 17] for detailed descriptions of the classical periodogram-based approaches as well as the more modern model-based approaches.

5.5 Complex Random Variables and Random Processes

In signal processing, it is common to convert real-valued signals to complex forms. For example, bandpass signals can be elegantly analyzed and efficiently processed using complex envelopes (e.g., see Sect. 7.3.1). Most statistical analysis has been developed for real random variables and real random processes. Resources for complex random variables and random processes include [15, 18–21]. When applied to complex data, statistical analysis begins by treating the real and imaginary parts as separate variables through the use of joint densities and distributions as in Sect. 5.3.6. Under certain conditions, the joint PDFs can be more easily characterized with a single complex argument rather than separate real and imaginary parts.

For example, suppose X and Y are jointly Gaussian, zero-mean random variables. The bivariate normal PDF from (5.46) is then

$$f_{X,Y}(x, y) = \frac{\exp\left\{-\frac{1}{2(1-\rho^2)}\left[\frac{x^2}{\sigma_X^2} - 2\rho\frac{xy}{\sigma_X\sigma_Y} + \frac{y^2}{\sigma_Y^2}\right]\right\}}{2\pi\sigma_X\sigma_Y\sqrt{1-\rho^2}}. \quad (5.105)$$

If X and Y are uncorrelated ($\rho = 0$) and have the same variance ($\sigma_X^2 = \sigma_Y^2 = \sigma^2$), then the PDF becomes

$$\begin{aligned} f_{X,Y}(x, y) &= \frac{1}{2\pi\sigma^2} e^{-\frac{1}{2\sigma^2}[x^2+y^2]} \\ &= \frac{1}{2\pi\sigma^2} e^{-\frac{1}{2\sigma^2}|z|^2} = f_Z(z) \end{aligned} \quad (5.106)$$

where $z = x + jy$ represents the observed value of the complex random variable $Z = X + jY$. Working with $f_Z(z)$ (and its multivariate counterpart) is often easier than maintaining the separate real and imaginary terms in $f_{X,Y}(x, y)$. This essentially requires that the joint PDF of the real and imaginary parts be characterizable as a function of the complex random variable while maintaining the relationships required to satisfy this under any transformation of the complex random variable necessary in the analysis. Although the complex Gaussian distribution (Sect. 5.6.7, [18]) is the most commonly encountered one, other distributions exist that satisfy these requirements.

For the multivariate case (i.e., a complex random vector $\mathbf{z} = \mathbf{x} + j\mathbf{y}$), the relationships required to describe the joint PDF of the real and imaginary parts as a function of their complex representation are maintained under affine transformations ($\mathbf{u} = \mathbf{Az} + \mathbf{b}$) when the following two conditions are satisfied:

1. The real and imaginary parts of \mathbf{z} have identical covariance matrices,

$$\boldsymbol{\Sigma}_{XX} = E[(\mathbf{x} - \boldsymbol{\mu}_X)(\mathbf{x} - \boldsymbol{\mu}_X)^T] = E[(\mathbf{Y} - \boldsymbol{\mu}_Y)(\mathbf{y} - \boldsymbol{\mu}_Y)^T] = \boldsymbol{\Sigma}_{YY} \quad (5.107)$$

2. The real and imaginary parts of \mathbf{z} have a skew-symmetric cross-covariance matrix,

$$\begin{aligned} \boldsymbol{\Sigma}_{YX} &= E[(\mathbf{y} - \boldsymbol{\mu}_Y)(\mathbf{x} - \boldsymbol{\mu}_X)^T] \\ &= -E[(\mathbf{x} - \boldsymbol{\mu}_X)(\mathbf{y} - \boldsymbol{\mu}_Y)^T] = -\boldsymbol{\Sigma}_{XY}, \end{aligned} \quad (5.108)$$

$$\text{so } \boldsymbol{\Sigma}_{YX} = -\boldsymbol{\Sigma}_{XY} = -\boldsymbol{\Sigma}_{YX}^T,$$

as detailed in [19], [21, Sect. 2.2], or [15, Sect. 3.7]. Taken together, these conditions are often referred to as *circularity* or *circular symmetry*. In most cases, data can be assumed to be circularly symmetric, although there has been recent interest in improper cases [21].

The mean of the complex vector \mathbf{z} is related to the means of the real and imaginary parts as would be expected, $E[\mathbf{z}] = \boldsymbol{\mu}_Z = \boldsymbol{\mu}_X + j\boldsymbol{\mu}_Y$. The covariance matrix of a complex vector \mathbf{z} with mean $\boldsymbol{\mu}_Z$ is defined as

$$\boldsymbol{\Sigma}_{ZZ} = E[(\mathbf{z} - \boldsymbol{\mu}_Z)(\mathbf{z} - \boldsymbol{\mu}_Z)^H] \quad (5.109)$$

where the conjugate-transpose (superscript H) is used rather than the transpose (superscript T). The relationship between the covariances of the complex and real representations is not as obvious as for the means. By expanding (5.109) into real and imaginary parts and applying the circularity conditions, the covariance matrix of the complex vector \mathbf{z} is seen to be

$$\begin{aligned} \boldsymbol{\Sigma}_{ZZ} &= \boldsymbol{\Sigma}_{XX} + \boldsymbol{\Sigma}_{YY} + j(\boldsymbol{\Sigma}_{YX} - \boldsymbol{\Sigma}_{XY}) \\ &= 2\boldsymbol{\Sigma}_{XX} + j2\boldsymbol{\Sigma}_{YX}. \end{aligned} \quad (5.110)$$

From this, the covariance and cross-covariance of the real and imaginary parts are

$$\boldsymbol{\Sigma}_{XX} = \boldsymbol{\Sigma}_{YY} = \frac{1}{2} \operatorname{Real}\{\boldsymbol{\Sigma}_{ZZ}\} \quad (5.111)$$

and

$$\boldsymbol{\Sigma}_{YX} = -\boldsymbol{\Sigma}_{XY} = \frac{1}{2} \operatorname{Imag}\{\boldsymbol{\Sigma}_{ZZ}\}. \quad (5.112)$$

As previously noted, the most common distribution for complex multivariate random variables in signal processing is the complex Gaussian distribution,

$$f(\mathbf{z}) = \frac{1}{\pi^n |\boldsymbol{\Sigma}_{ZZ}|} e^{-(\mathbf{z}-\boldsymbol{\mu}_Z)^H \boldsymbol{\Sigma}_{ZZ}^{-1} (\mathbf{z}-\boldsymbol{\mu}_Z)} \quad (5.113)$$

for $\mathbf{z} \in \mathbb{C}^n$, which has many similarities to the real multivariate Gaussian distribution. Derivation of the n -dimensional complex Gaussian PDF in (5.113) from the $2n$ -dimensional real Gaussian PDF, as shown in [15, Sect. 3.7], can be done by relating the eigenvalues and eigenvectors of $\boldsymbol{\Sigma}_{ZZ}$ to those of the covariance of the combined real and imaginary parts,

$$\boldsymbol{\Sigma}_R = \begin{bmatrix} \boldsymbol{\Sigma}_{XX} & \boldsymbol{\Sigma}_{XY} \\ \boldsymbol{\Sigma}_{YX} & \boldsymbol{\Sigma}_{YY} \end{bmatrix} = \begin{bmatrix} \boldsymbol{\Sigma}_{XX} & -\boldsymbol{\Sigma}_{YX} \\ \boldsymbol{\Sigma}_{YX} & \boldsymbol{\Sigma}_{XX} \end{bmatrix} \quad (5.114)$$

while exploiting the aforementioned circularity conditions.

Applying the circularity conditions to a complex random process $Z(t) = X(t) + jY(t)$ results in [19], [20, Sect. 60.2.3] requiring equal autocovariance functions

$$C_{XX}(t_1, t_2) = C_{YY}(t_1, t_2) \quad (5.115)$$

and a cross-covariance function satisfying

$$\begin{aligned} C_{XY}(t_1, t_2) &= E[X(t_1) - \mu_X(t_1)][Y(t_2) - \mu_Y(t_2)] \\ &= -C_{YX}(t_1, t_2) = -C_{XY}(t_2, t_1). \end{aligned} \quad (5.116)$$

The resulting autocovariance function of the complex random process $Z(t)$ is

$$C_{ZZ}(t_1, t_2) = E[(Z(t_1) - \mu_Z(t_1))^*[Z(t_2) - \mu_Z(t_2)]] \quad (5.117)$$

$$= 2C_{XX}(t_1, t_2) - j2C_{YX}(t_1, t_2) \quad (5.118)$$

and

$$E[Z(t_1)Z(t_2)] = 0. \quad (5.119)$$

Note that the convention in defining the autocovariance function in (5.117) is that the conjugation is applied to the random process at time t_1 . When $X(t)$ and $Y(t)$ are jointly WSS, their auto- and cross-covariance functions only depend on $\tau = t_2 - t_1$, implying $Z(t)$ is also WSS. The autocorrelation function is then defined by

$$R_{ZZ}(\tau) = E[Z^*(t)Z(t + \tau)]. \quad (5.120)$$

Exercise 5.13 If a complex random vector \mathbf{z} satisfies the circularity conditions, show that its *pseudo-covariance* is a matrix of zeros

$$E[(\mathbf{z} - \mu_z)(\mathbf{z} - \mu_z)^T] = \mathbf{0}.$$

The pseudo-covariance has a similar form to the covariance matrix in (5.109), but uses a transpose T as opposed to a conjugate-transpose H .

5.6 Common Statistical Distributions

This section contains the pertinent characteristics (e.g., as listed in Table 5.2) of many common statistical distributions (listed in Table 5.3). Useful handbook-type references containing most of the ensuing information include [6, 10], and Wikipedia [22]. Specific references are provided within each entry for distributions not easily found. More detailed descriptions, historical notes, and analysis for the majority of these distributions can be found in the series of texts initially written by Johnson and Kotz [23–26]. Many of the distributions described in this section are related to each other. Although several important relationships are noted, references such as [10, 11] provide a more extensive list.

The order in which the distributions are presented in Table 5.3 and the ensuing subsections is not alphabetical. Discrete distributions are presented first, followed by continuous ones. Within each of these categories, the sorting is a combination of importance/prevalence and inter-relationships (e.g., complex Gaussian follows Gaussian and Rician follows Rayleigh).

Table 5.2 Characterizing a statistical distribution

Property	Representation
PDF (probability density function)	$f(x) = \frac{d}{dx} F(x)$
CDF (cumulative distribution function)	$F(x) = \int_{-\infty}^x f(y) dy$
Mean	$\mu = E[X]$
Variance	$E[(X - \mu)^2]$
Power	$E[X^2]$
k th-order moment	$\mu'_k = E[X^k]$
k th-order central moment	$\mu_k = E[(X - \mu)^k]$
Median	η such that $F(\eta) = 0.5$
Mode	$\arg \max_x f(x)$
MGF (moment generating function)	$M(t) = E[e^{tX}]$
CF (characteristic function)	$\Phi(\omega) = E[e^{j\omega X}]$

Table 5.3 List of statistical distributions covered in this section

Distribution	Type	Notation	PDF support	Section
Bernoulli	Discrete	$\text{Be}(p)$	$\{0, 1\}$	5.6.1
Binomial	Discrete	$\text{Bin}(n, p)$	$\{0, 1, \dots, n\}$	5.6.2
Poisson	Discrete	$\text{Poi}(\lambda)$	$\{0, 1, 2, \dots\}$	5.6.3
Uniform	Continuous	$\text{Uni}(a, b)$	$[a, b]$	5.6.4
Beta	Continuous	$\text{Beta}(\alpha, \beta)$	$[0, 1]$	5.6.5
Gaussian (normal)	Continuous	$\mathcal{N}(\mu, \sigma^2)$	$\mathbb{R} = (-\infty, \infty)$	5.6.6
Complex Gaussian	Continuous	$\mathcal{CN}(\mu, \sigma^2)$	$\mathcal{C} = \mathbb{R}^2$	5.6.7
Multivariate Gaussian	Continuous	$\mathcal{N}(\boldsymbol{\mu}, \boldsymbol{\Sigma})$	\mathbb{R}^n	5.6.8
Complex multivariate Gaussian	Continuous	$\mathcal{CN}(\boldsymbol{\mu}, \boldsymbol{\Sigma})$	\mathcal{C}^n	5.6.9
Exponential	Continuous	$\text{Expon}(\lambda)$	$[0, \infty)$	5.6.10
Gamma	Continuous	$\text{Gamma}(\alpha, \beta)$	$[0, \infty)$	5.6.11
Rayleigh	Continuous	$\text{Rayl}(\sigma)$	$[0, \infty)$	5.6.12
Rician	Continuous	$\text{Rice}(\sigma, \alpha)$	$[0, \infty)$	5.6.13
Chi-squared	Continuous	χ_v^2	$[0, \infty)$	5.6.14
Non-central chi-squared	Continuous	$\chi_{v,\delta}^2$	$[0, \infty)$	5.6.15
F	Continuous	F_{v_1, v_2}	$[0, \infty)$	5.6.16
Non-central F	Continuous	$F_{v_1, v_2, \delta}$	$[0, \infty)$	5.6.17
Weibull	Continuous	$\text{Wbl}(\beta, \lambda)$	$[0, \infty)$	5.6.18
K	Continuous	$K(\alpha, \lambda)$	$[0, \infty)$	5.6.19
Generalized Pareto	Continuous	$\text{GP}(\gamma, \lambda)$	$[0, \infty)$	5.6.20
Log normal	Continuous	$\text{LN}(\mu, \lambda)$	$[0, \infty)$	5.6.21

5.6.1 Bernoulli Distribution

Notation $U \sim \text{Be}(p)$

Parameters/Moments/Characteristics

Mean $p \in [0, 1]$

Variance $p(1 - p)$

Support $u \in \{0, 1\}$ [discrete]

PDF $f(u) = p^u(1 - p)^{1-u}$

MGF $M(t) = 1 - p + pe^t$

CF $\Phi(\omega) = 1 - p + pe^{j\omega}$

Relationships and Properties

- History:
- Classic representation of the success ($U = 1$) or failure ($U = 0$) of an experiment where p is the probability of success.

- Relationships:
- Used to define several other random variables including binomial, geometric, and negative binomial.

5.6.2 Binomial Distribution

Notation $X \sim \text{Bin}(n, p)$

Parameters/Moments/Characteristics

Number of trials	n a natural number
Success probability	$p \in [0, 1]$
Mean	np
Variance	$np(1 - p)$
Support	$x \in \{0, 1, \dots, n\}$ [discrete]
PDF	$f(x) = \binom{n}{x} p^x (1 - p)^{n-x}$
MGF	$M(t) = (1 - p + pe^t)^n$
CF	$\Phi(\omega) = (1 - p + pe^{j\omega})^n$

Relationships and Properties

- Formation: • Sum of n iid Bernoulli random variables.
- Asymptotic: • Normal as $n \rightarrow \infty$.
- Special function: • n choose x : $\binom{n}{x} = \frac{n!}{x!(n-x)!}$

5.6.3 Poisson Distribution

Notation $X \sim \text{Poi}(\lambda)$

Parameters/Moments/Characteristics

Mean	$\lambda > 0$
Variance	λ
Support	$x \in \{0, 1, \dots\}$ [discrete]
PDF	$f(x) = \frac{\lambda^x e^{-\lambda}}{x!}$
MGF	$M(t) = e^{\lambda(e^t - 1)}$
CF	$\Phi(\omega) = e^{\lambda(e^{j\omega} - 1)}$

Relationships and Properties

- Note: • A discrete form of the exponential distribution.

5.6.4 Uniform Distribution

Notation $X \sim \text{Uni}(a, b)$

Parameters/Moments/Characteristics

Location $-\infty < a < b < \infty$

Mean $\frac{a+b}{2}$

Variance $\frac{(b-a)^2}{12}$

Median $\frac{a+b}{2}$

Support $x \in [a, b]$

PDF $f(x) = \begin{cases} \frac{1}{b-a} & \text{for } x \in [a, b] \\ 0 & \text{otherwise} \end{cases}$

CDF $F(x) = \begin{cases} 0 & \text{for } x < a \\ \frac{x-a}{b-a} & \text{for } x \in [a, b] \\ 1 & \text{for } x > b \end{cases}$

MGF $M(t) = \frac{e^{bt} - e^{at}}{t(b-a)}$

CF $\Phi(\omega) = \frac{e^{jb\omega} - e^{ja\omega}}{j\alpha(b-a)}$

Relationships and Properties

Note:

- A “standard” uniform random variable is $\text{Uni}(0, 1)$.

Simulation:

- Evaluating a random variable’s CDF at the random variable results in a standard uniform random variable: $F_X(X) \sim \text{Uni}(0, 1)$. If $F_X(x)$ is invertible, this can be used to simulate X (see Sect. 5.3.4).

5.6.5 Beta Distribution

Notation $X \sim \text{Beta}(\alpha, \beta)$

Parameters/Moments/Characteristics

Shape $\alpha > 0$ and $\beta > 0$

Mean $\frac{\alpha}{\alpha+\beta}$

Variance $\frac{\alpha\beta}{(\alpha+\beta)^2(\alpha+\beta+1)}$

k th moment $\mu'_k = \frac{B(\alpha+k, \beta)}{B(\alpha, \beta)} = \frac{\Gamma(\alpha+\beta)\Gamma(\alpha+k)}{\Gamma(\alpha+\beta+k)\Gamma(\alpha)}$

Mode $\frac{\alpha-1}{\alpha+\beta-2}$ for $\alpha > 1$ and $\beta > 1$

Support $x \in [0, 1]$

PDF $f(x) = \frac{\Gamma(\alpha+\beta)}{\Gamma(\alpha)\Gamma(\beta)} x^{\alpha-1} (1-x)^{\beta-1}$

Relationships and Properties

Simplification: • A standard uniform distribution arises when $\alpha = \beta = 1$.

Special function: • The beta function is

$$\begin{aligned} B(\alpha, \beta) &= \int_0^1 x^{\alpha-1} (1-x)^{\beta-1} dx \\ &= \frac{\Gamma(\alpha)\Gamma(\beta)}{\Gamma(\alpha+\beta)} \end{aligned} \quad (5.121)$$

CDF: • The CDF is the regularized incomplete beta function [27, Ch. 58].

5.6.6 Gaussian or Normal Distribution

Notation $X \sim \mathcal{N}(\mu, \sigma^2)$

Parameters/Moments/Characteristics

Mean	$\mu \in (-\infty, \infty)$
Variance	$\sigma^2, \sigma > 0$
Mode, median	μ
k th central moment	$\mu_k = \begin{cases} 0 & \text{for } k \text{ odd} \\ \sigma^k (k-1)(k-3)\cdots(3)(1) & \text{for } k \text{ even} \end{cases}$
Support	$x \in (-\infty, \infty)$
PDF	$f(x) = \frac{1}{\sqrt{2\pi}\sigma} e^{-\frac{(x-\mu)^2}{2\sigma^2}}$
CDF	$F(x) = \Phi\left(\frac{x-\mu}{\sigma}\right)$ [see below re $\Phi(\cdot)$ and $\Phi(\cdot)$]
MGF	$M(t) = e^{\mu t + \frac{1}{2}\sigma^2 t^2}$
CF	$\Phi(\omega) = e^{j\mu\omega - \frac{1}{2}\sigma^2\omega^2}$

Relationships and Properties

Note:

- Interchangeably known as the Gaussian or normal distribution. A standard normal distribution is $\mathcal{N}(0, 1)$.

Simulation:

- The Box–Muller transformation [24, Sect. 9.1] provides $X = \sqrt{-2 \log(U)} \cos(2\pi V)$ and $Y = \sqrt{-2 \log(U)} \sin(2\pi V)$ as independent $\mathcal{N}(0, 1)$ random variables if U and V are independent standard uniform random variables ($U, V \sim \text{Uni}(0, 1)$).

Special function:

- CDF of the standard normal distribution

$$\Phi(x) = \frac{1}{\sqrt{2\pi}} \int_{-\infty}^x e^{-z^2/2} dz \quad (5.122)$$

is related to the error function according to

$$\Phi(x) = \frac{1}{2} \left[1 + \operatorname{erf}\left(\frac{x}{\sqrt{2}}\right) \right]. \quad (5.123)$$

It should not be confused with the characteristic function (Sect. 5.3.9.2), which uses the same variable but with variant $\Phi(\omega)$ and an argument that is a frequency variable.

5.6.7 Complex Gaussian Distribution

Notation $X \sim \mathcal{CN}(\mu, \sigma^2)$

Parameters/Moments/Characteristics

Mean $\mu \in \mathbb{C}$ where \mathbb{C} is the complex plane

Variance $\sigma^2, \sigma > 0$

Support $x \in \mathbb{C}$

PDF $f(x) = \frac{1}{\pi\sigma^2} e^{-\frac{|x-\mu|^2}{\sigma^2}}$

Relationships and Properties

Interpretation: • The complex Gaussian distribution is primarily a convenient mathematical representation of what is truly a bivariate Gaussian distribution for the real and imaginary parts of the complex variable.

Formation: • $X = X_{\mathcal{R}} + jX_{\mathcal{I}} \sim \mathcal{CN}(\mu, \sigma^2)$ when $X_{\mathcal{R}}$ and $X_{\mathcal{I}}$ are independent, real Gaussian random variables with variance $\sigma^2/2$ and means $\mu_{\mathcal{R}} = \text{Real}\{\mu\}$ and $\mu_{\mathcal{I}} = \text{Imag}\{\mu\}$. More general forms allow different variances for and correlation between the real and imaginary parts.

References: • Goodman [18] and Kay [28, Sect. 15.4].

5.6.8 Multivariate Gaussian Distribution

Notation $\mathbf{x} \sim \mathcal{N}(\boldsymbol{\mu}, \boldsymbol{\Sigma})$

Parameters/Moments/Characteristics

Mean $\boldsymbol{\mu} \in \mathcal{R}^n$ where \mathcal{R} is the real line

Covariance matrix $\boldsymbol{\Sigma}, |\boldsymbol{\Sigma}| > 0$

Support $\mathbf{x} \in \mathcal{R}^n$

PDF $f(\mathbf{x}) = \frac{1}{(\sqrt{2\pi})^n |\boldsymbol{\Sigma}|^{\frac{1}{2}}} e^{-\frac{1}{2}(\mathbf{x}-\boldsymbol{\mu})^T \boldsymbol{\Sigma}^{-1}(\mathbf{x}-\boldsymbol{\mu})}$

MGF $M(\mathbf{t}) = E[e^{\mathbf{t}^T \mathbf{x}}] = e^{\boldsymbol{\mu}^T \mathbf{t} + \frac{1}{2} \mathbf{t}^T \boldsymbol{\Sigma} \mathbf{t}}$

CF $\Phi(\boldsymbol{\omega}) = E[e^{j\boldsymbol{\omega}^T \mathbf{x}}] = e^{j\boldsymbol{\omega}^T \boldsymbol{\mu} - \frac{1}{2} \boldsymbol{\omega}^T \boldsymbol{\Sigma} \boldsymbol{\omega}}$

Relationships and Properties

Formation: $\bullet \mathbf{x} = [X_1 \ X_2 \ \cdots \ X_n]^T$ is multivariate Gaussian $\mathcal{N}(\boldsymbol{\mu}, \boldsymbol{\Sigma})$ if the vector components are mutually Gaussian with mean $E[X_i] = \mu_i$ and covariances $E[(X_i - \mu_i)(X_j - \mu_j)] = \Sigma_{i,j}$, the (i, j) element of $\boldsymbol{\Sigma}$ for i and $j = 1, \dots, n$.

5.6.9 Complex Multivariate Gaussian Distribution

Notation $\mathbf{x} \sim \mathcal{CN}(\boldsymbol{\mu}, \boldsymbol{\Sigma})$

Parameters/Moments/Characteristics

Mean $\boldsymbol{\mu} \in \mathcal{C}^n$ where \mathcal{C} is the complex plane

Covariance matrix $\boldsymbol{\Sigma}, |\boldsymbol{\Sigma}| > 0$

Support $\mathbf{x} \in \mathcal{C}^n$

PDF $f(\mathbf{x}) = \frac{1}{\pi^n |\boldsymbol{\Sigma}|} e^{-(\mathbf{x}-\boldsymbol{\mu})^H \boldsymbol{\Sigma}^{-1}(\mathbf{x}-\boldsymbol{\mu})}$

Relationships and Properties

Formation: $\bullet \mathbf{x} = \mathbf{x}_{\mathcal{R}} + j\mathbf{x}_{\mathcal{I}} \sim \mathcal{CN}(\boldsymbol{\mu}, \boldsymbol{\Sigma})$ where $\mathbf{x}_{\mathcal{R}}$ and $\mathbf{x}_{\mathcal{I}}$ are real multivariate Gaussian random vectors with covariance $\frac{1}{2}\text{Real}(\boldsymbol{\Sigma})$, means $\boldsymbol{\mu}_{\mathcal{R}} = \text{Real}(\boldsymbol{\mu})$ and $\boldsymbol{\mu}_{\mathcal{I}} = \text{Imag}(\boldsymbol{\mu})$, and cross-covariance $E[(\mathbf{x}_{\mathcal{I}} - \boldsymbol{\mu}_{\mathcal{I}})(\mathbf{x}_{\mathcal{R}} - \boldsymbol{\mu}_{\mathcal{R}})^T] = \frac{1}{2}\text{Imag}(\boldsymbol{\Sigma})$ where $\text{Imag}(\boldsymbol{\Sigma}) = -\text{Imag}(\boldsymbol{\Sigma})^T$ (so $\boldsymbol{\Sigma} = \boldsymbol{\Sigma}^H$).

References:

\bullet Goodman [18] and Kay [28, Sect. 15.4].

5.6.10 Exponential Distribution

Notation $X \sim \text{Expon}(\lambda)$

Parameters/Moments/Characteristics

Scale	$\lambda > 0$
Mean	λ
Variance	λ^2
k th moment	$\mu'_k = \lambda^k \Gamma(k+1) = \lambda^k k!$
Mode	0
Median	$\lambda \log 2$
Support	$x \in [0, \infty)$
PDF	$f(x) = \frac{1}{\lambda} e^{-\frac{x}{\lambda}}$
CDF	$F(x) = 1 - e^{-\frac{x}{\lambda}}$
MGF	$M(t) = \frac{1}{1-\lambda t}$ for $t < 1/\lambda$
CF	$\Phi(\omega) = \frac{1}{1-\lambda j\omega}$

Relationships and Properties

Generalization: • Gamma random variable with shape $\alpha = 1$ is exponential.

Formation: • $X = -\log U \sim \text{Expon}(1)$ if $U \sim \text{Uni}(0, 1)$.

Property: • The exponential distribution is said to be *memoryless* in that if $X \sim \text{Expon}(\lambda)$, then conditioned on the event $\{X > h\}$, the amount over the threshold h , $Z = X - h$ is also $\sim \text{Expon}(\lambda)$.

5.6.11 Gamma Distribution

Notation $X \sim \text{Gam}(\alpha, \beta)$

Parameters/Moments/Characteristics

Shape	$\alpha > 0$
Scale	$\beta > 0$
Mean	$\alpha\beta$
Variance	$\alpha\beta^2$
k th moment	$\mu'_k = \beta^k \frac{\Gamma(\alpha+k)}{\Gamma(\alpha)}$
Mode	$(\alpha - 1)\beta$ when $\alpha \geq 1$; otherwise zero
Support	$x \in [0, \infty)$
PDF	$f(x) = \frac{x^{\alpha-1}}{\Gamma(\alpha)\beta^\alpha} e^{-\frac{x}{\beta}}$
CDF	$F(x) = \tilde{\gamma}(x/\beta; \alpha)$
MGF	$M(t) = \frac{1}{(1-\beta t)^\alpha}$ for $t < 1/\beta$
CF	$\Phi(\omega) = \frac{1}{(1-\beta j\omega)^\alpha}$

Relationships and Properties

- Simplification: • Exponential random variable when $\alpha = 1$.
- Simplification: • Chi-squared random variable when $\alpha = \frac{v}{2}$ and $\beta = 2$.
- Asymptotic: • Normal as $\alpha \rightarrow \infty$.
- Property: • Closed under addition when β is constant.
- Special function: • $\tilde{\gamma}(x; \alpha)$ is the normalized incomplete gamma function,

$$\tilde{\gamma}(x; \alpha) = \int_0^x \frac{t^{\alpha-1} e^{-t}}{\Gamma(\alpha)} dt = \frac{\gamma(\alpha, x)}{\Gamma(\alpha)}.$$

where $\Gamma(\alpha)$ is the gamma function and $\gamma(\alpha, x)$ is the (lower) incomplete gamma function (e.g., see [27, Ch. 45] or [29, Sect. 8.2]). See [30, Sect. 6.2] for numerical evaluation.

5.6.12 Rayleigh Distribution

Notation $X \sim \text{Rayl}(\sigma)$

Parameters/Moments/Characteristics

Scale $\sigma > 0$

$$\text{Mean} \quad \sigma \sqrt{\frac{\pi}{2}}$$

$$\text{Variance} \quad \left(2 - \frac{\pi}{2}\right) \sigma^2$$

$$\text{Power} \quad 2\sigma^2$$

$$\text{kth moment} \quad \mu'_k = (2\sigma^2)^{k/2} \Gamma\left(\frac{k}{2} + 1\right)$$

$$\text{Mode} \quad \sigma$$

$$\text{Median} \quad \sigma \sqrt{\log 4}$$

Support $x \in [0, \infty)$

$$\text{PDF} \quad f(x) = \frac{x}{\sigma^2} e^{-\frac{x^2}{2\sigma^2}}$$

$$\text{CDF} \quad F(x) = 1 - e^{-\frac{x^2}{2\sigma^2}}$$

Relationships and Properties

Gaussian: $\bullet \sqrt{X^2 + Y^2} \sim \text{Rayl}(\sigma^2)$ if X and Y are independent $\sim \mathcal{N}(0, \sigma^2)$.

Complex Gaussian: $\bullet |Z| \sim \text{Rayl}(\sqrt{\lambda/2})$ if $Z \sim \mathcal{CN}(0, \lambda)$.

Exponential: $\bullet \sqrt{Y} \sim \text{Rayl}(\sigma)$ if $Y \sim \text{Expon}(2\sigma^2)$.

Chi-Squared: $\bullet \sqrt{Y} \sim \text{Rayl}(1)$ if $Y \sim \chi_2^2$.

5.6.13 Rician Distribution

Notation $X \sim \text{Rice}(\sigma, \alpha)$

Parameters/Moments/Characteristics

Scale	$\sigma > 0$
Non-centrality	$\alpha \geq 0$
Power	$2\sigma^2 + \alpha^2$
Support	$x \in [0, \infty)$
PDF	$f(x) = \frac{x}{\sigma^2} e^{-\frac{(x^2+\alpha^2)}{2\sigma^2}} I_0\left(\frac{x\alpha}{\sigma^2}\right)$
CDF	$F(x) = 1 - Q_1\left(\frac{\alpha}{\sigma}, \frac{x}{\sigma}\right)$
Relationships and Properties	<ul style="list-style-type: none"> • Rayleigh distribution when $\alpha = 0$. • $X = \sqrt{Z_1^2 + Z_2^2}$ is Rician distributed with $\alpha = \sqrt{\mu_1^2 + \mu_2^2}$ when $Z_i \sim \mathcal{N}(\mu_i, \sigma^2)$ for $i = 1, 2$ and are independent. • $X = \sqrt{Y}$ is Rician with unit scale ($\sigma = 1$) when Y is non-central chi-squared with two degrees of freedom ($\nu = 2$) and non-centrality $\delta = \alpha^2$ ($Y \sim \chi_{2,\alpha^2}^2$). • $I_0(\cdot)$ is the zero-order modified Bessel function of the first kind. • Marcum Q function: $Q_1(a, b) = \int_b^\infty x e^{-(x^2+a^2)/2} I_0(ax) dx$ • Rice [31], Kay [32, Sect. 2.2.7], or McDonough and Whalen [33, Sect. 4.5].
Special functions	
References:	

5.6.14 Chi-Squared Distribution

Notation $X \sim \chi_v^2$

Parameters/Moments/Characteristics

Degrees of freedom $v > 0$

Mean v

Variance $2v$

k th moment $\mu'_k = 2^k \frac{\Gamma(\frac{v}{2} + k)}{\Gamma(\frac{v}{2})}$ for $k > -\frac{v}{2}$

Mode $\max\{v - 2, 0\}$

Support $x \in [0, \infty)$

PDF $f(x) = \frac{1}{2^{v/2} \Gamma(v/2)} x^{\frac{v}{2}-1} e^{-\frac{x}{2}}$

CDF $F(x) = \tilde{\gamma}\left(\frac{x}{2}; \frac{v}{2}\right)$

MGF $M(t) = \frac{1}{(1-2t)^{\frac{v}{2}}}$ for $t < \frac{1}{2}$

CF $\Phi(\omega) = \frac{1}{(1-2j\omega)^{\frac{v}{2}}}$

Relationships and Properties

Generalizations: • Gamma random variable (scale) and non-central chi-squared random variable.

Formation: • Formed from sum of squares of v iid $N(0, 1)$ random variables.

Asymptotic: • Normal as $v \rightarrow \infty$.

Special function: • $\tilde{\gamma}(x; \alpha)$ is the normalized incomplete gamma function (see Sect. 5.6.11).

5.6.15 Non-central Chi-Squared Distribution

Notation $X \sim \chi_{v,\delta}^2$

Parameters/Moments/Characteristics

Degrees of freedom $v > 0$

Non-centrality $\delta \geq 0$

Mean $v + \delta$

Variance $2(v + 2\delta)$

kth moment $\mu'_k = 2^k \Gamma\left(\frac{v}{2} + k\right) \sum_{j=0}^k \binom{k}{j} \frac{\left(\frac{\delta}{2}\right)^j}{\Gamma\left(\frac{v}{2} + j\right)}$

Support $x \in [0, \infty)$

$$\begin{aligned} \text{PDF } f(x) &= \sum_{k=0}^{\infty} \left[\frac{(\delta/2)^k e^{-\delta/2}}{k!} \right] \left[\frac{x^{v/2+k-1} e^{-x/2}}{2^{v/2+k} \Gamma(v/2+k)} \right] \\ &= \sum_{k=0}^{\infty} f_{\text{Poi}}(k; \delta/2) f_{\chi^2}(x; v + 2k) \\ &= s \frac{1}{2} e^{-\frac{(x+\delta)}{2}} \left(\frac{x}{\delta}\right)^{\frac{1}{2}(\frac{v}{2}-1)} I_{\frac{v}{2}-1}\left(\sqrt{\delta x}\right) \end{aligned}$$

$$\text{CDF } F(x) = 1 - Q_{v/2}\left(\sqrt{\delta}, \sqrt{x}\right)$$

$$\text{MGF } M(t) = \frac{1}{(1-2t)^{\frac{v}{2}}} e^{\delta t/(1-2t)} \text{ for } t < \frac{1}{2}$$

$$\text{CF } \Phi(\omega) = \frac{1}{(1-2j\omega)^{\frac{v}{2}}} e^{j\omega\delta/(1-2j\omega)}$$

Relationships and Properties

Note:

- The non-central-chi-squared PDF is a mixture of chi-squared distributions with parameters $v + 2k$ (PDF is $f_{\chi^2}(x; v + 2k)$) and weight from the Poisson distribution with mean $\delta/2$ (PDF is $f_{\text{Poi}}(k; \delta/2)$).

Formation:

- Arises from sum of squares of v iid $\mathcal{N}(\mu_i, 1)$ random variables where $\delta = \sum_i \mu_i^2$

CDF approximation:

- The CDF can be approximated by a shifted gamma distribution [25, Sect. 29.8].

Asymptotic:

- Normal as $v \rightarrow \infty$.

Special functions:

- $I_v(\cdot)$ is a modified Bessel function of the first kind and order v .

- Generalized Marcum Q function [34, App. C], [35]:

$$Q_M(a, b) = \frac{1}{a^{M-1}} \int_b^\infty x^M e^{-(x^2+a^2)/2} I_{M-1}(ax) dx$$

5.6.16 *F Distribution*

Notation $X \sim F_{v_1, v_2}$

Parameters/Moments/Characteristics

Degrees of freedom $v_1 > 0$ and $v_2 > 0$

Mean $\frac{v_2}{v_2 - 2}$ for $v_2 > 2$

Variance $\frac{2v_2^2(v_1+v_2-2)}{v_1(v_2-2)^2(v_2-4)}$ for $v_2 > 4$

k th moment $\mu'_k = \left(\frac{v_2}{v_1}\right)^k \frac{\Gamma(\frac{v_1}{2}+k)\Gamma(\frac{v_2}{2}-k)}{\Gamma(\frac{v_1}{2})\Gamma(\frac{v_2}{2})}$ for $k < \frac{v_2}{2}$

Mode $\frac{v_2(v_1-2)}{v_1(v_2+2)}$ for $v_1 > 2$

Support $x \in [0, \infty)$

PDF $f(x) = \frac{\Gamma(\frac{v_1+v_2}{2})v_1^{v_1/2}v_2^{v_2/2}}{\Gamma(\frac{v_1}{2})\Gamma(\frac{v_2}{2})(v_2+v_1x)^{(v_1+v_2)/2}}$

Relationships and Properties

Formation: $\bullet X = \frac{Y_1/v_1}{Y_2/v_2} \sim F_{v_1, v_2}$ if Y_1 and Y_2 are independent and $Y_i \sim \chi_{v_i}^2$.

Asymptotic: \bullet Normal as v_1 and v_2 both $\rightarrow \infty$.

Asymptotic: \bullet Scale of a chi-squared $\chi_{v_1}^2$ as $v_2 \rightarrow \infty$.

CDF: \bullet The CDF can be described in terms of an incomplete beta function [25, Sect. 27.2].

Special case: \bullet See Sect. 6.2.7 for the PDF and CDF when $v_1 = 2$.

5.6.17 Non-central F Distribution

Notation $X \sim F_{v_1, v_2, \delta}$

Parameters/Moments/Characteristics

Degrees of freedom $v_1 > 0$ and $v_2 > 0$

Non-centrality $\delta \geq 0$

Mean $\frac{v_2(v_1+\delta)}{v_1(v_2-2)}$ for $v_2 > 2$

Variance $2\left(\frac{v_2}{v_1}\right)^2 \left[\frac{(v_1+\delta)^2 + (v_1+2\delta)(v_2-2)}{(v_2-2)^2(v_2-4)} \right]$ for $v_2 > 4$

k th moment $\mu'_k = \left(\frac{v_2}{v_1}\right)^k \frac{\Gamma(\frac{v_1}{2}+k)\Gamma(\frac{v_2}{2}-k)}{\Gamma(\frac{v_2}{2})} \sum_{j=0}^k \binom{k}{j} \frac{\left(\frac{\delta}{2}\right)^j}{\Gamma(\frac{v_1}{2}+j)}$
for $k < \frac{v_2}{2}$

Support $x \in [0, \infty)$

$$\begin{aligned} f(x) &= \sum_{k=0}^{\infty} \left[\frac{(\delta/2)^k e^{-\delta/2}}{k!} \right] \frac{\Gamma(\frac{v_1+v_2}{2}+k)}{\Gamma(\frac{v_1}{2})\Gamma(\frac{v_2}{2})} x^{\frac{v_1}{2}+k} \frac{\frac{v_2}{2}}{x^{\frac{v_1+v_2}{2}+k}} \\ \text{PDF} &= \sum_{k=0}^{\infty} f_{\text{Poi}}(k; \delta/2) f_F\left(\frac{v_1 x}{v_1+2k}; v_1+2k, v_2\right) \frac{\frac{v_1}{v_1+2k}}{x^{\frac{v_1}{2}}} \end{aligned}$$

Relationships and Properties

Note:

- The non-central- F PDF is a mixture of scaled F distributions with parameters $v_1 + 2k$ and v_2 (PDF is $c_k f_F(c_k x; v_1 + 2k, v_2)$ where $c_k = v_1/(v_1 + k)$) and weight from the Poisson distribution with mean $\delta/2$ (PDF is $f_{\text{Poi}}(k; \delta/2)$).

Formation:

- $X = \frac{Y_1/v_1}{Y_2/v_2} \sim F_{v_1, v_2, \delta}$ if Y_1 and Y_2 are independent with $Y_1 \sim \chi_{v_1, \delta}^2$ and $Y_2 \sim \chi_{v_2}^2$.

Asymptotic:

- Normal as v_1 and $v_2 \rightarrow \infty$.

Asymptotic:

- Scale of a non-central chi-squared $\chi_{v_1, \delta}^2$ as $v_2 \rightarrow \infty$.

5.6.18 Weibull Distribution

Notation $X \sim \text{Wbl}(\beta, \lambda)$

Parameters/Moments/Characteristics

Shape	$\beta > 0$
Scale	$\lambda > 0$
Mean	$\lambda \Gamma(1 + \beta^{-1})$
Variance	$\lambda^2 \left\{ \Gamma(1 + 2\beta^{-1}) - [\Gamma(1 + \beta^{-1})]^2 \right\}$
k th moment	$\mu'_k = \lambda^k \Gamma(1 + k\beta^{-1})$
Mode	$\begin{cases} 0 & \text{for } \beta \in (0, 1] \\ \lambda(1 - \beta^{-1})^{\beta^{-1}} & \text{for } \beta > 1 \end{cases}$
Support	$x \in [0, \infty)$
PDF	$f(x) = \frac{\beta x^{\beta-1}}{\lambda^\beta} e^{-(x/\lambda)^\beta}$
CDF	$F(x) = 1 - e^{-(x/\lambda)^\beta}$

Relationships and Properties

- Simplification: • Exponential distribution when $\beta = 1$.
- Simplification: • Rayleigh distribution ($\sigma = \lambda/\sqrt{2}$) when $\beta = 2$.
- Generation: • If Y is standard exponential, then $X = \lambda Y^{(1/\beta)}$ is Weibull $\text{Wbl}(\beta, \lambda)$.
- Reference: • See Sect. 7.4.3.5 for usage in underwater acoustics.

5.6.19 *K Distribution*

Notation $X \sim K(\alpha, \lambda)$

Parameters/Moments/Characteristics

Shape	$\alpha > 0$
Scale	$\lambda > 0$
Mean	$\alpha\lambda$
Variance	$\lambda^2\alpha(\alpha + 2)$
k th moment	$\mu'_k = \lambda^k \Gamma(k+1) \frac{\Gamma(\alpha+k)}{\Gamma(\alpha)} = \lambda^k k! \frac{\Gamma(\alpha+k)}{\Gamma(\alpha)}$
Support	$x \in [0, \infty)$
PDF	$f(x) = \frac{2}{\lambda \Gamma(\alpha)} \left(\frac{x}{\lambda}\right)^{(\alpha-1)/2} K_{\alpha-1}\left(2\sqrt{\frac{x}{\lambda}}\right)$
CDF	$F(x) = 1 - \frac{2}{\Gamma(\alpha)} \left(\frac{x}{\lambda}\right)^{\alpha/2} K_\alpha\left(2\sqrt{\frac{x}{\lambda}}\right)$

Relationships and Properties

Formation: • The product description of a $K(\alpha, \lambda)$ random variable arises through $Y = VU$ where $V \sim \text{Expon}(\lambda)$ and $U \sim \text{Gam}(\alpha, 1)$.

Asymptotic: • Exponential distribution with mean μ when $\alpha \rightarrow \infty$ with $\lambda = \mu/\alpha$.

Note: • This form of the distribution is used to describe the matched-filter intensity. Transformations to the envelope \sqrt{X} or complex envelope $\sqrt{X}e^{j\theta}$ (where $\theta \sim \text{Uni}(0, 2\pi)$) are common.

References: • Jakeman and Pusey [36]. See Sect. 7.4.3.3 for usage in underwater acoustics.

5.6.20 Generalized Pareto Distribution

Notation $X \sim \text{GP}(\gamma, \lambda)$

Parameters/Moments/Characteristics

Shape	γ
Scale	$\lambda > 0$
Mean	$\frac{\lambda}{1-\gamma}$ for $\gamma < 1$
Variance	$\frac{\lambda^2}{(1-\gamma)^2(1-2\gamma)}$ for $\gamma < 0.5$
k th moment	$\mu'_k = \left(\frac{\lambda}{\gamma}\right)^k \frac{\Gamma(k+1)\Gamma(\gamma^{-1}-k)}{\Gamma(\gamma^{-1})}$ for $\gamma < k^{-1}$
Median	$\frac{\lambda}{\gamma}(2^\gamma - 1)$
Support	$x \in [0, \infty)$
PDF	$f(x) = \frac{1}{\lambda(1+\frac{\gamma}{\lambda}x)^{\gamma^{-1}+1}}$
CDF	$F(x) = 1 - \frac{1}{(1+\frac{\gamma}{\lambda}x)^{\gamma^{-1}}}$

Relationships and Properties

Simplification: • Exponential distribution with mean λ when $\gamma = 0$.

F distribution: • If $\lambda = 1$, then this form of the Pareto distribution is F distributed with $v_1 = 2$ and $v_2 = 2\gamma^{-1}$.

Note: • Arises in sonar in the analysis of extreme values of measured data [37].

Reference: • Pareto distribution of the second kind from [24, Ch. 20]. See Sect. 7.4.3.5 for usage in underwater acoustics.

5.6.21 Log Normal Distribution

Notation $X \sim \text{LN}(\mu, \gamma)$

Parameters/Moments/Characteristics

Shape	$\gamma \geq 0$
Scale	$e^\mu > 0, \mu \in (-\infty, \infty)$
Mean	$e^{\mu+\gamma/2}$
Variance	$e^{2\mu+\gamma}(e^\gamma - 1)$
k th moment	$\mu'_k = e^{k\mu+k^2\gamma/2}$
Median	e^μ
Mode	$e^{\mu-\gamma}$
Support	$x \in [0, \infty)$
PDF	$f(x) = \frac{1}{x\sqrt{2\pi\gamma}} e^{-(\log(x)-\mu)^2/(2\gamma)}$
CDF	$F(x) = \Phi\left(\frac{\log(x)-\mu}{\sqrt{\gamma}}\right)$

Relationships and Properties

Formation:

- The logarithm of X is normally (Gaussian) distributed with mean μ and variance γ so $Z = \log X \sim \mathcal{N}(\mu, \gamma)$.

Note:

- Although μ controls the location of $\log X$, it represents a scale parameter in the log normal distribution through e^μ . The shape parameter γ controls the tail heaviness.

Special function:

- $\Phi(z)$ is the CDF of the standard normal distribution (see Sect. 5.6.6).

Reference:

- See Sect. 7.4.3.5 for usage in underwater acoustics.

References

1. A. Papoulis, *Probability, Random Variables, and Stochastic Processes*, 3rd edn. (McGraw-Hill Inc., Boston, 1991)
2. R.D. Yates, D.J. Goodman, *Probability and Stochastic Processes* (Wiley, New York, 1999)
3. R.V. Hogg, A.T. Craig, *Introduction to Mathematical Statistics*, 4th edn. (Macmillan Publishers Co., New York, 1978)

4. B.W. Lindgren, *Statistical Theory*, 3rd edn. (Macmillan Publishers Co., New York, 1976)
5. N. Mukhopadhyay, *Probability and Statistical Inference* (Marcel Dekker, Inc., New York, NY, 2000)
6. C. Forbes, M. Evans, N. Hastings, B. Peacock, *Statistical Distributions*, 4th edn. (Wiley, Hoboken, NJ, 2011)
7. C.L. Nikias, M. Shao, *Signal Processing with Alpha-Stable Distributions and Applications* (Wiley-Interscience, New York, 1995)
8. L. DeVroye, *Non-Uniform Random Variate Generation* (Springer, New York, 1986)
9. S.M. Ross, *Simulation* (Harcourt Academic, New York, 1997)
10. E.B. Manoukian, *Modern Concepts and Theorems of Mathematical Statistics* (Springer, New York, 1985)
11. L.M. Leemis, J.T. McQueston, Univariate distribution relationships. *Am. Stat.* **62**(1), 45–53 (2008)
12. B.P. Lathi, *Linear Systems and Signals* (Berkeley-Cambridge Press, Carmichael, CA, 1992)
13. A.H. Nuttall, Accurate efficient evaluation of cumulative or exceedance probability distributions directly from characteristic functions. Technica Report 7023, Naval Underwater Systems Center, New London, CT, October (1983)
14. N.L. Johnson, S. Kotz (eds.), *Encyclopedia of Statistical Sciences*, vol. 2 (Wiley, New York, 1982)
15. R.G. Gallager, *Stochastic Processes: Theory for Applications* (Cambridge University Press, Cambridge, 2013)
16. S.M. Kay, *Modern Spectral Estimation Theory and Application* (Prentice Hall, Englewood Cliffs, NJ, 1988)
17. S.L. Marple, *Digital Spectral Analysis with Applications* (Prentice Hall Inc., Englewood Cliffs, 1987)
18. N.R. Goodman, Statistical analysis based on a certain multivariate complex Gaussian distribution (an introduction). *Ann. Math. Stat.* **34**, 152–177 (1963)
19. F.D. Neeser, J.L. Massey, Proper complex random processes with applications to information theory. *IEEE Trans. Inf. Theory* **39**(4), 1293–1302 (1993)
20. D.R. Fuhrmann, Complex random variables and stochastic processes, in *Digital Signal Processing Handbook*, ed. by V.K. Madisetti, D.B. Williams (CRC Press, Boca Raton, 1999)
21. P.J. Schreier, L.L. Scharf, *Statistical Signal Processing of Complex-Valued Data* (Cambridge University Press, Cambridge, 2010)
22. Wikipedia, http://en.wikipedia.org/wiki/List_of_probability_distributions
23. N.L. Johnson, S. Kotz, A.W. Kemp, *Univariate Discrete Distributions*, 2nd edn. (Wiley, New York, 1992)
24. N.L. Johnson, S. Kotz, N. Balakrishnan, *Continuous Univariate Distributions*, 2nd edn., vol. 1 (Wiley, New York, 1994)
25. N.L. Johnson, S. Kotz, N. Balakrishnan, *Continuous Univariate Distributions*, 2nd edn., vol. 2 (Wiley, New York, 1995)
26. S. Kotz, N. Balakrishnan, N.L. Johnson, *Continuous Multivariate Distributions, Models and Applications*, 2nd edn., vol. 1 (Wiley, New York, 2000)
27. K. Oldham, J. Myland, J. Spanier, *An Atlas of Functions*, 2nd edn. (Springer Science, New York, 2009)
28. S.M. Kay, *Fundamentals of Statistical Signal Processing: Estimation Theory* (Prentice Hall PTR, Englewood Cliffs, 1993)
29. F.W.J. Olver, D.W. Lozier, R.F. Boisvert, C.W. Clark (eds.), *NIST Handbook of Mathematical Functions* (Cambridge University Press, Cambridge, 2010)
30. W.H. Press et al., *Numerical Recipes in Fortran 77, The Art of Scientific Computing*, 2nd edn. (Cambridge University Press, Cambridge, 1992)
31. S.O. Rice, Mathematical analysis of random noise: Part III. *Bell Syst. Tech. J.* **24**(1), 46–156 (1945)
32. S.M. Kay, *Fundamentals of Statistical Signal Processing: Detection Theory* (Prentice Hall PTR, Englewood Cliffs, 1998)

33. R.N. McDonough, A.D. Whalen, *Detection of Signals in Noise*, 2nd edn. (Academic, San Diego, 1995)
34. C.W. Helstrom, *Elements of Signal Detection and Estimation* (Prentice Hall Inc., Englewood Cliffs, NJ, 1995)
35. J.I. Marcum, A statistical theory of target detection by pulsed radar. ASTIA Document AD101287, The RAND Corporation (1947)
36. E. Jakeman, P.N. Pusey, A model for non-Rayleigh sea echo. IEEE Trans. Antennas Propag. **24**(6), 806–814 (1976)
37. B.R. La Cour, Statistical characterization of active sonar reverberation using extreme value theory. IEEE J. Ocean. Eng. **29**(2), 310–316 (2004)

Chapter 6

Statistical Signal Processing



6.1 Introduction

The basic tenets of detection and estimation are presented in this chapter (respectively, in Sects. 6.2 and 6.3). These topics from statistical inference comprise the field of statistical signal processing and have numerous applications in underwater acoustics, as described in Sects. 6.2.1 and 6.3.1. The advantage of characterizing an application as a detection or estimation problem lies in the wealth of solutions that can be found in the statistics literature, along with the associated performance measures. The presentation found in this chapter begins with the performance measures and the techniques used to estimate them from simulated or real data (see Sects. 6.2.2 and 6.3.2). For estimation applications, the Cramér-Rao lower bound (CRLB) on the variance of unbiased¹ estimators is also presented (Sect. 6.3.3). Although the CRLB does not describe the performance achieved by a specific estimator, it characterizes the best achievable performance over all unbiased estimators and is therefore a very useful analysis tool. A number of standard techniques for developing detectors and estimators are then presented along with examples using both standard statistical models and those relevant to applications in underwater acoustics (Sects. 6.2.3–6.2.8 and 6.3.4–6.3.8).

6.2 Signal Detection Theory

In signal detection, a decision is made regarding the presence or absence of the signal of interest based on measured data. The theory supporting signal detection comes from the *hypothesis testing* arm of *statistical inference*. Most signal detection

¹As described in Sect. 6.3.2, an *unbiased* estimator has zero average error.

problems are a specific type of a binary hypothesis test where the null hypothesis (H_0) represents the no-signal or noise-only case and the alternative hypothesis (H_1) represents the signal-present case, which usually means the measured data contain both signal and noise. In developing, analyzing, and applying signal detection theory, the three basics steps are:

- describe the detection problem statistically under the H_0 and H_1 hypotheses,
- develop and implement a detection algorithm, and
- evaluate the performance of the detection algorithm.

The first step involves identifying an appropriate statistical characterization of the measured data, including their probability density functions (PDFs) and parameters related to the signal and noise. This step is usually situation specific and will be done throughout Part III for many common scenarios in underwater acoustics. To accomplish the second step, several standard approaches for developing detection algorithms are covered in this chapter (Sects. 6.2.3–6.2.8). As with the first step, evaluating the performance of detection algorithms is often scenario specific and covered in detail in Part III. However, the most common performance measures are presented here in Sect. 6.2.2. Additional information on signal detection can be found in [1–4] while resources from the more general hypothesis testing literature include [5–7].

6.2.1 Hypothesis Testing in Underwater Acoustics

Almost all remote-sensing applications of underwater acoustics have some component characterizable as a detector or hypothesis test. Obvious examples include sensing systems with the primary objectives of detecting the presence of and locating sound or echo sources such as earthquakes, fish, marine mammals, divers, submarines, or mines. However, cases can be found in most applications of underwater acoustics as illustrated in the following examples.

In underwater acoustic communications, information is encoded into signals which are modulated to acoustical frequencies and transmitted through the water from one location to another with the purpose of conveying information. Detectors and hypothesis tests are intrinsic to the receiver signal processing and required before the information can be extracted.

Detectors are also integral parts of systems used for measuring many physical properties of the ocean. The simplest example comes from depth sounding where the time delay between transmission of a signal and reception of the echo from the seabed allows estimation of the depth. The process of estimating time delay inherently requires detecting the echo. On a different spatial scale, time-delay estimation (with a detector in the processing) is used in ocean acoustic tomography where a signal is transmitted from one location to another a large distance away (e.g., exceeding 18,000 km as observed in the Heard Island Feasibility Test [8]) and the time delay used to infer ocean temperature through the average sound speed.

For most applications in underwater acoustics, the focus is on detecting weak signals (e.g., to maximize communications range). However, detectors and hypothesis testing can exist for strong signals as well. For example, a signal repeater in a communications or active-sonar-testing system generally needs to detect a loud signal in order to record it and transmit it back into the water. The challenge arises from the variety of forms in which the received signal might be observed and wanting to detect them all with few errors.

Not all applications of hypothesis testing in underwater acoustics entail binary hypothesis tests. Some are multiple- (or M -ary) hypothesis tests where M possible statistical models might represent the measured data and one must be chosen. For example, in a digital acoustic communications system, M distinct waveforms can be used to convey information, forcing an M -ary hypothesis test in the receiver. Another common application is signal classification where acoustic data are used to categorize the sound or echo source. Examples include classifying marine mammal acoustic emissions (e.g., determining which type of whale produced a particular frequency-modulated moan) and sea-bed classification or mapping (e.g., identifying areas of mud, silt, sand, or clay) from backscattering measurements.

6.2.2 Performance Measures, Implementation, and Analysis of Detectors

The performance of hypothesis tests is quantified by the so-called Type I and II errors that occur when making incorrect decisions [6, Sect. 8.2]. As applied to detection theory, a Type I error represents deciding signal is present (hypothesis H_1) when the data contain only noise (hypothesis H_0) and is referred to as a *false alarm*. A Type II error represents deciding the data only contain noise (H_0) when a signal is present (H_1) and is called a *missed detection*. Performance is quantified by the probability of observing these events: the probability of false alarm (P_f) and the probability of missed detection (P_m). Related to the probability of missed detection is the more common probability of detection, $P_d = 1 - P_m$; that is, the probability of correctly deciding a signal is present in the data. The performance measures are summarized in Table 6.1.

Table 6.1 Performance measures for detection

	Type I error	Type II error
Data condition (truth)	$H_0/\text{null/noise-only}$	$H_1/\text{altern./signal-present}$
Detector decision	$H_1/\text{altern./signal-present}$	$H_0/\text{null/noise-only}$
Detector error	False alarm	Missed detection
Performance measure	P_f	$P_m = 1 - P_d$

The detection process involves making the *signal-present* or *noise-only* decision based on measured data. If the measured data are represented by the n -dimensional random vector $\mathbf{x} = [X_1 \ X_2 \ \cdots \ X_n]^T$,² this amounts to partitioning the range of \mathbf{x} into two mutually exclusive and exhaustive sets. This is most easily accomplished by projecting the n -dimensional data to the real line in such a manner that the two sets are represented by values above or below a particular *threshold*. Mathematically, let the function $T(\mathbf{x})$ map the data \mathbf{x} to the real line as prescribed above where values above the threshold h come from the set representing *signal presence* and values at or below come from the set representing the *noise-only* condition. The detection decision is then obtained by choosing *signal present* (H_1) when $T(\mathbf{x}) \geq h$ and *noise only* (H_0) when $T(\mathbf{x}) < h$. The following notation succinctly describes the decision rule,

$$T(\mathbf{x}) \begin{cases} \stackrel{H_1}{\geq} h \\ \stackrel{H_0}{\leq} h \end{cases} \quad (6.1)$$

where $T(\mathbf{x})$ is called the *decision statistic* or *detection statistic*.

An example illustrating how this mapping results in the PDF of the detector decision statistic under the null hypothesis lying to the left of the PDF under the alternative hypothesis is shown in Fig. 6.1. In an ideal detector, there would be no overlap in the PDFs and the detector decision threshold would be placed in between the two PDFs to provide perfect separation between the two hypotheses. However, both PDFs in the example have probability mass above and below the decision threshold, which implies there will be errors in the detection process. Using (6.1), the performance measures can be described as the probability of observing $T(\mathbf{x}) \geq h$ under the appropriate hypothesis. The probability of false alarm is

$$P_f = \Pr\{T(\mathbf{x}) \geq h | H_0\} \quad (6.2)$$

where the conditioning on the null hypothesis (H_0) implies the probability is evaluated when the data are in the noise-only condition. Similarly, the probability of detection is

$$P_d = \Pr\{T(\mathbf{x}) \geq h | H_1\} \quad (6.3)$$

with evaluation when the data are in the signal-present condition. The shaded areas in Fig. 6.1 represent the two performance measures and it can be seen that P_f will generally be smaller than P_d because the PDF under H_0 lies to the left of that under H_1 .

The data-compressing transformation $T(\mathbf{x})$ is obtained as part of developing or deriving a detection algorithm. A key requirement for $T(\mathbf{x})$ is that it should

²Recall from the discussion in Sect. 5.3.6 that matrix-vector notation representing a vector as a lower-case bold letter (e.g., \mathbf{x}) takes precedence over the mathematical statistics notation of

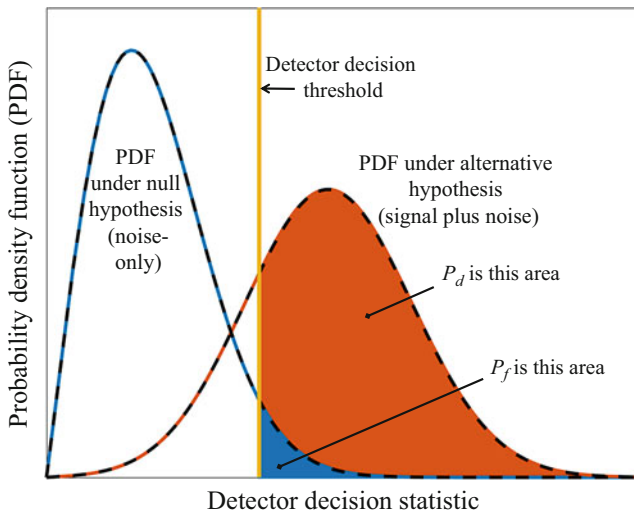


Fig. 6.1 PDFs of the detector decision statistic under the null and alternative hypotheses and how the probabilities of meeting or exceeding the detector decision threshold produce the probabilities of false alarm (P_f) and detection (P_d)

not depend on any unknown parameters (e.g., a signal or noise power or their ratio). Development approaches are covered in Sects. 6.2.4–6.2.8 for various cases of unknown noise and/or signal parameters. Once $T(\mathbf{x})$ is determined, the only other requirement for implementing the detector is to choose the threshold h , which is often called a *decision threshold* or *detector threshold*, but is not the Detection Threshold (DT) term in the sonar equation (see Sect. 2.3.5 or 6.2.2.1 for more details on this distinction). The specific choice of h defines what is called the *operating point* of the detector. It is most commonly chosen according to a desired false-alarm performance, which requires solving (6.2) to obtain h as a function of P_f . This enforces an additional constraint on $T(\mathbf{x})$ where the function in (6.2) cannot depend on any unknown parameters. The importance of this requirement is seen by assuming the contrary condition. Suppose h was a function of both P_f and an unknown noise power level λ_0 . It might be possible to choose an appropriate detector threshold h (i.e., it provides an acceptable P_f) based on some observed data. However, if the detector is then used in a new situation with a different noise power level, the probability of false alarm would be different and the detector at a different operating point than desired.

The detector output is generally a decision based on the observed data that signal is present or not. Another means of providing output is to obtain the *p*-value of the hypothesis test. The *p*-value describes the probability of observing a more extreme

random variables taking an upper-case letter and its observed value the lower case. Whether $\mathbf{x} = [X_1 \dots X_n]^T$ or $\mathbf{x} = [x_1 \dots x_n]^T$ must be discerned from context.

value when H_0 is true. If the observed data x_1, \dots, x_n produce a specific value $t = T(x_1, \dots, x_n)$ of the decision statistic, then the p -value is

$$p = \Pr\{T(X_1, \dots, X_n) \geq t) | H_0\} \quad (6.4)$$

where X_1, \dots, X_n are random variables and $t = T(x_1, \dots, x_n)$ is fixed by the observations. This is essentially P_f when the threshold is set to $t = T(x_1, \dots, x_n)$ instead of h . Use of p -values conveys the degree to which the data support the null hypothesis. Small values of p indicate H_0 is unlikely whereas large values support the null hypothesis. When a hypothesis test is described as being “level α ,” it implies the threshold is set so $P_f \leq \alpha$ and is equivalent to rejecting the null hypothesis (i.e., declaring signal-present) when the p -value is less than α .

6.2.2.1 Receiver Operating Characteristic (ROC) Curves

Detector performance measures are usually evaluated over a range of thresholds, forming a curve called a receiver operating characteristic (ROC). An example ROC curve is shown in Fig. 6.2 for a Gaussian-fluctuating signal in Gaussian noise for four different signal-to-noise power ratios (SNRs). Clearly, performance improves as SNR increases toward the ideal response of $(P_f, P_d) = (0, 1)$ in the upper-left corner. The curves can also be seen to each contain the points $(0, 0)$ and $(1, 1)$, which occur for, respectively, very large threshold values ($h \rightarrow \infty$) and very small ones ($h \rightarrow -\infty$) as can be seen by imagining that the decision threshold in Fig. 6.1 moves to the far right or far left. The chance line represents the antithesis of the ideal $(0, 1)$ point. It is the case where $P_d = P_f$ and indicates the detector and data provide no ability to distinguish between the two hypothesis. When signal detection problems are parameterized by a signal strength (or SNR), the ROC curve will tend to the chance line as signal strength goes to zero.

Generally, much smaller values of P_f are of interest relative to P_d so the abscissa is usually plotted logarithmically as shown in Fig. 6.3. Also shown in Fig. 6.3 are an operating point for $P_f = 10^{-2}$ and $P_d \approx 0.87$ for the 15 dB SNR case, and an estimated ROC curve for the 10 dB SNR case. A common measure of detection performance is the SNR required to achieve a specific operating point. For example, the SNR required to achieve the $(10^{-2}, 0.87)$ operating point in Fig. 6.3 is 15 dB. As described in Sect. 2.3.5, this is termed the Detection Threshold (DT) in the sonar equation. It is important to note the difference between DT and the decision threshold h . The former (DT) is only used in detector analysis and describes the SNR required to achieve a specific P_f and P_d operating point (it depends on both P_f and P_d). The latter (h) is used to implement the detector, is usually chosen solely as a function of P_f , and in conjunction with SNR dictates what value of P_d is achieved. The two are commonly confused when the detection statistic $T(\mathbf{x})$ can be interpreted as an estimate of SNR. When implementing a detector, $T(\mathbf{x})$ is always compared to a decision threshold h and never compared to the Detection Threshold (DT).

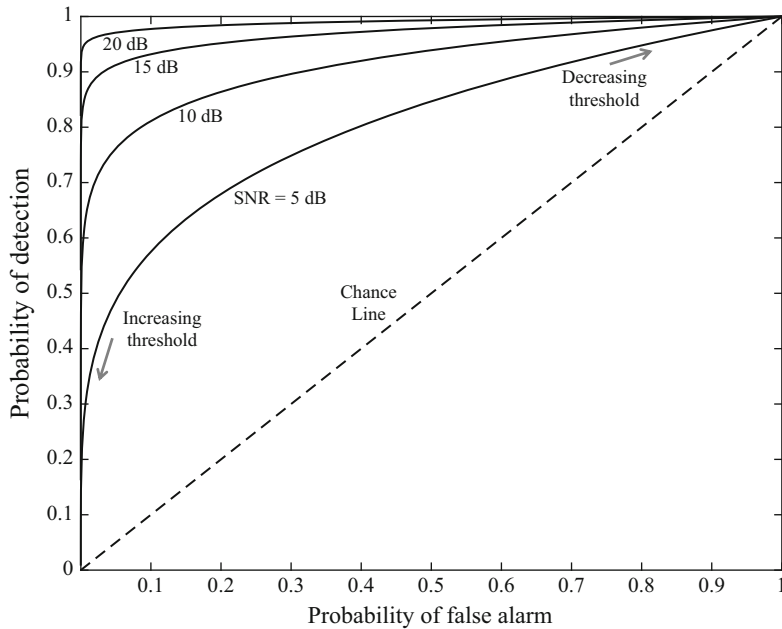


Fig. 6.2 ROC curve for fluctuating Gaussian signal in Gaussian noise

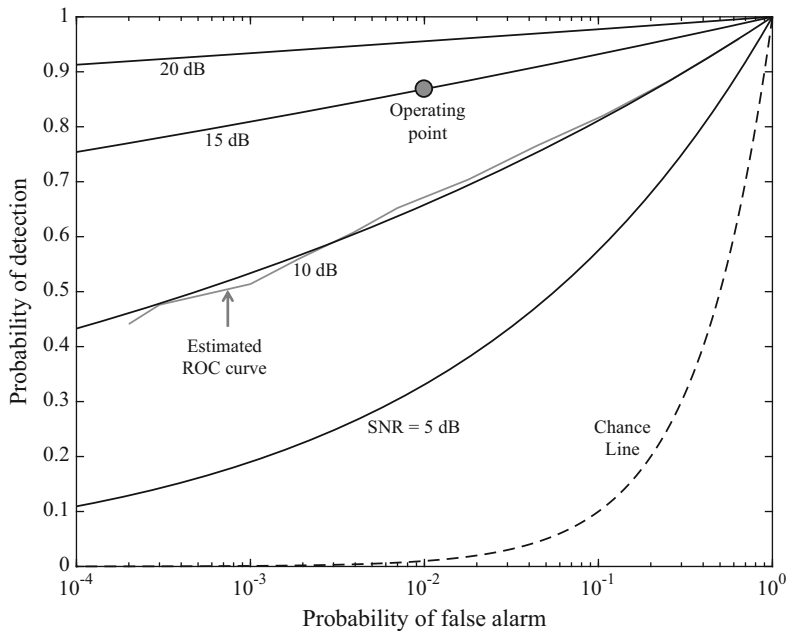


Fig. 6.3 ROC curve for fluctuating Gaussian signal in Gaussian noise with P_f on logarithmic scale, operating point, and estimated ROC curve

6.2.2.2 Estimating P_d and P_f

During the design stage, detectors can at times be analyzed analytically by evaluating the CDF of $T(\mathbf{x})$ under the null and alternative hypotheses. However, for situations involving complicated detectors or data, analytical evaluation of P_f and P_d can be difficult or impossible. An alternative lies in simulating the data \mathbf{x} for both the noise-only and signal-present cases followed by estimation of P_f and P_d . The estimation process follows that described in Sect. 5.3.5 for the histogram estimate of the CDF, but counts the occurrences of $T(\mathbf{x})$ exceeding the threshold h . If $\mathbf{x}_{0,i}$ and $\mathbf{x}_{1,i}$ are samples of the data under, respectively, hypotheses H_0 and H_1 for $i = 1, \dots, n$, the estimates are

$$\hat{P}_f = \frac{1}{n} \sum_{i=1}^n \mathbb{I}\{T(\mathbf{x}_{0,i}) \geq h\} \quad (6.5)$$

and

$$\hat{P}_d = \frac{1}{n} \sum_{i=1}^n \mathbb{I}\{T(\mathbf{x}_{1,i}) \geq h\} \quad (6.6)$$

where $\mathbb{I}\{\cdot\}$ is the indicator function returning one when the argument is true and zero otherwise. Confidence intervals (described in Sect. 6.3.8) for the estimates can be calculated as shown in Sect. 5.3.5. To provide an idea of how many simulation samples are necessary, consider the coefficient of variation of the estimate which is the ratio of its standard deviation to mean,

$$\frac{\sigma_{\hat{p}}}{\mu_{\hat{p}}} = \frac{\sqrt{p(1-p)/n}}{p} = \sqrt{\frac{1-p}{np}} \quad (6.7)$$

where p is either P_f or P_d and \hat{p} is its estimate. The coefficient of variation describes the standard deviation in units of the mean; for example, 0.1 means the standard deviation is one tenth the size of the mean, which is often an acceptable accuracy. Inverting this implies that achieving a 10% accuracy (i.e., coefficient of variation equal to 0.1) requires

$$n \geq 100(1-p)p^{-1} \approx 100p^{-1} \text{ for small } p. \quad (6.8)$$

When estimating P_d , often only values greater than 0.1 are of interest, so $n = 1000$ achieves adequate accuracy. However, when estimating P_f , smaller values (e.g., 10^{-6} to 10^{-2}) are usually of interest. For $P_f = 10^{-4}$, $n = 10^6$ observations are required to achieve the desired accuracy. An example estimated ROC curve is shown in Fig. 6.3 where $n = 10^5$ samples were used indicating the estimate has adequate accuracy only for values of $P_f \geq 10^{-3}$.

6.2.2.3 Importance Sampling

When the simulation requirement for estimating P_f becomes inhibitive, an alternative can be found in importance sampling [9]. The difficulty in estimating small values of P_f manifests in the form of infrequent threshold crossings. Importance sampling attempts to resolve this by simulating data more likely to produce a threshold crossing and correcting for the altered simulation by weighting the counting. Importance sampling begins by describing the parameter being estimated as an expectation, $p = E[g(\mathbf{x})]$, which for estimating an exceedance probability results in the function $g(\mathbf{x}) = \mathbb{I}\{T(\mathbf{x}) \geq h\}$. The expectation is then converted to being performed under a different PDF (say $f_0(\mathbf{x})$),

$$\begin{aligned} p &= E[g(\mathbf{x})] = \int g(\mathbf{x}) f_{\mathbf{x}}(\mathbf{x}) d\mathbf{x} \\ &= \int g(\mathbf{x}) \frac{f_{\mathbf{x}}(\mathbf{x})}{f_0(\mathbf{x})} f_0(\mathbf{x}) d\mathbf{x} \\ &= E_0[g(\mathbf{x}) w(\mathbf{x})] \end{aligned} \quad (6.9)$$

where $w(\mathbf{x}) = f_{\mathbf{x}}(\mathbf{x})/f_0(\mathbf{x})$. Data are simulated under the PDF $f_0(\mathbf{x})$ and the parameter is estimated according to

$$\hat{p} = \frac{1}{n} \sum_{i=1}^n g(\mathbf{x}_i) w(\mathbf{x}_i). \quad (6.10)$$

The estimate is unbiased ($E[\hat{p}] = p$) and the variance can be lower than that achieved by (6.5). The art in using importance sampling lies in how to choose the generating PDF $f_0(\mathbf{x})$. A reasonable place to start is to use the distribution of the data when signal is present.

The process for estimating P_d and P_f from real data is identical to that for simulated data. However, care needs to be taken when interpreting the estimates. ROC curves are defined for a specific scenario; for example, a given SNR and simulated data can achieve this precisely. In order to use real data to estimate P_d and P_f , the data acquisition experiment should be designed to produce a wide-sense-stationary (WSS), ergodic (Sect. 5.4) random process. This can be very difficult to achieve in practice, so it is common to consider the result as an average performance over the observed variations.

6.2.2.4 Equal-Error Point and Area Under the Curve

When evaluating multiple configurations or different design parameters (e.g., bandwidth), the ROC curve can be a cumbersome evaluation tool. If a specific operating point is of interest, the SNR required to achieve it is a useful performance

measure (e.g., the Detection Threshold term in the sonar equation). When no particular operating point is of interest, two other performance measures can distill the ROC-curve quality into a single scalar measure. The first is the area under the curve (AUC), which is one for an ideal detector and 0.5 for a bad one. An alternative is to identify the equal-error point. That is, the operating point on the ROC curve where $P_f = P_m = 1 - P_d$. This is the point at which the ROC curve intersects the anti-diagonal line formed by the equation $P_d = 1 - P_f$. The equal-error point is typically described by the achieved P_a , which also happens to be³ the AUC for a ROC curve linear from the equal-error point to both $(0, 0)$ and $(1, 1)$.

6.2.3 Design of Detectors: Neyman–Pearson Optimal

Given the statistical characterization of the data under the noise-only ($f_0(\mathbf{x})$) and signal-present hypotheses ($f_1(\mathbf{x})$), the optimal detector comes from the Neyman–Pearson (NP) lemma [2, Sect. 3.3], [3, Sect. 4.3], or [6, Sect. 8.3.1]. The optimality criterion consists of maximizing P_d while constraining P_f to be at or below a specified level. The NP lemma dictates that the detector formed by the following decision rule is optimal,

$$L(\mathbf{x}) \stackrel{H_1}{\geq} h \quad (6.11)$$

where $L(\mathbf{x})$ is the likelihood ratio (LR)

$$L(\mathbf{x}) = \frac{f_1(\mathbf{x})}{f_0(\mathbf{x})} \quad (6.12)$$

when $f_0(\mathbf{x}) \neq 0$. It is important to note the NP lemma assumes the distributions under H_0 and H_1 are known exactly (i.e., there are no unknown parameters). This is called a *simple-vs.-simple* hypothesis test whereas unknown parameters in either or both distributions result in at least one *composite* hypothesis for which (6.11) may not be implementable.

The NP optimality is preserved under any strictly monotonically increasing transformation of the likelihood ratio, although the specific value of the threshold h must change appropriately to preserve the same P_f . For example, it is often easier to work with the log-likelihood ratio (LLR), $l(\mathbf{x}) = \log L(\mathbf{x})$, yielding the test

$$\log L(\mathbf{x}) \stackrel{H_1}{\geq} \log(h) \text{ or } l(\mathbf{x}) \stackrel{H_1}{\geq} h' \quad (6.13)$$

³Thanks to J. Pitton (APL/UW) for pointing this out.

where $h' = \log h$. As seen in the following example, monotonic transformations are extremely useful in simplifying the detection statistic and removing dependence of the decision statistic on parameters.

Example:

Suppose n samples (X_1, \dots, X_n) measured from a conventional beamformer are assumed to be exponentially distributed with mean λ when only noise is present and mean $\lambda(1 + s)$ when noise and signal are present. Here, λ is the average noise power and s is an SNR.

Problem Derive the optimal detector to test the null hypothesis $H_0: X_i \stackrel{iid}{\sim} \text{Expon}(\lambda)$ against the alternative $H_1: X_i \stackrel{iid}{\sim} \text{Expon}(\lambda(1 + s))$ when λ and s are known.

Solution The joint PDF of the data under H_0 is

$$f_0(\mathbf{x}; \lambda) = \prod_{i=1}^n \frac{1}{\lambda} e^{-x_i/\lambda} \quad (6.14)$$

and under H_1 is

$$f_1(\mathbf{x}; s, \lambda) = \prod_{i=1}^n \frac{1}{\lambda(1+s)} e^{-x_i/[\lambda(1+s)]}. \quad (6.15)$$

The likelihood ratio is therefore

$$L(\mathbf{x}) = \frac{f_1(\mathbf{x}; s, \lambda)}{f_0(\mathbf{x}; \lambda)} = \frac{1}{(1+s)^n} \exp \left\{ \frac{s}{\lambda(1+s)} \sum_{i=1}^n x_i \right\} \quad (6.16)$$

which depends on both λ and s . By applying the monotonic transformation

$$g(L) = [\log(L) + n \log(1+s)] \left[\frac{\lambda(1+s)}{s} \right], \quad (6.17)$$

the detection statistic can be described as

$$g(L(\mathbf{x})) = \sum_{i=1}^n x_i \quad (6.18)$$

which does not depend on λ or s . The optimal detector is therefore

(continued)

$$T(\mathbf{x}) = \sum_{i=1}^n X_i \stackrel{H_1}{\underset{H_0}{\gtrless}} h. \quad (6.19)$$

Although the detection statistic here does not depend on either of the parameters, the threshold h will because the PDF of $T(\mathbf{x})$ under H_0 depends on λ . As such, for this detector to be implemented and optimal, λ must be known. However, the value of s does not need to be known; the detector described by (6.19) is optimal for any $s > 0$.

6.2.4 Composite Hypothesis Testing: Detecting When There Are Unknown Parameters

In most applications, there will be unknown parameters in the statistical characterization of the data for both the noise-only and signal-present conditions. When unknown parameters exist, at least one of the hypotheses is *composite* rather than *simple*. In detection applications, there are typically parameters related to the signal and parameters related to the noise. Although the signal parameters are only relevant under H_1 , the noise parameters usually (but not always) exist under both H_0 and H_1 . When noise parameters exist under both hypotheses and are unknown, they are considered *nuisance parameters* as they must be accounted for in the detector design, but do not distinguish H_1 from H_0 . Signal parameters usually contain a signal strength (e.g., an amplitude or power), which when set to zero yields the null hypothesis. It is common to have other signal parameters (e.g., frequency, bearing, and Doppler) that do not naturally distinguish H_1 from H_0 . Such *ancillary parameters* also produce a composite hypothesis when they are unknown.

The following sections describe various techniques for dealing with unknown parameters. Ideally, a uniformly most powerful (UMP) test or at least a UMP-invariant test (Sect. 6.2.5) can be derived as they provide optimal performance. When a UMP test does not exist and only the signal strength is unknown, a locally optimal detector (Sect. 6.2.6) can be derived with optimality as the signal strength tends to zero. More commonly, the generalized likelihood ratio (GLR) test is implemented (Sect. 6.2.7) to deal with both nuisance and ancillary parameters, which are replaced in the likelihood ratio by their maximum-likelihood estimates. A less common approach, which requires a prior distribution on unknown parameters, can be found in a Bayesian detector formulation (Sect. 6.2.8).

6.2.5 Design of Detectors: Uniformly Most Powerful Tests and Invariance

Recall the example from Sect. 6.2.3 where the optimal test did not depend on the SNR s . If the test had been characterized with an unknown value of $s > 0$ and a known noise power λ , it would have a simple null hypothesis and a composite alternative hypothesis; that is, it is a *simple-vs.-composite* hypothesis test. However, because the resulting detector had no dependence on s the detector presented in (6.19) is optimal for any $s > 0$. In this situation, the detector is termed *uniformly most powerful* (UMP) for the composite alternative hypothesis (i.e., the unknown SNR parameter).

The procedure for determining if a UMP test exists depends on whether the null hypothesis is known precisely (a simple hypothesis) or if it has unknown parameters (a composite hypothesis). When the null hypothesis is known precisely and the alternative has unknown parameters $\theta_1 \in \Theta_1$ (a simple-vs.-composite hypothesis test), the process starts by obtaining the NP-optimal detector for a given θ_1 . If the detector can be implemented without requiring specific knowledge of θ_1 , the detector is UMP. This essentially requires a strictly increasing monotonic transformation of the likelihood ratio to a form independent of θ_1 as was done in the example of Sect. 6.2.3.

When neither the null nor alternative hypotheses are known precisely, the hypothesis test is termed *composite-vs.-composite*. These are the most complicated situations and yet the most common. There are two approaches for obtaining UMP detectors for composite-vs.-composite hypothesis tests. Neither is guaranteed to work in all situations, so they are not covered in detail here. The first approach involves determining if the data distributions produce a monotone likelihood ratio [6, Sect. 8.4.2], [3, Sect. 4.7] in terms of a decision statistic $T(\mathbf{x})$, in which case the test comparing $T(\mathbf{x})$ to a threshold can be UMP. The second approach entails exploiting any invariances inherent in the detection problem with respect to nuisance parameters [5, Ch. 6], [3, Sect. 4.8] to compress the data to one or more statistics that do not depend on the nuisance parameters, but retain all necessary information required for the signal parameter (i.e., they are sufficient statistics). This in effect produces a *simple* null hypothesis within the space of invariant statistics, which enables use of the first approach to determine if a UMP-invariant detector can be formed from the likelihood ratio of the invariant statistics.

Several examples of UMP and UMP-invariant detectors can be found in [3, 5, 6]. Other approaches for dealing with composite-vs.-composite hypotheses are covered in Sects. 6.2.7 and 6.2.8.

6.2.6 Design of Detectors: Small-Signal Situations

Suppose only a signal strength parameter is unknown and no UMP detector exists. An attractive alternative can be found in optimizing performance for vanishingly weak signals. Let the data \mathbf{x} have PDF $f_{\mathbf{x}}(\mathbf{x}; a)$ where $a \neq 0$ is a signal amplitude and $a = 0$ represents the null hypothesis. The LLR is then

$$l(\mathbf{x}; a) = \log \left[\frac{f_{\mathbf{x}}(\mathbf{x}; a)}{f_{\mathbf{x}}(\mathbf{x}; 0)} \right] \quad (6.20)$$

for $a \neq 0$. A first-order Taylor series expansion of the LLR as function of a about the origin yields the approximation

$$l(\mathbf{x}; a) \approx l(\mathbf{x}; 0) + a \left[\frac{\partial}{\partial a} l(\mathbf{x}; a) \right] \Big|_{a=0} = a \frac{\left[\frac{\partial}{\partial a} f_{\mathbf{x}}(\mathbf{x}; a) \right] \Big|_{a=0}}{f_{\mathbf{x}}(\mathbf{x}; 0)}. \quad (6.21)$$

When a is small, the approximation is accurate and therefore useful in obtaining a detector for weak signals. Dividing by a produces the *locally optimal* decision statistic

$$T_{\text{LO}}(\mathbf{x}) = \frac{\left[\frac{\partial}{\partial a} f_{\mathbf{x}}(\mathbf{x}; a) \right] \Big|_{a=0}}{f_{\mathbf{x}}(\mathbf{x}; 0)} \quad (6.22)$$

which does not depend on the unknown value of a representing signal presence.

Note that P_d can be described as a function of the signal amplitude, $P_d(a)$. When $a \rightarrow 0$, probability of detection tends to the probability of false alarm, $P_d(a) \rightarrow P_f$. The locally optimal detector (i.e., using (6.22) as a decision statistic) can be shown [4, Sect. 1.4] to maximize the slope of $P_d(a)$ as $a \rightarrow 0$, implying P_d will grow faster than any other detector for vanishingly weak signals.

Example: Known Signal in Additive Non-Gaussian Noise

Suppose the data are of the form $X_i = as_i + V_i$ for $i = 1, \dots, n$ where a is the signal amplitude, s_i is a known signal, and V_i is an additive noise sample with PDF $f_V(v)$. The PDF of the data (assuming the noise samples are *iid*) when signal is present is

$$f_{\mathbf{x}}(\mathbf{x}; a) = \prod_{i=1}^n f_V(x_i - as_i) \quad (6.23)$$

which leads to the locally optimal detector

(continued)

$$\begin{aligned}
T_{\text{LO}}(\mathbf{x}) &= \sum_{i=1}^n s_i \left[-\frac{f'_V(x_i)}{f_V(x_i)} \right] \\
&= \sum_{i=1}^n s_i g_{\text{LO}}(x_i)
\end{aligned} \tag{6.24}$$

which is a generalized non-linear correlator. The function $g_{\text{LO}}(x)$, sometimes called a *detector non-linearity* or *detector function*, essentially warps the data to an appropriate scale prior to correlation. For example, in Gaussian noise $g_{\text{LO}}(x) = x$ and the data are used without modification. However, suppose the noise is Laplacian (i.e., double exponential) distributed,

$$f_V(v) = \frac{1}{2\lambda} e^{-|v|/\lambda} \tag{6.25}$$

which is heavier tailed (i.e., more frequent occurrence of large-amplitude values) than Gaussian noise. The detector function is

$$g_{\text{LO}}(x) = -\frac{f'_V(x)}{f_V(x)} = \frac{1}{\lambda} \text{sign}(x) \tag{6.26}$$

and the decision statistic is a sign correlator

$$T_{\text{LO}}(\mathbf{x}) = \sum_{i=1}^n \frac{s_i}{\lambda} \text{sign}(x_i) \tag{6.27}$$

which severely limits the contribution of the data to the detector's decision so large-amplitude noise values do not cause too many false alarms.

6.2.7 Design of Detectors: Generalized Likelihood Ratio (GLR)

When unknown parameters exist for both the null and alternative hypotheses and in particular when ancillary signal parameters exist, there are very few options for detector design. The approach described in this section essentially replaces unknown parameters with their maximum-likelihood estimates (MLEs, see Sect. 6.3.4) prior to forming the likelihood ratio. As such, it is called a generalized likelihood ratio (GLR) test or detector. If the PDF of the data is $f_{\mathbf{x}}(\mathbf{x}; \theta)$ where under $H_0 \theta \in \Theta_0$ and under H_1 is $\theta \in \Theta_1$, the decision statistic has the form

$$T_{\text{GLR}}(\mathbf{x}) = \frac{\max_{\theta \in \Theta_1} f_{\mathbf{x}}(\mathbf{x}; \theta)}{\max_{\theta \in \Theta_0} f_{\mathbf{x}}(\mathbf{x}; \theta)} \quad (6.28)$$

$$= \frac{f_{\mathbf{x}}(\mathbf{x}; \hat{\theta}_1)}{f_{\mathbf{x}}(\mathbf{x}; \hat{\theta}_0)} \quad (6.29)$$

where $\hat{\theta}_0$ and $\hat{\theta}_1$ maximize the likelihood function under the appropriate hypothesis. It is important to note the maximizations in (6.28) need to occur before the ratio is formed. Since nuisance parameters exist under both hypotheses, there will be two separate estimates (one within $\hat{\theta}_1$ and one within $\hat{\theta}_0$).

Example: Complex Gaussian Data with Unknown Variance

Suppose the data X_i are $\stackrel{iid}{\sim} \mathcal{CN}(\mu, \lambda)$ for $i = 1, \dots, n$ with signal presence represented by $\mu \neq 0$, the noise-only condition by $\mu = 0$, and λ is unknown. The PDF of the data under H_0 is

$$f_0(\mathbf{x}; \lambda) = \frac{1}{(\pi \lambda)^n} \exp \left\{ -\frac{1}{\lambda} \sum_{i=1}^n |x_i|^2 \right\} \quad (6.30)$$

Differentiating by λ and setting the resulting equation to zero requires choosing λ as

$$\hat{\lambda}_0 = \frac{1}{n} \sum_{i=1}^n |x_i|^2 \quad (6.31)$$

which is the MLE of λ under H_0 . Similar to the example shown in Sect. 6.3.4 for real Gaussian data, the MLEs for μ and λ under H_1 have form

$$\hat{\mu} = \frac{1}{n} \sum_{i=1}^n x_i \quad (6.32)$$

and

$$\hat{\lambda}_1 = \frac{1}{n} \sum_{i=1}^n |x_i - \hat{\mu}|^2. \quad (6.33)$$

Substituting these into the likelihood ratio results in

(continued)

$$\begin{aligned}
T_{\text{GLR}}(\mathbf{x}) &= \frac{f_1(\mathbf{x}; \hat{\mu}, \hat{\lambda}_1)}{f_0(\mathbf{x}; \hat{\lambda}_0)} = \left(\frac{\hat{\lambda}_0}{\hat{\lambda}_1} \right)^n \\
&= \left(\frac{\sum_{i=1}^n |X_i|^2}{\sum_{i=1}^n |X_i - \bar{X}|^2} \right)^n
\end{aligned} \tag{6.34}$$

where $\bar{X} = \frac{1}{n} \sum_{i=1}^n X_i$ is the sample mean. The GLR detector decision statistic can be transformed (monotonically) to the detector

$$T(\mathbf{x}) = \frac{n|\bar{X}|^2}{S_X} \stackrel[H_1]{\underset[H_0}{\gtrless} h \tag{6.35}$$

where

$$S_X = \frac{1}{n-1} \sum_{i=1}^n |X_i - \bar{X}|^2 = \frac{n}{n-1} \hat{\lambda}_1 \tag{6.36}$$

is the (unbiased) sample variance.

Under the signal-present hypotheses, the decision statistic in (6.35) is non-centrally F distributed (see Sect. 5.6.17) with parameters $\nu_1 = 2$, $\nu_2 = 2(n-1)$, and $\delta = 2n|\mu|^2/\lambda$. Under the noise-only hypothesis, it is $F_{2,2(n-1)}$ distributed. Note that $T(\mathbf{x})$ in (6.35) does not depend on μ or λ , nor does its PDF under the null hypothesis. This implies the detector is implementable when μ and λ are unknown and that the probability of false alarm depends only on the decision threshold h (i.e., the detector is invariant to λ).

Exercise 6.1 Using the information in Sect. 5.6.16, show that if $T \sim F_{2,2(n-1)}$, its PDF is

$$f_T(t) = \frac{1}{[1 + t/(n-1)]^n} \tag{6.37}$$

and its CDF is

$$F_T(t) = 1 - \frac{1}{[1 + t/(n-1)]^{n-1}} \tag{6.38}$$

for $t \geq 0$. For the GLR detector decision statistic in (6.35), find the threshold h as a function of P_f .

Exercise 6.2 Plot the ROC curves for $n = 10, 20, 50$, and 100 for $P_f \in [10^{-6}, 1]$ when $\lambda = 1$ and $\mu = (3 + 2j)/\sqrt{n}$. To obtain the CDF of the non-central F distribution, perform a numerical integration of the PDF. Although the larger values of n do not increase the total SNR (δ is a fixed 26), they do provide improved estimation of the unknown variance. The loss in performance incurred by estimating λ can be quantified by noting that as $n \rightarrow \infty$, the decision statistic becomes the scale of a chi-squared random variable with 2 degrees of freedom and the same non-centrality parameter. Plot the ROC curve for this case to see how close or how far from ideal the GLR detector is as a function of n .

6.2.7.1 Asymptotic Distribution of the GLR Detector Decision Statistic

Although the GLR detector does not enjoy the optimality of the previously described approaches, it is very useful because it can nearly always be implemented. By exploiting the asymptotic properties of MLEs, two times the logarithm of the GLR detector decision statistic can be shown to be approximately non-centrally chi-squared distributed when the number of samples available is large [10, Sect. 23.7],

$$2 \log T_{\text{GLR}}(\mathbf{x}) \sim \chi^2_{r,\delta} \quad [\text{approximately}] \quad (6.39)$$

where r is the number of signal parameters estimated (i.e., not counting nuisance parameters) and

$$\delta = (\boldsymbol{\theta}_s - \boldsymbol{\theta}_{s,0})^T \mathbf{I}(\boldsymbol{\theta}_s) (\boldsymbol{\theta}_s - \boldsymbol{\theta}_{s,0}) \quad (6.40)$$

where $\boldsymbol{\theta}_s$ are the signal parameters, $\boldsymbol{\theta}_{s,0}$ are their values under the null hypothesis, and $\mathbf{I}(\boldsymbol{\theta}_s)$ is the corresponding portion of the Fisher information matrix (FIM, see Sect. 6.3.2). Under the null hypothesis, the decision statistic (transformed as in (6.39)) is central chi-squared distributed ($\delta = 0$) with r degrees of freedom, which can be useful in setting thresholds for large data samples.

For many detection problems, statistical evaluation of the decision statistic is difficult, particularly when signal is present. However, it is often feasible to evaluate the FIM analytically or numerically which enables use of the asymptotic statistics to assess performance. For example, consider ancillary signal parameters which would retain the same value under H_0 and H_1 and therefore do not contribute to δ . With δ fixed and r increasing, detection performance degrades. However, if a signal parameter increases δ significantly enough, then the benefit may outweigh the cost of estimation.

In some applications, the ML estimate of unknown parameters can require a multidimensional numerical optimization of the likelihood function. When this is computationally prohibitive, simpler estimates (e.g., method-of-moments) for some or all of the parameters often work well enough within the GLR framework.

6.2.8 Design of Detectors: Bayesian Approaches

The Bayesian approach to statistical inference assumes the parameter θ is random and characterized by a PDF, $\pi(\theta)$. In this context, $\pi(\cdot)$ is a function commonly used to represent prior PDFs on parameters and not the symbol for the transcendental number. The function $\pi(\theta)$ needs to be defined before an experiment begins or a measurement is taken based on expert knowledge (e.g., previous experience or previous data analysis). Other approaches for forming priors exist (e.g., conjugate or non-informative priors [7, Sects. 3.3 & 4.2.2]), but are beyond the scope of this book.

A Bayesian hypothesis test incorporates the prior information on the unknown parameters into the decision statistic. Rather than the NP optimality criterion used in Sect. 6.2.3, a Bayesian detector minimizes the Bayes risk function, which in turn depends on a loss function describing the cost of making a correct or incorrect decision [7, Sect. 1.3]. Consider a composite-vs.-composite hypothesis test where $\theta \in \Theta_0$ represents the null hypothesis and $\theta \in \Theta_1$ the alternative. The detector minimizing the Bayes risk has the form

$$T_B(\mathbf{x}) = \frac{\int_{\theta \in \Theta_1} f_{\mathbf{x}}(\mathbf{x}|\theta) \pi(\theta) d\theta}{\int_{\theta \in \Theta_0} f_{\mathbf{x}}(\mathbf{x}|\theta) \pi(\theta) d\theta} \stackrel{H_1}{\gtrless} \stackrel{H_0}{\lessgtr} \frac{\pi_0(C_{10} - C_{00})}{\pi_1(C_{01} - C_{11})} \quad (6.41)$$

where π_i is the prior probability of observing hypothesis H_i ,

$$\pi_i = \int_{\theta \in \Theta_i} \pi(\theta) d\theta, \quad (6.42)$$

and C_{ij} is the cost of deciding i when j is true for i and $j \in \{0, 1\}$. Although the form of $T_B(\mathbf{x})$ is a type of likelihood ratio, a difference in the Bayesian hypothesis test is that the threshold is chosen as a function of the prior probabilities and loss function (i.e., C_{ij}). Generally, the cost of an error is greater than the cost of a correct decision ($C_{10} > C_{00}$ and $C_{01} > C_{11}$). Increasing the cost of a false alarm (C_{10}) results in an increase in the decision threshold whereas increasing the cost of a missed detection (C_{01}) results in a decrease.

6.3 Estimation Theory

The two main branches of statistical inference are decision theory (e.g., hypothesis testing) and estimation theory. Estimation is the process of learning something specific about a *state of nature* through measurements or observations. The process starts by characterizing the state of nature in terms of a parameter (θ) and then obtaining a statistical model for the observed data depending on the state of nature, $f_{\mathbf{x}}(\mathbf{x}; \theta)$. Given a statistical model, the approach for developing an estimator

depends on the situation and the type of estimator desired. Generally, parameter estimators produce what is termed a *point estimate*; that is, a specific value expected to be close to the true value. If there are p parameters to be estimated, the point estimate is a p -dimensional vector. Alternative approaches include defining an interval (or set) within which the true value is expected to lie (Sect. 6.3.8) and obtaining a PDF for the unknown parameter given the observed data (e.g., a Bayesian posterior PDF as described in Sect. 6.3.6).

Similar to detection theory, there exist optimal approaches for parameter estimation. In particular, certain scenarios will have a uniformly minimum-variance unbiased estimator (MVUE) [11, Ch. 2]. As existence of the MVUE is not guaranteed and the process for obtaining it is complicated, this section focuses instead on the more practical estimation techniques typically used in underwater acoustics. The following approaches to estimator design are covered in this section:

Maximum-likelihood estimation: (Sect. 6.3.4) Often the first choice in estimators owing to desirable asymptotic properties, but can result in a computationally intensive numerical optimization.

Method-of-moments estimation: (Sect. 6.3.5) Usually easier to derive and implement than the maximum-likelihood estimator, but sometimes fails to provide an estimate.

Bayesian inference: (Sect. 6.3.6) A useful approach when prior information exists about a parameter or the parameter is believed to be random.

Expectation-maximization algorithm: (Sect. 6.3.7) An iterative approach to maximum-likelihood estimation when the statistical model can be described with missing data (i.e., information associated with each data sample that was not measured or not observable).

Interval estimation: (Sect. 6.3.8) Confidence intervals and Bayesian credible sets provide an interval within which the parameter is believed to lie.

Once an estimator is developed, it is important to evaluate its performance. In many cases, an optimal estimator cannot be easily obtained, so performance evaluation is necessary to determine how sub-optimal an estimator might be. Even when an optimal estimator exists, it is important to know if an estimator will provide an accuracy acceptable to the situation at hand. The standard performance measures for estimation are found in Sect. 6.3.2 and the Cramér-Rao lower bound on the variance of unbiased estimators in Sect. 6.3.3.

Readers interested in more detail and broader coverage of estimation theory are referred to the signal-processing-oriented texts [3, 11] or [6, 12] from the statistics literature.

6.3.1 Point Estimation in Underwater Acoustics

Most underwater acoustical systems that can be characterized as remote sensing will include an estimation algorithm. The most obvious examples are from systems designed to measure physical and acoustical properties of the ocean. Examples from the sonar equation include systems designed to measure (i.e., estimate) propagation loss, ambient noise power, reverberation level, or scattering strength. Oceanographic properties that can be estimated from acoustical measurements include depth,

bathymetry, sound speed, and even the speed of internal waves. Examples can also be found within remote sensing systems used to locate sound or scattering sources. For example, the location of a mine on the seafloor, a fish school, or the relative range and bearing of a submarine. Each of these applications entails parameters, measured data, and requires estimators to map the measured data to parameter estimates.

6.3.2 Performance Measures and Analysis of Estimators

Suppose the parameter of interest is θ , the data to be measured are represented by the random vector $\mathbf{x} = [X_1 \cdots X_n]^T$ with joint PDF $f_{\mathbf{x}}(\mathbf{x}; \theta)$, and the estimator is

$$\hat{\theta} = T(\mathbf{x}). \quad (6.43)$$

The hat notation, $\hat{\theta}$, generally represents an estimator of θ . The *estimator* is the random variable $T(X_1, \dots, X_n)$ whereas the *estimate* $T(x_1, \dots, x_n)$ is a specific value obtained from the observed data x_1, \dots, x_n . In general, both θ and T can be vector quantities; however, this treatment is limited to the scalar case, with multivariate extensions only where necessary.

Estimation performance measures quantify in a statistical sense how far an estimate is from the true value. The first-order (in terms of powers of the error) performance measure is simply the average error

$$b_{\hat{\theta}} = E[\hat{\theta} - \theta] = \mu_{\hat{\theta}} - \theta, \quad (6.44)$$

which is called the estimator bias. The bias is also the difference between the average value of the estimator,

$$\mu_{\hat{\theta}} = E[\hat{\theta}], \quad (6.45)$$

and the true value. Ideally, an estimator has an average value equal to the true value, so the bias is zero ($b_{\hat{\theta}} = 0$). Such an estimator is called *unbiased*. A second-order performance measure is the variance of an estimator,

$$\sigma_{\hat{\theta}}^2 = E[(\hat{\theta} - \mu_{\hat{\theta}})^2], \quad (6.46)$$

which defines the spread of the estimator about its mean. Clearly, a small variance is a desirable trait in an estimator. However, there can often be a trade-off between bias and variance where decreasing one leads to an increase in the other. The two performance measures can be combined into the *mean squared error* (MSE) of the estimator,

$$\epsilon_{\hat{\theta}}^2 = E\left[\left(\hat{\theta} - \theta\right)^2\right] = b_{\hat{\theta}}^2 + \sigma_{\hat{\theta}}^2, \quad (6.47)$$

describing the average squared error between the estimator and the true value. Similar to the use of standard deviation in lieu of variance, it is common to use the *root mean squared error* (RMSE), $\epsilon_{\hat{\theta}}$, as it allows comparison in the same units as the estimate itself.

Although not common, it is sometimes possible to evaluate estimator performance measures theoretically. A common starting point, however, is to evaluate the Cramér-Rao lower bound (Sect. 6.3.3) which defines the lowest estimator variance achievable for an unbiased estimator. Simulation analysis is then typically used to assess how well an estimator performs relative to this bound. In simulation analysis, the expectations in the performance-measure definitions are replaced by Monte-Carlo integrations, which in this case essentially replaces moments by sample moments. For example, the sample mean

$$\bar{\theta} = \frac{1}{n} \sum_{i=1}^n \hat{\theta}_i \quad (6.48)$$

approximates the mean of $\hat{\theta}$ by the average of n simulation trials. The estimator performance measures and their simulation formulas are found in Table 6.2.

Table 6.2 Performance measures for estimation of θ by $\hat{\theta}$

Name	Description	Simulation formula	Units of
Bias	$b_{\hat{\theta}} = E[\hat{\theta} - \theta] = \mu_{\hat{\theta}} - \theta$	$\hat{b}_{\hat{\theta}} = \frac{1}{n} \sum_{i=1}^n \hat{\theta}_i - \theta = \bar{\theta} - \theta$	θ
Variance	$\sigma_{\hat{\theta}}^2 = E\left[\left(\hat{\theta} - \mu_{\hat{\theta}}\right)^2\right]$	$\hat{\sigma}_{\hat{\theta}}^2 = \frac{1}{n} \sum_{i=1}^n \left(\hat{\theta}_i - \bar{\theta}\right)^2$	θ^2
MSE	$\epsilon_{\hat{\theta}}^2 = E\left[\left(\hat{\theta} - \theta\right)^2\right]$ $= b_{\hat{\theta}}^2 + \sigma_{\hat{\theta}}^2$	$\hat{\epsilon}_{\hat{\theta}}^2 = \frac{1}{n} \sum_{i=1}^n \left(\hat{\theta}_i - \theta\right)^2$ $= \hat{b}_{\hat{\theta}}^2 + \hat{\sigma}_{\hat{\theta}}^2$	θ^2
RMSE	$\epsilon_{\hat{\theta}} = \sqrt{E\left[\left(\hat{\theta} - \theta\right)^2\right]}$ $= \sqrt{b_{\hat{\theta}}^2 + \sigma_{\hat{\theta}}^2}$	$\hat{\epsilon}_{\hat{\theta}} = \sqrt{\frac{1}{n} \sum_{i=1}^n \left(\hat{\theta}_i - \theta\right)^2}$ $= \sqrt{\hat{b}_{\hat{\theta}}^2 + \hat{\sigma}_{\hat{\theta}}^2}$	θ

6.3.3 Cramér-Rao Lower Bound (CRLB)

An extremely useful tool in the analysis of estimators and estimation problems is the Cramér-Rao lower bound (CRLB). It provides the lowest variance attainable by any unbiased parameter estimator when using data following the prescribed statistical model. This section reviews the key points related to the CRLB; the reader is referred to [11, Ch. 3] for an excellent detailed treatment of the subject.

Suppose an estimator $\hat{\theta} = T(\mathbf{x})$ of θ is unbiased, then

$$E[T(\mathbf{x}) - \theta] = \int_{\Omega_x} [T(\mathbf{x}) - \theta] f_{\mathbf{x}}(\mathbf{x}; \theta) d\mathbf{x} = 0 \quad (6.49)$$

where the integral is over Ω_x , the range of \mathbf{x} . Taking the partial derivative of (6.49) with respect to θ leads to

$$\int_{\Omega_x} [T(\mathbf{x}) - \theta] \frac{\partial}{\partial \theta} f_{\mathbf{x}}(\mathbf{x}; \theta) d\mathbf{x} = \int_{\Omega_x} f_{\mathbf{x}}(\mathbf{x}; \theta) d\mathbf{x} = 1. \quad (6.50)$$

This step requires the partial derivative with respect to θ to be brought inside the integral over Ω_x , which implies Ω_x cannot depend on the parameter θ (e.g., as it would for a uniform random variable on $[a, b]$ where a or b depend on θ). This requirement, along with unbiasedness of the estimator, defines the regularity conditions under which the CRLB exists. Noting $\frac{\partial}{\partial \theta} \log[g(\theta)] = [\frac{\partial}{\partial \theta} g(\theta)]/g(\theta)$ allows writing (6.50) as an expectation and then an inequality,

$$\begin{aligned} 1 &= \int_{\Omega_x} [T(\mathbf{x}) - \theta] \left\{ \frac{\partial}{\partial \theta} \log[f_{\mathbf{x}}(\mathbf{x}; \theta)] \right\} f_{\mathbf{x}}(\mathbf{x}; \theta) d\mathbf{x} \\ &= E \left[[T(\mathbf{x}) - \theta] \left\{ \frac{\partial}{\partial \theta} \log[f_{\mathbf{x}}(\mathbf{x}; \theta)] \right\} \right] \\ &\leq E \left[[T(\mathbf{x}) - \theta]^2 \right]^{\frac{1}{2}} E \left[\left\{ \frac{\partial}{\partial \theta} \log[f_{\mathbf{x}}(\mathbf{x}; \theta)] \right\}^2 \right]^{\frac{1}{2}} \end{aligned} \quad (6.51)$$

where the Cauchy–Schwarz inequality⁴ yields the final result. It is important to note the partial derivative with respect to θ only applies to the function within the braces; it does not affect the PDF $f_{\mathbf{x}}(\mathbf{x}; \theta)$ that is part of the expectation. The first term after the inequality in (6.51) is recognized as the standard deviation of the unbiased estimator $\hat{\theta} = T(\mathbf{x})$, which yields the Cramér-Rao lower bound on the variance

⁴The Cauchy–Schwarz inequality in integral form is $|\int f(x)g^*(x) dx|^2 \leq \int |f(x)|^2 dx \int |g(x)|^2 dx$ with the equality achieved non-trivially if and only if $g(x) = cf(x)$ for some constant c .

$$\text{Var}\{\hat{\theta}\} \geq E\left[\left\{\frac{\partial}{\partial\theta} \log[f_{\mathbf{x}}(\mathbf{x}; \theta)]\right\}^2\right]^{-1} = \frac{1}{I(\theta)} \quad (6.52)$$

The function in the denominator,

$$I(\theta) = E\left[\left\{\frac{\partial}{\partial\theta} \log[f_{\mathbf{x}}(\mathbf{x}; \theta)]\right\}^2\right] = E\left[-\left\{\frac{\partial^2}{\partial\theta^2} \log[f_{\mathbf{x}}(\mathbf{x}; \theta)]\right\}\right] \quad (6.53)$$

is called the Fisher information and indicates how much might be learned about θ from the data \mathbf{x} . The far right side of (6.53) provides an alternative but equivalent form of the CRLB,

$$\text{Var}\{\hat{\theta}\} \geq E\left[-\left\{\frac{\partial^2}{\partial\theta^2} \log[f_{\mathbf{x}}(\mathbf{x}; \theta)]\right\}\right]^{-1} = \frac{1}{I(\theta)}, \quad (6.54)$$

which is useful when taking a second derivative with respect to θ simplifies the ensuing expectation. Reiterating, it is important to note the partial derivatives with respect to θ in (6.52) and (6.54) only apply to the functions within the braces and not the PDF associated with the expectation. When an estimator achieves the CRLB (i.e., the equality holds in (6.52) or (6.54)), it is called an *efficient estimator*. When this occurs only as the amount of data grows to infinity, the estimator is termed *asymptotically efficient*.

Example: CRLB for *iid* Samples

Suppose the data X_1, \dots, X_n are $\stackrel{iid}{\sim} f_X(x; \theta)$, so the joint PDF factors into a product and the joint log-likelihood function (LLF) is the sum

$$\log f_{\mathbf{x}}(\mathbf{x}; \theta) = \sum_{i=1}^n \log f_X(x_i; \theta). \quad (6.55)$$

The second partial derivative of the LLF with respect to θ is also a sum and the expected value becomes

$$\begin{aligned} I(\theta) &= E\left[-\left\{\frac{\partial^2}{\partial\theta^2} \log[f_{\mathbf{x}}(\mathbf{x}; \theta)]\right\}\right] \\ &= \sum_{i=1}^n E\left[-\left\{\frac{\partial^2}{\partial\theta^2} \log[f_X(X_i; \theta)]\right\}\right] = nI_X(\theta) \end{aligned} \quad (6.56)$$

(continued)

where $I_X(\theta)$ is the Fisher information for one data sample (X). This result implies the CRLB is inversely proportional to the number of *iid* samples available for estimation.

In many cases, it will be easier to derive the CRLB than to evaluate the variance of an estimator analytically. As such, a common approach is to evaluate the CRLB and compare it to the achieved estimator performance via simulation. When the CRLB cannot be determined analytically, it is sometimes possible to simplify it to a partial derivative of a function involving θ (e.g., see [11, Sect. 3.9 & App. 15C] for general Gaussian cases), which can then be evaluated numerically by a finite difference.

Exercise 6.3 Derive the first form of the CRLB in (6.52) from the second form in (6.54). That is, show

$$E\left[-\left\{\frac{\partial^2}{\partial\theta^2}\log[f_{\mathbf{x}}(\mathbf{x};\theta)]\right\}\right]=E\left[\left\{\frac{\partial}{\partial\theta}\log[f_{\mathbf{x}}(\mathbf{x};\theta)]\right\}^2\right]. \quad (6.57)$$

Hint: After decomposing the left side, one of the terms requires exchanging the order of the partial derivative and the integral arising from the expectation.

6.3.3.1 CRLB for Multiple Parameters

When multiple parameters are estimated simultaneously, the CRLB extends to a matrix-vector formulation for any unbiased estimator. The scalar bias becomes a vector, which must be all zeros to satisfy the unbiased requirement. The scalar variance becomes a covariance matrix,

$$\Sigma_{\hat{\theta}}=E\left[\left(\hat{\theta}-\theta\right)\left(\hat{\theta}-\theta\right)^T\right] \quad (6.58)$$

and the Fisher information becomes the matrix

$$\begin{aligned} \mathbf{I}(\theta) &= E\left[\left(\frac{\partial}{\partial\theta}\log f_{\mathbf{x}}(\mathbf{x};\theta)\right)\left(\frac{\partial}{\partial\theta}\log f_{\mathbf{x}}(\mathbf{x};\theta)\right)^T\right] \\ &= -E\left[\frac{\partial}{\partial\theta}\left(\frac{\partial}{\partial\theta}\log f_{\mathbf{x}}(\mathbf{x};\theta)\right)^T\right]. \end{aligned} \quad (6.59)$$

The diagonal terms of the Fisher information matrix (FIM) are exactly the terms from the scalar case. However, the off-diagonal terms represent coupling between parameters,

$$\{\mathbf{I}(\boldsymbol{\theta})\}_{i,j} = E \left[\left\{ \frac{\partial}{\partial \theta_i} \log[f_{\mathbf{x}}(\mathbf{x}; \boldsymbol{\theta})] \right\} \left\{ \frac{\partial}{\partial \theta_j} \log[f_{\mathbf{x}}(\mathbf{x}; \boldsymbol{\theta})] \right\} \right] \quad (6.60)$$

$$= E \left[- \left\{ \frac{\partial^2}{\partial \theta_i \partial \theta_j} \log[f_{\mathbf{x}}(\mathbf{x}; \boldsymbol{\theta})] \right\} \right] \quad (6.61)$$

for i and $j = 1, \dots, p$ when there are p parameters.

The CRLB then dictates the inequality

$$\boldsymbol{\Sigma}_{\hat{\boldsymbol{\theta}}} \geq \mathbf{I}^{-1}(\boldsymbol{\theta}) \quad (6.62)$$

which for matrices implies the difference matrix $\boldsymbol{\Sigma}_{\hat{\boldsymbol{\theta}}} - \mathbf{I}^{-1}(\boldsymbol{\theta})$ is positive semi-definite (i.e., all eigenvalues are ≥ 0), so the matrix quadratic form satisfies

$$\mathbf{a}^T [\boldsymbol{\Sigma}_{\hat{\boldsymbol{\theta}}} - \mathbf{I}^{-1}(\boldsymbol{\theta})] \mathbf{a} \geq 0 \quad (6.63)$$

for any vector \mathbf{a} . Noting that the q th diagonal term in $\boldsymbol{\Sigma}_{\hat{\boldsymbol{\theta}}}$ is the variance of the q th parameter estimator, (6.63) can be used to show

$$\text{Var}\{\hat{\theta}_q\} \geq \left\{ \mathbf{I}^{-1}(\boldsymbol{\theta}) \right\}_{q,q} \quad (6.64)$$

by choosing \mathbf{a} as the q th unit vector (i.e., a vector of zeros except for a one in the q th element).

6.3.3.2 CRLB for Transformations

Often, a function of a parameter in a statistical model is of greater interest than the original parameter. For example, SNR is often evaluated in decibels whereas statistical models typically use linear forms. Another common example is when the cosine of an angle is estimated and the angle itself is desired. Fortunately, the CRLB for the function of a parameter is easily related to the CRLB for the parameter itself. If the function $g(\boldsymbol{\theta})$ is of interest, it is straightforward to see that the first definition of the Fisher information from (6.53) becomes

$$I(g(\boldsymbol{\theta})) = \frac{I(\boldsymbol{\theta})}{\left[\frac{\partial}{\partial \boldsymbol{\theta}} g(\boldsymbol{\theta}) \right]^2} \quad (6.65)$$

so the CRLB is

$$\text{Var}\{g(\hat{\boldsymbol{\theta}})\} \geq \frac{\left[\frac{\partial}{\partial \boldsymbol{\theta}} g(\boldsymbol{\theta}) \right]^2}{I(\boldsymbol{\theta})}. \quad (6.66)$$

For multiple parameters, the matrix inequality of (6.62) becomes

$$\boldsymbol{\Sigma}_{\hat{\theta}} \geq \frac{\partial \mathbf{g}(\boldsymbol{\theta})}{\partial \boldsymbol{\theta}} \mathbf{I}^{-1}(\boldsymbol{\theta}) \left[\frac{\partial \mathbf{g}(\boldsymbol{\theta})}{\partial \boldsymbol{\theta}} \right]^T \quad (6.67)$$

where $\partial \mathbf{g}(\boldsymbol{\theta})/\partial \boldsymbol{\theta}$ is a matrix of partial derivatives.

Example: Estimating SNR in Decibels

It is desired to estimate SNR (s) for a complex-Gaussian-fluctuating signal in zero-mean additive Gaussian noise where m complex-envelope samples of noise-only data are available to estimate the noise power for each of the n observations of the signal. The measured data are combined to form sufficient statistics for estimating s by taking the ratio of the magnitude-squared signal measurement to the estimated noise power in each observation. These sufficient statistics (T_1, \dots, T_n) follow an $F_{2,2m}$ distribution with a scale of $1 + s$, which has PDF

$$f_T(t) = \frac{(1+s)^m}{(1+s+t/m)^{m+1}} \quad (6.68)$$

for $t \geq 0$. The CRLB for s can be shown to be

$$\text{Var}(\hat{s}) \geq \frac{(1+s)^2}{n} \left(1 + \frac{2}{m} \right) \quad (6.69)$$

and indicates having multiple observations (n) provides the largest reduction in the lower bound. Better estimation of the noise power (increasing m) has minimal effect. Interestingly, for large s the bound is approximately proportional to the SNR squared so the bound on the standard deviation is proportional to the parameter itself.

Typically, SNR is evaluated in decibels, $S = 10 \log_{10} s$. Noting $\partial S / \partial s = s^{-1} 10 \log_{10}(e)$, the CRLB for S can be related to that for s by

$$\text{CRLB}_S = \frac{[10 \log_{10}(e)]^2}{s^2} \text{CRLB}_s \approx \frac{[4.34]^2}{s^2} \text{CRLB}_s. \quad (6.70)$$

Combining (6.69) and (6.70) and taking the square root produces a lower bound on the standard deviation of S

$$\text{Std}(\hat{S}) \geq \frac{4.34}{\sqrt{n}} \left(1 + \frac{1}{s} \right) \sqrt{1 + \frac{2}{m}} \quad (6.71)$$

(continued)

which is in decibel units. So, when s and m are large, the lower bound on the standard deviation for one observation is 4.34 dB. Assuming an unbiased, efficient estimator can be found, this implies at least 76 *iid* observations are necessary to obtain a standard deviation of 0.5 dB.

6.3.3.3 CRLB for a Multivariate Gaussian Model

The most common statistical model for multivariate data is the Gaussian model. In the general case, both the mean vector and covariance matrix can depend on the model parameters θ ,

$$\mathbf{x} \sim \mathcal{N}(\boldsymbol{\mu}(\boldsymbol{\theta}), \boldsymbol{\Sigma}(\boldsymbol{\theta})). \quad (6.72)$$

From [11, Sect. 3.9], the (i, j) element of the Fisher information matrix (FIM) has the form

$$\{\mathbf{I}(\boldsymbol{\theta})\}_{i,j} = \frac{\partial \boldsymbol{\mu}^T(\boldsymbol{\theta})}{\partial \theta_i} \boldsymbol{\Sigma}^{-1}(\boldsymbol{\theta}) \frac{\partial \boldsymbol{\mu}(\boldsymbol{\theta})}{\partial \theta_j} + \frac{1}{2} \text{tr} \left\{ \boldsymbol{\Sigma}^{-1}(\boldsymbol{\theta}) \frac{\partial \boldsymbol{\Sigma}(\boldsymbol{\theta})}{\partial \theta_i} \boldsymbol{\Sigma}^{-1}(\boldsymbol{\theta}) \frac{\partial \boldsymbol{\Sigma}(\boldsymbol{\theta})}{\partial \theta_j} \right\} \quad (6.73)$$

where $\text{tr}(\boldsymbol{\Sigma})$ is the trace of $\boldsymbol{\Sigma}$ (i.e., the sum of the diagonal elements of the matrix).

For situations where either the mean vector or covariance matrix does not depend on a particular parameter, one of the partial derivatives is zero and evaluation of the FIM is simplified by only requiring one of the terms in (6.73).

6.3.3.4 CRLB for a Complex Multivariate Gaussian Model

When the data are complex normally distributed as described in Sect. 5.6.9,

$$\mathbf{x} \sim \mathcal{CN}(\boldsymbol{\mu}(\boldsymbol{\theta}), \boldsymbol{\Sigma}(\boldsymbol{\theta})), \quad (6.74)$$

the (i, j) element of the Fisher information matrix has the form [11, App. 15C]

$$\begin{aligned} \{\mathbf{I}(\boldsymbol{\theta})\}_{i,j} &= 2\text{Re} \left\{ \frac{\partial \boldsymbol{\mu}^H(\boldsymbol{\theta})}{\partial \theta_i} \boldsymbol{\Sigma}^{-1}(\boldsymbol{\theta}) \frac{\partial \boldsymbol{\mu}(\boldsymbol{\theta})}{\partial \theta_j} \right\} \\ &\quad + \text{tr} \left\{ \boldsymbol{\Sigma}^{-1}(\boldsymbol{\theta}) \frac{\partial \boldsymbol{\Sigma}(\boldsymbol{\theta})}{\partial \theta_i} \boldsymbol{\Sigma}^{-1}(\boldsymbol{\theta}) \frac{\partial \boldsymbol{\Sigma}(\boldsymbol{\theta})}{\partial \theta_j} \right\}. \end{aligned} \quad (6.75)$$

6.3.4 Estimation Techniques: Maximum Likelihood

The maximum-likelihood (ML) estimator chooses the value of the parameter maximizing the likelihood function. The likelihood function is simply the function formed by the joint PDF of the data evaluated at the observed values (x_1, \dots, x_n) and taken as a function of the parameters of the distribution,

$$L(\boldsymbol{\theta}; \mathbf{x}) = f_{\mathbf{x}}(\mathbf{x}; \boldsymbol{\theta}). \quad (6.76)$$

Thus, the ML estimator has the form

$$\hat{\boldsymbol{\theta}} = \arg \max_{\boldsymbol{\theta}} L(\boldsymbol{\theta}; \mathbf{x}) \quad (6.77)$$

where “ $\arg \max$ ” returns the argument (here the value of $\boldsymbol{\theta}$) maximizing the ensuing function. Often, it is easier to work with the logarithm of the likelihood function,

$$\hat{\boldsymbol{\theta}} = \arg \max_{\boldsymbol{\theta}} \log L(\boldsymbol{\theta}; \mathbf{x}) \quad (6.78)$$

which results in the same estimator as (6.77) owing to the monotonicity of the logarithm function.

ML estimators are obtained using the same procedures as those required to maximize a function. The derivative of the likelihood or log-likelihood function with respect to the parameter to be estimated is set to zero and the resulting equation solved to obtain the parameter estimator $\hat{\boldsymbol{\theta}}$ as function of the data \mathbf{x} . When p parameters are to be estimated simultaneously, p partial derivatives are used to form p simultaneous equations. The solution to the simultaneous equations provides the parameter estimators as a function of the data. Similar to function optimization, the second derivative (or Hessian matrix) should be evaluated to ensure the stationary point is a maximum and not a minimum.

A distinct advantage of the ML estimation approach is that it is always feasible to obtain an estimate, even when closed-form solutions to the maximization problem are not readily available. As with function maximization, numerical optimization of the likelihood function can be employed to obtain the estimate. At times, numerical optimization can be computationally intensive (e.g., when simultaneously estimating multiple parameters) and fraught with problems such as converging to local rather than global maxima. However, not all estimation approaches are guaranteed to produce an estimate (e.g., see the method-of-moments approach in Sect. 6.3.5).

Example: Gaussian Distribution

Suppose the data are known to be Gaussian and it is desired to estimate the mean and variance. The log-likelihood function of the data, assuming they are $iid \mathcal{N}(\mu, \sigma^2)$ is

$$\begin{aligned} l(\boldsymbol{\theta}; \mathbf{x}) &= \log L(\boldsymbol{\theta}; \mathbf{x}) \\ &= -\frac{n}{2} \log \sigma^2 - \frac{1}{2\sigma^2} \sum_{i=1}^n (X_i - \mu)^2 - \frac{n}{2} \log(2\pi) \\ &= -\frac{n}{2} \left(\frac{S_x}{\sigma^2} + \log \sigma^2 \right) - \frac{n}{2\sigma^2} (\mu - \bar{X})^2 - \frac{n}{2} \log(2\pi) \quad (6.79) \end{aligned}$$

where $\bar{X} = \frac{1}{n} \sum_{i=1}^n X_i$ is the sample mean and

$$S_x = \frac{1}{n} \sum_{i=1}^n (X_i - \bar{X})^2 \quad (6.80)$$

is the sample variance.

The approach for finding the MLEs for μ and σ^2 entails differentiating the LLF with respect to the parameters, equating the derivative to zero and solving the resulting equations simultaneously. In this example, it can be seen that the ML estimator for the mean is simply $\hat{\mu} = \bar{X}$ by observing the second term in (6.79). The estimate of σ^2 can then be found by differentiating the LLF with respect to σ^2 and equating it to zero, which requires choosing $\hat{\sigma}^2 = S_x$. This is only a necessary and not sufficient condition for the LLF to be maximized; a second derivative should be taken and ensured to be negative to satisfy the sufficient conditions.

6.3.4.1 Properties of the MLE

An advantage of the ML technique is that the estimator is invariant under one-to-one mappings. That is, if the ML estimate of $\boldsymbol{\theta}$ is $\hat{\boldsymbol{\theta}}_{ML}$ and $\boldsymbol{\beta} = g(\boldsymbol{\theta})$ is an invertible transformation of the parameters, then the ML estimate of $\boldsymbol{\beta}$ is $\hat{\boldsymbol{\beta}}_{ML} = g(\hat{\boldsymbol{\theta}}_{ML})$.

Although the MLE is not necessarily optimal for a finite number of data samples (n), it enjoys several useful asymptotic properties as $n \rightarrow \infty$. First, the mean of the MLE tends to the true value of the parameter, so the estimator is at least asymptotically unbiased. Further, its variance tends to the CRLB so the estimator is also at least asymptotically efficient. Note that asymptotic unbiasedness or

efficiency does not preclude the possibility that the MLE is unbiased or efficient for finite values of n . The MLE is also considered a *consistent* estimator because the estimate converges (in probability) to the true parameter value as the amount of data grows to be infinite [10, Sects. 17.7 & 18.10].

In addition to these desirable properties, it can also be shown [11, Sect. 7.5] that the MLE is asymptotically Gaussian distributed,

$$\hat{\boldsymbol{\theta}}_{\text{ML}} \sim \mathcal{N}\left(\boldsymbol{\theta}, \mathbf{I}^{-1}(\boldsymbol{\theta})\right) \text{ as } n \rightarrow \infty \quad (6.81)$$

where $\mathbf{I}(\boldsymbol{\theta})$ is the Fisher information matrix for the n samples. In many cases, a surprisingly small number of samples are required before the asymptotic distribution is usefully accurate in characterizing the performance of the MLE.

6.3.5 Estimation Techniques: Method of Moments

The method-of-moments (MM) approach to parameter estimation uses theoretical relationships between the parameters to be estimated and the moments of the data distribution to map estimates of the moments back to estimates of the parameters. If there are p parameters to be estimated, p moment relationships must be formulated. For example, the first p moments

$$E[X^j] = h_j(\boldsymbol{\theta}), \quad (6.82)$$

for $j = 1, \dots, p$, can be approximated by the first p sample moments

$$h_j(\boldsymbol{\theta}) \approx \frac{1}{n} \sum_{i=1}^n X_i^j = \hat{\mu}'_j \quad (6.83)$$

where it is recalled from Sect. 5.3.2 that μ'_j is the j th moment about the origin (with μ_j being the j th moment about the mean). The set of p equations are then solved for the p unknown parameters. While it is common to use moments about the origin, central moments or even fractional moments (e.g., $E[X^q]$ where q is not necessarily an integer) will also work.

Example: Gamma Distribution Method-of-Moments Estimation

If the data X_i are gamma distributed with shape parameter α and scale β , the first two moments are

$$E[X_i] = \alpha\beta \text{ and } E[X_i^2] = \alpha(\alpha + 1)\beta^2. \quad (6.84)$$

(continued)

Approximating these by their respective sample moments results in the two equations

$$\hat{\mu}'_1 = \hat{\alpha}\hat{\beta} \text{ and } \hat{\mu}'_2 = \hat{\alpha}(\hat{\alpha} + 1)\hat{\beta}^2 \quad (6.85)$$

which, when solved for the parameter estimates, results in

$$\hat{\alpha} = \frac{\hat{\mu}'_1^2}{\hat{\mu}'_2 - \hat{\mu}'_1^2} \text{ and } \hat{\beta} = \frac{\hat{\mu}'_1}{\hat{\mu}'_2 - \hat{\mu}'_1^2}. \quad (6.86)$$

Noting that the sample variance is

$$\hat{\sigma}^2 = \hat{\mu}'_2 - \hat{\mu}'_1^2 \quad (6.87)$$

the MM parameter estimates can also be described as

$$\hat{\alpha} = \frac{\hat{\mu}'_1^2}{\hat{\sigma}^2} \text{ and } \hat{\beta} = \frac{\hat{\mu}'_1}{\hat{\sigma}^2}. \quad (6.88)$$

A distinct advantage of MM over ML lies in the ease of applicability when the data are identically distributed but not necessarily statistically independent. Dependent data can cause problems in ML estimation when the estimator is designed assuming the data are independent. Although the sample moments will have higher variability for statistically dependent data compared with independent data, which equates to a reduction in performance, the estimator structure does not change.

Disadvantages of the MM approach include non-uniqueness and the possibility of moment equations with no solution (i.e., they are not invertible to obtain a parameter estimate). With respect to non-uniqueness, there is no clear approach for which moments to use other than noting that some yield simpler moment equations than others and that lower-order moments are generally preferred over higher-order ones owing to their lower variance.

Example: *K*-Distributed Reverberation

Although reverberation in active sonar systems is traditionally assumed to have a Rayleigh-distributed envelope (or an intensity with an exponential PDF), it can exhibit heavier tails representative of a higher false-alarm rate

(continued)

(e.g., see Sect. 7.4.3). The K distribution [13] is a model commonly used to represent such heavy-tailed reverberation by introducing a shape parameter α in addition to the scale λ . However, the PDF (see Sect. 5.6.19 or 7.4.3.3), shown here for the matched-filter intensity,

$$f_X(x) = \frac{2}{\lambda \Gamma(\alpha)} \left(\frac{x}{\lambda} \right)^{(\alpha-1)/2} K_{\alpha-1} \left(2 \sqrt{\frac{x}{\lambda}} \right), \quad (6.89)$$

contains a K Bessel function which precludes a simple ML estimation. One of the MM estimators of α described in [14] uses the first moment of the intensity,

$$E[X] = \alpha \lambda \quad (6.90)$$

and the first moment of the envelope, which is a fractional moment of X ,

$$E[\sqrt{X}] = \lambda^{\frac{1}{2}} \Gamma(1.5) \frac{\Gamma(\alpha + 0.5)}{\Gamma(\alpha)}. \quad (6.91)$$

Although a simpler MM estimator can be obtained by using the second moment of the intensity rather than the fractional moment in (6.91), its performance is not so good (accurate estimation of high-order moments can require large amounts of data). Replacing the theoretical moments by their sample moments results in the two equations

$$\bar{X} = \frac{1}{n} \sum_{i=1}^n X_i = \hat{\alpha} \hat{\lambda} \quad (6.92)$$

and

$$T = \frac{\hat{\mu}'_{0.5}^2}{\bar{X}} = \frac{\pi}{4\hat{\alpha}} \left[\frac{\Gamma(\hat{\alpha} + 0.5)}{\Gamma(\hat{\alpha})} \right]^2 \quad (6.93)$$

where

$$\hat{\mu}'_{0.5} = \frac{1}{n} \sum_{i=1}^n \sqrt{X_i}. \quad (6.94)$$

While there is no closed-form solution to (6.93), an approximation [15] accurate for values of $\hat{\alpha} > 10$ and usable down to $\hat{\alpha} \approx 1$ is

(continued)

$$\hat{\alpha} \approx \frac{1}{-4 \log(4T/\pi)}. \quad (6.95)$$

For small values of $\hat{\alpha}$, (6.95) can be used to initialize a Newton–Raphson iteration to improve the accuracy. The shape parameter of the K distribution is always positive, which requires $T < \pi/4$. However, the range of T , as formed from the sample moments, is $(0, \infty)$ so it is possible there is no solution to (6.93), exemplifying one of disadvantages of the MM estimation approach.

6.3.6 Estimation Techniques: Bayesian Inference

Similar to Bayesian detection (Sect. 6.2.8), prior information about a random parameter can be incorporated into estimation. In Bayesian point estimation, the impact of errors is quantified by a *loss function*. For example, if the error is

$$\varepsilon = \hat{\theta} - \theta, \quad (6.96)$$

a squared-error loss function would have form

$$L(\varepsilon) = \varepsilon^2 = (\hat{\theta} - \theta)^2. \quad (6.97)$$

Estimator design then proceeds by minimizing the average or expected loss,

$$\mathcal{R} = E[L(\varepsilon)] \quad (6.98)$$

which is called the *Bayes risk*. For the squared-error loss function, the optimal Bayesian estimator is the average value of θ given the observed data. This requires the conditional distribution (see Sect. 5.3.8) on θ given the observed data $\mathbf{x} = [x_1 \dots x_n]^T$, which is related to the prior PDF $\pi(\theta)$ by the PDF of the data conditioned on the parameter, $f(\mathbf{x}|\theta)$, through Bayes' theorem,

$$f(\theta|\mathbf{x}) = \frac{f(\mathbf{x}|\theta)\pi(\theta)}{f(\mathbf{x})}. \quad (6.99)$$

In contrast to the prior PDF on θ , which describes the available information on the unknown parameter before any data are observed, the PDF in (6.99) describes the information after observing the data and is therefore termed the *posterior* PDF. The mean value of the posterior PDF, which minimizes the average squared-error loss, is

$$\hat{\theta} = \int_{-\infty}^{\infty} \theta f(\theta | \mathbf{x}) d\theta. \quad (6.100)$$

Generally, Bayesian estimators are a function of the posterior PDF. For example, if the loss function is the absolute value of the error,

$$L(\varepsilon) = |\varepsilon|, \quad (6.101)$$

the optimal Bayesian estimator is the median of the posterior PDF; that is, $\hat{\theta}$ such that

$$\int_{\hat{\theta}}^{\infty} f(\theta | \mathbf{x}) d\theta = \int_{-\infty}^{\hat{\theta}} f(\theta | \mathbf{x}) d\theta = \frac{1}{2}. \quad (6.102)$$

The absolute-error loss treats the error proportionately to its size compared with the squared-error loss, which emphasizes large errors. Another loss function is the “0-1” or “hit-or-miss” loss function, where the error is zero when the estimator is arbitrarily close to the truth and one otherwise,

$$L(\varepsilon) = \begin{cases} 0 & \text{if } \varepsilon = 0 \\ 1 & \text{if } \varepsilon \neq 0 \end{cases} \quad (6.103)$$

The optimal Bayesian estimator under the hit-or-miss loss function is the mode of the posterior PDF,

$$\hat{\theta} = \arg \max_{\theta} f(\theta | \mathbf{x}), \quad (6.104)$$

which is also known as the *maximum a posteriori* or MAP estimator.

6.3.7 Estimation Techniques: Expectation-Maximization (EM) Algorithm

As before, suppose the data $X_1, \dots, X_n \stackrel{iid}{\sim} f_X(x; \boldsymbol{\theta})$ and estimation of $\boldsymbol{\theta}$ is required. When the statistical model can be characterized as having missing (i.e., unobserved) data, the expectation-maximization (EM) algorithm [16, 17] provides an iterative algorithm for obtaining the MLE. A common missing-data scenario occurs when a PDF can be described as convex combinations of other PDFs. For example,

$$f_X(x; \boldsymbol{\theta}) = \sum_{m=1}^M \pi_m f_m(x; \boldsymbol{\theta}_m) \quad (6.105)$$

where $f_m(x; \boldsymbol{\theta}_m)$, $\boldsymbol{\theta}_m$, and $\pi_m \geq 0$ are, respectively, the PDF, parameter, and weight for the m th component of the combination with $\sum_{m=1}^M \pi_m = 1$. Such a PDF is called a mixture distribution [18] and the missing data \mathbf{y} are pointers or indices to which of the M components produces the i th data sample X_i for $i = 1, \dots, n$. If the missing data were available, the joint PDF of the observed and missing data, $f_{\mathbf{z}}(\mathbf{z}; \boldsymbol{\theta})$ where $\mathbf{z} = [\mathbf{x}^T \ \mathbf{y}^T]^T$, is commonly more amenable to calculating the MLE.

The EM algorithm has two steps, the Expectation step (E-step) and the Maximization step (M-step). An initial estimate of the parameters $\boldsymbol{\theta}^{[0]}$ is required before starting. After completing the two steps, a new estimate is formed, leading to $\boldsymbol{\theta}^{[k]}$ after k iterations. In this context, the superscript $[k]$ indicates the k th iteration of the EM algorithm. At each iteration, the likelihood function for $\boldsymbol{\theta}$ formed from the observed data (x_1, \dots, x_n) is guaranteed to not decrease, so the iteration will eventually converge if it is bounded above.

Defining the likelihood function of $\boldsymbol{\theta}$ based on the complete data $\mathbf{z} = [\mathbf{x}^T \ \mathbf{y}^T]^T$ as

$$L_c(\boldsymbol{\theta}) = f_{\mathbf{z}}(\mathbf{z}; \boldsymbol{\theta}) \quad (6.106)$$

the E-step is to form the conditional expectation of the full data log-likelihood function given the observed data

$$Q(\boldsymbol{\theta}, \boldsymbol{\theta}^{[k]}) = E_{\boldsymbol{\theta}^{[k]}}[\log L_c(\boldsymbol{\theta}) | \mathbf{X} = \mathbf{x}] \quad (6.107)$$

where the notation $\mathbf{X} = \mathbf{x}$ indicates $X_i = x_i$ for $i = 1, \dots, n$. The PDF used to carry out the expectation depends on an initial estimate $\boldsymbol{\theta}^{[k]}$ whereas the LLF within the argument of the expectation depends on $\boldsymbol{\theta}$. The M-step finds the new parameter estimate $\boldsymbol{\theta}^{[k+1]}$ as the value of $\boldsymbol{\theta}$ maximizing (6.107),

$$\boldsymbol{\theta}^{[k+1]} = \arg \max_{\boldsymbol{\theta}} Q(\boldsymbol{\theta}, \boldsymbol{\theta}^{[k]}). \quad (6.108)$$

EM iterations are usually truncated when either the LLF shows minimal increase and/or the parameters do not change substantially. In practice, obtaining a good initial estimate of $\boldsymbol{\theta}$ is critical to a quick convergence to the MLE. Sometimes, it is possible to start with a method-of-moments estimator or, for mixtures, to intelligently partition the data with some coming from each of the models. Without a good initial estimate, the EM algorithm can converge to a local rather than global maximum of the likelihood function, thereby failing to provide the MLE.

6.3.7.1 Example: Exponential Mixture

As an example, suppose $f_X(x; \boldsymbol{\theta})$ is an exponential mixture,

$$f_X(x; \boldsymbol{\theta}) = \sum_{m=1}^M \pi_m \left[\frac{1}{\lambda_m} e^{-\frac{x}{\lambda_m}} \right] \quad (6.109)$$

with parameters $\boldsymbol{\theta} = [\pi_1, \lambda_1, \dots, \pi_M, \lambda_M]^T$ where (π_m, λ_m) are the proportion and mean of the m th component in the mixture. Mixture distributions are useful in describing data randomly arising from multiple models, data with occasional corruptions, and as an extremely flexible distribution capable of representing a wide range of situations. An interesting characteristic of mixture distributions arises from the linear form of the PDF. Transformations of a random variable following a mixture distribution result in an identically weighted mixture of the transformations of the individual components. Thus, noting that the square root of an exponential random variable is a Rayleigh random variable, the square root of an exponential mixture will be a Rayleigh mixture. The Rayleigh-mixture distribution is commonly used to represent heavy-tailed matched-filter-envelope data in active sonar systems.

The complete data likelihood function for a mixture model is

$$L_c(\boldsymbol{\theta}) = \prod_{i=1}^n \prod_{m=1}^M [\pi_m f_m(x_i; \lambda_m)]^{Y_{i,m}} \quad (6.110)$$

where $Y_{i,m}$ is 1 when the observed data sample x_i comes from the m th model and zero otherwise. The LLF is then

$$\log L_c(\boldsymbol{\theta}) = \sum_{i=1}^n \sum_{m=1}^M Y_{i,m} \log[\pi_m f_m(x_i; \lambda_m)]. \quad (6.111)$$

The E-step requires taking the conditional expectation of (6.111), which in turn requires

$$\begin{aligned} w_{i,m}^{[k]} &= E_{\boldsymbol{\theta}^{[k]}}[Y_{i,m} | X_i = x_i] \\ &= \frac{\pi_m^{[k]} f_m(x_i; \lambda_m^{[k]})}{\sum_{l=1}^M \pi_l^{[k]} f_m(x_i; \lambda_l^{[k]})} = \frac{\frac{\pi_m^{[k]}}{\lambda_m^{[k]}} e^{-x_i/\lambda_m^{[k]}}}{\sum_{l=1}^M \frac{\pi_l^{[k]}}{\lambda_l^{[k]}} e^{-x_i/\lambda_l^{[k]}}} \end{aligned} \quad (6.112)$$

where the parameters from the k th iteration are used and the far right side of (6.112) represents the exponential mixture example. The function produced in the E-step is therefore

$$Q(\boldsymbol{\theta}, \boldsymbol{\theta}^{[k]}) = \sum_{i=1}^n \sum_{m=1}^M w_{i,m}^{[k]} [\log(\pi_m) + \log f_m(x_i; \lambda_m)] \quad (6.113)$$

$$= \sum_{i=1}^n \sum_{m=1}^M w_{i,m}^{[k]} \left[\log(\pi_m) + -\frac{x_i}{\lambda_m} - \log \lambda_m \right] \quad (6.114)$$

Maximizing (6.113) with respect to π_m for $m = 1, \dots, M$ subject to the constraint $\sum_{m=1}^M \pi_m = 1$ results in the very simple update

$$\pi_m^{[k+1]} = \frac{1}{n} \sum_{i=1}^n w_{i,m}^{[k]} \quad (6.115)$$

which applies for all such mixture distributions. The parameters of the m th model are isolated to the m th term in the sum of (6.113), which simplifies finding their update as maximization is usually only as difficult as it is for the underlying individual model. In the example, choosing

$$\lambda_m^{[k+1]} = \frac{\sum_{i=1}^n w_{i,m}^{[k]} x_i}{\sum_{i=1}^n w_{i,m}^{[k]}} \quad (6.116)$$

maximizes (6.114). While the MLE for the scale parameter (which is also the mean) of an exponential distribution is the sample mean, (6.116) can be recognized as a weighted average of the data with the weights indicating belief that the i th data sample is associated with the m th model.

The EM algorithm for a mixture of exponential distributions is summarized by (6.112) to accomplish the E-step and (6.115) and (6.116) to accomplish the M-step, which provide parameter estimates for the next iteration.

6.3.8 Confidence Intervals and Bayesian Credible Sets

The estimators described in Sects. 6.3.4–6.3.7 were all *point* estimators of an unknown p -dimensional parameter θ where the estimator transforms the data \mathbf{x} to one point in p -dimensional space. For the scalar case ($p = 1$), suppose the estimator takes the form of an interval [6, Ch. 9],

$$\mathcal{T} = (T_L(\mathbf{x}), T_U(\mathbf{x})) \quad (6.117)$$

where $T_L(\mathbf{x})$ and $T_U(\mathbf{x})$ are functions of the data and represent, respectively, lower and upper bounds on the interval. For example, in Sect. 5.3.5 an interval estimate of the CDF of a random variable was described and applied in Sect. 6.2.2 to the probability of detection. This type of estimator is known as a *confidence interval* and has an associated *confidence coefficient*

$$1 - \alpha = \Pr\{\theta \in (T_L(\mathbf{x}), T_U(\mathbf{x}))\}. \quad (6.118)$$

The confidence coefficient is also called a *coverage probability* and at times is defined as a percentage, $100(1 - \alpha)\%$. It is interpreted as the frequency with which the interval will include the true value over many independent trials. Once data are observed (i.e., $X_i = x_i$ for $i = 1, \dots, n$) and the interval estimate is formed as $(T_L(x_1, \dots, x_n), T_U(x_1, \dots, x_n))$, there is no randomness for which an associated probability can be described. In simpler terms, $1 - \alpha$ is the probability the interval will include the true value *before* any data are observed. Values of $1 - \alpha$ close to one will very frequently encompass the true value, but potentially be large intervals. Small values of $1 - \alpha$ may not lead to useful interval estimates. The approach for designing confidence intervals, which is usually application specific, is beyond the scope of this text. The reader is referred to [6, Ch. 9] for more detail.

In Bayesian analysis, the equivalent to the confidence interval is called a *credible set*. The highest posterior density (HPD) credible set [7, Sect. 4.3.2] takes the smallest region of the parameter space providing the desired coverage probability. The resulting credible set is defined as the region of the parameter space where the posterior PDF exceeds a value $h(\alpha)$,

$$\mathcal{T} = \{\theta : f(\theta|\mathbf{x}) \geq h(\alpha)\}, \quad (6.119)$$

where $h(\alpha)$ is chosen according to the desired coverage probability

$$1 - \alpha = \int_{\mathcal{T}} f(\theta|\mathbf{x}) d\theta = \Pr\{\theta \in \mathcal{T} | \mathbf{X} = \mathbf{x}\} \quad (6.120)$$

where $\mathbf{X} = \mathbf{x}$ indicates $X_i = x_i$ for $i = 1, \dots, n$. Contrary to confidence intervals, the coverage probability of a Bayesian credible set is interpreted as the probability the true value lies in the set *after* observing the data.

For a unimodal posterior PDF, the HPD credible set is an interval including the posterior mode with lower and upper bounds chosen to satisfy (6.120). In general, however, the HPD credible set criteria can result in disjoint intervals when the posterior PDF is not unimodal. This can occur when prior information conflicts with the observed data. Although forming credible sets often requires numerical evaluation, it is a straightforward computation as opposed to the more complicated derivation of confidence intervals.

References

1. R.N. McDonough, A.D. Whalen, *Detection of Signals in Noise*, 2nd edn. (Academic, San Diego, 1995)
2. S.M. Kay, *Fundamentals of Statistical Signal Processing: Detection Theory* (Prentice Hall PTR, Englewood Cliffs, 1998)
3. L.L. Scharf, *Statistical Signal Processing* (Addison-Wesley Publishing Co., Reading, MA, 1991)
4. S.A. Kassam, *Signal Detection in Non-Gaussian Noise* (Springer, New York, 1988)

5. E.L. Lehmann, J.P. Romano, *Testing Statistical Hypotheses*, 3rd edn. (Springer, New York, 2005)
6. N. Mukhopadhyay, *Probability and Statistical Inference* (Marcel Dekker Inc., New York, NY, 2000)
7. J.O. Berger, *Statistical Decision Theory and Bayesian Analysis* (Springer, New York, 1985)
8. W.H. Munk, R.C. Spindel, A. Baggeroer, T.G. Birdsall, The Heard Island feasibility test. *J. Acoust. Soc. Am.* **96**(4), 2330–2342 (1994)
9. R. Srinivasan, *Importance Sampling* (Springer, New York, 2002)
10. A. Stuart, J.K. Ord, *Kendall's Advanced Theory of Statistics*, 5th edn., vol. 2 (Oxford University Press, New York, 1991)
11. S.M. Kay, *Fundamentals of Statistical Signal Processing: Estimation Theory* (Prentice Hall PTR, Englewood Cliffs, 1993)
12. E.L. Lehmann, *Theory of Point Estimation* (Wiley, New York, 1983)
13. E. Jakeman, P.N. Pusey, A model for non-Rayleigh sea echo. *IEEE Trans. Antennas Propag.* **24**(6), 806–814 (1976)
14. I.R. Joughin, D.B. Percival, D.P. Winebrenner, Maximum likelihood estimation of K distribution parameters for SAR data. *IEEE Trans. Geosci. Remote Sens.* **31**(5), 989–999 (1993)
15. D.A. Abraham, A.P. Lyons, Reliable methods for estimating the K-distribution shape parameter. *IEEE J. Ocean. Eng.* **35**(2), 288–302 (2010)
16. A.P. Dempster, N.M. Laird, D.B. Rubin, Maximum likelihood from incomplete data via the EM algorithm. *J. R. Stat. Soc. Ser. B* **2**, 1–38 (1977)
17. G.J. McLachlan, T. Krishnan, *The EM Algorithm and Extensions* (Wiley, New York, 2008)
18. D.M. Titterington, A.F.M. Smith, U.E. Makov, *Statistical Analysis of Finite Mixture Distributions* (Wiley, Chichester, 1985)

Part III

Detection in Underwater Acoustics

Chapter 7

Underwater Acoustic Signal and Noise Modeling



7.1 Introduction

The first step in designing underwater acoustic signal detection or estimation algorithms is to represent acoustic signals with a mathematical model. The most common basis for doing so is in time and frequency. For example, underwater acoustic signals can be short duration (whale clicks), intermediate duration (active sonar or communications signals), or long duration (passive radiated noise). In a similar fashion the frequency content can vary from narrowband (radiated noise from a rotating propeller) to broadband (airguns in seismic exploration) or be instantaneously narrowband but broadband overall (dolphin whistles). In addition to the time-frequency characterization of a signal, detector design requires a probabilistic modeling to represent both the consistency of the signal and the level of knowledge about its structure.

The extremes of knowledge of signal structure (completely known and completely unknown) are rarely encountered abstractions. It is more common to know a limited amount about the signal structure. For example, it might be known that a communications system transmitted a 10-kHz, 0.1-s sinusoidal pulse at 100 dB re $\mu\text{Pa}^2\text{m}^2$. However, the detection algorithm needs to account for the effects of propagation through the underwater environment, which can change the signal's amplitude, phase, frequency, and duration. Statistical modeling of the measured signal characterizes the consistency of the measurement over repeated observations. Similar to the knowledge dimension, the extremes of consistency (deterministic and random) are uncommon. An example of a random signal is ambient noise; however, as described in Sect. 3.3, there is usually some knowledge available regarding the frequency content and the central limit theorem often allows assuming the noise follows a Gaussian distribution. With respect to deterministic signals, even repeated transmission of known signals (e.g., the aforementioned communications pulse) can result in variations from observation to observation in amplitude, delay, phase, or frequency owing to changes in the ocean environment. In many cases, consistency

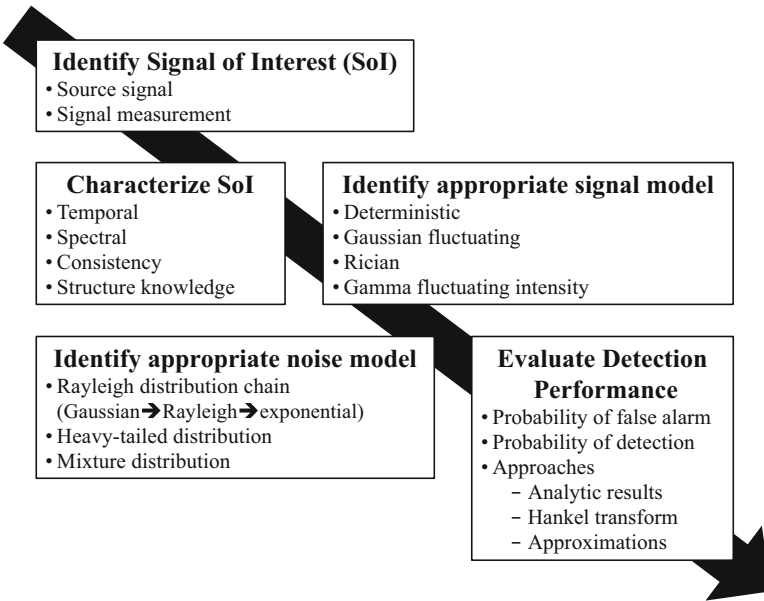


Fig. 7.1 Process of identifying a signal of interest (SoI), characterizing it, identifying mathematical signal and noise models, and evaluating detection performance

is inherently coupled with the extent of knowledge about signal structure. For example, if the signal's phase is unknown, the physics of the problem might dictate that it is random and uniformly distributed on $[0, 2\pi]$.

The material presented in this chapter details the process by which an underwater acoustic signal is categorized in terms of temporal extent, frequency content, consistency from observation to observation, and how much is known about its structure in order to identify one of several standard statistical models that can be used to design a signal detector and evaluate detection performance. This process (with the exception of designing the detection algorithm) is depicted in Fig. 7.1. Equally important to detector design is a similar characterization of the noise or interference hindering detection of the signal of interest. Descriptions of the four dimensions in which a signal is characterized (temporal, spectral, consistency, and structure) are presented in Sect. 7.2 along with the characterization of signals from common applications of underwater acoustic signal processing. A mapping from various points in the signal characterization dimensions to common statistical models is also presented. Because underwater acoustic signals generally have limited spectral content they can be modeled as bandpass signals. Simplifications to both signal processing and theoretical analysis of bandpass signals can then be obtained from their analytic signal, complex envelope, and baseband representations as described in Sect. 7.3. Spectral and statistical characterizations of noise and interfering signals (such as reverberation) are found in Sect. 7.4, including heavy-

tailed clutter distributions, mixture models, and the resulting probability of false alarm. The chapter is closed with a statistical characterization of common signal models as well as the combined signal-plus-noise measurement and associated probability of detection in Sect. 7.5.

7.2 Characterizing Underwater Acoustic Signals

The focus of this section is on characterizing the signal of interest in four different aspects or “dimensions.” These dimensions and their most relevant bifurcation are

- **Temporal character:** is the signal short or long duration?
- **Spectral content:** is the signal narrowband or broadband?
- **Measurement consistency:** is the measurement of the signal repeatable (deterministic) or in some way different in every observation (random)?
- **Knowledge of signal structure:** what is known and unknown about the signal of interest?

Where the signal of interest lies in these signal-character dimensions dictates what type of a detection algorithm should be used. In the ensuing chapters of this part of the book, detection algorithms are developed and analyzed for three general categories: signals with known form (Chap. 8), signals with unknown form (Chap. 9), and signals with unknown starting time and/or duration (Chap. 10). These signal categories represent subsets of the signal-character dimensions. Examples of signals of known form include active sonar and communications signals where most of the structure is known. Signals with unknown form include random signals that have little consistency from observation to observation but also encompass signals that are consistent across observations when very little is known about their structure. Particularly in remote sensing scenarios with either a moving object of interest or a moving sensing platform, the signal of interest persists for an unknown length of time. For example, in passive sensing of radiated ship noise the signal is only effectively present when the object of interest is close enough for there to be *signal excess* in the sonar equation. More specific details about the signal models and assumptions in each category are provided at the beginning of the chapter in which they are discussed. Signals of interest in most applications will fall into one of these three categories.

The signal of interest is usually first characterized according to how it is produced by (and at) the object of interest. For example, the clicks or whistles emitted by a dolphin or the reflection of an active sonar pulse from a mine. However, developing a detection algorithm requires characterizing the signal of interest after propagation from the object of interest to the sensor array. The effects of propagation can alter the signal’s characterization, most importantly in terms of consistency. When it is necessary to differentiate between the signal generated by the object of interest from that measured at the sensor array, the former will be called the “source signal”

Table 7.1 Source signals in several applications of underwater acoustic signal processing and their characterization in terms of consistency, knowledge, time, and frequency

Source signal and references	Characterization
Communications pulses General: [1, 2]; Underwater: [3, 4]	<ul style="list-style-type: none"> – Deterministic – Known form with unknown “information” – Short duration, high repetition rate – Generally BB
Active sonar reflections [5, Sect. 9.14] and [6, Part III]	<ul style="list-style-type: none"> – Deterministic (single dominant scatterer or specular reflection) – Random amplitude and phase (multiple scatterers or rough surface reflection) – Known form with unknown parameters (e.g., phase, amplitude, or Doppler) – Short duration, varying repetition rate – NB, BB, BB/INB – Doppler sensitive and insensitive
Radiated ship noise [5, Sects. 10.3–10.4], [7, Ch. 12] and [8]	<ul style="list-style-type: none"> – Random, unknown form – Long duration – <i>Machinery</i>: NB and BB – <i>Propeller</i>: NB and BB – <i>Hydrodynamic</i>: BB
Marine mammal sound emissions [9, Ch. 10]	<ul style="list-style-type: none"> – Unknown specific form within classes – Deterministic – <i>Clicks</i>: very short duration, BB; repeated in trains/bursts – <i>Whistles</i>: short to long duration, BB/INB; harmonics

The frequency character is described as being narrowband (NB), broadband (BB), or BB while being NB at any instant in time (BB/INB). Note that propagation through an acoustical channel can result in a different characterization of the signal *measurement* in a remote sensing system from that of the *source* signal

and the latter the “signal measurement” or simply the “signal.” Thus, the source signal is the forcing function (i.e., the source waveform) of the inhomogeneous wave equation described in Sect. 3.2.3.1 and the signal as measured at a sensor array is the ensuing solution. Source signals in several applications of underwater acoustic signal processing are listed in Table 7.1 along with where they lie in the different signal-characteristic dimensions. More detailed information on the various source signals can be found in the references listed in the first column.

Although the primary focus in characterizing the measurement is often on representing the signal of interest, characterizing the occluding noise or interference is equally important. Fortunately characterizing these is usually easier, both because of the ubiquity of noise measurements (i.e., measurements of signals of interest can be difficult to obtain over a wide span of conditions) and from the application of central-limit-theorem arguments to allow using Gaussian probability distributions. Acoustic noise in the ocean is generally assumed to be random and have a long duration relative to the signal of interest. Its frequency composition is typically broadband with some slope to the spectral density as described in Sect. 3.3.

However, nearby interferences (e.g., noise arising from mechanical components of a surface ship [8, Sect. 8.6]) can often be narrowband, intermediate duration, and come from specific directions.

To proceed, the signal measurement is considered to be either the pressure measurement from a single hydrophone or as obtained from the output of a beamformer applied to a sensor array. The relationships between measurements of an acoustic signal across an array of hydrophones and how they are exploited to implement a beamformer are described in Sect. 8.4. Suppose the measurement $x(t)$ is composed of a signal component $s(t)$ and a noise component $v(t)$. Generally, the physics and sensing system are considered a linear system so the measurement is the linear superposition of the two components,

$$x(t) = s(t) + v(t). \quad (7.1)$$

Although rare, there may be scenarios where the measurement involves other compositions (e.g., a multiplicative noise or the signal completely displacing the noise when it is present). All of the scenarios considered in this book assume linear superposition of signal and noise in the acoustical measurements. In general, the measurement $x(t)$ will be modeled as a random process. Although this may not be necessary for a purely deterministic signal, it is required when a deterministic signal has a random phase, an unknown starting time, or when adding random noise. Basic information on random processes can be found in Sect. 5.4. The remainder of this section describes each of the four dimensions characterizing signals of interest not falling under one of the types listed in Table 7.1.

7.2.1 *Signal Consistency and Knowledge*

The consistency of a signal measurement characterizes how similar it is expected to be from observation to observation. In a mathematical sense, multiple observations represent independent draws of a random process from the ensemble (i.e., the space of all possible outcomes). In a practical sense, multiple observations can represent either repeated experiments or multiple consecutive observations (e.g., several short processing epochs within a long-duration signal or echoes from consecutive transmissions in an active sensing system). In both cases, there is an assumption that the sensing scenario remains substantially the same, although not necessarily identical.

When a signal measurement is identical over multiple observations, it is called a *deterministic* signal. At the other extreme, where the signal measurement is significantly different from one observation to the next in an unpredictable manner, it might be characterized as a *random* signal. Most signals of interest will lie between these extremes. As an example, suppose a sinusoidal communications pulse is transmitted from a sound projector to a sensor in the basic ocean model described in Sect. 3.2. If the range is unknown, the amplitude (and arrival time)

of the signal measurement will be unknown but everything else will be known. Repeating the transmission results in an identical measurement as long as the range does not change, but the amplitude is still unknown. Thus, a signal measurement can be deterministic and yet have an unknown parameter. Suppose, however, that the pulse encounters significant boundary interaction affecting only the amplitude of the signal measurement. If the shape of the boundary changes from observation to observation (e.g., a moving sea surface or a sensing-system platform moving over a spatially varying seabed), the amplitude of the signal measurement might be different for each observation. Although such a signal measurement has some attributes that should be modeled as random, it is not a completely random signal because the shape of the pulse is consistent across observations even if its amplitude is not. These examples illustrate the importance of codifying not only signal consistency, but what knowledge is available about the signal measurement.

The amount of knowledge available about the signal measurement varies with each remote sensing scenario. In general more is known about the signal of interest in active remote sensing than passive because it is a reflection of a deliberately chosen sensing waveform. Even so, propagation through the ocean and reflection off the object of interest alters the transmitted waveform in ways that may be difficult to predict. The variation of signals of interest in passive remote sensing is exemplified by the sounds emitted by marine mammals, which include clicks, click trains or bursts, chirps, and whistles [9, Ch. 10]. When the knowledge about a deterministic signal becomes weak enough, the best detection algorithms are identical to those for random signals (i.e., energy detectors, as covered in Chap. 9). This highlights how knowledge about signal structure is as important as the consistency or statistical character of a signal. The commonality between random signals and deterministic signals with weak knowledge about structure lies in how the phase of a signal changes over time, which is unknown in both cases and results in a detector that does not exploit it.

Several useful signal models can be described by sampling a path between the extremes of the coupled consistency and knowledge dimensions. Bookending this path are the abstractions of a completely known deterministic signal and a random signal that is completely unknown. A progression between these two extremes might include the following signal categories:

1. Known exactly and deterministic (repeatable)
2. Known form: unknown deterministic parameters (e.g., arrival time, amplitude, phase, frequency, or Doppler scale)
3. Known form: unknown random parameters (e.g., amplitude or phase)
4. Partially known or unknown form: some consistency across observations
5. Unknown form: Gaussian wide-sense-stationary (WSS) random process with known power spectral density (PSD)
6. Unknown form: Gaussian WSS random process with unknown PSD
7. Unknown form: WSS random process with unknown probability density function (PDF) and PSD
8. Completely unknown and random

Categories 1 and 2 are considered perfectly repeatable; the measured signal will be identical over repeated observations, although for 2 there will be unknown but constant parameters. In category 3, although the form of the signal measurement is known (e.g., a communications pulse) it has unknown parameters that change in an unpredictable manner from one observation to the next and so the parameters are modeled as random.

In some scenarios a signal of interest can have consistency over repeated measurements and yet very little is known about its time-frequency structure before it is observed (category 4). Sound emissions from marine mammals fall under this category. They can be expected to have some consistency across repeated observations; however, only limited information may be available with respect to the form. The importance of the distinction between a signal with known form as opposed to an unknown form comes from the improvement in detection performance attained by exploiting the form, in particular how the phase changes over time, through the use of a matched filter.

The form of the signal measurement is clearly unknown when the generation process itself is random (e.g., the noise radiated by a body moving through water). Categories 5 and 6 describe a signal measurement with an unknown form as a wide-sense-stationary (WSS) Gaussian random process having either a known or unknown power spectral density (PSD). An example of such a signal measurement is the backscattering from a school of fish in an active sonar; the PSD is essentially the spectrum of the projected pulse as described in Sects. 3.5.6 and 7.4.2.3. Further along are a WSS random process with unknown distribution and PSD (category 7) and at the extreme a completely unknown and random signal (category 8).

Four different standard signal models are presented in Sects. 7.5.1–7.5.4. They are, respectively, deterministic, Gaussian-fluctuating, Rician, and gamma-fluctuating-intensity (GFI) signals models. A mapping from the above knowledge/consistency characteristics to the signal models is shown in Table 7.2. As seen in the table, signals with both known and unknown form can be represented by all four of the signal models. When it is not clear which signal model is appropriate, it is common to evaluate detection and estimation algorithms under both the deterministic and Gaussian-fluctuating signal models. While this (approximately) bounds the performance of a Rician signal, the GFI signal model can also be evaluated if the signal is expected to have fluctuations exceeding those of the Gaussian model.

With respect to noise and reverberation models, the basic Gaussian approximation to the pressure measurement leads to a Rayleigh-distributed envelope and an exponentially distributed instantaneous intensity, as shown in Sect. 7.3.6. The other scenarios listed in Table 7.2 and considered in Sect. 7.4.3 include heavy-tailed distribution models such as the K, Poisson-Rayleigh, and Weibull distributions as well as mixture models.

Table 7.2 Mapping from categories in the consistency/knowledge dimensions to standard signal and noise statistical models

Signal or noise category	Signal or noise model [section]
Signal with known form (e.g., active sensing)	
Deterministic parameters (known or unknown)	Deterministic [7.5.1]
Deterministic amplitude and uniformly random phase	Deterministic [7.5.1]
Random amplitude	Rician, Gaussian-fluctuating, or GFI [7.5.2–7.5.4]
Signal with unknown form (e.g., passive sensing)	
Some consistency across observations	Deterministic or Rician [7.5.1 or 7.5.3]
Gaussian WSS random process	Gaussian-fluctuating [7.5.2]
Non-Gaussian WSS random process	GFI [7.5.4]
Noise and reverberation models	
Gaussian WSS random process	Rayleigh/exponential [7.3.6]
Non-Gaussian WSS random process	Heavy-tailed models [7.4.3.3 and 7.4.3.5]
Multiple components	Mixture model [7.4.3.7]

Legend: WSS = wide-sense-stationary GFI = gamma-fluctuating-intensity

7.2.2 Time-Frequency Characterization of the Signal

As previously mentioned, the most important temporal characterization of a signal is its duration. For short-duration signals, the duration itself is important in the design of detection and estimation algorithms as is how much is known about it. For example, source signals with known form clearly have a known duration (e.g., active sonar or communication pulses); however, the effect of propagation through an underwater acoustical channel can alter this so the measurement has an unknown duration greater than that of the source signal. For short-duration signals of unknown form, it may be possible to define a maximum temporal extent (e.g., an impulsive source signal given some maximum propagation range in the CTBTO application or certain marine mammal sound emissions).

Long-duration signals are often random signals for which an important temporal characteristic is the time over which they can be considered correlated or coherent. For example, consider the signal arising from the flow of water through the oscillating forces produced by propeller blades [8, Sect. 9.2] or [5, Sect. 10.3]. These tonal signals have a narrow bandwidth at a center frequency related to the propeller blade rate (i.e., the number of blades times the rotational frequency) but are random in nature owing to the changing conditions in the water flow. Over some short period of time, however, the amplitude and phase of the signal does not change appreciably; it is coherent. The coherence time is approximately the inverse bandwidth of the signal, which illustrates the coupled nature of the time and frequency domains.

In the above examples of short- and long-duration signals, there was an inherent assumption that the signal was always present. In some scenarios, however, a signal measurement might be considered sparse in time. That is, the signal is not always observed throughout its duration or fades in and out. A fading signal can arise when the sonar platform, object of interest, or even the ocean itself move in such a way as to cause temporally overlapping multipath arrivals to alter between cancelling each other out and adding constructively. Another example can be found in multipath arrivals of short-duration signals (e.g., an active sonar echo or communications pulse) when the delay between arrivals on different paths exceeds the duration of the source signal, a common occurrence in deep water.

In order to discuss the spectral properties of signals of interest, it is useful to restrict consideration to signals and noise that can be modeled as wide-sense-stationary (WSS) random processes. Recall that the spectral content of a WSS random process can be described by its power spectral density (PSD), which is the Fourier transform of its autocorrelation function (ACF). Although it is possible to treat finite-duration deterministic signals separately through their Fourier transform, it is shown in Sect. 7.2.2.1 that they can be treated as WSS random processes when they have a random arrival time. The ACF of the resulting random signal is proportional to the (deterministic) correlation of the signal with itself and the PSD is proportional to the squared modulus of the Fourier transform of the signal. This allows a common analysis of either the noise or signal-plus-noise measurement. The ACF of a WSS random process can be used to describe the coherence time of a signal; however, it does not replace the aforementioned temporal characterization.

For many signals of interest, the PSD will be a sufficient characterization of the spectral characteristics of a signal. For example, many of the source signals listed in Table 7.1 were described as either narrowband (NB) or broadband (BB), which is essentially a statement about the spectral width (i.e., bandwidth) of the signal's PSD. As shown in Sect. 7.2.2.2, the definition of when a signal is considered NB or BB depends on the application. In many cases a signal is considered NB if its bandwidth is significantly less than its center frequency. However, in the important application of propagation of a source signal through an underwater acoustical channel, a signal is considered NB only if its bandwidth is narrow with respect to the channel bandwidth.

Unfortunately, the PSD of a signal is generally not adequate when there is time-varying spectral content. As described in [10], a joint time-frequency characterization of the signal can more accurately describe time-varying frequency content, which is commonly observed in underwater acoustic signals of interest and leads to the “broadband while instantaneously narrowband” (BB/INB) category in Table 7.1. For example, the whistle emitted by a dolphin (e.g., see [9, Ch. 10]) is decidedly narrowband at any instant in time, but can span a frequency band over 10-kHz wide in a short duration. Although the more detailed joint time-frequency characterizations are not always necessary, they can result in improved detection and estimation when there is an exploitable time-frequency structure (e.g., see how the time-frequency structure induced by dispersion can be exploited to improve classification [11]).

Other frequency characteristics that can play an important role in signal detection and estimation include the spectral shape of BB signals and the presence of harmonics. By their nature, the spectral shape of NB signals generally does not have an impact on detection or estimation. However, if the spectral shape of a signal or the noise in which it is observed varies significantly over its bandwidth, detection can be improved through the use of a whitening or frequency-weighting filter (e.g., the Eckart filter [12] or see Sect. 9.2.5.3). Harmonics can arise when a source signal undergoes a non-linear transformation prior to projection or measurement. This can occur in sound projectors [13, Ch. 9] and is clearly evident in marine mammal sound emissions (e.g., see [9, Ch. 10] or the example shown in Fig. 1.5).

7.2.2.1 Finite-Duration Signal Measurement as a Stationary Random Processes

Recall from Sect. 5.4.1 that a stationary random process is one whose statistical properties do not change with time. Therefore, it may be odd to think of a time-varying deterministic signal as having the potential to be represented as a stationary random process unless it is a constant. Suppose, however, that the deterministic signal $s(t)$ is only non-zero for $t \in (0, L)$ (i.e., it has finite duration) and that it arrives at some unknown time T , so the signal measurement is $X(t) = s(t - T)$. If there is no knowledge about the arrival time, it can be modeled as a uniform random variable on the interval $(-a, a)$. Assuming a is large enough to span the region of interest in t , the mean can be shown to be proportional to the time average of the signal,

$$\begin{aligned} E[X(t)] &= \frac{1}{2a} \int_{-a}^a s(t - r) dr \\ &= \frac{1}{2a} \int_{t-a}^{t+a} s(r) dr \end{aligned} \quad (7.2)$$

$$\approx \frac{1}{2a} \int_{-\infty}^{\infty} s(r) dr = 0, \quad (7.3)$$

which must be zero for an acoustic pressure measurement as described in Sect. 3.2.1.1. In a similar manner, it can be shown that the autocorrelation function (ACF) of the measurement is only a function τ ,

$$\begin{aligned} R_X(\tau) &= E[X(t)X(t + \tau)] \\ &\approx \frac{1}{2a} \int_{-\infty}^{\infty} s(r)s(r + \tau) dr. \end{aligned} \quad (7.4)$$

Thus, a finite-duration signal with a uniformly random arrival time is a wide-sense-stationary (WSS) random process.

The power spectral density (PSD) of the finite-duration signal with a random arrival time is the Fourier transform of the ACF. By noting that the form of (7.4) is a convolution between $s(t)$ and $s(-t)$, the PSD is seen to be proportional to the squared modulus of the Fourier transform of the signal,

$$\begin{aligned} S_X(f) &= \mathcal{F}\{R_X(\tau)\} \\ &= \frac{1}{2a} |\mathcal{F}\{s(t)\}|^2 = \frac{1}{2a} |S(f)|^2. \end{aligned} \quad (7.5)$$

By characterizing a finite-duration signal with a random arrival time as a WSS random process, the tools associated with WSS random processes and linear or LTI systems can be applied to both the noise¹ and signal-plus-noise measurements, which simplifies analysis.

7.2.2.2 Narrowband, Broadband, and Bandpass Signals

In an abstract sense, narrowband signals have a small bandwidth (W) and broadband signals have a large bandwidth. Before presenting more specific definitions of what constitutes “small” and “large” bandwidth, it is useful to define bandpass signals. As the name implies, a bandpass signal is one with spectral content limited to a band in frequency. In particular, a real-valued bandpass signal has no zero-frequency spectral content; its average value is zero. Bandpass signals can be described as a sinusoid modulated with a time-varying amplitude and phase,

$$s(t) = a(t) \cos(2\pi f_c t + \phi(t)), \quad (7.6)$$

where f_c is the center frequency, $a(t)$ is the amplitude, and $\phi(t)$ the phase. If a signal has an average value of zero (like the acoustic signals of interest in remote sensing) the so-called complex envelope $a(t)e^{j\phi(t)}$ must have bandwidth strictly less than $2f_c$.² It is important to note that bandpass signals can be either narrowband or broadband. In fact, any band-limited signal can be described using (7.6). More details on bandpass signals can be found in Sect. 7.3.

Determining if a signal is narrowband or broadband essentially amounts to choosing a particular bandwidth below which signals are narrowband and above which they are broadband. This is often done in the context of how large the bandwidth is relative to the center frequency. That is, a signal is narrowband if the ratio $W/f_c \ll 1$ and is otherwise broadband. This definition is important in many physical applications, ranging from sound production to the physics of

¹As noted in Sect. 7.4.1, ambient noise can be assumed stationary over short periods of time. However, as described in Sect. 7.4.2, a normalization process needs to occur in order to treat reverberation as a WSS random process.

²The bandwidth of the complex envelope accounts for both the positive and negative frequencies.

acoustic wave propagation. For example, the mechanical quality factor of a sound projector with resonant frequency f_r and producing a signal with bandwidth W is $Q_m = f_r/W$ [13, Sect. 2.8.3]. Because Q_m is also proportional to the ratio of the total energy produced to that dissipated in one cycle at projector resonance, a high- Q_m projector with a resonance at f_c is more efficient than a low- Q_m projector. As such, projecting narrowband signals defined by $W/f_c \ll 1$ is more efficient than projecting broadband signals.

An example from a sensing context can be found in the Doppler sensitivity of active sonar waveforms. Recall from Sect. 2.2.5 that the frequency shift induced by Doppler is (for a two-way monostatic system) $\Delta_f = 2v_r f_c/c_w$ where v_r is the relative radial velocity and c_w the speed of sound. For a fixed waveform bandwidth, the relative radial velocity must satisfy

$$v_r > \frac{c_w}{2} \cdot \frac{W}{f_c} \quad (7.7)$$

for an echo's spectrum to be outside of the zero-Doppler reverberation (see Sect. 2.2.6). Clearly narrowband waveforms ($W/f_c \ll 1$) have greater Doppler sensitivity than many broadband waveforms.³

As a final example, consider the case where the signal is an input to a mathematical system operator (e.g., representing propagation through an underwater acoustical channel). Recall from Sect. 4.2 that for a linear-time-invariant system, the response of the system to the signal $s(t)$ is the convolution

$$y(t) = \int_{-\infty}^{\infty} h(\tau)s(t - \tau) d\tau \quad (7.8)$$

where $h(t)$ is the system impulse response. Taking the Fourier transform of each side results in the product of the system frequency response $H(f)$ and the Fourier transform of the signal $S(f)$,

$$Y(f) = H(f)S(f). \quad (7.9)$$

Suppose the signal has a narrow enough bandwidth that $H(f)$ does not change appreciably over the frequency support of the signal. This results in

$$Y(f) \approx H(\text{sign}(f)f_c) S(f) \quad (7.10)$$

and the output of the system is then simply the input bandpass signal subject to an amplitude scale and phase shift induced by the frequency response of the system at the center frequency,

³As described in [14, Ch. 5] there exist broadband waveforms with significant Doppler sensitivity that are not subject to (7.7).

$$y(t) \approx |H(f_c)|a(t) \cos(2\pi f_c t + \phi(t) + \angle H(f_c)). \quad (7.11)$$

In order for (7.11) to be accurate, $a(t)$ and $\phi(t)$ need to vary slowly over the temporal extent of $h(t)$. A necessary but not sufficient condition for this to occur is for the signal bandwidth to be less than the system bandwidth. The sufficient condition is as previously stated: that $H(f) \approx H(\text{sign}(f)f_c)$ over the frequency support of the signal. An important difference between this example and the previous ones is that the signal bandwidth needs to be small relative to the bandwidth over which the system frequency response is flat at the center frequency as opposed to being small relative to the center frequency itself. In this context, the signal is said to be narrowband with respect to the system.

In each of these examples no specific demarcation between narrowband and broadband signals was noted. However, as bandwidth increases the relationships defining the narrowband regime will eventually break down, above which the signals can be considered broadband. Within the narrowband regime, however, projector efficiency, waveform Doppler sensitivity, or the approximation of the output of a system to a narrowband signal all improve as the bandwidth of the signal decreases (i.e., as it becomes more narrowband). Thus the distinction between narrowband and broadband signals may be more appropriately described as the conditions under which particular models or assumptions, respectively, hold or are violated.

Exercise 7.1 This exercise illustrates how propagation in a shallow-water multipath channel affects narrowband and broadband signals. For the shallow-water multipath channel described in Sect. 3.2.8.1, obtain the impulse response from (3.158). Use the following parameters: center frequency $f_c = 1 \text{ kHz}$, sampling frequency $f_s = 10f_c$, range $r = 5 \text{ km}$, water depth $z_b = 100 \text{ m}$, source depth $z_o = 45 \text{ m}$, receiver depth $z_r = 55 \text{ m}$. Noting that the n th path has $|n|$ bottom interactions, apply a bottom reflection loss factor of $0.5^{|n|}$ to the n th path in the impulse response. Approximate the impulse response of the propagation channel with an FIR filter with coefficients formed by sampling the first 100 ms of $h(t) * \text{sinc}(tf_s)$, which replaces the Dirac delta functions with a sinc function. Plot the impulse response and note the sinc-shaped functions representing each multipath, their alternating signs from the even and odd number of surface bounces, and the decaying amplitude arising from continued reflection from the bottom.

For a pulse duration $T_p = 0.5 \text{ s}$, generate a CW pulse $s(t)$ at frequency $f_c = 1 \text{ kHz}$ with a Tukey window shading the first and last 5% of the pulse. Generate the signal measured at the receiver by convolving the pulse with the impulse response, $y(t) = s(t) * h(t)$. Plot the signal and assess how much the channel altered its envelope. Is the Tukey window shape recognizable? Optional: obtain and plot the envelope of $y(t)$ rather than $y(t)$. Now generate an LFM waveform with bandwidth $W = 100 \text{ Hz}$ centered at $f_c = 1 \text{ kHz}$ and repeat the above process. How different is the amplitude? Is the LFM waveform broadband with respect to the channel? If so, how much should the bandwidth be reduced for it to be considered narrowband with respect to the channel? What changes when the pulse duration is increased to 2 s? What happens if the center frequency is 1422 Hz (which should be near a null in the channel frequency response)?

Simplifying hint: The signal measured at the receiver can be obtained directly by summing scaled and delayed versions of the transmit pulse or its complex envelope.

7.2.3 Effect of Propagation on Source-Signal Characterization

Source signals such as those listed in Table 7.1 must propagate from the object of interest to a sensor array. To evaluate the effect of propagation on the characterization of the source signal, suppose the propagation is treated as a linear time-invariant (LTI) system (see Sect. 4.2), that the signal of interest is bandpass,

$$p_o(t) = a(t) \cos(2\pi f_c t + \phi(t)), \quad (7.12)$$

and narrowband relative to the propagation channel. Further suppose the channel has a bulk propagation delay of τ_0 , so its frequency response is

$$H(f) = e^{-j2\pi f \tau_0} H_0(f). \quad (7.13)$$

If the source signal is narrowband with respect to $H(f)$, then $H_0(f)$ is essentially constant over the band $f_c \pm W/2$. The signal measurement is the convolution between the source signal and the channel impulse response, which then simplifies to

$$s(t) = \int_{-\infty}^{\infty} h(t - \tau) p_o(\tau) d\tau \quad (7.14)$$

$$= |H_0(f_c)| a(t - \tau_0) \cos(2\pi f_c(t - \tau_0) + \phi(t - \tau_0) + \angle H_0(f_c)). \quad (7.15)$$

Thus, when the signal is narrowband with respect to the channel, the signal measurement is a delayed version of the source signal with an amplitude factor $|H_0(f_c)|$ and a change in the phase of $\psi = \angle H_0(f_c)$ representing the cumulative effect of boundary interactions and any other propagation phenomena affecting the signal phase (e.g., caustics). When the source signal is broadband with respect to the propagation channel, the convolution in (7.14) spreads the signal of interest in some manner over time.

A final important alteration of the source signal arises from the Doppler effect (see Sect. 2.2.5) when there is relative motion between the sensing platforms and the object of interest. When the motion is slow relative to the speed of sound, the convolution in (7.14) can be used to approximate the signal measurement by imparting the Doppler effect as a time compression or expansion on the source signal before applying the convolution. If the source signal is narrowband with respect to the Doppler effect, the time scale is approximately a frequency shift in the frequency domain.

Table 7.3 Causative factors leading to changes in signal parameters and which signal characteristics are affected

Signal parameter	Causative factor	Characteristics affected
Amplitude	Range to object of interest, boundary interaction, multipath propagation	Knowledge, consistency
Travel time	Range to object of interest, sound speed, and complicated boundary interaction	Knowledge, consistency
Phase	Boundary interaction and other phenomena (e.g., caustics)	Knowledge, consistency
Temporal spreading	Multipath propagation, complicated boundary interaction	Temporal, knowledge, consistency
Doppler scale	Relative velocity between object of interest and sensing platforms	Spectral, temporal, knowledge, consistency

The affected characteristics are listed according to the most dominant or common effect

The effect of propagation can therefore be distilled to the impact on these four signal parameters: amplitude, phase, temporal spread, and Doppler scale. Several causative factors affecting each of these signal parameters are listed in Table 7.3. Clearly there are other factors affecting each of the signal parameters; however, these are the primary ones. Any changes in the characterization of the signal measurement in terms of the different dimensions (temporal, spectral, consistency, and knowledge of structure) from that of the source signal can be identified by how propagation changes the signal parameters. As seen in Table 7.3, knowledge and consistency can be affected by changes in any of the signal parameters. For example, when the range of the object of interest is unknown, the bulk delay or travel time is unknown as is the amplitude. As might be expected, changes in the temporal and spectral characterization are dominated by, respectively, signal spreading and Doppler. The following sections provide specific examples showing how propagation can cause a known source-signal phase or amplitude to be unknown or random in the signal measurement.

7.2.3.1 Unknown and Random Phases

Consider a single propagation path in a shallow-water channel with B reflections from the bottom. The change in phase arising from propagation is

$$\angle H(f_c) = -2\pi f_c \tau_0 + S\pi + \sum_{b=1}^B \psi_b \quad (7.16)$$

where S is the number of sign inversions (e.g., from surface reflection) and ψ_b is the phase change imparted on the signal during the b th bottom reflection. As described in Sect. 3.2.7.5, the phase change in a bottom reflection depends on the

grazing angle, the ratio of the speed of sound in the water to that of the bottom, and the ratio of their densities. This phase change can be zero, 180° (as for surface reflection), or in between during total internal reflection. In most scenarios, the detailed information required to determine the phase change induced by even one bottom reflection is not available. Because the bottom changes slowly with respect to most other processes in applications of underwater acoustic signal processing, the phase change induced by bottom reflection can generally be represented as a deterministic but unknown quantity.

Now suppose the time delay changes from observation to observation owing to motion of the sonar platform, object of interest, or the ocean itself. The phase difference between two observations (with delays τ_i and τ_j) is then

$$2\pi f_c(\tau_i - \tau_j) = 2\pi f_c \delta_\tau = \pi \left(\frac{c_w \delta_\tau}{\lambda_c / 2} \right) \quad (7.17)$$

where $\delta_\tau = \tau_i - \tau_j$, c_w is the speed of sound and λ_c is a wavelength at f_c so that $c_w \delta_\tau$ is the change in path length between the two observations. Thus, if the path length changes randomly over at least a half wavelength in each direction (e.g., a ± 0.5 -m change at 1500 Hz) between observations, the change in phase will vary over $(-\pi, \pi)$. For this reason it is common to assume the phase difference in active sonar echoes is random from ping to ping or for communications pulses that are separated enough in time for surface motion to alter the path length in an unpredictable manner. When the changes in path length are uniformly random, or large relative to a half wavelength, the phase change can be assumed to be uniformly random on $(-\pi, \pi)$, or equivalently $(0, 2\pi)$.

This example illustrates how, for a single observation along a single path, the phase of the signal measurement is mostly likely unknown but deterministic, whereas a random change in phase can arise from one observation to another when there are random perturbations in path length on the order of a wavelength.

7.2.3.2 Unknown and Random Amplitudes

Suppose the acoustical channel is characterized by a waveguide with a randomly rough surface and bottom and a fixed sound-speed profile. Using a ray-based solution to the wave equation results in a multipath channel with frequency response

$$H(f) = \sum_{i=1}^n A_i e^{-j2\pi f \tau_i + j\phi_i \text{sign}(f)} \quad (7.18)$$

where A_i , τ_i , and ϕ_i are the amplitude, delay, and phase of the i th of n paths. Extracting a linear-phase term to account for bulk travel time allows describing the remainder as

$$H_0(f) = e^{j2\pi f \tau_0} H(f) = \sum_{i=1}^n A_i e^{j\theta_i} \quad (7.19)$$

which is assumed to be constant for $f \in f_c \pm W/2$ when the source signal is narrowband with respect to the channel. The term

$$\theta_i = -2\pi f_c (\tau_i - \tau_0) + \phi_i \quad (7.20)$$

is the net phase (i.e., that not related to the travel time) on the i th path at f_c . How the amplitude and phase are modeled across the n paths dictates how the amplitude of the signal measurement will change relative to that of the source signal (i.e., $|H_0(f_c)|$).

Suppose the roughness of the surface and the bottom is small relative to a wavelength when taking into consideration the grazing angle (i.e., the Rayleigh roughness measure is much less than one). In this scenario, the amplitude and phase on each path will be very similar to that obtained when the surface and bottom are flat and so can be considered deterministic. If the source-signal amplitude is also deterministic, the propagation does not alter this and the measured signal can be represented by the deterministic or non-fluctuating signal model described in Sect. 7.5.1.

If the roughness increases, the disparity of the amplitudes and phases from the flat-surface condition does too. If there are B bottom reflections and S surface reflections for the i th path, then the path amplitude can be approximated by

$$A_i = \frac{\gamma_b^B \gamma_s^S}{(c_w \tau_i)^\rho} \quad (7.21)$$

where $\gamma_b = 10^{\text{BRL}/20}$ and $\gamma_s = 10^{\text{SRL}/20}$ represent the per-reflection reduction in amplitude arising from bottom loss (BRL) and surface loss (SRL), and ρ is the power-law dictating how the path amplitude is related to path length (e.g., $\rho = 1$ for spherical spreading). When the rough surface and bottom alter the i th path, the per-bounce BRL and SRL will change slightly as grazing angles change and the travel time will change as well. However, the relative change in travel time will be small when the range is large. Taken together, while the path amplitudes will be random, they will not vary as significantly as the phase. This can be seen from the form of the phase term in (7.20), which only requires a change in path length on the order of a wavelength for the variation to span $(0, 2\pi)$. The extreme case where the net phase on each path can be modeled as a uniform random variable on $(0, 2\pi)$ and be considered independent from path to path is called a *saturated* phase condition. As shown in [15], this results in $|H(f_c)|$ being a Rayleigh-distributed random variable. This follows from application of the central limit theorem to the sum in (7.19), so $\sum_{i=1}^n A_i e^{j\theta_i}$ is approximately a zero-mean complex-Gaussian random variable. When the source signal has a deterministic amplitude, propagation through such a channel results in a random (i.e., fluctuating) amplitude in the signal measurement.

For the saturated phase condition, the signal measurement can be represented by the Gaussian signal model described in Sect. 7.5.2.

In the intermediate regime where the phase is not completely saturated, the signal measurement will have some part that is deterministic and some part that is random. This *partially saturated* phase condition was considered in [16] by assuming the phase on each path to be Gaussian distributed with different means but a common variance. If the path amplitudes are assumed to be deterministic and the phases independent from path to path, the average of the sum in (7.20) is

$$E \left[\sum_{i=1}^n A_i e^{j\theta_i} \right] = e^{-\sigma_\theta^2/2} \sum_{i=1}^n A_i e^{j\mu_{\theta_i}} \quad (7.22)$$

and its variance is

$$\text{Var} \left\{ \sum_{i=1}^n A_i e^{j\theta_i} \right\} = \left(1 - e^{-\sigma_\theta^2} \right) \sum_{i=1}^n A_i^2 \quad (7.23)$$

where μ_{θ_i} and σ_θ^2 are the mean and variance of the phase on the i th path. Thus, as the phase variance $\sigma_\theta^2 \rightarrow 0$, the variance of the sum tends to zero to produce the deterministic signal previously mentioned. Conversely, increasing the phase variance causes the mean to tend to zero and results in the aforementioned saturated-phase condition. The waveguide scenario with a rough bottom was considered in [17] where the deterministic component was shown to decrease in power relative to the power in the random component as range increased. Clearly, as range increases in a waveguide there are more boundary reflections, which leads to an increase in the travel-time randomness and causes an increase in the single-path phase variance through (7.20). If the sum $\sum_{i=1}^n A_i e^{j\theta_i}$ can be assumed to be complex-Gaussian distributed with a non-zero mean, then the signal measurement can be represented by the Rician signal model developed in [18], applied to sonar in [19], and described here in Sect. 7.5.3. This may not be as precise as the results of [16] when n is small, but still spans the regime between deterministic and fully saturated phase.

When the boundaries off of which a propagating acoustic wave reflects are rough at an appropriate scale, the reflected wave can undergo an occasional focusing [20]. This produces a condition where the fluctuations are more extreme than those observed when the phase is saturated. This implies the need for models with heavier tails than the Gaussian-fluctuating signal model. Such signals can be represented by the gamma-fluctuating-intensity signal described in Sect. 7.5.4.

These examples illustrate how propagation through an acoustical channel can cause a deterministic amplitude in a source signal to be random at the receiver with an envelope that is Rician distributed, Rayleigh distributed, or even heavier-tailed. Randomness in the phase and amplitude on each path or mode, arising from randomness of the channel boundaries and travel time, controls how deterministic or random the amplitude of the signal measurement will be.

7.3 Bandpass and Baseband Representations of Signal and Noise

The signals of interest in underwater acoustical remote sensing are inherently real-valued bandpass signals. That is, their frequency content is limited to some band in frequency and there is no zero-frequency component (i.e., no direct current or “DC” component). The frequency support of such signals can be characterized by their center frequency (f_c) and bandwidth (W) where $W/2$ is required to be less than f_c in order to avoid a DC component. Limitations in bandwidth can arise either in how the signals are generated by the object of interest or from limitations of different components of the sensing system. Although propagation can play a role, it is usually the sensor array and projector (for active systems) that induce the most limitations. A (perhaps dated) rule of thumb from communications theory [21, Sect. 6.1] suggests that the bandwidth be no more than 10% of the center frequency, $W < 0.1 f_c$, to avoid distortion in the electrical components (e.g., amplifiers and antennas). Although it is certainly feasible to construct systems with low distortion and higher bandwidth-to-center-frequency ratios, at some point the cost can become prohibitive.

By restricting consideration to bandpass signals, simplifications in the mathematical representation of the signals, signal processing, and performance analysis can be exploited. The various representations, which are listed in Table 7.4 and presented in Sects. 7.3.1 and 7.3.2, include the analytic signal, complex envelope, envelope, and instantaneous intensity. The analytic signal, which can also be called the pre-envelope [22], is a complex-valued representation of the real-valued signal; it simplifies analysis because sine and cosine functions are represented as a complex exponential. It is also the means by which the complex envelope is formulated. The complex envelope is a lowpass representation of the bandpass signal obtained by removing the effect of the center (or carrier) frequency. Because it retains all

Table 7.4 Various representations of a bandpass signal $s(t)$ where $a(t)$ and $\phi(t)$ are, respectively, its amplitude and phase

Signal representation	Frequency content	Notation and formation
Signal	Bandpass	$s(t) = a(t) \cos(2\pi f_c t + \phi(t))$ $= \text{Real}\{\tilde{s}(t)\}$
Hilbert transform	Bandpass	$s_h(t) = \pi^{-1} \int_{-\infty}^{\infty} s(\tau)/(\tau - t) d\tau$
Analytic signal	Bandpass (positive freq.)	$\hat{s}(t) = s(t) + j s_h(t)$ $= a(t) e^{j2\pi f_c t + j\phi(t)}$ $= \tilde{s}(t) e^{j2\pi f_c t}$
Complex envelope	Lowpass	$\tilde{s}(t) = a(t) e^{j\phi(t)} = e^{-j2\pi f_c t} \hat{s}(t)$ $= 2\text{LPF}\{s(t) e^{-j2\pi f_c t}\}$
Envelope	Lowpass	$A(t) = \tilde{s}(t) = a(t) $
Instantaneous intensity	Lowpass	$I(t) = A^2(t) = \tilde{s}(t) ^2 = a^2(t)$

the information required for inference, detection and estimation algorithms can be derived by starting with a complex-envelope representation of the signal and noise. The signal envelope or instantaneous intensity is often the decision statistic used in detection algorithms. As such, it is important to know their probability density functions (PDFs). The relationship between the complex-envelope PDF and the envelope and instantaneous-intensity PDFs is derived in Sect. 7.3.6.

One of the significant changes in detection and estimation theory over the past several decades is the shift from working solely with analog signals (i.e., continuous-time and continuous-valued) to working with discrete-time (but still continuous-valued) signals. Clearly the shift to discrete-time (and discrete-valued) signals is prevalent in terms of how measurements are processed in most modern systems. However, there has also been a shift in terms of theoretical analysis where detection and estimation algorithms are derived from statistical representations of the discrete-time complex envelope. To enable this, the energy (for deterministic signals) and power spectral density (for random signals) of continuous-time signals are related to the statistical characterization of the discrete-time complex envelope in Sect. 7.3.5.

7.3.1 Analytic Signals

Bandpass signals can be represented mathematically as a cosine at the center frequency (f_c) with a time-varying amplitude $a(t)$ and phase $\phi(t)$,

$$s(t) = a(t) \cos(2\pi f_c t + \phi(t)). \quad (7.24)$$

In communications systems f_c is called a carrier frequency and the message content is encoded in $a(t)$ or $\phi(t)$. In the more general remote-sensing scenario, f_c is simply the center frequency (or a frequency close to it) and $a(t)$ and $\phi(t)$ often encode the state of nature. In order for $s(t)$ to be a bandpass signal, $a(t) \cos \phi(t)$ and $a(t) \sin \phi(t)$ must vary more slowly than $\cos(2\pi f_c t)$; that is, they are considered lowpass signals with respect to the center frequency. An example is shown in Fig. 7.2 where the bandpass signal exhibits very fast oscillations whereas its amplitude and phase change more slowly. The non-linear phase illustrates how the frequency content of the signal changes with time.

A more convenient representation of the bandpass signal in (7.24) can be found by using a complex sinusoidal kernel rather than the cosine in (7.24),

$$\hat{s}(t) = a(t) e^{j2\pi f_c t + j\phi(t)}. \quad (7.25)$$

This complex-valued representation of a real-valued bandpass signal is called the *analytic signal*. The real-valued signal is easily obtained from the analytic signal by taking the real part. The analytic signal is typically easier to work with than the real-valued bandpass signal. For example, recall from (7.11) that the response of a

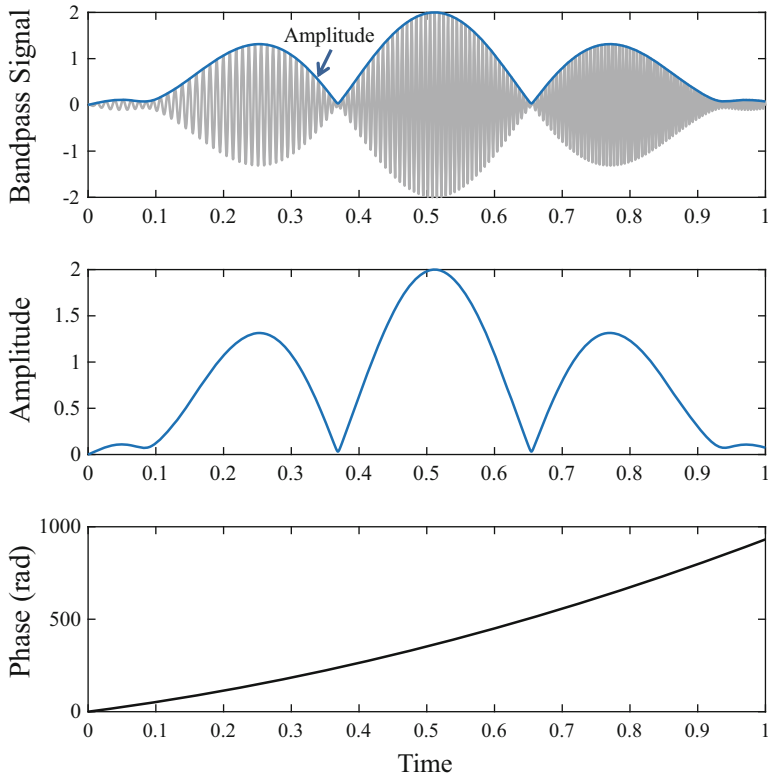


Fig. 7.2 Example of a bandpass signal, its amplitude, and phase

narrowband signal to an LTI system with transfer function $H(f)$ was

$$y(t) \approx |H(f_c)|a(t) \cos(2\pi f_c t + \phi(t) + \angle H(f_c)). \quad (7.26)$$

The analytic signal representation of this input/output relationship is much more compact:

$$\hat{y}(t) \approx H(f_c)\hat{s}(t). \quad (7.27)$$

Although using the cosine-kernel representation in (7.24) produces the real part of (7.27) without much more effort, the analytic-signal approach is quicker and easier, especially for narrowband signals.

The more general formulation of the analytic signal, which is not restricted to bandpass signals, is usually described as a means for removing redundant information from the Fourier transform of a real-valued signal (e.g., see [23, Sect. 3.1]). The Fourier transform of real-valued signals is conjugate symmetric: $S(-f) = S^*(f)$ where $S(f) = \mathcal{F}\{s(t)\}$. Because of this, the signal can be

completely defined from its Fourier transform for positive frequencies, so the negative-frequency information is redundant. The positive-frequency content can be isolated by passing the signal through a filter having frequency response

$$H_a(f) = \begin{cases} 0 & \text{for } f < 0 \\ 1 & \text{for } f = 0 \\ 2 & \text{for } f > 0 \end{cases} = 1 + \text{sign}(f). \quad (7.28)$$

To obtain a time-domain representation of this analytic-signal-producing filter, the Fourier-transform pair

$$h_h(t) = \frac{1}{\pi t} \leftrightarrow -j\text{sign}(f) = H_h(f) \quad (7.29)$$

is used to describe (7.28) as

$$H_a(f) = 1 + j[-j\text{sign}(f)] = 1 + jH_h(f). \quad (7.30)$$

The frequency response function $H_h(f)$ in (7.29) implements the Hilbert transform⁴ and the frequency response of “1” in (7.30) is an ideal all-pass filter with impulse response $\delta(t)$. In the time domain, the analytic signal of $s(t)$ is thus formed according to

$$\dot{s}(t) = s(t) + js_h(t) \quad (7.31)$$

where $s_h(t) = \mathcal{H}\{s(t)\}$ is the Hilbert transform of $s(t)$. That is, the analytic signal is a complex extension of the real-valued signal using its Hilbert transform in the imaginary dimension. In the frequency domain, the Fourier transform of the analytic signal is

$$\dot{S}(f) = H_a(f)S(f) = S(f) - j^2\text{sign}(f)S(f) = \begin{cases} 2S(f) & \text{for } f > 0 \\ S(0) & \text{for } f = 0 \\ 0 & \text{for } f < 0 \end{cases}, \quad (7.32)$$

which has no information for negative frequencies and is twice the signal’s Fourier transform for positive frequencies. The spectral content of $s(t)$ and $\dot{s}(t)$ is shown in the top two Fourier transform illustrations of Fig. 7.3.

⁴As shown in Sect. 4.4 or [24, Ch. 12], the Hilbert transform of $s(t)$ is $s_h(t) = \pi^{-1} \int_{-\infty}^{\infty} s(\tau)/(\tau - t) d\tau$. Note, however, that some texts define the Hilbert transform as the negative of that used here (i.e., with $t - \tau$ in the denominator of the definition rather than $\tau - t$).

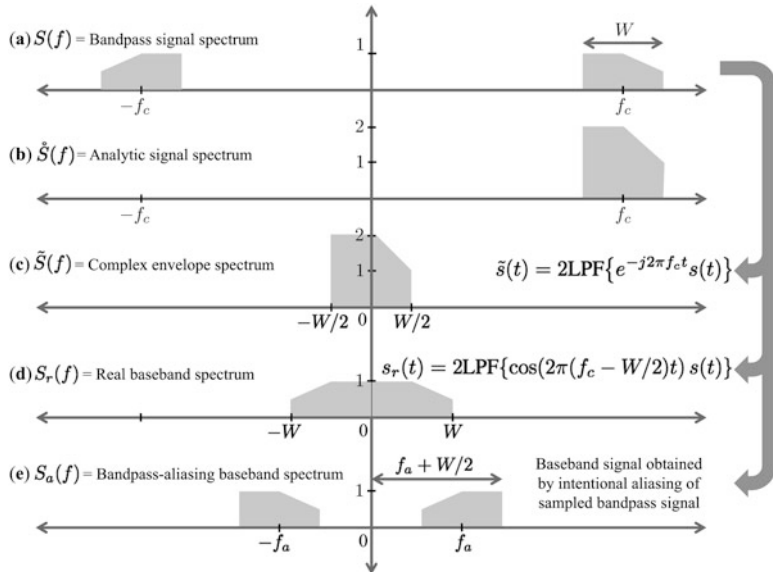


Fig. 7.3 Illustration of the spectral content of (a) a bandpass signal, (b) its analytic signal, (c) complex envelope, (d) real-baseband, and (e) bandpass-aliasing baseband signals. Note that the orientation of the spectral content in (e) depends on the aliasing. It is shown here with negative bandpass frequencies aliasing to positive baseband frequencies

Exercise 7.2 (Hilbert Transform of a Bandpass Signal) For the bandpass signal in (7.24), show that its Hilbert transform is

$$s_h(t) = a(t) \sin(2\pi f_c t + \phi(t)) \quad (7.33)$$

as long as the bandwidth of $\tilde{s}(t) = a(t)e^{j\phi(t)}$ is less than $2f_c$. Hint: write the cosine as a sum of complex exponentials, convert to the frequency domain, and apply (7.29) before taking an inverse Fourier transform. Use (7.33) with (7.24) to obtain the analytic signal of a bandpass signal in (7.25).

7.3.2 Basebanding and the Complex Envelope

It is important to note that the analytic signal $\tilde{s}(t)$ is still a bandpass signal with center frequency f_c and bandwidth W . It only differs from $s(t)$ in that the redundant negative-frequency information has been removed. When sampling the bandpass signal or analytic signal in time, Nyquist's theorem (see Sect. 4.6.1) indicates the sampling rate must be at least twice the highest frequency, $f_s \geq 2f_c + W$. When f_c is large, this can be computationally burdensome with respect to processing power and

storage requirements. When the state of nature is encoded in the signal's amplitude and/or phase, which are lowpass signals with respect to f_c , it is beneficial to remove the effect of the non-informative “carrier” frequency. By examining (7.25) it can be seen that this can be accomplished by demodulating the analytic signal,

$$\tilde{s}(t) = e^{-j2\pi f_c t} \mathring{s}(t) = a(t)e^{j\phi(t)}. \quad (7.34)$$

This process is called *basebanding* because it shifts the bandpass signal's frequency band from being centered at f_c to the “base” frequency band which is a lowpass band centered at zero frequency. The resulting signal $\tilde{s}(t)$ is called the *complex envelope* of $s(t)$. It is a complex lowpass signal with frequency content on the interval $f \in [-W/2, W/2]$. As such, it only needs to be sampled at $f_s \geq W$, which can be significantly less onerous than sampling and processing the bandpass signal. From (7.34), it can be seen that the Fourier transform of $\tilde{s}(t)$ is

$$\mathcal{F}\{\tilde{s}(t)\} = \tilde{S}(f) = \mathring{S}(f - f_c) = \begin{cases} 2S(f + f_c) & \text{for } |f| < \frac{W}{2} \\ 0 & \text{for } |f| \geq \frac{W}{2} \end{cases}. \quad (7.35)$$

Thus, the complex envelope characterizes the positive-frequency content of the signal after shifting it to be centered at zero and scaling by two. An example can be seen in Fig. 7.3c, which also illustrates how the Fourier-transform magnitude of the complex envelope is not necessarily symmetric about zero frequency as it is for real-valued signals.

Example: Complex Envelope of an LFM Transmit Waveform

Consider an LFM transmit waveform with center frequency f_c , bandwidth W , and duration T_p ,

$$s(t) = a(t) \cos\left(2\pi\left[(f_c - W/2)t + \frac{Wt^2}{2T_p}\right]\right), \quad (7.36)$$

where $a(t)$ is a lowpass amplitude weighting that is non-zero only for $t \in [0, T_p]$. When the bandwidth satisfies the bandpass-signal constraint ($W < 2f_c$), the analytic signal is

$$\mathring{s}(t) = a(t) \exp\left\{j\left(2\pi\left[(f_c - W/2)t + \frac{Wt^2}{2T_p}\right]\right)\right\}. \quad (7.37)$$

The complex envelope is then easily obtained by applying the demodulation described in (7.34), resulting in

(continued)

$$\tilde{s}(t) = a(t) \exp\left\{j\left(2\pi\left[-\frac{W}{2}t + \frac{Wt^2}{2T_p}\right]\right)\right\} \quad (7.38)$$

which is an identical LFM waveform (i.e., amplitude $a(t)$, duration T_p , and bandwidth W) except with a center frequency of zero instead of f_c .

Exercise 7.3 (Signal Energy) Show that the energy in the bandpass signal is half of that in its analytic signal or complex envelope,

$$\mathcal{E} = \int_{-\infty}^{\infty} s^2(t) dt = \frac{1}{2} \int_{-\infty}^{\infty} |\dot{s}(t)|^2 dt = \frac{1}{2} \int_{-\infty}^{\infty} |\tilde{s}(t)|^2 dt. \quad (7.39)$$

Hint: use Parseval's theorem from Sect. 4.3.2 with (7.32) and (7.35).

7.3.2.1 Signal Envelope and Instantaneous Intensity

Two quantities derived from the complex envelope are typically of interest in detection algorithms: the signal envelope and its instantaneous intensity. The signal envelope is simply the modulus of the complex envelope,

$$A(t) = |\tilde{s}(t)| = |a(t)|. \quad (7.40)$$

From (7.34), it can also be seen to be the absolute value of the amplitude $a(t)$ of the bandpass signal. In some descriptions of bandpass signals the amplitude $a(t)$ is restricted to be non-negative, in which case $A(t) = a(t)$.

The instantaneous intensity is the square of the signal envelope or the squared modulus of the complex envelope,

$$I(t) = A^2(t) = |\tilde{s}(t)|^2. \quad (7.41)$$

The descriptor *instantaneous* on the intensity is used to distinguish it from the average or peak intensity. Calling (7.41) an intensity carries with it an implicit assumption that $s(t)$ is in units of pressure normalized by the square root of the characteristic impedance so that $I(t)$ has proper units for intensity (e.g., pW/m² for pressure in μ Pa). Because the intensity is obtained as a squared pressure, there is also an assumption that it is an equivalent plane wave intensity (see Sect. 3.2.1.3).

An important distinction between the complex envelope and the envelope or instantaneous intensity arises from the non-linear operation forming the latter two from the former. The non-linear operation implies that the complex envelope is the last point in the signal processing chain where the different components of a measurement can be combined in a linear superposition. That is, although the signal-

plus-noise measurement is the sum of their respective complex-envelope components, it is not the sum of the envelope or instantaneous-intensity components.

7.3.2.2 Different Ways to Baseband a Signal

The approach described in (7.34) to obtain the complex envelope was a demodulation of the analytic signal. Rather than going through the intermediate stage of forming the analytic signal, it is possible to directly create the complex envelope from the bandpass signal. This method starts by demodulating the bandpass signal so the positive-frequency spectral content is centered at zero frequency. Because the demodulation is applied to the original bandpass signal and not the analytic signal, there is negative-frequency spectral content that is shifted to be centered at $-2f_c$. Applying an LPF only retaining frequencies $|f| < W/2$ then produces the complex envelope. For sampled data the LPF also removes the spectra repeated at integer multiples of the sampling frequency and the shifted negative-frequency content centered at $f_s - 2f_c$. If the notation $\text{LPF}\{\cdot\}$ represents the low-pass-filtering operation with unit gain in the passband, basebanding is accomplished using this technique by

$$\tilde{s}(t) = 2 \text{LPF} \left\{ s(t) e^{-j2\pi f_c t} \right\}. \quad (7.42)$$

Some digital processing architectures cannot indigenously perform complex-number arithmetic. For these systems, there are two options. The first is to obtain the “in-phase” and “quadrature” components of the complex envelope. They are, respectively, the real-valued real and imaginary parts of $\tilde{s}(t)$ and obtained by demodulating with $\cos(2\pi f_c t)$ and $\sin(2\pi f_c t)$ in lieu of $e^{j2\pi f_c t}$. The second option is to obtain a real baseband signal by demodulating with a cosine at the lowest frequency in the bandpass signal rather than a complex sinusoid at the center frequency,

$$s_r(t) = 2 \text{LPF} \{ s(t) \cos(2\pi(f_c - W/2)t) \}. \quad (7.43)$$

The result is a real lowpass signal with spectral content in the band $[-W, W]$ so the sampling frequency must be greater than twice the bandwidth, $f_s > 2W$. Although there is redundant negative-frequency content, this approach is essentially equivalent to the complex envelope in terms of computational effort (i.e., sampling a complex signal at W vice a real signal at $2W$). The disadvantage of this method is that it requires an extra step to obtain the signal envelope and $s(t)$ must be bandpass filtered (or minimally high-pass filtered) prior to demodulation to avoid aliasing of out-of-band energy.

In systems where there are significant computational constraints, it is possible to perform a basebanding operation simply by undersampling an analog bandpass signal or decimating an already sampled bandpass signal. This approach, called bandpass sampling [25, Sect. 2.3] relies on aliasing to move the bandpass spectral content to a band at lower frequency. As with the real baseband signal, it is

a real signal and requires an extra step to obtain the signal envelope. It also requires a bandpass filter to be applied before undersampling or decimation so out-of-band spectral content does not fold into and occlude the baseband signal. As described in [25, Sect. 2.4], this technique can cause the negative-frequency spectral content of the bandpass signal to appear as positive-frequency spectral content in the baseband signal (e.g., as depicted in Fig. 7.3e). Care must therefore be taken when creating signal replicas (e.g., for a matched filter) after bandpass sampling.

Exercise 7.4 Determine how to obtain the complex envelope from the real baseband signal $s_r(t)$ in (7.43).

Exercise 7.5 Using a sampling frequency of 5 kHz, generate an LFM waveform via (7.36) with a 100-Hz bandwidth, 2-kHz center frequency, and a Hann-window amplitude over a 1-s duration. Form the complex envelope using (7.42), decimate it by 50, and confirm the Hann-window amplitude is observable in the envelope. Upsample the complex envelope by a factor of 50 and reconstruct the bandpass signal using $s(t) = \text{Real}\{\tilde{s}(t)e^{j2\pi f_c t}\}$. Plot the error between the original and reconstructed bandpass signal. Is it acceptably low? How did you choose the LPF? Did you account for the phase delay of the filter?

7.3.2.3 Basebanding a Signal Subject to Delay and Doppler

Two of the most basic effects imparted on the signal of interest in remote sensing are a time delay from propagation and a Doppler scale from motion. As described in Sect. 2.2.5, the Doppler scale moves the spectral content of a signal, implying the center frequency also moves. Because the Doppler scale is typically unknown, the center frequency would also be unknown and so basebanding is usually performed using the center frequency of the original signal. Thus the measured signal is immediately basebanded and decimated so the remainder of the processing can be performed at the lower baseband sampling rate. The result is not precisely the complex envelope of the signal described in (7.34), but is related. To determine this relationship, suppose the signal measured by a sonar system is a bandpass signal $s(t)$ subjected to a time delay τ_0 and Doppler scale η (see Sect. 2.2.5),

$$x(t) = s(\eta[t - \tau_0]). \quad (7.44)$$

Because $s(t)$ is bandpass, it can be described according to (7.24), and $x(t)$ becomes

$$x(t) = a(\eta[t - \tau_0]) \cos(2\pi f_c \eta(t - \tau_0) + \phi(\eta[t - \tau_0])). \quad (7.45)$$

While $x(t)$ is still a bandpass signal, its center frequency is now ηf_c . If the demodulation frequency is kept at f_c , then the measured signal can be described as

$$x(t) = a_d(t) \cos(2\pi f_c t + \phi_d(t)) \quad (7.46)$$

where

$$a_d(t) = a(\eta[t - \tau_0]) \quad (7.47)$$

and

$$\phi_d(t) = 2\pi f_c[(\eta - 1)t - \eta\tau_0] + \phi(\eta[t - \tau_0]) \quad (7.48)$$

are the amplitude and phase of $x(t)$ accounting for delay and Doppler. Applying the basebanding process described in (7.42)–(7.46) results in

$$\begin{aligned} \tilde{x}_b(t) &= a_d(t) e^{j\phi_d(t)} \\ &= \tilde{s}(\eta[t - \tau_0]) \left[e^{-j2\pi f_c \eta \tau_0} \right] \left[e^{j2\pi f_c (\eta - 1)t} \right] \end{aligned} \quad (7.49)$$

where the notation $\tilde{x}_b(t)$ has been used to distinguish basebanding with the source-waveform carrier frequency (f_c) rather than the center frequency (ηf_c), the latter of which would produce the complex envelope of the measured signal. From (7.49) it can be seen that basebanding a signal subject to delay and Doppler results in the complex envelope of the original signal subject to the same effects and additional multiplicative terms for the bulk delay (first term in brackets) and Doppler (second term in brackets). This can also be seen in the frequency domain by taking the Fourier transform of (7.49),

$$\tilde{X}_b(f) = \frac{1}{|\eta|} e^{-j2\pi(f+f_c)\tau_0} \tilde{S}\left(\frac{f - (\eta - 1)f_c}{\eta}\right). \quad (7.50)$$

For a specific example, suppose $s(t)$ is a CW pulse at frequency f_c with a rectangular window having duration T_p (i.e., $a(t) = \text{rect}([t - T_p/2]/T_p)$ and $\phi(t) = 0$). The Fourier transform of the complex envelope is

$$\tilde{S}(f) = T_p \text{sinc}(f T_p) e^{-j\pi f T_p} \quad (7.51)$$

which leads to

$$\begin{aligned} \tilde{X}_b(f) &= \frac{T_p}{|\eta|} \text{sinc}\left(\frac{T_p}{\eta}[f - (\eta - 1)f_c]\right) \\ &\quad \exp\left\{-j\pi \frac{T_p}{\eta}[f - (\eta - 1)f_c] - j2\pi(f + f_c)\tau_0\right\} \end{aligned}$$

$$\begin{aligned} &\approx \frac{T_p}{|\eta|} \operatorname{sinc}\left(\frac{T_p}{\eta} \left[f - \frac{2v_r f_c}{c_w}\right]\right) \\ &\quad \exp\left\{-j\pi \frac{T_p}{\eta} \left[f - \frac{2v_r f_c}{c_w}\right] - j2\pi(f + f_c)\tau_0\right\} \end{aligned} \quad (7.52)$$

after accounting for delay and Doppler. The approximation in (7.52) arises from using $\eta \approx 1 + 2v_r/c_w$ for two-way propagation in a monostatic active sonar where v_r is the relative radial velocity between the sonar platform and the object of interest. When there is no Doppler ($\eta = 1$ or $v_r = 0$ m/s), the spectral content of the complex envelope (i.e., the sinc function in (7.52)) is centered at zero frequency. Doppler causes this to be centered at $(\eta - 1)f_c \approx 2v_r f_c/c_w$, which is the same offset as encountered by the bandpass signal. If the radial speed of the object of interest is the information required to describe the state of nature under investigation (e.g., is the object stationary or moving), this example illustrates how the information can be obtained after basebanding the signal when a fixed demodulation frequency is employed.

7.3.3 Bandpass Signals and Linear Time-Invariant Systems

Many of the physical processes and signal processing functions encountered in remote sensing can be characterized as linear time-invariant (LTI) systems. It is often advantageous to describe the input/output relationship of the linear system with respect to the analytic signals and complex envelopes. Suppose $y(t)$ is the response to an input $x(t)$ of an LTI system with impulse response $h(t)$. As described in Sect. 4.2, the time-domain representation of the output is a convolution $y(t) = h(t) * x(t)$ between the impulse response and input signal. In the frequency domain, the convolution becomes a product of the Fourier transforms,

$$Y(f) = H(f)X(f). \quad (7.53)$$

Using (7.32), the Fourier transform of the analytic signal of the LTI-system output is

$$\mathring{Y}(f) = H_a(f)Y(f) \quad (7.54)$$

where $H_a(f)$ is as described in (7.28). Using (7.53) in (7.54) immediately leads to an input/output relationship for the analytic signal in the frequency domain of

$$\mathring{Y}(f) = H(f)[H_a(f)X(f)] = H(f)\mathring{X}(f). \quad (7.55)$$

This implies the analytic signal of the LTI system output is the LTI system output of the analytic signal of the input. In the time domain it implies that $\mathring{y}(t)$ is the

convolution between $\dot{x}(t)$ and the impulse response,

$$\dot{y}(t) = h(t) * \dot{x}(t). \quad (7.56)$$

For bandpass signals (i.e., when there is no zero-frequency content so $X(f) = 0$ when $f = 0$), $\dot{Y}(f)$ can be described as

$$\dot{Y}(f) = \frac{1}{2}[H_a(f)H(f)][H_a(f)X(f)] = \frac{1}{2}\dot{H}(f)\dot{X}(f) \quad (7.57)$$

which exploits the fact that $H_a(f) = H_a^2(f)/2$ as long as $f \neq 0$. In the time domain this implies the analytic signal of the LTI system output is half the convolution between the analytic signals of the impulse response and input,

$$\dot{y}(t) = \frac{1}{2}\dot{h}(t) * \dot{x}(t). \quad (7.58)$$

Although this form is less useful than (7.56), it helps define the input/output relationship for complex envelopes. Recall from (7.34) that the complex envelope can be obtained by a demodulation of the analytic signal, $\tilde{y}(t) = e^{-j2\pi f_c t} \dot{y}(t)$, which in the frequency domain is

$$\tilde{Y}(f) = \dot{Y}(f - f_c) = \frac{1}{2}\tilde{H}(f - f_c)\tilde{X}(f - f_c). \quad (7.59)$$

In the time domain this implies the complex envelope of the LTI system output to a bandpass signal is half the convolution between the complex envelopes of the impulse response and input,

$$\tilde{y}(t) = \frac{1}{2}\tilde{h}(t) * \tilde{x}(t). \quad (7.60)$$

7.3.4 Complex Envelope of Bandpass Noise

In underwater acoustic signal processing basebanding is applied to measurements containing both signal and noise. Because noise is generally modeled as a random process, it is important to understand how basebanding affects the statistical characterization of random measurements as well as the deterministic signals considered in Sect. 7.3.2.

Suppose the noise measurement $z(t)$ can be represented as a bandpass wide-sense-stationary (WSS) random process. As described in Sect. 5.4, the autocorrelation function (ACF) of $z(t)$ is $R_{zz}(\tau) = E[z(t + \tau)z(t)]$ and the power spectral density (PSD) is $S_{zz}(f) = \mathcal{F}\{R_{zz}(\tau)\}$, the Fourier transform of the ACF. The bandpass nature of the process dictates that the PSD has frequency content centered

at f_c with bandwidth $W < 2f_c$. If the random process is also ergodic, then the bandpass nature (which requires its temporal average to be zero) implies it has zero mean.

Even though $z(t)$ is random, it can still be described using the bandpass representation in (7.24) and the complex envelope is still formed according to (7.34) or (7.42). Using the latter, the PSD of the complex envelope can be related to that of the bandpass noise. Suppose the complex demodulated signal is $z_d(t) = e^{-j2\pi f_c t} z(t)$. Using the definition of the ACF,⁵ it is straightforward to show that the ACF of $z_d(t)$ is

$$R_{z_d z_d}(\tau) = E[z_d^*(t) z_d(t + \tau)] = e^{-j2\pi f_c \tau} R_{zz}(\tau). \quad (7.61)$$

The PSD of $z_d(t)$ can then be obtained through the Fourier transform of (7.61),

$$S_{z_d z_d}(f) = S_{zz}(f + f_c), \quad (7.62)$$

and seen to be the bandpass-measurement PSD shifted down by f_c . Applying the lowpass filter in (7.42) and multiplying by two completes formation of the complex envelope. Because this is a linear-time-invariant (LTI) operation, the PSD of the filter output is the PSD of the input times the magnitude-squared filter transfer function (see Sect. 5.4.2). Thus, the PSD of the complex envelope is

$$S_{\tilde{z}\tilde{z}}(f) = \begin{cases} 4S_{zz}(f + f_c) & |f| < W/2 \\ 0 & \text{otherwise} \end{cases}. \quad (7.63)$$

The form of the ACF of $z_d(t)$ in (7.61) demonstrates that if $z(t)$ is a wide-sense-stationary (WSS) random process, then $z_d(t)$ will be too, as will $\tilde{z}(t)$. Coupling this with the LTI nature of the remainder of the complex envelope formation implies that if $z(t)$ is a bandpass, WSS, ergodic random process, then $\tilde{z}(t)$ will be a zero-mean, lowpass, WSS, ergodic random process. Using the results of [23, Sect. 3.5], it can also be seen that the real and imaginary parts of $\tilde{z}(t) = u(t) + jv(t)$ satisfy the affine-transformation circularity conditions described in Sect. 5.5 so that $\tilde{z}(t)$ is a *proper* complex random process.⁶

For a WSS random process, the PSD of the complex envelope in (7.63) provides the necessary second-order statistical description. The ACF of the complex envelope can be obtained from (7.63) through an inverse Fourier transform. As shown in [23, Sect. 3.5], it is also possible to relate the ACF of the real and imaginary parts of the complex envelope to the ACFs of the bandpass random process and its Hilbert transform (this is also the information required to show the complex envelope is

⁵Recall from Sect. 5.5 that the ACF for complex WSS random processes is $R_{zz}(\tau) = E[Z^*(t)Z(t + \tau)]$.

⁶Recall from Sect. 5.5 that $R_{\tilde{z}\tilde{z}}(\tau) = 2R_{uu}(\tau) + j2R_{vv}(\tau)$ and $R_{uv}(\tau) = -R_{vu}(-\tau)$ for a WSS proper complex random process.

a proper complex random process). It is also useful to relate the variance of the complex envelope (and its real and imaginary parts) to that of the bandpass random process. Noting that the variance of a zero-mean random process can be found by integrating its PSD over all frequencies, the variance of the complex envelope is seen to be twice that of the bandpass process,

$$\begin{aligned}\text{Var}\{\tilde{z}(t)\} &= \int_{-\infty}^{\infty} S_{\tilde{z}\tilde{z}}(f) df \\ &= 4 \int_{f_c-W/2}^{f_c+W/2} S_{zz}(f) df \\ &= 2 \int_{-\infty}^{\infty} S_{zz}(f) df \\ &= 2\sigma_z^2\end{aligned}\tag{7.64}$$

where $\sigma_z^2 = \text{Var}\{z(t)\}$. Because $\tilde{z}(t)$ is a proper complex random process, the ACFs of its real and imaginary parts are identical and so will be their variances. Using (7.64), this implies the variances of the real and imaginary parts of the complex envelope are the same as for the bandpass measurement,

$$\sigma_u^2 = \sigma_v^2 = \sigma_z^2 = \frac{1}{2}\sigma_{\tilde{z}}^2,\tag{7.65}$$

and half the variance of the complex envelope ($\sigma_{\tilde{z}}^2$).

For a specific example, suppose the bandpass measurement spectrum is white within the frequency band of interest, $f_c \pm W/2$. The PSD, which is defined for both positive and negative frequency, is

$$S_{zz}(f) = \begin{cases} \frac{P_0}{2} & |f| \in (f_c - W/2, f_c + W/2) \\ 0 & \text{otherwise} \end{cases}\tag{7.66}$$

with units $\mu\text{Pa}^2/\text{Hz}$. The variance of $z(t)$, which is also its average power,⁷ is easily seen to be $\sigma_z^2 = P_0 W$ by integrating (7.66). From (7.63) the PSD of the complex envelope for bandpass white noise is then

$$S_{\tilde{z}\tilde{z}}(f) = \begin{cases} 2P_0 & |f| < W/2 \\ 0 & \text{otherwise} \end{cases}.\tag{7.67}$$

As expected, integrating (7.67) results in $\sigma_{\tilde{z}}^2 = 2W P_0 = 2\sigma_z^2$ for the variance of the complex envelope. Applying an inverse Fourier transform to the complex-envelope

⁷Ergodicity in a WSS bandpass process with no zero-frequency content implies the ensemble mean is zero and that the temporally averaged power equals the variance.

PSD in (7.67) yields the ACF

$$R_{\tilde{z}\tilde{z}}(\tau) = 2P_0W\text{sinc}(W\tau). \quad (7.68)$$

The utility of this particular result arises when the complex envelope is sampled with sampling frequency $f_s = W$. From Nyquist's theorem (see Sect. 4.6.1), this is the minimum sampling frequency required to avoid aliasing (the highest frequency is $W/2$) and so it allows reconstruction of the continuous-time signal. The correlation between the n th sample $\tilde{z}(nT_s)$ and the m th sample $\tilde{z}(mT_s)$ is

$$\begin{aligned} E[\tilde{z}(nT_s)\tilde{z}^*(mT_s)] &= R_{\tilde{z}\tilde{z}}([n-m]T_s) \\ &= 2P_0W\text{sinc}(n-m) \\ &= 2P_0W\delta[n-m] \end{aligned} \quad (7.69)$$

where $T_s = 1/W$ and $\delta[n]$ is the Kronecker delta function returning one when the argument is zero and is otherwise zero. Thus, sampling the complex envelope of a white, bandpass, WSS, ergodic random process with a sampling rate equal to the bandwidth produces a sequence of uncorrelated random variables.

The results presented so far have only required the bandpass process to be WSS and ergodic (e.g., (7.63) and (7.64)) or additionally have a white bandpass spectrum (e.g., (7.69)). If the random process is further assumed to be Gaussian, then the linearity of the complex-envelope formation (which is easily seen from (7.42)) implies the complex envelope will be complex-Gaussian distributed. Because the complex envelope satisfies the conditions of a proper complex distribution under affine transformations, the correlation between its time-coincident real and imaginary parts is zero because their cross-covariance function is an odd function of delay so $R_{uv}(0) = 0$. When the complex envelope is Gaussian distributed, this zero correlation implies the time-coincident real and imaginary parts of the complex envelope are not only uncorrelated, but also statistically independent. If the Gaussian random process has a white bandpass spectrum, the independence extends to be between all temporal samples when $f_s = W$ because of the zero correlation observed in (7.69). This greatly simplifies the derivation of detection and estimation algorithms and theoretical analysis of their performance. In practice, however, it is common to sample at a higher rate (e.g., two or three times the minimum), which produces a sequence of correlated (and statistically dependent) samples. It is therefore very important to ensure any algorithms developed under the assumption of independent data samples are appropriately modified prior to applying the algorithms to such “over-sampled” data.

Exercise 7.6 Show that the real and imaginary parts of the complex envelope of a bandpass Gaussian random process are uncorrelated when taken at the same time (i.e., that $E[u(t)v(t)] = 0$ if $\tilde{z}(t) = u(t) + jv(t)$). Hint: exploit the properties of a proper complex random process for affine transformations as described in Sect. 5.5.

7.3.5 Modeling the Complex Envelope After Sampling in Time

Historically, detection performance modeling was carried out through the processing and analysis of analog signals [26]. An important quantity in characterizing an analog signal is the energy measured over an analysis window of length T_p . Signal energy together with the average noise power dictates detection performance. In order to extend analog performance modeling to the more tractable discrete-time statistical modeling, the pertinent analog signal and noise characterizations need to be related to equivalent ones for the sampled complex envelope. The relationships derived here are used in Chaps. 8 and 9 to obtain the SNR in the bandpass measurement required to achieve a detection performance specification (i.e., the detection threshold term in the sonar equation) for various signal types and detectors.

Sampling the complex envelope with period $T_s = 1/f_s$ results in the random variables

$$Z_{i+1} = \tilde{z}(t_0 + iT_s) = a(t_0 + iT_s) e^{j\phi(t_0 + iT_s)} \quad (7.70)$$

for $i = 0, \dots, N - 1$ where t_0 is the initial time considered for analysis. Over a window of length T_p there are $N = T_p/T_s = T_p f_s$ samples. To facilitate matrix–vector notation, place the data samples under consideration into a vector $\mathbf{z} = [Z_1 \cdots Z_N]^T$.

As indicated in Sect. 7.3.4, performance analysis is significantly simpler when the sampling rate of the complex envelope is at the Nyquist rate (i.e., $f_s = W$). In the following characterizations of signal and noise, the general case is derived and then the Nyquist sampling scenario is described as a special case. For example, at Nyquist sampling $N = T_p W$, which is known as the processing time-bandwidth product and can represent the gain achieved by coherent processing of the signal.

7.3.5.1 Deterministic Signal Energy

The most pertinent deterministic-signal characteristic in performance modeling is the energy in the bandpass signal $z(t)$. Using the bandpass description of (7.24) and starting at time t_0 , the energy in the analysis window is

$$\begin{aligned} \mathcal{E} &= \int_{t_0}^{t_0+T_p} z^2(t) dt \\ &= \int_{t_0}^{t_0+T_p} a^2(t) \cos^2(2\pi f_c t + \phi(t)) dt \\ &\approx \frac{1}{2} \int_{t_0}^{t_0+T_p} a^2(t) dt \end{aligned} \quad (7.71)$$

where the approximation is valid when T_p is large relative to $1/f_c$. The bandpass signal energy can be related to the sampled complex envelope by using a Riemann-sum approximation to the integral in (7.71), resulting in

$$\begin{aligned}\mathcal{E} &\approx \frac{T_s}{2} \sum_{i=0}^{N-1} a^2(t_0 + iT_s) \\ &= \frac{1}{2f_s} \sum_{i=1}^N |Z_i|^2 = \frac{\mathbf{z}^H \mathbf{z}}{2f_s}.\end{aligned}\quad (7.72)$$

In many of the detectors described in Part III, detection performance depends on the vector inner product of \mathbf{z} with itself,

$$\mathbf{z}^H \mathbf{z} = 2\mathcal{E} f_s = \frac{2\mathcal{E}}{T_p} N. \quad (7.73)$$

For Nyquist sampling it is simply $\mathbf{z}^H \mathbf{z} = 2\mathcal{E}W$. However, it is important to note that the factor W (or f_s and N in (7.73)) is simply a multiplicative factor related to sampling rate and does not imply a change in detection performance because the noise power is scaled similarly (i.e., increasing the sampling rate does not in general have a significant effect on the signal-to-noise power ratio).

7.3.5.2 Noise Covariance Matrix

From Sect. 7.3.4, sampling signal or noise measurements represented by bandpass, WSS, ergodic Gaussian random processes results in complex-envelope data Z_1, \dots, Z_N that are identically complex-Gaussian distributed with zero mean and variance $2\sigma_z^2$ where σ_z^2 is the average power in the bandpass process. The vector⁸ \mathbf{z} is therefore complex-multi-variate-Gaussian-distributed (see Sect. 5.6.9) with zero mean (the vector $\mathbf{0}$) and a covariance matrix Σ ,

$$\mathbf{z} \sim \mathcal{CN}(\mathbf{0}, \Sigma). \quad (7.74)$$

The (i, j) element of the covariance matrix is formed from the ACF of the complex envelope,

$$\{\Sigma\}_{i,j} = R_{\tilde{z}\tilde{z}}\left(\frac{i-j}{f_s}\right) \quad (7.75)$$

⁸Recall from the discussion in Sect. 5.3.6 that matrix–vector notation representing a vector as a lower-case bold letter (e.g., \mathbf{x}) takes precedence over the mathematical-statistics notation of random variables taking an upper case letter and its observed value the lower case. Whether $\mathbf{x} = [X_1 \dots X_n]^T$ or $\mathbf{x} = [x_1 \dots x_n]^T$ must be discerned from context.

for i and $j = 1, \dots, N$. The diagonal elements are the variance, $\sigma_z^2 = \{\boldsymbol{\Sigma}\}_{i,i} = R_{zz}(0) = 2\sigma_z^2$.

When the random process has a white bandpass spectrum with PSD $N_0/2$ and the complex envelope is sampled at the Nyquist rate ($f_s = W$), the samples are independent (see (7.69)) so $\boldsymbol{\Sigma} = 2\sigma_z^2 \mathbf{I}$ where \mathbf{I} is the identity matrix and the variance of each sample is $\lambda_z = \sigma_z^2 = 2N_0 W$. The sampled complex envelope then has distribution

$$\mathbf{z} \sim \mathcal{CN}(\mathbf{0}, 2N_0 W \mathbf{I}). \quad (7.76)$$

The simplicity of this representation allows facile derivation and analysis of detection and estimation algorithms.

Example: Perfectly Known Signal in Gaussian Noise

Consider the case of a perfectly known signal to be detected in white, bandpass, WSS, ergodic, Gaussian noise with spectral density $N_0/2$ for $|f| \in (f_c - W/2, f_c + W/2)$ and zero elsewhere. A more detailed consideration of this scenario may be found in Sect. 8.2.2. Let the Nyquist-rate-sampled complex envelope vector of the measured signal be

$$\mathbf{x} = \mathbf{s} + \mathbf{v} \quad (7.77)$$

where \mathbf{s} represents the deterministic signal and \mathbf{v} the random noise. Using (7.76) in conjunction with the known signal yields a sampled complex-envelope vector that follows a multivariate, complex-Gaussian distribution,

$$\mathbf{x} \sim \mathcal{CN}(\mathbf{s}, \lambda_0 \mathbf{I}), \quad (7.78)$$

with mean \mathbf{s} and covariance matrix $\lambda_0 \mathbf{I}$ where $\lambda_0 = 2N_0 W$.

As shown in Sect. 8.2.2, this scenario calls for a *coherent-matched-filter* detector, for which the detector decision statistic is

$$T = \text{Real}\left\{ \mathbf{s}^H \mathbf{x} \right\} \quad (7.79)$$

where $\text{Real}\{\cdot\}$ represents the real part of the argument. The detection statistic T is a (real) Gaussian-distributed random variable with mean $E_1[T] = \mathbf{s}^H \mathbf{s}$ when signal is present and $E_0[T] = 0$ for the noise-only case. The variance in both situations is $\text{Var}[T] = \mathbf{s}^H \mathbf{s} \lambda_0 / 2$ and so the detection index [26] or [5, Sect. 12.2] can be used to describe the performance. For the coherent matched filter applied to a deterministic signal (i.e., the amplitude is constant and the

(continued)

phase is known), the detection index

$$\begin{aligned} d &= \frac{(E_1[T] - E_0[T])^2}{\text{Var}[T]} \\ &= \frac{2(\mathbf{s}^H \mathbf{s})^2}{\mathbf{s}^H \mathbf{s} \lambda_0} = \frac{2\mathcal{E}}{N_0}, \end{aligned} \quad (7.80)$$

is the familiar $2\mathcal{E}/N_0$ from [26]. This example illustrates how analog statistical characterizations of a bandpass signal and noise can be carried through to a statistical characterization of the sampled complex envelope and used in detection performance analysis.

7.3.6 Statistics of the Complex Envelope, Envelope, and Instantaneous Intensity

When the envelope or instantaneous intensity of a signal is the decision statistic of a detector (as it is for the quadrature matched filter derived in Sect. 8.2.3), the probabilities of false alarm and detection require the evaluation of their cumulative distribution functions (CDFs). The first step in obtaining the CDFs is to obtain the envelope and instantaneous-intensity PDFs from the PDF of the complex envelope. By its nature, the PDF of the complex envelope is a joint PDF over the real and imaginary parts (see Sect. 5.5 for more about complex random variables). Suppose the PDF of a single complex-envelope sample $Z = U + jV$ is $f_Z(z) = f_{U,V}(u, v)$ where U and V are, respectively, the real and imaginary parts of Z . The PDF of the envelope $A = |Z|$ can be obtained by first transforming the joint PDF of U and V to an amplitude (A) and phase (θ) representation followed by integration over the phase (i.e., marginalization). The two pairs of random variables are related by the polar-to-Cartesian coordinate transformation,

$$\begin{aligned} U &= A \cos \theta \\ V &= A \sin \theta \end{aligned} \quad (7.81)$$

which has a Jacobian of $du dv = a da d\theta$. The joint PDF of A and θ is then

$$f_{A,\theta}(a, \theta) = af_{U,V}(a \cos \theta, a \sin \theta) \quad (7.82)$$

$$= af_Z(ae^{j\theta}) \quad (7.83)$$

for $a \geq 0$ and $\theta \in [0, 2\pi)$. The envelope PDF is then obtained by marginalizing over θ ,

$$f_A(a) = \int_0^{2\pi} f_{A,\theta}(a, \theta) d\theta \quad (7.84)$$

$$= a \int_0^{2\pi} f_Z(a e^{j\theta}) d\theta. \quad (7.85)$$

Because the instantaneous intensity is simply the square of the envelope ($I = A^2$) its PDF

$$f_I(\zeta) = \frac{1}{2\sqrt{\zeta}} f_A(\sqrt{\zeta}) \quad (7.86)$$

$$= \frac{1}{2} \int_0^{2\pi} f_Z(\sqrt{\zeta} e^{j\theta}) d\theta \quad (7.87)$$

can be found using the approach for one-to-one mappings described in Sect. 5.3.3. The variable ζ (zeta) is used to represent the instantaneous intensity in equations (outside of the subscripting) rather than I or i to avoid confusion with other common uses.

In the inverse direction, when starting with the distribution of the instantaneous intensity, the envelope distribution is also easily obtained by rewriting (7.86),

$$f_A(a) = 2a f_I(a^2). \quad (7.88)$$

However, it is generally not possible to describe the distribution of the complex envelope from the envelope or instantaneous-intensity distributions without some knowledge about how the phase is distributed.

7.3.6.1 Uniformly Random Phase

Suppose now that the complex-envelope PDF $f_Z(z)$ does not depend on the phase of z ; that is $f_Z(ae^{j\theta}) = f_Z(a)$. In the two-dimensional PDF of the real and imaginary parts of Z , this is represented as a constant at all angles for a given distance from the origin; that is, only a dependence on $a = \sqrt{u^2 + v^2}$. This is a type of circular symmetry that differs from the one described in Sect. 5.5 for complex random variables with proper PDFs under affine transformations. This type of symmetry results in a uniformly random phase on $[0, 2\pi)$. This can be seen by noting that the joint PDF of A and θ in (7.83) for this condition is separable into the product of the marginal PDFs

$$f_{A,\theta}(a, \theta) = [2\pi a f_Z(a)] \left[\frac{1}{2\pi} \right] = f_A(a) f_\theta(\theta) \quad (7.89)$$

where

$$f_A(a) = 2\pi a f_Z(a) \quad (7.90)$$

and $f_\theta(\theta) = 1/(2\pi)$ for $\theta \in [0, 2\pi]$. Thus, when the complex envelope has uniformly random phase, the envelope PDF is easily obtained by evaluating the complex-envelope PDF at $z = a$ and multiplying by $2\pi a$ as shown in (7.90). The PDF of the instantaneous intensity requires a similarly simple evaluation of the complex-envelope PDF,

$$f_I(\zeta) = \pi f_Z(\sqrt{\zeta}). \quad (7.91)$$

When starting with the envelope or instantaneous intensity, (7.90) and (7.91) can be rearranged under the assumption of uniformly random phase to provide the complex-envelope PDF as

$$f_Z(z) = \frac{1}{2\pi|z|} f_A(|z|) = \frac{1}{\pi} f_I(|z|^2). \quad (7.92)$$

As an example, suppose the original bandpass measurement is a WSS and ergodic Gaussian random process so a complex-envelope sample is a zero-mean complex-Gaussian random variable with variance λ_z . Its PDF,

$$f_Z(z) = \frac{1}{\pi\lambda_z} e^{-|z|^2/\lambda_z} \quad (7.93)$$

clearly does not depend on the phase of the argument so the random process has uniformly random phase. Using (7.90), the envelope PDF is then seen to be

$$f_A(a) = \frac{2a}{\lambda_z} e^{-a^2/\lambda_z} \quad \text{for } a \geq 0, \quad (7.94)$$

which is the Rayleigh distribution with power λ_z (e.g., see Sect. 5.6.12). Similarly, the instantaneous-intensity PDF is found through (7.91) to be

$$f_I(\zeta) = \frac{1}{\lambda_z} e^{-\zeta/\lambda_z} \quad \text{for } \zeta \geq 0, \quad (7.95)$$

which is an exponential distribution with mean λ_z (e.g., see Sect. 5.6.10).

This example illustrates how a zero-mean-Gaussian-distributed complex envelope leads to a Rayleigh-distributed envelope and an exponentially distributed instantaneous intensity. The relationship between the envelope and instantaneous

intensity is a one-to-one mapping and so the latter has an exponential PDF if and only if the envelope is Rayleigh distributed. As previously noted, the mapping from the complex envelope to the envelope is not one-to-one, implying a zero-mean-Gaussian distributed complex envelope may not be the only way to produce a Rayleigh-distributed envelope.⁹ When defining an envelope or instantaneous-intensity PDF, the uniform-random-phase assumption is usually made to allow using (7.92) to obtain $f_Z(z)$. However, not all proper complex distributions will have uniformly random phase. For example, simply shifting the zero-mean complex Gaussian to be centered away from the origin will have this effect, resulting in a phase distribution peaking at the angle of the mean. This particular scenario represents a deterministic signal with a constant phase in Gaussian noise and leads to a Rician-distributed envelope as will be described in Sect. 7.5.1.

It is common to describe a probability distribution for just one of the three variables of interest (complex envelope, envelope, or instantaneous intensity) and assume the others follow accordingly. Rather than referring to the distributions at each stage as a “family,” for which there already exists a connotation within statistics, the set of distributions for the complex envelope, envelope, and instantaneous intensity will be referred to as a distribution “chain.” For example, the Rayleigh distribution chain implies a zero-mean complex-Gaussian distributed complex envelope, a Rayleigh-distributed envelope, and an exponentially distributed instantaneous intensity.

Definition: A distribution “chain” is defined as the set of distributions linked by the formation of the envelope and instantaneous intensity from the complex envelope. The *Rayleigh distribution chain* implies a zero-mean complex-Gaussian distributed complex envelope, a Rayleigh-distributed envelope, and an exponentially distributed instantaneous intensity. The most common name will be used to define the chain (e.g., a Rayleigh or Rician distribution chain) or specified if there is potential for confusion (e.g., a gamma-fluctuating-intensity distribution chain implies the instantaneous intensity is gamma distributed).

7.4 Noise and Interference Models

In the analysis presented in this book there is a general assumption that the noise and interference signals encountered in underwater acoustics can be represented as WSS and ergodic random processes, at least for the short periods of time over which detection or estimation occurs. In most cases they will be assumed to be Gaussian

⁹A trivial example of this can be found by letting $\theta \sim \text{Unif}(0, 4\pi)$.

distributed and so are completely specified by either an ACF or a PSD. For the two primary noise and interference sources, ambient noise and reverberation, this is often an accurate assumption, although reverberation needs to be normalized to have a constant average power as will be described in Sect. 7.4.2.1. However, there are scenarios where real data exhibit non-Gaussian behavior. In particular, heavier-tailed distributions can be encountered where a larger than expected proportion of louder sounds are measured or when multiple disparate processes contribute to the noise.

The analysis of non-Gaussian noise is generally performed only after formation of the envelope or instantaneous intensity. This is partly because of the difficulty in analyzing non-Gaussian random processes and partly owing to the effect they have on detection performance (i.e., heavy-tailed non-Gaussian noise tends to increase the probability of false alarm). Noting that the envelope of a bandpass Gaussian random process is Rayleigh distributed (see Sect. 7.3.6), non-Gaussian noise may also be described as non-Rayleigh. Non-Rayleigh reverberation is commonly called “clutter” in the active sonar research community. This terminology differs from that in the radar community where “clutter” represents diffuse reverberation and heavy-tailed reverberation is usually described as a “clutter-discrete.”

This section presents basic information about ambient noise in Sect. 7.4.1, characterizes reverberation as a random process in Sect. 7.4.2, and introduces a variety of heavy-tailed distributions useful in representing active sonar clutter and non-Gaussian ambient noise in Sect. 7.4.3.

7.4.1 Ambient Noise

Ambient noise arises from a variety of different mechanisms in or near the ocean. For most sonar systems, it overwhelms any electronic noise induced by the measurement equipment. The cacophony of sounds audible in any given location, described as a *soundscape* [27], has enough variability in the different signal characterization dimensions that it precludes representation by a single or even a small set of models.

In terms of spectral character, some sources of noise are narrowband (e.g., radiated noise from a nearby ship or machinery noise from an oil-drilling platform) or broadband (e.g., airguns used for oil exploration, distant shipping, or wind-generated noise). As described in Sect. 3.3 through the Wenz curves [28], the PSD of broadband ambient noise is frequency dependent with different mechanisms dominating different frequency regimes. However, the bandwidth of many signals of interest is small enough that the PSD can be assumed constant over the signal band, which allows using the simplified description of the sampled complex envelope presented in Sect. 7.3.5. When it is not, the noise PSD needs to be included in its characterization and will affect derivation of an optimal detector.

The temporal character of ambient noise is as varied as the frequency content. Noise sources with very short temporal support include clicks or impulsive sounds

from marine fauna (e.g., sperm whales, dolphin, or snapping shrimp), ice cracks that are sharp but intermittent, and airgun blasts (< 0.1 s) that can be repeated as often as 4–6 times per minute [27]. An example spectrogram of airgun blasts measured¹⁰ at the CTBTO IMS hydrophone station off the Crozet Islands, France, is shown in Fig. 7.4. The decay of the spectrum with frequency and the extended temporal extent of the pulses illustrates how the effects of propagation must be accounted for when using a remote signal measurement to characterize a source signal. At the other extreme of the temporal-duration scale is the perpetual drone of distant shipping, wind-generated noise, or noise from persistent anthropogenic activities. Interestingly, the lower-level, longer-duration signals seen in the 18–50 Hz band in Fig. 7.4 are likely from a number of distant whales (blue and/or fin) each emitting sequences of pulses. Sources with an intermediate duration include other types of sound emissions from marine mammals and ephemeral anthropogenic interferences such as active sonar systems and nearby shipping.

From a statistical perspective, the central limit theorem (CLT; see Sect. 5.3.7) dictates that ambient noise will be approximately Gaussian distributed if it can be characterized as the linear superposition of many independent sources. Numerous analyses of experimental data [30, 31] support this model (although not ubiquitously) and confirm stationarity over short periods of time (e.g., 3 min was cited in [30]). However, a common scenario is for a long-duration noise source (e.g., distant shipping or wind-generated noise) to be temporarily dominated by a disparate mechanism. Examples of the latter include nearby shipping, movement of ice in the arctic, sound emissions of marine fauna, airguns, and even earthquakes [27, 32–36]. Such a combination of multiple mechanisms inherently produces non-Gaussian distributions and is naturally represented by mixture models, which are described in Sect. 7.4.3.7. An alternative can be found in Middleton's Class-A noise model [37], which was derived to represent a Gaussian measurement corrupted by impulsive noise with bandwidth not exceeding that of the sensor. The Class-A noise model was shown to represent ocean ambient noise dominated by snapping shrimp in [38] (as well as surface and bottom reverberation). As described in Sect. 7.4.3.4, the Class-A noise model is a Poisson-weighted mixture of bandpass Gaussian components leading to the Poisson-Rayleigh envelope distribution chain.

In theory, the parameters of both the multiple-mechanism mixture models and the Class-A noise model can be derived from physical characteristics of the noise sources. However, they are often used in a phenomenological manner by estimating the parameters from data. This approach has merit in that it restricts consideration to physically viable conditions. However, the generality of the models can weaken any inference made about the noise sources through the parameter estimates. Also in the category of phenomenological representation of noise distributions is the use of generalizations of standard distributions. For example, a generalized Gaussian distribution [39, Sect. 3.2.1] was shown to represent ambient noise arising from

¹⁰Acknowledgement: CTBTO [29] with gratitude to Drs. G. Haralabus, M. Zampolli, P. Nielsen, and A. Brouwer for their assistance in identifying, accessing, and interpreting the data.

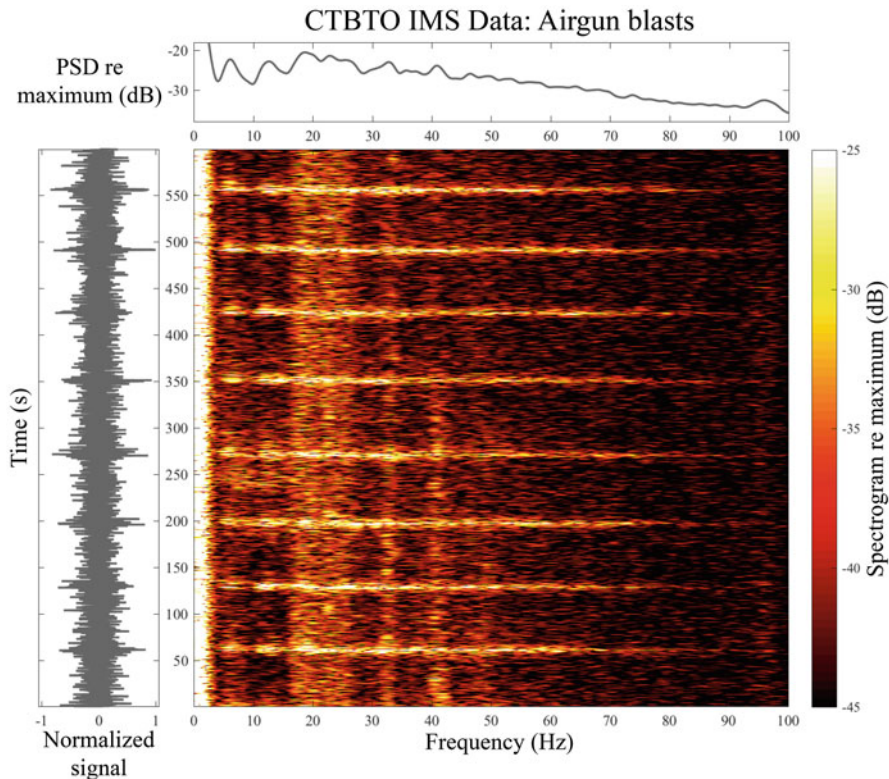


Fig. 7.4 Airgun blasts measured on May 14, 2017 at the CTBTO IMS hydrophone station off the Crozet Islands, France. Acknowledgement: CTBTO [29]

both seismic exploration and merchant ships in [40]. A key point made in [40] was how linear filtering can alter the single-sample distribution. When the filtering sums multiple independent samples, the central limit theorem (CLT) indicates a trend toward the Gaussian distribution. However, when the temporal structure of the noise does not support this, the filtering can make the distribution heavier tailed (e.g., as occurred for the noise arising from seismic exploration). One of the difficulties in working with generalized distributions is carrying the characterization through the distribution chain (i.e., from a bandpass representation to a complex envelope, envelope or instantaneous intensity). For example, it is not clear what a generalized-Gaussian-distributed bandpass signal produces at the envelope or instantaneous intensity without understanding how the phase is distributed. An alternative in the phenomenological approach is to use generalizations of distributions appropriate for an envelope or instantaneous intensity such as the generalized gamma [41, Sect. 8.7] or Weibull distributions (see Sects. 5.6.18 or 7.4.3).

7.4.2 Reverberation

Active remote sensing systems are often limited by backscattering of the projected pulse (i.e., reverberation) rather than ambient noise. Based on the preliminary analysis of reverberation presented in Sect. 3.5, it can be assessed that reverberation is zero-mean Gaussian distributed when it is formed from a large number of elemental scatterers, has a time-varying power level, and spectral character similar to that of the projected pulse. In this section, the objective is to work toward a description of reverberation as a WSS and ergodic Gaussian random process so the tools developed in Sect. 7.3 can be applied to the development and analysis of detection and estimation algorithms for active systems in the presence of reverberation. The key references for characterizing reverberation as a random process are [42, 43].

7.4.2.1 Reverberation as a Random Process

Suppose $r(t)$ is the reverberation measurement formed by a sum over a large number (n_e) of elemental scatterers,

$$r(t) = \sum_{i=1}^{n_e} \frac{A_i}{r_i^2} p_o(\eta_i t - \eta_i \tau_i) \quad (7.96)$$

where r_i , τ_i , η_i , and A_i are, respectively, the range, time delay, Doppler scale, and scattered amplitude of the i th elemental scatterer, and $p_o(t)$ is the projected pulse having duration T_p . The randomness inherent in reverberation arises from randomness in the characterization of each elemental scatterer (e.g., A_i and η_i) as well as its location (r_i and τ_i). Although these can be used to characterize reverberation as a random process, it is not WSS owing to the time-varying average power, nor is it necessarily ergodic.

In order to treat $r(t)$ as a WSS random process, the first two moments must be constant and the ACF must only depend on delay. Because $r(t)$ already has a constant mean (=zero), the second moment can be made constant by dividing $r(t)$ by its time-dependent standard deviation ($\sigma_r(t) = \sqrt{E[r^2(t)]}$) to form the normalized random process

$$z(t) = \frac{r(t)}{\sigma_r(t)}. \quad (7.97)$$

Before deriving the ACF of this random process, which will be shown to only depend on delay, it is useful to discuss when $z(t)$ might be ergodic. Ergodicity requires the temporal averages of a random process to be equivalent to its ensemble averages. Reverberation will violate this when the statistical distribution of $r(t)$

depends on the number of elemental scatterers contributing as this changes with time. However, when that number is always a very large number, the CLT dictates that the distribution is approximately Gaussian and therefore only dependent on the variance $\sigma_r^2(t)$. When this happens, the normalization in (7.97) is enough to make the resulting random process both WSS and ergodic.

7.4.2.2 Reverberation Autocorrelation Function

The ACF of the normalized reverberation time series $z(t)$ from (7.97) is

$$\begin{aligned} R_{zz}(\tau) &= E[z(t + \tau)z(t)] \\ &= \frac{1}{\sigma_r(t + \tau)\sigma_r(t)} \sum_{i=1}^{n_e} \sum_{j=1}^{n_e} E \left[\frac{A_i A_j}{r_i^2 r_j^2} p_o(\eta_i t + \eta_i \tau - \eta_i \tau_i) p_o(\eta_j t - \eta_j \tau_j) \right] \end{aligned} \quad (7.98)$$

$$= \frac{1}{\sigma_r(t + \tau)\sigma_r(t)} \sum_{i=1}^{n_e} E \left[\frac{A_i^2}{r_i^4} p_o(\eta_i t + \eta_i \tau - \eta_i \tau_i) p_o(\eta_i t - \eta_i \tau_i) \right] \quad (7.99)$$

where the expectation is over the set of triplets (A_i, τ_i, η_i) for $i = 1, \dots, n_e$. The simplification of the double summation in (7.98) to a single summation in (7.99) requires assuming the elemental scatterers are statistically independent and identically distributed and exploits the fact that reverberation is zero mean. The components of each triplet (A_i, τ_i, η_i) are also assumed to be statistically independent.

The normalization process accounts for the number of scatterers contributing, the average scattered power ($E[A_i^2]$), and the effects of propagation. The ACF of the normalized reverberation in (7.99) then simplifies to being proportional to

$$R_{zz}(\tau) \propto E[p_o(\eta_e t + \eta_e \tau - \eta_e \tau_e) p_o(\eta_e t - \eta_e \tau_e)] \quad (7.100)$$

where the expectation is over the delay (τ_e) and Doppler scale (η_e) of just one elemental scatterer. Assuming the scatterers are distributed uniformly in range, τ_e can be assumed to have a uniform distribution on $(0, T)$ where T is large relative to the pulse duration (T_p), t , and $|\tau|$. By assuming the time t and delay τ are such that there are no edge effects (i.e., the arguments of $p_o(\cdot)$ in (7.100) are not near 0 or T), the normalized-reverberation ACF can be simplified to an expectation over just the random Doppler scale,

$$R_{zz}(\tau) \propto E \left[\frac{1}{T} \int_0^T p_o(\eta_e t + \eta_e \tau - \eta_e \tau_e) p_o(\eta_e t - \eta_e \tau_e) d\tau_e \right]$$

$$\begin{aligned}
&= E \left[\frac{1}{T\eta_e} \int_{\eta_e(t-T)}^{\eta_e t} p_o(s + \eta_e \tau) p_o(s) ds \right] \\
&\propto E \left[\eta_e^{-1} \chi_p(\eta_e \tau) \right] = \int_{-\infty}^{\infty} \eta^{-1} \chi_p(\eta \tau) f_{\eta}(\eta) d\eta
\end{aligned} \tag{7.101}$$

where $\chi_p(\tau)$ is the ACF of the pulse,

$$\chi_p(\tau) = \int_{-\infty}^{\infty} p_o(t + \tau) p_o(t) dt \tag{7.102}$$

and $f_{\eta}(\eta)$ is the PDF of the Doppler scale of an elemental scatterer. Note that the ACF is now only a function of the delay τ and so the normalized reverberation process is wide-sense-stationary.

The normalization in (7.97) implies $R_{zz}(0) = 1$. From (7.101) it can be seen that this simply requires dividing by $\chi_p(0)E[\eta_e^{-1}]$, yielding

$$R_{zz}(\tau) = \frac{1}{\chi_p(0)E[\eta_e^{-1}]} \int_{-\infty}^{\infty} \eta^{-1} \chi_p(\eta \tau) f_{\eta}(\eta) d\eta. \tag{7.103}$$

If the relative radial velocity between the sonar and the elemental scatterers is zero (i.e., the sonar and scatterers are effectively stationary), then η_e is always 1 and the PDF of η_e is $f_{\eta_e}(\eta) = \delta(\eta - 1)$. The ACF of the normalized reverberation is then precisely that of the projected pulse scaled to have unit power,

$$R_{zz}(\tau) = \frac{\chi_p(\tau)}{\chi_p(0)}. \tag{7.104}$$

7.4.2.3 Reverberation Power Spectral Density

The PSD of the normalized reverberation random process can be obtained by taking the Fourier transform of (7.103) and exploiting the time-scale property (see Sect. 4.3.2),

$$\begin{aligned}
S_{zz}(f) &= \int_{-\infty}^{\infty} R_{zz}(\tau) e^{-j2\pi f \tau} d\tau \\
&= \frac{1}{\chi_p(0)E[\eta_e^{-1}]} \int_{-\infty}^{\infty} \frac{1}{\eta^2} S_p(f/\eta) f_{\eta}(\eta) d\eta
\end{aligned} \tag{7.105}$$

where it has been assumed that $\eta > 0$. As previously noted, the Doppler scale will always be one when the sonar platform and reverberation elemental scatterers are (effectively) stationary and the normalized-reverberation PSD is simply the scaled pulse spectrum,

$$S_{zz}(f) = \frac{S_p(f)}{\chi_p(0)} = \frac{S_p(f)}{\int_{-\infty}^{\infty} S_p(f) df}. \quad (7.106)$$

When the relative radial speed of the elemental scatterers with respect to the sonar platform is small compared to the speed of sound, the integral in (7.105) can be approximated by a convolution between the spectrum of the transmit waveform and the PDF $f_{\delta}(\delta_f)$ of the Doppler frequency shift induced by motion of the elemental scatterer,

$$\delta_f = (\eta - 1)f_c \approx \frac{2v_r f_c}{c_w} \quad (7.107)$$

where v_r is the relative radial velocity between a monostatic sonar platform and the elemental scatterer. The slow relative speed of the scatterers implies the Doppler scale is near one and allows replacing the denominator term $E[\eta_e^{-1}]\eta^2$ in (7.105) with the average Doppler scale $\bar{\eta} = 1 + 2\bar{v}_r/c_w = E[\eta_e] \approx 1/E[\eta_e^{-1}]$. The convolution approximation to $S_{zz}(f)$ can then be derived by assuming

$$S_p(f/\eta) \approx S_p(f - 2v_r f_c/c_w) \approx S_p(f - 2v_r f_c/c_w) \quad (7.108)$$

which essentially requires $S_p(f)$ to vary slowly within its frequency band. The resulting reverberation PSD has the form

$$\begin{aligned} S_{zz}(f) &\approx \frac{1}{\bar{\eta} \chi_p(0)} \int_{-\infty}^{\infty} S_p(f - \delta_f) f_{\delta}(\delta_f) d\delta_f \\ &= \frac{1}{\bar{\eta} \chi_p(0)} S_p(f) * f_{\delta}(f). \end{aligned} \quad (7.109)$$

This supports the intuition that the reverberation spectrum must spread when the elemental scatterers are in motion and provides an easily interpreted “spreading function” in the form of $f_{\delta}(\delta_f)$. The convolution approximation in (7.109) is surprisingly accurate, even for broadband waveforms.

Example: CW Pulse ACF and Spectrum

Consider a CW pulse with unit amplitude, duration T_p , and frequency f_c ,

$$p_o(t) = \begin{cases} \cos(2\pi f_c t) & \text{for } t \in [0, T_p] \\ 0 & \text{otherwise} \end{cases}. \quad (7.110)$$

The pulse ACF is easily shown to have a triangular shape modulated by a cosine at the pulse frequency,

(continued)

$$\begin{aligned}\chi_p(\tau) &= \int_{-\infty}^{\infty} p_o(t) p_o(t + \tau) dt \\ &\approx \begin{cases} \frac{1}{2}[T_p - |\tau|] \cos(2\pi f_c \tau) & \text{for } t \in [-T_p, T_p] \\ 0 & \text{otherwise} \end{cases}. \quad (7.111)\end{aligned}$$

The spectrum can be found either as the Fourier transform of the ACF in (7.111) or from the squared magnitude of the Fourier transform of the pulse itself. For the unit-amplitude CW pulse, the spectrum is approximately

$$S_p(f) \approx \frac{T_p^2}{4} \operatorname{sinc}^2(T_p[|f| - f_c]) \quad (7.112)$$

when $T_p f_c \gg 1$.

If an object of interest has a high enough radial velocity, the echo will be noise limited rather than reverberation limited. The spectrum of an echo from an object of interest with Doppler scale η_o is $S_p(f/\eta_o)/|\eta_o|$, which is a sinc^2 function centered at $\eta_o f_c \approx f_c + 2v_o f_c/c_w$ for the CW pulse and a monostatic sonar system. From (7.106), the reverberation spectrum is proportional to the pulse spectrum, which for the CW pulse has peak-to-null width of $1/T_p$ and 3-dB-down point occurring at a frequency offset of $\delta_f = 0.443/T_p$. If being in the noise-limited regime is defined by having the reverberation spectrum at least 3-dB down from its peak at the 3-dB-down point of the echo spectrum, then the object-of-interest's radial speed must exceed

$$|v_o| > \frac{0.443 c_w}{f_c T_p} \quad (7.113)$$

for it to be in a noise-limited regime. This result illustrates how increasing CW-pulse frequency or duration improves Doppler resolution.

7.4.2.4 Doppler Spreading of Reverberation

When either the sonar platform or reverberation scatterers are in motion, the measured reverberation can simultaneously contain different Doppler scales, which has the effect of spreading the reverberation spectrum. Among the sources of reverberation listed in Sect. 3.5.1, several can present motion in the elemental scatterers, with examples including fish, air bubbles, the ocean surface, and even sea grasses. Although some of these will affect the echo from the object of interest (i.e., those taking part in the propagation), the primary interest here is how the scatterer motion affects reverberation.

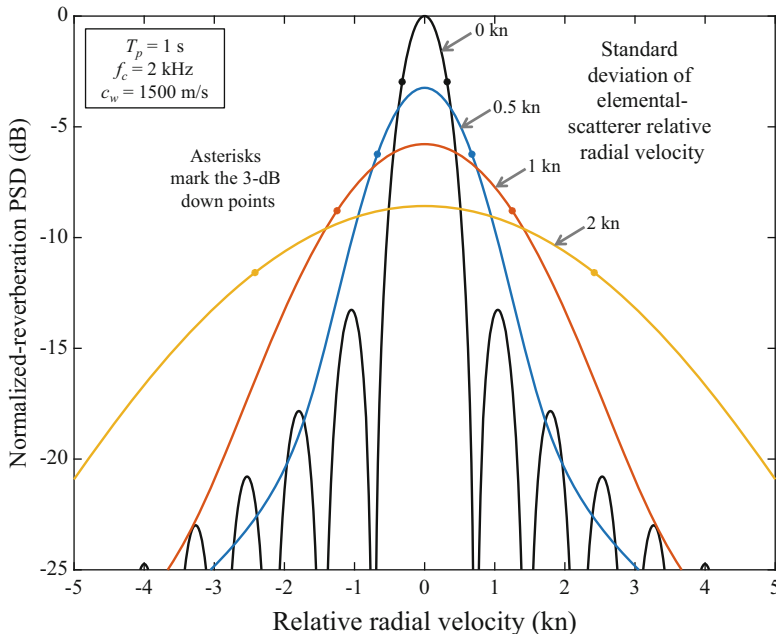
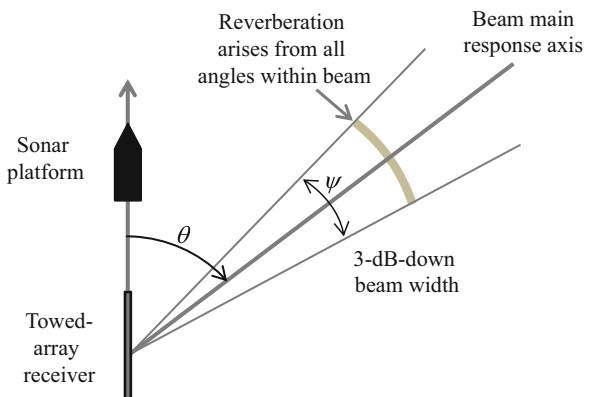


Fig. 7.5 PSD of the normalized reverberation process when the elemental scatterers have (zero-mean) Gaussian random radial velocity. Note that the abscissa has been converted from frequency to relative radial velocity through (7.107)

Suppose the relative radial velocity of the reverberation elemental scatterers is Gaussian distributed with zero mean and standard deviation σ_v . The spreading of the normalized-reverberation PSD is illustrated in Fig. 7.5 for an example CW-pulse spectrum using (7.112). Note that the PSD has been normalized by the $\chi_p(0)$ term in the denominator of (7.109) and that the abscissa is shown as converted to the units of relative radial velocity through (7.107). As expected, the PSD broadens as σ_v increases with a commensurate reduction in level to maintain the unit-power constraint induced by normalization.

The extent of the spreading for a CW pulse with duration T_p and Gaussian-distributed elemental-scatterer relative radial velocity can be assessed by approximating the sinc-squared function in $S_p(f)$ by a Gaussian PDF. The PSD in (7.109) is then the convolution of two Gaussian PDFs, which results in another Gaussian PDF with variance equal to the sum of the variances of the individual components. The 3-dB-down point in the Gaussian PDF is then $\sqrt{2\log 2} \approx 1.18$ times the standard deviation. This results in a reverberation-PSD 3-dB-down point, when described in the units of speed using (7.107), of

Fig. 7.6 Diagram of a moving sonar platform with a towed-array receiver forming a beam at angle θ from the platform heading. Reverberation in the beamformer output arises from angles near the beam main response axis within the beamwidth (i.e., within the angles $\theta \pm \psi/2$)



$$v_{3\text{dB}}(\sigma_v) \approx 1.18 \sqrt{\left(\frac{c_w}{2f_c}\right)^2 \frac{0.1415}{T_p^2} + \sigma_v^2} \quad (7.114)$$

where $v_{3\text{dB}}$, σ_v , and c_w have the same units (e.g., m/s). The “0.1415” in (7.114) is chosen so that as $\sigma_v \rightarrow 0$ the result tends to the 3-dB-down point for the sinc^2 function of the CW-pulse spectrum. An alternative approach is to approximate the logarithm of the sinc^2 function by a second-order Taylor-series expansion, which also produces a Gaussian shaped spectrum, and would require using $0.1520 = 1.5/\pi^2$ in lieu of the “0.1415.”

Motion of the elemental scatterers is not the only mechanism by which the reverberation spectrum can be spread. When one or both of the sonar components (projector and/or sensor array) are in motion, the effect of platform motion on the Doppler scale depends on the angle between the platform heading and the bearing to the object of interest (e.g., see the diagram in Fig. 7.6). Recall from Exercise 2.3 that the Doppler scale for a monostatic active sonar system with a ship speed v_a and an object of interest at a relative angle of θ_o from the ship’s heading was

$$\eta(\theta_o) \approx 1 + \frac{2v_a \cos \theta_o}{c_w}. \quad (7.115)$$

The reverberation arising from scatterers having this relative angle is similarly affected in that the spectrum is subject to a frequency scale shifting the zero-Doppler reverberation ridge to be centered at ηf_c where η is defined by (7.115). In most systems there will be a beamformer that limits the contributions from angles distant from θ_o ; however, reverberation scatterers from nearby angles will contribute to the reverberation measurement as depicted in Fig. 7.6. In the radar community this phenomenon is known as clutter spreading [44, Sect. 8.9.1]. Suppose the reverberation scatterers are dispersed uniformly in the horizontal plane so the spectrum of the reverberation is proportional to an integral over θ of the

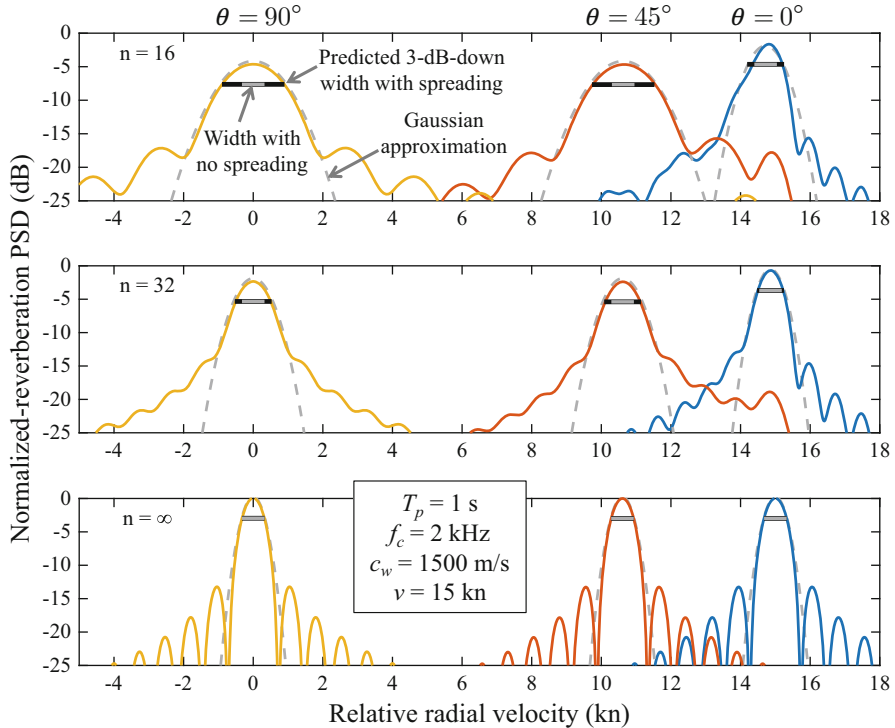


Fig. 7.7 PSD of the normalized reverberation process when a monostatic sonar platform is in motion and a line-array forms beams at various angles relative to the platform heading. The black lines are the spreading predicted from (7.121) whereas the gray lines are the width of the spectrum when there is no additional spreading (i.e., the sonar platform is stationary). Note that the abscissa has been converted from frequency to relative radial velocity through (7.107)

Doppler-scaled pulse spectrum weighted by $b(\theta; \theta_o)$, which is the beampattern of the beamformer pointed at θ_o ,

$$S_{zz}(f) \propto \int_{\theta} S_p \left(\frac{f}{\eta(\theta)} \right) b(\theta; \theta_o) d\theta. \quad (7.116)$$

Although this process is physically different than the spreading arising from random motion of the scatterers, the reverberation spectrum in (7.116) will clearly spread the pulse spectrum over the Doppler scales spanned by the beamwidth of the beamformer. This can be seen in Fig. 7.7 where the sensor is assumed to be a line array towed behind the sonar platform. The reverberation spectra for bearings of $\theta_o = 0^\circ$, 45° , and 90° are shown for line arrays with $n = 16$, 32 , or ∞ sensors at half-wavelength spacing and a 15-kn platform speed. The $n = \infty$ case implies perfect isolation of signals and reverberation arriving from the angle θ_o and

represents a lower bound on the Doppler spreading. As found in Sect. 8.4.3, the beampattern of a uniform line array with n sensors spaced every half wavelength is

$$b(\theta; \theta_o) = \frac{\text{sinc}^2\left(\frac{n}{2}[\cos \theta - \cos \theta_o]\right)}{\text{sinc}^2\left(\frac{1}{2}[\cos \theta - \cos \theta_o]\right)} \quad (7.117)$$

where $\theta = 0$ represents the array heading (assumed to be the same as that of the towing-platform). The colored lines in Fig. 7.7 are a numerical evaluation of (7.116) using (7.117) as the beampattern. The most dramatic change to the reverberation spectrum is the recentering of the spectrum to account for the base Doppler scale defined by (7.115): near 15 kn for $\theta = 0^\circ$, 10.6 kn for 45° , and 0 kn for 90° (broadside).

The line-array sensor is an interesting example because its beamwidth changes with the main response axis to be narrowest broadside to the array and widest at either array endfire. However, despite the wider beams near endfire, the Doppler spreading has a more egregious effect at broadside than endfire because of the rate of change of $\eta(\theta)$, which is at a maximum when $\theta = \pi/2$. This can also be seen by the difference between the black and gray bars in Fig. 7.7 which represent the 3-dB-down width of the reverberation spectrum, respectively, with and without the spreading arising from the sonar platform's motion.

Although both the pulse spectrum and line-array beampattern can be approximated by Gaussian PDF shapes, the form of (7.116) does not directly simplify to a convolution as was the case for random scatterer motion. As an alternative, suppose the spreading is represented by the span of Doppler scales encountered for a beam pointed at θ_o and having beamwidth ψ . Define θ_c as the mid-point between the two 3-dB-down points of the beampattern. For some arrays this will be identical to θ_o ; however, it can differ as will be described shortly for uniformly spaced line arrays. The difference between the largest and smallest Doppler scales is

$$\begin{aligned} \Delta_\eta &= \eta(\theta_c - \psi/2) - \eta(\theta_c + \psi/2) \\ &\approx \frac{2v_a}{c_w} [\cos(\theta_c - \psi/2) - \cos(\theta_c + \psi/2)] \end{aligned} \quad (7.118)$$

$$\begin{aligned} &= \frac{4v_a}{c_w} \sin \theta_c \sin\left(\frac{\psi}{2}\right) \\ &\approx \frac{2v_a}{c_w} \psi \sin \theta_c \end{aligned} \quad (7.119)$$

where it is assumed that $\theta_c \geq \psi/2$ and that ψ is small so that $\sin(\psi/2) \approx \psi/2$ to obtain the final result. Converting this to a spread in radial velocity for the monostatic active sonar scenario results in

$$\Delta_{v_r} \approx v_a \psi \sin \theta_c, \quad (7.120)$$

which illustrates that the Doppler spreading increases with speed of advance, beamwidth, and the beam angle relative to platform heading (up to broadside where $\theta_c = \pi/2$). This span of Doppler scales can then be used to predict the 3-dB-down width of the reverberation spectrum by combining it with the width of the unspread spectrum. The 3-dB-down spread in (7.120) can be converted to a standard deviation by dividing by 2 (to convert it to the distance from the center to the 3-dB-down point) and then dividing by $\sqrt{2 \log 2} = 1.18$ to match the 3-dB-down point of the Gaussian PDF, which will be used to approximate the spectrum near its peak. The distance from the center of the reverberation spectrum to the 3-dB-down point can then be approximated by

$$v_{3\text{dB}}(\sigma_v, v_a, \theta_c, \psi) \approx 1.18 \sqrt{\left(\frac{c_w}{2f_c}\right)^2 \frac{0.1415}{T_p^2} + \sigma_v^2 + \left(\frac{v_a \psi \sin \theta_c}{2\sqrt{2 \log 2}}\right)^2} \quad (7.121)$$

after accounting for forward motion of the sonar platform (v_a), the center angle of the beam (θ_c), beamwidth (ψ), and the standard deviation of the reverberation elemental-scatterer radial motion (σ_v). This approximation assumes the spreading arising from the sonar platform's motion acts in a similar manner to that of the reverberation scatterer motion—the total spread as a standard deviation is the square root of the sum of the variances. The accuracy of this approximation can be seen by the black bars in Fig. 7.7 and by the Gaussian PDF approximation (gray dashed lines), which uses (7.121) to form its standard deviation.

Because the beampattern of a line array is not symmetric in θ about the main response axis, the peak of the reverberation spectrum is not precisely at $v_a \cos \theta_o$, except at broadside. The frequency (or equivalent relative radial velocity) of the peak can be approximated using the average of $\eta(\theta)$ over the angles spanned by the 3-dB-down points of the beampattern. If these points are θ_1 and θ_2 , so the beamwidth $\psi = \theta_2 - \theta_1$ and beam center $\theta_c = (\theta_1 + \theta_2)/2$, then the reverberation spectrum is centered approximately at relative radial velocity

$$v_c = v_a \operatorname{sinc}\left(\frac{\psi}{2\pi}\right) \cos(\theta_c). \quad (7.122)$$

As shown in [45, Sect. 2.4.1, problem 2.4.7], approximating the beampattern through a Taylor series expansion provides a simple formula for the 3-dB-down points. For a uniform line array comprising n sensors these are

$$\theta_1 = \arccos\left[\cos(\theta_o) + \frac{a_w}{n\gamma}\right] \quad \text{and} \quad \theta_2 = \arccos\left[\cos(\theta_o) - \frac{a_w}{n\gamma}\right] \quad (7.123)$$

where a_w depends on the window function used to shade the array and $\gamma = f/f_d$ indicates if the frequency of the signal (f) is the same as the design frequency of the array ($f_d = c_w/(2d)$ where d is the sensor spacing). For a rectangular window, $a_w = 0.89$ whereas it is 1.31 for a Hamming window. The values for

other common windows can be found in the first column of Table 4.2 and [45, Sect. 3.1]. Using (7.123) in (7.122) results in

$$v_c = v_a \operatorname{sinc}\left(\frac{\psi}{2\pi}\right) \cos\left(\frac{1}{2} \arccos\left[\cos(\theta_o) + \frac{a_w}{n\gamma}\right] + \frac{1}{2} \arccos\left[\cos(\theta_o) - \frac{a_w}{n\gamma}\right]\right). \quad (7.124)$$

This illustrates how the reverberation spectrum is centered at $v_c = v_a \cos \theta_o$ only when $\theta_o = \pi/2$ (yielding $v_c = 0$) or as $n \rightarrow \infty$. The Gaussian PDF approximations to the reverberation spectra shown in Fig. 7.7 have a mean defined by (7.124) and a standard deviation of $v_{3\text{dB}}(\sigma_v, v_a, \theta_o, \psi)/1.18$ from (7.121). Before evaluating the Gaussian PDF, which is used to approximate the shape of the PSD as a function of frequency, these need to be converted back to a frequency shift (i.e., multiplying by $2f_c/c_w$) away from f_c .

In Sect. 2.2.6, a Doppler sensitive waveform (e.g., the CW pulse) was seen to be effective in differentiating an object of interest's echo from reverberation when the relative radial speed was large enough to shift the echo spectrum away from the reverberation spectrum. The impact of Doppler spreading of the reverberation spectrum is the need for a commensurately larger radial speed for the echo spectrum to be easily differentiated from the reverberation. When there is no Doppler spreading, the radial speed at which the reverberation and echo spectra overlap at their 3-dB-down points, which can be described as the beginning of the noise-limited regime, is $v_{\min} = 0.443c_w/(f_c T_p)$. When there is Doppler spreading, the minimum speed for being noise-limited increases to require a relative radial speed of

$$\begin{aligned} |v_r| &\geq \frac{v_{\min}}{2} + v_{3\text{dB}}(\sigma_v, v_a, \theta_c, \psi) \\ &= \frac{v_{\min}}{2} + \sqrt{\left(\frac{v_{\min}}{2}\right)^2 + (1.18\sigma_v)^2 + \left(\frac{v_a \psi \sin \theta_c}{2}\right)^2} \end{aligned} \quad (7.125)$$

where it is assumed that the motion of the reverberation elemental scatterers does not have an effect on the echo from the object of interest. Thus, when the platform speed and elemental-scatterer motion are small relative to the resolution capability of the waveform, there is no adverse effect whereas there will be if the waveform can discern the scatterer motion or beamformer-induced Doppler spreading. In the examples considered ($T_p = 1$ s, $f_c = 2$ kHz, and $v_a = 15$ kn), the waveform requires speeds greater than $v_{\min} = 0.65$ kn for noise-limited operation. The spreading for the $n = 16$ array with stationary reverberation scatterers results in requiring $|v_r| \geq 0.85$ kn at endfire and 1.2 kn at broadside, which is nearly double the minimum. If the reverberation scatterers have a 1-kn standard deviation, a 1.55 kn relative radial speed is required when the sonar platform is at rest. If the sonar platform has a 15-kn speed, these increase to 1.62 kn at endfire and 1.8 kn at broadside.

7.4.3 Heavy-Tailed Noise and Reverberation

In the previous sections it has been argued that ambient noise and reverberation are Gaussian distributed by describing them as a superposition of a multitude of independent sources and application of the CLT. However, when the number of sources becomes small, the bandpass noise or reverberation can no longer be assumed to be Gaussian distributed. The impact is generally to make the large positive or negative values (i.e., the “tails”) more likely to occur than they do under the Gaussian distribution. The data for such scenarios is termed “heavy tailed” because the PDF models have heavier tails than the Gaussian distribution. Owing to the relationship between bandpass reverberation or noise and its envelope and instantaneous intensity, this implies the upper tail of the envelope distribution will be heavier than that of the Rayleigh distribution and the upper tail of the instantaneous-intensity distribution will be heavier than that of the exponential distribution.

Heavy-tailed noise or reverberation distributions have an adverse effect on detection performance by requiring a higher decision threshold to achieve the same probability of false alarm as when the background follows the Rayleigh distribution chain, which results in a reduction in the probability of detection. Alternatively, if the same decision threshold is maintained as for a Rayleigh-distribution-chain background the probability of false alarm rises in the presence of heavy-tailed ambient noise or reverberation.

Reducing the number of elemental scatterers is not the only way in which reverberation and noise can become heavy tailed. Several mechanisms exist including:

- too few independent elemental scatterers for CLT to apply,
- as an adverse effect of signal-processing,
- multiple disparate noise sources, and
- non-stationarity within the analysis window.

In addition to the following brief introduction to these mechanisms, examples can be found as the various heavy-tailed distribution models are introduced throughout the remainder of this section.

The sonar-equation analysis found in Sect. 2.3 describes how different signal processing functions alter the average power of the signal and noise or reverberation. This generally results in a change in the scale parameter of the envelope or instantaneous-intensity distribution and is often all that is necessary to describe sonar performance. However, there are situations, both inexorable and avoidable, where signal processing can alter the statistical distribution of noise and reverberation with an adverse effect on sonar performance. Examples of an unavoidable change can be found when beamforming and matched filtering reduce the number of elemental scatterers contributing to reverberation to potentially make it heavier tailed and in a normalizer where the background power level is estimated from a finite sample of data. An avoidable scenario arises when the ambient noise or reverberation power level changes too much within the estimation window used by

a normalizer resulting in a biased normalization that appears as heavy-tailed data. This scenario is an example of mismatch errors dominating estimation errors.

Some ambient noise sources produce short-duration (transient) sounds at random intervals (e.g., ice movement or the sounds produced by fish and marine mammals as mentioned in Sect. 7.4.1) that lead to heavy-tailed distributions. Transient noise is usually measured in the presence of a background Gaussian noise source such as wind-generated surface noise or that arising from distant shipping. The PDF of the composite measurement can be approximated by a heavy-tailed mixture distribution where the transient noise occurs infrequently but completely dominates the background noise when it is present.

It is common to analyze the statistics of noise and reverberation with the data observed over a window in time. If the data are truly from an ergodic random process, this will properly characterize the PDF. However, ergodicity does not hold if the data change in certain fundamental ways throughout the window (i.e., the data are non-stationary). For example, the time-varying power level of un-normalized reverberation violates ergodicity. Estimating reverberation statistics from such a segment of data can cause a Rayleigh-distributed envelope with a slowly varying power level to appear very heavy tailed.

These mechanisms can be described as either arising from (1) the physical process or (2) from an improper application of signal processing or a failed assumption of ergodicity in the data analysis procedure. If the goal is to isolate, assess, or infer the physical process, it is important to ensure the signal processing and analysis procedure are not having an unintended effect.

7.4.3.1 Effect of Beamforming and Matched Filtering on Reverberation Statistics

Recall from (7.96) that reverberation can be represented as a sum of delayed and scaled copies of the projected pulse over a set of elemental scatterers,

$$r(t) = \sum_{i=1}^{n_e} \frac{A_i}{r_i^2} p_o(t - \tau_i), \quad (7.126)$$

where here it has been assumed there is no scatterer motion (i.e., the Doppler scale $\eta_i = 1$ for all i). The assessment presented in Sect. 3.5 that reverberation is Gaussian distributed arises from the assumption that the number of elemental scatterers contributing at any given time t is large enough for the CLT to hold. If the pulse $p_o(t)$ is only non-zero for $t \in [0, T_p]$, the only scatterers that contribute at time t are those satisfying $\tau_i \in [t - T_p, t]$. For example, consider bottom reverberation in the basic ocean model as described in Sect. 3.5.3. The number of elemental scatterers contributing at time t is on average

$$\bar{n}_e(t) = 2\pi \left[\frac{c_w t}{2} \right] \left[\frac{c_w T_p}{2 \cos \theta_g} \right] \beta \quad (7.127)$$

where β is the density of elemental scatterers (units: number per unit area), θ_g the grazing angle (assumed to be small), where the first term in brackets represents the slant range and the second the down-range ensonified extent on the bottom. The underlying assumption leading to Gaussianity is that $\bar{n}_e(t)$ is always large enough to support application of the CLT.

Two signal processing functions (beamforming and matched filtering) reduce the effective number of elemental scatterers contributing at a given time and therefore have the potential to alter the reverberation statistics. Beamforming a sensor array will limit the angles from which scatterers can contribute and would approximately result in replacing the “ 2π ” in (7.127) with the beamwidth (ψ) in radians. Matched filtering operates in the time-delay dimension and has the effect of reducing the effective ensonified down-range extent. The resulting region in angle and delay (or down-range extent) is called a “resolution cell,” within which it is generally not possible to resolve individual scatterers with conventional processing.

Applying a matched filter to the reverberation sum in (7.126) results in a similar sum of delayed and scaled copies of the waveform ACF,

$$\begin{aligned} x_r(\tau) &= \int_{-\infty}^{\infty} p_o(t) r(t + \tau) dt \\ &= \sum_{i=1}^{n_e} \frac{A_i}{r_i^2} \chi_p(\tau - \tau_i). \end{aligned} \quad (7.128)$$

In general, the temporal extent of the ACF of a waveform is inversely proportional to its bandwidth (W), which results in an effective number of elemental scatterers

$$\bar{n}_e(\tau) = \psi \left[\frac{c_w \tau}{2} \right] \left[\frac{c_w}{2W \cos \theta_g} \right] \beta \quad (7.129)$$

contributing at delay τ to reverberation after beamforming and matched filtering. Clearly reducing ψ (e.g., by increasing array size) and increasing bandwidth will reduce the number of elemental scatterers contributing at a given time delay. When there are not enough elemental scatterers for bandpass reverberation to follow the Gaussian distribution, there are a number of other distributions (as described in the remainder of this section) available for describing reverberation statistics, although generally only applied to the envelope or instantaneous intensity.

Although it is not uncommon to observe heavy-tailed reverberation, particularly with broadband pulses, it is important to note that Gaussian reverberation is very common. In many situations, the density of elemental scatterers is so large that the reduction in $\bar{n}_e(t)$ arising from beamforming and matched filtering does not produce any perceptible change in reverberation statistics.

7.4.3.2 Statistical Models for Heavy-Tailed Data

Heavy-tailed distribution models can be categorized as either having a basis in the physics of underwater acoustics (e.g., the K, Poisson-Rayleigh, and McDaniel distributions) or as being primarily descriptive in nature without a strong physical basis (e.g., the Weibull, log-normal, or generalized Pareto (GP) distributions). Clearly this is important when heavy-tailed distributions are used for inference on physical parameters related to the noise or reverberation source. However, they are more often used in a descriptive or phenomenological manner to represent observed data or data trends where the link to the physics can be immaterial. This provides a rationale for examining various standard distributions and their generalizations.

The scintillation index (SI), which is the ratio of the variance of the instantaneous intensity (ζ) to the square of its mean,

$$\text{SI} = \frac{\text{Var}\{\zeta\}}{E^2[\zeta]}, \quad (7.130)$$

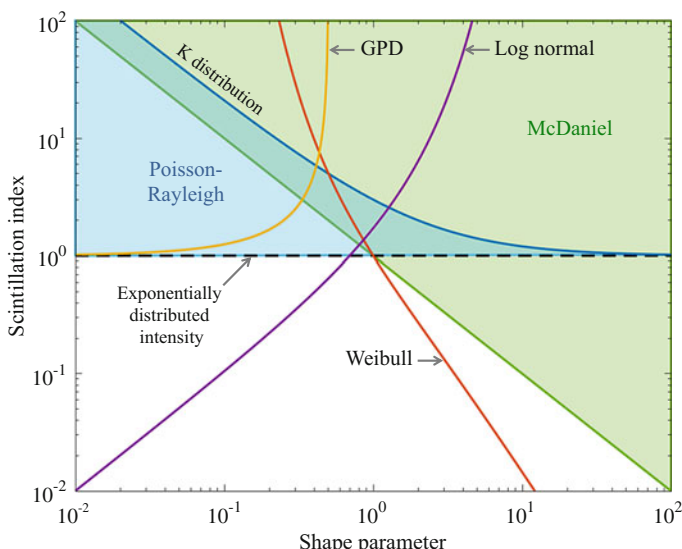
can be used as measure of a distribution model's tail heaviness owing to the sensitivity of higher-order moments to distribution tails. An exponentially distributed instantaneous intensity produces $\text{SI} = 1$, so a heavy-tailed distribution (with respect to the exponentially distributed instantaneous intensity) is assumed to produce $\text{SI} > 1$. Values of $\text{SI} < 1$ represent lighter tails and in the limit of $\text{SI} \rightarrow 0$ a constant instantaneous intensity, which is indicative of a deterministic signal as described in Sect. 7.5.1. The SI of several common models is presented in Table 7.5 along with the conditions resulting in the exponential distribution and the conditions for heavy tails. The SI is shown graphically in Fig. 7.8 as a function of the shape parameter where the two-parameter models are lines and the three-parameter models are regions. Although all of the models have the capacity to produce very heavy-tailed distributions ($\text{SI} \gg 1$), the K and Poisson-Rayleigh distributions cannot produce lighter-tailed distributions than the exponentially distributed instantaneous intensity (i.e., $\text{SI} < 1$). To illustrate how different the distributions can be, their probability of false alarm (P_f) is shown in Fig. 7.9 with the parameters chosen to have unit average intensity and $\text{SI} = 1.3$. The models illustrate a wide range of P_f despite having equal first and second instantaneous-intensity moments.

The analysis of heavy-tailed distributions presented in this text is primarily done for the instantaneous intensity, with mention of modeling the complex envelope or envelope only when necessary or appropriate. A derivation from a physical model is presented for the K distribution in Sect. 7.4.3.3. The Poisson-Rayleigh (envelope) model, which arises from Middleton Class-A bandpass noise, is described in Sect. 7.4.3.4. Other common models are briefly introduced in Sect. 7.4.3.5. Mixture models are treated separately in Sect. 7.4.3.7. All of the non-mixture models have a scale parameter (generally λ) and one or two shape parameters. More detailed information on the standard distributions can be found in Sect. 5.6. Additionally, the first three moments of the instantaneous intensity are presented in Table 7.8 in Sect. 7.5.6.5, which enables evaluation of the scintillation index (SI) shown here in

Table 7.5 Scintillation index (SI) for common heavy-tailed distribution models

Distribution and section	Scintillation index (SI)	Conditions for exponential distribution	Conditions for heavy PDF tails (i.e., SI > 1)
Exponential: Sect. 5.6.10	1	Always	Never
K: Sects. 5.6.19 and 7.4.3.3	$1 + \frac{2}{\alpha}$	$\alpha \rightarrow \infty$	All $\alpha \in (0, \infty)$
Poisson-Rayleigh: Sect. 7.4.3.5	$1 + \frac{2\alpha\lambda_d^2}{(\lambda_c + \alpha\lambda_d)^2}$	$\alpha = 0, \lambda_c \rightarrow \infty$, or $\alpha \rightarrow \infty$	$\alpha \in (0, \infty)$ when $\lambda_c < \infty$
McDaniel: Sect. 7.4.3.5	$\frac{1}{\alpha_1} + \frac{1}{\alpha_2} + \frac{1}{\alpha_1\alpha_2}$	$\alpha_1 \rightarrow \infty$ when $\alpha_2 = 1$	$\alpha_1 < \frac{\alpha_2+1}{\alpha_2-1}$ when $\alpha_2 > 1$
Generalized Pareto: Sect. 5.6.20	$\frac{1}{1-2\gamma}$	$\gamma = 0$	$\gamma > 0$
Weibull: Sect. 5.6.18	$\frac{\Gamma(1+\frac{2}{\beta})}{\Gamma^2(1+\frac{1}{\beta})} - 1$	$\beta = 1$	$\beta < 1$
Log-normal: Sect. 5.6.21	$e^\gamma - 1$	none	$\gamma > \log 2$

Each of the distributions and their parameters are described in Sect. 7.4.3; more details for the common distributions are found in the section cited in the first column. The first three moments of the distributions are found in Table 7.9

**Fig. 7.8** Scintillation index (SI) as a function of the shape parameter for common heavy-tailed probability distributions

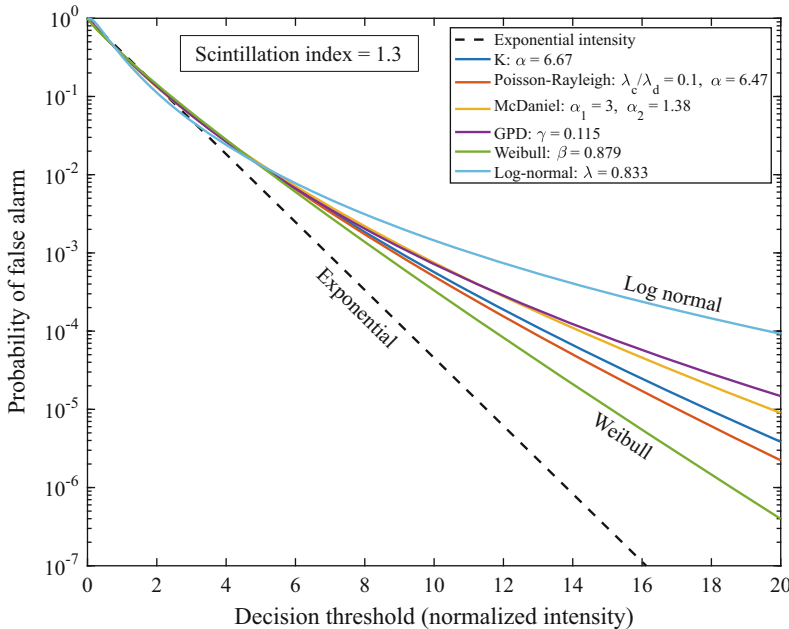


Fig. 7.9 Probability of false alarm for common heavy-tailed distributions as a function of the intensity threshold. Distribution parameters are chosen so the average intensity is one and the scintillation index (SI) is 1.3

Table 7.5 as well as providing the (uninverted) moment equations for method-of-moments estimation. Cramér-Rao lower bounds on parameter estimation for several common heavy-tailed distributions are presented in Sect. 7.4.3.6.

7.4.3.3 K Distribution

In Sect. 7.4.3.1, the effect of beamforming and matched filtering on reverberation statistics was articulated as a reduction in the number of elemental scatterers contributing at any given time. Suppose each elemental scatterer has size following an exponential distribution (e.g., the mud volcanoes described in [46]) in such a manner that the complex envelope of the i th scatterer is

$$Z_i = A_i e^{j\theta_i} \quad (7.131)$$

where $A_i \sim \text{Exp}(\mu)$ and θ_i is uniformly distributed on $[0, 2\pi]$. As noted in [47], this model presumes the scattered response is proportional to size, which occurs in the geometric scattering regime as described in Sect. 3.4.3. When some number n_e of the elemental scatterers contribute to a sonar resolution cell, the complex envelope is the sum

$$Z = \sum_{i=1}^{n_e} A_i e^{j\theta_i}. \quad (7.132)$$

In [47], this was shown to follow the K distribution [48]. A brief derivation following [47] is presented here before describing the properties of the K distribution. There is an extensive literature available on the K distribution owing to its applicability across many fields. Key resources on the K distribution include the early papers by Jakeman, Pusey, and Ward [48–50], the more recent texts [51, 52], and the sonar modeling applications in [47, 53, 54].

Assuming the elemental scatterers are statistically independent implies the characteristic function (CF) of the sum in (7.132) is the product of the CFs of the summands. The CF of Z_i is formed as a joint CF over the real and imaginary parts of Z_i ,

$$\begin{aligned} \Phi_{Z_i}(\omega, \gamma) &= E\left[e^{j\omega A_i \cos(\theta_i) + j\gamma A_i \sin(\theta_i)}\right] \\ &= \frac{1}{\sqrt{1 + \mu^2(\omega^2 + \gamma^2)}}. \end{aligned} \quad (7.133)$$

The CF of the sum is then (7.133) raised to the power n_e ,

$$\Phi_Z(\omega, \gamma) = \frac{1}{[1 + \mu^2(\omega^2 + \gamma^2)]^{n_e/2}}. \quad (7.134)$$

To obtain the PDF of the complex envelope, a two-dimensional inverse transform is applied to the characteristic function. The circular symmetry arising from the uniformly random phase, which presents itself in the CF domain as a dependence on ω and γ through $\rho = \omega^2 + \gamma^2$ so $\Phi_Z(\omega, \gamma) = \Phi_\rho(\omega^2 + \gamma^2)$, can be exploited to simplify the inversion. This results in an inversion formula that is valid for any circularly symmetric complex-envelope distribution

$$f_Z(z) = \frac{1}{4\pi^2} \iint_{-\infty}^{\infty} \Phi_Z(\omega, \gamma) e^{-j\omega u - j\gamma v} d\omega d\gamma \quad (7.135)$$

$$= \frac{1}{4\pi} \int_0^{\infty} \Phi_\rho(\rho) J_0(|z| \sqrt{\rho}) d\rho \quad (7.136)$$

where $z = u + jv$, $\rho = \omega^2 + \gamma^2$, and $J_0(x)$ is the zeroth-order Bessel function [55, Ch. 52]. Substituting (7.134) into (7.136) and using [56, 6.565-4] results in the K-distribution complex-envelope PDF

$$f_Z(z) = \frac{2}{\pi \lambda \Gamma(\alpha)} \left(\frac{|z|}{\sqrt{\lambda}} \right)^{\alpha-1} K_{\alpha-1} \left(2 \frac{|z|}{\sqrt{\lambda}} \right), \quad (7.137)$$

where $K_v(x)$ is the modified Bessel function of the third kind [55, Ch. 51] and α and λ are, respectively, shape and scale parameters. For the example entailing elemental scatterers with an exponentially distributed size, the shape parameter is driven by the number of elemental scatterers,

$$\alpha = \frac{n_e}{2}, \quad (7.138)$$

and the scale parameter by their average size,

$$\lambda = 4\mu^2. \quad (7.139)$$

It is important to note that this is only one example of how the K distribution can be derived; other examples will be discussed later in this section.

To complete the K-distribution-chain description, the PDF of the envelope can be stated as

$$f_A(a) = \frac{4}{\sqrt{\lambda} \Gamma(\alpha)} \left(\frac{a}{\sqrt{\lambda}} \right)^\alpha K_{\alpha-1} \left(\frac{2a}{\sqrt{\lambda}} \right) \quad \text{for } a \geq 0 \quad (7.140)$$

by using (7.90) and for the instantaneous intensity as

$$f_I(\zeta) = \frac{2}{\lambda \Gamma(\alpha)} \left(\frac{\zeta}{\lambda} \right)^{(\alpha-1)/2} K_{\alpha-1} \left(2\sqrt{\frac{\zeta}{\lambda}} \right) \quad \text{for } \zeta \geq 0 \quad (7.141)$$

from (7.91).

The probability of false alarm (P_f) for a detector implemented by comparing the envelope or instantaneous intensity to a decision threshold is one minus the cumulative distribution function (CDF) of the decision statistic. For example,

$$P_f = 1 - F_I(h) \quad (7.142)$$

where $F_I(\zeta)$ is the CDF of the instantaneous intensity and h is the decision threshold applied to the instantaneous intensity. Integrating either (7.135) or (7.136) from zero to the CDF argument yields the K-distribution CDF

$$F_I(\zeta) = F_A(\sqrt{\zeta}) \quad (7.143)$$

$$= 1 - \frac{2}{\Gamma(\alpha)} \left(\frac{\zeta}{\lambda} \right)^{\alpha/2} K_\alpha \left(2\sqrt{\frac{\zeta}{\lambda}} \right) \quad (7.144)$$

where the amplitude version is obtained from (7.144) by replacing ζ by a^2 . An example of how the shape parameter α controls the heaviness of the distribution tails is shown in Fig. 7.10. In the figure, the probability of false alarm is shown as a function of the normalized instantaneous intensity (i.e., the instantaneous intensity

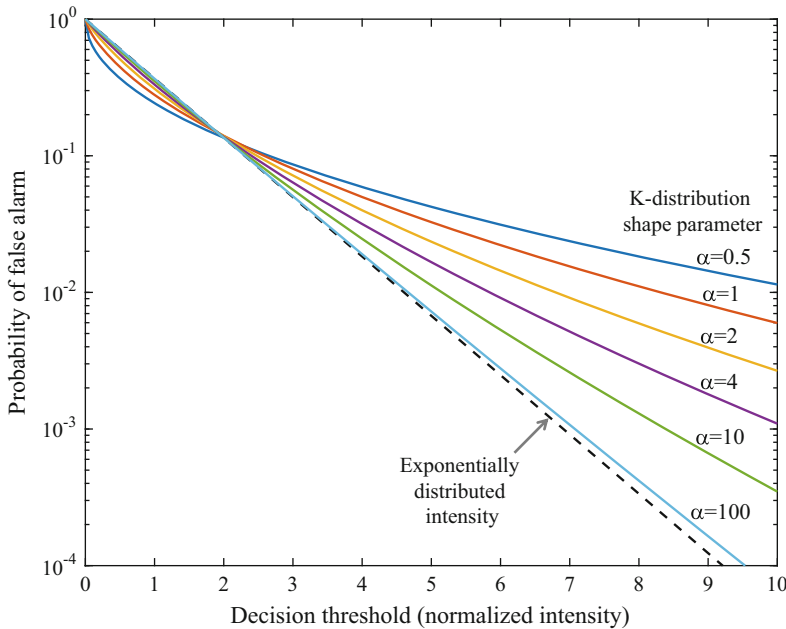


Fig. 7.10 Probability of false alarm for an exponentially distributed instantaneous intensity and the K distribution with various values of the shape parameter

has unit mean). When α is small, the distribution exhibits a very high P_f relative to the Gaussian-induced exponentially distributed instantaneous intensity at the larger decision thresholds. As would be expected from a central-limit-theorem argument and recalling that the number of elemental scatterers $n_e = 2\alpha$, increasing α moves the K distribution closer to the Gaussian-induced standard which is shown as an exponentially distributed instantaneous intensity in Fig. 7.10.

As previously mentioned, there is more than one physically meaningful derivation of the K distribution. In [47], a sum of a finite number of exponentially sized sea-floor patches, each comprising a large number of individual scatterers, was also shown to result in K-distributed reverberation. Both of the derivations in [47] are predicated on a finite number of contributors and a specific assumption about their size distributions. Although these assumptions provide a clear relationship between a physical-statistical description of the scatterers and the K-distribution shape and scale parameters, the K distribution has more general applicability as the limiting distribution of a random sum. As described in [49] or [51, Sect. 12.3], suppose the sum in (7.132) is over a random number N of scatterers,

$$Z = \sum_{i=1}^N A_i e^{j\theta_i}, \quad (7.145)$$

where N follows a negative binomial distribution. As the average number of scatterers $E[N]$ tends to infinity, Z converges in distribution to the K distribution irrespective of the distribution of the amplitudes (A_i); subject to some regularity conditions. The significance of this result lies both in not requiring knowledge of the PDF of the scatterer amplitudes to arrive at a reverberation distribution and as an example of how a large (random) number of scatterers does not automatically imply proximity to the Gaussian distribution.

One of the earlier characterizations of the K distribution comes from [50] for which a K-distributed instantaneous intensity (ζ) is described as the product

$$\zeta = VU \quad (7.146)$$

where V is gamma distributed with shape α and unit scale, U is exponentially distributed with mean λ , and U and V are assumed to be independent random variables. The exponentially distributed U represents the Gaussian-induced response of a large number of scatterers (sometimes called a speckle component) whereas V is a more slowly varying texture component representing a random modulation of the speckle. The product characterization of the K distribution is often much simpler to work with than the PDFs shown in (7.140) or (7.141). For example, it is straightforward to show the intensity moments are

$$\begin{aligned} E[\zeta^k] &= E[V^k]E[U^k] \\ &= \lambda^k \Gamma(k+1) \frac{\Gamma(\alpha+k)}{\Gamma(\alpha)} \end{aligned} \quad (7.147)$$

by noting the k th moment of a $\text{Gamma}(\alpha, \beta)$ distribution is $\beta^k \Gamma(\alpha+k)/\Gamma(\alpha)$ (see Sect. 5.6.11) and that the exponential distribution is a gamma distribution with a shape parameter equal to one. Using (7.147), the average intensity is easily seen to be

$$E[\zeta] = \alpha\lambda \quad (7.148)$$

and the average squared intensity

$$E[\zeta^2] = 2\lambda^2\alpha(\alpha+1). \quad (7.149)$$

From these, the variance of the instantaneous intensity is found to be

$$\text{Var}\{\zeta\} = E[\zeta^2] - E^2[\zeta] = (\alpha\lambda)^2 \left(1 + \frac{2}{\alpha}\right) \quad (7.150)$$

and the scintillation index

$$\text{SI} = \frac{\text{Var}\{\zeta\}}{E^2[\zeta]} = 1 + \frac{2}{\alpha} \quad (7.151)$$

is seen to only depend on the shape parameter. As $\alpha \rightarrow \infty$ the scintillation index tends to one, which represents an exponentially distributed intensity indicative of a Gaussian-distributed bandpass measurement.

The intensity moment equation in (7.147) can also be used to obtain the envelope moments via $E[A^k] = E[\zeta^{k/2}]$. For example, the envelope average is

$$E[A] = E\left[\zeta^{1/2}\right] = \frac{\sqrt{\pi\lambda}\Gamma(\alpha+0.5)}{2\Gamma(\alpha)}. \quad (7.152)$$

When α is large, the approximation $\Gamma(\alpha+0.5)/\Gamma(\alpha) \approx \sqrt{\alpha}$ can be used to show

$$E[A] \approx \frac{\sqrt{\pi\alpha\lambda}}{2} = \sigma\sqrt{\frac{\pi}{2}}, \quad (7.153)$$

where $\alpha\lambda = 2\sigma^2$ relates the K-distribution power to that of the Rayleigh distribution (e.g., see Sect. 5.6.12) as expected.

Parameter estimation for the K distribution can be complicated. A method-of-moments approach from [57] is described in Sect. 6.3.5, but has a non-zero probability of resulting in non-invertible moment equations. Maximum-likelihood estimation either requires a numerical search over a likelihood function or iterative techniques such as the expectation-maximization algorithm [58], both of which can be computationally intensive owing to the Bessel function in the PDF. A computationally efficient alternative found in [59] uses a Bayesian adaptation of the method-of-moments algorithm so as to always provide an estimate. Cramér-Rao lower bounds for the K-distribution parameters can be found in Sect. 7.4.3.6.

Exercise 7.7 Use the compound representation of the K distribution in (7.146) to derive the PDF of the instantaneous intensity.

Exercise 7.8 Use the compound representation of the K distribution in (7.146) to simulate K-distributed samples of the instantaneous intensity. Implement the method-of-moments estimator described in Sect. 6.3.5 to estimate the shape parameter for $\alpha = 1, 10$, and 50 using 200 samples at a time. After repeating this 100 times, what percentage of the trials produced invertible moment equations for each value of α ?

7.4.3.4 Poisson-Rayleigh Distribution

The Poisson-Rayleigh distribution [60] represents a scenario where a random number (M) of identically distributed zero-mean complex-Gaussian discrete con-

tributions are observed at the complex-envelope stage in background comprising zero-mean, complex-Gaussian distributed noise. An example from [60] can be found in scattering from M discrete bubble clouds in the presence of ambient noise. The number M is assumed to be Poisson distributed with mean α while the Gaussian contributions are zero mean and have power λ_c for the continuous background and λ_d for the discrete contributions. The most compact way to describe the Poisson-Rayleigh distribution chain is that, conditioned on M , the instantaneous intensity will be exponentially distributed with mean $\lambda_c + M\lambda_d$,

$$\zeta | M \sim \text{Expon}\{\lambda_c + M\lambda_d\}. \quad (7.154)$$

From this representation, the average intensity is easily seen to be

$$E[\zeta] = E_M[E[\zeta|M]] = \lambda_c + \alpha\lambda_d \quad (7.155)$$

and the variance as

$$\begin{aligned} \text{Var}\{\zeta\} &= E_M\left[E[\zeta^2|M]\right] - \{E_M[E[\zeta|M]]\}^2 \\ &= (\lambda_c + \alpha\lambda_c)^2 + 2\alpha\lambda_d^2. \end{aligned} \quad (7.156)$$

The instantaneous-intensity PDF can be described as a weighted sum over all possible values of M ,

$$f_I(\zeta) = \sum_{m=0}^{\infty} \left[\frac{\alpha^m e^{-\alpha}}{m!} \right] \left[\frac{1}{(\lambda_c + m\lambda_d)} e^{-\zeta/(\lambda_c + m\lambda_d)} \right] \quad (7.157)$$

for $\zeta \geq 0$. The first term in brackets is the Poisson PDF providing the probability $M = m$ that then weights the exponential PDF found in the second term in brackets.

The CDF of the instantaneous intensity for the Poisson-Rayleigh distribution chain is similarly a Poisson mixture of exponential CDFs,

$$F_I(\zeta) = \sum_{m=0}^{\infty} \left[\frac{\alpha^m e^{-\alpha}}{m!} \right] \left[e^{-\zeta/(\lambda_c + m\lambda_d)} \right]. \quad (7.158)$$

Because the characteristic function of the complex envelope of the Poisson-Rayleigh distribution has a very simple form (see Table 7.7 in Sect. 7.5.5), evaluation of the CDF can be performed very efficiently using the Hankel transform as described in Sect. 7.5.5.

The Poisson-Rayleigh distribution chain simplifies to the Rayleigh distribution chain when $\alpha \rightarrow 0$ and also when $\alpha \rightarrow \infty$ if $\lambda_d \propto 1/\alpha$. When $\lambda_c = \lambda_d$, the Poisson-Rayleigh is similar to a K distribution with a shape parameter $\alpha_k = \alpha(1 + 1/\alpha)^2$ and scale $\lambda_k = \lambda_d\alpha/(1 + \alpha)$, although not identical. This illustrates how the

Poisson-Rayleigh distribution is more general than the K distribution if it is to be used in a phenomenological manner.

Although the distribution chain described in Sect. 7.3.6.1 was characterized as starting with the complex envelope, it can also start with a real bandpass random process. For example, the Poisson-Rayleigh characterization could arise from a Poisson-weighted mixture of real zero-mean bandpass Gaussian components with variance $\lambda_c + m\lambda_d$ for $m = 0, 1, 2, \dots$. This is precisely the characterization of Middleton's Class-A noise model [37], which is used to represent impulsive noise with bandwidth less than that of the sensor.

Parameter estimation for the Poisson-Rayleigh distribution is generally accomplished through the method-of-moments [60, 61]. However, any of the techniques for estimating the parameters of the Middleton Class-A noise model are also applicable (e.g., see [62–64]).

7.4.3.5 Other Common Models

McDaniel's Model

The model derived by McDaniel in [65] describes the effect of limiting scattering contributions in both bearing and range. The result, as stated for the instantaneous intensity, can be described by the product

$$\zeta = \lambda V_1 V_2 \quad (7.159)$$

where λ is a scale parameter and V_1 and V_2 are independent gamma-distributed random variables with unit scale and shape parameters α_1 and α_2 , respectively. The product description allows simple evaluation of the average instantaneous intensity,

$$E[\zeta] = \lambda \alpha_1 \alpha_2. \quad (7.160)$$

and its variance,

$$\text{Var}\{\zeta\} = (\lambda \alpha_1 \alpha_2)^2 \left(\frac{1}{\alpha_1} + \frac{1}{\alpha_2} + \frac{1}{\alpha_1 \alpha_2} \right). \quad (7.161)$$

The PDF of the instantaneous intensity can be found by conditioning on V_2 to describe ζ as being gamma distributed with shape α_1 and scale λV_2 followed by taking an expectation over V_2 . The result, as found in [66], is

$$f_i(\zeta) = \frac{2}{\lambda \Gamma(\alpha_1) \Gamma(\alpha_2)} \left(\frac{\zeta}{\lambda} \right)^{\frac{\alpha_1 + \alpha_2}{2} - 1} K_{\alpha_2 - \alpha_1} \left(2\sqrt{\frac{\zeta}{\lambda}} \right) \quad (7.162)$$

for $\zeta \geq 0$. From the product formulation in (7.159), McDaniel's model can be seen as a generalization of the K distribution, which arises when one of the gamma random variables has shape parameter equal to one and is therefore exponentially distributed. It will simplify to the Rayleigh distribution chain when $\alpha_1 = 1$, $\alpha_2 \rightarrow \infty$ and $\lambda \propto 1/\alpha_2$.

As described in [66], the CDF of McDaniel's model requires evaluation of a generalized hypergeometric function, although a simpler finite-summation form exists when $\alpha_2 - \alpha_1$ is an integer. Alternatives include numerical integration of the PDF in (7.162) or the Hankel-transform approach presented in Sect. 7.5.5.

Parameter estimation for McDaniel's model is most easily accomplished by the method-of-moments [67]. However, similar to the K distribution, this approach occasionally results in non-invertible moment equations.

SIRV Models

One of the few multivariate heavy-tailed distribution models is the spherically invariant random vector (SIRV) model [68, 69]. At the complex-envelope stage, a vector of data (which could represent samples in time or space) is modeled as the product between a non-negative random amplitude (A) and a statistically independent zero-mean complex Gaussian random vector (\mathbf{z}),

$$\mathbf{x} = A\mathbf{z}. \quad (7.163)$$

Correlation between elements of the vector can be induced by defining a covariance matrix for \mathbf{z} while the heavy tails of the PDF are controlled by the PDF of A . The instantaneous intensity of a single element of the vector can be described by the product

$$\zeta = A^2 U \quad (7.164)$$

where U is an exponentially distributed random variable. Clearly the SIRV model simplifies to the Rayleigh distribution chain when A is constant. From the product formulation in (7.164), it can be seen that it also contains the K distribution as a sub-member when A^2 is gamma distributed.

Generalized Pareto (GP)

A common SIRV model is the generalized Pareto distribution (GPD) which is described in detail in [41, Ch. 20] and can be found here in Sect. 5.6.20. The GPD has a shape parameter γ and a scale parameter λ and contains the exponential distribution as a sub-member when $\gamma = 0$. As shown in [70] it arises in the product formulation of (7.164) when $1/A^2$ is gamma distributed with shape γ^{-1} and scale γ (i.e., A^2 is inverse-gamma distributed). The GPD instantaneous intensity can also

be described as the scale of an F_{2,v_2} random variable where $v_2 = 2/\gamma$ and as a limiting form used to represent the tails of a distribution, which allows representing very heavy-tailed clutter [71, 72]. The extent to which a heavy-tailed PDF can be represented by the GPD is emphasized by noting that the mean of the distribution ($= \lambda/(1 - \gamma)$) is infinite when the shape parameter $\gamma \geq 1$ and that the variance is infinite when $\gamma \geq 0.5$.

The PDF and CDF of the GPD are, respectively,

$$f_l(\zeta) = \frac{1}{\lambda(1 + \frac{\gamma}{\lambda}\zeta)^{\gamma^{-1}+1}} \quad (7.165)$$

and

$$F_l(\zeta) = 1 - \frac{1}{(1 + \frac{\gamma}{\lambda}\zeta)^{\gamma^{-1}}} \quad (7.166)$$

for $\zeta > 0$. The average and variance of the instantaneous intensity are, respectively,

$$E[\zeta] = \frac{\lambda}{1 - \gamma} \quad (7.167)$$

for $\gamma < 1$ and

$$\text{Var}\{\zeta\} = \frac{\lambda^2}{(1 - \gamma)^2(1 - 2\gamma)} \quad (7.168)$$

for $\gamma < 0.5$.

Although no closed-form solution exists for the maximum-likelihood estimators of the GPD parameters, it is amenable to an iterative evaluation and a simple alternative can be found using the method-of-moments.

Weibull

The Weibull distribution [41, Ch. 21] and Sect. 5.6.18 has seen significant development in the radar community [73–75]. The Weibull distribution arises when an exponential random variable U is raised to the power $1/\beta$,

$$\zeta = \lambda U^{1/\beta}. \quad (7.169)$$

The Weibull distribution might naturally be expected to represent the instantaneous intensity because it simplifies to an exponential distribution when $\beta = 1$. However, it also simplifies to the Rayleigh distribution when $\beta = 2$ and has been applied

to both stages. This arises because the Weibull distribution is a closed family¹¹ when raising the random variable to a power. As such, it is important to define if a Weibull parameterization is intended for the envelope or instantaneous intensity. For example, if the instantaneous intensity is Weibull distributed with parameterization $\zeta \sim \text{Wbl}(\beta, \lambda)$, then the envelope is also Weibull distributed but with parameterization $A = \sqrt{\zeta} \sim \text{Wbl}(2\beta, \sqrt{\lambda})$. Conversely, if the envelope is Weibull distributed with parameterization $A \sim \text{Wbl}(\beta, \lambda)$, the instantaneous intensity is Weibull distributed with parameterization $\zeta = A^2 \sim \text{Wbl}(\beta/2, \lambda^2)$.

The PDF and CDF of the Weibull distribution when used to describe the instantaneous intensity are, respectively,

$$f_I(\zeta) = \frac{\beta \zeta^{\beta-1}}{\lambda^\beta} e^{-(\zeta/\lambda)^\beta} \quad (7.170)$$

and

$$F_I(\zeta) = 1 - e^{-(\zeta/\lambda)^\beta} \quad (7.171)$$

for $\zeta > 0$. The average and variance of the instantaneous intensity are, respectively,

$$E[\zeta] = \lambda \Gamma\left(1 + \beta^{-1}\right) \quad (7.172)$$

and

$$\text{Var}\{\zeta\} = \lambda^2 \left\{ \Gamma\left(1 + 2\beta^{-1}\right) - \left[\Gamma\left(1 + \beta^{-1}\right) \right]^2 \right\}. \quad (7.173)$$

As can be seen by the SI curve shown in Fig. 7.8, the tails of the distribution become heavier tailed than the exponentially distributed intensity when $\beta < 1$. A mildly interesting coincidence occurs for $\beta = 0.5$ where the Weibull distribution and the K distribution are related: $K(0.5, \lambda) \equiv \text{Wbl}(0.5, \lambda/4)$.

The maximum-likelihood estimates of the Weibull distribution parameters require solution of a pair of simultaneous equations that can be accomplished in a simple iterative technique. The method-of-moments requires solution of one non-linear moment equation. Details for both estimation approaches are found in [41, Ch. 21] and [76, Ch. 22], the latter because the logarithm of a (two-parameter) Weibull-distributed random variable follows a Type-1 extreme value distribution.

¹¹A distribution family is closed under a mathematical operation if the result of the operation is still within the family. For example, the Gaussian distribution is closed under translation, scale, and the addition of other Gaussian random variables.

Log-Normal

The log-normal distribution [41, Ch. 14] and Sect. 5.6.21 has also been applied to both radar and sonar data [73, 77]. It is most easily described by noting that the logarithm of the random variable is Gaussian distributed with mean μ and variance γ ,

$$\log \zeta \sim \mathcal{N}(\mu, \gamma). \quad (7.174)$$

Because of this relationship, it is commonly used to represent the envelope or instantaneous intensity when data converted into decibels is determined to be Gaussian distributed. That is, the envelope or instantaneous-intensity is log-normally distributed. Similar to the Weibull distribution, the log-normal distribution is closed when the random variable is raised to a power. If the instantaneous intensity is log-normal distributed with parameterization $\zeta \sim \text{LN}(\mu, \gamma)$, then the envelope is also log-normal distributed, but with parameterization $A = \sqrt{\zeta} \sim \text{LN}(\mu/2, \gamma/4)$. Conversely, if the envelope is log-normal distributed with parameterization $A \sim \text{LN}(\mu, \gamma)$, the instantaneous intensity is log-normal distributed with parameterization $\zeta = A^2 \sim \text{LN}(2\mu, 4\gamma)$.

The PDF and CDF of the log-normal distribution are, respectively,

$$f_l(\zeta) = \frac{1}{\zeta \sqrt{2\pi\gamma}} e^{-(\log(\zeta)-\mu)^2/(2\gamma)} \quad (7.175)$$

and

$$F_l(\zeta) = \Phi\left(\frac{\log(\zeta) - \mu}{\sqrt{\gamma}}\right) \quad (7.176)$$

for $\zeta > 0$ where $\Phi(z)$ is the CDF of the standard Gaussian distribution. The average intensity is

$$E[\zeta] = e^{\mu+\gamma/2} = \lambda e^{\gamma/2}, \quad (7.177)$$

where $\lambda = e^\mu$ transforms μ into a proper scale parameter. The variance of the instantaneous intensity is

$$\text{Var}\{\zeta\} = e^{2\mu+\gamma} (e^\gamma - 1) = \lambda^2 e^\gamma (e^\gamma - 1). \quad (7.178)$$

Parameter estimation for the log-normal distribution is easily performed by taking the logarithm of the data and applying the standard estimation techniques for Gaussian-distributed data.

7.4.3.6 Performance Bounds on Parameter Estimation

When analyzing heavy-tailed data it is common to estimate the parameters of a particular distribution either for use in subsequent signal processing, to approximate the probability of false alarm, or for inference related to the parameters of the distribution. The Cramér-Rao lower bound (CRLB; see Sect. 6.3.3) describes the smallest variance attainable with an unbiased estimator. The CRLB of the shape, scale, and average intensity are shown in Table 7.6 for the two-parameter common heavy-tailed distributions (i.e., K, generalized Pareto, Weibull, and log-normal distributions). What is shown in the table is the CRLB given a single instantaneous-intensity sample. The CRLB for n independent and identically distributed instantaneous-intensity samples is the per-sample value from Table 7.6 divided by n . The square root of the bounds for the shape parameter and the average intensity are displayed in Figs. 7.11 and 7.12, respectively. The square root of the bound, which is a lower bound on the standard deviation of the parameter estimator, is used so the vertical axis is in the same scale as the parameter itself. As seen in Fig. 7.11, the CRLB for the shape parameter of the K, Weibull, and log-normal distributions is proportional to the parameter squared (i.e., the lower bound on the standard deviation is proportional to the parameter). For the K distribution the result is for $\alpha \geq 0.8$ and changes to a power-law relationship when the scale parameter is unknown.

The CRLB for the shape and scale parameters is shown both when the other parameter is known and when it is unknown. The difference describes how coupled the parameters are (e.g., there is no coupling in the log-normal distribution, minimal coupling for the Weibull distribution, and significant coupling in the K distribution). The effect can be seen in Fig. 7.11 where significant coupling of the parameters for the K distribution indicates that the variance of an unbiased estimator will be much larger when the scale parameter is unknown. The CRLBs for the K distribution shown in Table 7.6 are approximations valid only for $\alpha \geq 0.8$. The approximation for estimation of α when the scale is known comes from [47, App. B] whereas the others were obtained through least-squared-error fits¹² to numerical evaluation of the CRLB using the characteristic function method presented in [78]. When $\alpha < 0.8$, the numerically obtained bounds rose above the equations presented in Table 7.6, indicating these can still be used as loose lower bounds.

As described in [78], when one parameter (λ) is a scale parameter, the CRLB of the other parameter(s) does not depend on it. This can be seen in the first two rows of Table 7.6 where the bounds are strictly functions of the shape parameter. As seen in the second two rows of Table 7.6, it can also be seen that the CRLB for the scale parameter is proportional to its square (λ^2). By noting that the off-diagonal term in the Fisher information matrix (describing the coupling between the parameters)

¹²Note that the approximations in Table 7.6 for the K distribution are accurate enough for use as a CRLB, but not accurate enough to obtain the off-diagonal term of the Fisher information matrix without adding terms in the $1/\alpha$ polynomial.

Table 7.6 Cramér-Rao lower bound (CRLB) per sample on the variance of unbiased estimators for the shape and scale parameters of common heavy-tailed distribution models. The CRLB for the average intensity (P_I) is also shown when the other parameters are unknown

Distribution	K	Generalized Pareto	Weibull	Log-normal
CRLB for shape (known scale)	$\approx \alpha^2$	$(\gamma + 1/2)(\gamma + 1)$	$\frac{\beta^2}{1 + \psi^2(2) + \zeta(2, 2)} \approx (0.74\beta)^2$	$2\gamma^2$
CRLB for shape (unknown scale)	$\approx 5.75\alpha^{3.62}$	$\frac{(1 + 2\gamma)(1 + \gamma)^2}{1 + 4\gamma - \gamma^2}$	$\frac{\beta^2}{1 + \zeta(2, 2)} \approx (0.78\beta)^2$	$2\gamma^2$
CRLB for scale (known shape)	$\approx \lambda^2(1 + 1/\alpha)$	$\lambda^2(1 + 2\gamma)$	$\frac{\lambda^2}{\beta^2}$	γ (for μ)
CRLB for scale (unknown shape)	$\approx \lambda^2\alpha^{1.8}\left(3 + \frac{7.8}{\alpha}\right)$	$2\lambda^2 \frac{(1 + \gamma)(1 + 2\gamma)}{(1 + 4\gamma - \gamma^2)}$	$\frac{\lambda^2}{\beta^2} \left[1 + \frac{\psi^2(2)}{1 + \zeta(2, 2)}\right] \approx [1.053 \frac{\lambda}{\beta}]^2$	γ (for μ)
CRLB for P , the average intensity	$\approx P_I^2\left(1 + \frac{1.3}{\alpha}\right)$	$P_I^2 \frac{(1 + \gamma)^2(1 + 2\gamma)}{(1 + 4\gamma - \gamma^2)}$	$\frac{P_I^2}{\beta^2} \left[1 + \frac{[\psi(2) - \psi(1 + \beta^{-1})]^2}{1 + \zeta(2, 2)}\right]$	$P_I^2 \gamma \left(1 + \frac{\gamma}{2}\right)$

Note that the approximations for the K distribution are only accurate CRLBs for $\alpha \geq 0.8$; the actual CRLB for $\alpha < 0.8$ is higher

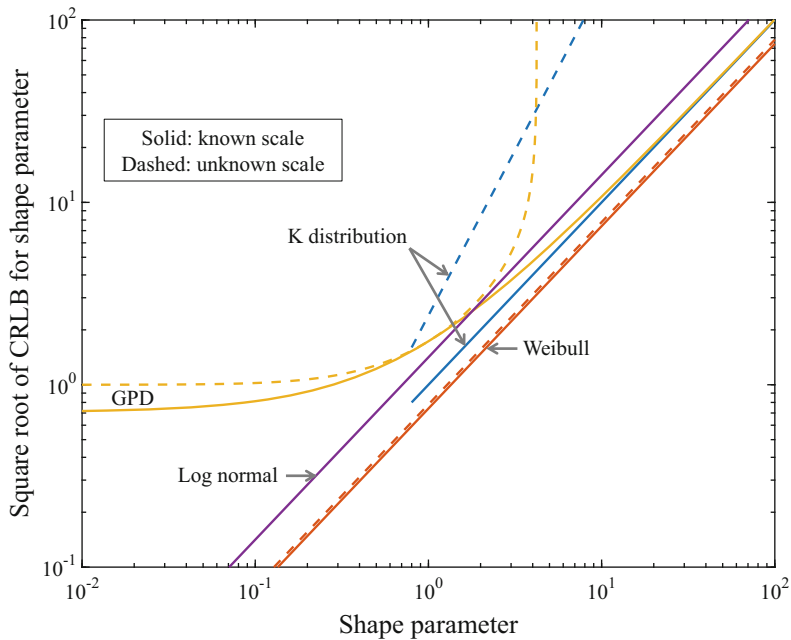


Fig. 7.11 Square root of the per-sample CRLB for the shape parameter of common heavy-tailed distributions. The solid lines are for when the scale parameter is known and the dashed lines are for when it is unknown

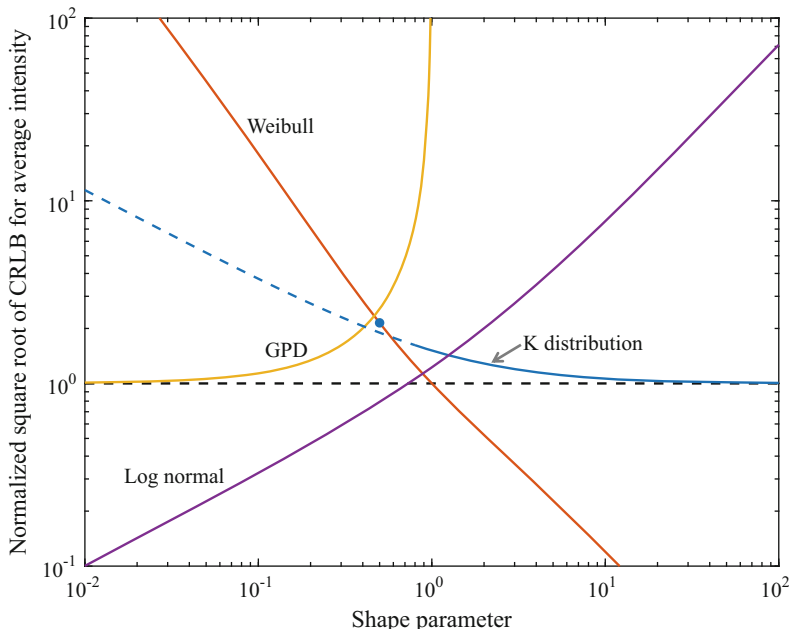


Fig. 7.12 Square root of the per-sample CRLB for the average intensity of common heavy-tailed distributions divided by the average intensity. The black dashed line is representative of an exponentially distributed instantaneous intensity

is inversely proportional to λ , it can also be shown that the CRLB of the average intensity (P_i) is proportional to the square of the true value, as seen in the last row of Table 7.6.

The square root of the CRLB of the average intensity (P_i) is shown in Fig. 7.12 with normalization by P_i . If the instantaneous intensity is exponentially distributed, the CRLB is P_i^2 so the normalized bound on the standard deviation is one, which is shown as a black dashed line in Fig. 7.12. The significance of this figure lies in the increase seen in the bound above that for an exponentially distributed instantaneous intensity, which implies estimation of the average power suffers relative to the nominal Rayleigh-distribution-chain scenario. This occurs when the tails of the distribution rise above the exponential, as identified in Table 7.5 when $SI > 1$. For example, when $\beta < 1$ in the Weibull distribution, when $\gamma > 0$ in the generalized Pareto, and $\alpha < \infty$ in the K distribution. Because the log-normal distribution does not contain the exponential distribution as a sub-member, the CRLB exceeds that of the exponential distribution when $\gamma > \sqrt{3} - 1 \approx 0.73$ rather than when its SI is greater than one (i.e., $\gamma > \log 2 \approx 0.69$). Thus, when the noise or reverberation has a heavy-tailed PDF, more data are required to obtain the same estimation accuracy as for the nominal Rayleigh distribution chain.

As an example, consider heavy-tailed K-distributed data with $\alpha = 1$, for which $SI = 1 + 2/\alpha = 3$. A minimum of $1 + 1.3/\alpha = 2.3$ times more data are necessary to achieve the same estimation performance of the average intensity as when the data follow the Rayleigh distribution chain. The loose lower bound of the CRLB for the K distribution is shown in Fig. 7.12 as a dashed line (for $\alpha < 0.8$). Noting that the K and Weibull distributions are identical when their shape parameters both equal 0.5, the CRLB on the average intensity should be identical and located at the blue dot on the Weibull bound. This illustrates how the actual CRLB is above the approximation found in Table 7.6 when $\alpha < 0.8$.

7.4.3.7 Mixture Distributions

When multiple sources of noise or reverberation are present in a measurement it is common for one of them to be considered a persistent, Gaussian-distributed, background component and the others assumed to intermittently produce transient or impulsive sounds that occasionally dominate the background. From a statistical perspective, this scenario naturally leads to using a mixture model to represent the distribution of a single instantaneous-intensity sample. The ambient-noise examples described in Sect. 7.4.1 include obvious transient events such as ice cracking, airgun blasts, and impulsive sounds from marine fauna. For a reverberation process, a temporally transient event in the delay domain represents a spatial inhomogeneity in the scattering sources. Examples of this include scattering from fish schools, rock outcrops, or otherwise patchy seafloors [79, 80]. A simulated example of normalized instantaneous-intensity samples from such a process is shown in Fig. 7.13a. In [81] such a scenario has been termed a “split aggregation” of scatterers in contrast to a “mixed assemblage” in which both types of sources are always present. A mixed assemblage is shown in Fig. 7.13b; it has an identical mixture distribution to that

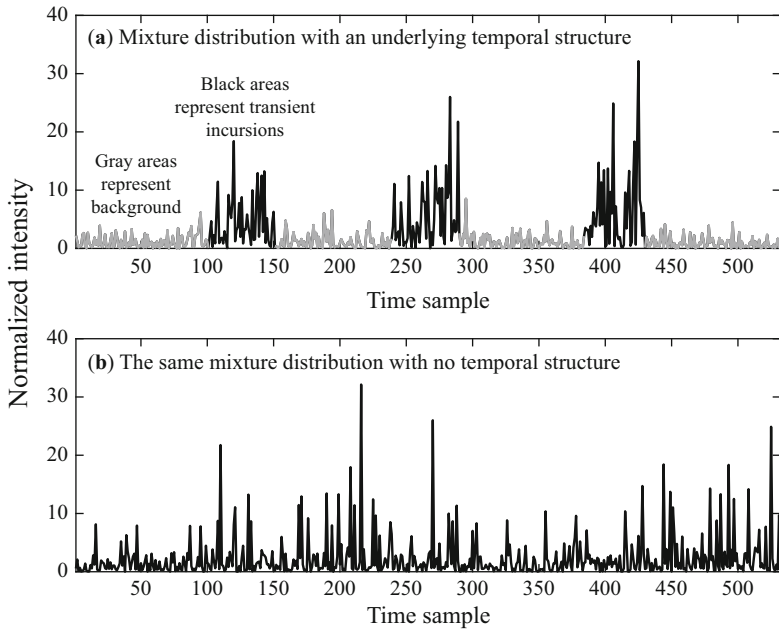


Fig. 7.13 Two examples of normalized intensity data from mixture distributions: **(a)** one with an underlying temporal structure and **(b)** one with the same mixture distribution but no temporal structure

shown in Fig. 7.13a, but no discernible temporal structure. These definitions clearly depend on the resolution of sensing system and the size of the analysis window in addition to the physical distribution of scatterers (e.g., decreasing the system resolution and increasing the analysis window in Fig. 7.13a might make the split aggregation a mixed assemblage). This example illustrates how the same mixture distribution can represent vastly difference physical scenarios. A priori knowledge of the existence of temporal structure such as that shown in Fig. 7.13a would allow incorporating it, perhaps as a hidden Markov model directing changes between the different sources.

The PDF of a mixture distribution is a weighted sum of the PDFs of each component,

$$f_i(\xi) = \sum_{i=1}^n \rho_i f_i^i(\xi), \quad (7.179)$$

where $f_i^i(\xi)$ is the instantaneous-intensity PDF for the i th component. In order for (7.179) to be a proper distribution, the weights must be non-negative ($\rho_i \geq 0$) and sum to one, $\sum_{i=1}^n \rho_i = 1$. The data from a random draw of a mixture distribution can be interpreted as arising from the i th component with probability

ρ_i . From this interpretation it is easy to see that the PDFs of the complex envelope or envelope are simply similarly weighted sums of the respective component PDFs; that is, if one member of a distribution chain is a mixture distribution, the other members of the chain are similarly composed mixtures. For example, the envelope PDF of the mixture in (7.179) is

$$f_A(a) = \sum_{i=1}^n \rho_i f_A^i(a), \quad (7.180)$$

where $f_I^i(\zeta)$ and $f_A^i(a)$ are related according to (7.86). Thus a mixture of zero-mean complex-Gaussian distributions at the complex envelope produces an identical mixture of Rayleigh distributions at the envelope and an identical mixture of exponential distributions for the instantaneous intensity.

It is important to note that when one of the components is an ever-present (i.e., continuous) background, as is common for ambient noise, the PDF of the data when the transient component occurs should represent the sum of the transient with the continuous background, which would be the convolution between their individual PDFs. However, if the transient component completely dominates the background noise when it is present, the PDF can be approximated by a mixture of the individual source PDFs.

Parameter estimation for mixture distributions is generally accomplished using the expectation-maximization (EM) algorithm [82, 83] or Sect. 6.3.7, which is an iterative means for obtaining a maximum-likelihood estimate (MLE). Global solutions are, however, not necessarily guaranteed so care must be taken both when initializing the algorithm and when interpreting physical meaning from the resulting parameter estimates. Within the iteration, the EM algorithm essentially requires a ML estimate for each component distribution. Because of this it is common to use distributions with simple ML estimators such as the Gaussian and Gaussian-induced distributions (i.e., Rayleigh for the envelope or exponential for the instantaneous intensity). The EM algorithm for a mixture of exponential distributions is derived in Sect. 6.3.7.

Mixture distributions provide a powerful tool in representing complicated ambient noise and reverberation distributions. For example, given enough components, a mixture of exponential random variables can represent any instantaneous-intensity distribution that can be described by a product $\zeta = VU$ where U is exponentially distributed. The difficulty in applying mixture distributions often lies in having enough data to estimate the parameters accurately. Because this becomes more difficult as the number of components increases, it is important to choose the model in each component carefully. When the data are known to primarily contain a background noise and a single transient or incursion component, it is sensible to combine an exponentially distributed background component with one of the previously described heavy-tailed distribution models. The instantaneous-intensity PDF then has the form

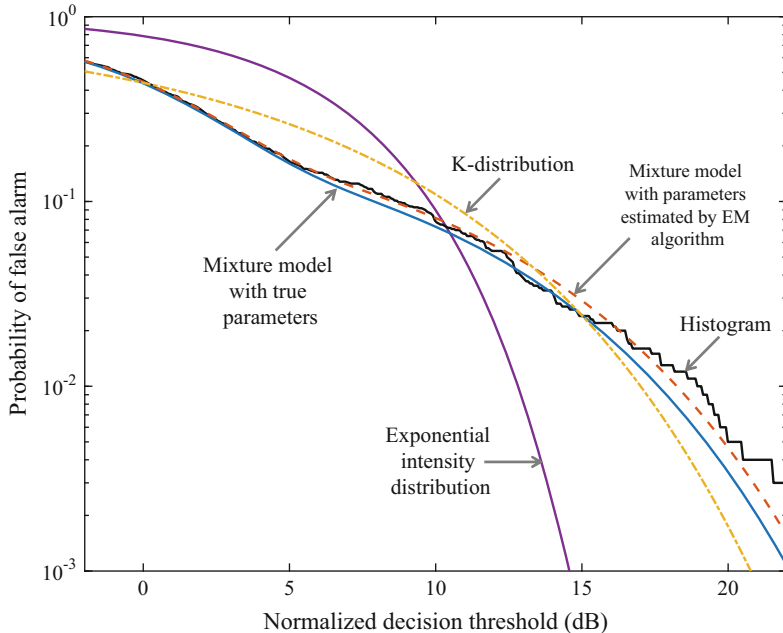


Fig. 7.14 Estimates of P_f for instantaneous-intensity data following an exponential-K mixture distribution

$$f_i(\zeta) = \frac{\rho}{\lambda_0} e^{-\zeta/\lambda_0} + (1 - \rho) f_c(\zeta; \theta) \quad (7.181)$$

where ρ is the background proportion which follows an exponential distribution with mean λ_0 and $f_c(\zeta; \theta)$ is the PDF of the non-background component having parameter vector θ . An example of the probability of false alarm (P_f) for an exponential-K mixture is shown in Fig. 7.14. As expected, estimates of P_f using single-component models fail to capture the details of the mixture model. In particular, the knee in the mixture-model P_f (beginning at a threshold of approximately 5 dB) is a key indicator that the data comprise more than one component.

As described in [84], the EM algorithm for the exponential/incursion-distribution mixture applied to n independent and identically distributed samples of the instantaneous intensity (ζ_1, \dots, ζ_n) has the following steps:

1. Obtain initial estimates of the parameters $\hat{\rho}$, $\hat{\lambda}_0$, and $\hat{\theta}$. Using a good initial estimate of the parameters both speeds convergence and makes obtaining a global maximum more likely. Options include the initialization algorithm presented in [84] or the following simpler alternative:
 - a. Estimate the background power according to

$$\hat{\lambda}_0 = \text{Median}\{\zeta_1, \dots, \zeta_n\} / \log 2 \quad (7.182)$$

- b. Obtain an estimate $\hat{\theta}$ of the incursion-distribution parameters from the full sample through standard techniques (i.e., assume all the data come from the PDF $f_c(\zeta; \theta)$).
- c. Estimate the background proportion by the fraction of samples with greater likelihood under the exponential model than the incursion distribution,

$$\hat{\rho} = \frac{1}{n} \sum_{i=1}^n \mathbb{I}\{\hat{\lambda}_0^{-1} e^{-\zeta_i/\hat{\lambda}_0} \geq f_c(\zeta_i; \hat{\theta})\} \quad (7.183)$$

where $\mathbb{I}\{\cdot\}$ is the indicator function returning one when the argument is true and is zero otherwise.

The cost of using this simple initialization algorithm over that presented in [84] is a larger number of iterations required for convergence of the ensuing EM algorithm and a higher probability of not achieving a global maximum.

- 2. In the “Expectation” step, calculate the background weight accorded each instantaneous intensity sample ζ_i for $i = 1, \dots, n$,

$$W_i = \frac{\hat{\rho} \hat{\lambda}_0^{-1} e^{-\zeta_i/\hat{\lambda}_0}}{\hat{\rho} \hat{\lambda}_0^{-1} e^{-\zeta_i/\hat{\lambda}_0} + (1 - \hat{\rho}) f_c(\zeta_i; \hat{\theta})} \quad (7.184)$$

- 3. For the “Maximization” step, use the weights to obtain new parameter estimates

$$\hat{\rho} = \frac{1}{n} \sum_{i=1}^n W_i, \quad (7.185)$$

$$\hat{\lambda}_0 = \frac{1}{n \hat{\rho}} \sum_{i=1}^n W_i \zeta_i, \quad (7.186)$$

and

$$\hat{\theta} = \arg \max_{\theta} Q(\theta) \quad (7.187)$$

where

$$Q(\theta) = \frac{1}{n} \sum_{i=1}^n (1 - W_i) \log f_c(\zeta_i; \theta) \quad (7.188)$$

is a weighted log-likelihood function for the incursion distribution. As described in [84], the maximization of $Q(\theta)$ can be exact or approximate. The exact or approximate result maximizing $Q(\theta)$ for several common distributions is presented following this algorithm description.

- 4. If the parameter estimates have not converged or if the likelihood function continues to increase significantly at each iteration, repeat from Step 2. Otherwise stop the iteration taking the current estimates of the parameters.

The maximization step in the EM algorithm results in the following parameter estimates. The description of each distribution and its parameters can be found in Sect. 7.4.3.3 (K) and 7.4.3.5 (others).

Exponential:

$$\hat{\lambda}_c = \frac{\sum_{i=1}^n (1 - W_i) \zeta_i}{\sum_{i=1}^n (1 - W_i)} \quad (7.189)$$

Log-normal:

$$\hat{\mu} = \frac{\sum_{i=1}^n (1 - W_i) \log(\zeta_i)}{\sum_{i=1}^n (1 - W_i)} \quad (7.190)$$

$$\hat{\gamma} = \frac{\sum_{i=1}^n (1 - W_i) [\log(\zeta_i) - \hat{\mu}]^2}{\sum_{i=1}^n (1 - W_i)} \quad (7.191)$$

K distribution: As described in Sect. 7.4.3.3, maximum-likelihood estimation of the K distribution parameters requires a numerical search and can be computationally intensive owing to the Bessel function evaluation. The computational intensity is exacerbated in the EM algorithm by its necessity in each iteration of the algorithm. As an alternative, the following implements the weighted method-of-moments EM algorithm described in [84] for the method-of-moments algorithm derived for the K distribution in the example found in Sect. 6.3.5:

$$T = \frac{[\sum_{i=1}^n (1 - W_i) \sqrt{\zeta_i}]^2}{[\sum_{i=1}^n (1 - W_i)][\sum_{i=1}^n (1 - W_i) \zeta_i]}, \quad (7.192)$$

$$\hat{\alpha} \approx \frac{1}{-4 \log(4\pi^{-1} \min\{T, T_{\max}\})}, \quad (7.193)$$

and

$$\hat{\lambda} = \frac{\sum_{i=1}^n (1 - W_i) \zeta_i}{\hat{\alpha} \sum_{i=1}^n (1 - W_i)} \quad (7.194)$$

where $T_{\max} = \frac{\pi}{4} e^{-1/(4\alpha_{\max})}$. To avoid the cases where the moment equations are not invertible, the shape parameter estimate is limited to $\alpha \leq \alpha_{\max}$, which can nominally be set at 100. The Bayesian adaptation of the method-of-moments estimator described in [59] as modified for use in the EM algorithm in [84] should be used if α is expected to be large. The approximate inversion from (6.95) of the non-linear moment-equation ratio relating T and $\hat{\alpha}$ is used in (7.193). An exact implementation of the inversion using the equation found in (6.93) may be useful when α is small.

Weibull or GPD: The Weibull and generalized Pareto distributions do not have simple closed-form maximum-likelihood estimators and so require an alternative to the standard EM algorithm. Because the derivatives of their log-likelihood functions are simply obtained, the EM Gradient algorithm [83, Sect. 4.13] is applicable. The resulting algorithm description and the gradient and Hessian matrix of $Q(\theta)$ for these distributions can be found in [84].

Exercise 7.9 Show that a mixture of intensity PDFs results in an identical mixture of the corresponding envelope PDFs (i.e., show (7.180) given (7.179)) using the approach described in Sect. 5.3.3 for one-to-one mappings of random variables.

Exercise 7.10 Simulate data from an exponential-K mixture where the exponentially distributed data have mean $\lambda_0 = 1$ and the K-distribution shape and scale parameters are, respectively, $\alpha = 0.5$ and $\lambda = 20$. Simulate $n = 1000$ samples for $\rho = 0.7$. If there are n samples, the number of background samples can be taken as a binomial (n, ρ) random variable with the remaining coming from the K distribution. Example random draws from the binomial $(1000, 0.7)$ distribution are 684, 716, 711, 688, and 697. Estimate P_f using a histogram and compare it to the model P_f .

Exercise 7.11 Implement the EM algorithm for an exponential-K mixture and apply it to the data simulated in the previous exercise. Compare P_f of the mixture model using the estimated parameters to the true P_f and the histogram.

Exercise 7.12 Implement the EM algorithm for an M -component exponential mixture and apply it to the previously simulated data from the exponential-K mixture. Compare P_f obtained from the exponential mixture approximation as a function of M . How many components are necessary to accurately represent the true P_f ?

7.5 Signal and Signal-Plus-Noise Statistical Models

As described in Sect. 6.2, detection algorithms are derived using a statistical characterization of the noise measurement and of the combined noise-plus-signal measurement. The latter can be obtained as a convolution of the PDF of the complex envelope of the noise measurement with that of the signal. In some scenarios, physical models can be used to predict the PDF of a signal measurement. The most basic example can be found in a communications pulse producing a deterministic signal when the sensor is close enough to the projector and the ocean is static. Another example can be found in how propagation through the underwater acoustical channel can produce either a Rayleigh- or Rician-distributed signal envelope as described in Sect. 7.2.3.2. In other cases the generation of the sound might dictate a particular distribution, such as when an active sonar echo comprises multiple independent sources to produce a Rayleigh-distributed envelope. Beyond these simple scenarios where either very simple physics or application of the central limit theorem simplify the analysis, it becomes difficult to obtain an accurate statistical model for the signal measurement. As a result of this, most detection algorithms are derived using one of several common statistical models under the assumption that the signal of interest is close enough for the resulting detector to provide adequate performance, which it generally does. The four common signal models presented in this section are the

- **deterministic signal** [alias: non-fluctuating, Marcum, or Swerling 0],
- **Gaussian-fluctuating signal** [alias: Rayleigh-envelope, fluctuating signal, or Swerling 1],
- **Rician signal** [alias: non-central chi-squared], and

- **gamma-fluctuating-intensity (GFI) signal** [alias: chi-squared or Weinstock].

The first two are often taken as the extremes of a “coherent” (deterministic) or “incoherent” (Gaussian-fluctuating) signal. The latter two can represent these two extremes with the Rician signal essentially a combination of the two and the gamma-fluctuating-intensity (GFI) signal a generalization that allows fluctuations more extreme than the Gaussian-fluctuating signal. This is illustrated in Fig. 7.15 where the probability of detection (P_d) is shown as a function of SNR for each signal type using a decision threshold yielding $P_f = 10^{-4}$. For the higher values of SNR, the deterministic signal presents the best P_d , followed by the Rician, Gaussian-fluctuating, and finally the GFI signal with $\alpha_o = 0.5$ (a shape parameter). As described in [85], signal fluctuations generally degrade a high-quality detection operating point whereas they can improve a low-quality one. An example of the latter scenario is seen in Fig. 7.15 at the lower values of SNR where the GFI signal has the highest P_d .

The four signal types are presented in Sects. 7.5.1–7.5.4. In addition to a statistical characterization of the signal, the PDF of the instantaneous intensity for the signal in the presence of additive, independent, zero-mean Gaussian noise is presented. These are used in Chaps. 8 and 9 to derive detection algorithms for signals with known and unknown form. As will be seen, the detectors have a coherent processing stage involving a matched filter or a bandpass filter tuned to the signal of interest. In general, the only difference in the statistical characterization before and after the filtering is a change in SNR. This means the CDF of the signal-plus-noise models presented in Sects. 7.5.1–7.5.4 can be used to obtain the probability of detection when the instantaneous intensity of the filter output is used as a detector decision statistic. Extension to the case where multiple instantaneous-intensity samples are summed prior to comparison to a decision threshold is also described (e.g., to combine echoes from multiple pulses, account for signal spreading, or to produce the decision statistic of an energy detector).

To facilitate analysis of detection performance in the presence of heavy-tailed noise or reverberation, an exact numerical technique is presented in Sect. 7.5.5 where P_d can be obtained by a Hankel transform of the signal-plus-noise complex-envelope characteristic function for the detector comparing a single instantaneous-intensity sample to a decision threshold. Several simple yet accurate approximation techniques for P_d that are applicable to the detector comprising either single or summed instantaneous-intensity samples are presented in Sect. 7.5.6.

7.5.1 Deterministic Signal

The deterministic-signal model is one where the response of the object of interest results in a complex envelope of $Z_o = A_o e^{j\theta_o}$ where $A_o > 0$ is a constant amplitude and ϕ_o is a phase that may or may not be constant from observation to observation. Regardless of the distribution of the phase, the envelope of the signal by itself is a

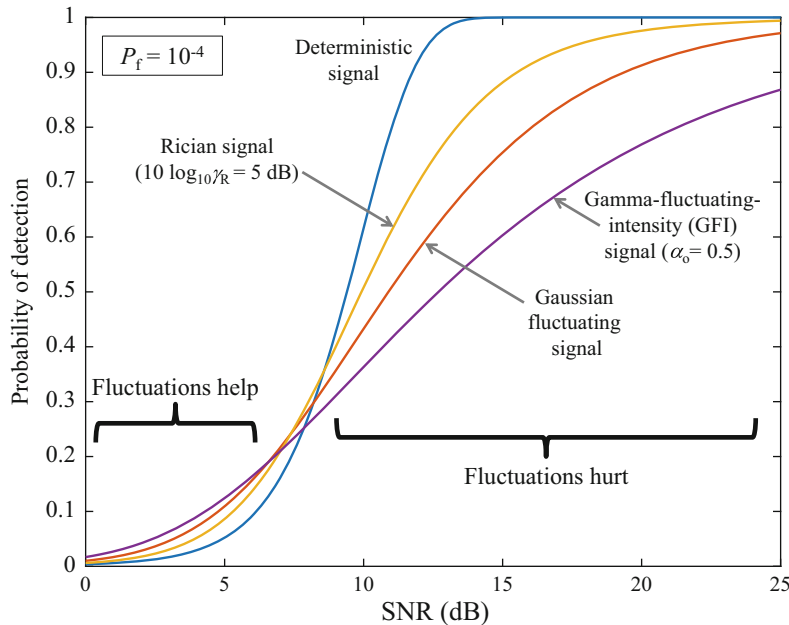


Fig. 7.15 Probability of detection as a function of SNR for examples from the four common signal models with $P_f = 10^{-4}$. While the Rician signal generally lies between the deterministic and Gaussian-fluctuating signals, the GFI signal can represent signals with more extreme fluctuations

constant $|Z_o| = A_o$ and its instantaneous intensity is a constant $|Z_o|^2 = P_o = A_o^2$. The signal is assumed to be measured in the presence of additive noise,

$$Z = A_o e^{j\theta_o} + W \quad (7.195)$$

where the noise component W is zero-mean complex-Gaussian distributed with variance λ .

The approach taken here to determine the distribution of the signal in the presence of additive Gaussian noise will be to first assume the phase is uniformly random, which allows using the simplifications and methodology described in Sects. 7.3.6 and 7.4.3.3. Interestingly, the signal-plus-noise PDFs of the envelope and instantaneous intensity are the same when the signal phase is either constant or uniformly random. The constant-phase deterministic signal case is examined in an exercise at the end of the section.

The PDF of the sum of the signal and noise at the complex envelope can be obtained from the convolution of their individual PDFs. Rather than evaluating the convolution directly, it will be carried out in the characteristic-function domain as a product and the complex-envelope PDF then obtained through an inverse transform. Under the uniformly random phase assumption, the spherically invariant form of the

characteristic function, which was introduced in Sect. 7.4.3.3, can be described as the expectation

$$\begin{aligned}\Phi_\rho(\rho) &= E[J_0(\sqrt{\rho}|Z|)] \\ &= E[J_0(\sqrt{\rho}A)] \\ &= E[J_0(\sqrt{\rho Y})].\end{aligned}\quad (7.196)$$

As shown in the latter lines of (7.196), the expectation can be carried out equivalently with the amplitude (A) or instantaneous-intensity ($Y = |Z|^2$) random variables by appropriately substituting for $|Z|$. Noting that the constant-valued response of the object of interest can be represented with a PDF through the use of a Dirac delta function placing all weight at that value, the instantaneous-intensity PDF of the signal component is

$$f_I(\zeta) = \delta(\zeta - P_o). \quad (7.197)$$

Using this in (7.196) very simply results in

$$\Phi_{\rho,o}(\rho) = J_0\left(\sqrt{\rho P_o}\right) \quad (7.198)$$

for the deterministic signal with uniformly random phase.

As noted in Sect. 7.3.6, Gaussian distributed noise with variance λ at the complex envelope produces an exponentially distributed instantaneous intensity with mean λ . Using this in (7.196) results in

$$\begin{aligned}\Phi_{\rho,n}(\rho) &= \int_0^\infty \frac{1}{\lambda} e^{-y/\lambda} J_0(\sqrt{\rho y}) dy \\ &= e^{-\rho\lambda/4}\end{aligned}\quad (7.199)$$

for the Rayleigh distribution chain where the solution to the integral is from [56, 6.614-1].

The characteristic function of the sum of the signal and noise for the deterministic signal is then the product

$$\begin{aligned}\Phi_\rho(\rho) &= \Phi_{\rho,o}(\rho)\Phi_{\rho,n}(\rho) \\ &= J_0\left(\sqrt{\rho P_o}\right) e^{-\rho\lambda/4}.\end{aligned}\quad (7.200)$$

The PDF of the complex envelope can be found using (7.136),

$$f_Z(z) = \frac{1}{4\pi} \int_0^\infty \Phi_\rho(\rho) J_0(|z| \sqrt{\rho}) d\rho$$

$$= \frac{1}{4\pi} \int_0^\infty J_0(\sqrt{\rho P_o}) e^{-\rho \lambda/4} J_0(|z| \sqrt{\rho}) d\rho \quad (7.201)$$

$$= \frac{1}{\pi \lambda} e^{-(|z|^2 + P_o)/\lambda} I_0\left(\frac{2}{\lambda} \sqrt{P_o} |z|\right) \quad (7.202)$$

where the solution to the integral in (7.201) is from [56, 6.615].

Noting that (7.202) only depends on $|z|$ and not the phase, it is clear that adding two independent components having uniformly random phase does not alter the condition; the sum also has uniform random phase. The envelope distribution can then be obtained from that of the complex envelope using (7.90), resulting in

$$\begin{aligned} f_A(a) &= 2\pi a f_Z(a) \\ &= \frac{2a}{\lambda} e^{-(a^2 + P_o)/\lambda} I_0\left(\frac{2a}{\lambda} \sqrt{P_o}\right) \text{ for } a \geq 0. \end{aligned} \quad (7.203)$$

This signal-plus-noise envelope distribution is attributed to Rice [18] and often called the Rician distribution (see Sect. 5.6.13 for more details). As will be seen in Sect. 7.5.3, this is the same distribution chain as for the “Rician” signal model. However, the parameterization of the Rician-signal or Rician-signal-plus-noise distributions differs from that of the deterministic-signal-plus-noise distribution. Noting that $I_0(0) = 1$, the Rician distribution is seen to simplify to the Rayleigh distribution with power λ when $P_o \rightarrow 0$, which appropriately arises from the Gaussian-distributed additive noise.

The instantaneous-intensity can be obtained from (7.203) using (7.86) to result in

$$\begin{aligned} f_I(\xi) &= \frac{1}{2\sqrt{\xi}} f_A(\sqrt{\xi}) \\ &= \frac{1}{\lambda} e^{-(\xi + P_o)/\lambda} I_0\left(\frac{2}{\lambda} \sqrt{\xi P_o}\right) \text{ for } \xi \geq 0, \end{aligned} \quad (7.204)$$

which simplifies to an exponential distribution with mean λ when $P_o \rightarrow 0$ to represent the noise-only scenario. Scaling the instantaneous intensity by $2/\lambda$,

$$T = \frac{2\xi}{\lambda} \sim \chi_{2,\delta}^2 \quad (7.205)$$

results in a non-central chi-squared distribution with $v = 2$ degrees of freedom and a non-centrality parameter $\delta = 2P_o/\lambda$. This allows using the tools arising from the statistics community for the non-central chi-squared distribution with the non-fluctuating signal-plus-noise model. More details on the non-central chi-squared distribution can be found in Sect. 5.6.15.

To summarize, the Rician distribution chain is characterized by a Gaussian-distributed complex envelope with a non-zero mean, an envelope following the Rician distribution, and an instantaneous intensity that is related to the non-central chi-squared distribution.

7.5.1.1 Probability of Detection

The deterministic signal is also known as a non-fluctuating signal and sometimes called a Swerling 0 or Marcum model [86, Table 2.3]. The probability of detection (P_d) for a detector comparing the instantaneous intensity to a threshold for a deterministic signal in Gaussian noise is one minus the CDF of the instantaneous-intensity PDF shown in (7.204). By using the scaling in (7.205), this can be seen to result in

$$P_d = 1 - F_{\chi^2_{2,\delta}}\left(\frac{2h}{\lambda}\right) \quad (7.206)$$

$$= Q_1\left(\sqrt{\frac{2P_o}{\lambda}}, \sqrt{\frac{2h}{\lambda}}\right) \quad (7.207)$$

where $h \geq 0$ is an intensity threshold, $F_{\chi^2_{2,\delta}}(t)$ is the CDF of the non-central chi-squared, and $Q_1(a, b)$ is the Marcum Q function. Numerical routines are readily available to evaluate both of these functions (e.g., [87], [88, App. C] or [89, App. 2D, pg. 52]) and many approximations exist for the non-central chi-squared CDF [76, Ch. 29].

7.5.1.2 Sum of Instantaneous-Intensity Samples

Suppose the detector decision statistic is formed from the sum of M samples of the instantaneous intensity,

$$\zeta_\Sigma = \sum_{m=1}^M \zeta_m \quad (7.208)$$

where the noise power λ is the same and the signal power $P_{o,m}$ allowed to vary. By applying the same scaling as in (7.205), T becomes the sum of M non-central chi-squared random variables,

$$T = \frac{2\zeta_\Sigma}{\lambda} = \sum_{m=1}^M \frac{2\zeta_m}{\lambda} \sim \chi^2_{2M,\delta_\Sigma} \quad (7.209)$$

each with two degrees of freedom and a non-centrality parameter $\delta_m = 2P_{o,m}/\lambda$. The resulting scaled decision statistic is still a non-central chi-squared distributed random variable, but with $v = 2M$ degrees of freedom and a non-centrality parameter

$$\delta_\Sigma = \sum_{m=1}^M \delta_m = \frac{2}{\lambda} \sum_{m=1}^M P_{o,m}. \quad (7.210)$$

Recall that when evaluating the ROC curve for a detector, the effect on the distribution of the decision statistic must be determined under both the signal-plus-noise and noise-only hypotheses. When no signal is present, the detector decision statistic can be seen from (7.209) to be the scale of the standard chi-squared distribution (i.e., $\delta_\Sigma \rightarrow 0$) with $2M$ degrees of freedom. Thus, when there is only noise, the decision statistic ζ_Σ is gamma distributed with shape parameter equal to M and scale parameter λ . For the additive-Gaussian noise case, all of the signal-plus-noise distributions must simplify to this distribution when the signal power is set to zero.

Exercise 7.13 Suppose a deterministic signal from the object of interest $Z_o = A_o e^{j\theta_o}$ has a constant phase as opposed to the uniformly random phase assumed earlier in this section. Because Z_o is constant, the complex-envelope of the signal-plus-noise is simply complex-Gaussian distributed with mean Z_o and variance λ . The PDF is

$$f_Z(z) = \frac{1}{\pi\lambda} e^{-|z-A_o e^{j\theta_o}|^2/\lambda}. \quad (7.211)$$

Using $f_{A,\theta}(a, \theta) = af_Z(ae^{j\theta})$ from (7.83), show that the joint PDF over the amplitude and phase of Z is then

$$f_{A,\theta}(a, \theta) = \frac{a}{\pi\lambda} \exp\left\{-\frac{(a^2 + A_o^2)}{\lambda} + \frac{2}{\lambda} A_o a \cos(\theta - \theta_o)\right\}. \quad (7.212)$$

Obtain the PDF of the envelope $A = |Z|$ by integrating (7.212) over $\theta \in (0, 2\pi)$ and show that it is identical to (7.203). The integral $I_0(z) = \pi^{-1} \int_0^\pi e^{z \cos \theta} d\theta$ from [56, 3.339] may be useful.

7.5.2 Gaussian-Fluctuating Signal

The Gaussian-fluctuating signal model arises when the response of the object of interest contains many independent random components with none dominating the others. At the complex envelope this results in a measurement

$$Z = Z_o + W \quad (7.213)$$

where Z_o is complex-Gaussian distributed with zero mean and variance P_o and the additive noise W is the same but with variance λ . The Gaussian-fluctuating signal model is known as a Swerling 1 signal [86, Table 2.5] and is often referred to as a “fluctuating” signal. In this text it is called a Gaussian-fluctuating signal to distinguish it from the gamma-fluctuating-intensity (GFI) signal model.

Because the Gaussian distribution is a closed family under addition, the signal-plus-noise measurement is also zero-mean complex-Gaussian distributed and has variance $P_o + \lambda$ owing to the independence of the signal and noise. Thus, the Gaussian-fluctuating signal produces the Rayleigh distribution chain by itself with average power P_o and also when added to Gaussian noise to produce a total power $P_o + \lambda$. The instantaneous-intensity distribution for the signal-plus-noise is simply that of an exponential random variable with mean $P_o + \lambda$,

$$f_I(\zeta) = \frac{1}{(P_o + \lambda)} e^{-\zeta/(P_o + \lambda)} \text{ for } \zeta \geq 0. \quad (7.214)$$

7.5.2.1 Probability of Detection

The probability of detection for a Gaussian-fluctuating signal in additive Gaussian noise is easily obtained by integrating (7.214) from the intensity threshold h to ∞ ,

$$P_d = e^{-h/(P_o + \lambda)} \quad (7.215)$$

for $h \geq 0$.

7.5.2.2 Sum of Instantaneous-Intensity Samples

When the detector decision statistic is a sum of instantaneous-intensity samples, as described in (7.208), the Gaussian-fluctuating signal model is the sum of M independent exponentially distributed random variables with mean $E[\zeta_m] = P_{o,m} + \lambda$ for $m = 1, \dots, M$. If the signal power is a constant P_o in each sample, the decision statistic is a gamma random variable with M degrees of freedom and scale $P_o + \lambda$; that is, $\zeta_\Sigma \sim \text{Gamma}(M, P_o + \lambda)$. This results in

$$\begin{aligned} P_d &= 1 - \int_0^h \frac{\zeta^{M-1}}{\Gamma(M)(P_o + \lambda)^M} e^{-\zeta/(P_o + \lambda)} d\zeta \\ &= 1 - F_G(h; M, P_o + \lambda) = 1 - \tilde{\gamma}(h/(P_o + \lambda); M) \end{aligned} \quad (7.216)$$

where $F_G(x; \alpha, \lambda)$ is the CDF of the gamma distribution, which is a normalized incomplete gamma function (see Sect. 5.6.11).

The assumption of independence between the multiple instantaneous-intensity samples results in what is known as a Swerling 2 multi-pulse model. As described in [86, Sect. 2.2.6] and here in Sect. 10.3.1.1 for a multiple-pulse context, the echoes decorrelate rapidly and so from pulse to pulse the instantaneous-intensity samples are statistically independent.

When the signal or noise power changes over the course of the M instantaneous-intensity samples, the distribution of the decision statistic is not a pure gamma distribution. It can be found by forming the moment-generating function (MGF) of the sum as a product of the MGFs of each term in the sum, performing a partial fraction expansion to describe it as a weighted sum of MGFs of gamma random variables followed by an inversion to the PDF. The result is a mixture of gamma distributions and so the CDF will be a mixture of incomplete gamma functions. Although this technique works well when M is not too large, numerical issues can arise if M is large and the partial fraction expansion can be tedious when there are multiple common values of the $P_{o,m}$. Viable alternatives include the approximations described in Sects. 7.5.6 and 9.2.7 and numerically inverting the characteristic function using the algorithm in [90] as described in Sect. 9.2.7.2.

7.5.3 Rician Signal

The Rician signal model [18] (but also see [91] and [92]) is used to represent a combination of the deterministic and Gaussian-fluctuating signals, which can be considered as, respectively, the coherent and incoherent components of the response of the object of interest. At the complex envelope, this results in a measurement

$$Z = A_o e^{j\theta_o} + Z_o + W \quad (7.217)$$

where $A_o = \sqrt{P_c}$ is the constant amplitude of the coherent component of the signal, θ_o its phase, Z_o is the zero-mean complex-Gaussian distributed incoherent component having power P_i , and W is the previously described additive noise. The total signal power is

$$P_o = P_c + P_i. \quad (7.218)$$

Noting that the sum $Z_o + W$ is itself a zero-mean complex-Gaussian random variable (as for the signal-plus-noise measurement of the Gaussian-fluctuating signal), the distribution of the Rician signal in noise follows the same distribution chain as for the deterministic signal in noise, but with different parameters. In particular, λ in Sect. 7.5.1 is replaced by $P_i + \lambda$ in the Rician signal model. Applying this parameterization to the scale in (7.205) results in

$$T = \frac{2\zeta}{P_i + \lambda} \sim \chi^2_{2,\delta_R} \quad (7.219)$$

following a non-central chi-squared distribution with two degrees of freedom and a non-centrality parameter

$$\delta_R = \frac{2P_c}{P_i + \lambda}. \quad (7.220)$$

Clearly when $P_i \rightarrow 0$, the Rician signal model simplifies to the deterministic signal model and when $P_c \rightarrow 0$ the Gaussian-fluctuating signal model.

7.5.3.1 Probability of Detection

Using (7.219) the probability of detection for the Rician signal in Gaussian noise can be shown to be

$$P_d = 1 - F_{\chi^2_{2,\delta_R}} \left(\frac{2h}{P_i + \lambda} \right) \quad (7.221)$$

$$= Q_1 \left(\sqrt{\frac{2P_c}{P_i + \lambda}}, \sqrt{\frac{2h}{P_i + \lambda}} \right) \quad (7.222)$$

where, as noted in Sect. 7.5.1, $h \geq 0$ is an intensity threshold, $F_{\chi^2_{2,\delta_R}}(t)$ is the CDF of the non-central chi-squared distribution, and $Q_1(a, b)$ is the Marcum Q function. At times it is useful to describe the Rician signal through the total power $P_o = P_c + P_i$ and the ratio of the coherent to incoherent power,

$$\gamma_R = \frac{P_c}{P_i}, \quad (7.223)$$

which is called the Rice power ratio. Given these two parameters, the coherent and incoherent signal powers are

$$P_c = \frac{\gamma_R}{(1 + \gamma_R)} P_o \quad \text{and} \quad P_i = \frac{P_o}{(1 + \gamma_R)}. \quad (7.224)$$

An example set of receiver operating characteristic (ROC) curves for the Rician signal is shown in Fig. 7.16 for values of the Rice power ratio ranging from -5 to 20 dB (i.e., $10 \log_{10} \gamma_R$). As expected, the Rician signal in Gaussian noise has performance ranging from that of a Gaussian-fluctuating signal in Gaussian noise (when γ_R is near zero) to that of a deterministic signal in Gaussian noise (when γ_R is large). As can be seen in Fig. 7.16, these are not bounds on P_d for all P_f , but rather represent the qualitative extremes of the Rician signal in terms of fluctuations.

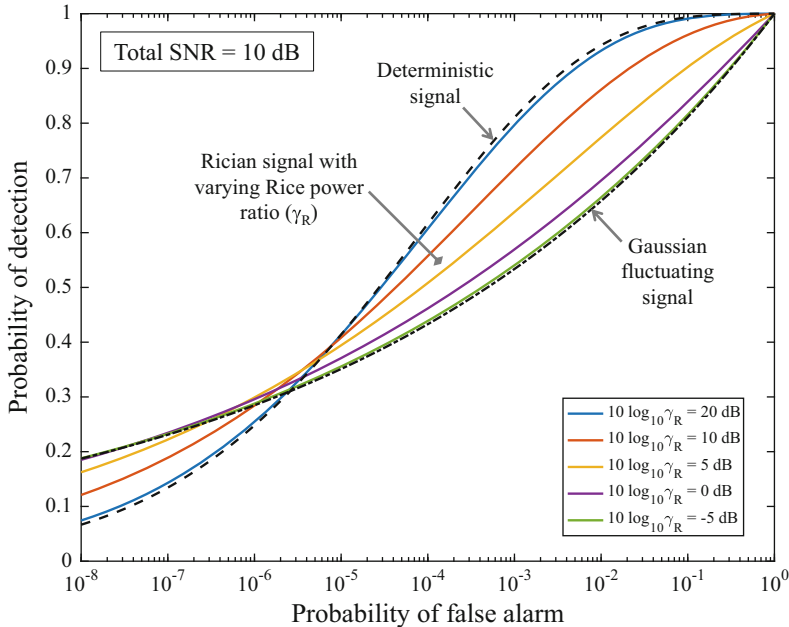


Fig. 7.16 ROC curve for a Rician signal in Gaussian noise with 10-dB total SNR and various Rice power ratios (γ_R). The figure illustrates how a Rician signal ranges between a Gaussian-fluctuating signal (low γ_R) and a deterministic signal (high γ_R)

7.5.3.2 Sum of Instantaneous-Intensity Samples

Similar to the deterministic signal in Gaussian noise, the decision statistic for a Rician signal in Gaussian noise can result in the scale of a non-central chi-squared distribution with $2M$ degrees of freedom when M independent instantaneous-intensity samples are summed. Here, however, the incoherent power of the signal must be constant across the M samples, $P_{i,m} = P_i$, which then results in

$$T = \frac{2\zeta_\Sigma}{P_i + \lambda} = \sum_{m=1}^M \frac{2\zeta_m}{P_{i,m} + \lambda} \sim \chi_{2M, \delta_\Sigma}^2, \quad (7.225)$$

where the non-centrality parameter is

$$\delta_\Sigma = \frac{2}{P_i + \lambda} \sum_{m=1}^M P_{c,m}. \quad (7.226)$$

If the incoherent signal power or noise variance change over the M samples so as to produce a non-constant power sum, the same options are available as for the Gaussian-fluctuating signal listed in the previous section.

7.5.4 Gamma-Fluctuating-Intensity (GFI) Signal

Similar to active sonar clutter, some signal fluctuations are so extreme that the Gaussian-fluctuating signal model cannot adequately represent them. Such a scenario was described in [20] as arising from focusing of a propagating sound wave during forward reflection as induced by the curvature of a rough reflecting boundary. Consider the scintillation index (SI) as a barometer of fluctuations. As shown in Table 7.8, SI for a deterministic signal is 0, SI for a Gaussian-fluctuating signal is 1, and SI for a Rician signal ranges between these extremes. The gamma-fluctuating-intensity (GFI) signal model allows direct control of SI. The GFI signal model has its roots in the radar community where Weinstock first proposed it in [93] and both Swerling [94] and Shnidman [94] have developed it further. As the name purports, the GFI signal is simply described as having a gamma-distributed instantaneous intensity,

$$\zeta_o \sim \text{Gamma}\left(\alpha_o, \frac{P_o}{\alpha_o}\right), \quad (7.227)$$

where α_o is the shape parameter and P_o the power (so the gamma scale parameter is P_o/α_o). The intensity moments found in Table 7.8 can be used to show that SI for the GFI model only depends on α_o via

$$\text{SI} = \frac{1}{\alpha_o}, \quad (7.228)$$

which has range $[0, \infty)$ for $\alpha_o \in (0, \infty]$. Thus the GFI model can represent a much wider range of signal fluctuations than the Rician signal model, and it exceeds the fluctuations of the Gaussian-fluctuating signal model when $\alpha_o < 1$. At the other extreme, as $\alpha_o \rightarrow \infty$, SI tends to zero and the GFI signal simplifies to a deterministic signal. This can be seen by noting that the variance of ζ_o tends to zero as $\alpha_o \rightarrow \infty$, so the gamma distribution described in (7.227) focuses all weight at its mean value $E[\zeta_o] = P_o$, yielding a deterministic signal. Finally, when $\alpha_o = 1$, the instantaneous intensity is exponentially distributed with mean P_o and so the GFI model also includes the Gaussian-fluctuating signal model as a sub-member of the family.

The complicated part of analyzing the GFI signal comes when it is measured in the presence of noise. Although the model only describes the PDF of the instantaneous intensity, the phase can be assumed as either constant or uniformly random so the complex envelope has form

$$Z = \sqrt{\zeta_o} e^{j\theta_o} + W. \quad (7.229)$$

The instantaneous intensity of the GFI signal plus Gaussian noise now has a rather complicated PDF and CDF. As shown in [85], they are finite sums of weighted gamma PDFs and CDFs if α_o is an integer greater than or equal to one and are otherwise infinite sums. The infinite-sum result,¹³ which is valid for all $\alpha_o > 0$, is

$$f_I(\zeta) = \sum_{i=0}^{\infty} \left[\frac{\beta^{\alpha_o} (1-\beta)^i \Gamma(\alpha_o + i)}{\Gamma(i+1) \Gamma(\alpha_o)} \right] \left[\frac{\zeta^i e^{-\zeta/\lambda}}{\Gamma(i+1) \lambda^{i+1}} \right] \quad (7.230)$$

where $\beta = \alpha_o / (\alpha_o + P_o / \lambda)$. As noted in [85], the first term in brackets can be recognized as a negative binomial PDF and the latter term in brackets as a gamma distribution with shape $i+1$ and scale λ . Thus, the GFI signal in Gaussian noise produces an instantaneous intensity that is a negative-binomial-weighted mixture of gamma PDFs.

7.5.4.1 Probability of Detection

From Sect. 7.4.3.7, the mixture representation of the PDF of the GFI signal in (7.230) implies the CDF is a similarly weighted mixture of gamma CDFs,

$$F_I(\zeta) = \sum_{i=0}^{\infty} \left[\frac{\beta^{\alpha_o} (1-\beta)^i \Gamma(\alpha_o + i)}{\Gamma(i+1) \Gamma(\alpha_o)} \right] \tilde{\gamma}\left(\frac{\zeta}{\lambda}; i+1\right) \quad (7.231)$$

where $\tilde{\gamma}(h; M)$ is the normalized incomplete gamma function (see Sect. 5.6.11). Although the sums converge quickly for many cases of interest, a much simpler alternative proposed in [85] is to use a shifted gamma distribution to approximate the distribution of $\zeta = |Z|^2$. This approach, called the three-moment shifted-gamma (TMSG) approximation is presented in detail in Sect. 7.5.6.2 in a more general context where it can be applied to any combination of signal and noise models.

A set of ROC curves illustrating detection performance for a GFI signal in Gaussian noise is shown in Fig. 7.17 for values of α_o ranging from 0.25 to 50 and a fixed SNR of 14 dB. The example illustrates how increasing fluctuations (i.e., decreasing α_o) in this regime of SNR and P_f reduces detection performance, even beyond that encountered for the Gaussian-fluctuating signal (the black circles). The exact CDF (solid colored lines) and the TMSG approximation (dashed gray lines) are shown to illustrate how accurate the latter is over a wide range of α_o .

¹³Note that this differs from that presented in [85] by not assuming the data have been normalized and by a factor of 2 so the average intensity is $P_o + \lambda$ rather than $2(P_o + \lambda)$.

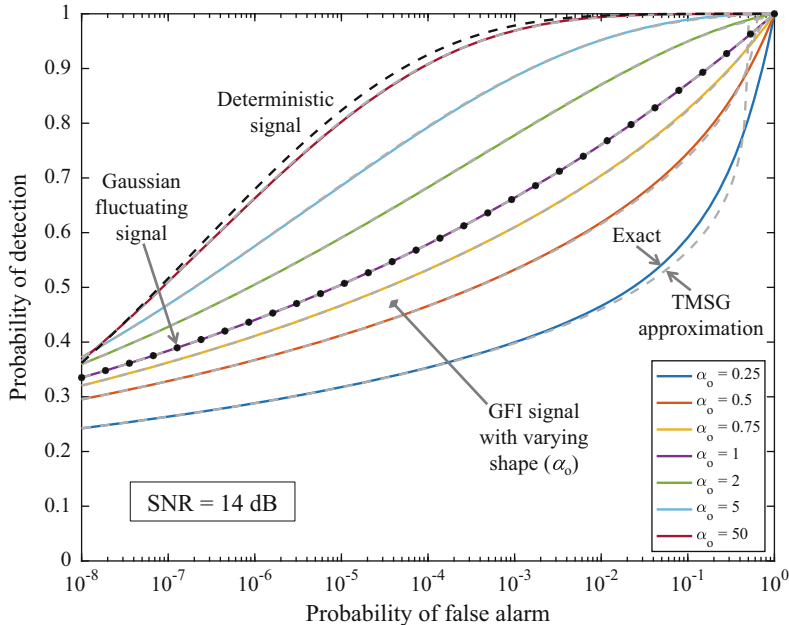


Fig. 7.17 ROC curves for a gamma-fluctuating-intensity (GFI) signal in Gaussian noise for various shape parameters (α_o). The figure illustrates how the GFI signal can range from a deterministic signal (large α_o) to a Gaussian-fluctuating signal ($\alpha_o = 1$) and beyond to even higher fluctuations ($\alpha_o < 1$). The exact results (solid colored lines) and the TMSG approximation (dashed gray lines) from Sect. 7.5.6.2 show the accuracy of the latter for most values of α_o

7.5.4.2 Sum of Instantaneous-Intensity Samples

The case involving the sum of instantaneous-intensity samples is covered in [85, 94, 95] when the incoherent sum of the signal component is gamma distributed, which essentially assumes the SNR is constant. Noting that the gamma distribution is a closed family under addition when the scale parameter is constant, the TMSG approximation described in Sect. 7.5.6.2 along with the moments of the sum in Sect. 7.5.6.4 can be used to approximate the distribution when summing instantaneous-intensity samples with a varying SNR.

7.5.5 Hankel Transform for Signal-Plus-Noise PDFs and CDFs

When both the signal and noise have a uniformly random phase, the characteristic function of the complex envelope provides a simple means for numerical evaluation

of very complicated signal-plus-noise PDFs and CDFs. By using (7.136) in (7.91), the PDF of the instantaneous intensity can be described as a single integral transformation of the circularly symmetric characteristic function of the complex envelope,¹⁴

$$f_I(\zeta) = \frac{1}{4} \int_0^\infty \Phi_\rho(\rho) J_0\left(\sqrt{\rho\zeta}\right) d\rho \quad (7.232)$$

$$= \frac{1}{2} \mathcal{H}_0\left\{\sqrt{\zeta}, \Phi_\rho(x^2)\right\} \quad (7.233)$$

where $J_0(x)$ is a zeroth-order Bessel function and

$$\mathcal{H}_v\{a, g(x)\} = \int_0^\infty x g(x) J_v(ax) dx \quad (7.234)$$

is a Hankel transform of order v [24, pg. 248]. Earlier sections introduced the simple form of the characteristic function of a deterministic signal with uniformly random phase, a Gaussian signal (or noise), and K-distributed noise; these are collated along with others in Table 7.7. The characteristic function of the sum of independent complex-envelope signals and noise is the product of the individual characteristic functions and therefore similarly simply formed. Combining simply formed characteristic functions with a numerical routine [98, 99]¹⁵ for computing the Hankel transform makes the PDF of the instantaneous intensity accessible for many combinations of signals and noise that would otherwise be very difficult to evaluate.

The list of distribution chains for which characteristic functions are available can be expanded by applying an inverse Hankel transform to the PDF of the instantaneous intensity

$$\Phi_\rho(\rho) = \int_0^\infty f_I(\zeta) J_0\left(\sqrt{\rho\zeta}\right) d\zeta. \quad (7.235)$$

Tables of Hankel transform pairs (e.g., [24, pg. 249]) can be used to obtain the characteristic function of the complex envelope (assuming circularly symmetry) for various instantaneous-intensity distributions. When the distribution has a closed-form k th moment, an infinite-series expansion of the Bessel function yields the characteristic function as an infinite summation,

¹⁴This technique has its origins in [96] and was applied in [97] to obtain the envelope PDF.

¹⁵The computational routine from [98] has been implemented as a MATLAB® subroutine in [99]. Note that the definition of the Hankel transform in [99] differs from that used here, which is from [24, pg. 248], by absorbing the “ x ” in the integrand of (7.234) into the function $g(x)$.

Table 7.7 Spherically invariant form of the characteristic function of the complex envelope for various target and noise distribution chains

Distribution chain	Characteristic function
	$\Phi_\rho(\rho) = \int_0^\infty f_i(\xi) J_0(\sqrt{\rho\xi}) d\xi$
Deterministic signal with uniformly random phase (non-fluctuating signal)	$J_0(\sqrt{\rho P_o})$
Gaussian-fluctuating signal or noise (Rayleigh distribution chain)	$e^{-\rho\sigma^2/4}$
Rician signal	$J_0(\sqrt{\rho P_c}) e^{-\rho P_t/4}$
Gamma-fluctuating-intensity(GFI) signal	$\sum_{m=0}^{\infty} \left(\frac{-\rho P_o}{4\alpha_o} \right)^m \frac{\Gamma(\alpha_o + m)}{(m!)^2 \Gamma(\alpha_o)}$ $= M\left(\alpha_o, 1, \frac{-\rho P_o}{4\alpha_o}\right) \text{ (Kummer function)}$
K distribution	$\frac{1}{(1 + \rho\lambda/4)^\alpha}$
Poisson-Rayleigh	$\exp\left\{-\rho \frac{\lambda_c}{4} - \alpha(1 - e^{-\rho\lambda_d/4})\right\}$
Weibull (intensity)	$\sum_{m=0}^{\infty} (-\rho\lambda/4)^m \frac{\Gamma(1 + m/\beta)}{(m!)^2}$
McDaniel	$\sum_{m=0}^{\infty} (-\rho\lambda/4)^m \frac{\Gamma(\alpha_1 + m)\Gamma(\alpha_2 + m)}{(m!)^2 \Gamma(\alpha_1)\Gamma(\alpha_2)}$

$$\Phi_\rho(\rho) = \sum_{m=0}^{\infty} (-1)^m \left(\frac{\rho}{4}\right)^m \frac{E[V^m]}{(m!)^2}. \quad (7.236)$$

The characteristic functions of the GFI signal, Weibull, and McDaniel distributions as shown in Table 7.7 were obtained through (7.236). Note that for some distributions (e.g., the log normal) the sum does not converge.

As shown in [53], the CDF of the instantaneous intensity can also be described as a single-integral transformation of the complex-envelope characteristic function by integrating (7.232),

$$\begin{aligned} F_I(\xi) &= \frac{\sqrt{\xi}}{2} \int_{\rho=0}^{\infty} \frac{1}{\sqrt{\rho}} \Phi_\rho(\rho) J_1(\sqrt{\rho\xi}) d\rho \\ &= \sqrt{\xi} \mathcal{H}_1\left\{\sqrt{\xi}, \frac{1}{x} \Phi_\rho(x^2)\right\}, \end{aligned} \quad (7.237)$$

where $\mathcal{H}_1\{a, g(x)\}$ is a first-order Hankel transform for which fast numerical routines exist [98, 99]. Using the characteristic functions listed in Table 7.7, a ROC

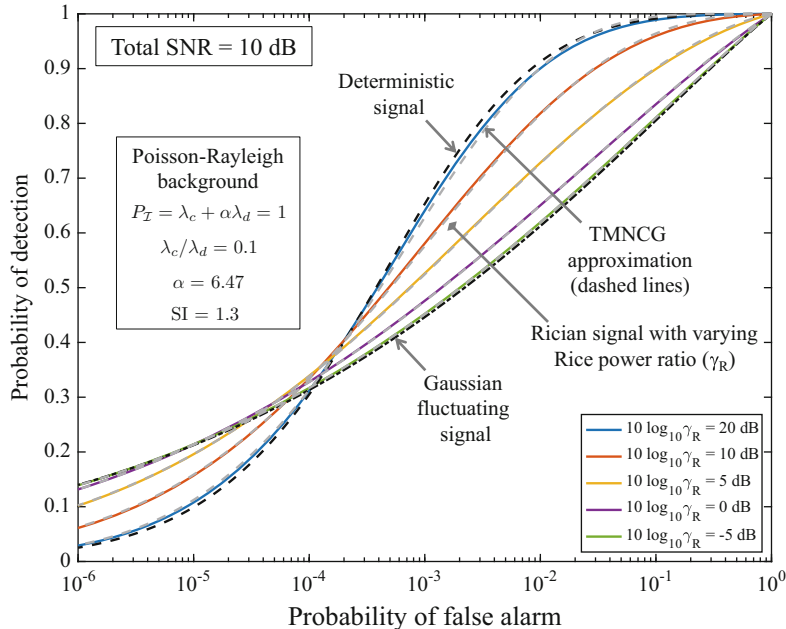


Fig. 7.18 ROC curve for a Rician signal with 10-dB total SNR and various Rice power ratios (γ_R) in a Poisson-Rayleigh-distributed background having $SI = 1.3$. Probability of detection is computed from the product of the signal and background characteristic functions using a first-order Hankel transform. The exact results (solid colored lines) and the TMNCG approximation (dashed gray lines) from Sect. 7.5.6.3 show the accuracy of the latter for most values of γ_R

curve for a Rician signal amid Poisson-Rayleigh-distributed noise is obtained and shown in Fig. 7.18. Compared with the Rician signal in Gaussian noise shown in Fig. 7.16, the Poisson-Rayleigh background degrades performance (note that the lower end of the abscissa in Fig. 7.18 stops at 10^{-6} where in Fig. 7.16 it extends to 10^{-8}).

7.5.6 Approximations to the CDF of Signals in Heavy-Tailed Noise

When the characteristic function of a particular signal or noise model is not easily evaluated or if some loss in accuracy is acceptable, there exist two very simple techniques for approximating the probability of detection for signals in heavy-tailed noise. The first is simply to use the CDF of the signal in Gaussian noise rather than the signal in the heavy-tailed background. The second is to assume a more general form of the distribution family from which the signal arises and obtain the parameters by matching the (theoretical) moments of the true and approximate distributions.

7.5.6.1 Signal in Gaussian Noise

When SNR is high, the signal component dominates the instantaneous intensity. As such, it is reasonable to expect the CDF of the signal in heavy-tailed noise to be similar to that of the signal in Gaussian noise at high SNR. Recalling that the characteristic function of the sum of the two components is the product of the individual characteristic functions, the accuracy of this approximation might be discerned from when the noise component will have an effect. The characteristic functions of the complex envelope for deterministic, Gaussian-fluctuating, and GFI signals are shown in Fig. 7.19 along with those of a Gaussian and K-distributed background. The noise examples all have unit average intensity and the signals all have 10-dB SNR. Comparing the characteristic functions for the signal types, it can be seen that the Gaussian-fluctuating signal tends toward zero very quickly relative to the various noise distributions. As such, the signal-plus-noise distribution in a heavy-tailed background will be nearly identical to that when the background is Gaussian (i.e., the Rayleigh distribution chain). However, the characteristic function of the GFI (for $\alpha_o < 1$) and deterministic signals are seen to decay more slowly and so are not expected to result in as good of an approximation, particularly when the background distribution is significantly heavy tailed.

This approach was used in [54] to approximate the detection threshold (DT) term in the sonar equation for deterministic and Gaussian-fluctuating signals in heavy-tailed noise. In this application or when evaluating a receiver operating characteristic (ROC) curve (i.e., P_d vs. P_f), it is important to use the correct heavy-tailed distribution when evaluating P_f or choosing a detector decision threshold.

7.5.6.2 Three-Moment Shifted-Gamma (TMSG) Approximation

Before it was common to have access to computational routines to evaluate the CDF of a non-central chi-squared distribution, it was often approximated by a shifted gamma distribution [76, Ch. 29]. Suppose the instantaneous intensity of the signal plus noise is

$$\zeta = \left| Z_o + \sqrt{V} e^{j\psi} \right|^2 \quad (7.238)$$

where Z_o is the complex envelope of the signal from the object of interest, V is the instantaneous intensity of the background noise or reverberation, and ψ its uniformly random phase. The shifted-gamma approximation can then be stated as

$$\zeta \approx b_g G + c_g \quad (7.239)$$

where G is a gamma random variable with shape parameter $a_g > 0$ and unit scale (alternatively the scale b_g induced in (7.239) can be absorbed into the gamma distribution). The CDF of the instantaneous intensity is approximated by that of a gamma distribution ($\tilde{\gamma}(x/\beta; \alpha)$, which is a normalized incomplete gamma function

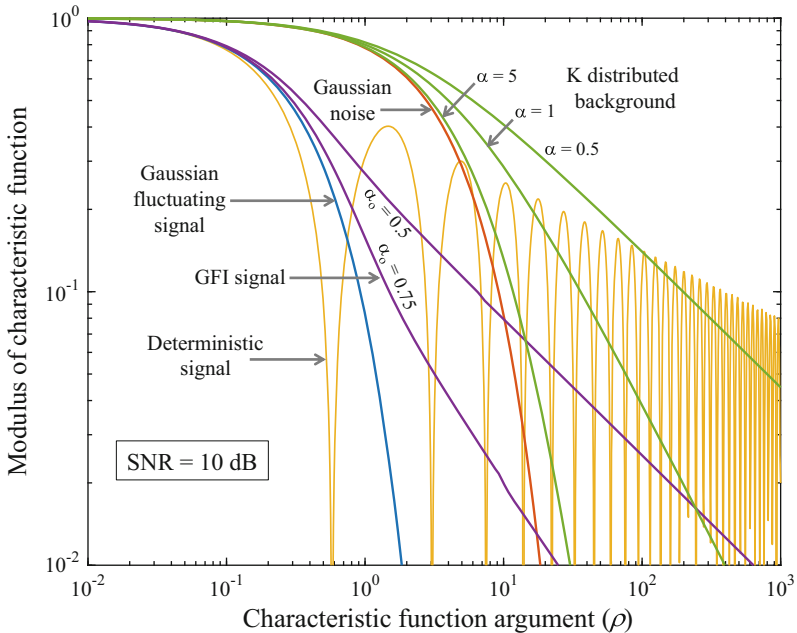


Fig. 7.19 Characteristic functions of the complex envelope for various signals and noise where SNR is always 10 dB

as described in Sect. 5.6.11),

$$\begin{aligned} F_l(\zeta) &\approx \tilde{\gamma}\left(\frac{\zeta - c_g}{b_g}; a_g\right) \\ &= \int_0^{(\zeta - c_g)/b_g} \frac{x^{a_g-1} e^{-x}}{\Gamma(a_g)} dx. \end{aligned} \quad (7.240)$$

The parameters of the shifted gamma distribution are obtained by matching the first three theoretical moments of the instantaneous intensity and of the shifted gamma distribution (i.e., each side of (7.239)). The first three moments of the instantaneous intensity are

$$E[\zeta] = \mu_1 = E[\zeta_o] + E[V] \quad (7.241)$$

$$E[\zeta^2] = \mu_2 = E[\zeta_o^2] + 4E[\zeta_o]E[V] + E[V^2] \quad (7.242)$$

$$E[\zeta^3] = \mu_3 = E[\zeta_o^3] + 9E[\zeta_o^2]E[V] + 9E[\zeta_o]E[V^2] + E[V^3] \quad (7.243)$$

where $\zeta_o = |Z_o|^2$ is the instantaneous intensity formed strictly from the complex envelope of the signal from the object of interest. As described in [53],¹⁶ solving the equations obtained by matching the first three moments of (7.239) results in the three-moment-shifted-gamma (TMSG) approximation, for which the parameters of the shifted gamma distribution are

$$b_g = \frac{\mu_3 - 3\mu_1\mu_2 + 2\mu_1^3}{2(\mu_2 - \mu_1^2)}, \quad (7.244)$$

$$a_g = \frac{\mu_2 - \mu_1^2}{b_g^2}, \text{ and} \quad (7.245)$$

$$c_g = \mu_1 - a_g b_g. \quad (7.246)$$

The instantaneous-intensity moments of common signal models and noise models are presented in Tables 7.8 and 7.9, respectively. They can be used in (7.241)–(7.243) to obtain the instantaneous-intensity moments of the combined signal plus noise and then used in (7.244)–(7.246) to obtain the parameters required for the approximation.

Despite the original application of the TMSG approximation to the non-central chi-squared distribution, it is more accurate when applied to the Gaussian-fluctuating signal or the GFI signal (e.g., see [53, 85]). This is explained by noting that the instantaneous intensity for these two signal types is itself a gamma distribution and so, based on the arguments presented in Sect. 7.5.6.1, should yield a good approximation at high SNR. The TMSG approximation is shown in Fig. 7.17 as dashed gray lines and seen to provide an excellent fit to the GFI signal in Gaussian noise, even as it tends toward a deterministic signal.

7.5.6.3 Three-Moment Non-central-gamma (TMNCG) Approximation

For a deterministic signal or a Rician signal with a high ratio of coherent to incoherent power, a natural alternative to the shifted gamma distribution can be found in the non-central gamma distribution. The non-central gamma random variable is a scaled non-central chi-squared random variable where the degrees of freedom are not restricted to the natural numbers. The three parameters available are the scale (λ_c), the degrees of freedom or shape ($\nu_c > 0$), and the non-centrality parameter ($\delta_c > 0$). In terms of the scaled non-central chi-squared distribution, the approximation is stated as

¹⁶Note that the parameter variables used here differ from those in [53] to align with the (α, β) gamma-distribution convention: a_g is the shape, b_g the scale, and c_g the location or shift parameter.

Table 7.8 Moments of the instantaneous intensity ζ_o for common target models and their scintillation index (SI)

Distribution chain	$E[\zeta_o]$	$E[\zeta_o^2]$	$E[\zeta_o^3]$	$E[\zeta_o^4]$	$E[\zeta_o^5]$	SI
Deterministic (non-fluctuating)	P_o	P_o^2	P_o^3	P_o^k	P_o^k	0
Gaussian-fluctuating	P_o	$2P_o^2$	$6P_o^3$	$k!P_o^k$	$k!P_o^k$	1
Rician	$P_c + P_i$	$P_c^2 + 4P_cP_i + 2P_i^2$	$P_c^3 + 9P_c^2P_i + 18P_cP_i^2 + 6P_i^3$	—	$1 - \frac{P_c^2}{(P_c + P_i)^2}$	
Gamma-fluctuating- intensity (GFI)	P_o	$P_o^2\left(1 + \frac{1}{\alpha_o}\right)$	$P_o^3\left(1 + \frac{1}{\alpha_o}\right)\left(1 + \frac{2}{\alpha_o}\right)$	$P_o^k \frac{\Gamma(\alpha_o + k)}{\alpha_o^k \Gamma(\alpha_o)}$	$P_o^k \frac{\Gamma(\alpha_o + k)}{\alpha_o^k \Gamma(\alpha_o)}$	$\frac{1}{\alpha_o}$

The distributions and parameter definitions of the various models are found in Sects. 7.5.1–7.5.4

Table 7.9 Moments of the instantaneous intensity V for common heavy-tailed distribution models

Intensity distribution	$E[V]$	$E[V^2]$	$E[V^3]$
Exponential	λ	$2\lambda^2$	$6\lambda^3$
K	$\alpha\lambda$	$2(\alpha\lambda)^2 \left(1 + \frac{1}{\alpha}\right)$	$6(\alpha\lambda)^3 \left(1 + \frac{1}{\alpha}\right) \left(1 + \frac{2}{\alpha}\right)$
Poisson-Rayleigh	$\lambda_c + \alpha\lambda_d$	$2(\lambda_c + \alpha\lambda_d)^2 + 2\alpha\lambda_d^2$	$6(\lambda_c + \alpha\lambda_d)^3 + 6\alpha\lambda_d^2[3(\lambda_c + \alpha\lambda_d) + \lambda_d]$
McDaniel	$\lambda\alpha_1\alpha_2$	$(\lambda\alpha_1\alpha_2)^2 \left(1 + \frac{1}{\alpha_1}\right) \left(1 + \frac{1}{\alpha_2}\right)$	$(\lambda\alpha_1\alpha_2)^3 \left(1 + \frac{1}{\alpha_1}\right) \left(1 + \frac{2}{\alpha_1}\right) \left(1 + \frac{1}{\alpha_2}\right) \left(1 + \frac{2}{\alpha_2}\right)$
Generalized Pareto	$\lambda(1 - \gamma)^{-1}$	$2\lambda^2(1 - \gamma)^{-1}(1 - 2\gamma)^{-1}$	$6\lambda^3(1 - \gamma)^{-1}(1 - 2\gamma)^{-1}(1 - 3\gamma)^{-1}$
Weibull	$\lambda\Gamma\left(1 + \frac{1}{\beta}\right)$	$\lambda^2\Gamma\left(1 + \frac{2}{\beta}\right)$	$\lambda^3\Gamma\left(1 + \frac{3}{\beta}\right)$
Log-normal	$e^{\mu+\gamma/2}$	$e^{2(\mu+\gamma)}$	$e^{3\mu+4.5\gamma}$

The distributions and their parameters are described in Sect. 7.4.3; more details for the common distributions are found in Chap. 5 as noted in Table 7.5

$$\frac{\zeta}{\lambda_c} \sim \chi_{v_c, \delta_c}^2 \quad (7.247)$$

and results in the instantaneous-intensity CDF

$$F_I(\zeta) \approx F_{\chi_{v_c, \delta_c}^2} \left(\frac{\zeta}{\lambda_c} \right) \quad (7.248)$$

where $F_{\chi_{v_c, \delta_c}^2}(x)$ is the CDF of the non-central chi-squared distribution (see Sect. 5.6.15).

Matching the moments of ζ from (7.241)–(7.243) and the scaled non-central chi-squared distribution results in choosing

$$\lambda_c = \frac{1}{2} \left[\frac{\mu_2}{\mu_1} - \mu_1 - \sqrt{\frac{\mu_2^2}{\mu_1^2} - \frac{\mu_2}{2} - \frac{\mu_3}{2\mu_1}} \right], \quad (7.249)$$

$$\delta_c = \max \left\{ 0, \frac{\mu_2 - \mu_1^2}{2\lambda_c^2} - \frac{\mu_1}{\lambda_c} \right\}, \text{ and} \quad (7.250)$$

$$v_c = \frac{\mu_1}{\lambda_c} - \delta_c. \quad (7.251)$$

The three-moment non-central gamma (TMNCG) approximation is perhaps better than the TMSG as it is more capable in representing the deterministic signal and also contains the (unshifted) gamma distribution as a sub-member, which handles the fluctuating signals. This can be seen in Fig. 7.18 where it is applied to a Rician signal in a Poisson-Rayleigh-distributed background with an SI = 1.3. The approximation is excellent when the Rician signal is mostly fluctuating (small values of γ_R) and still quite good as it tends to a deterministic signal (large values of γ_R). The disadvantage of the TMNCG approximation relative to the TMSG lies in the need for evaluation of the non-central chi-squared CDF. Although routines are not uncommon (e.g., see [87] or [89, App. 2D, pg. 52]), the incomplete gamma function required by the TMSG is more common.

7.5.6.4 Sums of Instantaneous-Intensity Samples

In situations where the decision statistic is formed as a sum of multiple instantaneous-intensity samples, it is feasible to apply either the TMSG or TMNCG models to the sum. If the detector decision statistic is

$$\zeta_\Sigma = \sum_{i=1}^M \zeta_i \quad (7.252)$$

then its first three moments are

$$E[\zeta_\Sigma] = M\mu_1 \quad (7.253)$$

$$E[\zeta_\Sigma^2] = M\mu_2 + M(M-1)\mu_1^2 \quad (7.254)$$

$$E[\zeta_\Sigma^3] = M\mu_3 + 3M(M-1)\mu_2\mu_1 + M(M-1)(M-2)\mu_1^3 \quad (7.255)$$

where it has been assumed the samples are identically distributed and where $\mu_j = E[\zeta_i^j]$ is the j th moment of ζ_i from (7.241)–(7.243). The moments in (7.253)–(7.255) can be extended to the more general case of non-identically distributed samples if necessary.

It is important to recall that forming the ROC curve for a detector summing a set of instantaneous-intensity samples requires a similar accounting for the effect on the distribution of the decision statistic for the noise-only case as for the signal-plus-noise case. As previously mentioned, this results in a $\text{Gamma}(M, \lambda)$ distribution for the decision statistic under the Gaussian noise assumption. Unfortunately, the result for most heavy-tailed distributions is much more complicated. Although it is feasible to evaluate characteristic or moment-generating functions for the instantaneous intensity of heavy-tailed distributions, they are generally not closed-form solutions (e.g., see [100] for the K distribution). An easier alternative is to apply the TMSG approximation to the noise-only case by using the noise-component moments in (7.253)–(7.255) to obtain P_f as a function of the decision threshold.

7.5.6.5 Signal and Noise Model Instantaneous-Intensity Moments

Instantaneous-intensity moments for common target and heavy-tailed distribution models are found, respectively, in Tables 7.8 and 7.9. Using the moments provided in these tables in the equations found in Sects. 7.5.6.2 for the TMSG or 7.5.6.3 for the TMNCG allows very simple approximation of the CDF of the instantaneous intensity comprising both signal and noise. In general, the TMSG approximation can be used for either a Gaussian-fluctuating signal or a GFI signal whereas the TMNCG should be used for a deterministic or Rician signal.

References

1. J.G. Proakis, *Digital Communications* (McGraw-Hill, New York 1983)
2. T.S. Rappaport, *Wireless Communications* (Prentice Hall, Englewood, 1996)
3. M. Stojanovic, Recent advances in high-speed underwater acoustic communications. *IEEE J. Ocean. Eng.* **21**(2), 125–136 (1996)
4. D. Brady, J.C. Preisig, Underwater acoustic communications, in *Wireless Communications: Signal Processing Perspectives*, ed. by H.V. Poor, G.W. Wornell, Chap. 8 (Prentice Hall PTR, Englewood, 1998)
5. R.J. Urick, *Principles of Underwater Sound*, 3rd edn. (McGraw-Hill, New York, 1983)

6. The physics of sound in the sea. Sum. Tech. Rep. 8, Office of Scientific Research and Development, Nat. Def. Res. Comm. Div. 6, 1946
7. W.S. Burdic, *Underwater Acoustic System Analysis*, 2nd edn. (Peninsula Publishing, Los Altos, 1991)
8. D. Ross, *Mechanics of Underwater Noise* (Peninsula Publishing, Los Altos, 1987)
9. W.W.L. Au, M.C. Hastings, *Principles of Marine Bioacoustics* (Springer, Berlin, 2008)
10. L. Cohen, *Time-Frequency Analysis* (Prentice Hall PTR, Englewood Cliffs, 1995)
11. G. Okopal, P.J. Loughlin, L. Cohen, Dispersion-invariant features for classification. *J. Acoust. Soc. Am.* **123**(2), 832–841 (2008)
12. C. Eckart, Optimal rectifier systems for the detection of steady signals. *Tech. Rpt. 52-11*, University of California, Marine Physical Laboratory of the Scripps Institute of Oceanography, La Jolla, California, March 1952
13. C.H. Sherman, J.L. Butler, *Transducers and Arrays for Underwater Sound* (Springer, Berlin, 2007)
14. D.W. Ricker, *Echo Signal Processing* (Kluwer Academic Publishers, Boston, 2003)
15. I. Dyer, Statistics of sound propagation in the ocean. *J. Acoust. Soc. Am.* **48**(1B), 337–345 (1970)
16. P.N. Mikhalevsky, Envelope statistics of partially saturated processes. *J. Acoust. Soc. Am.* **72**(1), 151–158 (1982)
17. A.D. Seifer, M.J. Jacobson, Ray transmissions in an underwater acoustic duct with a pseudorandom bottom. *J. Acoust. Soc. Am.* **43**(6), 1395–1403 (1968)
18. S.O. Rice, Mathematical analysis of random noise: part III. *Bell Syst. Tech. J.* **24**(1), 46–156 (1945)
19. R.J. Urick, Models for the amplitude fluctuations of narrow-band signals and noise in the sea. *J. Acoust. Soc. Am.* **62**(4), 878–887 (1977)
20. C.H. Harrison, The influence of propagation focusing on clutter statistics. *IEEE J. Ocean. Eng.* **35**(2), 175–184 (2010)
21. A.B. Carlson, *Communication Systems* (McGraw-Hill, New York, 1986)
22. J. Dugundji, Envelopes and pre-envelopes of real waveforms. *IRE Trans. Inf. Theory* **4**(1), 53–57 (1958)
23. R.N. McDonough, A.D. Whalen, *Detection of Signals in Noise*, 2nd edn. (Academic Press, San Diego, 1995)
24. R.N. Bracewell, *The Fourier Transform and Its Applications*, 2nd edn. (McGraw-Hill, New York, 1986)
25. R.G. Lyons, *Understanding Digital Signal Processing* (Prentice Hall, Englewood Cliffs, 2011)
26. W.W. Peterson, T.G. Birdsall, W.C. Fox, The theory of signal detectability. *Trans. IRE Prof. Group Inf. Theory* **4**(4), 171–212 (1954)
27. S.M. Haver, H. Klinck, S.L. Nieuirkirk, H. Matsumoto, R.P. Dziak, J.L. Miksis-Olds, The not-so-silent world: measuring Arctic, Equatorial, and Antarctic soundscapes in the Atlantic Ocean. *Deep Sea Res. I* **122**, 95–104 (2017)
28. G.M. Wenz, Acoustic ambient noise in the ocean: spectra and sources. *J. Acoust. Soc. Am.* **34**(12), 1936–1956 (1962)
29. Acknowledgement: The author thanks and acknowledges the Preparatory Commission for the Comprehensive Nuclear-Test-Ban Treaty Organization (CTBTO; <https://www.ctbto.org/specials/vdec/>) for providing access to the data used to produce these figures. The CTBTO is not responsible for the views of the author.
30. T. Arase, E.M. Arase, Deep-sea ambient-noise statistics. *J. Acoust. Soc. Am.* **44**(6), 1679–1684 (1968)
31. W.J. Jobst, S.L. Adams, Statistical analysis of ambient noise. *J. Acoust. Soc. Am.* **62**(1), 63–71 (1977)
32. A.R. Milne, J.H. Ganton, Ambient noise under arctic sea ice. *J. Acoust. Soc. Am.* **36**(5), 855–863 (1964)
33. I. Dyer, Statistics of distant shipping noise. *J. Acoust. Soc. Am.* **53**(2), 564–570 (1973)

34. J.G. Veitch, A.R. Wilks, A characterization of Arctic undersea noise. *J. Acoust. Soc. Am.* **77**(3), 989–999 (1985)
35. M. Bouvet, S.C. Schwartz, Underwater noises: statistical modeling, detection, and normalization. *J. Acoust. Soc. Am.* **83**(3), 1023–1033 (1988)
36. A.B. Baggeroer, E.K. Scheer, The NPAL Group, Statistics and vertical directionality of low-frequency ambient noise at the North Pacific Acoustics Laboratory site. *J. Acoust. Soc. Am.* **117**(3), 1643–1665 (2005)
37. D. Middleton, Statistical-physical models of electromagnetic interference. *IEEE Trans. Electromagn. Compat.* **EMC-19**(3), 106–127 (1977)
38. G.R. Wilson, D.R. Powell, Experimental and modeled density estimates of underwater acoustic returns, in *Statistical Signal Processing*, ed. by E.J. Wegman, J.G. Smith (Marcel Dekker, New York, 1984), pp. 223–219
39. S.A. Kassam, *Signal Detection in Non-Gaussian Noise* (Springer, New York, 1988)
40. F.W. Machell, C.S. Penrod, Probability density functions of ocean acoustic noise processes, in *Statistical Signal Processing*, ed. by E.J. Wegman, J.G. Smith (Marcel Dekker, New York, 1984), pp. 211–221
41. N.L. Johnson, S. Kotz, N. Balakrishnan, *Continuous Univariate Distributions*, vol. 1, 2nd edn. (Wiley, Hoboken, 1994)
42. P. Faure, Theoretical model of reverberation noise. *J. Acoust. Soc. Am.* **36**(2), 259–266 (1964)
43. V.V. Ol'shevskii, *Characteristics of Sea Reverberation* (Consultants Bureau, New York, 1967)
44. M.A. Richards, J.A. Scheer, W.A. Holm, *Principles of Modern Radar* (SciTech Publishing, Raleigh, 2010)
45. H.L. Van Trees, *Optimum Array Processing* (Wiley, New York, 2002)
46. C.W. Holland, J.R. Preston, D.A. Abraham, Long-range acoustic scattering from a shallow-water mud-volcano cluster. *J. Acoust. Soc. Am.* **122**(4), 1946–1958 (2007)
47. D.A. Abraham, A.P. Lyons, Novel physical interpretations of K -distributed reverberation. *IEEE J. Ocean. Eng.* **27**(4), 800–813 (2002)
48. E. Jakeman, P.N. Pusey, A model for non-Rayleigh sea echo. *IEEE Trans. Antennas Propag.* **24**(6), 806–814 (1976)
49. E. Jakeman, On the statistics of k -distributed noise. *J. Phys. A Math. Gen.* **13**, 31–48 (1980)
50. K.D. Ward, Compound representation of high resolution sea clutter. *Electron. Lett.* **17**(16), 561–563 (1981)
51. E. Jakeman, K.D. Ridley, *Modeling Fluctuations in Scattered Waves* (Taylor & Francis, Boca Raton, 2006)
52. K.D. Ward, R.J.A. Tough, S. Watts, *Sea Clutter: Scattering, the K Distribution and Radar Performance* (The Institution of Engineering and Technology, London, 2006)
53. D.A. Abraham, Signal excess in K -distributed reverberation. *IEEE J. Ocean. Eng.* **28**(3), 526–536 (2003)
54. D.A. Abraham, Detection-threshold approximation for non-Gaussian backgrounds. *IEEE J. Ocean. Eng.* **35**(2), 355–365 (2010)
55. K. Oldham, J. Myland, J. Spanier, *An Atlas of Functions*, 2nd edn. (Springer Science, New York, 2009)
56. I.S. Gradshteyn, I.M. Ryzhik, *Table of Integrals, Series, and Products*, ed. by D. Zwillinger, 8th edn. (Elsevier Academic Press, Waltham, 2015)
57. I.R. Joughin, D.B. Percival, D.P. Winebrenner, Maximum likelihood estimation of K distribution parameters for SAR data. *IEEE Trans. Geosci. Remote Sens.* **31**(5), 989–999 (1993)
58. W.J.J. Roberts, S. Furui, Maximum likelihood estimation of K -distribution parameters via the expectation-maximization algorithm. *IEEE Trans. Signal Process.* **48**(12), 3303–3306 (2000)
59. D.A. Abraham, A.P. Lyons, Reliable methods for estimating the K -distribution shape parameter. *IEEE J. Ocean. Eng.* **35**(2), 288–302 (2010)
60. J.M. Fialkowski, R.C. Gauss, D.M. Drumheller, Measurements and modeling of low-frequency near-surface scattering statistics. *IEEE J. Ocean. Eng.* **29**(2), 197–214 (2004)
61. J.M. Fialkowski, R.C. Gauss, Methods for identifying and controlling sonar clutter. *IEEE J. Ocean. Eng.* **35**(2), 330–354 (2010)

62. S.M. Zabin, H.V. Poor, Parameter estimation for Middleton Class A interference processes. *IEEE Trans. Commun.* **37**(10), 1042–1051 (1989)
63. S.M. Zabin, H.V. Poor, Recursive algorithms for identification of impulse noise channels. *IEEE Trans. Inf. Theory* **36**(3), 559–578 (1990)
64. S.M. Zabin, H.V. Poor, Efficient estimation of Class A noise parameters via the EM algorithm. *IEEE Trans. Inf. Theory* **37**(1), 60–72 (1991)
65. S.T. McDaniel, Seafloor reverberation fluctuations. *J. Acoust. Soc. Am.* **88**(3), 1530–1535 (1990)
66. M. Gu, D.A. Abraham, Using McDaniel's model to represent non-Rayleigh reverberation. *IEEE J. Ocean. Eng.* **26**(3), 348–357 (2001)
67. M. Gu, D.A. Abraham, Parameter estimation for McDaniel's non-Rayleigh reverberation model, in *Proceedings of Oceans 99 Conference*, Seattle, Washington (1999), pp. 279–283
68. E. Conte, M. Longo, Characterisation of radar clutter as a spherically invariant random process. *IEE Proc. F Radar Signal Process.* **134**(2), 191–197 (1987)
69. T.J. Barnard, D.D. Weiner, Non-Gaussian clutter modeling with generalized spherically invariant random vectors. *IEEE Trans. Signal Process.* **44**(10), 2384–2390 (1996)
70. T.J. Barnard, F. Khan, Statistical normalization of spherically invariant non-Gaussian clutter. *IEEE J. Ocean. Eng.* **29**(2), 303–309 (2004)
71. B.R. La Cour, Statistical characterization of active sonar reverberation using extreme value theory. *IEEE J. Ocean. Eng.* **29**(2), 310–316 (2004)
72. J.M. Gelb, R.E. Heath, G.L. Tipple, Statistics of distinct clutter classes in mid-frequency active sonar. *IEEE J. Ocean. Eng.* **35**(2), 220–229 (2010)
73. G.B. Goldstein, False-alarm regulation in log-normal and Weibull clutter. *IEEE Trans. Aerosp. Electron. Syst.* **AES-9**(1), 84–92 (1973)
74. D.C. Schleher, Radar detection in Weibull clutter. *IEEE Trans. Aerosp. Electron. Syst.* **AES-12**(6), 736–743 (1976)
75. M. Sekine, Y. Mao, *Weibull Radar Clutter* (Peter Peregrinus, London, 1990)
76. N.L. Johnson, S. Kotz, N. Balakrishnan, *Continuous Univariate Distributions*, vol. 2, 2nd edn. (Wiley, New York, 1995)
77. N.P. Chotiros, H. Boehme, T.G. Goldsberry, S.P. Pitt, R.A. Lamb, A.L. Garcia, R.A. Altenburg, Acoustic backscattering at low grazing angles from the ocean bottom. Part II. Statistical characteristics of bottom backscatter at a shallow water site. *J. Acoust. Soc. Am.* **77**(3), 975–982 (1985)
78. S. Kay, C. Xu, CRLB via the characteristic function with application to the K-distribution. *IEEE Trans. Aerosp. Electron. Syst.* **44**(3), 1161–1168 (2008)
79. P.A. Crowther, Fluctuation statistics of sea-bed acoustic backscatter, in *Bottom Interacting Ocean Acoustics*, ed. by W.A. Kuperman, F.B. Jensen (Plenum, New York, 1980), pp. 609–622
80. A.P. Lyons, D.A. Abraham, Statistical characterization of high-frequency shallow-water seafloor backscatter. *J. Acoust. Soc. Am.* **106**(3), 1307–1315 (1999)
81. W.J. Lee, T.K. Stanton, Statistics of echoes from mixed assemblages of scatterers with different scattering amplitudes and numerical densities. *IEEE J. Ocean. Eng.* **39**(4), 740–754 (2014)
82. A.P. Dempster, N.M. Laird, D.B. Rubin, Maximum likelihood from incomplete data via the EM algorithm. *J. R. Stat. Soc. Ser. B* **2**, 1–38 (1977)
83. G.J. McLachlan, T. Krishnan, *The EM Algorithm and Extensions* (Wiley, Hoboken, 2008)
84. D.A. Abraham, J.M. Gelb, A.W. Oldag, Background and clutter mixture distributions for active sonar statistics. *IEEE J. Ocean. Eng.* **36**(2), 231–247 (2011)
85. D.A. Abraham, Application of gamma-fluctuating-intensity signal model to active sonar, in *Proceedings of 2015 IEEE Oceans Conference*, Genoa, Italy (2015)
86. M.A. Richards, *Fundamentals of Radar Signal Processing* (McGraw-Hill, New York, 2005)
87. D.A. Shnidman, The calculation of the probability of detection and the generalized Marcum Q-function. *IEEE Trans. Inf. Theory* **35**(2), 389–400 (1989)

88. C.W. Helstrom, *Elements of Signal Detection and Estimation* (Prentice Hall, Englewood Cliffs, 1995)
89. S.M. Kay, *Fundamentals of Statistical Signal Processing: Detection Theory* (Prentice Hall PTR, Englewood Cliffs, 1998)
90. A.H. Nuttall, Accurate efficient evaluation of cumulative or exceedance probability distributions directly from characteristic functions. Tech. Rpt. 7023, Naval Underwater Systems Center, New London, CT, October 1983
91. S.O. Rice, Mathematical analysis of random noise. Bell Syst. Tech. J. **23**(3), 282–332 (1944)
92. S.O. Rice, Statistical properties of a sine wave plus random noise. Bell Syst. Tech. J. **27**(1), 109–157 (1948)
93. W.W. Weinstock, Target cross section models for radar systems analysis. Ph.D. dissertation, University of Pennsylvania, Philadelphia, PA, 1964
94. D.A. Shnidman, Expanded Swerling target models. IEEE Trans. Aerosp. Electron. Syst. **39**(3), 1059–1069 (2003)
95. P. Swerling, Radar probability of detection for some additional fluctuating target cases. IEEE Trans. Aerosp. Electron. Syst. **33**(2), 698–709 (1997)
96. R.D. Lord, The use of the Hankel transform in statistics I. general theory and examples. Biometrika **41**, 44–55 (1954)
97. D.M. Drumheller, Padé approximations to matched filter amplitude probability functions. IEEE Trans. Aerosp. Electron. Syst. **35**(3), 1033–1045 (1999)
98. W.L. Anderson, Computer program numerical integration of related Hankel transforms of orders 0 and 1 by adaptive digital filtering. Geophysics **44**(7), 1287–1305 (1979)
99. B. Borchers, Hankel Transform Routines in MATLAB. <http://www.nmt.edu/~borchers/hankel.html>
100. H. Amindavar, J.A. Ritcey, Padé approximations for detectability in K-clutter and noise. IEEE Trans. Aerosp. Electron. Syst. **30**(2), 425–434 (1994)

Chapter 8

Detecting Signals with Known Form: Matched Filters



8.1 Introduction

The focus of this chapter is on the detection of signals that have a known form or structure when they are occluded by additive noise. The most common example of signals with known form is from active remote sensing where a known *source signal* is projected into the underwater environment and the sounds measured by a sensor are then analyzed to achieve one of the inferential objectives. The signal observed at the sensor, termed the *signal measurement*, can be viewed as the output of a linear system whose input is the source waveform or signal. When the linear system alters the signal in a predictable and repeatable manner, detectors can be derived that exploit knowledge of the source signal. For example, when the range of an object of interest is unknown in the basic ocean model, the arrival time and amplitude of an active sonar echo will be unknown. However the form of the signal measurement is still known, with the exception of a translation on the time axis and a scale in amplitude. Several such examples of how propagation in an underwater acoustical channel affects various signal parameters (arrival time, amplitude, phase, or Doppler scale) were presented in Sect. 7.2.3. Thus, the topic of this chapter may be viewed as detection of signals with known form and potentially unknown parameters.

In Sect. 8.2 the most basic case of a completely known signal is seen to result in a coherent matched-filter detector. Matched-filtering, which is also called replica correlation or pulse compression, compares the signal-plus-noise measurement with the known source signal to produce a decision statistic with a large value when they have a similar shape and a small value when they do not. The matched-filter is also shown to arise in detecting signals when the signal strength or phase are unknown or random. Extensions to account for other unknown deterministic parameters such as arrival time and Doppler scale result in a maximization (or search) over the matched-filter detector decision statistic formed assuming the parameters are known, an implementation known as a Doppler filter bank. The derivations presented in Sect. 8.2 include the probabilities of false alarm and detection required to form

the detector receiver operating characteristic (ROC) curve and, for certain signal models, the detection threshold term in the sonar equation. While the focus of this chapter is on deriving optimal or sub-optimal detectors under various assumptions on the signal model and in the presence of additive, stationary, white Gaussian noise, matched filters also maximize the filter output signal-to-noise power ratio (SNR) under the weaker assumptions of stationary and white noise (e.g., see [1]).

Two important tools used in the design and analysis of matched filter detectors, the waveform autocorrelation and ambiguity functions, are presented in Sect. 8.3. The autocorrelation function characterizes the response of the matched filter when it is mis-aligned in time with the signal measurement while the ambiguity function extends the analysis to include a mismatch in Doppler scale. The autocorrelation and ambiguity functions for the common active sonar pulses, described below in the introductory examples, are derived or approximated.

Signal detection is most commonly applied to signals as a function of time. However, in underwater acoustic signal processing applications, signals are functions of both time and space. A signal in the spatial dimension, which must obey the wave equation, can be described as having a known form with some unknown parameters. Using a plane-wave propagation model and a temporally narrowband signal, the conventional beamforming process is shown in Sect. 8.4 to arise from a detection inferential objective. The beampattern and beam response are related to the ambiguity function, and directivity and array gain are evaluated for a uniform line array.

Although the focus of this chapter is on detection, estimation performance for arrival time and Doppler scale is closely related and therefore the topic of Sect. 8.5. An important distinction is made between the resolution capabilities of a waveform in the time and Doppler-scale dimensions and the accuracy with which the parameters can be estimated. The resolution of a waveform represents a change-point where two signals with separation greater than the resolution can be easily identified, whereas they may or may not be separable when they are both within a “resolution cell.” Estimation accuracy describes more specifically how well the parameter can be estimated in terms of the estimation performance metrics described in Sect. 6.3.2. In particular, the Cramér-Rao lower bound (CRLB) on the variance of unbiased estimators is derived for various combinations of known and unknown parameters. Several examples are presented including how many observations are required to obtain a desired accuracy when estimating a sound pressure level in decibels and the estimation of arrival time and/or Doppler scale using the standard sonar pulses.

One of the key assumptions in the derivation of matched-filter detectors in Sect. 8.2 is that the background noise and reverberation power is known. In practice it is not known, varies over time (especially in reverberation-limited scenarios), and must be estimated. This process, described in Sect. 8.6, is called *normalization* because the matched-filter detector decision statistic is divided by the background power estimate before it is compared to a decision threshold. The normalization process provides what is known as a constant-false-alarm-rate (CFAR) detector because the false alarm performance of the detector is invariant to (i.e., does

not change with) the background power level. Both a basic cell-averaging CFAR processor and a more complicated order-statistic CFAR processor are presented along with their impact on detection performance.

In applications where the object of interest is moving, its radial velocity is most likely unknown and may in fact be an important quantity related to the state of nature under investigation. The generalized likelihood ratio (GLR) detector for an unknown Doppler scale requires a maximization or search over a bank of matched filters tuned to span the Doppler scales of interest. The details of implementing such a Doppler filter bank are covered in Sect. 8.7, including the impact on false alarm and detection performance, implementation through use of a fast Fourier transform for continuous-wave pulses, and normalization considerations.

The final topic of this chapter is the temporal spreading arising from propagation through the underwater acoustical channel and reflection or scattering from an object of interest. In Sect. 8.8, the *energy spreading loss* incurred by the matched-filter detector is approximated using simple spreading models. An approach to recoup the lost energy by incoherently integrating the matched-filter instantaneous intensity is presented and evaluated.

The material presented in this chapter requires a knowledge of detection and estimation theory as well as probability and statistics. The basic principles of these topics can be found in Chaps. 5 and 6. Other resources in detection theory include [2–4]. Detection in non-Gaussian noise can be found in [5] or more general mathematical statistics and hypothesis testing texts such as [6, 7]. Texts with specific applications of detection theory to sonar or radar include [8–13]. Additional information on the different waveforms used in active sensing, their autocorrelation and ambiguity functions can be found in [14–18].

8.1.1 Introductory Examples

In signal detection, the data measurement (e.g., a period of time observed on a hydrophone or at the output of a beamformer) is compressed or distilled to form a scalar detector *decision statistic* containing all the information necessary to decide if a signal is present in the data or if it is only noise. The decision itself is made by comparing the decision statistic to a *decision threshold* with a detection (true or false) declared when the decision statistic exceeds the decision threshold. The decision threshold is generally chosen to meet a probability of false alarm (P_f) specification (e.g., see Sect. 6.2.2), which is the probability the decision statistic exceeds the decision threshold when only noise is present. The accompanying performance metric related to the signal is the probability of detection (P_d), which is the probability the decision statistic exceeds the decision threshold when signal is present. To first order, P_d depends on the signal-to-noise power ratio (SNR). An example of this is found in Fig. 8.1 where a sequence of signals with varying SNR have been added to noise at equal intervals in time. Also shown on the figure

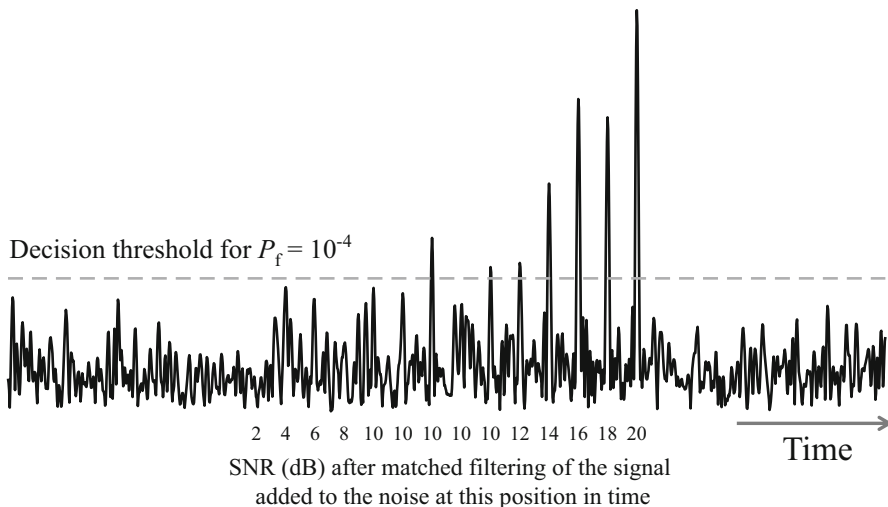


Fig. 8.1 Matched filter response (i.e., the detector decision statistic) for signals amid noise with varying SNR

is the threshold achieving $P_f = 10^{-4}$. An exceedance of this threshold by the decision statistic (which in this case is the matched-filter envelope) produces either a false alarm or a true detection. The signals with the lowest SNRs do not produce a detection for this observation and they are unlikely to produce one in repeated observations because detecting signals with low SNR is very difficult and therefore unlikely. Conversely, the signals with the highest SNR produce detections here and would do so in most observations because detecting signals with high SNR is easy and occurs frequently. In between there are SNRs where signals will be detected only some of the time, such as the 10-dB-SNR examples shown in Fig. 8.1. Of the five occurrences, only two produced detections, which is not unreasonable given the expectation of $P_d = 0.6$ for this example. In deriving detection algorithms, these cases are of most interest because the detector design can make a difference. Nearly any detection algorithm will detect high SNR signals with minimal loss compared to an optimal detector and almost no detection algorithm will reliably detect signals at very low SNR.

Many of the examples in this chapter use one of the three most common active-sensing waveforms in underwater acoustics applications: continuous-wave (CW), linear-frequency-modulated (LFM), and hyperbolic-frequency-modulated (HFM) pulses. Examples of these pulses are shown in Fig. 8.2 where it can be seen that the CW pulse maintains a constant frequency throughout whereas the LFM and HFM pulses have an instantaneous frequency that changes, respectively, linearly and hyperbolically with time. The primary characteristics of the pulses can be found in Table 8.1, which indicates that temporal resolution is inversely proportional to bandwidth (W) and that Doppler resolution for the CW pulse is inversely

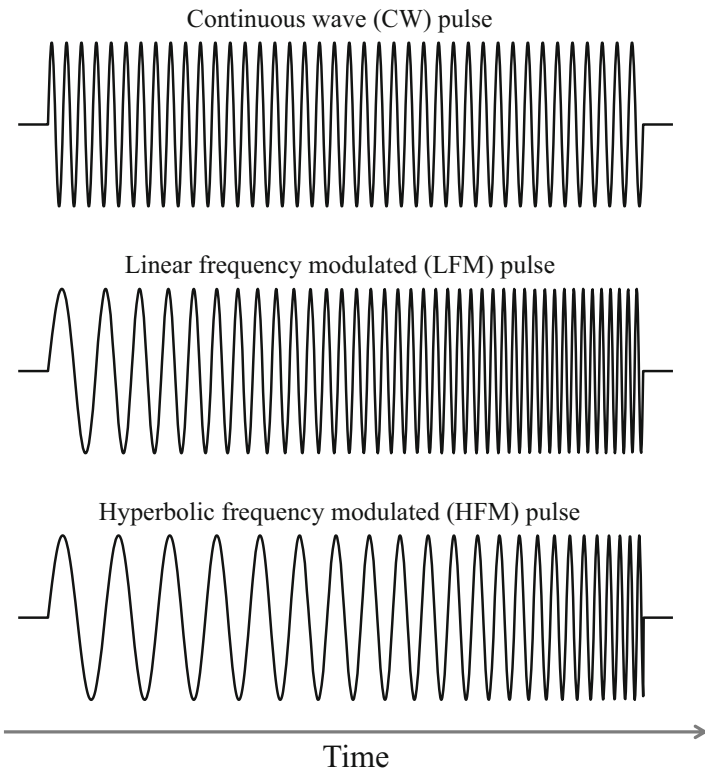


Fig. 8.2 Common sonar pulses: continuous wave (CW), linear frequency modulated (LFM), and hyperbolic frequency modulated (HFM)

proportional to pulse duration (T_p). Although more details are presented in later sections, these are the basic concepts conveyed in the introductory examples.

When the arrival time of a signal is unknown, the matched-filter detector applies a correlation at all possible arrival times and chooses the maximum response. By examining the signals in Fig. 8.2, the CW pulse is expected to have poor resolution in time because shifting by a full period still provides a large correlation. However, shifting one of the FM waveforms by enough will cause a mismatch in the frequencies and therefore a low correlation. This is illustrated in Fig. 8.3 where a signal-plus-noise measurement is shown at the top. Noting how low the signal envelope is compared with the signal-plus-noise envelope, it is clear the measurement is dominated by noise. The lower three signals show the envelope response of a matched filter in time when using the three standard sonar pulses. The ability of matched filtering to increase the SNR is evident in the large response of the signals relative to the noise background. The poor overall temporal resolution of the CW pulse is seen by the triangularly shaped response. The excellent temporal resolution of the FM waveforms illuminates that there are actually three signals

Table 8.1 Common sonar pulse types and their characteristics

Pulse type	Freq./time character	Temporal resolution	Doppler resolution
CW	Constant	Poor unless short ($\propto T_p$)	Good unless short ($\propto 1/T_p$)
LFM	Linear	Good unless NB ($\propto 1/W$)	Poor unless broadband
HFM	Hyperbolic	Good unless NB ($\propto 1/W$)	Poor

Legend:*CW* = continuous wave*LFM* = linear frequency modulated*HFM* = hyperbolic frequency modulated*NB* = narrowband*T_p* = pulse duration*W* = pulse bandwidth

* These assessments assume that both signal arrival time and Doppler scale are unknown and for the FM waveforms do not account for the bias introduced by the coupling between arrival time and Doppler scale (see Sect. 8.5 for more details)

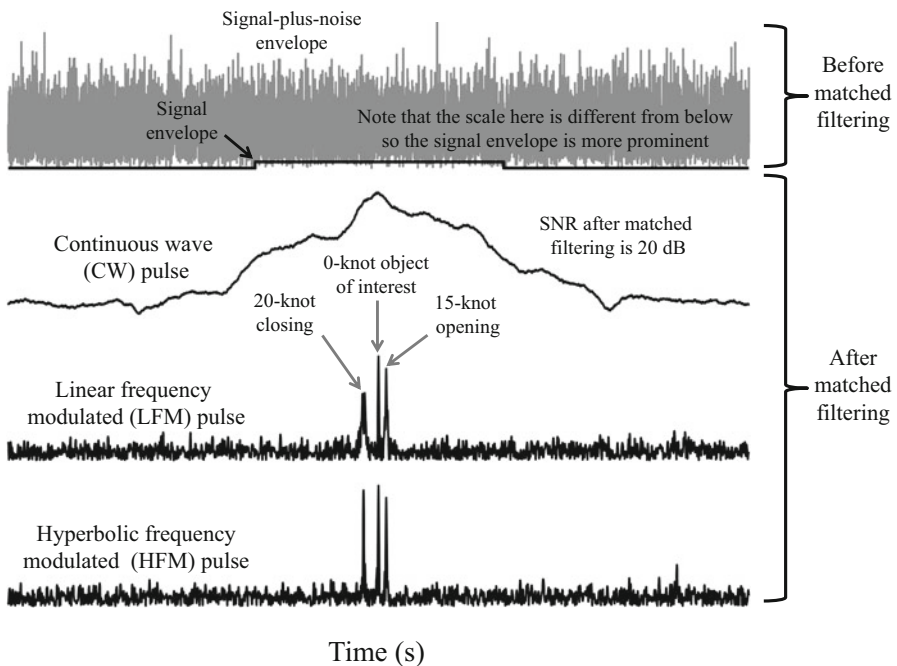


Fig. 8.3 Example illustrating how a signal that is completely occluded by noise can be easily detected after matched filtering. The frequency-modulated pulses show there are three echoes in the signal measurement. Although the CW pulse cannot separate these in time, it can easily do so in a Doppler filter bank because they are from objects moving with 0, 15, and 20 kn speed

in the measurement. The signals have Doppler scales for 0-kn, 15-kn-opening, and 20-kn-closing radial velocities. Although not shown, the CW-pulse can easily

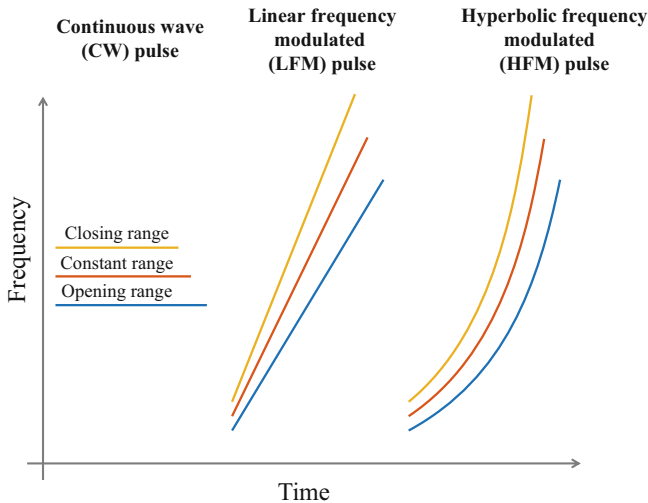


Fig. 8.4 The impact of Doppler scale on the time-frequency character of the common sonar pulses. Objects of interest with opening range result in lower-frequency/longer-duration echoes whereas those with closing range result in higher-frequency/shorter-duration echoes. Note that the change in signal duration and frequency scaling have been exaggerated from typical sonar conditions so they are more prominent

separate these signals in the Doppler dimension. They are separated in the temporal dimension by the FM pulses only because of the different radial velocities and their associated time-delay bias induced by a coupling between arrival time and Doppler scale.

The poor time resolution and good Doppler resolution capabilities of the CW pulse can also be ascertained from a plot of its time-frequency structure, which is shown in Fig. 8.4. A temporal shift results in a significant overlap in both frequency and time. However, the Doppler effect shifts the signal up or down in frequency and (very slightly in sonar) shortens or lengthens the signal in time. The signals are therefore easily separated once the shift is greater than the inverse pulse duration because there is no overlap in frequency. Similarly, the poor Doppler resolution and good time resolution of the FM pulses can be seen from the time-frequency characterization. A shift in time causes a mis-alignment of the frequency content that leads to good temporal resolution. In essence, variation of the instantaneous frequency throughout the pulse makes a temporal displacement more obvious. However, the Doppler effect for wideband signals is a frequency scale (this simplifies to a frequency shift for narrowband waveforms). In underwater acoustics applications, the speeds of objects of interest are generally much less than the speed of sound so the frequency scaling often leaves significant overlap in frequency between a source signal (which is not affected by Doppler) and a signal measurement subject to Doppler. The potential for some Doppler resolution with the LFM pulse is seen by the (exaggerated) change in slope, which reduces the

correlation between a Doppler-scaled signal measurement and an un-scaled source signal. This can also be seen in Fig. 8.3 where the opening and closing signals have a lower response than the 0-kn signal measurement that is perfectly matched to the source signal. However, the hyperbolic time-frequency shape of the HFM pulse has a self-consistency when subjected to a Doppler scale. The Doppler-scaled instantaneous frequency matches precisely with that of the un-scaled source signal at an earlier or later time so the only loss in correlation comes from a reduced overlap in time. This is also seen in Fig. 8.3 where the opening and closing signals only suffer a small amount of decorrelation compared with the 0-kn signal measurement.

8.2 Matched-Filter Detectors

In designing a detection algorithm for an underwater acoustic signal, it will be assumed that sensor data have been beamformed, basebanded, and sampled in time (though not necessarily in this order). This allows using the statistical characterization of the basebanded signal and noise from Sect. 7.3.5. If the sampling frequency is f_s , so a sample is obtained every $T_s = 1/f_s$ seconds, there will be $n = T_p/T_s = T_p f_s$ discrete-time samples representing the signal if its duration is T_p . Assuming the arrival time (τ_p) of the signal is known, the sampled basebanded data available for detection can be placed into a vector

$$\mathbf{x} = [\tilde{x}(\tau_p) \ \tilde{x}(\tau_p + T_s) \ \cdots \ \tilde{x}(\tau_p + (n-1)T_s)]^T \quad (8.1)$$

$$= \mathbf{u}_\Theta + \mathbf{v} \quad (8.2)$$

containing a noise component \mathbf{v} and the signal \mathbf{u}_Θ where Θ represents the signal parameters.

As described in Sect. 7.4, the standard noise model is a zero-mean Gaussian distribution. By assuming the (two-sided) noise power spectral density (PSD) is a constant $N_0/2$ [units: $\mu\text{Pa}^2/\text{Hz}$] and sampling the complex envelope at the signal bandwidth (W), the basebanded noise samples are statistically independent from sample to sample with variance

$$\lambda = 2N_0 W \quad (8.3)$$

as shown in Sect. 7.3.5.2. Thus, under the null (noise only) hypothesis the data are zero-mean, complex Gaussian distributed with covariance matrix $\lambda \mathbf{I}$,

$$\mathbf{x} \sim \mathcal{CN}(\mathbf{0}, \lambda \mathbf{I}), \quad (8.4)$$

and probability density function (PDF)

$$f(\mathbf{x}|H_0) = \frac{1}{(\pi \lambda)^n} e^{-\mathbf{x}^H \mathbf{x} / \lambda}. \quad (8.5)$$

The signal vector \mathbf{u}_θ can be described as a complex amplitude (Z_s) multiplying a unit-norm vector (\mathbf{s}_θ),

$$\mathbf{u}_\theta = Z_s \mathbf{s}_\theta \quad (8.6)$$

where θ represents deterministic parameters directly affecting the temporal form of the signal such as Doppler scale or the information encoded in a communications pulse. The known-form assumption implies \mathbf{s}_θ is known perfectly given θ . The unit-norm requirement on \mathbf{s}_θ implies $\mathbf{s}_\theta^H \mathbf{s}_\theta = 1$. How Z_s is distributed then dictates which type of signal is formed. A general formulation describing most of the signals considered in Sect. 7.5 is

$$Z_s = Ae^{j\psi} + V_s \quad (8.7)$$

where the first term describes the deterministic component having amplitude A and phase ψ and the second term a statistically independent, zero-mean Gaussian-fluctuating component with variance λ_s (i.e., $V_s \sim \mathcal{CN}(0, \lambda_s)$). It is assumed that A is always non-negative and that a sign inversion is implemented by adding π to the phase ψ . A deterministic signal (Sect. 7.5.1) is formed when setting $A > 0$ and $\lambda_s = 0$ in (8.7), a Gaussian-fluctuating signal (Sect. 7.5.2) when $\lambda_s > 0$ and $A = 0$, and a Rician signal (Sect. 7.5.3) when both $A > 0$ and $\lambda_s > 0$.

For signals with known form, the phase terms (ψ for a deterministic signal, the angle of V_s for a Gaussian-fluctuating signal, or the angle of Z_s for a Rician signal) represent a rotation of the complex amplitude as can arise during propagation through an underwater acoustical channel. In particular, it is assumed that the phase progression of the known-signal form encapsulated in \mathbf{s}_θ is not affected. As noted in Sect. 7.2.3.1, common assumptions for the signal phase include

- deterministic and known,
- deterministic and unknown, and
- random with a uniform distribution on $[0, 2\pi)$.

Recall from Sect. 7.5.1 that although the distributions of the complex basebanded signal differ when the phase is deterministic or uniformly random, the envelope or instantaneous-intensity distributions are the same. This holds both for the signal by itself and when added to zero-mean complex-Gaussian distributed noise.

When ψ is deterministic or when conditioning on ψ if it is random, the data are complex-Gaussian distributed with the deterministic-signal component entering the mean and the random-signal component adding a rank-one term ($\lambda_s \mathbf{s}_\theta \mathbf{s}_\theta^H$) to the covariance matrix,

$$\mathbf{x}|\psi \sim \mathcal{CN}\left(Ae^{j\psi} \mathbf{s}_\theta, \lambda_s \mathbf{s}_\theta \mathbf{s}_\theta^H + \lambda \mathbf{I}\right). \quad (8.8)$$

When the deterministic-signal phase is random, the PDF of the data can be obtained by taking the expectation over ψ of the data PDF described by (8.8), which results in the integral

$$f(\mathbf{x}|H_1) = \int_0^{2\pi} \frac{\exp\left\{-(\mathbf{x} - Ae^{j\psi}\mathbf{s}_\theta)^H (\lambda_s \mathbf{s}_\theta \mathbf{s}_\theta^H + \lambda \mathbf{I})^{-1} (\mathbf{x} - Ae^{j\psi}\mathbf{s}_\theta)\right\}}{\pi^n |\lambda_s \mathbf{s}_\theta \mathbf{s}_\theta^H + \lambda \mathbf{I}|} f_\psi(\psi) d\psi \quad (8.9)$$

where $f_\psi(\psi)$ is the PDF of ψ , which is simply $1/(2\pi)$ for $\psi \in [0, 2\pi]$ when it is uniformly random. The PDF in (8.9) will be used in subsequent sections to derive the detectors for various combinations of assumptions in the knowledge and consistency signal-characterization dimensions. The combinations to be considered are listed in Table 8.2 along with the resulting detector, its optimality, and in which section the detector is derived.

When the phase of a deterministic signal is known, the detector (derived in Sect. 8.2.2) is called a coherent matched filter (CMF). When the signal phase is unknown or uniformly random the detector has the form of an “incoherent” or “quadrature” matched filter (QMF). The QMF detector incoherently combines the in-phase and quadrature components of the signal envelope, thereby ignoring the signal phase. The decision statistic of the QMF detector, which is derived in Sect. 8.2.3, is the squared modulus of the inner product between the data vector (\mathbf{x}) and the unit-norm signal vector (\mathbf{s}_θ) divided by the noise variance,

$$T(\mathbf{x}) = \frac{|\mathbf{s}_\theta^H \mathbf{x}|^2}{\lambda}. \quad (8.10)$$

The QMF detector is implemented by comparing the detector decision statistic in (8.10) to a detector decision threshold h . The mathematical notation for this decision process is

$$T(\mathbf{x}) \stackrel{H_1}{\geqslant} h \quad (8.11)$$

which indicates the noise-only or null hypothesis (H_0) is chosen when $T(\mathbf{x})$ is less than h and the signal-present or alternative hypothesis (H_1) is chosen when $T(\mathbf{x})$ is greater than or equal to h .

Noting that perfect knowledge of signal phase is a rare occurrence and seeing from Table 8.2 how many different signal characterizations result in the QMF detector with some degree of optimality, it is not surprising that it is the most commonly used type of detection processor for signals with known form. As such, references to a “matched filter” generally imply the QMF. From (8.10), it can be seen that the coherent portion of detection processing is the vector inner product

$$X = \mathbf{s}_\theta^H \mathbf{x}. \quad (8.12)$$

As will be seen, this is also the coherent portion of detection processing when using the CMF. This form of the matched filter is commonly called a *replica correlator* owing to the correlation implied by the vector inner product of the

Table 8.2 Various signal models, the underlying assumptions about their parameters, the resulting detector, its optimality, and the section in which the detector is derived. The signal component is $Z_s = Ae^{j\psi} + V_s$ from (8.7) where $V_s \sim \mathcal{CN}(0, \lambda_s)$. For each case, the additive Gaussian noise is assumed to have a constant and known PSD in the signal band. Additionally, the arrival time of the signal and any other signal parameters (e.g., Doppler scale) are assumed to be known

Signal [Section]	Signal strengths ¹ (A and λ_s)	Signal phase (ψ)	Detector & Optimality conditions
Deterministic (known phase) [8.2.2]	Deterministic $ Z_s = A$	Deterministic and Known	CMF NPO & UMP(A)
Deterministic (unknown phase) [8.2.3]	Deterministic $ Z_s = A$	Deterministic and Unknown	QMF GLR(ψ)
Deterministic (random phase) [8.2.4]	Deterministic $ Z_s = A$	Random $\psi \sim \text{Uni}(0, 2\pi)$	QMF NPO & UMP(A)
Gaussian-fluctuating [8.2.5]	Random $ Z_s \sim \text{Rayl}(\lambda_s)$	Random $\psi \sim \text{Uni}(0, 2\pi)$	QMF NPO & UMP(λ_s)
Rician (known phase) [8.2.7]	Mixed $ Z_s \sim \text{Rice}(\sqrt{\lambda_s}, A)$	Deterministic and Known	Mixed CMF/QMF NPO & UMP(A/λ_s)
Rician (unknown phase) [8.2.6 & 8.2.7]	Mixed $ Z_s \sim \text{Rice}(\sqrt{\lambda_s}, A)$	Deterministic and Unknown	QMF GLR(ψ), GLR(A, ψ)
Rician (random phase) [8.2.6 & 8.2.7]	Mixed $ Z_s \sim \text{Rice}(\sqrt{\lambda_s}, A)$	Random $\psi \sim \text{Uni}(0, 2\pi)$	QMF NPO & UMP(A, λ_s)
Arbitrary amplitude (unknown phase) [8.2.6]	Random $ Z_s \sim f_A(a; \theta_A)$	Deterministic and Unknown	QMF GLR(ψ)
Arbitrary amplitude (random phase) [8.2.6]	Random $ Z_s \sim f_A(a; \theta_A)$	Random $\psi \sim \text{Uni}(0, 2\pi)$	QMF NPO & UMP(θ_A)

Legend:

Detectors

MF = matched filter

CMF = coherent MF

QMF = quadrature MF

Optimality

NPO = Neyman-Pearson optimal

UMP(θ) = uniformly most powerful for θ

GLR(θ) = generalized likelihood ratio detector for θ

Notes:

1. The deterministic-signal amplitude (A) and random-signal variance (λ_s) can be either known or unknown in each of the scenarios presented and maintain the stated optimality, with the exception of the Rician signal with known phase where the ratio A/λ_s must be known.

data with a signal “replica” \mathbf{s}_θ . The “filtering” context arises when the arrival time of the signal is unknown and the replica correlator in (8.12) is applied at every possible time through the use of a finite-impulse-response (FIR) filter formed from the signal replica. By setting the filter impulse response equal to the time-inverted and conjugated signal, the convolution between it and the input data results in a correlation (see Exercise 8.1 for an example implementation). The matched-filtering process is also called *pulse compression* because the temporal response of the matched filter has a peak magnitude at the time of the signal arrival, but can fall off rapidly when the replica and the signal are misaligned temporally. The width of this response is generally narrower than the duration of the pulse itself and significantly so for broadband waveforms, which explains the pulse-compression moniker.

To recapitulate, *matched filtering*, *replica correlation*, and *pulse compression* all represent the same process: one that can be derived from a detection inferential objective. Derivations for various assumptions about the signal strengths and phase (e.g., deterministic or random) are presented in Sects. 8.2.2–8.2.7 and summarized in Table 8.2 along with the associated optimality conditions. It is important to note that these derivations assume that the noise variance (λ) and any other signal parameters (such as Doppler scale and arrival time) are known. As described in Sect. 8.2.8, unknown parameters are generally estimated from the data and used to form a generalized likelihood ratio (GLR) detector which degrades the optimality condition of the original detector. When the noise PSD is not flat in the frequency band of the signal and the data sampled at the signal bandwidth, the noise covariance matrix of the sample data vector is no longer a scaled identity matrix. When the shape of the noise PSD is unknown it must be estimated to form an adaptive matched filter, as described in Sect. 8.2.9. The trade-off between the small increase in performance obtained by oversampling a matched-filter detector and the small decrease in performance from the ensuing higher false-alarm-rate is examined in Sect. 8.2.10.

Exercise 8.1 (Implementing a matched-filter) Use the following MATLAB® code to implement a matched filter for an LFM pulse. The `filter` command implements a linear-time-invariant (LTI) filter. A finite-impulse-response (FIR) filter is implemented by placing the filter coefficients in the first argument and a one in the second. To implement a correlation between the complex envelopes of the signal replica and the data using this command, the replica must be conjugated and time-reversed (recall that the output of an LTI filter is the convolution between its impulse response and input). The first $n - 1$ samples of the filter response represent negative delays where the replica and data sample do not fully overlap and are therefore discarded.

```
% Design parameters
Tp=1; W=50; taup=1;
fs=max(100,10*W); % Set the sampling rate
t=(0:1/fs:Tp)'; % Time sampling for the replica
% Generate the LFM-pulse complex envelope
s=exp(1j*2*pi*(-t*W/2+(W/(2*Tp))*t.^2));
s=s/sqrt(s'*s); % Scale the replica so it is unit length
% Place the replica in the middle of a data sample
```

```

x=[zeros(round(fs*taup*1.5),1); s; zeros(round(fs*taup*1.5),1)];
% Matched filter the data
y=filter(conj(s(end:-1:1)),1,x);
% Remove samples until replica fully overlaps data
y=y(length(s):end);
tau=(0:length(y)-1)/fs; % Delay for each filter output sample
plot(tau,abs(y)); % Plot the envelope

```

What is the width of the response at the 3-dB-down points (where the envelope is a factor $\sqrt{0.5}$ of its peak)? How does the shape of the response change as the bandwidth (W) is lowered? What is the shape when $W = 0$, which represents a CW pulse?

8.2.1 SNR Gain of the Matched Filter

The simple form of the statistical model for basebanded data sampled at the signal bandwidth under the constant-in-band noise PSD assumption makes derivation of detectors for the various signal characterizations straightforward. However, it is still important to relate the parameters used in the sampled baseband data model to those describing the continuous-time bandpass signal. This in turn provides the connections between the ratio of the bandpass signal energy to the noise power spectral density (\mathcal{E}/N_0), the SNR after the coherent portion of the detection process (S^d), and the probabilities of detection and false alarm (P_d and P_f) for a given detector and signal model, that are required to obtain the detection threshold (DT) term in the sonar equation.

From (8.3) the noise variance of the sampled data is $\lambda = 2N_0W$ where $N_0/2$ is the (two-sided) noise PSD. Using the results of Sect. 7.3.5.1, the inner product of the baseband signal vector with itself can be related to the signal energy \mathcal{E} in the continuous-time bandpass signal (over the signal duration T_p) according to

$$\mathbf{u}_\Theta^H \mathbf{u}_\Theta = 2\mathcal{E}f_s = 2\mathcal{E}W \quad (8.13)$$

where, as before, it is assumed that $f_s = W$. This relationship can also be seen by recalling from Exercise 7.3 that the signal energy \mathcal{E} is half that of the analytic signal $\dot{s}(t)$ or its complex envelope $\tilde{s}(t)$,

$$\mathcal{E} = \int_{-\infty}^{\infty} s^2(t) dt = \frac{1}{2} \int_{-\infty}^{\infty} |\dot{s}(t)|^2 dt = \frac{1}{2} \int_{-\infty}^{\infty} |\tilde{s}(t)|^2 dt. \quad (8.14)$$

When the signal has a random component, an expectation must be applied to (8.13) and \mathcal{E} can be interpreted as the average bandpass signal energy throughout the signal duration T_p . For the baseband signal model in (8.6) and (8.7), the average statistical

power of the signal is

$$E[\mathbf{u}_\Theta^H \mathbf{u}_\Theta] = E[|Z_s|^2] = A^2 + \lambda_s \quad (8.15)$$

which leads to

$$A^2 + \lambda_s = 2\mathcal{E}W. \quad (8.16)$$

While these results individually relate the parameters of the sampled baseband signal and noise models to the continuous-time bandpass signal energy and noise PSD, they also provide the means to describe the SNR after the coherent portion of detection, which is used in the sonar-equation analysis presented in Sect. 2.3. The average statistical power of $X = \mathbf{s}_\theta^H \mathbf{x}$ in (8.12),

$$E[|X|^2] = A^2 + \lambda_s + \lambda, \quad (8.17)$$

contains a signal component ($A^2 + \lambda_s$) and a noise component (λ). The SNR after the coherent portion of detection is simply the ratio of these two, yielding

$$S^d = \frac{A^2 + \lambda_s}{\lambda} = \frac{\mathcal{E}}{N_0}, \quad (8.18)$$

which is clearly equal to the ratio of the bandpass signal energy to noise-PSD ratio (\mathcal{E}/N_0). The SNR required to achieve a desired detector operating point (i.e., \overline{SNR}^d) can then be obtained through the analysis of the detectors derived in this section for each of the different signal models and be interpreted as a requirement on the bandpass signal energy to (one-sided) noise PSD ratio.

In order to determine the gain in SNR achieved by the matched filter, the SNR at its input must be assessed. The SNR for the i th input sample is simply

$$\frac{E[|Z_s \mathbf{s}_\theta[i]|^2]}{\lambda} = \frac{(A^2 + \lambda_s)|\mathbf{s}_\theta[i]|^2}{\lambda} \quad (8.19)$$

where $\mathbf{s}_\theta[i]$ is the i th element of the vector \mathbf{s}_θ . Because the signal can vary throughout the n input samples, the individual SNRs in (8.19) are averaged to form

$$\begin{aligned} S_{in}^d &= \frac{(A^2 + \lambda_s)}{n\lambda} \sum_{i=1}^n |\mathbf{s}_\theta[i]|^2 \\ &= \frac{(A^2 + \lambda_s)}{n\lambda}. \end{aligned} \quad (8.20)$$

The SNR gain achieved by the matched filter can then be obtained from the ratio of (8.18) (here labeled as $S_{\text{out}}^{\text{d}}$) to the average input SNR from (8.20),

$$G_{\text{d}} = \frac{S_{\text{out}}^{\text{d}}}{S_{\text{in}}^{\text{d}}} = n = T_p W. \quad (8.21)$$

It is important to note that using (8.18) requires the sampling rate to be equal to the signal bandwidth so $n = T_p W$ and the SNR gain in (8.21) is that obtained when applying a matched filter after the data have been filtered to the frequency band of the signal. Thus, the matched filter provides a gain in SNR equal to the time-bandwidth product of the signal.

For sinusoidal signals (e.g., a CW pulse) the bandwidth is one over the duration, $W = 1/T_p$, so the matched filter does not provide any improvement in SNR irrespective of pulse duration. This does not imply that the SNR after matched filtering does not improve with pulse duration; from (8.18) it clearly will increase with pulse duration or amplitude in an ambient-noise background. The unity SNR gain of the matched filter for sinusoidal signals implies that there is no structure exploitable beyond filtering the data to the frequency band of the signal. However, for frequency modulated signals (e.g., an LFM or HFM pulse) where there is structure within the frequency band of the signal, the SNR gain of the matched filter is proportional to both pulse duration and bandwidth.

8.2.2 *Detector for Signals with Known Form, Known Amplitude, and Known Phase*

When a deterministic signal is known perfectly, the PDF of the data under the alternative hypothesis (H_1) is that of (8.8) where ψ is assumed to be known or (8.9) with all weight in $f_{\psi}(\psi)$ at a known phase and $\lambda_s = 0$, resulting in

$$f(\mathbf{x}|H_1) = \frac{1}{(\pi\lambda)^n} e^{-(\mathbf{x}-Ae^{j\psi}\mathbf{s}_{\theta})^H(\mathbf{x}-Ae^{j\psi}\mathbf{s}_{\theta})/\lambda}. \quad (8.22)$$

The Neyman-Pearson optimal (NPO) detector (Sect. 6.2.3), which maximizes the probability of detection given a fixed probability of false alarm, can be formed from the log-likelihood ratio (LLR). The LLR is simply the logarithm of the ratio of the PDFs under the alternative and null hypotheses,

$$l(\mathbf{x}) = \log \left\{ \frac{f(\mathbf{x}|H_1)}{f(\mathbf{x}|H_0)} \right\}. \quad (8.23)$$

Using $f(\mathbf{x}|H_0)$ from (8.5) with (8.22), the LLR for a perfectly known signal in additive white Gaussian noise can be shown to be

$$l(\mathbf{x}) = \frac{2A \operatorname{Real}\{e^{-j\psi} \mathbf{s}_\theta^H \mathbf{x}\}}{\lambda} - \frac{A^2}{\lambda}. \quad (8.24)$$

As described in Sect. 6.2.3, the NPO condition of a detector is preserved under any strictly monotonically increasing transformation. In fact any detector can be modified by such a transformation without affecting performance because it is always possible to invert the transformation to obtain the original form of the detector. The detector in (8.24) can therefore be simplified to

$$\begin{aligned} T(\mathbf{x}) &= \frac{1}{A} \sqrt{\frac{\lambda}{2}} \left[l(\mathbf{x}) + \frac{A^2}{\lambda} \right] \\ &= \sqrt{\frac{2}{\lambda}} \cdot \operatorname{Real}\{e^{-j\psi} \mathbf{s}_\theta^H \mathbf{x}\} \end{aligned} \quad (8.25)$$

In this transformation, dependence on the amplitude A has been removed and allows implementing the detector without a priori knowledge of its value (recall it has been assumed that $A > 0$ so there is no concern about a sign inversion). Thus, the detector has the same form regardless of what the actual value of A is and is therefore uniformly most powerful over A ; that is, it is $\text{UMP}(A)$. Recall that the noise variance λ was assumed to be known. It has been left in the detector to emphasize the need for estimating it when it is unknown through the normalization process described in Sect. 8.6 and also to form a decision statistic exhibiting a constant false alarm rate (CFAR). A CFAR detector has, for a given detector decision threshold, the same probability of false alarm irrespective of the noise variance. Removing λ from the detector decision statistic in (8.25) does not change the net detection performance (i.e., probability of detection as a function of probability of false alarm); it simply shifts the dependence on λ to the detector decision threshold.

The detector in (8.25) is known as a coherent matched filter (CMF) because of its dependence on the phase of the signal. The importance of the phase is underscored by rewriting (8.25) as a function of the modulus and angle of $\mathbf{s}_\theta^H \mathbf{x}$,

$$T(\mathbf{x}) = \sqrt{\frac{2}{\lambda}} |\mathbf{s}_\theta^H \mathbf{x}| \cos(\psi - \angle \mathbf{s}_\theta^H \mathbf{x}). \quad (8.26)$$

This shows how $|\mathbf{s}_\theta^H \mathbf{x}|$ is scaled, through the cosine term, based on how far the phase is from the assumed value of ψ . As the magnitude of the phase separation increases to $\pi/2$, $|\mathbf{s}_\theta^H \mathbf{x}|$ is scaled all the way down to zero. When the phase separation exceeds $\pm\pi/2$, $T(\mathbf{x})$ becomes negative making a decision error unlikely except when the probability of false alarm is allowed to be very high.

When a signal is present, the decision statistic formed by (8.25) or (8.26) is a real-valued, Gaussian distributed random variable with mean $A/\sqrt{\lambda/2} = \sqrt{2S^d}$ and unit variance,

$$T(\mathbf{x})|H_1 \sim \mathcal{N}\left(\sqrt{2S^d}, 1\right). \quad (8.27)$$

The distribution of the decision statistic under the null (noise-only) hypothesis can be obtained from (8.27) by setting $S^d = 0$, which leads to a standard normal random variable,

$$T(\mathbf{x})|H_0 \sim \mathcal{N}(0, 1). \quad (8.28)$$

The probability of false alarm (P_f) is then simply one minus the cumulative distribution function (CDF) of the standard normal random variable

$$\begin{aligned} P_f &= \Pr\{T(\mathbf{x}) \geq h|H_0\} \\ &= 1 - \Phi(h) \end{aligned} \quad (8.29)$$

where h is the detector decision threshold and $\Phi(\cdot)$ is the standard-normal CDF. The detector decision threshold can be obtained as a function of P_f by inverting (8.29) to form

$$h = \Phi^{-1}(1 - P_f) \quad (8.30)$$

where $\Phi^{-1}(\cdot)$ is the functional inverse. The probability of detection (P_d) can then be described either as a function of the decision threshold or P_f ,

$$\begin{aligned} P_d &= \Pr\{T(\mathbf{x}) \geq h|H_1\} \\ &= 1 - \Phi\left(h - \sqrt{2S^d}\right) \end{aligned} \quad (8.31)$$

$$= 1 - \Phi\left(\Phi^{-1}(1 - P_f) - \sqrt{2S^d}\right). \quad (8.32)$$

The receiver operating characteristic (ROC) curve for the perfectly known signal with a 10-dB signal-to-noise power ratio (SNR) is shown in Fig. 8.5. By solving (8.32) for S^d , the SNR in decibels required by the CMF to achieve a desired (P_d , P_f) operating point when detecting a deterministic signal with known phase is found to be

$$\overline{\text{SNR}}^d = 10 \log_{10}(S^d) = 10 \log_{10} \left[\frac{(\phi_f - \phi_d)^2}{2} \right] \quad (8.33)$$

where $\phi_f = \Phi^{-1}(1 - P_f)$ and $\phi_d = \Phi^{-1}(1 - P_d)$.

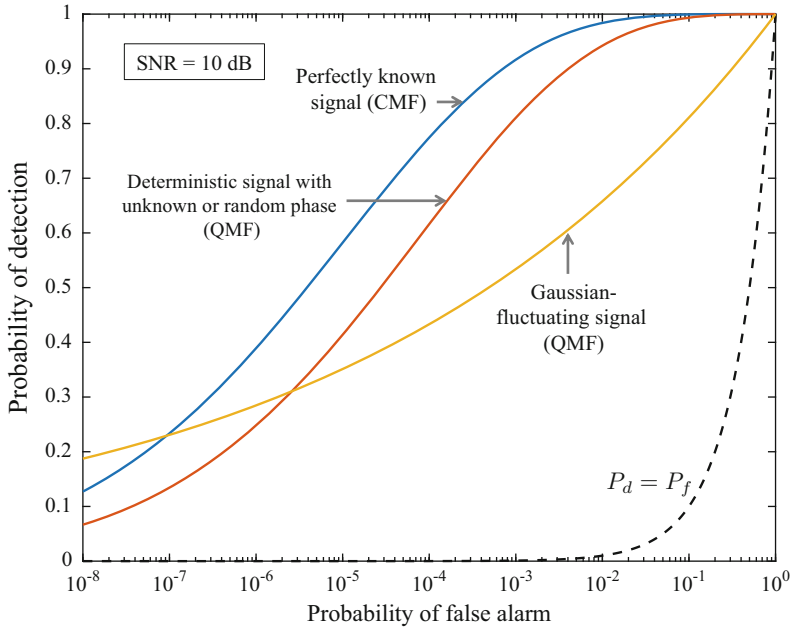


Fig. 8.5 ROC curve showing the performance of various signal and detector combinations for a 10-dB SNR

If there is error in the assumed phase of $\Delta_\psi \in (-\pi/2, \pi/2)$, the mean of the decision statistic is reduced by a factor $\cos \Delta_\psi$,

$$T(\mathbf{x})|H_1 \sim \mathcal{N}\left(\sqrt{2S^d \cos^2(\Delta_\psi)}, 1\right). \quad (8.34)$$

The SNR required to achieve a specific operating point is therefore subject to a decibel loss of

$$\text{Loss}_{\text{dB}} = -10 \log_{10} [\cos^2(\Delta_\psi)]. \quad (8.35)$$

Noting that a 1-dB loss occurs when Δ_ψ is $\sim \pm 27^\circ$ and a 3-dB loss at $\pm 45^\circ$, it can be seen that the phase does not necessarily need to be known very accurately for the CMF to be useful. However, a large phase error can result in a significant degradation in performance.

8.2.3 Detector for Signals with Known Form and Unknown Phase

As previously noted, it is not common for the phase of a signal to be known accurately enough to implement the CMF. The next step along the combined knowledge and consistency signal-characterization dimension explored in Sect. 7.2.1 is to let the phase remain deterministic, but assume it is unknown.

Because ψ is unknown and does not distinguish the signal-present from the noise-only hypotheses, it is considered an ancillary signal parameter (see Sect. 6.2.4). With no knowledge about the signal phase other than its determinism, it must be estimated from the data and used to form a generalized likelihood ratio (GLR) detector as described in Sect. 6.2.7. For now it is still assumed that A , η , and λ are known. The GLR detector over ψ then has the form

$$T(\mathbf{x}) = \frac{\max_{\psi} f(\mathbf{x}|H_1)}{f(\mathbf{x}|H_0)}. \quad (8.36)$$

The PDF of the data under H_1 is still that shown in (8.22). However, because the LLR depends on ψ only through the numerator in (8.36) (i.e., because ψ does not exist as a parameter under H_0), the maximization can be applied directly to (8.26), yielding

$$\begin{aligned} T(\mathbf{x}) &= \max_{\psi} \sqrt{\frac{2}{\lambda}} \left| \mathbf{s}_{\theta}^H \mathbf{x} \right| \cos(\psi - \angle \mathbf{s}_{\theta}^H \mathbf{x}) \\ &= \sqrt{\frac{2}{\lambda}} \left| \mathbf{s}_{\theta}^H \mathbf{x} \right| \end{aligned} \quad (8.37)$$

$$\stackrel{D}{\equiv} \frac{|\mathbf{s}_{\theta}^H \mathbf{x}|^2}{\lambda} \quad (8.38)$$

where the notation $\stackrel{D}{\equiv}$ is introduced to represent application of an invertible function to yield an equivalent detector. As previously mentioned, this detector is called an *incoherent* or *quadrature* matched filter (QMF) [19, Sect. 7.6.2] because it combines the squared amplitudes of both the in-phase and quadrature components of the demodulated bandpass signal after matched filtering. As done for the CMF, a dependence on the noise variance has been left in the detector decision statistic both to emphasize the need for it and to produce a CFAR detector. Note that the form of the detector does not depend on the amplitude A , which is assumed to be deterministic. As a result of this, the QMF can be used either when A is known or unknown; in both cases, it is a GLR detector because of the unknown phase.

When signal is present, the coherent component of the detector ($\mathbf{s}_\theta^H \mathbf{x}$) is complex-Gaussian distributed with mean $Ae^{j\psi}$ and variance λ ,

$$X = \mathbf{s}_\theta^H \mathbf{x} \sim \mathcal{CN}\left(Ae^{j\psi}, \lambda\right). \quad (8.39)$$

This implies the real (X_r) and imaginary (X_i) components, which are statistically independent, individually have variance $\lambda/2$ and, respectively, means of $A \cos \psi$ and $A \sin \psi$. Dividing by their standard deviation, squaring and summing the two components then produces

$$\left(\frac{X_r}{\sqrt{\lambda/2}}\right)^2 + \left(\frac{X_i}{\sqrt{\lambda/2}}\right)^2 \sim \chi_{2,\delta}^2, \quad (8.40)$$

which is non-central chi-squared distributed (see Sect. 5.6.15) with two degrees of freedom and a non-centrality parameter

$$\delta = \left(\frac{A \cos \psi}{\sqrt{\lambda/2}}\right)^2 + \left(\frac{A \sin \psi}{\sqrt{\lambda/2}}\right)^2 = \frac{2A^2}{\lambda} = 2S^d. \quad (8.41)$$

Noting that the sum of squares in (8.40) is simply two times $T(\mathbf{x})$, the decision statistic under H_1 is said to be the scale of a non-central chi-squared distribution,

$$2T(\mathbf{x})|H_1 \sim \chi_{2,\delta}^2 \quad (8.42)$$

with $\delta = 2S^d$.

Under the null hypothesis, which is obtained from (8.42) by setting $S^d = 0$, this simplifies to the standard chi-squared distribution with two degrees of freedom,

$$2T(\mathbf{x})|H_0 \sim \chi_2^2. \quad (8.43)$$

The probability of false alarm is easily obtained as one minus the CDF of the chi-squared distribution (see Sect. 5.6.14) evaluated at the decision threshold (h) multiplied by two to account for the two multiplying $T(\mathbf{x})$ in (8.43),

$$P_f = 1 - F_{\chi_2^2}(2h) = e^{-h}. \quad (8.44)$$

This can be inverted to obtain the decision threshold as a function of P_f ,

$$h = -\log P_f. \quad (8.45)$$

In some formulations of the QMF as a detector, the scale of two in (8.42) is included in the decision statistic itself, which results in a decision threshold that is two times that shown in (8.45).

The probability of detection is similarly obtained as one minus the CDF of the non-central chi-squared distribution evaluated at $2h$,

$$\begin{aligned} P_d &= 1 - F_{\chi^2_{2,\delta}}(2h) \\ &= 1 - F_{\chi^2_{2,\delta}}(-2 \log P_f) \end{aligned} \quad (8.46)$$

with non-centrality parameter $\delta = 2S^d$. As described in Sects. 5.6.15 and 7.5.1, the CDF of the non-central chi-squared distribution, which can be approximated by the CDF of a shifted gamma distribution, is a generalized Marcum Q function. Inversion of (8.46) to solve for S^d in terms of the (P_d, P_f) operating point, which then produces the DT term in the sonar equation for detecting a deterministic signal with the QMF, can be accomplished using the results of Albersheim [20] or Hmam [21] as described in Sect. 2.3.5.2.

A ROC curve for the QMF detector with a deterministic signal with 10-dB SNR is shown in Fig. 8.5, where it is seen to have reduced performance relative to the CMF. This difference is the cost of not knowing the phase or in ignoring it if it is known. The severity of the loss can be quantified in terms of the SNR as follows. Given a signal measurement with an SNR and a desired P_d essentially dictates what the detector decision threshold must be in the CMF through (8.31) and the resulting P_f through (8.30) or (8.32). The SNR required to obtain this particular operating point when using the QMF can then be found through Hmam's equation (specifically, (2.87) with $M = 1$). The difference between the SNR required by the QMF and that required by the CMF also describes the SNR loss when the signal phase is unknown, uniformly random, or when it is known but ignored relative to when it is known precisely. As shown in Fig. 8.6, the loss decreases as SNR increases or the desired P_d decreases. Noting that the loss is less than one decibel when SNR exceeds 10 dB and the P_d operating point is less than 0.95, use of the QMF over the CMF may be warranted if there is any possibility that the assumed knowledge of the phase is incorrect.

8.2.4 Detector for Signals with Known Form and Uniformly Random Phase

When the phase of a deterministic signal is uniformly random on $[0, 2\pi]$, the PDF of \mathbf{x} under H_1 can be obtained from (8.9) by setting $\lambda_s = 0$ and letting $f_\psi(\psi) = 1/(2\pi)$ for $\psi \in [0, 2\pi]$,

$$f(\mathbf{x}|H_1) = \int_0^{2\pi} \frac{1}{(\pi\lambda)^n} e^{-(\mathbf{x} - Ae^{j\psi}\mathbf{s}_\theta)^H(\mathbf{x} - Ae^{j\psi}\mathbf{s}_\theta)/\lambda} \frac{1}{2\pi} d\psi$$

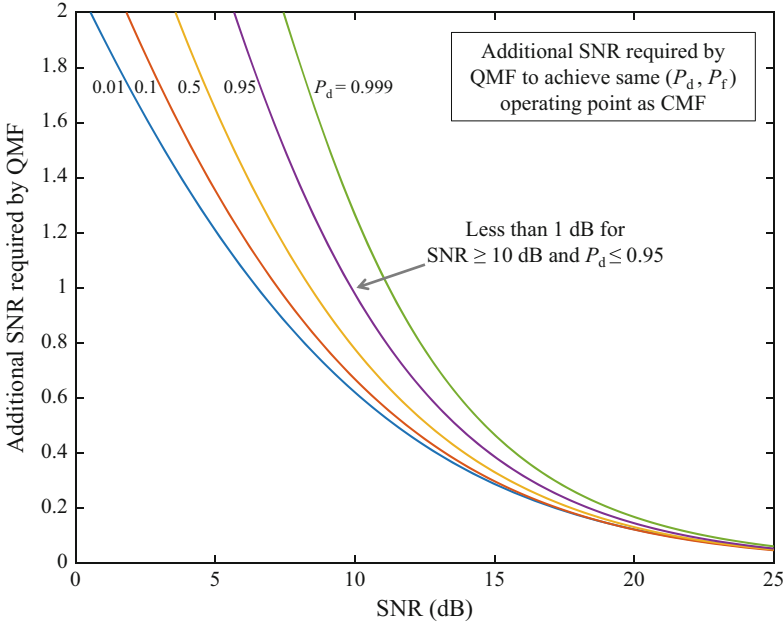


Fig. 8.6 Additional SNR required by the QMF to achieve the same performance as the CMF when phase is known or the loss in SNR when using the QMF because phase is unknown, uniformly random, or ignored

$$= \frac{e^{-(\mathbf{x}^H \mathbf{x} + A^2)/\lambda}}{(\pi \lambda)^n} \frac{1}{2\pi} \int_0^{2\pi} e^{2A\lambda^{-1}|\mathbf{s}_\theta^H \mathbf{x}| \cos(\psi - \angle \mathbf{s}_\theta^H \mathbf{x})} d\psi \quad (8.47)$$

$$= \frac{e^{-(\mathbf{x}^H \mathbf{x} + A^2)/\lambda}}{(\pi \lambda)^n} I_0\left(\frac{2A|\mathbf{s}_\theta^H \mathbf{x}|}{\lambda}\right) \quad (8.48)$$

where $I_0(x)$ is the order-zero modified Bessel function [22, Ch. 49]. The simplification from (8.47) to (8.48), which comes from application of [23, 3.339], is seen to remove the dependence on the phase of $\mathbf{s}_\theta^H \mathbf{x}$. The likelihood ratio can then be formed from (8.48) and (8.5) for the noise PDF to result in

$$L(\mathbf{x}) = \frac{f(\mathbf{x}|H_1)}{f(\mathbf{x}|H_0)} = e^{-A^2/\lambda} I_0\left(\frac{2A|\mathbf{s}_\theta^H \mathbf{x}|}{\lambda}\right). \quad (8.49)$$

In order to claim that the likelihood-ratio detector is equivalent to the QMF,

$$L(\mathbf{x}) \stackrel{D}{\equiv} \frac{|\mathbf{s}_\theta^H \mathbf{x}|^2}{\lambda}, \quad (8.50)$$

it is only necessary to show that $I_0(x)$ is strictly monotonically increasing for positive arguments. Using the infinite-sum definition of the modified Bessel function,

$$I_0(x) = \sum_{j=0}^{\infty} \frac{(x^2/4)^j}{(j!)^2}, \quad (8.51)$$

from [22, Sect. 49:6] $I'_0(x)$ is easily seen to be non-negative when $x > 0$. Thus, the QMF is NPO for a deterministic signal with uniformly random phase. Because the QMF does not depend on knowledge of the amplitude A , it is also UMP(A).

Recall from Sect. 7.5.1 that the distributions of the instantaneous intensity for a deterministic signal in additive Gaussian noise are the same regardless of whether the signal's phase is deterministic or uniformly random. Because both scenarios also result in the QMF, which is proportional to the instantaneous intensity, their detection performance is also identical and can be taken from the results presented in Sect. 8.2.3.

8.2.5 Detector for Signals with Known Form and Gaussian Amplitude Fluctuations

The Gaussian-fluctuating signal can be represented in (8.9) by setting $A = 0$, which results in the PDF

$$f(\mathbf{x}|H_1) = \frac{1}{\pi^n |\lambda_s \mathbf{s}_\theta \mathbf{s}_\theta^H + \lambda \mathbf{I}|} \exp \left\{ -\mathbf{x}^H (\lambda_s \mathbf{s}_\theta \mathbf{s}_\theta^H + \lambda \mathbf{I})^{-1} \mathbf{x} \right\} \quad (8.52)$$

$$= \frac{1}{(\pi \lambda)^n (1 + \lambda_s/\lambda)} \exp \left\{ -\frac{\mathbf{x}^H \mathbf{x}}{\lambda} + \frac{|\mathbf{s}_\theta^H \mathbf{x}|^2}{\lambda(1 + \lambda/\lambda_s)} \right\}. \quad (8.53)$$

The simplification from (8.52) to (8.53) requires solution of the determinant in the denominator and exploiting the matrix inversion lemma [24, Sect. A.21]

$$(\mathbf{A} + \mathbf{U} \mathbf{B} \mathbf{V}^H)^{-1} = \mathbf{A}^{-1} - \mathbf{A}^{-1} \mathbf{U} (\mathbf{V}^H \mathbf{A}^{-1} \mathbf{U} + \mathbf{B}^{-1})^{-1} \mathbf{V}^H \mathbf{A}^{-1}, \quad (8.54)$$

also known as the Woodbury identity, to simplify the matrix–vector quadratic form in the exponent of (8.52). Recalling that $\mathbf{s}_\theta^H \mathbf{s}_\theta = 1$, the matrix inverse in (8.52) simplifies to

$$(\lambda_s \mathbf{s}_\theta \mathbf{s}_\theta^H + \lambda \mathbf{I})^{-1} = \frac{1}{\lambda} \mathbf{I} - \frac{1}{\lambda(1 + \lambda/\lambda_s)} \mathbf{s}_\theta \mathbf{s}_\theta^H \quad (8.55)$$

Noting that the determinant of a matrix is the product of its eigenvalues and that $\lambda_s \mathbf{s}_\theta \mathbf{s}_\theta^H + \lambda \mathbf{I}$ has $n - 1$ eigenvalues equal to λ and one equal to $\lambda_s \mathbf{s}_\theta^H \mathbf{s}_\theta + \lambda$, this results in

$$|\lambda_s \mathbf{s}_\theta \mathbf{s}_\theta^H + \lambda \mathbf{I}| = (\lambda_s \mathbf{s}_\theta^H \mathbf{s}_\theta + \lambda) \lambda^{n-1} = \lambda^n (1 + \lambda_s/\lambda). \quad (8.56)$$

The LLR is then obtained by combining (8.53) with (8.5) to produce

$$\begin{aligned} l(\mathbf{x}) &= \frac{|\mathbf{s}_\theta^H \mathbf{x}|^2}{\lambda(1 + \lambda/\lambda_s)} - \log(1 + \lambda_s/\lambda) \\ &\stackrel{D}{=} \frac{|\mathbf{s}_\theta^H \mathbf{x}|^2}{\lambda}, \end{aligned} \quad (8.57)$$

which is seen to be equivalent to the QMF. Thus, the QMF is NPO for detection of a Gaussian-fluctuating signal in Gaussian noise. Because it does not depend on the signal power λ_s , it is also UMP(λ_s).

When signal is present, the coherent component of the detector ($\mathbf{s}_\theta^H \mathbf{x}$) is a zero-mean complex-Gaussian distributed random variable with variance $\lambda_s + \lambda$. By noting that the squared modulus of a zero-mean complex-Gaussian random variable is exponentially distributed, the QMF decision statistic is seen to have distribution

$$T(\mathbf{x})|H_1 \sim \text{Expon}\left(1 + S^d\right) \quad (8.58)$$

where $S^d = \lambda_s/\lambda$. Under the noise-only hypothesis, obtained by setting $\lambda_s = 0$, this simplifies to

$$T(\mathbf{x})|H_0 \sim \text{Expon}(1), \quad (8.59)$$

which is the same as that derived in Sect. 8.2.3 (i.e., a χ_2^2 random variable divided by two) and so P_f is as found in (8.44). Using $h = -\log(P_f)$ from (8.45), it can be seen that for the Gaussian-fluctuating signal

$$P_d = e^{-h/(1+S^d)} \quad (8.60)$$

$$= P_f^{1/(1+S^d)}. \quad (8.61)$$

Solving (8.61) for S^d produces the SNR required to achieve an operating point,

$$S^d = \frac{\log(P_f)}{\log(P_d)} - 1 \quad (8.62)$$

or, in decibels,

$$\overline{\text{SNR}}^d = 10 \log_{10}(S^d) = 10 \log_{10} \left[\frac{\log(P_f)}{\log(P_d)} - 1 \right]. \quad (8.63)$$

Thus, the DT term in the sonar equation for detecting a Gaussian-fluctuating signal with the QMF has a simple closed-form solution.

8.2.6 *Detector for Signals with Known Form and an Arbitrary Amplitude Distribution*

Before proceeding to evaluate a Rician signal, a more general form of amplitude distribution is considered for the unknown or uniformly random phase scenarios. Suppose the amplitude A is random with a distribution $f_A(a)$ with support only on $a > 0$. The PDF of the data when signal is present is similar to (8.9), but with $\lambda_s = 0$ and an additional integral over the random amplitude,

$$f(\mathbf{x}|H_1) = \int_0^{\infty} \int_0^{2\pi} \frac{\exp\{-(\mathbf{x} - ae^{j\psi} \mathbf{s}_\theta)^H (\mathbf{x} - ae^{j\psi} \mathbf{s}_\theta)/\lambda\}}{(\pi\lambda)^n} f_\psi(\psi) f_A(a) d\psi da \quad (8.64)$$

$$= \int_0^{\infty} \int_0^{2\pi} \frac{\exp\{-[\mathbf{x}^H \mathbf{x} + a^2 - 2a|\mathbf{s}_\theta^H \mathbf{x}| \cos(\psi - \angle \mathbf{s}_\theta^H \mathbf{x})]/\lambda\}}{(\pi\lambda)^n} f_\psi(\psi) f_A(a) d\psi da. \quad (8.65)$$

If ψ is deterministic but unknown, $f_\psi(\psi)$ in (8.65) is a Dirac delta function at the unknown value (e.g., ψ_o), which collapses the integral over ψ placing all weight at $\psi = \psi_o$. The GLR detector is then obtained by evaluating the resulting integral over a choosing $\psi_o = \angle \mathbf{s}_\theta^H \mathbf{x}$ to maximize the integrand for every value of $a > 0$. Coupled with the noise-only PDF from (8.5), this results in a detector having the form

$$T(\mathbf{x}) = \int_0^{\infty} \exp\left\{-a^2/\lambda + 2a|\mathbf{s}_\theta^H \mathbf{x}|/\lambda\right\} f_A(a) da. \quad (8.66)$$

Equivalence of (8.66) to the QMF can be shown by noting its derivative with respect to $|\mathbf{s}_\theta^H \mathbf{x}|$ is always positive under the previously mentioned assumption that $f_A(a)$ only has support on $a > 0$. Thus, the QMF is a GLR(ψ) detector for any random-amplitude signal when ψ is deterministic.

When the phase is uniformly random and independent of the amplitude, the PDF in (8.65) can be simplified to

$$f(\mathbf{x}|H_1) = \int_0^\infty \frac{1}{(\pi\lambda)^n} e^{-[\mathbf{x}^H \mathbf{x} + a^2]/\lambda} I_0(2a\lambda^{-1}|\mathbf{s}_\theta^H \mathbf{x}|) f_A(a) da \quad (8.67)$$

where $I_0(x)$ is the order-zero modified Bessel function and the simplification requires application of [23, 3.339]. The likelihood ratio detector can then be formed by the ratio of (8.67) and (8.5),

$$L(\mathbf{x}) = \int_0^\infty e^{-a^2/\lambda} I_0(2a\lambda^{-1}|\mathbf{s}_\theta^H \mathbf{x}|) f_A(a) da. \quad (8.68)$$

Similar to the previous scenario, (8.68) can be shown to be a strictly monotonically increasing function of $|\mathbf{s}_\theta^H \mathbf{x}|$ and therefore equivalent to the QMF detector by showing its derivative (using (8.51)) to be positive when $f_A(a)$ has support on $a > 0$. Thus the QMF detector is NPO for any random-amplitude signal when ψ is uniformly random on $[0, 2\pi]$.

These results apply to the deterministic signal, the Gaussian-fluctuating signal (which has a uniformly random phase), the Rician signal to be discussed in the following section (unless the deterministic-signal component has a known phase), and the gamma-fluctuating-intensity signal described in Sect. 7.5.4 under the proper phase assumptions.

8.2.7 Detector for Signals with Known Form and a Rician Distributed Amplitude

A Rician signal requires the general form of the PDF described in (8.9) where both A and λ_s are greater than zero. Of the three different phase assumptions, the deterministic-but-unknown and uniformly random are covered by the results of Sect. 8.2.6 to result in the QMF detector as, respectively, GLR(ψ) and NPO detectors. When the phase is uniformly random, the QMF is additionally UMP over A and λ_s for the Rician signal. This leaves for consideration the case where the phase of the deterministic-signal component is known, which simplifies (8.9) to

$$f(\mathbf{x}|H_1) = \frac{\exp\left\{-(\mathbf{x} - Ae^{j\psi}\mathbf{s}_\theta)^H (\lambda_s\mathbf{s}_\theta\mathbf{s}_\theta^H + \lambda\mathbf{I})^{-1} (\mathbf{x} - Ae^{j\psi}\mathbf{s}_\theta)\right\}}{\pi^n |\lambda_s\mathbf{s}_\theta\mathbf{s}_\theta^H + \lambda\mathbf{I}|} \quad (8.69)$$

$$= \frac{\exp\left\{-\frac{\mathbf{x}^H \mathbf{x}}{\lambda} + \frac{\lambda_s |\mathbf{s}_\theta^H \mathbf{x}|^2}{\lambda(\lambda + \lambda_s)} - \frac{[A^2 - 2A \operatorname{Re}[e^{-j\psi}\mathbf{s}_\theta^H \mathbf{x}]]}{(\lambda + \lambda_s)}\right\}}{(\pi\lambda)^n (1 + \lambda_s/\lambda)} \quad (8.70)$$

where the determinant and inverse of $\lambda_s\mathbf{s}_\theta\mathbf{s}_\theta^H + \lambda\mathbf{I}$ can be found in Sect. 8.2.5.

Using (8.5) for the PDF under the null hypothesis with (8.70), the LLR can be seen to be

$$l(\mathbf{x}) = \frac{\lambda_s}{(\lambda + \lambda_s)} \left[\frac{|\mathbf{s}_\theta^H \mathbf{x}|^2}{\lambda} + \frac{2A}{\lambda_s} \operatorname{Real} \left\{ e^{-j\psi} \mathbf{s}_\theta^H \mathbf{x} \right\} - \frac{A^2}{\lambda_s} \right] - \log(1 + \lambda_s/\lambda) \quad (8.71)$$

$$\stackrel{D}{=} \frac{2|\mathbf{s}_\theta^H \mathbf{x}|^2}{\lambda} + 2\sqrt{2}\gamma \frac{|\mathbf{s}_\theta^H \mathbf{x}|}{\sqrt{\lambda/2}} \cos(\psi - \angle \mathbf{s}_\theta^H \mathbf{x}) + 2\gamma^2 \quad (8.72)$$

where

$$\gamma = \frac{A\sqrt{\lambda}}{\lambda_s} = \frac{\sqrt{\frac{A^2}{\lambda}}}{\frac{\lambda_s}{\lambda}} \quad (8.73)$$

is essentially a ratio of the deterministic-signal amplitude to the noise standard deviation to the SNR of the random-signal component. Note that the form of the detector in (8.72) is chosen to simplify the analysis of its performance; only the first two terms are required for implementation. The detector in (8.72) is NPO and UMP over all values of (A, λ_s) such that γ is fixed. Noting that γ is proportional to A and inversely proportional to λ_s , the detector will approximate the CMF when the deterministic component of the signal dominates and approximate the QMF when the random component dominates. In between, the detector balances between the two detector structures.

To analyze detection performance, it is helpful to define an intermediate variable by normalizing the coherent component of the CMF and QMF ($\mathbf{s}_\theta^H \mathbf{x}$) by $\sqrt{\lambda/2}$, which is the standard deviation of its real and imaginary parts under H_0 , and rotating it in angle by $-\psi$ so the deterministic-signal component lies completely in the real part,

$$Z = \frac{e^{-j\psi} \mathbf{s}_\theta^H \mathbf{x}}{\sqrt{\lambda/2}} = U + jV. \quad (8.74)$$

In terms of Z and its real and imaginary parts, the decision statistic in (8.72) can be written as

$$\begin{aligned} T(\mathbf{x}) &= |Z|^2 + 2\sqrt{2}\gamma \operatorname{Real}\{Z\} + 2\gamma^2 \\ &= V^2 + U^2 + 2(\sqrt{2}\gamma)U + 2\gamma^2 \\ &= V^2 + (U + \sqrt{2}\gamma)^2. \end{aligned} \quad (8.75)$$

When signal is present Z, U , and V have the following statistical distributions:

$$Z \sim \mathcal{CN}(A/\sqrt{\lambda/2}, 2 + 2\lambda_s/\lambda), \quad (8.76)$$

$$U \sim \mathcal{N}(A/\sqrt{\lambda/2}, 1 + \lambda_s/\lambda), \quad \text{and} \quad (8.77)$$

$$V \sim \mathcal{N}(0, 1 + \lambda_s/\lambda). \quad (8.78)$$

The distributions for the noise-only hypothesis are obtained by setting A and λ_s to zero in (8.76)–(8.78). However, because γ comes from the likelihood ratio and is used to implement the detector, it is the same under both hypotheses. Because U and V are independent Gaussian random variables and have unit variance under H_0 , the sum of squares in (8.75) results in a non-central chi-squared distribution with two degrees of freedom and a non-centrality parameter equal to $2\gamma^2$,

$$T(\mathbf{x})|H_0 \sim \chi_{2,2\gamma^2}^2. \quad (8.79)$$

Under H_1 , $T(\mathbf{x})$ similarly follows the non-central chi-squared distribution, but first needs to be scaled by the variance $1 + \lambda_s/\lambda$,

$$\frac{T(\mathbf{x})}{1 + \lambda_s/\lambda} \sim \chi_{2,\delta_1}^2 \quad (8.80)$$

where the non-centrality parameter is

$$\delta_1 = \frac{2(A + \sqrt{\lambda}\gamma)^2}{\lambda + \lambda_s}. \quad (8.81)$$

Thus, the probability of false alarm is

$$P_f = 1 - F_{\chi_{2,2\gamma^2}^2}(h) \quad (8.82)$$

and the probability of detection is

$$P_d = 1 - F_{\chi_{2,\delta_1}^2}(h/(1 + \lambda_s/\lambda)) \quad (8.83)$$

where $F_{\chi_{2,\delta}^2}(x)$ is the CDF of the non-central chi-squared distribution.

An example illustrating how choosing the correct value of γ leads to optimal performance (in the Neyman-Pearson sense) is shown in Fig. 8.7. In this example, the power of the deterministic-signal component is set to be 3 dB higher than that of the random-signal component (i.e., $\lambda_s = A^2/2$). Setting γ according to (8.73) results in a multiplicative error of 0 dB in the figure, which provides the highest P_d over any other choice of γ in the Rician LLR detector and over the QMF or CMF detectors. If the choice of γ is off by multiplicative factor of 0.5 or 2 (i.e., a -3 or $+3$ dB error), there is very little loss in P_d . In all the cases shown in Fig. 8.7, the Rician LLR detector with such error in γ is still better than either the QMF or CMF detectors. However, the QMF and CMF detectors both provide reasonable, though sub-optimal, performance.

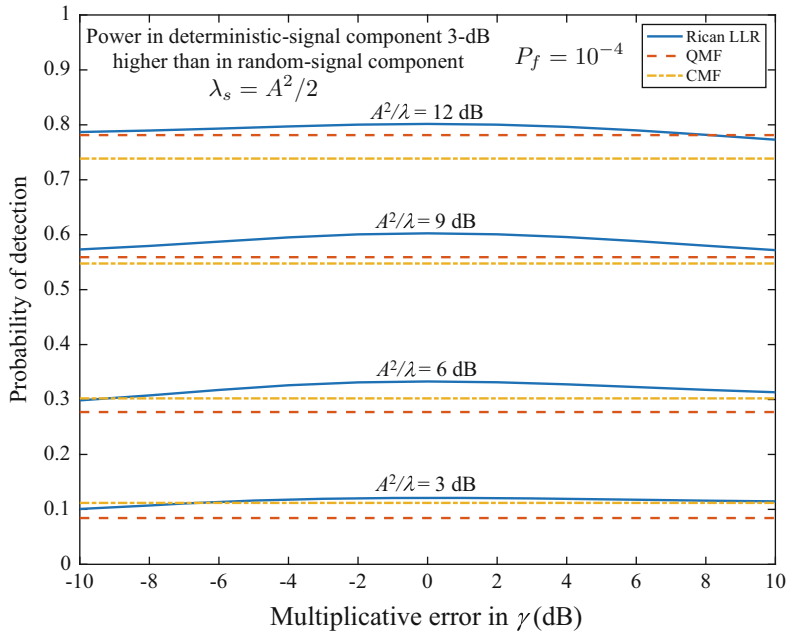


Fig. 8.7 Probability of detection for a Rician signal (with $\lambda_s = A^2/2$) for the Rician LLR, QMF, and CMF detectors as a function of the multiplicative error in the γ term of the Rician LLR. The correct value of γ results in a 0-dB multiplicative error

8.2.8 Detectors When Parameters Other Than Phase and Amplitude Are Unknown

The matched-filter detectors presented in Sects. 8.2.2–8.2.7 considered different signal amplitude and phase conditions, but were all derived under the assumption that the noise background power and the signal arrival time and Doppler were known perfectly. In practice, however, none of these quantities are known, so they need to be estimated. The general approach for dealing with unknown noise or signal parameters is described in this section with specific scenarios of unknown arrival time and unknown Doppler scale discussed in more detail in Sect. 8.5.

8.2.8.1 Detectors for Unknown Noise Parameters

When noise parameters are unknown in a detection problem they are considered *nuisance* parameters because they do not contribute to the separation between the null and alternative hypotheses, but still must be accounted for in the detector design. Suppose the noise parameters are placed in a vector Λ and, as described

at the beginning of Sect. 8.2, Θ is a vector containing the signal parameters. The GLR detector for this scenario, assuming Θ is also unknown, has the form

$$T(\mathbf{x}) = \frac{\max_{\Theta, \Lambda} f(\mathbf{x}; \Theta, \Lambda | H_1)}{\max_{\Lambda} f(\mathbf{x}; \Lambda | H_0)} \quad (8.84)$$

where the dependence of the data PDF on the signal and noise parameters has been made explicit for each hypothesis. It is important to note that there are two separate maximizations over Λ . The one in the numerator of (8.84) is over the likelihood function¹ formed from the data PDF under the alternative hypothesis and would produce an estimate $\hat{\Lambda}_1$. The one in the denominator is over the likelihood function formed using the data PDF under the null hypothesis and would produce the standard maximum-likelihood estimate (MLE) $\hat{\Lambda}_0$. Using these estimates, the GLR detector can be described as having the form

$$T(\mathbf{x}) = \frac{\max_{\Theta} f(\mathbf{x}; \Theta, \hat{\Lambda}_1 | H_1)}{f(\mathbf{x}; \hat{\Lambda}_0 | H_0)}. \quad (8.85)$$

In general, it can be difficult to jointly maximize $f(\mathbf{x}; \Theta, \Lambda | H_1)$ over both Θ and Λ . When it can be done, there is often not much information available on Λ within the data because \mathbf{x} is usually chosen to focus on the signal. To address this, it is common to identify signal-free data, called *auxiliary data*, that can be assumed to have the same noise distribution as in the test data. When the auxiliary data (\mathbf{y}) are statistically independent of the test data (\mathbf{x}), the GLR detector has the form

$$T(\mathbf{x}) = \frac{\max_{\Theta, \Lambda} f(\mathbf{x}; \Theta, \Lambda | H_1) f(\mathbf{y}; \Lambda | H_0)}{\max_{\Lambda} f(\mathbf{x}; \Lambda | H_0) f(\mathbf{y}; \Lambda | H_0)} = \frac{\max_{\Theta} f(\mathbf{x}; \Theta, \hat{\Lambda}_1 | H_1) f(\mathbf{y}; \hat{\Lambda}_1 | H_0)}{f(\mathbf{x}; \hat{\Lambda}_0 | H_0) f(\mathbf{y}; \hat{\Lambda}_0 | H_0)} \quad (8.86)$$

where $\hat{\Lambda}_0$ and $\hat{\Lambda}_1$ maximize the joint PDF of the test and auxiliary data under, respectively, the noise-only and signal-plus-noise hypotheses. The maximizations over the joint test and auxiliary data PDFs in (8.86) present an even more difficult optimization than in (8.84) when only the test data are considered. When the information contained in the auxiliary data about Λ significantly exceeds that in the test data, an approximation to (8.86) can be obtained by estimating Λ solely from the auxiliary data and using that estimate in both the numerator and denominator of (8.86). For example, it is common to use the MLE of Λ over the auxiliary data, which has form

¹As described in Sect. 6.3.4, the likelihood function of a parameter is simply the PDF taken as a function of the parameter.

$$\hat{\Lambda} = \arg \max_{\Lambda} f(\mathbf{y}; \Lambda | H_0). \quad (8.87)$$

Using this in (8.86) for Λ in both the numerator and denominator results in

$$T(\mathbf{x}) = \frac{\max_{\Theta} f(\mathbf{x}; \Theta, \hat{\Lambda} | H_1) f(\mathbf{y}; \hat{\Lambda} | H_0)}{f(\mathbf{x}; \hat{\Lambda} | H_0) f(\mathbf{y}; \hat{\Lambda} | H_0)} = \frac{\max_{\Theta} f(\mathbf{x}; \Theta, \hat{\Lambda} | H_1)}{f(\mathbf{x}; \hat{\Lambda} | H_0)}, \quad (8.88)$$

which is only approximately a GLR detector and structured the same as assuming Λ is known and using the estimate from the auxiliary data in one of the detectors derived in Sects. 8.2.2–8.2.7.

As an example, consider the case of detecting a Gaussian-fluctuating signal in Gaussian noise. The QMF output for the test cell without normalization, $X = |\mathbf{s}_\theta^H \mathbf{x}|^2$ from (8.10), has an exponential distribution with mean $\lambda + \lambda_s$ when signal is present,

$$X \sim \text{Expon}(\lambda + \lambda_s). \quad (8.89)$$

The auxiliary data, Y_1, \dots, Y_L , are similarly exponentially distributed but with mean λ . The joint PDF of the test and auxiliary data under H_1 is

$$f(x, \mathbf{y}; \lambda_s, \lambda | H_1) = \frac{1}{(\lambda + \lambda_s) \lambda^L} \exp \left\{ -\frac{x}{\lambda + \lambda_s} - \frac{1}{\lambda} \sum_{l=1}^L y_l \right\}. \quad (8.90)$$

A joint maximization of (8.90) over λ_s and λ results in the estimators

$$\hat{\lambda}_1 = \frac{1}{L} \sum_{l=1}^L y_l \quad \text{and} \quad \hat{\lambda}_s = x - \hat{\lambda}_1. \quad (8.91)$$

However, the likelihood function for λ formed from the joint PDF of the test and auxiliary data under H_0 is maximized over λ by the sample mean of the combined data,

$$\hat{\lambda}_0 = \frac{1}{L+1} \left[x + \sum_{l=1}^L y_l \right] \quad (8.92)$$

$$= \left(1 - \frac{1}{L+1} \right) \hat{\lambda}_1 + \frac{x}{L+1}. \quad (8.93)$$

If L is large, which would be indicative of the auxiliary data carrying much more information about λ than the test data, then clearly $\hat{\lambda}_0 \approx \hat{\lambda}_1$ so the approach using only the auxiliary data to estimate λ will be very similar to the GLR detector. In this example, the estimator in (8.91) is coincidentally the same as that formed solely

from the auxiliary data (i.e., $\hat{\lambda} = L^{-1} \sum_{l=1}^L y_l$). Inserting this estimator into (8.88) results in

$$T(x) = \frac{\hat{\lambda}}{x} e^{x/\hat{\lambda}-1} \stackrel{D}{\equiv} \frac{x}{\hat{\lambda}}. \quad (8.94)$$

This example illustrates a practical case of how the test data can be normalized by an estimate of the background noise power. Recalling that X was defined as the QMF detector without normalization from (8.10), the approximate GLR detector in (8.94) results in

$$T(\mathbf{x}) = \frac{|\mathbf{s}_\theta^H \mathbf{x}|^2}{\hat{\lambda}} \quad (8.95)$$

for the QMF detector with normalization, where $\hat{\lambda}$ is the estimate of λ . As will be shown in Sect. 8.6, the detector in (8.95) has a constant false alarm rate (CFAR), which is a requirement for implementing a detector without prior knowledge of the background noise power. The impact of normalization on detection performance is presented in Sect. 8.6 along with the more robust order-statistic normalizer.

8.2.8.2 Detectors for Unknown Signal Parameters

The cases of an unknown signal amplitude or phase have been treated in various combinations in earlier sections. The case where other deterministic signal parameters ($\boldsymbol{\theta}$) are unknown is treated here. The most common examples of such parameters are arrival time and Doppler. The primary detectors for such signals are the GLR detectors shown in (8.85) for test data and (8.86) for combined test and auxiliary data. If the particular assumptions about the signal amplitude lead to the QMF detector and λ is assumed to be known, the GLR detector from (8.85) results in a maximization over $\boldsymbol{\theta}$ of the QMF detector from (8.38)

$$\begin{aligned} T(\mathbf{x}) &= \max_{\boldsymbol{\theta}} T(\mathbf{x}|\boldsymbol{\theta}) \\ &= \max_{\boldsymbol{\theta}} \frac{|\mathbf{s}_\theta^H \mathbf{x}|^2}{\lambda} \end{aligned} \quad (8.96)$$

where $T(\mathbf{x}|\boldsymbol{\theta})$ is the QMF tuned to the signal replica formed using $\boldsymbol{\theta}$. The maximization is essentially a search over the unknown parameter $\boldsymbol{\theta}$ and is often implemented as a search over a finite set of discretized values of $\boldsymbol{\theta}$ (e.g., $\boldsymbol{\theta}_1, \dots, \boldsymbol{\theta}_n$) that span its region of support.

The GLR detector implementation for unknown deterministic signal parameters has several aliases. In a filtering context, it is called a filter bank with the i th filter “tuned” to $\boldsymbol{\theta}_i$. In an image processing context it would be called template matching where each $\boldsymbol{\theta}_i$ represents a different signal template. As one would expect, searching

over an unknown parameter comes at the expense of a reduction in performance relative to the case where it is known. In each of the signal types considered in Sect. 8.2, detection performance only depended on the SNR and not on the specific value of θ or form of \mathbf{s}_θ , as long as $\mathbf{s}_\theta^H \mathbf{s}_\theta = 1$. This implies that for a given decision threshold h , the probability of detection will be similar to the case where θ is known. The cost in searching over θ , however, comes in the form of an increase in the probability of false alarm. Suppose the n values of θ form an orthogonal signal set; that is,

$$\mathbf{s}_{\theta_i}^H \mathbf{s}_{\theta_j} = \delta[i - j] \quad (8.97)$$

where $\delta[i]$ is the Kronecker delta function equal to one when the argument is zero and is otherwise zero. Recalling the Gaussian statistical characterization of the random data vector \mathbf{x} under the noise-only hypothesis from (8.4), it can be seen that the coherent component of the QMF for θ_i (i.e., $\mathbf{s}_{\theta_i}^H \mathbf{x}$) will be uncorrelated with that for θ_j if $i \neq j$. Because zero correlation in the Gaussian distribution implies statistical independence, the GLR detector in (8.96) is, under the noise-only hypothesis, the maximum of n independent, exponentially distributed random variables each having a mean of one. It is then straightforward to show that the probability of false alarm is

$$P_f(n) = 1 - (1 - P_0)^n \quad (8.98)$$

$$\approx n P_0 \quad (8.99)$$

where $P_0 = e^{-h}$ is the probability of false alarm when θ is known from (8.44). The approximation in (8.99) comes from a first order Maclaurin series and so is accurate when P_0 is small. It clearly demonstrates the cost in searching over an n -dimensional signal subspace: an n -fold increase in the probability of false alarm.

More details on estimating the time of arrival are found in Sect. 8.5.3 and on estimating Doppler in Sect. 8.5.4.

Exercise 8.2 If T_1, \dots, T_n are independent and identically distributed with CDF $F_0(t)$, show that the CDF of $T = \max_i T_i$ is $F_T(t) = F_0^n(t)$. Hint: show that $\Pr\{\max_i T_i < h\} = \Pr\{\cap_{i=1}^n T_i < h\}$.

8.2.9 Noise-Normalized and Adaptive Matched Filters

Before deriving the matched filter, it was assumed in the beginning of Sect. 8.2 that the noise PSD was constant over frequency. However, as described in Sect. 3.3, ocean ambient noise (i.e., excluding thermal noise) typically has a PSD proportional to an inverse power law $1/f^p$, with p ranging from 1.59 for mid-frequency wind-generated noise to as high as 4 at very low frequencies. In Sect. 3.5.6 it was shown

that the PSD of reverberation is proportional to the spectrum of the sonar pulse and in Sect. 7.4.2.4 it was shown how it can be spread by motion of the sonar platform or elemental scatters. Although many sensing waveforms have approximately constant spectra in the signal band (e.g., the CW and LFM pulses), some may not. For example, the spectrum of an HFM pulse has a $1/f^4$ dependence (this can be seen from (8.187) as will be presented in Sect. 8.3.6.1). If the variation of the noise PSD over the signal band is small, using the matched filters of the previous sections is a prudent and common practice. For situations where the variation in the background PSD over the signal band is large, a *noise-normalized* matched filter should be used.

For the constant noise PSD, sampling the complex envelope at the signal bandwidth led to uncorrelated noise samples that could be assumed independent when they were Gaussian distributed. When the noise PSD is not constant, the noise samples are correlated and the distribution of the basebanded and sampled data for a deterministic signal conditioned on the signal phase ψ is

$$\mathbf{x}|\psi \sim \mathcal{CN}\left(A e^{j\psi} \mathbf{s}_\theta, \Sigma\right) \quad (8.100)$$

where $\Sigma = E[\mathbf{v}\mathbf{v}^H]$ is the covariance matrix of the noise vector \mathbf{v} . Because the noise vector contains consecutive samples of a wide-sense-stationary random process, its covariance matrix has a Toeplitz structure with each element in the i th diagonal equal to

$$\{\Sigma\}_{j,j+i} = R_{vv}(i/f_s) \quad (8.101)$$

for $j = 1, \dots, n$ and $i = -(n-1), \dots, (n-1)$ such that $1 \leq j+i \leq n$, where $R_{vv}(\tau)$ is the autocorrelation function (ACF) of the basebanded noise. Recall from Sect. 7.3.4 that a constant noise PSD filtered to the signal band resulted in $R_{vv}(\tau) = 2N_0 W \text{sinc}(W\tau)$. Thus, sampling at $f_s = W$ results in the scaled identity matrix used in previous sections, $\Sigma = 2N_0 W \mathbf{I} = \lambda \mathbf{I}$.

Using the PDF of the Gaussian model in (8.100) to form the log-likelihood ratio results in

$$l(\mathbf{x}) = 2A \operatorname{Real}\left\{e^{j\psi} \mathbf{x}^H \Sigma^{-1} \mathbf{s}_\theta\right\} - A^2 \mathbf{s}_\theta^H \Sigma^{-1} \mathbf{s}_\theta. \quad (8.102)$$

If Σ is known and ψ is either unknown or uniformly random, the noise-normalized QMF detector then has the form

$$T(\mathbf{x}) = \frac{|\mathbf{s}_\theta^H \Sigma^{-1} \mathbf{x}|^2}{\mathbf{s}_\theta^H \Sigma^{-1} \mathbf{s}_\theta}. \quad (8.103)$$

The term in the denominator has the effect of making the distribution of $T(\mathbf{x})$ independent of the noise covariance matrix Σ under the noise-only hypothesis so (8.103) is a CFAR detector.

The numerator of (8.103) can be interpreted as a noise-whitening stage applied to both the signal ($\Sigma^{-1/2}\mathbf{s}_\theta$) and data ($\Sigma^{-1/2}\mathbf{x}$) before forming the QMF derived in Sect. 8.2.3 or 8.2.4. Derivation of the noise-normalized matched filter for a continuous-time deterministic signal in Gaussian noise (e.g., see [25, Sect. 5.4]) results in a closely related decision statistic

$$T = \left| \int_{-\infty}^{\infty} \frac{S^*(f)X(f)}{P_{nn}(f)} df \right|^2 \quad (8.104)$$

where $S(f)$ is the Fourier transform of the known signal form, $X(f)$ is the Fourier transform of the data and $P_{nn}(f)$ is the PSD of the noise. Here the interpretation as a noise-whitening filter applied to the signal and data has a more apparent effect. Whitening the data via $X(f)/\sqrt{P_{nn}(f)}$ clearly produces a constant PSD when there is only noise. Whitening the signal through $S^*(f)/\sqrt{P_{nn}(f)}$ then imparts a weighting that emphasizes frequencies with high SNR and diminishes those with low SNR.² This weighting is similar to that found in the locally optimal energy detector and Eckart filter, which are derived in Sects. 9.2.5.2 and 9.2.5.3 for Gaussian random signals in Gaussian noise. The primary difference between the two forms is that the integral is inside the squared-modulus in (8.104) to exploit the phase structure of the known signal form. In the energy detector, the squared modulus is formed first and then the information accrued over frequency.

In order to implement the noise-normalized matched filter, the noise PSD must be known or estimated. When it is estimated, the detector is known as an adaptive matched filter because it adapts to the local background noise PSD. There are a number of ways in which the noise PSD or, equivalently, the noise ACF can be estimated (e.g., see [26]). Care must be taken when employing these adaptive filters to ensure the estimation error does not dominate the potential mismatch error incurred when using the standard matched filter. In many scenarios, the background PSD changes so rapidly that there are not enough stationary data samples available to get a good estimate.

8.2.10 Effect of Oversampling on a Matched-Filter Detector

As previously mentioned, basebanded data are sampled at the signal bandwidth ($f_s = W$) to simplify the statistical characterization and subsequent derivation of the optimal detector. In doing so, there is an inherent assumption that the data after that sampling are *sufficient statistics*. That is, that they contain all the necessary information required to implement the optimal detector. To determine how accurate

²This is more accurately described as a fractional SNR.

this assumption was, suppose the data were sampled at a higher rate to more precisely represent the continuous signal. The sampled data for a deterministic signal are then distributed according to (8.100) when conditioning on ψ and Σ is formed from (8.101) using the ACF of the noise. When the noise has a constant PSD and has been filtered to the signal band, recall that $R_{vv}(\tau) = 2N_0W\text{sinc}(W\tau)$. Sampling at a rate higher than W then results in a noise covariance matrix with some non-zero values in the off-diagonal elements.

Suppose the standard matched filter is used even though Σ is not a scaled identity matrix. The coherent component of the matched filter subject to oversampling for a deterministic signal can be described as being complex-Gaussian distributed,

$$\mathbf{s}_\theta^H \mathbf{x} \sim \mathcal{CN}\left(Ae^{j\psi}, \mathbf{s}_\theta^H \Sigma \mathbf{s}_\theta\right), \quad (8.105)$$

with the same mean ($Ae^{j\psi}$) as before because of the unit-length requirement on \mathbf{s}_θ , but a variance equal to $\mathbf{s}_\theta^H \Sigma \mathbf{s}_\theta$. The SNR after the coherent portion of detection processing is then

$$S^d = \frac{A^2}{\mathbf{s}_\theta^H \Sigma \mathbf{s}_\theta}. \quad (8.106)$$

When $\Sigma = \lambda \mathbf{I}$, this simplifies to $S^d = A^2/\lambda$ as in (8.18) with $\lambda_s = 0$. As an example, consider the SNR shown in Fig. 8.8 as a function of the oversampling factor (f_s/W) for an LFM pulse with time-bandwidth product $T_p W = 50$. Three different background scenarios are considered: an ambient-noise-limited scenario with a flat-in-band noise PSD and a reverberation-limited scenario with and without Doppler spreading. In each scenario, the SNR increases with the oversampling factor; however, the increase is only on the order of one tenth of a decibel for this particular signal. The increase in SNR occurs rapidly with most of the gain achieved when oversampling by a factor of two. Oversampling by more than a factor of three is clearly excessive. Slightly more gain is observed when the reverberation is subject to Doppler spreading compared to when it is not, likely because the spreading has the effect of whitening the reverberation PSD.

Noting that detection performance improves with SNR, the implication of the results illustrated by Fig. 8.8 is that sampling at $f_s = W$ does not produce a sufficient statistic and so some gain can be obtained simply by oversampling and using the matched filter. Recall from Sect. 4.6.1 that sampling a band-limited signal at the Nyquist rate implies that it can be reconstructed perfectly. Although this seems to imply the sampled data contain all the information available in the original signal, the interpolation filter required to implement the reconstruction has an infinite-duration impulse response so edge effects will be observable when working with finite-duration segments of data. This gain observed in SNR from oversampling arises from the edge effects. Noting that there are $T_p W$ samples of the signal at Nyquist sampling, the edge effects (and therefore potential for SNR gain) are expected to decrease as $T_p W$ increases. This is shown in Fig. 8.9 as the gain in SNR

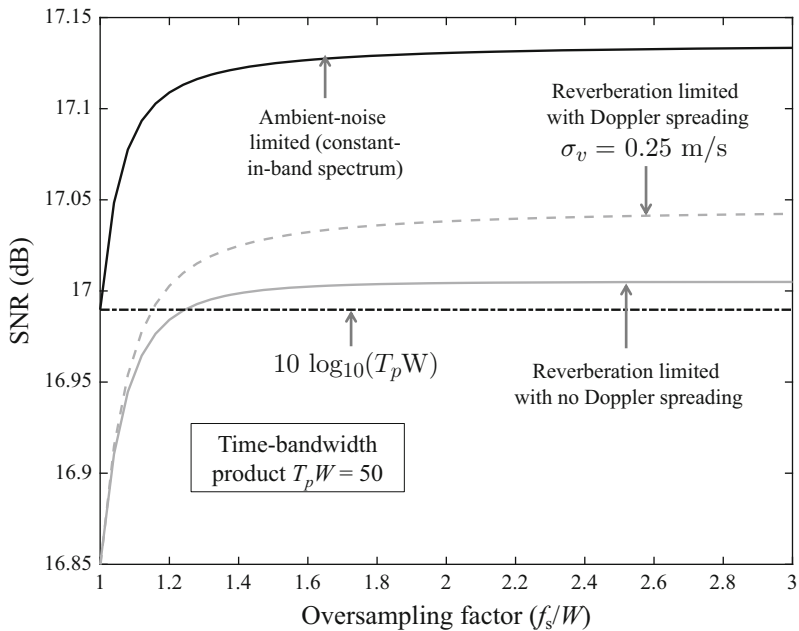


Fig. 8.8 SNR achieved by oversampling by a factor f_s/W in the matched filter for ambient-noise- and reverberation-limited scenarios for an LFM pulse

achieved when oversampling by a factor of three for an LFM waveform in the same noise and reverberation scenarios as noted above. Thus, oversampling by a factor of two or three is prudent for small time-bandwidth-product waveforms but might not be worth the effort when $T_p W$ is large.

If oversampling changes the noise covariance matrix so it is not an identity matrix, it is reasonable to ask if the noise-normalized matched filter can provide any gain. However, when the noise is assumed to be filtered to the signal band, its covariance matrix under oversampling has a rank that is approximately $T_p W$. This implies that Σ is not invertible and so the noise-normalized matched filter cannot be implemented.

Exercise 8.3 Plot the eigenvalues of the noise covariance matrix for the previously considered LFM pulse with $T_p W = 50$ in ambient noise with a constant-in-band PSD and reverberation when the data are sampled at the signal bandwidth and when they are oversampled by a factor of two. Which of these matrices are invertible?

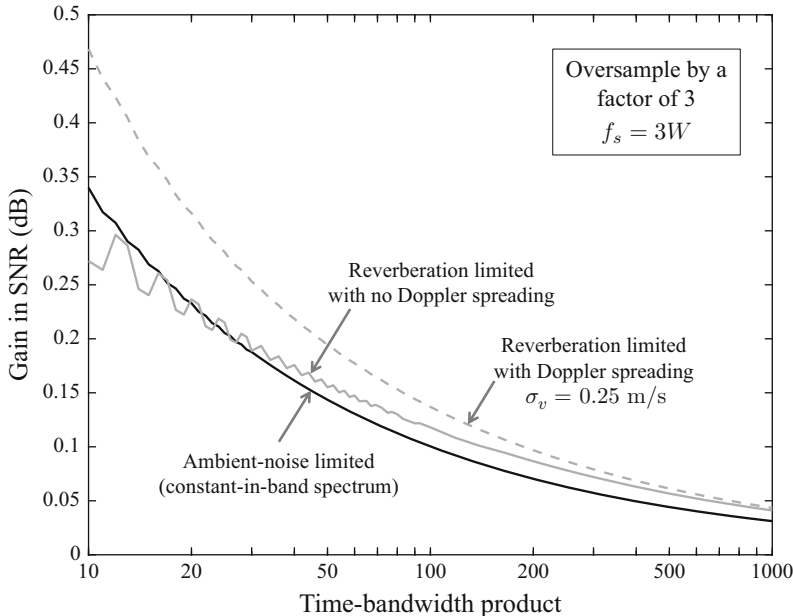


Fig. 8.9 Gain in SNR achieved by oversampling in the matched filter by a factor of three as a function of the time-bandwidth product for an LFM pulse

8.2.11 False-Alarm Rate (FAR)

To this point, the derivation and analysis of detectors has assumed that the arrival time of the signal is known. As was mentioned at the beginning of Sect. 8.2, the signal arrival time is generally not known in practice so every possible time is tested by the *filter* implementation of the detector, which slides the signal replica along a time series. The impact of this approach for dealing with an unknown arrival time on false alarm performance is assessed in this section by introducing the false-alarm-rate (FAR) performance metric and determining the effect of oversampling on FAR.

When basebanded data are sampled at the signal bandwidth, the arrival times that are evaluated are spaced every $1/W$, which represents a single sonar resolution cell. If the total time under evaluation is T_e , there are $N = T_e W$ resolution cells spanning the analysis time. Under the assumption that there is only one signal within the evaluation time, the GLR detector for an unknown arrival time compares the maximum of the N individual matched-filter decision statistics (T_i for the i th resolution cell) to a decision threshold,

$$\max_{1 \leq i \leq N} T_i \stackrel{H_1}{\underset{H_0}{\gtrless}} h. \quad (8.107)$$

Define the probability of a false alarm arising from the GLR detector applied to data with duration T_e as $P_f(T_e)$ while retaining the notation of P_f alone as the probability of a false alarm when testing a single resolution cell. For most waveforms, sampling at the waveform bandwidth produces matched-filter decision statistics that are statistically independent of each other. Under this assumption the probability of false alarm for the GLR detector is

$$\begin{aligned} P_f(T_e) &= \Pr \left\{ \max_{1 \leq i \leq N} T_i > h \mid H_0 \right\} = 1 - \Pr \left\{ \max_{1 \leq i \leq N} T_i \leq h \mid H_0 \right\} \\ &= 1 - F_0^N(h) \end{aligned} \quad (8.108)$$

$$= 1 - [1 - P_f]^N \approx NP_f \quad (8.109)$$

where $F_0(t) = \Pr\{T \leq t \mid H_0\}$ is the CDF of the matched-filter decision statistic for a single resolution cell under the null hypothesis and $P_f = 1 - F_0(h)$ is the associated single-resolution-cell probability of false alarm. The approximation in (8.109) is accurate when $P_f \ll 1$ and illustrates the impact of an unknown arrival time on false alarm performance. Searching over N independent sonar resolution cells for a signal results in an N -fold increase in the single-resolution-cell probability of false alarm. The implication is that the single-resolution-cell probability of false alarm must be set N times smaller than that desired over an evaluation time $T_e = N/W$.

In practice it is common for there to be more than one signal present within the data being evaluated. In this case the matched-filter decision statistic in each resolution cell is compared to a decision threshold with every threshold exceedance representing a signal detection or false alarm. When false alarms are a rare occurrence, a common measure of the false-alarm performance when testing N resolution cells for multiple signals is the *probability of observing one or more false alarms*. Assuming independence, the probability of observing i false alarms within the N resolution cells is the binomial probability

$$\begin{aligned} \Pr\{i \text{ false alarms in } N \text{ cells}\} &= \binom{N}{i} P_f^i [1 - P_f]^{N-i} \\ &= \frac{N!}{i!(N-i)!} P_f^i [1 - P_f]^{N-i}. \end{aligned} \quad (8.110)$$

The probability of one or more false alarms (FAs) in testing N statistically independent resolution cells can then be obtained by summing (8.110) for $i = 1$ up to N or by one minus the probability of observing no false alarms,

$$\begin{aligned}\Pr\{\text{at least one FA in } N \text{ cells}\} &= 1 - \Pr\{\text{no FAs in } N \text{ cells}\} \\ &= 1 - [1 - P_f]^N \approx NP_f.\end{aligned}\quad (8.111)$$

Thus, the same decision threshold is used either when testing for a single signal over N resolution cells or when testing for an unknown number of signals in N resolution cells.

The number of false alarms observed when testing N independent resolution cells can be phrased as the number of successes in N Bernoulli trials and is therefore a binomial random variable with success probability P_f (e.g., see Sect. 5.6.2). This means the average number of false alarms observed in the N resolution cells is NP_f . When N exceeds $1/P_f$, more than one false alarm may occur and a more relevant false alarm performance measure can be found in the *false-alarm rate* (FAR), which is the average number of false alarms observed per unit of time. When sampling is done at the waveform bandwidth, the FAR is easily seen to be the bandwidth times the probability of false alarm per resolution cell,

$$\text{FAR} = \frac{NP_f}{T_e} = WP_f.\quad (8.112)$$

When searching over a number (N_c) of independent channels (e.g., beams or Doppler channels), FAR increases proportionately (i.e., $\text{FAR} = N_c W P_f$). Solving this for P_f and converting to a base-ten logarithmic scale results in

$$\log_{10} P_f = \log_{10} \text{FAR} - \log_{10}(N_c W).\quad (8.113)$$

As shown in Table 8.3, this can then be used to easily relate FAR to the P_f required for a single resolution cell when $N_c W = 10^D$ (i.e., $D = \log_{10}(N_c W)$) and bandwidth-rate sampling is performed. For example, from Table 8.3, a FAR of one per day requires $P_f = 10^{-(4.94+D)}$. If there are ten channels of a 100-Hz bandwidth waveform, then $D = 3$ and the decision threshold should be chosen to achieve $P_f \approx 10^{-8}$ for a single resolution cell.

Table 8.3 Negative base-ten exponent (C) of the probability of false alarm ($P_f = 10^{-C}$) required at a resolution cell for various false alarm rates (FARs) when $N_c W = 10^D$ where W is the signal bandwidth and N_c is the number of independent channels

FAR	$C = -\log_{10} P_f$
1/minute	$1.78 + D$
1/hour	$3.56 + D$
1/day	$4.94 + D$
1/week	$5.78 + D$
1/year	$7.50 + D$
Double (e.g., 2/day)	Subtract $\log_{10} 2 \approx 0.3$ (e.g., $4.64 + D$)
Factor of 5	Subtract $\log_{10} 5 \approx 0.7$

8.2.11.1 FAR Under Oversampling

As previously noted, sampling at the waveform bandwidth simplifies the derivation and performance analysis of detectors. In practice, however, it is common to oversample by a factor of two to three. This is done in part to mitigate the small loss in SNR from sampling and edge effects (as described in Sect. 8.2.10), but more so to reduce the loss in SNR that occurs when the signal arrival time falls in between samples (i.e., the scalloping loss arising from mismatch between the echo and the closest replica). Using the sinc-function approximation to the autocorrelation function (ACF) of an LFM or HFM pulse, this is seen to result in about a 4-dB scalloping loss in SNR when the signal is directly between samples and a little over one decibel of loss on average when its alignment is uniformly random. Oversampling can significantly reduce this loss: sampling at $2W$ has a maximum scalloping loss of 0.9 dB and an average of 0.3 dB for the sinc ACF while sampling at $3W$ reduces the maximum loss to 0.4 dB and the average to 0.13 dB.

From an estimation perspective, the time of the peak matched-filter instantaneous intensity is the maximum-likelihood estimator of the signal arrival time. Sampling at the waveform-bandwidth rate usually only produces a coarse estimate of the arrival time. As described in Sects. 8.5.1.2 and 8.5.3.1, the accuracy (standard deviation) of the signal arrival time estimator using an LFM waveform is inversely related to both the bandwidth and square root of SNR; it can be significantly more precise than the size of the sonar resolution cell. Although oversampling by a factor of two to three is an improvement over sampling at the waveform bandwidth with respect to estimating the signal arrival time, a second vernier stage is often necessary to refine the estimate. Whether oversampling is performed to improve detection or estimation performance, there is a cost in terms of an increase in the FAR arising from testing $f_s T_e > WT_e = N$ resolution cells. To address the higher FAR, the decision threshold must be raised slightly to meet a desired FAR specification. Although this will have a negative impact on the probability of detection, it will be seen to be less egregious than the scalloping loss that occurs when signals arrive in between two adjacent samples.

Fortunately, the FAR does not rise proportionately with the oversampling factor because the decision statistics from the newly sampled resolution cells are correlated with those obtained at the bandwidth-rate sampling. The most expeditious means for relating the decision threshold to FAR when testing correlated samples is to suppose the oversampling is increased to the point where the matched-filter output can be considered a continuous random process. The FAR can then be determined using solutions to the “level crossing” problem (e.g., see [27, Sect. 16–1]). Application of the level-crossing problem to the squared modulus of a zero-mean complex-Gaussian random process can be found in [28, Sect. 17.9 & App. B] or [8, Sect. 7.3.4]. This represents the case where the background noise and reverberation are Gaussian distributed and the normalization is perfect. Recall that the probability of observing a false alarm in a single resolution cell is

$$P_f = e^{-h} \quad (8.114)$$

where h is the decision threshold applied to the (perfectly) normalized instantaneous intensity. The resulting FAR for the detector thresholding the continuous-time (i.e., an infinite oversampling factor) matched-filter instantaneous intensity is

$$\text{FAR}_{\infty} = 2\sigma_f \sqrt{\pi h} e^{-h}, \quad (8.115)$$

where σ_f is the square root of the frequency variation of the pulse. The frequency variation (σ_f^2) of the pulse is described in Sect. 8.5.3 where it is used to define the Cramér-Rao lower bound (CRLB) on estimating the arrival time. A large value of σ_f^2 is good for estimation of arrival time (the CRLB is inversely proportional to it). However, it is clear that this has the opposite effect on FAR. For the sinc-function approximation to the ACF of an LFM or HFM pulse, $\sigma_f^2 = W^2/12$, which yields a FAR

$$\text{FAR}_{\infty} = W \sqrt{\frac{\pi}{3} h} e^{-h} \quad (8.116)$$

$$= WP_f \sqrt{-\frac{\pi}{3} \log P_f}. \quad (8.117)$$

Comparing (8.117) to (8.112), it can be seen that oversampling results in a FAR at most a factor $\sqrt{-\frac{\pi}{3} \log P_f} = \sqrt{\pi h/3}$ higher than sampling at the bandwidth.

This ranges from 2.2 when $P_f = 10^{-2}$ to only 4.4 when $P_f = 10^{-8}$. Although doubling or quadrupling FAR sounds like a bad idea, it requires less than a one-decibel increase in SNR to recover the original FAR specification (e.g., WP_f) for either a deterministic or Gaussian-fluctuating signal for the above range of P_f and P_d above about 0.4. As this is less than the average SNR loss from scalloping when sampling at the waveform-bandwidth rate and well below the worst-case scenario, oversampling is clearly beneficial both for detection and arrival time estimation.

8.3 Waveform Autocorrelation and Ambiguity Functions

The detectors developed in Sect. 8.2 inherently assumed that the signal replica or waveform and signal measurement were perfectly aligned in time and that the Doppler scale (η) of the echo was known. In practice it is often the case that neither the arrival time of the signal measurement nor its Doppler scale is known. The GLR approach was suggested in Sect. 8.2.8.2 for handling such unknown parameters. This approach requires a search over the unknown parameters that is often carried out by quantizing the parameters and evaluating a finite grid of values over the intervals of interest to create a bank of matched-filter detectors (e.g., the Doppler filter bank to be described in Sect. 8.7). When the true parameter value falls in between grid points, there is a loss in SNR. This mismatch loss is quantified by the response of the matched filter to a signal measurement having a different

parameterization than that of the signal replica. The autocorrelation function (ACF) of a signal waveform describes this when there is only a temporal offset between the signal measurement and replica. The ambiguity function (AF), which generalizes the ACF, describes the response of the matched filter when there is both a temporal offset and a difference in Doppler scale between the signal measurement and replica. To reiterate, in this context, the ACF and AF describe the response of a fixed matched filter to time offset (τ) and Doppler-scale (η) differences in the signal measurement. For any given waveform, these functions should be used to design the grid spacing in a GLR detector so the maximum SNR loss arising from mismatch is small enough to be an acceptable trade-off to the additional computational effort required by finer spacing and the subsequent increase in FAR described in Sect. 8.2.11.1. In this section reference made to the AF implicitly implies that the ACF, which is often simpler in form than the AF, can be used if only time offset is of interest and Doppler scale is known perfectly.

The AF is not only useful in assessing detection performance and designing the grid spacing in a bank of matched-filter detectors. The previously mentioned GLR approach to detection also provides estimates of the arrival time and Doppler scale of a measurement. Because these estimation algorithms rely on the matched filter, the AF can be used to assess their performance. In this context the AF is described as representing the response of a large bank of filters to a fixed signal measurement. From an estimation perspective, an ideal ACF or AF is one tightly focused around the origin (i.e., the true parameter values) so the estimation error is minimized. The “ambiguity” terminology is also clear from the estimation context: two different parameter estimates having large values in the AF are more likely to be confused by an estimator than if one has a large value and the other a small value.

One measure of the accuracy of an estimator is to assess the minimum variance attainable by an unbiased estimator through the Cramér-Rao lower bound (CRLB). As will be shown in Sects. 8.5.3–8.5.5, the CRLBs for estimating arrival time and Doppler scale can be described using the AF. In a qualitative context, the very slow decay of the AF of a CW pulse in time offset indicates it is a poor choice for estimating time of arrival. However, the rapid decay of the AF with Doppler scale indicates the CW pulse is good at estimating an object’s radial velocity. Part of the discussion about accuracy in range and velocity estimation involves the estimator bias imparted by a coupling of the two dimensions that arises for certain waveforms (e.g., LFM and HFM pulses). The coupling exhibits itself in the AF as a slowly decaying ridge occurring at a predictable angle in the time-offset/Doppler dimensions of the AF and illustrates heightened ambiguity for (τ, η) pairs lying on it.

It is important to differentiate *accuracy* from *resolution*. The CRLBs derived in Sect. 8.5 describe the accuracy with which it may be possible to estimate the arrival time of a single signal. The resolution capability of a waveform describes how close two signals can be in time and/or Doppler under the condition that they are reliably discerned from one another with standard processing. Many factors impact resolution, which complicates its analysis (e.g., the detection/estimation algorithm and its assumptions, how many signals are present, and their SNR and/or phase

differences). As such, it is common to use some distillation of the main-lobe width of the AF to describe the resolution capability of a waveform. The two primary metrics for resolution are the distance between the 3-dB down points in the mainlobe and the Rayleigh criterion for resolution [29, Sect. 41–5], which is the distance from the peak response to the first zero.

This section is organized as follows. The SNR loss arising from mismatch in time of arrival and Doppler scale is derived in Sect. 8.3.1 and then related to the complex ambiguity function, which is also shown to represent the response of a Doppler filter bank. Specific details and definitions (compiled in Table 8.4) of the AF and ACF are presented in Sects. 8.3.2 and 8.3.3, including the narrowband AF. The section closes with Sects. 8.3.4–8.3.6 where the ACF and AF are presented for the primary sonar pulses: CW, LFM, and HFM.

8.3.1 SNR Loss from Waveform Mismatch

Suppose the signal vector used in the matched filter is an exact replica \mathbf{s}_r based on the transmitted waveform whereas the form of the measured signal, \mathbf{s}_m , is potentially different. When \mathbf{s}_m differs from \mathbf{s}_r , matched-filter detectors are subject to a mismatch loss. The complex matched-filter response, $X = \mathbf{s}_r^H \mathbf{x}$ is still complex-Gaussian distributed, but with altered signal components,

$$X|\psi \sim \mathcal{CN}\left(A e^{j\psi} \mathbf{s}_r^H \mathbf{s}_m, \lambda_s |\mathbf{s}_r^H \mathbf{s}_m|^2 + \lambda\right), \quad (8.118)$$

where it has been assumed that both \mathbf{s}_r and \mathbf{s}_m have unit length. Noting that $|\mathbf{s}_r^H \mathbf{s}_m|^2 \leq \mathbf{s}_m^H \mathbf{s}_m \cdot \mathbf{s}_r^H \mathbf{s}_r = 1$, the power of the signal components in the mean and variance of (8.118) will be lower than when the replica and measured signal are identical (or when they only differ by a constant phase term). The SNR loss arising from waveform mismatch is now derived for the CMF and QMF detectors for a general signal measurement \mathbf{s}_m . The complex ambiguity function is then shown to arise when describing the vector inner product $\mathbf{s}_r^H \mathbf{s}_m$ for mismatch in the arrival-time and Doppler-scale dimensions. The SNR loss arising from this mismatch can then be obtained for the CMF and QMF directly from the ambiguity function.

8.3.1.1 Coherent Matched Filter

The decision statistic of the CMF from (8.25),

$$\begin{aligned} T(\mathbf{x}) &= \sqrt{\frac{2}{\lambda}} \cdot \text{Real}\left\{e^{-j\psi} \mathbf{s}_r^H \mathbf{x}\right\} \\ &\sim \mathcal{N}\left(\sqrt{2S^d} \left| \mathbf{s}_r^H \mathbf{s}_m \right| \cos\left(\angle \mathbf{s}_r^H \mathbf{s}_m\right), 1\right), \end{aligned} \quad (8.119)$$

is still normally distributed with unit variance when there is a mismatch between the measured signal (\mathbf{s}_m) and the assumed signal (\mathbf{s}_r). However, the mean can have a smaller amplitude and even be negative. The latter scenario occurs when $|\angle \mathbf{s}_r^H \mathbf{s}_m| > \pi/2$, assuming the angle is on $(-\pi, \pi]$. This results in a biased detector where the probability of detection is less than the probability of false alarm and is therefore considered too extreme of a mismatch for a usable detector. Under the assumption that the mismatch in angle yields $|\angle \mathbf{s}_r^H \mathbf{s}_m| < \pi/2$, the detector decision statistic can be described as

$$T(\mathbf{x}) \sim \mathcal{N}\left(\sqrt{2S_m^d}, 1\right) \quad (8.120)$$

where the SNR obtained under mismatch is

$$S_m^d = S^d \left| \mathbf{s}_r^H \mathbf{s}_m \right|^2 \cos^2\left(\angle \mathbf{s}_r^H \mathbf{s}_m\right). \quad (8.121)$$

Clearly if $\mathbf{s}_m = \mathbf{s}_r$, there is no mismatch and $S_m^d = S^d$. From this, the loss in SNR arising from mismatch in the CMF can be described by the factor

$$\mathcal{L}_C^d(\mathbf{s}_m) = \frac{S_m^d}{S^d} = \left| \mathbf{s}_r^H \mathbf{s}_m \right|^2 \cos^2\left(\angle \mathbf{s}_r^H \mathbf{s}_m\right) \quad (8.122)$$

as long as $|\angle \mathbf{s}_r^H \mathbf{s}_m| < \pi/2$.

8.3.1.2 Quadrature Matched Filter

The decision statistic of the quadrature matched filter (QMF), defined in (8.38), is

$$T(\mathbf{x}) = \frac{|\mathbf{s}_r^H \mathbf{x}|^2}{\lambda} \quad (8.123)$$

Using the characterization in (8.118), the expected value of $T(\mathbf{x})$ when a mismatched signal is present is seen to be

$$E[T(\mathbf{x})] = \frac{(A^2 + \lambda_s)}{\lambda} |\mathbf{s}_r^H \mathbf{s}_m|^2 + 1 \quad (8.124)$$

where the first term represents the normalized signal and the “1” represents the normalized noise. Thus, for the QMF, the SNR after the coherent portion of matched filtering when there is mismatch between the replica and measured signal is

$$S_m^d = S^d |\mathbf{s}_r^H \mathbf{s}_m|^2. \quad (8.125)$$

The loss in SNR arising from mismatch, when described as a multiplicative factor, is

$$\mathcal{L}_Q^d(\mathbf{s}_m) = \frac{S_m^d}{S^d} = |\mathbf{s}_r^H \mathbf{s}_m|^2, \quad (8.126)$$

which differs from that for the CMF by not depending on the phase of $\mathbf{s}_r^H \mathbf{s}_m$.

8.3.1.3 The Complex Ambiguity Function and SNR Loss

The SNR loss factors for both the CMF and QMF depend on the vector inner product between the assumed form of the signal and that actually observed, $\mathbf{s}_r^H \mathbf{s}_m$. This inner product can be approximated by an integral over the complex envelope of the transmitted and measured signals (respectively, $\tilde{s}_r(t)$ and $\tilde{s}_m(t)$),

$$\mathbf{s}_r^H \mathbf{s}_m = \sum_{i=1}^n \tilde{s}_r[i]^* \tilde{s}_m[i] \approx W \int_{-\infty}^{\infty} \tilde{s}_r^*(t) \tilde{s}_m(t) dt \quad (8.127)$$

where the vectors contain $n = T_p W$ samples ($\tilde{s}_r[i]$ and $\tilde{s}_m[i]$ for $i = 1, \dots, n$) spaced every $1/W$. Recalling that the analytic signals that form $\tilde{s}_r(t)$ and $\tilde{s}_m(t)$ are, respectively, $\dot{s}_r(t) = e^{j2\pi f_c t} \tilde{s}_r(t)$ and $\dot{s}_m(t) = e^{j2\pi f_c t} \tilde{s}_m(t)$, the vector inner product $\mathbf{s}_r^H \mathbf{s}_m$ can be equivalently described as

$$\mathbf{s}_r^H \mathbf{s}_m \approx W \int_{-\infty}^{\infty} \dot{s}_r^*(t) \dot{s}_m(t) dt. \quad (8.128)$$

Characterizing $\mathbf{s}_r^H \mathbf{s}_m$ in terms of the analytic signal simplifies relating it to mismatch arising from differences in arrival time and Doppler. Using the unit-length assumptions for the sampled complex-envelope signal vectors \mathbf{s}_r and \mathbf{s}_m (i.e., $\mathbf{s}_r^H \mathbf{s}_r = 1$ and $\mathbf{s}_m^H \mathbf{s}_m = 1$) in (8.127) and (8.128) illustrates that the energy in the complex envelope or analytic signal “form” is

$$\int_{-\infty}^{\infty} |\tilde{s}_r(t)|^2 dt = \int_{-\infty}^{\infty} |\tilde{s}_m(t)|^2 dt = \int_{-\infty}^{\infty} |\dot{s}_r(t)|^2 dt = \int_{-\infty}^{\infty} |\dot{s}_m(t)|^2 dt \approx \frac{1}{W}. \quad (8.129)$$

Suppose the signal measurement is observed with Doppler scale η_1 so

$$\dot{s}_m(t) = \sqrt{\eta_1} \dot{s}(\eta_1 t), \quad (8.130)$$

where $\dot{s}(t)$ is the transmitted pulse and the multiplication by $\sqrt{\eta_1}$ is required to satisfy (8.129). The general scenario under consideration then requires the signal

replica to be designed for a Doppler scale η_0 that might differ from η_1 and be misaligned in time by an amount τ , which implies

$$\dot{s}_r(t) = \sqrt{\eta_0} \dot{s}(\eta_0[t - \tau]). \quad (8.131)$$

The similarity between the assumed replica and the signal measurement form under Doppler-scale and time-alignment mismatch can be captured using the right-hand side of (8.128) and dividing by W to produce the function

$$\begin{aligned} R(\tau, \eta_0, \eta_1) &= \int_{-\infty}^{\infty} \dot{s}_r^*(t) \dot{s}_m(t) dt \\ &= \sqrt{\eta_0 \eta_1} \int_{-\infty}^{\infty} \dot{s}^*(\eta_0[t - \tau]) \dot{s}(\eta_1 t) dt \end{aligned} \quad (8.132)$$

$$= \sqrt{\frac{\eta_0}{\eta_1}} \int_{-\infty}^{\infty} \dot{s}(t) \dot{s}^*\left(\frac{\eta_0}{\eta_1}[t - \eta_1 \tau]\right) dt. \quad (8.133)$$

The function shown in (8.132) and (8.133) taken as a function of τ and $\eta = \eta_0$ with $\eta_1 = 1$ is termed the *complex ambiguity function*,

$$\chi(\tau, \eta) = \sqrt{\eta} \int_{-\infty}^{\infty} \dot{s}(t) \dot{s}^*(\eta[t - \tau]) dt. \quad (8.134)$$

The general function $R(\tau, \eta_0, \eta_1)$ in (8.132), and therefore the complex ambiguity function, can be interpreted in two different manners. When η_1 is fixed and $R(\tau, \eta_0, \eta_1)$ is taken as a function of τ and $\eta = \eta_0$ it describes the response of a Doppler filter bank to a specific signal measurement with Doppler scale η_1 . If that fixed signal measurement is for an object with zero-radial velocity (i.e., $\eta_1 = 1$), the response of the filter-bank in time offset and Doppler scale is precisely the complex ambiguity function,

$$R_{FB}(\tau, \eta) = R(\tau, \eta, 1) = \chi(\tau, \eta). \quad (8.135)$$

Now suppose that $R(\tau, \eta_0, \eta_1)$ is taken as a function of $\eta = \eta_1$ with η_0 fixed so as to represent the response of a single matched filter subject to varying Doppler mismatch in the signal measurement. Using the definition of the complex ambiguity function, (8.132) can be represented as

$$R(\tau, \eta_0, \eta_1) = \chi\left(\eta_1 \tau, \frac{\eta_0}{\eta_1}\right) = \chi^*\left(-\eta_0 \tau, \frac{\eta_1}{\eta_0}\right), \quad (8.136)$$

which illustrates a type of conjugate symmetry about the time-offset and Doppler-scale axes. With η_0 fixed, (8.136) results in what can be considered a Doppler-scale “transfer function” of the filter in the sense that it is the response to a test signal with Doppler scale $\eta = \eta_1$. If the matched filter is tuned to have zero radial velocity ($\eta_0 = 1$), the single-filter (SF) output is also easily described in terms of the complex ambiguity function,

$$R_{\text{SF}}(\tau, \eta) = R(\tau, 1, \eta) = \chi(\eta\tau, \eta^{-1}) = \chi^*(-\tau, \eta). \quad (8.137)$$

Thus, the complex ambiguity function can be used either to represent the response of a Doppler filter bank to a fixed signal measurement or to obtain the response of a single matched filter to a varying input. The two interpretations differ by a conjugation and reflection about the time-offset axis.

Unfortunately, there are many small variations in the naming and definition³ of the ambiguity functions. The “ambiguity” terminology, which is a common thread, appears to arise from Woodward’s discussion of it in a section titled “Ambiguity in Range and Velocity,” [14, Sect. 7.2]. This early development focused on narrowband signals where the Doppler scale found in (8.134) is approximated by a complex modulation in the time domain. The wideband version of an ambiguity function was proposed in [30] for targets with both radial velocity and acceleration. The wideband ambiguity function in (8.134) is related to the modulated-carrier form presented in [30] when setting the acceleration component to zero, but defined in terms of the analytic function as found in [31] or in [11, Sect. 3.4] where it is termed an uncertainty function. The derivation in [30] only uses the real part of (8.134) because of its focus on the CMF. As will be seen below, the complex form in (8.134) is necessary to define the SNR loss for the QMF. Other important results for wideband ambiguity functions include exact solutions for LFM pulses [32], stationary-phase approximations [33], and their application to HFM pulses [31, 34]. The variety in nomenclature and definition comes not only in the narrowband-wideband distinction, but also because the squared modulus of (8.134) and its form normalized by the peak value are more commonly used than the complex form and can also be referred to as an ambiguity function, a squared ambiguity function or a normalized ambiguity function. In this text the more specific nomenclature will be included when necessary (e.g., complex, squared, normalized, narrowband, wideband, etc.). As may be expected from the filter-bank and single-filter interpretations found in (8.135) and (8.137), definitions of the complex ambiguity function can also differ by a conjugation (e.g., the complex form in [30, eq. 36] differs from (8.134) by a conjugation in addition to being for a narrowband signal) and the sign on τ (e.g., as in [35]), which arises from applying a delay to the signal measurement rather than the replica. All of the results presented in this text follow (8.134).

³One might say there is ambiguity in the definition.

More important than the name of the function, however, is how it is related to the loss in SNR arising from mismatch in time-offset or Doppler scale. Using the single-filter interpretation of the ambiguity function from (8.137), it can be seen that the vector inner product formulating the SNR loss in the CMF and QMF detectors when they are fixed and the signal measurement varies is

$$\mathbf{s}_r^H \mathbf{s}_m = \frac{\chi^*(-\tau, \eta)}{\chi(0, 1)} \quad (8.138)$$

by noting $\chi(0, 1) = 1/W$ from (8.129). It is then straightforward to obtain from (8.122) the SNR loss in the CMF as

$$\mathcal{L}_C^d(\tau, \eta) = \frac{|\chi(-\tau, \eta)|^2}{|\chi(0, 1)|^2} \cos^2(\angle \chi(-\tau, \eta)) \quad (8.139)$$

assuming $|\angle \chi(-\tau, \eta)| < \pi/2$. The term $|\chi(-\tau, \eta)| \cos(\angle \chi(-\tau, \eta))$ is then precisely the real part of $\chi(-\tau, \eta)$ as presented in [30]. The SNR loss in the QMF can be obtained similarly from (8.126), to result in

$$\mathcal{L}_Q^d(\tau, \eta) = \frac{|\chi(-\tau, \eta)|^2}{|\chi(0, 1)|^2}. \quad (8.140)$$

As would be expected when there is no time offset or mismatch in Doppler scale (and from the Cauchy-Schwarz inequality), $|\chi(\tau, \eta)|$ is at a maximum when $\tau = 0$ and $\eta = 1$ and so this represents the “origin” in τ and η where there is no loss incurred by the matched filters. The SNR loss factors for the CMF and QMF detectors and their relationship to various forms of the ambiguity function can also be found in Table 8.4.

Conversion of the SNR loss from a multiplicative factor to a decibel loss (where positive values represent a loss) is accomplished by

$$\begin{aligned} \text{SNR Loss} &= -10 \log_{10} \mathcal{L}_Q^d(\tau, \eta) \\ &= -10 \log_{10} \left[\left| \frac{\chi(-\tau, \eta)}{\chi(0, 1)} \right|^2 \right] \geq 0, \end{aligned} \quad (8.141)$$

for the QMF with a similar form for the CMF. It is worth emphasizing that the ratios in (8.139) and (8.140) represent ratios of powers and so the $10 \log_{10}(\cdot)$ conversion to decibels is appropriate. The apparent “squaring” of the signal waveform that occurs when $\chi(\tau, \eta)$ is formed is not the relevant quantity. Rather the deterministic-signal amplitude A in (8.118) that is multiplied by $\mathbf{s}_r^H \mathbf{s}_m$ (which is proportional to $\chi^*(-\tau, \eta)$) or the random-signal power λ_s that is multiplied by $|\mathbf{s}_r^H \mathbf{s}_m|^2$ (which is proportional to $|\chi(-\tau, \eta)|^2$) are the relevant quantities.

Table 8.4 Ambiguity and autocorrelation function definitions, inter-relationships, and their relationship to the SNR loss factor in the CMF and QMF detectors

Function or quantity & mathematical definition	Reference
Wideband ambiguity function (WAF) [complex]	
$\chi(\tau, \eta) = \sqrt{\eta} \int_{-\infty}^{\infty} \hat{s}(t) \hat{s}^*(\eta[t - \tau]) dt$	(8.134) & (8.142)
Narrowband ambiguity function (NAF) [complex]	
$\xi(\tau, \delta) = \int_{-\infty}^{\infty} \tilde{s}(t) \tilde{s}^*(t - \tau) e^{-j2\pi\delta t} dt$	(8.149)
$= e^{-j2\pi f_c \tau} \int_{-\infty}^{\infty} \hat{s}(t) \hat{s}^*(t - \tau) e^{-j2\pi\delta t} dt$	(8.150)
where $\delta = f_c(\eta - 1) \approx 2v_r f_c/c_w$ (see notes d. and e.)	
Relating the NAF to the WAF	
$\chi(\tau, \eta) \approx \sqrt{\eta} e^{j2\pi f_c \eta \tau} \xi(\tau, \delta)$	(8.148)
Response of a filter bank to a signal measurement with Doppler scale η_1 [complex]	
$R_{FB}(\tau, \eta; \eta_1) = \chi\left(\eta_1 \tau, \frac{\eta}{\eta_1}\right) = \chi^*\left(-\eta \tau, \frac{\eta_1}{\eta}\right)$	(8.151)
Response of a single filter matched to Doppler scale η_0 [complex]	
$R_{SF}(\tau, \eta; \eta_0) = \chi\left(\eta \tau, \frac{\eta_0}{\eta}\right) = \chi^*\left(-\eta_0 \tau, \frac{\eta}{\eta_0}\right)$	(8.152)
Autocorrelation function [complex]	
$\chi(\tau) = \chi(\tau, 1) = \int_{-\infty}^{\infty} \hat{s}(t) \hat{s}^*(t - \tau) dt = \int_{-\infty}^{\infty} \hat{s}(t + \tau) \hat{s}^*(t) dt$	(8.153)
$= e^{j2\pi f_c \tau} \int_{-\infty}^{\infty} \tilde{s}(t) \tilde{s}^*(t - \tau) dt = e^{j2\pi f_c \tau} \xi(\tau, 0)$	(8.154)
CMF SNR loss factor	
$\mathcal{L}_C^d(\tau, \eta) = \frac{ \chi(-\tau, \eta) ^2}{ \chi(0, 1) ^2} \cos^2(\angle \chi(-\tau, \eta)) \text{ for } \angle \chi(-\tau, \eta) < \pi/2$	(8.139)
$= \frac{ \xi(-\tau, \delta) ^2}{ \xi(0, 0) ^2} \cos^2(\angle e^{-j2\pi f_c \tau} \xi(-\tau, \delta)) \text{ for NB signals}$	
QMF SNR loss factor [often called a normalized ambiguity function]	
$\mathcal{L}_Q^d(\tau, \eta) = \frac{ \chi(-\tau, \eta) ^2}{ \chi(0, 1) ^2} = \frac{ \xi(-\tau, \delta) ^2}{ \xi(0, 0) ^2}$	(8.140)
$= \frac{ \xi(-\tau, \delta) ^2}{ \xi(0, 0) ^2} \text{ for NB signals}$	

Notes:

- a. $\hat{s}(t)$ is the analytic signal of the transmit waveform (ref. Table 7.4)
- b. $\tilde{s}(t) = \hat{s}(t)e^{-j2\pi f_c t}$ is the complex envelope of the transmit waveform
- c. η is the Doppler scale with $\eta > 1$ representing objects closing range and $\eta < 1$ objects opening range
- d. $\delta = f_c(\eta - 1)$ is the Doppler-frequency-shift [units: Hz] approximation of a Doppler frequency scale
- e. $\delta \approx 2v_r f_c/c_w$ for a monostatic active sonar echo where c_w is the speed of sound and v_r is the relative radial velocity ($v_r > 0$ is a closing-range object and $v_r < 0$ is an opening-range object)

8.3.2 Ambiguity Functions

The complex ambiguity function

$$\chi(\tau, \eta) = \sqrt{\eta} \int_{-\infty}^{\infty} \dot{s}(t) \dot{s}^*(\eta[t - \tau]) dt \quad (8.142)$$

which was introduced in (8.134) and in Table 8.4 is what is considered a *wideband* ambiguity function (WAF) [11, 30]. It can be used for any waveform, irrespective of its bandwidth or center frequency. However, it has as an underlying assumption that the matched-filter signal replica is subject to a time-offset τ and that the signal measurement is the signal replica only subject to a Doppler scale. This is representative of an object of interest that is a point target with a constant relative radial velocity throughout the pulse-reflection process. Extension of this “range-velocity” ambiguity function to include a radial-acceleration component can be found in [30]. The WAF is considered first in this text owing to its more general applicability relative to its narrowband approximation, which will be discussed in Sect. 8.3.2.1, and because it is more often required in sonar than in radar applications.

The various properties of the WAF can be found in [30, 31, 35–37]. An important property of the ambiguity function is that its modulus is at a maximum when $\tau = 0$ and $\eta = 1$, which represents the case of zero mismatch between the signal replica and measurement and therefore no SNR loss in the matched filter. In addition to providing the loss in SNR arising from mismatch in arrival time and Doppler, the ambiguity function also represents the temporal response of the matched filter to a signal measurement having Doppler scale η .

Although the complex ambiguity function is defined using the analytic signal of the transmit waveform, $\dot{s}(t) = \tilde{s}(t)e^{j2\pi f_c t}$, it can be described in terms of the complex envelope,

$$\chi(\tau, \eta) = \sqrt{\eta} e^{j2\pi f_c \eta \tau} \int_{-\infty}^{\infty} \tilde{s}(t) \tilde{s}^*(\eta[t - \tau]) e^{j2\pi f_c (1-\eta)t} dt. \quad (8.143)$$

Although this appears more complicated than (8.142), it simplifies significantly when the signal is narrowband with respect to the carrier frequency (i.e., the waveform bandwidth $W \ll f_c$) as will be described below in Sect. 8.3.2.1.

Applying a Fourier transform over τ to the complex ambiguity function in (8.142) results in

$$\int_{-\infty}^{\infty} \chi(\tau, \eta) e^{-j2\pi f \tau} d\tau = \frac{1}{\sqrt{\eta}} \mathring{S}(f) \mathring{S}^*(f/\eta) \quad (8.144)$$

where $\mathring{S}(f) = \mathcal{F}\{\mathring{s}(t)\}$ is the Fourier transform of the analytic function of the pulse. When $\mathring{S}(f)$ has a simple form it can be easier to obtain the AF as the inverse Fourier transform,

$$\chi(\tau, \eta) = \mathcal{F}^{-1} \left\{ \frac{1}{\sqrt{\eta}} \mathring{S}(f) \mathring{S}^*(f/\eta) \right\}, \quad (8.145)$$

than to evaluate (8.142) directly.

8.3.2.1 Narrowband Signals

If a signal is narrowband with respect to its carrier frequency, its envelope and phase vary slowly relative to the carrier. Recalling that for a stationary monostatic active sonar system $\eta = (1 + v_r/c_w)/(1 - v_r/c_w) \approx 1 + 2v_r/c_w$ where v_r is the radial velocity of the object of interest ($v_r > 0$ represents a closing object) and c_w is the speed of sound, η will be close to one for most scenarios of interest in sonar (e.g., if the radial speed is less than 43 knots then $\eta \in (0.97, 1.03)$ when $c_w = 1500$ m/s and $\eta \in (0.99, 1.01)$ for radial speed less than 14 knots). The complex envelope of a narrowband signal subject to a time scale of η , when η is near one, does not change significantly. Thus,

$$\tilde{s}(\eta t) \approx \tilde{s}(t) \quad (8.146)$$

which allows simplifying (8.143) to

$$\chi(\tau, \eta) \approx \sqrt{\eta} e^{j2\pi f_c \eta \tau} \int_{-\infty}^{\infty} \tilde{s}(t) \tilde{s}^*(t - \tau) e^{j2\pi f_c (1 - \eta)t} dt \quad (8.147)$$

$$= \sqrt{\eta} e^{j2\pi f_c \eta \tau} \xi(\tau, \delta) \quad (8.148)$$

where $\delta = f_c(\eta - 1)$ is the Doppler frequency shift approximation of a Doppler scale and

$$\xi(\tau, \delta) = \int_{-\infty}^{\infty} \tilde{s}(t) \tilde{s}^*(t - \tau) e^{-j2\pi \delta t} dt \quad (8.149)$$

is generally described as the *narrowband ambiguity function*⁴ (NAF). For a monostatic active sonar system with $\eta \approx 1 + 2v_r/c_w$, the Doppler frequency shift is $\delta \approx 2v_r f_c / c_w$. This simplified version of the ambiguity function is very

⁴Note that definitions of the NAF can vary in the sign on δ .

common in radar (e.g., see [14, Sect. 7.2], [16, Sect. 5.1] [18, Ch. 3], or [9, Sect. 4.4]). Although it is useful in many sonar applications, the more general wideband ambiguity function is often required.

An important distinction between the narrowband ambiguity function of (8.149) and the wideband ambiguity function defined in (8.134) is that the complex envelope of the transmit waveform is used in (8.149) rather than its analytic signal. However, it is straightforward to convert (8.149) to be a function of the analytic signal,

$$\xi(\tau, \eta) = e^{-j2\pi f_c \tau} \int_{-\infty}^{\infty} \dot{s}(t) \dot{s}^*(t - \tau) e^{-j2\pi \delta t} dt. \quad (8.150)$$

Two points may be taken from these results when only the modulus of $\chi(\tau, \eta)$ is important (e.g., for the SNR loss in the QMF). The first is that the common definition of the narrowband ambiguity function in (8.149) can be used in lieu of $\chi(\tau, \eta)$ as they only differ by a phase term in the normalized form required for SNR loss. The second is that the modulus of $\chi(\tau, \eta)$ can be obtained using either the complex envelope or analytic signal of the transmit waveform in the definition of the narrowband ambiguity function. An important counterpoint arises when the phase of $\chi(\tau, \eta)$ is important (e.g., for the SNR loss in the CMF). The common definition of the narrowband ambiguity function $\xi(\tau, \delta)$ in (8.149) must be modified as represented in (8.148) in order to incorporate the phase at the carrier frequency before taking the angle required in the CMF SNR loss.

8.3.2.2 Cross-Ambiguity

In the Doppler filter bank interpretation of (8.135), the signal measurement was assumed to have a Doppler scale $\eta_1 = 1$. The more general case is represented by (8.133) taken as a function of τ and $\eta = \eta_0$,

$$R_{FB}(\tau, \eta; \eta_1) = \chi\left(\eta_1 \tau, \frac{\eta}{\eta_1}\right) = \chi^*\left(-\eta \tau, \frac{\eta_1}{\eta}\right) \quad (8.151)$$

where τ is the temporal offset of the filter, η represents the Doppler channel, and η_1 is the fixed Doppler scale of the signal measurement. Recalling that $|\chi(\tau, \eta)|$ achieves its maximum value at $\tau = 0$ and $\eta = 1$, it is seen that $R_{FB}(\tau, \eta; \eta_1)$ also achieves its maximum modulus for zero temporal offset but the maximum occurs in the Doppler channel where η equals η_1 .

Similarly, the more general case of the single-filter representation in (8.137) is formed by taking (8.133) as a function of τ and $\eta = \eta_1$,

$$R_{SF}(\tau, \eta; \eta_0) = \chi\left(\eta \tau, \frac{\eta_0}{\eta}\right) = \chi^*\left(-\eta_0 \tau, \frac{\eta}{\eta_0}\right) \quad (8.152)$$

where η is the Doppler scale of the echo and η_0 is the fixed Doppler scale of the signal replica used in the matched filter. As should be expected, the maximum here occurs when the Doppler scale of the echo matches the tuning of the filter ($\eta = \eta_0$).

The general functions in (8.151) and (8.152) are at times called cross ambiguity functions [16, Sect. 5.5]. However, it is also common to describe the even more general response to a completely different signal as a cross-ambiguity function.

8.3.3 Autocorrelation Functions

In many scenarios the temporal response of the matched filter is more important than mismatch in Doppler (e.g., when neither the sonar platform nor the object of interest are moving). Rather than evaluating the ambiguity function in such scenarios, it is simpler to evaluate the autocorrelation function (ACF) of the transmit waveform. The ACF is the slice of the ambiguity function taken when there is no mismatch in Doppler (i.e., for $\eta = 1$ or $\delta = 0$). It can be described as a function of the analytic signal of the transmit waveform or its complex envelope,

$$\chi(\tau) = \chi(\tau, 1) = \int_{-\infty}^{\infty} \dot{s}(t) \dot{s}^*(t - \tau) dt = \int_{-\infty}^{\infty} \dot{s}(t + \tau) \dot{s}^*(t) dt \quad (8.153)$$

$$= e^{j2\pi f_c \tau} \int_{-\infty}^{\infty} \tilde{s}(t) \tilde{s}^*(t - \tau) dt = e^{j2\pi f_c \tau} \int_{-\infty}^{\infty} \tilde{s}(t + \tau) \tilde{s}^*(t) dt, \quad (8.154)$$

and also as a correlation of the signal with itself. Using the definition of the inverse Fourier transform, the ACF can be described as the inverse Fourier transform of the squared modulus of the Fourier transform of the analytic signal or complex envelope,

$$\chi(\tau) = \mathcal{F}^{-1}\{|\dot{S}(f)|^2\} \quad (8.155)$$

$$= e^{j2\pi f_c \tau} \mathcal{F}^{-1}\{|\tilde{S}(f)|^2\} \quad (8.156)$$

where $\dot{S}(f)$ and $\tilde{S}(f)$ are, respectively, the Fourier transforms of $\dot{s}(t)$ and $\tilde{s}(t)$. This relationship is analogous to the Fourier-transform relationship between the autocorrelation function and power spectrum of a wide-sense-stationary random process (e.g., see Sect. 5.4).

Because of its relationship to the ambiguity function, the maximum modulus of the ACF is achieved at $\tau = 0$. Other properties of the ACF will be explored in the following sections where it is evaluated for different pulses.

Exercise 8.4 Show that the peak of the ACF of a finite-duration waveform occurs at $\tau = 0$. This can be done by differentiating $\chi(\tau)$ with respect to τ to show that

at $\tau = 0$ the first derivative is zero and the second derivative is negative. Hint: use the definition of the ACF as the inverse Fourier transform of the waveform spectrum from (8.155).

8.3.4 CW Pulses

As described in Sect. 8.1.1, a continuous-wave (CW) pulse is a sinusoidal signal at frequency f_c with duration T_p ,

$$s(t) = \begin{cases} \cos(2\pi f_c t) & 0 < t < T_p \\ 0 & \text{otherwise} \end{cases}. \quad (8.157)$$

The analytic signal of a CW pulse is a complex-exponential pulse,

$$\dot{s}(t) = \begin{cases} e^{j2\pi f_c t} & 0 < t < T_p \\ 0 & \text{otherwise} \end{cases}, \quad (8.158)$$

and the complex envelope is simply the rectangular pulse,

$$\begin{aligned} \tilde{s}(t) &= \begin{cases} 1 & 0 < t < T_p \\ 0 & \text{otherwise} \end{cases} \\ &= \text{rect}\left(\frac{t - T_p/2}{T_p}\right). \end{aligned} \quad (8.159)$$

Although it is common to apply a window function in time to reduce the sharp transitions at the beginning and end of the pulse, the pulse described and evaluated here has a constant envelope (i.e., uses a rectangular window).

8.3.4.1 Autocorrelation Function for a CW Pulse

In many situations, it is easiest to evaluate the ACF using the form described in (8.154) for the complex envelope of the signal. Applying this to (8.159) results in

$$\begin{aligned} \chi(\tau) &= e^{j2\pi f_c \tau} \int_{-\infty}^{\infty} \tilde{s}(t) \tilde{s}^*(t - \tau) dt \\ &= e^{j2\pi f_c \tau} \int_{-\infty}^{\infty} \text{rect}\left(\frac{t - T_p/2}{T_p}\right) \text{rect}\left(\frac{t - \tau - T_p/2}{T_p}\right) dt \end{aligned}$$

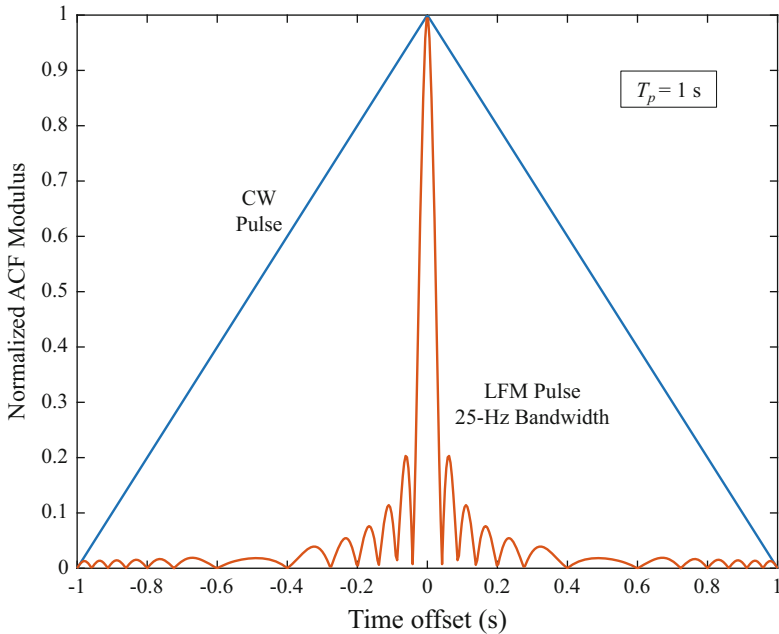


Fig. 8.10 Normalized autocorrelation function (ACF) modulus for 1-s duration CW and LFM pulses normalized by its value at zero offset. The bandwidth of the LFM pulse is 25 Hz

$$= \begin{cases} e^{j2\pi f_c \tau} (T_p - |\tau|) & |\tau| < T_p \\ 0 & \text{otherwise} \end{cases}. \quad (8.160)$$

As seen in Fig. 8.10 for $T_p = 1 \text{ s}$, the modulus of $\chi(\tau)$, which is essentially the convolution between two rectangular pulses, is a triangular function centered at the origin and extending from $\tau = -T_p$ to T_p . The ACF modulus for the CW pulse shown in Fig. 8.10 exhibits three characteristics of the ACF:

- the peak of the ACF occurs at zero time offset ($\tau = 0$),
- the ACF can only be non-zero for $\tau \in (-T_p, T_p)$, and
- the ACF modulus has symmetry about the origin; the ACF itself has conjugate symmetry: $\chi(-\tau) = \chi^*(\tau)$.

That the peak occurs at $\tau = 0$ was the subject of Exercise 8.4. That the ACF can only be non-zero on $(-T_p, T_p)$ arises from the ACF being a correlation or convolution between two signals with duration T_p . The conjugate symmetry is easily proven from the definition.

8.3.4.2 Ambiguity Function for a CW Pulse

The CW pulse is narrowband as long as its duration is long relative to one period of the carrier frequency, which can be seen to arise from assuming $f_c \gg 1/T_p = W$. Because this is generally true in underwater acoustic applications, the NAF in (8.149) is the appropriate form of the ambiguity function. The resulting NAF is

$$\xi(\tau, \delta) = \int_{-\infty}^{\infty} \tilde{s}(t)\tilde{s}^*(t - \tau) e^{-j2\pi\delta t} dt \quad (8.161)$$

$$= \int_{-\infty}^{\infty} \text{rect}\left(\frac{t - T_p/2}{T_p}\right) \text{rect}\left(\frac{t - \tau - T_p/2}{T_p}\right) e^{-j2\pi\delta t} dt \quad (8.162)$$

$$= \begin{cases} T_p \left(1 - \frac{|\tau|}{T_p}\right) \text{sinc}\left(\delta T_p \left[1 - \frac{|\tau|}{T_p}\right]\right) e^{-j\pi\delta[T_p - |\tau|]} & |\tau| < T_p \\ 0 & \text{otherwise} \end{cases} \quad (8.163)$$

where $\delta = f_c(\eta - 1)$ is the Doppler frequency-shift approximation to the frequency scale. The modulus of $\xi(\tau, \delta)$ is that of a triangularly weighted sinc function where the primary argument of the sinc function, δT_p , also includes a triangular weighting. When there is no Doppler mismatch, $\delta = 0$ and $\xi(\tau, 0)$ has the triangularly shaped modulus seen in the ACF of (8.160). At zero time offset, the modulus as a function of δ is that of $\text{sinc}(\delta T_p)$, which first reaches zero when the Doppler frequency shift is $\delta = 1/T_p$. Thus, the CW pulse has a Rayleigh-resolution limit requiring a Doppler frequency shift $\delta \geq 1/T_p$ [unit: Hz], which is precisely its bandwidth. This implies that the minimum separation in radial velocity between two resolvable echoes in a monostatic active sensing geometry is $v_r \geq c_w/(2f_c T_p)$ when using standard processing. The normalized NAF modulus for a 1-s CW pulse at 2 kHz is shown in Fig. 8.11. The figure illustrates the poor resolution of the CW pulse in time, which was also observed in the ACF, and the good resolution in Doppler. How the ambiguity function represents the response of a Doppler filter bank can be seen in the introductory example found in Fig. 1.6. The hourglass-shaped structure seen in Fig. 8.11 (when rotated by 90°) is visible in the strong echo in Fig. 1.6, including the first few sidelobes in the Doppler dimension.

When taken as a function of the Doppler frequency shift δ for a given value of τ , the NAF in (8.161) can be described as the Fourier transform of $\tilde{s}(t)\tilde{s}^*(t - \tau)$. For the CW pulse, the complex envelope $\tilde{s}(t)$ is simply the amplitude shading of the pulse (e.g., the rect(.) functions in (8.162) for the rectangular window). Thus, an FFT can be used to easily evaluate $\xi(\tau, \delta)$ for a given value of τ . The most interesting time offset is of course $\tau = 0$, which represents the Doppler response of the matched filter when the replica and echo are aligned in time. At $\tau = 0$, the Doppler response to a shaded CW pulse is simply the Fourier transform of the squared window

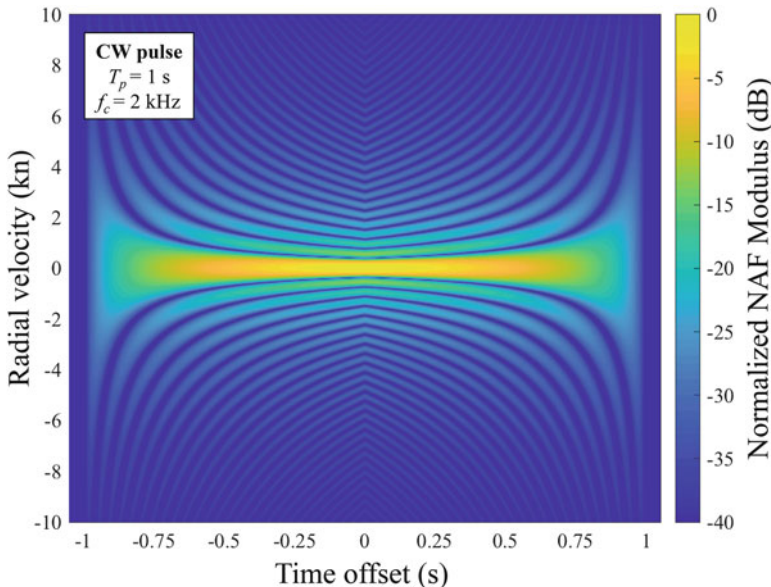


Fig. 8.11 Normalized narrowband ambiguity function (NAF) for a 1-s duration CW pulse at $f_c = 2 \text{ kHz}$

function. As would be expected, shading a CW pulse helps to reduce the sidelobes in the Doppler response. This effect is illustrated in Fig. 8.12 for a 1-s CW pulse at 1.5 kHz (so the Doppler resolution is approximately 1 kn). Applying a Tukey window with 10% (total) shading is seen to have minimal impact on the mainlobe and sidelobes; however, it is beneficial to reduce transient effects in sound projectors subject to sharp power transitions. Using a Hamming window significantly reduces the Doppler sidelobes, but at the expense of a significant increase in the mainlobe width. Finally, a Taylor window with $\bar{n} = 5$ and $R = 25 \text{ dB}$ is seen to reduce the sidelobes at minimal expense to the mainlobe width. It is important to note that there is an additional cost in using each of these windows: the reduction in transmitted energy (which drives performance in noise-limited scenarios) when the peak amplitude and duration of the pulse are kept constant.

Exercise 8.5 Use an FFT to form the Doppler slice of the AF shown in Fig. 8.12 for the Tukey and Taylor windows. From the AF Doppler slice, evaluate the 3-dB-down mainlobe width, the first time the AF is zero (the Rayleigh resolution), and the level of the largest sidelobe. Plot these metrics as a function of the reduction in total transmit energy when the duration and peak pulse amplitude are held constant. Varying the window parameters will trace out curves for each metric as a function of the energy reduction. Such curves can be used to compare the Tukey and Taylor windows. Which one is better and why?

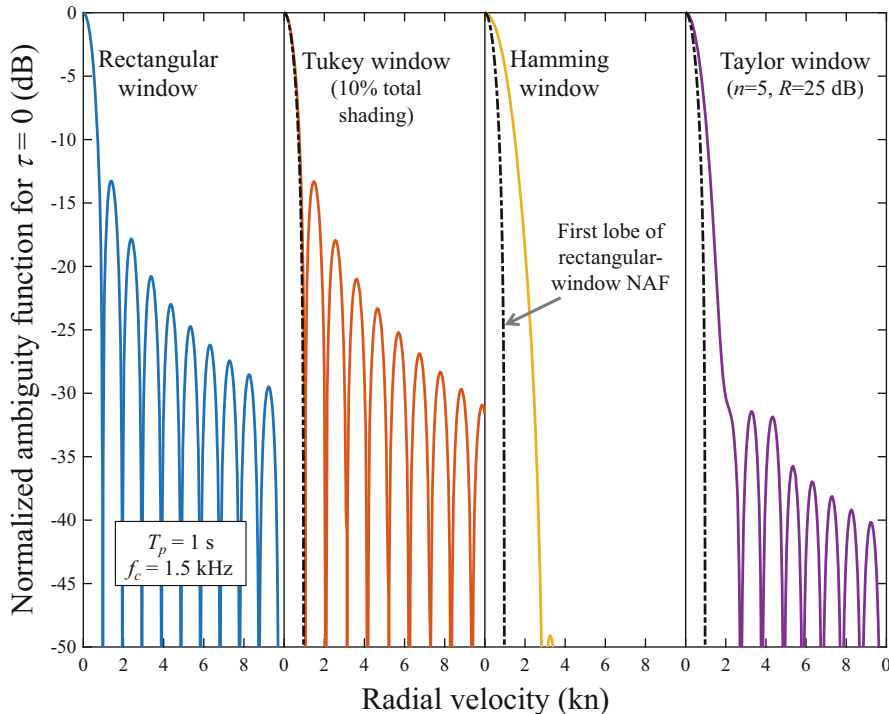


Fig. 8.12 Doppler slice of the normalized narrowband ambiguity function (NAF) at $\tau = 0$ for a 1-s CW pulse at 1.5 kHz with different window functions. The first lobe of the rectangular-window NAF is repeated for the other window functions as a dashed line

8.3.5 LFM Pulses

A linear-frequency-modulated (LFM) pulse has an instantaneous frequency that changes linearly with time from $f_0 = f_c - W/2$ to $f_1 = f_c + W/2$ where f_c is the center frequency and W is the bandwidth. Noting that the instantaneous frequency is the derivative of the phase, the LFM waveform will have a phase varying quadratically in time. A constant-envelope pulse with duration T_p has the form

$$s(t) = \begin{cases} \cos\left[2\pi\left(f_0 t + \frac{\beta}{2}t^2\right)\right] & 0 < t < T_p \\ 0 & \text{otherwise} \end{cases} \quad (8.164)$$

where $\beta = W/T_p$ is called the sweep rate [units: Hz/s]. The analytic signal is a similarly phased *complex exponential* pulse,

$$\hat{s}(t) = \begin{cases} e^{j2\pi(f_0 t + \frac{\beta}{2} t^2)} & 0 < t < T_p \\ 0 & \text{otherwise} \end{cases}. \quad (8.165)$$

The complex envelope is an LFM pulse with the same bandwidth and duration,

$$\tilde{s}(t) = \begin{cases} e^{j2\pi(-\frac{W}{2}t + \frac{\beta}{2}t^2)} & 0 < t < T_p \\ 0 & \text{otherwise} \end{cases}, \quad (8.166)$$

but spans the frequency band $(-W/2, W/2)$.

These equations are generally used to represent an up-sweeping LFM pulse. That is, one where $f_0 < f_1$ so the instantaneous frequency increases with time. A down-sweeping LFM pulse can be achieved in the above equations by letting the variable W be negative, which produces $f_0 > f_1$ and $\beta < 0$ so the instantaneous frequency decreases over time. The bandwidth in this scenario is, of course, not negative but $|W|$.

8.3.5.1 Autocorrelation Function for an LFM Pulse

The ACF of an LFM pulse can be obtained by starting with (8.154) and assuming $\tau \in [0, T_p]$, which leads to

$$\begin{aligned} \chi(\tau) &= e^{j2\pi f_c \tau} \int_{-\infty}^{\infty} \tilde{s}(t + \tau) \tilde{s}^*(t) dt \\ &= e^{j2\pi f_c \tau} e^{-j\pi\tau(W+\beta\tau)} \int_{\tau}^{T_p} e^{j2\pi\beta\tau t} dt \\ &= e^{j2\pi f_c \tau} \left[\frac{\sin(\pi\beta\tau[T_p - \tau])}{\pi\beta\tau} \right]. \end{aligned} \quad (8.167)$$

Combining this with the result for $\tau \in [-T_p, 0]$ (which simply requires replacing each occurrence of τ within the brackets in (8.167) with $-\tau$) and noting that the ACF must be zero for $|\tau| > T_p$ results in the complex ACF,

$$\chi(\tau) = \begin{cases} T_p \left(1 - \frac{|\tau|}{T_p} \right) \operatorname{sinc}\left(W\tau \left[1 - \frac{|\tau|}{T_p} \right] \right) e^{j2\pi f_c \tau} & |\tau| \leq T_p \\ 0 & |\tau| > T_p \end{cases}. \quad (8.168)$$

Thus, for $\tau \in (-T_p, T_p)$, the modulus of the ACF of an LFM pulse is that of the product between the triangular function found in the ACF of a CW pulse and a sinc function with an argument of $W\tau$ that is modulated by the same triangular function. When $W \rightarrow 0$, the LFM pulse becomes a CW and its ACF correspondingly tends to that found in (8.160).

When the time-bandwidth product of the pulse ($T_p W$) is much greater than one, the ACF is approximately

$$\chi(\tau) \approx T_p \operatorname{sinc}(W\tau) e^{j2\pi f_c \tau}, \quad (8.169)$$

especially when $|\tau|$ is small. This can be seen by noting that the first few zero crossings of the sinc function will occur near where $W\tau$ is an integer (i.e., $W\tau = \pm 1, \pm 2, \dots$), so the magnitude of the ACF decreases rapidly with τ and the triangle function has minimal impact. The sinc-function approximation implies the Rayleigh-resolution capability of an LFM pulse is approximately $1/W$. The example shown in Fig. 8.10 for $T_p = 1$ and $W = 25$ illustrates this with zero crossings occurring near $\tau = \pm 0.04$ s and a width of approximately 0.04 s.

8.3.5.2 Narrowband Ambiguity Function for an LFM Pulse

To obtain the NAF of an LFM pulse, it is instructive to describe the complex envelope of the LFM pulse as a quadratic phase modulation of another pulse,

$$\tilde{s}(t) = \tilde{s}_0(t) e^{j\pi(-Wt + \beta t^2)}. \quad (8.170)$$

Because this modulation adds $f_m(t) = -(W/2) + \beta t$ to the instantaneous frequency of $\tilde{s}_0(t)$, the NAF of a CW pulse can then be used to obtain the NAF of an LFM pulse. Using this description in (8.149) results in

$$\begin{aligned} \xi(\tau, \delta) &= \int_{-\infty}^{\infty} \tilde{s}_0(t) e^{j\pi(-Wt + \beta t^2)} \left[\tilde{s}_0(t - \tau) e^{j\pi[-W(t - \tau) + \beta(t - \tau)^2]} \right]^* e^{-j2\pi\delta t} dt \\ &= e^{-j\pi(W\tau + \beta\tau^2)} \int_{-\infty}^{\infty} \tilde{s}_0(t) \tilde{s}_0^*(t - \tau) e^{-j2\pi(\delta - \beta\tau)t} dt \end{aligned} \quad (8.171)$$

$$= e^{-j\pi(W\tau + \beta\tau^2)} \xi_0(\tau, \delta - \beta\tau) \quad (8.172)$$

where $\xi_0(\tau, \delta)$ is the NAF of $\tilde{s}_0(t)$. Thus, the NAF of an LFM pulse can be formed from that of a CW pulse by evaluating it at a time-offset-dependent Doppler frequency shift of $\delta - \beta\tau$.

For the LFM pulse with a constant envelope this results in the squared NAF

$$|\xi(\tau, \delta)|^2 = \begin{cases} (T_p - |\tau|)^2 \operatorname{sinc}^2\left(T_p[\delta - \beta\tau]\left[1 - \frac{|\tau|}{T_p}\right]\right) & |\tau| < T_p \\ 0 & \text{otherwise} \end{cases}. \quad (8.173)$$

For a given value of τ , the peak in the δ dimension occurs when the argument of the sinc function is zero, which requires $\delta = \beta\tau$. This coupling of τ and δ can be

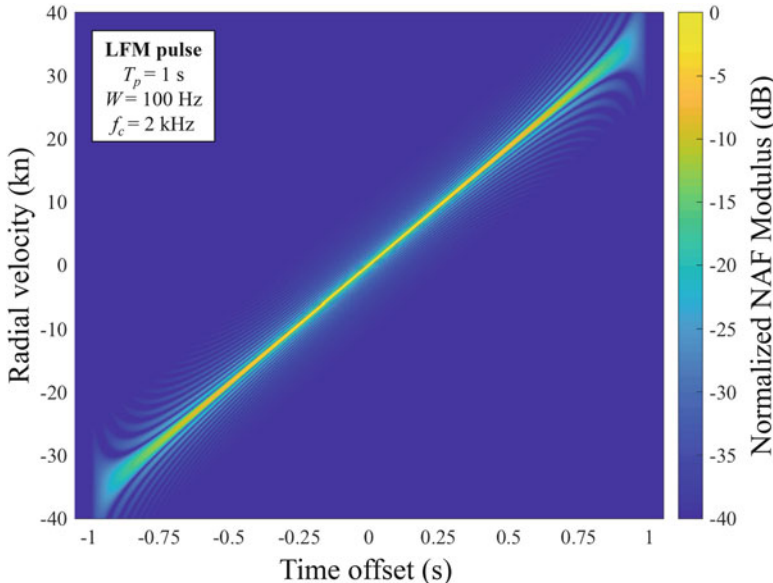


Fig. 8.13 Normalized narrowband ambiguity function (NAF) modulus for a 1-s duration, 100-Hz bandwidth LFM pulse centered at $f_c = 2$ kHz

seen in Fig. 8.13 and implies it will be difficult to simultaneously estimate both the arrival time and Doppler scale using a narrowband LFM pulse.

It is important to recall that the AF $\chi(\tau, \eta)$ was defined in Sect. 8.3.1.3 as most directly representing the response of a Doppler filter bank to a signal measurement. For example, from Fig. 8.13, the Doppler channel for a 10-kn (closing) radial velocity will have a peak in its response approximately 0.3 s after the actual arrival time of a 0-kn signal measurement. Recall from (8.137) that the response of a single matched filter for a zero-radial-velocity signal replica to a signal measurement with Doppler scale η is

$$R_{SF}(\tau, \eta) = \chi^*(-\tau, \eta) = \chi(\eta\tau, \eta^{-1}). \quad (8.174)$$

The time-offset argument of $-\tau$ in the AF implies that for the modulus shown in Fig. 8.13 this is simply a reflection about the temporal-offset axis. Thus, a signal measurement exhibiting a 10-kn (closing) radial velocity will appear in the filter matched to a 0-kn radial velocity approximately 0.3 s before the actual arrival time of the signal measurement. Intuitively this can be remembered by noting that closing objects result in a scale to higher frequencies and that the replica of an up-sweeping FM waveform will align with the higher frequencies at an earlier time rather than a later time (e.g., see the time-frequency diagrams in Fig. 8.4). The converse applies for a down-sweeping FM waveform where echoes from closing objects appear later in time in the matched filter tuned to a 0-kn radial velocity.

Table 8.5 Limits on t , which are used in (8.178), for the two regions of τ required to evaluate the LFM WAF when $\eta \neq 1$

Region of τ	t_1	t_2
$-\frac{T_p}{\eta} \leq \tau \leq T_p - \frac{T_p}{\eta}$	$\max(0, \tau)$	$\frac{T_p}{\eta} + \tau$
$T_p - \frac{T_p}{\eta} \leq \tau \leq \frac{T_p}{\max\{1, \eta\}}$	$\max(0, \tau)$	T_p

8.3.5.3 Wideband Ambiguity Function for an LFM Pulse

Analytical results for the WAF of the LFM pulse can be found in [32]. The basic form of the result is

$$\chi(\tau, \eta) = e^{j\phi} \left[\frac{\eta}{2|\beta(\eta^2 - 1)|} \right]^{\frac{1}{2}} \{C(z_2) - C(z_1) - j\text{sign}(\beta[\eta - 1])[S(z_2) - S(z_1)]\} \quad (8.175)$$

where

$$C(z) = \int_0^z \cos\left(\frac{1}{2}\pi t^2\right) dt \quad \text{and} \quad S(z) = \int_0^z \sin\left(\frac{1}{2}\pi t^2\right) dt \quad (8.176)$$

are the Fresnel cosine and sine integrals (e.g., see [38, Ch. 7]) and

$$\phi = \frac{\pi[(\eta - 1)f_0 + \eta\beta\tau]^2}{\beta(\eta^2 - 1)} \quad (8.177)$$

describes the phase. The Fresnel cosine and sine integrals are evaluated at values

$$z_i = \sqrt{2(\eta + 1)|\beta(\eta - 1)|} \left[t_i + \frac{(\eta - 1)f_0 - \beta\eta^2\tau}{\beta(\eta^2 - 1)} \right] \quad (8.178)$$

for $i = 1$ and 2 where t_1 and t_2 are found in Table 8.5 for different conditions on η and τ . Outside of the regions of τ described in Table 8.5, $\chi(\tau, \eta) = 0$. When $\eta = 1$, the ACF in (8.168) should be used. If only the squared modulus of the WAF is required, (8.175) yields the slightly simpler

$$|\chi(\tau, \eta)|^2 = \left[\frac{\eta}{2(\eta + 1)|\beta(\eta - 1)|} \right] \{[C(z_2) - C(z_1)]^2 + [S(z_2) - S(z_1)]^2\}. \quad (8.179)$$

A comparison between the NAF and WAF of an LFM pulse is found in Fig. 8.14 where the bandwidth is 500 Hz and the center frequency 2 kHz so $\xi = W/f_c = 0.25$. The NAF clearly fails to capture both the spreading of the response in time and the lower levels of the AF at non-zero radial velocity. The AF slices shown in Fig. 8.15 (lower pane) emphasize how significant the spreading and mismatch loss are.

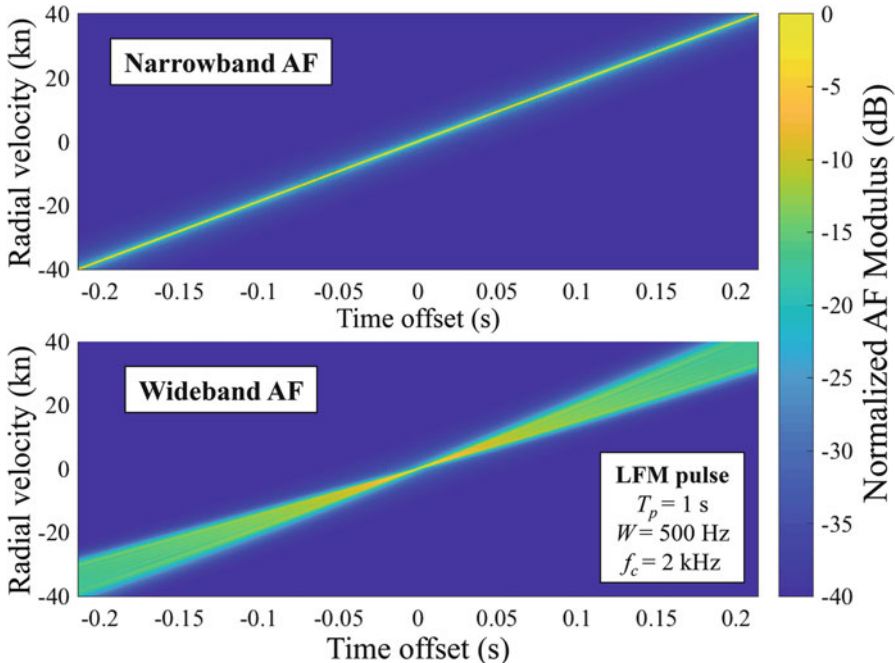


Fig. 8.14 Normalized narrowband and wideband ambiguity functions for a 1-s duration, 500-Hz bandwidth LFM pulse centered at $f_c = 2$ kHz

Exercise 8.6 Use the WAF of the LFM to evaluate its maximum modulus over τ as a function of η , $\max_{\tau} |\chi(\tau, \eta)|$ for a 1-s LFM pulse with a 2-kHz center frequency and bandwidth of 100 Hz. What is the maximum radial velocity allowable for no more than a 3-dB SNR loss in the QMF detector designed for $\eta = 1$? What if the bandwidth of the LFM pulse is 500 Hz?

8.3.6 HFM Pulses

A hyperbolic-frequency-modulated (HFM) pulse has an instantaneous frequency described by a hyperbola. For example, suppose the instantaneous frequency for $t \in [0, T_p]$ is defined by the rectangular hyperbola

$$f(t) = \frac{f_0}{1 - bf_0 t} \quad (8.180)$$

where b is chosen so the instantaneous frequency is $f_1 = f_0 + W$ at the end of the pulse,

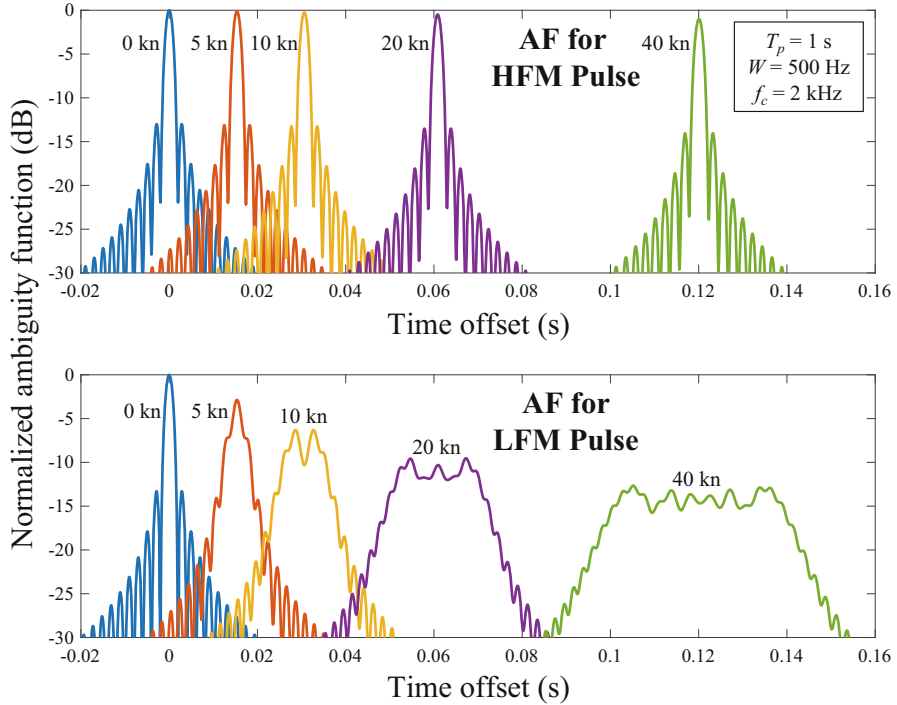


Fig. 8.15 Slices of the normalized ambiguity function (AF) for 1-s duration, 500-Hz LFM and HFM pulses centered at $f_c = 2\text{ kHz}$ with various radial velocities. The greater sensitivity of the broadband LFM pulse relative to the HFM is evident in both the reduced level of the AF and the temporal spreading

$$b = \frac{f_1 - f_0}{f_0 f_1 T_p} = \frac{W}{f_0 f_1 T_p}. \quad (8.181)$$

Although this describes an up-sweeping HFM pulse, it can also be used to form a down-sweeping pulse when $f_1 < f_0$ and W is redefined to be $f_0 - f_1$. Recalling that the instantaneous frequency can be obtained from the derivative of the phase, $f(t) = \frac{1}{2\pi}\phi'(t)$, the phase of the HFM waveform is seen to be logarithmic [39],

$$\begin{aligned} \phi(t) &= 2\pi \int_0^t f(s) \, ds \\ &= -\frac{2\pi}{b} \log(1 - bf_0 t). \end{aligned} \quad (8.182)$$

A constant-envelope HFM pulse with duration T_p therefore has the form

$$s(t) = \begin{cases} \cos\left(\frac{2\pi}{-b} \log[1 - bf_0 t]\right) & 0 < t < T_p \\ 0 & \text{otherwise} \end{cases}. \quad (8.183)$$

The analytic signal is a similarly phased complex exponential pulse,

$$\dot{s}(t) = \begin{cases} \exp\{-j2\pi b^{-1} \log[1 - bf_0 t]\} & 0 < t < T_p \\ 0 & \text{otherwise} \end{cases}. \quad (8.184)$$

The complex envelope is easily obtained from the analytic signal via $\tilde{s}(t) = e^{-j2\pi f_c t} \dot{s}(t)$; however, it is no more than a frequency-shifted version of the bandpass analytic signal. In particular, the complex envelope is not an HFM pulse in the base frequency band (e.g., with $f_0 = -W/2$ and $f_1 = W/2$) as occurs for the complex envelope of an LFM pulse.

Noting that the period of a sinusoid is the inverse of its frequency, the HFM pulse is also seen to produce a linear period modulation (LPM),

$$\text{Period}(t) = \frac{1}{f_0} - bt, \quad (8.185)$$

ranging from f_0^{-1} at $t = 0$ to f_1^{-1} at $t = T_p$. This description also indicates that b is the rate at which the period decreases with time throughout the pulse.

8.3.6.1 Autocorrelation Function for an HFM Pulse

There are two useful approximations to the ACF of an HFM pulse. The first can be used when the waveform bandwidth is small relative to the center frequency (i.e., $\zeta = W/f_c \ll 1$), in which case the LFM ACF is a good approximation [34]. A third-order Maclaurin series approximation to the phase of the HFM pulse results in

$$\begin{aligned} \phi(t) &= -\frac{2\pi}{b} \log(1 - bf_0 t) \\ &\approx 2\pi \left\{ f_0 t + \frac{W(1 - \zeta/2)}{2T_p(1 + \zeta/2)} t^2 \left[1 + \frac{2t\zeta}{3T_p(1 + \zeta/2)} \right] \right\}. \end{aligned} \quad (8.186)$$

When ζ is small, the second term within the brackets in (8.186) can be discarded to form the 2nd-order Maclaurin series approximation. The resulting quadratic phase represents an LFM waveform with duration T_p and frequency ranging from f_0 to $f_0 + W(1 - \zeta/2)/(1 + \zeta/2)$. When ζ is small, the ACF of an LFM with bandwidth W can therefore be used to approximate the ACF of the HFM waveform. This is illustrated in Fig. 8.16 where the LFM ACF is seen to be accurate for small values of ζ and the mainlobe reasonably accurate even when ζ is as high as one.

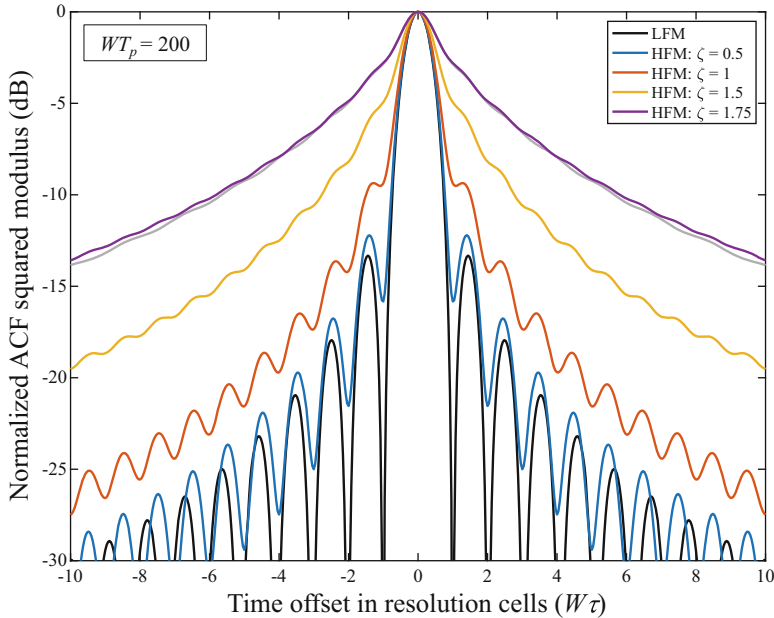


Fig. 8.16 Squared modulus of the autocorrelation function (ACF) of 1-s-duration/200-Hz-bandwidth HFM pulses for various values of $\zeta = W/f_c$ and an LFM pulse, normalized by the ACF value at zero offset. The offset is shown in terms of the number of resolution cells (i.e., $W\tau$). The gray line is a numerical evaluation of the HFM ACF for $\zeta = 1.75$ whereas the colored lines use the stationary phase approximation found in (8.190)

When ζ is not small but the time-bandwidth product is large, the stationary-phase approximation to the Fourier transform of the HFM pulse can be used with the frequency-domain definition of the ACF in (8.155). This approach was used in [31, 34] to obtain the Fourier transform of the ambiguity function of the HFM pulse via (8.145), but is applied here to obtain the ACF. The stationary-phase approximation to the Fourier transform of the analytic signal of the unit-amplitude HFM pulse illustrates that its modulus has a $1/f^2$ dependence,

$$S(f) = \mathcal{F}\{\chi(\tau)\} \approx \begin{cases} \frac{1}{bf^2} & f_0 < f < f_1 \\ 0 & \text{otherwise} \end{cases}. \quad (8.187)$$

Using this in (8.155) results in the ACF approximation

$$\chi(\tau) \approx \int_{f_0}^{f_1} \frac{1}{bf^2} e^{j2\pi f\tau} df \quad (8.188)$$

$$= \frac{2\pi}{b} \left[\frac{e^{j\omega_0\tau}}{\omega_0} - \frac{e^{j\omega_1\tau}}{\omega_1} + j\tau \int_{\omega_0\tau}^{\omega_1\tau} \frac{e^{js}}{s} ds \right] \quad (8.189)$$

$$= \frac{2\pi}{b} \left\{ \frac{e^{j\omega_0\tau}}{\omega_0} - \frac{e^{j\omega_1\tau}}{\omega_1} + j\tau [E_1^*(j\omega_0\tau) - E_1^*(j\omega_1\tau)] \right\} \quad (8.190)$$

where $\omega_0 = 2\pi f_0$, $\omega_1 = 2\pi f_1$ and

$$E_1(x) = \int_x^\infty \frac{e^{-s}}{s} ds \quad (8.191)$$

is the exponential integral [38, Ch. 5] (e.g., available as the `expint` function in MATLAB®). This approximation is shown in Fig. 8.16 for $WT_p = 200$ and several values of ζ . The gray line near $\zeta = 1.75$ is a numerical evaluation of the ACF and illustrates how the approximation is adequate for most purposes, but not necessarily precise away from the main lobe of the ACF.

Exercise 8.7 Evaluate the temporal resolution of the HFM pulse using the 3-dB down width of the mainlobe ($\tau_{3\text{dB}}$) as a function of $\zeta = W/f_c$ ranging from 0.1 to 1.75 with $f_c = 2\text{ kHz}$ and $T_p = 1\text{ s}$. How much larger is the resolution cell size relative to an LFM pulse when $\zeta = 1$? How does $W\tau_{3\text{dB}}$ change with f_c and T_p ?

8.3.6.2 Ambiguity Function for an HFM Pulse

Suppose an HFM pulse is subject to a Doppler scale η . The replica then has the form

$$\dot{s}(\eta t) = \begin{cases} \exp\{-j2\pi b^{-1} \log[1 - b\eta f_0 t]\} & 0 < t < T_p/\eta \\ 0 & \text{otherwise} \end{cases}. \quad (8.192)$$

The instantaneous frequency is

$$f_\eta(t) = \frac{\eta f_0}{1 - b\eta f_0 t}, \quad (8.193)$$

which varies from ηf_0 at $t = 0$ to ηf_1 for $t = T_p/\eta$ when the pulse ends. Thus, the Doppler-scaled pulse is itself an HFM waveform with a period-rate parameter

$$b_\eta = \frac{\eta f_1 - \eta f_0}{(T_p/\eta)(\eta f_0)(\eta f_1)} = b \quad (8.194)$$

which is identical to that of the original pulse.

Plots of the instantaneous frequency of an echo from objects that have zero relative radial velocity ($\eta = 1$), closing-range objects ($\eta > 1$) and opening-range

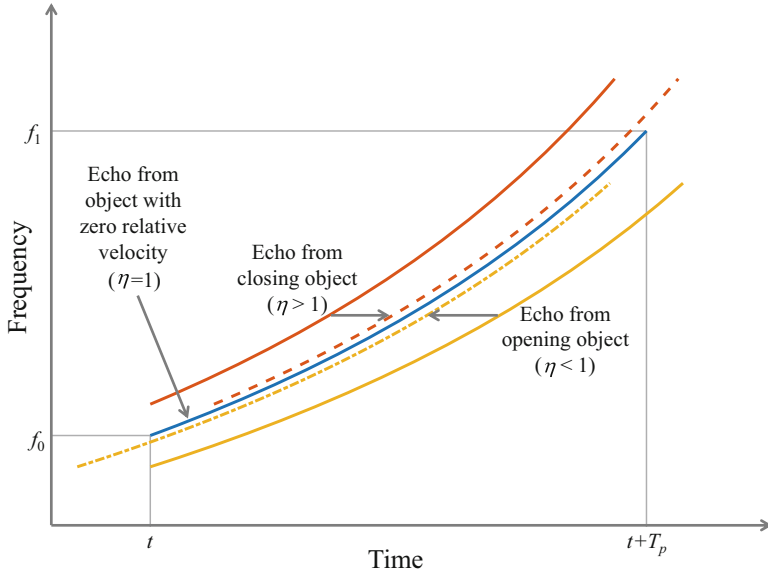


Fig. 8.17 Instantaneous frequency of the echo from opening, closing, and zero-relative-velocity objects for an HFM pulse. The echoes from opening or closing objects have the same instantaneous frequency profile as that of an object with zero relative velocity but are subject to a Doppler-dependent temporal offset. The dashed lines represent the respective echoes at a time offset closer to that of the zero-relative-velocity profile

objects ($\eta < 1$) are shown in Fig. 8.17. The new start and stop frequencies of ηf_0 and ηf_1 are evident and either below the original frequencies when $\eta < 1$ or above when $\eta > 1$. The primary advantage the HFM pulse enjoys over the LFM pulse with respect to Doppler is seen in the figure when the echoes from the objects having some relative velocity are shifted in time (the dashed lines). The instantaneous-frequency functions of the time-shifted echoes illustrate how their time-frequency structure is identical to that of the HFM pulse for $\eta = 1$ where they overlap. This implies that where the waveforms overlap there is no SNR loss from mismatch, but only from having a smaller overlap than if there was no Doppler scale to begin with. The preservation of the time-frequency structure of the HFM pulse when subject to a Doppler scale has been described as “optimizing a frequency-modulation law” [34] and as being *optimally invariant* to Doppler [40].

The time offset required to align the pulses is obtained for $\eta > 1$ by finding the time at which the frequency in (8.180) is ηf_0 ,

$$\tau_\eta = \frac{1 - \eta^{-1}}{bf_0} = \frac{T_p(1 - \eta^{-1})}{1 - f_0/f_1}. \quad (8.195)$$

When $\eta < 1$, a time advancement (negative time offset) is required and obtained as the time when the frequency in (8.193) equals f_0 . In time-offset form it is functionally the same as (8.195).

The AF of an HFM pulse can thus be approximated by the ACF of an HFM pulse with rate parameter b and frequency range $(\eta f_0, f_1)$ for $\eta > 1$ or $(f_0, \eta f_1)$ for $\eta < 1$. Normalizing the HFM ACF from (8.190) by $\sqrt{\eta}$ as required by the AF definition in (8.142) results in

$$\chi(\tau, \eta) \approx \frac{2\pi\sqrt{\eta}}{b} \left\{ \frac{e^{j\omega_{0,\eta}(\tau-\tau_\eta)}}{\omega_{0,\eta}} - \frac{e^{j\omega_{1,\eta}(\tau-\tau_\eta)}}{\omega_{1,\eta}} + j\tau [E_1^*(j\omega_{0,\eta}(\tau-\tau_\eta)) - E_1^*(j\omega_{1,\eta}(\tau-\tau_\eta))] \right\} \quad (8.196)$$

where the lower and upper radian frequencies, as a function of η , are

$$\omega_{0,\eta} = 2\pi f_0 \cdot \max\{1, \eta\} \quad \text{and} \quad \omega_{1,\eta} = 2\pi f_1 \cdot \min\{1, \eta\}. \quad (8.197)$$

Slices of the AF for various radial velocities are shown in Fig. 8.15 for both HFM and LFM pulses with duration $T_p = 1$ s, bandwidth $W = 500$ Hz, and center frequency $f_c = 2$ kHz. As the radial velocity increases, the HFM-pulse AF slice maintains its shape, but is subject to the shift in time offset (τ_η) and a slight mismatch loss relative to the $\eta = 1$ scenario. In contrast, the LFM-pulse AF experiences a significant broadening of the response (also seen in Fig. 8.14) and a significantly larger mismatch loss.

The Doppler mismatch loss for the HFM pulse can be assessed by evaluating the AF at τ_η , where its modulus peaks for any given value of η . According to the approximation used to form (8.196), the AF modulus at the peak is approximately $\sqrt{\eta}$ times the temporal extent of the overlap ($T_p - |\tau_\eta|$) between the replica and Doppler-scaled echo. Describing this as an SNR loss factor (for the QMF detector) results in

$$\begin{aligned} \mathcal{L} &= \max_{\tau} \left| \frac{\chi(\tau, \eta)}{\chi(0, 1)} \right|^2 = \left| \frac{\chi(\tau_\eta, \eta)}{\chi(0, 1)} \right|^2 \\ &= \frac{\eta}{T_p^2} \left[\frac{T_p}{\min\{1, \eta\}} - |\tau_\eta| \right]^2 \end{aligned} \quad (8.198)$$

$$= \frac{1}{4\bar{\eta}} \left[1 + \bar{\eta} - \frac{2(\bar{\eta} - 1)}{\zeta} \right]^2 \quad (8.199)$$

where $\bar{\eta} = \max\{\eta, 1/\eta\}$ and $\zeta = W/f_c$. Because $\bar{\eta} \geq 1$, the loss factor $\mathcal{L} \leq 1$ and is exacerbated by increasing $\bar{\eta}$ or decreasing ζ . That is, broader band HFM pulses are less sensitive to Doppler than narrower band HFM pulses, as would be expected from the larger percentage of overlap for a given η .

8.4 Beamforming as a Detection Process

In developing the matched-filter detector in Sect. 8.2 it was assumed that the data consisted of a temporal signal as measured from a single hydrophone or as the output of a beamformer steered to a particular direction. The beamforming itself can be described as a detection process by starting with the measurements from the hydrophones within the array. This requires representing the signal and noise as functions of both space and time that satisfy the wave equation as described in Sect. 3.2.2.1. The structure imposed on the space-time signal by the wave equation allows characterizing it as a signal with known form and some unknown parameters. The intent in this section is to demonstrate that a “spatial” matched-filter detector is in fact a conventional beamformer. Because of the focus on the detection process, consideration is restricted to the simple case of plane-wave propagation and a uniformly spaced line array of sensors. The beampattern and beam-response functions are shown to be the spatial equivalent of the ambiguity function for conventional array processing. Array gain and directivity index are presented owing to their relevance to the sonar equation. Other resources for array signal processing include [41–45].

8.4.1 Plane Waves and Line Arrays

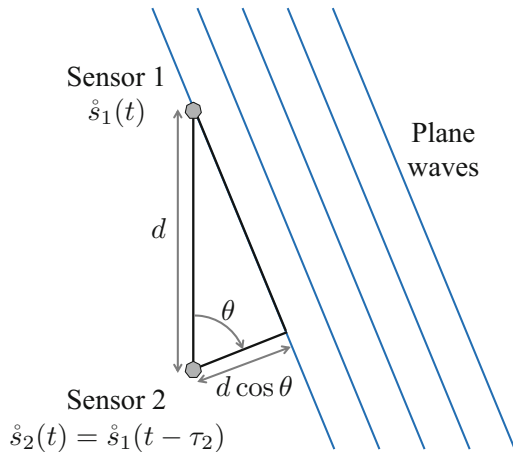
As described in Sect. 3.2.2.4, spherical propagation of a sound wave can be approximated by planar wavefronts when the distance from the sound source is large enough. This condition is satisfied when the sensor array is in the far-field of the source (cf. Sect. 3.2.2.5) and implies that the signal observed at one sensor is simply a delayed version of the signal observed at another. Using the analytic signal observed at sensor 1 as the reference, this means the analytic signal observed at the l th sensor can be described as

$$\dot{s}_l(t) = \dot{s}_1(t - \tau_l) \quad (8.200)$$

where the delay τ_l depends on both the position of the l th sensor relative to the first and the direction from which the plane wave is propagating. As shown in Fig. 8.18, the additional distance a wavefront travels to reach a sensor a distance d away is $d \cos \theta$ where θ is the angle between the line connecting the sensors and the direction from which the plane waves are propagating. The delay between the first and second sensor is then $\tau_2 = d \cos(\theta)/c_w$ where c_w is the speed of sound. For a uniformly spaced line array with inter-sensor spacing d , the distance between the first and l th sensor is $(l - 1)d$ so the delay between the first and l th sensors is

$$\tau_l = (l - 1) \frac{d \cos \theta}{c_w}. \quad (8.201)$$

Fig. 8.18 Plane waves impinging on two sensors illustrating the additional distance traveled by a wavefront to reach the second sensor relative to the first



Note that these delays are independent of the temporal frequency, but depend on $\cos \theta$, which can be viewed as a spatial frequency. For a line array, only the conical angle θ relative to the array heading is required to define the delays in (8.201). This could represent a depression/elevation angle if the line array is placed vertically in the water or represent an azimuthal angle if the array is horizontal and the signals arrive in the horizontal plane. The extension to include both dimensions is straightforward.

8.4.2 Narrowband Beamformer

Suppose the signal of interest is narrowband so its analytic signal can be described by

$$\dot{s}_1(t) = a(t)e^{j2\pi f_c t + j\phi(t)} \quad (8.202)$$

where the amplitude $a(t)$ and phase $\phi(t)$ vary slowly with respect to the carrier frequency f_c . The signal observed at the l th sensor is then

$$\dot{s}_l(t) = a(t - \tau_l)e^{j2\pi f_c(t - \tau_l) + j\phi(t - \tau_l)} \quad (8.203)$$

$$\approx a(t)e^{j2\pi f_c(t - \tau_l) + j\phi(t)} \quad (8.204)$$

where the approximation requires $a(t)$ and $\phi(t)$ to vary slowly over the interval $t \in [0, \tau_l]$. When this condition is satisfied, the signal is said to be narrowband with respect to the beamforming application (recall the discussion in Sect. 7.2.2 regarding the definitions of narrowband and broadband signals). If the source signal

has bandwidth W , it will change over a time interval $1/W$, so the narrowband beamforming requirement is

$$\max_{l,\theta} \tau_l \ll \frac{1}{W} \quad (8.205)$$

or

$$W \ll \frac{c_w}{d(m-1)} \quad (8.206)$$

for the uniformly spaced line array with m sensors where the maximum delay occurs for $\theta = 0$ or π . Although this may appear to not be a function of the carrier frequency, it is when the inter-sensor spacing is chosen to be every half wavelength, $d = \lambda/2 = c_w/(2f_d)$, where f_d is called the design frequency of the array. When operating the array at the design frequency (i.e., $f_c = f_d$), this then requires the bandwidth-to-center-frequency ratio to be inversely related to the number of half-wavelength spaced sensors,

$$\frac{W}{f_c} \ll \frac{2}{m-1}. \quad (8.207)$$

When the source signal does not satisfy this constraint, a broadband beamformer must be implemented. While this is beyond the scope of this text, it is simply accomplished by converting the data to the frequency domain using a DFT and implementing a separate narrowband beamformer on each frequency bin.

8.4.2.1 Array Signal and Noise Models

As was done in Sect. 8.2, the data measured on each of the sensors are basebanded and sampled in time because of the ensuing simple statistical characterizations. Starting with the signal component requires the complex envelope of the signal measurement from the l th sensor, which is

$$\begin{aligned} \tilde{s}_l(t) &\approx a(t)e^{-j2\pi f_c \tau_l + j\phi(t)} \\ &= \tilde{s}_l(t)e^{-j2\pi f_c \tau_l}, \end{aligned} \quad (8.208)$$

where the delay τ_l in the bandpass signal equates to a change in phase of $-2\pi f_c \tau_l$. Placing the sampled basebanded signal measurements over the time period $[\tau_p, \tau_p + T_p]$ from the l th sensor into the l th column of a matrix results in

$$\mathbf{S} = \begin{bmatrix} \tilde{s}_1(\tau_p) & \cdots & \tilde{s}_m(\tau_p) \\ \tilde{s}_1(\tau_p + T_s) & \cdots & \tilde{s}_m(\tau_p + T_s) \\ \vdots & & \vdots \\ \tilde{s}_1(\tau_p + [n-1]T_s) & \cdots & \tilde{s}_m(\tau_p + [n-1]T_s) \end{bmatrix}, \quad (8.209)$$

where $T_s = 1/f_s$ is the sampling period and $n = T_p f_s$. Using (8.208), the matrix \mathbf{S} , which has dimension n -by- m , can be factored into the vector outer product

$$\mathbf{S} = \mathbf{s}\mathbf{d}^T \quad (8.210)$$

that decouples the temporal structure into \mathbf{s} and the spatial structure into \mathbf{d} . The sampled signal vector

$$\mathbf{s} = [\tilde{s}_1(\tau_p) \quad \tilde{s}_1(\tau_p + T_s) \quad \cdots \quad \tilde{s}_1(\tau_p + (n-1)T_s)]^T \quad (8.211)$$

is identical to that developed in Sect. 8.2. The spatial structure of the signal is captured by a vector of complex rotations,

$$\mathbf{d} = [1 \quad e^{-j2\pi f_c \tau_1} \quad \cdots \quad e^{-j2\pi f_c \tau_m}]^T, \quad (8.212)$$

where the phases represent the time-delays from the first sensor. The vector \mathbf{d} is known as the steering vector of the array because it points the beamformer to the arrival angle used to form the time delays.

Recall from Sect. 8.2 that sampling temporally white noise at the signal bandwidth results in uncorrelated samples that are also statistically independent if they are Gaussian distributed. If a similar assumption is made for the spatial sampling, the noise samples in the n -by- m data matrix (\mathbf{X}) corresponding to the signal matrix in (8.209) will all be uncorrelated. The conditions producing this spatially white noise scenario will be described in Sect. 8.4.4.

Under these assumptions, the array signal and noise models for the sampled complex envelope are identical to the characterization presented in Sect. 8.2 for derivation of the matched-filter detector. Thus, the detector and optimality conditions presented in Table 8.2 also hold for the narrowband array signal and noise model. Similar to how the signal after sampling in time and space was placed into the matrix \mathbf{S} in (8.209), suppose the sampled complex envelope data from each sensor (\mathbf{x}_l being from the l th sensor) are placed in the data matrix

$$\mathbf{X} = [\mathbf{x}_1 \dots \mathbf{x}_m]. \quad (8.213)$$

The coherent matched filter output, equivalent to (8.12), can then be described as

$$X = \mathbf{s}^H \mathbf{X} \mathbf{d}^* = \mathbf{d}^H (\mathbf{X}^H \mathbf{s})^* \quad (8.214)$$

and used to form either the CMF or QMF detectors. The form shown in (8.214) can be obtained by rearranging the n -by- m data matrix \mathbf{X} into an nm -by-1 vector and forming the inner product as was done in Sect. 8.2 (or by exploiting notation for the covariance of a matrix of random variables). The multiplication of \mathbf{X} by \mathbf{d}^* is precisely a narrowband conventional beamformer (e.g., see [41, Sect. 2.2]). Thus, the narrowband conventional beamformer is itself a matched filter where the replica is obtained by exploiting the form of the signal enforced by propagation that must follow the wave equation (e.g., here using plane waves as a solution when the array is in the far field of the source).

For uniformly spaced line arrays there are many similarities between beamforming and spectral estimation or Doppler-bank filtering for CW pulses. The most important is related to how a single narrowband filter in spectral estimation accepts signals within its passband and rejects frequency content outside. Beamforming to a specific angle θ similarly implements a spatial filter accepting signals originating near angle θ and rejecting signals coming from other directions.

8.4.3 Array Beam Response and Beampattern

The linearity of the temporal matched filtering (pre-multiplication of \mathbf{X} in (8.214) by \mathbf{s}^H) and the narrowband conventional beamformer (post-multiplication of \mathbf{X} by \mathbf{d}^*) implies they can be done in either order. Consider first performing the temporal matched filtering⁵ and forming an m -by-1 vector comprising the conjugated complex matched filter response to the sampled complex envelope measured at each sensor,

$$\mathbf{x}_s = (\mathbf{X}^H \mathbf{s})^* = \begin{bmatrix} (\mathbf{x}_1^H \mathbf{s})^* \\ \vdots \\ (\mathbf{x}_m^H \mathbf{s})^* \end{bmatrix} \quad (8.215)$$

Using the Rician signal model from (8.8), it can be shown that the array data vector after matched filtering is complex multivariate Gaussian distributed,

$$\mathbf{x}_s \sim \mathcal{CN}\left(A e^{j\psi} \mathbf{d}, \nu_s \mathbf{d} \mathbf{d}^H + \nu \mathbf{I}\right), \quad (8.216)$$

with a mean vector proportional to the array steering vector to represent the deterministic signal component and a rank-one component ($\nu_s \mathbf{d} \mathbf{d}^H$) in the covariance matrix to represent the random signal component. Note that ν_s and ν have been used in (8.216) for the random-signal and noise powers, respectively, in lieu of λ_s and λ

⁵The matched filtering can equivalently be replaced by a narrowband filter for frequency-domain processing of random signals or signals with unknown form.

in (8.8) to avoid the soon-to-be-encountered conflict with wavelength. The QMF detector decision statistic is then the squared modulus of the vector inner product between the array signal form \mathbf{d} and the array data \mathbf{x}_s ,

$$T(\mathbf{x}_s) = |\mathbf{d}^H \mathbf{x}_s|^2. \quad (8.217)$$

Normalization by the noise variance has been deferred to conform with standard array signal processing notation.

Similar to the development of the matched filter where the signal arrival time and Doppler were assumed to be known, the direction from which the signal emanated (θ) has been assumed to be known here. In general, however, it is not and a bank of filters matched to all possible values of θ are formed in an identical construct to the Doppler filter bank. The output of the filter bank formed by taking (8.217) as a function of θ ,

$$R(\theta; \mathbf{x}_s) = |\mathbf{d}^H(\theta) \mathbf{x}_s|^2, \quad (8.218)$$

is called the array beam response. Similar to the output of the Doppler filter bank or a DFT filter bank used in spectral estimation, this is a random quantity representing the system response to a data measurement. The value of θ maximizing the beam response provides an estimate of the angle of arrival of the signal. Suppose now that the signal originates from angle ϕ . The average beam response, which is taken as a function of the pointing direction θ , is

$$\begin{aligned} \bar{R}(\theta; \phi) &= E[R(\theta; \mathbf{x}_s)] \\ &= \mathbf{d}^H(\theta) E[\mathbf{x}_s \mathbf{x}_s^H] \mathbf{d}(\theta) \\ &= (A^2 + v_s) |\mathbf{d}^H(\theta) \mathbf{d}(\phi)|^2 + m v. \end{aligned} \quad (8.219)$$

The function $\mathbf{d}^H(\theta) \mathbf{d}(\phi)$ that describes how much of the signal enters into the average response is directly analogous to the complex ambiguity function from Sect. 8.3.1.3 when it is interpreted as describing the response of a Doppler filter bank to a specific signal.

The interpretation of the ambiguity function as representing the response of a single matched filter to a varying signal has the same form, but is taken as a function of the direction of arrival of the test signal (ϕ) rather than the main response axis of the beamformer beam (θ). In array signal processing, the squared modulus of this function is called the beampattern and is typically described for a more general beamforming vector $\mathbf{w}(\theta)$,

$$b(\phi; \theta) = |\mathbf{w}^H(\theta) \mathbf{d}(\phi)|^2. \quad (8.220)$$

For example, choosing $\mathbf{w}(\theta) = \mathbf{W}\mathbf{d}(\theta)$ where $\mathbf{W} = \text{diag}\{w_1, \dots, w_m\}$ is a diagonal matrix allows shading the array with a window to reduce the sidelobes at the expense of increasing the mainlobe. As a beampattern, (8.220) describes the response of a fixed beamformer pointing to θ to a signal arriving from ϕ . Although the average beam response in (8.219) contains the beampattern function (assuming $\mathbf{w}(\theta) = \mathbf{d}(\theta)$), it is taken as a function of θ for a fixed ϕ . Although this difference may seem minor, it is an important one in adaptive beamforming where the beamforming vector is chosen as a function of the observed data.

8.4.4 Array Gain and Directivity

Similar to a temporal matched filter, a spatial matched filter increases the SNR of a signal. In the array processing context, this is called array gain. The SNR at the input to the beamformer is that at a single sensor, which is obtained from (8.216) as

$$S_{\text{in}}^{\text{a}} = \frac{(A^2 + v_s)}{\nu}. \quad (8.221)$$

The SNR after beamforming can be obtained from the average beam response in (8.219) when evaluated at $\theta = \phi$ by forming the ratio of the signal and noise components, which results in

$$\begin{aligned} S_{\text{out}}^{\text{a}} &= \frac{(A^2 + v_s)|\mathbf{d}^H(\phi)\mathbf{d}(\phi)|^2}{m\nu} \\ &= \frac{m(A^2 + v_s)}{\nu}. \end{aligned} \quad (8.222)$$

The SNR gain achieved by the beamformer is then the ratio

$$G_{\text{a}} = \frac{S_{\text{out}}^{\text{a}}}{S_{\text{in}}^{\text{a}}} = m \quad (8.223)$$

so the array gain term in the sonar equation is $\text{AG} = 10 \log_{10} G_{\text{a}} = 10 \log_{10} m$ where m is the number of half-wavelength-spaced sensors in a line array operated at the design frequency. It is important to recall the assumption of spatially white noise required to obtain this result.

This process of using the average beam response to obtain the SNR after beamforming allows consideration of very complex scenarios involving interferences and noise that are not spatially white. As described in Sect. 2.3.2, it is common in sonar equation analysis to use array gain assuming the noise is isotropic (i.e., the noise originates from all angles equally) in which case the array gain is called the *directivity index* or DI of the array. To determine DI, the statistical characterization

of the array data vector from (8.216) is first generalized to account for correlation between the noise observed on different sensors, resulting in

$$\mathbf{x}_s \sim \mathcal{CN}\left(Ae^{-j\psi} \mathbf{d}, v_s \mathbf{d} \mathbf{d}^H + \mathbf{Q}\right), \quad (8.224)$$

where \mathbf{Q} is the covariance matrix of the noise across the array sensors. The sensor-to-sensor correlation of isotropic noise for temporally overlapping measurements is then obtained from [46, Table 3.1] as

$$\rho = \text{sinc}\left(\frac{2f_c d}{c_w}\right) \quad (8.225)$$

when the sensors are separated by a distance d . For a uniform line array, the (i, j) element of the noise covariance matrix is then

$$\{\mathbf{Q}\}_{i,j} = v \text{sinc}\left(\frac{2f_c(i-j)d}{c_w}\right). \quad (8.226)$$

By choosing the sensor spacing

$$d = \frac{c_w}{2f_c} = \frac{\lambda}{2}, \quad (8.227)$$

which is placing them every half wavelength (λ), the noise covariance matrix is $\mathbf{Q} = v\mathbf{I}$, so the noise is uncorrelated from sensor to sensor and therefore spatially white. That is, isotropic noise results in a spatially white array covariance matrix when the sensors are spaced every half wavelength.

While arrays are often built for a particular design frequency, $f_d = c_w/(2d)$, they are typically operated at a wider range of frequencies. Rewriting (8.226) to be a function of the design frequency of the array rather than the sensor spacing yields

$$\{\mathbf{Q}\}_{i,j} = v \text{sinc}\left(\frac{f_c(i-j)}{f_d}\right) \quad (8.228)$$

which produces the desired $\mathbf{Q} = v\mathbf{I}$ when $f_c = f_d$, but otherwise exhibits correlations in the noise observed across the sensors in the array.

For a general noise covariance matrix \mathbf{Q} , beamforming vector \mathbf{w} , and plane-wave propagation of the signal across the array, the array gain is

$$G_a = \frac{v|\mathbf{w}^H \mathbf{d}|^2}{\mathbf{w}^H \mathbf{Q} \mathbf{w}}. \quad (8.229)$$

In the specific case of a uniformly spaced line array, conventional beamformer with shading weights w_i , isotropic noise, and plane-wave propagation, the directivity index when pointed broadside to the array is approximately

$$\text{DI} \approx 10 \log_{10} \left[\frac{f_c}{f_d} \frac{\left(\sum_{i=1}^m w_i \right)^2}{\sum_{i=1}^m w_i^2} \right]. \quad (8.230)$$

Using rectangular array shading ($w_i = 1$) at the design frequency ($f_c = f_d$) then simplifies this to $\text{DI} = 10 \log_{10} m$, but illustrates a 10-dB-per-decade reduction when operating the array at frequencies below the design.

8.5 Signal-Parameter Estimation Performance

In Sect. 8.2 matched-filter detectors were derived for various assumptions regarding the knowledge about or statistical modeling of the amplitude and phase. However, in all cases it was assumed that the arrival time and Doppler scale were known perfectly. Generalized likelihood ratio (GLR) detectors were described for when these parameters or the background noise variance were unknown in Sect. 8.2.8. In the detection application, the state of nature for which inference is being made is the presence or absence of the signal of interest. However, in many cases one of the signal parameters is also of interest (e.g., the range to an object of interest or its radial velocity). Parameter estimators are generally straightforward to determine; for example, GLR detectors are formed using maximum-likelihood parameter estimates and so are obtained during detection. For the unknown arrival time, it is the time of the peak matched-filter intensity. For an unknown Doppler scale, it is the Doppler associated with the channel in which the peak response occurs in a Doppler filter bank (e.g., see Sect. 8.7). The focus of this section is on using the statistical characterization of the sampled baseband data to derive the Cramér-Rao Lower Bound (CRLB) on the variance of unbiased estimators of the various signal parameters, but with a focus on arrival time and Doppler scale. The CRLB was briefly described in Sect. 6.3.3; more detailed information and examples can be found in [47, Ch. 3]. CRLBs are useful in performance prediction and system design where they can be used, in a manner similar to the sonar equation, to determine the SNR (or array size or signal bandwidth) required to achieve a desired estimation performance (e.g., see Sect. 2.3.6). In analyzing the estimation of arrival time and Doppler scale, it is important to differentiate the information conveyed by the CRLB, which is a measure of *accuracy*, from the *resolution* provided by a particular waveform. This topic is covered in Sect. 8.5.1 for the standard sonar pulses.

The same statistical model used in deriving the detectors in Sect. 8.2 is used for the CRLB analysis in this section. It includes as parameters the amplitude (A) and phase (ψ) of the deterministic signal component, variance of a Gaussian random signal component (λ_s), signal arrival time (τ) and Doppler scale (η), and the additive noise variance (λ). The model from (8.8) describes the sampled basebanded data using a multivariate complex Gaussian distribution,

$$\mathbf{x} \sim \mathcal{CN}\left(Ae^{j\psi}\mathbf{s}_\theta, \lambda_s\mathbf{s}_\theta\mathbf{s}_\theta^H + \lambda\mathbf{I}\right) \quad (8.231)$$

where here it is assumed that the phase ψ is a deterministic unknown parameter. The elements of the Fisher information matrix (FIM), which is used to form the CRLB, for the multivariate complex Gaussian distribution can be found in [47, App. 15C] or here in Sect. 6.3.3.4. As previously noted, this model can represent the deterministic, Gaussian-fluctuating, and Rician signals in additive, Gaussian-distributed noise.

In general most or all of the parameters in the model will be unknown. This is accounted for in CRLB analysis by forming the FIM over only the unknown parameters. The diagonal elements of the inverse of the FIM are then the CRLB on the variance of unbiased estimators for each of the parameters individually under the assumption that all of the parameters used to form the FIM are unknown. As will be described in Sect. 8.5.3, an uncoupled parameter simplifies the CRLB analysis in that whether it is known or unknown does not affect the CRLB for the other parameters. The various combinations of which parameters are assumed to be unknown, the accompanying assumptions for which parameters are known or uncoupled, and in which section they are considered is summarized in Table 8.6.

Estimation of the signal amplitude, phase, and variance and the noise variance is covered in Sect. 8.5.2, including an example regarding estimation of a sound pressure level (SPL) in decibels. Estimation of arrival time when Doppler scale is known is considered in Sect. 8.5.3 whereas estimation of Doppler scale when arrival time is known is covered in Sect. 8.5.4. In most cases, however, both the arrival time and Doppler scale of the signal measurement are unknown and need to be estimated jointly as described in Sect. 8.5.5. Other resources for derivations of the CRLB for the various signal parameters can be found in [2, Ch. 10], [8, Ch. 6], and [13, Ch. 10]. The derivations in this section are limited to the effect of Doppler arising from a constant radial velocity imparted on the signal measurement. The case of a non-zero acceleration component can be found in [48, 49] for narrowband waveforms.

Table 8.6 Configurations of unknown, known, and uncoupled parameters for the CRLB analyses, in which section they are considered, and the examples provided

Section	Unknown parameters	Known parameters	Uncoupled parameters	Example
8.5.2	$A, \psi, \lambda_s, \lambda$	τ, η	A, ψ	SPL in dB
8.5.3	τ, ψ	η	$A, \lambda + \lambda_s$	LFM, HFM & CW pulses
8.5.4	η, ψ	τ	$A, \lambda + \lambda_s$	Shaded CW pulse
8.5.5	τ, η, ψ	—	$A, \lambda + \lambda_s$	LFM pulse

Legend:

A = deterministic signal amplitude

ψ = deterministic signal phase

λ_s = Gaussian random signal variance

λ = noise variance

τ = signal arrival time

η = signal Doppler scale

Although most derivations exploit narrowband arguments to simplify the CRLB and therefore focus on the bound for estimation of the Doppler frequency shift, the case of broadband waveforms and Doppler-scale estimation (which is presented in Sects. 8.5.4 and 8.5.5) can be found in [50]. It is important to note that the CRLB is known to be a very loose bound at low SNR. It primarily represents what might be considered small or local errors. As SNR decreases, there is an increasing probability of observing a large error, which can be defined as an error greater than the resolution capability of the waveform. Other bounds, as described in [51], can provide a better assessment of performance in these scenarios.

8.5.1 *Waveform Resolution vs. Estimation Accuracy*

At the beginning of Sect. 8.3, the *resolution* of a waveform was defined either by the distance between the 3-dB-down points in the ambiguity function (AF) modulus in a particular dimension or by the Rayleigh resolution, which is the distance from the peak modulus to the first zero [29, Sect. 41–5]. Although other measures can be extracted from the AF [14, Sect. 7.1], the 3-dB-down or Rayleigh-resolution definitions are sufficient for most waveforms. The 3-dB-down width is also called the half-power width and is generally defined by when the squared modulus of the AF equals half of its peak value. As described in [16, Sect. 4.3], waveform *resolution* essentially represents the size of the sonar resolution cell (here in the temporal or Doppler-scale dimensions). This can be taken to mean that the majority of the response of a signal under standard (matched-filter) processing will lie within this extent. In the context of resolving two closely spaced signals, these resolution measures are neither absolute limits on resolution nor guarantees that resolution will occur. Rather, they represent a change-point of sorts where signals with somewhat greater separation are easily resolved with standard processing techniques whereas signals more closely spaced might be resolved through use of an inverse filter, adaptive or parametric signal processing algorithms.

8.5.1.1 **Resolution of the Standard Sonar Pulses**

The standard definitions of resolution in arrival time and Doppler make an assumption that the other quantity is known. For example, that Doppler scale is known when determining the resolution in arrival time. The AF modulus is then evaluated at the origin in the dimension of the known parameter. Thus, the temporal resolution of a waveform can be obtained from either the ACF or the AF. However, the resolution in the Doppler dimension must be obtained from the AF with $\tau = 0$. When both parameters are unknown and must be estimated, it is more reasonable to define resolution using the maximum over the other dimension. For example, this would trace out the peak along the ridge seen in the LFM AF shown in Figs. 8.13 and 8.14.

For a CW pulse, the modulus of the ACF from (8.160) is a triangle function with width $2T_p$. Thus the Rayleigh resolution is simply $\tau_{\text{Ray}} = T_p$ and the 3-dB-down width is $\tau_{3\text{dB}} = 2T_p(1 - 1/\sqrt{2}) \approx 0.6T_p$. This reinforces the need for short CW pulses if arrival-time estimation is important. The disadvantage of this is that any reduction in duration must be matched with an increase in the peak amplitude of the pulse in order to keep a constant total energy in the transmitted pulse (recalling that performance in noise-limited scenarios depends on the total transmitted energy in the pulse). In the Doppler dimension, the CW-pulse AF from (8.163) is proportional to $\text{sinc}(\delta T_p)$ when $\tau = 0$ so its Rayleigh resolution in the Doppler-frequency-shift (δ) dimension is $\delta_{\text{Ray}} = 1/T_p$. Noting that $\text{sinc}(0.443) \approx \sqrt{0.5}$, the 3-dB-down resolution is $\delta_{3\text{dB}} = 0.886/T_p$.

For an LFM waveform with a high duration-bandwidth product, the modulus of the ACF from (8.169) is approximately that of a sinc function, so $\tau_{3\text{dB}} \approx 0.886/W$. Using the exact LFM ACF from (8.168), the Rayleigh resolution can be obtained by the time at which the argument of the sinc function is one, resulting in

$$\tau_{\text{Ray}} = \frac{T_p}{2} \left[1 - \sqrt{1 - \frac{4}{T_p W}} \right] \quad (8.232)$$

$$\approx \frac{1}{W} + \frac{1}{T_p W^2} \approx \frac{1}{W} \quad (8.233)$$

where the approximations require either a high duration-bandwidth product or at least a high bandwidth. This identifies the advantage of LFM pulses over CW pulses: the temporal resolution can be improved by increasing the pulse bandwidth while keeping the pulse duration constant. From the narrowband AF for the LFM pulse in (8.173), the same $\text{sinc}(\delta T_p)$ dependence as for the CW pulse is seen. However, the form of the wideband AF shown in Sect. 8.3.5.3 prohibits simple evaluation of the Doppler resolution for wideband pulses. An approximate result obtained through numerical evaluation of the wideband AF followed by functional approximation results in

$$\delta_{3\text{dB}} \approx \frac{0.886}{T_p} \exp\{-2.5\zeta/(\zeta + 5)\}, \quad (8.234)$$

where $\zeta = W/f_c$ is the ratio of the LFM pulse bandwidth to its center frequency. This illustrates how the Doppler resolution of the LFM improves as ζ increases. In the Doppler dimension, the wideband AF does not necessarily have a null descending all the way to zero (especially when ζ is large), so the Rayleigh resolution is a less useful measure.

Table 8.7 Resolution of the standard sonar pulses in time and Doppler frequency shift based on the width of the ambiguity function in each dimension. These results inherently assume the other quantity is known

Pulse	Time (s)	Doppler frequency shift (Hz)
CW	$\tau_{\text{Ray}} = T_p$	$\delta_{\text{Ray}} = 1/T_p$
	$\tau_{3\text{ dB}} \approx 0.6T_p$	$\delta_{3\text{ dB}} \approx 0.886/T_p$
LFM	$\tau_{\text{Ray}} \approx 1/W$	—
	$\tau_{3\text{ dB}} \approx 0.886/W$	$\delta_{3\text{ dB}} \approx \frac{0.886}{T_p} \exp\{-2.5\zeta/(\zeta + 5)\}$
HFM	$\tau_{3\text{ dB}} \approx \gamma(\zeta) 0.886/W$ where $\gamma(\zeta) = \exp\{0.11\zeta^{1.59}/(2 - \zeta)^{0.81}\}$	$\delta_{3\text{ dB}} \approx \gamma(\zeta) \frac{0.886}{T_p} \exp\{-2.5\zeta/(\zeta + 5)\}$

Legend:

T_p = pulse duration

W = pulse bandwidth

f_c = pulse center frequency

$\zeta = W/f_c$ is the ratio of pulse bandwidth to center frequency

Recall from Fig. 8.16 how the ACF of the HFM pulse widened when ζ was increased. Clearly when ζ is small enough the HFM pulse will have the same temporal resolution as that of the LFM pulse. As ζ increases, however, the resolution of the HFM pulse degrades relative to an LFM pulse with the same duration and bandwidth. Because the HFM ACF does not necessarily decay to zero in a rapid manner (e.g., see any of the HFM ACFs in Fig. 8.16), only the 3-dB-down resolution is relevant. The ratio between the HFM 3-dB-down temporal resolution and the LFM 3-dB-down temporal resolution is approximately

$$\frac{\tau_{\text{HFM},3\text{ dB}}}{\tau_{\text{LFM},3\text{ dB}}} \approx \exp\left\{ \frac{0.11\zeta^{1.59}}{(2 - \zeta)^{0.81}} \right\} = \gamma(\zeta). \quad (8.235)$$

Although this starts out as a very small increase (2.7% when $\zeta = 0.5$), it is appreciable when $\zeta = 1$ (11.6% increase) and significant when $\zeta = 1.5$ (44% increase). However, it is still on the order of the LFM-pulse resolution (i.e., within a factor of 10) until $\zeta > 1.9$. Interestingly, the same proportionality is observed in the Doppler dimension.

The resolution of the basic sonar pulses in the time and Doppler-frequency-shift dimensions is summarized in Table 8.7. These results illustrate that the temporal resolution of each pulse type is inversely proportional to the waveform bandwidth (note that the CW bandwidth is approximately $1/T_p$) whereas the resolution in Doppler-frequency-shift is inversely proportional to pulse duration. Because neither of the resolution measures precisely or specifically defines the waveform's resolution capability, which is itself a vaguely defined concept, it is common and accepted to define the temporal resolution of a waveform as one over the bandwidth and the Doppler-frequency-shift resolution as one over the duration. However, care should be used when bandwidth is an appreciable fraction of the center frequency.

It is important to remember that these measures of resolution assume the quantity in the other dimension is known and so they do not account for the coupling between the two dimensions exhibited by the LFM and HFM waveforms. The case where neither parameter is known was considered in [52] by approximating the AF for high time-bandwidth product LFM waveforms. The distance between the 3-dB-down points of the AF along the ridge, as projected onto the Doppler-frequency-shift dimension is approximately

$$\delta_{3\text{dB}} \approx \min \left\{ 0.6W, \frac{3.48f_c}{T_p W} \right\} \quad (8.236)$$

where the narrowband result of $\delta_{3\text{dB}} \approx 0.6W$, obtained from the triangular shaped fall-off of the AF modulus along the ridge from (8.173), has been used to limit the result from [52] when W and T_p are not large enough to satisfy the high time-bandwidth product requirement. The combined result in (8.236) is reasonably accurate, with some error at the transition between the two models. The 3-dB-down point in the temporal dimension can be obtained by using (8.236) in the equation defining the ridge. From the narrowband LFM AF in (8.173), the ridge is defined along $\delta = \beta\tau = (W/T_p)\tau$ yielding

$$\tau = \frac{T_p}{W} \delta = \frac{T_p f_c}{W} (\eta - 1) \quad (8.237)$$

recalling that $\delta = f_c(\eta - 1)$. When the 3-dB-down point of the AF is on the main part of the ridge, which occurs both in the narrowband case (small W/f_c) and in the large duration-bandwidth product case (large $T_p W$), (8.237) can be used to obtain $\tau_{3\text{dB}}$. However, outside of these cases (8.237) cannot be used because the 3-dB-down point lies on the ridge after it has deformed from a single dominant peak. This can be seen in the widening of the ridge in the wideband AF in Fig. 8.14 away from the origin or in the AF slices for the LFM pulse in Fig. 8.15.

8.5.1.2 Accuracy vs. Resolution

In contrast to the *resolution* capabilities of a waveform, which describe when two closely spaced signals might be resolvable, the *accuracy* with which the arrival time or Doppler can be estimated is defined by the bias and variance of their estimators (e.g., see the estimation metrics described in Sect. 6.3.2). Because evaluating the variance of a specific estimator can be difficult, it is common to exploit the Cramér-Rao lower bound (CRLB) on the variance of unbiased estimators. As will be seen in Sect. 8.5.3, the CRLB for arrival-time estimation is inversely proportional to both SNR and a measure of the variation of the frequency content of the pulse. The latter depends on the waveform ACF and is greater when it falls off more sharply from its peak at zero time offset, which equates to a broader band signal for many pulse

types. It can therefore be said that the accuracy with which the arrival time can be estimated improves with both the waveform resolution (or bandwidth) and SNR. To illustrate this, consider the CRLB for the arrival-time estimator $\hat{\tau}$ when using an LFM pulse,

$$\text{Var}\{\hat{\tau}\} \geq \text{CRLB}(\tau) = \frac{3}{2\pi^2 S^d W^2} \quad (8.238)$$

which is derived in Sect. 8.5.3.1 and has units of s^2 . In order to relate this to the resolution of the LFM pulse ($\tau_{\text{Ray}} = 1/W$), the square root of the CRLB is used to describe a lower bound on the standard deviation of the estimator,

$$\text{Std}\{\hat{\tau}\} \geq \frac{\sqrt{1.5}}{W\pi\sqrt{S^d}} \approx \frac{\tau_{\text{Ray}}}{2.56\sqrt{S^d}}. \quad (8.239)$$

This implies that the estimation accuracy can be significantly better than the resolution. For example, the lower bound on the standard deviation is 26 times smaller than the Rayleigh resolution for a 20-dB SNR. With a 100-Hz bandwidth, this results in a 0.4-ms standard deviation. If the estimator achieves the CRLB (i.e., it is an efficient estimator) and has Gaussian-distributed errors, the estimate will be within 2.6 standard deviations (i.e., ± 1 ms) 99% of the time, which is five times smaller than the 10-ms Rayleigh resolution.

8.5.2 Performance Bounds for Estimating Signal Strength and Phase

With respect to estimating the phase of the deterministic signal, ψ is assumed to be deterministic and unknown. The maximum-likelihood estimators (MLEs) for the parameters of the deterministic-signal model can be obtained by maximizing the likelihood function over ψ , A , and λ to yield

$$\begin{aligned} \hat{A} &= |\mathbf{s}_\theta^H \mathbf{x}| \\ \hat{\psi} &= \angle \mathbf{s}_\theta^H \mathbf{x} \\ \hat{\lambda} &= \frac{1}{n-1} \mathbf{x}^H (\mathbf{I} - \mathbf{s}_\theta \mathbf{s}_\theta^H) \mathbf{x}. \end{aligned} \quad (8.240)$$

The estimates of the amplitude and phase are obtained directly from the complex matched filter output $\mathbf{s}_\theta^H \mathbf{x}$ whereas the estimate of the noise variance utilizes basebanded data before matched filtering.

Under the Gaussian-fluctuating-signal model, the MLEs are obtained by jointly maximizing the likelihood function over λ_s and λ to result in

$$\begin{aligned}\hat{\lambda} &= \frac{1}{n} \mathbf{x}^H (\mathbf{I} - \mathbf{s}_\theta \mathbf{s}_\theta^H) \mathbf{x} \\ \hat{\lambda}_s &= |\mathbf{s}_\theta^H \mathbf{x}|^2 - \hat{\lambda}.\end{aligned}\quad (8.241)$$

The estimate of the noise variance is similar to that for the deterministic signal model, but divides by n rather than $n - 1$, which produces a biased estimate. However, that noise estimate is then used to estimate the random-signal variance.

Estimation of the parameters of the Rician signal model is complicated by the difficulty in distinguishing between the random-signal variance and the noise variance in the presence of a deterministic-signal component. This can be seen by using the formulation of the CRLB for a complex multivariate Gaussian model from Sect. 6.3.3.4 or [47, Ch. 3 & App. 15C] to obtain the Fisher information matrix for the parameter vector $\boldsymbol{\theta} = [A \ \psi \ \lambda_s \ \lambda]^T$,

$$\text{FIM}(\boldsymbol{\theta}) = \begin{bmatrix} \frac{2}{\lambda + \lambda_s} & 0 & 0 & 0 \\ 0 & \frac{2A^2}{\lambda + \lambda_s} & 0 & 0 \\ 0 & 0 & \frac{1}{(\lambda + \lambda_s)^2} & \frac{1}{(\lambda + \lambda_s)^2} \\ 0 & 0 & \frac{1}{(\lambda + \lambda_s)^2} & \frac{1}{(\lambda + \lambda_s)^2} + \frac{n-1}{\lambda^2} \end{bmatrix}. \quad (8.242)$$

The zero-value entries imply there is no coupling between the deterministic-signal amplitude and phase and that they are uncoupled from the random signal or noise power. However, as anticipated, the random-signal power and the noise power are coupled. Inverting the FIM results in

$$\text{FIM}^{-1}(\boldsymbol{\theta}) = \begin{bmatrix} \frac{\lambda + \lambda_s}{2} & 0 & 0 & 0 \\ 0 & \frac{\lambda + \lambda_s}{2A^2} & 0 & 0 \\ 0 & 0 & \frac{(\lambda + \lambda_s)^2 + \frac{\lambda^2}{n-1}}{n-1} & -\frac{\lambda^2}{n-1} \\ 0 & 0 & -\frac{\lambda^2}{n-1} & \frac{\lambda^2}{n-1} \end{bmatrix}, \quad (8.243)$$

which provides on its diagonal the CRLB for joint parameter estimation (i.e., all the parameters are unknown) of the parameters in the Rician signal model. Results for the other models can be obtained by removing from the FIM in (8.242) the row and column associated with the parameter known to be zero. For example, the Gaussian-

fluctuating signal model is formed from the two-by-two matrix in the lower-right quadrant of (8.242). Because of the decoupling the inverse of this two-by-two FIM is precisely the matrix in the lower-right quadrant of (8.243). The CRLB for unbiased estimators of the random-signal variance in the Gaussian-fluctuating signal model is then

$$\begin{aligned}\text{Var}\left\{\hat{\lambda}_s\right\} &\geq (\lambda + \lambda_s)^2 + \frac{\lambda^2}{n-1} \\ &= \lambda_s^2 \left(1 + \frac{1}{S^d}\right)^2 + \frac{\lambda^2}{n-1}.\end{aligned}\quad (8.244)$$

This indicates that even if the SNR after the coherent portion of detection processing ($S^d = \lambda_s/\lambda$) and the time-bandwidth product ($n = T_p W$) are large, the CRLB is proportional to the parameter itself squared (i.e., the lower bound on the standard deviation is proportional to the parameter). This implies that multiple independent observations, which cause the CRLB to go down by a factor equal to their number (see Sect. 6.3.3), are the primary means for improving the estimate. The example in Sect. 6.3.3.2 describing estimation of SNR for the Gaussian-fluctuating signal model examines this in more detail, including the benefit of estimating it in decibels.

For the deterministic-signal model, the FIM for the amplitude, phase, and noise variance can be obtained from (8.242) by removing the third row and third column and setting $\lambda_s = 0$, which results in a three-by-three diagonal matrix. The CRLB on the variance of unbiased estimators of the parameters is then easily obtained by inverting the diagonal elements,

$$\text{Var}\left\{\hat{A}\right\} \geq \text{CRLB}(A) = \frac{\lambda}{2} = \frac{A^2}{2S^d} \quad (8.245)$$

$$\text{Var}\left\{\hat{\psi}\right\} \geq \text{CRLB}(\psi) = \frac{1}{2S^d} \quad (8.246)$$

$$\text{Var}\left\{\hat{\lambda}\right\} \geq \text{CRLB}(\lambda) = \frac{\lambda^2}{n}. \quad (8.247)$$

In contrast to the Gaussian-fluctuating signal, increasing SNR for the deterministic signal ($S^d = A^2/\lambda$) directly improves estimation performance for the amplitude and phase. For all the signal models, the time-bandwidth product ($n = W T_p$) drives estimation performance for the noise variance.

It is more common to estimate the decibel level of a sound pressure relative to $1\mu\text{Pa}^2$ than the amplitude,

$$\hat{P} = 10 \log_{10} \left(\frac{\hat{A}^2}{1\mu\text{Pa}^2} \right) \quad (8.248)$$

The CRLB on this estimate can be easily obtained from that for the estimate of the amplitude using the results of Sect. 6.3.3.2, which indicate that

$$\begin{aligned}\text{CRLB}(P) &= \left[\frac{\partial P}{\partial A} \right]^2 \text{CRLB}(A) \\ &= \frac{2[10 \log_{10}(e)]^2}{S^d} \approx \frac{37.7}{S^d}\end{aligned}\quad (8.249)$$

in units of squared decibels. If M independent measurements are averaged to improve the estimate of P and it is assumed that the estimator achieves the CRLB, its standard deviation is

$$\text{Std}(\hat{P}) = \frac{6.14}{\sqrt{MS^d}} \quad (8.250)$$

in units of decibels. By the central limit theorem, the estimator can be assumed to be Gaussian distributed as long as M is large enough. If it is further assumed that the estimator is unbiased, this implies that a confidence interval with a coverage probability of $1 - \alpha$ is

$$\hat{P} \mp z_{\alpha/2} \frac{6.14}{\sqrt{MS^d}} \quad (8.251)$$

where $z_{\alpha/2}$ is the $\alpha/2$ quantile of the standard normal distribution (i.e., $\Phi(z_{\alpha/2}) = \alpha/2$). This information can now be used to identify how many samples at a given SNR are required to achieve a desired confidence-interval extent. Keeping the confidence interval less than \mathcal{L} [units: dB] requires

$$10 \log_{10}(MS^d) \geq 21.8 + 10 \log_{10}(z_{\alpha/2}^2) - 20 \log_{10} \mathcal{L}. \quad (8.252)$$

As an example, suppose it is desired for the confidence interval to be no larger than one decibel with 95% coverage, which requires $z_{0.025} = -1.96$. The constraint on the combined SNR and number of observations is then

$$10 \log_{10}(MS^d) \geq 27.7 \text{ dB}, \quad (8.253)$$

which can come from one measurement with an SNR of 27.7 dB or ten measurements with an SNR of 17.7 dB. Although one might expect the Gaussian assumption on the errors to be invalid when M is small, this is not an issue unless the SNR is also very low. The probability distribution function (PDF) of the estimator is essentially that of the logarithm of a non-central chi-squared distribution, which becomes increasingly Gaussian as the non-centrality parameter increases. As such, the “sampling” requirements dictated by (8.252) are accurate even for $M = 1$ as long as the SNR is above about five decibels. What changes at low SNR (e.g.,

below 15 dB) when $M = 1$ is the symmetry of the distribution about its mean. The PDF of the estimate is skewed whereas that of the Gaussian assumption is not, which implies the confidence interval in (8.251) should not be symmetric about the estimate.

8.5.3 Performance Bounds for Estimating Arrival Time

In order to derive CRLBs for estimating arrival time and Doppler scale, the effect of the parameters needs to be introduced into the statistical characterization of the basebanded data. The parameters enter through the sampled signal vector \mathbf{s}_θ , which can be seen from (8.231) to affect both the mean and covariance matrix of the data under the Rician signal model. CRLB analysis for multiple unknown parameters entails obtaining all the terms of the Fisher information matrix (FIM), inverting the matrix, and taking the diagonal terms as a lower bound on the estimator variance of each parameter. When one parameter is uncoupled from the others, the cross terms in the FIM are zero and estimation of the other parameters is not impacted by estimation of the uncoupled parameter. For example, in the CRLB analysis of Sect. 8.5.2, the signal amplitude and phase parameters were uncoupled from the others. When a parameter is uncoupled, CRLB analysis can be simplified to focus solely on the coupled parameters (i.e., forming and inverting only the portion of the FIM containing the coupled parameters).

Under the assumption of Gaussian-distributed data, parameters solely entering the mean are uncoupled from parameters solely entering the covariance (this can easily be seen by the form of (6.75) in Sect. 6.3.3.4). In order to simplify the analysis presented here, it will be assumed that the signal is deterministic so $\lambda_s = 0$. This implies τ and η only enter the mean and are therefore uncoupled from the noise power λ , but remain coupled with the deterministic signal amplitude and phase. Except where it has been noted otherwise, the amplitude shading of the pulse is assumed to be rectangular. In this section the bound for estimating the arrival time is derived under the assumption that the Doppler scale is known, as might occur when all participants in the remote sensing system are stationary.

As was done in Sect. 8.5.2, CRLB analysis starts with the statistical model of the measured data. Recall from (8.8) or (8.231) that the sampled basebanded data, assuming $\lambda_s = 0$ and that the phase ψ is deterministic, are complex-Gaussian distributed,

$$\mathbf{x}|\psi \sim \mathcal{CN}(\mathbf{u}_\Theta, \lambda \mathbf{I}), \quad (8.254)$$

with covariance matrix $\lambda \mathbf{I}$ and a mean vector $\mathbf{u}_\Theta = Ae^{j\psi}\mathbf{s}_\tau$ where \mathbf{s}_τ represents the sampled and normalized complex envelope of the signal incorporating a delay τ and $\Theta = [\tau \ \psi \ A]^T$ because the Doppler scale η is assumed to be known. Note that \mathbf{s}_τ differs from \mathbf{s}_θ in (8.8) in that it is subject to an offset in arrival time of τ and can be assumed to have $\eta = 1$ without loss of generality. The continuous-time basebanded

signal measurement $\tilde{u}_{\Theta}(t)$ producing \mathbf{u}_{Θ} can be described by the complex envelope of the signal form and by demodulating the analytic signal,

$$\begin{aligned}\tilde{u}_{\Theta}(t) &= Ae^{j\psi}\tilde{s}(t - \tau) \\ &= Ae^{j\psi}\dot{\tilde{s}}(t - \tau)e^{-j2\pi f_c(t-\tau)}.\end{aligned}\quad (8.255)$$

Although it is possible to derive the CRLB for τ directly from the complex envelope $\tilde{s}(t)$, it will be necessary to use the analytic signal when Doppler scale is included. Because of this, derivation of the CRLB for arrival time will be done using the analytic signal.

In the following CRLB analysis τ , ψ , and A are the unknown parameters and the objective is to estimate τ . This will be done by inverting the Fisher information matrix (FIM), which is described for complex, multivariate Gaussian data in [47, App. 15C] and can be found here in (6.75) from Sect. 6.3.3.4. Simplifying the FIM entry for parameters θ_i and θ_j in the case of a parameter only entering the mean results in

$$\begin{aligned}\text{FIM}_{\theta_i, \theta_j} &= 2 \text{Real} \left\{ \left(\frac{\partial \mathbf{u}_{\Theta}}{\partial \theta_i} \right)^H [\lambda \mathbf{I}]^{-1} \left(\frac{\partial \mathbf{u}_{\Theta}}{\partial \theta_j} \right) \right\} \\ &= \frac{2}{\lambda} \text{Real} \left\{ \left(\frac{\partial \mathbf{u}_{\Theta}}{\partial \theta_i} \right)^H \left(\frac{\partial \mathbf{u}_{\Theta}}{\partial \theta_j} \right) \right\} \\ &\approx \frac{2W}{\lambda} \text{Real} \left\{ \int_{-\infty}^{\infty} \frac{\partial \tilde{u}_{\Theta}^*(t)}{\partial \theta_i} \frac{\partial \tilde{u}_{\Theta}(t)}{\partial \theta_j} dt \right\}.\end{aligned}\quad (8.256)$$

The approximation in (8.256) arises from representing the vector inner product by an integral, which also introduces the factor of W to account for the sample spacing (i.e., $dt \approx 1/W$). The derivatives of $\tilde{u}_{\Theta}(t)$ with respect to τ , ψ , and A are evaluated at their true values, represented by the vector Θ_0 . In this scenario the true value of τ is zero indicating perfect alignment with the arrival time. The amplitude is left as A and without a loss of generality ψ can be set to zero. The derivatives are then obtained from (8.255) and described as a function of the analytic signal as follows:

$$\begin{aligned}\left. \frac{\partial}{\partial \tau} \tilde{u}_{\Theta}(t) \right|_{\Theta_0} &= -A\dot{\tilde{s}}'(t)e^{-j2\pi f_c t} + j2\pi f_c A\dot{\tilde{s}}(t)e^{-j2\pi f_c t} \\ &= -A[\dot{\tilde{s}}'(t) - j2\pi f_c \dot{\tilde{s}}(t)]e^{-j2\pi f_c t}\end{aligned}\quad (8.257)$$

$$\left. \frac{\partial}{\partial \psi} \tilde{u}_{\Theta}(t) \right|_{\Theta_0} = jA\dot{\tilde{s}}(t)e^{-j2\pi f_c t}\quad (8.258)$$

$$\left. \frac{\partial}{\partial A} \tilde{u}_{\Theta}(t) \right|_{\Theta_0} = \dot{\tilde{s}}(t)e^{-j2\pi f_c t}.\quad (8.259)$$

Before evaluating the FIM, the properties of the Fourier transform can be used to simplify some of the integrals that will be encountered involving $\dot{s}'(t)$. First, if $\dot{S}(f)$ is the Fourier transform of $\dot{s}(t)$, then the Fourier transform of $\dot{s}'(t)$ is $\mathcal{F}\{\dot{s}'(t)\} = j2\pi f \dot{S}(f)$. Another useful Fourier transform property is Parseval's theorem as stated for two different signals,

$$\int_{-\infty}^{\infty} a(t)b^*(t) dt = \int_{-\infty}^{\infty} A(f)B^*(f) df. \quad (8.260)$$

Now, the $\text{FIM}_{\tau,A}$ term requires the integral

$$\int_{-\infty}^{\infty} \dot{s}'(t)\dot{s}^*(t) dt = \int_{-\infty}^{\infty} j2\pi f |\dot{S}(f)|^2 df = \frac{j2\pi \bar{f}}{W} \quad (8.261)$$

where \bar{f} is defined as the average frequency of the signal based on a spectral weighting,

$$\bar{f} = \frac{\int_{-\infty}^{\infty} f |\dot{S}(f)|^2 df}{\int_{-\infty}^{\infty} |\dot{S}(f)|^2 df}, \quad (8.262)$$

and the fact that

$$\int_{-\infty}^{\infty} |\dot{S}(f)|^2 df = \int_{-\infty}^{\infty} |\dot{s}(t)|^2 dt = \int_{-\infty}^{\infty} |\tilde{s}(t)|^2 dt \approx W^{-1} \quad (8.263)$$

has been exploited. Noting that (8.261) is purely imaginary means that $\text{FIM}_{\tau,A}$ and $\text{FIM}_{\psi,A}$ are zero because (8.256) only takes the real part. This implies that A is uncoupled from both τ and ψ and can therefore be eliminated from the remaining CRLB analysis. It is important to note that this assumes the conditions in the Fourier transforms used to simplify (8.261) hold.

Using (8.261) and (8.263), the $\text{FIM}_{\tau,\psi}$ term is seen to be

$$\begin{aligned} \text{FIM}_{\psi,\tau} &= \frac{2A^2}{\lambda} \text{Real} \left\{ j \int_{-\infty}^{\infty} \dot{s}'(t)\dot{s}^*(t) dt + 2\pi f_c \int_{-\infty}^{\infty} |\dot{s}(t)|^2 dt \right\} \\ &= -\frac{4\pi(\bar{f} - f_c)A^2}{\lambda} = -4\pi \tilde{f} S^d \end{aligned} \quad (8.264)$$

where $S^d = A^2/\lambda$ is the SNR after the coherent portion of detection and $\tilde{f} = \bar{f} - f_c$ is the center frequency of the complex envelope. This implies a coupling between

arrival time and phase with the implication that estimation of the signal phase will suffer when the arrival time is unknown.

The integral required in the $\text{FIM}_{\tau,\tau}$ term can be simplified by exploiting the aforementioned Fourier transform properties to produce

$$\int_{-\infty}^{\infty} |\dot{s}'(t)|^2 dt = 4\pi^2 \int_{-\infty}^{\infty} f^2 |\dot{S}(f)|^2 df = \frac{4\pi^2}{W} (\sigma_f^2 + \bar{f}^2), \quad (8.265)$$

where σ_f^2 is the spectrally weighted frequency variance of the signal,

$$\sigma_f^2 = \frac{\int_{-\infty}^{\infty} (f - \bar{f})^2 |\dot{S}(f)|^2 df}{\int_{-\infty}^{\infty} |\dot{S}(f)|^2 df}. \quad (8.266)$$

The $\text{FIM}_{\tau,\tau}$ term can then be formed using (8.265) and (8.261),

$$\begin{aligned} \text{FIM}_{\tau,\tau} &= \frac{2WA^2}{\lambda} \int_{-\infty}^{\infty} |\dot{s}'(t) - j2\pi f_c \dot{s}(t)|^2 dt \\ &= \frac{2WA^2}{\lambda} \int_{-\infty}^{\infty} \left[|\dot{s}'(t)|^2 + j2\pi f_c \dot{s}'(t) \dot{s}^*(t) - j2\pi f_c [\dot{s}'(t)]^* \dot{s}(t) + 4\pi^2 f_c^2 |\dot{s}(t)|^2 \right] dt \\ &= 8\pi^2 S^d (\sigma_f^2 + \bar{f}^2 - 2\bar{f} f_c + f_c^2) \\ &= 8\pi^2 S^d (\sigma_f^2 + \bar{f}^2). \end{aligned} \quad (8.267)$$

The final term required to form the FIM is

$$\text{FIM}_{\psi,\psi} = \frac{2W}{\lambda} \int_{-\infty}^{\infty} A^2 |\dot{s}(t)|^2 dt = 2S^d, \quad (8.268)$$

which is readily obtained from (8.263).

Combining the elements of the FIM for τ and ψ results in the two-by-two matrix

$$\text{FIM}(\tau, \psi) = 2S^d \begin{bmatrix} 4\pi^2(\sigma_f^2 + \bar{f}^2) & -2\pi \bar{f} \\ -2\pi \bar{f} & 1 \end{bmatrix} \quad (8.269)$$

which can easily be inverted to obtain the CRLB for τ from the first diagonal entry as

$$\text{CRLB}(\tau) = \frac{1}{8\pi^2 S^d \sigma_f^2}. \quad (8.270)$$

Although the CRLB has been derived here using the analytic signal, it can also be formulated using the complex envelope. This is especially straightforward when simply recasting \tilde{f} and σ_f^2 to depend on $\tilde{S}(f) = \dot{\tilde{S}}(f + f_c)$ instead of $\dot{S}(f)$ in (8.262) and (8.266). As previously noted, the average frequency in the complex envelope becomes $\bar{f} = \tilde{f} - f_c$. The frequency variation in the complex envelope,

$$\sigma_f^2 = \frac{\int_{-\infty}^{\infty} (f - \bar{f})^2 |\tilde{S}(f)|^2 df}{\int_{-\infty}^{\infty} |\tilde{S}(f)|^2 df}, \quad (8.271)$$

is invariant to a frequency translation and so produces the same result under both definitions. Using $f_c = \bar{f}$ to demodulate the bandpass signal centers the complex envelope spectrum so $\bar{f} = 0$, which further simplifies (8.271).

It is also possible to relate \bar{f} and σ_f^2 to the complex wideband ambiguity function. Recalling from (8.142) that the AF can be described according to

$$\chi(\tau, \eta) = \sqrt{\eta} \int_{-\infty}^{\infty} \dot{s}(t) \dot{s}^*(\eta[t - \tau]) dt = \sqrt{\eta} \int_{-\infty}^{\infty} \dot{s}(t + \tau) \dot{s}^*(\eta t) dt \quad (8.272)$$

it can be seen that

$$\bar{f} = \frac{W}{j2\pi} \int_{-\infty}^{\infty} \dot{s}'(t) \dot{s}^*(t) dt = \frac{\frac{\partial}{\partial \tau} \chi(\tau, 1) \Big|_{\tau=0}}{j2\pi \chi(0, 1)} \quad (8.273)$$

The frequency variance can similarly be described through the AF,

$$\begin{aligned} \sigma_f^2 &= \frac{W}{4\pi^2} \int_{-\infty}^{\infty} |\dot{s}'(t)|^2 dt - \bar{f}^2 \\ &= \frac{-\frac{\partial^2}{\partial \tau^2} \chi(\tau, 1) \Big|_{\tau=0}}{4\pi^2 \chi(0, 1)} - \bar{f}^2. \end{aligned} \quad (8.274)$$

Note that these both require the AF to be differentiable at $\tau = 0$, a condition violated by both the CW- and LFM-pulse AFs.

8.5.3.1 Frequency-Modulated Pulses

Recall that frequency-modulated pulses (including CW, LFM, and HFM pulses) can be described by an amplitude function $a(t)$ subject to a time-varying phase, $\phi(t)$

$$\dot{s}(t) = a(t)e^{j\phi(t)}. \quad (8.275)$$

Pulses with this form, assuming $a(t)$ varies slowly enough, have a CRLB that can be simply described using the instantaneous frequency of the pulse,

$$f(t) = \frac{\phi'(t)}{2\pi}. \quad (8.276)$$

To see this, note that the derivative of the analytic signal in (8.275) is

$$\dot{s}'(t) = a'(t)e^{j\phi(t)} + j\phi'(t)\dot{s}(t), \quad (8.277)$$

which has a term related to the amplitude derivative and a term related to the phase derivative. When the pulse amplitude varies slowly enough, which is often the case for active sonar pulses, the analytic-signal derivative can be approximated solely by the phase-derivative component,

$$\dot{s}'(t) \approx j\phi'(t)\dot{s}(t) = j2\pi f(t)\dot{s}(t). \quad (8.278)$$

For a constant-envelope pulse (i.e., a rectangular weighting), the amplitude of $\dot{s}(t)$ must be $a(t) = 1/\sqrt{T_p W}$ for $t \in [0, T_p]$ to satisfy $\int_0^{\infty} |\dot{s}(t)|^2 dt = 1/W$. This then allows describing \bar{f} as the average of the instantaneous frequency,

$$\bar{f} = \frac{W}{j2\pi} \int_{-\infty}^{\infty} \dot{s}'(t)\dot{s}^*(t) dt = \frac{1}{T_p} \int_0^{T_p} f(t) dt. \quad (8.279)$$

The frequency variation is similarly formed from the instantaneous frequency,

$$\begin{aligned} \sigma_f^2 &= \frac{W}{4\pi^2} \int_{-\infty}^{\infty} |\dot{s}'(t)|^2 dt - \bar{f}^2 \\ &= \frac{1}{T_p} \int_0^{T_p} f^2(t) dt - \bar{f}^2 = \frac{1}{T_p} \int_0^{T_p} [f(t) - \bar{f}]^2 dt. \end{aligned} \quad (8.280)$$

For an LFM waveform over the frequency interval $(f_0, f_0 + W)$ and duration T_p , the instantaneous frequency is $f(t) = f_0 + tW/T_p$, the average frequency is $\bar{f} = f_0 + W/2$ and $\sigma_f^2 = W^2/12$. These combine to produce

$$\text{CRLB}(\tau) = \frac{3}{2\pi^2 S^d W^2} \quad (8.281)$$

which illustrates how SNR and bandwidth drive arrival-time estimation accuracy for the LFM pulse.

For an HFM waveform spanning f_0 to $f_1 = f_0 + W$, the average frequency,

$$\bar{f} = \frac{f_0 f_1}{W} \log\left(\frac{f_1}{f_0}\right), \quad (8.282)$$

is not the center of the band. However, the frequency variation about the average is adequately approximated by that of the LFM,

$$\sigma_f^2 = f_0 f_1 - \bar{f}^2 \approx \frac{W^2}{12} \quad (8.283)$$

unless the bandwidth becomes large relative to the center frequency (the approximation in (8.283) is within 5% when $(W/f_0) \leq 0.85$). Thus, the LFM and HFM waveforms have essentially the same CRLB for estimation of the arrival time, which is inversely proportional to the squared bandwidth, except for very wideband HFM pulses.

It is important to note that pulse duration does not enter the CRLB on arrival-time estimation for the LFM or HFM pulses as long as the pulse duration is longer than the inverse bandwidth. For FM pulses with a duration shorter than the inverse of their design bandwidth, the actual bandwidth of the pulse is effectively the inverse duration. The CRLB in this scenario is likely closer to that of a CW pulse.

Exercise 8.8 Assuming the pulse amplitude $a(t)$ varies slowly enough for (8.278) to hold, show that the average frequency for a shaped pulse is

$$\bar{f} = \frac{\int_0^{T_p} f(t) a^2(t) dt}{\int_0^{T_p} a^2(t) dt} \quad (8.284)$$

and that the frequency variation is

$$\sigma_f^2 = \frac{\int_0^{T_p} [f(t) - \bar{f}]^2 a^2(t) dt}{\int_0^{T_p} a^2(t) dt}. \quad (8.285)$$

8.5.3.2 Continuous-Wave Pulses

Noting that σ_f^2 describes the frequency variation of the signal about the average frequency, it is not surprising that continuous-wave (CW) pulses can pose problems in evaluating the CRLB. Consider a CW pulse with a rectangular weighting and duration T_p , for which the complex envelope is constant over the pulse duration and the squared modulus of its Fourier transform is a squared sinc function,

$$|\tilde{S}(f)|^2 = \text{sinc}^2(T_p f). \quad (8.286)$$

The numerator in (8.271), which requires multiplying (8.286) by f^2 (when $f_c = \tilde{f}$ so $\tilde{f} = 0$), results in an integral over $\sin^2(\pi T_p f)$. Because this will be infinite, $\sigma_f^2 \rightarrow \infty$ and the CRLB is zero, which is not a very useful lower bound on the variance of an estimator. In practice, the CW pulse is typically windowed to limit the transient effects of amplifiers, which themselves are subject to physical limitations in terms of how large of a bandwidth they can transmit. This implies the integral in (8.271) describing σ_f^2 should not span all frequencies. By restricting it to the interval $f \in [-\gamma/T_p, \gamma/T_p]$, it can be shown that

$$\sigma_f^2 \approx \frac{\gamma}{\pi^2 T_p^2}. \quad (8.287)$$

Setting $\gamma = 1$ uses the complete main lobe of $|\tilde{S}(f)|^2$ whereas $\gamma = 0.5$ uses a bandwidth equal to $1/T_p$. Using this in (8.270) produces the CRLB for a band-limited, uniformly weighted CW pulse,

$$\text{CRLB}(\tau) = \frac{T_p^2}{8\gamma S^d}. \quad (8.288)$$

The key points to take from (8.288) are that the CRLB is proportional to the square of the pulse duration and inversely proportional to SNR. This emphasizes that CW pulses are not particularly good for estimating arrival time unless they are very short pulses and SNR is high.

If a pulse has amplitude weighting $w(t)$, then the complex envelope modulus $|\tilde{s}(t)| \propto w(t)$ and

$$\sigma_f^2 = \frac{\int_{-\infty}^{\infty} [w'(t)]^2 dt}{4\pi^2 \int_{-\infty}^{\infty} w^2(t) dt}. \quad (8.289)$$

As an example, a Hann window can be shown to result in

$$\sigma_f^2 = \frac{1}{3T_p^2}, \quad (8.290)$$

which results in a $\text{CRLB}(\tau) \propto T_p^2$ similar to the band-limited rectangularly weighted CW pulse. It can be seen from (8.290) that the effective shortening of the pulse imposed by the Hann window results in a 5 to 8 dB higher σ_f^2 than that for the rectangular window with γ between 0.5 and 1. However, noting that a Hann window results in a signal loss of about 6 dB, the net difference is likely insignificant when the two pulses are designed to have the same total transmit energy.

The CRLB is not the only bound on the variance of an estimator. Estimation of arrival time for a pulse having a constant complex envelope (as does the CW pulse used here) was considered in [53] using a Barankin bound [54] and by Ziv and Zakai in [55]. Without delving into the specifics of each bound, what they have in common is a proportionality to T_p^2 as was observed in the CRLB of the band-limited CW pulse,

$$\text{Bound} \propto \left[\frac{T_p}{S^d} \right]^2, \quad (8.291)$$

but also an inverse dependence on SNR squared. An advantage of alternative bounds such as that of Ziv-Zakai [55] lies in the ability to account for large errors arising when the initial estimation window is large.

8.5.4 Performance Bounds for Estimating Doppler Scale

Similar to the derivation of the CRLB in Sect. 8.5.3 for the arrival time, the CRLB for estimation of the Doppler scale starts by describing the demodulated signal in terms of the analytic signal subject to a Doppler scale η . Assuming the arrival time is known perfectly, this results in

$$\tilde{u}_{\Theta}(t) = A e^{j\psi} \dot{s}(\eta t) e^{-j2\pi f_c t}, \quad (8.292)$$

where $\Theta = [\eta \ \psi \ A]^T$. Note that the time-scale arising from Doppler only affects the analytic signal in (8.292) and not the demodulation. When evaluating the partial derivatives of (8.292) at Θ_0 , it can be assumed without a loss of generality that the true value of η is one. The derivatives with respect to ψ and A are, respectively, the same as those derived in (8.258) and (8.259) for the case of an unknown arrival time. The partial derivative of $\tilde{u}_{\Theta}(t)$ with respect to η is

$$\frac{\partial}{\partial \eta} \tilde{u}_{\Theta}(t) \Big|_{\Theta_0} = A t \dot{s}'(t) e^{-j2\pi f_c t}. \quad (8.293)$$

The integral over $t\dot{s}'(t)\dot{s}^*(t)$, which is required for both the $\text{FIM}_{A,\eta}$ and $\text{FIM}_{\psi,\eta}$ terms, can be described in terms of its real and imaginary parts using the general form of $\dot{s}'(t)$ from (8.277),

$$\int_{-\infty}^{\infty} t\dot{s}'(t)\dot{s}^*(t) dt = \int_{-\infty}^{\infty} ta'(t)a(t) dt + j2\pi \int_{-\infty}^{\infty} tf(t)|\dot{s}(t)|^2 dt. \quad (8.294)$$

Because the $\text{FIM}_{A,\eta}$ term requires the real part of (8.294), assuming $a'(t) \approx 0$ (as was done for the CRLB on τ) leads to $\text{FIM}_{A,\eta} = 0$. Thus the amplitude is uncoupled from the Doppler scale as well as the arrival time when the signal amplitude varies slowly and so can be removed from consideration in the CRLB analysis. However, from the imaginary part of (8.294) it can be seen that the $\text{FIM}_{\psi,\eta}$ term is

$$\begin{aligned} \text{FIM}_{\psi,\eta} &= 2S^d W \operatorname{Real} \left\{ -j \int_{-\infty}^{\infty} t\dot{s}'(t)\dot{s}^*(t) dt \right\} \\ &= 4\pi S^d W \int_{-\infty}^{\infty} tf(t)|\dot{s}(t)|^2 dt = 4\pi S^d \bar{c} \end{aligned} \quad (8.295)$$

where the average of the time/instantaneous-frequency product,

$$\bar{c} = \frac{\int_{-\infty}^{\infty} tf(t)|\dot{s}(t)|^2 dt}{\int_{-\infty}^{\infty} |\dot{s}(t)|^2 dt}, \quad (8.296)$$

represents the time-frequency correlation of a signal as described in [56, Sect. 1.8]. In the context of estimating a time-scale the time/instantaneous-frequency product can be interpreted as representing time normalized by the instantaneous period of the signal,

$$tf(t) = \frac{t}{\text{Period}(t)}. \quad (8.297)$$

Thus, \bar{c} represents the average time of the signal in units of periods or cycles, which is why the variable c is used. It is worth noting that most derivations of the CRLB for estimating Doppler assume the phase after removing the carrier varies slowly (i.e., $f(t) \approx f_c$), which is a narrowband assumption that will be discussed in more detail below. The more general form presented here, which can be found in [50], means the result will be applicable to more waveforms and, in particular, broadband waveforms with Doppler sensitivity.

The $\text{FIM}_{\eta,\eta}$ term can now be simplified by subtracting and adding \bar{c} to “center” the $tf(t)$ time-in-units-of-periods term inside the integral,

$$\begin{aligned}\text{FIM}_{\eta,\eta} &= 2S^d W \int_{-\infty}^{\infty} t^2 |\dot{s}'(t)|^2 dt = 8\pi^2 S^d W \int_{-\infty}^{\infty} [tf(t) - \bar{c} + \bar{c}]^2 |\dot{s}(t)|^2 dt \\ &= 8\pi^2 S^d (\sigma_c^2 + \bar{c}^2).\end{aligned}\quad (8.298)$$

Similar to its frequency-variation counterpart, this results in a term σ_c^2 describing the variation of the time-in-units-of-periods throughout the pulse,

$$\sigma_c^2 = \frac{\int_{-\infty}^{\infty} [tf(t)]^2 |\dot{s}(t)|^2 dt}{\int_{-\infty}^{\infty} |\dot{s}(t)|^2 dt} - \bar{c}^2 = \frac{\int_{-\infty}^{\infty} [tf(t) - \bar{c}]^2 |\dot{s}(t)|^2 dt}{\int_{-\infty}^{\infty} |\dot{s}(t)|^2 dt}.\quad (8.299)$$

Intuitively, one expects a signal traversing a large number of periods or cycles to be better at estimating a time-scale parameter because of the larger number of zero crossings (e.g., this is why increasing the frequency of a CW pulse heightens its sensitivity to Doppler).

The FIM for η and ψ can now be formed as a function of the time-in-units-of-periods average (\bar{c}) and variance (σ_c^2) using (8.295), (8.298), and $\text{FIM}_{\psi,\psi}$ from (8.268), to result in

$$\text{FIM}(\eta, \psi) = 2S^d \begin{bmatrix} 4\pi^2(\sigma_c^2 + \bar{c}^2) & 2\pi\bar{c} \\ 2\pi\bar{c} & 1 \end{bmatrix}.\quad (8.300)$$

This can easily be inverted to obtain the CRLB for the variance of unbiased estimators of η from the first diagonal entry of $\text{FIM}(\eta, \psi)^{-1}$,

$$\text{CRLB}(\eta) = \frac{1}{8\pi^2 S^d \sigma_c^2}.\quad (8.301)$$

Narrowband derivations of the CRLB that assume the phase varies slowly after removal of the carrier essentially assume $f(t) \approx f_c$, which is the same as for CW pulses. This results in $\bar{c} = f_c \bar{t}$ and $\sigma_c^2 = f_c^2 \sigma_t^2$, where \bar{t} and σ_t^2 are the weighted time average and variance of the signal. This results in the lower bound

$$\text{CRLB}(\eta) = \frac{1}{8\pi^2 S^d f_c^2 \sigma_t^2}.\quad (8.302)$$

Similar to the frequency-variation measure of the LFM pulse ($\sigma_f^2 = W^2/12$), which was derived assuming a constant spectrum, a CW pulse with a constant envelope results in

$$\sigma_t^2 = \frac{T_p^2}{12} \quad (8.303)$$

where T_p is the pulse duration. This confirms the expectation that increasing pulse duration (or SNR) improves estimation of the Doppler scale.

Although the CRLB was derived for the Doppler scale, it can be converted to describe estimation of the Doppler frequency shift, $\delta = (\eta - 1)f_c$, by multiplying by $(\partial\delta/\partial\eta)^2 = f_c^2$,

$$\text{CRLB}(\delta) = \frac{1}{8\pi^2 S^d \sigma_t^2} \quad (8.304)$$

with units of Hz^2 , or to radial velocity for a monostatic-active-sonar geometry via $\eta = 1 + 2v_r/c_w$,

$$\text{CRLB}(v_r) = \frac{c_w^2}{32\pi^2 S^d f_c^2 \sigma_t^2}. \quad (8.305)$$

The CRLB can also be described as a lower bound on the standard deviation of an unbiased estimator. For example, the CW pulse with a constant envelope results in

$$\text{Std}\{\hat{v}_r\} \geq \left(\frac{c_w}{2f_c T_p} \right) \frac{\sqrt{1.5}}{\pi \sqrt{S^d}} \approx \frac{v_{r,\text{Ray}}}{2.56 \sqrt{S^d}} \quad (8.306)$$

as a lower bound for estimation of the radial velocity where $v_{r,\text{Ray}} = c_w/(2f_c T_p)$ is the Rayleigh resolution in radial velocity for a stationary monostatic active sonar, which can easily be obtained from the Rayleigh resolution in the Doppler frequency shift $\delta_{\text{Ray}} = 1/T_p$ found in Sect. 8.5.1. The result in (8.306) illustrates that when estimating radial velocity with a CW pulse, SNR provides a similar improvement over the Rayleigh resolution as that seen for estimating arrival time when using the LFM pulse as described in Sect. 8.5.1.2.

8.5.4.1 Shaded CW-Pulse Example

As described in Sect. 8.3.4.2, shading the transmit waveform helps limit the sidelobes in the Doppler dimension at the expense of a widened mainlobe. The impact of the widened mainlobe is a reduction in Doppler estimation performance, which is captured in σ_t^2 . For a CW pulse with amplitude shading $a(t)$, the time-variance of the pulse is

$$\sigma_t^2 = \frac{\int_{-\infty}^{\infty} [t - \bar{t}]^2 a^2(t) dt}{\int_{-\infty}^{\infty} a^2(t) dt}. \quad (8.307)$$

As long as the pulse has symmetric shading, \bar{t} is at the center (i.e., $\bar{t} = T_p/2$ if the pulse occurs during $t \in (0, T_p)$).

As an example, consider Tukey-shading (see Sect. 4.10.2) of a CW pulse. Tukey shading is often used to limit the transient response of sound projectors by shading a small portion at the beginning and end of the pulse, but also produces the Hann window when the window is fully shaded. Evaluating (8.307) with the Tukey window amplitude function from Sect. 4.10.2 results in

$$\sigma_t^2 = \frac{T_p^2}{12\left(1 - \frac{5\alpha}{8}\right)} \left[1 - \frac{15\alpha}{8} + \left(\frac{15}{8} - \frac{6}{\pi^2}\right)\alpha^2 + \left(\frac{51}{16\pi^2} - \frac{5}{8}\right)\alpha^3 \right] \quad (8.308)$$

$$\approx \frac{T_p^2}{12} \left(1 - \frac{15}{2\pi^2}\right)^\alpha \quad (8.309)$$

where α is the total shaded fraction (i.e., $\alpha = 0.1$ implies 5% of each side is shaded). The resulting increase in the CRLB on the standard deviation (e.g., using the square root of (8.305)) relative to that for a rectangular window is shown in Fig. 8.19 for

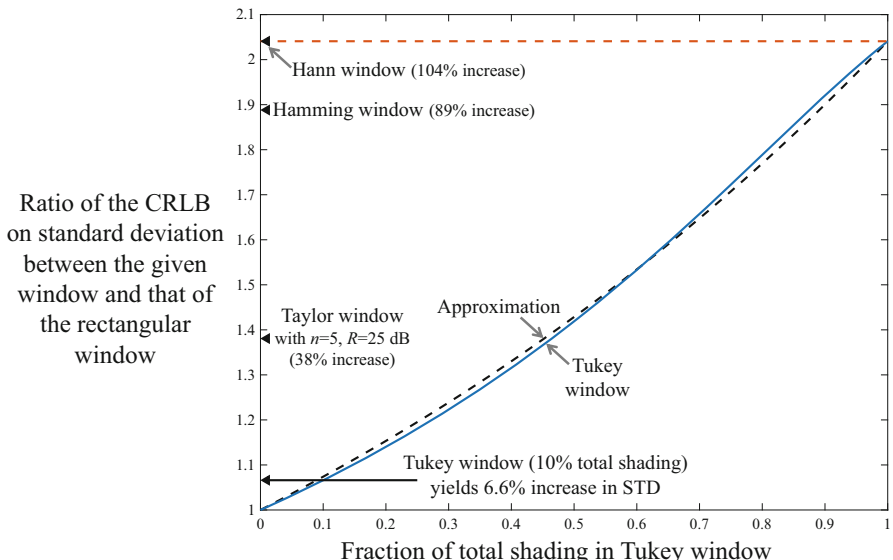


Fig. 8.19 Ratio of the CRLB on the standard deviation for the Tukey window as a function of the total shaded fraction (α) relative to that for a rectangular window

the Tukey window as a function of α as well as for other common windows. The value of 1.38 shown for the Taylor window (with $n = 5$ and $R = 25$ dB) has the implication of a 38% increase in estimation error in the units of the parameter.⁶ When $\alpha = 0$ there is no shading and (8.308) simplifies to the rectangular-window result ($T_p^2/12$). When $\alpha = 1$, the Tukey window is identical to the Hann window, which results in a 24% reduction in σ_t^2 from the rectangular window,

$$\sigma_t^2 = \frac{T_p^2}{12} \left(1 - \frac{15}{2\pi^2}\right) \approx \left(\frac{T_p^2}{12}\right) 0.24. \quad (8.310)$$

Commensurate with the severity with which the Hann window tapers, this produces a 104% increase in the lower bound on the standard deviation. The approximation in (8.309) for the Tukey shading, shown in Fig. 8.19 as the black dashed line, illustrates an exponential progression. Using 10% total shading ($\alpha = 0.1$) results in a 6.6% increase in the CRLB for the standard deviation, which is generally an acceptable trade-off to limit the transient response of the sound projector.

8.5.5 Performance Bounds for Joint Estimation of Arrival Time and Doppler Scale

In most realistic scenarios both the arrival time and Doppler scale of the signal measurement are unknown and need to be estimated. The CRLB for this joint estimation problem can be constructed using the same approach as in previous sections, by expanding the Fisher information matrix to include both arrival time and Doppler scale (so $\Theta = [\tau \ \eta \ \psi \ A]^T$). Fortunately, most of the entries of the FIM are the same as those previously obtained where it was assumed either arrival time or Doppler scale is known. These cases are simply the more general case with $\tau = 0$ (known arrival time) or with $\eta = 1$ (known Doppler scale). Under the slowly-varying-amplitude approximation of (8.278), this implies the amplitude parameter is uncoupled from arrival time, Doppler scale, and phase so it can be eliminated from consideration. The one term in the FIM that remains to be calculated is then that describing the information between τ and η . This requires describing the basebanded signal measurement $\tilde{u}_\Theta(t)$ in terms of the unknown signal parameters. When both arrival time and Doppler are unknown, the basebanded signal is most easily described by subjecting the analytic signal to the Doppler scale, basebanding, and then applying the offset in arrival time,

$$\tilde{u}_\Theta(t) = Ae^{j\psi} \hat{s}(\eta[t - \tau])e^{-j2\pi f_c(t - \tau)}. \quad (8.311)$$

⁶Note that because this is based on the CRLB, the achieved estimation performance will vary unless the estimator is efficient and therefore meets the bound.

This can also be obtained from (7.49) by noting $\tilde{s}(t) = \dot{s}(t)e^{-j2\pi f_c t}$. The derivatives from (8.257) and (8.293) can then be used in (8.256) along with (8.294) to produce the final FIM term

$$\begin{aligned}
 \text{FIM}_{\tau,\eta} &= -2S^d W \operatorname{Real} \left\{ \int_{-\infty}^{\infty} t |\dot{s}'(t)|^2 dt + j2\pi f_c \int_{-\infty}^{\infty} t \dot{s}'(t) \dot{s}^*(t) dt \right\} \\
 &\approx -2S^d W \left[\int_{-\infty}^{\infty} t [\phi'(t)]^2 |\dot{s}(t)|^2 dt - 4\pi^2 f_c \int_{-\infty}^{\infty} t f(t) |\dot{s}(t)|^2 dt \right] \\
 &= -8\pi^2 S^d \left[W \int_{-\infty}^{\infty} t f^2(t) |\dot{s}(t)|^2 dt - \bar{c} f_c \right] \\
 &= -8\pi^2 S^d [\rho \sigma_c \sigma_f + \bar{c}(\bar{f} - f_c)] \\
 &= -8\pi^2 S^d [\rho \sigma_c \sigma_f + \bar{c}\bar{f}] \tag{8.312}
 \end{aligned}$$

where the coupling between the Doppler scale and arrival time parameters is described by

$$\rho = \frac{W \int_{-\infty}^{\infty} t f^2(t) |\dot{s}(t)|^2 dt - \bar{c}\bar{f}}{\sigma_c \sigma_f} = \frac{\int_{-\infty}^{\infty} [tf(t) - \bar{c}][f(t) - \bar{f}] |\dot{s}(t)|^2 dt}{\sigma_c \sigma_f \int_{-\infty}^{\infty} |\dot{s}(t)|^2 dt}. \tag{8.313}$$

From the Cauchy-Schwarz inequality, it can be seen that $\rho \in [-1, 1]$ and so can be considered a correlation between the pulse's time-in-units-of-periods and instantaneous frequency.

Combining the terms of the FIM from (8.269) and (8.300) along with (8.312) results in the FIM for the three unknown coupled parameters (τ, η, ψ) ,

$$\text{FIM}(\tau, \eta, \psi) = 8\pi^2 S^d \begin{bmatrix} \sigma_f^2 + \bar{f}^2 & -(\rho \sigma_c \sigma_f + \bar{c}\bar{f}) & -\bar{f}/(2\pi) \\ -(\rho \sigma_c \sigma_f + \bar{c}\bar{f}) & \sigma_c^2 + \bar{c}^2 & \bar{c}/(2\pi) \\ -\bar{f}/(2\pi) & \bar{c}/(2\pi) & 1/(4\pi^2) \end{bmatrix} \tag{8.314}$$

Of primary interest is the upper-left two-by-two matrix of the inverted FIM describing the covariance of the (τ, η) estimates. This can be obtained by using the matrix inverse equation for a block (or partitioned) matrix (e.g., see [4, Sect. 2.9]), which results in

$$\left\{ \text{FIM}^{-1}(\tau, \eta, \psi) \right\}_{\tau, \eta} = \frac{1}{8\pi^2 S^d (1 - \rho^2)} \begin{bmatrix} \frac{1}{\sigma_f^2} & \frac{\rho}{\sigma_c \sigma_f} \\ \frac{\rho}{\sigma_c \sigma_f} & \frac{1}{\sigma_c^2} \end{bmatrix}. \quad (8.315)$$

Recall from Sect. 6.3.3.1 that this matrix acts as a lower bound for the covariance matrix of the parameter estimates in the sense of positive definiteness (i.e., the difference matrix is positive definite). The lower bound on the variance of the individual estimators in the joint-estimation scenario comes from the diagonal terms,

$$\text{Var}\{\hat{\tau}\} \geq \frac{1}{8\pi^2 S^d \sigma_f^2 (1 - \rho^2)} \quad (8.316)$$

$$\text{Var}\{\hat{\eta}\} \geq \frac{1}{8\pi^2 S^d \sigma_c^2 (1 - \rho^2)} \quad (8.317)$$

which illustrates how an increase in the coupling between arrival time and Doppler scale (i.e., $\rho \rightarrow 1$) degrades the estimation of each parameter.

8.5.5.1 LFM-Pulse Example

As before, suppose the instantaneous frequency of the LFM pulse is $f(t) = f_0 + tW/T_p$ for $t \in (0, T_p)$. Using this in (8.296) results in an average time-in-units-of-periods of

$$\bar{c} = \frac{T_p f_c}{2} \left(1 + \frac{\zeta}{6} \right) \quad (8.318)$$

where $f_c = f_0 + W/2 = \bar{f}$ is the center frequency and $\zeta = W/f_c$ is the ratio of the bandwidth to the center frequency. Similar application in (8.299) results in the variance

$$\sigma_c^2 = \frac{T_p^2 f_c^2}{12} \left(1 + \zeta + \frac{19}{60} \zeta^2 \right). \quad (8.319)$$

As expected, both of these simplify to the CW-pulse results when $\zeta = 0$. Evaluating the correlation in (8.313) produces

$$\rho = \frac{1 + \zeta/2}{\sqrt{1 + \zeta + \frac{19}{60} \zeta^2}} \quad (8.320)$$

which is seen to be one when $\zeta = 0$, implying a full coupling between delay and Doppler scale for the constant-envelope CW pulse. As ζ increases, ρ decreases very slowly: $\rho = 0.9947$ for $\zeta = 0.5$ and reaches a minimum of 0.9682 when $\zeta = 2$. This implies that even for very broadband LFM waveforms, there is significant coupling

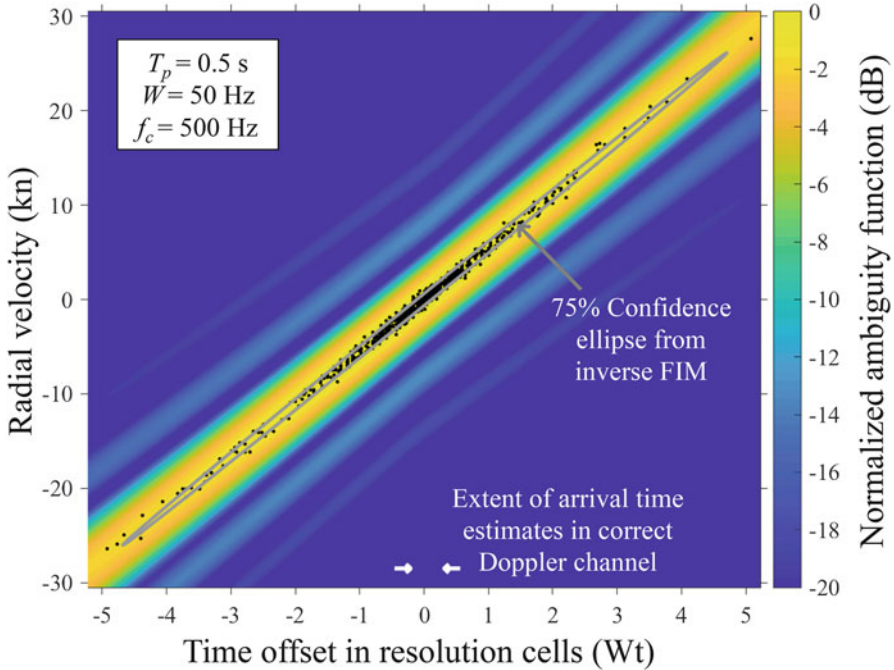


Fig. 8.20 Estimates of arrival time and radial velocity from 1000 trials overlaid on the normalized ambiguity function for a 0.5-s duration, 50-Hz bandwidth LFM pulse centered at $f_c = 500 \text{ Hz}$. The gray line is a 75%-coverage confidence ellipse formed by using the inverse Fisher information matrix (FIM) as a covariance matrix for the estimates and assuming Gaussian-distributed errors

between arrival time and Doppler. This is, of course, no surprise for either the CW or LFM pulses based on the shapes of the AFs found in Sect. 8.3.

The impact of the coupling between the arrival time and Doppler scale on joint estimates of the parameters can be seen in the example presented in Fig. 8.20 for a 0.5-s, 50-Hz LFM pulse centered at 500 Hz. The errors in the joint estimates from 1000 trials are shown overlaid on the normalized ambiguity function and seen to cluster on the ridge with the heaviest concentration near the origin where the error is zero. The white arrows near the abscissa indicate the spread of all 1000 estimates of delay when taken from the correct Doppler channel (i.e., assuming η is known), whereas the estimates when the Doppler scale is unknown extend throughout all of the temporal resolution cells shown.

One of the uses of the CRLB is to provide a prediction for estimation performance when it can be assumed that an estimator ($\mathbf{v} = [\hat{\tau} \ \hat{\eta}]^T$) is efficient, unbiased, and produces Gaussian-distributed errors. Under these assumptions, the quadratic form $R = \mathbf{v}^T \boldsymbol{\Sigma}^{-1} \mathbf{v}$ is chi-squared distributed with two degrees of freedom (i.e., exponentially distributed with mean two) where $\boldsymbol{\Sigma}$ is the inverse FIM matrix for the parameters. The probability that $R < r$ is then $q = 1 - e^{-r/2}$, which can be used to form a confidence ellipse with coverage probability q . For the LFM pulse, the

inverse FIM matrix in (8.315) results in the confidence ellipse

$$\begin{aligned}\tau(\rho, \theta) &= \frac{\cos \theta}{\sigma_f} \sqrt{\frac{-2 \log(1-q)}{8\pi^2 S^d(1-\rho^2)}} \\ v_r(\rho, \theta) &= \left(\frac{c_w}{2}\right) \frac{\sin(\theta + \arcsin \rho)}{\sigma_c} \sqrt{\frac{-2 \log(1-q)}{8\pi^2 S^d(1-\rho^2)}}\end{aligned}\quad (8.321)$$

for $\theta \in [0, 2\pi]$, where the Doppler scale has been converted to radial velocity for a monostatic-active-sonar geometry via $\eta = 1 + 2v_r/c_w$. The $q = 0.75$ coverage ellipse is shown in Fig. 8.20 (gray line) where it provides an approximate representation of the performance (i.e., the estimators do not necessarily satisfy all of the aforementioned constraints).

The extrema of the confidence ellipse can be obtained from (8.321) by evaluating it at $\theta = 0$ and π . This projection of the ellipse onto either axis can be interpreted as a confidence interval for the case where both arrival time and Doppler are unknown. Although the area of the ellipse may be a better representation of the potential estimation error, the single-dimension confidence intervals can be compared with the projections of the 3-dB-down points of the ambiguity function described in Sect. 8.5.1 (e.g., see Table 8.7). Such a comparison is shown in Fig. 8.21 for an LFM pulse with 1-s duration and center frequency of 1 kHz. The confidence-interval lengths (colored lines) are formed assuming a 15-dB SNR and 90% coverage. The corresponding 3-dB-down resolution measures are shown in gray and lie directly above the confidence-interval lengths. Both approaches convey the same information: increasing the bandwidth of an LFM pulse relative to its center frequency improves the joint estimation of arrival time and radial velocity.

8.6 Normalization: Background Power Estimation

In deriving the detectors in Sects. 8.2.2–8.2.7 it was assumed that the variance of the noise in the complex envelope (λ) was known. This generally resulted in a detector decision statistic with the variance or standard deviation in the denominator. For example, the QMF detector from (8.38) has the form

$$T(\mathbf{x}) = \frac{|\mathbf{s}_\theta^H \mathbf{x}|^2}{\lambda}. \quad (8.322)$$

Recall that the detector is implemented by comparing $T(\mathbf{x})$ to a threshold (h) and declaring a signal detected if $T(\mathbf{x}) \geq h$. Although multiplying both sides of this inequality by λ successfully removes it from the detector decision statistic on the left side, it merely forces it to be absorbed into the threshold on the right side. The *normalized* form shown in (8.322) is preferred over the un-normalized

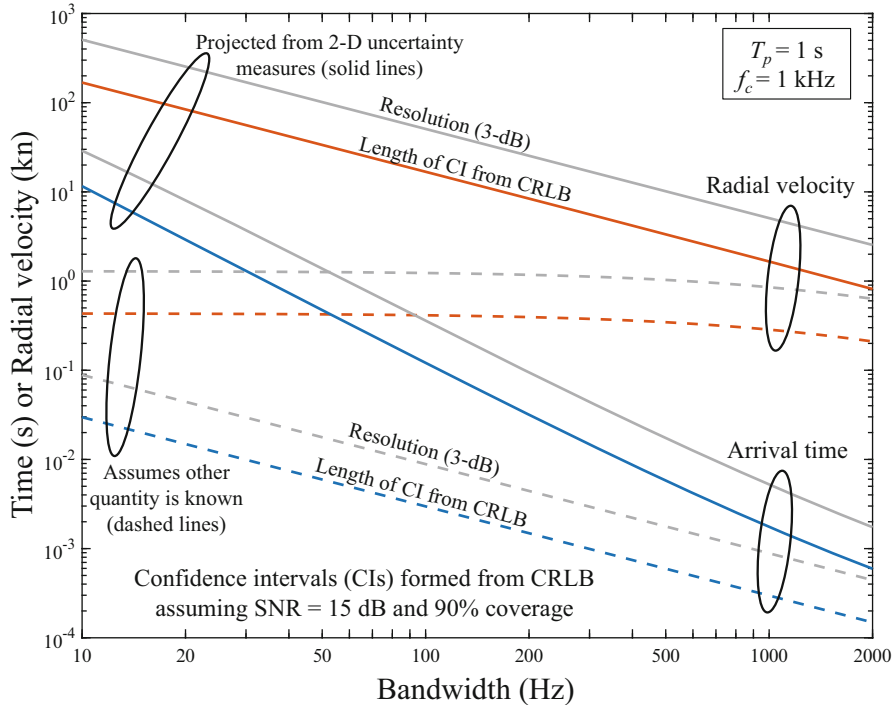


Fig. 8.21 Comparison of the 3-dB-down resolutions (gray lines) and the length of CRLB-based confidence intervals (colored lines) for arrival time and radial velocity when using an LFM pulse as a function of its bandwidth. The dashed lines represent the case where either arrival time or Doppler is assumed to be known. The solid lines represent projections of the two-dimensional uncertainty onto each dimension

version precisely because the resulting threshold does not depend on λ , rather it only depends on the desired probability of false alarm (P_f).

In practice the variance λ is generally not known and in some cases can change very rapidly. An example of rapidly varying reverberation levels in an active sonar system can be seen in the upper panel of Fig. 8.22. The data in this example are beamformed and matched-filtered measurements of a 1-s-duration, 1-kHz-bandwidth LFM pulse obtained during the NATO Undersea Research Centre (NURC) Clutter 2007 Experiment.⁷ The experiment occurred in shallow water (nominally a 100-m depth) and initially exhibits the $1/r^2$ decay in reverberation power expected from Sect. 3.5.3, which produces a very rapid decay at early times as can be seen in the figure. Reverberation from features on the bottom results in increases above this and at later times it can be seen to follow the $1/r^3$ decay

⁷Acknowledgement: NURC Clutter JRP [57] with gratitude to Dr. P. Nielsen (scientist in charge, Clutter 2007 Experiment).

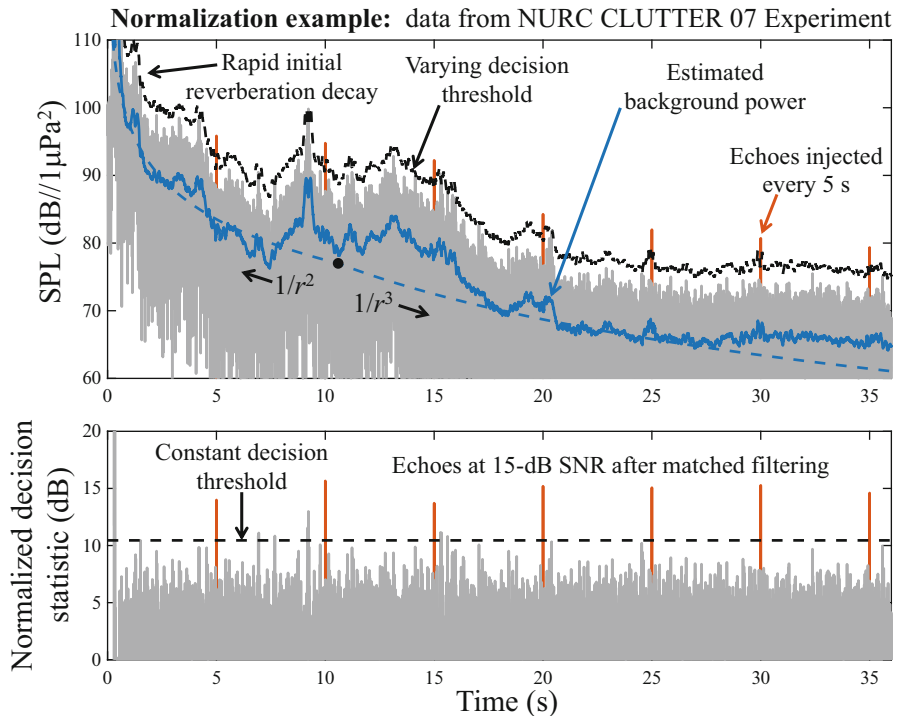


Fig. 8.22 Example matched-filter response with a time-varying background power (upper panel) from a 1-kHz bandwidth LFM pulse. The varying background power level requires the use of a time-varying threshold or the application of a normalizer (lower panel) before using a constant decision threshold. Acknowledgement: NURC Clutter JRP [57]

predicted in [58] until the ambient noise begins to dominate. A number of synthetic echoes that were added to the time-series data at 5-s intervals are also visible.

Using an estimate of the background reverberation and noise variance to form a threshold results in the black dashed line in the upper panel of Fig. 8.22. Using the estimate to form the normalized decision statistic as in (8.322) produces the lower panel in the figure where the background power now has a constant level and therefore allows the use of a constant decision threshold. Although both methods produce identical automated detection results, the injected signals are clearly easier to identify in the lower pane owing to the smaller dynamic range that can be used after normalization. The threshold was chosen so that if the reverberation had a Rayleigh-distributed envelope there would be on average one threshold exceedance over the data shown in the figure (i.e., $P_f = 1/(T_r W)$ where T_r is the time extent of the window and W the waveform bandwidth.) At this threshold, the seven echoes injected with an estimated SNR of 15 dB (after matched filtering) are all easily detected. However, additional detections are seen and represent false alarms from active sonar clutter, which can be modeled using the techniques described in Sect. 7.4.3.

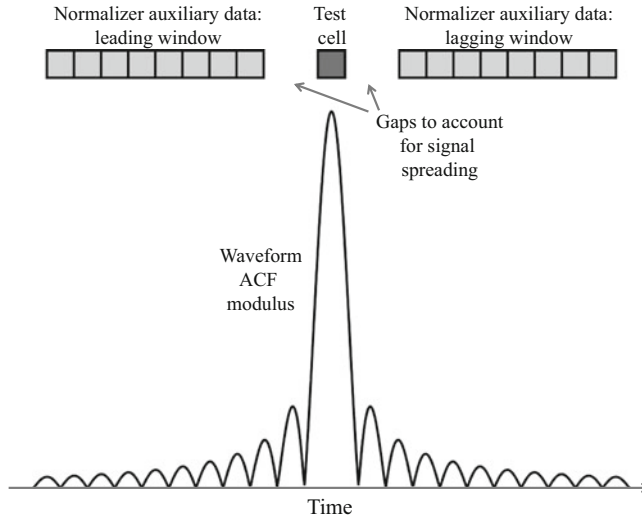


Fig. 8.23 Location of the normalizer auxiliary data and test cell relative to the modulus of the waveform autocorrelation function (ACF) for a signal perfectly aligned with the test cell

As noted in Sect. 8.2.8.1, the noise variance is generally estimated from sonar resolution cells near enough in time to the cell being tested for them to have the same noise variance but be free from signal. The location of such auxiliary data is illustrated in Fig. 8.23 relative to both the test cell in the center and the modulus of the waveform ACF for a signal perfectly aligned with the test cell. This configuration of the auxiliary data is known as a split-window normalizer. A gap is generally placed between the test cell and auxiliary data to account for spreading of signal from multipath propagation and/or reflection from extended objects.

Under the assumption that the information content on λ in the auxiliary data dominates that found in the test cell (e.g., see Sect. 8.2.8.1), the GLR detector is obtained by replacing λ in (8.322) by its maximum-likelihood estimate (MLE) $\hat{\lambda}$ as formed using the auxiliary data,

$$T(\mathbf{x}) = \frac{|\mathbf{s}_\theta^H \mathbf{x}|^2}{\hat{\lambda}} \quad (8.323)$$

$$= \left[\frac{|\mathbf{s}_\theta^H \mathbf{x}|^2}{\lambda} \right] \div \left[\frac{\hat{\lambda}}{\lambda} \right]. \quad (8.324)$$

The formation of the detector decision statistic in (8.323) with estimation of λ from auxiliary data is called a normalizer. When implementing a normalizer on an extended measurement time series, the auxiliary data window is slid along the time-series output of the matched filter as each new sonar resolution cell is tested. In designing a normalizer it is helpful to define the gap and auxiliary data windows

in terms of a temporal extent rather than a number of samples. This is a more natural dimension for determining gaps related to signal spreading and the time over which the background is assumed stationary. It also avoids confusion as to when the data are assumed to be sampled at a rate equal to the signal bandwidth (e.g., as occurs in the analysis) or are oversampled (as often occurs in practice).

The form of the normalized detector decision statistic in (8.324) is that of a perfectly normalized decision statistic (the quantity in the first set of brackets) divided by $\hat{\lambda}/\lambda$. Two important points come from this description. The first is that there will be an inherent loss in detection performance arising from the randomness of the estimator. That is, when the QMF is Neyman-Pearson optimal (NPO), $T(\mathbf{x})$ in (8.323) will not be NPO unless $\hat{\lambda} = \lambda$, which essentially means λ is known. The second key point is that the statistical distribution of $T(\mathbf{x})$ in (8.323) under the noise only hypothesis (and therefore P_f) will not depend on λ as long as $\hat{\lambda}/\lambda$ does not depend on λ . The invariance of $\hat{\lambda}/\lambda$ to λ only requires that the mean of the estimate be proportional to the true value,

$$E[\hat{\lambda}] \propto \lambda. \quad (8.325)$$

The invariance to an unknown noise power of the probability of false alarm in a detector with normalization is called a *constant false alarm rate* (CFAR) property. This is an important enough property that the loss in performance, called a CFAR loss, is deemed an acceptable tradeoff. The basic cell-averaging (CA) CFAR normalizer is described and analyzed in Sect. 8.6.1. Two common problems encountered when the auxiliary data are corrupted by non-background interferences are discussed in Sect. 8.6.2. The order-statistic (OS) normalizer, which addresses some corruption of the auxiliary data is described and analyzed in Sect. 8.6.3.

8.6.1 Cell-Averaging CFAR Normalizer

The development and analysis of a normalizer is generally performed by considering only a single test cell and the corresponding set of auxiliary data. Because the QMF only depends on the data through the squared modulus of the matched-filter response, the test cell data can be taken as

$$Y = |\mathbf{s}_\theta^H \mathbf{x}|^2 \quad (8.326)$$

and the auxiliary data available to the normalizer for estimation of the noise variance as

$$Y_l = |\mathbf{s}_\theta^H \mathbf{x}_l|^2 \quad (8.327)$$

where \mathbf{x}_l is the vectorized input to the matched filter producing the l th auxiliary-data sample. Let the auxiliary data from the leading and lagging windows be combined into one set indexed by $l = 1, \dots, L$ where L is the total number of independent samples. As previously noted, the matched-filter outputs and their corresponding instantaneous intensities will be statistically independent when the samples are taken at a rate equal to the bandwidth of the signal.

Assuming the auxiliary data have the same noise variance as the test cell and are signal-free leads to

$$Y_l \stackrel{iid}{\sim} \text{Expon}(\lambda) \quad (8.328)$$

under both the noise-only (H_0) and signal-present (H_1) hypotheses. The test cell is similarly exponentially distributed with mean λ under H_0 ; however, its distribution changes under H_1 . Although the particular distribution under H_1 affects the probability of detection (P_d), it does not change how the noise variance is estimated nor the relationship between the detector decision threshold and P_f .

As shown in the example in Sect. 8.2.8.1, the MLE for λ over the auxiliary data $\{Y_1, \dots, Y_L\}$ is the sample mean

$$\hat{\lambda} = \frac{1}{L} \sum_{l=1}^L Y_l. \quad (8.329)$$

The cell-averaging normalizer takes its name because this is simply an average of the instantaneous intensity formed over the auxiliary data cells.

8.6.1.1 Decision-Threshold Analysis

In terms of the instantaneous intensity samples, the detector decision statistic is

$$T = \frac{|\mathbf{s}_\theta^H \mathbf{x}|^2}{\hat{\lambda}} = \frac{Y}{\hat{\lambda}} = \frac{Y}{\frac{1}{L} \sum_{l=1}^L Y_l} \quad (8.330)$$

where the dependence on \mathbf{x} in T has been removed. The distribution of T under H_0 can be determined by noting that Y , when no signal is present, is the scale of a chi-squared random variable with two degrees of freedom,

$$U_n = \frac{2Y}{\lambda} \sim \chi_2^2 \quad (8.331)$$

and that $\hat{\lambda}$ is similarly the scale of a chi-squared random variable with $2L$ degrees of freedom,

$$U_d = \frac{2L\hat{\lambda}}{\lambda} = 2 \sum_{l=1}^L \frac{Y_l}{\lambda} \sim \chi_{2L}^2. \quad (8.332)$$

The detector decision statistic is then the ratio of the two chi-squared random variables, with both being divided by their degrees of freedom,

$$T = \frac{Y}{\hat{\lambda}} = \frac{U_n/2}{U_d/(2L)}. \quad (8.333)$$

As described in Sect. 5.6.16, this ratio is F distributed with $\nu_1 = 2$ and $\nu_2 = 2L$ degrees of freedom. In order to relate the decision threshold to P_f , the cumulative distribution function (CDF) of T is required. Although the CDF of the F distribution is in general related to an incomplete beta function, there is a simpler form when $\nu_1 = 2$. This can be obtained by integrating the PDF of T , which is

$$f_T(t|H_0) = \frac{1}{(1+t/L)^{L+1}} \quad \text{for } t \geq 0, \quad (8.334)$$

from Sect. 5.6.16 with $\nu_1 = 2$ and $\nu_2 = 2L$. The CDF is then easily obtained by integrating (8.334) from zero to t ,

$$F_T(t|H_0) = \int_0^t f_T(x) dx = 1 - \frac{1}{(1+t/L)^L} \quad \text{for } t \geq 0. \quad (8.335)$$

The decision threshold is found by solving the equation $P_f = 1 - F_T(h|H_0)$ for h , which results in

$$h = L \left(P_f^{-1/L} - 1 \right). \quad (8.336)$$

It is straightforward to show using L'Hopital's rule that as $L \rightarrow \infty$, the threshold

$$\lim_{L \rightarrow \infty} h = -\log P_f, \quad (8.337)$$

which is what it would be if the noise variance were known perfectly (i.e., as in (8.45)). Noting that the MLE is a consistent estimator (see Sect. 6.3.4.1), the estimate converges in probability to the true value, $\hat{\lambda} \rightarrow \lambda$, so this is an expected as well as a desired result. The detector decision thresholds for various values of L are shown in Fig. 8.24 as a function of P_f , where the progression toward $h = -\log P_f$ can be seen as L increases. One indication of the loss in performance is that, for a given P_f , the decision threshold when λ is estimated is always greater than the asymptotic value. The higher decision threshold results in a lower P_d , as will be shown in Sect. 8.6.1.3.

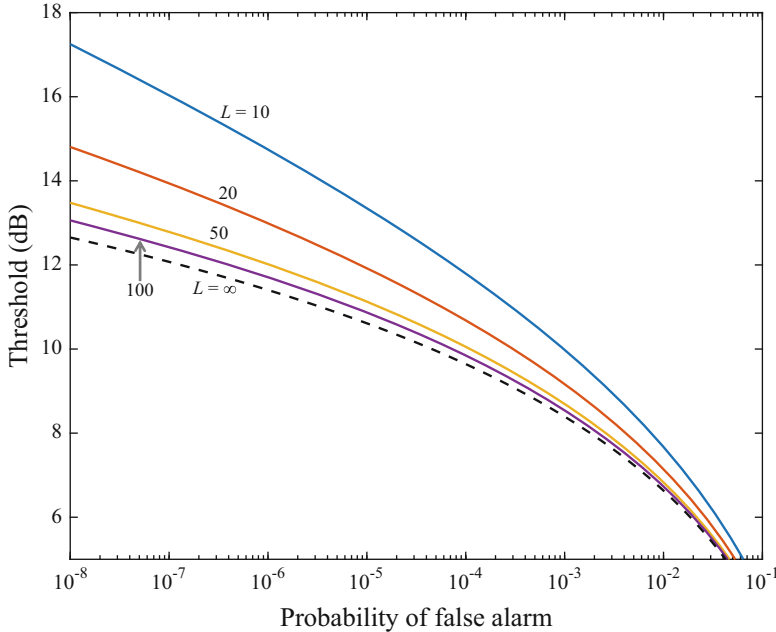


Fig. 8.24 Decision threshold for a cell-averaging normalizer as a function of P_f for various quantities of auxiliary data. As $L \rightarrow \infty$, the threshold converges to that used when λ is known perfectly

8.6.1.2 Equivalent Number of Independent Samples

Recall that the auxiliary data were assumed to be statistically independent because they were sampled at a rate equal to the signal bandwidth. When they are oversampled, the cell-averaging normalizer is identical in terms of forming the estimate as an average over the instantaneous intensity samples. However, the relationship in (8.336) should be modified to use the effective number of independent squared-envelope samples (L_{eq}) in lieu of L . For a single contiguous auxiliary data window with temporal extent T_a and waveform bandwidth W this is approximated by

$$L_{\text{eq}} = T_a W + 1. \quad (8.338)$$

The temporal extent is defined as the time from the first sample to the last, which means that $T_a = 0$ if only one sample is used and results in $L = 1$. For a split-window normalizer like that shown in Fig. 8.23 where each side covers a temporal extent T_{half} , the total time span if the windows were contiguous would be $T_a = 2T_{\text{half}} + 1/W$ with the $1/W$ used to separate the two windows. This then results in

$$L_{\text{eq}} = 2T_{\text{half}}W + 2, \quad (8.339)$$

which illustrates a minimum number of samples equal to two rather than one.

When the PSD of the matched-filter noise and reverberation output is not reasonably flat over the band, these approximations can be inaccurate. In this case, the autocorrelation function $R_{zz}(\tau)$ of the matched-filter output can be used to obtain an equivalent number of independent squared-envelope samples following the approach of [59, App. A]. The equivalent number of independent squared-envelope samples is derived by equating the mean and variance of $\hat{\lambda}$ to that of a gamma distribution and using the shape parameter as L_{eq} .⁸ Suppose the complex matched filter output for the l th auxiliary data sample is $Z_l = \mathbf{s}_\theta^H \mathbf{x}_l$ and the set of auxiliary data samples is arranged into a vector $\mathbf{z} = [Z_1 \dots Z_L]^T$. This vector is complex-Gaussian distributed,

$$\mathbf{z} \sim \mathcal{CN}(\mathbf{0}, \boldsymbol{\Sigma}), \quad (8.340)$$

with zero mean and a Toeplitz covariance matrix $\boldsymbol{\Sigma}$ with (i, j) element

$$\{\boldsymbol{\Sigma}\}_{i,j} = R_{zz} \left(\frac{i-j}{f_s} \right) \quad (8.341)$$

where f_s is the sampling rate. If the PSD of the noise and reverberation response of the matched filter is flat in the signal band, then $R_{zz}(\tau) = \lambda \text{sinc}(W\tau)$ and sampling at the bandwidth produces $\boldsymbol{\Sigma} = \lambda \mathbf{I}$. The estimate of the background power in terms of \mathbf{z} can be described as its vector inner product divided by L ,

$$\hat{\lambda} = \frac{\mathbf{z}^H \mathbf{z}}{L}. \quad (8.342)$$

Its mean can then be found by equating the vector inner product to the trace⁹ of the vector outer product, $\mathbf{z}^H \mathbf{z} = \text{tr}\{\mathbf{z}\mathbf{z}^H\}$. This results in

$$\begin{aligned} E[\hat{\lambda}] &= \frac{1}{L} \text{tr}\left\{ E\left[\mathbf{z}\mathbf{z}^H \right] \right\} \\ &= \frac{1}{L} \text{tr}\{\boldsymbol{\Sigma}\} \end{aligned} \quad (8.343)$$

where the trace is taken outside of the expectation, the latter of which results in the covariance matrix of \mathbf{z} . For the Toeplitz covariance structure described by (8.341), this simplifies to

$$E[\hat{\lambda}] = R_{zz}(0) = \lambda, \quad (8.344)$$

⁸This is because a gamma random variable with shape parameter α and scale β has the same distribution as the sum of α independent exponential random variables with mean β .

⁹The trace of a matrix is the sum of the diagonal elements.

which is as expected because the sample mean is an unbiased estimator. Using a similar procedure, the second moment of the estimator can be shown to be

$$\begin{aligned} E[\hat{\lambda}^2] &= \frac{1}{L^2} \text{tr} \left\{ E \left[\mathbf{z} \mathbf{z}^H \mathbf{z} \mathbf{z}^H \right] \right\} \\ &= \frac{1}{L^2} \left[\text{tr}^2 \{ \boldsymbol{\Sigma} \} + \text{tr} \left\{ \boldsymbol{\Sigma}^2 \right\} \right] \end{aligned} \quad (8.345)$$

through the use of

$$E \left[\mathbf{z}^H \mathbf{A} \mathbf{z} \mathbf{z}^H \mathbf{B} \mathbf{z} \right] = \text{tr} \{ \mathbf{A} \boldsymbol{\Sigma} \} \text{tr} \{ \mathbf{B} \boldsymbol{\Sigma} \} + \text{tr} \{ \mathbf{A} \boldsymbol{\Sigma} \mathbf{B} \boldsymbol{\Sigma} \} \quad (8.346)$$

from [47, pg. 564] which requires \mathbf{z} to be complex-Gaussian distributed as in (8.340) and for \mathbf{A} and \mathbf{B} to be Hermitian symmetric (i.e., $\mathbf{A} = \mathbf{A}^H$ and $\mathbf{B} = \mathbf{B}^H$).

Equating the first two moments of $\hat{\lambda}$ to a gamma random variable with L_{eq} degrees of freedom results in

$$L_{\text{eq}} = \frac{\left\{ E[\hat{\lambda}] \right\}^2}{\text{Var}\{\hat{\lambda}\}} \quad (8.347)$$

Using (8.343) and (8.345) and noting that the variance is the mean-square minus the squared mean produces

$$L_{\text{eq}} = \frac{\text{tr}^2 \{ \boldsymbol{\Sigma} \}}{\text{tr} \{ \boldsymbol{\Sigma}^2 \}} \quad (8.348)$$

for a general covariance matrix. For the Toeplitz covariance structure described in (8.341) and a single contiguous window with temporal extent $T_a = (L - 1)/f_s$, this simplifies to

$$L_{\text{eq}} = \frac{L R_{zz}^2(0)}{\sum_{k=-L}^L \left(1 - \frac{|k|}{L} \right) R_{zz}^2 \left(\frac{k T_a}{L-1} \right)}, \quad (8.349)$$

which is the result found in [59, App. A, eq. A-9].

When L_{eq} is large enough (e.g., $L_{\text{eq}} > 10$), the gamma approximation leading to (8.336) is most likely adequate. However, when it is small and there is oversampling or a shaped PSD it may not be accurate. In these scenarios, P_f should be evaluated using the characteristic-function approach described in [60] or here in Sect. 9.3.4.

8.6.1.3 Performance Analysis and CFAR Loss

As previously mentioned, the cost of not knowing the background power and having to estimate it is a reduction in performance. Although there are several ways to articulate this performance loss, describing it as the additional SNR required to maintain a desired performance specification provides congruity with sonar-equation analysis. Evaluating this CFAR loss requires choosing an operating point and assuming a particular signal model. Of the standard signal models, closed-form results can be obtained for the Gaussian-fluctuating signal. When the signal has Gaussian amplitude fluctuations with SNR S^d , the test cell data are exponentially distributed with mean $\lambda(1 + S^d)$,

$$Y = |\mathbf{s}_\theta^H \mathbf{x}|^2 \sim \text{Expon}\left\{\lambda(1 + S^d)\right\} \quad (8.350)$$

which can be seen from (8.58) after accounting for multiplying by λ . Following the same process as for the P_f analysis, the numerator in the normalizer decision statistic is the scale of a chi-squared random variable with two degrees of freedom,

$$U_n = \frac{2Y}{\lambda(1 + S^d)} \sim \chi_2^2. \quad (8.351)$$

This results in

$$T = \frac{Y}{\hat{\lambda}} = (1 + S^d) \left[\frac{U_n/2}{U_d/(2L)} \right] \quad (8.352)$$

where the term in the brackets is, as before, F distributed with $\nu_1 = 2$ and $\nu_2 = 2L$. The CDF of T is then

$$F_T(t|H_1) = 1 - \left[1 + \frac{t}{L(1+S^d)} \right]^{-L} \quad \text{for } t \geq 0. \quad (8.353)$$

so the probability of detection is

$$P_d = 1 - F_T(h|H_1) = \left(\frac{S^d + 1}{S^d + P_f^{-1/L}} \right)^L. \quad (8.354)$$

As expected, $P_d \rightarrow P_f$ when $S^d \rightarrow 0$. Solving (8.354) for S^d yields the SNR required to achieve the performance specification (P_f , P_d) when using a normalizer with L independent observations of the noise,

$$S^d = \frac{\left(\frac{P_d}{P_f}\right)^{1/L} - 1}{1 - P_d^{1/L}}. \quad (8.355)$$

As $L \rightarrow \infty$, this tends to $S^d = (\log P_f / \log P_d) - 1$ as in (8.62). The CFAR loss is then the ratio of (8.355) to the asymptotic result, which results in

$$\text{Loss}_{\text{dB}} = 10 \log_{10} \left\{ \frac{\log(P_d) \left[1 - \left(\frac{P_d}{P_f} \right)^{1/L} \right]}{\log(P_d/P_f) \left[1 - P_d^{1/L} \right]} \right\} \quad (8.356)$$

$$\leq 10 \log_{10} \left\{ \frac{L \left[P_f^{-1/L} - 1 \right]}{-\log P_f} \right\} \quad (8.357)$$

after conversion to decibels. The CFAR loss for various values of P_f and P_d is shown in Fig. 8.25 as a function of L . The tight grouping over P_d implies the upper bound in (8.357) is a useful approximation (the black dashed lines formed by letting $P_d \rightarrow 1$). Noting that other losses arising in the implementation of signal processing algorithms on real data are on the order of one decibel, it seems reasonable to choose L to allow no more than a 1-dB CFAR loss (as long as stationarity holds within the auxiliary data window). As P_f decreases, more samples are required to achieve this. For example, although the 1-dB CFAR loss can be achieved with only $L = 11$ independent samples in the auxiliary data for $P_f = 10^{-2}$, it requires $L = 32$ for $P_f = 10^{-6}$. Achieving $L = 32$ independent samples in the auxiliary data is not difficult for broadband waveforms where the resolution-cell extent is one over the bandwidth. For example, with a 100-Hz bandwidth this only requires a combined auxiliary data window extent of $T_a = 0.31$ s, or, using (8.339), just 0.15 s per side in the split-window normalizer. Achieving this with a CW pulse, however, can stress the stationarity assumptions because the resolution cell extent is equal to the signal duration. As described in Sect. 8.7.3, this can be mitigated by using data from nearby Doppler channels in a Doppler filter bank.

For a deterministic signal, the signal component enters the complex envelope in the mean rather than the variance as for the Gaussian-fluctuating signal. This results in the instantaneous intensity Y being the scale of a non-central chi-squared random variable,

$$U_n = \frac{2Y}{\lambda} \sim \chi^2_{2,\delta} \quad (8.358)$$

where the non-centrality parameter is $\delta = 2S^d$. The normalized detector decision statistic is then non-centrally F distributed

$$T = \frac{Y}{\hat{\lambda}} = \frac{U_n/2}{U_d/(2L)} \sim F_{2,2L,\delta}. \quad (8.359)$$

Obtaining P_d requires evaluation of the CDF of the non-central F distribution, which is most easily described in the form of an infinite summation as found in

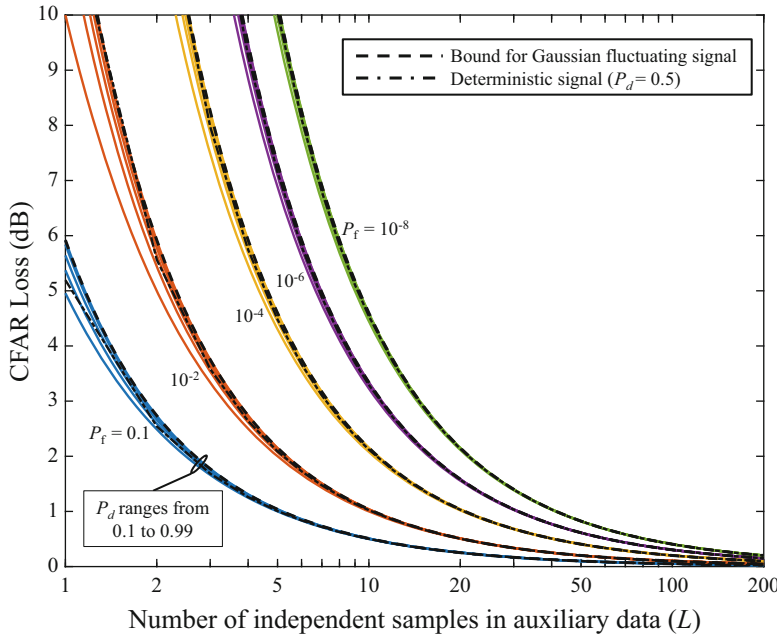


Fig. 8.25 CFAR loss for a signal with Gaussian amplitude fluctuations as a function of L , the number of independent samples contained in the auxiliary data. For each value of P_f , the values of $P_d = 0.1, 0.3, 0.5, 0.7, 0.9$, and 0.99 are shown. The black dashed lines represent the upper bound from (8.357) obtained by letting $P_d \rightarrow 1$ and the black dash-dot lines are for a deterministic signal with $P_d = 0.5$

Sect. 5.6.17. Approximations can be found in [61, Ch. 30] and subroutines are available in some numerical packages (e.g., the statistics toolbox in MATLAB[®]). The lack of a closed-form solution makes evaluation of the SNR required to achieve an operating point cumbersome in that the P_d equation must be numerically solved for S^d . The results of this for $P_d = 0.5$ are shown in Fig. 8.25 (black dash-dot lines) where they are seen to be very similar to the results of the Gaussian-fluctuating signal.

8.6.2 Target Masking and False-Alarm-Rate Inflation

The underlying premise of using auxiliary data to estimate the noise variance is that it has the same variance as in the test cell. The most common problem with normalizers occurs when interfering signals occupy the auxiliary data cells. This causes the noise variance estimate to be biased high, $E[\hat{\lambda}] > \lambda$, which results in a reduction in P_d . Because of the reduction in P_d , the phenomenon is called

target masking. Target masking is common both in the presence of spatially compact clutter and in the regions near strong signals.

At the other extreme is a bias of the noise-variance estimate below the true value, $E[\hat{\lambda}] < \lambda$. Although this acts to increase P_d , which is not an issue, it also increases P_f and is therefore known as false-alarm-rate (FAR) inflation. FAR inflation is common when the auxiliary-data window is so large that the noise variance changes throughout it in such a way as to bias it low.

Both of these issues can be mitigated through the use of alternative normalizers that trade-off some performance for robustness to interferences or mismatch in assumptions. For example, forming the estimate of the background variance using the logarithm of the instantaneous intensity was shown in [62] to require $L_{\log} = 1.65L_{\text{lin}} - 0.65$ cells of auxiliary data to achieve the same performance as a cell-averaging normalizer using L_{lin} cells. Other approaches include forming separate estimates of the noise variance from the leading and lagging windows and using either the larger (to mitigate FAR inflation) or the smaller (to mitigate target masking). These are known as, respectively, *greater-of* (GO) and *lesser-of* (LO) normalizers. A more computationally intensive approach is found in order-statistic (OS) normalizers. For example, estimating the noise variance using the median (where half of the samples are above and half below) of the instantaneous-intensity samples in the auxiliary-data windows can mitigate both FAR inflation and target masking. This comes at the computational expense of having to sort the auxiliary data. Order statistic normalizers are covered in the next section; details on the GO, LO, and trimmed-mean order-statistic normalizers can be found in [9, Ch. 7] and [63]. The trimmed-mean order-statistic normalizer, which forms an average of the order statistics after trimming some of the largest and smallest values, was shown in [63] to be a good choice when the noise variance is changing throughout the window.

8.6.3 Order-Statistic CFAR Normalizer

The *ordered statistics* of a data set Y_1, \dots, Y_L are simply the data samples ordered from smallest to largest,

$$Y_{(1)} \leq Y_{(2)} \leq \dots \leq Y_{(L-1)} \leq Y_{(L)}. \quad (8.360)$$

The notation in $Y_{(k)}$ with the parentheses surrounding the subscript means it is the k th ordered sample with $Y_{(1)}$ being the smallest and $Y_{(L)}$ the largest. The concept behind an order-statistic normalizer is that using $Y_{(k)}$ to estimate λ where k is somewhere near the middle can avoid target masking because the interfering signals within the auxiliary data with an average intensity above λ are more likely to be ordered above $Y_{(k)}$, leaving $Y_{(k)}$ largely unaffected. Similarly, if some number of the auxiliary data samples have average intensity less than λ , they are more likely to be ordered below $Y_{(k)}$, which mitigates FAR inflation.

To evaluate the performance of an order-statistic normalizer, suppose λ is estimated by the k th order statistic,

$$\hat{\lambda} = Y_{(k)} \quad (8.361)$$

so the normalized detector decision statistic is

$$T = \frac{Y}{\hat{\lambda}} = \frac{Y}{Y_{(k)}}. \quad (8.362)$$

Such a normalizer will be referred to as an $OS(L, k)$ normalizer. It is important to note that this does not produce an unbiased estimate of λ , but is within a multiplicative scale of λ (i.e., $E[\hat{\lambda}] = c_k \lambda$). The scale c_k is inherently absorbed into the decision threshold of the order-statistic normalizer as it is implemented here. If an unbiased estimate of the noise variance is desired for other applications, c_k should be obtained and used to scale $Y_{(k)}$.

As long as the auxiliary-data samples are *iid*, the CDF of the k th order statistic is simply the probability that k or more of the samples are below the threshold [64, Sect. 2.1],

$$F_{\hat{\lambda}}(z) = \Pr\{Y_{(k)} \leq z\} = \sum_{l=k}^L \binom{L}{l} F_0^l(z)[1 - F_0(z)]^{L-l} \quad (8.363)$$

where $F_0(y) = F_Y(y|H_0)$ is the CDF of both the test cell under the noise-only hypothesis and of the auxiliary data. Using [65, 6.6.4, pg. 263], the CDF of $Y_{(k)}$ can be related to the incomplete beta function,

$$\begin{aligned} F_{\hat{\lambda}}(z) &= \frac{B(k, L - k + 1, F_0(z))}{B(k, L - k + 1)} \\ &= \frac{1}{B(k, L - k + 1)} \int_0^{F_0(z)} p^{k-1} (1 - p)^{L-k} dp, \end{aligned} \quad (8.364)$$

where $B(u, v) = \Gamma(u)\Gamma(v)/\Gamma(u + v)$ is the beta function. This form can then be differentiated to obtain the PDF,

$$f_{\hat{\lambda}}(z) = k \binom{L}{k} F_0^{k-1}(z)[1 - F_0(z)]^{L-k} f_0(z). \quad (8.365)$$

These forms are useful when working with instantaneous-intensity data that are not exponentially distributed (e.g., the heavy-tailed distributions described in Sect. 7.4.3). When the auxiliary data follow the Rayleigh distribution chain and have an exponentially distributed instantaneous intensity, P_f and P_d can be obtained through finite summations as shown in the following sections.

8.6.3.1 Decision-Threshold Analysis

To evaluate P_f in terms of the detector decision threshold for data following the Rayleigh distribution chain, it is first required to map the L order statistics to an alternative set of L random variables consisting of the minimum (i.e., $U_1 = Y_{(1)}$) and the $L - 1$ differences between consecutive order statistics,

$$U_l = Y_{(l)} - Y_{(l-1)} \quad (8.366)$$

for $l = 2, \dots, L$. The k th order statistic can then be described by the sum of the first k ,

$$Y_{(k)} = \sum_{l=1}^k U_l. \quad (8.367)$$

When the auxiliary data are *iid* exponentially distributed with mean λ , it can be shown [64, Sect. 6.7] that U_l is itself exponentially distributed with mean $\lambda/(L - l + 1)$,

$$U_l \sim \text{Expon}\{\lambda/(L - l + 1)\}, \quad (8.368)$$

and is independent of U_m for $l \neq m$.

In order to determine P_f , recall that the detector decision statistic is

$$T = \frac{Y}{\hat{\lambda}} \quad (8.369)$$

so the probability of false alarm is

$$P_f = \Pr\{T \geq h | H_0\} = \Pr\left\{Y \geq \hat{\lambda}h | H_0\right\}. \quad (8.370)$$

Because Y is exponentially distributed (with mean λ) under H_0 , the probability in (8.370) can be obtained through the CDF of the exponential distribution by conditioning on $\hat{\lambda}$,

$$P_f = E_{\hat{\lambda}}\left[1 - F_0(\hat{\lambda}h)\right] = E\left[e^{-h\hat{\lambda}/\lambda}\right] \quad (8.371)$$

Inserting (8.367) into (8.371) for $\hat{\lambda}$ and exploiting the separability of the expectations arising from independence of the difference variables, it can be seen that P_f is the product over the moment generating functions (MGFs) of U_l for $l = 1, \dots, k$,

$$\begin{aligned}
P_f &= \prod_{l=1}^k E\left[e^{-hU_l/\lambda}\right] = \prod_{l=1}^k M_{U_l}(-h/\lambda) \\
&= \prod_{l=1}^k \frac{1}{1 + h/(L - l + 1)}
\end{aligned} \tag{8.372}$$

where the MGF of an exponentially distributed random variable with mean $\lambda/(L - l + 1)$,

$$M_{U_l}(t) = E[e^{tU_l}] = \frac{1}{1 - t\lambda/(L - l + 1)}, \tag{8.373}$$

can be obtained from Sect. 5.6.10. This provides a simple formula for relating the detector decision threshold h to P_f for an OS(L, k) normalizer. Most importantly, the CFAR nature of the OS(L, k) normalizer is exhibited by P_f not depending on λ , but only L, k , and the decision threshold h .

This derivation of P_f enables analysis of other order-statistic-based normalizers such as the trimmed-mean [63] where the noise variance is estimated by a sum over the order statistics excluding some of the largest and smallest. A simpler evaluation of P_f for the OS(L, k) normalizer can be found in [66] by directly evaluating (8.371) using $f_{\hat{\lambda}}(\hat{\lambda})$ from (8.365). This results in

$$\begin{aligned}
P_f &= \int_0^\infty e^{-h\hat{\lambda}/\lambda} f_{\hat{\lambda}}(\hat{\lambda}) d\hat{\lambda} \\
&= \frac{1}{B(k, L - k + 1)} \int_0^1 p^{h+L-k} (1-p)^{k-1} dp \\
&= \frac{B(h + L + 1 - k, k)}{B(k, L - k + 1)} = \frac{\Gamma(h + L + 1 - k)\Gamma(L + 1)}{\Gamma(h + L + 1)\Gamma(L - k + 1)},
\end{aligned} \tag{8.374}$$

which is identical to (8.372).

Exercise 8.9 Show that (8.374) simplifies to (8.372). Hint: $\Gamma(x + 1) = x\Gamma(x)$.

8.6.3.2 Performance Analysis

In a similar fashion to how P_f was obtained, the probability of detection can be described as an expectation over $\hat{\lambda}$,

$$\begin{aligned}
P_d &= \Pr\{T > h | H_1\} = \Pr\left\{Y > h\hat{\lambda} | H_1\right\} \\
&= E_{\hat{\lambda}}\left[1 - F_1(h\hat{\lambda})\right],
\end{aligned} \tag{8.375}$$

where $F_1(y) = F_r(y|H_1)$ is the CDF of the test data when signal is present.

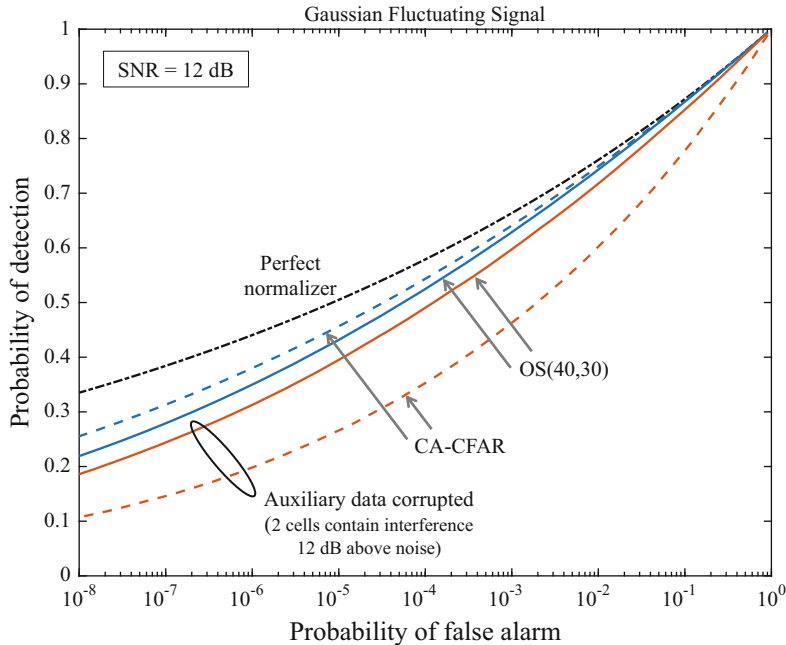


Fig. 8.26 ROC curve for a Gaussian-fluctuating signal with a 12-dB SNR for perfect normalization, cell-averaging normalizer, and an OS(40, 30) normalizer. The reddish-brown lines represent a target masking example where two of the forty auxiliary-data cells are corrupted by interference 12 dB above the noise

For a Gaussian-fluctuating signal, Y is exponentially distributed with mean $\lambda(1 + S^d)$, so $F_1(y) = 1 - \exp\{-y/[\lambda(1 + S^d)]\}$ to result in

$$\begin{aligned}
 P_d &= \prod_{l=1}^k E\left[e^{-hU_l/[\lambda(1+S^d)]}\right] = \prod_{l=1}^k M_{U_l}\left(-h/[\lambda(1+S^d)]\right) \\
 &= \prod_{l=1}^k \left[1 + \frac{h}{(L-l+1)(1+S^d)}\right]^{-1} = \frac{\Gamma\left(\frac{h}{1+S^d} + L + 1 - k\right) \Gamma(L + 1)}{\Gamma\left(\frac{h}{1+S^d} + L + 1\right) \Gamma(L - k + 1)}. \tag{8.376}
 \end{aligned}$$

The ROC curve for the order-statistic normalizer formed from (8.372) or (8.374) and (8.376) is shown in Fig. 8.26 for a 12-dB SNR signal with $L = 40$ and $k = 30$. Restricting attention to the blue lines in the ROC curve where the auxiliary data are pristine, it is seen that a cell-averaging normalizer (also using $L = 40$ cells of auxiliary data) is better than the OS(40, 30), but not as good as the unrealizable perfect normalization. A target-masking example is shown by corrupting two of the forty cells of the auxiliary data with interference 12 dB above the noise. The

robustness of the order-statistic normalizer relative to the cell-averaging normalizer is evident in that the reduction in P_d is significantly less when the auxiliary data are corrupted by large interferences.

The expectation describing P_d in (8.375) can be written in integral form using either the PDF of $\hat{\lambda}$,

$$P_d = \int_0^\infty [1 - F_1(h\hat{\lambda})] f_{\hat{\lambda}}(\hat{\lambda}) d\hat{\lambda} \quad (8.377)$$

$$= \frac{1}{h} \int_0^\infty f_1(y) F_{\hat{\lambda}}(y/h) dy, \quad (8.378)$$

or the CDF, after performing integration by parts, where $f_1(y) = f_Y(h|H_1)$ is the PDF of the test cell when signal is present. These integral equations, coupled with (8.363)–(8.365) allow a straightforward evaluation of P_d when the noise data do not follow the Rayleigh distribution chain or when the signal does not have Gaussian fluctuations. For example, the ROC curve for detecting a deterministic signal in Gaussian noise is shown in Fig. 8.27 for a perfect normalizer,

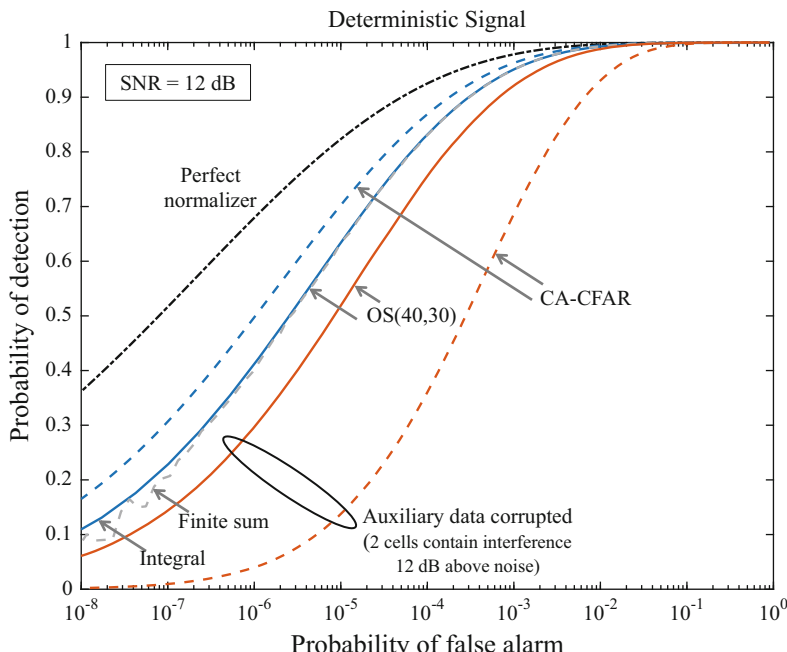


Fig. 8.27 ROC curve for a deterministic signal with a 12-dB SNR for perfect normalization, cell-averaging normalizer, and OS(40, 30). The gray dashed line represents obtaining P_d through the finite sum in (8.379) whereas the solid blue line is via the integral equation in (8.377)

an OS(40, 30) normalizer, and a cell-averaging normalizer having forty independent samples of auxiliary data. The integral representation of P_d in (8.377) is used with (8.365) to obtain the solid blue line. Similar to the Gaussian-fluctuating signal, the order-statistic normalizer is seen to be more robust to target masking than the cell-averaging normalizer when the auxiliary data are corrupted.

When the signal-plus-Gaussian-noise model has a simple MGF for the instantaneous-intensity data (as do the deterministic, Rician, and gamma-fluctuating-intensity signals) the form of $F_{\hat{\lambda}}(z)$ in (8.363) can be exploited to write P_d as a finite sum. Recalling that under the Rayleigh distribution chain $F_0(z) = 1 - e^{-z/\lambda}$, the CDF of $\hat{\lambda}$ can be expanded into a double sum of weighted exponentials. Using such a representation in (8.378) results in

$$P_d = \frac{1}{h} \sum_{l=k}^L \sum_{j=0}^l \binom{L}{l} \binom{l}{j} (-1)^j M_1\left(\frac{-(L+j-l)}{h\lambda}\right) \quad (8.379)$$

where $M_1(t) = E[e^{tY}|H_1]$ is the MGF of the instantaneous intensity under H_1 . The $(-1)^j$ term in (8.379) indicates that numerical evaluation may result in errors when L is large. This can be seen in Fig. 8.27 for $L = 40$ at the lower values of P_d and P_f where the gray dashed curve departs from the numerical evaluation of P_d through the integral in (8.377).

In situations where the PDF of the background estimator or the CDF of the test cell are not easily evaluated and so (8.377) is not a viable option, an alternative can be found by describing the CDF of a ratio of independent random variables as a single integral involving their characteristic functions. This approach, which exploits the results of [67, Thm. 16], is described more fully in Sect. 9.3.4 and [60]. From (9.226), the integral relationship is

$$P_d = \frac{1}{2} - \frac{1}{\pi} \int_0^\infty \text{Imag}\left\{\omega^{-1} \Phi_{\hat{\lambda}}(\omega) \Phi_1^*(\omega/h)\right\} d\omega \quad (8.380)$$

where $\Phi_{\hat{\lambda}}(\omega) = E[e^{j\omega\hat{\lambda}}]$ and $\Phi_1(\omega) = E[e^{j\omega Y}|H_1]$ are the characteristic functions of, respectively, $\hat{\lambda}$ and the test cell Y under H_1 . When the auxiliary data are *iid* exponentially distributed with mean λ , the characteristic function of the k th order statistic (i.e., using $\hat{\lambda} = Y_{(k)}$) is

$$\Phi_{\hat{\lambda}}(\omega) = \prod_{l=1}^K \left[1 - \frac{j\omega\lambda}{L-l+1} \right]^{-1}, \quad (8.381)$$

which can be seen from (8.367) and (8.368). Evaluation of the detection performance of an OS(L, k) normalizer for deterministic, Rician, or gamma-fluctuating-intensity signals can all be done with essentially equal effort through (8.380) using (8.381) and the characteristic functions for the test cell as found in Table 9.2.

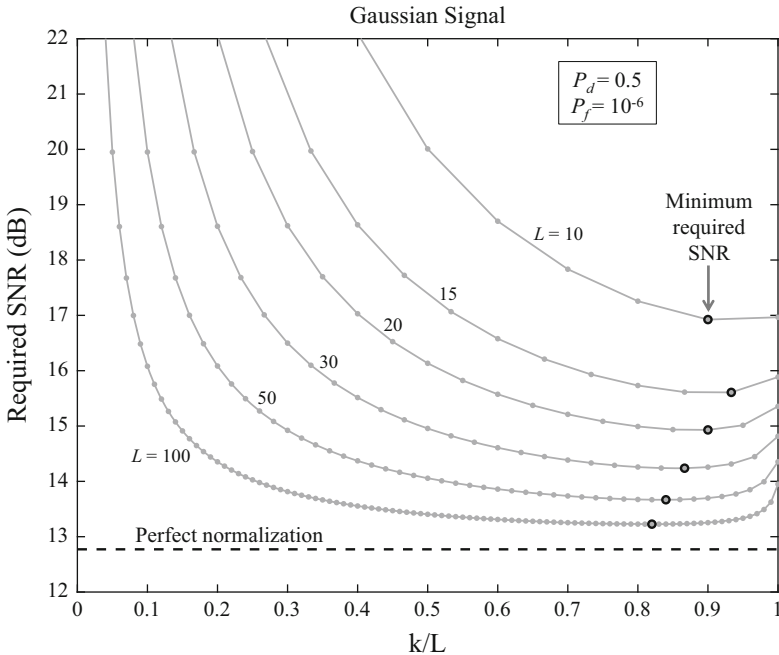


Fig. 8.28 SNR required to achieve $P_d = 0.5$ and $P_f = 10^{-6}$ when using an OS(L, k) normalizer as a function of k/L for various values of L

8.6.3.3 Which Order Statistic to Use?

The analysis presented in [66] recommends using $k = \frac{3}{4}L$ based on the “average decision threshold” (ADT). Although slightly better performance was obtained for k closer to $\frac{7}{8}L$, the difference was minimal and justified by the increased robustness to target masking. The ADT measure is a proxy for the SNR required to achieve a performance specification, which can be evaluated by numerical inversion of (8.374) to obtain h as a function of P_f and then (8.376), (8.379), or (8.380) to obtain S^d as a function of P_d and h . The result for the Gaussian-fluctuating signal is shown in Fig. 8.28 as a function of k/L for $P_d = 0.5$ and $P_f = 10^{-6}$. In this example, which is typical for a large range of operating points, the optimal value of k/L ranges from over 0.9 when L is small down to approximately 0.8 as L increases. This result supports the conclusions of [66] indicating minimal loss when k is chosen in the range of $\frac{3}{4}L$ to $\frac{7}{8}L$, with greater sensitivity when L is small.

Although the numerical analysis presented in Fig. 8.28 can be used to evaluate the CFAR loss for the OS(L, k) normalizer, an asymptotic analysis for large values of L is also informative. The CFAR processors form an estimate of the noise variance λ using L cells of auxiliary data. When the auxiliary data are uncorrupted, the variance of the unbiased estimate obtained by the order-statistic normalizer is larger than that for the cell-averaging normalizer. The increase in the number of auxiliary

data cells required by the order-statistic normalizer to achieve the same estimator variance as the cell-averaging normalizer is a measure of how poorly it does in benign background conditions. For example, it was shown in [62] that the number of samples required by a log normalizer to achieve the same performance as the cell-averaging normalizer is $L_{\log} = 1.65L_{\text{lin}} - 0.65$, nominally a 65% increase.

For a cell-averaging normalizer, the variance of the estimator is simply $1/L$ times the variance of a single auxiliary data cell,

$$\text{Var}\{\hat{\lambda}_{\text{CA}}\} = \frac{\lambda^2}{L}. \quad (8.382)$$

The mean of the k th order statistic, which is required to form an unbiased estimate of λ , can be obtained by using the description of $Y_{(k)}$ from (8.367),

$$E[Y_{(k)}] = \lambda \sum_{i=1}^k \frac{1}{L-i+1} \quad (8.383)$$

The variance, obtained similarly, is

$$\text{Var}\{Y_{(k)}\} = \lambda^2 \sum_{i=1}^k \frac{1}{(L-i+1)^2}. \quad (8.384)$$

Scaling the $\text{OS}(L, k)$ estimate of the noise variance to be unbiased results in

$$\text{Var}\{\hat{\lambda}_{\text{os}}\} = \lambda^2 \frac{\sum_{i=1}^k \frac{1}{(L-i+1)^2}}{\left[\sum_{i=1}^k \frac{1}{L-i+1} \right]^2}. \quad (8.385)$$

When L is large, the summations in (8.385) can be approximated by integrals to yield

$$\text{Var}\{\hat{\lambda}_{\text{os}}\} \approx \frac{\frac{k}{L} - \frac{1}{L}}{L \left(1 - \frac{k}{L} + \frac{1}{L} \right) \left[\log \left(1 - \frac{k}{L} + \frac{1}{L} \right) \right]^2}. \quad (8.386)$$

By differentiating (8.386) with respect to $r = (k-1)/L$, it can be shown that the variance will be minimized when

$$\frac{k-1}{L} = \log \left(\frac{1}{\sqrt{1 - \frac{(k-1)}{L}}} \right) \quad (8.387)$$

which occurs when $k \approx 0.8L + 1$. This result also corresponds to the limiting trend seen in Fig. 8.28 where the optimum value of k approaches $0.8L$ as L increases.

Using $k = 0.8L + 1$ while equating the variances in (8.382) and in (8.386) then results in

$$L_{\text{os}} = \frac{4 L_{\text{CA}}}{[\log(0.2)]^2} \approx 1.54 L_{\text{CA}}, \quad (8.388)$$

which indicates the $\text{OS}(L, 0.8L+1)$ normalizer requires 54% more cells of auxiliary data to achieve the same performance as the cell-averaging normalizer in a benign background. As shown in [63] and Figs. 8.26 and 8.27, this may be worth the cost when interferences cause target masking.

Although this analysis indicates how much larger a window of auxiliary data is required by the order-statistic normalizer, the CFAR loss for a given value of L is a more direct measure of the loss in performance. This can be approximated using the CFAR loss from the cell-averaging normalizer in (8.356) or (8.357) by using (8.388) to describe an equivalent value of L ,

$$L_{\text{eq}} = \frac{\left[\sum_{i=1}^k \frac{1}{L-i+1} \right]^2}{\sum_{i=1}^k \frac{1}{(L-i+1)^2}} \approx \frac{L}{1.54}, \quad (8.389)$$

for which a cell-averaging normalizer produces the same variance as the order-statistic normalizer. Note that the approximation on the far right side of (8.389) assumes $k = 0.8L+1$. Using L_{eq} from (8.389) in (8.356) to obtain an approximation to the CFAR loss for the $\text{OS}(L, 0.8L + 1)$ processor improves in accuracy as either L or P_f increase. When $L < 30$ using the exact moment ratio in (8.389) (i.e., evaluating the sums) is worthwhile compared with using $L_{\text{eq}} \approx L/1.54$.

8.7 Doppler Processing

In remote sensing systems with moving components the signal measurement is affected by Doppler. In active sensing, motion by any combination of the sound projector, object of interest, or sensor platform induces a Doppler effect on the signal measurement and potentially on interfering signals such as reverberation and ambient noise. As described in Sect. 2.2.5, this results in either a time compression or dilation in the measurement relative to the source signal. The basic Doppler relationships presented in earlier sections are summarized in Table 8.8. The sensitivity of the source signal to these effects, quantified by the ambiguity function (Sect. 8.3.2), dictates whether or not detection processing requires a search over an unknown Doppler scale and if estimation of the radial velocity is feasible or not. This section describes several topics within the context of Doppler processing for detection and estimation. In Sect. 8.7.1, the filter-bank implementation of a search over unknown Doppler is described along with an FFT approximation for

Table 8.8 Summary of Doppler relationships and where key results are found

Item	Description	Reference
Doppler time/frequency scale	η	Sect. 2.2.5
Radial velocity	v_r	
Closing range	$\eta > 1$ and $v_r > 0$	
Opening range	$\eta < 1$ and $v_r < 0$	
One-way propagation		
Doppler scale	$\eta \approx 1 + v_r/c_w$	Eq. (2.19)
Doppler frequency shift	$\Delta_f \approx v_r f_c/c_w$	Eq. (2.20)
Two-way monostatic geometry		
Doppler scale	$\eta \approx 1 + 2v_r/c_w$	Eq. (2.31)
Doppler shift	$\delta_f \approx 2v_r f_c/c_w$	Eq. (2.21)
Source signal	$s_o(t) \xleftrightarrow{\mathcal{F}} S_o(f)$	
Signal with Doppler		
Broadband	$s_o(\eta t) \xleftrightarrow{\mathcal{F}} \frac{1}{ \eta } S_o(f/\eta)$	Eq. (2.22)
Narrowband	$S_o(f/\eta) \approx S_o(f - \Delta_f)$ or $S_o(f - \delta_f)$	Eq. (7.108)
Approximations		
	$\pm 1 \text{ kn} \approx \pm 1 \text{ Hz}$ Doppler shift at 1.5 kHz (2-way) or 3 kHz (1-way)	
	$\eta = 1.001$ is 1.5 kn (2-way closing) or 3 kn (1-way closing)	
	$\eta = 0.999$ is 1.5 kn (2-way opening) or 3 kn (1-way opening)	
Speed conversions		
	$1 \text{ m/s} = 1.944 \text{ kn} = 3.6 \text{ kph} = 3.28 \text{ fps} = 2.24 \text{ mph}$	
	$1 \text{ kn} = 0.5144 \text{ m/s} = 1.85 \text{ kph} = 1.69 \text{ fps} = 1.15 \text{ mph}$	
	$c_w = 1500 \text{ m/s} = 2916 \text{ kn}$	

Legend: $\xleftrightarrow{\mathcal{F}}$ indicates a Fourier transform pair
 kn = knot
 m/s = meters per second
 kph = kilometers per hour
 fps = feet per second
 mph = miles per hour

CW pulses. A MATLAB® example of the FFT-based Doppler filter bank can be found in Appendix 8.A. The impact of reverberation on detection for Doppler-sensitive waveforms is covered in Sect. 8.7.2, including the reverberation ridge and the reverberation level (RL) term in the sonar equation. Finally, the topic of normalization (i.e., background noise power estimation) for CW pulses is covered in Sect. 8.7.3.

8.7.1 Doppler Filter Bank

A Doppler filter bank is simply a discrete implementation of the generalized likelihood ratio (GLR) detector described in Sect. 8.2.8.2 when the radial velocity of the object of interest is unknown. For the given sensing scenario there will be a subset of radial velocities expected to be encountered; for example, the interval $(-v_{\max}, v_{\max})$. A Doppler filter bank implements N matched filters tuned to a discrete set of velocities spanning this interval. The spacing of the filters, which are often called Doppler “channels,” is dictated by the width of the ambiguity function in the Doppler-scale dimension. The maximum (normalized) response of the Doppler filter bank provides estimates of the arrival time and Doppler scale (or shift) of the signal.

At a given point in time, the GLR detector decision statistic is the maximum over the decision statistics of the individual matched filters (i.e., Doppler channels). If the sampled complex envelope data for time sample i are in the vector \mathbf{x}_i , then the normalized instantaneous intensity for the filter tuned to Doppler scale η_j is

$$Y_{i,j} = \frac{|\mathbf{s}_{\eta_j}^H \mathbf{x}_i|^2}{\lambda}. \quad (8.390)$$

The decision statistic for time sample i , when searching for just one signal of interest, is then

$$T_i = \max_j Y_{i,j}. \quad (8.391)$$

In practice there may be more than one signal of interest, so each of the Doppler channels is compared with a threshold instead of just the largest.

Analyzing the detection performance of a Doppler filter bank is most easily done under the assumption that $Y_{i,j}$ is independent of $Y_{i,k}$ when $j \neq k$. This can be achieved by choosing the set of Doppler scales η_1, \dots, η_N so that \mathbf{s}_{η_j} is orthogonal to \mathbf{s}_{η_k} when $j \neq k$,

$$\mathbf{s}_{\eta_k}^H \mathbf{s}_{\eta_j} = 0 \text{ for } j \neq k. \quad (8.392)$$

When the Doppler channels are statistically independent of each other, the CDF of the decision statistic is easily seen to be the product

$$\begin{aligned} F_T(t) &= \Pr\{T \leq t\} \\ &= \Pr\left\{\max_j Y_{i,j} \leq t\right\} \\ &= \Pr\{Y_{i,1} \leq t, \dots, Y_{i,N} \leq t\} \end{aligned}$$

$$= \prod_{j=1}^N F_{Y_{i,j}}(t) \quad (8.393)$$

of the CDFs of $Y_{i,j}$ for $j = 1, \dots, N$.

8.7.1.1 Probability of False Alarm in a Filter Bank

Under the noise-only hypothesis and with perfect normalization, the instantaneous-intensity samples from the Doppler channels are exponentially distributed with unit mean,

$$Y_{i,j}|H_0 \sim \text{Expon}(1). \quad (8.394)$$

Using $F_0(y) = 1 - e^{-y}$ for $y \geq 0$, the CDF of the unit-mean exponential distribution from Sect. 5.6.10, in (8.393), the probability of false alarm is seen to be

$$P_f = 1 - F_T(h|H_0) = 1 - \left(1 - e^{-h}\right)^N. \quad (8.395)$$

Solving (8.395) for the detector decision threshold results in

$$h = -\log \left[1 - (1 - P_f)^{1/N} \right] \quad (8.396)$$

$$\approx -\log(P_f) \left[1 + \log(N) \frac{(1 - P_f) \log(1 - P_f)}{P_f \log P_f} \right] \quad (8.397)$$

$$\approx -\log(P_f) + \log(N) \quad (8.398)$$

where the approximation in (8.397) is obtained as a first-order Maclaurin series for $\log(N)$ and (8.398) is formed by assuming $P_f \ll 1$. The approximation illustrates what is intuitively obvious: as more Doppler channels are added, the decision threshold must be increased in order to maintain a desired probability of false alarm. When P_f is small, the decision threshold as applied to the normalized instantaneous intensity for a single matched filter must be increased by approximately $\log N$ when there are N Doppler channels. This is the same analysis as that presented in Sect. 8.2.11 for the false-alarm-rate when the arrival time is unknown, as can be seen from the similarity between (8.395) and (8.109). This allows interpreting the effect of searching over N statistically independent Doppler channels as requiring a probability of false alarm that is N times smaller at an individual Doppler channel than the desired P_f .

8.7.1.2 Probability of Detection in a Filter Bank

When signal is present and its radial velocity is precisely matched by one of the Doppler channels, it only enters the filter bank in this channel because of the orthogonality assumption made in (8.392). The remaining $N - 1$ channels contain only noise. With this characterization, the probability of detection is

$$\begin{aligned} P_d &= 1 - F_T(h|H_1) \\ &= 1 - F_Y(h|H_1)(1 - e^{-h})^{N-1} \\ &= 1 - F_Y(h|H_1)(1 - P_f)^{1-1/N} \end{aligned} \quad (8.399)$$

$$\approx 1 - F_Y(h|H_1). \quad (8.400)$$

The approximation forming (8.400), which assumes $P_d \gg P_f$, implies that P_d in the filter bank for a given decision threshold is the same as it is for the individual filter tuned to the correct Doppler scale. It can also be argued that (8.400) is a more appropriate measure of the probability of detection than (8.399) because it only allows the threshold exceedance to occur in the filter matched to the signal of interest, ignoring any serendipitous threshold crossings from the Doppler channels dominated by noise. The case of a signal of interest having radial velocity in between the discrete sampling implemented in the filter bank is handled in practice by forming more densely spaced Doppler channels with an effect on P_d and P_f similar to that discussed in Sect. 8.2.11.1 when the matched filter is oversampled in time.

The cost of using a Doppler filter bank when the radial velocity of the object of interest is unknown starts with the increase in the probability of false alarm for a given threshold relative to testing a single matched filter. In order to maintain a desired probability of false alarm, a higher threshold (via (8.396)) is necessary than for a single matched filter. Given the higher threshold, an increase in SNR is then required to maintain a desired probability of detection. The SNR loss associated with the Doppler filter bank is the additional SNR required to maintain a (P_d, P_f) performance specification given there are N statistically independent Doppler channels.

Using the CDF of Y for a Gaussian-fluctuating signal in Gaussian noise, $F_Y(h|H_1) = 1 - e^{-h/(1+S^d)}$, in (8.400) and solving for the SNR required to achieve the desired operating point results in

$$S^d = \frac{h}{-\log P_d} - 1 = \frac{\log[1 - (1 - P_f)^{1/N}]}{\log P_d} - 1. \quad (8.401)$$

This can then be used to evaluate the SNR loss associated with implementing the filter bank,

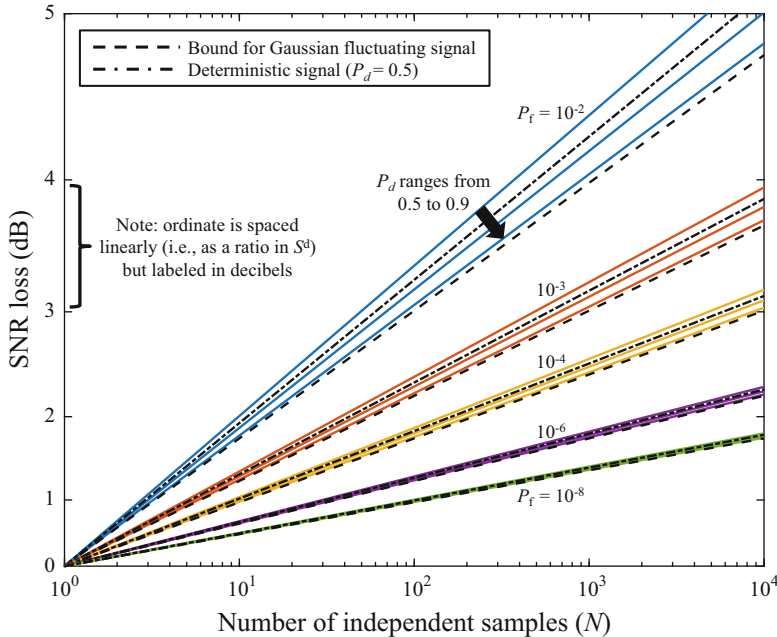


Fig. 8.29 SNR loss when searching over N independent samples (e.g., Doppler channels and/or time samples) for several values of P_f and P_d . The colored lines are from (8.402) whereas the black dashed line is the lower bound from (8.404) with both representing a Gaussian-fluctuating signal. The black dash-dot line is the result for a deterministic signal when $P_d = 0.5$, obtained using Hmam's equation

$$\text{Loss}_{\text{dB}} = 10 \log_{10} \left\{ \frac{\log P_d - \log [1 - (1 - P_f)^{1/N}]}{\log P_d - \log P_f} \right\} \quad (8.402)$$

$$\approx 10 \log_{10} \left\{ 1 + \frac{\log N}{\log P_d - \log P_f} \right\} \quad (8.403)$$

$$\geq 10 \log_{10} \left\{ 1 - \frac{\log N}{\log P_f} \right\}. \quad (8.404)$$

The approximation in (8.403) comes from using (8.398) whereas the lower bound in (8.404) is obtained by letting $P_d \rightarrow 1$. The SNR loss for the Gaussian-fluctuating signal from (8.402) is shown in Fig. 8.29 for $P_d = 0.5, 0.7$, and 0.9 and several values of P_f as the colored lines. It can immediately be seen that the loss incurred by implementing a Doppler filter bank to account for an object of interest's unknown radial velocity is not overly large. Note that the results shown in Fig. 8.29 apply not only to searching over Doppler channels but also over arrival time when it is unknown, which is why the abscissa is labeled as the number of independent samples. The lower bound from (8.404) (black dashed line in Fig. 8.29) is seen to be

an adequate approximation to the SNR loss when P_f is small or when P_d is large. Note that the ordinate in Fig. 8.29 is spaced according to an SNR ratio in linear form (i.e., S_d); however, it is labeled in decibels and the abscissa is logarithmically spaced in N . The linearity of the colored lines in Fig. 8.29 using these scales represents the linearity with $\log N$ of the SNR loss from (8.402) in the form $10^{\text{LOSS}_{\text{dB}}/10}$, and indicates (8.403) and (8.404) are good approximations. This also emphasizes that the SNR loss does not increase proportionally with the number of Doppler channels, but only by $\log N$ for the linear SNR ratio.

The SNR loss for a deterministic signal can be obtained by using the approximation in (8.400) and either Albersheim's or Hmam's equation from Sect. 2.3.5.2. Although Hmam's equation is more accurate and can be easily implemented numerically, Albersheim's equation yields a useful analytic result. The SNR loss is obtained by the difference in $\overline{\text{SNR}}^d$ (i.e., the SNR in decibels required to meet a performance specification) using the same value of P_d and then

$$\tilde{P}_f = 1 - (1 - P_f)^{1/N} \approx \frac{P_f}{N} \quad (8.405)$$

for the Doppler filter bank compared with using P_f for a single Doppler channel. Albersheim's equation from (2.85) requires the intermediate variables $B = \log[P_d/(1 - P_d)]$ and $A_1 = \log(0.62/P_f)$ for a single Doppler channel or $A_N = \log(0.62/\tilde{P}_f) \approx A_1 + \log N$ for N of them. The SNR loss is then approximately

$$\begin{aligned} \text{Loss}_{\text{dB}} &= 10 \log_{10}(A_N + 0.12A_N B + 1.7B) - 10 \log_{10}(A_1 + 0.12A_1 B + 1.7B) \\ &\approx 10 \log_{10} \left\{ 1 + \frac{\log N}{\frac{1.7B}{1+0.12B} + \log 0.62 - \log P_f} \right\} \end{aligned} \quad (8.406)$$

where M is set to one in (2.85). The form of (8.406) is identical to the approximation in (8.403) for the Gaussian-fluctuating signal when $P_d = 0.456$ (i.e., where $\log P_d = 1.7B/(1 + 0.12B) + \log 0.62$). This can be seen in Fig. 8.29 where the loss for the deterministic signal (the black dash-dot line) for $P_d = 0.5$ is similar to that for the Gaussian-fluctuating signal. However, as P_d decreases or increases from 0.456 there will be an increase or decrease, respectively, in the loss relative to that for the Gaussian-fluctuating signal that can be significant when P_d nears the extremes of zero or one.

8.7.1.3 Doppler Filter Bank Example

As an example design of a Doppler filter bank, suppose the sensing waveform is a $T_p = 1$ s CW pulse at $f_c = 2$ kHz and that the object of interest is expected to have radial velocity within ± 15 kn. From the ambiguity function of the CW pulse in (8.163) it can be seen that when $\tau = 0$ the first zero-crossing in the Doppler dimension occurs when the frequency shift $\delta = 1/T_p$. This means independent

Doppler channels should be spaced in frequency every $1/T_p$. For a monostatic active sonar system, for which $\delta = 2v_r f_c / c_w$, the spacing in radial velocity is

$$\Delta_v = \frac{c_w}{2f_c T_p}. \quad (8.407)$$

To span the range $(-v_{\max}, v_{\max})$, this requires

$$N = \frac{2v_{\max}}{\Delta_v} = \frac{4f_c T_p v_{\max}}{c_w} \quad (8.408)$$

Doppler channels. For the example, this results in $N = 42$ channels where 15 kn converts to 7.7 m/s and assuming $c_w = 1500$ m/s.

An example normalized instantaneous intensity produced by the Doppler filter bank is shown in Fig. 8.30 (note that the normalization is with respect to the ambient noise power). The echo from an object of interest is seen at 30 s with a radial velocity of 5 kn. This echo appears very similar to the reverberation occasionally

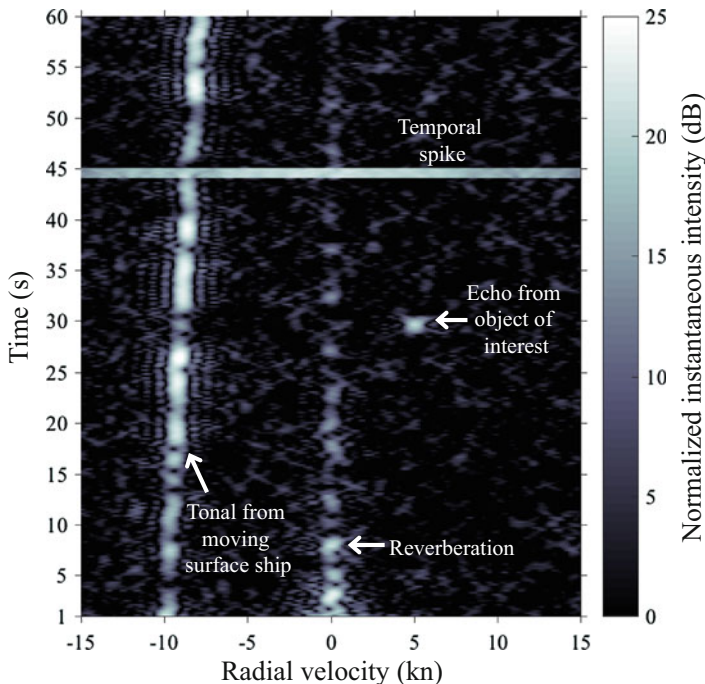


Fig. 8.30 Instantaneous intensity of a Doppler filter bank for a 1-s CW-pulse at 2 kHz, searching over ± 15 kn, and normalized by the ambient background noise power. The echo from an object of interest is seen at 30 s with a 5-kn radial velocity. Common interferences include the reverberation ridge at zero radial velocity, broadband temporal spikes, and tonal signals with time-varying frequency from moving surface ships

dominating the zero-Doppler channel (i.e., a radial velocity of 0 kn) and illustrates how difficult it is to detect echoes from objects having no radial velocity with a CW pulse. Other common interferences affecting detection of CW pulses include temporal spikes such as the one shown at 45 s. When even one temporal sample is corrupted with an abnormally large value, the Doppler filter bank can be affected over the extent of the pulse and across a wide range of Doppler channels. A source of narrowband interference is found in the tonal components radiated by surface ships (Sect. 7.2). The example shown in Fig. 8.30 illustrates how the frequency of the tone, and therefore the affected Doppler channel, can vary with the motion of the surface ship.

8.7.1.4 FFT Implementation of a CW-Pulse Doppler Filter Bank

When a finite-duration sensing waveform (i.e., a pulse) is subjected to a Doppler scale, its duration changes. If the pulse $s(t)$ has duration T_p , then under the Doppler scale η , $s(\eta t)$ will have duration T_p/η . For the stationary monostatic active sonar scenario where $\eta \approx 1 + 2v_r/c_w$ and v_r is the radial velocity, this represents a change of approximately

$$\Delta_t = T_p - \frac{T_p}{\eta} \approx \frac{2v_r T_p}{c_w}. \quad (8.409)$$

When the object of interest is closing ($v_r > 0$) the echo is shorter than the projected pulse and when it is opening ($v_r < 0$) the echo is longer.

This implies that the replica used to form the matched filter for a particular Doppler channel will have a temporal duration that depends on η . However, as noted in [30], the change in pulse length need only be accounted for if the waveform has the capability to sense it. If the pulse bandwidth is W , the pulse cannot sense the time difference when

$$\frac{2|v_r|}{c_w} T_p W \ll 1. \quad (8.410)$$

For a CW pulse where $W = 1/T_p$, this only requires

$$|v_r| \ll \frac{c_w}{2}, \quad (8.411)$$

which is satisfied in essentially all applications of underwater acoustics. This means the signal replica across the whole Doppler filter bank can have a fixed pulse duration of T_p without concern for the loss arising from mismatch. For broadband pulses with large bandwidth-duration products, however, (8.410) may indicate a need for careful construction of the replica for each Doppler channel.

There is a distinct advantage to using a replica with the same duration across the Doppler filter bank for CW pulses in that a fast-Fourier transform (FFT)

applied to the basebanded signal measurement can be used to simultaneously obtain the response of all the filters in the filter bank for a given time delay. Because the Doppler scale is unknown, the signal measurement is basebanded using the frequency of the original CW pulse (f_c). When $\eta \neq 1$, this is different from the center frequency of the signal measurement and so (7.49) must be used to obtain the baseband signal replica to be used in the matched filter. For a CW pulse with an amplitude function $a(t)$, Doppler scale η , and zero temporal offset, this results in

$$\begin{aligned}\tilde{s}_\eta(t) &= a(\eta t) \left[e^{j2\pi f_c(\eta-1)t} \right] \\ &\approx a(t) \left[e^{j2\pi \delta t} \right],\end{aligned}\quad (8.412)$$

which is an amplitude-weighted sinusoid at frequency $\delta = f_c(\eta - 1)$. The matched filter simply correlates the signal measurement with the replica in (8.412). When δ is discretized, the correlation can be accomplished efficiently through the use of an FFT applied to the signal measurement using a window with the form of $a(t)$. If the basebanded replica and signal measurement have been sampled at rate f_s with $T = 1/f_s$, then the complex form of the matched filter response at delay τ is

$$\begin{aligned}y[\tau, k] &= \sum_{n=0}^{N-1} \tilde{s}_\eta^*(nT) \tilde{x}_b(\tau + nT) \\ &= \sum_{n=0}^{N-1} a(nT) \exp \left\{ -j2\pi \left(\frac{kf_s}{N} \right) (nT) \right\} \tilde{x}_b(\tau + nT) \\ &= \sum_{n=0}^{N-1} a(nT) \tilde{x}_b(\tau + nT) e^{-j2\pi kn/N}\end{aligned}\quad (8.413)$$

where δ is replaced with $f_s k / N$ for $k = 0, \dots, N - 1$ to implement the FFT. For a given delay τ , the sum in (8.413) is the FFT of $x_a[n] = a(nT) \tilde{x}_b(\tau + nT)$ for $n = 0, \dots, N - 1$. This process is then repeated for all the delay values of interest. Because the temporal resolution of the (unshaded) CW pulse is equal to its duration, this is not particularly burdensome. Example MATLAB® code implementing the FFT-based Doppler filter can be found in Appendix 8.A.

The radial velocity associated with the k th FFT bin (producing the k th Doppler channel) can be obtained using the FFT index-to-frequency mapping from (4.99) and $\delta = 2v_r f_c / c_w$ from the stationary monostatic active sonar application,

$$v_{r,k} = \begin{cases} \frac{k}{N} \frac{c_w f_s}{2f_c} & 0 \leq k < \frac{N}{2} \\ \left(\frac{k-N}{N} \right) \frac{c_w f_s}{2f_c} & \frac{N}{2} \leq k \leq N-1 \end{cases}\quad (8.414)$$

$$\approx \begin{cases} \frac{c_w}{2f_c T_p} k & 0 \leq k < \frac{N}{2} \\ \frac{c_w}{2f_c T_p} (k - N) & \frac{N}{2} \leq k \leq N - 1 \end{cases} \quad (8.415)$$

where (8.415) is formed by noting that $T_p \approx N/f_s$. The maximum speed represented by the filter bank, $\max_k |v_{r,k}| = c_w f_s / (4f_c)$, is controlled by the sampling rate f_s (i.e., higher speeds require more bandwidth which requires a higher sampling rate). The Doppler bin spacing described by (8.415) assumes that $N = T_p f_s + 1$ is a power of two. When it is not, f_s can be increased until it is (and the resulting higher-speed Doppler channels ignored) or the N samples of $x_a[n]$ can be zero-padded to the closest power of two $N_f = 2^{\lceil \log_2 N \rceil}$ greater than N . Recalling that zero-padding an FFT is equivalent to interpolating the N -point DFT, this will produce Doppler channels with a finer spacing in radial velocity,

$$v_{r,k} = \begin{cases} \frac{c_w}{2f_c T_p} k \left(\frac{N}{N_f} \right) & 0 \leq k < \frac{N_f}{2} \\ \frac{c_w}{2f_c T_p} (k - N_f) \left(\frac{N}{N_f} \right) & \frac{N_f}{2} \leq k \leq N_f - 1 \end{cases}, \quad (8.416)$$

which also results in correlation between channels.

8.7.2 Reverberation in a Doppler Filter Bank

In the Doppler-filter-bank response shown in Fig. 8.30, reverberation is seen as a decaying instantaneous intensity at 0 kn radial velocity because both the sonar platform and the reverberation scatterers are stationary in the example. This response is known as the *reverberation ridge* because it is typically limited to a small range of radial velocities. The shape of the reverberation ridge in the radial velocity dimension depends predominantly on the pulse spectrum as described in Sect. 7.4.2.3. Recall, however, that it can be shifted and/or spread in the radial-velocity dimension by motion of the sonar platform or the scattering sources (e.g., see Sect. 7.4.2.4). When ownship Doppler nullification (ODN) is applied, as described in Sect. 3.5.7, the abscissa in the Doppler filter bank becomes the radial velocity relative to the sonar receiving platform and so the reverberation ridge is located at the zero-Doppler channel. However, spreading arising from platform motion and beamforming will still vary with the beam direction.

When a matched filter is applied to the measured reverberation, elemental scatterers with an arrival time in the interval $[\tau - T_p, \tau + T_p]$ can impact the matched filter response for time τ . In terms of detection, the average instantaneous intensity of the reverberation signal after matched filtering drives performance. To determine this, suppose the reverberation for time τ out of the matched filter comprises n_r statistically independent elemental scatterers. The analytic signal of the reverberation measurement can then be described as the sum

$$\dot{s}(t) = \sum_{i=1}^{n_r} Z_{r,i} \dot{s}(t - U_i) \quad (8.417)$$

where $Z_{r,i}$ and U_i are, respectively, the complex amplitude and arrival time of the i th scatterer. Using (8.128), the response to a sampled reverberation time series (\mathbf{r}) of a filter matched to delay τ and Doppler scale η is

$$\begin{aligned} \mathbf{s}^H \mathbf{r} &\approx W \int_{-\infty}^{\infty} \dot{s}^*(\eta[t - \tau]) \dot{s}(t) dt \\ &= W \sum_{i=1}^{n_r} Z_{r,i} \int_{-\infty}^{\infty} \dot{s}^*(\eta[t - \tau]) \dot{s}(t - U_i) dt \\ &\approx W \sum_{i=1}^{n_r} Z_{r,i} \chi(\tau - U_i, \eta) \end{aligned} \quad (8.418)$$

Now suppose the reverberation scatterers are significantly smaller than the temporal resolution capability of the waveform and the acoustical conditions (i.e., propagation and scattering) do not change significantly over the ensonified extent of the ocean for a delay time of τ . Under these conditions, the complex amplitude of the elemental reverberation scatterers can be assumed to be zero mean with a constant variance σ_r^2 and be independent of their arrival time. The average instantaneous intensity of the reverberation response to the matched filter is then

$$\begin{aligned} \lambda_r &= E[|\mathbf{s}^H \mathbf{r}|^2] \\ &= W^2 \sum_{i=1}^{n_r} \sum_{j=1}^{n_r} E[Z_{r,i} Z_{r,j}^*] E[\chi^*(\tau - U_i, \eta) \chi(\tau - U_j, \eta)] \\ &= W^2 \sigma_r^2 n_r E[|\chi(\tau - U_i, \eta)|^2]. \end{aligned} \quad (8.419)$$

If the elemental reverberation scatterers occur in the time response in a uniformly random manner over a temporal extent T_r that contains the interval $[\tau - T_p, \tau + T_p]$, then

$$\lambda_r(\eta) = W^2 \sigma_r^2 \beta_r \int_{-\infty}^{\infty} |\chi(\tau, \eta)|^2 d\tau \quad (8.420)$$

where $\beta_r = n_r / T_r$ [units: #/s] is a measure of the density of the elemental scatterers in time as their echoes arrive at the sensor. Using (8.129) it can be seen that $W^{-1} = \chi(0, 1)$ so defining the function

$$Q_r(\eta) = \int_{-\infty}^{\infty} \left| \frac{\chi(\tau, \eta)}{\chi(0, 1)} \right|^2 d\tau \quad (8.421)$$

results in $\lambda_r(\eta) = \sigma_r^2 \beta_r Q_r(\eta)$, which isolates the waveform-dependent effects into a single function. This function, which has units of time (s), can be interpreted as the effective temporal extent from which the waveform allows reverberation scatterers to contribute to the matched filter response—a waveform-dependent reverberation temporal-support function. It is colloquially known as the “ Q ” function (not to be confused with Marcum’s Q function). When $Q_r(\eta)$ is larger for one waveform than another it implies the former waveform will observe a larger reverberation power level after matched filtering than the latter. When a signal is reverberation-limited, this means the detection performance of the waveform with the larger $Q_r(\eta)$ will be worse.

The average reverberation intensity in (8.420) and the reverberation temporal-support function in (8.421) are described as functions of η . However, this is a simplification enabling the current objective of assessing the impact of reverberation on different waveforms given a specific delay time τ (i.e., both the density and σ_r^2 will change with the range of the elemental scatterers and therefore τ). The more general case is described in [68] and [13, Sect. 13.2.1] where reverberation can be non-uniform and is described through use of a scattering function which allows consideration of more general scenarios than the simple one considered here.

8.7.2.1 Detection in Reverberation and Noise

When reverberation is assumed to follow the Rayleigh-envelope distribution chain, detection performance can be evaluated through the same formulas as for detecting a signal in Gaussian noise by replacing the noise power with the noise-plus-reverberation power. The resulting SNR is more properly described as a signal-to-interference-and-noise ratio (SINR). However, the SINR must be evaluated after matched filtering. Toward this end, suppose the sampled-data measurement \mathbf{x} for delay time τ contains a signal reflected from a point target with radial velocity η_o ($Z_s \mathbf{s}_{\eta_o}$), reverberation (\mathbf{r}) and ambient noise (\mathbf{v}),

$$\mathbf{x} = Z_s \mathbf{s}_{\eta_o} + \mathbf{r} + \mathbf{v}. \quad (8.422)$$

The complex response of the Doppler filter bank in the channel tuned to Doppler scale η is

$$\mathbf{s}_\eta^H \mathbf{x} = Z_s \mathbf{s}_\eta^H \mathbf{s}_{\eta_o} + \mathbf{s}_\eta^H \mathbf{r} + \mathbf{s}_\eta^H \mathbf{v}. \quad (8.423)$$

Using (8.3), the average instantaneous intensity of the noise component $\mathbf{s}_\eta^H \mathbf{v}$ is

$$E\left[|\mathbf{s}_\eta^H \mathbf{v}|^2\right] = 2N_0 W \quad (8.424)$$

where $N_0/2$ is the two-sided noise PSD. The average instantaneous intensity of the signal component can be found by using (8.16) and (8.126),

$$E\left[|Z_s \mathbf{s}_\eta^H \mathbf{s}_{\eta_o}|^2\right] = 2\mathcal{E}_o W \mathcal{L}_Q^d\left(0, \frac{\eta_o}{\eta}\right) \quad (8.425)$$

where \mathcal{E}_o is the energy in the bandpass signal measurement and $\mathcal{L}_Q^d(\tau, \eta)$ is the SNR loss factor for the QMF from (8.140). Because the reverberation essentially comprises reflections of the projected pulse, $\sigma_r^2 = 2\mathcal{E}_r W$ from (8.16) where \mathcal{E}_r is the energy in the bandpass reflection from a single elemental scatterer.

Combining these average instantaneous intensities to produce the signal-to-reverberation-and-noise power ratio results in

$$\begin{aligned} \text{SINR} &= \frac{\mathcal{E}_o \mathcal{L}_Q^d\left(0, \frac{\eta_o}{\eta}\right)}{N_0 + \beta_r \mathcal{E}_r Q_r(\eta)} \\ &\leq \frac{\mathcal{E}_o}{N_0 + \beta_r \mathcal{E}_r Q_r(\eta)} \end{aligned} \quad (8.426)$$

where the equality in the upper bound is achieved when the Doppler filter bank channel perfectly matches the Doppler scale of the signal, $\eta = \eta_o$. As would be expected, the SINR simplifies to \mathcal{E}_o/N_0 when the ambient noise dominates and $\mathcal{E}_o/[\beta_r \mathcal{E}_r Q_r(\eta)]$ when reverberation dominates. These relationships confirm the sonar-equation analysis from Sect. 2.3.3 where increasing the energy of the projected pulse improves performance in noise-limited conditions whereas it does not in reverberation limited conditions because both \mathcal{E}_o and \mathcal{E}_r are proportional to the energy in the transmitted pulse. The significance of the reverberation temporal-support function $Q_r(\eta)$ term in (8.426) is that it encapsulates all the other effects of the waveform on detection performance in reverberation.

8.7.2.2 Reverberation Temporal-Support Function for CW and FM Pulses

The reverberation temporal-support function $Q_r(\eta)$ from (8.421), which is the integrated squared-modulus of the normalized waveform AF over delay is easily evaluated for a CW pulse. Using the narrowband AF for the CW pulse from (8.163) in (8.421) results in

$$Q_r(v_r) = \frac{1}{T_p \delta^2 \pi^2} [1 - \text{sinc}(2\delta T_p)]$$

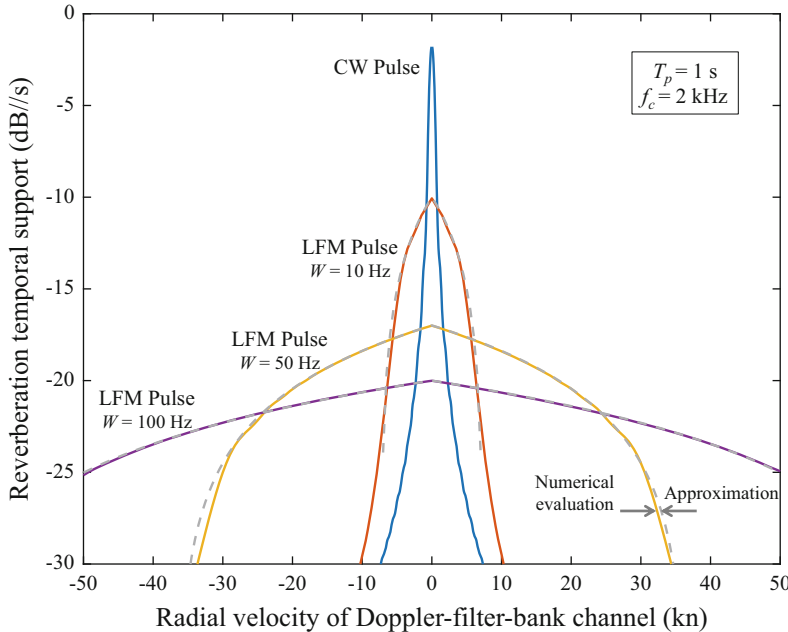


Fig. 8.31 Reverberation temporal-support function, $Q_r(v_r)$, for CW and LFM pulses as a function of the radial velocity of the Doppler-filter-bank channel. For pulses having equal energy in their projection, the function encapsulates the other effects of the waveform on the average instantaneous intensity of reverberation after matched filtering. For the LFM pulse the gray lines are the approximation in (8.428) whereas the colored lines are a numerical evaluation of (8.421)

$$= \frac{1}{T_p} \left(\frac{c_w}{2\pi f_c v_r} \right)^2 \left[1 - \text{sinc}\left(\frac{4T_p v_r f_c}{c_w}\right) \right] \quad (8.427)$$

where η has been converted to radial velocity v_r using the Doppler frequency shift $\delta = 2v_r f_c / c_w \approx (\eta - 1)f_c$ for a stationary monostatic active sonar system. An example is shown in Fig. 8.31 for $T_p = 1$ and $f_c = 2$ kHz as a function of the relative radial velocity v_r . For the CW pulse, the peak value $\max_{v_r} Q_r(v_r) = 2T_p/3$ (which occurs when $v_r = 0$) is proportional to pulse duration. This implies that decreasing CW-pulse duration while keeping the energy of the projected pulse constant (i.e., by increasing the source power level) can improve performance in reverberation limited scenarios. This is expected because a shorter pulse ensonifies fewer elemental scatterers thereby reducing the reverberation level, as was noted in Sect. 3.5 for volume and boundary reverberation.

Integrating the LFM-pulse AF over delay is not as simple as for the CW pulse. However an approximation to the reverberation temporal-support function for the LFM pulse can be obtained by arguing that the width of its ACF is $1/W$ and noting that a Doppler scale results in less overlap in frequency between the replica and zero-Doppler reverberation measurement. Assuming the pulse only allows contributions from a temporal extent of $1/W$ for the full overlap observed in the zero-Doppler

channel (i.e., when $\eta = 1$ or $v_r = 0$) and proportionately less for partial overlap, the approximation becomes the triangularly shaped function

$$Q_r(v_r) \approx \frac{1}{W} \left(1 - \frac{2|v_r|f_c}{c_w W} \right) \quad (8.428)$$

for $|v_r| < c_w W/(2f_c)$. The approximation is compared to a numerical evaluation of (8.421) for bandwidths of 10, 50, and 100 Hz (with $T_p = 1$ and $f_c = 2$ kHz as for the CW pulse) in Fig. 8.31. The approximation (gray dashed lines) is quite good when the magnitude of the Doppler frequency shift is small relative to the waveform bandwidth. Noting the similarity of the LFM and HFM AFs when W/f_c is small, the approximation is also useful for HFM pulses. Even when W/f_c is large, the overlap may be large enough for the approximation to be accurate at the more moderate Doppler frequency shifts encountered in most underwater acoustics applications. The peak value, $\max_{v_r} Q_r(v_r) = 1/W$, illustrates how increasing LFM-pulse bandwidth has a direct impact on performance in reverberation limited conditions by a proportionate increase in the signal to reverberation power ratio. Here increasing bandwidth has the effect of reducing the effective ensonified volume or area after the pulse-compression achieved by matched filtering.

As can be seen in Fig. 8.31, the reverberation temporal-support for the LFM pulse is clearly lower than that for a CW pulse for the Doppler-filter-bank channels that reside within the CW-pulse reverberation ridge. However, above some radial speed (that increases with the LFM-pulse bandwidth and Doppler-spreading of the reverberation) the temporal support of the reverberation for the CW-pulse is less than that of the LFM-pulse. In this regime, the CW-pulse is limited by ambient noise whereas the LFM-pulse may still be limited by reverberation.

When assessing a waveform for use in active sensing, it is important to consider how well it will work in reverberation-limited conditions. Beyond the CW- and LFM-pulse examples presented here, some waveforms have “thumbtack”-like AFs [11, Ch. 5] with a very narrow peak in the time and Doppler dimensions that rides on a lower-level plateau. The narrow peak can provide simultaneously good resolution in both time and Doppler. However, the waveform may not perform well in reverberation relative to an LFM pulse having an equivalent bandwidth if the plateau integrates up to a value greater than $1/W$.

8.7.3 Normalization for CW Pulses

In Sect. 8.6 a split-window normalizer was introduced where leading and lagging windows surrounding the test cell were used to estimate the average instantaneous intensity of the noise. An inherent assumption in such a structure is that the noise is stationary (i.e., its level does not vary) over the temporal extent of the window (T_a). If the bandwidth of the waveform is W , then $L \approx T_a W$ independent samples are available. For broadband waveforms, T_a can usually be chosen to satisfy the

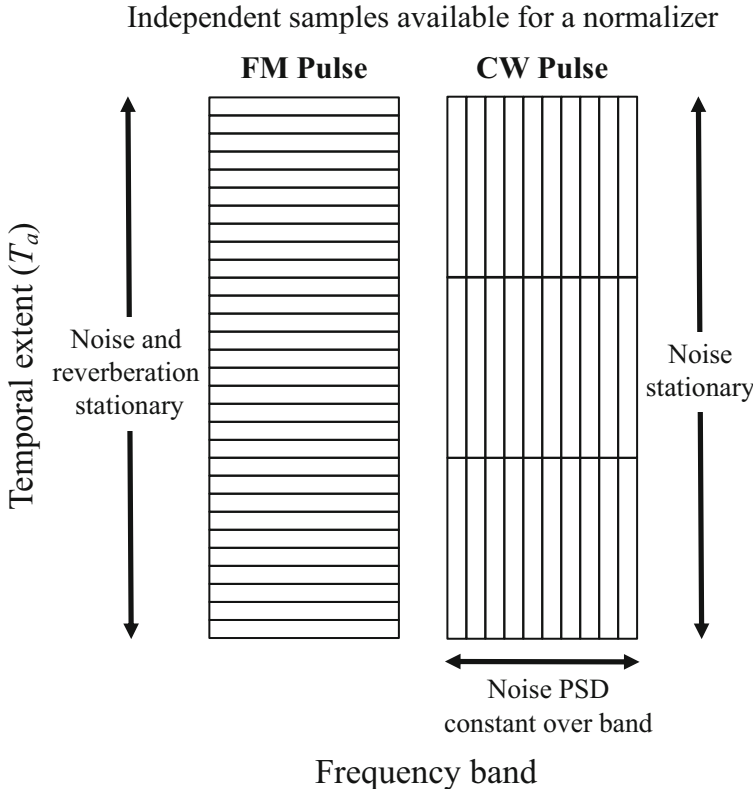


Fig. 8.32 Time-frequency arrangement of independent samples available in normalization for CW and FM pulses

balance between being large enough to keep the CFAR loss small while being small enough to satisfy the stationarity requirements. However, for CW pulses where $W = 1/T_p$, this only produces $L \approx T_a/T_p$ independent samples which might not be enough to reduce the CFAR loss to an acceptable level. However, if the Doppler filter bank is restricted to using noise-limited channels (i.e., excluding the channels within the reverberation ridge) the stationarity of the ambient noise, which can be up to three minutes as noted in [69] (see Sect. 7.4.1), should provide an adequate number of independent samples. A second alternative also exists where the noise PSD is assumed to be constant over some small frequency band and data from other Doppler channels are used to augment the estimate [70]. A comparison of where independent samples are obtained for FM and CW pulses is shown in Fig. 8.32 for a fixed region of the time-frequency plane. The FM pulse approach obtains L samples with a $1/W$ spacing in time under the assumption that the background level is stationary over the whole extent. Although the CW pulse makes the same assumption when $T_a > T_p$ (e.g., the window shown is $T_a = 3T_p$) the differences

will be less owing to the longer resolution cells and there is no such requirement if $T_a = T_p$. However, when multiple Doppler channels are used in the CW-pulse normalizer to estimate the background noise power, the noise PSD is assumed to be constant over the frequency band. In either approach, the total number of independent samples available is the time-bandwidth product ($L \approx T_a W$).

From the characterization of ambient noise in Sect. 3.3, the noise PSD can have a frequency dependence as sharp as $1/f^4$ in the infrasonic region and encounter up to $1/f^2$ and $1/f^{1.59}$ in, respectively, the shipping and wind-related noise regimes. As described in Sect. 3.5, reverberation power can vary with range up to $1/r^2$ for spherical spreading and volume scatterers. To determine the impact of a frequency- or range-dependent background power in the normalizer auxiliary data, suppose the l th of L samples has average λ_l ; that is, $Y_l \sim \text{Expon}(\lambda_l)$ as opposed to the *iid* assumption made in (8.328). The cell-averaging estimate $\hat{\lambda}$ of the background power is still the sample mean over Y_1, \dots, Y_L found in (8.329). However, its average value is

$$\bar{\lambda} = \frac{1}{L} \sum_{l=1}^L \lambda_l \quad (8.429)$$

which may differ from the true value λ and result in a biased estimator. When L is not too small, it is reasonable to approximate $\hat{\lambda}$ as being gamma distributed with the parameters obtained by equating the first two moments of $\hat{\lambda}$ and the gamma distribution. Defining

$$\sigma_{\lambda}^2 = \frac{1}{L} \sum_{l=1}^L (\lambda_l - \bar{\lambda})^2 \quad (8.430)$$

as the variability of the background power in the auxiliary data, the moment-matched gamma-distribution has shape parameter

$$\alpha_{\lambda} = \frac{L}{1 + \frac{\sigma_{\lambda}^2}{\bar{\lambda}^2}} \quad (8.431)$$

and scale parameter

$$\beta_{\lambda} = \frac{\bar{\lambda}}{L} \left(1 + \frac{\sigma_{\lambda}^2}{\bar{\lambda}^2} \right). \quad (8.432)$$

For a Gaussian-fluctuating signal, the detector decision statistic formed using the biased estimate of λ ,

$$T = \frac{X}{\hat{\lambda}} = \left[\frac{\lambda(1 + S^d)}{\alpha_\lambda \bar{\lambda}} \right] \left[\frac{\frac{X}{2\lambda(1 + S^d)}}{\frac{\hat{\lambda}}{2\alpha_\lambda \bar{\lambda}}} \right], \quad (8.433)$$

can be described as the scale (first term in brackets) of an $F_{2,2\alpha_\lambda}$ distributed random variable (second term in brackets). By choosing a detector decision threshold as a function of α_λ and β_λ to achieve the desired P_f , the SNR required to achieve the (P_d, P_f) operating point is identical to (8.355) replacing L with α_λ ,

$$S^d = \frac{\left(\frac{P_d}{P_f}\right)^{1/\alpha_\lambda} - 1}{1 - P_d^{1/\alpha_\lambda}}. \quad (8.434)$$

The CFAR loss in (8.357) is an *estimation* loss in that it represents the loss in performance arising from the need to estimate an unknown parameter. When the data used to estimate the unknown parameter do not follow the model for which the estimator was developed, the resulting additional loss in performance is a *mismatch* loss. There is a trade-off between the conflicting desires of reducing mismatch loss through more complicated modeling and reducing estimation loss through more compact or restrictive models. The ideal balance is achieved by a parsimonious enough model to represent the requisite physics while being simple enough to easily and accurately estimate the unknown parameters. In the present application, the mismatch loss can be evaluated by the ratio of (8.434) to (8.355), which after conversion to decibels is

$$\begin{aligned} \text{Loss}_{\text{dB}} &= 10 \log_{10} \left\{ \frac{\left[\left(\frac{P_d}{P_f} \right)^{1/\alpha_\lambda} - 1 \right] \left[1 - P_d^{1/L} \right]}{\left[\left(\frac{P_d}{P_f} \right)^{1/L} - 1 \right] \left[1 - P_d^{1/\alpha_\lambda} \right]} \right\} \\ &\leq 10 \log_{10} \left\{ \frac{\alpha_\lambda \left[P_f^{-1/\alpha_\lambda} - 1 \right]}{L \left[P_f^{-1/L} - 1 \right]} \right\} \end{aligned} \quad (8.435)$$

$$\approx 10 \log_{10} \left\{ 1 - \frac{1}{2L} \left(\frac{\sigma_\lambda^2}{\bar{\lambda}^2} \right) \log P_f \right\}. \quad (8.436)$$

The upper bound in (8.435) is achieved by letting $P_d \rightarrow 1$ as was done for the CFAR loss in (8.357) and is quite accurate for all useful values of P_d . The approximation in (8.436) is obtained as a first-order Maclaurin series on $\log P_f$ and so is more accurate as $P_f \rightarrow 1$. However, the trends of less mismatch error as $\sigma_\lambda^2/\bar{\lambda}^2$ decreases or L or P_f increase hold even for small values of P_f . In particular, increasing the size of the auxiliary data window will only improve performance if L increases more than $\sigma_\lambda^2/\bar{\lambda}^2$.

Recalling the ambient noise PSD and reverberation power examples, suppose the average power in the auxiliary data varies with x (which could be frequency or range) according to an inverse power law $\rho \geq 0$,

$$\lambda(x) = \frac{\lambda_c}{(x/x_0)^\rho}. \quad (8.437)$$

If the auxiliary data span the interval $(x_0, x_0 + \delta)$, the ratio of the variance to squared mean is

$$\frac{\sigma_\lambda^2}{\bar{\lambda}^2} = \left(\frac{\delta}{x_0}\right) \frac{(\rho - 1)^2 \left[1 - \left(1 + \frac{\delta}{x_0}\right)^{1-2\rho} \right]}{(2\rho - 1) \left[1 - \left(1 + \frac{\delta}{x_0}\right)^{1-\rho} \right]^2}. \quad (8.438)$$

This function is approximately proportional to $(\delta/x_0)^2$ when $\delta < x_0$ and proportional to δ/x_0 when $\delta > x_0$, so it increases slowly as a function of δ/x_0 . This implies that mismatch loss for the power-law variation shown in (8.437) will only be an issue if ρ is large, P_f is very small, and δ is large relative to x_0 . As an example, suppose a CW pulse has a 0.5-s duration and $L = 50$ independent samples are desired from adjacent Doppler channels taking 25 from each side of the test cell. Because independent Doppler channels are spaced every $1/T_p = 2$ Hz, this requires a span of 100 Hz. With $\rho = 2$ and $P_f = 10^{-6}$, the mismatch loss is approximately 1 dB if the center frequency is 100 Hz, where $\delta/x_0 = 2$. However at 1 kHz where $\delta/x_0 \approx 0.1$ the mismatch loss is less than 0.01 dB.

8.8 Temporal Spreading and Incoherent Integration

In previous sections, the impact of an unknown arrival time and Doppler scale on detection performance has been investigated. In each of these cases, the signal measurement was assumed to differ from the source signal in very simple and specific ways. However, in most applications of underwater acoustic signal processing the source signal is altered in more complex ways by propagation through the underwater acoustical channel. In active remote sensing, reflection and scattering off the object of interest further alters the signal measurement. As a simple example of spreading in time, consider propagation from a sound source to a sensor along two paths, one traveling directly from the source to the sensor and the other taking a longer path involving a reflection off the surface. Because the source signal arrives at the sensor along two paths with different lengths, the signal measurement is spread in time relative to the source signal. This temporal spreading can have a deleterious effect on signal detection when paths have opposite signs or phases leading to cancellation and therefore a very large propagation loss, as was

seen in the Lloyd mirror example of Sect. 3.2.7.3. This destructive combination of multiple paths assumes the path length and signal resolution (after matched filtering) are such that the paths overlap in time. Thus, the loss in detection performance arising from temporal spreading depends on the signal resolution, which is inversely related to its bandwidth. With the goal of balancing the accuracy of propagation modeling against the need to keep the model simple enough for a useful analysis of detection performance, the impact of temporal spreading on the matched-filter detector is evaluated in Sect. 8.8.1 as a function of the signal resolution using simple spreading models. Although spreading in frequency can also occur, the focus here is on spreading in time. The reduction in the peak SNR for a spread signal relative to the case where there is no spreading, called the *energy spreading loss*, approximates the loss in performance of the matched-filter detector. When signal spreading is unavoidable, incoherently integrating the matched-filter instantaneous intensity over multiple resolution cells is shown in Sect. 8.8.2 to be a locally optimal detector for a deterministic signal and to improve performance when the spreading is on-par with or exceeds the signal resolution. Early research on spreading in the underwater acoustical channel and the impact on matched filtering and waveform design can be found in [68, 71, 72].

8.8.1 Energy Spreading Loss (ESL)

To describe the effect of propagation on a source signal it is convenient to use the linear-system model of a remote sensing system where the signal measurement is the convolution between the source signal and the system impulse response, $h(t)$. The impulse response contains all the effects of propagation and (for active sensing) reflection or scattering from the object of interest. For example, $h(t)$ might represent propagation as a sum over ray paths or modes (see Sect. 3.2.8), which has the effect of spreading the source signal in time before it is measured at the sensor.

In this analysis, suppose the sampled basebanded signal has form

$$\mathbf{x} = Ae^{j\psi} \mathbf{s}_m + \mathbf{v} \quad (8.439)$$

where \mathbf{s}_m represents the normalized signal measurement including the spreading and \mathbf{v} is the additive noise. For this analysis consideration is restricted to the deterministic signal with amplitude A and phase ψ that is either unknown or uniformly random so the quadrature matched filter (QMF) is the appropriate detector. The vector \mathbf{s}_m is formed by basebanding and sampling the analytic signal measurement $\dot{s}_m(t)$. From (7.56), this is the convolution between the impulse response $h(t)$ and the analytic source signal $\dot{s}(t)$,

$$\dot{s}_m(t) = h(t) * \dot{s}(t). \quad (8.440)$$

When there is no spreading, the impulse response is simply a Dirac delta function placing all weight at the arrival time τ ; that is, $h(t) = \delta(t - \tau)$, so $\dot{s}_m(t) = \dot{s}(t - \tau)$.

To assess the impact of temporal spreading on detection performance, the response of the matched filter to \mathbf{x} must be evaluated. This process is similar to the analysis of Sect. 8.3.1.3 relating the ambiguity function to the SNR loss arising from mismatch. The SNR after the coherent portion of detection processing is

$$S_m^d = \frac{A^2}{\lambda} |\mathbf{s}^H \mathbf{s}_m|^2 = S^d |\mathbf{s}^H \mathbf{s}_m|^2, \quad (8.441)$$

so the squared modulus of the complex matched filter response $\mathbf{s}^H \mathbf{s}_m$ isolates the change in the SNR. At time t , the complex matched filter output is

$$\mathbf{s}^H \mathbf{s}_m \approx W \int_{-\infty}^{\infty} \dot{s}^*(u - t) \dot{s}_m(u) du \quad (8.442)$$

$$= W \dot{s}^*(-t) * \dot{s}_m(t) \quad (8.443)$$

$$= W h(t) * \dot{s}^*(-t) * \dot{s}(t) \quad (8.444)$$

$$= W h(t) * \chi_{\tau}(t) \quad (8.445)$$

where the correlation in (8.442) is described as a convolution (with a time reversal) in (8.443) and the convolutions in (8.444) have been rearranged (recall convolution is commutative) as a convolution between the system impulse response and the autocorrelation function (ACF) of the projected pulse,

$$\chi_{\tau}(t) = \dot{s}^*(-t) * \dot{s}(t). \quad (8.446)$$

The form shown in (8.445) provides some intuition on how much the spreading effects of propagation will affect detection performance. If the impulse response $h(t)$ is narrow with respect to the width of the ACF, there will be minimal impact—the matched-filter response will closely resemble a scaled version of the ACF. However, if the impulse response is spread beyond the resolution of the pulse, the matched-filter response will also be spread in time and have a lower peak squared modulus than when there is no spreading. This reduction of the peak squared modulus of the matched filter is called an energy spreading loss (ESL).

Now consider a high time-bandwidth product LFM waveform where the ACF, which from (8.169) has a sinc-function shape, can be approximated by a rectangular function with width $1/W$,

$$\chi_{\tau}(t) \approx \frac{1}{W} \text{rect}(Wt) e^{j2\pi f_c t}. \quad (8.447)$$

Note that the phase imparted by the ACF, which depends on the center frequency of the pulse, is retained in the approximation and the scale $1/W$ enforces the previously assumed normalization of $\dot{s}(t)$. Using this in (8.445) results in

$$|\mathbf{s}^H \mathbf{s}_m|^2 \approx \left| \int_{t-1/(2W)}^{t+1/(2W)} h(s) e^{-j2\pi f_c s} ds \right|^2. \quad (8.448)$$

As an example, suppose the spreading consists of only two paths so $h(t) = a_1 \delta(t - \tau_1) + a_2 \delta(t - \tau_2)$. If W is large enough that only one path contributes, $|\mathbf{s}^H \mathbf{s}_m|^2 = |a_1|^2$ when the matched filter is aligned with the first path and $|a_2|^2$ when aligned with the second and the maximum response is $\max\{|a_1|^2, |a_2|^2\}$. However, if the bandwidth is small enough that both paths contribute,

$$|\mathbf{s}^H \mathbf{s}_m|^2 = \left| a_1 e^{-j2\pi f_c \tau_1} + a_2 e^{-j2\pi f_c \tau_2} \right|^2, \quad (8.449)$$

which could be as large as $(|a_1| + |a_2|)^2$ if the paths combine constructively and as small as zero if they combine destructively. If there is assumed to be a uniformly random phase offset between the two paths, the result is $|a_1|^2 + |a_2|^2$ when both paths are included in the response. Under this assumption, the case where both paths are included will always be larger than when one is not, which articulates the impact of signal spreading on detection performance. Extending the random-phase assumption to the general form results in

$$|\mathbf{s}^H \mathbf{s}_m|^2 \approx \int_{t-1/(2W)}^{t+1/(2W)} |h(u)|^2 du \quad (8.450)$$

when it is assumed that the phase between paths decorrelates rapidly with respect to the variation in the amplitude.

Recall from the analysis in Sect. 8.3.1.3 that the analytic source signal was assumed to be normalized so $\int_{-\infty}^{\infty} |\dot{s}(t)|^2 dt = 1/W$. When $\dot{s}_m(t)$ was only affected by delay and Doppler it could be similarly normalized simply by multiplying by $\sqrt{\eta}$, as seen in (8.131). In order for A in (8.439) to distill the effects of propagation and scattering off the object of interest when the sensing waveform is such that all paths are included *and under the random-phase assumption*, the impulse response must be normalized so that (8.450) is one when all paths are included,

$$\int_{-\infty}^{\infty} |h(u)|^2 du = 1. \quad (8.451)$$

This also implies that the *incoherent* propagation loss (see Sect. 3.2.4.2) should be used to form A .

Now suppose that time \hat{t} produces the maximum response. The loss factor as a function of the temporal resolution of the source signal ($T_{\text{res}} = 1/W$) is then

$$\mathcal{L}_h(T_{\text{res}}) = \frac{S_m^d}{S^d} \approx \frac{\int_{\hat{t}-T_{\text{res}}/2}^{\hat{t}+T_{\text{res}}/2} |h(u)|^2 du}{\int_{-\infty}^{\infty} |h(u)|^2 du} \quad (8.452)$$

where a term has been included in the denominator to enforce the normalization described by (8.451).

Because $|h(u)|^2$ is non-negative and when normalized according to (8.451) integrates to one for $u \in (-\infty, \infty)$, it can be viewed as a probability density function (PDF). Weston [71] proposed using a Gaussian distribution based on the argument that propagation on multiple legs leads to consecutive convolutions of the per-leg PDFs, which results in a Gaussian distribution by appealing to the central limit theorem. An example of this can be seen in Fig. 8.33 where two-way

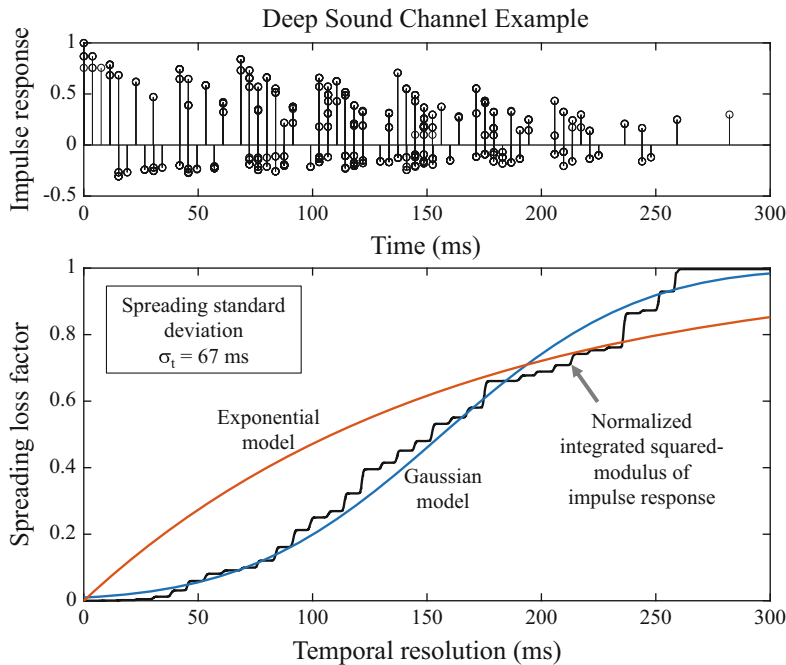


Fig. 8.33 Example of temporal spreading in the deep sound channel. The channel impulse response is shown in the upper panel. The resulting spreading loss factor, $\mathcal{L}_h(T_{\text{res}})$, is shown in the lower panel, along with that for the Gaussian and exponential spreading models, as a function of the temporal resolution

propagation in the deep sound channel (see Sect. 3.2.6) results in almost 300 ms of spreading in the impulse response. Although the path amplitudes do not fall off in a Gaussian taper, the spreading loss factor $\mathcal{L}_h(T_{\text{res}})$ is well fit by a Gaussian model, especially in comparison to the exponential model. When using a symmetric spreading model such as the Gaussian distribution, it is reasonable to assume the peak response \hat{t} occurs at the mean,

$$\hat{t} = \frac{\int_{-\infty}^{\infty} u |h(u)|^2 du}{\int_{-\infty}^{\infty} |h(u)|^2 du}. \quad (8.453)$$

The spreading standard deviation is then obtained as

$$\sigma_t = \sqrt{\frac{\int_{-\infty}^{\infty} (u - \hat{t})^2 |h(u)|^2 du}{\int_{-\infty}^{\infty} |h(u)|^2 du}}. \quad (8.454)$$

Centering the spreading distribution in this manner results in a spreading loss function that can be described as a function of the spreading standard deviation (σ_t) in terms of the resolution (T_{res}); that is, the ratio σ_t/T_{res} which is also the product $W\sigma_t$ and the ratio W/W_c where $W_c = 1/\sigma_t$ can be viewed as the bandwidth of the channel. Converting $\mathcal{L}_h(T_{\text{res}})$ for the Gaussian model to a decibel loss then results in

$$\text{Loss}_{\text{dB}}(\sigma_t/T_{\text{res}}) = -10 \log_{10} \mathcal{L}_h(T_{\text{res}}) = -10 \log_{10} \left\{ 2 \left[\Phi\left(\frac{T_{\text{res}}}{2\sigma_t}\right) - \frac{1}{2} \right] \right\} \quad (8.455)$$

where $\Phi(x)$ is the standard normal CDF. As seen in Fig. 8.34, this loss tends to zero when the spreading standard deviation is much less than the signal resolution (i.e., signal bandwidth \ll channel bandwidth). As the spreading standard deviation increases relative to the signal resolution, the matched filter begins to resolve the signal measurement and leads to an increase in the loss. For the Gaussian model this results in ~ 4.2 dB loss when $\sigma_t = T_{\text{res}}$ and then quickly enters a 10-dB-per-decade increase.

Although the Gaussian model is appealing for its intuitive derivation, it may not be appropriate when the impulse response is not symmetric as can occur in shallow water channels. The example shown in Fig. 8.35 illustrates an exponentially decaying impulse response arising from the geometric progression of steeper ray paths having more surface and bottom bounces and a longer travel time. As seen in the lower plot, the exponential model is a better fit than the Gaussian, especially for very small resolutions. In this example, the peak response is assumed to occur at a

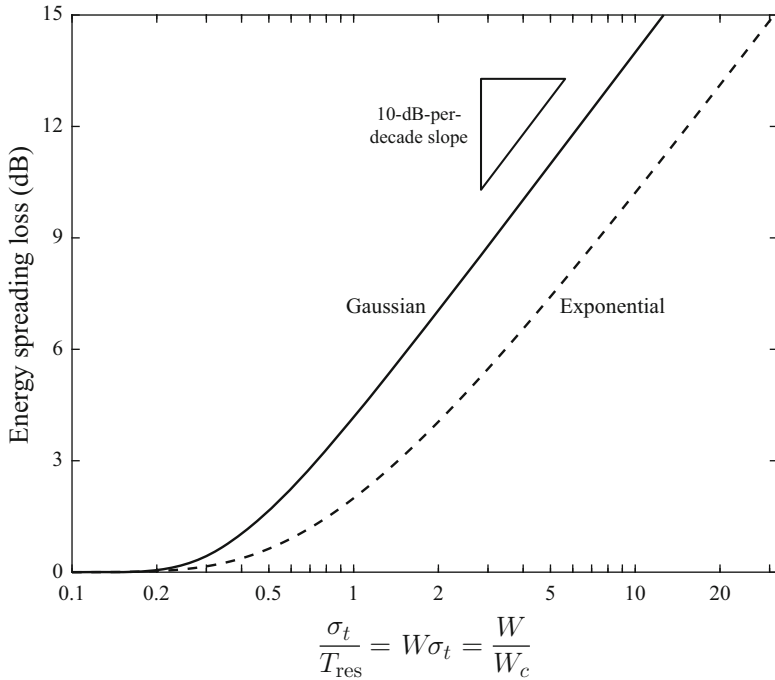


Fig. 8.34 Energy spreading loss (ESL) in the peak matched-filter output for exponential and Gaussian spreading models as a function of the spreading standard deviation relative to the signal resolution ($\sigma_t/T_{\text{res}} = W\sigma_t = W/W_c$)

time $\hat{t} = T_{\text{res}}/2$ so the integral in (8.452) spans $(0, T_{\text{res}})$. This results in a spreading loss of

$$\text{Loss}_{\text{dB}}(\sigma_t / T_{\text{res}}) = -10 \log_{10} \left(1 - e^{-T_{\text{res}}/\sigma_t} \right) \quad (8.456)$$

for the exponential model. As seen in Fig. 8.34, this results in a slower decay in performance with only a 2-dB loss when $\sigma_t = T_{\text{res}}$ compared with the Gaussian model. The sharp increase in the energy spreading loss observed for both models when the signal measurement is resolved (i.e., σ_t rises above $T_{\text{res}} = 1/W$) implies the waveform resolution should be kept below the spreading standard deviation. This is, of course, the same as requiring that the waveform bandwidth is less than the channel bandwidth ($W < 1/\sigma_t = W_c$).

Although this sort of coarse modeling can be useful in performance prediction, it is important to note that actual results may vary depending on the applicability of the random-phase assumption made in (8.450). In particular, when the signal resolution is very fine with respect to the spreading (the right side of Fig. 8.34), actual results can be very sensitive to the multipath structure. These results are also restricted to a detector formed by comparing the matched filter instantaneous intensity to a

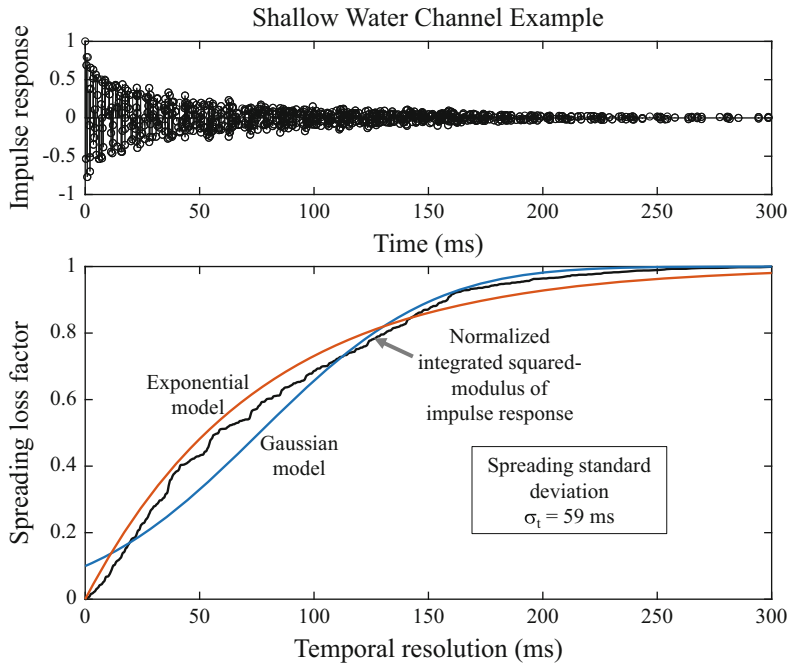


Fig. 8.35 Example of temporal spreading in a shallow water channel. The channel impulse response is shown in the upper panel. The resulting spreading loss factor, $\mathcal{L}_h(T_{\text{res}})$, is shown in the lower panel, along with that for the Gaussian and exponential spreading models, as a function of the temporal resolution

decision threshold. As will be seen in the following section, this may not be the best detector when a signal is spread over many temporal resolution cells.

8.8.2 Incoherent Integration

The examples of the previous section (Figs. 8.33 and 8.35) illustrate propagation spreading with standard deviations of 33 and 59 ms, which equate to channel bandwidths of, respectively, 30 and 17 Hz. Recalling that increasing bandwidth improves performance in reverberation limited scenarios, it may be desirable to use a bandwidth larger than $1/\sigma_t$ despite the increased spreading loss. The spreading loss analysis of the previous section inherently assumed performance was dominated by the peak SNR of the signal measurement. However, when the spreading does not have a sharp falloff (e.g., see the deep sound channel example in Fig. 8.33) detection opportunities in other resolution cells may contribute significantly to performance. An analysis of the receiver operating characteristic (ROC) curve would identify such scenarios.

An alternative, as suggested in [72], is to change the detection processing to account for the spreading. Under the deterministic signal model, the squared modulus of the i th matched-filter resolution cell with perfect normalization is non-central chi-squared distributed,

$$Y_i = \frac{2|\mathbf{s}^H \mathbf{x}_i|^2}{\lambda} \sim \chi_{2,\delta_i}^2 \quad (8.457)$$

with two degrees of freedom and non-centrality parameter $\delta_i = 2S_i^d$ for $i = 1, \dots, M$ where M represents the extent of the spreading in terms of resolution cells. The specific values of δ_i are generally not known so implementation of a likelihood ratio detector is not feasible. However, under a small-signal assumption (i.e., that the δ_i are not large), a locally optimal detector can be derived. As described in Sect. 6.2.6 the locally optimal detector function for a single sample is

$$T(y) = \frac{\left[\frac{\partial}{\partial \delta} f_1(y; \delta) \right]_{\delta=0}}{f_0(y)} \quad (8.458)$$

where $f_1(y; \delta)$ is in this case the non-central chi-squared PDF with two degrees of freedom and non-centrality parameter δ and $f_0(y)$ is the central chi-squared PDF with two degrees of freedom. The PDF of the non-central chi-squared distribution with two degrees of freedom is (from Sect. 5.6.15),

$$f_1(y; \delta) = \sum_{k=0}^{\infty} \frac{\delta^k e^{-\delta/2} x^k e^{-x/2}}{(k!)^2 2^{2k+1}}. \quad (8.459)$$

When taking the derivative with respect to δ and evaluating it at $\delta = 0$, only the first two terms in the infinite sum will have non-zero values. Combining this with the central chi-squared PDF for two degrees of freedom, $f_0(y) = e^{-y/2}/2$, results in a detector function

$$T(y) = \frac{1}{2} \left(\frac{y}{2} - 1 \right) \quad (8.460)$$

$$\stackrel{D}{=} \frac{y}{2} \quad (8.461)$$

that is equivalent to using the normalized instantaneous intensity by itself. When formed over multiple samples, which can each have a different non-centrality parameter, this results in the sum

$$T(\mathbf{y}) = \sum_{i=1}^M \frac{y_i}{2} = \sum_{i=1}^M \frac{|\mathbf{s}^H \mathbf{x}_i|^2}{\lambda}. \quad (8.462)$$

Thus the locally optimal decision statistic for a spread deterministic signal is an incoherent integration of the normalized matched-filter response or the sum of the

quadrature matched filter (QMF) detector decision statistics. It is sometimes called post-matched-filter integration (PMFI).

8.8.2.1 Decision-Threshold Analysis

In order to evaluate the detection performance of the PMFI detector, two factors need to be considered. The most obvious one is that the distribution of $T(\mathbf{y})$ changes with M , the number of independent normalized QMF samples summed to form a decision statistic. The second factor is that the rate at which decisions (i.e., threshold comparisons) are made changes—with respect to independent decision statistics, it is slower by a factor of M . Because of the changing decision rate, a fair comparison of the PMFI detector as a function of M or against other detectors requires the false alarm rate (FAR) to be constant as opposed to the probability of observing a false alarm in any one decision statistic. Recall from Sect. 8.2.11 that FAR and the probability of false alarm in a single independent decision statistic are related according to

$$\text{FAR} = \frac{P_f}{T_{\text{res}}} \quad (8.463)$$

where T_{res} is the temporal extent or resolution of the independent decision statistic. The effect of the PMFI detector is to increase the time over which a single decision is made by a factor of M . This means a decision is made every M/W where W is the bandwidth of the signal and therefore

$$\text{FAR} = \frac{P_f(M)}{M/W} \quad (8.464)$$

where $P_f(M)$ is the probability of a false alarm in the PMFI decision statistic summed over M independent QMF samples. This can be related to that used in the QMF detector, which is obtained by simply setting M to one,

$$P_f(M) = \frac{M}{W} \cdot \text{FAR} = M P_f(1). \quad (8.465)$$

Thus, maintaining a constant FAR as M increases results in a probability of false alarm in a single decision statistic a factor M larger than that when decisions are made at every QMF sample. Although this may appear to be a significant relaxation of the operating point, it may not be that large when $P_f(1)$ is already very small. Under the noise-only hypothesis and assuming perfect normalization, the decision statistic in (8.462) is the scale of a chi-squared random variable with $2M$ degrees of freedom,

$$2T(\mathbf{y})|H_0 \sim \chi^2_{2M}. \quad (8.466)$$

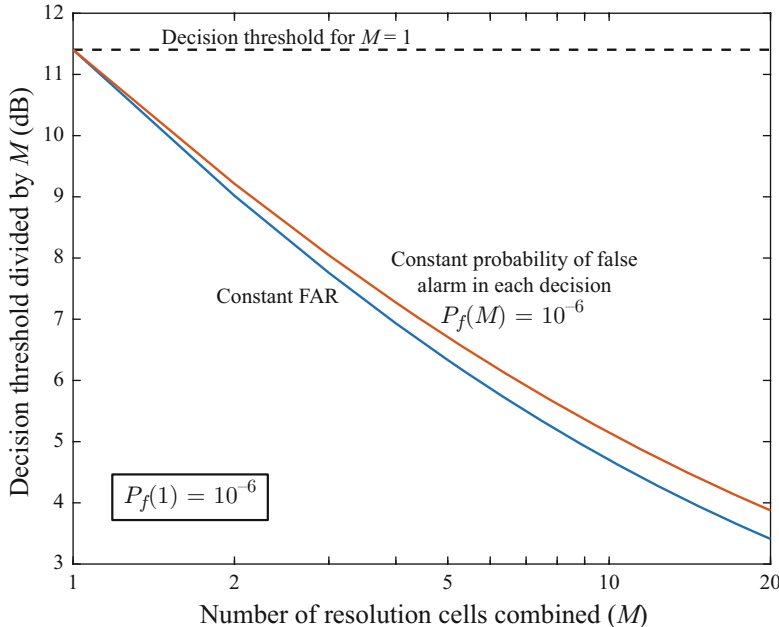


Fig. 8.36 Decision threshold for the PMFI detector divided by the number of resolution cells combined (M) for the case of holding false alarm rate (FAR) constant and when the probability of false alarm in each decision is held constant

Obtaining the decision threshold as a function of $P_f(M)$ requires inversion of the CDF of the chi-squared distribution with $2M$ degrees of freedom. This is generally accomplished numerically and is available in common software packages (e.g., `h=chi2inv(1-Pf1, 2*M)` in MATLAB®). The decision threshold, divided by M and converted to decibels (i.e., $10 \log_{10}(h/M)$), is shown as a function of M in Fig. 8.36 for the case of a constant FAR (blue line) and a constant probability of false alarm for each decision (reddish-brown line) where $P_f(M) = P_f(1)$. The difference between the two approaches is small for the $P_f(1) = 10^{-6}$ case shown. Although the difference increases with M and $P_f(1)$, it is still less than one decibel for $M = 10$ when $P_f(1) \leq 3.8 \cdot 10^{-3}$. Because the threshold for a constant probability of false alarm is larger than the threshold for a constant FAR, the achieved FAR and probability of detection will be lower using the former threshold compared to the latter.

The reason Fig. 8.36 displays the threshold divided by M , which can be interpreted as the decision threshold that would be applied to the QMF decision statistic *averaged* over M resolution cells rather than summed, is to illustrate how the incoherent averaging reduces the variability of the decision statistic. The decreasing variability under H_0 as the number of averages increases allows a commensurately smaller decision threshold. As seen in Fig. 8.36, the rate of change is steepest when M is small (e.g., more than a 2-dB decrease per doubling) and lessens as M increases because the PDF of the decision statistic tends to a Gaussian distribution.

8.8.2.2 Performance Analysis

When a deterministic signal is present, the decision statistic in (8.462) is the scale of a non-central chi-squared random variable with $2M$ degrees of freedom,

$$2T(\mathbf{y})|H_1 \sim \chi^2_{2M, \delta_M} \quad (8.467)$$

and non-centrality parameter

$$\delta_M = \sum_{i=1}^M \delta_i = 2 \sum_{i=1}^M S_i^d. \quad (8.468)$$

This result assumes the data in the M resolution cells are independent and that the normalization is perfect. The implication of (8.468) is that making M large enough allows recoupling all of the spread signal energy. However, if the SNR in each additional resolution cell is not large enough, performance may degrade rather than improve by increasing the incoherent integration. The minimum SNR required in the next resolution cell to be included in a PMFI detection that maintains a P_d specification is shown in Fig. 8.37 for $P_f(1) = 10^{-6}$ (with the decision thresholds

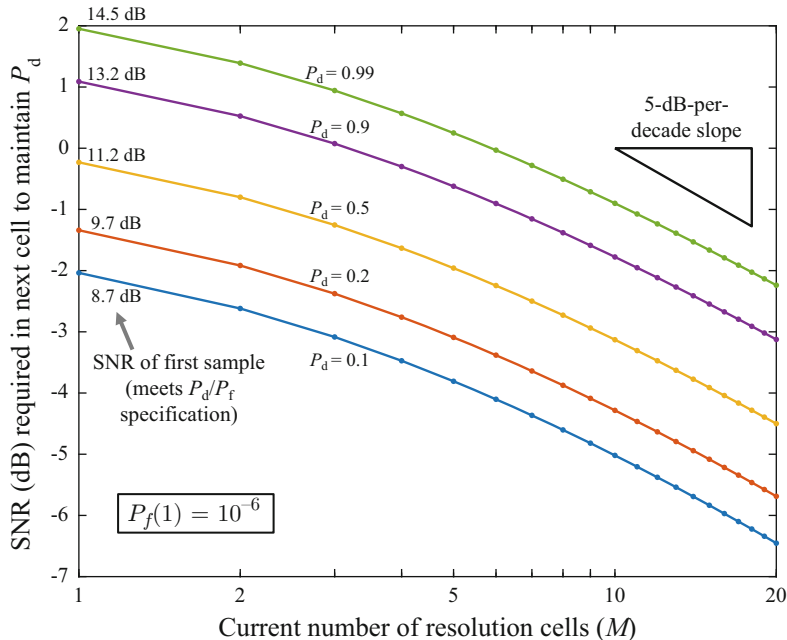


Fig. 8.37 SNR required in the next resolution cell in a PMFI detector in order to maintain the operating point when extending incoherent integration

chosen to produce a constant FAR). For example, when $M = 1$ and the SNR ($= 13.2$ dB) is already such that $P_d = 0.9$, adding a second resolution cell requires it to have slightly over a one-decibel SNR in order to maintain $P_d = 0.9$. If the SNR in the second resolution cell is greater, then P_d will increase and it is better to use the PMFI detector than thresholding the QMF decision statistic in each resolution cell. However, if it is smaller P_d will decrease and the QMF detector provides better performance. As M increases, the SNR required in the next resolution cell decreases because it has less impact on the total SNR, which can be defined by $\delta/2 = \sum_{i=1}^M S_i^d$. For large M , it can be seen in Fig. 8.37 that the required SNR in the next resolution cell decreases at a 5-dB-per-decade rate (i.e., $5 \log_{10}(M)$)—as would be expected from the incoherent averaging.

The SNR requirements shown in Fig. 8.37 are small enough that the PMFI detector is expected to improve performance in many spreading scenarios. To illustrate this, suppose the spreading results in an exponential SNR decay, $S_i = S_0 e^{-(i-1)/\mathcal{T}}$ for $i = 1, \dots, M$ as shown in the top panel of Fig. 8.38. Such spreading arises from the exponential model of Sect. 8.8.1 and is described here in terms of the average extent \mathcal{T} in units of resolution cells, which is the abscissa of Fig. 8.34 (i.e., $\mathcal{T} = \sigma_t / T_{\text{res}} = \sigma_t W$). Assuming the SNR for the resolution cell with the peak

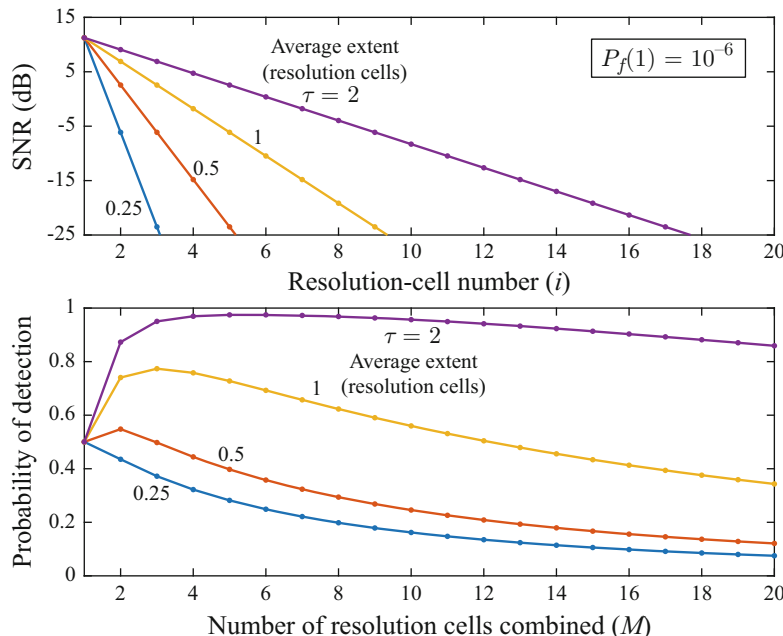


Fig. 8.38 Probability of detection (lower panel) under incoherent integration for four different average extents of an exponentially decaying SNR (shown in the upper panel). The PMFI detector only improves performance when the average extent of the spreading is on par with or exceeds the signal resolution

response is 11.2 dB to produce $P_d = 0.5$ with $P_f(1) = 10^{-6}$, the P_d achieved by the PMFI detector is shown in the lower panel of Fig. 8.38. When the spreading is small relative to the signal resolution ($\tau = 0.25$), performance degrades and when the spreading is relatively large, there is considerable improvement. These results can be related to those shown in Fig. 8.37: the $\tau = 0.25$ average extent produces an SNR (-6.1 dB) in the second resolution cell that is below that required to maintain $P_d = 0.5$, which was -0.23 dB. All of the other average extents resulted in a higher SNR in this second example and therefore a performance improvement.

These results indicate that PMFI should be used when the spreading is on-par with or exceeds the signal resolution. For the exponential model at the $P_f(1) = 10^{-6}$ operating point, using enough resolution cells to cover three times the spreading standard deviation provides nearly optimal performance over a wide range of P_d . The slower decay of the Gaussian PDF near its peak relative to the exponential PDF implies a slightly larger PMFI window: four times the spreading standard deviation at the $P_f(1) = 10^{-6}$ operating point.

Appendix 8.A: Example MATLAB® Code for a Doppler Filter Bank

The following MATLAB® code implements a Doppler filter bank using fast Fourier transforms (FFTs) as described in Sect. 8.7.1.4. It is assumed that the data have been basebanded and decimated to a band appropriate to the radial velocities of interest. In producing the filter bank, a 50% overlap in time has been implemented and zero-padding of the FFT has been used to interpolate in frequency, which produces correlated Doppler channels. The response of the filter bank is converted to radial velocity assuming a monostatic active sonar geometry. The sample signal generated includes reverberation and an echo near 30 s with approximately 10-kn radial velocity.

```
% Setup for Doppler filter bank
Ts=60; % Pulse repetition period (s)
Tp=1; % Pulse duration (s)
fc=1500; % Frequency of pulse
fs=40; % Sampling frequency (Hz)
cwkn=2916; % Speed of sound (kn)
%-----
% Generate sample complex-envelope data
Nx=round(Ts*fs); tx=(0:Nx-1)'/fs;
x=randn(Nx,2)*[1;1j]/sqrt(2)+5./sqrt(1+tx)...
+2*exp(1j*2*pi*10*tx).*abs(tx-Tp/2-30)<Tp/2;
%-----
% Number of samples in pulse duration
N=round(Tp*fs);
% FFT size (increase the '1' to interpolate more in frequency)
Nfft=2^(nextpow2(N)+1);
% Number of FFTs without overlapping
Nt=floor((length(x)-N/2)/N);
% Pulse shading vector & matrix
```

```

a=tukeywin(N,0.1); A=a*ones(1,Nt);
% FFTs for non-overlapped windows
Y1=fftshift(fft(A.*reshape(x(1:Nt*N),N,Nt),Nfft),1);
% FFTs for 50% overlapping
Y2=fftshift(fft(A.*reshape(x(round(N/2)...
+(1:Nt*N),N,Nt),Nfft),1);
% Combine into one matrix
Y=10*log10(abs(reshape([Y1;Y2],Nfft,2*Nt)).^2)';
% Velocity and time vectors for plotting
vkn=[((Nfft/2):(Nfft-1))-Nfft 0:(Nfft/2-1)]' * ...
    fs*cwkn/(2*fc*Nfft);
ts=(0:size(Y,2)-1)*(N/2)/fs;
%-----
% Plot normalized intensity in decibels
figure(2); clf;
imagesc(vkn,ts,Y-median(Y(:)));
set(gca,'YDir','normal');
set(gca,'TickDir','out');
shading flat
xlabel('Radial velocity (kn)');
ylabel('Time (s)');
caxis([-5 25]);
colorbar;

```

References

1. G. Turi,. An introduction to matched filters. IRE Trans. Inf. Theory **6**(3), 311–329 (1960)
2. R.N. McDonough, A.D. Whalen, *Detection of Signals in Noise*, 2nd edn. (Academic Press, San Diego, 1995)
3. S.M. Kay, *Fundamentals of Statistical Signal Processing: Detection Theory* (Prentice Hall PTR, 1998)
4. L.L. Scharf, *Statistical Signal Processing* (Addison-Wesley, Reading, MA, 1991)
5. S.A. Kassam, *Signal Detection in Non-Gaussian Noise* (Springer, New York, 1988)
6. N. Mukhopadhyay, *Probability and Statistical Inference* (Marcel Dekker, New York, NY, 2000)
7. E.L. Lehmann, J.P. Romano, *Testing Statistical Hypotheses*, 3rd edn. (Springer, New York, 2005)
8. C.W. Helstrom, *Elements of Signal Detection and Estimation* (Prentice Hall, Englewood Cliffs, NJ, 1995)
9. M.A. Richards, *Fundamentals of Radar Signal Processing* (McGraw-Hill, New York, 2005)
10. P.Z. Peebles, Jr., *Radar Principles* (Wiley, New York, 1998)
11. D.W. Ricker, *Echo Signal Processing* (Kluwer Academic, Boston, MA, 2003)
12. R.O. Nielsen, *Sonar Signal Processing* (Artech House, Norwood, MA, 1991)
13. H.L. Van Trees, *Detection, Estimation, and Modulation Theory: Part III* (Wiley, New York, 1971)
14. P.M. Woodward, *Probability and Information Theory, with Applications to Radar* (Pergamon Press, New York, 1964)
15. A.W. Rihaczek, Delay-Doppler ambiguity function for wideband signals. IEEE Trans. Aerosp. Electron. Syst. **AES-3**(4), 705–711 (1967)
16. A.W. Rihaczek, *Principles of High Resolution Radar* (McGraw-Hill, New York, 1969)

17. D.W. Ricker, The Doppler sensitivity of large TW phase modulated waveforms. *IEEE Trans. Signal Process.* **40**(10), 2406–2413 (1992)
18. N. Levanon, E. Mozeson, *Radar Signals* (Wiley-Interscience, 2004)
19. S.M. Kay, *Modern Spectral Estimation Theory and Application* (Prentice Hall, Englewood Cliffs, NJ, 1988)
20. W.J. Albersheim, A closed-form approximation to Robertson's detection characteristics. *Proc. IEEE* **69**(7), 839 (1981)
21. H. Hamm, SNR calculation procedure for target types 0, 1, 2, 3. *IEEE Trans. Aerosp. Electron. Syst.* **41**(3), 1091–1096 (2005)
22. K. Oldham, J. Myland, J. Spanier, *An Atlas of Functions*, 2nd edn. (Springer Science, New York, 2009)
23. I.S. Gradshteyn, I.M. Ryzhik, in *Table of Integrals, Series, and Products*, 8th edn., ed. by D. Zwillinger (Elsevier Academic Press, Waltham, MA, 2015)
24. T. Kailath, *Linear Systems* (Prentice Hall, Englewood Cliffs, NJ, 1980)
25. A.B. Carlson, *Communication Systems* (McGraw-Hill, New York, 1986)
26. S. Haykin, *Adaptive Filter Theory*, 3rd edn. (Prentice Hall, Englewood Cliffs, NJ, 1996)
27. A. Papoulis, *Probability, Random Variables, and Stochastic Processes*, 3rd edn. (McGraw-Hill, Boston, 1991)
28. J.V. DiFranco, W.L. Rubin, *Radar Detection* (Artech House, Dedham, MA, 1980)
29. D. Halliday, R. Resnick, *Fundamentals of Physics* (Wiley, New York, 1981)
30. E.J. Kelly, R.P. Wishner, Matched-filter theory for high-velocity accelerating targets. *IEEE Trans. Mil. Electron.* **Mil-9**, 56–69 (1965)
31. Z. Lin, Wideband ambiguity function of broadband signals. *J. Acoust. Soc. Am.* **83**(6), 2108–2116 (1988)
32. D.M. Russo, C.L. Bartberger, Ambiguity diagram for linear FM sonar. *J. Acoust. Soc. Am.* **38**(2), 183–190 (1965)
33. B. Harris, S.A. Kramer, Asymptotic evaluation of the ambiguity functions of high-gain FM matched filter sonar systems. *Proc. IEEE* **56**(12), 2149–2157 (1968)
34. J.J. Kroszczynski, Pulse compression by means of linear-period modulation. *Proc. IEEE* **57**(7), 1260–1266 (1969)
35. R.A. Altes, Some invariance properties of the wideband ambiguity function. *J. Acoust. Soc. Am.* **53**(4), 1154–1160 (1973)
36. D.A. Swick, A review of wideband ambiguity functions. NRL Report 6994, Naval Research Laboratory, December 1969
37. L.H. Sibul, E.L. Titlebaum, Volume properties for the wideband ambiguity function. *IEEE Trans. Aerosp. Electron. Syst.* **AES-17**(1), 83–87 (1981)
38. F.W.J. Olver, D.W. Lozier, R.F. Boisvert, C.W. Clark (eds.), *NIST Handbook of Mathematical Functions* (Cambridge University Press, Cambridge, 2010)
39. R.C. Thor, A large time-bandwidth product pulse-compression technique. *IRE Trans. Mil. Electron.* **MIL-6**(2), 169–173 (1962)
40. R.A. Altes, E.L. Titlebaum, Bat signals as optimally Doppler tolerant waveforms. *J. Acoust. Soc. Am.* **48**(4), 1014–1020 (1970)
41. H.L. Van Trees, *Optimum Array Processing* (Wiley, New York, 2002)
42. D.H. Johnson, D.E. Dudgeon, *Array Signal Processing: Concepts and Techniques* (Prentice Hall, Englewood Cliffs, NJ, 1993)
43. S. Haykin (ed.), *Array Signal Processing* (Prentice Hall, Englewood Cliffs, NJ, 1985)
44. B.D. Van Veen, K.M. Buckley, Beamforming: a versatile approach to spatial filtering. *IEEE ASSP Mag.* **5**(2), 4–24 (1988)
45. H. Krim, M. Viberg, Two decades of array signal processing research: the parametric approach. *IEEE Signal Process. Mag.* **13**(4), 67–94 (1996)
46. R.J. Urick, *Principles of Underwater Sound*, 3rd edn. (McGraw-Hill, New York, 1983)
47. S.M. Kay, *Fundamentals of Statistical Signal Processing: Estimation Theory* (Prentice Hall PTR, 1993)

48. P. Bello, Joint estimation of delay, Doppler, and Doppler rate. *IRE Trans. Inf. Theory* **6**(3), 330–341 (1960)
49. E.J. Kelly, The radar measurement of range, velocity and acceleration. *IRE Trans. Mil. Electron.* **MIL-5**(2), 51–57 (1961)
50. J.P. Ovarlez, Cramer Rao bound computation for velocity estimation in the broad-band case using the Mellin transform, in *1993 IEEE International Conference on Acoustics, Speech, and Signal Processing*, vol. 1, pp. 273–276, 1993
51. H.L. Van Trees, K.L. Bell (eds.), *Bayesian Bounds for Parameter Estimation and Nonlinear Filtering/Tracking* (IEEE Press Wiley-Interscience, 2007)
52. S.A. Kramer, Doppler and acceleration tolerances of high-gain, wideband linear FM correlation sonars. *Proc. IEEE* **55**(5), 627–636 (1967)
53. P. Swerling, Parameter estimation for waveforms in additive Gaussian noise. *J. Soc. Ind. Appl. Math.* **7**(2), 152–166 (1959)
54. E.W. Barankin, Locally best unbiased estimates. *Ann. Math. Stat.* **20**(4), 447–501 (1949)
55. J. Ziv, M. Zakai, Some lower bounds on signal parameter estimation. *IEEE Trans. Inf. Theory* **15**(3), 386–391 (1969)
56. L. Cohen, *Time-Frequency Analysis* (Prentice Hall PTR, Englewood Cliffs, NJ, 1995)
57. Acknowledgement: These data were made possible by funding from the Office of Naval Research (Codes 321US and 322OA) and the CLUTTER Joint Research Project (JRP), including as Participants the NATO Undersea Research Centre (NURC), Pennsylvania State University - ARL-PSU (USA), Defence Research and Development Canada - DRDC-A (CAN), and the Naval Research Laboratory - NRL (USA). Scientist in charge: Dr. P. Nielsen
58. C.H. Harrison, Closed-form expressions for ocean reverberation and signal excess with mode stripping and Lambert's law. *J. Acoust. Soc. Am.* **114**(5), 2744–2756 (2003)
59. A.H. Nuttall, A.F. Magaraci, Signal-to-noise ratios required for short-term narrowband detection of Gaussian processes. Tech. Rpt. 4417, Naval Underwater Systems Center, Newport, RI, October 1972
60. D.A. Abraham, Performance analysis of constant-false-alarm-rate detectors using characteristic functions. *IEEE J. Ocean. Eng.* (2017). <https://doi.org/10.1109/JOE.2017.2771878>
61. N.L. Johnson, S. Kotz, N. Balakrishnan, *Continuous Univariate Distributions*, vol. 2, 2nd edn. (Wiley, New York, 1995)
62. V.G. Hansen, H.R. Ward, Detection performance of the cell averaging LOG/CFAR receiver. *IEEE Trans. Aerosp. Electron. Syst.* **AES-8**(5), 648–652 (1972)
63. P.P. Gandhi, S.A. Kassam, Analysis of CFAR processors in nonhomogenous background. *IEEE Trans. Aerosp. Electron. Syst.* **24**(4), 427–445 (1988)
64. H.A. David, H.N. Nagaraja, *Order Statistics*, 3rd edn. (Wiley, Hoboken, NJ, 2003)
65. M. Abramowitz, I.A. Stegun (eds.), *Handbook of Mathematical Functions* (Dover Publications, New York, 1972)
66. H. Rohling, Radar CFAR thresholding in clutter and multiple target situations. *IEEE Trans. Aerosp. Electron. Syst.* **AES-19**(4), 608–621 (1983)
67. H. Cramér, *Random Variables and Probability Distributions*. Number 36 in Cambridge Tracts in Mathematics and Mathematical Physics (Cambridge University Press, Cambridge, 1937)
68. H.L. Van Trees, Optimum signal design and processing for reverberation-limited environments. *IEEE Trans. Mil. Electron.* **9**(3), 212–229 (1965)
69. T. Arase, E.M. Arase, Deep-sea ambient-noise statistics. *J. Acoust. Soc. Am.* **44**(6), 1679–1684 (1968)
70. D.R. Morgan, Two-dimensional normalization techniques. *IEEE J. Ocean. Eng.* **12**(1), 130–142 (1987)
71. D.E. Weston, Correlation loss in echo ranging. *J. Acoust. Soc. Am.* **37**(1), 119–124 (1965)
72. S.M. Garber, High resolution sonar signals in a multipath environment. *IEEE Trans. Aerosp. Electron. Syst.* **AES-2**(6), 431–440 (1966)

Chapter 9

Detecting Signals with Unknown Form: Energy Detectors



9.1 Introduction

In many applications of underwater acoustic signal processing very little is known about the structure of signals of interest either because they are inherently random (e.g., radiated ship noise) or because of insufficient a priori knowledge about the sound source (e.g., marine mammal acoustic emissions). Such signals cannot be characterized as having a known form with some unknown parameters and so the matched-filter detectors derived in Chap. 8 cannot be used. The three signals shown in Fig. 9.1 illustrate the character of random signals as well as how the rapidity with which the temporal structure changes depends on the bandwidth of the signal. However, random signals are not the only ones for which the form can be unknown. There are many applications where the source signal is deterministic but very little is known about it. Examples of such signals include the aforementioned marine mammal sound emissions and, in many cases, anthropogenic noise in the ocean. A spectrogram of a sound emission from a right whale is shown in Fig. 9.2 (Acknowledgement: data provided by Prof. S. Parks, Syracuse University).¹ After observing these particular signals, several defining characteristics can be identified including harmonics and frequency modulation. However, the variations from one observation to the next are generally too great to easily implement a matched filter, especially noting the differences in emission types.

A common trait of signals with unknown form is a lack of knowledge about the phase of the signal. The analytic representation of a bandpass signal (from Sect. 7.3.1) is

¹Acknowledgment with gratitude to Prof. S. Parks, Biology Dept., Syracuse University, who acquired the data under funding from the National Oceanic and Atmospheric Administration (NOAA) and a Department of Fisheries and Oceans (DFO) Canada permit.

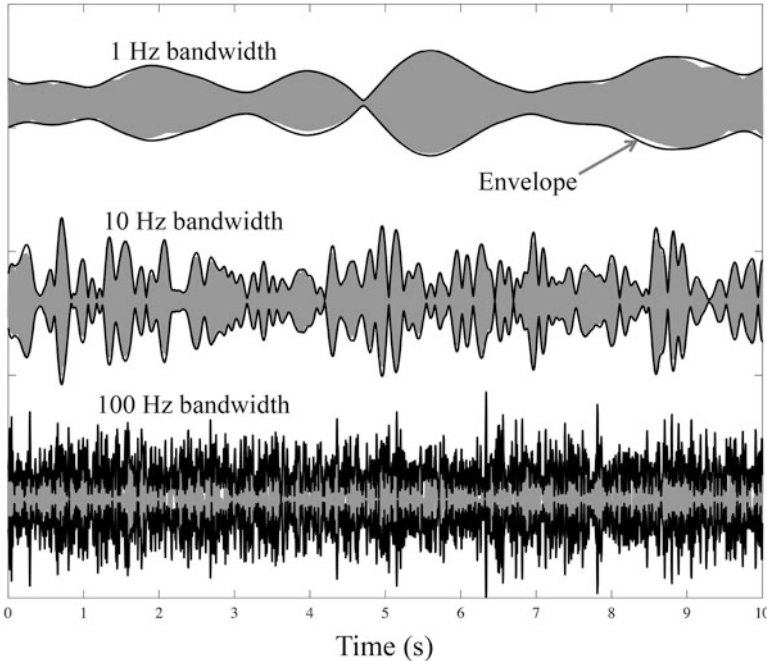


Fig. 9.1 Gaussian random signals with different bandwidths. The gray regions are the signal at the carrier frequency while the black lines define the envelope of the signal

$$\dot{s}(t) = a(t)e^{j\phi(t)}e^{j2\pi f_c t} \quad (9.1)$$

where f_c is the center frequency, $a(t)$ is the amplitude, and $\phi(t)$ is the phase. When the phase is unknown, the only information remaining related to the signal of interest lies in the amplitude. One can therefore imagine that the energy of the signal, which can be obtained from the real or analytic signal or its Fourier transform,

$$\mathcal{E} = \int_{-\infty}^{\infty} s^2(t) dt = \frac{1}{2} \int_{-\infty}^{\infty} |\dot{s}(t)|^2 dt = \frac{1}{2} \int_{-\infty}^{\infty} |\dot{S}(f)|^2 df, \quad (9.2)$$

might encapsulate the signal information encoded in the amplitude while ignoring the phase. As shown in Sect. 9.2, this is the case and results in what is known as an *energy detector*. In (9.2), Parseval's theorem is used to describe the signal energy as an integral over frequency of the squared modulus of $\dot{S}(f)$, which is the Fourier transform of the analytic signal. This indicates the energy detector can be implemented with either time- or frequency-domain processing. A comparison of the two approaches is found in Sect. 9.2.10 where the time-domain processor is seen to be (approximately) coherent integration followed by incoherent integration.

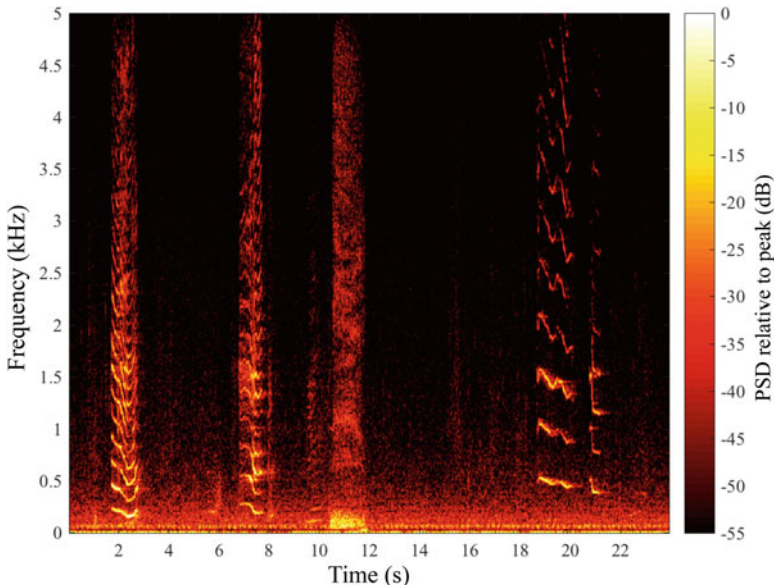


Fig. 9.2 Example spectrogram of acoustic emissions from a right whale. Acknowledgement: data provided by Prof. S. Parks, Biology Dept., Syracuse University

Recall the four dimensions used to characterize underwater acoustic signals in Sect. 7.2: *temporal character*, *spectral content*, *measurement consistency*, and *knowledge of signal structure*. As described above, signals with unknown form clearly tend to be those that are not strongly consistent from one observation to the next and either little signal structure to exploit or not enough knowledge of the signal structure to exploit it in a detector. The remaining dimensions represent the temporal character and spectral content of the signal. The applications where these signals of unknown form are important typically involve passive remote sensing. As described in Sect. 7.2, the signals of interest might persist for long periods of time or be very short. The focus in this chapter is on detection processing when the signal of interest is assumed to exist throughout a given analysis window. Techniques for detecting signals across such temporal epochs are covered in Chap. 10. The spectral content of the signal of interest and how much is known about it plays an important role in what type of energy detector should be used. A flow chart can be found in Fig. 9.3 describing how the characteristics of and knowledge about a signal measurement lead to which detector to use. Although the consistency and knowledge characteristics of some signals will fall between these demarcations, the majority of commonly encountered scenarios can be found in this list. Broadly, the chart ranges vertically along the combined consistency and knowledge dimensions described in Sect. 7.5 from consistent signals with high knowledge to random signals with very little knowledge. The detectors for these signals similarly range from a coherent matched filter to a quadrature matched filter to energy detectors

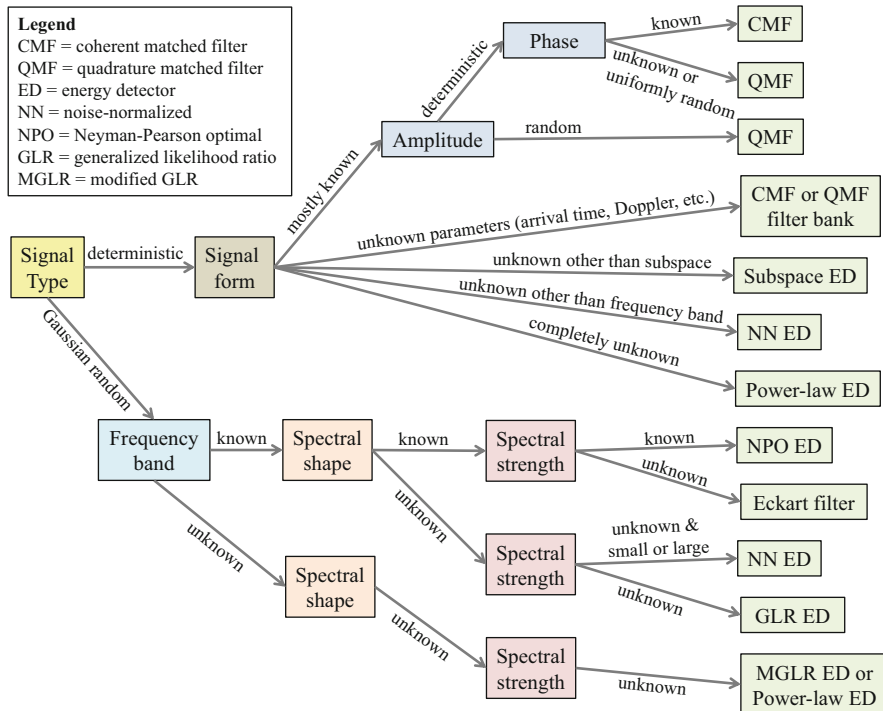


Fig. 9.3 Flow chart of how to choose a detector (green boxes) based on signal characteristics

requiring less and less knowledge of the signal. This progression of energy detectors is presented in Sect. 9.2 along with techniques for the analysis of their detection performance, including evaluation of the detection threshold when energy detectors are used on deterministic and Gaussian random signals. It is worth noting that, from the perspective of detector derivation, whether a random signal is narrowband or broadband does not play a large role. Both signal types require the use of an energy detector with the type dependent upon how much is known about the shape and spectral strength, not the bandwidth. Areas where signal bandwidth is important in detector design include tuning one of the more general detectors (see Sect. 9.2.8) when the center frequency is unknown and normalization. As covered in Sect. 9.3, estimation of the background noise power as a function of frequency is paramount to the implementation of an energy detector. Where the auxiliary data used in the estimation are obtained from is dictated in part by signal bandwidth. Estimation for narrowband signals can exploit adjacent frequency bands whereas the auxiliary data for broadband signals must come from another dimension (e.g., time or space).

Although the focus of this chapter is on energy detectors and their analysis, an important aspect of underwater acoustic signal processing in passive remote sensing is time-delay estimation. As described in Sect. 2.2.3.3, the difference between the times at which a common source signal is measured on two physically separated

remote sensors can be used to localize the object of interest to a hyperbolic line of location. Cross-correlation processing is shown in Sect. 9.4.1 to arise in the maximum-likelihood estimation of the inter-sensor time delay. On a single sensing platform, the time delay between multipath arrivals can similarly be used to localize an object of interest (e.g., see the example in Sect. 2.2.3.4). Estimation of the multipath time delay is shown to require autocorrelation processing in Sect. 9.4.2. Both of these applications require the signals of interest to be broadband. Narrowband signals can carry information both in their center frequency and bandwidth. Estimation of these narrowband signal parameters and the resulting estimator performance is discussed in Sect. 9.5.

Among the material presented in this chapter are three very powerful and useful analysis or estimation methods whose applicability extends well beyond the present application. In Sect. 9.2.7.2, the technique of [1] for numerical evaluation of the cumulative distribution function of a random variable from its characteristic function is presented for the analysis of the detection performance of a weighted-sum energy detector. The MATLAB® code implementing an example is found in Appendix 9.A and presented in a manner enabling adaptation to other applications. In Sect. 9.4.2.1, the technique described in [2] for estimating the parameters of a modeled power spectral density (PSD) for Gaussian random signals and evaluation of the corresponding Cramér-Rao lower bounds for parameter estimation is described and then applied to the estimation of multipath delay. Subsequently in Sect. 9.5.2.1 it is used to evaluate the Cramér-Rao lower bounds for estimating the center frequency and bandwidth of a narrowband Gaussian random signal with a Gaussian-shaped PSD measured in the presence of Gaussian noise. Finally, the histogram-based PSD estimation of [3, 4] is applied in Sect. 9.5.2.2 to the estimation of the bandwidth and center frequency of the aforementioned narrowband Gaussian signal. The algorithm enables estimation of the PSD of a signal through the lens of a mixture of probability density functions, exploiting the expectation-maximization algorithm (see Sect. 6.3.7) to obtain the parameters of each component of the mixture. The algorithm implementing the estimator for the narrowband-signal parameter estimation problem, which is characterized as a Gaussian-shaped signal PSD mixed with a noise PSD that is uniform over the signal band, is described in pseudocode in Appendix 9.C.

9.2 Energy Detectors

As described in Sect. 7.2.1, certain signals of interest can be modeled as Gaussian wide-sense-stationary random processes. The wide-sense-stationarity assumption (see Sect. 5.4.1) implies the random process has an autocorrelation function (ACF) that depends only on delay and whose Fourier transform is the power spectral density (PSD). The Gaussianity assumption means that either the ACF or PSD completely characterizes the signals. In addition to using the frequency domain

to characterize the signal, the signal detector can be derived, analyzed, and implemented in the frequency domain.

As previously mentioned, the focus in this chapter is on detecting a signal when it is assumed to occupy an analysis period with a given temporal extent. Although it may persist for longer periods of time, the detector decision statistic is derived for the given temporal epoch. In the frequency domain, the focus is typically limited to a particular frequency band both because many signals of interest are naturally bandpass and because measurement systems can have inherent frequency responses that limit consideration to particular bands. For example, sensor arrays are often built to a design frequency, above which spatial aliasing occurs and below which the array gain degrades.

The objective of this section is to develop or present the various forms of energy detectors and analyze their performance. Because of the interdependencies of these two topics, the sequence of their appearance is interleaved. For example, the basic energy detector is developed in Sect. 9.2.3 in the time domain along with its performance analysis in the simple scenario of noise and signal PSDs that are constant in the processing band. The energy detector is then characterized in Sect. 9.2.4 as a frequency-domain processor operating on the squared moduli of the discrete Fourier transform (DFT) bin data. Other forms of the energy detector are derived in later sections for varying levels of knowledge about the signal PSD. Table 9.1 contains a list of these assumptions, the resulting energy detector, its optimality and the section in which it can be found. The various forms of energy detectors can be classified as either a weighted incoherent sum over the frequency-domain data or as the sum of a non-linear function applied to each DFT bin. The weighted-sum energy detectors are generally used when the frequencies containing adequate SNR are known. When the location of the signal in frequency is unknown, non-linear functions can limit the adverse effects of summing over many noise-dominated DFT bins. The time-domain implementation of the energy detector is then revisited in Sect. 9.2.10 where it is seen to approximately represent a noise-normalization filter followed by coherent integration over an extent equal to the inverse bandwidth of the signal and then finished with incoherent integration. A key restriction made throughout this section is the assumption that the noise PSD is known perfectly. Estimation of the background noise power, its use in the energy detector to normalize each DFT bin (equivalently to whiten the time-domain data), and an analysis of the resulting loss in performance can be found in Sect. 9.3.

The parts of this section focusing on analysis of energy detectors begin with a description of the SNR after the coherent portion of detection processing (S^d) in Sect. 9.2.2 where it is seen to be a convex combination of the ratio of the signal PSD to the noise PSD in the processing band. A performance analysis of the basic energy detector, which assumes the signal and noise PSDs are constant in the processing band, is found in Sect. 9.2.3.1 and is suitable for use in the sonar equation. A more detailed analysis of the detection threshold term in the sonar equation is presented in Sect. 9.2.11 for the noise-normalized energy detector where it is seen that S^d for this common detector is the average PSD-SNR over the processing band. The means to precisely evaluate or approximate the detection performance of a

Table 9.1 Various signal models, the underlying assumptions about the signal spectrum, the resulting detector, its optimality, and the section in which the detector is derived. The noise PSD is assumed to be known or perfectly estimated in all cases. With the exception of the first case, the noise PSD is assumed to vary with frequency

Spectral shape ¹	Spectral strength ¹	Frequency band	Detector	Optimality conditions	Section
Gaussian random signals					
Constant ²	Known or unknown	Known	Basic ED	NPO and UMP	9.2.3
Known	Known	Known	Weighted ED	NPO	9.2.5.1
Known	Unknown and small	Known	Eckart filter	LO	9.2.5.2
Known	Unknown	Known	Eckart filter	Maximum DI	9.2.5.3
Unknown	Unknown and large	Known	NN ED	Asympt. NPO	9.2.6.1
Unknown	Unknown and small	Known	NN ED	LO	9.2.6.1
Unknown	Unknown	Known	GLR ED	GLR	9.2.6.2
Unknown	Unknown	Unknown	MGLR ED or power-law ED	None	9.2.8
Deterministic signals					
Unknown	Unknown	Known	NN ED	GLR, LO phase invariant	9.2.9.1
Unknown	Unknown	Partially known	Subspace ED	GLR	9.2.9.2
Unknown	Unknown	Unknown	Power-law ED	None	9.2.9.3

Legend:

Detectors

ED = energy detector

NN = noise-normalized

Optimality

NPO = Neyman-Pearson optimal

LO = Locally optimal

UMP = uniformly most powerful

GLR = generalized likelihood ratio

MGLR = modified GLR

DI = detection index

Notes:

1. The shape and strength of the spectrum are described separately; the shape characterizes the frequency dependence and the strength characterizes the average level
2. The noise and signal PSDs for this case are assumed to be constant within the signal band

weighted-sum energy detector is presented in Sect. [9.2.7](#) and various techniques for evaluating or approximating the performance of the non-linear-sum energy detectors are presented along with the detectors themselves.

9.2.1 Statistical Characterization of the Signal and Noise

As has been noted previously, underwater acoustic signals generally have bandpass spectra. Detector design can then proceed by basebanding the bandpass signal in order to exploit the simple statistical characterizations of sampled complex envelope data as described in Sect. 7.3.5. Take for consideration a segment of the complex envelope signal $\tilde{x}(t)$ starting at time τ_p and having duration T_p . Sampling the complex envelope every $T_s = 1/f_s$ and placing the $M = T_p/T_s = T_p f_s$ samples into a vector results in

$$\mathbf{x} = [\tilde{x}(\tau_p) \ \tilde{x}(\tau_p + T_s) \ \cdots \ \tilde{x}(\tau_p + (M-1)T_s)]^T \quad (9.3)$$

$$= \mathbf{s} + \mathbf{v}, \quad (9.4)$$

which can be characterized as the sum of signal (\mathbf{s}) and noise (\mathbf{v}) components. The vector of noise complex-envelope samples,

$$\mathbf{v} \sim \mathcal{CN}(\mathbf{0}, \mathbf{\Lambda}_t), \quad (9.5)$$

is complex-Gaussian distributed with zero mean and a Toeplitz covariance matrix $\mathbf{\Lambda}_t$. The (i, j) element of $\mathbf{\Lambda}_t$ is

$$\{\mathbf{\Lambda}_t\}_{i,j} = R_{\tilde{v}\tilde{v}}\left(\frac{i-j}{f_s}\right) \quad (9.6)$$

where $R_{\tilde{v}\tilde{v}}(\tau)$ is the ACF of the noise complex envelope. Thus, the elements on the l th diagonal of $\mathbf{\Lambda}_t$ for $l = 0, \pm 1, \dots, \pm(M-1)$, where $l = 0$ is the main diagonal, are the same and formed by taking the l th sample of the noise ACF spaced every $T_s = 1/f_s$. The subscript t on $\mathbf{\Lambda}_t$ is used to indicate that this covariance matrix represents the sampled data in the time domain; it does not imply the covariance matrix is a function of time. The wide-sense-stationarity assumption implies $\mathbf{\Lambda}_t$ does not change with the time τ_p of the data sample. Similar assumptions for the signal PSD result in

$$\mathbf{s} \sim \mathcal{CN}(\mathbf{0}, \mathbf{\Psi}_t), \quad (9.7)$$

where $\mathbf{\Psi}_t$ is the covariance matrix of the sampled complex signal envelope. Assuming the signal and noise are statistically independent means their covariances add so the signal-plus-noise measurement is distributed according to

$$\mathbf{x} \sim \mathcal{CN}(\mathbf{0}, \mathbf{\Lambda}_t + \mathbf{\Psi}_t). \quad (9.8)$$

Applying the probability density function (PDF) of the multivariate complex Gaussian distribution from Sect. 5.6.9 to (9.8), the PDF of \mathbf{x} is seen to be

$$f(\mathbf{x}|H_1) = \frac{1}{\pi^M |\boldsymbol{\Lambda}_t + \boldsymbol{\Psi}_t|} e^{-\mathbf{x}^H (\boldsymbol{\Lambda}_t + \boldsymbol{\Psi}_t)^{-1} \mathbf{x}} \quad (9.9)$$

when signal is present and

$$f(\mathbf{x}|H_0) = \frac{1}{\pi^M |\boldsymbol{\Lambda}_t|} e^{-\mathbf{x}^H \boldsymbol{\Lambda}_t^{-1} \mathbf{x}} \quad (9.10)$$

when only noise is present.

The signal covariance matrix is also a Toeplitz matrix populated by sampling the ACF of the complex envelope of the signal envelope, $R_{\tilde{s}\tilde{s}}(\tau)$, with the (i, j) element taking on value

$$\{\boldsymbol{\Psi}_t\}_{i,j} = R_{\tilde{s}\tilde{s}}\left(\frac{i-j}{f_s}\right). \quad (9.11)$$

The ACF of the signal is most easily described as the inverse Fourier transform of the PSD of the complex envelope,

$$R_{\tilde{s}\tilde{s}}(\tau) = \mathcal{F}^{-1}\{S_{\tilde{s}\tilde{s}}(f)\}. \quad (9.12)$$

Recall from Sect. 7.3.4 that the PSD of the complex envelope has the same shape as the positive-frequency half of the PSD of the bandpass signal,

$$S_{\tilde{s}\tilde{s}}(f) = \begin{cases} 4S_{ss}(f + f_c) & |f| < f_s/2 \\ 0 & \text{otherwise} \end{cases}. \quad (9.13)$$

Thus, if the signal has bandwidth W , so does the complex envelope and the ACF can then be expected to have a width of approximately $1/W$. The diagonal term of the signal covariance matrix is two times the total power in the signal,

$$\begin{aligned} \psi_t = R_{\tilde{s}\tilde{s}}(0) &= \int_{-f_s/2}^{f_s/2} 4S_{ss}(f + f_c) df \\ &= 2 \int_{-\infty}^{\infty} S_{ss}(f) df, \end{aligned} \quad (9.14)$$

where it has been assumed that the signal is properly bandpass (i.e., $W < 2f_c$) and that the basebanding captures all of the signal's positive-frequency spectral content (i.e., $f_s > W$).

9.2.2 SNR After the Coherent Portion of Detection Processing

As will be seen in Sect. 9.2.10, detection processing for random signals can be described as a coherent or linear portion followed by an incoherent or non-linear one. Although the SNR metric can easily be carried through linear processing, it cannot typically be extended through non-linear processing owing to cross terms involving signal and noise products.

Linear processing of the sampled data vector \mathbf{x} can be described by the vector inner product $\mathbf{a}^H \mathbf{x}$, which is zero-mean complex Gaussian distributed,

$$X = \mathbf{a}^H \mathbf{x} \sim \mathcal{CN}\left(0, \mathbf{a}^H \boldsymbol{\Lambda}_t \mathbf{a} + \mathbf{a}^H \boldsymbol{\Psi}_t \mathbf{a}\right), \quad (9.15)$$

with a variance equal to the sum of the variances of the noise and signal components, respectively, $\mathbf{a}^H \boldsymbol{\Lambda}_t \mathbf{a}$ and $\mathbf{a}^H \boldsymbol{\Psi}_t \mathbf{a}$. The ratio of these components yields the SNR after the coherent portion of detection processing,

$$S^d = \frac{\mathbf{a}^H \boldsymbol{\Psi}_t \mathbf{a}}{\mathbf{a}^H \boldsymbol{\Lambda}_t \mathbf{a}} = \frac{\mathbf{b}^H \boldsymbol{\Lambda}_t^{-1/2} \boldsymbol{\Psi}_t \boldsymbol{\Lambda}_t^{-1/2} \mathbf{b}}{\mathbf{b}^H \mathbf{b}}. \quad (9.16)$$

Pre- and post-multiplication of $\boldsymbol{\Psi}_t$ by $\boldsymbol{\Lambda}_t^{-1/2}$ has the effect of normalizing the signal PSD by the noise PSD to produce a Rayleigh quotient [5, Sect. 6.4] in the vector $\mathbf{b} = \boldsymbol{\Lambda}_t^{1/2} \mathbf{a}$ and matrix $\boldsymbol{\Lambda}_t^{-1/2} \boldsymbol{\Psi}_t \boldsymbol{\Lambda}_t^{-1/2}$. The quadratic forms in \mathbf{b} in the numerator and denominator can be converted to the frequency domain by characterizing the product $\boldsymbol{\Lambda}_t^{-1/2} \boldsymbol{\Psi}_t \boldsymbol{\Lambda}_t^{-1/2}$ as a noise whitening, approximating the summations as integrals, and using the inverse-Fourier-transform definition of the ACFs and the linear filter forming \mathbf{b} . By doing this, the SNR after the coherent portion of detection processing is seen to be an average over the ratio of bandpass signal and noise PSDs (respectively $S_{ss}(f)$ and $S_{vv}(f)$),

$$S^d \approx \left[\int_{f_c - f_s/2}^{f_c + f_s/2} P_b(f) \frac{S_{ss}(f)}{S_{vv}(f)} df \right] \div \left[\int_{f_c - f_s/2}^{f_c + f_s/2} P_b(f) df \right] \quad (9.17)$$

where

$$P_b(f) = \begin{cases} |B(f - f_c)|^2 & \text{for } |f - f_c| < f_s/2 \\ 0 & \text{otherwise} \end{cases} \quad (9.18)$$

is the frequency-shifted squared modulus of the transfer function of the linear filtering implied by \mathbf{b} . Because $P_b(f)$ is non-negative, the normalization in (9.17) implies S^d must be between the minimum and maximum ratio of the signal and noise PSDs within the processing band. As will be seen in Sect. 9.2.11 for an energy detector with noise normalization, the average SNR over frequency,

$$S^d \approx \frac{1}{W} \int_{f_c-W/2}^{f_c+W/2} \frac{S_{ss}(f)}{S_{vv}(f)} df \quad (9.19)$$

can be used if there is not too much variation in the signal-to-noise PSD ratio.

If the signal and noise PSDs conspire to have a constant ratio, S_0/N_0 , within the signal band of $f_c \pm W/2$, then this simplifies to

$$S^d \approx \frac{S_0}{N_0} \left[\frac{\int_{f_c-W/2}^{f_c+W/2} P_b(f) df}{\int_{f_c-f_s/2}^{f_c+f_s/2} P_b(f) df} \right] \leq \frac{S_0}{N_0} \quad (9.20)$$

where it is important to notice the differences between the limits of integration in the numerator and denominator integrals. Clearly, sampling at the signal bandwidth when the signal-to-noise PSD ratio is constant achieves the upper bound. However, designing the linear filtering so $P_b(f)$ decays rapidly for $|f - f_c| > W/2$ achieves the same effect, so sampling at the signal bandwidth is not a requirement. This can be accomplished by restricting the coherent processing to have a temporal extent $T_{coh} \approx 1/W$.

For example, suppose the sampling is above the bandwidth and coherent processing is done with $b(t) = \text{sinc}(t/T_{coh})$ which results in a Fourier transform $B(f)$ that is a rectangular function

$$B(f) = T_{coh}\text{rect}(T_{coh}f) \quad (9.21)$$

spanning $f \in \pm 1/(2T_{coh})$. The SNR after coherent detection processing over a bandwidth W for the scenario of a constant signal-to-noise PSD ratio is then

$$S^d = \frac{S_0}{N_0} \min\{WT_{coh}, 1\}. \quad (9.22)$$

Choosing $T_{coh} = 1/W$ achieves the maximum SNR and when $T_{coh} < 1/W$, increasing it improves SNR at the rate of ten decibels per decade of increase (3 dB per doubling),

$$\text{SNR}^d = 10 \log_{10} \left(\frac{S_0}{N_0} \right) + 10 \log_{10} W + 10 \log_{10} T_{coh} \quad \text{with} \quad T_{coh} \leq \frac{1}{W}. \quad (9.23)$$

As previously mentioned, the concept of a ratio of signal power to noise power does not easily extend to non-linear processing because of cross terms between the signal and noise. The following is a more detailed explanation of what conditions foil the direct use of SNR as a performance measure for this scenario. The context

in which this discussion occurs is in sonar equation analysis where one desires a particular detection operating point in a remote sensing system and wishes to solve the performance equation for some quantity entering into it (e.g., see Sect. 2.3). Examples of such quantities include the range at which the performance is achieved, the size of an array required to obtain the operating point, the bandwidth of the signal measurement, or the time-bandwidth product of the signal measurement used in the decision. The first three of these examples impact the SNR after the coherent portion of detection processing; however, they do not otherwise alter the statistical distribution of the detector decision statistic. Because of this, the SNR required to achieve an operating point ($\overline{\text{SNR}}^d$) is only a function of the operating point and not the quantity for which the performance equation is being inverted. In these situations the achieved SNR after the coherent portion of detection processing (SNR^d) can be used as a proxy for achieving the operating point. That is, any conditions where $\text{SNR}^d = \overline{\text{SNR}}^d$ will achieve the operating point.

Although this constraint of not altering the PDF of the decision statistic is satisfied for any changes affecting the linear portion of processing and Gaussian-distributed data (at the complex envelope), it may and may not hold for non-Gaussian data or for non-linear processing. An example of where it does not hold can be found in accounting for the incoherent integration in an energy detector. As will be seen in Sect. 9.2.3.1, application of an energy detector to a Gaussian random signal results in a decision statistic whose PDF depends on the amount of incoherent integration, which is quantified by the time-bandwidth product ($M = T_p W$). Thus, the relationship between $\overline{\text{SNR}}^d$ and the operating point depends on the operating point and the processing time-bandwidth product. For an energy detector, this results in $\overline{\text{SNR}}^d$ decreasing asymptotically at a rate of five decibels per decade of increase in the time-bandwidth product (i.e., 1.5 dB per doubling). Although it is tempting to interpret this as implying a 5-dB-per-decade increase in the SNR achieved after incoherent integration as is done for parameters affecting the linear portion of the processing chain, such an interpretation would be incorrect—*incoherent integration does not increase the SNR after the coherent portion of detection processing and in general there is no signal-to-noise power ratio that can be formed after non-linear processing*. What incoherent integration does is to alter the statistical distribution of the decision statistic so as to increase the separation between the PDFs of the detector decision statistic under the signal-present and noise-only conditions.

9.2.3 Detector for Random Signals and Noise Having Constant Spectra in a Known Frequency Band

In order to introduce the energy detector, a basic scenario consisting of both signal and noise with a constant PSD is considered. The ensuing simple characterization of the sampled complex envelope allows derivation of the detector using time-domain data. More complicated scenarios involving varying signal and noise

PSDs are considered in later sections after introducing a transformation of the sampled complex envelope data to the frequency domain through a discrete Fourier transform.

If the signal PSD is assumed to be constant within its frequency band with (two-sided) level $S_0/2$ [units: $\mu\text{Pa}^2/\text{Hz}$], then the ACF of the complex envelope is

$$R_{\tilde{s}\tilde{s}}(\tau) = 2S_0 W \text{sinc}(W\tau). \quad (9.24)$$

Sampling the complex envelope at $f_s = W$ then results in zero correlation between the samples, which are also statistically independent owing to the assumption of Gaussianity. For this scenario, the signal covariance matrix is simply $\Psi_t = \psi_t \mathbf{I}$ where $\psi_t = R_{\tilde{s}\tilde{s}}(0) = 2S_0 W$. Assuming the noise similarly has a constant PSD within the signal band implies the sampled complex noise envelope data have covariance matrix $\Lambda_t = \lambda_t \mathbf{I}$ where $\lambda_t = 2N_0 W$.

The first step in deriving a detector is to obtain the PDF of the data when signal is present (H_1) and when there is only noise (H_0). The PDF of \mathbf{x} when signal is present from (9.9) can be simplified in the case of constant signal and noise PSDs with sampling at the bandwidth to

$$f(\mathbf{x}|H_1) = \frac{1}{[\pi(\lambda_t + \psi_t)]^M} e^{-\mathbf{x}^H \mathbf{x}/(\lambda_t + \psi_t)}. \quad (9.25)$$

The PDF of the data when only noise is present is then easily obtained from (9.25) by setting ψ_t to zero,

$$f(\mathbf{x}|H_0) = \frac{1}{(\pi\lambda_t)^M} e^{-\mathbf{x}^H \mathbf{x}/\lambda_t}. \quad (9.26)$$

The Neyman-Pearson-optimal (NPO) detector (Sect. 6.2.3) is obtained by forming the likelihood ratio,

$$T(\mathbf{x}) = \frac{f(\mathbf{x}|H_1)}{f(\mathbf{x}|H_0)} = \frac{1}{\left(1 + \frac{\psi_t}{\lambda_t}\right)^M} \exp\left\{\frac{\mathbf{x}^H \mathbf{x}}{1 + \lambda_t/\psi_t}\right\} \quad (9.27)$$

The form of the detector can be simplified further by applying any transformation that is strictly monotonically increasing. Because such transformations are one-to-one or invertible, they do not affect the optimality of the Neyman-Pearson optimal (NPO) detector, which maximizes the probability of detection given a fixed probability of false alarm. Multiplying (9.27) by $(1 + \psi_t/\lambda_t)^M$, taking the logarithm, and then multiplying by $(1 + \lambda_t/\psi_t)/\lambda_t$ simplifies the decision statistic to be simply the inner product of the signal-plus-noise measurement vector scaled by the noise variance,

$$T(\mathbf{x}) \stackrel{D}{\equiv} \frac{\mathbf{x}^H \mathbf{x}}{\lambda_t} \quad (9.28)$$

where the notation $\stackrel{D}{\equiv}$ implies an equivalent detector decision statistic. As was done in developing the matched filter, a dependence on the noise variance λ_t is retained to reinforce that it is required to implement the detector. Because the NPO decision statistic in (9.28) is invariant to the actual value of the signal variance ψ_t , the detector is also uniformly most powerful (UMP) over ψ_t .

From the form of (9.28), the coherent portion of detection processing stops with formation of the complex envelope for this scenario of constant signal and noise PSDs and sampling at the signal bandwidth. As such, the SNR after the coherent portion of detection processing is the ratio of ψ_t to λ_t ,

$$S^d = \frac{\psi_t}{\lambda_t} = \frac{2S_0 W}{2N_0 W} = \frac{S_0}{N_0}. \quad (9.29)$$

This simplifies to the ratio of the signal and noise PSDs as was shown in Sect. 9.2.2.

9.2.3.1 The Basic Energy Detector and Its Performance Analysis

The structure of the detector in (9.28), which discards the phase of the signal and combines the squared moduli of the complex envelope samples, is known as an *energy detector* (ED). The nomenclature is easily understood when the sum formed by the vector inner product in (9.28) is approximated by an integral. The decision statistic is then seen to be proportional to the energy in the continuous-time complex envelope $[\tilde{x}(t)]$, analytic signal $[\dot{x}(t)]$, and bandpass signal $[x(t)]$,

$$\frac{\mathbf{x}^H \mathbf{x}}{W} \approx \int_{\tau_p}^{\tau_p + T_p} |\tilde{x}(t)|^2 dt = \int_{\tau_p}^{\tau_p + T_p} |\dot{x}(t)|^2 dt \approx 2 \int_{\tau_p}^{\tau_p + T_p} x^2(t) dt. \quad (9.30)$$

Using Parseval's theorem (Sect. 4.3.2), the time-domain representation of (9.30) can be converted to a frequency-domain representation. This will be done in Sect. 9.2.4 when shaped PSDs are considered.

Recalling that the detector is implemented by comparing the decision statistic $T(\mathbf{x})$ to a decision threshold h ,

$$T(\mathbf{x}) \stackrel[H_1]{\gtrless}{<} h, \quad (9.31)$$

the probability of false alarm (P_f) is obtained as

$$P_f = \Pr\{T(\mathbf{x}) \geq h | H_0\} \quad (9.32)$$

where H_0 is the noise-only hypothesis and the probability of detection as

$$P_d = \Pr\{T(\mathbf{x}) \geq h | H_1\} \quad (9.33)$$

where H_1 is the signal-plus-noise hypothesis. The i th sample of the complex envelope $X_i = \tilde{x}(\tau_p + (i - 1)T_s)$ is a zero-mean complex-Gaussian distributed random variable with variance $\lambda_t + \psi_t$ when signal is present. From Sect. 7.3.6, this is part of the Rayleigh-envelope distribution chain so its squared modulus will be exponentially distributed with mean $\lambda_t + \psi_t$. When the sampling is done at the rate of the signal bandwidth ($f_s = W$), the decision statistic is then the sum of $M = WT_p$ independent and identically distributed exponential random variables with mean $1 + S^d$ (recall that $S^d = \psi_t/\lambda_t = S_0/N_0$). This sum is gamma distributed,

$$T(\mathbf{x}) = \sum_{i=1}^M \frac{|X_i|^2}{\lambda_t} \sim \text{Gamma}\left(M, 1 + S^d\right) \quad (9.34)$$

with a shape parameter of M and a scale parameter $1 + S^d$.

When the processing time-bandwidth product is one ($M = WT_p = 1$), there is only one term in the sum and so the detection performance of the energy detector for a Gaussian random signal is identical in form to that described for a matched filter detecting a signal with known form and Gaussian amplitude fluctuations. Using the results of Sect. 8.2.5, the probabilities of false alarm and detection for $M = 1$ are

$$P_f = e^{-h} \quad \text{and} \quad P_d = e^{-h/(1+S^d)} = P_f^{1/(1+S^d)}. \quad (9.35)$$

For this case of constant signal and noise PSDs and $M = WT_p = 1$, the SNR required to achieve a desired operating point is easily seen to be

$$\overline{\text{SNR}}^d = 10 \log_{10}(S^d) = 10 \log_{10} \left[\frac{\log(P_f)}{\log(P_d)} - 1 \right]. \quad (9.36)$$

At the other extreme where the time-bandwidth product is large ($M = WT_p \gg 1$), the decision statistic is approximately Gaussian distributed. Using the mean and variance of the gamma distribution from Sect. 5.6.11 results in

$$\mu_1 = M(1 + S^d) \quad \text{and} \quad \sigma_1^2 = M(1 + S^d)^2 \quad (9.37)$$

when signal is present and

$$\mu_0 = M \quad \text{and} \quad \sigma_0^2 = M \quad (9.38)$$

when there is only noise. For a Gaussian-distributed decision statistic with parameters (μ_0, σ_0^2) under H_0 and (μ_1, σ_1^2) under H_1 , the probabilities of detection and false alarm are

$$P_d = 1 - \Phi\left(\frac{h - \mu_1}{\sigma_1}\right) \quad \text{and} \quad P_f = 1 - \Phi\left(\frac{h - \mu_0}{\sigma_0}\right) \quad (9.39)$$

where h is the decision threshold and $\Phi(x)$ is the CDF of the standard normal distribution. To more easily describe the relationship between P_d and P_f , define $\phi_f = \Phi^{-1}(1 - P_f)$ and $\phi_d = \Phi^{-1}(1 - P_d)$ where $z = \Phi^{-1}(p)$ is the functional inverse of the CDF of the standard normal distribution (i.e., so $p = \Phi(z)$). These definitions result in the equation

$$\phi_d = \frac{\sigma_0}{\sigma_1} \left[\phi_f - \frac{(\mu_1 - \mu_0)}{\sigma_0} \right] \quad (9.40)$$

defining the relationship between P_d , P_f and the means and variances of the decision statistic under H_0 and H_1 . Using the moments for the energy detector in (9.40) produces

$$\phi_d = \frac{1}{1 + S^d} \left[\phi_f - \sqrt{M} S^d \right] \quad (9.41)$$

which can be solved for S^d to result in

$$S^d = \frac{\phi_f - \phi_d}{\sqrt{M} \left(1 + \frac{\phi_d}{\sqrt{M}} \right)}. \quad (9.42)$$

Converting this to decibels,

$$\overline{\text{SNR}}^d = -5 \log_{10} M + 10 \log_{10} (\phi_f - \phi_d) - 10 \log_{10} \left(1 + \frac{\phi_d}{\sqrt{M}} \right) \quad (9.43)$$

$$\approx -5 \log_{10} M + 10 \log_{10} (\phi_f - \phi_d), \quad (9.44)$$

illustrates how increasing the amount of incoherent integration reduces the SNR required to achieve an operating point at the rate of five decibels per decade (i.e., 1.5 dB per doubling) both when M is large and when $P_d = 0.5$ which results in $\phi_d = 0$.

This leaves the region where M is greater than one but not large enough to satisfy the Gaussian approximation and forces use of the gamma distribution described in (9.34). The cumulative distribution function (CDF) of a $\text{Gamma}(\alpha, \beta)$ random variable G ,

$$\begin{aligned}
F_G(g; \alpha, \beta) &= \Pr\{G \leq g\} = \int_0^g \frac{x^{\alpha-1} e^{-x/\beta}}{\Gamma(\alpha)\beta^\alpha} dx \\
&= \int_0^{g/\beta} \frac{y^{\alpha-1} e^{-y}}{\Gamma(\alpha)} dy = \tilde{\gamma}\left(\frac{g}{\beta}; \alpha\right),
\end{aligned} \tag{9.45}$$

can be obtained from the normalized incomplete gamma function $\tilde{\gamma}(x; \alpha) = \gamma(\alpha, x)/\Gamma(\alpha)$. The incomplete gamma function $\gamma(\alpha, x)$ exists in many common computational packages (e.g., `gammainc` in MATLAB®, which includes the normalization) and is easily implemented through various numerical routines [6, Sect. 6.2]. Using (9.45) to describe the probabilities of false alarm and detection results in

$$P_f = 1 - \tilde{\gamma}(h; M) \quad \text{and} \quad P_d = 1 - \tilde{\gamma}\left(\frac{h}{1+S^d}; M\right). \tag{9.46}$$

If $x = \tilde{\gamma}^{-1}(p; \alpha)$ is the functional inverse of the incomplete gamma function (i.e., so that $p = \tilde{\gamma}(x; \alpha)$), then the detector decision threshold is

$$h = \tilde{\gamma}^{-1}(1 - P_f; M) \tag{9.47}$$

and the SNR required to achieve the operating point is

$$S^d = \frac{\tilde{\gamma}^{-1}(1 - P_f; M)}{\tilde{\gamma}^{-1}(1 - P_d; M)} - 1. \tag{9.48}$$

The MATLAB® code evaluating the required SNR in decibels ($\overline{\text{SNR}}^d = 10 \log_{10} S^d$) is simply

```
DT = 10*log10(gaminv(1-Pf,M)/gaminv(1-Pd,M)-1)
```

A comparison of the SNR required to achieve an operating point as obtained either through inversion of the incomplete gamma functions in (9.48) or the Gaussian approximations in (9.43) and (9.44) is shown in Fig. 9.4 as a function of the processing time-bandwidth product M . Although the Gaussian approximations are accurate when M is very large, they can be very inaccurate if used when M is small. While (9.43) can be useful as low as $M = 20$ in some scenarios, (9.44) generally requires a substantially larger value of M before it is accurate.

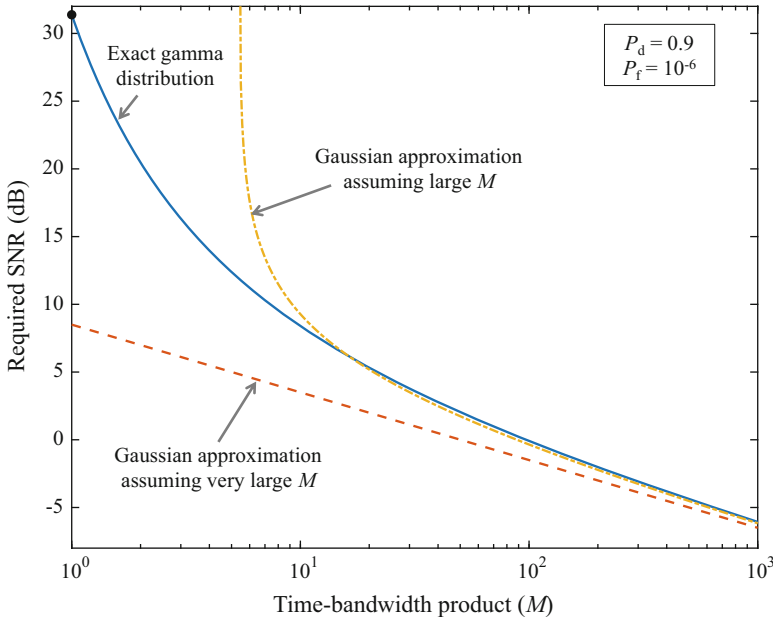


Fig. 9.4 SNR required to achieve $P_d = 0.9$ and $P_f = 10^{-6}$ as a function of the processing-time-bandwidth product (M) when detecting a Gaussian random signal with an energy detector. The approximations assuming a Gaussian-distributed decision statistic are not always accurate unless M is very large

9.2.4 Frequency-Domain Processing for Shaped Signal and Noise Spectra

The assumption of constant noise and signal PSDs in Sect. 9.2.3 was convenient for derivation of the basic energy detector and is a reasonable assumption for narrowband signals. However, as signal bandwidth increases, so does the variation expected in both the noise and signal PSDs. When either or both PSDs are shaped, sampling at the bandwidth will not necessarily produce uncorrelated samples in the time domain. Rather than working with correlated samples in the time domain, transformation of the data to the frequency domain has the effect of decorrelating the data owing to the orthogonality of frequency bins spaced every $1/T_p$ where T_p is the temporal extent of the analysis window. As described in [7], this frequency domain approach dates to early work in time-series analysis by Whittle [8]. Transformation to the frequency domain is accomplished analytically on the sampled data by the linear operation

$$\mathbf{y} = \mathbf{D}^H \mathbf{x} \quad (9.49)$$

where \mathbf{D} is an M -by- M discrete-Fourier-transform (DFT) matrix with (i, k) element

$$\{\mathbf{D}\}_{i,k} = \frac{1}{\sqrt{M}} e^{j2\pi ik/M} \quad (9.50)$$

with both i and k ranging from 0 to $M - 1$ (using DFT notation of indexing from 0 rather than 1). The covariance matrix of \mathbf{y} is then

$$\begin{aligned} \boldsymbol{\Sigma}_y &= \mathbf{D}^H \boldsymbol{\Lambda}_t \mathbf{D} + \mathbf{D}^H \boldsymbol{\Psi}_t \mathbf{D} \\ &= \boldsymbol{\Lambda} + \boldsymbol{\Psi} \end{aligned} \quad (9.51)$$

$$\approx \text{diag}\{\psi_0, \dots, \psi_{M-1}\} + \text{diag}\{\lambda_0, \dots, \lambda_{M-1}\}. \quad (9.52)$$

The DFT matrix \mathbf{D} has some interesting properties. It is full rank and therefore the transformation is invertible (i.e., the inverse of \mathbf{D} exists and $\mathbf{x} = \mathbf{D}^{-H} \mathbf{y}$). It is also orthonormal, which implies that $\mathbf{D}^H \mathbf{D} = \mathbf{I}$ so $\mathbf{D}^{-1} = \mathbf{D}^H$. Using this to describe the (un-normalized) time-domain energy detector from (9.28) in terms of the frequency-domain data results in

$$\mathbf{x}^H \mathbf{x} = \mathbf{x}^H \mathbf{D} \mathbf{D}^{-1} \mathbf{x} = \mathbf{x}^H \mathbf{D} \mathbf{D}^H \mathbf{x} = \mathbf{y}^H \mathbf{y}, \quad (9.53)$$

which can also be obtained using Parseval's theorem.

However, these properties do not directly indicate that the frequency-domain noise covariance matrix $\mathbf{D}^H \boldsymbol{\Lambda}_t \mathbf{D}$ or signal covariance matrix $\mathbf{D}^H \boldsymbol{\Psi}_t \mathbf{D}$ are approximately diagonal, which is the primary objective of the transformation. In the limit of an asymptotically large analysis window (i.e., $T_p \rightarrow \infty$), the elements of \mathbf{y} , which are Fourier series coefficients, are known to be uncorrelated [9, Sect. 12–3]. Thus, asymptotically as $T_p \rightarrow \infty$, the frequency-domain covariance matrices are diagonal and it is reasonable to expect finite analysis windows to approximate this ideal. Smaller windows were examined in [10] to determine how large T_p should be with a recommendation for $T_p > 8/W$. The covariance between two DFT bins (i.e., elements of \mathbf{y}) is related to the PSD in the following section where it is seen that the diagonal approximation is more accurate when the PSD is constant over the extent of the DFT bin.

When the covariance matrix of the frequency domain data is diagonal, the PDF for the signal-present case is

$$f_Y(\mathbf{y}) = \frac{\exp\left\{-\sum_{m=0}^{M-1} |Y_m|^2 / (\lambda_m + \psi_m)\right\}}{\pi^M \prod_{m=0}^{M-1} (\lambda_m + \psi_m)}. \quad (9.54)$$

The PDF when there is only noise can then be obtained from (9.54) by setting ψ_m to zero. Note how only the squared modulus of Y_m is used in either the signal or noise PDF; the phase of Y_m is not used. This implies that any detector formed using the PDFs can be described as a function of $U_m = |Y_m|^2$ for $m = 0, \dots, M - 1$ and

will not depend on any of the phases.² Detector derivation can therefore begin with a statistical characterization of the squared moduli in $\mathbf{u} = [U_0 \cdots U_{M-1}]^T$. Because the zero-mean complex Gaussian distribution is part of the Rayleigh-envelope distribution chain (see Sect. 7.3.6), the squared modulus of Y_m is exponentially distributed with mean λ_m when there is only noise,

$$U_m | H_0 \sim \text{Expon}\{\lambda_m\}, \quad (9.55)$$

and with mean $\lambda_m + \psi_m$ when signal is present,

$$U_m | H_1 \sim \text{Expon}\{\lambda_m + \psi_m\}. \quad (9.56)$$

The assumption of zero correlation between Y_m and Y_n when $m \neq n$ coupled with the Gaussianity of the data implies Y_m and Y_n , and therefore U_m and U_n , are independent when $m \neq n$.

9.2.4.1 Decorrelation of DFT Bin Data

To assess the correlation between DFT bins, consider the noise covariance matrix Λ whose (m, n) element is the covariance between the noise in the m th and n th DFT frequency bin. The (m, n) element can be represented as a matrix–vector bilinear form

$$\{\Lambda\}_{m,n} = E[Y_m Y_n^* | H_0] = \mathbf{d}_m^H \boldsymbol{\Lambda} \mathbf{d}_n \quad (9.57)$$

where \mathbf{d}_m is the m th column of \mathbf{D} , which produces the m th DFT bin via $Y_m = \mathbf{d}_m^H \mathbf{x}$. The bilinear form can be described as a double sum, which can then be approximated by a double integral,

$$\{\Lambda\}_{m,n} = \frac{1}{M} \sum_{i=0}^{M-1} \sum_{k=0}^{M-1} e^{-j2\pi im/M} e^{j2\pi kn/M} R_{\tilde{v}\tilde{v}}\left(\frac{i-k}{f_s}\right) \quad (9.58)$$

$$\approx \frac{f_s^2}{M} \iint_0^{T_p} e^{-j2\pi t f_m} e^{j2\pi s f_n} R_{\tilde{v}\tilde{v}}(t-s) dt ds, \quad (9.59)$$

where f_m is the frequency of the m th DFT bin from Sect. 4.8,

²In mathematical statistics, this condition arises from the sufficiency [11, Sect. 6.2] of the squared moduli for the model parameters.

$$f_m = \begin{cases} \left(\frac{m}{M}\right) f_s & \text{for } 0 \leq m < \frac{M}{2} \\ \left(\frac{m-M}{M}\right) f_s & \text{for } \frac{M}{2} \leq m \leq M-1 \end{cases} \quad (9.60)$$

Using the definition of the inverse Fourier transform for $R_{\tilde{v}\tilde{v}}(t-s)$ in (9.59) then allows describing the double integral as a single integral over a sinc function that represents the transfer function of the narrowband filters comprising the DFT operation,

$$\{\Lambda\}_{m,n} \approx T_p f_s e^{j\pi(n-m)} \int_{-\infty}^{\infty} \text{sinc}(fT_p - n) \text{sinc}(fT_p - m) S_{\tilde{v}\tilde{v}}(f) df. \quad (9.61)$$

When the PSD is constant, the orthogonality of the sinc functions,

$$\int_{-\infty}^{\infty} \text{sinc}(fT_p - n) \text{sinc}(fT_p - m) df = \frac{1}{T_p} \delta[m-n], \quad (9.62)$$

where $\delta[m-n]$ is the Kronecker delta function, diagonalizes the covariance matrix. When the signal PSD is not constant, increasing the analysis time T_p makes the narrowband filter transfer functions (the sinc functions in (9.61)) even narrower. As described in [10], when T_p is large enough that the PSD varies slowly over a frequency span on the order of $1/T_p$, which is the width of the sinc functions, the signal covariance matrix will be useably close to diagonal. The rectangular PSD examined in [10] satisfied this when $T_p > 8/W$.

If the noise PSD of the complex envelope satisfies this condition, then the variance of the m th DFT bin under H_0 is

$$\lambda_m \approx f_s S_{\tilde{v}\tilde{v}}(f_m) = 4f_s S_{vv}(f_c + f_m) \quad (9.63)$$

where $S_{vv}(f)$ is the PSD of the bandpass noise. If the (two-sided) bandpass noise PSD is a constant $N_0/2$, this simplifies to $\lambda_m = 2N_0 f_s$. This result applies identically to the signal components in the DFT bin data and leads to

$$\psi_m \approx f_s S_{\tilde{s}\tilde{s}}(f_m) = 4f_s S_{ss}(f_c + f_m) \quad (9.64)$$

where $S_{\tilde{s}\tilde{s}}(f)$ and $S_{ss}(f)$ are, respectively, the PSDs of the complex envelope and bandpass signals. Similarly, a constant (two-sided) bandpass signal PSD equal to $S_0/2$ leads to $\psi_m = 2S_0 f_s$.

9.2.5 Detectors for Random Signals with Known Spectra in a Known Frequency Band

In this section detectors are derived under two different assumptions regarding how much is known about the signal PSD subject to knowledge or perfect estimation of the noise PSD. When the signal PSD is known precisely, the Neyman-Pearson optimal (NPO) detector can be implemented. As will be seen, this requires knowing its absolute or average level relative to the noise and is therefore an unlikely scenario. However, the performance of the NPO detector provides an upper bound on the performance of sub-optimal detectors derived under weaker knowledge conditions. For example, if the shape of the signal PSD is known but not its absolute or average level, the locally optimal detector can be derived and provide nearly optimal performance when SNR is low. As seen in Sect. 9.2.5.3, the locally optimal detector in this case is the same as the Eckart filter [12] which maximizes detection index. Presentation of techniques for evaluating the performance of these detectors is delayed until Sect. 9.2.7 where the general class of weighted energy detectors is considered.

9.2.5.1 Optimal Detector for a Signal with a Known Spectrum

The Neyman-Pearson-optimal (NPO) detector for the case where the signal and noise PSDs are known precisely can be derived from the log-likelihood ratio formed using the statistical characterization of the DFT-frequency-bin squared moduli $\mathbf{u} = [U_0 \cdots U_{M-1}]^T$ in (9.55) and (9.56). This results in

$$T(\mathbf{u}) = \sum_{m=0}^{M-1} \left[\frac{\psi_m}{\lambda_m(\lambda_m + \psi_m)} \right] U_m - \sum_{m=0}^M \log \left(1 + \frac{\psi_m}{\lambda_m} \right) \quad (9.65)$$

$$\stackrel{D}{\equiv} \sum_{m=0}^{M-1} \left[\frac{\psi_m}{\lambda_m(\lambda_m + \psi_m)} \right] U_m \quad (9.66)$$

where the notation $\stackrel{D}{\equiv}$ implies an invertible transformation to produce an equivalent detector decision statistic. Note that the detector is formed by a weighted sum of the DFT-bin squared moduli and that the weight

$$c_m = \frac{\psi_m}{\lambda_m(\lambda_m + \psi_m)} \quad (9.67)$$

depends on the relative level of the signal PSD (via ψ_m) to that of the noise PSD (via λ_m). In what will be a common theme, the frequency weighting in (9.67) can be described as having a noise normalization term, $1/\lambda_m$, followed by an SNR-

dependent weighting, $s_m/(1 + s_m)$ where $s_m = \psi_m/\lambda_m$ is the SNR in the m th DFT bin.

9.2.5.2 Locally Optimal Detector for a Signal with a Known Spectral Shape

The absolute level of the signal PSD or its relative level in reference to the noise PSD are unlikely to be known in most applications, which precludes implementation of the NPO detector. However, if at least the signal shape is known a locally optimal detector can be derived under a small signal assumption. Suppose the signal power in the m th DFT is

$$\psi_m = A\tilde{\psi}_m \quad (9.68)$$

where $A > 0$ is an unknown signal strength parameter and $\tilde{\psi}_m$ is the known shape scaled so that

$$\sum_{m=0}^{M-1} \tilde{\psi}_m = 1. \quad (9.69)$$

As described in Sect. 6.2.6, the locally optimal detector function is formed by taking the derivative of the joint PDF of the data under H_1 with respect to the signal strength parameter and evaluating it at zero. Because the DFT bin data are independent, the derivation can be applied to a single DFT bin and then the decision statistic formed by summing the data over all DFT bins after applying a scalar detector function (similar to the example in Sect. 6.2.6). The PDF for the m th DFT bin when signal is present is

$$f_1(u; A) = \frac{1}{\lambda_m + A\tilde{\psi}_m} e^{-u/(\lambda_m + A\tilde{\psi}_m)}. \quad (9.70)$$

When there is only noise it is simply

$$f_0(u) = \frac{1}{\lambda_m} e^{-u/\lambda_m}. \quad (9.71)$$

Using these to form the locally optimal detector function for the m th DFT bin results in

$$T(u) = \frac{\left[\frac{\partial}{\partial A} f_1(u; A) \right]_{A=0}}{f_0(u)} \quad (9.72)$$

$$= \frac{\tilde{\psi}_m}{\lambda_m} \left(\frac{u}{\lambda_m} - 1 \right). \quad (9.73)$$

The detector decision statistic is then formed by summing (9.73) over frequency,

$$T_{\text{LO}}(\mathbf{u}) = \sum_{m=0}^{M-1} \frac{\tilde{\psi}_m}{\lambda_m} \left(\frac{u}{\lambda_m} - 1 \right) \quad (9.74)$$

$$\stackrel{D}{\equiv} \sum_{m=0}^{M-1} \left[\frac{\tilde{\psi}_m}{\lambda_m^2} \right] U_m. \quad (9.75)$$

As should be expected, the LO detector can also be obtained from the NPO detector in (9.66) by assuming $\psi_m \ll \lambda_m$ so the denominator term $\lambda_m(\lambda_m + \psi_m) \approx \lambda_m^2$.

The term in parentheses in (9.73) has a mean of $A\tilde{\psi}_m/\lambda_m$ under H_1 and so can be considered as an estimate of the SNR in the m th DFT bin. The detector decision statistic in (9.74) then represents a correlation between the estimated SNR and the known form of the SNR.

9.2.5.3 Eckart Filter for Maximum Detection Index

The NPO and LO decision statistics in (9.66) and (9.75) are simply a weighted sum of the squared moduli of the DFT bins.

$$T(\mathbf{u}) = \sum_{m=0}^{M-1} c_m U_m. \quad (9.76)$$

Early work by Eckart [12] used the central-limit-theorem to approximate the sum as being Gaussian distributed for large values of M to argue that the weighting coefficients (c_m for $m = 0, \dots, M-1$) should be chosen to maximize the detection index. The detection index, which can be a proxy for SNR in representing detection performance when the decision statistic is Gaussian, is the ratio of the square of the difference in the means of the decision statistic under H_1 and H_0 to the variance under H_0 ,

$$d(\mathbf{c}) = \frac{\{E_1[T(\mathbf{u})] - E_0[T(\mathbf{u})]\}^2}{\text{Var}_0\{T(\mathbf{u})\}}. \quad (9.77)$$

Noting that U_m is an exponentially distributed random variable with mean $\lambda_m + \psi_m$ and therefore variance $(\lambda_m + \psi_m)^2$, the detection index for the decision statistic in (9.76) is seen to be

$$d(\mathbf{c}) = \frac{\left[\sum_{m=0}^{M-1} c_m \psi_m \right]^2}{\sum_{m=0}^{M-1} c_m^2 \lambda_m^2}. \quad (9.78)$$

There are many ways to determine which values of c_m will maximize $d(\mathbf{c})$. One way is to describe it as the Rayleigh quotient [5, Sect. 6.4] of a rank-one matrix. Suppose $\boldsymbol{\psi}$ is a vector with ψ_m in the m th element and as before Λ is a diagonal matrix with λ_m in the (m, m) element. The detection index can then be described as the Rayleigh quotient of the matrix $\Lambda^{-1} \boldsymbol{\psi} \boldsymbol{\psi}^T \Lambda^{-1}$ with the vector $\mathbf{d} = \Lambda \mathbf{c}$,

$$d(\mathbf{c}) = \frac{\mathbf{c}^T \boldsymbol{\psi} \boldsymbol{\psi}^T \mathbf{c}}{\mathbf{c}^T \Lambda^2 \mathbf{c}} = \frac{\mathbf{d}^T [\Lambda^{-1} \boldsymbol{\psi} \boldsymbol{\psi}^T \Lambda^{-1}] \mathbf{d}}{\mathbf{d}^T \mathbf{d}}. \quad (9.79)$$

The Rayleigh quotient is maximized when \mathbf{d} is chosen as proportional to the eigenvector associated with the maximum eigenvalue. Because the matrix in (9.79) is a vector outer product (i.e., $\mathbf{x}\mathbf{x}^T$) it has only one non-zero eigenvalue and the associated eigenvector is simply the vector itself (i.e., \mathbf{x}) normalized to unit length. Thus, choosing \mathbf{d} proportional to $\Lambda^{-1} \boldsymbol{\psi}$ will maximize the detection index. Converting this back to \mathbf{c} yields

$$\mathbf{c} \propto \Lambda^{-2} \boldsymbol{\psi}. \quad (9.80)$$

When only the form of the signal PSD is known and not its absolute level (i.e., $\psi_m = A \tilde{\psi}_m$ where A is unknown), it is sensible to use $\mathbf{c} = \Lambda^{-2} \boldsymbol{\psi} / A$ so \mathbf{c} will not depend on A . This results in

$$c_m = \frac{\tilde{\psi}_m}{\lambda_m^2} \quad (9.81)$$

as the weighting that maximizes the detection index.

A filter whose transfer function within the signal band has a squared modulus formed by (9.81) at frequency f_m is known as an Eckart filter. It results in a detector decision statistic with the form

$$T_{\text{EF}}(\mathbf{u}) = \sum_{m=0}^{M-1} \left[\frac{\tilde{\psi}_m}{\lambda_m^2} \right] U_m, \quad (9.82)$$

which is identical to the LO detector in (9.75). As with the NPO detector, the weighting on the m th DFT-bin data here is also a noise-normalization term, $1/\lambda_m$, followed by an SNR-dependent weighting, $\tilde{\psi}_m/\lambda_m$.

Although the Eckart filter maximizes the detection index metric, it does not satisfy the Neyman-Pearson criteria of maximizing the probability of detection

given the probability of false alarm except asymptotically as $A \rightarrow 0$ owing to its equivalence to the LO detector. The sub-optimality (with respect to the Neyman-Pearson criteria) continues to hold even when M is large and the Gaussian approximation is accurate. This apparent incongruity can be explained by noting that although detection index plays an important role in the P_d/P_f relationship for Gaussian-distributed data (e.g., see where it enters into (9.40)), it does not completely define this relationship unless the variance of the decision statistic is the same under both the signal-present and noise-only hypotheses. In the case of a weighted sum of DFT-bin squared moduli, the variances under the two hypotheses are different, which explains why the Eckart filter is not NPO. However, the Eckart filter does have an advantage over the NPO detector in that it can be implemented when the shape of the signal PSD is known but its amplitude is not (as with the LO detector). These reasons make the LO detector/Eckart filter an attractive option when the signal structure is known to within a scale factor.

9.2.6 Detectors for Random Signals with Unknown Spectra in a Known Frequency Band

In many scenarios, the signal PSD is not known except for the frequency band. In this section, two detectors are derived to handle this under the assumption that the noise PSD is known or can be perfectly estimated.

9.2.6.1 Large and Small Signal-to-Noise Spectral-Density Ratios

Recalling the form of the NPO detector when the signal PSD is known from (9.66),

$$T(\mathbf{u}) = \sum_{m=0}^{M-1} \left[\frac{\psi_m}{\lambda_m(\lambda_m + \psi_m)} \right] U_m, \quad (9.83)$$

it is clear that if the signal PSD is always large relative to the noise PSD (i.e., $\psi_m \gg \lambda_m$), the optimal detector is approximately

$$T(\mathbf{u}) \approx \sum_{m=0}^{M-1} \frac{U_m}{\lambda_m}, \quad (9.84)$$

which can be viewed as a noise-normalized energy detector.

In the opposite scenario where the signal PSD is always small relative to the noise PSD, the locally optimal (LO) detector (Sect. 6.2.6) can be used. In contrast to the LO detector derived in Sect. 9.2.5.2, here the signal-to-noise PSD ratio is assumed to be small in all of the DFT bins. If $s_m = \psi_m/\lambda_m$ is this SNR for the m th DFT bin,

then its PDF under H_1 is

$$f_1(u; s_m) = \frac{1}{\lambda_m(1+s_m)} e^{-u/[\lambda_m(1+s_m)]}. \quad (9.85)$$

Using this along with the PDF under H_0 from (9.71) results in

$$T(u) = \frac{\left[\frac{\partial}{\partial s_m} f_1(u; s_m) \right]_{s_m=0}}{f_0(u)} \quad (9.86)$$

$$= \frac{u}{\lambda_m} - 1 \quad (9.87)$$

as the LO detector function for the m th DFT bin. Combining³ this over the M DFT bins, which are assumed to be independent, produces the sum

$$T_{\text{LO}}(\mathbf{u}) = \sum_{m=0}^{M-1} \left(\frac{U_m}{\lambda_m} - 1 \right) \stackrel{D}{\equiv} \sum_{m=0}^{M-1} \frac{U_m}{\lambda_m} \quad (9.88)$$

which is identical to the noise-normalized energy detector from (9.84). Thus, the noise-normalized energy detector is optimal asymptotically as the SNR in every DFT bin becomes either very small or very large.

9.2.6.2 Generalized Likelihood Ratio Energy Detector for an Unknown Signal Spectrum

For broadband signals there may be scenarios where the signal fades within the band (e.g., from destructive combination of multiple propagation paths) and so satisfies neither the large- nor small-SNR assumptions made in the previous section. By treating the SNR s_m in the m th DFT-bin as an unknown parameter, a generalized likelihood ratio (GLR) energy detector can be derived. Because s_m is formed from the ratio of PSDs it must be non-negative. Enforcing this in maximum-likelihood estimation results in an estimator

$$\hat{s}_m(u) = \begin{cases} \frac{u}{\lambda_m} - 1 & \text{for } \frac{u}{\lambda_m} > 1 \\ 0 & \text{otherwise} \end{cases} \quad (9.89)$$

³A somewhat arcane difference between the development of the LO detector here and in Sect. 9.2.5.2 is that here there are M partial derivatives with respect to the DFT-bin SNRs that are then evaluated at zero whereas in Sect. 9.2.5.2 there is only one partial derivative with respect to A . In both cases, application to the joint PDF of the independent DFT-bin data results in a decision statistic comprising a sum over the detector non-linearities formed for the individual DFT bins.

for the SNR in the m th DFT bin where $z = u/\lambda_m$ represents the normalized squared modulus. Inserting this back into the PDF forms the GLR energy detector function

$$g(z) = \log \left\{ \frac{f_1(u; \hat{s}_m(u))}{f_0(u)} \right\} = \begin{cases} z - 1 - \log z & \text{for } z > 1 \\ 0 & \text{otherwise} \end{cases}. \quad (9.90)$$

The GLR energy detector decision statistic over all DFT bins is then formed by the sum

$$T_{\text{GLR}}(\mathbf{u}) = \sum_{m=0}^{M-1} g\left(\frac{U_m}{\lambda_m}\right) \quad (9.91)$$

which will tend to suppress DFT bins dominated by noise and include DFT bins with higher SNR. Because the probability of U_m exceeding λ_m under the null hypothesis is $e^{-1} \approx 0.37$, this detector will suffer if the frequency band includes too many noise-dominated DFT bins. However, a modification described in Sect. 9.2.8.1 that generalizes the GLR energy detector function in (9.90) ameliorates the problem. Techniques for analyzing the performance of the GLR energy detector are also discussed in Sect. 9.2.8.1.

9.2.7 Performance of a Weighted-Sum Energy Detector for Gaussian Random Signals and Noise

Each of the detectors derived in Sects. 9.2.3 and 9.2.6.1 can be described as a linear combination of the squared moduli of the DFT bin data. If $U_m = |Y_m|^2$ is the squared modulus of the data from the m th DFT bin, the detector decision statistic can be represented by the weighted sum

$$T(\mathbf{u}) = \sum_{m=0}^{M-1} c_m U_m. \quad (9.92)$$

This general form can be considered a *weighted* energy detector. Recall from Sect. 9.2.4 that under the assumption of a Gaussian random signal in Gaussian random noise U_m is exponentially distributed with a mean λ_m when there is only noise,

$$U_m | H_0 \sim \text{Expon}\{\lambda_m\}, \quad (9.93)$$

and with mean $\lambda_m + \psi_m$ when signal is present,

$$U_m | H_1 \sim \text{Expon}\{\lambda_m + \psi_m\}. \quad (9.94)$$

As long as the temporal extent of the data sample is large enough to ensure the DFT bin data are independent (see Sect. 9.2.4), the detector decision statistic in (9.92) is equivalent in a statistical sense to one comprising the sum of M independent exponentially distributed random variables with means $p_{m,0} = c_m \lambda_m$ under H_0 and $p_{m,1} = c_m (\lambda_m + \psi_m)$ under H_1 .

Two approaches for a direct evaluation of the probabilities of false alarm and detection of the weighted energy detector are described in Sects. 9.2.7.1 and 9.2.7.2: a potentially unstable finite sum and a numerical approach using an inversion of the characteristic function of the detector decision statistic. Approximations are also presented assuming $T(\mathbf{u})$ is Gaussian distributed (Sect. 9.2.7.3), gamma distributed (Sect. 9.2.7.4), or shifted-gamma (Sect. 9.2.7.5). In general, the gamma approximation provides a good balance between accuracy and effort when M is large (e.g., $M > 100$). When M is smaller, the error in the gamma approximation makes using the shifted-gamma approximation a better choice. The Gaussian approximation is not usefully accurate unless M is extremely large. This is illustrated in Fig. 9.5 where the approaches are compared for obtaining the ROC curve of an Eckart filter when M is small and large. Note that the figure is plotted using a “normal probability” scale for both P_d and P_f . On this scale Gaussian-distributed decision statistics result in linear performance curves. This is a common scale for energy detectors owing to the accuracy of the Gaussian approximation for large processing time-bandwidth products.

The shifted-gamma approximation described in Sect. 9.2.7.5 is now used to examine the performance of the various detectors previously derived; the results are shown in Fig. 9.6. In order for the comparison to illustrate any difference, the noise and signal PSDs must vary with frequency. As such, the noise PSD is chosen so $\lambda_m \propto 1/f_m^2$ and the signal PSD is chosen so $\psi_m \propto 1/f_m^{1/4}$. As described in Sect. 3.3, the $1/f^2$ noise PSD is commensurate with distant shipping noise for frequencies between 100 Hz and 1 kHz and somewhat greater than the $1/f^{1.59}$ dependence expected for wind-related surface noise above about 2 kHz. To ensure a large variation in noise is observed, the bandwidth is taken to be 1.5 times the center frequency, which leads to a 17-dB spread in the noise PSD within the processing band. The signal PSD, which is chosen arbitrarily, results in slightly more than a 10-dB spread. The overall SNR was chosen to achieve $P_d = 0.5$ at $P_f = 10^{-4}$ with the NPO detector. By choosing a processing time-bandwidth product of $M = T_p W = 50$, the SNR is not necessarily small in all of the frequency bins so there is a small difference in the performance between the NPO detector and the Eckart filter. The effect of increasing M is to reduce the SNR required in each DFT-bin to achieve this operating point, which makes the Eckart filter more like the NPO detector as was described in Sect. 9.2.5.3. The different shapes for the noise and signal PSDs cause the degradation in the noise-normalized energy detector. If they have the same shape, then the SNR is the same in each DFT bin and the NPO detector, Eckart filter, and noise-normalized energy detector are identical. Clearly, the shaped PSDs make the basic energy detector, which includes no noise normalization, an unattractive option.

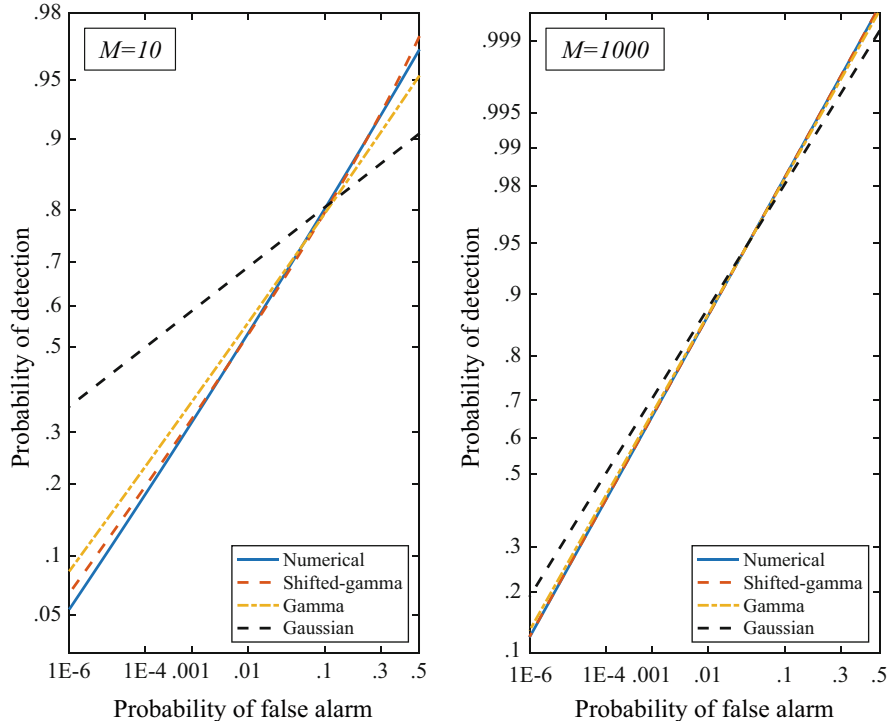


Fig. 9.5 Example ROC curves for an Eckart filter using the numerical approach from Appendix 9.A, Gaussian, gamma, and shifted-gamma approximations for small and large time-bandwidth product (M). The shifted-gamma approximation provides the best approximation when M is small

It is important to note that the analysis presented in this section focuses on detecting a Gaussian random signal in Gaussian noise. The techniques presented in Sects. 9.2.7.2–9.2.7.5 can all be applied to detecting a deterministic signal in Gaussian noise (although the non-central gamma approximation described in Sect. 7.5.6.3 may be a better candidate for a deterministic signal than the shifted gamma distribution found in Sect. 9.2.7.5). These techniques also exploit the frequency-domain implementation of a weighted energy detector, where the individual frequency bins are assumed to be statistically independent. However, they can also be applied to a time-domain implementation (see Sect. 9.2.10) involving the incoherent combination of overlapped windowed segments of the data (e.g., the case of a sinusoid in Gaussian noise can be found in [13]).

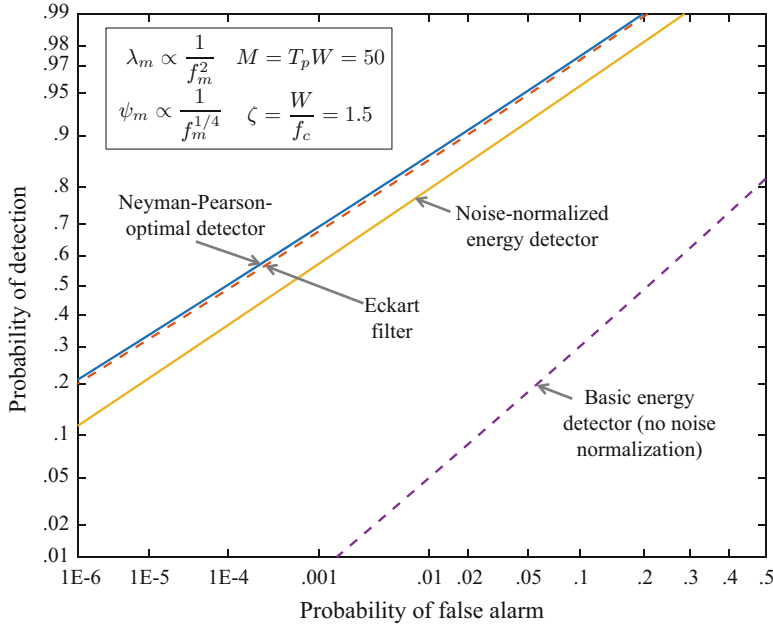


Fig. 9.6 Example ROC curves for various detectors when both the noise and signal PSDs are shaped

9.2.7.1 Exact Solution via the Characteristic Function

The characteristic function of the detector decision statistic T can be described as the product of the characteristic functions of the terms in the sum because they are independent. Recall from Sect. 5.6.10 that the characteristic function of an exponentially distributed random variable with mean λ is $1/(1 - j\omega\lambda)$. The characteristic function of T under H_1 is then

$$\Phi_T(\omega) = E[e^{jT(u)}] = \prod_{m=0}^{M-1} \frac{1}{1 - j\omega c_m(\lambda_m + \psi_m)}. \quad (9.95)$$

When the mean of each scaled term (i.e., $p = c_m(\lambda_m + \psi_m)$) is constant for all m , the characteristic function of T can be seen to have the form of a gamma random variable with shape M and scale equal to p . This leads to the analysis of the energy detector presented in Sect. 9.2.3. When each term in the sum has a different mean, a partial fraction expansion can be used to describe the characteristic function of T as a sum over each of the unique poles

$$\Phi_T(\omega) = \sum_{m=0}^{M-1} \frac{b_m}{1 - j\omega p_m} \quad (9.96)$$

where $p_m = c_m(\lambda_m + \psi_m)$ and the coefficient for the m th pole is

$$b_m = \prod_{\substack{n=1 \\ n \neq m}}^M \frac{p_m}{p_m - p_n}. \quad (9.97)$$

Noting that each term in the sum in (9.96) represents an exponentially distributed random variable with mean p_m , the PDF of T can be described as

$$f_T(t) = \sum_{m=0}^{M-1} \frac{b_m}{p_m} e^{-t/p_m}, \quad (9.98)$$

which is a mixture of exponential PDFs. When M is small enough and the poles are unique enough, it is feasible to use (9.98) to obtain the CDF of T as a similarly proportioned mixture of exponential CDFs.

Alternative partial fraction expansions can be applied when there are repeated poles, which results in a mixture of gamma distributions [14]. Although it is feasible to evaluate these numerically [15], the computation becomes untenable as M increases or when the poles are unique but do not differ greatly. In such situations, a better approach to obtaining the CDF of T is to perform a numerical inversion of the characteristic function as described in the next section.

9.2.7.2 Numerical Evaluation of the CDF from the Characteristic Function

Many scenarios in signal detection result in a decision statistic formed by the sum of independent random variables. The commonality of this result can be seen by noting that the logarithm of the likelihood ratio for independent data is the sum of the log-likelihood-ratio of the individual samples. Evaluating detection performance (i.e., P_d and P_f) requires evaluation of the CDF of the sum. If there are N independent terms in the sum, the PDF of the sum requires $N - 1$ convolutions and then an integral to obtain the CDF. Exploiting the product-representation of a convolution after converting the PDFs to their characteristic functions can be significantly simpler. However, even when the individual characteristic functions are known and easily evaluated, it can be difficult to analytically invert the characteristic function to obtain the PDF of the decision statistic. An alternative approach can be found in the numerical routine presented by Nuttall in [1], which exploits a fast Fourier transform (FFT) to efficiently perform an inversion of the characteristic function to directly obtain the CDF. Although application of the algorithm is straightforward, the algorithm is more involved than simply applying the FFT and an important enough

tool in evaluating detection performance to deserve a more detailed explanation. An example applying the algorithm to a sum of independent exponentially distributed random variables that are not identically distributed is presented in Appendix 9.A. The more general algorithm is described in this section.

The following derivation summarizes that presented in [1] for evaluation of the CDF of a random variable X from its characteristic function,

$$\Phi(\omega) = E[e^{j\omega X}] = \int_{-\infty}^{\infty} e^{j\omega x} f(x) dx \quad (9.99)$$

Recall from Sect. 5.3.9.2 that the characteristic function is the Fourier transform of the PDF of the random variable evaluated at $-\omega$; the Fourier transform (Sect. 4.3) uses a minus sign in the transform to the frequency domain (i.e., $e^{-j\omega t}$ rather than the $e^{j\omega x}$ in (9.99)). This means that Fourier transforms and properties of the transform can be used, but need to be applied carefully to account for the difference in sign.

Nuttall's algorithm samples the characteristic function in the ω variable, say every δ . Similar to how sampling in time results in repeated spectra at integer multiples of the sampling frequency (see Sect. 4.6.1), this sampling produces repeated PDFs at integer multiples of $2\pi/\delta$. Suppose the PDF of X is zero or very small outside of the interval $[x_0, x_1]$. In order to avoid aliasing of the repeated PDFs, the characteristic-function sampling must satisfy

$$\delta \leq \frac{2\pi}{x_1 - x_0}. \quad (9.100)$$

Inherent in this choice is that the characteristic function varies slowly over any interval of length δ . In the code presented in Appendix 9.A, x_0 and x_1 are chosen as being some number of standard deviations below and above the mean of the random variable. This may require modification if a random variable has heavy upper tails (increase x_1) or if it is known to always be above some value (e.g., set $x_0 = 0$ for positive random variables).

The core of Nuttall's algorithm exploits the following relationship between the characteristic function and the CDF,

$$F(x) = \frac{1}{2} - \frac{1}{\pi} \int_0^{\infty} \text{Imag} \left\{ \frac{\Phi(\omega)}{\omega} e^{-j\omega x} \right\} d\omega. \quad (9.101)$$

As noted in [16], this relationship can be found in [17, Sect. 4.3]. It can also be derived using the definition of the inverse Fourier transform, the integration property of the Fourier transform (carefully accounting for the previously mentioned difference in sign) and noting that, because $f(x)$ is real, the characteristic function is conjugate symmetric about $\omega = 0$; that is, $\Phi(-\omega) = \Phi^*(\omega)$. This last point

is what changes the Fourier integral from an interval of $(-\infty, \infty)$ to $(0, \infty)$ and results in taking the imaginary part.

Now define the integrand in (9.101) as the function $g(\omega, x)$ and apply a composite trapezoidal rule [18, Sect. 7.2] to approximate the integral,

$$\int_0^\infty g(\omega, x) d\omega \approx \frac{\delta}{2} [g(0, x) + g(\infty, x)] + \delta \sum_{m=1}^{\infty} g(m\delta, x). \quad (9.102)$$

Because $f(x)$ integrates to one, $|\Phi(\omega)|$ is bounded from above so $\lim_{\omega \rightarrow \infty} g(\omega, x) = 0$. The value of $g(0, x)$ can be obtained by describing it as a derivative,

$$\begin{aligned} g(0, x) &= \lim_{\omega \rightarrow 0} \operatorname{Imag} \left\{ \frac{\Phi(\omega) e^{-j\omega x}}{\omega} \right\} \\ &= \frac{\partial}{\partial \omega} \operatorname{Imag} \left\{ \Phi(\omega) e^{-j\omega x} \right\} \Big|_{\omega=0} \\ &= \operatorname{Imag} \{ j\mu - jx \} = \mu - x \end{aligned} \quad (9.103)$$

where μ is the mean of X . Combining these back into (9.101) produces

$$F(x) \approx \frac{1}{2} - \frac{\delta}{2\pi} (\mu - x) - \frac{\delta}{\pi} \sum_{m=1}^{\infty} \operatorname{Imag} \left\{ \frac{\Phi(m\delta)}{m\delta} e^{-jm\delta x} \right\}. \quad (9.104)$$

Now suppose the CDF of X is evaluated at the points

$$x_k = x_0 + \frac{k(x_1 - x_0)}{M} \quad (9.105)$$

for $k = 0, \dots, M-1$. Using these particular points in (9.104) with $\delta = 2\pi/(x_1 - x_0)$ results in

$$F(x_k) \approx \frac{1}{2} + \frac{k}{M} - \frac{\delta}{2\pi} (\mu - x_0) - \frac{1}{\pi} \operatorname{Imag} \left\{ \sum_{m=1}^{\infty} \left[\frac{\Phi(m\delta) e^{-jm\delta x_0}}{m} \right] e^{-j2\pi km/M} \right\} \quad (9.106)$$

where the complex exponential term $e^{-j2\pi km/M}$ is now what is used in an M -point FFT operation. However, two modifications to (9.106) are required in order to describe the sum as an FFT operation. First, the $\delta(\mu - x_0)/(2\pi)$ term is brought inside the operation taking the imaginary part by multiplying it by $j\pi$ and then it is used as the first term in the sum (i.e., for a new $m = 0$ term). This can be done by defining a sequence

$$Z_m = \begin{cases} j(x_0 - \mu)\delta/2 & m = 0 \\ \frac{\Phi(m\delta)}{m} e^{-jm\delta x_0} & m > 0 \end{cases} \quad (9.107)$$

to replace the term in brackets in the sum. Note that the $m = 0$ term came from $\delta g(0, x)/2$ and so is simply half (from the trapezoidal-rule integration approximation) what the $m > 0$ term would be if evaluated as the frequency went to zero. The second modification is to break the infinite sum into two nested sums,

$$\begin{aligned} \sum_{m=0}^{\infty} Z_m e^{-j2\pi km/M} &= \sum_{l=0}^{\infty} \sum_{m=0}^{M-1} Z_{m+lM} e^{-j2\pi k(m+lM)/M} \\ &= \sum_{m=0}^{M-1} e^{-j2\pi km/M} \left[\sum_{l=0}^{\infty} Z_{m+lM} \right], \end{aligned} \quad (9.108)$$

and note that there are only M unique complex exponential terms $e^{-j2\pi km/M}$ for $m = 0, \dots, M-1$. The result in (9.108) is then seen to be an FFT applied to the term in brackets, which is a function of m . Returning these modifications to (9.106) results in the final algorithm,

$$F(x_k) \approx \frac{1}{2} + \frac{k}{M} - \frac{1}{\pi} \operatorname{Imag} \left\{ \text{FFT} \left\{ \sum_{l=0}^{L-1} Z_{m+lM} \right\} \right\} \quad (9.109)$$

where the infinite sum in (9.108) is terminated at $L-1$. L should be chosen so $|Z_{ML}| = |\Phi(ML\delta)|/(ML)$ is small relative to the largest term, which can be taken as $(\mu - x_0)\delta$.

9.2.7.3 Gaussian Approximation

A Gaussian approximation to T can be accurate if M is large enough. The approximation only requires the mean and variance of T ,

$$\mu_{T,i} = \sum_{m=0}^{M-1} p_{m,i} \quad \text{and} \quad \sigma_{T,i}^2 = \sum_{m=0}^{M-1} p_{m,i}^2, \quad (9.110)$$

where $p_{m,0} = c_m \lambda_m$ and $p_{m,1} = c_m (\lambda_m + \psi_m)$ are the means of the m th term in the sum under H_0 and H_1 . The probabilities of false alarm and detection are then

$$P_f \approx \Phi \left(\frac{h - \mu_{T,0}}{\sigma_{T,0}} \right) \quad \text{and} \quad P_d \approx \Phi \left(\frac{h - \mu_{T,1}}{\sigma_{T,1}} \right) \quad (9.111)$$

where $\Phi(z)$ is the CDF of the standard normal distribution. The disadvantage of the Gaussian approximation lies in how large M needs to be before it is accurate.

9.2.7.4 Gamma Approximation

The gamma distribution is a good alternative to the Gaussian when approximating the performance of a weighted energy detector. Matching the moments of T to that of a gamma-distributed random variable results in a shape parameter

$$\alpha_i = \frac{\mu_{T,i}^2}{\sigma_{T,i}^2} = \frac{\left[\sum_{m=0}^{M-1} p_{m,i} \right]^2}{\sum_{m=0}^{M-1} p_{m,i}^2} \quad (9.112)$$

and a scale parameter

$$\beta_i = \frac{\sigma_{T,i}^2}{\mu_{T,i}} = \frac{\sum_{m=0}^{M-1} p_{m,i}^2}{\sum_{m=0}^{M-1} p_{m,i}}. \quad (9.113)$$

Using the definition of the normalized incomplete gamma function from (9.45), the probabilities of detection and false alarm are then approximated by

$$P_f \approx 1 - \tilde{\gamma}\left(\frac{h}{\beta_0}; \alpha_0\right) \quad \text{and} \quad P_d \approx 1 - \tilde{\gamma}\left(\frac{h}{\beta_1}; \alpha_1\right). \quad (9.114)$$

9.2.7.5 Shifted Gamma Approximation

As described in Sect. 7.5.6.2, an improvement to the gamma approximation can be obtained by generalizing it to include a shift in location. This results in a model with three parameters that can be obtained by matching the first three moments of T ,

$$\mu_{1,i} = \sum_{m=0}^{M-1} p_{m,i} \quad (9.115)$$

$$\mu_{2,i} = \left[\sum_{m=0}^{M-1} p_{m,i} \right]^2 + \sum_{m=0}^{M-1} p_{m,i}^2 \quad (9.116)$$

$$\mu_{3,i} = \left[\sum_{m=0}^{M-1} p_{m,i} \right]^3 + 3 \left[\sum_{m=0}^{M-1} p_{m,i} \right] \left[\sum_{m=0}^{M-1} p_{m,i}^2 \right] + 2 \sum_{m=0}^{M-1} p_{m,i}^3 \quad (9.117)$$

with those of a shifted gamma distribution. As described in Sect. 7.5.6.2, the parameters of the shifted gamma distribution are then obtained according to

$$b_{g,i} = \frac{\mu_{3,i} - 3\mu_{1,i}\mu_{2,i} + 2\mu_{1,i}^3}{2(\mu_{2,i} - \mu_{1,i}^2)}, \quad (9.118)$$

$$a_{g,i} = \frac{\mu_{2,i} - \mu_{1,i}^2}{b_{g,i}^2}, \text{ and} \quad (9.119)$$

$$c_{g,i} = \mu_{1,i} - a_{g,i}b_{g,i} \quad (9.120)$$

where $a_{g,i}$ is the shape parameter, $b_{g,i}$ is the scale parameter, and $c_{g,i}$ is the location (shift) parameter. The probabilities of detection and false alarm are then approximated using the incomplete gamma function from (9.45) according to

$$P_f \approx 1 - \tilde{\gamma}\left(\frac{h-c_{g,0}}{b_{g,0}}; a_{g,0}\right) \quad \text{and} \quad P_d \approx 1 - \tilde{\gamma}\left(\frac{h-c_{g,1}}{b_{g,1}}; a_{g,1}\right). \quad (9.121)$$

9.2.8 Detectors for Random Signals with Unknown Spectra in an Unknown Frequency Band

The detectors developed in Sects. 9.2.3–9.2.6 assumed the band in which the signal occurs is known and so only those DFT bins are used to form the detector. In many situations the exact band in which the signal occurs is not known precisely. For example, objects of interest moving at different speeds will have signals of interest that are affected by a frequency scale (or shift for narrowband signals) that depends on the relative radial velocity, which can change over time. Another example can be found in marine mammal acoustic emissions whose spectral content can vary with many factors. Detailed derivations of the detectors presented in this section can be found in the sequence of reports by A. Nuttall [19–24] on detection of Gaussian random signals when little is known about the structure of the frequency content.

Two detectors are presented in this section that account for an unknown signal PSD in an unknown frequency band. The first is a modification of the GLR energy detector from Sect. 9.2.6.2 and the second is a general class of power-law detectors that includes as sub-members both the noise-normalized energy detector and a detector formed by taking the value of the largest normalized DFT bin as a decision statistic. In describing and analyzing these detectors, the DFT-bin data are assumed to be normalized by a (perfect) estimate of the noise PSD,

$$Z_m = \frac{|Y_m|^2}{\lambda_m} = \frac{U_m}{\lambda_m} \quad (9.122)$$

for $m = 1, \dots, M$. When only noise is present, the m th sample Z_m is exponentially distributed with unit mean. When a Gaussian random signal is present the data are still exponentially distributed, but with a mean of $1+S^d$. In order to simplify analysis of the detectors, it will be assumed signals only occupy $M_s \leq M$ of the DFT bins

with a constant per-DFT-bin SNR of S^d . The total SNR available to the detector is therefore $M_s S^d$.

9.2.8.1 Modified Generalized Likelihood Ratio Energy Detector

Recall that the GLR energy detector function in (9.90) was formed by requiring the MLE of the SNR in each DFT bin to be non-negative, which resulted in only using those bins where the normalized squared modulus $Z_m > 1$. A generalization of this detector function, attributed by A. Nuttall in [19] to J. Wolcin, requires the SNR to be greater than some minimum value $S_{\min} \geq 0$. The resulting modified GLR energy detector function is then

$$g(z) = \begin{cases} z - z_0 - \log\left(\frac{z}{z_0}\right) & \text{for } z > z_0 \\ 0 & \text{otherwise} \end{cases} \quad (9.123)$$

where $z_0 = 1 + S_{\min}$. Note that (9.90) has also been modified by adding $1 - z_0 + \log z_0$ so $g(z_0) = 0$. The detector decision statistic is then the sum over the M DFT bins

$$T(\mathbf{z}) = \sum_{m=0}^{M-1} g(Z_m), \quad (9.124)$$

however, only the DFT bins with $Z_m > z_0$ will contribute.

The performance of the modified GLR energy detector has been extensively analyzed in [19]. The non-linear nature of $g(z)$ and the subsequent sum over M bins preclude a direct analytical performance evaluation. The approaches presented in [19] include approximating $g(z)$ as piecewise linear for large breakpoints and approximating the characteristic function by a fourth-order expansion for small breakpoints. An alternative is presented here where the distribution of the decision statistic is approximated by that of the shifted gamma, which requires the first three moments of $g(Z)$. In [19], the moments were obtained through a numerical integration. An alternative approach involving numerical differentiation of the moment generating function of $g(Z)$, which only requires evaluation of an incomplete gamma function, is presented in Appendix 9.B. The accuracy of the shifted-gamma distribution is shown in Fig. 9.7 for the standard GLR energy detector (i.e., $z_0 = 1$) with various values of M when half of the DFT bins contain signal so that the total SNR is 14 dB. Approximations using the first two moments of $T(\mathbf{z})$ to match to the gamma and Gaussian distributions are also shown. Although all the approximations are accurate when M is very large, the Gaussian approximation degrades rapidly as M decreases (note that it is not shown for $M = 10$ or 40). The gamma distribution is reasonably accurate except when M is small, where the shifted-gamma distribution is clearly the best approximation.

When the number of signal-occupied DFT bins is a small portion of the total number of bins, increasing the breakpoint z_0 can lead to improved performance.

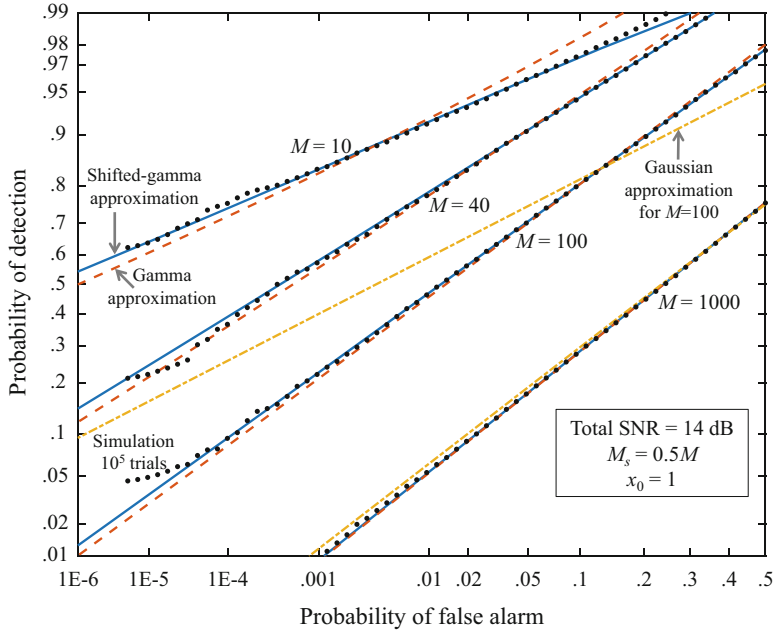


Fig. 9.7 ROC curves via simulation and various approximations for the GLR energy detector for various values of M with half of the bins occupied by signal ($M_s = 0.5M$). Although all the approximations are accurate when M is large, the shifted-gamma approximation provides a better fit when M is small

This is illustrated in Fig. 9.8 where there are only $M_s = 10$ signal-occupied DFT bins out of a total of $M = 1000$. Increasing the breakpoint to $z_0 = 8$ provides a significant improvement in performance by reducing the dilution of $T(\mathbf{z})$ by so many noise-dominated DFT bins. This example also depicts the degradation of the gamma and shifted-gamma approximations for large breakpoints, where the probability of observing a noise-dominated DFT bin exceeding z_0 becomes so small the sum does not contain a large enough number of non-zero entries. The quality of the fit can be predicted by the gamma-distribution shape parameter, which should be above about five. In the examples, the $M = 10$ case in Fig. 9.7 and the $x_0 = 8$ case in Fig. 9.8 fail this condition and so are not expected to provide an accurate approximation. The $M = 40$ case for the gamma approximation in Fig. 9.7 was right on the cusp with a shape parameter of 5.08 under H_0 .

9.2.8.2 Power-Law Energy Detector

The GLR energy detectors from Sects. 9.2.6.2 and 9.2.8.1 were derived under the assumption that every DFT bin might contain signal and that the SNR in each bin could be different, which constitutes very little information about the structure of the

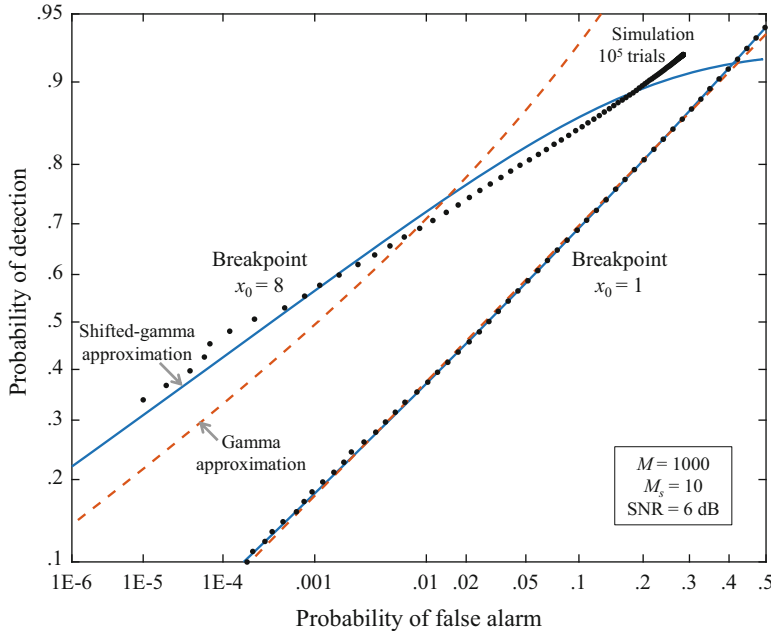


Fig. 9.8 ROC curves via simulation and the gamma-distribution approximations for the modified GLR energy detector for $M = 1000$, $M_s = 10$, and two different breakpoints. The shifted-gamma approximation performs better than the gamma approximation when the breakpoint increases but can be inaccurate in the tails

signal PSD. An alternative scenario was considered in [21] where it was assumed the signal occupied a subset of bins ($M_s \leq M$), but that the location of those bins within the frequency band was unknown. Although the previously described example of a source signal being affected by an unknown Doppler scale is represented in this scenario, the assumptions are more general because the DFT bins containing signal do not necessarily need to be contiguous. As an example, suppose the signal is known to exist in only one DFT bin but not which one. Applying the generalized likelihood ratio detector formalism to the unknown location results in a decision statistic equal to the value of the largest normalized DFT-bin squared moduli,

$$T(\mathbf{z}) = \max_m Z_m \quad (9.125)$$

$$= \lim_{p \rightarrow \infty} \left[\sum_{m=0}^{M-1} Z_m^p \right]^{1/p}. \quad (9.126)$$

The “max” operation in (9.125) can also be described by raising each data sample to a power p , summing over the data, raising the sum to the power $1/p$, and letting p tend to infinity as is shown in (9.126). As p increases, the maximum of

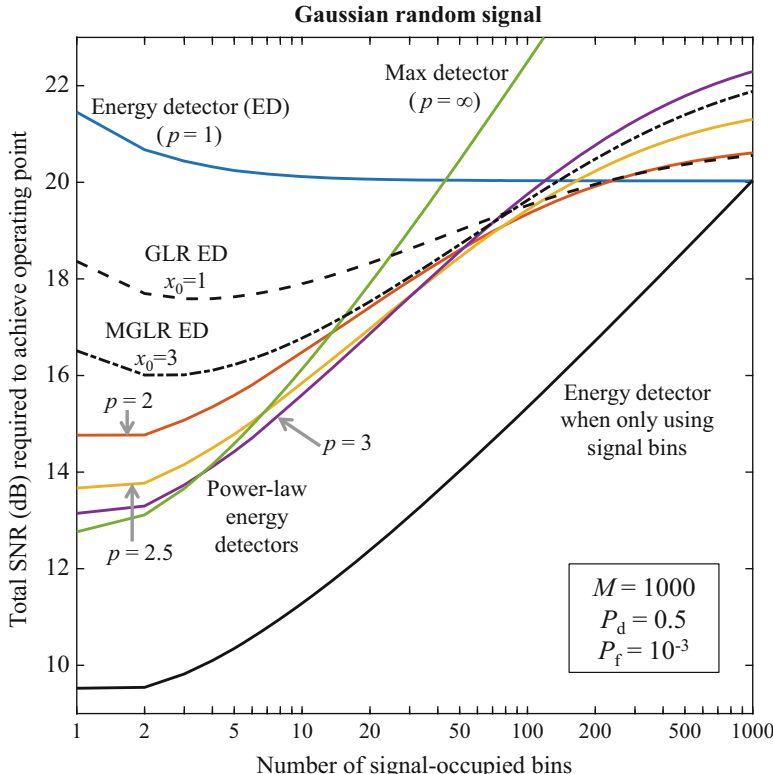


Fig. 9.9 Total SNR in decibels (i.e., $10 \log_{10}(M_s S^d)$) required for a Gaussian random signal to achieve $P_d = 0.5$ and $P_f = 10^{-3}$ for various detectors as a function of the number of signal-occupied bins (M_s) for $M = 1000$

Z_1, \dots, Z_m dominates the other terms in the sum and is extracted alone as $p \rightarrow \infty$. In [21], Nuttall shows how a GLR detector for a signal occupying M_s DFT bins with unknown locations behaves in a similar manner to a power-law energy detector formed by the sum of Z_m^p over all the DFT bins,

$$T_p(\mathbf{z}) = \sum_{m=0}^{M-1} Z_m^p, \quad (9.127)$$

where p is large when M_s is small and is one when the signal occupies all the DFT bins ($M_s = M$). Thus, the power-law processor in (9.127) can range between the noise-normalized energy detector ($p = 1$) appropriate when all frequency bins contain signal to the “max” detector ($p \rightarrow \infty$) appropriate when only one bin contains signal. Such a power-law processor was also applied to the detection of a Gaussian-random signal burst occurring at an unknown time in a longer sample of

Gaussian noise in [25]. The signal-burst application only differs from the current one in that it was applied to the absolute value of (real) Gaussian-distributed time-series data rather than the squared moduli of DFT bin outputs (i.e., the data are χ_1^2 distributed rather than χ_2^2 distributed). In both [21, 25] it was noted that a single power law ($p = 2.5$ for the DFT-bin application) provided good performance over the full range of M_s . This can be seen in Fig. 9.9, which is similar to the performance curves found in [21, 22], showing the total SNR in decibels (i.e., $10 \log_{10}(M_s S^d)$) required to achieve an operating point of $P_d = 0.5$ and $P_f = 10^{-3}$. The result for the $p = 2.5$ power-law detector is within 1.3 dB of the best power-law detector for M_s ranging from 1 to 1000 with $M = 1000$. Also shown on the figure are the GLR energy detector from Sect. 9.2.6.2 (dashed black line), the modified GLR energy detector from Sect. 9.2.8.1 with $x_0 = 3$ (dash-dot black line), and a noise-normalized energy detector only using the occupied signal bins (solid black line). Although the modified GLR energy detector outperforms the GLR energy detector when M_s is small, it does not match the performance achieved by the $p = 2.5$ power-law energy detector. The total SNR required by the noise-normalized energy detector operating only on the signal bins is shown to illustrate the loss in performance incurred by weakening the knowledge about the signal PSD. In [22], Nuttall introduces knowledge of a limited, hypothetical structure to the signal frequency-bin locations in order to derive a performance bound for comparison against the weaker assumptions under which the other detectors were derived and operate. Given M_s , a power-law processor could always be found that was within 0.1 dB of the bound in terms of the SNR required to achieve an operating point. For the case considered in [22], the power-law $p = 2.4$ was found to be within 1.2 dB of the best processor over the tested range of M_s even when the SNR varied across the signal-occupied bins [23]. Accounting for normalization [24] resulted in the expected degradation in performance, but also a decrease in the sensitivity to the optimal power law.

As proposed in [21], the performance of the power-law processor is most accurately obtained through the characteristic-function inversion method derived in [1] and described here in Sect. 9.2.7.2 and Appendix 9.A. Unfortunately, neither the gamma nor shifted-gamma distributions provide adequate approximations, even when M is large. The characteristic function of the decision statistic in (9.127) can be obtained as the product of the characteristic functions of the terms in the sum, which are assumed to be independent. The characteristic function of Z^p when $Z \sim \text{Expon}(\mu)$ is

$$\Phi_\mu(\omega) = E[e^{j\omega Z^p}] = \frac{1}{\mu} \int_0^\infty \exp\left\{j\omega z^p - \frac{z}{\mu}\right\} dz \quad (9.128)$$

$$= \frac{e^{j\pi/(2p)}}{\mu} \int_0^\infty \exp\left\{-\omega r^p - \frac{r e^{j\pi/(2p)}}{\mu}\right\} dr. \quad (9.129)$$

As noted in [21], the form in (9.129) is obtained by rotating the path of the integration to remove the oscillatory $e^{j\omega z^p}$ term so the integral is suitable for numerical evaluation. The characteristic function of the decision statistic when signal is present in M_s bins with SNR S^d is

$$\Phi_T(\omega|H_1) = [\Phi_{1+S^d}(\omega)]^{M_s} [\Phi_1(\omega)]^{M-M_s} \quad (9.130)$$

To implement the characteristic-function inversion algorithm of [1], the mean of the decision statistic is required and the variance is helpful but not required. For the decision statistic in (9.127), these are

$$E[T|H_1] = \left[M - M_s + M_s(1 + S^d)^p \right] \Gamma(p+1) \quad (9.131)$$

and

$$\text{Var}\{T|H_1\} = \left[M - M_s + M_s(1 + S^d)^{2p} \right] \left[\Gamma(2p+1) - \Gamma^2(p+1) \right] \quad (9.132)$$

when signal is present in M_s bins with SNR S^d .

The SNR required to achieve an operating point for the power-law detectors shown in Fig. 9.9 was formulated following [21] by using the characteristic-function inversion approach (i.e., (9.130)–(9.132) with $S^d = 0$ and the algorithm from [1]) to set the decision threshold as a function of P_f and then a simulation analysis with 10^5 trials to obtain the SNR required to achieve P_d . If a single ROC curve is desired, the characteristic-function inversion approach via (9.130)–(9.132) may be a more appealing approach to obtaining P_d and can also be generalized to account for signals with an SNR that varies over the frequency band.

9.2.9 Detectors for Deterministic Signals with Unknown or Partially Known Form

The detectors presented in earlier sections of this chapter have all assumed the signal to be a zero-mean Gaussian random process. Suppose now that the signal of interest is deterministic, but that very little is known about it. For example, when it is desired to detect the presence of a marine mammal through their acoustic emissions when the type of emission or mammal is unknown. These assumptions differ from those made in Chap. 8 where the form of the signal was known subject to a few potentially unknown parameters. Here the signal itself is presumed to be unknown within a given frequency band (Sect. 9.2.9.1), partially known in the sense that it is assumed to reside in a subspace (Sect. 9.2.9.2), or completely unknown (Sect. 9.2.9.3). In the first two scenarios, an energy detector arises from application of the generalized likelihood ratio detector formalism, either as applied directly to the frequency-domain DFT-bin data as in previous sections or as applied after

a projection on the noise-normalized signal subspace. Thus, the energy detector and matched filter represent the detectors applied at the extremes of the knowledge dimension for deterministic signals: the matched filter is used when the form of the signal is known precisely and the energy detector when it is unknown other than the frequency band. The subspace energy detector is the complement to the subspace matched filter described in [26, 4.11]. It spans the knowledge dimension through the size of the signal subspace. When the signal-subspace dimension is one, the subspace energy detector is a quadrature matched filter. When the signal-subspace dimension equals the dimension of the data, the subspace energy detector is identical to an energy detector applied directly to the frequency-domain data.

9.2.9.1 Deterministic Signals with Unknown Structure in a Known Frequency Band

Application of an energy detector to unknown deterministic signals is discussed in [27] with the assumption that a noise-whitening filter is applied before characterizing the time-series data. In the development here, the frequency-domain approach presented for random signals is used so the noise-whitening or normalization is derived as part of the detection process. As before, the noise PSD is assumed to be known or perfectly estimated. As described at the beginning of Sect. 9.2, the complex envelope of the basebanded data is sampled in time to produce the time-series data \mathbf{x} for the interval over which a detection decision is to be made. This implies some knowledge of the signal with respect to its duration. Because the signal is assumed to be deterministic, it enters into the mean of the complex-Gaussian distribution,

$$\mathbf{x} \sim \mathcal{CN}(\mathbf{s}, \boldsymbol{\Lambda}_t), \quad (9.133)$$

where \mathbf{s} is the sampled complex signal envelope and as before $\boldsymbol{\Lambda}_t$ is the covariance matrix of the sampled complex noise envelope. Transformation of the time series data to the frequency domain via $\mathbf{y} = \mathbf{D}^H \mathbf{x}$ will still (approximately) diagonalize the noise covariance matrix, which leads to the simple statistical description of the m th DFT bin being complex Gaussian distributed,

$$Y_m \sim \mathcal{CN}\left(A_m e^{j\phi_m}, \lambda_m\right), \quad (9.134)$$

with a mean $A_m e^{j\phi_m}$ and noise variance λ_m and independent of Y_n for $n \neq m$. The amplitude A_m and phase ϕ_m of the signal in the m th DFT bin, which is the m th element of $\mathbf{D}^H \mathbf{s}$, can be obtained from the spectrum of the signal of interest. The amplitudes define the signal-present hypothesis by requiring at least one DFT bin to have a non-zero amplitude ($A_m > 0$ for some m), but are otherwise assumed to be unknown as are the phases. The unknown parameters can be handled by forming maximum-likelihood estimates and using them to produce the generalized

likelihood ratio detector. Expanding the exponent in the PDF of the m th DFT bin data when signal is present,

$$\begin{aligned} f_1(y; A_m, \phi_m, \lambda_m) &= \frac{1}{\lambda_m} \exp \left\{ \frac{-|y - A_m e^{j\phi_m}|^2}{\lambda_m} \right\} \\ &= \frac{1}{\lambda_m} \exp \left\{ \left[-|y|^2 + 2A_m |y| \cos(\angle y - \phi_m) - A_m^2 \right] / \lambda_m \right\} \end{aligned} \quad (9.135)$$

illustrates that it can be maximized by choosing the phase estimate $\hat{\phi}_m = \angle y$. Substituting this back into the PDF leads to

$$\begin{aligned} f_1(y; A_m, \hat{\phi}_m, \lambda_m) &= \frac{1}{\lambda_m} \exp \left\{ \left[-|y|^2 + 2A_m |y| - A_m^2 \right] / \lambda_m \right\} \\ &= \frac{1}{\lambda_m} \exp \left\{ -(|y| - A_m)^2 / \lambda_m \right\}, \end{aligned} \quad (9.136)$$

which can then be maximized by choosing the amplitude estimate $\hat{A}_m = |y|$. Using these estimates in the GLR detector for a single DFT bin produces

$$\frac{f_1(y; \hat{A}_m, \hat{\phi}_m, \lambda_m)}{f_0(y; \lambda_m)} = e^{|y|^2 / \lambda_m}. \quad (9.137)$$

The independence of the DFT bin data implies the joint PDF of the data is the product of their marginal PDFs. The product of the marginal PDFs results in a sum of the exponents in (9.137),

$$\begin{aligned} T(\mathbf{y}) &= \prod_{m=0}^{M-1} e^{|y_m|^2 / \lambda_m} = \exp \left\{ \sum_{m=0}^{M-1} |y_m|^2 / \lambda_m \right\} \\ &\stackrel{D}{=} \sum_{m=0}^{M-1} \frac{|y_m|^2}{\lambda_m}, \end{aligned} \quad (9.138)$$

which is equivalent to the noise-normalized energy detector. Thus, the noise-normalized energy detector is a GLR detector for an unknown deterministic signal in noise. Another approach to the problem is to treat the DFT-bin phases as nuisance parameters and obtain a detector that is *invariant* to ϕ_m . Using [28, Ch. 6] or [26, Sect. 4.8], it can be shown that $|Y_m|^2$ is a maximally invariant statistic for the phase ϕ_m and so only detectors formed from $|Y_m|^2$ need to be considered. It can then be shown that the noise-normalized energy detector is the locally optimal invariant detector as the SNR (A_m^2 / λ_m) tends to zero.

9.2.9.2 Deterministic Signals with Partially Known Form

Depending on the application, varying amounts of knowledge will be available about the structure of a deterministic signal. When the form of the signal within the analysis window is known subject to an unknown amplitude, phase, and some other signal parameter (e.g., center frequency), a GLR detector or bank of matched filters can be implemented as described in Sects. 8.2.8.2 or 8.7.1. An example where less information is available can be found in the narrowband radiated noise seen in Fig. 8.30, which changed in frequency⁴ because of the motion of the source platform. Such quasi-linear motion can be accounted for by a piecewise-linear frequency modulation. A maximum a posteriori (MAP) detector for such a signal model was developed in [29] where the initial frequency was assumed unknown and prior information limited the rate of change in each linear component.

In many scenarios, however, the potential variation in the observed signal of interest is so diverse that it defies a simple parameterization for which a specific detector can be derived. For example, consider the marine mammal acoustic emissions described at the beginning of Sect. 9.2.9. As seen in [30, Ch. 10], the sounds emitted by marine mammals contain significant structure while still being very diverse. Although the structure is not robust enough to implement a matched filter, enough information may exist to improve on the noise-normalized energy detector by identifying the subspace in which the signals of interest exist. For example, suppose the signal of interest is a combination of chirps where the specific details are not known with enough precision to implement a bank of matched filters. The discrete Fourier transform of the sampled complex envelope of the signal of interest (ψ) can be described by a matrix–vector product

$$\psi = \mathbf{S}\mathbf{a} \quad (9.139)$$

where \mathbf{S} is an M -by- N matrix with $N \leq M$ of all the possible chirps that may combine to form the signal of interest and the N -by-1 vector \mathbf{a} represents the unknown manner in which they are combined. When the signal is present, the DFT-bin data are then described as being complex Gaussian distributed with mean $\mathbf{S}\mathbf{a}$ and covariance Λ ,

$$\mathbf{y}|H_1 \sim \mathcal{CN}(\mathbf{S}\mathbf{a}, \Lambda). \quad (9.140)$$

Using (9.140) to form the likelihood ratio results in

$$\frac{f_1(\mathbf{y}; \mathbf{a})}{f_0(\mathbf{y})} = \exp\left\{\mathbf{a}^H \mathbf{S}^H \Lambda^{-1} \mathbf{y} + \mathbf{y}^H \Lambda^{-1} \mathbf{S} \mathbf{a} - \mathbf{a}^H \mathbf{S}^H \Lambda^{-1} \mathbf{S} \mathbf{a}\right\}$$

⁴Note that Fig. 8.30 is shown as radial velocity, which is related to the measured frequency through an affine transformation.

$$= \exp \left\{ \mathbf{b}^H \mathbf{Q}^{-2} \mathbf{b} - \left(\mathbf{Q}^{-1} \mathbf{b} - \mathbf{Q} \mathbf{a} \right)^H \left(\mathbf{Q}^{-1} \mathbf{b} - \mathbf{Q} \mathbf{a} \right) \right\} \quad (9.141)$$

where $\mathbf{Q} = (\mathbf{S}^H \mathbf{\Lambda}^{-1} \mathbf{S})^{1/2}$ and $\mathbf{b} = \mathbf{S}^H \mathbf{\Lambda}^{-1} \mathbf{y}$. Choosing

$$\hat{\mathbf{a}} = \mathbf{Q}^{-2} \mathbf{b} = (\mathbf{S}^H \mathbf{\Lambda}^{-1} \mathbf{S})^{-1} \mathbf{S}^H \mathbf{\Lambda}^{-1} \mathbf{y} \quad (9.142)$$

will maximize $f_1(\mathbf{y}; \mathbf{a})$ to produce the GLR decision statistic

$$\begin{aligned} T(\mathbf{y}) &= \frac{f_1(\mathbf{y}; \hat{\mathbf{a}})}{f_0(\mathbf{y})} = \exp \left\{ \mathbf{b}^H \mathbf{Q}^{-2} \mathbf{b} \right\} \stackrel{D}{=} \mathbf{b}^H \mathbf{Q}^{-2} \mathbf{b} \\ &= \mathbf{y}^H \mathbf{\Lambda}^{-1} \mathbf{S} (\mathbf{S}^H \mathbf{\Lambda}^{-1} \mathbf{S})^{-1} \mathbf{S}^H \mathbf{\Lambda}^{-1} \mathbf{y} \\ &= \mathbf{z}^H \mathbf{P}_\psi \mathbf{z} \end{aligned} \quad (9.143)$$

where $\mathbf{z} = \mathbf{\Lambda}^{-1/2} \mathbf{y}$ is the noise-normalized complex DFT-bin data and

$$\mathbf{P}_\psi = \mathbf{\Lambda}^{-1/2} \mathbf{S} (\mathbf{S}^H \mathbf{\Lambda}^{-1} \mathbf{S})^{-1} \mathbf{S}^H \mathbf{\Lambda}^{-1/2} \quad (9.144)$$

is a projection matrix for the noise-whitened signal subspace. Because \mathbf{P}_ψ is a projection matrix, $\mathbf{P}_\psi = \mathbf{P}_\psi^2$ so the GLR decision statistic can be described as

$$T(\mathbf{y}) = (\mathbf{P}_\psi \mathbf{z})^H (\mathbf{P}_\psi \mathbf{z}) \quad (9.145)$$

which is an energy detector applied in the noise-normalized signal subspace.

Performance analysis of the subspace energy detector described in (9.143) is simplified by noting that $\mathbf{z} \sim \mathcal{CN}(\mathbf{0}, \mathbf{I})$ and that \mathbf{P}_ψ has M_s eigenvalues equal to one and $M - M_s$ equal to zero. This can be used to show that two times the decision statistic is chi-squared distributed,

$$2T(\mathbf{y})|H_0 \sim \chi_{2M_s}^2, \quad (9.146)$$

with $2M_s$ degrees of freedom when there is only noise and non-central chi-squared-distributed when signal is present,

$$2T(\mathbf{y})|H_1 \sim \chi_{2M_s, 2M_s \bar{s}}^2, \quad (9.147)$$

with non-centrality parameter $2M_s \bar{s}$ where $M_s \bar{s}$ is the total SNR over the frequency band,

$$\begin{aligned} M_s \bar{s} &= \mathbf{a}^H \mathbf{S}^H \mathbf{\Lambda}^{-1/2} \mathbf{P}_\psi \mathbf{\Lambda}^{-1/2} \mathbf{S} \mathbf{a} \\ &= \mathbf{a}^H \mathbf{S}^H \mathbf{\Lambda}^{-1} \mathbf{S} \mathbf{a}. \end{aligned} \quad (9.148)$$

With this description, \bar{s} can be interpreted as the SNR per signal subspace dimension and be obtained as a function of a (P_d, P_f) operating point using Albersheim's or Hmam's equations.

One of the risks in using a subspace detector lies in incorrectly describing it so some of the signal is lost to projection onto the orthogonal subspace. Albersheim's equation (2.85) can be used to assess how much loss in the total SNR a subspace energy detector can withstand and still perform better than using a noise-normalized energy detector operating on the full M dimensions. Noting that Albersheim's equation produces the average SNR, the maximum loss allowed in total SNR in order to benefit from using a subspace energy detector of dimension M_s relative to using the noise-normalized energy detector applied to the full M dimensions is

$$\text{Loss}_{\text{dB}} = 5 \log_{10} \left(\frac{M}{M_s} \right) - 4.54 \log_{10}(A + 0.12AB + 1.7B) \left[\frac{1}{\sqrt{M_s - 0.44}} - \frac{1}{\sqrt{M - 0.44}} \right] \quad (9.149)$$

where A and B are functions of the (P_d, P_f) operating point used in Albersheim's equation and defined in (2.86). When M and M_s are large, the first term dominates, indicating an SNR-loss tolerance changing at the rate of five decibels per decade (i.e., 1.5 dB per doubling) of reduction in dimension. For example, reducing the dimension by a factor of ten ($M_s = M/10$) when M and M_s are large implies tolerance to a 5-dB loss in SNR. However, when M or M_s are small, the latter term, which is negative, implies a greater sensitivity to SNR loss.

The dimension of the signal subspace is the rank of \mathbf{S} , so significant gains can be obtained when it can be kept to a small number of dimensions. In the chirp example, this means limiting the chirp characteristics as much as possible (i.e., as narrow a range of center frequencies and sweep rates as possible). An example where this is not possible is when the signal comprises a sum of sinusoids with frequencies that span the band. In this case \mathbf{S} has full rank so $M_s = M$ and \mathbf{P}_ψ is an identity matrix.

Exercise 9.1 Show that $2T(\mathbf{y})$ is chi-squared distributed with $2M_s$ degrees of freedom under H_0 . Hint: obtain the moment generating function of $2T(\mathbf{y})$ using the multivariate complex Gaussian PDF. Can the same approach be used to show $2T(\mathbf{y})$ is non-central chi-squared distributed with $2M_s$ degrees of freedom and non-centrality parameter $2M_s\bar{s}$ under H_1 ?

9.2.9.3 Completely Unknown Deterministic Signals

When the frequency band of the signal is unknown in addition to its spectral content, the noise-normalized energy detector derived in Sect. 9.2.9.1 will not perform well when the number of signal-occupied bins is a small portion of the total. Similar to how the GLR energy detector was modified in Sect. 9.2.8.1 to discard more noise-only bins, the noise-normalized energy detector could be modified by applying a

non-linear function requiring each normalized DFT bin statistic (i.e., $|Y_m|^2/\lambda_m$) to exceed a particular level before entering the sum over the frequency band. Noting, however, that the power-law energy detector from Sect. 9.2.8.2 performed better than the modified GLR energy detector, it is considered more appropriate for application to a completely unknown deterministic signal. Similar arguments to those presented in [21] and summarized in Sect. 9.2.8.2 for use of a power law to emphasize signal-occupied bins over noise-occupied bins for a Gaussian random signal can be applied to a deterministic signal occupying $M_s \leq M$ frequency bins.

An example evaluation of the total SNR required to meet a performance specification ($P_d = 0.5$ and $P_f = 10^{-3}$) is shown in Fig. 9.10. Similar to the process used to form Fig. 9.9, the characteristic function inversion method of [1] was applied to obtain the threshold required to achieve P_f and a simulation analysis was used to obtain the SNR S^d required in each of the M_s signal-occupied bins to achieve P_d . As seen in Fig. 9.10, the $p = 2.5$ power-law provides good performance through the full range of signal-occupied bins and is clearly a good choice when the signal is not expected to occupy all the frequency bins and how many are occupied is unknown. In this example, the $p = 2.5$ power law is within 1.5 dB of the best power-law processor through all values of M_s and better than the energy detector applied to all bins when $M_s \leq 81$. Although applying the energy detector to all bins is a better choice when it is known that more than about 8% of the bins (in this scenario) will contain signal, the power law detector is a reasonable choice when M_s might also be small.

9.2.10 Time-Domain Energy Detector: Coherent and Incoherent Averaging

As formulated in the frequency domain, the noise-normalized energy detector results in an incoherent combination of the DFT bin data formed over the full analysis window after they have been normalized by the noise power in each bin. As seen in Fig. 9.11, this structure can be implemented in the time domain as a noise-whitening filter followed by a combination of coherent and incoherent integration. The coherent integration filters the data to lie within the frequency band of the signal. This implies that the temporal extent of the filter impulse response is approximately the inverse signal bandwidth, over which the phase of the signal is stable. When the total analysis window exceeds this, the ensuing incoherent integration discards the phase before combining the filter output over the extent of the window to form a decision statistic.

The equivalence of the time- and frequency-domain approaches can be seen by first noting that the Neyman-Pearson optimal detector, noise-normalized energy detector, and Eckart filter can be described as a weighted sum of the squared moduli of the DFT bin data,

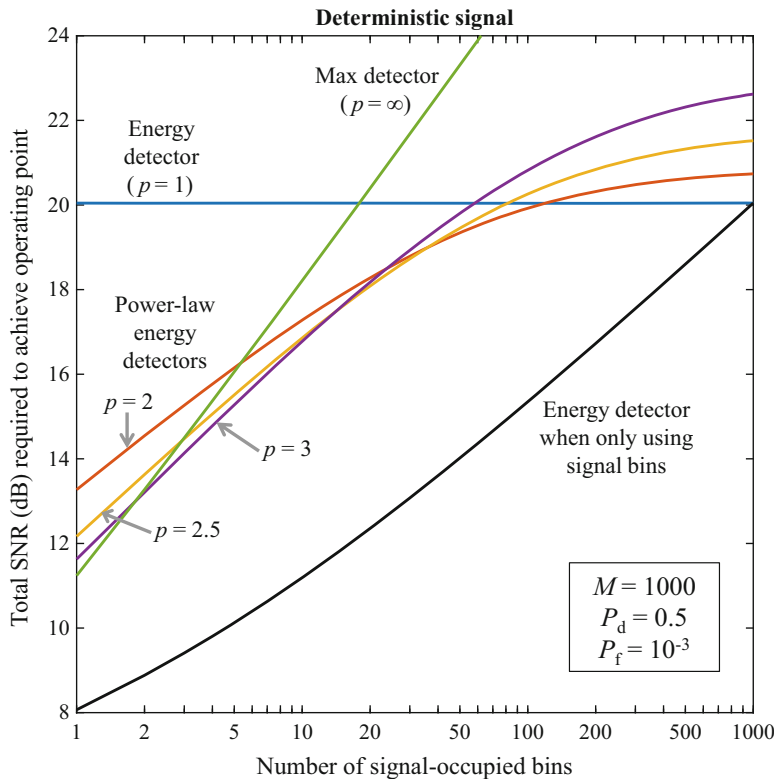


Fig. 9.10 Total SNR in decibels (i.e., $10 \log_{10}(M_s S^d)$) required for a deterministic signal to achieve $P_d = 0.5$ and $P_f = 10^{-3}$ for various detectors as a function of the number of signal-occupied bins (M_s) for $M = 1000$

$$T(\mathbf{y}) = \sum_{m=0}^{M-1} c_m |Y_m|^2. \quad (9.150)$$

In each of the detectors, the coefficients implement a noise normalization followed by an SNR-dependent weighting. For the noise-normalized energy detector, $c_m = 1/\lambda_m$ for frequencies within the signal band and is otherwise zero. The noise normalization can be implemented in the time domain using a *noise whitening* filter with a magnitude-squared transfer function equal to $1/\lambda_m$ at frequency f_m . The SNR-dependent weighting within the signal band can similarly be implemented in the coherent integration. However, to simplify this discussion of representing an energy detector as a combination of coherent and incoherent integration, it is assumed that noise-normalization has been done and that SNR is constant in the signal band so c_m is one for frequencies in the signal band and is otherwise zero. If \mathbf{C} is a diagonal matrix with c_m in the (m, m) element, the detector decision statistic can be described as

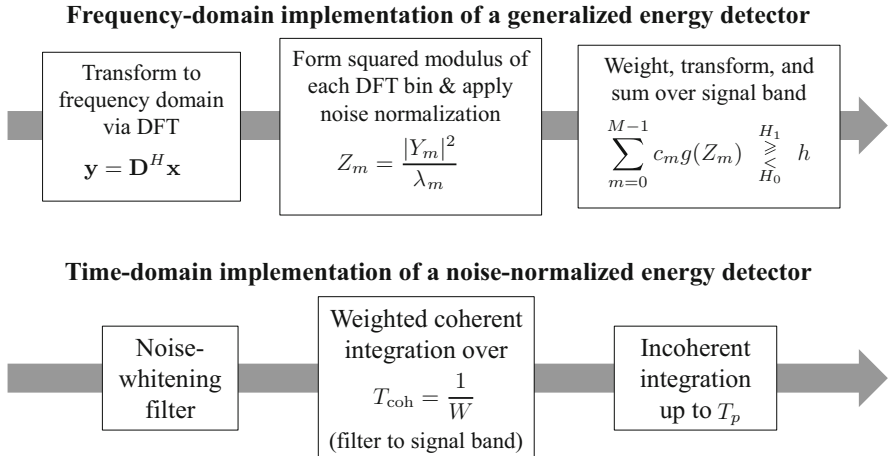


Fig. 9.11 Frequency and time-domain implementations of an energy detector. Note that by using the detector function $g(Z_m)$, the frequency-domain implementation is more general than the time-domain energy detector

$$\begin{aligned} T(\mathbf{y}) &= \mathbf{y}^H \mathbf{C} \mathbf{y} = \mathbf{x}^H \mathbf{D} \mathbf{C} \mathbf{D}^H \mathbf{x} \\ &= \mathbf{x}^H \mathbf{D}_s \mathbf{D}_s^H \mathbf{x} \end{aligned} \quad (9.151)$$

$$= \sum_{m=0}^{M_s-1} |\mathbf{d}_m^H \mathbf{x}|^2 \quad (9.152)$$

where $\mathbf{D}_s = [\mathbf{d}_0 \cdots \mathbf{d}_{M_s-1}]$ contains the M_s DFT vectors representing the frequencies in the signal band (enumerated here with indices 0 to $M_s - 1$). Although (9.152) can be described as coherent processing to form $\mathbf{d}_m^H \mathbf{x}$ followed by an incoherent combination, it is not the desired time-domain characterization of coherent integration followed by incoherent integration. If the signal is not oversampled, then $\mathbf{D}_s = \mathbf{D}$ and the orthonormality of \mathbf{D} implies that $\mathbf{D} \mathbf{D}^H = \mathbf{I}$ and the decision statistic simplifies to $\mathbf{x}^H \mathbf{x}$ as was shown in Sect. 9.2.3. Thus, if noise-normalized data are filtered to the signal bandwidth (W) and then decimated by f_s/W , the energy detector would have the simple form of a vector inner product because the samples are independent and identically distributed. Toward this end, suppose filtering to the signal bandwidth is implemented by a finite impulse response (FIR) filter with temporal extent T_t and coefficients $\mathbf{w} = [w_1 \dots w_{n_t}]^T$ where $n_t = f_s T_t$. The combined filtering and decimation process can be characterized by

$$\mathbf{z} = \mathbf{A}^H \mathbf{x} \quad (9.153)$$

where the matrix \mathbf{A} is formed by placing the filter vector \mathbf{w} , surrounded by zeros (the vertical lines in the following equation), in each column so as to perform both

the filter and decimation operations,

$$\mathbf{A} = \begin{bmatrix} \mathbf{w} & | & & \\ | & \mathbf{w} & \cdots & | \\ & | & & \mathbf{w} \end{bmatrix}. \quad (9.154)$$

For example, the j th column of \mathbf{A} contains \mathbf{w} starting in element $(j - 1)M/M_s + 1$ for $j = 1, \dots, M_s$ and is otherwise zero,

$$\mathbf{a}_j^T = [0 \cdots 0 \ \mathbf{w}^T \ 0 \cdots 0]. \quad (9.155)$$

Filtering to the signal band can be accomplished by using a sinc-function-shaped impulse response (e.g., $h(t) = \text{sinc}(Wt)$) to extract the frequency band $(-W/2, W/2)$. If T_t is large enough relative to $1/W$ and \mathbf{x} is large enough to ignore the edge effects, then the vector inner product $\mathbf{a}_j^H \mathbf{a}_i \approx 0$ when $i \neq j$. This means the elements of $\mathbf{z} = \mathbf{A}^H \mathbf{x}$ are independent and identically distributed so the optimal detector is

$$T(\mathbf{x}) = \mathbf{z}^H \mathbf{z} = \mathbf{x}^H \mathbf{A} \mathbf{A}^H \mathbf{x} \quad (9.156)$$

$$= \sum_{j=0}^{M_s-1} |\mathbf{a}_j^H \mathbf{x}|^2. \quad (9.157)$$

This detector structure is precisely coherent integration (i.e., forming $\mathbf{a}_j^H \mathbf{x}$) followed by incoherent integration. It is typically implemented without the full decimation, which is primarily required to claim optimality of the $\mathbf{z}^H \mathbf{z}$ decision statistic.

The detectors in (9.156) and (9.151) appear vastly different—are they equivalent? The primary difference lies in using either an FIR filter or a DFT operation to isolate the frequency band of the signal. Thus, the approaches might be equivalent if the transition and rejection bands in the FIR filter match the sharpness of the DFT in limiting frequency content outside of the signal band. In order to assess the difference in performance, suppose the detector has the general form

$$T(\mathbf{x}) = \mathbf{x}^H \mathbf{P} \mathbf{x} \quad (9.158)$$

where $\mathbf{P} = \mathbf{D}_s \mathbf{D}_s^H$ for the frequency-domain implementation and $\mathbf{P} = \mathbf{A} \mathbf{A}^H$ for the time-domain approach. Rather than directly evaluating a receiver operating characteristic (ROC) curve for the two detectors, the detection index from (9.77) provides a simpler assessment of how much difference in performance there might be between the two approaches. It can be shown that detection index for a Gaussian signal in noise using the detector in (9.158) is

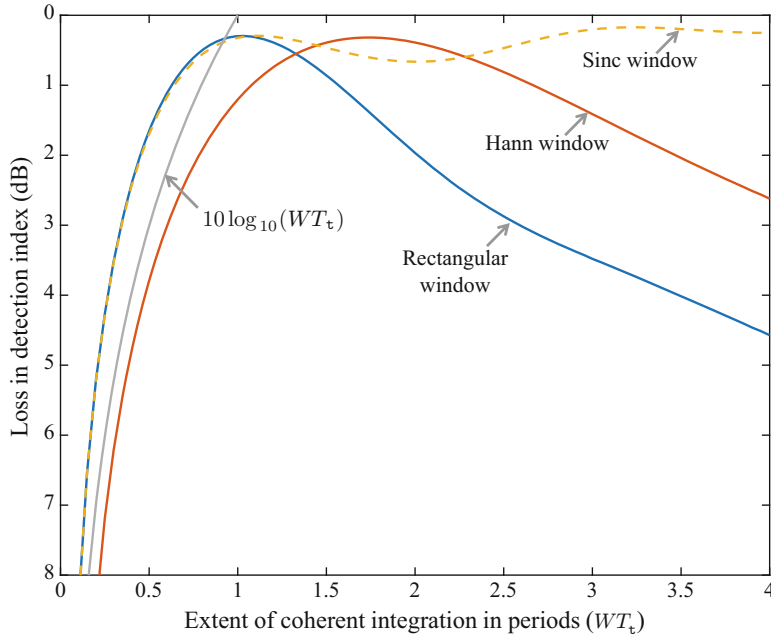


Fig. 9.12 Loss in detection index when using windowed coherent processing followed by incoherent combination as a function of the extent of the coherent integration

$$d = \frac{\left[\text{trace}(\mathbf{P} \boldsymbol{\Lambda}_t^{-1/2} \boldsymbol{\Psi}_t \boldsymbol{\Lambda}_t^{-1/2}) \right]^2}{\text{trace}(\mathbf{P}^2)} \quad (9.159)$$

where $\boldsymbol{\Lambda}_t^{-1/2} \boldsymbol{\Psi}_t \boldsymbol{\Lambda}_t^{-1/2}$ is the noise-normalized signal covariance matrix of the sampled complex envelope data. The loss in detection index for the time-domain energy detector relative to the frequency-domain implementation is shown in Fig. 9.12 as a function of the temporal extent of the filter (T_t) in terms of signal periods (i.e., WT_t). As T_t increases, the loss for the sinc-shaped filter impulse response (dashed line in Fig. 9.12) tends to zero, so the two approaches are equivalent asymptotically when the impulse response of the coherent filtering is allowed to be large enough to implement the sharp filtering accomplished by selecting the DFT bins in the frequency domain.

As seen in Fig. 9.12, setting $T_t = 1/W$ strikes a balance between a long filter impulse response and the loss in performance relative to the frequency-domain implementation (which is about one third of a decibel). Suppose instead that a rectangular window was used without the sinc-function shape, which is simply a coherent integration over T_t . This results in very similar performance to the sinc-shaped impulse response until T_t exceeds $1/W$, where performance begins to degrade (blue line in Fig. 9.12). Thus, the extent of a coherent integration operation

can be used to dictate the width of the frequency band over which the time-domain energy detector operates. Choosing the coherent processing interval (CPI) $T_{\text{coh}} = T_t = 1/W$ clearly optimizes performance for a signal bandwidth of W and a rectangular window in the integration. A longer integration time, which results in a performance degradation, coherently combines the signal beyond the point of its phase stability. In the frequency domain, the passband is narrower than the signal band, which discards some signal and some noise. Using a shorter integration time, which opens up the processing band to allow more noise in, has the effect of a ten-decibels-per-decade decrease in detection index (see the gray line in Fig. 9.12). Recalling the asymptotic five-decibels-per-decade decrease in detection threshold achieved by incoherent processing, it is clear that coherent integration should be extended to the point where it achieves maximum gain (and not further), which is generally on the order of $T_{\text{coh}} = 1/W$ as was discussed in Sect. 9.2.2.

The disadvantage of using $T_{\text{coh}} = T_t = 1/W$ and a rectangular window lies in the sidelobe structure of the filter transfer function outside of the signal band. As noted in Table 4.2, the highest sidelobe of the frequency response of a rectangular window is only 13.3 dB down from the peak and the decay rate is only 6 dB per octave, which implies out-of-band interferences might adversely impact detection performance. An alternative can be found in using one of the many other window functions that better control the sidelobes, but at the expense of an increase in the CPI. This can be seen in Fig. 9.12 for the Hann window (highest sidelobe 31.5 dB down and an 18 dB-per-octave decay rate) where the CPI must be $T_{\text{coh}} \approx 1.75/W$ to attain optimal performance for a signal bandwidth of W (reddish-brown line in Fig. 9.12).

9.2.10.1 Choosing the Coherent-Processing-Window Size and Spacing

The issue of choosing window size and spacing (i.e., overlap) in spectral estimation was considered in [31]. The window size was chosen to keep a constant 3-dB-down spectral width whereas the spacing was chosen to realize a large percentage of the number of equivalent degrees of freedom in the total analysis window. Using a shaped window function required a longer window to maintain spectral width and also a larger overlap between adjacent windows.

The same considerations come into play in the detection application. The size of the CPI window should be chosen so the filter transfer function isolates the signal band and the CPI spacing so as to retain all the independent samples in the total analysis window. For the standard window functions presented in Table 4.2, the CPI duration can be approximated by

$$T_{\text{coh}} = \frac{\Psi_w}{W\Psi_{\text{rect}}} \quad (9.160)$$

where Ψ_w is the 3 dB-down mainlobe width (in terms of DFT bins) for the desired window and $\Psi_{\text{rect}} = 0.89$ for the rectangular window. Using $\Psi_{\text{Hann}} = 1.45$, this

results in $T_{\text{coh}} = 1.63/W$ which is close to the optimal value of 1.75 seen in Fig. 9.12.

Recall that the decimation required to produce independent samples in the analysis of the time-domain energy detector was so the sampling rate equalled the bandwidth (i.e., one sample every $1/W$). When using a window function in the coherent integration and adjusting the size through (9.160), the filter bandwidth is still W and so the decimation must still yield a bandwidth of at least W . However, as noted in [31], overlapping the windows more (i.e., sampling faster) improves performance. An approximate minimum sampling rate for a given window can be obtained from the independent sample rate (η_w) described in Sect. 4.10,

$$f_s \geq \frac{\eta_w}{T_{\text{coh}}} = \frac{\eta_w \Psi_{\text{rect}}}{\Psi_w} W. \quad (9.161)$$

The maximum temporal distance between CPI windows is then

$$\Delta_t \leq \frac{T_{\text{coh}}}{\eta_w} = \frac{\Psi_w}{\eta_w \Psi_{\text{rect}} W}. \quad (9.162)$$

Using $\eta_{\text{Hann}} = 2.1$, this results in $\Delta_t = 0.48 T_{\text{coh}} = 0.78/W$ for the Hann window, which is approximately a 50% overlap of adjacent windows and a finer spacing than one every inverse bandwidth. In a different application, use of the Hann window with certain ratios of window size to spacing has been shown to allow reconstruction of other window sizes post windowing [32].

9.2.10.2 Choosing the Analysis Window Extent

At the beginning of Sect. 9.2, the analysis window was assumed to have duration T_p with the only requirement that the signal and noise be wide-sense stationary within the window. As described in Sect. 9.2.4, the independence of DFT bins assumed in the detector derivations required $T_p > 8/W$ from [10] where W is the smallest signal bandwidth of interest. This can be described as a smoothness requirement on the signal and noise PSDs; they need to vary slowly over the extent of each DFT bin, which is $1/T_p$ Hz. Although this points to making T_p as large as possible, estimation of the noise power in each DFT bin, as will be described in Sect. 9.3, improves with the number of observations of the noise, with one observation obtained from each DFT (i.e., each analysis window of duration T_p). These two competing objectives dictate how to choose T_p : large enough for the signal and noise PSDs to be smooth within each DFT bin and small enough to provide a large number of stationary observations of the noise in each DFT bin. This is identical to the classic trade-off between bias and variance in spectral estimation [33, Sect. 4.4].

If the stationarity time T_{sta} is larger than T_p , the frequency-domain energy detector simply combines the DFT bins incoherently over all the analysis windows. In the time-domain implementation, the process is even simpler in that the coher-

ent/incoherent integration process simply continues through to T_{sta} . In scenarios where T_p is chosen much smaller than T_{sta} because of processing constraints, it is possible to perform coherent processing over multiple analysis windows as shown in [34] (and see [35, 36]), for example to detect or more accurately estimate the center frequency of a long-duration narrowband signal.

9.2.11 Detection Threshold for the Noise-Normalized Energy Detector

The detection threshold term of the sonar equation was described in Sect. 9.2.3.1 for the basic energy detector applied to a signal and noise with constant PSDs over frequency. The SNR requirement that was obtained as a function of the (P_d, P_f) ROC-curve operating point was seen to be applied to the ratio $S^d = S_0/N_0$ of the signal and noise PSDs. The objectives in this section are to extend the analysis to the noise-normalized energy detector, allow for signal and noise PSDs that vary with frequency, and describe the SNR required when the noise-normalized energy detector is applied to a deterministic signal.

The process for evaluating the SNR required to meet an operating point is to obtain the decision threshold h as a function of P_f and then obtain the SNR providing the desired P_d when using that decision threshold. Inherent in this process is choosing a detector, a noise model, and a signal model. The detector under consideration is the noise-normalized energy detector. A similar analysis could be made for the Eckart filter or the Neyman-Pearson optimal detector. However, such an evaluation for the GLR or power-law energy detectors would be more complicated. Recall from Sect. 9.2.6.1 that the decision statistic for the noise-normalized energy detector was

$$T(\mathbf{u}) = \sum_{m=0}^{M-1} \frac{U_m}{\lambda_m}. \quad (9.163)$$

Under the noise-only hypothesis, the normalized squared modulus of the m th DFT bin, U_m/λ_m , is exponentially distributed with unit mean. Because all of the DFT bin data are independent of each other (when T_p is large enough), the sum forming $T(\mathbf{u})$ is gamma distributed with shape parameter M and unit scale,

$$T(\mathbf{u})|H_0 \sim \text{Gamma}(M, 1). \quad (9.164)$$

The decision threshold can therefore be described using the functional inverse of the normalized incomplete gamma function,

$$h = \tilde{\gamma}^{-1}(1 - P_f; M). \quad (9.165)$$

When M is large, the gamma distribution can be approximated with a Gaussian distribution by matching their first two moments. From the description of the gamma distribution in Sect. 5.6.11, the mean and variance of $T(\mathbf{u})$ under H_0 can be seen to be

$$\mu_{T,0} = M \quad \text{and} \quad \sigma_{T,0}^2 = M. \quad (9.166)$$

Under the Gaussian approximation, the decision threshold is described in a similar manner to the gamma by using the functional inverse of the standard Gaussian cumulative distribution function,

$$h = \mu_{T,0} + \sigma_{T,0}\Phi^{-1}(1 - P_f) = M + \sqrt{M}\phi_f \quad (9.167)$$

where $\phi_f = \Phi^{-1}(1 - P_f)$.

Obtaining the SNR required to achieve a particular probability of detection for the decision threshold h requires choosing a statistical model to represent the signal. The following sections cover deterministic and Gaussian-random signals with a signal PSD that is allowed to vary with frequency.

9.2.11.1 Deterministic Signals

Recall from (9.134) that under the deterministic signal model the m th complex DFT bin was complex-Gaussian distributed with the signal entering the mean,

$$Y_m \sim \mathcal{CN}\left(A_m e^{j\phi_m}, \lambda_m\right). \quad (9.168)$$

Multiplying the squared modulus by $2/\lambda_m$ therefore results in a non-central chi-squared-distributed random variable,

$$\frac{2|Y_m|^2}{\lambda_m} = \frac{2U_m}{\lambda_m} \sim \chi_{2,\delta}^2 \quad (9.169)$$

with two degrees of freedom and non-centrality parameter $\delta = 2s_m$ where $s_m = A_m^2/\lambda_m$.

Summing over the M DFT bins then produces a non-central chi-squared-distributed random variable,

$$2T(\mathbf{u}) \sim \chi_{2M,\bar{\delta}}^2 \quad (9.170)$$

with $2M$ degrees of freedom and non-centrality parameter $\bar{\delta} = 2M\bar{s}$ where \bar{s} is the average SNR over the frequency band,

$$\bar{s} = \frac{1}{M} \sum_{m=0}^{M-1} s_m. \quad (9.171)$$

If the squared modulus of the Fourier transform of the signal, $S_{ss}(f)$, and the noise PSD, $S_{vv}(f)$, vary slowly over the width of each DFT bin, the average SNR can be approximated by the integral

$$\bar{s} \approx \frac{1}{W} \int_{f_c-W/2}^{f_c+W/2} \frac{S_{ss}(f)}{S_{vv}(f)} df. \quad (9.172)$$

The scenario of the deterministic signal in Gaussian noise, producing the scaled non-central chi-squared-distributed decision statistic, is precisely that represented by Hmam's equation [37] and approximately that represented by Albersheim's equation [38] (which was developed for summing envelopes rather than squared envelopes). Their equations, which can be found in Sect. 2.3.5.2 can be used to obtain the SNR required under these statistical models to produce the desired (P_d , P_f) operating point. The SNR requirement is then interpreted as applying to the average SNR over the frequency band used to form the decision statistic.

Although the region of validity for M in the Albersheim and Hmam equations is stated as being small by energy-detector standards (respectively, $M \leq 16$ and $M \leq 20$), both equations can be used at larger values. Hmam's equation is very accurate for large M when the decision threshold is computed precisely (i.e., using (9.165)). Albersheim's equation is less accurate (especially for P_d near zero or one), but does not require evaluation of any special functions.

The performance of an energy detector applied to a deterministic signal can also be examined when M is large through a Gaussian approximation to the decision statistic. Using the mean and variance of a non-central chi-squared-distributed random variable from Sect. 5.6.15, it can be seen that the mean and variance of $T(\mathbf{u})$ when signal is present are

$$\mu_{T,1} = M(1 + \bar{s}) \quad \text{and} \quad \sigma_{T,1}^2 = M(1 + 2\bar{s}). \quad (9.173)$$

Recall from (9.40) that when a detector decision statistic is Gaussian distributed, P_d and P_f can be related to its means and variances according to

$$\phi_d = \frac{\sigma_{T,0}}{\sigma_{T,1}} \left[\phi_f - \frac{(\mu_{T,1} - \mu_{T,0})}{\sigma_{T,0}} \right] \quad (9.174)$$

where $\phi_d = \Phi^{-1}(1 - P_d)$ and as previously noted $\phi_f = \Phi^{-1}(1 - P_f)$. Solving this equation for \bar{s} results in the average SNR as a function of M and the (P_d , P_f) operating point,

$$\bar{s} = \frac{\phi_f}{\sqrt{M}} \left[1 + \frac{\phi_d^2}{\sqrt{M}\phi_f} - \frac{\phi_d}{\phi_f} \sqrt{\left(1 + \frac{\phi_f}{\sqrt{M}}\right)^2 + \frac{(\phi_d^2 - \phi_f^2)}{M}} \right] \quad (9.175)$$

$$\approx \frac{\phi_f - \phi_d}{\sqrt{M}}, \quad (9.176)$$

where the approximation in (9.176) assumes M is large. Converting (9.176) to decibels results in

$$\overline{\text{SNR}}^d \approx -5 \log_{10} M + 10 \log_{10} (\phi_f - \phi_d), \quad (9.177)$$

which exhibits the expected reduction in DT at a rate of five decibels per decade as the processing time-bandwidth product (M) is increased. It is also identical to (9.44) for the energy detector operating on Gaussian random signal and noise with constant PSDs when M is large. These will be compared with the approximation for a Gaussian random signal in the next section.

9.2.11.2 Gaussian-Based Approximation for Gaussian Random Signals

The detector decision statistic in (9.163) can be described as a sum of independent exponentially distributed random variables as was done in Sect. 9.2.7 where the means of the m th term under H_0 and H_1 are

$$p_{0,m} = 1 \quad \text{and} \quad p_{1,m} = 1 + s_m. \quad (9.178)$$

Using the results of Sect. 9.2.7.3 for the mean and variance of the sum from (9.110) when signal is present results in

$$\mu_{T,1} = M(1 + \bar{s}) \quad \text{and} \quad \sigma_{T,1}^2 = M \left[(1 + \bar{s})^2 + \sigma_s^2 \right] \quad (9.179)$$

where \bar{s} is the average SNR from (9.171) or (9.172) and σ_s^2 represents the variability of the SNR over the frequency band,

$$\sigma_s^2 = \frac{1}{M} \sum_{m=0}^{M-1} (s_m - \bar{s})^2 \approx \frac{1}{W} \int_{f_c-W/2}^{f_c+W/2} \left(\frac{S_{ss}(f)}{S_{vv}(f)} - \bar{s} \right)^2 df. \quad (9.180)$$

It is interesting to note that the variability of the SNR does not affect, in either a good or bad way, the performance of an energy detector operating on a deterministic signal. However, when operating on a Gaussian random signal, this variability increases the variance of the decision statistic and will therefore affect the performance.

Using the performance equation for the Gaussian approximation from (9.174) with (9.166) and (9.179) and solving for \bar{s} results in

$$\begin{aligned}\bar{s} &= \frac{\phi_f}{\sqrt{M}(1 - \phi_d^2/M)} \left[1 + \frac{\phi_d^2}{\sqrt{M}\phi_f} - \frac{\phi_d}{\phi_f} \sqrt{\left(1 + \frac{\phi_f}{\sqrt{M}}\right)^2 + \sigma_s^2 \left(1 - \frac{\phi_d^2}{M}\right)} \right] \\ &\approx \frac{\phi_f - \phi_d - \phi_d\sigma_s^2}{\sqrt{M}}\end{aligned}\quad (9.181)$$

where the approximation in (9.181) assumes M is large. This describes the average SNR over the DFT frequency bins required to achieve a (P_d, P_f) operating point given a specific variability in the SNR. Comparing the large- M approximation in (9.181) to that for the deterministic signal in (9.176), it can be seen that a higher SNR is required to achieve the operating point for a Gaussian random signal when $\phi_d < 0$, which occurs when $P_d > 0.5$. Conversely, the deterministic signal requires a higher SNR when $\phi_d > 0$ which occurs when $P_d < 0.5$. This reinforces the expectation that signal variation can improve a low-quality operating point and degrade a high-quality one.

Except for very stringent operating points (i.e., very high P_d and very low P_f), the SNR in any one cell when M is large is likely to be less than one. Because the variability scales with the square of the SNRs, this implies σ_s^2 will also be small. In this scenario, the performance of the energy detector on Gaussian random signals and deterministic signals will be similar. This can be seen both from the large- M approximations in (9.176) and (9.181) and in the variances of the decision statistics in (9.173) and (9.179).

Converting (9.181) to decibels results in

$$\overline{\text{SNR}}^d = -5 \log_{10} M + 10 \log_{10}(\phi_f - \phi_d) + 10 \log_{10} \left(1 - \frac{\phi_d \sigma_s^2}{\phi_f - \phi_d} \right), \quad (9.182)$$

which exhibits the expected reduction in DT at a rate of five decibels per decade as the processing time-bandwidth product is increased. When it can be assumed that $\sigma_s^2 \ll \phi_f - \phi_d$ or if P_d is near 0.5 so ϕ_d is near zero, this result is identical to that found in (9.44) for the energy detector operating on Gaussian random signal and noise with constant PSDs and for the deterministic signal in (9.177). Thus, when the SNR variability over the frequency band is small or the operating point is near the minimum detectable level, the same DT relationships as those derived in Sect. 9.2.3.1 for the constant signal and noise PSDs can be used when M is large simply by interpreting the SNR requirement as applying to the average SNR over the frequency band.

The difference in performance for a Gaussian random signal with a varying SNR over the frequency band is captured in the last term in (9.182). For an unbiased detector where $P_d > P_f$, the difference $\phi_f - \phi_d$ will always be positive. This implies that the sign of the third term will be positive when $\phi_d < 0$, which represents an

increase in the SNR required to meet the desired operating point and a degradation in performance relative to the case of a random signal with a constant SNR over frequency or a deterministic signal. Thus, the variability of SNR over frequency improves low-quality operating points (i.e., those for which $P_d < 0.5$ so $\phi_d > 0$) and degrades high-quality operating points (i.e., those for which $P_d > 0.5$ so $\phi_d < 0$) relative to the case of a constant SNR or a deterministic signal.

9.2.11.3 Gamma-Based Approximation for Gaussian Random Signals

Approximating the noise-normalized energy detector decision statistic as being Gaussian distributed was seen in Sect. 9.2.7 to only be accurate for very large time-bandwidth products, whereas the gamma distribution or a shifted gamma distribution was seen to provide a better fit for more moderate values. The P_d and P_f relationships derived for the gamma approximation in (9.114) can be combined into one equation,

$$\frac{\beta_1}{\beta_0} = \frac{\tilde{\gamma}^{-1}(1 - P_f; \alpha_0)}{\tilde{\gamma}^{-1}(1 - P_d; \alpha_1)}, \quad (9.183)$$

that relates P_f and P_d to \bar{s} and σ_s^2 through the gamma parameters (α_0, β_0) and (α_1, β_1) . For the noise-normalized energy detector, the shape and scale parameters of the gamma approximation can be shown to be

$$\alpha_0 = M \quad \text{and} \quad \beta_0 = 1 \quad (9.184)$$

when there is only noise and

$$\alpha_1 = \frac{M}{\kappa} \quad \text{and} \quad \beta_1 = (1 + \bar{s})\kappa \quad (9.185)$$

when signal is present, where the impact of the SNR variability over the frequency band is isolated to

$$\kappa = 1 + \frac{\sigma_s^2}{(1 + \bar{s})^2}. \quad (9.186)$$

These illustrate how variation in the SNR over the frequency band decreases the degrees of freedom parameter (α_1) by a factor κ , but also increases the scale parameter by the same factor. Using these parameters in (9.183) and solving for \bar{s} in terms of P_f , P_d , M , and κ results in

$$\bar{s} = \frac{\tilde{\gamma}^{-1}(1 - P_f; M)}{\kappa \tilde{\gamma}^{-1}(1 - P_d; \frac{M}{\kappa})} - 1 \quad (9.187)$$

which is not directly useful unless the right-hand side does not depend strongly on \bar{s} even though it enters through κ . Although this does occur when the average SNR is small (i.e., $\bar{s} \ll 1$), it is possible to simplify (9.187) further through the use of the approximation

$$\tilde{\gamma}^{-1}\left(1 - P_d; \frac{M}{\kappa}\right) \approx \frac{1}{\kappa} \tilde{\gamma}^{-1}(1 - P_d; M), \quad (9.188)$$

which improves as P_d nears 0.5 and as M increases. Inserting (9.188) into (9.187) results in

$$\bar{s} \approx \frac{\tilde{\gamma}^{-1}(1 - P_f; M)}{\tilde{\gamma}^{-1}(1 - P_d; M)} - 1, \quad (9.189)$$

which is the identical relationship to the result for a constant SNR found in (9.48) with $S^d = \bar{s}$. Thus, the DT relationship found in (9.48) for constant signal and noise PSDs can be used for a noise-normalized energy detector when the time-bandwidth product is moderate and the SNR variation not too severe by interpreting the SNR requirement as applying to the average SNR over the frequency band.

Exercise 9.2 Evaluate the error in (9.189) relative to (9.187) by their decibel difference as a function of $\kappa \in [1, 2]$ for $M = 10, 100$, and 1000 , $P_d = 0.5$ and 0.9 , and $P_f = 10^{-4}$. Is the approximation optimistic or pessimistic? Are the errors reasonable for use in sonar-equation analysis when $M = 10$ and $P_d = 0.9$? Suppose the SNR has a raised sinusoidal shape as a function of frequency, $s_m = \bar{s}[1 + \rho \sin(100f_m/W)]$, so there are many cycles over the frequency bandwidth (W), the average value is \bar{s} , and where $|\rho| \leq 1$ so the SNR is always non-negative. Show that the SNR variance is $\sigma_s^2 = (\rho\bar{s})^2/2$. What is the maximum value of κ when $\bar{s} \gg 1$? Is the approximation of (9.189) useful in this regime?

9.3 Normalization: Background Power Estimation

Development of the energy detectors in Sect. 9.2 assumed the PSD of the background noise was known or able to be estimated perfectly. In general, the noise PSD is not known with any precision and needs to be estimated. Similar to the normalization process described for matched filters (Sect. 8.6), the background noise power used in an energy detector is estimated using auxiliary data. The characteristics of the auxiliary data and where they come from when detecting narrowband and broadband signals are described in Sect. 9.3.1. The primary objective in this section is to present and analyze the effect on an energy detector of estimating the noise background with cell-averaging (Sect. 9.3.2) and exponential averaging estimators (Sect. 9.3.3). These can both be described as *weighted-average* normalizers, which are discussed in Sect. 9.3.4.

In this section, the normalizers are assumed to be applied to each DFT bin individually. The m th normalized DFT bin has the form

$$Z_m = \frac{|Y_m|^2}{\hat{\lambda}_m} \quad (9.190)$$

where Y_m is the complex DFT bin output and $\hat{\lambda}_m$ is the estimate of the noise power in the DFT bin. The detector decision statistic is assumed to be the noise-normalized energy detector described in Sect. 9.2.6.1,

$$T(\mathbf{y}) = \sum_{m=0}^{M-1} Z_m. \quad (9.191)$$

Extension of the analysis to the Neyman-Pearson optimal or Eckart filter energy detectors requires changing (9.191) to a weighted sum. Although this is not overly difficult to analyze using gamma approximations to the decision statistic, it may be computationally exorbitant when M is large in the characteristic-function approaches.

When the noise PSD does not vary significantly over DFT bins, the auxiliary data can be combined to form a single background power estimate and the decision statistic becomes a ratio of sums, $T(\mathbf{y}) = \sum_{m=0}^{M-1} |Y_m|^2 / \sum_{m=0}^{M-1} \hat{\lambda}_m$, rather than the sum of ratios described by (9.190) and (9.191). As shown in [39], this normalization after incoherent combination yields a performance improvement over normalization before, but at the expense of less robustness to a change in the noise PSD. Analysis of normalizing after incoherent integration can be performed by using the characteristic-function-based approach presented in Sect. 9.3.4.2 or by a generalization to the approaches found in Sect. 8.6.1. The latter simply requires using chi-squared-distributed terms in the ratio with $2M$ degrees of freedom in the numerator and $2ML$ in the denominator rather than, respectively, 2 and $2L$. This then results in F -distributed decision statistics with $v_1 = 2M$ and $v_2 = 2ML$.

9.3.1 Auxiliary Data for Narrowband and Broadband Processing

The auxiliary data used to estimate the background noise power in the m th DFT bin (i.e., the “test cell”) are assumed to be independent and identically distributed with the same average noise power level as that of the test cell. When the signal is persistent in time (e.g., when the source signal is a radiated noise), auxiliary data need to come from nearby cells in a different dimension than the temporal one. For narrowband signals, the DFT bins of nearby frequencies can be used as was described for normalization of CW pulses in Sect. 8.7.3. For broadband signals, auxiliary data can be obtained from nearby beams under the assumption that the

noise spectrum does not have a strong angular dependence. When the background is ambient ocean noise, it can be stationary for several minutes, which generally provides a long enough time to obtain accurate estimates of the background noise power in each DFT bin.

Subject to these stationarity conditions, the auxiliary data used to estimate the background noise power in the m th DFT bin can be described as being independent and identically exponentially distributed with mean λ_m ,

$$V_{m,n} \sim \text{Expon}(\lambda_m) \quad (9.192)$$

for $n = 1, \dots, L$. The maximum-likelihood estimate of the background noise power in the m th DFT bin is then the sample mean

$$\hat{\lambda}_m = \frac{1}{L} \sum_{l=1}^L V_{m,l}. \quad (9.193)$$

This estimator is identical to the cell-averaging background power estimator derived for the matched filter in Sect. 8.6.1 and is an unbiased estimator so its average is the true value

$$E\left[\hat{\lambda}_m\right] = \lambda_m. \quad (9.194)$$

The importance of this is that the ratio $|Y_m|^2/\hat{\lambda}_m$ does not depend on λ_m under the noise-only hypothesis (H_0) and so neither will the decision statistic $T(\mathbf{y})$ in (9.191). Because the noise PSD only enters into the statistical characterization of the decision statistic under H_0 through λ_m , the normalized energy detector is said to be invariant to the noise PSD. As described in Sect. 8.6, the decision threshold therefore only depends on the probability of false alarm and so the detector has a constant false alarm rate (CFAR).

The analysis presented in this section assumes that L independent samples are available to estimate each DFT bin and that these are independent of both the test cells (i.e., Y_m for $m = 0, \dots, M - 1$) and the auxiliary data for all the other DFT bins. This then implies that each term Z_m of the sum in (9.191) that forms the decision statistic is independent of the others. There is a common scenario for which the independence assumption is broken and so the analysis of this section does not directly apply. When the noise PSD varies slowly, it is sensible to share the auxiliary data across frequency. This is what was previously described for narrowband signals where DFT bins from adjacent frequencies are used to form the estimate of the m th bin (similar to the split-window normalizer described for detecting CW pulses in Sect. 8.7.3), but can also occur when the auxiliary data come from a different beam. This expansion of the auxiliary data to overlapping sets can improve performance in practice when the mismatch error is small (e.g., see Sect. 8.7.3), but complicates theoretical analysis owing to the correlation it introduces between the terms in (9.191). Taking L equal to the total number of

independent observations available in the auxiliary data divided by M and using the analysis presented in this section should provide an assessment of the worst-case performance when the auxiliary data are shared across estimates.

9.3.2 Cell-Averaging Normalizer

If the estimate of the background power in the m th DFT bin is formed by an average of the squared moduli of L independent DFT bins, each of which is exponentially distributed with mean λ_m , the estimate is gamma distributed with mean λ_m and shape parameter L ,

$$\hat{\lambda}_m \sim \text{Gamma}\left(L, \frac{\lambda_m}{L}\right). \quad (9.195)$$

Multiplying $\hat{\lambda}_m$ by $2L/\lambda_m$ results in a chi-squared-distributed random variable with $2L$ degrees of freedom. For a Gaussian random signal, Z_m is exponentially distributed with mean $\lambda_m(1+s_m)$ where $s_m = \psi_m/\lambda_m$ is the SNR in the m th DFT bin. Multiplying Z_m by $2/[\lambda_m(1+s_m)]$ results in a chi-squared random variable with two degrees of freedom. Using this along with the definition of an F -distributed random variable from Sect. 5.6.16 as a ratio of chi-squared random variables divided by their degrees-of-freedom parameters, it is seen that the m th term in the sum forming the decision statistic is related to an F distribution with 2 and $2L$ degrees of freedom,

$$\frac{Z_m}{1+s_m} = \frac{\left[\frac{2|Y_m|^2}{\lambda_m(1+s_m)}\right]/2}{\left[\frac{2L\hat{\lambda}_m}{\lambda_m}\right]/(2L)} \sim F_{2,2L}. \quad (9.196)$$

The terms in brackets are the numerator and denominator of Z_m scaled so as to be, respectively, χ_2^2 and χ_{2L}^2 distributed random variables.

The same approaches as those described in Sect. 9.2.7 are available for evaluating the performance of the energy detector when the background power is estimated in each DFT bin and then used to normalize it before summing over frequency. These approaches include characteristic function inversion and approximation by Gaussian, gamma, and shifted-gamma distributions. Unfortunately, the F distribution does not have a simply described characteristic function. For the present application it is most expeditiously evaluated by numerical integration. Using the PDF of the $F_{2,2L}$ distribution from Sect. 5.6.16, the characteristic function of Z_m with SNR s is

$$\Phi_s(\omega) = E[e^{j\omega Z_m}] = \int_0^\infty \frac{e^{j\omega(1+s)z}}{(1+z/L)^{L+1}} dz \quad (9.197)$$

$$= j \int_0^\infty \frac{e^{-\omega(1+s)r}}{(1 + jr/L)^{L+1}} dr \quad (9.198)$$

where the form in (9.198), which rotates the integration in the complex plane through the transformation $r = ze^{-j\pi/2}$, is more suitable to numerical evaluation because it converts the oscillatory complex exponential into an exponential decay. The characteristic function in (9.198) can be used to obtain P_f and P_d using the inversion technique described in Appendix 9.A as was done for the power-law detector in Sect. 9.2.8.2.

Application of the characteristic function inversion approach requires the mean and variance of the decision statistic, which can be obtained using (9.377)–(9.379) from Appendix 9.B where $\mu_{G,k}$ are replaced with the moments of Z_m , which are

$$\mu_{z,k} = E[Z_m^k] = \frac{L^k \Gamma(k+1)\Gamma(L-k)}{\Gamma(L)} (1+s)^k. \quad (9.199)$$

These moments can also be used to form the Gaussian, gamma, and shifted-gamma approximations as described in Sect. 9.2.7. These approaches are compared in Fig. 9.13 for a case where $L = 10$, $M = 100$, and the total SNR (i.e., $10 \log_{10}(Ms)$ with $s_m = s$) is 16 dB. The accuracy of the approximations is the same as that encountered in Sect. 9.2.7: the Gaussian approximation is worst, followed by the gamma and then the shifted-gamma. The accuracy of the two gamma approximations improves as M or L increases. The Gaussian approximation is only accurate when M is very large.

The SNR loss arising the normalization, termed a CFAR loss in Sect. 8.6, can be assessed using the gamma approximation, which will be adequate when L or M is reasonably large. This approximation results in the shape and scale parameters

$$\alpha_0 = M \left(1 - \frac{2}{L} \right) \quad \text{and} \quad \beta_0 = \frac{L^2}{(L-1)(L-2)} \quad (9.200)$$

when there is only noise and

$$\alpha_1 = M \left(1 - \frac{2}{L} \right) \quad \text{and} \quad \beta_1 = \frac{L^2(1+s)}{(L-1)(L-2)} \quad (9.201)$$

when signal is also present with an SNR of s in each DFT bin. Using these in (9.183), which relates the (P_d , P_f) operating point to the gamma-approximation parameters, and solving for s results in

$$s = \frac{\tilde{\gamma}^{-1}(1 - P_f; M[1 - 2/L])}{\tilde{\gamma}^{-1}(1 - P_d; M[1 - 2/L])} - 1. \quad (9.202)$$

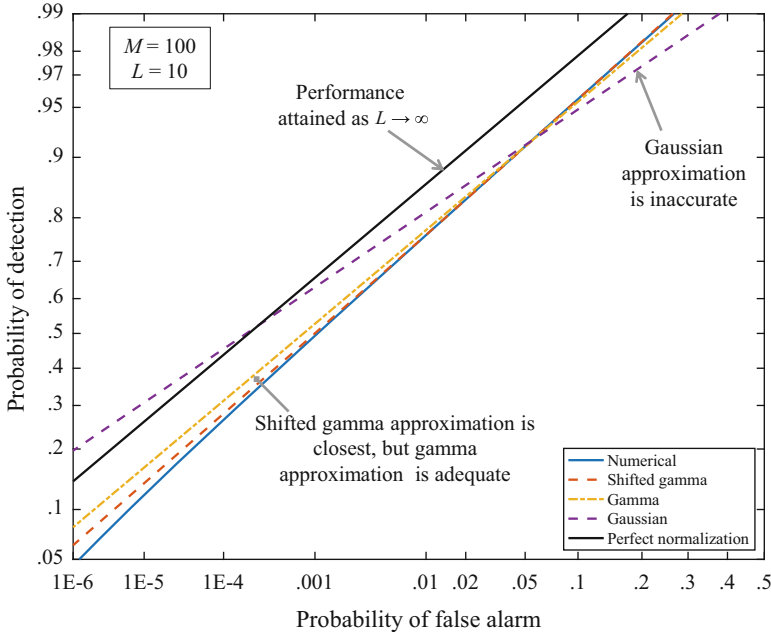


Fig. 9.13 Various approaches to obtaining the ROC curve for a noise-normalized energy detector using $L = 10$ independent observations to estimate the background noise power in each DFT bin when $M = 100$ and the total SNR is 16 dB. The case of perfect normalization is also shown to illustrate the loss incurred by not knowing the background noise power

As should be expected when the amount of auxiliary data is increased ($L \rightarrow \infty$), the SNR required to achieve an operating point tends to that derived for perfect normalization in (9.48). Qualitatively within the gamma approximation to the decision statistic, normalization with an estimated background noise power manifests as a reduction in the degrees-of-freedom parameter. Because this increases the tails of the distribution, it results in an increase in the SNR required to achieve an operating point. Because the gamma distribution tends to be Gaussian as its shape parameter increases, it can also be expected that the CFAR loss has less of an impact when M is large. The CFAR loss in decibels is easily formed from the ratio of (9.202) and (9.48),

$$\text{CFAR Loss} = -10 \log_{10} \left\{ \frac{\frac{\tilde{\gamma}^{-1}(1-P_f; M[1-2/L])}{\tilde{\gamma}^{-1}(1-P_d; M[1-2/L])} - 1}{\frac{\tilde{\gamma}^{-1}(1-P_f; M)}{\tilde{\gamma}^{-1}(1-P_d; M)} - 1} \right\}. \quad (9.203)$$

As seen in Fig. 9.14, the loss decreases rapidly as both L and M increase. The result for $M = 1$, which is obtained from (8.356), is shown to provide a comparison to normalization in matched filtering. The averaging over $M \gg 1$ frequency bins

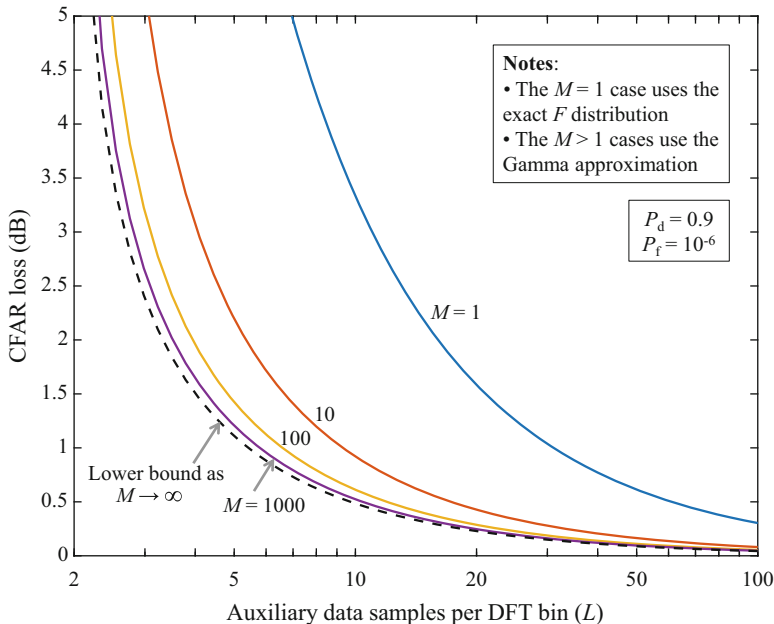


Fig. 9.14 CFAR loss (i.e., the increase in detection threshold) for $P_d = 0.9$ and $P_f = 10^{-6}$ when estimating the background noise power in each DFT bin as a function of the number of independent samples used in each estimate (L) for various values of M . The $M = 1$ case is shown for comparison with normalization when applied to a matched filter; M is generally much larger than one in an energy detector

mitigates the deleterious effects of an extreme value in the estimated background noise power, which more easily causes a false alarm ($\hat{\lambda}_m \ll \lambda_m$) or a missed detection ($\hat{\lambda}_m \gg \lambda_m$) when there is only one term in the sum.

When M is large, the CFAR loss can be shown to tend to the lower bound (when $P_d \geq 0.5$),

$$\text{CFAR Loss} > -5 \log_{10} \left(1 - \frac{2}{L} \right) \quad (9.204)$$

through use of the Gaussian approximation and (9.174). This bound is convenient because it is independent of the operating point and can be used to provide a rule of thumb requiring $L = 10$ for a 0.5-dB CFAR loss, $L \approx 20$ for a 0.25-dB loss and $L = 50$ for a loss less than one tenth of a decibel.

9.3.3 Exponential-Average Normalizers

When there are a large number of DFT bins in an energy detector and L is large, the memory required for implementation of sliding-window background power

estimators can be a challenge in real-time systems. One solution to this is to use an *exponential averager* rather than the sliding-window estimator. The exponential averager is a one-step update combining the newly observed data at time-index l with the previous estimate from time-index $l - 1$ in the form

$$\hat{\lambda}_m[l] = \alpha \hat{\lambda}_m[l - 1] + (1 - \alpha) V_{m,l} \quad (9.205)$$

where $\alpha \in (0, 1)$ is known as a forgetting factor because it de-emphasizes the previous estimate before adding in the new data. When α is near one, the previous estimate is favored over the new data whereas α near zero emphasizes the new data. The form of the exponential averager is that of a first-order infinite-impulse-response (IIR) filter (see Sect. 4.9.1). This allows describing the output as a convolution between the input and the impulse response,

$$\hat{\lambda}_m[l] = \sum_{i=1}^l (1 - \alpha) \alpha^{l-i} V_{m,i}. \quad (9.206)$$

Using the geometric series sum (e.g., from [40, Sect. 8.6]),

$$\sum_{i=0}^{l-1} x^i = \frac{1 - x^l}{1 - x} \quad \text{for } x \neq 1, \quad (9.207)$$

the mean of the estimator at time l can be shown to be

$$E[\hat{\lambda}_m[l]] = \lambda_m (1 - \alpha^l). \quad (9.208)$$

Thus, the estimator is essentially unbiased once it is in its steady state (i.e., l is large). It can similarly be shown that the variance of the estimator is

$$\text{Var}\{\hat{\lambda}_m[l]\} = \lambda_m^2 (1 - \alpha^{2l}) \frac{(1 - \alpha)}{(1 + \alpha)}. \quad (9.209)$$

Noting that the cell-averaging estimate in (9.193) is also unbiased and reduces the variance by a factor of L , the two approaches can be related by equating their variances, which results in

$$L = \frac{1 + \alpha}{1 - \alpha} \quad \text{or} \quad \alpha = \frac{L - 1}{L + 1}. \quad (9.210)$$

This relationship between α and L is shown in Fig. 9.15 (blue line) and illustrates that choosing $\alpha = 0.5$ results in approximately three independent samples, choosing $\alpha = 0.9$ achieves $L = 19$ and $\alpha = 0.98$ yields $L \approx 100$. As will be seen, the accuracy of this approximation degrades as α decreases.

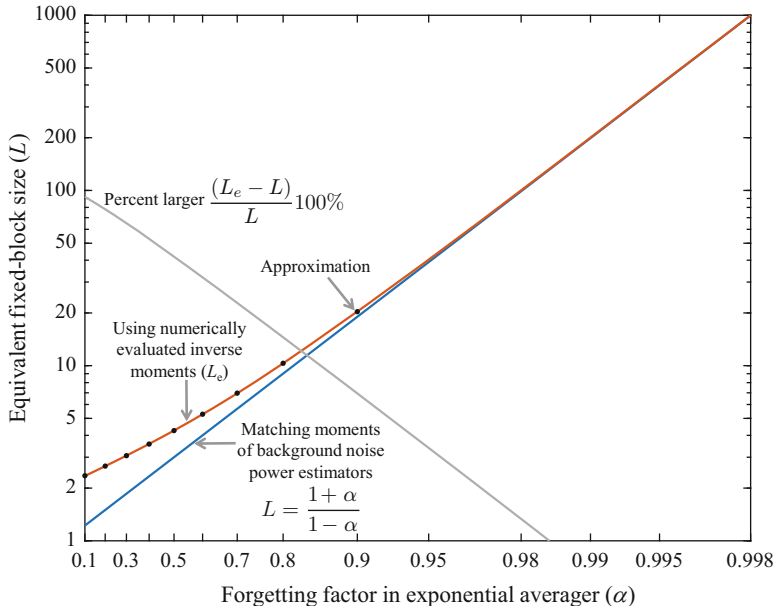


Fig. 9.15 Relationship between the exponential averager forgetting factor (α) and the equivalent number of samples in a fixed sliding block estimator (L)

Recall from (9.190) and (9.191) that the decision statistic of the noise-normalized energy detector is the sum over the normalized DFT-bin squared moduli,

$$T(\mathbf{y}) = \sum_{m=0}^{M-1} \frac{|Y_m|^2}{\hat{\lambda}_m}. \quad (9.211)$$

There are limited options available for evaluating detection performance when using an exponential averager. The most accurate method would be to apply Nuttall's characteristic-function-inversion method [1] as described in Sect. 9.2.7.2. Although it is straightforward to obtain the characteristic function of $\hat{\lambda}_m[l]$, the characteristic function of $|Y_m|^2/\hat{\lambda}_m$ is more complicated and will be described in Sect. 9.3.4.2 for the general case of a normalizer using a weighted-average background estimator. Recalling how useful the gamma distribution has been in approximating scaled sums of exponential random variables, it is reasonable to approximate $\hat{\lambda}_m$ as being gamma distributed with shape parameter L and scale λ_m/L using $L = (1 + \alpha)/(1 - \alpha)$ from (9.210). Each term in the sum in (9.211) is then $F_{2,2L}$ distributed after dividing by $1 + s_m$ as in (9.196). The results of Sect. 9.3.2 can then be used to assess performance through the gamma or shifted gamma distributions. This approach is accurate when α is near one and near the mode of the distribution, but can be inaccurate in the tails. Because $\hat{\lambda}_m$ enters through the denominator, a better approximation can be obtained by using the inverse moments of $\hat{\lambda}_m$, coupled

with the moments of $U_m = |Y_m|^2$ directly in the gamma or shifted gamma approximations. When U_m is exponentially distributed with mean $\lambda_m(1 + s_m)$ and is independent of the background noise power estimate, then the k th moment of a single normalized DFT bin is

$$\mu_{z,k} = E[Z_m^k] = k!(1 + s_m)^k E\left[\frac{\lambda_m^k}{\hat{\lambda}_m^k}\right]. \quad (9.212)$$

Using these moments in the gamma approximation to the distribution of $T(\mathbf{y})$ results in a shape parameter

$$\alpha_T = \frac{M\mu_{z,1}^2}{\mu_{z,2} - \mu_{z,1}^2}. \quad (9.213)$$

When the normalizer is perfect, the exponential distribution dictates that $\mu_{z,2} = 2\mu_{z,1}^2$ and so $\alpha_T = M$. Otherwise, $\mu_{z,2} > 2\mu_{z,1}^2$ and $\alpha_T < M$, which implies the decision statistic will have heavier PDF tails and degrade the performance of high-quality operating points. Equating α_T in (9.213) to the shape parameter $\alpha = M(1 - 2/L)$ arising in the cell-averaging normalizer from (9.200) or (9.201) results in an equivalent number of independent auxiliary data samples

$$L_e = \frac{2\sigma_z^2}{\sigma_z^2 - \mu_{z,1}^2} \quad (9.214)$$

where $\sigma_z^2 = \mu_{z,2} - \mu_{z,1}^2$ is the variance of $Z_m = U_m/\hat{\lambda}_m$. As previously mentioned, approximating $\hat{\lambda}_m$ by a gamma distribution results in $L = (1 + \alpha)/(1 - \alpha)$. Using the approach described in Sect. 9.3.4.2 to obtain the exact values of $\mu_{z,k}$ for an exponential averager as a function of α results in L_e as shown in Fig. 9.15 (reddish-brown line). This illustrates how the F distribution approximation is accurate when α is large, but degrades as α decreases. As described in [39], the equivalent number of independent auxiliary data samples obtained using an exponential averager is approximately

$$L_e(\alpha) \approx \left(\frac{1 + \alpha}{1 - \alpha}\right) \exp\left\{0.734 - 0.799\alpha + 0.065\alpha^2\right\} \quad (9.215)$$

which is seen in Fig. 9.15 as the black dots. This can then be used to obtain the CFAR loss using (9.203) or (9.204), which is shown in Fig. 9.14.

9.3.4 Weighted-Average Normalizers

Both the cell-averaging and exponential-averaging background estimators are examples of a class of weighted-average normalizers where the background power estimate has the form

$$\hat{\lambda} = \sum_{l=1}^L c_l V_l. \quad (9.216)$$

The estimator here has the same form as that encountered in the analysis of the weighted energy detector in Sect. 9.2.7. Thus, the exact PDF of $\hat{\lambda}$ can be obtained numerically via the characteristic-function inversion described in Sect. 9.2.7.2 or approximately through one of the distribution models presented in Sects. 9.2.7.3–9.2.7.5. Given the PDF of $\hat{\lambda}$, the PDF of one normalized test cell (i.e., $Z_m = U_m/\hat{\lambda}_m$) can be obtained through the integral

$$f_Z(z) = \int_{-\infty}^{\infty} v f_U(vz) f_{\hat{\lambda}}(v) dv \quad (9.217)$$

where $f_U(u)$ is the PDF of the test cell $U_m = |Y_m|^2$ which is assumed to be independent of the auxiliary data. The CDF of Z_m is seen to be a similar integral over the CDF of U_m ,

$$F_Z(z) = \int_{-\infty}^{\infty} F_U(vz) f_{\hat{\lambda}}(v) dv. \quad (9.218)$$

Because the decision statistic in (9.191) is the sum over many such normalized test cells, it will most likely need to be evaluated using characteristic functions as described in Sect. 9.2.7.2. As with the PDF and CDF, the characteristic function of Z_m is also an integral over the characteristic function of U_m ,

$$\Phi_Z(\omega) = \int_{-\infty}^{\infty} \Phi_U(\omega/v) f_{\hat{\lambda}}(v) dv. \quad (9.219)$$

Noting that the PDF of $\hat{\lambda}$ is likely to be obtained through a numerical inversion of its characteristic function, it is sensible to consider approaches for evaluating the PDF, CDF, and characteristic function of Z_m that start with the characteristic function of $\hat{\lambda}$, which is easily obtained for a weighted-average normalizer.

9.3.4.1 Characteristic Function of a Weighted-Average Background Estimate

The characteristic function of $\hat{\lambda}$ can be obtained by first describing it as the matrix–vector quadratic form

$$\hat{\lambda} = \mathbf{v}^H \mathbf{C} \mathbf{v} \quad (9.220)$$

where \mathbf{C} is a diagonal matrix with c_l in the (l, l) element and \mathbf{v} is a vector containing the complex DFT bin data comprising the auxiliary data. In general \mathbf{v} can be assumed to be complex Gaussian distributed with zero mean and covariance $\mathbf{\Lambda}$,

$$\mathbf{v} \sim \mathcal{CN}(\mathbf{0}, \mathbf{\Lambda}). \quad (9.221)$$

When the auxiliary data are independent and have the same noise power as the test cell, $\mathbf{\Lambda} = \lambda \mathbf{I}$. When they are correlated, $\mathbf{\Lambda}$ is a Toeplitz matrix formed by sampling the autocorrelation function of the noise.

Starting with the PDF of the multivariate complex Gaussian distribution (see Sect. 5.6.9), the characteristic function of the estimator in (9.220) can be derived by completing the square of the terms in the exponent. This results in

$$\Phi_{\hat{\lambda}}(\omega) = \frac{1}{|\mathbf{I} - j\omega \mathbf{C} \mathbf{\Lambda}|} = \frac{1}{\prod_{l=1}^L (1 - j\omega \sigma_l)} \quad (9.222)$$

where σ_l are the eigenvalues of the matrix product $\mathbf{C} \mathbf{\Lambda}$. When the auxiliary data are independent and identically distributed with mean λ , $\mathbf{C} \mathbf{\Lambda}$ is a diagonal matrix so the eigenvalues are simply $\sigma_l = \lambda c_l$. However, the characteristic function of $\hat{\lambda}$ is also easily evaluated after only one eigen-decomposition for the more general $\mathbf{\Lambda}$ that can represent both correlated and non-stationary auxiliary data.

9.3.4.2 Single-Sample Normalizer Distribution, Characteristic Function and Moments

In [41, Thm. 16], Cramér describes the PDF and CDF of a ratio of independent random variables as single-integral functions where the integrand only requires the characteristic functions of the numerator and denominator of the ratio. These results were adapted and applied to the analysis of constant-false-alarm-rate detectors in [39] for describing the statistics of a single normalized test cell in terms of the characteristic functions of the background power estimate and the un-normalized test cell ($U = |Y_m|^2$). They can be used to analyze the performance of the noise-normalized energy detector by combining the results over the M terms in the sum that forms the decision statistic (i.e., by raising the characteristic function to the right

power or by obtaining the moments of the sum from moments of the summands). A single normalized test cell has the form

$$Z = \frac{U}{\hat{\lambda}} \quad (9.223)$$

where U is the squared modulus of the DFT bin data with PDF $f_U(u)$.

The integral describing the PDF of Z is easily obtained by first describing the PDF of $\hat{\lambda}$ in terms of its characteristic function,

$$f_{\hat{\lambda}}(v) = \frac{1}{2\pi} \int_{-\infty}^{\infty} \Phi_{\hat{\lambda}}(\Omega) e^{-j\Omega v} d\Omega, \quad (9.224)$$

which is very similar to an inverse Fourier transform. Using this definition in the PDF of the normalized test cell Z from (9.217), interchanging the order of the two integrals, and simplifying the result produces

$$f_Z(z) = \frac{1}{\pi z^2} \int_0^{\infty} \text{Imag}\{\Phi_{\hat{\lambda}}^*(\omega)\Phi_U'(\omega/z)\} d\omega \quad (9.225)$$

where $\Phi_U(\omega)$ is the characteristic function of U . The CDF of Z can then be obtained (see [39, App. A]) essentially by integrating (9.225) to produce

$$F_Z(z) = \frac{1}{2} + \frac{1}{\pi} \int_0^{\infty} \text{Imag}\left\{\omega^{-1} \Phi_{\hat{\lambda}}(\omega) \Phi_U^*(\omega/z)\right\} d\omega. \quad (9.226)$$

Suppose that U represents a Rician signal with both a deterministic ($Ae^{j\psi}$) and Gaussian-fluctuating component with power λ_s . The complex random variable forming U is then

$$Y \sim \mathcal{CN}(Ae^{j\psi}, \lambda + \lambda_s) \quad (9.227)$$

where the phase of the deterministic component (ψ) is either deterministic and unknown or uniformly random. When appropriately scaled, U is non-central chi-squared distributed with two degrees of freedom and non-centrality parameter $\delta = 2A^2/(\lambda + \lambda_s)$,

$$W = \frac{2U}{\lambda + \lambda_s} \sim \chi_{2,\delta}^2. \quad (9.228)$$

The characteristic function of U is simply that of the non-central chi-squared distribution (see Sect. 5.6.15) evaluated at $\omega(\lambda + \lambda_s)/2$,

$$\begin{aligned}\Phi_U(\omega) &= E\left[e^{j\omega U}\right] = E\left[\exp\left\{j\frac{\omega(\lambda + \lambda_s)}{2}W\right\}\right] \\ &= \frac{1}{1 - j\omega(\lambda + \lambda_s)} \exp\left\{\frac{j\omega A^2}{(\lambda + \lambda_s)^{-1} - j\omega}\right\}. \quad (9.229)\end{aligned}$$

This and the derivative found in Table 9.2 can be used with (9.225) and (9.226) to obtain the PDF and CDF of the normalized test cell not only for a Rician signal in Gaussian noise but also for

- Gaussian noise: $A = 0$ and $\lambda_s = 0$,
- deterministic signals: $A > 0$ and $\lambda_s = 0$, and
- Gaussian-fluctuating signals: $A = 0$ and $\lambda_s > 0$,

where the signals are assumed to occur in the presence of Gaussian noise. Also shown in Table 9.2 are the characteristic functions and their derivative for a gamma-fluctuating-intensity signal in Gaussian noise and Poisson-Rayleigh-distributed noise. Only the characteristic function of K -distributed noise is shown and not its derivative. Clearly, the integrals in (9.225) and (9.226) are easily evaluated even for complicated scenarios such as using an exponential averager on correlated auxiliary data to detect a gamma-fluctuating-intensity (GFI) signal.

These results for the PDF and CDF of a single normalized test cell are useful for narrowband processing and matched-filtering. However, when the decision statistic comprises the sum of multiple normalized DFT bins, as for the noise-normalized energy detector, the characteristic-function approach described in Sect. 9.2.7.2 is the best approach for performance analysis. This requires the characteristic function of Z which from [39, App. B] is

$$\Phi_Z(\omega) = \frac{1}{2} + \frac{1}{2\pi j} \int_{-\infty}^{\infty} s^{-1} \Phi_{\hat{\lambda}}\left(\frac{s}{\omega\lambda}\right) [1 + se^s E_i(-s)] ds \quad (9.230)$$

under the noise-only hypothesis where $E_i(x)$ is the exponential integral (e.g., see [43, Ch. 6]). Note that the “1/2” in (9.230) accounts for the singularity of the integrand at $s = 0$ so the integral represents the Cauchy principal value. Evaluating it numerically is best accomplished by reflecting $(-\infty, 0)$ to $(0, \infty)$ and integrating the result from some small value suitably close to zero to avoid the singularity. In MATLAB®, $E_i(x)$ as required in (9.230) is evaluated through `-conj(expint(-x))` where the `expint` command represents $E_1(x)$. The characteristic function for a single normalized test cell containing a Gaussian-fluctuating signal in Gaussian noise can be obtained from (9.230) by evaluating it at $\omega(1 + \lambda_s/\lambda)$. The results for deterministic or Rician signals require a more complicated function than the exponential integral.

An alternative to the characteristic function approach that may be well suited to evaluating P_d when the decision statistic is the sum over many normalized DFT bins are the various gamma-distribution approximations. These only require the moments of $Z = U/\hat{\lambda}$. Because U and $\hat{\lambda}$ are assumed to be independent, the moment

Table 9.2 Characteristic functions [$\Phi(\omega)$] and their derivatives [$\Phi'(\omega)$] of the instantaneous intensity for various signals in Gaussian noise and noise-only models

Model	$\Phi(\omega)$	$\Phi'(\omega)$
Gaussian signal	$\frac{1}{1 - j\omega(\lambda + \lambda_s)}$	$\frac{j(\lambda + \lambda_s)}{[1 - j\omega(\lambda + \lambda_s)]^2}$
Deterministic signal	$\frac{\exp\left\{\frac{j\omega A^2}{1 - j\omega\lambda}\right\}}{1 - j\omega\lambda}$	$\frac{j}{(1 - j\omega\lambda)^2} \left[\lambda + \frac{A^2}{1 - j\omega\lambda} \right]$ $\times \exp\left\{\frac{j\omega A^2}{1 - j\omega\lambda}\right\}$
Rician signal	$\frac{\exp\left\{\frac{j\omega A^2}{1 - j\omega(\lambda + \lambda_s)}\right\}}{1 - j\omega(\lambda + \lambda_s)}$	$\left[\frac{j}{1 - j\omega(\lambda + \lambda_s)} \right] \times$ $\left[\lambda + \lambda_s + \frac{A^2}{1 - j\omega(\lambda + \lambda_s)} \right] \Phi(\omega)$
GFI signal ¹	$\frac{(1 - j\omega\lambda)^{\alpha_s - 1}}{(1 - j\omega[\lambda + \beta_s])^{\alpha_s}}$	$\frac{[\omega\lambda(\lambda + \beta_s) + j(\lambda + \alpha_s\beta_s)]}{(1 - j\omega\lambda)(1 - j\omega[\lambda + \beta_s])} \Phi(\omega)$
Gaussian noise	$\frac{1}{1 - j\omega\lambda}$	$\frac{j\lambda}{(1 - j\omega\lambda)^2}$
Poisson-Rayleigh noise	$\sum_{m=0}^{\infty} \frac{\alpha^m e^{-\alpha}}{m! [1 - j\omega(\lambda_c + m\lambda_d)]}$	$\sum_{m=0}^{\infty} \frac{j(\lambda_c + m\lambda_d) \alpha^m e^{-\alpha}}{m! [1 - j\omega(\lambda_c + m\lambda_d)]^2}$
K -distributed noise ^{2,3}	$\Phi_{\alpha}(\omega) = \frac{j [1 - \Phi_{\alpha-1}(\omega)]}{\lambda\omega(\alpha - 1)}$ with $\Phi_1(\omega) = \frac{j}{\lambda\omega} e^{j/(\lambda\omega)} E_1\left(\frac{j}{\lambda\omega}\right)$ $(\alpha \text{ must be an integer})$	

Notes:

1. Gamma-fluctuating-intensity (GFI) signal: $\beta_s = S\lambda/\alpha_s$ where S is the SNR
2. $E_1(x)$ is an exponential integral (e.g., see [42, 5.1.1])
3. The characteristic-function derivative for K -distributed noise is not shown

of their ratio is the product of the k th moment of U and the k th moment of the inverse of $\hat{\lambda}$,

$$E[Z^k] = E[U^k] E\left[\frac{1}{\hat{\lambda}^k}\right]. \quad (9.231)$$

The moments of U are easily obtained for each of the common signal types. For example, under the Rician signal assumption of (9.228), the k th moment is

$$E[U^k] = \Gamma(k+1) \sum_{l=0}^k \binom{k}{l} \frac{(A^2)^l (\lambda + \lambda_s)^{k-l}}{\Gamma(l+1)}. \quad (9.232)$$

When $A = 0$ this simplifies to the moments of the Gaussian-fluctuating signal intensity of $(\lambda + \lambda_s)^k \Gamma(k+1)$. Similar to how the moments of a random variable can be obtained by differentiating the moment generating function (MGF) and evaluating it at zero, the inverse moments of a random variable can be obtained by integrating the MGF. However, this requires a k -dimensional integral to obtain the k th moment. A simpler alternative can be found in the one-dimensional integral

$$E\left[\frac{1}{\hat{\lambda}^k}\right] = \frac{1}{\Gamma(k)} \int_0^\infty t^{k-1} M_{\hat{\lambda}}(-t) dt \quad (9.233)$$

from [44] where $M_{\hat{\lambda}}(t)$ is the MGF of $\hat{\lambda}$. As described in [39], this can be converted to an integral over the characteristic function,

$$E\left[\frac{1}{\hat{\lambda}^k}\right] = \frac{j^k}{\Gamma(k)} \int_0^\infty \omega^{k-1} \Phi_{\hat{\lambda}}(-\omega) d\omega. \quad (9.234)$$

These integral equations only require that the moment exist, which essentially implies $|\Phi_{\hat{\lambda}}(-\omega)|$ must decay faster than $1/\omega^k$ as $\omega \rightarrow \infty$. This can be interpreted as requiring more than k independent samples in the estimator for the k th inverse moment to exist. The parameters of a gamma or shifted gamma distribution that is used to approximate the PDF of Z can then be obtained from (9.231)–(9.234) using, respectively, (9.112)–(9.113) or (9.118)–(9.120). The non-central gamma distribution described in Sect. 7.5.6.3 may be more appropriate for deterministic and Rician signals.

An example application of these techniques is shown in Fig. 9.16 where the probability of false alarm is evaluated for an energy detector combining $M = 100$ DFT bins with each utilizing an exponential averager with $\alpha = 0.6$. The decision threshold is shown when T in (9.191) is divided by M and then converted to decibels. The characteristic function inversion method described in Sect. 9.2.7.2 is employed using the characteristic function in (9.230) (with $\lambda_s = 0$) and $\Phi_{\hat{\lambda}}(\omega)$ from (9.222) with the coefficients from (9.206). The moments evaluated via (9.231) and (9.234) are used in the gamma and shifted-gamma approximations and the mean is required for the characteristic-function inversion approach. The accuracy of the different approaches is as expected; however, the approximation to Z_m using the F distribution and $L = (1 + \alpha)/(1 - \alpha)$ is particularly poor for this combination of M and α (i.e., large M and small α). This can be understood by noting from the gray line in Fig. 9.15 showing that L from (9.214) is more than 30% larger than that for the F-distribution approximation. When M is large, this can amount to a significant change in the distribution of the decision statistic. As seen in Fig. 9.16, one would not wish to use the F-distribution approximation to obtain a threshold as a function of P_f . However, in an SNR loss analysis or when using the F-distribution approximation for both P_f and P_d , the smaller value of L has a similar impact

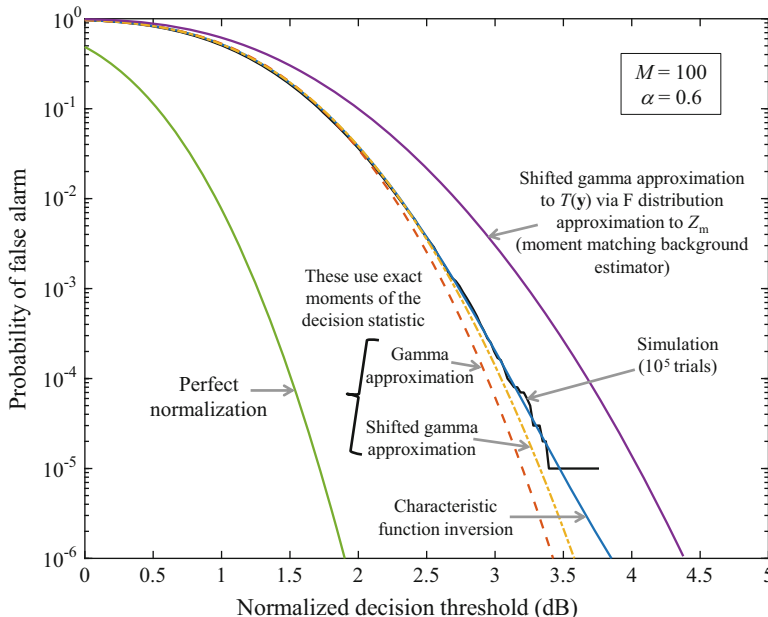


Fig. 9.16 Probability of false alarm as a function of the detector decision threshold for an energy detector combining $M = 100$ DFT bins with an exponential-average normalizer ($\alpha = 0.6$) using various approaches. Inverting the characteristic function is the most accurate, followed by the shifted gamma and gamma approximations utilizing the exact moments of the decision statistic. The accuracy of the shifted gamma approximation relying on the F distribution approximation obtained by matching moments with the background estimator degrades as M increases or as α decreases

under both hypotheses and therefore a small net impact. This example illustrates the importance of ensuring the accuracy of approximations and in their consistent use for analysis of the probabilities of false alarm and detection.

9.4 Time-Delay Estimation

Detection of signals with unknown form is generally an application of passive remote sensing where the object of interest emits the signal of interest (e.g., see Sect. 7.2) and it is measured by the system's sensors after propagation through the underwater acoustical channel. When the signals of interest are broadband, it is sometimes possible to obtain time-delay information that enables or facilitates localization of the object of interest. Two such examples are considered in this section: cross-correlation processing to estimate the time delay when the same source signal is observed at two physically separated sensors and autocorrelation processing to estimate the delay between a source signal arriving at a single sensor

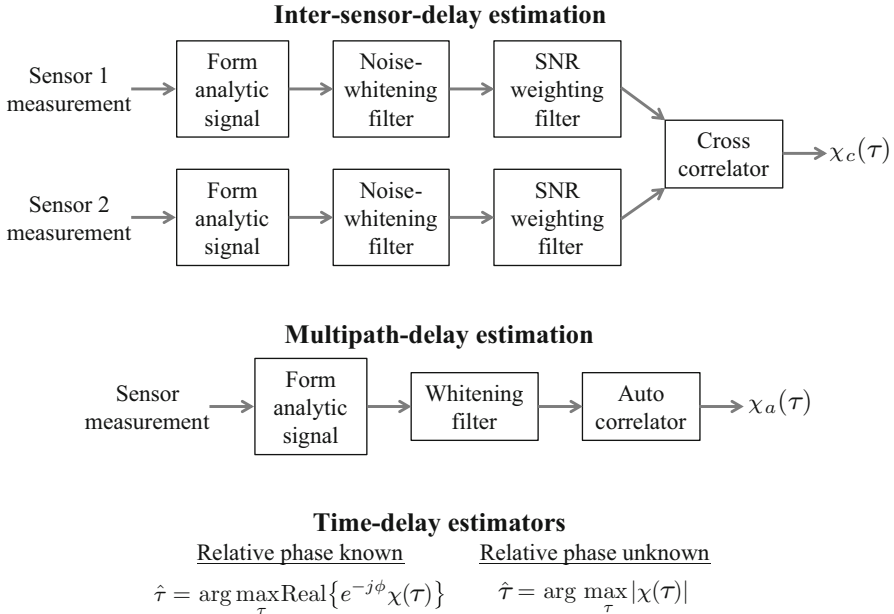


Fig. 9.17 Block diagram of cross- and auto-correlators with spectral-conditioning filters for estimation of inter-sensor delay and multipath delay and the subsequent time-delay estimators when the relative phase is known or unknown

along a primary and secondary multipath. The cross- and auto-correlation processors are derived, respectively, in Sects. 9.4.1 and 9.4.2 as maximum-likelihood estimators (under certain conditions). Both sections also include evaluation of the Cramér-Rao lower bound (CRLB) for the time-delay estimate. The cross-correlation processor is derived first in order to emphasize the assumptions made in the analysis, which can have an impact when processing small temporal segments. Derivation and analysis of the autocorrelation processor is performed within the context of estimating the parameters of a power spectral density (PSD) model via the results of [2]. A significant body of work exists in time-delay estimation related to these two applications; a number of papers have been compiled in [45]. Key references for the two-sensor delay estimation problem also include [46–53]. Similarly seminal papers for estimating multipath delays are [2, 52, 54, 55]. What follows now is an introduction describing the delay-estimation process with examples to illuminate potential difficulties.

As described in Fig. 9.17, the processing begins for both scenarios with the analytic signal of the sensor measurement, which is then filtered to whiten and/or shape the frequency spectrum. This is followed by either a cross- or auto-correlation operation that provides a function of delay from which the time of the maximum is the delay estimate. The models used in both scenarios account for a difference in the amplitude, phase, and delay of the second signal observation relative to

the first. These arise from differences in the propagation paths along which the source signals travel from the object of interest to the sensor. The amplitude and delay differences are clearly related to differences in the propagation path lengths. However, differences in boundary interaction can also alter the amplitude and, more importantly, the phase. The simplest difference in phase arises when the secondary path involves an odd-numbered difference in surface reflections, which results in a sign inversion or a phase difference of π . However, when the secondary path involves a different number of bottom bounces or a difference in the grazing angle, the phase difference can be something other than 0 or π (e.g., see the effect of total internal reflection on phase in Sect. 3.2.7.5) and would generally be unknown, which requires a slight difference in the processing and results in a significant difference in performance. As might be expected, the primary performance drivers in delay estimation are SNR, processing time, bandwidth, and potentially center frequency. As seen in Sects. 9.4.1.2 and 9.4.2.3, the CRLB can be considerably smaller when the phase is known. To illustrate this, consider the example cross-correlation function for the two-sensor scenario shown in Fig. 9.18, as normalized by its peak value. In this case, the phase is assumed to be unknown and the modulus of the analytic-signal correlation function is used for delay estimation. The inverse proportionality of the main-lobe width of the function to processing bandwidth illustrates how bandwidth drives performance when the phase is unknown. The correlation function for the same scenario is shown in Fig. 9.19 when the phase difference is known to be zero, which results in using the real part of the analytic-signal correlation function (note that the abscissa in Fig. 9.19 has a scale four times smaller than that shown in Fig. 9.18). When the phase is known, the envelope of the cross-correlation-function from Fig. 9.18 undergoes a modulation at a rate equal to the center frequency of the signal of interest. Clearly, this can result in a more accurate delay estimate—the estimation performance now also depends on the center frequency. However, if the bandwidth is not large enough, the decay of the envelope is slow and can result in a high probability of a “large error” occurring. A large error is when the addition of random noise causes the peak of the correlation function to occur near a sidelobe peak (i.e., a peak in the signal-only response other than the mainlobe at the true value). While this happens often at low SNR, it can also happen when the sidelobe peaks have nearly as large a value as the mainlobe peak as for the 50-Hz example in Fig. 9.19.

An example of the autocorrelation function used to estimate multipath delays is shown in Fig. 9.20 both when the phase is unknown (black line) and when it is known to be either 0 or π , in which case the absolute value of the real part of the analytic-signal autocorrelation function is used to estimate the delay. The figure then includes the portions of the real part of the correlation function that are negative compared with the example shown in Fig. 9.19 where the phase was assumed to be perfectly known (those negative values are not shown when plotting the normalized correlation function in decibels). As with the cross-correlation example, estimation performance can be significantly better when the phase is known. The example in Fig. 9.20 shows how the autocorrelation function is dominated by the primary path at zero delay. This implies the multipath need to have a delay large enough

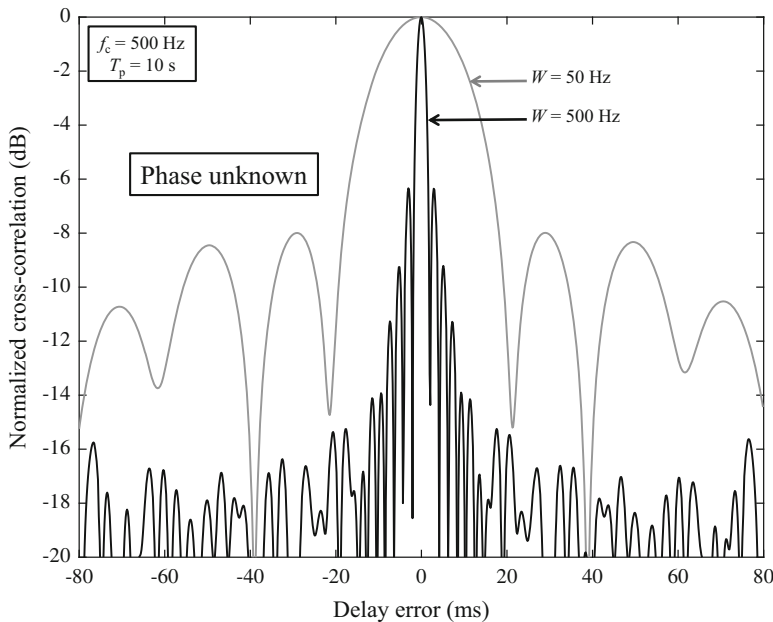


Fig. 9.18 Example output of a cross-correlator when the relative phase is unknown and must be estimated. The processing bandwidth has a large impact on performance

be easily separated from the primary-path response. The example contains only two multipath (at delays of 20 and 30 ms); however, the sidelobes can complicate estimation.

A final example illustrates the importance of whitening or shaping the spectrum. The correlation function obtained without whitening when there is a narrowband component is seen in Fig. 9.21 to have significantly higher sidelobes than when the spectrum is whitened. Clearly, the correlation function response will be sharpest when the signal bandwidth is as high as possible. The narrowband component, when it is not whitened, has the effect of reducing the effective bandwidth and degrading performance.

9.4.1 Cross-Correlation Processing

Suppose two sensors are separated enough that the noise measured on each is statistically independent. If both sensors measure a signal from the same object of interest, the time delay between the two observations can be measured and provides information useful in localizing the object of interest (e.g., see [56] or the example in Sect. 2.2.3.3). As with the energy detector, analysis is most easily

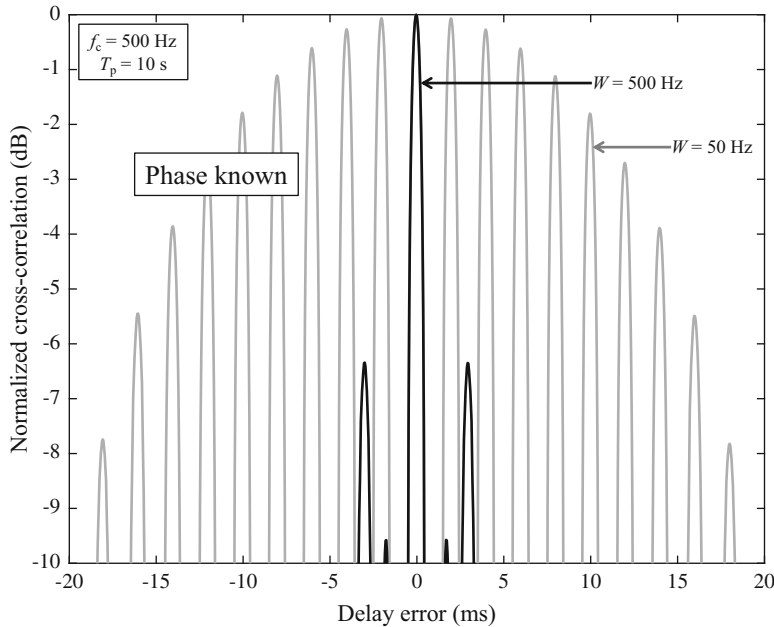


Fig. 9.19 Example output of a cross-correlator when the relative phase is known. Although the lower bandwidth can attain a high accuracy, it has a higher probability of a “large error” occurring than the higher bandwidth because of the extremely high sidelobes in the correlation function. Note that the abscissa here is four times smaller than that shown in Fig. 9.18

accomplished by converting the sampled time-domain data to the frequency domain. However, it is important to start with the time-domain data to understand the approximations required to enable the analysis. Let the form of the analytic source signal measurement at the first sensor be $\dot{s}(t)$ and assume that noise with analytic signal $\dot{v}_i(t)$ is observed at sensor i for $i = 1$ and 2. Now suppose the signal measurement at the second sensor has an identical form to that observed at the first sensor, but is subject to a time delay τ and a phase change ϕ , both of which are assumed to be constant over the time and frequency support of the signal. Both the known- and unknown-phase cases will be considered in the estimation and analysis of the time delay. This is essentially the model used in [49] except that ϕ is assumed constant here, as was done in [46], rather than random. The analytic signal measurements at the two sensors can then be described as

$$\dot{x}_1(t) = A_1 \dot{s}(t) + \dot{v}_1(t) \quad (9.235)$$

and

$$\dot{x}_2(t) = A_2 e^{j\phi} \dot{s}(t - \tau) + \dot{v}_2(t) \quad (9.236)$$

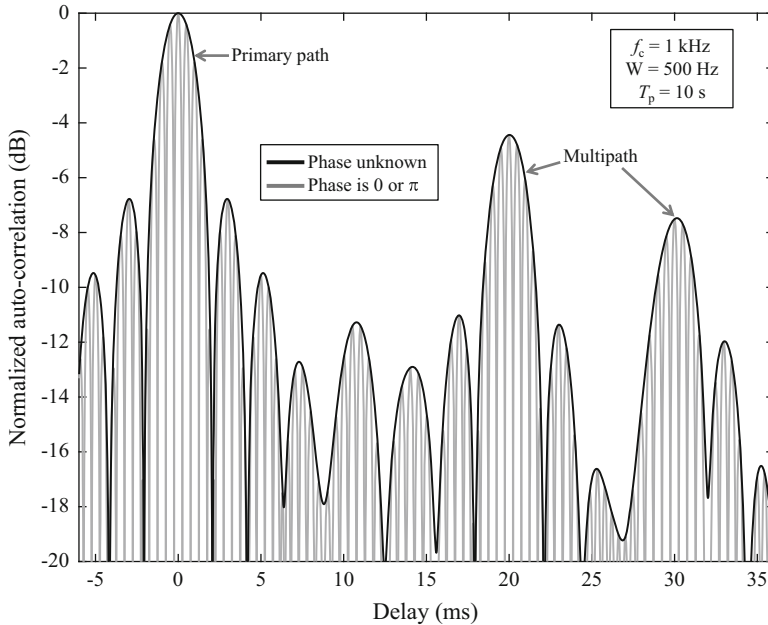


Fig. 9.20 Example output of an auto-correlator for multipath-delay estimation showing the primary path and multipath at delays of 20 and 30 ms. Here the phase is assumed to be either unknown (black line) or known except for the sign (i.e., $\phi = 0$ or π ; gray line)

where A_i is the signal amplitude at sensor i . Although not strictly necessary, this analysis will be done using the complex envelope of the signal measurements for consistency with the derivations of the CRLBs of time-of-arrival estimators for signals with known form in Sect. 8.5. Using (7.34) from Sect. 7.3.2, the complex envelopes of the signal measurements are

$$\tilde{x}_1(t) = A_1 \tilde{s}(t) + \tilde{v}_1(t) \quad (9.237)$$

and

$$\begin{aligned} \tilde{x}_2(t) &= A_2 e^{j\phi} \tilde{s}(t - \tau) e^{-j\omega_c t} + \tilde{v}_2(t) \\ &= A_2 e^{j(\phi - \omega_c \tau)} \tilde{s}(t - \tau) + \tilde{v}_2(t) \end{aligned} \quad (9.238)$$

where $\omega_c = 2\pi f_c$ is the frequency used in the basebanding.

As described in Sect. 9.2.4, sampling the complex envelope and applying a discrete Fourier transform (DFT) produces statistically independent samples, assuming the observation time is long enough and the signals and noise are Gaussian random processes. The following development will be applied to a single DFT bin and the

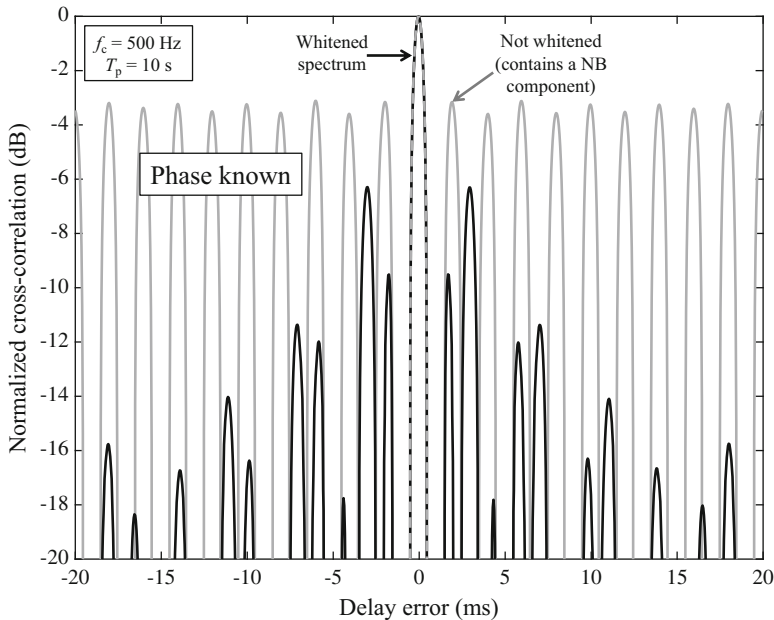


Fig. 9.21 Example output of a cross-correlator when the spectrum is not whitened and contains a narrowband (NB) component (gray line). Compared to the correlation function for a whitened spectrum (black line), the sidelobes in the correlation function are much higher and degrade estimation performance

index over frequency omitted until the frequency-domain data are combined. For example, the k th DFT bin of the noise measurement from sensor i is (omitting the index on k)

$$V_i = \sum_{n=0}^{N-1} \tilde{v}_i(\tau_p + nT_s) e^{-j2\pi kn/N} \quad (9.239)$$

where $T_s = 1/f_s$ is the sampling period and the processing time starts at time τ_p , has extent T_p , and $N = f_s T_p$ samples. Applying this to (9.237) results in

$$X_1 = A_1 \left[\sum_{n=0}^{N-1} \tilde{s}(\tau_p + nT_s) e^{-j2\pi kn/N} \right] + V_1 \quad (9.240)$$

$$= A_1 S + V_1 \quad (9.241)$$

where S , the term in brackets in (9.240), is the k th DFT bin output for the signal. Applying this to the signal measurement from the second sensor produces

$$X_2 = A_2 e^{j(\phi - \omega_c \tau)} \sum_{n=0}^{N-1} \tilde{s}(\tau_p + nT_s - \tau) e^{-j2\pi kn/N} + V_2 \quad (9.242)$$

$$= A_2 e^{j[\phi - \omega_c \tau - 2\pi k\tau/(T_s N)]} \left[\sum_{m=-\tau/T_s}^{N-1-\tau/T_s} \tilde{s}(\tau_p + mT_s) e^{-j2\pi km/N} \right] + V_2 \quad (9.243)$$

$$\approx \tilde{A}_2 S + V_2 \quad (9.244)$$

where the sum over the signal in (9.242) undergoes a change in variables of $mT_s = nT_s - \tau$, with an implicit assumption that τ/T_s is an integer.⁵ The approximation creating (9.244) assumes τ/T_s is much smaller than N ; that is, that the delay is small relative to the processing duration, $\tau \ll T_p$. When this is true, the term in brackets in (9.243) is approximately S . When this is not true, the effect is (approximately) a reduction in SNR at both sensors (i.e., the non-overlapping signals components are treated as noise). Also note that in forming (9.244) the phase terms in (9.243) have been combined into a complex signal amplitude

$$\tilde{A}_2 = A_2 e^{j[\phi - \omega_c \tau - 2\pi k\tau/(T_s N)]} \quad (9.245)$$

$$= A_2 e^{j(\phi - \omega_k \tau)} \quad (9.246)$$

where

$$\omega_k = 2\pi(f_c + \tilde{f}_k) \quad (9.247)$$

and \tilde{f}_k is the frequency of the k th DFT bin from (9.60) or Sect. 4.8. The tilde accent has been used in \tilde{f}_k to emphasize that these frequencies apply to the complex envelope and so are centered about zero (i.e., covering the band $\pm f_s/2$). Recall that \tilde{f}_k is formed by subtracting N from the “ k ” in the exponent of (9.245) when $k \geq N/2$.

When both the signal and noise are bandpass Gaussian random processes, the DFT bin data are complex-Gaussian distributed with zero mean and a power that is approximately the average level of the PSD in the frequency band of the bin. Thus,

$$S \sim \mathcal{CN}(0, \psi) \quad \text{and} \quad V_i \sim \mathcal{CN}(0, \lambda_i). \quad (9.248)$$

When taken individually, X_1 and X_2 are also complex Gaussian distributed with zero mean and a variance comprising the sum of $A_i^2 \psi$ and λ_i when it is assumed that the signal and noise are independent. However, because S enters into both X_1

⁵This assumption is pertinent only in the CRLB analysis and not in deriving the delay estimator itself.

and X_2 , they are correlated with correlation

$$E[X_1 X_2^*] = E[(A_1 S + V_1)(\tilde{A}_2 S + V_2)^*] = A_1 \tilde{A}_2^* \psi \quad (9.249)$$

when it is assumed that the sensors are far enough apart for the noises V_1 and V_2 to be independent (of course, the signal is also assumed to be independent of the noises). Thus, $\mathbf{x} = [X_1 \ X_2]^T$ has covariance matrix

$$\boldsymbol{\Sigma} = \begin{bmatrix} A_1^2 \psi + \lambda_1 & A_1 \tilde{A}_2^* \psi \\ A_1 \tilde{A}_2 \psi & A_2^2 \psi + \lambda_2 \end{bmatrix} \quad (9.250)$$

with inverse

$$\boldsymbol{\Sigma}^{-1} = \frac{1}{|\boldsymbol{\Sigma}|} \begin{bmatrix} A_2^2 \psi + \lambda_2 & -A_1 \tilde{A}_2^* \psi \\ -A_1 \tilde{A}_2 \psi & A_1^2 \psi + \lambda_1 \end{bmatrix} \quad (9.251)$$

and determinant

$$|\boldsymbol{\Sigma}| = (A_1^2 \psi + \lambda_1)(A_2^2 \psi + \lambda_2) - (A_1 A_2 \psi)^2. \quad (9.252)$$

It is important to note that the determinant does not depend on τ or ϕ , but only the signal and noise powers.

9.4.1.1 Inter-Sensor-Delay Estimation

The maximum-likelihood estimates of τ and ϕ are obtained by maximizing the joint PDF of the data over all frequency bins. To simplify the derivation, the pertinent terms from the PDF of the data for a single frequency bin will be extracted before combining over frequency. Recall from Sect. 5.6.9 that the PDF of the bivariate complex Gaussian distribution with zero mean is

$$f(\mathbf{x}) = \frac{1}{\pi^2 |\boldsymbol{\Sigma}|} e^{-\mathbf{x}^H \boldsymbol{\Sigma}^{-1} \mathbf{x}}. \quad (9.253)$$

Noting that neither τ nor ϕ enter in the determinant or in the diagonal entries of $\boldsymbol{\Sigma}^{-1}$, the only terms of interest are those arising from the off-diagonal terms of $\boldsymbol{\Sigma}^{-1}$. Taking the logarithm of (9.253) and using $\boldsymbol{\Sigma}^{-1}$ from (9.251) results in

$$\begin{aligned} \log f(\mathbf{x}) &= \frac{1}{|\boldsymbol{\Sigma}|} \left[X_1 X_2^* A_1 \tilde{A}_2 \psi + X_1^* X_2 A_1 \tilde{A}_2^* \psi \right] + \text{O.T.} \\ &= \frac{A_1 A_2 \psi}{|\boldsymbol{\Sigma}|} \left[X_1 X_2^* e^{j(\phi - \omega_k \tau)} + X_1^* X_2 e^{-j(\phi - \omega_k \tau)} \right] + \text{O.T.} \end{aligned} \quad (9.254)$$

where “O.T.” represents other terms that do not depend on τ or ϕ . Summing (9.254) over frequency, discarding the terms that do not depend on τ or ϕ , and (arbitrarily) multiplying by T_p/N^2 results in a gain function (i.e., a monotonically increasing transformation of the likelihood function)

$$G(\tau, \phi) = \frac{T_p}{N^2} \sum_{k=0}^{N-1} \left\{ Y_1[k]Y_2^*[k]e^{j(\phi - \omega_k \tau)} + Y_1^*[k]Y_2[k]e^{-j(\phi - \omega_k \tau)} \right\} \quad (9.255)$$

where $Y_i[k] = H_i[k]X_i[k]$ represents a filtering of the measurement from the i th sensor by a filter with transfer function $H_i[k]$. The filtering, which is described below, appropriately compensates each frequency bin based on its signal and noise powers. The maximum-likelihood estimates of τ and ϕ are the values maximizing (9.255) as long as the terms $H_i[k]$ satisfy

$$H_1[k]H_2^*[k] = \frac{A_1 A_2 \psi_k}{|\boldsymbol{\Sigma}_k|} = \left[\frac{1}{A_1 A_2 \psi_k} \right] Q[k]. \quad (9.256)$$

where ψ_k and $\boldsymbol{\Sigma}_k$ are simply ψ and $\boldsymbol{\Sigma}$ for the k th DFT bin (note that similar constructs are used to index the other variables over frequency) and

$$Q[k] = \frac{(A_1 A_2 \psi_k)^2}{|\boldsymbol{\Sigma}_k|} = \frac{\gamma_{12}^2[k]}{1 - \gamma_{12}^2[k]} \quad (9.257)$$

represents a weighting emphasizing frequencies with high coherence via the squared coherence function between the two sensor measurements, $\gamma_{12}^2[k]$ [45, pg. 1].

In this application, the squared coherence function has the form

$$\gamma_{12}^2[k] = \frac{A_1^2 A_2^2 \psi_k^2}{(A_1^2 \psi_k + \lambda_1[k])(A_2^2 \psi_k + \lambda_2[k])} \quad (9.258)$$

and can be seen to be a product across the two sensors of the ratio of the signal power to the total power. Describing the SNR in the k th DFT bin at the i th sensor as

$$\mathcal{S}_i[k] = \frac{A_i^2 \psi[k]}{\lambda_i[k]} \quad (9.259)$$

the “high-coherence” weighting can also be seen to be a function of the SNR at each sensor,

$$Q[k] = \frac{\mathcal{S}_1[k]\mathcal{S}_2[k]}{1 + \mathcal{S}_1[k] + \mathcal{S}_2[k]}. \quad (9.260)$$

Given this description of the weighting applied to the frequency-domain sensor data, the results can be compared with the continuous-time derivation found in [47, eq. 47a]. The effect of this weighting is to more strongly de-emphasize frequency bins

for which both sensors have low SNR (i.e., $\mathcal{S}_1[k] + \mathcal{S}_2[k] \ll 1$) than those where at least one sensor has appreciable SNR (i.e., $\max_i \mathcal{S}_i[k] > 1$). This can be seen by noting that when both sensors have low SNR, the weighting is approximately the product of the SNRs whereas it is otherwise on the order of the lower SNR of the two. In practical terms, at least one sensor needs to have a high SNR in order to know what the source signal is.

Choosing the filters according to

$$H_i[k] = \frac{\sqrt{\mathcal{Q}[k]}}{A_i \sqrt{\psi_k}} \quad (9.261)$$

will satisfy (9.256) and can be seen to have both a signal whitening term (the division by $A_i \sqrt{\psi_k}$) and the high-coherence weighting. Alternatively, choosing the filters as

$$H_i[k] = \left[\frac{1}{\sqrt{\lambda_i[k]}} \right] \left[\sqrt{\frac{\mathcal{S}_i[k]}{1 + \mathcal{S}_1[k] + \mathcal{S}_2[k]}} \right] \quad (9.262)$$

represents a noise-whitening term (the first term in brackets) followed by an SNR-proportion weighting (the second term in brackets). Several other weightings are considered in [47] or [57, Ch. 3], illustrating how one can trade some of the resolution capability attained by the maximum-likelihood estimator for robustness to errors in knowledge of the signal and noise PSDs.

Now proceeding with development of the estimator, notice that the first and second terms within the sum in (9.255) are related by a complex conjugation. The maximum-likelihood gain function can therefore be described as

$$\begin{aligned} G(\tau, \phi) &= e^{-j\phi} \chi_c(\tau) + e^{j\phi} \chi_c^*(\tau) \\ &= 2|\chi_c(\tau)| \cos[\phi - \angle \chi_c(\tau)] \end{aligned} \quad (9.263)$$

where

$$\chi_c(\tau) = \frac{T_p}{N^2} \sum_{k=0}^{N-1} Y_1^*[k] Y_2[k] e^{j\omega_k \tau}. \quad (9.264)$$

Thus, if ϕ is known then the maximum-likelihood estimator of τ is the value of τ maximizing (9.263). For example, if $\phi = 0$ then the estimator takes the real part of $\chi_c(\tau)$,

$$\hat{\tau} = \arg \max_{\tau} \text{Real}\{\chi_c(\tau)\}. \quad (9.265)$$

Similarly, if ϕ is known to be π the delay estimator simply takes the time of largest negative peak of the real part of $\chi_c(\tau)$. However, when ϕ is unknown it

can be estimated by its maximum-likelihood estimator which is $\hat{\phi} = \angle \chi_c(\tau)$ by examination of (9.263). This then results in a delay estimator taking the time of the maximum modulus of $\chi_c(\tau)$,

$$\hat{\tau} = \arg \max_{\tau} |\chi_c(\tau)|. \quad (9.266)$$

Whether the phase difference between the two signal measurements (ϕ) is known or not is an important distinction. While there is clearly an impact on the estimation algorithm itself, the impact on performance is even more important, as will be seen in the CRLB analysis of Sect. 9.4.1.2.

Although the filtering, formation of $\chi_c(\tau)$, and estimation of τ can all be accomplished in the frequency domain, it is instructive to assess what form $\chi_c(\tau)$ has in the time domain. This can be accomplished by using the definition of the DFT for $Y_1[k]$ in (9.264) and recalling from (9.247) that $\omega_k = 2\pi(f_c + \tilde{f}_k)$,

$$\begin{aligned} \chi_c(\tau) &= \frac{T_p}{N^2} \sum_{k=0}^{N-1} \left[\sum_{n=0}^{N-1} \tilde{y}_1[n] e^{-j2\pi kn/N} \right]^* Y_2[k] e^{j\omega_k \tau} \\ &= \frac{T_p}{N} \sum_{n=0}^{N-1} \tilde{y}_1^*[n] \left[\frac{1}{N} \sum_{k=0}^{N-1} Y_2[k] e^{j2\pi k(n+\tau/T_s)/N} \right] e^{j\omega_c \tau} \end{aligned} \quad (9.267)$$

$$= T_p e^{j\omega_c \tau} \frac{1}{N} \sum_{n=0}^{N-1} \tilde{y}_1^*[n] \tilde{y}_2[n + \tau/T_s] \quad (9.268)$$

where the normalized frequency of the k th DFT bin (\tilde{f}_k/f_s) has been converted back to the ratio k/N . The simplification from (9.267) to (9.268) is achieved by noting the term in the brackets in (9.267) represents an inverse DFT operation from (4.100) evaluated at time index $n + \tau/T_s$. The function $\chi_c(\tau)$ in (9.268) is completely described in terms of the complex envelopes of the filtered sensor measurements $\tilde{y}_i(t)$. It can be seen to be a correlation of the two complex envelopes and a multiplication by $e^{j\omega_c \tau}$. This multiplicative phase term is only important when the phase ϕ is known—it accounts for the basebanding in the estimate. When ϕ is unknown and τ is estimated through the modulus of $\chi_c(\tau)$, the delay estimate is simply that achieving the largest absolute cross-correlation between $\tilde{y}_1[n]$ and $\tilde{y}_2[n]$.

In a somewhat cleaner representation, $\chi_c(\tau)$ can also be described in terms of the continuous-time measurement complex envelopes and analytic signals by approximating the sum in (9.268) as an integral and using $\dot{\tilde{y}}_1(t) = \tilde{y}_1(t)e^{j\omega_c t}$ to produce

$$\chi_c(\tau) = e^{j\omega_c \tau} \int_{\tau_p}^{\tau_p+T_p} \tilde{y}_1^*(t) \tilde{y}_2(t + \tau) dt$$

$$= \int_{\tau_p}^{\tau_p + T_p} \ddot{y}_1^*(t) \ddot{y}_2(t + \tau) dt. \quad (9.269)$$

Thus, if the cross-correlation is performed using analytic signals rather than complex envelopes, the phase term $e^{j\omega_c\tau}$ in (9.268) is not required.

Recall that the approximation made between (9.243) and (9.244) assumed that $\tau \ll T_p$. In practice this may not always hold firmly. In order to reduce the impact of the non-overlapping signal segments being treated as noise when the correlator is implemented in the frequency domain, it is helpful in practice to zero-pad the signals so as to compute a true correlation. Without zero-padding, the FFT operation implements a circular correlation, analogous to the circular convolution described in Sect. 4.9.4, where the values at one end of the time sequence wrap around and are repeated at the other end as the sequence is shifted. Correlating two length- N sequences results in a sequence with length $2N - 1$, which is the minimum size of the DFT and requires padding with $N - 1$ zero values before applying the DFT. An advantage of implementing delay estimation in the frequency domain using (9.264) is that a single optimization routine allows calculating an estimate to a desired precision or quantization level (e.g., defined by the optimization algorithm's termination criteria). Implementation in the time domain via (9.268) results in a sampled correlation function, $\chi_c(nT_s)$, and a delay estimate quantized with steps of T_s . The samples of the correlation function can be interpolated or the sensor measurements can be oversampled (i.e., $f_s \gg W$) to reduce the quantization error. Note that this only relates to how precisely any particular estimate is calculated. When done correctly, it is not the limiting factor in the overall estimation accuracy.

9.4.1.2 Cramér-Rao Lower Bound for Inter-Sensor Delay

The parameters potentially requiring estimation in the two-sensor scenario include not only the signal delay and phase difference between the two channels but also the noise and signal spectral strengths. Fortunately these are uncoupled from the delay and phase (e.g., see [52] for the delay decoupling) and are therefore not considered in this analysis. Because the parameters only enter into the complex-Gaussian distribution PDF through the covariance matrix, the element of the Fisher information matrix from [58, App. 15C] or (6.75) in Sect. 6.3.3.4 describing the coupling between parameters θ_i and θ_j can be simplified to

$$\{\mathbf{I}(\boldsymbol{\theta})\}_{i,j} = \text{tr} \left\{ \boldsymbol{\Sigma}^{-1}(\boldsymbol{\theta}) \frac{\partial \boldsymbol{\Sigma}(\boldsymbol{\theta})}{\partial \theta_i} \boldsymbol{\Sigma}^{-1}(\boldsymbol{\theta}) \frac{\partial \boldsymbol{\Sigma}(\boldsymbol{\theta})}{\partial \theta_j} \right\}. \quad (9.270)$$

Differentiating $\boldsymbol{\Sigma}$ from (9.250) with respect to τ and ϕ and evaluating the result at their true values (assumed in this analysis to be $\tau = 0$ and $\phi = 0$) results in

$$\frac{\partial \boldsymbol{\Sigma}}{\partial \tau} = j A_1 A_2 \psi \omega_k \begin{bmatrix} 0 & 1 \\ -1 & 0 \end{bmatrix} = j A_1 A_2 \psi \omega_k \mathbf{J} \quad (9.271)$$

and

$$\frac{\partial \boldsymbol{\Sigma}}{\partial \phi} = -j A_1 A_2 \psi \begin{bmatrix} 0 & 1 \\ -1 & 0 \end{bmatrix} = -j A_1 A_2 \psi \mathbf{J} \quad (9.272)$$

where

$$\mathbf{J} = \begin{bmatrix} 0 & 1 \\ -1 & 0 \end{bmatrix}. \quad (9.273)$$

It can then be seen that each term in the Fisher information matrix will be proportional to

$$\text{tr}\left\{\boldsymbol{\Sigma}^{-1} \mathbf{J} \boldsymbol{\Sigma}^{-1} \mathbf{J}\right\} = \frac{-2}{(A_1^2 \psi + \lambda_1)(A_2^2 \psi + \lambda_2) - (A_1 A_2 \psi)^2} = \frac{-2}{|\boldsymbol{\Sigma}|}. \quad (9.274)$$

Using (9.271), (9.272) and (9.274) in (9.270) then results in the Fisher information matrix for the k th DFT bin having form

$$\begin{aligned} \text{FIM}_{\tau, \phi}[k] &= \frac{-2}{|\boldsymbol{\Sigma}_k|} \begin{bmatrix} (j A_1 A_2 \psi_k \omega_k)^2 & (j A_1 A_2 \psi_k \omega_k)(-j A_1 A_2 \psi_k) \\ (j A_1 A_2 \psi_k \omega_k)(-j A_1 A_2 \psi_k) & (-j A_1 A_2 \psi_k)^2 \end{bmatrix} \\ &= 2Q[k] \begin{bmatrix} \omega_k^2 & -\omega_k \\ -\omega_k & 1 \end{bmatrix} \end{aligned} \quad (9.275)$$

where $Q[k] = (A_1 A_2 \psi_k)^2 / |\boldsymbol{\Sigma}_k|$ is the high-coherence weighting from (9.257) for frequency $\omega_k = 2\pi(f_c + \tilde{f}_k)$.

Combining (9.275) over frequency results in weighted sums over ω_k and ω_k^2 . To simplify the final form of the Fisher information matrix, it is convenient to describe the following terms. Define Γ^d as the average of the weighting function $Q[k]$ over the frequency band, which is assumed to be the interval (f_0, f_1) ,

$$\Gamma^d = \frac{1}{N} \sum_{k=0}^{N-1} Q[k] \approx \frac{1}{W} \int_{f_0}^{f_1} Q(f) df \quad (9.276)$$

$$= \frac{1}{W} \int_{f_0}^{f_1} \frac{\mathcal{S}_1(f)\mathcal{S}_2(f)}{1 + \mathcal{S}_1(f) + \mathcal{S}_2(f)} df. \quad (9.277)$$

The variables $Q(f)$ and $S_i(f)$ are simply the continuous-frequency counterparts of $Q[k]$ and $S_i[k]$. For example, $S_i(f) = A_i^2 S_{s,s}(f)/S_{v_i,v_i}(f)$ is the SNR at the i th sensor as a function of frequency where $S_{s,s}(f)$ and $S_{v_i,v_i}(f)$ are the PSDs of the bandpass signal and noise. The approximation of (9.276) as an integral assumes $df = W/N$. Recalling that the weighting $Q[k]$ is linear when at least one sensor has high SNR, Γ^d can be interpreted as the average SNR available for estimation. Now define as a weighted average frequency

$$\bar{f} = \frac{\sum_{k=0}^{N-1} Q[k](f_c + \tilde{f}_k)}{\sum_{k=0}^{N-1} Q[k]} \approx \frac{\int_{f_0}^{f_1} f Q(f) df}{\int_{f_0}^{f_1} Q(f) df} \quad (9.278)$$

and a similarly constructed frequency spread,

$$\sigma_f^2 = \frac{\sum_{k=0}^{N-1} Q[k](f_c + \tilde{f}_k - \bar{f})^2}{\sum_{k=0}^{N-1} Q[k]} \approx \frac{\int_{f_0}^{f_1} (f - \bar{f})^2 Q(f) df}{\int_{f_0}^{f_1} Q(f) df}. \quad (9.279)$$

It is then straightforward to show that the weighted sum over ω_k^2 from the (1, 1) element of (9.275) results in $4\pi^2 N \Gamma^d (\sigma_f^2 + \bar{f}^2)$.

Summing each Fisher information matrix from (9.275) over frequency can now be seen to result in

$$\text{FIM}_{\tau,\phi} = 2N \Gamma^d \begin{bmatrix} 4\pi^2 (\sigma_f^2 + \bar{f}^2) & -2\pi \bar{f} \\ -2\pi \bar{f} & 1 \end{bmatrix}. \quad (9.280)$$

When the phase ϕ is known, the CRLB on τ is simply the inverse of the (1,1) element of the Fisher information matrix in (9.280),

$$\text{CRLB}(\tau|\phi) = \frac{1}{8\pi^2 N \Gamma^d (\sigma_f^2 + \bar{f}^2)}. \quad (9.281)$$

This illustrates how time-delay estimation performance improves by increasing the processing time-bandwidth product ($N = T_p W$), average SNR measure Γ^d , weighted average frequency (\bar{f}), or the weighted frequency spread (σ_f^2). When the signal has a high enough SNR throughout the frequency band, σ_f^2 will be proportional to the square of the processing bandwidth, so the CRLB is proportional to $1/W^3$. Clearly increasing the processing bandwidth to the maximum extent supported by the signal and noise PSDs will have the most impact on performance.

The CRLB in (9.281) is the same result as can be found in [47, eq. A4] or [52, eq. 10], but in a different form and with integrals that are only over the positive-frequency signal band owing to the use of the analytic signal in this derivation.

When ϕ is unknown, the CRLB on τ is the $(1, 1)$ element of the inverse of the Fisher information matrix in (9.280), which is easily seen to be

$$\text{CRLB}(\tau) = \frac{1}{8\pi^2 N \Gamma^d \sigma_f^2}. \quad (9.282)$$

Comparing this with (9.281) when the phase is known illustrates a potentially significant degradation. The CRLB when the phase is unknown is a factor $1 + \bar{f}^2 / \sigma_f^2$ larger than when it is known.

It is interesting to note that the structure of the Fisher information matrix is nearly identical to that developed in Sect. 8.5.3 for arrival-time estimation when the form of the signal is known. Comparing (9.280) with (8.269) illustrates they are in fact the same if the SNR after matched filtering (S^d in (8.269)) is equated to $N \Gamma^d$. Suppose the SNR in the two-sensor scenario is large and constant over frequency and between the two sensors (i.e., $S_i(f) = S^d$). At high SNR the measurement from the first sensor can be viewed as a slightly noisy replica and applied as in a matched filter to the measurement from the second sensor. Under these assumptions, $\Gamma^d \approx S^d/2$, which illustrates how having noise in both measurements is like having no noise in the replica and twice the noise in the measurement: a doubling of the CRLB.

9.4.2 Autocorrelation Processing

When a signal measurement is known to contain a source signal arriving along two different propagation paths, the time-of-arrival difference between the paths can be used in localization (e.g., see the example found in Sect. 2.2.3.4 or the material in [59] and [57, Ch. 6]). The multipath time delay can be estimated through use of an autocorrelation processor similar to the cross-correlation processor described in Sect. 9.4.1.1. Adding a delayed copy of a signal to itself has the effect of applying a multiplicative interference pattern to the source-signal spectrum. Because of this encoding of the parameter of interest in the PSD of the sensor measurement, the results of [2] can be used to obtain both the maximum-likelihood estimator and the CRLB. The key results of [2], which are general and apply to many scenarios, are reviewed in Sect. 9.4.2.1 and then applied to the multipath-delay estimation problem to derive the estimator in Sect. 9.4.2.2 and to obtain the CRLB in Sect. 9.4.2.3.

9.4.2.1 Estimating Parameters of a PSD

In many scenarios of interest, the information desired in remote sensing is encoded in the frequency spectrum of the signal measurement. The example to be considered here is estimation of the time delay associated with a multipath arrival relative to the direct path. Estimation of the parameters of a PSD for wide-sense-stationary, zero-mean, bandpass, Gaussian random processes was described in [2] along with providing the means for a CRLB analysis.

Following [2], suppose the sensor measurement has PSD $P(f; \boldsymbol{\theta})$ where $\boldsymbol{\theta}$ is a vector of parameters describing the PSD. As noted in [2], when the sensor measurement comprises both signal and noise, they are assumed to be independent so $P(f; \boldsymbol{\theta})$ represents the sum of the individual PSDs. Given a time sample of length T_p and a processing bandwidth of W , there are $N = T_p W$ independent DFT bins spanning the frequency band of interest, which is assumed to be (f_0, f_1) . This assumes T_p is large enough to ensure the DFT bins are independent as described in Sect. 9.2.4.

Rather than working with complex envelopes as was done in Sect. 9.4.1, the derivations in this section will utilize analytic signals. Summations over frequency will be denoted solely by an index k (or l) which is assumed to combine the bins from the band of interest. Under the zero-mean bandpass Gaussian random process model, the squared modulus of the k th DFT bin is exponentially distributed with a mean that is approximately the PSD at the frequency of interest,

$$U_k \sim \text{Expon}\{P(f_k; \boldsymbol{\theta})\} \quad (9.283)$$

for $k = 0, \dots, N - 1$. Independence amongst the DFT bin data then implies the log-likelihood function is the sum of the individual log-likelihoods over the frequency band,

$$\begin{aligned} l(\boldsymbol{\theta}; \mathbf{u}) &= \log f_U(\mathbf{u}; \boldsymbol{\theta}) \\ &= - \sum_k \left[\frac{U_k}{P(f_k; \boldsymbol{\theta})} + \log P(f_k; \boldsymbol{\theta}) \right] \end{aligned} \quad (9.284)$$

$$= - \sum_k \left[\frac{U_k}{P_k} + \log P_k \right] \quad (9.285)$$

where the power spectrum evaluated at the frequency of the k th DFT bin is defined as $P_k = P(f_k; \boldsymbol{\theta})$ to simplify subsequent derivations and analysis. This implies U_k is exponentially distributed with mean P_k , which is understood to depend on $\boldsymbol{\theta}$. For a specific PSD model, the maximum-likelihood estimator of $\boldsymbol{\theta}$ is obtained from the argument jointly maximizing (9.284).

A CRLB analysis for a multiple-parameter model requires the Fisher information matrix as described in Sect. 6.3.3.1. The term describing the information between θ_i and θ_j from (6.60) is

$$\{\mathbf{I}(\boldsymbol{\theta})\}_{i,j} = E \left[\left\{ \frac{\partial}{\partial \theta_i} \log f_{\mathbf{u}}(\mathbf{u}; \boldsymbol{\theta}) \right\} \left\{ \frac{\partial}{\partial \theta_j} \log f_{\mathbf{u}}(\mathbf{u}; \boldsymbol{\theta}) \right\} \right]. \quad (9.286)$$

The term inside the braces in (9.286) is then

$$\frac{\partial}{\partial \theta_i} \log f_U(\mathbf{u}; \boldsymbol{\theta}) = \sum_k \left(\frac{\partial P_k / \partial \theta_i}{P_k} \right) \left[\frac{U_k}{P_k} - 1 \right]. \quad (9.287)$$

Noting that U_k/P_k is an exponential random variable with unit mean, the term inside the brackets can be seen to have zero mean and a variance of one (e.g., from Sect. 5.6.10). Using (9.287) in (9.286) results in

$$\{\mathbf{I}(\boldsymbol{\theta})\}_{i,j} = \sum_k \sum_l \left(\frac{\frac{\partial P_k}{\partial \theta_i}}{P_k} \right) \left(\frac{\frac{\partial P_l}{\partial \theta_j}}{P_l} \right) E \left[\left(\frac{U_k}{P_k} - 1 \right) \left(\frac{U_l}{P_l} - 1 \right) \right] \quad (9.288)$$

$$= \sum_k \left[\frac{\partial P_k / \partial \theta_i}{P_k} \right] \left[\frac{\partial P_k / \partial \theta_j}{P_k} \right] \quad (9.289)$$

$$\approx T_p \int_{f_0}^{f_1} \left[\frac{\partial P(f; \boldsymbol{\theta}) / \partial \theta_i}{P(f; \boldsymbol{\theta})} \right] \left[\frac{\partial P(f; \boldsymbol{\theta}) / \partial \theta_j}{P(f; \boldsymbol{\theta})} \right] df \quad (9.290)$$

where the double sum collapses to a single sum because of the independence of U_k and U_l when $k \neq l$ and because each term within the expectation in (9.288) has zero mean. When $k = l$, the expectation in (9.288) represents the variance of U_k/P_k , which was previously noted to be one.

9.4.2.2 Multipath-Delay Estimation

The single-sensor multipath delay estimation problem assumes that a broadband source signal arrives at a sensor through two different paths where the only difference between the individual-path signal measurements is a change in amplitude, phase, and arrival time. Suppose that the SNR is large so that any noise in the sensor measurement can be ignored. The analytic signal of the sensor measurement under the multipath model is then

$$\dot{x}(t) = A \left[\dot{s}(t) + ae^{j\phi} \dot{s}(t - \tau) \right] \quad (9.291)$$

where $\hat{s}(t)$ is the form of the analytic signal from the primary path, A is its amplitude and a , ϕ , and τ are, respectively, the relative amplitude, phase, and delay of the multipath arrival. This model differs from that presented in [2, Sect. VIII] only through the inclusion of the phase change ϕ , which is assumed along with the delay to be constant over the time and frequency support of the signal. In many scenarios, the multipath arrival will have had an additional boundary reflection or entailed boundary reflection at a different angle than the primary path, which can result in a phase change.

There are multiple ways in which the PSD of $\dot{x}(t)$ can be obtained as a function of the PSD of $\hat{s}(t)$, including describing $\dot{x}(t)$ as the output of a linear-time-invariant system whose input is $\hat{s}(t)$ and by describing the autocorrelation function (ACF) of $\dot{x}(t)$ in terms of the ACF of $\hat{s}(t)$. Consider the latter approach where the ACF of $\dot{x}(t)$ is

$$\begin{aligned} R_{\dot{x}\dot{x}}(\delta) &= E[\dot{x}(t + \delta)\dot{x}^*(t)] \\ &= A^2 \left[(1 + a^2)R_{\hat{s}\hat{s}}(\delta) + ae^{j\phi}R_{\hat{s}\hat{s}}(\delta - \tau) + ae^{-j\phi}R_{\hat{s}\hat{s}}(\delta + \tau) \right], \end{aligned} \quad (9.292)$$

where $R_{\hat{s}\hat{s}}(\delta)$ is the ACF of $\hat{s}(t)$. The PSD of $\dot{x}(t)$ is then the Fourier transform of its ACF. Using the time-delay property of the Fourier transform (see Sect. 4.3.2), this can be shown to be

$$\begin{aligned} P_{\dot{x}\dot{x}}(f) &= \mathcal{F}\{R_{\dot{x}\dot{x}}(\delta)\} = A^2 \left[1 + a^2 + ae^{j\phi - j2\pi f\tau} + ae^{-j\phi + j2\pi f\tau} \right] \Psi(f) \\ &= A^2 \left[1 + 2a \cos(\phi - 2\pi f\tau) + a^2 \right] \Psi(f) \end{aligned} \quad (9.293)$$

where $\Psi(f)$ is the PSD of the signal and the Fourier transform of $R_{\hat{s}\hat{s}}(\delta)$.

To simplify derivation of the maximum-likelihood estimator of τ , define $\psi_k = \Psi(f_k)$ and

$$b_k = \cos(\phi - 2\pi f_k \tau) \quad (9.294)$$

so the PSD for the k th DFT bin is

$$P_k = A^2 \left(1 + 2ab_k + a^2 \right) \psi_k. \quad (9.295)$$

Under this model, the log-likelihood function becomes

$$\begin{aligned} l(A, a, \tau, \phi; \mathbf{u}) &= \frac{-1}{A^2} \sum_k \left[\frac{U_k}{\psi_k(1 + 2ab_k + a^2)} \right] - N \log A^2 \\ &\quad - \sum_k \log \left(1 + 2ab_k + a^2 \right) + \text{O.T.} \end{aligned} \quad (9.296)$$

where “O.T.” is understood to encapsulate *other terms* not depending on the parameters. Differentiating (9.296) with respect to A and solving for the value of A setting the derivative to zero results in the maximum-likelihood parameter estimator for A ,

$$\hat{A} = \left\{ \frac{1}{N} \sum_k \frac{U_k}{\psi_k(1 + 2ab_k + a^2)} \right\}^{\frac{1}{2}}. \quad (9.297)$$

Using this in the likelihood function then produces

$$\begin{aligned} l(\hat{A}, a, \tau, \phi; \mathbf{u}) &= -N \log \left\{ \sum_k \frac{U_k}{\psi_k(1 + 2ab_k + a^2)} \right\} + \text{O.T.} \\ &\quad - \sum_k \log(1 + 2ab_k + a^2) \end{aligned} \quad (9.298)$$

By assuming a is small ($\ll 1$), the term on the second line of (9.298) can be ignored,

$$\sum_k \log(1 + 2ab_k + a^2) \approx 2a \sum_k b_k = 2a \sum_k \cos(\phi - 2\pi f_k \tau) \quad (9.299)$$

$$\approx 2a T_p W \text{sinc}(W\tau) \cos(\phi - 2\pi f_c \tau) \approx 0, \quad (9.300)$$

where $f_c = (f_0 + f_1)/2$ is the center frequency of the band. The approximation yielding (9.299) uses the first-order Taylor series approximation of $\log(1 + x) \approx x$, which requires a to be small. In order for the result in (9.300) to be small as the processing-time-bandwidth product ($T_p W$) increases, the sum in (9.299) must span many periods of the cosine, which requires $\tau \gg 1/W$. That is, the delay between the multipath arrivals must be large relative to the resolution capability of the signal.

The likelihood function then becomes the first line of (9.298),

$$l(\hat{A}, a, \tau, \phi; \mathbf{u}) \approx -N \log \left\{ \sum_k \frac{U_k}{\psi_k(1 + 2ab_k + a^2)} \right\} + \text{O.T.} \quad (9.301)$$

so the maximum-likelihood estimate of a can be obtained by subtracting the *other terms* and applying a transformation $\exp\{-l/N\}$. This results in a requirement to minimize the cost function

$$C(a, \tau, \phi) = \sum_k \frac{U_k}{\psi_k(1 + 2ab_k + a^2)} \approx \sum_k \frac{U_k}{\psi_k} \left[1 - 2ab_k + (4b_k^2 - 1)a^2 \right] \quad (9.302)$$

where the approximation arises from a second-order Maclaurin series approximation to $(1 + 2ab_k + a^2)^{-1}$. Taking the partial derivative of (9.302) with respect to a results in

$$\frac{\partial C(a, \tau, \phi)}{\partial a} = -2 \sum_k \frac{U_k}{\psi_k} b_k + 2a \sum_k \frac{U_k}{\psi_k} (4b_k^2 - 1). \quad (9.303)$$

Equating this to zero and solving for a results in the estimator

$$\hat{a} = \frac{\sum_k \frac{U_k}{\psi_k} b_k}{\sum_k \frac{U_k}{\psi_k} (4b_k^2 - 1)} \approx \frac{\sum_k \frac{U_k}{\psi_k} b_k}{\sum_k \frac{U_k}{\psi_k}} \quad (9.304)$$

where the approximation arises from $b_k^2 = 0.5 + 0.5 \cos(2\phi - 4\pi f_k \tau)$ and the earlier arguments about summing over the cosine when $\tau \gg 1/W$. Inserting the estimate \hat{a} into (9.302) and neglecting the \hat{a}^2 term results in

$$C(\hat{a}, \tau, \phi) \approx \sum_k \frac{U_k}{\psi_k} - 2 \left[\sum_k \frac{U_k b_k}{\psi_k} \right]^2 \left[\sum_k \frac{U_k}{\psi_k} \right]^{-1}. \quad (9.305)$$

Because the parameters τ and ϕ only enter (9.305) through the first term in brackets, they can be estimated by the arguments maximizing the gain function (arbitrarily multiplying the pertinent sum by $2/T_p$)

$$G(\tau, \phi) = \frac{2}{T_p} \sum_k \frac{U_k}{\psi_k} b_k = \frac{2}{T_p} \sum_k \frac{U_k}{\psi_k} \cos(\phi - 2\pi f_k \tau) \quad (9.306)$$

$$\approx \int_{f_0}^{f_1} \frac{\dot{U}(f)}{\Psi(f)} \left[e^{j(\phi - 2\pi f \tau)} + e^{-j(\phi - 2\pi f \tau)} \right] df \quad (9.307)$$

$$= e^{-j\phi} \chi_a(\tau) + e^{j\phi} \chi_a^*(\tau) \quad (9.308)$$

$$= 2|\chi_a(\tau)| \cos[\phi - \angle \chi_a(\tau)] \quad (9.309)$$

where $\dot{U}(f) = |\dot{X}(f)|^2$ is the squared modulus of the Fourier transform of the analytic signal measurement ($\dot{X}(f) = \mathcal{F}\{\dot{x}(t)\}$) and

$$\chi_a(\tau) = \int_{f_0}^{f_1} \frac{\dot{U}(f)}{\Psi(f)} e^{j2\pi f \tau} df. \quad (9.310)$$

Noting that (9.308) is identical in form to (9.263) from the development of delay estimation in the two sensor problem, the following proceeds identically when ϕ is unknown. Estimating ϕ by

$$\hat{\phi} = \angle \chi_a(\tau) \quad (9.311)$$

maximizes $G(\tau, \phi)$ and the multipath delay is then estimated by the argument maximizing the modulus of $\chi_a(\tau)$,

$$\hat{\tau} = \arg \max_{\tau} |\chi_a(\tau)|. \quad (9.312)$$

If there is no phase difference ($\phi = 0$) between the two paths, then the maximum would be taken over the real part of $\chi_a(\tau)$. If it is assumed to be either zero or π (i.e., a sign inversion as might occur from the multipath having an additional surface reflection), the maximum is taken over the absolute value of the real part of $\chi_a(\tau)$.

The ratio $\dot{U}(f)/\Psi(f)$ in (9.310) represents a whitening of the measured spectrum (although not a normalization, so the absolute level of the signal spectrum is not required). If $\dot{z}(t)$ is the whitened measurement, with Fourier transform $\dot{Z}(f) = X(f)/\sqrt{\Psi(f)}$ and there is no frequency content outside of the band (f_0, f_1) , then (9.310) can be described as its autocorrelation using a sample of size T_p starting at τ_p ,

$$\chi_a(\tau) = \int_{f_0}^{f_1} \dot{Z}^*(f) \dot{Z}(f) e^{j2\pi f \tau} df \quad (9.313)$$

$$= \int_{-\infty}^{\infty} \dot{z}^*(t) \dot{z}(t + \tau) dt, \quad (9.314)$$

by using the definition of the Fourier transform and its inverse for $Z(f)$ in (9.313). Recalling the requirement that $\tau \gg 1/W$ and noting that the maximum-likelihood estimate is subject to large errors, it is clear in this scenario that the search for τ must avoid the inevitable peak in $|\chi_a(\tau)|$ at $\tau = 0$.

Converting the analytic signals in (9.314) to complex envelopes,

$$\chi_a(\tau) = e^{j\omega_c \tau} \int_{-\infty}^{\infty} \tilde{z}^*(t) \tilde{z}(t + \tau) dt. \quad (9.315)$$

is seen to result in a form similar to that for the cross-correlation processor in (9.269) where the phase term $e^{j\omega_c \tau}$ must be used to form $\chi_a(\tau)$ from a correlation of complex envelopes when the relative phase is known.

The derivation here has focused on the case of high SNR to illustrate under what conditions the autocorrelation estimator approximates the maximum-likelihood estimator. Extensions to more realistic conditions can be found in [54, 55] as well as a large number of papers examining numerical techniques handling multiple paths. The same comments related to the discrete-time frequency-domain implementation as those made at the end of Sect. 9.4.1.1 apply (i.e., the inherent arbitrary precision of the frequency-domain approach in evaluating the arg max function and zero padding of the sequence before applying the DFT).

9.4.2.3 Cramér-Rao Lower Bound for Multipath Delay

Recalling the form of the (i, j) element of the Fisher information matrix when estimating parameters from a PSD in (9.290), the derivatives of the PSD with respect to each parameter as evaluated at their true values are required. Without a loss of generality in the result, it can be assumed that the true value of ϕ in the multipath model is zero. However, the other variables will retain their form. For the multipath-model PSD in (9.293),

$$P_{\ddot{x}\dot{x}}(f) = A^2 \left[1 + 2a \cos(\phi - 2\pi f \tau) + a^2 \right] \Psi(f) \quad (9.316)$$

the derivatives of the PSD with respect to the parameters are

$$\frac{\partial P_{\ddot{x}\dot{x}}(f)}{\partial A} = \frac{2}{A} P_{\ddot{x}\dot{x}}(f) \quad (9.317)$$

$$\frac{\partial P_{\ddot{x}\dot{x}}(f)}{\partial a} = 2[a + \cos(2\pi f \tau)] A^2 \Psi(f) \quad (9.318)$$

$$\frac{\partial P_{\ddot{x}\dot{x}}(f)}{\partial \phi} = -2a \sin(2\pi f \tau) A^2 \Psi(f) \quad (9.319)$$

$$\frac{\partial P_{\ddot{x}\dot{x}}(f)}{\partial \tau} = 4\pi a f \sin(2\pi f \tau) A^2 \Psi(f). \quad (9.320)$$

As described in (9.290), the Fisher information matrix is then formed by integrating products of the derivatives in (9.317)–(9.320) for various parameter pairs divided by the squared PSD. Assuming a is small (i.e., $a \ll 1$), the PSD in the denominator can be approximated by

$$P_{\ddot{x}\dot{x}}(f) \approx A^2 \Psi(f), \quad (9.321)$$

which will cancel the last two terms in (9.318)–(9.320) before taking the integral to leave simple integrands comprising products of powers of f and the sine and cosine terms. When $\tau \gg 1/W$, the integrals over any products containing $\sin(2\pi f \tau)$ when it is not squared will be approximately zero. This implies that A and a are uncoupled from τ and ϕ , but that τ and ϕ are coupled. Carrying out the integrations described in (9.290) for τ and ϕ and with the aforementioned assumptions results in the Fisher information matrix

$$\text{FIM}_{\tau,\phi} = 2a^2 T_p \begin{bmatrix} \frac{4}{3}\pi^2(f_1^3 - f_0^3) & -\pi(f_1^2 - f_0^2) \\ -\pi(f_1^2 - f_0^2) & f_1 - f_0 \end{bmatrix}. \quad (9.322)$$

When ϕ is known, the CRLB for τ is simply the inverse of the (1,1) element of (9.322),

$$\text{CRLB}(\tau|\phi) = \frac{3}{8\pi^2 a^2 T_p (f_1^3 - f_0^3)} \quad (9.323)$$

$$= \frac{3}{8\pi^2 a^2 T_p W [W^2 + 3f_0 f_1]} \quad (9.324)$$

which is identical to [2, eq. 44]. This result illustrates how estimation performance will improve with increases in the multipath amplitude, processing time, bandwidth, and the center frequency of the band.

When ϕ is unknown, the CRLB for τ is the (1, 1) element of the inverse of the Fisher information matrix in (9.322),

$$\text{CRLB}(\tau) = \frac{3}{2\pi^2 a^2 T_p W^3} \quad (9.325)$$

where $W = f_1 - f_0$. In sonar applications, $4(f_1^3 - f_0^3)$ will generally be much larger than W^3 , illustrating the loss incurred when the multipath phase is unknown. Similar to the two-sensor cross-correlation scenario in Sect. 9.4.1.2, the lack of phase information removes the dependence of the bound on the center frequency and can result in a significant loss of information. The CRLB in (9.325) is larger than that in (9.324) by a factor

$$\frac{\text{CRLB for } \tau \text{ if } \phi \text{ is unknown}}{\text{CRLB for } \tau \text{ given } \phi} = 4 + 3\left(\frac{4}{\zeta^2} - 1\right) \quad (9.326)$$

where $\zeta = W/f_c$ is the bandwidth to center-frequency ratio (i.e., the inverse of the quality factor, $Q = f_c/W$, of the processing band). When the bandwidth is small relative to the center frequency (ζ is small, Q is large), the reduction in performance is significant—because there is relatively little data available to estimate the multipath phase. Conversely, as bandwidth increases to equal the center frequency, the ratio is 13, which is still a significant reduction in performance. In the limit as $\zeta \rightarrow 2$, estimating phase in the multipath still results in a bound four times higher than if it were known.

9.5 Narrowband-Signal Parameter Estimation

In Sect. 7.3.1 the analytic form of a bandpass signal was represented by

$$\hat{s}(t) = A(t)e^{j\phi(t)}e^{j2\pi f_c t} \quad (9.327)$$

where f_c is the center frequency and $A(t)$ and $\phi(t)$ are the time-varying amplitude and phase. The signal can be considered narrowband if the amplitude and phase vary

slowly with respect to the complex exponential, which implies the bandwidth W of the complex envelope $A(t)e^{j\phi(t)}$ is small compared to f_c .

The statistical characteristics of the amplitude dictate how parameter estimation proceeds for a narrowband signal. When the amplitude and phase are constant over the analysis period, the signal in (9.327) is effectively a complex sinusoid for $t \in (\tau_p, \tau_p + T_p)$,

$$\hat{s}(t) \approx Ae^{j\phi}e^{j2\pi f_c t}. \quad (9.328)$$

This might imply a short observation period or a consistent signal (see Sect. 7.2.1). Parameter estimation and Cramér-Rao lower bounds for sinusoids are presented in Sect. 9.5.1.

Recall that the Fourier transform of (9.328) is an impulse function at f_c . When the signal is windowed by a rectangular function with duration T_p , the Fourier transform is a sinc function centered at f_c with width $1/T_p$. This implies that the observed bandwidth of the sinusoidal signal measurement decreases as the measurement duration increases. At some point, conditions will change and alter the amplitude and phase of the signal measurement. For example, the sound source itself might change, or there may be relative motion between the object of interest and the sensor, or the underwater acoustical channel through which the acoustic wave propagates might change because of a moving boundary or water mass. When this happens on a time scale that is shorter than the analysis window, the complex envelope $A(t)e^{j\phi(t)}$ must be treated as a narrowband Gaussian random process with bandwidth W . Under this model, increasing T_p (as long as $T_p \gg 1/W$) does not change the observed bandwidth of the signal measurement. Estimation processing and analysis of narrowband Gaussian random processes is presented in Sect. 9.5.2.

9.5.1 Sinusoidal Signals

The topic of this section is the estimation of the amplitude, frequency, and phase of a sinusoidal signal in noise. The development follows that of [60], some of which can also be found in [33, Ch. 13]. In order to exploit the simple statistical characterization of the sampled complex envelope of bandpass signals and noise from Sect. 7.3.5, the signal measurement must be basebanded. However, because the frequency of the sinusoidal signal is not known a priori, the basebanding is done by shifting a band with center frequency f_b that is known to include the sinusoid. The basebanded sensor measurement is then

$$\tilde{x}(t) = \hat{x}(t)e^{-j2\pi f_b t} = Ae^{j\phi}e^{j2\pi \tilde{f}t} + \tilde{v}(t) \quad (9.329)$$

where $\tilde{v}(t)$ is the complex envelope of additive zero-mean Gaussian noise and

$$\tilde{f} = f_c - f_b \quad (9.330)$$

is the frequency of the sinusoid after basebanding. The estimate of f_c can then be obtained from an estimate of \tilde{f} simply by adding f_b . Sampling the complex envelope data every $T_s = 1/f_s$ starting at τ_p and placing the N samples in a vector results in

$$\mathbf{x} = Ae^{j\psi}\mathbf{s}_{\tilde{f}} + \mathbf{v} \quad (9.331)$$

where the n th element of $\mathbf{s}_{\tilde{f}}$ is

$$\{\mathbf{s}_{\tilde{f}}\}_n = e^{j2\pi\tilde{f}nT_s} \quad (9.332)$$

for $n = 0, \dots, N - 1$ and the phase associated with the initial sampling time is absorbed into $\psi = \phi + 2\pi\tilde{f}\tau_p$. Note that DFT indexing (i.e., starting from zero rather than one) will be used in this section. The maximum-likelihood estimate of ϕ can be obtained from those of ψ and \tilde{f} . Assuming that the sinusoidal amplitude and phase are deterministic parameters and that the noise is white and Gaussian results in \mathbf{x} being complex-Gaussian distributed,

$$\mathbf{x} \sim \mathcal{CN}(\mathbf{u}, \lambda\mathbf{I}), \quad (9.333)$$

with mean

$$\mathbf{u} = Ae^{j\psi}\mathbf{s}_{\tilde{f}} \quad (9.334)$$

and covariance matrix $\lambda\mathbf{I}$ where $\lambda = 2N_0f_s$ if $N_0/2$ is the two-sided bandpass noise PSD, which is assumed to be constant within the processing band.

9.5.1.1 Estimation of the Frequency, Phase, and Amplitude of a Sinusoid

The parameters of interest are the sinusoid frequency, phase, and amplitude. As will be seen, the noise power λ does not need to be estimated in order to estimate the other parameters. Using the complex multivariate Gaussian model in (9.333), the log-likelihood function for the signal parameters can be written as a function of the complex signal amplitude $\tilde{A} = Ae^{j\psi}$ as follows,

$$\begin{aligned} l(A, \psi, \tilde{f}; \mathbf{x}) &= \frac{-1}{\lambda}(\mathbf{x} - Ae^{j\psi}\mathbf{s}_{\tilde{f}})^H(\mathbf{x} - Ae^{j\psi}\mathbf{s}_{\tilde{f}}) + \text{O.T.} \\ &= \frac{1}{N\lambda}|\mathbf{s}_{\tilde{f}}^H\mathbf{x}|^2 - \frac{N}{\lambda}|\tilde{A} - \frac{1}{N}\mathbf{s}_{\tilde{f}}^H\mathbf{x}|^2 + \text{O.T.} \end{aligned} \quad (9.335)$$

where “O.T.” represents other terms that do not depend on the signal parameters and it is noted that $\mathbf{s}_{\tilde{f}}^H\mathbf{s}_{\tilde{f}} = N$. From the form shown in (9.335), it can be seen that choosing

$$\hat{A} = \frac{1}{N} |\mathbf{s}_{\tilde{f}}^H \mathbf{x}| \quad (9.336)$$

and

$$\hat{\psi} = \angle \mathbf{s}_{\tilde{f}}^H \mathbf{x} \quad (9.337)$$

will maximize the second term to a value of zero irrespective of \tilde{f} or λ . Thus, the MLEs for the amplitude and phase are (9.336) and (9.337) evaluated at the MLE of \tilde{f} , which is obtained by maximizing

$$l(\hat{A}, \hat{\psi}, \tilde{f}; \mathbf{x}) = \frac{1}{N\lambda} |\mathbf{s}_{\tilde{f}}^H \mathbf{x}|^2 + \text{O.T..} \quad (9.338)$$

The inner product between the data \mathbf{x} and the sinusoidal signal model $\mathbf{s}_{\tilde{f}}$ is seen to be the discrete Fourier transform (DFT) of the data

$$\mathbf{s}_{\tilde{f}}^H \mathbf{x} = \sum_{n=0}^{N-1} \tilde{X}[n] e^{-j2\pi n \tilde{f}/f_s} \quad (9.339)$$

where $\tilde{X}[n] = \tilde{x}(\tau_p + nT_s)$. Thus, the maximum-likelihood frequency estimate is the frequency maximizing the squared modulus of the DFT,

$$\hat{\tilde{f}} = \arg \max_{\tilde{f}} \left| \sum_{n=0}^{N-1} \tilde{X}[n] e^{-j2\pi n \tilde{f}/f_s} \right|^2. \quad (9.340)$$

This is generally implemented using a fast Fourier transform (FFT), which only provides samples at frequency intervals of $1/T_p$. Finer spacing can be achieved by zero-padding the FFT or through a numerical search to refine the estimate of \tilde{f} about the frequency obtained using the FFT.

Exercise 9.3 (Random Amplitude Sinusoid) If the complex amplitude ($\tilde{A} = Ae^{j\psi}$) of the sinusoid is complex Gaussian distributed with zero mean and variance λ_s , the signal enters the covariance matrix rather than the mean of the sampled complex envelope data distribution,

$$\mathbf{x} \sim \mathcal{CN}\left(\mathbf{0}, \lambda_s \mathbf{s}_{\tilde{f}} \mathbf{s}_{\tilde{f}}^H + \lambda \mathbf{I}\right). \quad (9.341)$$

Show that the maximum-likelihood estimate of \tilde{f} has the same form as when A and ψ are assumed to be deterministic. Hint: use the matrix inversion lemma from (8.54) to obtain $(\lambda_s \mathbf{s}_{\tilde{f}} \mathbf{s}_{\tilde{f}}^H + \lambda \mathbf{I})^{-1}$.

9.5.1.2 Phase Estimator Distribution

If the frequency of the sinusoid is known, the phase estimator from (9.337) is the angle of $\mathbf{s}_{\tilde{f}}^H \mathbf{x}$ where the signal-model vector $\mathbf{s}_{\tilde{f}}$ is formed using the known frequency \tilde{f} . This vector inner product is a complex-Gaussian distributed random variable with mean $NAe^{j\psi}$ and variance $N\lambda$,

$$\mathbf{s}_{\tilde{f}}^H \mathbf{x} \sim \mathcal{CN}\left(NAe^{j\psi}, N\lambda\right). \quad (9.342)$$

Because the real and imaginary parts of a complex Gaussian random variable are independent, the PDF of the phase estimate can be shown to be (e.g., see [61, Sect. 9.2–2])

$$f_{\hat{\psi}}(\hat{\psi}) = \frac{e^{-S^d}}{2\pi} + \frac{\sqrt{S^d}}{\sqrt{\pi}} \cos(\hat{\psi} - \psi) e^{-S^d \sin^2(\hat{\psi} - \psi)} \left[1 - \Phi\left(-\sqrt{2S^d} \cos(\hat{\psi} - \psi)\right) \right] \quad (9.343)$$

for $\hat{\psi} \in (-\pi, \pi]$ where, as before, the SNR after coherent processing is $S^d = NA^2/\lambda$. The importance of SNR is clearly seen in Fig. 9.22 where the PDF is shown as a function of the error for various levels of SNR. As expected, a higher SNR tightens the PDF around the true value. Alternatively, in the limit of $S^d \rightarrow 0$ as the signal vanishes, the estimator is non-informative with a uniform PDF on $(-\pi, \pi)$, which arises from the first term in (9.343).

One of the complications in working with and estimating phase is that it uses an interval on the real line $(-\pi, \pi]$ to represent a position on a circle. For example, $\psi = \pi$ and $\psi = -\pi$ represent the same point on the circle but are on opposite ends of the phase interval. One of the issues that arises is that the traditional performance metrics may not be sufficient to characterize an estimator. For example, the MLE of the phase from (9.337) with a PDF in (9.343) for a known frequency has been shown to be a biased estimator [62] when using the traditional definition of bias (i.e., $E[\hat{\psi}] \neq \psi$). This is not surprising, noting that averaging $\pi - \varepsilon$ and $-\pi + \varepsilon$ yields zero instead of π or $-\pi$ as it would on a circle. This points to using an expectation on the unit-circle [63, Ch. 3], for which the MLE of the phase is in fact unbiased,

$$\angle E[e^{j\hat{\psi}}] = \psi. \quad (9.344)$$

This also provides an appropriate means for combining phase estimates. Given multiple estimates $\hat{\psi}_1, \dots, \hat{\psi}_N$ of the phase of a signal, it is better to combine them with a unit-circle average,

$$\hat{\psi} = \angle \frac{1}{N} \sum_{n=1}^N e^{j\hat{\psi}_n}, \quad (9.345)$$

than an arithmetic one, $\hat{\psi} = \sum_{n=1}^N \hat{\psi}_n / N$.

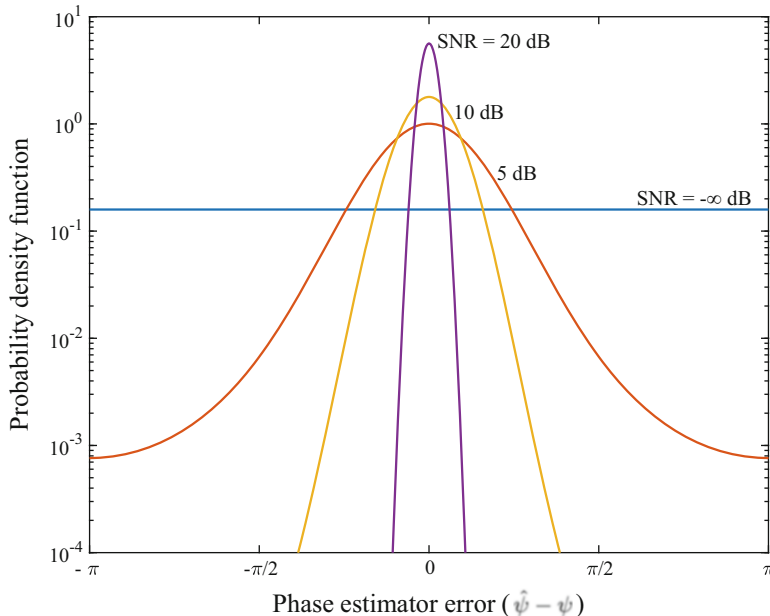


Fig. 9.22 Probability density function of the phase estimator error when a sinusoid's frequency is known perfectly

Exercise 9.4 (Variance of the Phase Estimator) Numerically evaluate the variance of the phase estimator in (9.337) for a known frequency from the PDF in (9.343) with $\psi = 0$, SNR ranging from -15 dB to 15 dB, and integrating from $-\pi$ to π . Note that when $\psi = 0$ the error has zero mean (this is the only phase value for which the MLE is unbiased in the traditional sense), so only one integral is required. Compare this with the CRLB from Sect. 8.5.2 when the sinusoid's frequency is known, which is $1/(2S^d)$ from (8.246). Also compare it with CRLB from Sect. 9.5.1.3 when the frequency is not known, which is $2/S^d$ from (9.358). At what SNR does the estimator achieve the CRLB? Compare the variance of $\hat{\psi}$ at low SNR to the variance of a uniform distribution on $(-\pi, \pi)$ (e.g., see Sect. 5.6.4).

Approximate the variance of the phase estimate when the frequency is also estimated through a simulation. At high SNR this can be quickly accomplished in MATLAB® using the function `fminbnd` by restricting the search to be within $1/(2T_p)$ of the true value (or using `fminsearch` and starting at the true value). This means there will be no “large errors” (i.e., errors away from the correct lobe of the DFT), but they are very rare at high SNR. Does the combined frequency/phase estimator achieve the CRLB at high SNR?

9.5.1.3 Cramér-Rao Lower Bounds

The (i, j) element of the Fisher information matrix (FIM) for the general complex Gaussian model from [58, App. 15C] or (6.75) in Sect. 6.3.3.4 has the form

$$\{\mathbf{I}(\boldsymbol{\theta})\}_{i,j} = 2\operatorname{Re}\left\{\frac{\partial \boldsymbol{\mu}^H(\boldsymbol{\theta})}{\partial \theta_i} \boldsymbol{\Sigma}^{-1}(\boldsymbol{\theta}) \frac{\partial \boldsymbol{\mu}(\boldsymbol{\theta})}{\partial \theta_j}\right\} + \operatorname{tr}\left\{\boldsymbol{\Sigma}^{-1}(\boldsymbol{\theta}) \frac{\partial \boldsymbol{\Sigma}(\boldsymbol{\theta})}{\partial \theta_i} \boldsymbol{\Sigma}^{-1}(\boldsymbol{\theta}) \frac{\partial \boldsymbol{\Sigma}(\boldsymbol{\theta})}{\partial \theta_j}\right\}. \quad (9.346)$$

This illustrates that two parameters are uncoupled if one appears only in the mean and the other appears only in the covariance matrix. This implies that λ is uncoupled from A , ψ , and \tilde{f} and so λ can be ignored in this analysis. For parameters only entering the mean, it can be seen that the elements of the FIM require the partial derivatives of the mean with respect to the parameters. For the sampled sinusoid, these result in

$$\frac{\partial \mathbf{u}}{\partial A} = e^{j\psi} \mathbf{s}_{\tilde{f}}, \quad (9.347)$$

$$\frac{\partial \mathbf{u}}{\partial \psi} = jAe^{j\psi} \mathbf{s}_{\tilde{f}}, \quad \text{and} \quad (9.348)$$

$$\frac{\partial \mathbf{u}}{\partial \tilde{f}} = j2\pi T_s A e^{j\psi} \mathbf{N} \mathbf{s}_{\tilde{f}}, \quad (9.349)$$

where \mathbf{N} is a diagonal matrix with the (n, n) element equal to n for $n = 0, \dots, N-1$. These are used in only the first term in (9.346) because the second term is zero for the parameters of interest. The matrix–vector bilinear form in the first term in (9.346) is simply $1/\lambda$ times the inner product between the various pairs of vectors in (9.347)–(9.349) because $\boldsymbol{\Sigma}^{-1}(\boldsymbol{\theta}) = \lambda^{-1} \mathbf{I}$. Noting that the inner product between $\partial \mathbf{u} / \partial A$ and either of the others is purely imaginary, it can be seen that A is uncoupled from \tilde{f} and ψ . Thus the FIM entry for A is

$$\operatorname{FIM}_{A,A} = \frac{\mathbf{s}_{\tilde{f}}^H \mathbf{s}_{\tilde{f}}^H}{\lambda} = \frac{N}{\lambda} \quad (9.350)$$

and the Cramér-Rao lower bound formed by its inverse. The FIM for (\tilde{f}, ψ) is formed from the inner products of (9.348) and (9.349) to result in

$$\operatorname{FIM}_{\tilde{f},\psi} = \frac{2A^2}{\lambda} \begin{bmatrix} 4\pi^2 T_s^2 (\mathbf{s}_{\tilde{f}}^H \mathbf{N}^2 \mathbf{s}_{\tilde{f}}) & 2\pi T_s (\mathbf{s}_{\tilde{f}}^H \mathbf{N} \mathbf{s}_{\tilde{f}}) \\ 2\pi T_s (\mathbf{s}_{\tilde{f}}^H \mathbf{N} \mathbf{s}_{\tilde{f}}) & \mathbf{s}_{\tilde{f}}^H \mathbf{s}_{\tilde{f}} \end{bmatrix} \quad (9.351)$$

$$= \frac{2A^2}{\lambda} \begin{bmatrix} \frac{2}{3}\pi^2 T_s^2 N(N-1)(2N-1) & \pi T_s N(N-1) \\ \pi T_s N(N-1) & N \end{bmatrix}. \quad (9.352)$$

The simplification from (9.351) to (9.352) requires solution of the following quadratic forms,

$$\mathbf{s}_{\tilde{f}}^H \mathbf{N} \mathbf{s}_{\tilde{f}} = \sum_{n=0}^{N-1} n = \frac{N(N-1)}{2} \quad \text{and} \quad (9.353)$$

$$\mathbf{s}_{\tilde{f}}^H \mathbf{N}^2 \mathbf{s}_{\tilde{f}} = \sum_{n=0}^{N-1} n^2 = \frac{N(N-1)(2N-1)}{6}. \quad (9.354)$$

Noting that the SNR after coherent processing (i.e., forming $\mathbf{s}_{\tilde{f}}^H \mathbf{x}$) is

$$S^d = \frac{|\mathbf{u}^H \mathbf{s}_{\tilde{f}}|^2}{\lambda \mathbf{s}_{\tilde{f}}^H \mathbf{s}_{\tilde{f}}} = \frac{NA^2}{\lambda} \quad (9.355)$$

the CRLBs for the amplitude, frequency, and phase of the sinusoid can be described as

$$\frac{\text{CLRB}(A)}{A^2} = \frac{\lambda}{2NA^2} = \frac{1}{2S^d}, \quad (9.356)$$

$$\text{CLRB}(\tilde{f}) = \frac{3\lambda}{2\pi^2 A^2 T_s^2 N(N^2 - 1)} \approx \frac{3}{2\pi^2 S^d T_p^2}, \quad \text{and} \quad (9.357)$$

$$\text{CLRB}(\psi) = \frac{\lambda(2N-1)}{A^2 N(N+1)} \approx \frac{2}{S^d}. \quad (9.358)$$

Note that the results found in [60] differ only in that the variance of the in-phase and quadrature components of the noise was taken as $\sigma^2 = \lambda/2$. These results can be related to those described in Sect. 8.5.2 for estimation of the amplitude and phase of a deterministic signal, which is what was assumed here with the difference of an unknown frequency. Although the amplitude bound is identical, the bound for the phase in (8.246) is the inverse of the (2, 2) element in (9.352), which would represent the case when the frequency is known. The bound for the frequency estimate in (9.357) is identical to that shown in (8.302) for estimating the Doppler scale η when it is multiplied by f_c^2 to convert a frequency scale to a frequency and σ_t^2 set to $T_p^2/12$ as in (8.303).

9.5.2 Narrowband Gaussian Random Signals

The information content carried by narrowband random signals can be encoded in both the center frequency and bandwidth of the signal. In order to develop estimation algorithms for these parameters a model is required to describe how the

parameters impact the data. The sinusoidal model of Sect. 9.5.1 is one such model that is useful when the complex signal amplitude is very consistent throughout the analysis window. However, when the source signal is subject to significant boundary interaction, the complex amplitude can be assumed to be a zero-mean Gaussian random process (e.g., see the saturated-phase condition of [64] as described in Sect. 7.2.3). Assuming the signal measurement is wide-sense stationary over at least the analysis time allows modeling the power spectral density (PSD) of the random process as a function of the bandwidth and center frequency through a PSD model. The advantage of this approach is that it allows using the techniques of [2] (described in Sect. 9.4.2.1) for evaluation of the Cramér-Rao lower bound and potentially for estimating the model parameters.

Assuming the narrowband signal has already been detected, the PSD model only needs to describe the signal and a small band in frequency around it. There is a balance in choosing a model that can be both representative of the signals observed in practice and yet tractable enough to yield parameter estimators. One such model is to assume the signal PSD has a Gaussian shape and that the PSD of the noise in the processing band is constant,

$$P(f; \boldsymbol{\theta}) = \lambda + \lambda_s e^{-c(f-f_c)^2/W^2} \quad (9.359)$$

where λ is the noise PSD and λ_s is the peak signal PSD. Choosing $c = 4 \log(2)$ implies that the signal PSD is at half its peak power ($\lambda_s/2$) a distance $W/2$ from the center frequency f_c so W is the half-power bandwidth of the PSD's signal component.

9.5.2.1 Cramér-Rao Lower Bounds

From (9.290) in Sect. 9.4.2.1, the Fisher information matrix (FIM) entry for PSD parameters θ_i and θ_j is

$$\{\mathbf{I}(\boldsymbol{\theta})\}_{i,j} = T_p \int_{f_0}^{f_1} \left[\frac{\partial P(f; \boldsymbol{\theta})/\partial \theta_i}{P(f; \boldsymbol{\theta})} \right] \left[\frac{\partial P(f; \boldsymbol{\theta})/\partial \theta_j}{P(f; \boldsymbol{\theta})} \right] df. \quad (9.360)$$

For the purposes of estimating center frequency and bandwidth, the signal would already have been detected and so the frequency band (f_0, f_1) can be chosen with the signal coarsely in its center. The processing band should be large enough to contain a large majority of the signal PSD (i.e., $W_p = f_1 - f_0 > W$ where W_p is the bandwidth of the processing band).

The partial derivatives of the PSD for the parameters in (9.359) are

$$\frac{\partial P(f; \boldsymbol{\theta})}{\partial \lambda} = 1, \quad (9.361)$$

$$\frac{\partial P(f; \boldsymbol{\theta})}{\partial \lambda_s} = e^{-c(f-f_c)^2/W^2}, \quad (9.362)$$

$$\frac{\partial P(f; \boldsymbol{\theta})}{\partial f_c} = \frac{2c(f-f_c)\lambda_s}{W^2} e^{-c(f-f_c)^2/W^2}, \text{ and} \quad (9.363)$$

$$\frac{\partial P(f; \boldsymbol{\theta})}{\partial W} = \frac{2c(f-f_c)^2\lambda_s}{W^3} e^{-c(f-f_c)^2/W^2}. \quad (9.364)$$

Under the previous assumptions, the derivatives with respect to λ , λ_s , and W are approximately symmetric functions of f about f_c whereas the derivative with respect to f_c is an odd function. This implies that the Fisher information matrix cross terms between f_c and the other parameters will be approximately zero, implying f_c is decoupled from the other parameters. The Fisher information matrix diagonal entry for f_c is

$$\text{FIM}_{f_c, f_c} = \frac{4T_p c^2 \lambda_s^2}{W^4} \int_{f_0}^{f_1} \frac{(f-f_c)^2 e^{-2c(f-f_c)^2/W^2}}{\left[\lambda + \lambda_s e^{-c(f-f_c)^2/W^2}\right]^2} df \quad (9.365)$$

$$\approx \frac{16\sqrt{\log 2} T_p}{3W} \left[\log\left(\frac{\lambda_s}{2\lambda}\right) \right]^{3/2} \quad (9.366)$$

where the approximation producing (9.366) assumes high SNR ($\lambda_s \gg \lambda$) and essentially approximates the denominator in the integrand while truncating the limits to $f_c \pm W/2$. This results in the approximate Cramér-Rao lower bound for the center frequency of

$$\text{CRLB}\{f_c\} \approx \frac{3W}{16\sqrt{\log 2} T_p \left[\log\left(\frac{\lambda_s}{2\lambda}\right) \right]^{3/2}}, \quad (9.367)$$

which increases with bandwidth and decreases with T_p and peak SNR, although in a non-linear manner with respect to the peak SNR. Truncating the integrand in approximating (9.365) required assuming

$$W_p > \frac{W}{2\log 2} \sqrt{\left(\frac{\lambda_s}{2\lambda}\right)}, \quad (9.368)$$

which provides an indication of the minimum size of the processing band. Noting that W_p does not enter into (9.367), it appears that the precise value of W_p is less important than the requirement that it satisfy (9.368).

Evaluation of the Cramér-Rao lower bound for the bandwidth requires inversion of the three-by-three Fisher information matrix for W , λ , and λ_s . Although it may be feasible to derive an approximation similar to (9.367), the elements of the matrix and the matrix inverse are straightforward to obtain numerically. Consider as a nominal

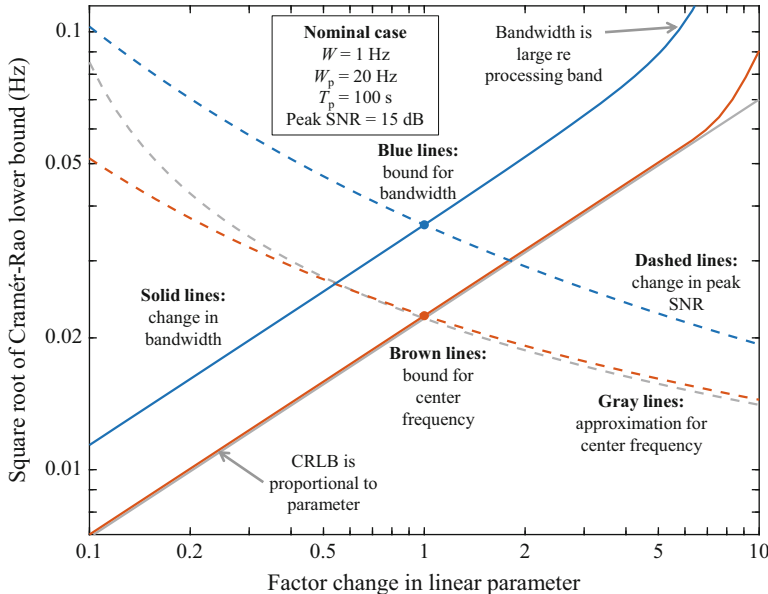


Fig. 9.23 Square root of the Cramér-Rao lower bounds for estimation of bandwidth and center frequency as a function of changes in bandwidth and peak SNR (i.e., λ_s/λ) from the nominal case

case $W = 1 \text{ Hz}$, $W_p = f_1 - f_0 = 20 \text{ Hz}$, $T_p = 100 \text{ s}$, and a 15-dB peak SNR (i.e., $10 \log_{10}(\lambda_s/\lambda) = 15$). The variations in the CRLB from this nominal case for a multiplicative factor change in either W or λ_s/λ are shown in Fig. 9.23. The numerically evaluated CRLBs are in blue for the bandwidth and in reddish-brown for the center frequency. The approximation in (9.367) for the center frequency is shown in gray. The dashed lines represent changing the peak SNR from the nominal case and illustrate how this reduces the bound as SNR increases. The solid lines represent changes in bandwidth from the nominal case and demonstrate how the bounds are proportional to W when the previously made assumptions are satisfied. As bandwidth increases to the point where W_p is not significantly larger than W , the bounds are seen to rise precipitously. Estimation of the bandwidth is clearly more difficult than estimation of the center frequency. At the nominal point (and for some region around it), the CRLB for the bandwidth is almost 2.6 times higher than that for the center frequency. Loosely this may be explained by noting that estimating the bandwidth requires estimating the two frequencies at which the power is at half of the maximum. In terms of absolute performance, (9.367) can be used as a guide for what is feasible or, for example, how large an analysis window (T_p) is required to achieve a desired performance.

9.5.2.2 Estimation of the Center Frequency and Bandwidth

There are four unknown parameters in the PSD model (f_c , W , λ_s , λ). The maximum-likelihood estimator described in Sect. 9.4.2.1 requires a four-dimensional optimization of the log-likelihood function in (9.285). The derivatives in (9.361)–(9.364) can be used to implement a constrained gradient ascent algorithm, ensuring the bandwidth and power parameters are non-negative, but still requires optimization over a four-dimensional function. An alternative approach can be found in the *histogram* expectation-maximization estimator as applied to spectral estimation. This approach, which was derived in [3, Ch. 2] and used in [4], first changes the representation of the PSD to that of a probability density function by scaling the model to integrate to one and then interprets the DFT bin data as if they were obtained through a histogram counting observations within each (DFT) bin. A tutorial on the technique can be found in [65].

When the PSD of a measurement comprises multiple components, the PDF approximation to the PSD is represented by a mixture model (e.g., see Sect. 7.4.3.7) and the expectation-maximization (EM) algorithm (see Sect. 6.3.7) is used to obtain the parameter estimates. This combination provides a very powerful tool where complex PSDs can be represented and their parameters estimated without requiring a high-dimensional optimization routine. Applying the technique to estimation of the bandwidth and center frequency of the narrowband random signal in noise PSD of (9.359) is done by describing the noise PSD with a uniform PDF and noting that the mean of the Gaussian component is $\mu = f_c$ and its variance is related to the bandwidth according to $\sigma^2 = W^2/(2c)$. The PSD is therefore

$$P(f; \theta) = \lambda + \lambda_s e^{-c(f-f_c)^2/W^2} \quad (9.369)$$

$$= \gamma \left[\frac{\pi_0}{f_1 - f_0} + (1 - \pi_0) f_z(f; \mu, \sigma) \right] \quad (9.370)$$

where π_0 is the mixture proportion for the noise component, $f_z(f; \mu, \sigma)$ is the Gaussian PDF, and the processing band is assumed to be (f_0, f_1) . The scale γ is such that the term within the brackets in (9.384) integrates to one (i.e., it is a proper PDF).

Derivation of the estimation algorithm is beyond the scope of this text. However, the distilled algorithm for the case at hand (a single Gaussian component mixed with a uniform component) is presented in pseudocode in Appendix 9.C. The algorithm was implemented for the nominal case described in Sect. 9.5.2.1 as a function of SNR. The standard deviation of the bandwidth and center-frequency estimates over 1000 trials is shown in Fig. 9.24 along with the Cramér-Rao lower bounds. Each trial was initialized in the neighborhood of the true values (i.e., each parameter was displaced randomly with variance from the bound). As such, the low-SNR performance unrealistically does not have any “large” errors. As SNR increases, where large errors are not an issue, the algorithm does not achieve the CRLBs. This effect was also noted in [3, Sect. 2.2.3] where the time-domain bounds (effectively

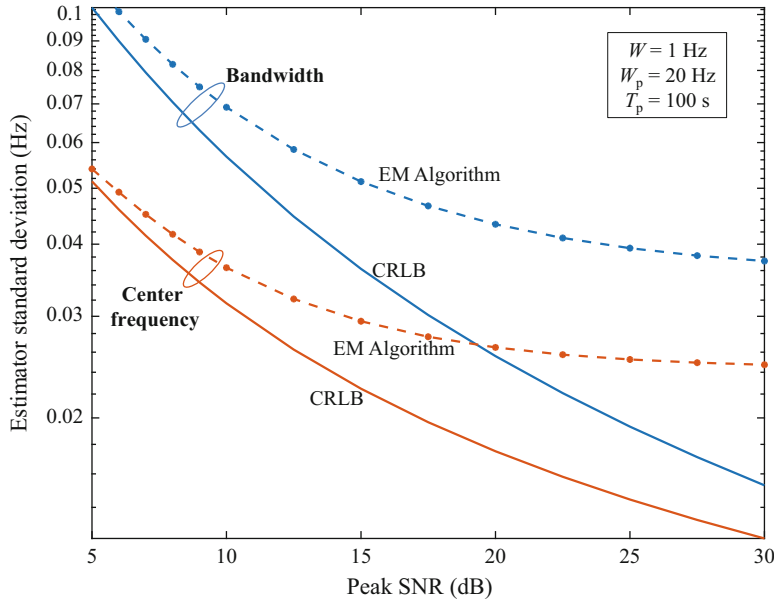


Fig. 9.24 Standard deviation of the EM-algorithm estimates of bandwidth and center frequency compared to the square root of the Cramér-Rao lower bound (CRLB) as a function of the peak SNR (λ_s/λ)

what is obtained in Sect. 9.5.2.1) are lower than those obtained when starting with the frequency-domain data. It is also not unexpected in that the estimation algorithm does not fully or directly exploit the statistical characterization of the DFT bin data.

Appendix 9.A: Numerical Evaluation of the CDF of a Sum of Exponential Random Variables

The following MATLAB[®] code evaluates the cumulative distribution function (CDF) of the sum of a number of independent exponentially distributed random variables with arbitrary mean values. That is, the CDF of

$$T = \sum_{m=0}^{M-1} U_m \quad (9.371)$$

where U_m is exponentially distributed with mean λ_m and independent of U_n for $m \neq n$. The technique used to obtain the CDF is from [1] and is described in detail in Sect. 9.2.7.2. Because the technique may be more generally applied to obtain the CDF of any random variable for which the characteristic function can be obtained,

the lines specific to this example are noted by [EXSPEC] and set in blue type. These lines provide the

- mean and standard deviation of T ,
- the characteristic function of T , and
- the simulation to assess the result.

Noting that the mean and standard deviation can be obtained from the characteristic function itself through numerical differentiation, it is possible to generalize the code to only require the characteristic function. The standard deviation is only used to define the interval over which the CDF is evaluated and so is not a strict requirement.

```
% % % % % % % % % % % % % % % % % % % % % % % % % % % % % %
% EXAMPLE PARAMETERS
prmM=20; % [EXSPEC] Number of terms in sum
prm=linspace(1,10,prmM)'; % [EXSPEC] Mean of each term
u=sum(prm); % Mean of random variable [EXSPEC]
sig=sqrt(sum(prm.^2)); % Standard deviation [EXSPEC]
% Characteristic function (CF) as a function Phi=cfun(w,prm)
% [EXSPEC]
cfun=@(w,prm) reshape(1./prod(1-1j*prm*w(:)'),size(w));
%%%%%%%%%%%%%%%
% PROGRAM TO OBTAIN CDF VIA CHARACTERISTIC FUNCTION
%---Setup in RV domain---
% Minimum CDF argument [EXSPEC: no lower than zero]
x0=max(0,u-5*sig);
x1=u+5*sig; % Maximum CDF argument [increase 5 if necessary]
Mfft=512; % FFT size
k=0:(Mfft-1); % CDF argument index
x=x0+k*(x1-x0)/Mfft; % CDF argument
%---Setup in CF domain---
dw=2*pi/(x1-x0); % Spacing in CF domain
TOL=1e-10; % Relative modulus of CF term at maximum frequency
L=1; % Get maximum CF argument
while (abs(cfun(Mfft*L*dw,prm)/(Mfft*L*dw*(u-x0)))>TOL),
    L=ceil(L*1.2); % Increase until meet criteria
end;
%---Evaluate CF & form input to FFT in matrix Z---
indw=reshape(0:Mfft*L-1,Mfft,L)'; % index=m+1*M
% Input to FFT
Z=(cfun(dw*indw,prm)./indw).*exp(-1j*indw*dw*x0);
% Replace zero-frequency entry with correct value
Z(1,1)=1j*(u-x0)*dw/2;
%---Form CDF---
F=0.5+k/Mfft-imag(fft(sum(Z,1)))/pi; % CDF
%---Remove regions outside of [0,1] from round-off errors---
ikp=find(F>=0,1,'first'):find(F<=1,1,'last');
F=F(ikp); x=x(ikp); % Keep valid values
%%%%%%%%%%%%%%%
% SIMULATION TO ASSESS RESULT
% [plots exceedance distribution function]
ni=10^4; % Number of trials in simulation
```

```
% [EXSPEC] Simulate sum
T=sum(exprnd(1,prmM,ni).*repmat(prm,1,ni));
% Estimate CDF via histogram
Ft=cumsum(hist(T,x))/ni;
% Plot exceedance distribution function
figure(1); semilogy(x,1-F,x,1-Ft);
```

Appendix 9.B: Moments of the Modified GLR Energy Detector Decision Statistic

The distribution of the modified GLR energy detector decision statistic described in Sect. 9.2.8.1 can be approximated by that of a shifted gamma random variable. The parameters are obtained by matching the moments of the shifted gamma distribution with that of $T(\mathbf{z})$ in (9.124), which depend on the moments of $G = g(Z)$ where

$$g(z) = \begin{cases} z - z_0 - \log(z/z_0) & \text{for } z > z_0 \\ 0 & \text{otherwise} \end{cases} \quad (9.372)$$

is the modified GLR energy detector function and

$$Z \sim \text{Expon}(\lambda) \quad (9.373)$$

with $\lambda = 1$ under H_0 and $\lambda = 1 + S^d$ under H_1 . The moments of G can be obtained from its moment generating function (MGF),

$$\begin{aligned} M_G(t) &= E[e^{tg(Z)}] \\ &= 1 - e^{-z_0/\lambda} + \lambda^{-1} z_0^t \left(\lambda^{-1} - t \right)^{t-1} e^{-z_0 t} \Gamma(1-t, [\lambda^{-1} - t] z_0) \end{aligned} \quad (9.374)$$

for $t < 1/\lambda$. This requires evaluation of the upper incomplete gamma function $\Gamma(\alpha, x) = \Gamma(\alpha) - \gamma(\alpha, x)$ (see [43, Sect. 8.2]). The k th moment of G is simply the k th derivative of $M_G(t)$ evaluated at zero,

$$\mu_{G,k} = E[G^k] = \left[\frac{d^k M_G(t)}{dt^k} \right]_{t=0}. \quad (9.375)$$

As described in [18, Sect. 6.2], these can be obtained by numerical differentiation; for example,

$$\mu_{G,1} = \frac{M_G(\delta/2) - M_G(-\delta/2)}{\delta} \quad (9.376)$$

where δ is small. This must be done using $\lambda = 1$ for the DFT bins containing noise and using $\lambda = 1 + S^d$ for the DFT bins containing both signal and noise.

When $T(\mathbf{z})$ is formed by summing over n identically distributed samples $g(Z_m)$ for $m = 1, \dots, n$, with each having k th moment $\mu_{G,k}$, the moments of the sum are

$$\mu_{T,1} = E[T(\mathbf{z})] = n\mu_{G,1} \quad (9.377)$$

$$\mu_{T,2} = E[T^2(\mathbf{z})] = n\mu_{G,2} + n(n-1)\mu_{G,1}^2 \quad (9.378)$$

$$\begin{aligned} \mu_{T,3} &= E[T^3(\mathbf{z})] \\ &= n\mu_{G,3} + 3n(n-1)\mu_{G,1}\mu_{G,2} + n(n-1)(n-2)\mu_{G,1}^3. \end{aligned} \quad (9.379)$$

Under the noise-only hypothesis, (9.377)–(9.379) can be used with $n = M$ and $\lambda = 1$ to form the decision-statistic moments required to approximate P_f . For the signal structure used in the analysis, comprising M_s bins with signal and noise and $M - M_s$ bins with only noise, the moments $\mu_{N,k}$ and $\mu_{S,k}$ need to be formed using (9.377)–(9.379) with $n = M - M_s$ and $\lambda = 1$ for the noise bins and $n = M_s$ and $\lambda = 1 + S^d$ for the signal-occupied bins. These are then combined to form the decision statistic moments under H_1 ,

$$\mu_{T,1} = \mu_{S,1} + \mu_{N,1} \quad (9.380)$$

$$\mu_{T,2} = \mu_{S,2} + 2\mu_{S,1}\mu_{N,1} + \mu_{N,2} \quad (9.381)$$

$$\mu_{T,3} = \mu_{S,3} + 3\mu_{S,2}\mu_{N,1} + 3\mu_{S,1}\mu_{N,2} + \mu_{N,3}. \quad (9.382)$$

The gamma approximation to the decision-statistic distribution is then obtained by using the moments in (9.112) and (9.113) (with $\sigma_T^2 = \mu_{T,2} - \mu_{T,1}^2$) while the shifted-gamma approximation can be obtained by using (9.118)–(9.120).

Appendix 9.C: Algorithm for Estimating the Bandwidth and Center-Frequency of a Narrowband Random Signal in Noise

The algorithm described in this appendix obtains estimates of the parameters of a power spectral density (PSD) with the form

$$P(f; \boldsymbol{\theta}) = \lambda + \lambda_s e^{-c(f-f_c)^2/W^2} \quad (9.383)$$

$$= \gamma \left[\frac{\pi_0}{f_1 - f_0} + (1 - \pi_0) f_z(f; \mu, \sigma) \right] \quad (9.384)$$

as was described in Sect. 9.5.2.2. The algorithm is an expectation-maximization (EM) algorithm applied to DFT bin data that are interpreted as if they were obtained

from a histogram. More detailed descriptions of the algorithm can be found in [3, Ch. 2] and [4, 65]. A limitation of the algorithm that is presented here is that it assumes the Gaussian component lies entirely within the processing band. When this is not the case, the algorithm can be modified as described in [65] to account for truncated components.

The input to the algorithm are the (squared moduli) DFT bin data $Y[k]$ for $k = 0, \dots, N - 1$ from the frequency band of interest. If the bandwidth of the processing band is W_p and the analysis window extent T_p , then $N = T_p W_p$. The algorithm requires definition of the edges of the frequency bins. By defining the $N + 1$ DFT bin edges as

$$l_k = W_p \left(-\frac{1}{2} + \frac{k}{N} \right) - \frac{0.5}{T_p}, \quad (9.385)$$

for $k = 0, \dots, N$, the k th DFT bin is then assumed to span $f \in (l_k, l_{k+1})$ for $k = 0, \dots, N - 1$. This describes the case when the data have been basebanded by the center frequency of the processing band (i.e., $f_b = (f_0 + f_1)/2$). The bandpass center frequency of the narrowband signal can then be obtained by adding f_b to the final estimate or it can be added to (9.385).

The following describes one iteration of the expectation-maximization algorithm for estimating the parameters (π_0, μ, σ) of the PDF model within (9.384) (i.e., the term in brackets). As described in Sect. 9.5.2.2, the center frequency is the mean ($f_c = \mu$) of the Gaussian component and the bandwidth is proportional to the standard deviation, $W = \sqrt{2c}\sigma = 2\sqrt{2\log 2}\sigma$ where $c = 4\log 2$.

The algorithm must be initialized with sensible parameter estimates (e.g., the location of the peak for μ , an estimate of the spread about it for σ , and an average of the samples deemed dominated by noise using μ and σ). The iteration can be halted when the difference in consecutive parameter estimates or the value of the likelihood function they achieve is less than a given tolerance.

Define the current parameter estimates as $\hat{\pi}_0$, $\hat{\mu}$, and $\hat{\sigma}$ and let

$$\hat{P} = \sum_{k=0}^{N-1} Y[k], \quad (9.386)$$

which represents the total number of points in the histogram interpretation of the DFT bin data. The iteration updating the parameters then requires the following steps.

- Evaluate the PDF and CDF at the DFT bin edges

$$\phi_k = \phi\left(\frac{l_k - \hat{\mu}}{\hat{\sigma}}\right) \quad \text{and} \quad \Phi_k = \Phi\left(\frac{l_k - \hat{\mu}}{\hat{\sigma}}\right)$$

for $k = 0, \dots, N$, where $\phi(x) = f_Z(x; 0, 1)$ and $\Phi(x) = F_Z(x; 0, 1)$ are the PDF and CDF of a standard Gaussian random variable.

2. Evaluate the total probability for each DFT bin

$$P_b[k] = \frac{\hat{\pi}_0}{N} + (1 - \hat{\pi}_0)[\Phi_{k+1} - \Phi_k] \quad \text{for } k = 0, \dots, N - 1$$

3. Obtain the data weighting under the noise model

$$w_0[k] = \frac{\hat{\pi}_0/N}{P_b[k]} \quad \text{for } k = 0, \dots, N - 1$$

4. Update the proportion for the noise model

$$\hat{\pi}_0 = \frac{1}{\hat{P}} \sum_{k=0}^{N-1} Y[k] w_0[k]$$

5. Obtain estimates of the signal model parameters (Gaussian distribution)

a. Evaluate the mean and variance contributions for each DFT bin

$$\begin{aligned} \mu_1[k] &= \hat{\mu} [\Phi_{k+1} - \Phi_k] - \hat{\sigma}^2 [\phi_{k+1} - \phi_k] \\ \sigma_1^2[k] &= \hat{\sigma}^2 [\Phi_{k+1} - \Phi_k - (l_{k+1} - \hat{\mu})\phi_{k+1} + (l_k - \hat{\mu})\phi_k] \end{aligned}$$

for $k = 0, \dots, N - 1$

b. Obtain the proportion of the total histogram observations attributed to the signal model

$$N_1 = \sum_{k=0}^{N-1} (1 - w_0[k]) Y[k]$$

c. Update the signal-model parameters

$$\begin{aligned} \hat{\mu} &= \frac{(1 - \hat{\pi}_0)}{N_1} \sum_{k=0}^{N-1} \frac{Y[k]\mu_1[k]}{\Phi_{k+1} - \Phi_k} \\ \hat{\sigma} &= \sqrt{\frac{(1 - \hat{\pi}_0)}{N_1} \sum_{k=0}^{N-1} \frac{Y[k]\sigma_1^2[k]}{\Phi_{k+1} - \Phi_k}} \end{aligned}$$

References

1. A.H. Nuttall, Accurate efficient evaluation of cumulative or exceedance probability distributions directly from characteristic functions. Tech. Rpt. 7023, Naval Underwater Systems Center, New London, CT, October 1983
2. M. Levin. Power spectrum parameter estimation. *IEEE Trans. Inf. Theory* **11**(1), 100–107 (1965)
3. T.E. Luginbuhl, *Estimation of General, Discrete-Time FM Processes*. PhD thesis, University of Connecticut, 1999
4. T.E. Luginbuhl, P.K. Willett, Estimating the parameters of general frequency modulated signals. *IEEE Trans. Signal Process.* **52**(1), 117–131 (2004)
5. G. Strang, *Linear Algebra and Its Applications*, 3rd edn. (Harcourt Brace Jovanovich, Publishers, San Diego, 1988)
6. W.H. Press et al., *Numerical Recipes in Fortran 77, The Art of Scientific Computing*, 2nd edn. (Cambridge University Press, Cambridge, 1992)
7. M. Calder, R.A. Davis, Introduction to Whittle (1953) ‘The Analysis of multiple stationary time series’, in *Breakthroughs in Statistics*, vol. III, ed. by S. Kotz, N.L. Johnson (Springer, New York, 1997)
8. P. Whittle, *Hypothesis Testing in Time Series Analysis* (Almqvist & Wiksell boktr., Uppsala, 1951)
9. A. Papoulis, *Probability, Random Variables, and Stochastic Processes*, 3rd edn. (McGraw-Hill, Inc., Boston, 1991)
10. W.S. Hodgkiss, L.W. Nolte, Covariance between Fourier coefficients representing the time waveforms observed from an array of sensors. *J. Acoust. Soc. Am.* **59**(3), 582–590 (1976)
11. N. Mukhopadhyay, *Probability and Statistical Inference* (Marcel Dekker, Inc., New York, 2000)
12. C. Eckart, Optimal rectifier systems for the detection of steady signals. Tech. Rpt. 52–11, University of California, Marine Physical Laboratory of the Scripps Institute of Oceanography, La Jolla, California, March 1952
13. A.H. Nuttall, Probability distribution of spectral estimates obtained via overlapped FFT processing of windowed data. Tech. Rpt. 5529, Naval Underwater Systems Center, New London, CT, December 1976
14. S.V. Amari, R.B. Misra, Closed-form expressions for distribution of sum of exponential random variables. *IEEE Trans. Reliab.* **46**(4), 519–522 (1997)
15. C. Pottle, On the partial fraction expansion of a rational function with multiple poles by digital computer. *IEEE Trans. Circuit Theory* **11**(1), 161–162 (1964)
16. A.H. Nuttall, Numerical evaluation of cumulative probability distribution functions directly from characteristic functions. *Proc. IEEE* **57**(11), 2071–2072 (1969)
17. A. Stuart, J.K. Ord, *Kendall's Advanced Theory of Statistics*, vol. 1, 5th edn. (Oxford University Press, New York, 1987)
18. J.H. Mathews, K.D. Fink, *Numerical Methods Using MATLAB* (Prentice Hall, Upper Saddle River, 1999)
19. A.H. Nuttall, Detection performance of a modified generalized likelihood ratio processor for random signals of unknown location. Tech. Rpt. 10539, Naval Undersea Warfare Center, New London, CT, November 1993
20. A.H. Nuttall, Detection performance of generalized likelihood ratio processors for random signals of unknown location, structure, extent, and strength. Tech. Rpt. 10739, Naval Undersea Warfare Center, Newport, RI, August 1994
21. A.H. Nuttall, Detection performance of power-law processors for random signals of unknown location, structure, extent, and strength. Tech. Rpt. 10751, Naval Undersea Warfare Center, Newport, RI, September 1994
22. A.H. Nuttall, Limiting detection performance for random signals of unknown location, structure, extent, and strength. Tech. Rpt. 10839, Naval Underwater Systems Center, Newport, RI, March 1995

23. A.H. Nuttall, Near-optimum detection performance of power-law processors for random signals of unknown locations, structure, extent, and arbitrary strengths. Tech. Rpt. 11123, Naval Undersea Warfare Center, Newport, RI, April 1996
24. A.H. Nuttall, Performance of power-law processor with normalization for random signals of unknown structure. Tech. Rpt. 10760, Naval Undersea Warfare Center, Newport, RI, May 1997
25. J.A. Fawcett, B.H. Maranda, The optimal power law for the detection of a Gaussian burst in a background of Gaussian noise. *IEEE Trans. Inf. Theory* **IT-37**(1), 209–214 (1991)
26. L.L. Scharf, *Statistical Signal Processing* (Addison-Wesley Pub. Co., Reading, 1991)
27. H. Urkowitz, Energy detection of unknown deterministic signals. *Proc. IEEE* **55**(4), 523–531 (1967)
28. E.L. Lehmann, J.P. Romano, *Testing Statistical Hypotheses*, 3rd edn. (Springer, New York, 2005)
29. J.J. Wolcin, Maximum a posteriori estimation of narrowband signal parameters. *J. Acoust. Soc. Am.* **68**(1), 174–178 (1980)
30. W.W.L. Au, M.C. Hastings, *Principles of Marine Bioacoustics* (Springer, New York, 2008)
31. A.H. Nuttall, Spectral estimation by means of overlapped fast Fourier transform processing of windowed data. Tech. Rpt. 4169, Naval Underwater Systems Center, New London, CT, October 1971
32. P.M. Bagenstoss, On the equivalence of Hanning-weighted and overlapped analysis windows using different window sizes. *IEEE Signal Process. Lett.* **19**(1), 27–30 (2012)
33. S.M. Kay, *Modern Spectral Estimation Theory and Application* (Prentice Hall, Englewood Cliffs, 1988)
34. A.H. Nuttall, An approximate fast Fourier transform technique for vernier spectral analysis. Tech. Rpt. 4767, Naval Underwater Systems Center, New London, CT, August 1974
35. D.R.A McMahon, R.F Barrett, An efficient method for the estimation of the frequency of a single tone in noise from the phases of discrete Fourier transforms. *Signal Process.* **11**(2), 169–177 (1986)
36. D.R.A McMahon, R.F Barrett, Generalisation of the method for the estimation of the frequencies of tones in noise from the phases of discrete Fourier transforms. *Signal Process.* **12**(4), 371–383 (1987)
37. H. Hmam, SNR calculation procedure for target types 0, 1, 2, 3. *IEEE Trans. Aerosp. Electron. Syst.* **41**(3), 1091–1096 (2005)
38. W.J. Albersheim, A closed-form approximation to Robertson's detection characteristics. *Proc. IEEE* **69**(7), 839 (1981)
39. D.A. Abraham, Performance analysis of constant-false-alarm-rate detectors using characteristic functions. *IEEE J. Ocean. Eng.* (2017). <https://doi.org/10.1109/JOE.2017.2771878>
40. L. de Rå, B. Westergren, *Mathematics Handbook*, 5th edn. (Springer, Berlin, 2004)
41. H. Cramér, *Random Variables and Probability Distributions*. Cambridge Tracts in Mathematics and Mathematical Physics, vol. 36 (Cambridge University Press, Cambridge, 1937)
42. M. Abramowitz, I.A. Stegun (eds.), *Handbook of Mathematical Functions* (Dover Publications, New York, 1972)
43. F.W.J. Olver, D.W. Lozier, R.F. Boisvert, C.W. Clark (eds.), *NIST Handbook of Mathematical Functions* (Cambridge University Press, Cambridge, 2010)
44. N. Cressie, A.S. Davis, J.L. Folks, G.E. Policello, The moment-generating function and negative integer moments. *Am. Stat.* **35**(3), 148–150 (1981)
45. G.C. Carter, *Coherence and Time Delay Estimation* (IEEE Press, Piscataway, 1993)
46. B.V. Hamon, E.J. Hannan, Spectral estimation of time delay for dispersive and non-dispersive systems. *J. R. Stat. Soc. Ser. C Appl. Stat.* **23**(2), 134–142 (1974)
47. C.H. Knapp, G.C. Carter, The generalized correlation method for estimation of time delay. *IEEE Trans. Acoust. Speech Signal Process.* **24**(4), 320–327 (1976)
48. C.H. Knapp, G.C. Carter, Estimation of time delay in the presence of source or receiver motion. *J. Acoust. Soc. Am.* **61**(6), 1545–1549 (1977)
49. M. Wax, The estimate of time delay between two signals with random relative phase shift. *IEEE Trans. Acoust. Speech Signal Process.* **29**(3), 497–501 (1981)

50. S.-K. Chow, P.M. Schultheiss, Delay estimation using narrow-band processes. *IEEE Trans. Acoustics Speech Signal Process.* **29**(3), 478–484 (1981)
51. J.P. Ianniello, Time delay estimation via cross-correlation in the presence of large estimation errors. *IEEE Trans. Acoust. Speech Signal Process.* **30**(6), 998–1003 (1982)
52. B. Friedlander, On the Cramer-Rao bound for time delay and Doppler estimation. *IEEE Trans. Inf. Theory* **30**(3), 575–580 (1984)
53. G.C. Carter, Coherence and time delay estimation. *Proc. IEEE* **75**(2), 236–255 (1987)
54. J. Ianniello, Large and small error performance limits for multipath time delay estimation. *IEEE Trans. Acoust. Speech Signal Process.* **34**(2), 245–251 (1986)
55. J.P. Ianniello, High-resolution multipath time delay estimation for broad-band random signals. *IEEE Trans. Acoust. Speech Signal Process.* **36**(3), 320–327 (1988)
56. H.E. Daniels, The theory of position finding. *J. R. Stat. Soc. Ser. B Methodol.* **13**(2), 186–207 (1951)
57. J.C. Hassab, *Underwater Signal and Data Processing* (CRC Press, Boca Raton, 1989)
58. S.M. Kay, *Fundamentals of Statistical Signal Processing: Estimation Theory* (Prentice Hall PTR, Englewood Cliffs, 1993)
59. J.C. Hassab, Contact localization and motion analysis in the ocean environment: a perspective. *IEEE J. Ocean. Eng.* **8**(3), 136–147 (1983)
60. D. Rife, R. Boorstyn, Single tone parameter estimation from discrete-time observations. *IEEE Trans. Inf. Theory* **20**(5), 591–598 (1974)
61. D. Middleton, *An Introduction to Statistical Communication Theory* (IEEE Press, Piscataway, 1996)
62. K. Peters, S. Kay, Unbiased estimation of the phase of a sinusoid, in *2004 IEEE International Conference on Acoustics, Speech, and Signal Processing*, vol. 2, May 2004, pp. 493–496
63. K.V. Mardia, P.E. Jupp, *Directional Statistics* (Wiley, Chichester, 2000)
64. I. Dyer, Statistics of sound propagation in the ocean. *J. Acoust. Soc. Am.* **48**(1B), 337–345 (1970)
65. P.L. Ainsleigh, A Tutorial on EM-based density estimation with histogram intensity data. Tech. Rpt. 11,807, Naval Undersea Warfare Center, 2009

Chapter 10

Detecting Signals with Unknown Duration and/or Starting Time: Sequential Detectors



10.1 Introduction

The focus of this chapter is on detecting signals whose duration or starting time violates one or more of the assumptions made in Chaps. 8 and 9. In particular, this chapter deals with cases where

- the signal extends beyond one coherent processing interval (CPI),
- the duration of the signal is unknown, and/or
- the starting time of the signal is unknown.

Of primary interest are signals that persist beyond one CPI, which breaks one of the fundamental assumptions made in the earlier chapters. As an example, consider the scenario of passively detecting a moving object of interest through a narrowband component of its radiated noise. The tonal radiated by a surface ship seen in the Doppler filter bank of Fig. 8.30 might represent such a signal. Because the object of interest is moving relative to the sensing platform, the center frequency of the narrowband signal measurement is changing over time. As described in Sect. 9.2.10, coherent processing for such a signal should be applied over a temporal extent equal to one over the bandwidth of the signal. The changing center frequency of the measured narrowband signal therefore limits the temporal extent of the CPI. Other examples where the extent of the CPI is limited include narrowband signals of interest with an inherent non-zero bandwidth and traversal of the contact from one beam to another when applying detection to the output of a beamformer. While earlier chapters described how to form the decision statistic for a single CPI, the focus of this chapter is on how to combine the decision statistics formed in each CPI across multiple ones in order to best detect a signal.

In the example of detecting a moving object of interest through its radiated noise, the starting time and duration of the signal are clearly unknown *a priori*. These depend on the geometry of the scenario, motion of the object of interest and sensing platform, and the many parameters found in the sonar equation. However, such a

signal can readily be assessed as having duration greater than one CPI, but only persist for a finite amount of time because propagation loss generally increases with range. This type of signal is said to have an *intermediate* duration to distinguish it from both a single-CPI signal and an infinite- or long-duration signal. A long-duration signal is one that, once it commences, persists to the end of the observation period or at least until some other action is taken as a result of detection. The quintessential example of this type of signal is found in an object-avoidance system where the signal from a colliding object continues until a maneuver is made to avoid the collision. For single-CPI and long-duration signals, the duration is implied and so it is effectively known. Although the introductory example described an intermediate-duration signal with an unknown duration, there are scenarios where the duration is known. For example, when an active sonar echo is subject to temporal spreading as described in Sect. 8.8, the duration of the signal might be known from a general characterization of the environment. With these examples, signals have been categorized as being short- (i.e., single-CPI), intermediate-, or long-duration and as having a known/implied or unknown specific duration.

In most applications of remote sensing with a detection inferential objective, the starting time of the signal is unknown because the distance between the object of interest and the sensing system is unknown. There are, however, examples where the starting time can be characterized as being known. These are generally found in scenarios where the signals of interest, when they do occur, pre-exist any sensor measurements. Other examples can be found in post-detection classification where it is required to classify an object of interest using subsequent measurements that each have an associated cost. The “signal” for the classification inferential objective starts with the detection and a quick classification decision is desired in order to reduce the total cost.

The composite characterization of a signal by its duration, knowledge of duration, and knowledge of the starting time is delineated in Table 10.1 along with the relevant performance measures, appropriate detector and its optimality, and the section in which each signal type is covered. Although the focus of this chapter is on signals with a duration greater than a single CPI, the case of a single-CPI signal with an unknown starting time is used in Sect. 10.2 as an example to introduce the concept of *sequential detection* and its performance measures. Most of the detectors presented in this chapter are sequential detectors, which come from the area of *sequential analysis* in the field of mathematical statistics. Reference texts for sequential analysis include [1–5]. In sequential detection, the data are observed in an ordered sequence (i.e., X_1, X_2, X_3, \dots) and a decision is desired to be made using as little data as possible. This implies that after observing k samples, one option is that there is not enough evidence to make a decision and that another sample must be obtained. This is in contrast to the *fixed-sample-size* hypothesis testing used to form single-CPI decision statistics. In this chapter, each observation is assumed to be the decision statistic formed for a single CPI according to the tenets presented in Chaps. 8 and 9. Additionally, the combination over multiple CPIs to make a decision is assumed to be done incoherently. That is, the input data to the sequential detector have had their phase dependence removed or accounted for so there is no coherent

Table 10.1 Categorization of signals types based on their duration, knowledge of duration, and knowledge of starting time along with the appropriate detectors, their optimality conditions, performance metrics, and the section in which they are covered

Duration ^{1,2}	Starting time	Performance measures ³	Detector	Optimality conditions	Section
Short-duration signals (single CPI)					
Implied	Known	P_d & P_f	ED or MF	Varies	Chaps. 8 & 9
Implied	Unknown	P_d & F	Sliding ED or MF	Varies	10.2
Intermediate-duration signals (multiple CPIs)					
Known	Known	P_d & P_f	Incoherent sum	Varies	10.3
Known	Known	P_d & P_f	M -of- N	None/robust	10.3.1
Known	Unknown	P_d & F	Sliding incoherent sum	GLR	10.4.1
Known	Unknown	P_d & F	Sliding M -of- N	None/robust	10.4.2
Unknown	Known	P_d , P_f , ASN	SPRT	GLR	10.6.1
Unknown	Unknown	P_d , D & F	Alter.-hyp. (AH) Page's test	GLR	10.6.2
Long-duration signals (all CPIs after onset)					
Implied	Known	P_d , P_f , ASN	SPRT	MASN	10.5.1
Implied	Unknown	D & F	Page's Test	QD & GLR	10.5.2

Legend:

Detectors

ED = energy detector

Optimality

GLR = generalized likelihood ratio

MF = matched filter

MASN = minimum average sample number

SPRT = sequential probability ratio test

QD = quickest detector

AH = alternating hypothesis

Notes:

1. The measure of signal duration is with respect to the coherent processing interval (CPI) and the total observation time as follows.

Short: signal duration is less than or equal to the CPI

Intermediate: longer than one CPI but less than the total observation time

Long: extends throughout the observation time after onset (effectively infinite duration)

2. Knowledge of the signal duration is *implied* when it is short or long (i.e., one CPI for short-duration signals and every CPI from the starting time to the end of the observation for long-duration signals).

3. Performance measures (see Sect. 10.2 for more details):

P_d & P_f : probabilities of detection and false alarm

ASN: average number of samples to decision

D : average number of signal samples required for detection

F : average number of samples to a false alarm

combination of data across CPIs. This generally means the input to a sequential detector is a one-to-one mapping of the single-CPI matched-filter or energy-detector decision statistics.

Although the standard probabilities of detection (P_d) and false alarm (P_f) are still applicable to some sequential detection scenarios, the focus on using as few samples as possible to make a decision provokes the use of a different performance measure. The number of samples used to make a decision in a sequential detector can vary from one realization to the next and so it is represented as a random variable (K) defined by the index of the data sample when a decision is finally made and the hypothesis test is stopped. The performance metric commonly used in sequential detection is then the average number of samples required to make a decision (i.e., $E[K]$), which can be interpreted as an average cost to the decision when each sample has an equal cost to its acquisition. When the starting time of a signal is unknown, the average time before a false alarm ($F = E[K|H_0]$) is the relevant false-alarm performance metric. When a signal is present the pertinent measure is the average number of samples required to detect the signal once it has started; i.e., the average number of *signal* samples. This is often called detection *latency* and is defined as $D = E[K|H_1, S] - (D_o - 1)$ where D_o is the time index of the first sample containing signal and the event S represents the signal being detected. Depending on the application, but predominantly for intermediate-duration signals, the probability of detecting a signal remains a very important performance metric. These performance metrics, and how they are related to the probability density function of the sample size or stopping time of the test (i.e., K), are described in Sect. 10.2.

The case of a known signal duration and known starting time is briefly discussed in Sect. 10.3. This scenario is similar to that covered in Sects. 8.8 and 9.2.10 and so the focus is instead on an M -of- N detector, which is useful when the signal structure is either highly fluctuating or sparse (i.e., it only occurs in M out of the N consecutive CPIs). The assumption of a known starting time is relaxed in Sect. 10.4, which results in sliding the detectors developed for a known starting time over all possible starting times. Detectors for long-duration signals are then covered in Sect. 10.5, where it is seen that a sequential probability ratio test (SPRT) is used when the starting time is known and Page's test is used when the starting time is unknown. Approximations to the average sample numbers for these tests are derived and corrections improving their accuracy are presented. The chapter is then closed by applying the SPRT and Page's test to intermediate-duration signals in Sect. 10.6. Analysis of the probability of detection and detection latency is performed by quantizing the single-CPI data and describing the tests as discrete-time, finite-state Markov chains. The performance metrics can then be obtained from matrix–vector equations involving the state transition probability matrix. The alternating-hypothesis Page's test (AHPT) is presented in Sect. 10.6.2.1 to sequentially detect multiple signals occurring with both unknown duration and an unknown time between signals. Finally, an example is presented for Page's test in Sect. 10.6.2.3 to illustrate the design and analysis process.

10.2 Performance Measures for Sequential Signal Detectors

The standard probability of detection and probability of false alarm performance measures are generally adequate when the quantity of data used for detection is fixed and finite. There are, however, scenarios where these measures do not usefully represent the performance of a detector. For example, if a detector for a signal with an unknown starting time is applied to an infinitely long sequence of data, the probability of false alarm equals one. In this scenario, the average number of samples from one false alarm to the next is a more appropriate measure of false-alarm performance. When the signal exists forever once it commences, the probability of detection is also one, so a similar argument leads to the average number of samples required for detection as the more appropriate detection performance measure. This focus on the number of samples before a false alarm or a signal detection arises from the desire to make a decision as quickly as possible, generally because there is a cost to each observation.

Consider the scenario where a detector is provided an infinite sequence of data X_1, X_2, \dots and the objective is to detect signal presence as quickly as possible. The null hypothesis (H_0) is that the data always follow the probability density function (PDF) $f_0(x)$. The alternative hypothesis (H_1) is that a signal producing data with PDF $f_1(x)$ is present starting with sample D_o and persists for some time with noise-only data occurring before and after the signal. The signal starting time and duration can be either known or unknown and the duration can be finite or infinite.

As an introductory example, suppose the starting time D_o is unknown and that the signal duration is infinite so once the signal starts it never stops. The data are then distributed according to

$$X_k \sim \begin{cases} f_0(x) & \text{for } k < D_o \\ f_1(x) & \text{for } k \geq D_o \end{cases}. \quad (10.1)$$

In this text, the data used in sequential detectors are assumed to have been formed as single-CPI decision statistics under the assumptions made in Chaps. 8 and 9. They are expected to be independent and identically distributed within the confines of the signal models described in Table 10.1. The stationarity of the data under the noise-only hypothesis generally implies normalization, which can introduce dependence when there is overlap in the auxiliary data used to estimate the background power in consecutive samples. However, the analysis in this section ignores this potential correlation, assuming it is small enough to not largely affect the results.

After observing the k th sample, a sequential detector forms a decision statistic $T_k(\mathbf{x}_k)$ using the current and previously observed data, $\mathbf{x}_k = [X_1 \ \cdots \ X_k]^T$. A signal is then declared present if the decision statistic meets or exceeds a decision threshold,

$$T_k(\mathbf{x}_k) \stackrel{H_1}{\underset{H_0}{\gtrless}} h_k. \quad (10.2)$$

If the threshold is not met or crossed, then the detector remains in a *noise-only* state (H_0) and waits for the next observation. Note that in general the decision threshold h_k can depend on the time index k , although it is common to transform the time-varying portion of h_k to be part of the decision statistic so the decision threshold is constant over time. The detector stops processing data the first time one of the decision statistics exceeds the appropriate threshold. This is called the *stopping time* of the sequential detector. If the stopping time is K , then all of the previous decision statistics resulted in choosing H_0 ,

$$T_k(\mathbf{x}_k) < h_k \quad \text{for } k = 1, \dots, K - 1, \quad (10.3)$$

and the K th exceeds its threshold, $T_K(\mathbf{x}_K) \geq h_K$. Mathematically, the stopping time (K) can be described as the minimum¹ over the set of integers $\{k \geq 1\}$ such that $T_k(\mathbf{x}_k)$ exceeds h_k ,

$$K = \min\{k \geq 1 : T_k(\mathbf{x}_k) \geq h_k\}. \quad (10.4)$$

Note that $T_k(\mathbf{x}_k)$ may (or may not) exceed h_k after the stopping time; however, this is irrelevant because signal detection has already occurred.

It is important to note that K is a random variable: the stopping time can vary from one realization of the data to the next. This implies that the amount of data used to form a decision can vary from one realization to the next and that the decision thresholds must be chosen to account for this. A complete characterization of the performance of a sequential detector can be obtained from the probability density function of K under the noise-only and signal-present hypotheses. Because of the discrete nature of K , it is more appropriate to refer to its density function as a probability mass function (PMF). Except in the simplest scenarios, analytical evaluation of the PMF of K can be difficult. This generally leads to using the average number of samples required to make a decision under H_0 and H_1 as performance metrics. In this text, these will be referred to as *average sample numbers* (ASNs) but are sometimes called average record lengths or average stopping times.

For the introductory example, suppose the decision statistic of the sequential detector at time k is simply the single-CPI decision statistic X_k and that the decision threshold is fixed. This particular sequential detector is appropriate for use when a signal is known to reside within a single CPI but has an unknown starting time. It is essentially the scenario presented in Sect. 8.2.8.2 for matched filtering and sampling at the signal bandwidth, but will now be described in the context of sequential detection.

¹In some texts the stopping time is described using the infimum (“inf”) rather than minimum so as to include the limiting case of $K \rightarrow \infty$.

Under the noise-only hypothesis, the probability of observing a threshold exceedance is constant for all k ,

$$p_0 = \Pr\{X_k \geq h|H_0\}. \quad (10.5)$$

The sequence of threshold comparisons implementing the sequential detector represent repeated independent Bernoulli trials with success probability p_0 . The stopping time for the detector can therefore be described as the number of Bernoulli(p_0) trials required to achieve a single success. From [6, Ch. 23], this is one plus a geometric random variable with “success” probability p_0 . The PMF of K under H_0 is therefore

$$f_K(k|H_0) = p_0(1 - p_0)^{k-1} \quad \text{for } k = 1, 2, 3, \dots \quad (10.6)$$

which for $K = k$ can be seen to require $k - 1$ “failures,” each occurring with probability $1 - p_0$, followed by one “success.” The average number of samples before a false alarm occurs can then be found as one plus the mean of the geometric random variable, which yields

$$F = E[K|H_0] = \sum_{k=1}^{\infty} kf_K(k|H_0) \quad (10.7)$$

$$= \frac{1}{p_0} \quad (10.8)$$

where (10.7) is the general definition and (10.8) is the result for the introductory example. It can be seen from (10.8) that F is expected to be large because p_0 is the CPI-level probability of false alarm and should therefore small.

The average number of signal samples required for detection is

$$D = E[K|H_1] - (D_o - 1) \quad (10.9)$$

where it is assumed that the signal begins with sample D_o , exists for all remaining samples, and that no false alarms occur before D_o (which implies the signal causes the detection). In the theoretical evaluation of D there are two approaches for handling the noise-only samples occurring before the signal starts at D_o . The more rigorous approach accounts for the testing of the noise samples under the condition that no false alarms occur. A simpler alternative is to assume the noise samples leave the detector in the worst possible state for detection. The difference between these two approaches is highlighted by the case of a decision statistic with memory (i.e., correlation) and noise samples that leave the decision statistic very close to the threshold, or very far from it, just before the signal starts. The worst-case ASN for detection is the more common approach and is essentially equivalent to evaluating the ASN as if the signal starts in the first sample (i.e., $D_o = 1$). In the introductory example, the decision statistic has no memory so the two approaches are equivalent. If the signal starts in the first sample, then $f_K(k|H_1)$ has the same form as that

shown in (10.6) under H_0 but replacing p_0 with $p_1 = \Pr\{X_k \geq h|H_1\}$, which is the single-CPI probability of detection. Similar to (10.8), this then leads to $D = 1/p_1$.

In fixed-sample-size detection an *unbiased* detector exhibits the desirable characteristic of a larger P_d than P_f . In sequential detection this transforms into requiring $F > D$, which is clearly satisfied in the introductory example if $P_d > P_f$. The ideal sequential detection performance measures are $F \rightarrow \infty$ and $D \rightarrow 1$, the latter of which represents always detecting the signal after observing only one sample. The relationship between F and D as a function of the detector decision threshold (when it is a constant $h = h_k$ over time) is similar to that observed between P_f and P_d . The receiver operating characteristic (ROC) curve for a sequential detector is a plot of D as a function of F that is formed by varying the decision threshold h . Reducing the decision threshold h makes it easier to detect a signal (i.e., reduces D), but causes false alarms to occur more frequently (i.e., it also reduces F).

Now suppose that the signal in the introductory example only persists for a total of N samples where the duration N is unknown but finite. Using the worst-case detection analysis approach (i.e., letting $D_o = 1$), the PMF of the stopping time under H_1 can be described as

$$f_K(k|H_1) = \begin{cases} p_1(1 - p_1)^{k-1} & \text{for } k \leq N \\ (1 - p_1)^N p_0(1 - p_0)^{k-N-1} & \text{for } k > N \end{cases}. \quad (10.10)$$

The ASN when signal is present can then be shown to be

$$E[K|H_1] = \sum_{k=1}^{\infty} kf_K(k|H_1) \quad (10.11)$$

$$= \frac{1}{p_1} + \left(\frac{1}{p_0} - \frac{1}{p_1} \right) (1 - p_1)^N. \quad (10.12)$$

This illustrates how $D \rightarrow 1/p_1$ as $N \rightarrow \infty$, which corresponds to the previously derived result for the case of an infinite length signal and how $D \rightarrow F = 1/p_0$ when $p_1 \rightarrow p_0$ irrespective of N . The sequential detector receiver operating characteristic (ROC) curve is shown in Fig. 10.1 for this constant-threshold detector applied to intensity data for a Gaussian-fluctuating signal in Gaussian distributed noise where

$$p_0 = e^{-h} \quad \text{and} \quad p_1 = e^{-h/(1+s)} \quad (10.13)$$

and s is the SNR.² The solid lines represent the average number of samples required for detection (D) for the infinite-duration signal whereas the dashed lines are $E[K|H_1]$ when only the first $N = 10$ samples contain signal. At large threshold

²The SNR s here is equivalent to the S^d used in earlier chapters. However, owing to the applicability of sequential detectors to other scenarios a generic SNR term is used.

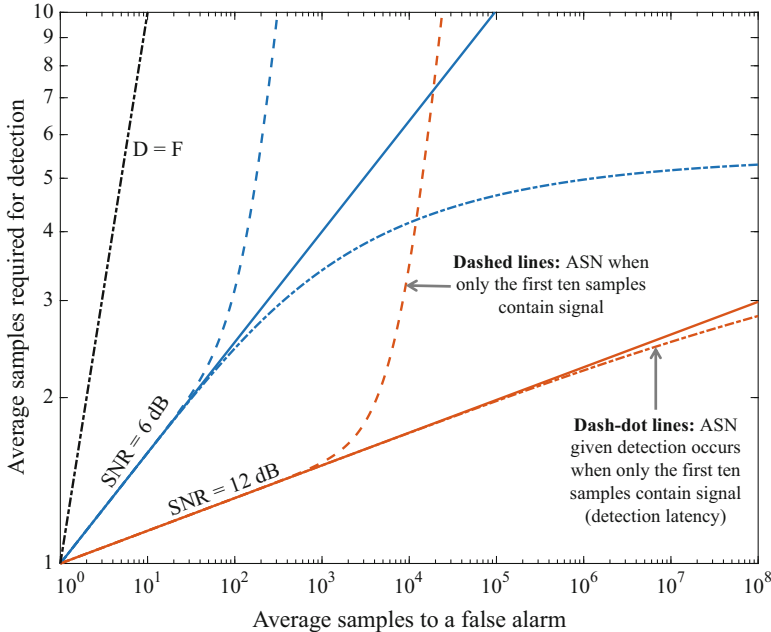


Fig. 10.1 Sequential detector ROC curve showing the average sample numbers (ASNs) for detection and false alarms for a constant-threshold sequential detector applied to *iid* intensity data and a Gaussian-fluctuating signal in Gaussian noise. When only the first ten samples contain signal, the unconditioned ASN is shown as dashed lines and the ASN conditioned on the signal being detected as dash-dot lines

values, which correspond to large values of F , the ASN for detecting the finite-duration signal exhibits exponential growth similar to that observed in F —in fact in those regions it does not accurately represent detection of the signal because it is dominated by threshold exceedances occurring after the signal has ended. This difference illustrates why finite-duration signals need to be analyzed differently when using sequential detectors.

The latter term on the right side of (10.12) describes the contribution to the ASN from realizations where the signal is not detected within the first N samples. In essence, this means the signal itself is not detected and that the threshold exceedance arises solely from the noise. Let detection of a signal with duration N be denoted by the event \mathcal{S} and be defined as requiring the decision statistic at the stopping time to have been affected by presence of the signal. In the more general formulation, the ASN can be decomposed into terms related to when the signal is detected and when it is not, which is represented by the event $\bar{\mathcal{S}}$,

$$E[K|H_1] = E[K|H_1, \mathcal{S}] \Pr\{\mathcal{S}|H_1\} + E[K|H_1, \bar{\mathcal{S}}] \Pr\{\bar{\mathcal{S}}|H_1\}. \quad (10.14)$$

The information pertinent to detection performance of a finite-duration signal is then captured in the first term in (10.14). The ASN given detection occurs, $E[K|H_1, \mathcal{S}]$, is commonly referred to as detection *latency* and $\Pr\{\mathcal{S}|H_1\}$ is simply P_d of the sequential detector. In the introductory example where the signal is present in only the first N samples and the decision statistic has no memory (i.e., $T_k(\mathbf{x}_k)$ only depends on X_k), signal detection is represented by the event $\mathcal{S} = \{K \leq N\}$. The probability of detection is then the sum of $f_K(k)$ over the first N samples,

$$P_d = \sum_{k=1}^N f_K(k|H_1) \quad (10.15)$$

$$= 1 - (1 - p_1)^N. \quad (10.16)$$

This illustrates both how P_d can be formed from the PMF of K and how $P_d \rightarrow 1$ when the signal persists for infinite time (the same formula holds under the null hypothesis so $P_f \rightarrow 1$ as previously noted).

The detection latency for the introductory example can be shown to be

$$D|\mathcal{S} = E[K|H_1, \mathcal{S}] - (D_o - 1) = \frac{1}{p_1} - \frac{N(1 - p_1)^N}{1 - (1 - p_1)^N}. \quad (10.17)$$

As seen in Fig. 10.1, the detection latency ($D|\mathcal{S}$, shown as dash-dot lines) is very similar to the average number of samples required for detection (D , solid lines) of an infinite-duration signal when the decision threshold is low enough or the SNR high enough for there to be a high probability of detecting the finite-duration signal. By conditioning on the signal being detected, it is also useful when P_d is not overly large, where the unconditioned ASN is dominated by behavior similar to F .

To summarize, the average number of samples to a false alarm (F) and the average number of signal samples required for detection (D) are the performance measures for a sequential detector applied to a signal with unknown starting time that persists forever once it occurs. When applying a sequential detector to a finite-duration signal with an unknown starting time, the ASN under H_1 should be conditioned on detection of the signal ($D|\mathcal{S}$) to describe detection latency and the probability of detection $P_d = \Pr\{\mathcal{S}\}$ also evaluated.

10.3 Detectors for Signals with Known Duration and Known Starting Time

In the scenario where the starting time and duration of a signal are known, the data available for detection are X_1, \dots, X_N where N is a known, non-random, quantity describing how many samples contain signal. The data are assumed to be either all noise-only samples (under H_0) or all signal-plus-noise samples (under H_1).

When the data represent a log-likelihood ratio (LLR) or generalized log-likelihood ratio, they should be combined into a single decision statistic by a sum under the independence assumption noted in Sect. 10.2. This is identical to the incoherent integration described in Sect. 8.8 to counter energy spreading loss or that from Sect. 9.2.10 for a time-domain energy detector.

When the signal is highly fluctuating or appears broken up with some number of the N samples containing only noise, a detector accounting for this transitory signal structure can provide better performance than the incoherent sum. The GLR, MGLR, and power-law energy detectors described in Chap. 9 are examples where the data are summed after application of a non-linear function reducing the effect of the noise-only samples. A similar approach, called an M -of- N detector, is presented in the following section where the detector function represents a binary quantization of the data.

10.3.1 M -of- N Detector: Binary Integration

The mapping from observed intensity data to a log-likelihood-ratio represents a type of *statistical* normalization making the transformed data suitable for combination by summing. For example, the mapping may de-emphasize larger values when the PDF of the noise is heavy-tailed relative to an exponential intensity. In the extreme this can result in a binary quantization of the data as occurs in the locally optimally detector for a constant signal in additive Laplacian (double-exponential) noise [7, Sect. 2.3.2]. The binary quantization provides both a very simple detector to implement and a robustness to unknown signal and noise distributions. The cost comes in a reduction in performance when the noise is known to follow a particular distribution with lighter PDF tails.

The detector decision statistic combining N samples of data after binary quantization is

$$T(\mathbf{x}) = \sum_{n=1}^N \mathbb{I}\{X_n \geq h_x\} \quad (10.18)$$

where h_x is the quantization threshold and $\mathbb{I}\{\cdot\}$ is an indicator function returning one when the argument is true and is otherwise zero. The decision statistic is now a discrete random variable potentially taking on values $0, 1, \dots, N$. If the threshold is M , then a signal is declared present if at least M of the N data samples exceed the quantization threshold. This M -of- N detector is also known as *binary integration* [8, Sect. 6.4] or [9, Sect. 14.1] and is commonly found in data fusion applications where decisions made locally by individual sensors are combined remotely to form an overall fused decision (e.g., [10, Sect. 3.3]).

Two commonly known detector structures arise from the extreme thresholds in the M -of- N detector. When $M = 1$, only one sample must exceed the quantization

threshold. It might be the first sample, or the second, or the n th—which names this as an “OR” processor. It is also identical to comparing the maximum sample to the quantization threshold, and so is also a “MAX” processor. At the other extreme, where the decision threshold is $M = N$, all of the samples must exceed the quantization threshold. This is therefore called an “AND” processor and is identical to comparing the minimum sample to the quantization threshold (i.e., it is also a “MIN” processor). The M -of- N detector itself can be represented as comparing the $(N - M + 1)$ st order statistic to the data threshold h_x ,

$$X_{(N-M+1)} \stackrel{H_1}{\stackrel{\geq}{\leq}} h_x. \quad (10.19)$$

This can be seen by noting that when $X_{(N-M+1)}$ meets or exceeds h_x , each of the $M - 1$ larger order statistics also meet or exceed h_x and so a total of M of the samples do, which satisfies the M -of- N requirement.

Analysis of the M -of- N processor when the data are identically distributed follows readily by noting the decision statistic is a binomial (N, p_i) random variable where the success probability $p_i = \Pr\{X_n \geq h_x | H_i\}$ for $i = 0$ and 1. The probability of false alarm is then obtained by summing over the binomial PMF from M to N ,

$$P_f = \sum_{n=M}^N \binom{N}{n} p_0^n (1 - p_0)^{N-n} \quad (10.20)$$

For the AND/MIN detector ($M = N$) this simplifies to

$$P_f = p_0^N \quad (10.21)$$

and for the OR/MAX detector ($M = 1$) to

$$P_f = 1 - (1 - p_0)^N. \quad (10.22)$$

Because of the discrete nature of the decision statistic, describing the exceedance probability in terms of the CDF of the binomial distribution requires evaluating it at $M - 1$ (e.g., in MATLAB® use `Pf=1-binocdf(M-1, N, p0)`). The results for P_d have similar form when all samples contain signal (i.e., replace p_0 with p_1 or see

Table 10.2 OR and AND processors, their relationship to the MAX and MIN processors and an M -of- N detector and the associated exceedance probability

Description	Min/Max	Order Statistic	M in M -of- N	Exceedance probability
OR	MAX	$X_{(N)}$	1	$1 - F_X^N(h_x)$
AND	MIN	$X_{(1)}$	N	$[1 - F_X(h_x)]^N$

the equations in Table 10.2). The case where not all samples contain signal under H_1 is more complicated to evaluate analytically.

As an example, consider the ROC curve shown in Fig. 10.2 for $N = 10$ and a ubiquitous 5-dB-SNR deterministic signal in Gaussian noise. Over a wide range of P_f , choosing $M = 6$ maximizes P_d . The difference between this best choice of M and the AND/MIN or OR/MAX detectors is significant, indicating it is important to choose M based on the expected temporal structure of the signal. For example, if the signal were anticipated to be observed in only one of the N samples, choosing $M = 1$ provides the best performance and can be derived under a GLR framework. When it is known that M_s of the N samples contain signal, but not which ones, choosing $M = M_s$ provides the best performance at high SNR, but choosing a smaller value can perform better when the SNR is lower because of the higher probability that some noise-only samples will exceed the data threshold h_x . This was illustrated in Fig. 10.2 where $M_s = N$; the following section describes how to choose M in this scenario of all samples containing signal.

10.3.1.1 M -of- N Detector Design: Choosing Thresholds

Given N , detector design requires choosing the data quantization threshold h_x and the detector decision threshold M . Early approaches to this problem chose h_x to

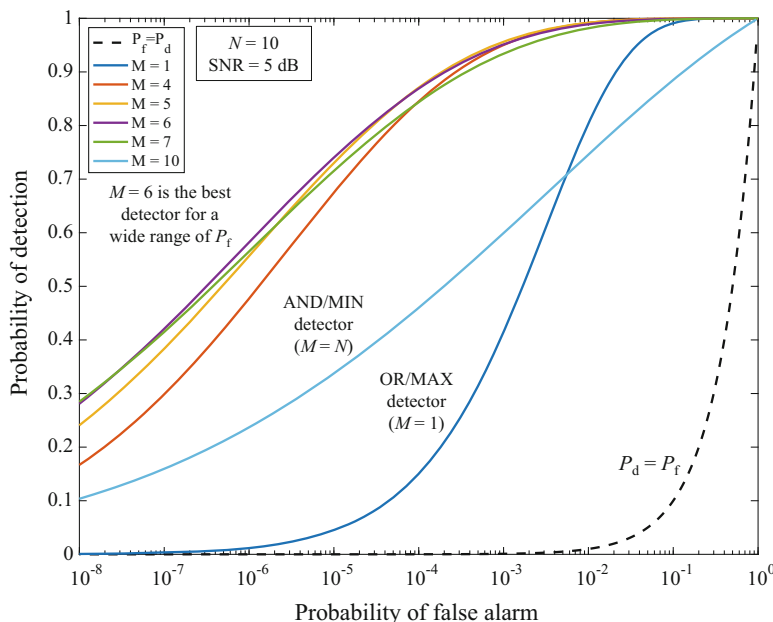


Fig. 10.2 ROC curve for various M -of- N processors when $N = 10$ with an SNR of 5 dB for a deterministic signal in Gaussian noise

Table 10.3 Swerling target models as described by their envelope distribution, whether they are consistent or fluctuate in the short or long term, and the parameters found in [12] used to obtain the (approximately) optimal value of M in an M -of- N detector via (10.23) when data are combined over the short term

Model number	Envelope distribution	Short-term character	Long-term character	(a, b) for M_{opt} in (10.23)	Validity over N
0	Deterministic	Consistent	Consistent	(0.8, -0.02)	[5, 700]
1	Rayleigh	Consistent	Fluctuates	(0.8, -0.02)	[6, 500]
2	Rayleigh	Fluctuates	Fluctuates	(0.91, -0.38)	[9, 700]
3	Chi w/ 4 dof ¹	Consistent	Fluctuates	(0.8, -0.02)	[6, 700]
4	Chi w/ 4 dof ¹	Fluctuates	Fluctuates	(0.873, -0.27)	[10, 700]

Notes:

1. The Swerling 3 and 4 models use a chi-distributed envelope with four degrees of freedom (dof) as an approximation to a Rician signal (with a particular Rice power ratio). Squaring a chi-distributed (χ_v) envelope produces a chi-squared-distributed intensity (χ_v^2) in the same manner that squaring a Rayleigh-distributed envelope produces an exponentially distributed intensity.

optimize the detection index (DI) of $T(\mathbf{x})$ and then M to achieve a desired P_f [11] (also found in [9, Sect. 14.3]). When N is large, the detector decision statistic $T(\mathbf{x})$ is approximately Gaussian, which partially justifies the approach. However, it is not a shift-in-mean Gaussian detection problem so DI is only an approximate proxy for optimizing detection performance. This technique also limits the choices of P_f to the finite set achieved by the values of M ranging from one to N .

An alternative approach is to design the detector to be optimal in the Neyman-Pearson sense of optimizing P_d given a fixed P_f (see Sect. 6.2.3). As described in [12], the SNR required to achieve an operating point only depends weakly on M for a wide range of operating points. This implies that there is little loss in choosing M to maximize P_d solely as a function of N and then choosing h_x to achieve the P_f specification. Evidence of this can be seen in Fig. 10.2 where choosing $M = 6$ leads to an optimal detector over a wide range of P_f . Choosing $M = 5$ or 7 is optimal at, respectively, higher and lower values of P_f and only slightly sub-optimal where $M = 6$ is optimal. Using this approach, Shnidman [12] approximates the value of M optimizing P_d according to

$$M_{\text{opt}} \approx 10^b N^a \quad (10.23)$$

where a and b are chosen according to the signal fluctuation model. For example, $a = 0.8$ and $b = -0.02$ for a deterministic signal when $N \in [5, 700]$. P_d as a function of M for various values of P_f is shown in Fig. 10.3 for $N = 20$ and a 3-dB SNR. Shnidman's equation for this scenario indicates the optimal value of M is approximately 10. As seen in Fig. 10.3, this is within one of the values maximizing P_d for $P_f \in [10^{-4}, 10^{-8}]$, but not $P_f = 10^{-2}$, the former of which corresponds to the region of validity noted in [12].

The basic Swerling fluctuation models, as described in [8, Sect. 2.2.6], represent three different statistical models for a signal measurement and whether repeated

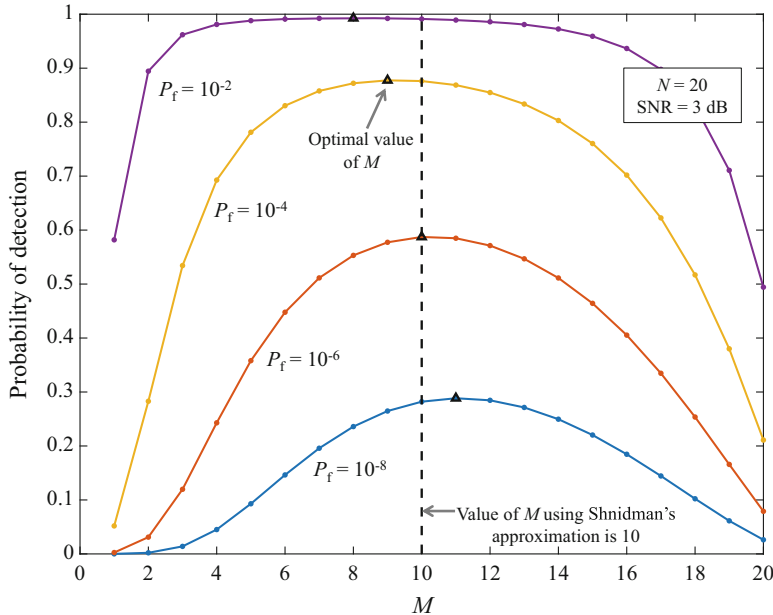


Fig. 10.3 Probability of detection as a function of M for various values of P_f when $N = 20$ with an SNR of 3 dB for a deterministic signal in Gaussian noise

observations are consistent or fluctuate in either the short term or the long term. The models, their envelope distribution and temporal fluctuation characteristics are listed in Table 10.3 along with the values of (a, b) required for (10.23) and the corresponding region of validity in N . When a signal fluctuates from one observation to the next the observations are represented as being statistically independent. In radar systems where one scan consists of multiple pulses, this is generally described as pulse-to-pulse (short-term) or scan-to-scan (long-term) fluctuation. In sonar applications, the distinction between short-term and long-term fluctuations depends on the application. Fluctuations most commonly arise from changes in the acoustical channel, but can also arise intrinsically in the generation of the source signal (e.g., as occurs for ship radiated noise). Changes in the acoustical channel most obviously arise from motion of the object of interest, a sensing platform, or the ocean boundaries themselves. The acoustical channel can also change as a result of time-varying oceanography such as internal waves or changes in temperature from solar heating. An example of the importance of the sensing geometry in characterizing whether a signal is fluctuating or not can be found in reflection from a moving surface. The acoustical roughness of the surface $g_r = 4k^2\sigma_z^2 \sin^2 \theta_g$ (see Sect. 3.2.7.6) depends on frequency through the wavenumber $k = 2\pi f_c/c_w$, the RMS sea-surface height σ_z , and the sine of the grazing angle θ_g . Thus, even if the surface is moving, it will not affect the acoustical channel at low frequencies or low grazing angles (such that $g_r \ll 1$). As seen in

Table 10.3, only the deterministic signal is consistent over the long term. Thus it suffices to define the time over which signals are consistent with observations separated by greater times assumed to fluctuate.

In choosing the optimal value of M for the M -of- N detector when combining over the short term, the same values of a and b as for the deterministic signal are used in (10.23) for the signal models with consistency among the N short-term observations (Swerling models 1 and 3). However, the minimum value of N for which they are valid varies, as shown in the last column of Table 10.3. When the signal fluctuates within the N observations, the values are different. For example, a Gaussian-fluctuating signal (i.e., a Swerling 2 signal) uses $a = 0.91$ and $b = -0.38$ for $N \in [6, 500]$. The operating points evaluated in [12] were $P_d = 0.2$ and 0.9 and $P_f = 10^{-4}, 10^{-6}$, and 10^{-8} . When N is less than the minimum value noted in the region of validity in Table 10.3, tables found in [12] provide the optimal value of M .

For Swerling models 0 and 2, the optimal value of M was approximated in [13] when the noise-only data are heavy tailed. The first scenario considered was for a cell-averaging constant-false-alarm-rate (CA-CFAR) normalizer, which produces $F_{2,2L}$ -distributed noise data. An empirical formula for the optimal value of M was then obtained as a function of N , the desired operating point, and the number of independent observations (L) in the auxiliary data used to estimate the background power. The second scenario entailed K -distributed noise-only data and obtained the minimax value of M over a range of shape parameters. Although the approximations found in [13] require more coefficients than (10.23), they help optimize performance for more realistic noise conditions.

10.4 Detectors for Signals with Known Duration and Unknown Starting Time

When the duration of a signal (N) is known but its starting time is not, the GLR approach evaluates every possible starting time to find the maximum decision statistic formed over N consecutive samples. If the detector function applied to an individual observation is a log-likelihood ratio and the observations are independent, this produces a running sum over every N consecutive samples. When more than one signal is expected to be observed, the detector implementation can be viewed as thresholding the output of a constant-coefficient, length- N , finite-impulse-response (FIR) filter applied to the individual observation data. The filtering clearly introduces correlation between samples that complicates performance analysis. A lower bound on the probability of detection can be obtained from P_d for the known-starting-time scenario as described in Sect. 10.3. The lower bound formed in this manner only excludes observations where a threshold exceedance occurs when the integration window and signal are mis-aligned and no threshold exceedance occurs when they are aligned. Therefore, the bound is increasingly tight as SNR increases and generally adequate for performance prediction. When higher accuracy

is required, simulating P_d is a reasonable alternative. As such, the focus here is on the average number of samples before a false alarm (F). Obtaining analytic results relating decision or quantization thresholds to F is important owing to the difficulty in using simulation to evaluate false-alarm performance when the average number of samples between false alarms is extremely high.

Similar to the development of Sect. 10.3, two detectors are considered here: a sliding incoherent-sum detector and a sliding M -of- N detector. It is important to be cognizant of the loss in performance encountered in using the M -of- N detector when the incoherent sum detector is more appropriate. An example of this *quantization* loss can be seen in the ROC curve found in Fig. 10.4 for a deterministic signal with 5-dB SNR and duration $N = 10$. This ROC curve shows the aforementioned lower bound on the probability of detection as a function of the average number of samples to a false alarm obtained using the techniques described later in this section. For this type of ROC curve, performance improves as the operating point shifts toward the upper right (i.e., higher P_d and F). As expected, the sliding incoherent sum detector performs better than the sliding M -of- N detector. For this scenario with the deterministic signal, the quantization loss of the sliding M -of- N detector is approximately equivalent to a loss in SNR of one decibel (reddish-brown dashed line in the figure) in the sliding incoherent sum

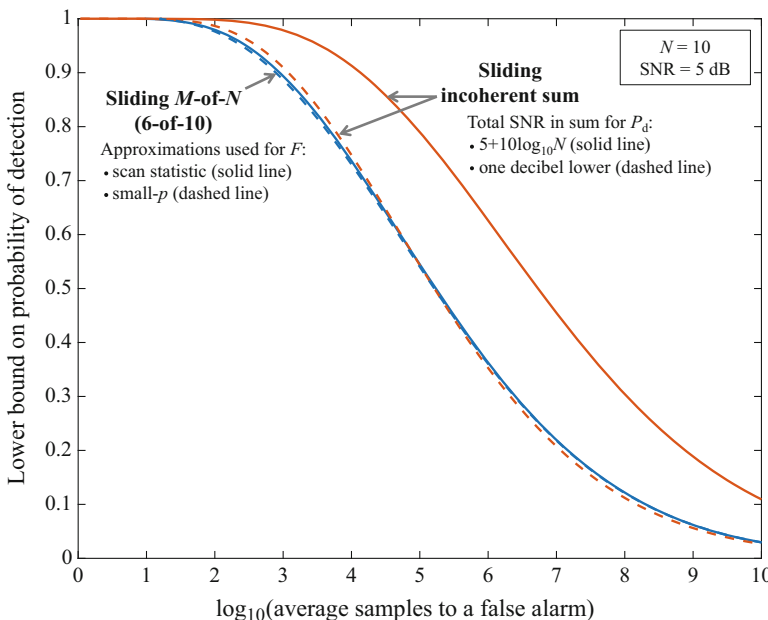


Fig. 10.4 ROC curve for detecting a 5-dB-SNR deterministic signal with known duration ($N = 10$) and unknown starting time using a sliding M -of- N processor with the optimal value of $M = 6$ from (10.23) or a sliding incoherent sum. In this scenario, the loss incurred by quantizing the data in the sliding M -of- N detector is approximately equivalent to a loss of 1 dB in SNR

detector. Although not shown, a Gaussian-fluctuating signal (Swerling 2) exhibits a loss of approximately 1.4 dB. This is commensurate with the maximum loss of 1.5 dB reported in [12] for the scenario of a known starting time.

10.4.1 Sliding Incoherent Sum Detector

When a signal with a duration of N samples occurs at an unknown time and the data samples X_1, X_2, \dots are independent and represent a log likelihood ratio, the GLR detector over the unknown starting time effectively compares the incoherent sum

$$T_k = \sum_{i=0}^{N-1} X_{k-i} \quad (10.24)$$

to a threshold h for every value of $k \geq N$. In a quickest detection scenario, a detection is declared the first time T_k meets or exceeds the threshold (h). This sliding incoherent sum detector is known as a finite-moving-average control chart [4, Sect. 8.1.3] where the *control chart* terminology comes from the manufacturing and process control literature.

In underwater acoustic signal processing applications, this detector is typically applied to instantaneous-intensity samples so under the noise-only hypothesis the data are exponentially distributed, $X_k \sim \text{Expon}(\lambda)$, assuming the normalization is perfect. The decision statistic at time k is then gamma distributed with shape N and scale λ ,

$$T_k | H_0 \sim \text{Gamma}(N, \lambda). \quad (10.25)$$

In order to obtain the average number of samples to a false alarm, $F = E[K|H_0]$, where the stopping time is

$$K = \min\{k \geq N : T_k \geq h\}, \quad (10.26)$$

suppose that only every N th sample were compared to a threshold. The resulting sequence is then independent and identically distributed and so satisfies the assumptions made in Sect. 10.2. Modifying (10.8) to account for the decision occurring only every N th sample results in

$$F \approx \frac{N}{1 - F_G(h; N, \lambda)} \quad (10.27)$$

where $F_G(h; \alpha, \beta)$ is the cumulative distribution function (CDF) of the gamma distribution.

Similar to how oversampling in a matched filter (see Sect. 8.2.10) increases the probability of a false alarm, comparing every sample T_k to a threshold instead of every N th sample will increase the false alarm rate, which means a decrease in F in the context of sequential detection. Analysis of the detector comparing a sequence of correlated samples to a threshold is in general difficult; analytic solutions are not known to exist [4, Sect. 8.1.3]. However, upper and lower bounds on the average sample number (\tilde{N}) can be obtained from [14] that only depend on the CDFs of the partial sums $\sum_{l=1}^i X_l$ for $i = 1, \dots, N$. The upper bound is

$$F \leq \frac{N}{1 - \Pr\left\{\sum_{l=1}^N X_l < h\right\}}, \quad (10.28)$$

which is precisely the approximation shown in (10.27) that only tests every N samples (and when the data are exponentially distributed). The lower bound is

$$F \geq \frac{\prod_{i=1}^{N-1} \Pr\left\{\sum_{l=1}^i X_l < h\right\}}{1 - \Pr\left\{\sum_{l=1}^N X_l < h\right\}}, \quad (10.29)$$

which has the same denominator as the upper bound, but replaces the numerator with the product of the CDF of the partial sums up to $N - 1$. As a side note, the bounds described in [14] handle the more general case of a weighted sum; they are simplified here to the sum in (10.24). These bounds on the average number of samples to a false alarm when $N = 10$ for the example of exponentially distributed data are shown in Fig. 10.5 as a function of the normalized decision threshold (i.e., h/λ). A simulation analysis illustrates how the upper bound is tight when the threshold is small whereas the lower bound may be tighter when the threshold is large. Tighter bounds can be found in [14, 15]; however, they require evaluation of the joint cumulative distribution function of N consecutive values of T_k which is not particularly easy to evaluate, even for the rather simple exponential distribution considered here.

The net effect of the correlation induced by comparing every sample to a threshold is reasonably described by assuming N is slightly larger and using (10.27). That is, the model

$$F \approx \frac{\tilde{N}}{1 - F_G(h; \tilde{N}, \lambda)} \quad (10.30)$$

where initially $\tilde{N} > N$ will be chosen so the model matches the lower bound in (10.29) for some adequately large decision threshold. This is illustrated in Fig. 10.5 where matching (10.30) and (10.29) at a threshold of $h = 40\lambda$ resulted in $\tilde{N} = 11.8$. As seen in the figure, using this in the model from (10.30) leads to a good

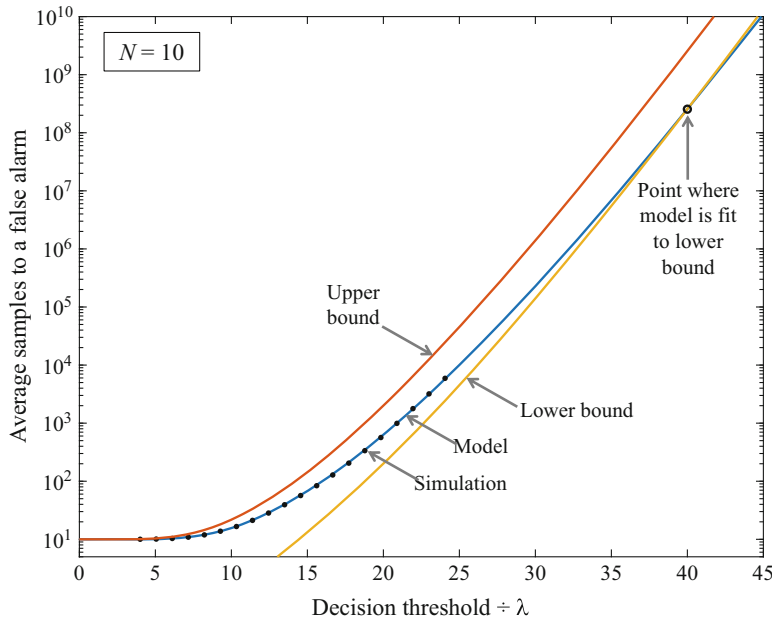


Fig. 10.5 Average number of samples to a false alarm as a function of the normalized decision threshold (h/λ) for a sliding incoherent sum of exponentially distributed intensity samples

approximation to F for smaller thresholds. Unfortunately, changing N results in a slightly different value of \tilde{N}/N with the ratio decreasing toward one as N increases. A practical approach to choosing the decision threshold as a function of F is to use simulation analysis at lower thresholds to obtain \tilde{N} by fitting to (10.30) and then the maximum of the model result in (10.30) and the lower bound in (10.29) as an approximation to F for larger thresholds. This approach is expected to be accurate for other data distributions (e.g., if the data are normalized first and therefore F distributed) as long as an accurate distribution is used for the sum. In the case of F -distributed data, the gamma distribution can be used in (10.30) as an approximation (by matching moments) to the sum if N is large enough. When the model in (10.30) is appropriate, it can be solved for the decision threshold h as a function of F ,

$$h = \lambda \tilde{\gamma}^{-1}\left(1 - \tilde{N}/F; \tilde{N}\right), \quad (10.31)$$

where $\tilde{\gamma}^{-1}(p; \alpha)$ is the functional inverse of the normalized incomplete gamma function. Because the inverse incomplete gamma function is an increasing function, increasing F clearly results in the anticipated increase in h .

10.4.2 Sliding M-of-N Detector

When the structure of the signal is such that an M -of- N detector is the appropriate detector when the starting time is known (see Sect. 10.3.1), the extension to an unknown starting time entails sliding the M -of- N detector along the data sequence to test every possible starting time. As shown in [16], a sliding M -of- N detector can be described as a discrete-time, finite-state Markov chain. A discrete-time Markov chain is one where the statistical model of the current state only depends on the state of the process at the previous time step. For the sliding M -of- N detector, the set of states essentially enumerates the 2^N combinations of the current and $N - 1$ previous binary samples formed by quantizing the data. The states of the process are described as either *accepting* or *non-accepting* with respect to satisfying the M -of- N criteria, so transition to an accepting state implies a detection and transition to a non-accepting state implies a continuation of the search for a signal. As shown in [17], the PMF of the stopping time (i.e., $f_k(k)$), ASNs, and even P_d for finite-duration signals can be obtained from the state transition matrix. However, the large number of states limits the practical utility of the approach to values of N not much larger than 10.

The sliding M -of- N detector can also be described as a type of *scan statistic*, which is used to represent counts of events occurring within a sliding window. Approximations to the ASN for a sliding M -of- N detector can be found in [18] or [19, Sect. 4.2]. Because these approximations assume a minimum stopping time of N , they are primarily useful for evaluating F or D when it is much larger than N . A modification to the approximation was presented in [13] to allow a detection to occur starting with M samples, which is useful for scenarios where D is on the order of N . A simpler alternative can be found when the single-sample success probability is sufficiently small, which is typical for the noise-only scenario. Using the terminology of Bernoulli trials, a *success* in a single sample is simply the observation of a threshold exceedance (i.e., $X_k \geq h_x$) whereas a *failure* occurs when there is no threshold exceedance. Thus, the single-sample success probability under the noise-only hypothesis is $p = \Pr\{X_k \geq h_x | H_0\}$. As described in [17, Sect. 3.3.1], a detection at time k in the sliding M -of- N detector requires the following three events to occur in sequence:

1. a failure at time $k - N$,
2. $M - 1$ successes occurring in the ensuing $N - 1$ samples, and
3. a success at time k .

The probability of these three events occurring is

$$\begin{aligned}\tilde{p} &\approx (1 - p) \cdot \left[\binom{N-1}{M-1} p^{M-1} (1-p)^{N-M} \right] \cdot p \\ &= \frac{\Gamma(N) p^M (1-p)^{N-M+1}}{\Gamma(M) \Gamma(N-M+1)}.\end{aligned}\tag{10.32}$$

Now define the event \mathcal{D}_i as an M -of- N detection occurring at the i th sample. The probability that the first M -of- N detection occurring at time k is then

$$f_k(k) = \Pr\{\overline{\mathcal{D}}_1 \overline{\mathcal{D}}_2 \cdots \overline{\mathcal{D}}_{k-1} \mathcal{D}_k\}. \quad (10.33)$$

When \tilde{p} is small, the probability of not observing an M -of- N detection at time $i-1$ (i.e., $\Pr\{\overline{\mathcal{D}}_{i-1}\}$) is nearly one so $\Pr\{\overline{\mathcal{D}}_i | \overline{\mathcal{D}}_{i-1}\} \approx \Pr\{\overline{\mathcal{D}}_i\}$ and

$$\Pr\{\overline{\mathcal{D}}_{i-1} \overline{\mathcal{D}}_i\} = \Pr\{\overline{\mathcal{D}}_i | \overline{\mathcal{D}}_{i-1}\} \Pr\{\overline{\mathcal{D}}_{i-1}\} \quad (10.34)$$

$$\approx \Pr\{\overline{\mathcal{D}}_i\} \Pr\{\overline{\mathcal{D}}_{i-1}\} = (1 - \tilde{p})^2. \quad (10.35)$$

Using this in (10.33) results in

$$f_k(k) \approx \tilde{p}(1 - \tilde{p})^{k-1} \quad (10.36)$$

for $k = 1, 2, \dots$, which is the PMF of one plus a geometric random variable as found in (10.6). The form of the stopping time PMF in (10.36) can also be shown to arise asymptotically as $k \rightarrow \infty$ with \tilde{p} as the largest eigenvalue of the sub-matrix formed from the continuing (i.e., non-accepting) states of the Markov chain [17]. Using (10.8), the average number of samples to a false alarm is then

$$F \approx \frac{1}{\tilde{p}} = \frac{\Gamma(M)\Gamma(N-M+1)}{\Gamma(N) p^M (1-p)^{N-M+1}}. \quad (10.37)$$

This small- p approximation is shown in Fig. 10.6 along with the scan-statistic approximation from [19, Sect. 4.2]. The agreement between the two for small values of p is evident as are the computational problems encountered in evaluating the scan-statistic approximation when $1/F$ reaches machine precision (i.e., for small p and large M). Analysis of a limited number of scenarios in [17] illustrated up to 10% relative logarithmic error in the small- p approximation (compared to the Markov-chain result) when $Np \leq 0.7$ or less than a 1% error when $Np \leq 0.07$. As seen in Fig. 10.6, the errors are worst for $M = 2$ (note that the exact result of $F = 1/p$ should be used for $M = 1$). The impact of this approximation on a ROC curve can be seen in Fig. 10.4 where a small difference is observed below roughly $\log_{10} F = 4.5$. Noting that $Np \approx 0.7$ when $\log_{10} F = 5$ for this scenario a 10% error might be expected in this region for smaller values of M ; however, less error is observed because the optimal M is six.

In the sliding M -of- N detector, using \tilde{p} from (10.32) is more accurate than using the probability of observing M successes in N trials, which is P_f in the known-starting-time scenario, however the difference is slight. This similarity can be used to argue that the optimal value of M described in Sect. 10.3.1.1, which approximately maximizes P_d for a wide range of P_f , will approximately maximize

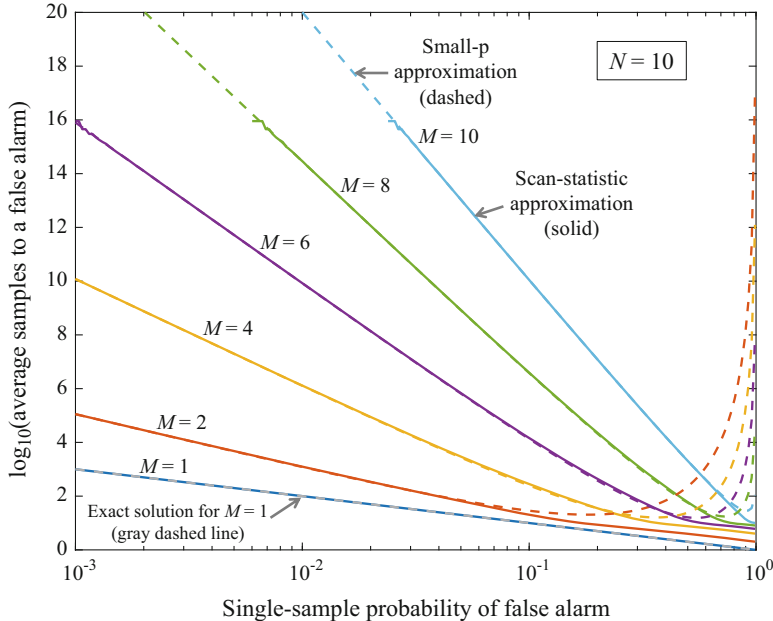


Fig. 10.6 Average number of samples to a false alarm for a sliding M -of- N detector as a function of the single-sample probability of false alarm for $N = 10$ and various values of M

P_d over a wide range of F in the sliding M -of- N detector as long as F is large. Alternatively, the approximations presented in [13] allow choosing M subject to using F as the false-alarm specification rather than P_f .

Given M , the quantization threshold h_x must then be chosen to satisfy the false alarm performance specification. This can be accomplished by solving (10.37) for p and then obtaining h_x by inverting the exceedance distribution function of the data (e.g., $h_x = -\lambda \log p$ for exponentially distributed data with mean λ). Solving (10.37) for p may be done by finding the roots of the polynomial

$$(-1)^{N-M+1} p^M (p-1)^{N-M+1} - \frac{\Gamma(M)\Gamma(N-M+1)}{F\Gamma(N)} = 0. \quad (10.38)$$

The correct root is generally the smallest positive real root. As seen in Fig. 10.6, there will be a root closer to one that is in the region where the approximation is not accurate. When F is large enough that $(1-p)^{N-M+1}$ can be assumed to be approximately one, (10.37) can be solved explicitly,

$$p \approx \left[\frac{\Gamma(M)\Gamma(N-M+1)}{F\Gamma(N)} \right]^{1/M}. \quad (10.39)$$

This can also be used to initialize a numerical search for the correct value, which becomes more important as p increases.

10.5 Detectors for Long-Duration Signals

In some scenarios the duration of a signal can be considered essentially infinite. These are often scenarios where action is required to change the underlying state of nature, such as occurs in obstacle avoidance. The infinite-duration signal also represents the traditional sequential detection framework, within which there are two fundamental types of hypothesis tests: the sequential probability ratio test (SPRT) and Page's test.

The SPRT, as described in Sect. 10.5.1, is used to quickly decide between two hypotheses. With respect to signal detection, this implies the starting time of the signal is known and the objective is to decide if it has occurred or not. This is an uncommon *detection* scenario in underwater acoustic signal processing applications, but is often applicable in the context of post-detection classification. Once an object has been detected, one of the ensuing inferential objectives is classification. In applications where repeated observations can be made with each having a fixed cost, a classification decision is required as quickly as possible so as to limit the total cost. The SPRT is also the building block of Page's test, which can be described as a sequence of SPRTs terminating at the noise-only hypothesis followed by one SPRT terminating at the signal-present hypothesis. As described in Sect. 10.5.2, Page's test is designed to rapidly detect a change that occurs at an unknown time. The unknown starting time is more common in remote-sensing applications and typified by the obstacle-avoidance example.

The performance metrics for the SPRT include the traditional Type I and II error probabilities (respectively P_f and $1 - P_d$ in the signal-detection context), but also the average number of samples required to make a decision. In Page's test the probabilities of false alarm and detection (for the infinite-duration signal) are both one when the test is allowed to run forever. Thus, its performance evaluation focuses on the average number of samples to detect a signal (D) and the average number of samples before a false alarm (F). Note that D and F differ from the average sample numbers of the SPRT in that the latter include both correct and incorrect decisions where D only reflects a correct decision and F an incorrect decision. Various approximations to these performance metrics are presented in Sects. 10.5.1 and 10.5.2. The application and analysis of an SPRT and Page's test to a finite-duration signal is covered later in Sect. 10.6.

10.5.1 Known Starting Time: Sequential Probability Ratio Test (SPRT)

When data are obtained sequentially in time and the inferential objective is to decide which of two hypotheses represent the data, the sequential probability ratio test (SPRT) uses less data on average than any other test with equal or smaller error probabilities. Before applying the SPRT to underwater acoustics application, the general form of this sequential hypothesis test will be developed and analyzed. In this scenario the observed data X_1, X_2, \dots are assumed to be independent and identically distributed, but are observed in sequence and so are not all immediately available for evaluation. The hypotheses to be tested,

$$\begin{aligned} H_0 : \quad X_k &\sim f_0(x) \\ H_1 : \quad X_k &\sim f_1(x), \end{aligned} \tag{10.40}$$

are similar to those previously considered in fixed sample size tests. Recall from Sect. 6.2.2 that there are two types of errors that can be made in hypothesis testing (Types I and II). In signal detection a Type I error is a false alarm and a Type II error is a missed detection (e.g., see Table 6.1). When testing a fixed quantity of data (e.g., the N samples X_1, \dots, X_N where N is fixed) the test is generally designed to control the probability of a Type I error (false alarm) and to minimize the probability of a Type II error (i.e., to maximize the probability of detection). In a sequential testing framework, the test is designed to control the probabilities of both errors occurring while using as little data as possible in making the decision. This is especially important when there is a cost associated with each observation. Although it can be advantageous to know that the test achieves specific error probabilities, the uncontrollable part becomes the amount of data required to make a decision, which is itself a random variable. Similar to how reducing P_f in a fixed-sample-size detector leads to an increase in the decision threshold and therefore a reduction in P_d , reducing the error probabilities in a sequential detector will lead to more extreme thresholds and consequently a need for more data.

As before, define the data up to the k th time sample as $\mathbf{x}_k = [X_1 \ \dots \ X_k]^T$. The SPRT decision statistic is simply the likelihood ratio of all of the data observed through time k ,

$$T_k(\mathbf{x}_k) = \frac{f_1(\mathbf{x}_k)}{f_0(\mathbf{x}_k)} \tag{10.41}$$

where $f_i(\mathbf{x}_k)$ is the joint PDF of the first k samples of data under hypothesis H_i . After observing the k th data sample one of three possible decisions is made:

1. Decide H_1 if $T_k(\mathbf{x}_k) \geq B$
2. Decide H_0 if $T_k(\mathbf{x}_k) \leq A$
3. Remain undecided and obtain another sample if $T_k(\mathbf{x}_k) \in (A, B)$

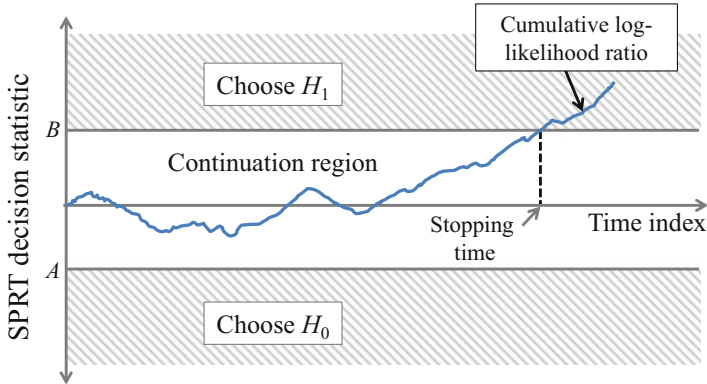


Fig. 10.7 Example decision statistic for a sequential probability ratio test (SPRT) illustrating the regions where each hypothesis is chosen and the continuation region where more data must be obtained before a decision can be made

where A and B are the decision thresholds. This decision process is described through an example in Fig. 10.7. The stopping time³ of the test is the first time the decision statistic departs the continuation region,

$$K = \min\{k \geq 1 : T_k(\mathbf{x}_k) \notin (A, B)\}. \quad (10.42)$$

The number of samples required to make a decision can change each time the test is run. Approximations for the average number of samples used are presented in Sect. 10.5.1.2 and generally used to assess performance. Noting the continuation region in Fig. 10.7, it seems possible for the test to never produce a decision and continue ad infinitum. Fortunately, as long as the log-likelihood ratio does not place all weight at zero, the probability of a finite stopping time is one.⁴ However, it is possible for a very large number of samples to be required. This can be avoided by forcing a decision after a certain number of observations have been obtained using a *truncated SPRT* (see Sect. 10.6.1.2 for more details).

The SPRT is optimal in the context of the sequential testing of two simple hypotheses with independent and identically distributed data. More specifically, the Wald-Wolfowitz theorem ([21] or [2, Sect. 2.9]) dictates that the SPRT has the smallest average sample numbers under H_0 and H_1 of all tests having equal or lower Type I and II error probabilities. It is important to note that the requirement

³Note that in most texts on sequential detection and hypothesis testing the variable N is used to describe the stopping time. In this text the variable K is used so as to avoid confusion with the N in M -of- N detectors.

⁴This can be shown using the results of [20] which dictate that if the data are *iid* and $\Pr\{\log[f_1(X)/f_0(X)] = 0\} < 1$, then $\Pr\{K > k\} < cr^k$ for some $c > 0$ and $r \in (0, 1)$ with the stopping time K as in (10.42).

for simple hypotheses in the SPRT and its optimality implies there is explicit knowledge of the likelihood ratio—both $f_0(x)$ and $f_1(x)$ must be completely specified. Extensions to handle composite hypothesis tests or dependent data are beyond the scope of this text; however, the former are addressed in [1, Ch. 4], [2, Ch. 3], or [4, Sects. 3.5 & 3.6, Ch. 5] and the latter in [2, Sect. 2.12] and [4, Sects. 3.3 & 3.4]. Of particular interest are the locally optimal version for weak signals [22] or [4, Sect. 3.5], the robust version [23] that censors (limits) the log-likelihood ratio from above and below, and sequential tests that are invariant to nuisance parameters [24] or [4, Sect. 3.6]. Dependence of the data sequence in the form of a Markov model can be found in [25] and [26].

10.5.1.1 Decision Thresholds and Error Probabilities

Let the probability of a Type I error be α and that of a Type II error be β . Wald's approximations [1, Sect. 3.2]⁵ to the decision thresholds in the SPRT then satisfy the inequalities

$$\frac{\beta}{1 - \alpha} \leq A \quad \text{and} \quad B \leq \frac{1 - \beta}{\alpha}. \quad (10.43)$$

In the derivation of these bounds it is assumed that the value of the likelihood ratio for \mathbf{x}_K when the test stops (which is indicated by the use of K rather than k) exceeds the threshold. For example, when the test terminates in a “decide H_1 ” state the second inequality in (10.43) arises from assuming

$$B \leq \frac{f_1(\mathbf{x}_K)}{f_0(\mathbf{x}_K)} = \left[\frac{f_1(\mathbf{x}_{K-1})}{f_0(\mathbf{x}_{K-1})} \right] \left[\frac{f_1(X_K)}{f_0(X_K)} \right]. \quad (10.44)$$

The right side of (10.44) factors the decision statistic at time K into the product of the decision statistic at time $K - 1$ and the likelihood ratio of the data observed at time K . Because the test stops at time K and not $K - 1$, the decision statistic at time $K - 1$, which is the first term in brackets in (10.44), must be less than B . Stopping at time K then implies that the likelihood ratio for the data observed at time K is far enough above unity to push the decision statistic above the threshold. When the error probabilities are small, the decision thresholds and number of samples to a decision will be large. This final contribution from the likelihood ratio of the data observed at time K is therefore expected to be small relative to the decision statistic at time $K - 1$. The amount by which the decision statistic exceeds the threshold will therefore also be small, which implies the equalities in (10.43) can be used to approximately set the thresholds.

⁵Note that in Wald's book [1] and some others on sequential analysis, A and B are the opposite of the variables used here.

In order to examine what occurs when the bounds are not very tight, suppose the thresholds are chosen based on design values of α_d and β_d for the error probabilities,

$$A = \frac{\beta_d}{1 - \alpha_d} \quad \text{and} \quad B = \frac{1 - \beta_d}{\alpha_d}. \quad (10.45)$$

Using these in the inequalities in (10.43) where α and β are the actual error probabilities encountered using A and B then results in the inequalities

$$\beta(1 - \alpha_d) \leq \beta_d(1 - \alpha) \quad \text{and} \quad \alpha(1 - \beta_d) \leq \alpha_d(1 - \beta). \quad (10.46)$$

Summing these two inequalities results in

$$\alpha + \beta \leq \alpha_d + \beta_d, \quad (10.47)$$

so the total probability of error (if H_0 and H_1 are equally likely to occur) observed will always be less than that of the design.

10.5.1.2 Average Sample Numbers for the SPRT

Before approximating the ASNs of the SPRT, it is useful to transform the test to a log-likelihood-ratio representation. Define

$$Z_k = \log \left[\frac{f_1(X_k)}{f_0(X_k)} \right] \quad (10.48)$$

as the log-likelihood ratio of the k th data sample and transform the decision thresholds to

$$a = \log A \quad \text{and} \quad b = \log B. \quad (10.49)$$

The stopping time from (10.42) is then

$$K = \min \left\{ k \geq 1 : \sum_{i=1}^k Z_i \notin (a, b) \right\}, \quad (10.50)$$

which assumes the data are independent so the joint PDFs factor into products that become sums in the log-likelihood ratio. The decision statistic at time k is therefore the sum of the log-likelihood functions of the data samples up to time k ,

$$\Sigma_k = \sum_{i=1}^k Z_i. \quad (10.51)$$

The ASNs can now be derived using Wald's fundamental identity [2, Sect. 2.5], which states that

$$E\left[e^{t\Sigma_K} M(t)^{-K}\right] = 1 \quad (10.52)$$

for all t such that the moment generating function of Z_k ,

$$M(t) = E\left[e^{tZ_k}\right], \quad (10.53)$$

exists and as long as $\Pr\{Z_k = 0\} < 1$. Note that the use of K in (10.52) indicates that it is the random stopping time of the test and Σ_K is the corresponding decision statistic at the stopping time that must have traversed one of the decision thresholds. If K were in fact a non-random positive integer, the validity of (10.52) is obvious.

Differentiating both sides of (10.52) with respect to t results in

$$E\left[\Sigma_K e^{t\Sigma_K} M(t)^{-K} - K e^{t\Sigma_K} M(t)^{-K-1} M'(t)\right] = 0. \quad (10.54)$$

Evaluating this at $t = 0$, noting that $M(0) = 1$ and $M'(0) = E[Z_k]$, and rearranging terms results in Wald's first equation,

$$E[K] = \frac{E[\Sigma_K]}{E[Z_k]}, \quad (10.55)$$

which describes the ASN in terms of the average value of the decision statistic when the test terminates and the average of the log-likelihood ratio of the data. The expected value of the decision statistic at the stopping time can be approximated by assuming it is near one of the thresholds. Under the null hypothesis, it is near the upper threshold (b) with probability α (i.e., a Type I error occurs) and near the lower threshold (a) when H_0 is correctly chosen, which occurs with probability $1 - \alpha$. This results in

$$E[\Sigma_K | H_0] \approx (1 - \alpha)a + \alpha b \quad (10.56)$$

and similar arguments lead to

$$E[\Sigma_K | H_1] \approx \beta a + (1 - \beta)b \quad (10.57)$$

for the alternative hypothesis. Using these approximations in (10.55) results in the ASN approximations

$$E[K | H_0] \approx \frac{(1 - \alpha)a + \alpha b}{E_0[Z_k]} \quad (10.58)$$

and

$$E[K|H_1] \approx \frac{\beta a + (1 - \beta)b}{E_1[Z_k]} \quad (10.59)$$

which only require the error probabilities, decision thresholds, and average log-likelihood ratio under the two hypotheses.

When the decision thresholds are not overly large, the assumption that the decision statistic only just crosses it when the test terminates may not be accurate. As described in Sect. 10.5.1.3, correction terms have been developed [27] that improve the approximation.

As an example, suppose a sequential detector is used to initiate a track when the data are exponentially distributed with unit mean under the noise-only hypothesis and with mean $1 + s$ when signal is present,

$$\begin{aligned} H_0 : X_k &\sim \text{Expon}\{1\} \\ H_1 : X_k &\sim \text{Expon}\{1 + s\}. \end{aligned} \quad (10.60)$$

The log-likelihood ratio is easily shown to be

$$Z_k = \frac{sX_k}{1+s} - \log(1+s). \quad (10.61)$$

Note that its mean when there is only noise present,

$$E[Z_k|H_0] = \frac{s}{1+s} - \log(1+s) < 0, \quad (10.62)$$

is negative and when there is signal present,

$$E[Z_k|H_1] = s - \log(1+s) > 0, \quad (10.63)$$

is positive. Using these with (10.58) and (10.59) to evaluate the ASN produces ROC curves like those found in Fig. 10.8 where the average number of samples required to correctly accept a track on an object of interest is shown as a function of the average number of samples required to reject a false track (which occur under H_0). These curves are produced by varying the SNR of the data, which makes them different from standard ROC curves, but illustrates how increasing SNR produces quicker decisions. In this example, a Type I error (α) implies a false track was generated while a Type II error (β) implies no track was formed on an object of interest. The error operating points evaluated illustrate a desire to correctly detect tracks most of the time (i.e., with probability 0.9 for which $\beta = 0.1$ or probability 0.99 for which $\beta = 0.01$) while rarely ($\alpha = 10^{-2}$) or very rarely ($\alpha = 10^{-4}$) forming false tracks. From (10.43), the effect of decreasing β is to increase the magnitudes of the logarithmic decision thresholds (i.e., a and b), but more dramatically for the

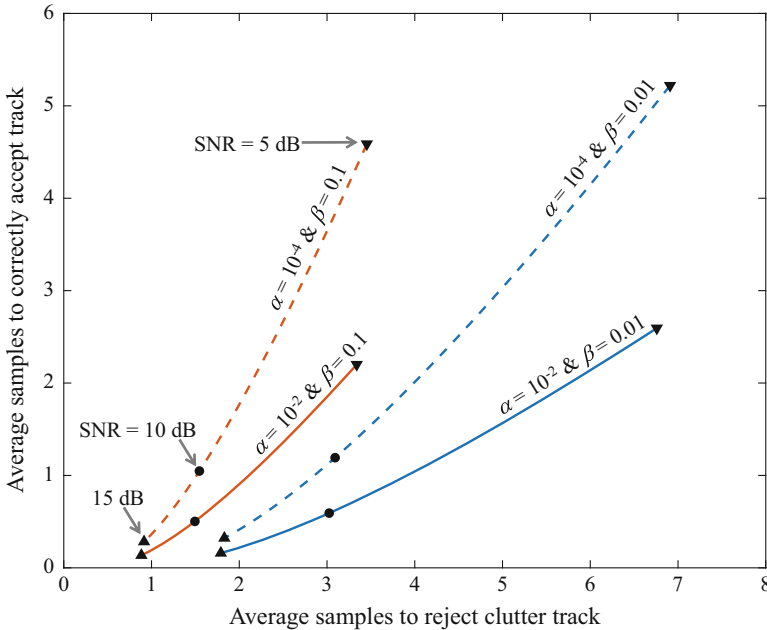


Fig. 10.8 Average number of samples to correctly accept a track on an object of interest as a function of that required to reject a false track for various error probabilities and SNRs

lower threshold $a = \log A = \log(\beta) - \log(1 - \alpha)$. Reducing this decision threshold makes it harder to reject a false track, which can be seen in Fig. 10.8 by the blue lines ($\beta = 0.01$) being to the right of the reddish-brown lines ($\beta = 0.1$). Because it is harder to reject a false track, it is also harder to incorrectly reject a target track, which corresponds to the decrease in β .

Given the error operating points and an SNR, it is possible to evaluate the smallest fixed-sample-size test achieving the same performance as the SPRT. Consider the highest-quality operating point shown in Fig. 10.8 (i.e., $\alpha = 10^{-4}$ and $\beta = 0.01$) and an SNR of 10 dB, which is the circle on the blue dashed line in the figure. A fixed-sample-size test would require six samples to achieve the same performance as the SPRT, which only requires on average 3.1 samples to reject false tracks and 1.2 samples to accept correct tracks. Although this appears to be a significant savings, there are disadvantages to the SPRT. For example, some realizations may require many more samples than the average to make a decision. There will also be a performance loss arising from mismatch when there is a difference between the SNR the track detector is designed for and the SNR of the observed data. However, a distinct advantage of the SPRT in this application lies in its ability to make a decision at every update, whereas the fixed-sample-size detector requires some finite number of samples to make a decision. Forcing a decision with the SPRT, for example when the track ends abruptly, can also be done with an

understanding of how this changes the error probabilities (e.g., see the truncated SPRT in Sect. 10.6.1.2).

10.5.1.3 Overshoot Corrections to the SPRT Average Sample Numbers

The assumption that the SPRT decision statistic equals the decision threshold when the test stops can be inaccurate when the threshold is not large as compared to the update itself. Corrections that account for overshooting the threshold were developed by Siegmund [27] (also found in [5, Ch. X]) through the use of a Brownian-motion approximation to the decision statistic. The correction terms are employed by increasing the magnitude of the thresholds a and b in (10.58) and (10.59) by an amount equal to the average overshoot, ρ_i^\pm . That is, using the log-likelihood-ratio thresholds

$$a_{c,i} = a + \rho_i^- \quad \text{and} \quad b_{c,i} = b + \rho_i^+ \quad (10.64)$$

where $\rho_i^- < 0 < \rho_i^+$ represent the average overshoot of the two thresholds. The subscript i indicates that the correction is evaluated under hypothesis H_i . As described in [28, Sect. 4.2.3.2], this also necessitates updating the likelihood-ratio thresholds A and B by using (10.64) in (10.49). These are then used to correct the probabilities of stopping at either threshold by solving (10.45) for α_d and β_d , which then results in

$$\alpha_c = \frac{1 - e^{a_{c,0}}}{e^{b_{c,0}} - e^{a_{c,0}}} \quad (10.65)$$

and

$$\beta_c = \frac{e^{a_{c,1}}(e^{b_{c,1}} - 1)}{e^{b_{c,1}} - e^{a_{c,1}}}. \quad (10.66)$$

The average sample numbers are now formed by using the corrected thresholds and stopping probabilities in (10.56) and (10.57), resulting in

$$E[K|H_0] \approx \frac{(1 - \alpha_c)(a + \rho_0^-) + \alpha_c(b + \rho_0^+)}{E_0[Z_k]} \quad (10.67)$$

and

$$E[K|H_1] \approx \frac{\beta_c(a + \rho_1^-) + (1 - \beta_c)(b + \rho_1^+)}{E_1[Z_k]}. \quad (10.68)$$

The average overshoots ρ_i^\pm are obtained by first standardizing the SPRT update $Z = Z_k$ to have zero mean and unit variance,

$$Y = \frac{Z - \mu_Z}{\sigma_Z} \quad (10.69)$$

where μ_Z and σ_Z are, respectively, the mean and standard deviation of Z . The characteristic function of Y is then seen to be $e^{-j\omega\mu_Z/\sigma_Z}$ times the characteristic function of Z evaluated at ω/σ_Z ,

$$\Phi_Y(\omega) = E[e^{j\omega Y}] = e^{-j\omega\mu_Z/\sigma_Z} E[e^{j(\omega/\sigma_Z)Z}]. \quad (10.70)$$

The average overshoots can now be described as

$$\rho_i^\pm = \sigma_Z \left(\frac{\eta_{3,Z}}{6} \mp \frac{\phi}{\pi} \right) \quad (10.71)$$

where all expectations occur under hypothesis H_i ,

$$\eta_{3,Z} = \frac{E[(Z - \mu_Z)^3]}{\sigma_Z^3} = E[Y^3] \quad (10.72)$$

is the skewness of Z , and the function

$$\phi = \int_{\omega=0}^{\infty} \omega^{-2} \operatorname{Real} \left[\log \left\{ \frac{2}{\omega^2} [1 - \Phi_Y(\omega)] \right\} \right] d\omega \quad (10.73)$$

generally needs to be evaluated numerically. As described in [28, Sect. 4:1.11], the correction factors for Gaussian data are $\rho^\pm = \pm 0.5826\sigma_Z$ and from [29] the correction factors for exponentially distributed data are $\rho_i^+ = \sigma_Z$ and $\rho_i^- = -\sigma_Z/3$. The correction factors for the gamma distribution, which spans these two distributions, are shown in Fig. 10.9 as a function of the shape parameter (note that what is plotted is ρ_i^+/σ_Z and $-\rho_i^-/\sigma_Z$). For very large shape parameters, the gamma distribution is approximately Gaussian and so the correction factors converge on the aforementioned $\rho^\pm = \pm 0.5826\sigma_Z$, which represents symmetry in the overshoot when traversing the upper and lower thresholds arising from symmetry in the distribution of Z . As the gamma shape parameter decreases, it becomes increasingly skewed, which results in a larger overshoot for the upper threshold than the smaller. This is quantified above by the correction factors for exponentially distributed data, which are the black dots seen in Fig. 10.9 when the gamma shape parameter is one.

An example evaluation of the average sample numbers with and without correction is shown in Fig. 10.10 when the data are exponentially distributed with mean $1 + s$ under H_1 , which represents the intensity of a Gaussian-fluctuating

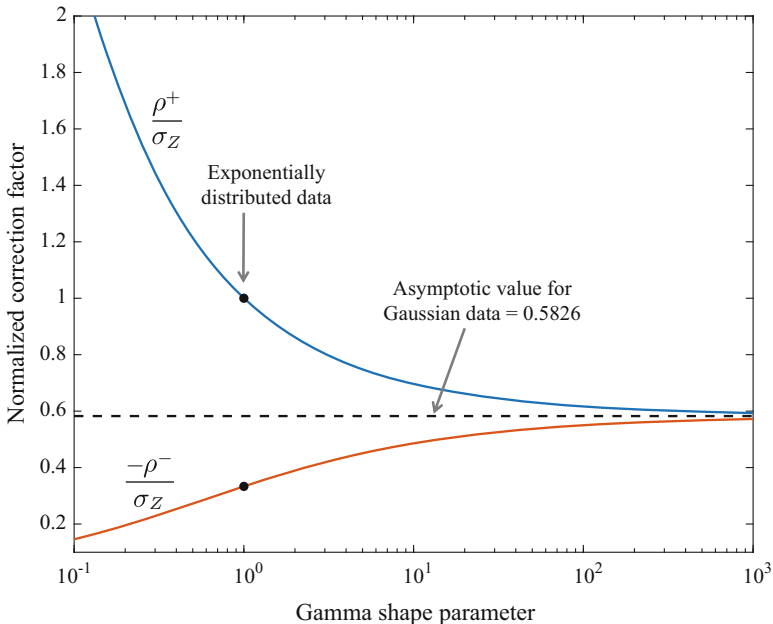


Fig. 10.9 Normalized correction factors to the thresholds for calculating the average sample number of an SPRT when the update is gamma distributed as a function of the shape parameter

signal in Gaussian noise. In the example the errors are symmetric (i.e., $\alpha_d = \beta_d$) so the thresholds have a common amplitude ($a = -b$). The corrected approximations are better than the standard approximations over a wide range of decision thresholds. Compared with a simulation, the correction is quite accurate under H_1 and still somewhat low under H_0 . The quantization approach, which is described in Sect. 10.6.1.1, will generally be the most accurate if the quantization is done finely enough.

10.5.2 Unknown Starting Time: Page's Test

In some remote sensing scenarios where the starting time of the signal of interest is unknown, the signal persists indefinitely or at least for a very long time once it appears. This signal characterization is commonly used to represent failure of a machinery component in manufacturing and detectors are designed to quickly detect the change in order to minimize production loss. An underwater acoustics application can be found in collision avoidance where a signal from an object on a colliding path persists until action is taken to maneuver.

The data are assumed to follow a noise-only model up until the time at which the signal appears, when they then begin to follow the signal-plus-noise model. If p

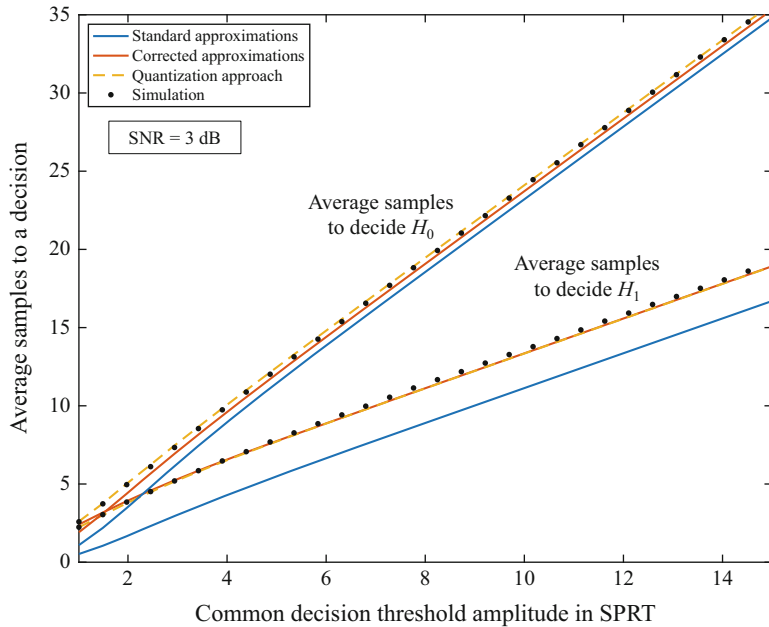


Fig. 10.10 Average number of samples to a decision as a function of the common threshold amplitude (i.e., $a = -b$) in an SPRT using the standard approximations, the corrected approximations, quantization approach from Sect. 10.6.1.1, and via simulation

is the last noise-only sample before the signal is observed, the data are assumed to follow the distributions according to

$$X_k \sim \begin{cases} f_0(x) & k \leq p \\ f_1(x) & k > p \end{cases}. \quad (10.74)$$

The noise-only hypothesis can be represented by letting $p \rightarrow \infty$ so the data always follow PDF $f_0(x)$. In what is known as a *quickest detection* or *change-point* problem, it is desired to detect that a change has occurred as soon as possible after it happens.

If the data are independent of each other, the likelihood ratio describing (10.74) for data through time k is

$$L(\mathbf{x}_k; p) = \frac{\prod_{i=1}^p f_0(x_i) \prod_{i=p+1}^k f_1(x_i)}{\prod_{i=1}^k f_0(x_i)} \quad (10.75)$$

$$= \prod_{i=p+1}^k \frac{f_1(x_i)}{f_0(x_i)}. \quad (10.76)$$

If the signal has not occurred yet (i.e., $p \geq k$), the likelihood ratio is simply one because the numerator and denominator in (10.75) will be identical. As can be seen from (10.76), the data up to time p do not play a role in forming the likelihood ratio when p is known. However, p is assumed to be unknown and therefore must be estimated. Toward this end, define the detector function

$$g(x) = \log \left[\frac{f_1(x)}{f_0(x)} \right] \quad (10.77)$$

as the logarithm of the ratio of the PDFs of one data sample containing signal to the noise PDF.⁶ Given the starting time of the signal, the log-likelihood ratio (LLR) representing the data model in (10.74) when p is known is then the sum over this detector function applied to the data when the signal is present,

$$l(\mathbf{x}_k; p) = \sum_{i=p+1}^k g(x_i). \quad (10.78)$$

By defining the cumulative sum of $g(x)$ applied to the data through time sample k as

$$\Sigma_k = \sum_{i=1}^k g(x_i) \quad (10.79)$$

the LLR can be described by

$$l(\mathbf{x}_k; p) = \Sigma_k - \Sigma_p. \quad (10.80)$$

For the scenario where the signal starts with the first observation (i.e., $p = 0$), define an initial value for the cumulative sum as $\Sigma_0 = 0$. Because p is unknown, a GLR detector can be formed by estimating p . Because p does not enter into the null hypothesis (i.e., it is not in the denominator of (10.75)), its maximum-likelihood estimate can be obtained by maximizing (10.80). This results in choosing the time index of the minimum observed cumulative sum of the log-likelihood ratio,

$$\hat{p} = \arg \min_{i \leq k} \Sigma_i. \quad (10.81)$$

⁶As an arcane side note, $g(x)$ in (10.77) is not specifically a log-likelihood ratio of the data model in (10.74) because it does not differentiate whether signal is present or not based on the time index.

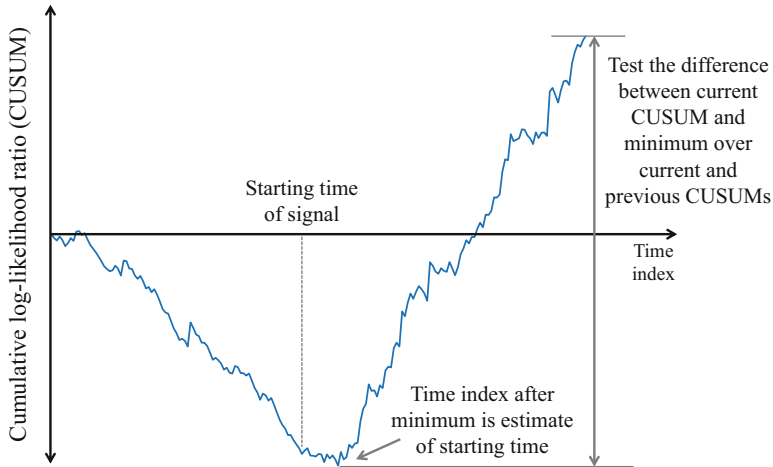


Fig. 10.11 Example illustrating the decision statistic for Page's test as the difference between the current value and minimum of the cumulative log-likelihood ratio

Inserting \hat{p} into (10.80) results in the GLR detector decision statistic given k observations,

$$T_k = l(\mathbf{x}_k; \hat{p}) = \Sigma_k - \min_{i \leq k} \Sigma_i \quad (10.82)$$

where the dependence of T_k on \mathbf{x}_k has been suppressed. If the minimum observed cumulative sum occurs at time k (i.e., $\hat{p} = k$) when only k samples have been observed, then $T_k = 0$ and there is no support in the data for a signal having started. An example cumulative log-likelihood ratio is depicted in Fig. 10.11, showing how the decision statistic is the difference between the current cumulative LLR and the minimum previously observed.

This detector is known as a CUSUM (cumulative summation) detector [4, Sect. 8.2], but is commonly called Page's test owing to its derivation by E. S. Page [30]. It is typically implemented sequentially in the following manner. The data through time k are used to form T_k in (10.82) and a signal detection is declared only if T_k exceeds a threshold h . If no signal is detected at time k , another sample is obtained in order to form the decision statistic at time $k+1$ and again assess if a detection has occurred. The stopping time is therefore as defined in (10.4) with a fixed decision threshold,

$$K = \min\{k \geq 1 : T_k \geq h\}. \quad (10.83)$$

When the detector function is the LLR between the signal-present and noise-only PDFs (i.e., $g(x)$ as in (10.77)), Page's test is optimal in the sense of minimizing the worst-case average number of samples required for detection (D) given a

constrained average number of samples to a false alarm (F) [31, 32]. The definition of “worst-case” with respect to D is that the signal starts in the sample directly following one at which the cumulative sum in (10.79) achieves a new minimum and so has the furthest to travel before a threshold exceedance can occur.

The form of the detector decision statistic in (10.82) appears to require retaining data observations back to the most recent minimum. Fortunately, an iterative update can be derived by breaking up the “min” in (10.82) into a minimum over the cumulative sum through k and through $k - 1$, carrying the negative sign inside to convert the minimum to a maximum, and simplifying to yield

$$\begin{aligned} T_k &= \Sigma_k - \min_{i \leq k} \Sigma_i \\ &= \Sigma_k - \min \left\{ \Sigma_k, \min_{i \leq k-1} \Sigma_i \right\} \\ &= \max \left\{ 0, \Sigma_k - \min_{i \leq k-1} \Sigma_i \right\}. \end{aligned} \quad (10.84)$$

Now by describing the cumulative sum at time k as the cumulative sum at time $k - 1$ plus the update at time k , $\Sigma_k = \Sigma_{k-1} + g(x_k)$, the iterative update is revealed as

$$T_k = \max \{0, T_{k-1} + g(x_k)\}. \quad (10.85)$$

This one-step-update form of the Page’s test decision statistic is clearly seen to saturate at a lower boundary of zero when it believes there is only noise. Once the signal starts, $g(x_k)$ will generally be positive and so T_k is also positive and the maximum operation always returns the latter argument, which performs a cumulative summation over the data after applying the detector function. A plot of the decision statistic as formed from the cumulative sum from Fig. 10.11 is shown in Fig. 10.12. In this form of the decision statistic, the starting time estimate can be obtained as the time after the most recent reset to zero [33].

10.5.2.1 Average Sample Numbers for Page’s Test

If the Page’s test detector described by (10.85) is run with an infinite observation time, it will eventually produce a threshold exceedance and stop. This implies that the probabilities of detection and false alarm are both equal to one. For this reason, the performance metrics are the average number of samples required for detection (D) and the average number of samples to a false alarm (F).

In order to determine the average sample numbers (ASNs) for Page’s test, it is necessary to describe it as a sequence of SPRTs. In essence, every time T_k resets to zero it represents an SPRT terminating at the noise-only hypothesis. When T_k exceeds the decision threshold h , it is a final SPRT terminating at the signal-present hypothesis. Although the SPRT thresholds described in Sect. 10.5.1 should be $a = 0$

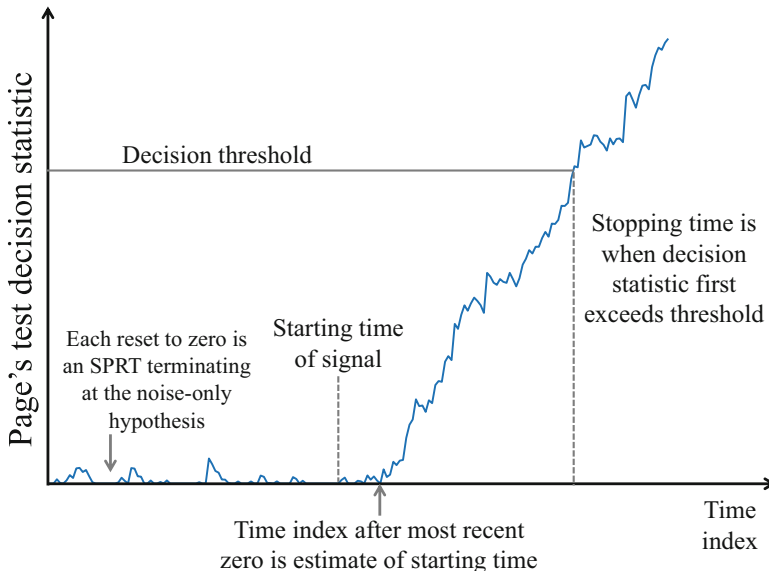


Fig. 10.12 Page's test decision statistic and threshold illustrating detecting the signal and estimating its starting time

and $b = h$, suppose initially that each SPRT is constructed with the lower decision threshold at a generic value a and for congruity retain the label b on the upper threshold. Let $s \geq 0$ be an SNR measure such that $s = 0$ is the noise-only case and suppose the data are identically distributed. While this clearly occurs when there is only noise, it implies that for this analysis the signal is assumed to start in the first sample when it is present. The resulting ASN when signal is present will therefore be the average number of samples required for detection (i.e., the “ $D_0 - 1$ ” in (10.9) has already been subtracted). To facilitate deriving approximations to the ASNs, define the following variables:

$\text{SPRT}(a, b)$ = an SPRT with continuation region (a, b)

$P_a(s)$ = probability an $\text{SPRT}(a, b)$ ends at a

$\bar{N}(s)$ = ASN for an $\text{SPRT}(a, b)$

$\bar{N}_a(s)$ = ASN for an $\text{SPRT}(a, b)$ ending at a

$\bar{N}_b(s)$ = ASN for an $\text{SPRT}(a, b)$ ending at b

$\bar{K}_a(s)$ = ASN for Page's test with a reset to a (rather than 0)

The desired ASN for Page's test is then $\lim_{a \rightarrow 0} \bar{K}_a(s)$ with $b = h$. Because the data are identically distributed, the probability $P_a(s)$ of the $\text{SPRT}(a, b)$ terminating at a is the same for each SPRT. The probability that there are l such SPRTs terminating at a followed by one terminating at b is then

$$f_L[l] = [P_a(s)]^l [1 - P_a(s)] \quad \text{for } l = 0, 1, \dots, \quad (10.86)$$

which describes the probability mass function of a geometric random variable. Thus, the number of SPRT terminations at a in a Page's test with a lower absorbing boundary at a is a geometric random variable with success probability $1 - P_a(s)$ (i.e., the probability the SPRT terminates at b).

Given that there are L SPRTs terminating at a before a final one terminating at b , the average number of samples for Page's test is

$$\bar{K}_a(s)|L = L\bar{N}_a(s) + \bar{N}_b(s), \quad (10.87)$$

where as noted above $\bar{N}_a(s)$ and $\bar{N}_b(s)$ are the ASNs for the $\text{SPRT}(a, b)$ terminating at, respectively, a and b . The ASN for Page's test can then be found by taking the expectation of (10.87) over L . Noting that the mean of a geometric random variable with success probability $1 - p$ is $p/(1 - p)$, this results in

$$\begin{aligned} \bar{K}_a(s) &= E[L\bar{N}_a(s) + \bar{N}_b(s)] \\ &= \frac{P_a(s)\bar{N}_a(s)}{1 - P_a(s)} + \bar{N}_b(s) \\ &= \frac{\bar{N}(s)}{1 - P_a(s)} \end{aligned} \quad (10.88)$$

where

$$\bar{N}(s) = P_a(s)\bar{N}_a(s) + [1 - P_a(s)]\bar{N}_b(s) \quad (10.89)$$

is the ASN for an $\text{SPRT}(a, b)$. Using Wald's first equation from (10.55) and assuming the value of the decision statistic when the test ends is equal to the decision threshold, this can be approximated by

$$\bar{N}(s) = \frac{E[\Sigma_N]}{E[Z_n]} \approx \frac{aP_a(s) + b[1 - P_a(s)]}{E_s[g(X)]} \quad (10.90)$$

where N is used for the stopping time of the SPRT to differentiate it from K for Page's test. A subscript s or 0 on an expectation is used where necessary to note that the PDF is either for the data with the given SNR or for the noise-only case. Here it must also be assumed that the mean of the update is not zero,

$$E_s[g(X)] \neq 0 \quad (10.91)$$

where X represents a data observation with SNR s . Inserting (10.90) into (10.88) results in

$$\bar{K}_a(s) = \frac{a}{E_s[g(X)]} \left[\frac{P_a(s)}{1 - P_a(s)} \right] + \frac{b}{E_s[g(X)]}. \quad (10.92)$$

A difficulty is now encountered when a tends to zero because this causes $P_a(s)$ to tend to one, which results in the undefined ratio 0/0 in the first term in (10.92). Application of L'Hôpital's rule to simplify (10.92) requires the derivative of $1 - P_a(s)$ with respect to a evaluated as $a \rightarrow 0$. Recall Wald's fundamental identity from (10.52),

$$E\left[e^{t\Sigma_N} M(t)^{-N}\right] = 1, \quad (10.93)$$

which relates the stopping time (N) of the SPRT, the corresponding value of the decision statistic (Σ_N), and the moment generating function (MGF) of the update, $M(t) = E[e^{tg(X)}]$. An approximation to $P_a(s)$ can be obtained through the use of Wald's fundamental identity under some mild regularity conditions on $g(X)$ that are described in detail in Sect. 10.5.2.2. When the detector function satisfies the regularity conditions, there exists a unique value t_s not equal to zero for which $M(t_s) = 1$. Using this value in Wald's fundamental identity results in

$$\begin{aligned} 1 &= E\left[e^{t_s \Sigma_N}\right] \\ &\approx P_a(s)e^{t_s a} + [1 - P_a(s)]e^{t_s b}, \end{aligned} \quad (10.94)$$

where $1^N = 1$ even if N is random and it has been assumed that the SPRT decision statistic takes on the value of the threshold when it terminates. Solving (10.94) for $P_a(s)$ then results in

$$P_a(s) = \frac{1 - e^{bt_s}}{e^{at_s} - e^{bt_s}} \quad (10.95)$$

which leads to the desired derivative

$$\frac{d}{da}[1 - P_a(s)]\Big|_{a=0} = \frac{t_s}{1 - e^{bt_s}}. \quad (10.96)$$

The ASN for Page's test can now be approximated by using (10.96) with L'Hôpital's rule applied to (10.92) to produce

$$\bar{K}(s) = \lim_{a \rightarrow 0} \bar{K}_a(s) \approx \frac{h + t_s^{-1}[1 - e^{ht_s}]}{E_s[g(X)]} \quad (10.97)$$

where b has been set to h to correspond to the definition of the stopping time in (10.83). Before proceeding to explore the properties of the ASN for Page's test under the noise-only and signal-present hypotheses, an excursion is taken to describe t_s , the non-zero unity root of the MGF.

10.5.2.2 Unity Roots of the Moment Generating Function

A unity root of the moment generating function (MGF) of a random variable $Z = g(X)$ is a value t such that

$$M(t) = E[e^{tZ}] = 1. \quad (10.98)$$

Clearly $t = 0$ satisfies this for any random variable Z . Under mild regularity conditions, a non-zero value of t will also satisfy (10.98). The fundamental enabling condition is that the MGF exist on some large enough region (t_-, t_+) including zero in the interior of the interval. This can be described as requiring Z to have finite moments. For example, the MGF of the F distribution does not exist for $t > 0$ and so does not satisfy this condition, nor are all its moments finite.

Depictions of the MGF when the mean of Z is positive and negative are shown in Fig. 10.13. Note that in both cases the MGF passes through one when $t = 0$ and that the slope at zero is the mean of Z (i.e., $M'(0) = E[Z]$). Thus, the MGF decreases from one either as t decreases from zero when the mean of Z is positive or as t increases from zero when the mean of Z is negative. Clearly this requires $E[Z] \neq 0$. Now note that the second derivative of the MGF is always positive,

$$M''(t) = E\left[Z^2 e^{tZ}\right] > 0, \quad (10.99)$$

so the function is strictly convex, with the exclusion of the degenerate case where Z equals zero with probability one. The expectation form of the MGF can be decomposed by conditioning on the three events $\{Z < 0\}$, $\{Z > 0\}$ and $\{Z = 0\}$, and then removing the conditioning to produce

$$M(t) = E\left[e^{tZ} | Z < 0\right] \Pr\{Z < 0\} + E\left[e^{tZ} | Z > 0\right] \Pr\{Z > 0\} + \Pr\{Z = 0\}. \quad (10.100)$$

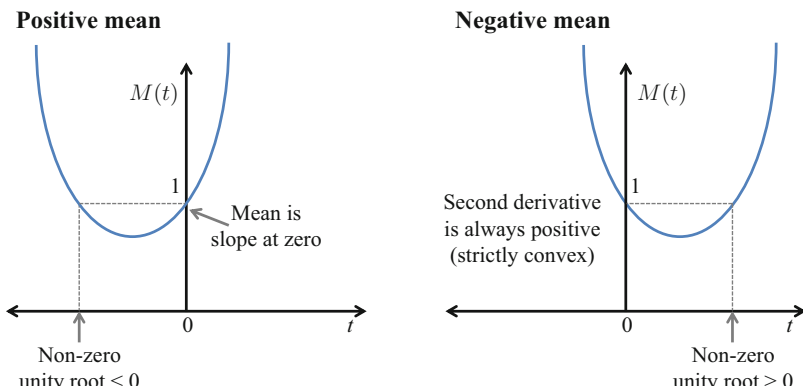


Fig. 10.13 Unity roots of the moment generating function when the mean is positive and negative

Now suppose that the MGF exists over the whole real line. It can then be seen that the first term in (10.100) increases to infinity as $t \rightarrow -\infty$ as long as $\Pr\{Z < 0\} > 0$. Similarly, the second term tends to infinity as $t \rightarrow \infty$ when $\Pr\{Z > 0\} > 0$.

Taking these points together implies, as depicted in Fig. 10.13, that there is a unique minimum to the MGF (which is also guaranteed by the convexity of $M(t)$), that it will be below one, and that there is a unique non-zero unity root occurring at an argument with a larger magnitude than the argument of the minimum.

The regularity conditions for the existence of a non-zero unity root of the MGF of Z can be summarized as follows:

1. $E[Z] \neq 0$
2. The MGF $M(t) = E[e^{tZ}]$ must exist for some large enough interval (t_-, t_+) including zero
3. $\Pr\{Z > 0\} > 0$ and $\Pr\{Z < 0\} > 0$

A more precise description of the second and third conditions is that the MGF must tend to infinity as t approaches t_- if the mean of Z is positive or t_+ if the mean is negative.

As an example, consider the detector function

$$g(x) = x - \tau \quad (10.101)$$

when the observed data, represented by X , are exponentially distributed with mean λ . Noting that Z must have support on the negative real line (i.e., $\Pr\{Z < 0\} > 0$), the biasing term τ must be positive because X is always greater than zero. The MGF of Z is easily obtained using the MGF of the exponential distribution from Sect. 5.6.10,

$$M(t) = E[e^{tZ}] = e^{-t\tau} E[e^{tX}] = \frac{e^{-t\tau}}{1 - \lambda t} \quad (10.102)$$

for $t < 1/\lambda$. The non-zero unity root of the MGF can then be found by the solution of the equation

$$1 - \lambda t - e^{-t\tau} = 0. \quad (10.103)$$

From the forms of the MGF seen in Fig. 10.13, any numerical solution to (10.103) needs to be initialized at a value beyond the argument of the minimum so it does not settle back on $t = 0$ as a solution. In the example presented here, the minimum occurs when $t = (1 - \lambda/\tau)/\lambda$. When there is no closed-form solution for the minimum point, a numerical routine for finding the non-zero unity root should increase the magnitude of t in steps to either get past the minimum or bound the root. The latter, which entails finding t_a and t_b such that $M(t_a) < 1 < M(t_b)$, is a more robust approach. The root can then be found by successively shrinking the interval while continuing to bound the root.

Care needs to be taken if unconstrained root-finding algorithms (e.g., the Newton-Raphson method [34, Sect. 2.4]) are used because they can either end up returning the $t = 0$ solution when the non-zero root is desired or produce an update where the MGF is not valid. In the exponential-data example, it was required that $t < 1/\lambda$ because $M(t) \rightarrow \infty$ as $t \rightarrow 1/\lambda$ from below. This must be taken into account both in the initialization and in each update of the root-finding algorithm by constraining the solution to satisfy $t < 1/\lambda$.

Exercise 10.1 Code an algorithm to solve (10.103) for the non-zero unity root. Test the algorithm when $\lambda = 2$ and $\tau = 1$ or $\tau = 3$ and generate plots like those shown in Fig. 10.13.

10.5.2.3 ROC Curves and Asymptotic Performance of Page's Test

Using the ASN for Page's test from (10.97) when signal is present results in the average number of samples required for detection,

$$D \approx \frac{h + t_s^{-1} [1 - e^{ht_s}]}{E_s[g(X)]} \quad (10.104)$$

and the average number of samples to a false alarm,

$$F \approx \frac{h + t_0^{-1} [1 - e^{ht_0}]}{E_0[g(X)]}, \quad (10.105)$$

when there is only noise. The analysis in Sect. 10.5.2.2 indicated that the non-zero unity root of the MGF of $g(X)$ has the opposite sign to the mean of $g(X)$. Because D is ideally small and F is ideally large, this implies that it is desirable that

$$E_0[g(X)] < 0 < E_s[g(X)] \quad (10.106)$$

so

$$t_s < 0 < t_0. \quad (10.107)$$

When this condition holds, D will approximately be a linear function of h whereas F will approximately be exponentially related.⁷ The resulting log-linear relationship between F and D (i.e., $\log F \sim D$) can be seen in Fig. 10.14 where ROC curves are

⁷Note that if $E_0[g(X)] = 0$ and $E_s[g(X)] > 0$, the relationship between D and F is quadratic ($F \sim D^2$); clearly this should be avoided.

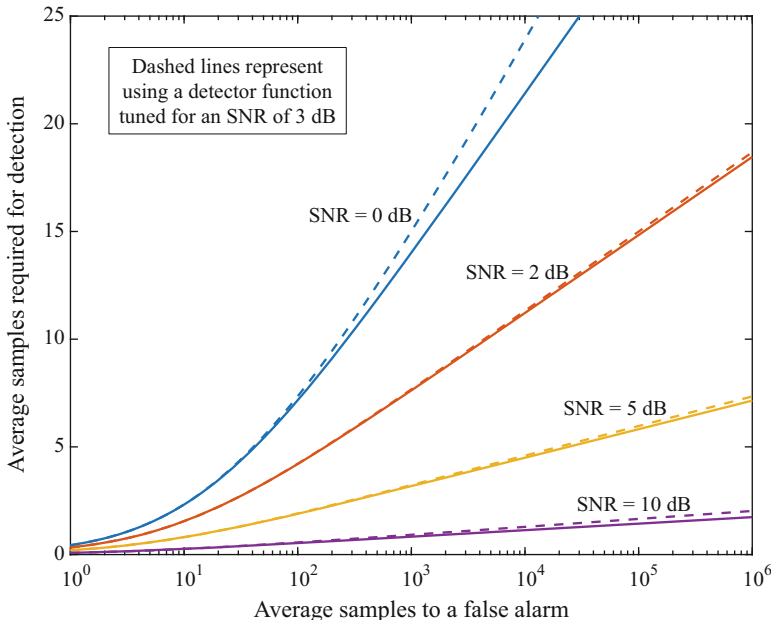


Fig. 10.14 Page's test ROC curves for a Gaussian-fluctuating signal in Gaussian noise for various per-sample SNRs. The solid curves use the log-likelihood ratio for the given SNR as the detector function whereas the dashed lines incorrectly use one tuned for an SNR of 3 dB

shown for detecting a Gaussian-fluctuating signal in Gaussian noise, which results in the exponentially distributed data example of Sect. 10.5.2.2. When the data are exponentially distributed with mean $\lambda = 1 + s$ where s is the per-sample SNR, the log-likelihood ratio results in a detector function

$$g(x) = x - \frac{(1+s)\log(1+s)}{s} \quad (10.108)$$

where the scale factor on x has been removed with an appropriate adjustment to the bias term to conform with the example in Sect. 10.5.2.2. Note that this is equivalent to a scale factor on the decision threshold and does not change the performance in terms of the ROC curves. The solid curves in Fig. 10.14 represent when the detector is implemented using (10.108) and the observed data have the same SNR when signal is present (i.e., the detector function is precisely the log-likelihood ratio). The dashed lines represent using a bias term in (10.108) tuned for an SNR of 3 dB regardless of the actual SNR of the data. Note that this results in an increase in D both when the actual SNR is higher or lower than the design value of 3 dB. This illustrates how using the log-likelihood ratio in Page's test minimizes the average number of samples required for detection. Note that if the detector is tuned to a design SNR too much above the observed SNR, D can become exponentially related

to h if the right-hand inequality in (10.106) is violated. It is therefore important to choose a design SNR close enough to the minimum expected SNR to maintain the inequalities shown in (10.106).

Detector operating points are generally chosen using large values of F , so it can be assumed that h is also large. When (10.106) is satisfied, the ASNs in (10.104) and (10.105) can be approximated by

$$D \approx \frac{h}{E_s[g(X)]} \quad \text{and} \quad F \approx \frac{e^{ht_0}}{-t_0 E_0[g(X)]}. \quad (10.109)$$

Combining these equations then allows describing D in terms of F ,

$$D \approx \frac{\log(F) + \log\{-t_0 E_0[g(X)]\}}{t_0 E_s[g(X)]}, \quad (10.110)$$

with the log-linear relationship now clearly evident. An asymptotic (large h) measure was extracted from this relationship by Broder in [35, Sect. 2.3],

$$\eta = t_0 E_s[g(X)], \quad (10.111)$$

to represent the performance of Page's test for large thresholds. From (10.110), this performance measure is seen to be the inverse slope relating $\log F$ to D ; that is, $D \approx \log(F)/\eta$ when F is large enough. Clearly increasing η results in improved performance.

Suppose the detector function $g(x)$ is the log-likelihood ratio. The MGF under the noise-only hypothesis is then

$$E_0\left[e^{tg(X)}\right] = \int_{-\infty}^{\infty} \left[\frac{f_1(x)}{f_0(x)}\right]^t f_0(x) dx. \quad (10.112)$$

The non-zero MGF unity root can easily be seen to be $t_0 = 1$, which implies the asymptotic performance is driven by

$$E_s[g(X)] = E_s\left[\log\left(\frac{f_1(X)}{f_0(X)}\right)\right] \quad (10.113)$$

which is the Kullback-Liebler divergence [36]. Owing to the optimality of using the log-likelihood ratio in Page's test, this provides an easily evaluated upper bound on asymptotic performance when other detector functions are used.

Exercise 10.2 In the example presented in Fig. 10.14, the detector function in (10.108) was not precisely the log-likelihood ratio, but within a scale factor of it. Suppose the detector function is $y(x) = cg(x)$ where $g(x)$ is the log-likelihood ratio and c is a scale factor. Show that Broder's asymptotic performance measure

(η) is invariant to the scale factor c . Show that the scale invariance extends to the ROC curve (i.e., D as a function of F).

10.5.2.4 Biasing a General Input to Page's Test

When the log-likelihood-ratio cannot be characterized explicitly (e.g., because of unknown parameters), it is common to use one of the other more practical approaches to determine how data should be transformed before applying Page's test. For example, Dyson [37] showed that using a locally optimal detector function could yield the lowest worst-case average delay to detection asymptotically as $F \rightarrow \infty$ (i.e., in the sense of Lorden [31]) for a vanishingly small signal strength. When noise parameters are unknown, it may be necessary to resort to the logarithm of a GLR detector function.

Because in general these approaches do not guarantee that the means of the detector function will satisfy the inequalities in (10.106), the detector function may need to be biased. If the generic detector function is $g_0(x)$, then consider using

$$g_\tau(x) = g_0(x) - \tau \quad (10.114)$$

in Page's test where the bias τ is chosen to satisfy (10.106). In [37, Sect. 4.3], Dyson assumed the locally optimal detector function had a zero mean when only noise was present and proposed using a bias equal to half the mean when signal is present. As noted in [38], this can easily be extended to account for a non-zero noise mean,

$$\tau = \frac{E_0[g_0(X)] + E_s[g_0(X)]}{2}, \quad (10.115)$$

which puts the means of $g_\tau(x)$ equidistant from zero and so satisfies (10.106).

It is also possible to choose the bias τ to maximize the asymptotic performance of Page's test. Suppose that t_τ is the non-zero unity root of the MGF of $g_\tau(X)$ when there is only noise so

$$\begin{aligned} 1 &= E_0[e^{t_\tau g_\tau(X)}] \\ &= e^{-t_\tau \tau} E_0[e^{t_\tau g_0(X)}] \\ &= e^{-t_\tau \tau} M_0(t_\tau) \end{aligned} \quad (10.116)$$

where $M_0(t)$ is the MGF of $g_0(X)$ when there is only noise. Solving this for the τ in the exponent of (10.116) results in

$$\tau = \frac{\log M_0(t_\tau)}{t_\tau}. \quad (10.117)$$

Using this in the asymptotic performance measure from (10.111) results in

$$\begin{aligned}\eta &= t_\tau \{E_s[g_0(X)] - t_\tau\} \\ &= t_\tau \left\{E_s[g_0(X)] - \frac{\log M_0(t_\tau)}{t_\tau}\right\} \\ &= t_\tau E_s[g_0(X)] - \log M_0(t_\tau).\end{aligned}\quad (10.118)$$

Assuming there is a one-to-one mapping between τ and t_τ , maximizing η with respect to t_τ will lead to an optimal value of the bias τ . Differentiating (10.118) with respect to t_τ and setting the result to zero produces

$$E_s[g_0(X)] = \frac{M'_0(t_\tau)}{M_0(t_\tau)}. \quad (10.119)$$

The optimal bias is then found by solving (10.119) for t_τ and inserting it in (10.117). The uniqueness of the result and concavity of η in t_τ can be shown by evaluating the derivatives of (10.118) and using the Cauchy-Schwarz inequality (e.g., see [38]).

As an example, suppose an energy detector summing α independent frequency bins is applied to a Gaussian-fluctuating signal so the data are gamma distributed with shape parameter α and scale $1 + s$ when signal is present with s being the SNR in each frequency bin. Letting $g_0(x) = x$ results in $M_0(t) = 1/(1-t)^\alpha$ and $M'_0(t) = \alpha/(1-t)^{\alpha+1}$. Using these in (10.119) with the mean of $\alpha(1+s)$ and solving for t_τ results in

$$t_\tau = \frac{s}{1+s}. \quad (10.120)$$

Inserting this in (10.117) then results in the optimal bias

$$\tau = \frac{\alpha(1+s)\log(1+s)}{s} \quad (10.121)$$

which is exactly that found in (10.108) with $\alpha = 1$ to represent the exponential distribution used in the prior example. In this example Dyson's bias from (10.115) results in

$$\tau = \alpha \left(1 + \frac{s}{2}\right). \quad (10.122)$$

Noting that Dyson's bias was derived to be optimal for vanishingly small signals, it is no surprise that (10.122) is also a first-order Maclaurin series approximation to the optimal bias in (10.121). However, when SNR is not small the asymptotically optimal bias may provide a large enough improvement in performance to justify the additional effort required to derive it.

Suppose the signal was deterministic rather than Gaussian-fluctuating so that, when appropriately scaled, the data are non-central chi-squared distributed ($2X \sim \chi_{2\alpha,\delta}^2$) with 2α degrees of freedom and a non-centrality parameter $\delta = 2\alpha s$. Interestingly, this scenario results in exactly the same biases as for the Gaussian-fluctuating signal. This can be explained by noting that the noise distributions under the two models are identical (i.e., if $2X \sim \chi_{2\alpha}^2$, then $X \sim \text{Gamma}(\alpha, 1)$) and the means when signal is present are the same. Because the bias terms do not depend on the distribution of the data when signal is present other than through the mean, the specific shape of the distribution can otherwise vary and not change the biases.

Exercise 10.3 Show that the only noise distribution for which Dyson's bias and the asymptotically optimal bias are identical is when $g_0(X)$ is Gaussian distributed. Hints: equate the definitions of the biases from (10.115) and (10.117),

$$\frac{\log M_0(t)}{t} = \frac{E_0[g_0(X)] + E_s[g_0(X)]}{2}, \quad (10.123)$$

and describe each term using the cumulant generating function (CGF; Sect. 5.3.9.3), which is the logarithm of the MGF, $K(t) = \log M(t)$. Note that $K'(t) = M'(t)/M(t)$, which can be used with (10.119), and that $K'(0)$ is the mean. Solve the resulting ordinary differential equation for $K(t)$ and show that it has the form of a CGF of Gaussian random variable, $K(t) = \mu t + t^2\sigma^2/2$. What constraints are placed on the signal distribution in this derivation?

10.5.2.5 Page's Test with Nuisance Parameter Estimation

When there are unknown nuisance parameters (e.g., noise powers), it is possible to exploit the structure of Page's test to automatically identify data believed to contain only noise samples. As described in [29], this essentially involves using data prior to the most recent reset to zero of the Page's test decision statistic. Given an initial estimate $\hat{\lambda}$ of the nuisance parameter λ , Page's test can be operated using a detector function $g_{\hat{\lambda}}(x)$. The parameter estimate can then be updated each time that there is a reset to zero, although it may be prudent to wait until more than one reset has occurred. Such a paradigm helps avoid contamination of the presumed noise-only data by samples containing signal, which can lead to target masking (e.g., see Sect. 8.6.2). This can be implemented efficiently by continually estimating the nuisance parameters at each update with either a trailing window or an exponential averager and only when there is a reset to zero entering the current estimate into a finite-length, first-in-first-out (FIFO) queue which forces out the oldest value. The oldest value remaining in the FIFO queue is then used in the detector function until there is another reset to zero. Thus, the size of the queue dictates how many resets to zero are required to occur before an estimate is used.

As with any estimation of an unknown parameter, there is a cost in terms of a reduction in detection performance. As shown in [29], estimating a nuisance

parameter results in an average sample number that is approximately

$$\bar{K}(s) \approx E_{\hat{\lambda}} \left[\frac{\left[1 + t_s h(1 - e^{t_s h})^{-1} \right]}{E_s \left[g_{\hat{\lambda}}(X) | \hat{\lambda} \right]} \right] \div E_{\hat{\lambda}} \left[\frac{t_s}{(1 - e^{t_s h})} \right] \quad (10.124)$$

where the unity-root of the MGF (t_s) is formed while conditioning on the nuisance parameter estimate and is therefore the solution to

$$1 = E_s \left[e^{t_s g_{\hat{\lambda}}(X)} | \hat{\lambda} \right]. \quad (10.125)$$

The result shown in (10.124) is obtained by following the derivation in Sect. 10.5.2.1 while assuming each individual SPRT utilizes an independent estimate of $\hat{\lambda}$. Taking expectations over $\hat{\lambda}$ at the appropriate points produces (10.124), which can be seen to simplify to (10.97) when $\hat{\lambda}$ is constant.

Suppose the exponential data example had an unknown noise power λ so the data when signal is present are exponentially distributed with mean $\lambda(1 + s)$. The Page's test detector function from (10.108) must be modified to account for the unknown nuisance parameter according to

$$g_{\hat{\lambda}}(x) = \frac{x}{\hat{\lambda}} - \frac{(1 + s) \log(1 + s)}{s}. \quad (10.126)$$

If L independent noise samples are available to estimate λ using a sample mean (e.g., as in a cell-averaging normalizer), then the noise power estimate is gamma distributed,

$$\hat{\lambda} \sim \text{Gamma}\left(L, \frac{\lambda}{L}\right), \quad (10.127)$$

with L degrees of freedom and a scale parameter of λ/L . Using these in (10.124) and (10.125) results in the Page's test ROC curves shown in Fig. 10.15 when the SNR is 5 dB. For a fixed average number of samples to a false alarm, the average number of samples required for detection increases dramatically when L is decreased. The accuracy with which the nuisance parameter must be estimated (quantified by L) clearly increases as F increases, which is indicative of a need to control the distribution of the Page's test input further out in the tails.

10.5.2.6 Overshoot Corrections to Page's Test Average Sample Numbers

The overshoot corrections developed for the SPRT in Sect. 10.5.1.3 can be carried through the derivation of the average sample numbers in Page's test (i.e., the derivation in Sect. 10.5.2.1). The result is to modify the decision threshold in (10.97) to account for the overshoot,

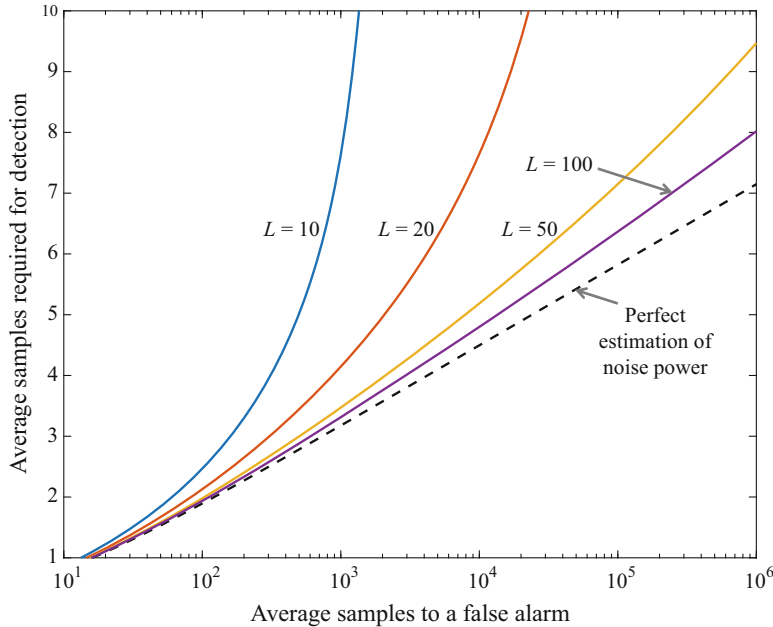


Fig. 10.15 ROC curve for Page's test with nuisance parameter estimation for various window sizes (L) and an SNR of 5 dB

$$h_c = h + \rho_s^+ - \rho_s^-, \quad (10.128)$$

where the subscript s is used to indicate signal presence or absence. The corrected average sample number in Page's test is then

$$\bar{K}(s) \approx \frac{h + \rho_s^+ - \rho_s^- + t_s^{-1} \left[1 - e^{(h+\rho_s^+-\rho_s^-)t_s} \right]}{E_s[g(X)]}. \quad (10.129)$$

As shown in [29], the average overshoot can also be incorporated into the analysis of a Page's test with nuisance parameter estimation, but results in a more complicated form than that obtained by modifying the threshold in (10.124).

10.6 Detectors for Signals with Unknown, Intermediate Duration

The final type of signal to be examined are those signals with an intermediate duration. That is, signals persisting for more than a single CPI, but not so long as to be considered infinite duration. Applying the generalized likelihood ratio (GLR)

principle to the unknown duration results in the SPRT and Page's test, respectively, for signals with known and unknown starting times. An example of an intermediate-duration signal with a known starting time comes from track classification where a tracking algorithm associates data over multiple updates and it is desired to determine if the track represents an object of interest or not using a classification algorithm. Application of the SPRT to this scenario is evaluated in Sect. 10.6.1, including truncation of the test if the track ends precipitously. A more common scenario for intermediate-duration signals is for them have an unknown starting time, in which case Page's test is the appropriate detector. This is described in Sect. 10.6.2 along with an alternating-hypothesis form of Page's test useful when multiple signals of interest can occur at different times.

Because of the finite duration of these signals, the probability of making a correct decision becomes an important performance metric. For an SPRT, these probabilities (which are related to the Type I and II error probabilities) become a function of the sample number and the decision threshold. When Page's test is applied to a finite-duration signal, the probability of false alarm is still one when the test runs forever so the average time before a false alarm from Sect. 10.5.2.1 or 10.5.2.3 is still the appropriate metric. However, the probability of detection will be less than one and therefore needs to be evaluated as a function of signal duration. As described in Sect. 10.2, detection latency can also be of interest.

If an intermediate-duration signal exists for n samples and Z_k is the update of the SPRT or Page's test (e.g., Z_k is optimally the log-likelihood ratio), then a lower bound on the probability of detection can be obtained by comparing the sum of Z_k over the n samples containing the signal to the same decision threshold used in the sequential test,

$$P_d(n) \geq \Pr \left\{ \sum_{k=1}^n Z_k \geq h | H_1 \right\}. \quad (10.130)$$

This is a lower bound because it ignores detections that might occur when the decision statistic exceeds h before reaching n but then decreases below h at time index n (i.e., $\sum_{k=1}^n Z_k < h$) and for Page's test ignores the reflecting boundary at zero. Also ignored are any detections that do not occur until after the signal stops, but still arise from presence of the signal—this can happen because both the SPRT and Page's test decision statistics have memory. Such detections are termed *latent* detections [39] and are generally not a significant contributor to detection unless the update has a very heavy-tailed distribution or the threshold is small.

Evaluation of the probability of detection in sequential detectors is in general difficult. In Sects. 10.6.1.1 and 10.6.2.2, an analysis technique entailing quantization of the SPRT or Page's test update is presented. Quantization allows representation of the decision-statistic sequence by a discrete-time, finite-state Markov chain. The advantage of this approach lies in simple matrix–vector formulae for the distribution of the stopping time, the average sample numbers, and error probabilities. The

primary disadvantage is the potential need for a very fine quantization, which results in very large matrices.

10.6.1 Known Starting Time: Sequential Probability Ratio Test (SPRT)

When the starting time of an intermediate-duration signal is known, the hypothesis test can be described as

$$X_1, \dots, X_n \sim \begin{cases} f_0(x) & \text{under } H_0 \\ f_1(x) & \text{under } H_1 \end{cases} \quad (10.131)$$

where the signal duration $n \geq 1$ is unknown and the data X_k for $k > n$ are assumed to have PDF $f_0(x)$. If the data are assumed to be independent, a generalized likelihood ratio (GLR) test over the unknown value of n has the form

$$\begin{aligned} L(\mathbf{x}) &= \frac{\max_{n \geq 1} \prod_{k=1}^n f_1(x_k) \prod_{k>n} f_0(x_k)}{\prod_{k \geq 1} f_0(x_k)} \\ &= \max_{n \geq 1} \prod_{i=1}^n \frac{f_1(x_k)}{f_0(x_k)}. \end{aligned} \quad (10.132)$$

Thus, a GLR test over the unknown starting time results in choosing the value of n maximizing the cumulative sum of the log-likelihood ratio and then comparing the resulting sum to a decision threshold. This can be generalized to the cumulative sum of a detector function $z = g(x)$ applied to the data to account for unknown signal and noise parameters, resulting in

$$\Sigma_n = \sum_{i=1}^n Z_k \quad (10.133)$$

where $Z_k = g(X_k)$. To observe a maximum in Σ_n , data will usually need to be observed beyond the duration of the signal. Because this is often not practical and it is typically desirable to make a decision as quickly as possible, Σ_n is simply compared to a threshold chosen based on desired Type I and II error probabilities (i.e., α_d and β_d). This is precisely the design of the SPRT after the addition of a termination decision at the H_0 hypothesis when Σ_n passes below a lower threshold.

An example of the probability of making a correct decision with the SPRT is shown as a function of the number of samples in Fig. 10.16. The data are exponentially distributed with mean $1 + s$ under H_1 and with unit mean under H_0

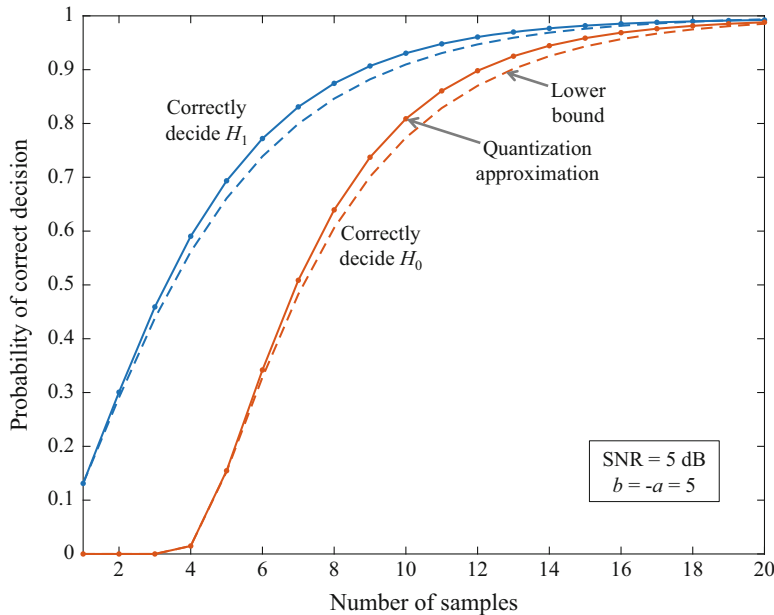


Fig. 10.16 Example probability of correctly deciding H_0 and H_1 using a symmetric (i.e., equal-error) SPRT as a function of sample number using the quantization approach and the lower bound formed from the fixed-length decision

with $10 \log_{10} s = 5$ dB used in the example. The design error probabilities were chosen to induce symmetric thresholds (i.e., $a = -b$) in the SPRT. The lower bound from (10.130) is shown along with the quantization approximation from (10.152) which is derived below in Sect. 10.6.1.1. This illustrates how P_d (i.e., correctly choosing H_1) increases rapidly with the duration of the signal, for example this 5-dB-SNR (per sample) signal only needs to be nine samples long to achieve P_d exceeding 90 percent. The asymmetry of the data (i.e., non-zero skewness of Z_k) leads to it taking longer to attain the same level of performance in correctly choosing H_0 (i.e., that there is no signal of interest present in the data).

In this example, the lower bound on P_d from (10.130) provides a useful measure of the performance attained by the SPRT with much less effort than the quantization approach (2000 quantization levels were used in this example). Qualitatively the approximation from (10.130) improves when the data are less heavy tailed and degrades when the PDF tails are higher.

Exercise 10.4 Suppose a deterministic signal is observed instead of a Gaussian-fluctuating signal, but the same detector function is used in the SPRT (i.e., $g(x) = sx/(1+s) - \log(1+s)$). How many samples are then required to achieve $P_d = 0.9$? This can be approximated using the lower bound in (10.130). The decision statistic on the right side of (10.130) in terms of the data is

$$\sum_{k=1}^n Z_k = \frac{s}{1+s} \left[\sum_{k=1}^n X_k \right] - n \log(1+s). \quad (10.134)$$

For a deterministic signal with perfect normalization, two times $\sum_{k=1}^n X_k$ is non-central chi-squared distributed, which means Albersheim's or Hmam's equation can be used to relate a desired (P_d, P_f) operating point and number of independent samples summed to the required SNR. Show that comparing the left side of (10.134) to a threshold b is equivalent to comparing $\sum_{k=1}^n X_k$ to a threshold $h = [b + n \log(1+s)](1+s)/s$. Now using Hmam's equation from (2.87) with this value of h and $P_d = 0.9$, show that the value of n for which the SNR required to achieve the desired performance is less than the 5 dB used in the example shown in Fig. 10.16 is seven samples. This implies that if a deterministic signal is observed instead of a Gaussian-fluctuating signal that it will be detected on average two samples earlier than the Gaussian-fluctuating signal.

10.6.1.1 SPRT Analysis by Quantization

The decision statistic of an SPRT from (10.133) can be described recursively by

$$\begin{aligned} \Sigma_k &= \sum_{i=1}^k Z_i \\ &= \Sigma_{k-1} + Z_k. \end{aligned} \quad (10.135)$$

By quantizing the input sequence (i.e., $Z = Z_k$ where the indexing on k is omitted when there is no conflicting notation) the SPRT decision statistic can be approximated with a discrete-time, finite-state Markov chain where the probability that Σ_k lies in a given state only depends on the observed state at time $k-1$ and a set of transition probabilities. Suppose the update Z is quantized to levels

$$z_i = (i - i_0)\delta \quad (10.136)$$

for $Z \in (z_i - \delta/2, z_i + \delta/2]$ where δ is the quantization step, i is an integer, and the index i_0 will be used to represent when $Z = 0$ in the following manner. If the test has not stopped yet, the SPRT decision statistic Σ_k must lie on (a, b) . Suppose there are n levels on the interval (a, b) and let them be indexed in increasing order by $i = 1, \dots, n$. Thus $i = 1$ represents the smallest value Σ_k can attain without passing the lower threshold a and i_0 is the index for zero

$$i_0 = \left\lceil \frac{-a - \delta/2}{\delta} \right\rceil \quad (10.137)$$

where $\lceil \cdot \rceil$ is the ceiling function returning the next largest integer.

The levels z_i for $i = 1, \dots, n$ can be described as continuing states because the test continues while Σ_k is in one of them. Given that Σ_{k-1} is in the i th state, the probability of Σ_k being in the j th state is called the state transition probability,

$$P_{i,j} = \Pr\{\Sigma_k = z_j | \Sigma_{k-1} = z_i\} = p[i_0 + j - i] \quad (10.138)$$

where

$$p[i] = F_Z(z_i + \delta/2) - F_Z(z_i - \delta/2) \quad (10.139)$$

is the probability Z quantizes to the i th level. Removing the conditioning on the state at time $k-1$ in (10.138) results in the probability that the SPRT is in state j at time k ,

$$\begin{aligned} \pi_{k,j} &= \Pr\{\Sigma_k = z_j\} \\ &= \sum_{i=1}^n \Pr\{\Sigma_k = z_j | \Sigma_{k-1} = z_i\} \Pr\{\Sigma_{k-1} = z_i\} \end{aligned} \quad (10.140)$$

$$= \sum_{i=1}^n P_{i,j} \pi_{k-1,i}. \quad (10.141)$$

This update of the state probabilities can be described efficiently using matrix–vector notation by placing the state probabilities at time k into a vector $\boldsymbol{\pi}_k^T = [\pi_{k,1} \dots \pi_{k,n}]$ and the one-step transition probabilities into a state-transition matrix

$$\mathbf{P} = \begin{bmatrix} p[i_0] & p[i_0 + 1] & \cdots & p[n] \\ p[i_0 - 1] & p[i_0] & \cdots & p[n - 1] \\ p[i_0 - 2] & p[i_0 - 1] & \cdots & p[n - 2] \\ \vdots & \vdots & \ddots & \vdots \\ p[1] & p[2] & \cdots & p[i_0] \end{bmatrix}. \quad (10.142)$$

The update in (10.141) over all the states is then represented by the vector–matrix product

$$\boldsymbol{\pi}_k^T = \boldsymbol{\pi}_{k-1}^T \mathbf{P}. \quad (10.143)$$

Note that the more common convention for describing state transition probability matrices and the one-step update for Markov chains is as described in (10.142) and (10.143); that is, as a row vector multiplying a matrix. Using the transpose of (10.142) and a matrix-column-vector product is not uncommon.

When describing the SPRT as a cumulative summation, the initial value is zero (i.e., $\Sigma_0 = 0$). Thus, the state-probability vector at time zero is $\boldsymbol{\pi}_0 = \mathbf{e}_{i_0}$ where \mathbf{e}_i is a unit vector with zeros in all elements except for the i th where it contains a

one. The state probability vector after the first update is then simply $\mathbf{e}_{i_0}^T \mathbf{P}$ and after k updates is $\mathbf{e}_{i_0}^T \mathbf{P}^k$. The probability that the test stops after time k is the probability that the decision statistic remains within the continuing states at time k , which is the sum over the state probabilities. In matrix–vector form this is

$$\Pr\{K > k\} = \mathbf{e}_{i_0}^T \mathbf{P}^k \mathbf{1} \quad (10.144)$$

where $\mathbf{1}$ is a vector of ones. The probability mass function (PMF) of the stopping time can be obtained by differencing (10.144),

$$\begin{aligned} f_K(k) &= \Pr\{K > k - 1\} - \Pr\{K > k\} \\ &= \mathbf{e}_{i_0}^T \mathbf{P}^{k-1} (\mathbf{I} - \mathbf{P}) \mathbf{1}. \end{aligned} \quad (10.145)$$

Although the primary interest in this section is on the probability of detection, this characterization of the stopping time can easily be used to obtain the average sample number

$$\begin{aligned} \bar{K} &= \sum_{k=1}^{\infty} k f_K(k) \\ &= \mathbf{e}_{i_0}^T \left[\sum_{k=1}^{\infty} k \mathbf{P}^{k-1} \right] (\mathbf{I} - \mathbf{P}) \mathbf{1} \end{aligned} \quad (10.146)$$

$$= \mathbf{e}_{i_0}^T (\mathbf{I} - \mathbf{P})^{-1} \mathbf{1}. \quad (10.147)$$

This requires exploiting $\sum_{k=1}^{\infty} kp^{k-1} = 1/(1-p)^2$ and requires that $\mathbf{I} - \mathbf{P}$ be invertible, which implies that \mathbf{P} does not have any eigenvalues equal to one. Because the test is guaranteed to terminate, the eigenvalues must in fact have magnitude strictly less than one so the probability of being in a continuing state tends to zero. That is, $\mathbf{e}_{i_0}^T \mathbf{P}^k \rightarrow \mathbf{0}^T$ as $k \rightarrow \infty$ where $\mathbf{0}$ is a vector of zeros.

The probability that the test stops at time k by crossing the upper threshold can be described by conditioning on the state at time $k-1$ and summing over the resulting probabilities of observing a threshold exceedance in the next update,

$$\Pr\{\Sigma_k \geq b\} = \sum_{j=1}^n \Pr\{Z + z_j \geq b | \Sigma_{k-1} = z_j\} \Pr\{\Sigma_{k-1} = z_j\}. \quad (10.148)$$

In matrix–vector form this results in

$$f_K^b(k) = \mathbf{e}_{i_0}^T \mathbf{P}^{k-1} \mathbf{p}_b \quad (10.149)$$

where \mathbf{p}_b is a vector with the j th element equal to

$$\begin{aligned}\{\mathbf{p}_b\}_j &= \Pr\{\Sigma_k \geq b | \Sigma_{k-1} = z_j\} = \Pr\{Z + z_j \geq b\} \\ &= 1 - F_Z(b - z_j)\end{aligned}\quad (10.150)$$

for $j = 1, \dots, n$. The probability of terminating at b within the first n samples is then

$$\begin{aligned}P_b(n) &= \sum_{k=1}^n f_K^b(k) \\ &= \mathbf{e}_{i_0}^T \left[\sum_{k=1}^n \mathbf{P}^{k-1} \right] \mathbf{p}_b\end{aligned}\quad (10.151)$$

$$= \mathbf{e}_{i_0}^T (\mathbf{I} - \mathbf{P}^n) (\mathbf{I} - \mathbf{P})^{-1} \mathbf{p}_b \quad (10.152)$$

where the matrix function in brackets is simplified using $\sum_{k=1}^n p^{k-1} = (1 - p^n)/(1 - p)$.

The solid blue line in the example presented in Fig. 10.16 was formed using $P_b(n)$ in (10.152) with a state transition matrix $\mathbf{P} = \mathbf{P}_1$ formed under H_1 . The result showing the probability of correctly deciding H_0 (solid reddish-brown line) is obtained using a similar formula,

$$P_a(n) = \mathbf{e}_{i_0}^T (\mathbf{I} - \mathbf{P}^n) (\mathbf{I} - \mathbf{P})^{-1} \mathbf{p}_a, \quad (10.153)$$

where the state transition matrix $\mathbf{P} = \mathbf{P}_0$ is formed under H_0 and \mathbf{p}_a is a vector whose j th element is the probability of terminating at H_0 in the next update when the current state is z_j ,

$$\begin{aligned}\Pr\{\Sigma_k \leq a | \Sigma_{k-1} = z_j\} &= \Pr\{Z + z_j \leq a\} \\ &= F_Z(a - z_j).\end{aligned}\quad (10.154)$$

The state probability vectors π_k can also be used to approximate the PDF of the decision statistic as a function of the sample number by dividing by the quantization step size. An example is shown in Fig. 10.17 under H_1 illustrating how the PDF of the decision statistic (the part between a and b) evolves over time. At the first time sample, it is simply a shifted and truncated exponential PDF. As the sample number increases, it spreads and migrates higher. The integral of the PDF of Σ_k over (a, b) , which is the probability that the test continues, clearly decreases as the sample number increases. This is because with each new sample there is some probability of crossing the upper or lower thresholds and ending the test. The upper and lower portions of the figure (above and below the white lines) show, respectively, the cumulative probability of deciding H_1 and H_0 . The former is precisely what is found

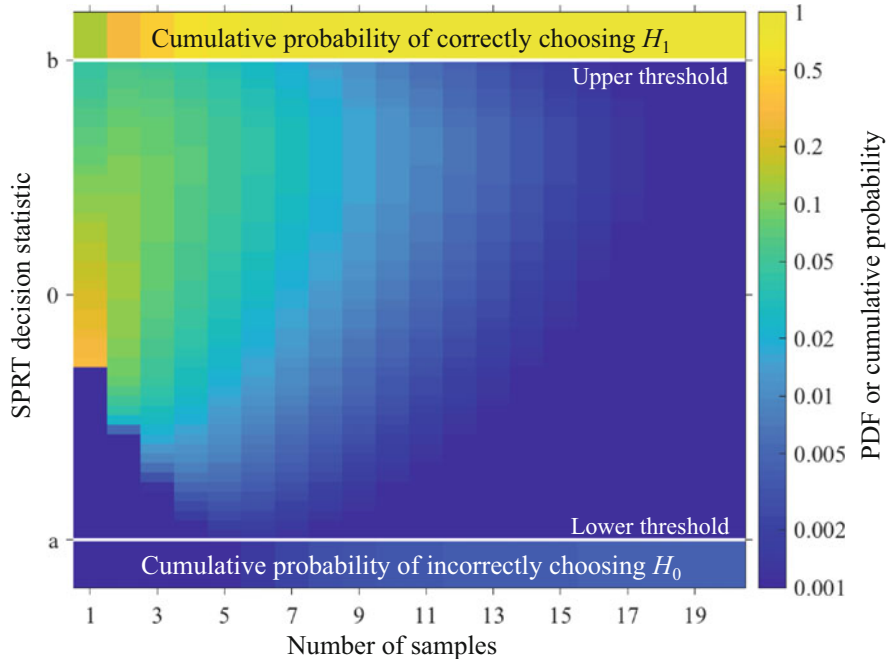


Fig. 10.17 PDF of the SPRT decision statistic as a function of the sample number under H_1 and the cumulative probabilities of correctly choosing H_1 and incorrectly choosing H_0

in Fig. 10.16 and the latter is small because of the design of the test and because H_1 is true.

The quantization approach is also useful in obtaining more accurate error probabilities than either the standard or corrected approximations described in Sect. 10.5.1. The probability of a Type I error can be obtained from (10.152) by letting $n \rightarrow \infty$,

$$\alpha = \mathbf{e}_{i_0}^T (\mathbf{I} - \mathbf{P}_0)^{-1} \mathbf{p}_b, \quad (10.155)$$

and using the state transition matrix formed under H_0 . The Type II error probability can similarly be described as

$$\beta = \mathbf{e}_{i_0}^T (\mathbf{I} - \mathbf{P}_1)^{-1} \mathbf{p}_a \quad (10.156)$$

where the state transition matrix under H_1 is required.

Latency, as defined in Sect. 10.2, is the average number of samples required for detection given a signal is present (H_1) and detected (the event \mathcal{S}). The PMF of the stopping time K for a signal of length n conditioned on it being present and detected is

$$f_K(k|H_1, \mathcal{S}) = \frac{\mathbf{e}_{i_0}^T \mathbf{P}_1^{k-1} \mathbf{p}_b}{\sum_{j=1}^n \mathbf{e}_{i_0}^T \mathbf{P}_1^{j-1} \mathbf{p}_b} \quad (10.157)$$

for $k = 1, \dots, n$ where detection requires terminating at b under H_1 in the first n samples. The latency is then the average of K using the PMF in (10.157),

$$E[K|H_1, \mathcal{S}] = \frac{\sum_{k=1}^n k \mathbf{e}_{i_0}^T \mathbf{P}_1^{k-1} \mathbf{p}_b}{\sum_{k=1}^n \mathbf{e}_{i_0}^T \mathbf{P}_1^{k-1} \mathbf{p}_b}. \quad (10.158)$$

It is also feasible to extract other measures from the PMF of K to represent the time it takes to detect the signal (e.g., the median time to decision).

Exercise 10.5 Show that $\sum_{k=1}^{\infty} k \mathbf{P}^{k-1} = (\mathbf{I} - \mathbf{P})^{-2}$ by describing \mathbf{P} using an eigenvalue/eigenvector decomposition, $\mathbf{P} = \mathbf{U} \Lambda \mathbf{U}^{-1}$ where Λ is a diagonal matrix of the eigenvalues and exploiting the infinite sum $\sum_{k=1}^{\infty} kp^{k-1} = 1/(1-p)^2$ for $|p| < 1$.

Exercise 10.6 Show that $(\mathbf{I} - \mathbf{P}^n)(\mathbf{I} - \mathbf{P})^{-1} = (\mathbf{I} - \mathbf{P})^{-1}(\mathbf{I} - \mathbf{P}^n)$ so the order of the matrix product in (10.152) is arbitrary.

10.6.1.2 Truncated SPRT

In scenarios where a decision must be forced before an SPRT has terminated properly, as might occur at the end of a track where no more data exist, the test can be truncated. The process simply compares the final decision statistic to zero,

$$\Sigma_n \stackrel{H_1}{\gtrless} \stackrel{H_0}{\lessdot} 0. \quad (10.159)$$

The cost of such a premature termination lies in an increase in the error probabilities. Upper bounds for the error probabilities, as found in [2, Sect. 2.8], are

$$\alpha(n) \leq \alpha + (1 - e^{-b}) \int_0^b [1 + e^{a-b-y}] f_n(y|H_0) dy \quad (10.160)$$

and

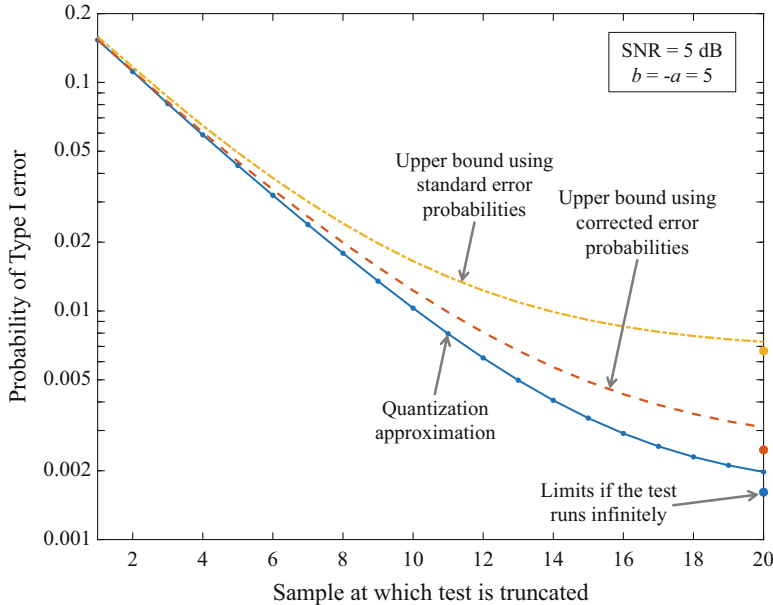


Fig. 10.18 Example probability of Type I error (i.e., choose H_1 when H_0 is true) for a truncated SPRT as a function of the stopping time using the quantization approach and the upper bound with either the standard or corrected error probabilities

$$\beta(n) \leq \beta + (1 - e^a) \int_a^0 [1 + e^{a-b+y}] f_n(y|H_1) dy \quad (10.161)$$

where $f_n(y|H_i)$ is the PDF of Σ_n under hypothesis i .

Continuing the example from Fig. 10.16, the probability of a Type I error (i.e., choosing H_1 when H_0 is true) is shown in Fig. 10.18 as a function of the sample number at which the test is truncated. The bound in (10.160) is shown for a symmetric SPRT using the standard approximations to the error probability (i.e., α via the equality in (10.45) using $b = -a = 5$) and the corrected approximation from (10.65). The error probabilities in the limit of an infinite-length test are shown as circles on the right edge of the plot. As seen in the figure, the errors decrease rapidly as the sample size of the test increases, but are initially very high. This is as should be expected; there is not much power in a test designed for long signals that is truncated after only a few samples.

The quantization approach from Sect. 10.6.1.1 is used to assess the accuracy of the approximations. Although the bound using the corrected error probabilities is better than the standard approximations to the error probabilities, it is still not as accurate as the quantization approach. For the Type I error of the truncated SPRT this entails calculating $P_b(n)$ in (10.152) using \mathbf{P}_0 and adding the probability that

the state at time n is non-negative (i.e., $\Sigma_n \geq 0$) If \mathbf{e}_+ is a vector with ones for each state that is non-negative and zeros in the other elements, then the Type I error for the truncated SPRT is

$$\alpha(n) = \mathbf{e}_{i_0}^T (\mathbf{I} - \mathbf{P}_0^n)(\mathbf{I} - \mathbf{P}_0)^{-1} \mathbf{p}_b + \mathbf{e}_{i_0}^T \mathbf{P}_0^n \mathbf{e}_+ . \quad (10.162)$$

The Type II error is similarly approximated as

$$\beta(n) = \mathbf{e}_{i_0}^T (\mathbf{I} - \mathbf{P}_1^n)(\mathbf{I} - \mathbf{P}_1)^{-1} \mathbf{p}_a + \mathbf{e}_{i_0}^T \mathbf{P}_1^n \mathbf{e}_- , \quad (10.163)$$

where \mathbf{e}_- is a vector of ones for the negative states with zeros in the other elements.

10.6.2 Unknown Starting Time: Page's Test

Similar to the development of the SPRT for intermediate-duration signals with a known starting time and unknown duration, the GLR approach can be applied to a signal with both an unknown starting time and unknown duration. As seen in Sect. 10.6.2.1, the signal-onset detection is identical in form to Page's test while including detection of the end of the signal can be described as an alternating-hypothesis Page's test (AHPT). This form is particularly useful for scenarios where multiple signals occur with periods of noise in between occurrences. Similar to the SPRT, the probability of detecting a signal with Page's test (or the AHPT) as a function of its duration can be evaluated by quantizing the Page's test update (Sect. 10.6.2.2). The detector design and analysis process is then illustrated through an example in Sect. 10.6.2.3.

10.6.2.1 Alternating Hypothesis Page's Test

If both the starting time and duration of an intermediate-duration signal are unknown, the data can be described as having the following distributions

$$X_i \sim \begin{cases} f_0(x) & \text{for } i \leq p \text{ and } i > q \\ f_1(x) & \text{for } p < i \leq q \end{cases} \quad (10.164)$$

where both p and q are unknown. Here the signal starts in sample $p + 1$ and has duration $q - p$. The noise-only condition can be implemented by letting $p \rightarrow \infty$. If the data are assumed to be independent, a generalized likelihood ratio (GLR) test applied to the first k samples has the form

$$\begin{aligned}
L(\mathbf{x}_k) &= \frac{\max_{p,q} \prod_{i=1}^p f_0(x_i) \prod_{i=p+1}^q f_1(x_i) \prod_{i=q+1}^k f_0(x_i)}{\prod_{i=1}^k f_0(x_i)} \\
&= \max_{p,q} \prod_{i=p+1}^q \frac{f_1(x_i)}{f_0(x_i)}. \tag{10.165}
\end{aligned}$$

Using the notation

$$\Sigma_k = \sum_{i=1}^k Z_i \tag{10.166}$$

for the cumulative sum over the log-likelihood ratio of the data (Z_i) through time k results in an objective function

$$\tilde{T}_k = \max_{p,q} \Sigma_q - \Sigma_p \tag{10.167}$$

$$= \max_q \left\{ \Sigma_q - \min_{p \leq q} \Sigma_p \right\}. \tag{10.168}$$

In a sequential detection context, the maximization over p occurs first in that a signal must be detected before its end point can be estimated. This implies the standard Page's test decision statistic from (10.82)

$$T_k = \Sigma_k - \min_{p \leq k} \Sigma_p \tag{10.169}$$

is used until it exceeds a detection threshold at time $q_0 > \hat{p}$ where \hat{p} is the estimate of p taken as the most recent reset of the decision statistic to zero. Now that the onset of a signal has been detected, the ending time q can be estimated. Conceptually this is identical to detecting the end of the finite-duration signal, as its onset was detected using Page's test. The objective function at time k can be described as

$$\tilde{T}_k = \max_{q_0 \leq q \leq k} \Sigma_q - \Sigma_{\hat{p}} \tag{10.170}$$

$$= [\Sigma_k - \Sigma_{\hat{p}}] + \left[\max_{q_0 \leq q \leq k} \Sigma_q - \Sigma_k \right] \tag{10.171}$$

where the two terms in brackets represent, respectively, the distances from the current total log-likelihood to the minimum and maximum. The latter term in brackets in (10.171) represents the decision statistic required to detect the end of the signal. This can be seen to be identical to the formulation of Page's test to

detect signal onset but with the hypotheses switched, which provides the naming convention of an *alternating hypothesis Page's test* (AHPT) [40]. A recursive implementation of the decision statistic can be formulated as it was for signal onset detection,

$$U_k = \max_{q_0 \leq q \leq k} \Sigma_q - \Sigma_k \quad (10.172)$$

$$= \max \left\{ \Sigma_k, \max_{q_0 \leq q \leq k-1} \Sigma_q \right\} - \Sigma_k \quad (10.173)$$

$$= \max \{0, U_{k-1} - Z_k\}. \quad (10.174)$$

Thus, when U_k exceeds a threshold the end of the signal is declared. Similar to how the starting time of the signal is estimated using the reset of the detection statistic T_k to zero (see Fig. 10.12), the end of the signal can be estimated by the most recent time at which U_k reset to zero.

In many applications multiple signals of interest can occur with periods of noise in between each occurrence. This is handled with the AHPT by re-starting signal-onset detection at the end of each detected signal. Although the decision threshold used to detect the end of a signal does not have to be the same as the one used to detect signal onset, a simple form for the decision statistic arises when they are the same,

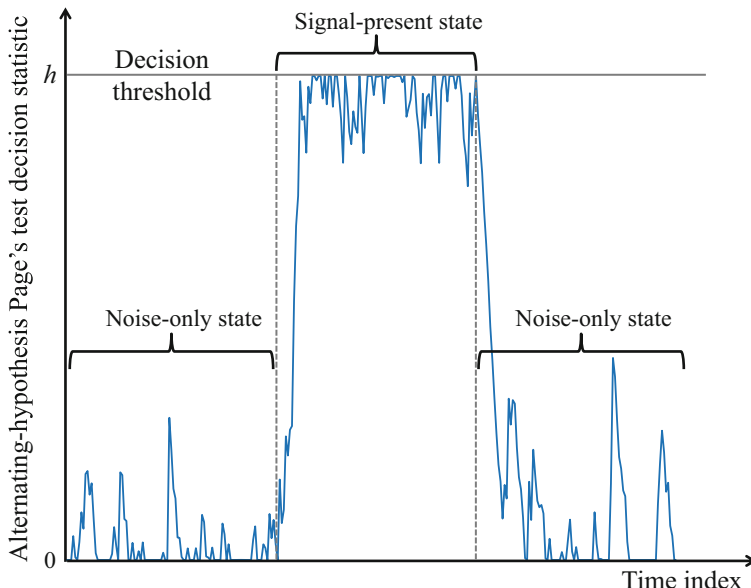


Fig. 10.19 Example decision statistic for an alternating-hypothesis Page's test (AHPT) with equal thresholds in the signal-present and signal-absent decisions

$$V_k = \min\{h, \max\{0, V_{k-1} + Z_k\}\} \quad (10.175)$$

with $V_0 = 0$. As seen in the example in Fig. 10.19, this decision statistic is always between zero and the common decision threshold h . Each reset to zero confirms the noise-only state and each reset to h confirms the signal-present state. When the decision statistic leaves one of the boundaries, the detector can be considered in a pending state with the decision confirmed only when it next reaches a boundary. As seen in Fig. 10.19 the end of the signal is estimated by the last time at which the decision statistic $V_k = h$, which corresponds to $U_k = 0$.

As a final point about the AHPT, recall the decision statistic from (10.167) was developed under a GLR formulation. Because signal detection in the AHPT is performed only using the maximization over the unknown starting time p via the standard Page's test decision statistic in (10.169), it is not clear that it is a GLR detector in the strictest sense. Suppose, however, that a secondary threshold comparison was made against the decision statistic in (10.167), which evaluates the largest negative-to-positive excursion of the cumulative sum after the signal has ended. Because this maximum excursion must be equal to or greater than the decision threshold used to declare a signal present in (10.169), this staged onset-detection and duration estimation also implements the GLR formulation.

10.6.2.2 Page's Test Analysis by Quantization

When done properly, the quantization approximation to SPRT analysis presented in Sect. 10.6.1.1 provided a more accurate assessment of performance than the other approximations or bounds. It is similarly possible to evaluate Page's test as described in [39, 41]. The majority of the following development can be found in [39]. Recall that the iterative form of the Page's test decision statistic from (10.85) was

$$T_k = \max\{0, T_{k-1} + Z_k\} \quad (10.176)$$

where here $z = g(x)$ represents the data after application of the detector function. Although the focus in this section is on the standard Page's test, the results can be applied to the AHPT directly for evaluation of the probability of detection and with little additional effort to characterize the PDF of the decision statistic after the signal has ended.

Now suppose the Page's test update z is quantized to the levels $z_i = (i + 0.5)\delta$ when $z \in [z_i - \delta/2, z_i + \delta/2]$ for integer values of i . The probability of the update lying in the i th interval is then

$$p[i] = F_Z(i\delta + \delta) - F_Z(i\delta) \quad (10.177)$$

where the CDF of the update $F_Z(z)$ is assumed to be continuous. The probability that the update is in or below the i th interval is then

$$P[i] = \sum_{j=-\infty}^i p[j] = F_Z(i\delta + \delta). \quad (10.178)$$

If the step size is chosen so there are n levels on $[0, h)$, then $\delta = h/n$ and there will be n continuing states in the discrete-time, finite-state Markov chain describing the Page's test decision statistic. The state transition matrix, whose (i, j) element describes the probability that T_k will be in state j given that T_{k-1} is in state i , is then

$$\mathbf{P} = \begin{bmatrix} P[0] & p[1] & p[2] & \cdots & p[n-1] \\ P[-1] & p[0] & p[1] & \cdots & p[n-2] \\ P[-2] & p[-1] & p[0] & \cdots & p[n-3] \\ \vdots & \vdots & \vdots & \ddots & \vdots \\ P[1-n] & p[2-n] & p[3-n] & \cdots & p[0] \end{bmatrix}. \quad (10.179)$$

Note that the first column contains cumulative probabilities from (10.178) whereas the remaining columns contain single-level probabilities from (10.177). The first column represents cases where the update Z_k is zero or negative enough that the sum $T_{k-1} + Z_k$ is less than or equal to zero and so the decision statistic is limited at the lower reflecting boundary (i.e., $T_k = 0$). The remainder of the matrix is similar in form to (10.142) for the SPRT with $i_0 = 0$.

The probability mass function (PMF) of the stopping time, average sample numbers (ASNs), and probability of detection as a function of sample number (i.e., $P_d(n)$) for Page's test have identical forms to those presented in Sect. 10.6.1.1 for a quantized SPRT. These are presented below with the following modifications. The unit vector \mathbf{e}_{i_0} has been replaced with \mathbf{e}_0 to represent a vector with a one in the first element, which assumes Page's test is initialized at zero. The vector \mathbf{p}_b is replaced by

$$\mathbf{p}_h^T = [1 - F_Z(h) \quad 1 - F_Z(h - \delta) \quad 1 - F_Z(h - 2\delta) \quad \cdots \quad 1 - F_Z(\delta)] \quad (10.180)$$

to reflect the use of h as a decision threshold and the specific values of the continuing states. Because Page's test only stops when it crosses the upper threshold, the PMF of the stopping time is

$$f_K(k) = \mathbf{e}_0^T \mathbf{P}^{k-1} \mathbf{p}_h \quad (10.181)$$

from (10.149). However, it is easily shown that for \mathbf{P} in (10.179),

$$(\mathbf{I} - \mathbf{P})\mathbf{1} = \mathbf{p}_h \quad (10.182)$$

so this is identical in form to the result in (10.145) for the SPRT. From (10.147), the average sample number is simply

$$\bar{K} = \mathbf{e}_0^T (\mathbf{I} - \mathbf{P})^{-1} \mathbf{1}. \quad (10.183)$$

Starting with (10.152) and using (10.182) to produce $(\mathbf{I} - \mathbf{P})^{-1} \mathbf{p}_h = \mathbf{1}$, the probability of detecting a signal in n samples simplifies to

$$\begin{aligned} P_d(n) &= \mathbf{e}_0^T (\mathbf{I} - \mathbf{P}^n) (\mathbf{I} - \mathbf{P})^{-1} \mathbf{p}_h \\ &= 1 - \mathbf{e}_0^T \mathbf{P}^n \mathbf{1}. \end{aligned} \quad (10.184)$$

From (10.158) the detection latency of a signal with duration n for Page's test is

$$E[K|H_1, \mathcal{S}] = \frac{\sum_{k=1}^n k \mathbf{e}_0^T \mathbf{P}^{k-1} \mathbf{p}_h}{\sum_{k=1}^n \mathbf{e}_0^T \mathbf{P}^{k-1} \mathbf{p}_h}. \quad (10.185)$$

Simplifying this using

$$\sum_{k=1}^n kp^{k-1} = \left\{ (1-p)^{-1} - p^n \left[n + (1-p)^{-1} \right] \right\} (1-p)^{-1} \quad (10.186)$$

adapted from [42, eq. 0.113] and $(\mathbf{I} - \mathbf{P})^{-1} \mathbf{p}_h = \mathbf{1}$ results in

$$E[K|H_1, \mathcal{S}] = \frac{\mathbf{e}_0^T (\mathbf{I} - \mathbf{P})^{-1} \mathbf{1} - \mathbf{e}_0^T \mathbf{P}^n \mathbf{1} \left[n + \frac{\mathbf{e}_0^T \mathbf{P}^n}{\mathbf{e}_0^T \mathbf{P}^n \mathbf{1}} (\mathbf{I} - \mathbf{P})^{-1} \mathbf{1} \right]}{1 - \mathbf{e}_0^T \mathbf{P}^n \mathbf{1}} \quad (10.187)$$

$$= \frac{E[K|H_1] - \Pr\{\bar{\mathcal{S}}|H_1\} E[K|H_1, \bar{\mathcal{S}}]}{\Pr\{\mathcal{S}|H_1\}}. \quad (10.188)$$

This is seen to be a rearrangement of the ASN of an infinite-duration signal in (10.14) to define detection latency in terms of the probability of detecting the signal (or not) and the ASNs for an infinite-duration signal unconditioned on signal detection and conditioned on not detecting the signal in the first n samples. Recall that latent detections (those occurring after the signal has ended but that still arise from signal presence) have been ignored. However, as described in [39], it is possible to include them using the quantization approach to evaluating the performance of Page's test.

Use of \mathbf{e}_0 in (10.181), (10.183)–(10.185) and (10.187) when signal is present implies the *worst-case* detection scenario; that is, the signal starts just after a reset of the Page's test decision statistic to zero. The quantization approximation allows evaluation of the more realistic scenario of the detector being in a steady-state under the noise-only hypothesis. To evaluate this, suppose $\tilde{\pi}_k$ is defined as the state probability vector under the condition that the test has not stopped yet (i.e., $K > k$). As described in [39], this is simply the update from (10.143) divided by

the probability that the test continues,

$$\tilde{\pi}_k^T = \frac{\tilde{\pi}_{k-1}^T \mathbf{P}}{\tilde{\pi}_{k-1}^T \mathbf{P} \mathbf{1}}. \quad (10.189)$$

Iteratively replacing each $\tilde{\pi}_{k-1}^T \mathbf{P}$ with this definition allows describing the state probability vector at time k in terms of the initial one (\mathbf{e}_0) and the state transition probability matrix,

$$\tilde{\pi}_k^T = \frac{\mathbf{e}_0^T \mathbf{P}^k}{\mathbf{e}_0^T \mathbf{P}^k \mathbf{1}}. \quad (10.190)$$

As k increases, the matrix \mathbf{P}^k tends to $\lambda_1^k \mathbf{m}_1 \mathbf{m}_1^T$ where λ_1 is the largest eigenvalue of \mathbf{P} and \mathbf{m}_1 is its associated eigenvector. Thus, the state probability vector conditioned on the test not stopping yet tends to the eigenvector associated with the largest eigenvalue of \mathbf{P} scaled to sum to one,

$$\tilde{\pi}_\infty = \lim_{k \rightarrow \infty} \tilde{\pi}_k = \frac{\mathbf{m}_1}{\mathbf{m}_1^T \mathbf{1}}, \quad (10.191)$$

as $k \rightarrow \infty$. Using $\tilde{\pi}_\infty$ in lieu of \mathbf{e}_0 in (10.181)–(10.184) allows evaluation of the more realistic steady-state condition.

An example evaluation of the probability of detection for Page's test is shown in Fig. 10.20. Using the steady-state state probability vector from (10.191) (reddish-brown line in the figure) illustrates how much difference there is between this expected performance and the worst-case scenario (blue line) of the signal starting in the sample following a reset of the decision statistic to zero. Also shown for comparison are the results for the SPRT presented in Fig. 10.17 and the lower bound from (10.130) (black dashed line). The worst-case Page's test performance is slightly better than the SPRT because of the limiting of the Page's test decision statistic to be non-negative, which does not occur in the SPRT. This implies the lower bound in (10.130), which provides a reasonable approximation to SPRT performance, is less accurate in approximating the performance of Page's test.

10.6.2.3 Design Example

Suppose it is desired to use Page's test to detect a signal of interest arriving at an unknown time and with unknown duration. If the signal is deterministic, the noise is Gaussian, and a cell-averaging CFAR normalizer has been used, then the normalized data are non-centrally F distributed when the signal is present as described in Sect. 8.6.1.3. If the normalizer uses L independent samples of auxiliary data at each observation, then the data are independent and identically distributed,

$$X_k \sim F_{v_1, v_2, \delta} \quad (10.192)$$

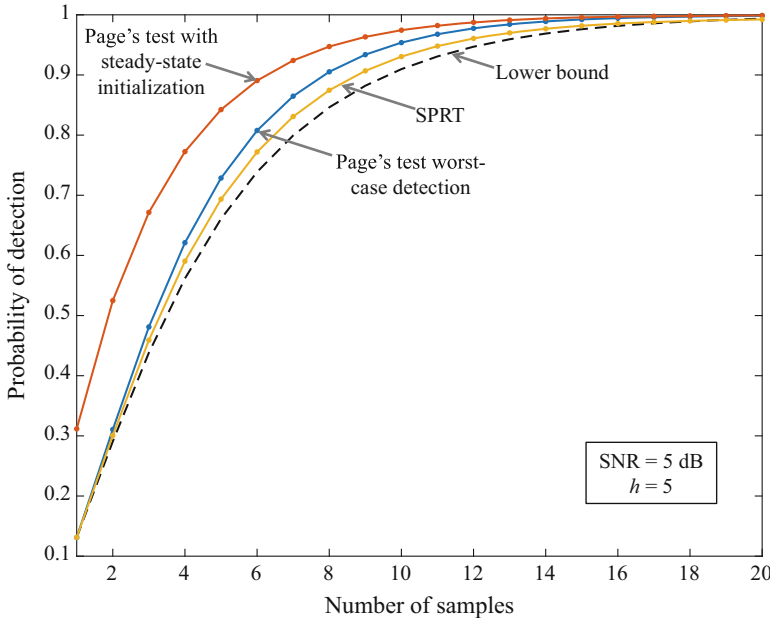


Fig. 10.20 Example probability of detection for Page's test as a function of sample number evaluated using a worst-case initialization ($\pi_0 = \mathbf{e}_0$) and the steady-state state probability under the noise-only hypothesis ($\pi_0 = \tilde{\pi}_\infty$) compared with the performance of an equal-error SPRT with the same upper threshold and the lower bound from (10.130)

with degrees of freedom parameters $v_1 = 2$ and $v_2 = 2L$ and a non-centrality parameter of $\delta = 2s$ where s is the SNR. Under the noise-only condition, the data are centrally F distributed (i.e., $\delta = 0$) with the same degrees-of-freedom parameters. The following covers the steps of designing the detector function, appropriately biasing the Page's test update, choosing a decision threshold based on the average number of samples to a false alarm, and evaluating detection performance as a function of signal duration.

- 1. Design the detector function:** As can be seen from Sect. 5.6.17, the PDF of the non-central F distribution is an infinite summation. Direct application to data in the form of a likelihood ratio is therefore not pragmatic. Although it is possible to choose a design SNR and implement the corresponding log-likelihood ratio through a table-lookup function, the locally optimal detector provides a simple and attractive alternative. As described in (6.22) from Sect. 6.2.6, the locally optimal detector function is

$$g_{\text{LO}}(x) = \frac{\frac{\partial}{\partial \delta} f_1(x; \delta)|_{\delta=0}}{f_0(x)} \quad (10.193)$$

where $f_1(x; \delta)$ and $f_0(x)$ are the PDFs of the data under, respectively, the signal-present and noise-only hypotheses. Similar to the derivation of the

locally optimal detector function for the non-central chi-squared distribution in Sect. 8.8.2, only the first two terms in the infinite-sum form of the non-central F PDF are required because when δ is set to zero in (10.193) all the remaining terms will be zero. Recall from Sect. 5.6.17 the infinite-sum form of the PDF using the central F and Poisson distributions,

$$\begin{aligned} f_1(x; \delta) &= \sum_{k=0}^{\infty} f_{\text{Poi}}(k; \delta/2) f_F\left(\frac{\nu_1 x}{\nu_1 + 2k}; \nu_1 + 2k, \nu_2\right) \frac{\nu_1}{\nu_1 + 2k} \\ &= e^{-\delta/2} f_F(x; \nu_1, \nu_2) + \frac{\delta}{2} e^{-\delta/2} f_F\left(\frac{\nu_1 x}{\nu_1 + 2}; \nu_1 + 2, \nu_2\right) \frac{\nu_1}{\nu_1 + 2} + \dots \end{aligned} \quad (10.194)$$

where $f_F(x; \nu_1, \nu_2)$ is the F_{ν_1, ν_2} PDF and $f_{\text{Poi}}(k; \lambda)$ is the Poisson PDF with rate λ . Substituting this in (10.193) results in the locally optimal detector function for the non-central F distribution,

$$g_{\text{LO}}(x) = \frac{(\nu_1 + \nu_2)x}{2(\nu_2 + \nu_1 x)} - \frac{1}{2}. \quad (10.195)$$

The pertinent portion of this detector function in the present application is the first term because the constant term can be accounted for during the biasing of the update. After an appropriate, though arbitrary, scaling this simplifies to

$$g_0(x) = \frac{x}{1 + x/L}. \quad (10.196)$$

As seen in Fig. 10.21, this function is approximately linear when $x \ll L$ and saturates at L as $x \rightarrow \infty$. This has the effect of de-emphasizing the tails of the non-central F distribution based on the quality of the background power estimator.

- 2. Obtain the bias for Page's Test:** In deriving the locally optimal detector function, the constant term was discarded to form (10.196). The reason the locally optimal detector function cannot be used exactly as it is derived is because it has a zero mean under the noise-only condition and would therefore violate (10.106). This can be seen by using the definition of the locally optimal detector function in the following expectation,

$$\begin{aligned} E_0[g_{\text{LO}}(X)] &= E_0\left[\frac{\frac{\partial}{\partial \delta} f_1(x; \delta)|_{\delta=0}}{f_0(x)}\right] \\ &= \frac{\partial}{\partial \delta} \int_{-\infty}^{\infty} f_1(x; \delta) dx \Big|_{\delta=0} \quad (10.197) \\ &= 0, \quad (10.198) \end{aligned}$$

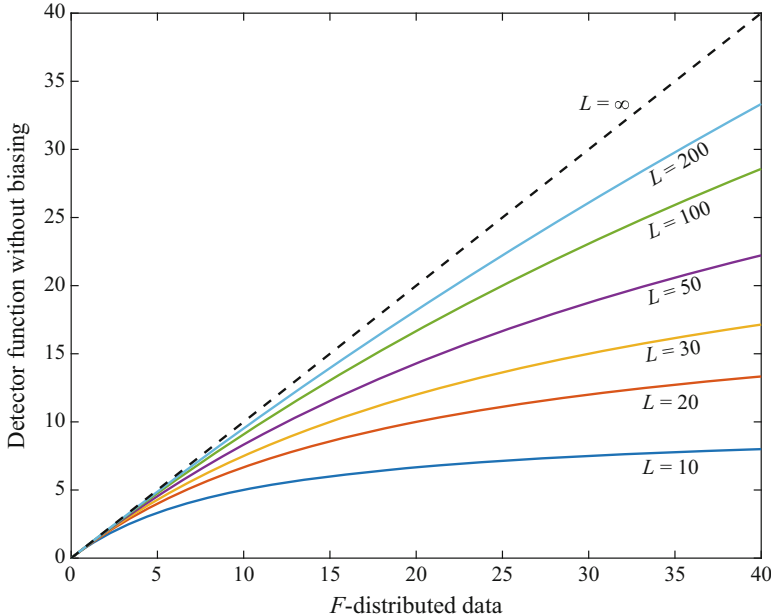


Fig. 10.21 Locally optimal detector function from (10.196) for non-centrally F distributed data with L independent samples of auxiliary data in the background estimation. The black dashed line represents the case of perfect estimation (i.e., $L \rightarrow \infty$)

and noting that the integral in (10.197) is over a PDF and is therefore always equal to one. Thus, either Dyson's bias or the asymptotically optimal bias from Sect. 10.5.2.4 must be used to force the mean of the biased detector function to be negative when there is only noise and positive when signal is present. For the present application, both of these require numerical evaluation. Dyson's bias as found in (10.115) only requires numerical evaluation of the mean of (10.196) for a design SNR. Under the noise-only hypothesis, the mean of the unbiased detector function is

$$E_0[g_0(X)] = \frac{L}{L+1}. \quad (10.199)$$

The asymptotically optimal bias in (10.117) not only requires evaluation of the moment generating function of (10.196) (under the noise-only condition), but also its derivative and solution of the equation in (10.119). After performing the numerical evaluations for this example, the resulting bias options are presented in Fig. 10.22. Although Dyson's bias is easier to evaluate, use of the asymptotically optimal bias provides not only better performance but also a smaller bias which means it can be subject to a greater mismatch in SNR. The optimal bias for perfect normalization, which is simply $(1 + 1/s) \log(1 + s)$, is shown as the

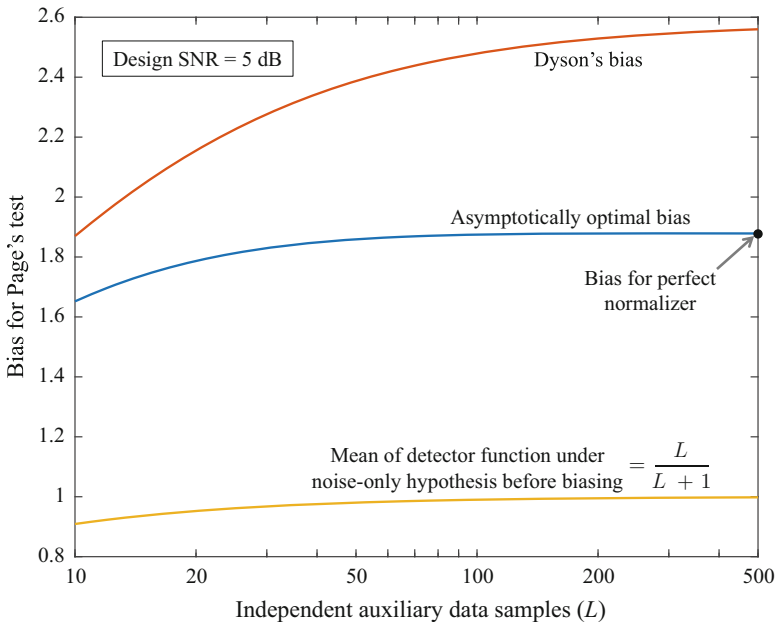


Fig. 10.22 Biases for Page's test when the input data are F distributed

black circle on the right-side axis. Except for small values of L , using this bias appears not only expedient, but nearly optimal.

3. **Choose the decision threshold:** The next step in the design of this detector is to choose the decision threshold as a function of the false-alarm performance specification, which is the average number of samples to a false alarm. The options for evaluating this include the approximation of (10.97), the approximation using the Brownian-motion-based correction in (10.129), or using the quantization approach described in Sect. 10.6.2.2. The first two require numerical evaluation of the unity root of the moment generating function as described in Sect. 10.5.2.2 and the correction requires evaluation of the variance and skewness of $g_0(X)$ and ϕ in (10.73), which requires the characteristic function of $g_0(X)$. By comparison, the quantization approach is much simpler because it primarily requires evaluation of the cumulative distribution function (CDF) of $g_0(X)$, which is easily described in terms of the CDF of X .

The average number of samples to a false alarm (F) as obtained by the three approaches for $L = 30$, a design SNR of 5 dB, and the asymptotically optimal bias is shown in Fig. 10.23. Based on the higher accuracy expected from the quantization approach and the relative ease with which it is obtained for this example, it is the best option for choosing the decision threshold as a function of the false-alarm specification. For a design average number of samples between false alarms of $F = 10^4$ the decision threshold is $h = 7.7$. Using one of the other approximations would result in a larger threshold. This implies the

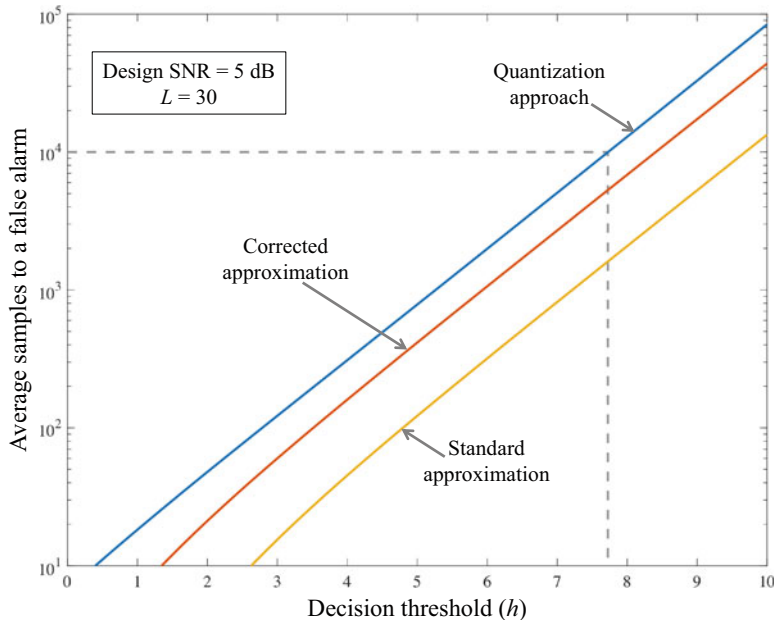


Fig. 10.23 Average number of samples to a false alarm as a function of the decision threshold for Page’s test with an F distributed input, the locally optimal detector function, and the asymptotically optimal bias for a design SNR of 5 dB

achieved detector operating point is conservative with respect to the false-alarm specification at the expense of a reduction in probability of detection.

4. **Evaluate detection performance:** The final task in developing this detector is to assess its performance in detecting the signal using the decision threshold chosen in the previous step. Because the signal is of intermediate duration, the probability of detection is the relevant performance metric and it needs to be evaluated as a function of the signal duration. The two options for evaluating this include the lower bound described in (10.130) and the quantization approach from (10.184).

Although the lower bound does not have any simple closed-form solution, it can be adequately approximated by matching moments with a shifted gamma distribution. This can be done by using the first three moments of the sum of $g_0(X_k)$ via (9.377)–(9.379), finding the parameters of the shifted gamma distribution using (9.118)–(9.120), modifying the shift parameter ($c_{g,i}$) by subtracting $n\tau$ where τ is the bias, and evaluating P_d in (9.121). The result of this is shown in Fig. 10.24 along with the results of a simulation to ensure its accuracy.

The results of the quantization approach are also shown, both for the worst-case scenario where the signal starts immediate after a reset of the decision statistic to zero and when the test is in the steady state of a noise-only condition

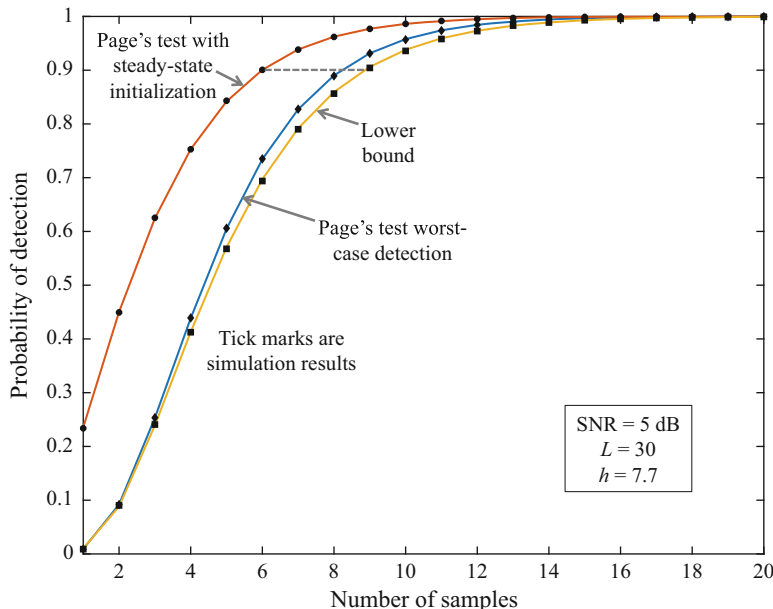


Fig. 10.24 Probability of detection for Page’s test as a function of sample number evaluated using a worst-case initialization ($\pi_0 = \mathbf{e}_0$) and the steady-state state probability under the noise-only hypothesis ($\pi_0 = \tilde{\pi}_\infty$) compared with the lower bound from (10.130). The solid lines are obtained using the quantization approach for Page’s test and a shifted-gamma approximation for the lower bound. The black tick marks are simulation results illustrating the accuracy of the approximations

(i.e., using $\tilde{\pi}_\infty$ from (10.191) in lieu of \mathbf{e}_0 in (10.184)). The worst-case detection results illustrate that the lower bound is useful in this example and the steady-state noise condition indicates the signal is likely to be detected a full two samples earlier than indicated by the worst-case scenario.

Note that implementing Page’s test in MATLAB[®] is most easily accomplished by exploiting the definition in (10.82) rather than the iteration in (10.85). Using (10.82) leads to

$$T = \text{cumsum}(Z) - \text{cummin}(\min(0, \text{cumsum}(Z))) ;$$

where the input data are in the vector Z . However, simulating the steady-state noise-only scenario requires the iteration in (10.85).

References

1. A. Wald, *Sequential Analysis* (Wiley, 1947)
2. Z. Govindarajulu, *The Sequential Statistical Analysis of Hypothesis Testing, Point and Interval Estimation, and Decision, Theory* (American Sciences Press, 1987)
3. B.K. Ghosh, P.K. Sen (eds.), *Handbook of Sequential Analysis* (Marcel Dekker, 1991)
4. A. Tartakovsky, I. Nikiforov, M. Basseville, *Sequential Analysis: Hypothesis Testing and Changepoint Detection* (CRC Press, Boca Raton, 2014)
5. D. Siegmund, *Sequential Analysis* (Springer, 1985)
6. C. Forbes, M. Evans, N. Hastings, B. Peacock, *Statistical Distributions*, 4th edn. (Wiley, Hoboken, NJ, 2011)
7. S.A. Kassam, *Signal Detection in Non-Gaussian Noise* (Springer, New York, 1988)
8. M.A. Richards, *Fundamentals of Radar Signal Processing* (McGraw-Hill, New York, 2005)
9. J.V. DiFranco, W.L. Rubin, *Radar Detection* (Artech House, Dedham, MA, 1980)
10. P.K. Varshney, *Distributed Detection and Data Fusion* (Springer, New York, 1996)
11. J.V. Harrington, An analysis of the detection of repeated signals in noise by binary integration. *IRE Trans. Inf. Theory* **1**(1), 1–9 (1955)
12. D.A. Shnidman, Binary integration for Swerling target fluctuations. *IEEE Trans. Aerosp. Electron. Syst.* **34**(3), 1043–1053 (1998)
13. D.A. Abraham, Optimization of M -of- N detectors in heavy-tailed noise, in *Proceedings of 2018 IEEE/MTS Oceans Conference*, Charleston, SC, 2018
14. T.L. Lai, Control charts based on weighted sums. *Ann. Stat.* **2**(1), 134–147 (1974)
15. W. Böhm, P. Hackl, Improved bounds for the average run length of control charts based on finite weighted sums. *Ann. Stat.* **18**(4), 1895–1899 (1990)
16. P. Williams, Evaluating the state probabilities of m out of n sliding window detectors. *Tech. Rpt. DSTO-TN-0132*, Maritime Operations Division Aeronautical and Maritime Research Laboratory, February 1998
17. D.A. Abraham, Analysis and design of sliding m -of- n detectors. *Tech. Rpt. 2011-01*, CausaSci LLC, <http://www.dtic.mil/get-tr-doc/pdf?AD=ADA565377>, 2011
18. J.I. Naus, Approximations for distributions of scan statistics. *J. Am. Stat. Assoc.* **77**(377), 177–183 (1982)
19. J. Glaz, J. Naus, S. Wallenstein, *Scan Statistics* (Springer, New York, 2001)
20. C. Stein, A note on cumulative sums. *Ann. Math. Stat.* **17**(4), 498–499 (1946)
21. A. Wald, J. Wolfowitz, Optimum character of the sequential probability ratio test. *Ann. Math. Stat.* **19**(3), 326–339 (1948)
22. R.H. Berk, Locally most powerful sequential tests. *Ann. Stat.* **3**(2), 373–381 (1975)
23. P.J. Huber, A robust version of the probability ratio test. *Ann. Math. Stat.* **36**(6), 1753–1758 (1965)
24. W.J. Hall, R.A. Wijsman, J.K. Ghosh, The relationship between sufficiency and invariance with applications in sequential analysis. *Ann. Math. Stat.* **36**(2), 575–614 (1965)
25. R.M. Phatarfod, Sequential analysis of dependent observations. I. *Biometrika* **52**(1/2), 157–165 (1965)
26. C.D. Fuh, SPRT and CUSUM in hidden Markov models. *Ann. Stat.* **31**(3), 942–977 (2003)
27. D. Siegmund, Corrected diffusion approximations and their applications, in *Proc. Berkeley Conference in Honor of Jerzy Neyman and Jack Kiefer*, ed. by L.M. Le Cam, R.A. Olshan (Wadsworth, 1985), pp. 599–617
28. R.A. Wijsman, Stopping times: Termination, moments, distribution, in *Handbook of Sequential Analysis*, ed. by B.K. Ghosh, P.K. Senn (Marcel Dekker, 1991)
29. D.A. Abraham, A Page test with nuisance parameter estimation. *IEEE Trans. Inf. Theory* **42**(6), 2242–2252 (1996)
30. E.S. Page, Continuous inspection schemes. *Biometrika* **41**, 100–114 (1954)
31. G. Lorden, Procedures for reacting to a change in distribution. *Ann. Math. Stat.* **42**(6), 1897–1908 (1971)

32. G.V. Moustakides, Optimal stopping times for detecting changes in distributions. *Ann. Stat.* **14**(4), 1379–1387 (1986)
33. D.A. Abraham, Analysis of a signal starting time estimator based on the Page test statistic. *IEEE Trans. Aerosp. Electron. Syst.* **33**(4), 1225–1234 (1997)
34. J.H. Mathews, K.D. Fink, *Numerical Methods Using MATLAB* (Prentice Hall, 1999)
35. B. Broder, *Quickest Detection Procedures and Transient Signal Detection*, PhD thesis, Princeton University, Princeton, NJ, 1990
36. S. Kullback, R.A. Leibler, On information and sufficiency. *Ann. Math. Stat.* **22**(1), 79–86 (1951)
37. T.F. Dyson, *Topics in Nonlinear Filtering and Detection*, PhD thesis, Princeton University, Princeton, NJ, 1986
38. D.A. Abraham, Asymptotically optimal bias for a general non-linearity in Page’s test. *IEEE Trans. Aerosp. Electron. Syst.* **32**(1), 360–367 (1996)
39. C. Han, P.K. Willett, D.A. Abraham, Some methods to evaluate the performance of Page’s test as used to detect transient signals. *IEEE Trans. Signal Process.* **47**(8), 2112–2127 (1999)
40. R.L. Streit, Load modeling in asynchronous data fusion systems using Markov modulated Poisson processes and queues, in *Proceedings of Signal Processing Workshop*, Washington, D.C., March 24–25, 1995. Maryland/District of Columbia Chapter of the IEEE Signal Processing Society
41. D. Brook, D.A. Evans, An approach to the probability distribution of cusum run length. *Biometrika* **59**(3), 539–549 (1972)
42. I.S. Gradshteyn, I.M. Ryzhik, *Table of Integrals, Series, and Products*, 8th edn., ed. by D. Zwillinger (Elsevier Academic Press, Waltham, MA, 2015)

Index

A

Absorption, 124
Acoustic quantities & units (table), 98
Acoustic wave, 95, 99, 102
Acronyms and abbreviations, list of, xxix
Active sonar
 noise-limited, 68, 69, 70, 72, 396, 492, 597, 599
 reverberation-limited, 68, 70, 189, 492, 597, 598, 610
Albersheim's equation, *see* Detection threshold
Algorithm development process, 9
Aliasing, 220, 221, 626, 653
Ambient noise, 62, 158, 349, 389
 anthropogenic, 390, 423
 deep vs. shallow water, 162, 163
 earthquakes, 390
 ice related, 390, 404, 423
 impulsive, 415, 423
 isotropic, 86, 533, 534
 Knudsen curves, 162
 level, 63, 74
 non-Gaussian (*see* Heavy-tailed distributions)
 precipitation, 159, 163
 shipping, 161, 404, 601, 649
 snapping shrimp, 390
 spatial properties, 164
 spectral characterization, 158, 160, 353, 389, 490, 600, 649
 statistical characterization, 164, 352, 355, 359, 390
 surface related, 162, 404, 601, 649

temporal characterization, 164, 353, 389, 600, 684
thermal, 163
turbulence, 160
wave–wave interaction, 160
Wenz curves, 158
Ambiguity
 cone, 39, 528
 left/right, 20, 39, 40
Ambiguity function, 56, 498, 507, 584, 586, 590
 and matched-filter SNR mismatch loss, 505–507, 509, 605
 as filter-bank response, 499, 503, 506, 509, 532
 as single-filter response, 498, 503, 504–507, 509, 518, 532
 complex, 503, 506, 507, 532
 Fourier transform, 507
 cross-ambiguity, 509
 frequency-average relationship, 549
 frequency-variance relationship, 549
 narrowband, 506, 508
 quadratic phase modulation, 517
 table of definitions, 506
 thumbtack shaped, 599
 wideband, 504, 506, 507
Analytic signal, xxxiii, 192, 367, 368, 371, 374
 LTI system response, 377
Ancillary parameters, 318, 321, 324, 475
Angle estimation, 20, 38, 39, 532
 CRLB for line array, 86
Array gain, 62–64, 74, 77, 533, 626
Array of sensors, 5, 35
 See also Line array

- Array signal processing, 7, 15
 isotropic noise, 533, 534
 signal and noise modeling, 529, 531
 spatially white noise, 530, 533
- Autocorrelation function, 283
 random process, 274, 357, 358, 378, 389, 625
 waveform, 405, 498, 506, 510, 540, 605
 Fourier transform, 510, 511
 properties, 511
- Autocorrelation processing, *see* Time-delay estimation
- Autocovariance function, 275, 283
- Auxiliary data, *see* Normalization
- B**
- Backscattering strength, *see* Scattering strength
- Bandpass signal, 281, 350, 359, 362, 367, 368, 371, 378, 382, 621, 626
- Bandwidth
 channel, 357, 608, 610
 signal, 217, 357, 361, 367, 405, 621, 625
- Basebanding, 16, 372, 374, 628
 unknown Doppler, 375
 via bandpass sampling, 374
- Basic ocean model, 96, 99, 102, 105, 118, 156, 166, 170, 182, 353
 channel impulse response, 112
 waveguide, 148, 151, 154, 157
- Bayes' theorem, 253, 271
- Bayesian
 confidence interval (*see* Credible sets)
 detection, 325
 estimation, 340
 loss function, 325, 340
 MAP estimator, 341
 posterior mean, 340
 posterior median, 341
 posterior mode, 341
 posterior PDF, 340
 risk function, 325, 340
- Beamforming, 16, 19, 20, 39, 97, 102, 194, 353, 398, 403, 405, 527, 594
 beam response, 532, 533
 main response axis, 400, 401, 532
 steering vector, 530
 wavefront-curvature, 20, 43, 110
 See also Array signal processing
- Beampattern, 399, 532
 uniform line array, 400
- Beamwidth, 400, 401, 405
- Bearing estimation, *see* Angle estimation
- Bearing-time record, 36
- Bellhop model, 129
- Beta function, xxxiv, 288
- Bias, *see* Estimation
- Binary integration, *see* M-of-N detector
- Bistatic sonar, 37, 41, 45
 bistatic angle, 47, 167
 blanking region, 47
 Doppler scale, 52
 ellipse, 45
 equivalent monostatic range, 46
 range estimation, 46
 resolution cell, 47
 target scattering (*see* Scattering)
- Box-Muller transformation, 289
- Broadband signal, 351, 357, 359, 625
 contrasted with narrowband, 359, 361
 instantaneously narrowband, 357
 normalization, 683
- Bubbles, 125, 148, 162, 182, 188, 396, 414
- Bulk modulus, 125
- C**
- Carrier frequency, 368
- Cauchy-Schwarz inequality, 329, 505, 559, 790
- Causality of a system, 234
- Central limit theorem, 268, 349, 390, 391, 403, 404, 429
 applications, 76, 78, 365, 411, 607, 644
- Chance line, 312
- Channel capacity, 25
- Channel frequency response, 114, 362
 Lloyd mirror, 135
 multipath channel, 114
 related to propagation loss factor, 122
- Channel impulse response, 112, 114, 182, 362
 basic ocean model, 112, 156
 multipath channel, 113
 units, 112
- Chapman-Harris, *see* Scattering strength, surface
- Characteristic function, xxxiv, 272, 409, 432, 581, 651, 652, 693
- Characteristic function
 inverse moments via, 697
- Circularity or circular symmetry, 282, 379, 386, 409, 443
- Classification, 8, 15, 24, 180, 357
 contrasted with detection, 24
 features, 26
 historical training data, 27
- Clustering, 23
- Clutter, *see* Heavy-tailed distributions
- Coherence function, 707, 711

- Coherent processing interval, 23, 674, 743
Complex envelope, xxxiii, 359, 367, 372, 373, 374, 406, 408, 429
bandpass noise, 378
characteristic function, 409, 432, 442–444, 446
impact of delay and Doppler, 375
LTI system response, 378
statistical modeling, 381, 382, 383, 385, 432, 469, 489, 628
Complex random variables, *see* Random variables
Comprehensive Nuclear-Test-Ban Treaty Organization, 4, 5
airgun blasts, 390
fin whale acoustic emissions, 11
iceberg grounding, 4
volcano activity, 11
Cone of ambiguity, *see* Ambiguity
Confidence interval, 263, 326, 344, 544
confidence coefficient, 265, 344
coverage probability, 265, 345
ellipse, 561
interpretation, 345
Constant false alarm rate, 488, 490, 566, 684
CFAR loss (*see* Normalization) detector, 472
Control chart, 760
Convergence zone, *see* Propagation
Convolution, 206, 225
application, 261, 272, 359, 397, 425, 429
circular vs. linear, 238
continuous time, xxxiii, 112, 206, 214, 360, 377, 604
discrete time, xxxiii, 225, 227, 689
Coordinate system, 36, 40
spherical, 113
spherical/Cartesian conversion, 40
Correlation coefficient, 267, 268
Correlation matrix, 268
Correlation time, 61, 65, 356
Covariance matrix, 268
pseudo, 284
Cramér-Rao lower bound, 85, 328, 329, 499, 535
deterministic-signal amplitude and phase, 543, 728
Doppler scale, 553, 555, 560
Doppler shift, 555, 556
frequency of a sinusoid in noise, 86
Gaussian-fluctuating-signal power, 543
heavy-tailed noise parameters, 420
iid samples, 330
line-array angle estimation, 86
looseness at low SNR, 537
multiple parameters, 331, 536, 545
multivariate Gaussian
complex, 334
real, 334
narrowband signal parameters, 729
parameter transformations, 332
power-spectral-density parameters, 715
radial velocity, 556
sinusoidal signal parameters, 728
SNR estimation, 333
sound pressure level, 543
time-Doppler (joint), 558, 560
time delay, 710, 720
time of arrival, 540, 545, 549, 550, 552, 560, 713
Credible sets, 345
interpretation, 345
Creeping wave, *see* Scattering
Critical angle, 121, 128, 137, 139, 141
Critical depth, 130
CRLB, *see* Cramer-Rao lower bound
Cross-correlation processing, *see* Time-delay estimation
Cross-covariance function, 283
CTBTO, *see* Comprehensive Nuclear-Test-Ban Treaty Organization
Cumulant, 273
generating function, 272, 791
Cumulative distribution function, 253, 385, 410
characteristic function relationship, 653
conditional, 269
joint, 265
numerical evaluation from characteristic function, 272, 437, 625, 652, 662, 669, 686, 690, 733
of a ratio, 693
CUSUM detector, *see* Page's test
CW pulse, 192, 361, 395, 460, 511, 590
ambiguity function, 513, 538, 590
analytic signal, 511
autocorrelation function, 395, 511, 538
complex envelope, 511
Doppler sensitivity, 54, 463, 499, 555, 592
estimating radial velocity, 54
own-ship Doppler nullification, 196
resolution, 513, 537, 556
reverberation temporal support ('Q') function, 598
spectrum, 54, 192, 396, 397, 463

D

- Data fusion, 37
 DCLT, 3, 8, 15
 as inference problems, 8
 Decade, *see* Frequency
 Decibel, 58
 $10 \log_{10}$ vs. $20 \log_{10}$, 59
 reference units, 59
 Decidecade, *see* Frequency
 Decimation, 246, 374, 671
 and aliasing, 247
 impact on the Fourier transform, 247
 Deep scattering layer, 185, 186
 Deep sound channel, *see* Propagation
 Delta function, *see* Impulse function
 Density (volumetric mass)
 air, 134
 and reciprocity, 157
 bottom, 136, 364
 typical values, 126
 water, 61, 99, 364
 Depth excess, 130
 Depth sounding, 4
 Detection, 8, 16, 307
 area under the ROC curve, 315
 as a binary hypothesis test, 24, 308
 Bayesian, 325
 CFAR (*see* Constant false alarm rate)
 coherent portion of, 64, 70, 75, 83, 88, 466,
 470, 492, 626, 630, 632
 contrasted with classification, 24
 decision statistic, 17, 310, 459
 decision threshold, 17, 311, 459
 decision threshold vs. detection threshold,
 312
 detector function, 321, 643, 647, 648,
 778
 envelope vs. squared-envelope, 78
 equal error point, 315
 flow chart by signal characterization, 624
 generalized likelihood ratio, 318, 321, 486,
 487, 495, 498, 794
 asymptotic distribution, 324
 examples, 459, 475, 481, 565, 586, 647,
 658, 660, 664, 667, 795, 804
 known signals, 457
 locally optimal, 320, 789
 examples, 604, 611, 643, 665, 811
 Neyman-Pearson optimal (*see* Neyman-Pearson)
 non-linearity (*see* Detection, detector
 function)
 operating point, 75, 80, 81, 311

-value, 311

performance measures, 309, 312, 315, 745,
 747
 probability of detection, 309, 310, 403, 459
 approximation, 445, 446, 451
 probability of false alarm, 309, 310, 389,
 403, 406
 required SNR, 312
 ROC curve, 312, 750
 estimation (*see* Histogram)
 uniformly most powerful, 318, 319
 examples, 472, 479, 480, 483, 634
 invariant, 318, 319
 unknown noise parameters, 485
 unknown signal parameters, 488
 weak signal (*see* Detection, locally
 optimal)
 Detection index, 82, 384, 642, 644, 672, 756
 Gaussian decision statistics, 646
 Detection threshold, 74, 75, 81, 311, 312, 316,
 469
 Albersheim's equation, 78, 590, 668, 678
 alternative definition using noise PSD, 82
 deterministic signal
 known phase, 83, 84, 473
 unknown phase, 78, 84, 477, 677
 Gaussian-fluctuating signal, 76, 84, 481,
 635, 637, 679, 681
 Hamm's equation, 79, 668, 678
 non-Gaussian background, 80
 related to required SNR, 83
 Rician signal, 79
 Detector threshold, *see* Detection, decision
 threshold
 Deterministic signal, 75, 80, 86, 90, 353, 355,
 356, 365, 366, 384, 429, 430, 438,
 448, 452, 465, 467, 498, 536, 545,
 573, 581, 590, 604, 614, 664, 677,
 695, 755, 756, 758, 759, 796
 characteristic function, 444, 446, 696
 detection threshold, 78, 83, 84
 detector, 471, 475, 477
 incoherent integration, 434
 moments of the instantaneous intensity, 449
 parameter estimation, 541
 probability of detection, 433
 scintillation index, 440, 449
 Direct blast, 45
 blanking, 46
 Directivity index, 64, 533, 534
 line array, 64
 Dirichlet kernel, 243
 Discrete Fourier transform, *see* Fourier
 transform
 Dispersion, 124, 154, 156, 357

- intrinsic vs. geometric, 154
- Distortionless response
 - window scaling, 241
- Distribution-approximation models
 - F* distribution, 690, 697
 - gamma, 601, 649, **656**, 658, 662, 681, 683, 686, 690, 695, 697, 762
 - non-central, 448, 451, 697
 - shifted, 297, 441, 442, **446**, 451, 477, 649, 656, 658, 662, 681, 686, 691, 697, 735, 815
 - Gaussian, 80, 90, 269, 644, 649, 655, 658, 677–679, 681, 686
 - Distribution chain, 388, 391, 428, 443
 - K* distribution, 410, 416
 - mixture distribution, 425
 - Poisson Rayleigh, 414
 - Rayleigh, 388, 414, 416, 423, 432, 446, 576, 596, 635, 640
 - Rician, 388, 433, **434**, 437
 - Distributions, 284
 - Bernoulli, 265, **285**, 286, 496, 749
 - beta, 285, **288**
 - binomial, 265, 285, **286**, 429, 496, 754
 - chi-squared, 296
 - examples, 79, 324, 429, 435, 476, 561, 567, 572, 611, 612, 667, 668, 685
 - properties, 262, 285, 293, 294, **296**, 298, 756
 - chi-squared, non-central, 297, 446, 448
 - examples, 78, 324, 429, 433, 438, 476, 544, 573, 611, 614, 667, 668, 677, 694, 791, 797, 812
 - properties, 255, 261, 273, 285, 295, 296, **297**, 299, 324, 434
 - exponential, 292, 403
 - examples, 260, 261, 265, 317, 338, 355, 356, 387, 388, 408, 410, 413, 414, 416, 425, 429, 432, 436, 486, 487, 489, 561, 567, 570, 572, 576, 577, 579, 581, 587, 608, 615, 640, 644, 648, 652, 653, 657, 676, 679, 684, 685, 691, 714, 715, 733, 753, 760, 761, 765, 772, 775, 785, 787, 792, 795
 - moments, 292, 450
 - properties, 255, 261, 262, 269, 273, 285, 286, **292**, 293, 294, 300–302, 343, 344, 406, 407, 411, 416, 417, 423, 440, 480, 578, 635, 651, 690, 756
 - F* distribution, 262, 285, **298**, 299, 302, 323, 333, 602, 685, 812
 - characteristic function, 685
 - non-central, 285, **299**, 323, 324, 573, 810
 - when ν_1 equals two, 323, 568, 572, 685
 - gamma, 293, 337, 685, 760
 - examples, 337, 412, 415, 416, 435, 436, 440–442, 446, 448, 451, 570, 571, 601, 635, 636, 651, 656, 658, 676, 677, 690, 691, 760, 775, 790, 792
 - non-central, 448
 - properties, 255, 261, 262, 269, 285, 293, 301, 687
 - gamma shifted (*see* Distribution-approximation models)
 - Gaussian or normal, 253, 256, **289**
 - bivariate, 281, 290
 - complex, 281, 283, **290**, 322, 333, 387
 - complex multivariate, 283, **291**, 416, 464, 531, 542, 628, 706, 710
 - examples, 24, 29, 65, 76, 78, 80, 82, 88, 145, 164, 190, 256, 257, 263, 265, 267, 269, 336, 349, 352, 366, 384, 388, 390, 397, 403–405, 412, 414, 423, 464, 473, 484, 541, 544, 561, 607, 608, 625, 636, 644, 756, 775
 - multivariate, 291
 - properties, 255, 267, 273, 285, 286, 289, 293, 294, 303, 337, 397, 418, 419, 436, 489, 633, 791
 - generalized Pareto, 285, **302**, **416**, 420, 428
 - moments, 302, 450
 - scintillation index, 407
 - geometric, 285, 749, 764, 782
 - heavy-tailed (*see* Heavy-tailed distributions)
 - K distribution, 285, **301**, 406, **408**, 429, 695
 - characteristic function, 444, 446, 696
 - genesis, 262, 301, 409, 411
 - moments, 301, 412, 450
 - parameter estimation, 338, 413, 420, 428
 - scintillation index, 407, 412
 - Laplacian/double-exponential, 321, 753
 - log normal, 90, 285, **303**, 419, 420
 - moments, 303, 450
 - scintillation index, 407
 - mixtures (*see* Mixture distribution)
 - negative binomial, 285, 412, **441**
 - Poisson, 285, **286**, 297, 299, 390, 414, 415, 812
 - Rayleigh, 261, **294**
 - examples, 261, 338, 355, 356, 365, 366, 387, 388, 403, 404, 413, 425, 429, 436, 564, 576, 577, 596, 635

- Distributions (*cont.*)
 properties, 285, 294, 295, 300, 343, 389, 414, 416, 417, 423, 433, 581, 756
 Rician, 295
 examples, 366, 388, 433
 properties, 261, 285, 295
 See also Rician signal
 standard exponential, normal, or uniform, 256, 262, 269, 287–289
 uniform, 183, 190, 258, 260, 287, 289, 329, 358, 365
 Weibull, 285, 300, 391, 417, 420, 428, 444
 characteristic function, 444
 moments, 300, 450
 scintillation index, 407
- Divergence, *see* Kullback-Liebler divergence
- Doppler, 48
 derivation of effect, 51, 115
 effect on reverberation, 193
 ownship Doppler nullification, 195, 594
 radial acceleration, 53
 scale, 49, 50, 118, 193, 195, 394, 396, 463, 508, 585, 660
 scale for bistatic active, 52
 scale for monostatic active, 53, 585
 scale for one-way propagation, 52, 585
 sensitive vs. tolerant waveforms, 54
 sensitive waveform, 402, 584
 shift, 50, 360, 362, 377, 585, 657
 spreading (*see* Reverberation)
 table summary, 585
 time compression or dilation, 49, 592
- Doppler estimation, 535, 584
 CRLB (*see* Cramer-Rao lower bound)
 Doppler channel, 586
 Doppler filter bank, 54, 55, 194, 498, 513, 531, 532, 586, 594, 616
 decision threshold, 587
 example, 13, 590
 implementation, 592, 616
 normalization, 600
 performance analysis, 587, 588, 596
- Dynamic range, *see* Quantization
- E**
- Echo ranging, *see* Localization, ranging, active
 Eckart filter, 358, 491, 644, 649, 669, 676, 683
 Eikonal equations, 148
 Energy detector, 64, 622, 624, 625, 682, 745
 basic, 632, 649
 performance analysis, 634
 coherent and incoherent integration, 622, 669
 deterministic signals, 663, 666, 668
 Eckart filter (*see* Eckart filter)
 frequency domain, 622, 626, 638, 669
 generalized likelihood ratio, 647, 662, 676
 modified, 658, 662, 668, 735
 performance analysis, 658
 locally optimal, 491, 643, 644–646
 Neyman-Pearson optimal, 642, 643–646, 649, 669, 676, 683
 examples, 633
 noise normalized, 630, 646, 649, 657, 661, 662, 665, 668, 669, 676, 681, 683, 690, 693
 decision threshold, 676
 power law, 659, 669, 676
 performance analysis, 662, 669
 SNR after coherent processing, 630, 634
 statistical modeling, 628, 664
 subspace, 664, 666
 performance analysis, 667
 table of assumptions & optimality, 627
 time domain, 622, 626, 639, 669
 weighted frequency sum, 642, 644, 646, 648, 669, 692
 performance analysis, 649, 651, 652, 655, 656
- Energy flux density, 101
 Energy of a signal, 101, 209, 214, 368, 373, 382, 470, 622, 634
 Energy spreading loss, 604, 605
 Ensemble, 353
 Envelope, 367, 373, 403, 406
 statistical modeling, 386, 387, 433
 Ergodicity, 275, 276, 388, 392, 404
 distribution ergodic, 277
 mean ergodic, 277
 power ergodic, 277
- Error function, 77
- Estimation, 7, 325
 Bayesian, 326 (*see also* Bayesian, estimation)
 bias, 327, 576, 601, 684
 consistency, 337, 568
 efficiency, 330
 asymptotic, 330
 EM algorithm (*see* Expectation-maximization algorithm)
 estimator vs. estimate, 327
 maximum likelihood, 326, 335, 425, 486, 535
 examples, 413, 418, 497, 565, 567, 647, 658, 664, 684, 706, 716, 778
 ML estimator asymptotic properties, 336
 mean squared error, 328

- method of moments, 326, 337, 413, 416
 - examples, 415, 418
- minimum-variance unbiased estimator, 326
- Monte-Carlo analysis, 328
- performance measures, 327, 540
- point, interval, or posterior PDF, 326, 344
- root mean squared error, 328
- unbiased estimator, 327
- variance, 327
 - with dependent data, 338
- Estimators
 - angle of arrival, 532
 - arrival time and Doppler, 586
 - background noise power, 567, 576, 689, 692
 - deterministic signal strength & phase, 541, 725
 - exponential mixture parameters, 342
 - gamma shape and scale, 337
 - Gaussian-fluctuating signal power, 647
 - Gaussian mean and variance, 336
 - histogram for PDF & CDF, 263
 - K distribution shape parameter, 338
 - narrowband signal parameters, 732
 - parameters of a PSD, 714
 - sinusoidal signal parameters, 723
 - SNR in decibels, 333
 - time delay, 699, 706, 715
- Exceedance distribution function, 255
- Expectation-maximization algorithm, 326, 341, 425, 625
 - exponential-incursion, 426
 - exponential-K, 429
 - exponential mixture, 344, 429
 - histogram, 732, 736
- Expectation operator, 257
- F**
 - False alarm, 18
 - average time between, 746, 749
 - rate, 494, 496, 612
 - oversampled data, 497, 498
 - See also* Detection performance measures
- False-alarm-rate inflation, *see* Normalization
- Far-field, *see* Propagation
- Fast Fourier transform, *see* Fourier transform
- Filtering, 16, 231
 - design approaches, 234
 - design of band-pass FIR filters, 236
 - design of high-pass FIR filters, 236
 - design of low-pass FIR filters, 235
 - design parameters, 235
 - filter order selection, 235
- finite impulse response filters, 232, 671
- frequency response, ideal, 231
- group delay, 231, 233
- implementation, 237
- infinite impulse response filters, 232, 689
- random process response, 277, 280
- Fisher information, 330, 332
 - matrix, 324, 331, 337, 558, 561, 715
 - Gaussian model, 334, 535, 536, 710
- Fourier series, 221, 639
 - discrete, 229
- Fourier transform, xxxiv, 208, 272, 622, 625, 653
 - continuous-discrete relationships, 230
 - discrete-time signal, 226
 - discrete Fourier transform, xxxiv, 228, 529, 639, 673, 703, 709
 - frequencies, xxxv, 228, 593
 - interpretations, 230
 - inverse, xxxiv, 229, 709
 - uncorrelated frequency bins, 639, 640, 675, 714
 - zero padding (*see* Zero padding)
 - fast Fourier transform, 229, 593, 616, 652, 724
 - generalized for power signals, 209
 - inverse, xxxiv, 209, 694
 - properties for continuous-time signals, 211
 - properties for discrete-time signals, 227
- Frequency
 - decade, decidecade, logit, 160
 - octave, third-octave, 160
- Frequency response, 208, 226, 360, 626
- G**
 - Gamma-fluctuating-intensity signal, 79, 88, 90, 355, 356, 366, 430, 440, 444, 448, 452, 581, 695
 - characteristic function, 444, 446, 696
 - detector, 482
 - incoherent integration, 442
 - moments of the instantaneous intensity, 449
 - probability of detection, 441
 - scintillation index, 440, 449
- Gamma function, xxxiv
 - incomplete, 76, 293, 637
- Gaussian-fluctuating signal, 75, 80, 84, 90, 355, 356, 366, 430, 435, 438, 440, 441, 452, 465, 467, 498, 536, 572, 579, 588, 601, 635, 657, 661, 679, 681, 695, 750, 756, 758, 760, 775, 787, 790, 791, 796
 - characteristic function, 444, 446, 696

- Gaussian-fluctuating signal (*cont.*)
 detection threshold, 76, 84
 detector, 479, 487
 incoherent integration, 436
 moments of the instantaneous intensity, 449
 parameter estimation, 542
 probability of detection, 436
 scintillation index, 440, 449
- Generalized likelihood ratio, *see* Detection
- Goodness-of-fit tests, 263
- Gradient, 99
 cylindrical coordinates, 153
 spherical coordinates, 104
- Grazing angle, 72, 121, 128, 137, 142, 144, 146, 154, 155, 166, 187, 188, 190, 364, 365, 405, 700, 757
- Green's function, 114
- Group delay
 filter (*see* Filtering)
 waveguide (*see* Waveguide)
- H**
- Hankel transform, xxxv, 414, 416, 443, 444
- Harmonics, 358
- Heavy-tailed distributions, 164, 356, 389, 403, 406
 causes, 403, 404
 generalized gamma, 391
 generalized Gaussian, 390
 generalized Pareto (*see* Distributions)
 K distribution (*see* Distributions)
 log normal (*see* Distributions)
 McDaniel's model, 415, 444
 Middleton Class-A noise, 390, 415
 mixtures (*see* Mixture distributions)
 moments of the instantaneous intensity, 450
 parameter estimation performance bounds, 420
 physics-based vs. phenomenological, 406
 Poisson Rayleigh, 390, 406, 413, 444, 445, 451, 695
 scintillation index, 407
 spherically invariant random vectors, 416
 Weibull (*see* Distributions)
- Helmholtz equation, 114, 115, 150, 153, 157
- HFM pulse, 170, 460, 520
 ambiguity function, 524
 analytic signal, 522
 autocorrelation function, 497, 522, 539
 complex envelope, 522
 optimal Doppler tolerance, 54, 464, 525
 resolution, 539
- reverberation temporal support ('Q')
 function, 599
 spectrum, 193, 490, 524
 time-Doppler coupling (*see* Waveform)
- Hilbert transform, xxxv, 141, 215, 367, 370
 bandpass signal, 371
- Histogram, 263, 314
- Hmam's equation, *see* Detection threshold
- Huygen's principle, 130
- Hydrophone, 5, 34, 39, 353, 527
 frequency response, 35
- Hypothesis, null & alternative, 308
- Hypothesis test, 7
 binary, 8, 308
 composite, 316, 319
 multiple, 24, 309
 simple, 316, 318
 Type I and II errors, 309, 767, 769, 803
See also Detection
- I**
- Images, method of, *see* Propagation
- Impedance
 characteristic, 61, 100, 133, 134, 373
 mismatch, 134, 136
- Importance sampling, 315
- Impulse function, xxxiv, 205, 209
 delta function
 Dirac, 112, 172, 205, 361, 432, 605
 Kronecker, 151, 225, 489, 641
 sifting property, 116, 205
- Impulse response, 205, 225, 360, 604, 689
 target (*see* Scattering, impulse response)
- Incidence angle, 127, 128, 142
- Independence
 and identically distributed (*iid*), 267
 probability, 253
 random variables, 266
 vs. correlation, 267
- Indicator function, xxxiv
- Inference, 7, 404
 DCLT objectives, 8
 design process, 9
- Information, 6, 25
- Integration
 coherent, 7, 17, 21, 622, 631, 669
 incoherent, 7, 17, 64–66, 70, 78, 80, 84, 434, 436, 439, 442, 451, 604, 610, 622, 626, 669
 decision threshold, 613
 impact on required SNR, 632, 636
 performance analysis, 614
- Intensity, 100, 103

equivalent plane wave, 100, 373
 units, 100, 373

Intensity, instantaneous, 100, 367, 373, 403, 406
 moments, 452
 statistical modeling, 386, 387, 433, 443, 444, 446
 table of characteristic functions, 696

Interpolation, 246, 375
 and new information, 247, 248

Invariance, 319, 665, 684

K

Kalman filter, *see* Tracking
 Kullback-Liebler divergence, 788
 Kurtosis, 259

L

Lambert's rule, *see* Scattering strength, bottom
 Lamb wave, *see* Scattering
 Laplace transform, 271
 Laplacian operator
 Cartesian coordinates, 102
 cylindrical coordinates, 106, 153
 spherical coordinates, 103
 Latency, 746, 752, 801, 809
 Level-crossing problem, 497
 LFM pulse, 170, 192, 361, 460, 492, 515
 ambiguity function
 narrowband, 518, 538
 wideband, 519, 526
 analytic signal, 372, 515
 autocorrelation function, 497, 516, 538, 605
 complex envelope, 372, 516
 Doppler insensitivity, 54, 463
 resolution, 517, 538, 541
 reverberation temporal support ('Q')
 function, 598
 spectrum, 55, 192, 463
 time-Doppler confidence ellipse, 561
 time-Doppler coupling (*see* Waveform)
 Likelihood ratio, 316, 767
 monotone, 319
 Linear period modulation, *see* HFM pulse
 Line array, 35, 39, 399, 527
 CRLB for angle estimation, 86
 design frequency, 66, 86, 529, 534, 626
 directivity index, 64
 Linear system, 204, 353, 359, 604
 time-invariant, 204, 359, 360, 362, 377, 379
 Lloyd mirror, *see* Propagation

Localization, 8, 15, 18, 37, 625, 701, 713
 angle estimation (*see* Angle estimation)
 contrasted with tracking, 21
 errors, 41, 47
 examples, 19
 exploiting propagation effects, 43
 matched-field processing, 44
 multilateration, 21, 41
 ranging
 active, 18, 38, 41
 bistatic, 41, 46
 multipath, 43
 passive, 20, 40, 43, 44
 triangulation, 21, 40, 41
 Logit, *see* Frequency

M

Main response axis, *see* Beamforming
M-of-*N* detector, 746, 753
 detector design, 755
 MAX/OR processor, 657, 660, 753
 MIN/AND processor, 753
 order-statistic detector, 754
 performance analysis, 754, 763
 sliding, 745, 763
 Marcum *Q* function, xxxiv, 295, 297, 434, 438, 477
 Marginal distribution, 266
 Markov model, 424, 763, 769, 797
 Matched-field processing, *see* Localization
 Matched filter, 13, 18, 47, 69, 148, 355, 375, 403, 405, 430, 457, 586, 604, 621, 664, 713, 745, 748
 adaptive, 491
 beamforming as a, 530
 coherent, 82, 384, 466, 472, 483, 530, 623
 decision threshold, 473
 SNR mismatch loss, 501, 505
 implementation example, 468
 maximizing SNR, 458, 461
 noise normalized, 489, 493
 pulse compression, 14, 468
 quadrature, 70, 78, 466, 475, 478, 480, 481, 483, 488, 531, 532, 604, 612, 623, 664
 decision threshold, 476
 SNR mismatch loss, 502, 505, 597
 replica correlator, 466
 SNR after coherent processing, 469
 SNR gain, 69, 470
 statistical modeling, 464
 subspace, 664
 table of assumptions & optimality, 467

- Matrix inversion lemma, 479
 Maximum likelihood estimation, *see* Estimation
 Mean squared error, *see* Estimation
 Mean squared pressure, *see* Pressure
 Median, *see* Probability density function
 Minimum detectable level, 74, 80
 Mixture distribution, 342, 356, 390, 404, 423, 625
 applied to spectral estimation, 732
 exponential, 342, 425, 652
 exponential-incursion, 426
 gamma, 437, 441, 652
 parameter estimation, 425
 Rayleigh, 343, 425
 Modeling
 accuracy vs. tractability, 44, 97, 604, 649, 729
 estimation vs. mismatch errors, 22, 404, 491, 600, 602
 Moment generating function, xxxv, 271, 577, 581
 inverse moments via, 697
 unity root, 784, 786
 Multilateration, *see* localization
 Multipath channel, 113, 123, 149, 206, 357, 361, 565, 603, 699, 713
 delay estimation, 715
 frequency response, 114, 364
 impulse response, 113
 saturated phase, 90
- N**
 Narrowband signal, 23, 64, 122, 134, 139, 144, 145, 148, 169, 351, 359, 507, 624, 625, 676, 701, 721, 732
 contrasted with broadband, 359, 361
 examples, 11, 349, 352, 353, 356, 357, 389, 592, 728
 LTI system response, 360, 369
 normalization, 600, 683
 parameter estimation, 625, 721, 724, 732, 737
 re beamforming, 528
 re center frequency, 357, 359, 507
 re Doppler, 362, 537, 554, 657
 re propagation channel, 357, 362, 365
 re system response, 361
 Near-field, *see* Propagation
 Neyman-Pearson
 lemma, 316
 optimal detector, 316, 471, 633
 examples, 479, 480, 483
- Non-fluctuating signal, *see* Deterministic signal
 Normalization, 18, 393, 403, 488, 562, 614, 624, 657, 664, 670, 675, 682
 auxiliary data, 486, 487, 488, 565, 566, 682, 683
 correlated, 693, 695
 independent samples in, 569, 691
 non-stationary, 601, 693
 cell averaging, 566, 580, 583, 684, 685, 692
 decision threshold, 568
 performance analysis, 572, 601
 CFAR loss, 566, 572, 582, 602, 686
 exponential averaging, 688, 692, 695, 697
 false-alarm-rate inflation, 575
 greater-of and lesser-of, 575
 logarithmic, 575
 order statistic, 575
 decision threshold, 577
 design, 582
 performance analysis, 578
 trimmed mean, 575, 578
 performance via characteristic functions, 581, 693, 697
 split window, 565, 569, 599
 target masking, 575, 579, 582, 791
 weighted average, 692
 Normal modes, *see* Propagation; Waveguide
 Notation conventions, list of, xxiii
 Nuisance parameters, 318, 324, 485, 665, 769, 791
 Nyquist, *see* Sampling
- O**
 Object of interest, 3, 5, 6, 96, 603
 Ocean acoustic tomography, 4, 308
 Oceanography, 96
 horizontal stratification, 113, 125, 126, 128, 131
 surface waveheight, 142
 Octave, *see* Frequency
 Order statistics, 575
 cumulative distribution function, 576
 differences, 577
 probability density function, 576
 Overlap and add, *see* Filtering, implementation
 Overlap and save, *see* Filtering, implementation
 Oversampling, 23, 220, 381, 468, 491, 494, 566, 569, 588, 671, 710, 761
 and false alarm rate, 496
 Ownship Doppler nullification (ODN), *see* Doppler

P

- Page's test, 745, 746, 776, 804
 alternating hypothesis, 745, 804
 asymptotic performance measure, 788
 average sample numbers, 783, 786, 792,
 793, 808
 biasing the detector function, 789, 812
 nuisance parameters, 791
 one-step update, 780, 806
 optimality, 779
 performance analysis, 780, 807, 815
 probability of detection, 809
 Parseval's theorem, 122, 169, 184, 214, 279,
 622, 634, 639
 discrete-time signals, 228
 disparate signals, 547
 Partial fraction expansion, 273, 437, 651
 Particle velocity, 99, 100, 153, 154
 cylindrical wavefront, 99
 plane wave, 99, 108
 spherical wave, 99, 104
 Periodic signals, 104, 135
 Plane wave, 107, 142, 154, 167, 169, 175, 527
 intensity (*see* Intensity)
 particle velocity (*see* Particle velocity)
 Point source, *see* Source, point
 Positive semi-definite matrix, 332
 Post-matched-filter integration, *see* Integration,
 incoherent
 Power, acoustic, 100, 103
 units, 101
 Power signal, 209
 Power spectral density, 191, 276, 279, 355,
 357, 359, 368, 378, 389, 699
 parameter estimation for, 714
 units, 280
 Power sum, 68
 Pre-envelope, *see* Analytic signal
 Pressure, 96, 98
 acoustic vs. total, 96
 level, 99
 mean square, 61, 98, 100, 102
 peak, 98
 units, 60, 98
 Prior distribution, 325, 340
 conjugate, 325
 non-informative, 325
 Probability, 251
 conditional, 252
 intersection or union, 252
 Probability density function, 253
 conditional, 270
 independent random variables, 266
 joint, 266

P median, 258

- mode, 258
 of a ratio, 693
 parameter types, 255, 406
 Probability of detection, *see* Detection
 performance measures
 Projection matrix, 667
 Propagation, 96
 convergence zone, 68, 130, 182
 deep sound channel, 4, 129, 130, 608, 610
 image source, 43, 136, 149, 157
 Lloyd mirror, 134, 604
 near-field/far-field, 20, 37, 43, 109, 527
 non-linear effects, 102
 normal modes, 126 (*see also* Waveguide)
 ray tracing, 126, 129, 130
 reciprocity, 37, 156
 reliable acoustic path, 130
 spreading, 70, 604, 610, 615
 Propagation loss, 62, 63, 67, 74, 119, 120, 169
 absorption effect, 124
 broadband signals, 123
 contrasted with transmission loss, 120
 cylindrical spreading, 107, 121, 151
 factor, 120, 121
 incoherent, 123, 606
 mode-stripping, 122, 187
 reference units, 120
 related to figure of merit, 90
 spherical spreading, 103, 119, 121, 184,
 187, 365

Propeller blade rate, 356

Pulse compression, *see* Matched filter

p-value, *see* Detection

Q

- Q* function, *see* Marcum *Q* function;
 Reverberation, temporal support
 ('Q') function
 Quantile, 265
 Quantization, 223
 dynamic range, 224
 error, 223
 SQNR, 224
 Quickest detection, *see* Page's test

R

- Radar, 398
 cross section (*see* Scattering)
 equation, 58, 168
 wave polarization, 168
 Random process, 273, 353, 358

- Random process (*cont.*)
 complex, 283, 379
 Gaussian, 61, 64, 663, 714
 examples, 147, 261, 355, 387, 392, 497,
 625, 722, 729
 properties, 274–276, 278, 381, 383, 389,
 703, 705
 non-Gaussian, 389
- Random variables, 253
 complex, 281
 continuous, discrete, or mixed, 256
 functions of, 260
 independent, 266
 moments, 257, 258, 271, 273
 central, 258, 273
 inverse, 697
 multiple, 265
 PDF of a sum, 261, 271, 652
 simulating, 262
 uncorrelated vs. independent, 267
- Range estimation, *see* Localization, ranging
- Rayleigh parameter, 142, 365
- Rayleigh quotient, 630, 645
- Rayleigh resolution, *see* Resolution, metrics
- Rayleigh scattering, *see* Scattering
- Ray tracing, *see* Propagation
- Receiver operating characteristic (ROC) curve, *see* Detection, ROC curve
- Reciprocity, *see* Propagation
- Recognition differential, *see* Sonar equation
- Rectangular pulse, xxxiv, 205
- Reflection, 127, 132, 603
 constant-density layers, 133
 contrasted with scattering, 164
 diffuse, 165
 phase change, 138, 363, 716
 rough surface, 142, 182, 188, 365, 757
 specular, 142, 144, 164, 175
 surface, 134, 700
 total internal, 128, 137, 138, 149, 364,
 700
- Reflection loss, 131, 133, 150
 bottom, 121, 136, 137
 surface, rough, 145
- Refraction, 127, 130, 132, 133, 186
- Reliable acoustic path, *see* Propagation
- Remote sensing, 3
 active, 5, 68, 180
 applications, 6
 passive, 5, 6, 34, 623
- Repeater, 309
- Replica correlator, *see* Matched filter
- Required SNR, 9, 57, 75, 632, 662
- overline notation, 75
See also Detection threshold
- Resolution, 458, 535, 537, 539, 599, 604, 608
 Doppler, 396, 402, 460
 metrics, 500, 537
 temporal, 460
 vs. accuracy, 499, 540
- Resolution cell, 47, 405, 408, 458, 494, 495,
 537, 601, 611, 615
 bistatic, 47
- Reverberation, 13, 68, 180, 389, 392, 404, 563,
 594
 autocorrelation function, 393
 boundary, 182, 186
 Doppler spreading, 395, 396, 401, 492, 594
 moving source, 193, 395, 398
 non-Rayleigh (*see* Heavy-tailed distributions)
 ridge, 594, 599
 sources, 182
 spectrum, 54, 191, 194, 196, 394, 490, 594
 statistical characterization, 190, 355, 359,
 392, 594
 temporal support ('Q') function, 595, 597
 volume, 182
- Reverberation level, 68, 74, 182, 563
 boundary, 186
 characteristics, 68, 69
 volume, 184
- Rician signal, 355, 356, 366, 429, 433, 437,
 448, 452, 465, 467, 531, 536, 545,
 581, 694, 756
 characteristic function, 444, 696
 detection threshold, 79
 detector, 482
 incoherent integration, 439
 moments of the instantaneous intensity, 449
 parameter estimation, 542
 probability of detection, 438
 Rice power ratio, 438
 scintillation index, 440, 449
- Robertson's detection performance curves, 78
- Root mean squared error, *see* Estimation
- Rough surface, *see* Reflection, rough surface
- S**
- Salinity, 126, 129
- Sampling, 219, 371
 bandpass, 374
 impact in frequency domain, 221, 653
- Nyquist, 221, 381, 383, 384
 frequency, 221
 rate, 221, 492

- Saturated phase, *see* Signal phase
Scalloping loss, 497
Scattering, 164, 603
 bistatic, 174, 187
 contrasted with reflection, 164
 creeping wave, 177
 cross section, 68, 168, 172, 175, 176
 cylindrical object, 177, 180
 diffraction, 172, 176, 177
 form function, 179, 180
 forward scattering, 176, 180
 frequency response, 169, 172, 173, 175
 geometric, 72, 142, 172, 174, 179, 186,
 408
 impulse response, 165, 169, 170, 182
 ka dependence, 172, 179
 Lamb wave, 177
 modal solution, 174, 177
 physical optics, 172, 175, 176
 Rayleigh, 172, 173, 179, 186
 spherical object, 166, 170, 173, 176, 177,
 179, 186
- Scattering strength
 bottom, 187, 188
 surface, 187, 188
 volume, 184, 186
- Scintillation index, 90, 406, 412, 418, 423, 440,
 449
- Sensor array, *see* Array of sensors
Sequential detection, 744
 average sample numbers, 748, 749
 known starting time (*see* Sequential
 probability ratio test)
 latent detection, 794
 performance measures, 747, 752, 794
 sliding incoherent sum, 745, 760
 sliding M -of- N detector (*see* M -of- N
 detector)
 stopping time, 748, 768
 table of assumptions & optimality, 745
 unknown starting time (*see* Page's test)
- Sequential probability ratio test, 745, 746, 767,
 795
 average sample numbers, 771, 774, 799,
 802
 decision threshold, 769
 optimality, 768
 performance analysis, 770, 774, 797
 truncated, 768, 774, 802
- Signal amplitude, 535, 622
 detection for arbitrary distribution, 481
 effect of propagation, 364
 estimation, 723
 fluctuations or statistics, 90, 365, 441, 465
- gamma (*see* Gamma-fluctuating-
 intensity signal)
Gaussian (*see* Gaussian-fluctuating
 signal)
Swerling signal models, 430, 434, 436,
 437, 756, 760
- Signal characterization
 consistency, 349, 351, 353, 623
 effect of propagation, 148, 349, 351, 356,
 362, 390, 429, 440, 465, 700, 757
 flow chart for detection, 624
 in the presence of noise, 353, 430
 joint time-frequency, 357
 knowledge of structure, 349, 351, 354, 621,
 623, 642, 664
 known vs. unknown form, 355, 621, 663
 spectral, 349, 351, 357, 623, 657
 temporal, 349, 351, 356, 623, 743, 776,
 794
- Signal excess, *see* Sonar equation
Signal fluctuations, *see* Signal amplitude
Signal of interest, 4, 6, 8
 active-sonar echoes, 11, 13, 18, 25
 airgun blasts, 390
 examples, 10, 11, 352
 marine mammal acoustic emissions, 11,
 12, 621
 radiated noise, 11, 20
- Signal phase, 535, 621, 694
 deterministic, 364, 435, 465, 471, 475, 481,
 482, 604, 702
 effect of propagation, 363
 estimation, 724
 estimator distribution, 725
 saturated & partially saturated, 365, 729
 uniformly random, 364, 386, 408, 431, 433,
 440, 465, 477, 481, 604, 606
- Signal processing
 as inference, 7, 8
 vs. information processing, 8
- Sign correlator, 321
- Sinc function, xxxiv, 209
- Skewness, 259
- Snell's law, 127, 130, 132, 133
- SOFAR channel, *see* Propagation, deep sound
 channel
- Sonar, 3
- Sonar equation, 9, 58
 active sonar, 67
 array gain (*see* Array gain)
 detection threshold (*see* Detection
 threshold)
 differences in definitions, 63
 energy form, 67, 101

- Sonar equation (*cont.*)

figure of merit, 75, 90

linear and non-linear processing, 64, 632

list of terms, 73

passive sonar, 63, 66

processing-band constraint, 62

propagation loss (*see* Propagation loss)

recognition differential, 75, 82

reverberation level (*see* Reverberation level)

reverberation target strength, 69, 189

signal-to-reverberation power ratio, 189

signal excess, 75, 88, 351

SNR notation (S^h , S^a , & S^d), 62, 62, 70, 74

source level (*see* Source level)

to specify detection performance, 81

to specify estimation performance, 85

target strength (*see* Target strength)

transition curve, 88

using intensity vs. MSP, 61
- Sonar pulses, *see* Waveform
- Sonar system, 4, 33

active vs. passive, 34, 38

bistatic (*see* Bistatic sonar)

components, 34

distributed, 21, 37

monostatic, 37

parametric, 102
- Sound pressure level, *see* Pressure, level
- Sound projector, 5, 18, 34, 37, 38, 45, 47, 51, 54, 58, 67, 96, 97, 100, 102, 104, 115, 118, 165, 181, 193, 353, 358, 360, 367
- Soundscape, 389
- Sound speed, 125, 128, 364

air, 134

bottom, 136

downward refracting, 186

empirical model, 126

linear, 150

Munk profile, 129

typical values, 126
- Source

factor, 61, 101, 119, 120, 166, 169, 184, 191

units, 119

point, 25, 102, 111, 113, 114, 118, 119, 130, 169

waveform, 60, 96, 118, 352, 457

units, 112
- Source level, 61, 63, 67, 73, 118, 120

interpreted as MSP at 1 m, 119

measurement, 119

reference units, 120
- relation to source factor, 119

units, 63
- Spectral estimation, 281, 531, 532, 675

histogram based, 625, 732, 736

parameterized, 625
- Spherical coordinates, *see* Coordinate system
- Spherical wave, 102, 103, 111

particle velocity (*see* Particle velocity)

power, 101
- Spreading, *see* Propagation loss
- Standard deviation, 257
- State of nature, 3, 6, 9, 34, 325, 372, 459, 535

as a question, 8
- Stationarity, 275, 358

strict sense, 275

wide sense, 191, 276, 355, 357, 358, 379, 388, 392, 625, 628, 675
- Statistical inference, 307, 325
- Steering vector, *see* Beamforming
- Stochastic process, *see* Random process
- Sturm-Liouville problem, 150, 156
- Sufficient statistic, 26, 319, 491
- Surface

reflection (*see* Reflection)

spatial correlation function, 147
- Swerling signal models, *see* Signal amplitude
- T**
- Target gain, 68
- Target impulse response, *see* Scattering, impulse response
- Target masking, *see* Normalization
- Target strength, 67, 74, 165, 170, 176, 179

broadband signals, 170

fish with swim bladder, 185

integrated vs. peak, 170

narrowband signals, 169

radar cross section relationship, 168

sphere, 72, 166

target gain, 166, 169
- Telemetry, 35, 37
- Template matching, 488
- Time-bandwidth product

Gaussian-shaped signal, 219

lower bound, 218

processing, 25, 65, 83, 86, 218, 543, 569, 632, 635, 649, 679, 680, 712, 717

signal, 216, 471, 492, 515, 537, 605
- Time-delay estimation, 4, 38, 41, 44, 56, 308, 624, 698

autocorrelation processing, 44, 625, 698, 713, 719

- CRLB (*see* Cramer-Rao lower bound)
 cross-correlation processing, 625, 698, 701
 continuous-time, 709
 known & unknown phase, 708, 712, 713
 time-domain, 709
 whitening, 701, 708, 719
- Time-of-arrival estimation, 535, 703
 accuracy, 497
- CRLB (*see* Cramer-Rao lower bound)
 and false alarm rate, 494
- Time invariance, 204
 violated by Doppler, 206, 208
- Total internal reflection, *see* Reflection
- Total probability theorem, 270
- Towed array, *see* Line array
- Tracking, 8, 15, 21, 42
 $\alpha\text{-}\beta$ filter, 24
 $\alpha\text{-}\beta\text{-}\gamma$ filter, 24
 applications in underwater acoustics, 24
 as a motion filter, 21
 bearings-only, 23
 contrasted with localization, 21
 Kalman filter, 24
 measurement model, 23
 process noise, 22
 state variables, 21
- Transducer, 34
- Transient signal or noise, 101, 404, 425
- Transmission loss, 120
 contrasted with propagation loss, 120
- Trapezoidal rule, 654
- Triangulation, *see* Localization
- Turning depth, 130
- Two's complement binary representation, 223
- U**
- Uniformly most powerful, *see* Detection
- V**
- Variance, 257, 268
See also Estimation
- W**
- Wald's first equation, 771
 Wald's fundamental identity, 771, 783
 Wave
 acoustic (*see* Acoustic wave)
 evanescent, 153
 longitudinal, 99
- mechanical, 95
 periodic, 105, 109
 plane (*see* Plane wave)
 spherical (*see* Spherical wave)
 transverse, 99
- Wave equation, 101, 111, 113, 126, 148
 Cartesian coordinates, 102
 cylindrical coordinates, 106
 frequency domain (*see* Helmholtz equation)
 inhomogeneous, 48, 111, 115, 118, 120, 169, 352
 normal-mode solution, 44
 spherical coordinates, 103
 varying density and sound speed, 126
 varying sound speed, 126
- Waveform
 Doppler sensitive, 56, 68
 frequency-modulated (FM), 550
 frequency average, 547
 FM pulse, 550
 shaded pulse, 551
 frequency variance, 548, 549
 ambiguity function relationship, 549
 CW pulse, 552
 FM pulse, 497, 550
 shaded pulse, 551, 552
 instantaneous frequency, 460, 463, 515, 517, 520, 524, 550, 559
 time-Doppler coupling, 499, 517, 540, 559, 560
 time average, 554
 LFM pulse, 560
 shaded pulse, 557
 time variance, 555
 CW pulse, 556
 LFM pulse, 560
 shaded pulse, 556
- Wavefront, 16, 48, 96, 97, 142
- Wavefront-curvature processing, *see* Beamforming
- Waveguide, 44, 113, 364, 366
 dispersion, 125, 154
 frequency response, 150–152
 group delay, 155, 156
 group velocity, 156
 impulse response, 149, 153, 157
 invariant, 44
 modal solution, 148, 150
 mode cutoff, 153
 mode functions, 151
 multipath solution, 149
- Wavelength, 35, 105, 142, 172, 176, 364
 half-wavelength spacing, 399, 534

- Wavenumber, 105, 142, 172
horizontal, 151, 153, 154
vector, 108
vertical, 154
- Wenz curves, *see* Ambient noise
- Wideband signal, *see* Broadband signal
- Window functions
- Blackman, 246
 - Dolph-Chebyshev, 244
 - Hamming, 243, 401, 514
 - Hann or Hanning, 64, 66, 245, 375, 552, 558, 674, 675
 - Kaiser, 245
 - rectangular, uniform, or boxcar, 242, 401, 558, 673
 - Taylor, 244, 514, 558
 - Tukey, 243, 361, 514, 557
- Windows, 239
3-dB main-lobe width, 240, 674
distortionless response scaling, 241
equivalent noise bandwidth, 241
independent sample rate, 242, 675
noise gain & relative noise gain, 241
sidelobe decay rate, 243
sidelobe level, 242
signal loss, 239
trading accuracy for purity, 242
- Woodbury identity, *see* Matrix inversion lemma
- Z**
- Zero padding, 238, 594, 616, 710, 719, 724
- Z transform, 226